Toshio Moritani
Sven Ekholm
Per-Lennart Westesson

Diffusion-Weighted MR Imaging of the Brain

Second Edition

Springer

Diffusion-Weighted MR Imaging of the Brain

Moritani · Ekholm · Westesson

T. Moritani
S. Ekholm
P.-L. Westesson

Diffusion-Weighted MR Imaging of the Brain

Second Edition

Springer

Toshio Moritani, MD, PhD
Assistant Professor
Department of Radiology
University of Iowa Hospitals and Clinics
200 Hawkins Drive
Iowa City, IA 52242-1009
USA

Sven Ekholm, MD, PhD
Professor of Radiology and Director of Research
Division of Diagnostic
and Interventional Neuroradiology
Department of Radiology
University of Rochester
School of Medicine and Dentistry
602 Elmwood Avenue
Rochester, NY 14642-8623
USA

Per-Lennart Westesson, MD, PhD, DDS
Professor of Radiology
and Director of Division of Diagnostic
and Interventional Neuroradiology
Department of Radiology and
Professor of Clinical Dentistry
University of Rochester
School of Medicine and Dentistry
602 Elmwood Avenue
Rochester, NY 14624-8623
USA

ISBN 978-3-540-78784-6 e-ISBN 978-3-540-78785-3
DOI 10.1007/978-3-3540-78785-3

Springer Dordrecht Heidelberg London New York

Library of Congress Control Number: 2009926632

Cover design: eStudio Calamar Figueres, Berlin

Printed on acid-free paper

Springer is part of Springer Science+Business Media (www.springer.com)

Foreword

Few advances in MR imaging have had the impact that diffusion-weighted (DW) imaging has had in the evaluation of brain. From the time of the early descriptions by LeBihan and colleagues of the ability to image and measure the micromovement of water molecules in the brain to the present time, diffusion imaging and its derivatives have made an impact in the evaluation of multiple disease processes, primarily in ischemia, but also in other conditions of the brain. In most medical centers diffusion imaging is no longer considered a sequence to be used in special circumstances, but rather it is employed as part of routine MR imaging of the brain. Because the information derived from diffusion measurements can improve our understanding of pathologic processes and can influence patient care, knowledge of the principles and applications of DW imaging is critical.

It is therefore of great interest that the group from the University of Rochester (Drs. Moritani, Ekholm, and Westesson) have assembled under one cover a collection of material which encompasses all the clinical aspects of DW imaging. Those who have attended recent meetings of the ASNR know the quality of the exhibits and presentations which have come from this group. They, early on, demonstrated the wide spectra of diseases that can cause restricted diffusion and they warned us of mimickers of infarction and ischemia.

In this richly illustrated volume the authors take the reader from the basic principles of DW imaging, through the pulse sequences used, to mathematical concepts behind the derivation of apparent diffusion coefficients. Following explanations of the different types of edema which can effect the brain and the appearance of DW images, this book allows the reader to see the variety of conditions that alter diffusion, including infarction, hemorrhage, cerebral infections, degenerative neurologic disorders, white matter diseases, toxic/metabolic disorders, and tumors. As one can easily see from the table of contents, the authors have systematically covered all major areas of neuroradiology. This will allow cross-referencing to problematic cases which one may encounter. Additionally, knowledge of what represents a normal adult brain and a normal developing brain along with an explanation of artifacts seen in DW imaging makes this a valuable book. It is noteworthy that the authors have chosen to abundantly illustrate the clinical material, drawing on pathologic correlations in a number of areas.

I believe that this book will benefit not only those who deal routinely with neuro-MR imaging, but also those who want to establish a basis for understanding of diffusion images in the hope of taking these principles of diffusion further into more exotic areas of neuroimaging such as white matter tract mapping with diffusion tensor imaging, analyzing alterations in highly organized structures with fractional anisotropy, or delving into macromolecular alterations with ever-higher b values. The authors are to be congratulated for putting their considerable experience together in this form, and I am sure that the collection of cases herein will serve to educate not only those who are just entering the clinical neurosciences, but also those who daily use diffusion imaging to arrive at a proper clinical diagnosis.

Robert M. Quencer, M.D.
Chairman, Department of Radiology
The Robert Shapiro, M.D. Professor of Radiology
University of Miami/Jackson Memorial
Medical Center
Miami, Florida, USA

Preface

Progress in the field of diffusion imaging is occurring at a very fast pace, with many papers on the clinical application of diffusion-weighted (DW) imaging being published in the last few years. Today, DW imaging has become one of the routine MR imaging sequences of the brain; therefore, the correct interpretation of brain MR images is mandatory. Without accurate knowledge of DW imaging, correct diagnoses are often difficult to make.

Furthermore, remarkable progress has been made in the fields of diffusion tensor imaging, including fractional anisotropy mapping, diffusion tensor color mapping, and fiber tractography, as well as in high-b-value diffusion imaging, as exemplified by numerous articles published recently. The second edition of *Diffusion-Weighted Imaging of the Brain* contains new cutting-edge images from these fields. Those images that are clinically most useful were carefully selected for inclusion, as the clinical applications are sometimes not straightforward.

For this second edition, almost all the chapters were rewritten and new cases were added – particularly the most clinically useful cases with recent references and images, including diffusion tensor imaging and high-b-value imaging. Consequently, the total number of images in this edition is almost double that of the first one.

In Chap. 1, the description of the principle of diffusion tensor imaging, including fractional anisotropy mapping, diffusion tensor color mapping, and fiber tractography, was added. In Chaps. 2 and 3, we display the normal findings in adult and pediatric brain imaging, along with the pitfalls and artifacts encountered, and explain the anatomy of white matter fiber tracts by using diffusion tensor color maps and fiber tractography.

Abnormal findings in DW imaging are based on such diverse pathological conditions as edema (cytotoxic /cellular edema vs vasogenic edema), necrosis (coagulative necrosis vs liquefactive necrosis), cellularity of tissue or tumor (hypercellular vs hypocellular tumor), viscosity of fluid (abscess, hematoma), etc. In the present volume, we have given more consideration to the pathophysiological mechanisms. I included my own hypothesis of "excitotoxic mechanisms," which accounts for cytotoxic/cellular edema in different pathological conditions. For instance, cytotoxic/cellular edema (Chap. 4) is seen not only in ischemia/infarction (Chap. 5), but also in epilepsy (Chap. 8), demyelination and degeneration (Chap. 9), toxic and metabolic disease (Chap. 10), infectious disease (Chap. 11), trauma (Chap. 12), or sometimes in relation to brain neoplasm (Chap. 13). Interestingly, their distributions are sometimes similar even though the pathological processes are quite different.

Each chapter presents correlations between many DW images and pathological tissues. In Chap. 13, we have classified brain neoplasms based on the WHO 2007 classification, and displayed many cases with pathology. All pathology reports and figure legends were reviewed and checked by two experienced neuropathologists, namely, Patricia Kirby MD (Neuropathology, Department of Pathology, The University of Iowa Hospitals and Clinics) and Barbara Germin, MD (Neuropathology, Department of Pathology, University of Rochester).

The pediatric brain is not a "small adult brain"; different types of diseases and their mechanisms in the pediatric brain are remarkably different from those of the adult brain. For example, the postnatal period of brain development is vulnerable to excitotoxic injury. In Chap. 14, we have collected DW and diffusion tensor images of pediatric conditions encompassing various common and uncommon diseases. We also added a new chapter (Chap. 15) on scalp and skull lesions, since DW imaging is executed routinely in this area.

I hope that *Diffusion-Weighted Imaging of the Brain* will be useful for the understanding of the anatomy and the pathophysiological background of brain diseases, contributing to a better interpretation of DW images and thereby to correct clinical diagnoses in daily clinical work.

Toshio Moritani MD, PhD
April 2009

Preface to the 1st Edition

This book is the result of many years of clinical and academic interest in diffusion-weighted MR (DW) imaging of the brain. Researchers and clinicians at the University of Rochester started to collect DW images of a spectrum of abnormalities affecting the brain immediately after this technique became available. Several case series with clinical and radiographic correlations have been presented at the annual meetings of the American Society of Neuroradiology and the Radiological Society of North America via posters and scientific reports. Over time it became quite clear that we had a collection of DW images representing the majority of conditions that affect the brain and we felt a need to put them all together under one cover.

MR imaging has evolved dramatically since its introduction into clinical work in the mid-1980s. Looking back, there are several major steps that took MR imaging of the central nervous system to the next level. One of the first steps was the introduction of the clinical usefulness of contrast agents. Other steps were the development of fat suppression techniques, fast spin echo imaging, and,more recently, the development of a clinically useful DW imaging technique. DW imaging has revolutionized the imaging diagnosis of acute infarction in the brain. It is,however,quite clear from the series of cases shown in this book that DW imaging is useful for many other conditions.The time it takes to obtain a DW image is so short that in many institutions it is now being used as a routine part of any MR imaging of the brain.

The initial chapters on principles of DW imaging, normal DW appearance, and pitfalls and artifacts provide the bases for understanding DW imaging. This technique is complex and is associated with many pitfalls and artifacts. The following chapter on brain edema provides the basis for understanding the pathophysiology of signal alterations in DW images related to various pathological conditions. The images are correlated to corresponding neuropathologic slides and aid the understanding of the DW imaging representation of various types of brain edema. Chapters 5–13 cover DW imaging characteristics of different pathologic conditions and in Chap. 14 (pediatrics) we have collected DW images of pediatric conditions.

The book is organized according to major disease categories. This brings structure to the book, but is not optimal for the clinician sitting in front of a set of images and wondering what they might represent. For that reason we have a summary chapter entitled "How to Use This Book" (Chap. 15, Chap. 16 in 2nd ed), which is organized from the opposite perspective. Thus, in Chap. 15 we have started with DW images and grouped them according to imaging characteristics. In each table we have listed differential diagnoses for each specific set of DW imaging characteristics and added thumbnail images with references to the corresponding chapters. The clinician can go directly to Chap. 15, determine the signal on the DW imaging, combine it with the T2 and ADC signal characteristics, and get a list of the conditions that match these imaging characteristics. The thumbnail images, the reference to corresponding chapter and knowledge about the patient's clinical presentation should allow the clinician to formulate a relatively narrow differential diagnosis for most clinical conditions. We think that this "reversed" chapter will make the book very useful for everyday work with DW imaging of the brain.

We are grateful for many pathological slides and fruitful discussions with Barbara Germin, MD, Department of Pathology, University of Rochester. We acknowledge the case contribution from the Department of Radiology,Showa University, Japan, collected during the primary author's time at Showa University. We would also like to thank Masahiro Ida,MD,Department of Radiology, Ebara Municipal Hospital, Japan; Minoru Morikawa, MD, Department of Radiology, Nagasaki University, Japan; R.Nuri Sener,MD, Department of Radiology, Ege University Hospital,Turkey;and Ryutarou Ukisu,MD,Department of Radiology, Showa University, Japan, all of whom contributed case studies. Our deepest gratitude goes to

Ms Margaret Kowaluk and Ms Theresa Kubera,Medical Graphic Designers, Department of Radiology, University of Rochester, and Ms Belinda De Libero for her secretary work.We also wish to thank Yuji Numaguchi, MD, PhD, Department of Radiology, University of Rochester and St. Luke's Hospital, Japan, who gave us encouragement and support.

We want to thank the editorial staff at Springer-Verlag, without whose guidance, skills and knowledgeable advice this book would not have become a reality. We would also like to thank our colleagues, fellows and coworkers at the University of Rochester. Finally, but not least, we thank our families for giving us the time to complete this project.

It is our hope that our readers will find this book on "Diffusion-Weighted Imaging of the Brain" instructional and clinically useful.

Toshio Moritani
Sven Ekholm
Per-Lennart Westesson
October 2003

Acknowledgments

Many new images, such as those of diffusion tensor imaging, fiber tractography, high-b-value imaging, as well as new cases were provided by leading neuroradiologists who take active roles in neuroradiology. We are deeply grateful to: Matthew L. White MD and Yan D. Zhang MD (Department of Radiology, The University of Nebraska Medical Center, USA); Jinsuh Kim MD (Department of Radiology, The University of Iowa Hospitals and Clinics, USA); Noriko Salamon MD (Department of Radiology, The University of California, Los Angeles, USA); Shigeki Aoki MD (Department of Radiology, Juntendo University, Japan); Kei Yamada MD (Department of Radiology, Kyoto Prefectural University of Medicine, Japan); Toshiaki Taoka MD (Department of Radiology, Nara Medical University, Japan); Keiko Toyoda MD (Department of Radiology, Kameda Medical Center, Japan); and Hidetsuna Utsunomiya MD (Department of Radiology, Graduate School of Radiology, International University of Health and Welfare, Japan).

Many neuroradiologists and clinicians kindly provided us with valuable cases and pathology reports. We hereby express our deepest gratitude to: R. Nuri Sener MD (Department of Radiology, Ege University Hospital, Turkey); Michael Sacher MD (Department of Radiology, Mount Sinai Medical Center, USA); Ho Kyu Lee MD (Department of Radiology, Wayne State University Detroit Medical Center, USA); Jain Vikas MD (Metro Health Hospital, Case Western Reserve University, USA); Edip M. Gurol MD (Department of Neurology, Massachusetts General Hospital, USA); Andrew Lee MD (Department of Ophthalmology, Methodist Hospital, Houston, USA); Toshibumi Kinoshita MD (Research Institute for Brain and Blood Vessels, Akita, Japan); Masaki Oka MD (Department of Radiology, Kikuna Memorial Hospital, Japan); Harushi Mori MD (Department of Radiology, The University of Tokyo, Japan); Masahiro Ida MD (Department of Radiology, Ebara Municipal Hospital, Japan); Minoru Morikawa MD (Department of Radiology, Nagasaki University, Japan); Ryutaro Ukisu, MD (Department of Radiology, Showa University Northern Yokohama Hospital, Japan); Hisao Nakamura MD and Takashi Kitanosono MD (Department of Radiology, The University of Rochester Medical Center, USA); Syrbu Sergei MD (Department of Pathology, The University of Iowa Hospitals and Clinics, USA); Takashi S. Sato MD (The University of Iowa Carver College of Medicine, USA); Bruno Policeni MD, Andres Capizzano MD, and Limin Yang MD (Department of Radiology, The University of Iowa Hospitals and Clinics, USA).

We would like to especially thank James M. Powers MD (Former Director, Neuropathology, Department of Pathology, The University of Rochester Medical Center), who gave me valuable advice on brain cutting.

Most of the new adult and pediatric cases come from the University of Iowa Hospitals and Clinics, and we are sincerely grateful to Wendy R.K. Smoker MD (Director of Neuroradiology) and Yutaka Sato MD (Director of Pediatric Radiology, Department of Radiology, The University of Iowa Hospitals and Clinics).

I also wish to thank Laurie Fajardo MD (Chairman, Department of Radiology, The University of Iowa Hospitals and Clinics), Takehiko Gokan MD (Chairman, Department of Radiology, Showa University of School of Medicine, Japan), Hirotsugu Munechika MD (Department of Radiology, Southern Tohoku Research Institute for Neuroscience, Japan, and Former Chairman, Showa University of School of Medicine, Japan), and Yuji Numaguchi, MD (Department of Radiology, University of Rochester, USA, and St. Luke's International Hospital, Japan), who gave us encouragement and support.

This book is also an outcome of the daily clinical work, lectures, and seminars at the University of Iowa Hospitals and Clinics. I hereby wish to thank the residents, fellows, colleagues, and coworkers at the University of Iowa who constantly provided insightful comments, stimulating discussions, and interesting questions.

I also wish to express my deepest gratitude to the editorial staff at Springer for their skills and knowledgeable advice.

Last but not least, I would like to thank my wife for her support and secretarial work. I also thank my parents in Japan for their warm support.

Toshio Moritani MD, PhD
April 2009

Contents

Contributors

Germin Barbara, MD
Senior Instructor
Neuropathology, Department of Pathology and Laboratory Medicine
University of Rochester
School of Medicine and Dentistry
Rochester, New York, USA

Sven Ekholm, MD, PhD
Professor of Radiology and Director of Research
Division of Diagnostic and Interventional Neuroradiology
Department of Radiology
University of Rochester
School of Medicine and Dentistry
Rochester, New York, USA

Professor of Radiology
University of Gothenburg
Gothenburg, Sweden

Ramon R. de Guzman, MD
Fellow, Division of Diagnostic and Interventional Neuroradiology
Department of Radiology
University of Rochester Medical Center
Rochester, New York, USA

Akio Hiwatashi, MD
Assistant Research Professor
Division of Diagnostic and Interventional Neuroradiology
Department of Radiology
University of Rochester
School of Medicine and Dentistry
Rochester, New York, USA

Jack Kademian, MD, DDS
Clinical Assistant Professor
Department of Radiology
University of Iowa Hospitals and Clinics
Iowa City, Iowa, USA

Jianhui Zhong, PhD
Professor of Radiology, Biomedical Engineering, and Physics
Director of MR Imaging Research
Department of Radiology
University of Rochester
School of Medicine and Dentistry
Rochester, New York, USA

Associate Professor of Radiology
Yale University School of Medicine
New Haven, Connecticut, USA

Patricia Kirby, MD
Clinical Professor
Department of Pathology
University of Iowa Hospitals and Clinics
Iowa City, Iowa, USA

Toshio Moritani, MD, PhD
Assistant Professor
Department of Radiology
University of Iowa Hospitals and Clinics
Iowa City, Iowa, USA

Adjunct Assistant Professor
Division of Diagnostic and Interventional Neuroradiology
Department of Radiology
University of Rochester
School of Medicine and Dentistry
Rochester, New York, USA

Adjunct Assistant Professor
Department of Radiology
Showa University, School of Medicine
Tokyo, Japan

Yoshimitsu Ohgiya, MD, PhD
Assistant Professor
Department of Radiology
Showa University, School of Medicine
Tokyo, Japan

Per-Lennart Westesson, MD, PhD, DDS
Professor of Radiology
and Director of Division of Diagnostic
and Interventional Neuroradiology
Department of Radiology and
Professor of Clinical Dentistry
University of Rochester
School of Medicine and Dentistry
Rochester, New York, USA

Professor of Oral Diagnostic Sciences
State University of New York at Buffalo
Buffalo, New York, USA

Associate Professor of Oral Radiology
University of Lund
Lund, Sweden

Basics of Diffusion Measurements by MRI

In collaboration with J. Zhong

Diffusion occurs as a result of the constant movement of water molecules. Water makes up 60–80% of our body weight. The heat associated with our body temperature energizes the water molecules, causing them to "jerk" around randomly. This phenomenon is called "Brownian motion" after the scientist who first described it [1, 2]. It can be demonstrated by adding a few drops of ink to a still bucket of water. Initially, the ink will be concentrated in a very small volume, but it will quickly spread out (diffuse) and mix with the rest of the water. The speed of this process of diffusion gives physicists a measure of the property of water. Similarly, if we could put some "magic ink" into the brain tissue and follow its progress, we would gain knowledge about the brain tissue itself, as well as the kind of changes that may occur in the brain when it is affected by various disease processes.

1.1 Diffusion Imaging in MR

In the measurement of diffusion by MR, the "magic ink" is created by the magnetic field gradients [3]. When the patient enters the large tunnel of a static magnetic field, nuclear spins (small magnets inside each proton nucleus) are lined up along the direction of the big magnet. Magnetic field gradients of a certain duration will then add a smaller magnetic field to spins located in different regions within the tissue. This is similar to marking the spins with "magic ink". By applying another gradient pulse at a later time, information is obtained about how much the spins have spread (diffused) during this time. This is analogous to comparing two snapshots, one taken at the moment when the ink is dropped into the water and one taken later, to obtain information about how the ink has spread in the water. However, the analogy of ink in water and what happens in the brain stops here.

1.2 Diffusion Imaging of the Brain

The brain is complex and full of fibrous, globular, and other structures and membranes, which may or may not allow water to move freely. Because water spins will run into constituents of cells of different concentrations in different cellular compartments, they will spread at different rates when labeled with the "magic ink". In addition, they will not behave in the same way when they are moving in different directions. As described below, the former is measured as the diffusion rate, diffusion coefficient, or simply diffusivity, depending on the unit used, and the latter is more formally described as diffusion anisotropy, with a variety of parameters defined [4–7].

1.3 Magnetic Resonance Principles of Diffusion Imaging

In order to perform diffusion studies, one needs to apply field gradients in addition to the radiofrequency and gradient pulses used for conventional MR imaging. A simplified version of the most commonly used pulse-gradient spin-echo pulse sequence for diffusion imaging is shown in Fig. 1.1. During the time evolution (TE), a pair of field gradients is used to perform "diffusion-encoding." Each gradient in this gradient pair will last a time δ, with strength G (usually in units of mT/m), and the pair is separated by a time Δ. A more formal analysis will tell us that the intensity of the signal will depend on all these parameters, given by

$$S=S_0\exp(-b\ ADC), \quad (1)$$

where ADC is the apparent diffusion coefficient, and b is the gradient factor, sometimes simply called the b-factor. S_0 is the signal intensity obtained when no diffusion gradients are used. The diffusion coefficient calculated in this way is usually called "apparent" be-

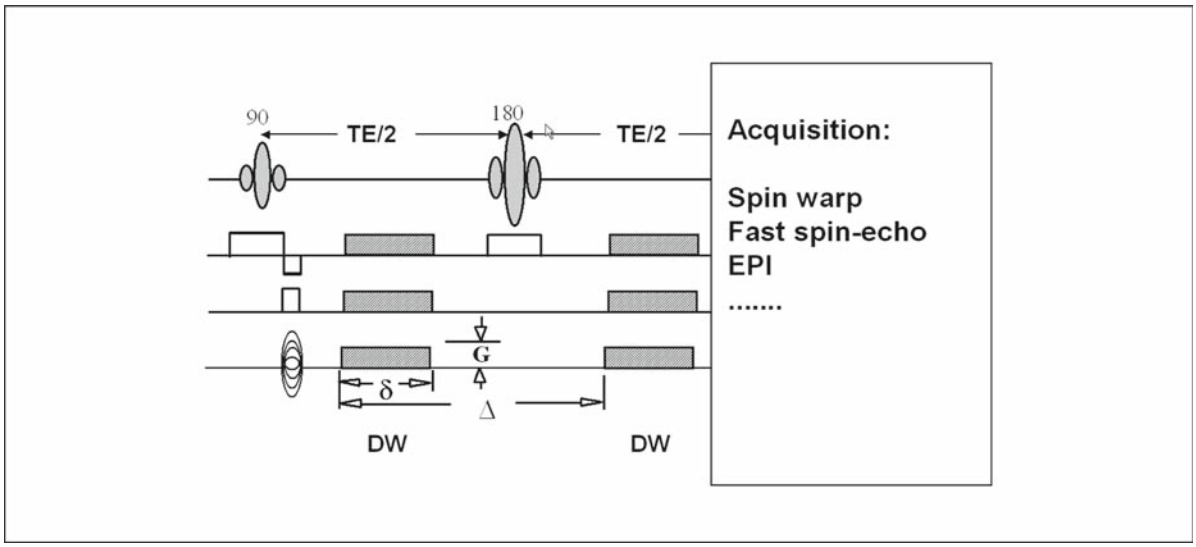

Figure 1.1

A typical pulse sequence for diffusion imaging. The shaded areas represent field gradient pulses. DW diffusion weighted, TE time evolution

cause it is often an average measure of much more complicated processes in the tissues, as discussed below. The b-factor is related to the gradient parameters δ, G and Δ (Fig. 1.1), usually in the form $b \mu (dG)^2 (\Delta - \delta / 3)$, and is set by the experimenter. The formula for the b-factor tells us that we can increase diffusion weighting (DW) by increasing either gradient timing, δ or Δ, or gradient strength, G.

Equation 1.1 suggests that there is a reduction in the measured signal intensity when DW is applied, $b \neq 0$, which can be understood with some simple reasoning. As the diffusing spins are moving inside the field gradient (an additional magnetic field varying in intensity from location to location), each spin is affected differently by the field. The alignment of the spins with each other is thus destroyed. Since the measured signal is a summation of tiny signals from all individual spins, the misalignment, or "dephasing", caused by the gradient pulses results in a drop in signal intensity; the longer the diffusion distance, the lower the signal (more dephasing; Fig. 1.2).

1.4 Apparent Diffusion Coefficient

From Eq. 1.1 it can be seen that when a fixed DW b-factor is used, tissues with a higher ADC value produce a lower signal intensity. Since brain cerebrospinal fluid (CSF) contains water that can move around freely, its ADC value is much higher than that of other brain tissues (either gray matter or white matter), which contain many more cellular structures and constituents. Consequently, in a DW image one typically sees dark CSF space (pronounced dephasing) and brighter tissue signals (less dephasing). It is also clear from Eq. 1.1 that if we collect a series of DW images with different b-values, we can calculate according to the expression for every pixel and obtain a parametric map of ADC values. The result is sometimes referred to as an ADC map. The calculated ADC map would have image pixel intensities reflecting the strength of diffusion in the pixels. Regions of CSF will therefore have higher intensity than other brain tissues – a reversal of DW images. There are several reasons why it is sometimes desirable to calculate an ADC map instead of just using DW images. One is the so-called T2-shine-through effect, which will be discussed in a later chapter. It can also be noted that S_0 in Eq. 1.1 is equal to the signal when no DW is used. Figure 1.1 suggests that this is actually the same as would be obtained from a simple spin-echo sequence. In most clinical scanners, a long TE time (tens of milliseconds) is needed to accommodate the diffusion pulses, so S_0 is often T2-weighted.

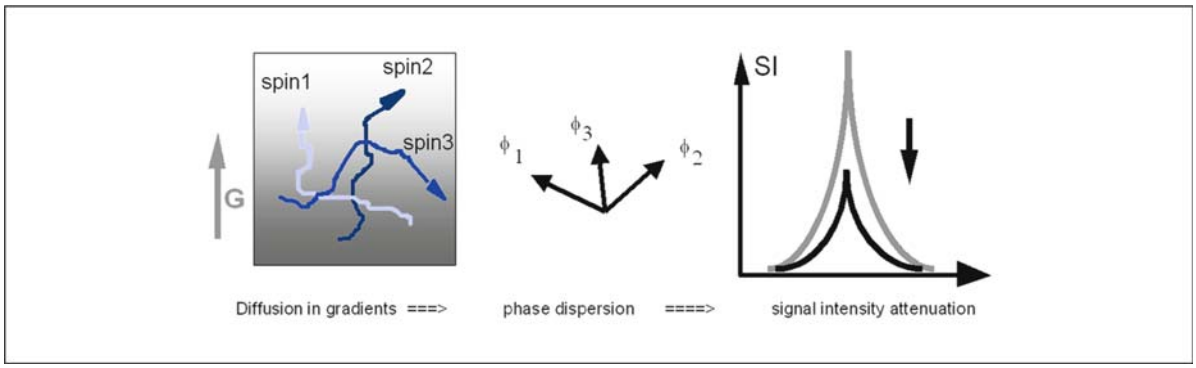

Figure 1.2

Effects of gradients on diffusing spins. Diffusion in the gradient causes dephasing of spins and therefore reduction in the measured signal intensity

1.5 Diffusion Represents a Molecular Event

Even though an image pixel size in the order of millimeters is used in most clinical MR imaging, the information provided by diffusion imaging reflects cellular or molecular events in much smaller scales. This is because the molecular diffusion process is highly modulated by these events. It can be shown that water spins diffuse about tens of micrometers during a typical MR imaging measurement time, which coincides with the dimension of typical cellular structures. If spins experience minimal obstruction from cellular structures during this time (such as for spins in the CSF space), the measured diffusion is "free" and "isotropic", and ADC is just the intrinsic molecular diffusion coefficient. On the other hand, when diffusing spins run into cellular constituents and membranes, the value of ADC will be reduced when compared with the value in free space. What happens at the cellular level is represented schematically in Fig. 1.3. For patients with neurological abnormalities that change the water distribution in various cellular compartments, or change the ability of water to pass through cell membranes, the measured ADC values will also be altered [4–7]. Therefore the MR diffusion measurement offers a unique opportunity to obtain information about morphology otherwise inaccessible to conventional MR imaging methods. A wide range of pathological conditions can be explored with water diffusion measurements, as described later in this book. The measured ADC may also vary depending on the duration of the diffusion process, the direction in which diffusion is measured, and other factors. For diffusion in an anisotropic environment (such as in brain white matter, where bundles of axons with myelin layers wrapped around them make diffusion along the bundle much easier than across the bundle), diffusion becomes more complicated and a complete description of the process relies on what is called tensor analysis [8, 9].

1.6 Requirements in Clinical Diffusion Imaging

In a clinical environment, certain requirements are imposed for diffusion studies. A reasonable imaging time is often limited to a few minutes for each type of measurement (T1-W, T2-W, diffusion, and others). Multiple slices (15–20) are required to cover most of the brain. A good spatial resolution (~5–8 mm thick, 1–3 mm in-plane) is required. A reasonably short TE (120 ms) to reduce T2 decay, and an adequate diffusion sensitivity (ADC ~0.2–1×10^{-3} mm^2/s for brain tissues) are also needed. However, most essential is the almost complete elimination of sensitivity to subject motion during scanning. The best compromise so far in most clinical practices of diffusion imaging is the use of the multi-directional (x,y,z), 2 b-factor (b=0, and b~1/ADC) single-shot echo-planar imaging technique. Sometimes fluid attenuation with inversion recovery (FLAIR) is used to eliminate signal in the highly diffusive CSF space. Separation from relaxation effects is achieved with calculation of ADC instead of just using DW,

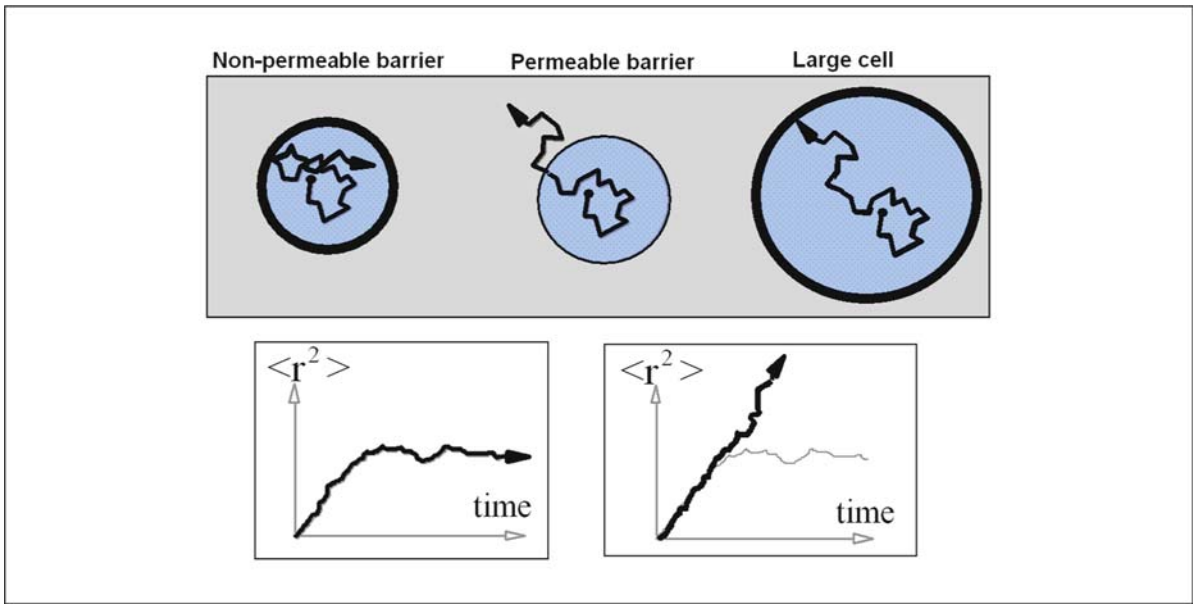

Figure 1.3

When water spins are diffusing among cellular structures, depending on the mean displacement ($<r^2>$) during the measurement time and the size of the cellular structure, their behavior can be quite different. Water inside a non-permeable cell (top and bottom left) experiences restriction or hindrance to diffusion. Diffusion barrier effects are minimal for water inside a permeable cell, or in a cell that is much larger than the mean displacement during diffusion (top middle and right, and bottom right)

and elimination of anisotropic diffusion is achieved by averaging the diffusion measurements from three orthogonal directions.

1.7 Setting the b-Value in Clinical DW Imaging

In a clinical setting it is advisable to maintain the same b-value for all examinations, making it easier to learn to interpret these images and become aware of the appearance of findings in various disease processes. The studies and discussions presented in this book are limited to DW imaging using b-values of 0 and 1,000. An upper b-factor around 1,000 is available on most clinical scanners and DW imaging at these standard values has been shown to be a sensitive tool in detecting and delineating restricted diffusion, e.g., in acute ischemic lesions of the brain. DW imaging has become clinically important in many other disease processes, which will be discussed in this book.

1.8 Future Trends in Clinical Diffusion Imaging

Newer DW imaging techniques are using even higher b-values: 8.000 and more. Some recent articles that explore the use of higher b-values imply that they will simplify clinical diffusion imaging [10]. The increased b-values may free up routine DW imaging from its most pressing problem, "T2 shine-through". At high b-values more attention will be focused on the actual physiological basis of restricted and facilitated diffusion. Clearly, much of the advantage of increased b-values may lie not with the diagnosis of lesions with restricted diffusion, especially acute infarcts, but with allowing a more complete understanding of other types of diseases.

The benefits of improved diffusion contrast at high b values come with the complication of prescription dependent measures of apparent diffusion. The ADC is conventionally derived from images taken at two different b-values. Because tissues are described by

fast and slow components, the results of a two-point measurement will depend on the specific b-values chosen. If the lower b-value is set to 0 (a T2-weighted image) and the upper value is allowed to vary, the ADC will vary as a function of the upper value. Specifically, one would expect the measured ADC to decrease as the upper b-value increases.

Another area of diffusion imaging that has become more commonly used is diffusion tensor (DT) imaging, which is now available in modern clinical scanners. Instead of monitoring "magnitude" or strength of water movement alone, DT imaging detects both the magnitude and directionality of the water diffusion process in three dimensions and allows the investigation of the microstructure of the CNS by measuring the diffusion properties of water protons in the CNS microenvironment. It is expected that water molecules move less impeded, e.g., along the axonal bundles, and have higher directionality of movement (higher anisotropy, i.e., in white matter tracts) than perpendicular to these bundles (lower anisotropy, i.e., cortical gray matter); on the other hand, in areas with high concentration of cerebrospinal fluid (i.e., ventricles), there would be little preferential directionality of movement (high isotropy) and minimal hindrance to diffusion (highest diffusivity). Fractional anisotropy (FA) and mean diffusivity (<D>) are common DT imaging indices used to measure microscopic motion of tissue water at each image voxel. In a DT imaging measurement, six or more DWI measurements are required, and tensor eigenvalues ($\lambda 1$, $\lambda 2$, and $\lambda 3$) and eigenvectors are derived from these measurements [8]. Maps of <D> and FA can then be generated from $\lambda 1$, $\lambda 2$, and $\lambda 3$ with the following relations:

$$\langle D\rangle = \frac{1}{3}(\lambda_1+\lambda_2+\lambda_3),$$

$$FA = \sqrt{\frac{2}{3}}\,\frac{\sqrt{(\lambda_1-\langle D\rangle)^2+(\lambda_2-\langle D\rangle)^2+(\lambda_3-\langle D\rangle)^2}}{\sqrt{\lambda_1^2+\lambda_2^2+\lambda_3^2}}$$

FA represents anisotropy of the diffusion process, yielding values between 0 (perfectly isotropic diffusion) and 1 (completely anisotropic diffusion). <D> represents the overall strength of water mobility in different brain areas. A useful representation of DT imaging measurement results is given by a "color FA" map in which red, green, and blue colors are used to represent the orientation of the largest eigenvalue along left-right (LR), anterior-posterior (AP) and superior-inferior (SI) directions, respectively, while image intensity represents FA values in each voxel.

By following the main direction of water movement (the largest tensor eigenvalue) and its connection in adjacent voxels in the three-dimensional space, fiber tractography in white matter can be formed. This further increases the diagnostic ability of diffusion imaging in degenerative neurological diseases where damage to axon bundles or demyelination can be directly detected and visualized.

References

1. Brown R (1928) A brief account of microscopical observations made in the months of June, July, and August, 1827, on the particles contained in the pollen of plants; and on the general existence of active molecules in organic and inorganic bodies. Phil Mag 4:161–173
2. Doob JL (1942) The Brownian movement and stochastic equations. Ann Math 43:351–369
3. Stejeskal EO, Tanner JE (1965) Spin diffusion measurements: spin echoes in the presence of time-dependent field gradient. J Chem Phys 42:288–292.
4. Le Bihan D, Breton E, Lallemand D, Grenier P, Cabanis E, Laval-Jeantet M (1986) MR imaging of intravoxel incoherent motions: application to diffusion and perfusion in neurologic disorders. Radiology Nov; 161(2):401–407
5. Moseley ME, Kucharczyk J, Mintorovitch J (1990) Diffusion-weighted MR imaging of acute stroke: correlation with T2-weighted and magnetic susceptibility-enhanced MR imaging in cats. AJNR Am J Neuroradiol 11:423
6. Moonen CT, Pekar J, Vleeschouwer de MHM, Gelderen van P, Zijl van PCM, DesPres D (1991) Restricted and anisotropic displacement of water in healthy cat brain and in stroke studied by NMR diffusion imaging. Magn Reson Med 19:327
7. Zhong J, Petroff OAC, Prichard JW, Gore JC (1993) Changes in water diffusion and relaxation properties of rat cerebrum during status epilepticus. Magn Reson Med 30:241
8. Basser PJ, Mattiello J, Le Bihan D (1994) Estimation of the effective self-diffusion tensor from the NMR spin-echo. J Magn Reson 103:247–254
9. Le Bihan D, Van Zijl P (2002) From the diffusion coefficient to the diffusion tensor. NMR Biomed Nov-Dec; 15(7–8):431–434
10. Clark CA, Le Bihan D (2000) Water diffusion compartmentation and anisotropy at high b values in the human brain. Magn Reson Med Dec; 44(6):852–859

Diffusion-Weighted and Tensor Imaging of the Normal Brain

2.1 Introduction

Diffusion-weighted (DW) images are usually obtained in three orthogonal orientations using spin-echo type single-shot DW echo-planar imaging with b-values around 0 and 1,000 s/mm^2. These three planes are combined into isotropic DW images, and apparent diffusion coefficient (ADC) maps are calculated on a pixel-by-pixel basis (Fig. 2.1). To avoid misinterpretations, it is important to recognize the normal findings on DW images and ADC maps.

2.2 Adult Brain

2.2.1 Low Signal in Basal Ganglia

Isotropic DW imaging in adult brain often shows low signal intensity in the basal ganglia (Fig. 2.1). This low signal is caused by normal iron deposition. The hypointensity on DW images of these areas is essentially related to T2 contrast, which is also shown on b_0 images. ADC maps usually show the areas as isointense, but it can be hyper- or hypointense depending on the paramagnetic susceptibility artifact of iron deposition.

2.2.2 Diffusion-Weighted Imaging of Gray and White Matter

Gray matter on DW images is generally hyperintense when compared with white matter. ADC values of gray matter ($0.76 \pm 0.13 \times 10^{-3}$ mm^2/s) and white matter ($0.77 \pm 0.18 \times 10^{-3}$ mm^2/s) are, however, identical in the adult brain [1]. There are several reports about ADC increasing with age [2–8], but this increase is minimal and has been observed in all parts of the brain. It is usually more apparent in the white matter and lentiform nucleus than in the rest of the brain. Focal areas of DW hyperintensities are often seen in the posterior limbs of the internal capsule, corticospinal tract, cingulate gyrus, insula, medial lemniscus, and the decussation of the superior cerebellar peduncles (Figs. 2.1 and 2.2). These DW hyperintensities are caused by T2 contrast and represent normal findings without clinical significance. ADC maps are usually isointense in these areas [2].

2.2.3 Choroid Plexus

The choroid plexus occasionally shows prominent hyperintensity on DW imaging associated with mild elevation of ADC. In these situations the ADC is often higher than in white matter, but lower than in cerebrospinal fluid. The high DW signal is believed to represent gelatinous cystic changes of the choroid plexus, which can occur with age (Fig. 2.3)[9].

2.3 Pediatric Brain

2.3.1 Diffusion-Weighted Imaging and ADC of the Pediatric Brain

The normal brain of neonates and infants has significantly higher ADC values than the adult brain [10–15] (Fig. 2.4). ADC in neonates and infants varies markedly within different areas of the brain and is higher in white matter (1.13×10^{-3} mm^2/s) than in gray matter (1.02×10^{-3} mm^2/s) [13]. ADC at birth is higher in subcortical white matter (1.88×10^{-3} mm^2/s) than in both the anterior (1.30×10^{-3} mm^2/s) and posterior limbs of the internal capsule (1.09×10^{-3} mm^2/s). It is also higher in cortex and the caudate nucleus (1.34×10^{-3} mm^2/s) than in the thalamus and the lentiform nucleus (1.20×10^{-3} mm^2/s) [15]. With the exception of the cerebrospinal fluid (CSF), there is a trend of decreasing ADC with increasing maturation in most areas of the pediatric brain. These ADC changes seem to reflect a combination of different factors, including

a reduction of overall water content, cellular maturation and white matter myelination. In neonates and infants, ischemia is usually global and can therefore resemble the normal image with elevated DW signal and decreased ADC. White matter diseases can also be mimicked by the normal, age-related appearance of DW imaging and ADC. Out of necessity, the ADC values will therefore have to be age related for a correct interpretation of the DW images of the pediatric brains.

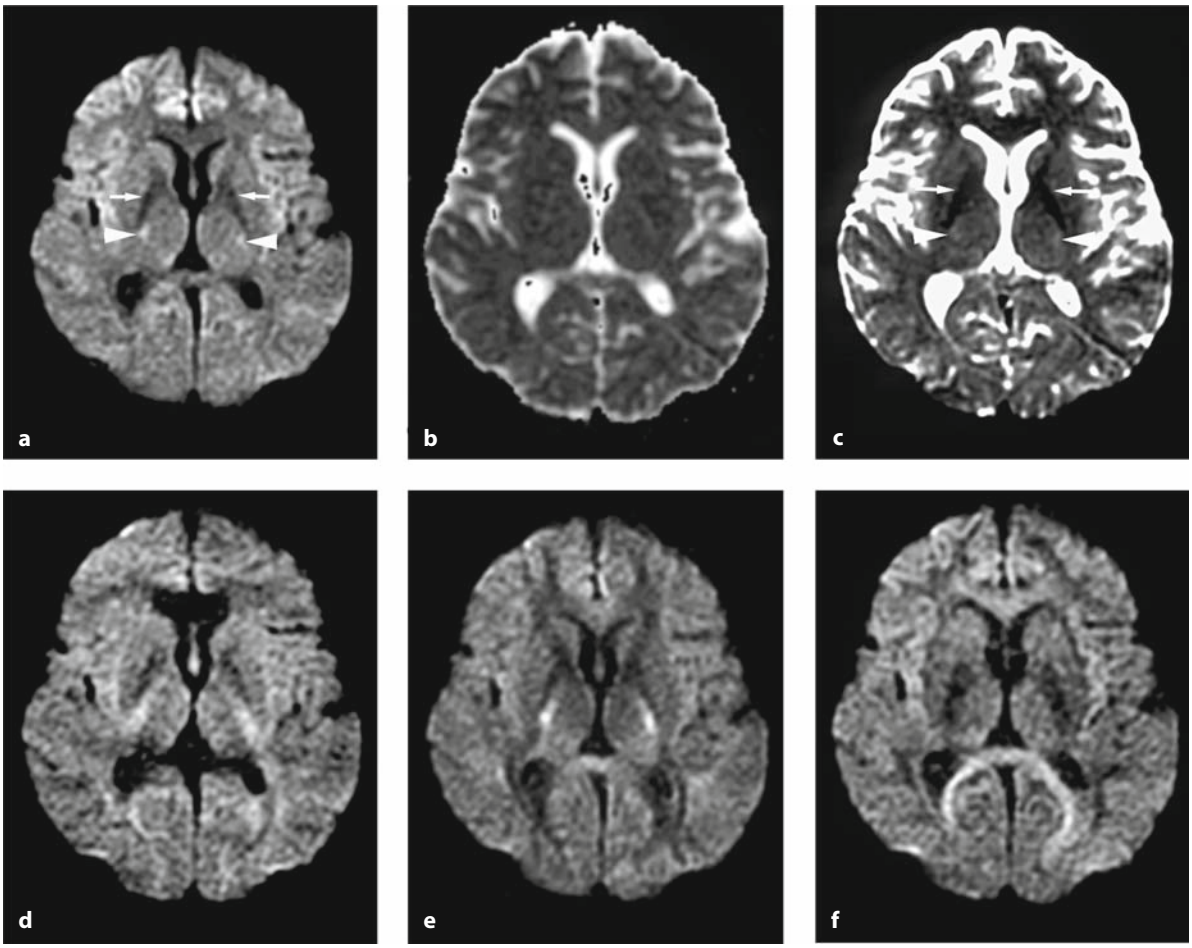

Figure 2.1 a–f

Normal adult brain of a 40-year-old male without neurological deficits. **a** Isotropic DW image is obtained by combining b_0 image and three orthogonal unidirectional images (x, y, z axis). The bilateral globi pallidi have low signal on DW image as a result of physiological iron deposition (*arrows*). Corticospinal tracts have mildly high signal on DW image (*arrowheads*). Gray matter shows mildly high signal compared to white matter. These signal changes on isotropic DW imaging are normal and are caused by T2 contrast. **b** ADC map shows homogeneous ADC values in globi pallidi, corticospinal tracts, gray and white matter. **c** b_0 image shows low signal in globi pallidi (*arrows*), high signal in corticospinal tracts (*arrowheads*), and the gray–white matter contrast. **d–f** Diffusion weighting is applied in x axis (**d**), y axis (**e**), and z axis (**f**)

Figure 2.2 a, b

a Decussation of the superior cerebellar peduncle has mildly high signal on DW image (*arrow*). **b** ADC map shows similar ADC values in the decussation of the superior cerebellar peduncle to those in cerebral peduncles (*arrow*).

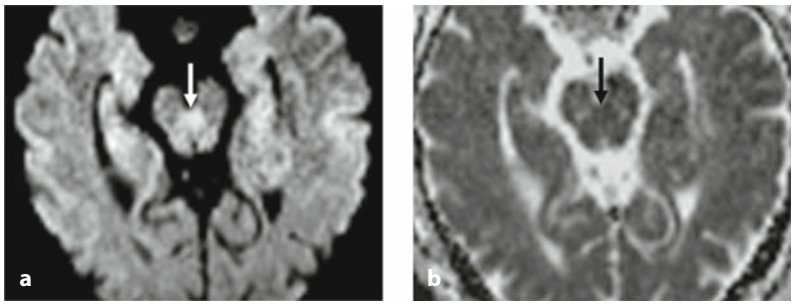

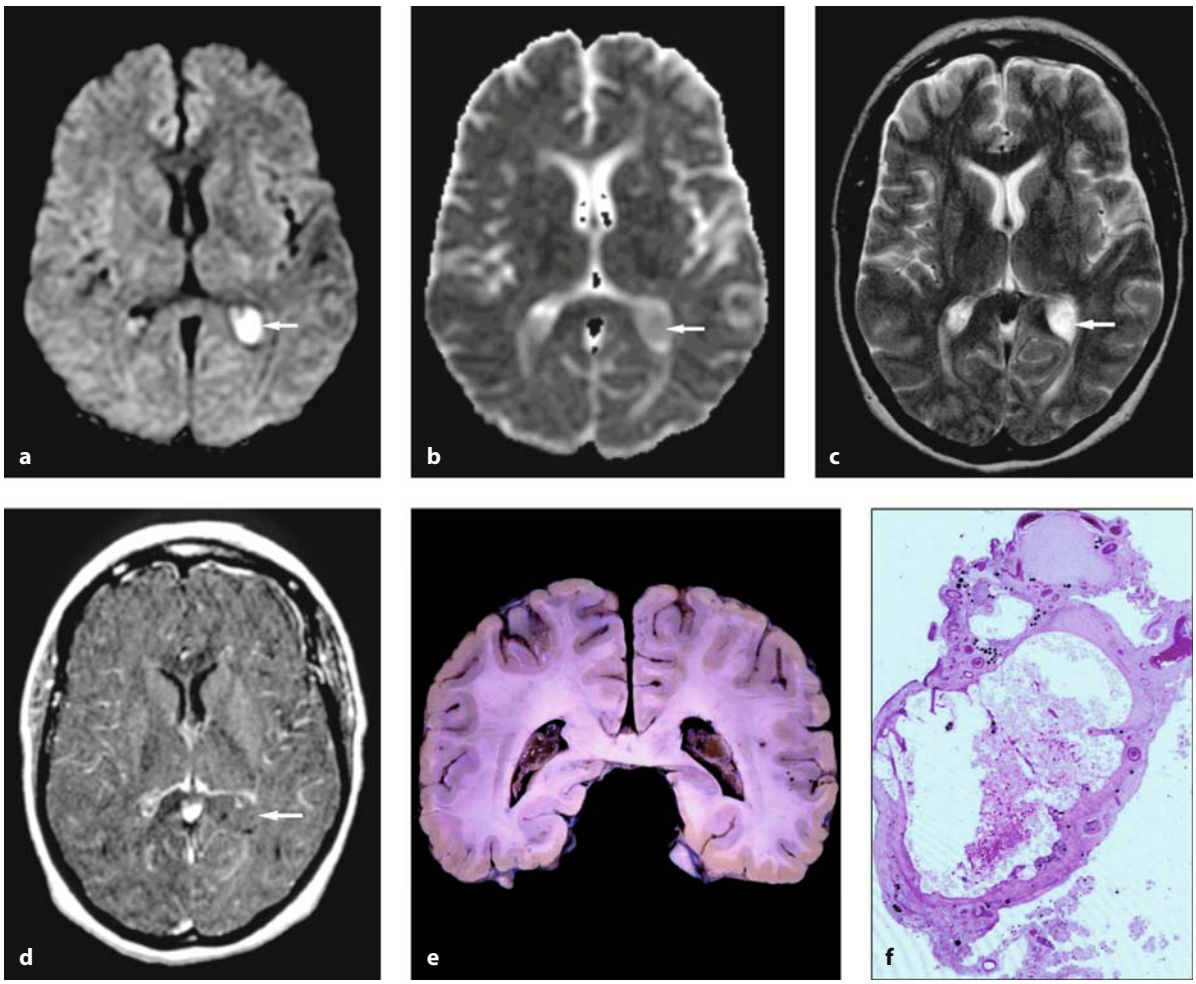

Figure 2.3 a–f

Cystic changes in the choroid plexus. **a** DW image shows hyperintensity in cystic changes of the left choroid plexus (*arrow*). **b** ADC values of the cystic changes are lower than those of the CSF, which probably represent viscous gelatinous materials, but higher than those of brain parenchyma (*arrow*). **c** T2-weighted image shows the cystic changes as hyperintensity (*arrow*). **d** Gadolinium-enhanced T1-weighted image with magnetization transfer contrast reveals no enhancement in it (*arrow*). **e** Macropathology of choroids plexis cyst (another case). **f** Micropathology shows gelatinous content, foci of calcification with a thickened fibrous wall containing blood vessels. (Courtesy of Kinoshita T, MD, Research Institute for Brain and Blood Vessels Akita, Japan)

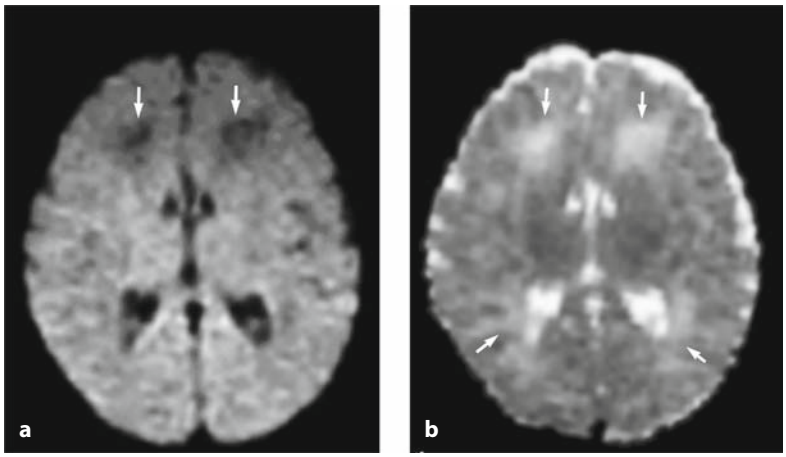

Figure 2.4 a, b

Normal neonatal brain. **a** The appearance of the pediatric brain on DW images varies with age. In neonates it is normal to have low DW signal intensities in the frontal deep white matter (*arrows*). **b** ADC values of the corresponding areas are high in neonatal brain, especially in the white matter (*arrows*). These ADC changes seem to reflect a combination of factors, including a reduction of overall water content, cellular maturation, and white matter myelination.

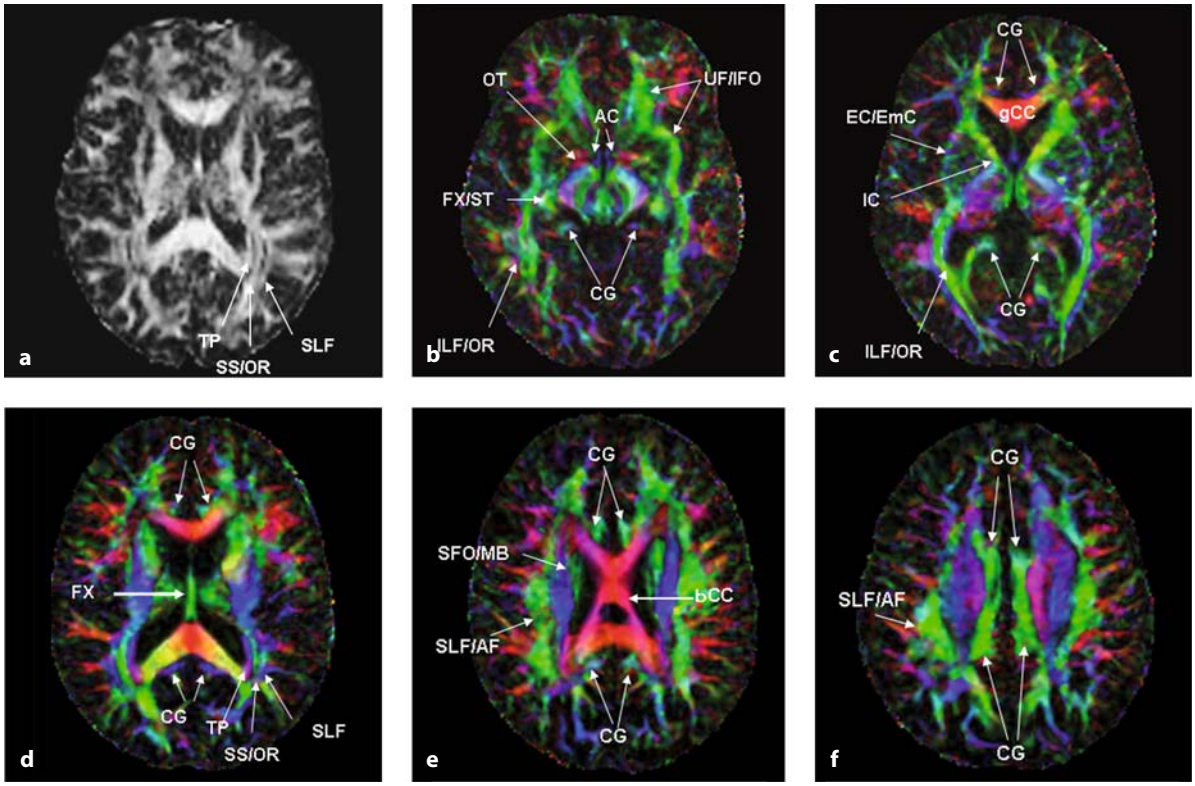

Figure 2.5 a–f

a Fractional anisotropy (FA) map, **b-f** Axial DTI color maps, **g-i** Coronal DTI color maps, **j-m** Sagittal DTI color maps

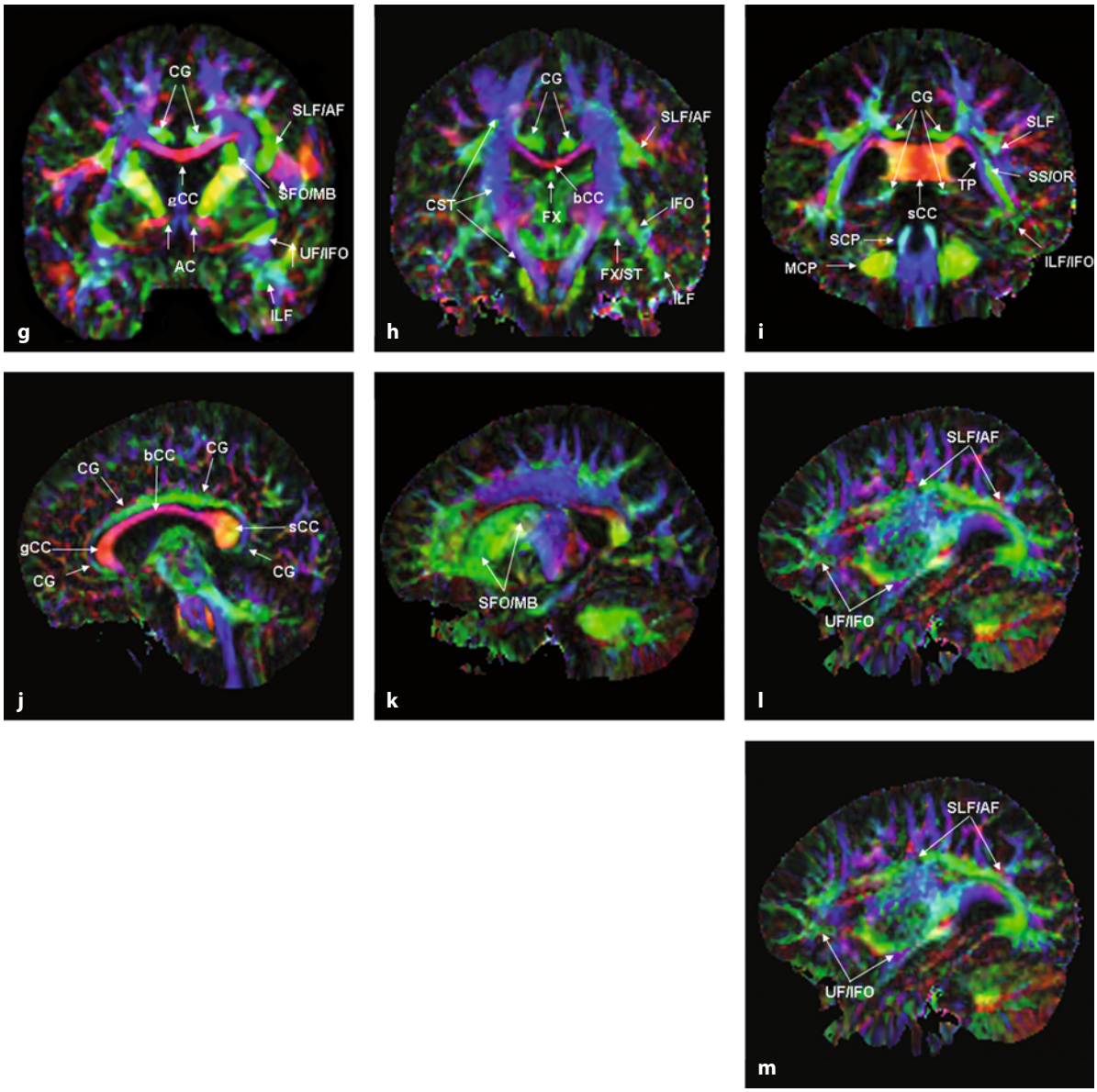

Figure 2.5 g–m

g-i Coronal DTI color maps, **j-m** Sagittal DTI color maps. DTI shows the white matter lateral to the posterior horn as three parts: the tapetum (TP), internal and external sagittal strata including optic radiation (SS/OR), and SLF. SLF/AF connects the frontal lobe to temporal and occipital lobes. SFO/MB is situated beneath the corpus callosum (CC) and medial to the corona radiata (CR). ILF connects temporal and occipital lobe cortices. The cingulum (CG) is situated on both sides of the midline on the surface of CC. The uncinate fasciculus (UF) connects the ventral and lateral fontal lobe with the anterior temporal lobe. EmC/EC is hard to be separately seen on DTI. SLF superior longitudinal fasciculus, AF arcuate fasciculus, ILF inferior longitudinal fasciculus, CG cingulum, UF uncinate fasciculus, SFO superior fronto-occipital fasciculus, IFO inferior fronto-occipital fasciculus, EmC extreme capsule, EC external capsule, MB subcallosal fasciculus of Muratoff, IC internal capsule, CST corticospinal tract, OT optic tract, OR optic radiation, SS sagittal stratum, gCC genu of corpus callosum, bCC body of corpus callosum, sCC splenium of corpus callosum, TP tapatum, AC anterior commissure, FX fornix, ST stria terminalis, SCP superior cerebellar peduncle, MCP middle cerebellar peduncle. (Courtesy of Kim J MD, The University of Iowa Hospitals and Clinics, USA, and White ML MD and Zhang Y MD, The University of Nebraska Medical Center, USA)

2.4 Diffusion Tensor Imaging and White Matter Anatomy

Diffusion tensor (DT) imaging is available in many modern clinical scanners. A fractional anisotropy (FA) map represents the magnitude of the anisotropy of the diffusion process at each image voxel, yielding values between 0 (perfectly isotropic diffusion) and 1 (completely anisotropic diffusion) (Fig. 2.5). A color FA map represents the directionality of the anisotropy based on the orientation of the largest eigenvalue along left-right (red), anterior-posterior (green), and superior-inferior directions (blue) (Fig. 2.5).

A fiber tractography map is made by following the main direction of water movement(the largest tensor eigenvalue) and its connection in adjacent voxels in the three-dimensional space (Figs. 2.6-2.11). DT imaging with these maps has been used to investigate the microstructure of the CNS, and their clinical usefulness has been reported in the literature [16-18]. DT imaging can beautifully demonstrate white matter fiber tracts of the CNS in detail that is useful for understanding the anatomy.

White matter fiber tracts consist of myelinated fiber bundles, called the fasciculus. The white matter fibers are traditionally classified as follows: (1) association fibers that interconnect various cortical areas of the same hemisphere, (2) projection fibers that interconnect cortical areas with the thalami, brain stem, cerebellum, and spinal cord, and (3) commissural fibers that interconnect corresponding cortical areas of the two hemispheres [19-22]. However, the classification of the fiber bundles is complex and to date has remained unresolved [23-27].

2.4.1 Association Fibers

Short association fibers arch beneath the six layers of the cortex referred to as U-fibers or arcuate fibers. In long association fibers, the superior longitudinal fasciculus (SLF) is the largest bundle, connecting the frontal lobe cortex to the temporal and occipital lobe cortices (Fig. 2.6). The arcuate fasciculus (AF) is the part of the SLF that forms a curved shape and connects the Broca area (motor area of speech) with the Wernicke area (language comprehension). The inferior longitudinal fasciculus (ILF) connects the temporal and occipital lobe cortices, which are concerned with visual perception, object identification, and recognition.

The cingulum (CG) is situated on both sides of the midline on the peripheral surface of the corpus callosum and courses within the cingulate gyrus that is concerned with behavior and regulation of emotional processing (Fig. 2.7). The cingulum bundle contains variable-length fibers which connect the frontal and parietal lobes with the parahippocampal gyrus and adjacent temporal lobe cortex. The uncinate fasciculus (UF) connects the ventral and lateral fontal lobe cortex with the anterior temporal lobe cortex, which is concerned with memory integration (retrograde amnesia).

The existence of the superior or inferior fronto-occipital (occipitofrontal) fasciculus is controversial [23-27]. The superior fronto-occipital fasciculus (SFO) connects the frontal and parietal lobes. It is thought to be concerned with space perception. Ventrally its base rests on the subcallosal fasciculus of Muratoff (MB) [24, 26]. The SFO/MB is situated beneath the corpus callosum and medial to the corona radiata (Fig. 2.5). The SFO may not exist based on analyses using fiber dissection techniques [23]. The inferior fronto-occipital fasciculus (IFO) connects the frontal and temporo-occipital areas intermingled with the uncinate fasciculus antero-inferiorly, possibly concerned with auditory-visual association [24] (Fig. 2.7). The IFO may not exist based on analyses using isotope anterograde tract tracer in the macaque monkey [24-27].

The extreme capsules (EmC) contain association fibers parallel to the external capsule (EC), which are separated by a sheet of gray matter known as the claustrum.

Corticostriatal fibers interconnect the cortex with the striatum including the external capsule and the subcallosal fasciculus of Muratoff (MB) concerned with motor and cognitive–affective performance. The corticostriatal fibers are not exactly association fibers, based on the definition [25, 28].

2.4.2 Projection Fibers

The corona radiata and internal capsule (IC) are composed of afferent and efferent fibers to and from the entire cerebral cortex. Efferent fibers in the internal capsule arise from the cortex and project to the brain stem and spinal cord and are categorized as corticothalamic, corticopontine, corticobulbar, and corticospinal tracts (Fig. 2.8) [29, 30]. The most posterior component of the posterior limb of the internal capsule contains fibers, connecting the lateral geniculate nucleus to the calcarine sulcus (geniculocalcarine tract), also known as optic radiation (OR) (Fig. 2.9). The ventral bundle of the optic radiation

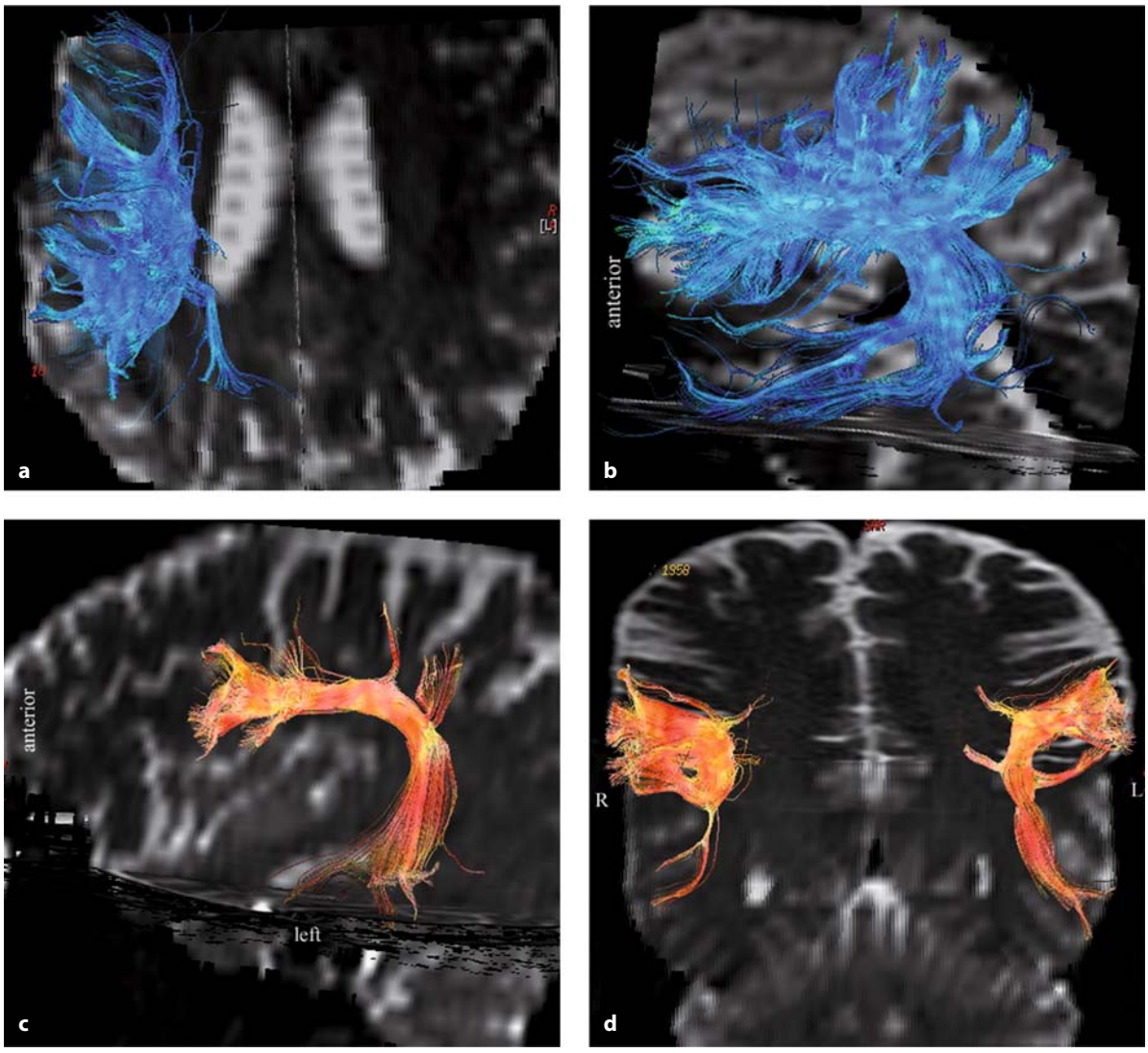

Figure 2.6 a–d

a, b The superior longitudinal fasciculus (SLF) interconnects frontal lobe cortex to temporal and occipital lobe cortices. The inferior longitudinal fasciculus (ILF) connects temporal and occipital lobe cortices. **c** The arcuate fasciculus (AF) is the part of the SLF that forms a curved shape and connects the Wernicke area with Broca area. **d** There is asymmetry in right and left side of arcuate fasciculi (Courtesy of White ML MD and Zhang Y MD, The University of Nebraska Medical Center, USA)

passes anteriorly before making a sharp turn, known as the Meyer loop, and terminating in the inferior bank of the calcarine cortex. The temporal stem is a critical landmark in temporal lobe surgery, which is crossed by the uncinate fasciculus, inferior fronto-occipital fasciculus, and Meyer's loop [24, 31]. The optic radiation is part of the sagittal stratum. The sagittal stratum not only conveys fibers from parietal, occipital, temporal, and cingulate regions to the thalamus and brain stem, but also conveys principally from the thalamus to the cortex. The thalamocortical (afferent) and corticothalamic (efferent) fibers are arrayed around the thalamus, termed thalamic radiations or peduncles (Fig. 2.10).

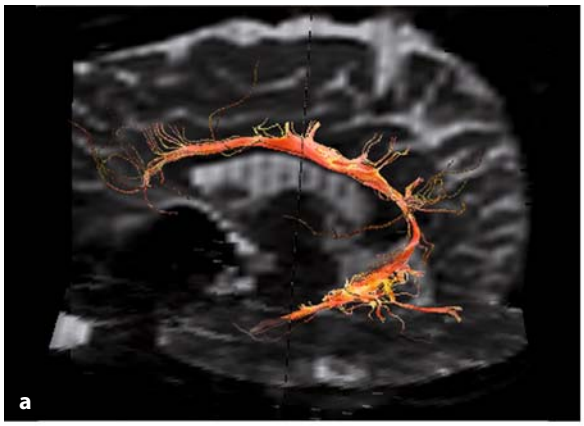

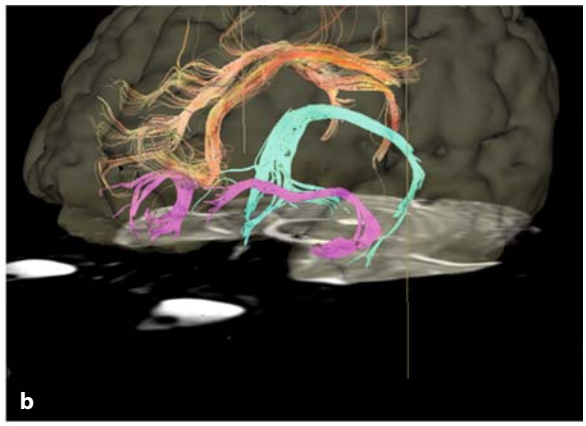

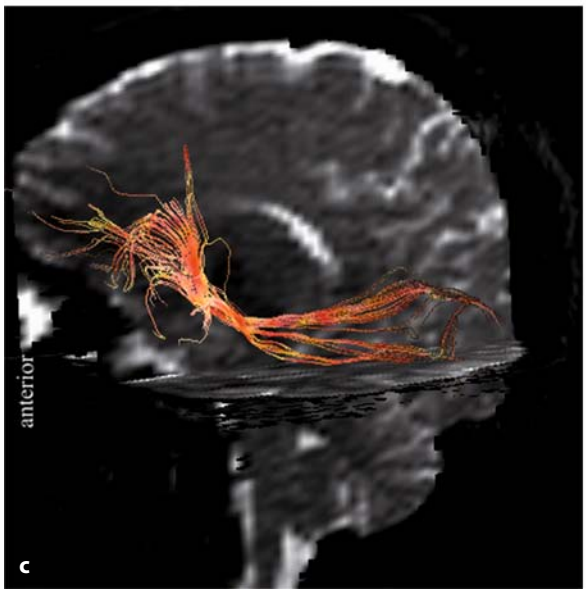

Figure 2.7 a–c

a The cingulum bundle contains variable length fibers which connect frontal and parietal lobes with parahippocampal gyrus and adjacent temporal lobe cortex (Courtesy of White ML, MD and Zhang Y MD, University of Nebraska Medical Center, USA). **b** The cingulum (orange) is situated on both sides of the midline on the peripheral surface of the corpus callosum and courses within the cingulate gyrus. The uncinate fasciculus (UF) (pink) connects the ventral and lateral fontal lobe cortex with the anterior temporal lobe cortex. The fornix (FX) (light blue) is also demonstrated (Courtesy of Aoki S, MD, The University of Tokyo, Japan). **c** The inferior fronto-occipital fasciculus (IFO) connects frontal and temporo-occipital areas intermingled with the uncinate fasciculus antero-inferiorly (Courtesy of White ML MD and Zhang Y MD, The University of Nebraska Medical Center, USA)

2.4.3 Commissural Fibers

The corpus callosum (CC) is a broad thick plate of dense myelinated fibers that reciprocally interconnect broad regions of the cortex (Fig. 2.11). The genu (gCC) contains fibers interconnecting rostral parts of the frontal lobes. Fibers from the remaining parts of the frontal lobe and the parietal lobe traverse the body of the corpus callosum (bCC). Fibers transversing the splenium relate regions of the temporal and occipital lobes. The tapetum comprises the fibers in the splenium (sCC) which sweep inferiorly along the lateral margin of the posterior horn of the lateral ventricle. The white matter lateral to the posterior horn is divided into four layers: the tapetum, the internal and external sagittal strata, and the SLF [22, 32]. The anterior commissure (AC) is a small compact bundle that crosses the midline rostral to the columns of the fornix. The posterior commissure connects the right and left peritectal region. The hippocampal commissure joins the right and left hippocampi also known as the commissure of the fornix (FX). The fornix is the main efferent fiber system of the hippocampal formation, including both projection and commissural fibers, associated with antegrade amnesia. The stria terminalis is an efferent pathway from the amygdala, which arches along the medial border of the caudate nucleus and terminates in the hypothalamic nuclei lateral to the fornix. The stria terminalis is associated with the hypothalamus-pituitary-adrenal axis.

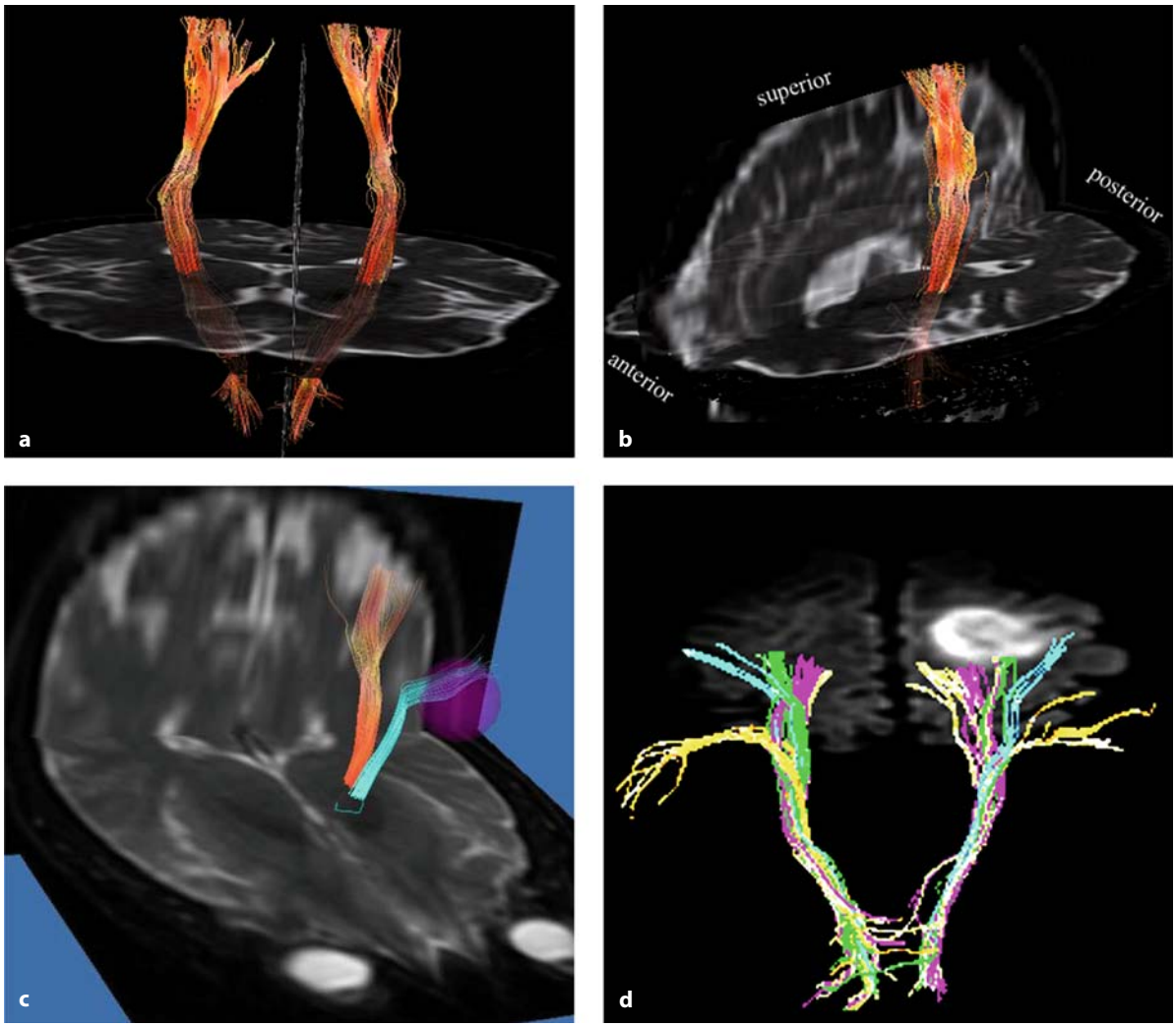

Figure 2.8 a–d

a, b Anterior-posterior and oblique lateral views of the corticospinal tract (Courtesy of White ML MD and Zhang Y MD, University of Nebraska Medical Center, USA). **c** The corticospinal tract (orange) and corticobulbar tract (light blue) are demonstrated (Courtesy of Aoki S, MD, The University of Tokyo, Japan). **d** Multi-tensor DTI separate each corticospinal fiber projecting special areas: hand (green),tongue (orange), trunk (purple), face (blue), and lower extremity (yellow) (Courtesy of Yamada K MD, Kyoto Prefectural University of Medicine, Japan) (from [30])

2.4.4 Fibers of the Brain Stem and Cerebellum

The complex anatomy of the brain stem includes a large number of tracts, nuclei, commissures, and decussations (Fig. 2.12) [19, 33].

In the midbrain, the tegmentum and crus cerebri are separated by the substantia nigra. The crus cerebri consists of corticopontine, corticobulbar, and corticospinal fibers. The superior cerebellar peduncle (SCP) is seen on each side of the upper part of the fourth ventricle, and decussates completely in the caudal midbrain tegmentum. The SCP is made up of predominantly efferent pathways arising from the cerebellar cortex and deep cerebellar nuclei to the thalamus and cerebral cortex but it also caries afferent pathways. It is associated with coordination of

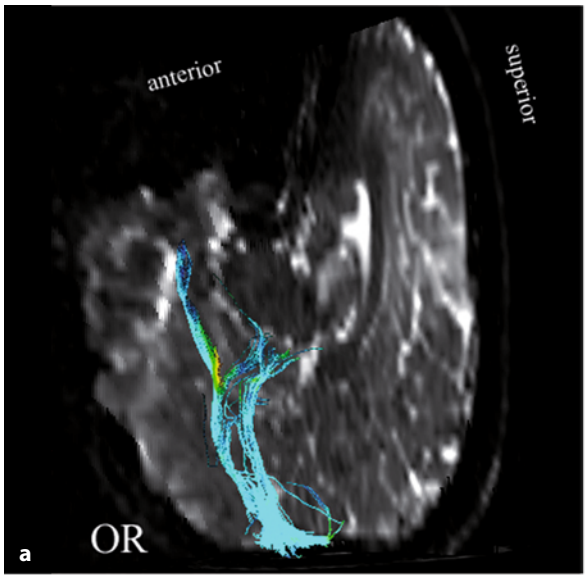

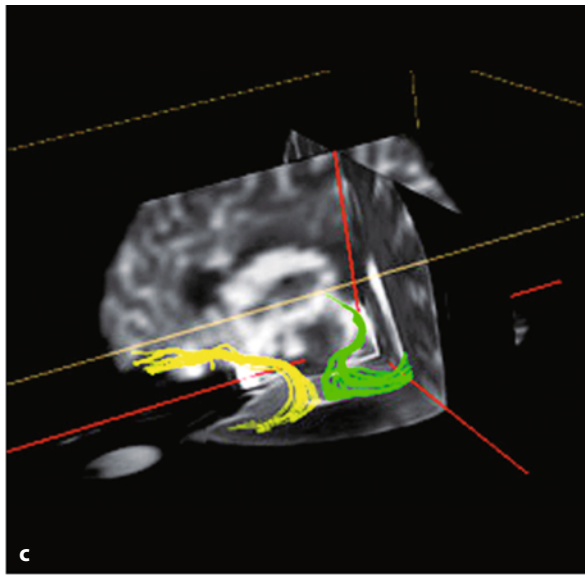

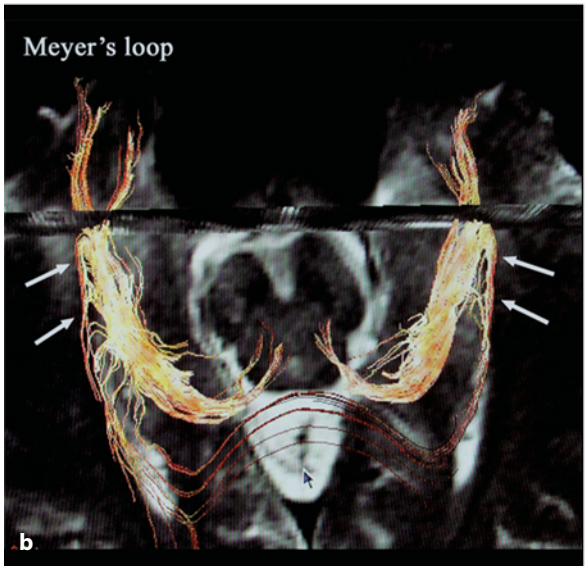

Figure 2.9 a–c

a Optic radiations on the right (OR), **b** Meyer's loop (*arrows*) (Courtesy of White ML MD and Zhang Y MD, The University of Nebraska Medical Center, USA). **c** The relationship between the Meyer's loop (green) and the uncinate fasciculus (Courtesy of Taoka T MD, Nara Medical University, Japan)

motor function. The ventral part of the pons consists of longitudinal descending fibers, pontine nuclei, and transverse pontine fibers projecting to the cerebellum. The dorsal tegmental portion contains the reticular formation, medial lemniscus, and cranial nerve nuclei. The medial lemniscus comprises large ascending fibers and terminates in the ventral posterolateral nucleus of the thalamus, which is concerned with sensation of touch, vibration, proprioception, and two-point discrimination.

The middle cerebellar peduncle (MCP) also known as the brachium pontis consists of predominantly afferent fibers arising from the pontine nuclei, and most of them decussate and terminate as mossy fibers projecting to the cerebellar hemisphere. The function of the MCP includes initiation, planning, and voluntary movement. The medulla contains the inferior olivary nuclei, cranial nerve nuclei, and decussation of the medullary pyramids and medial lemniscus.

The inferior cerebellar peduncle (ICP), seen on each side of the lower part of the fourth ventricle, connects

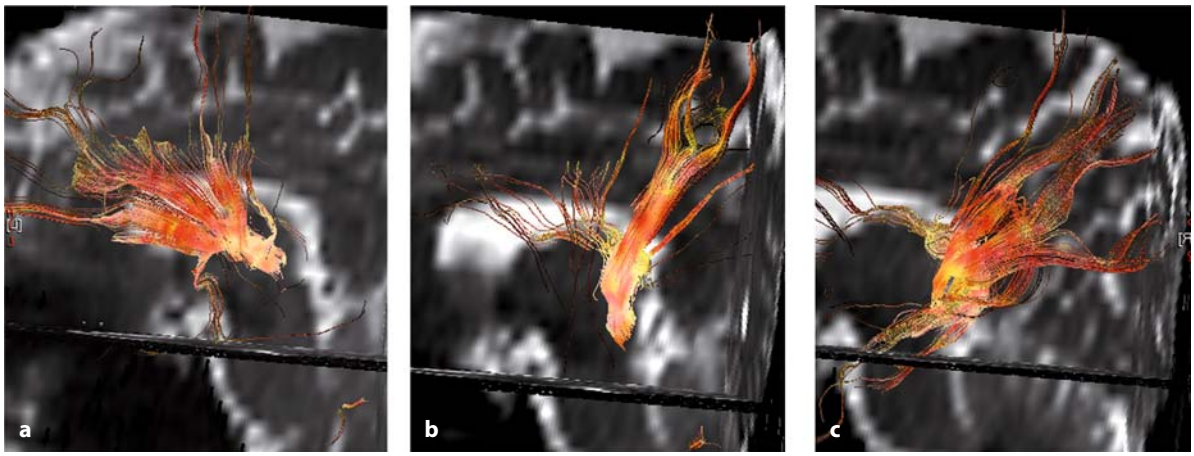

Figure 2.10 a–c

Thalamic radiations (**a** anterior, **b** superior, **c** posterior) (Courtesy of White ML MD and Zhang Y MD, The University of Nebraska Medical Center, USA)

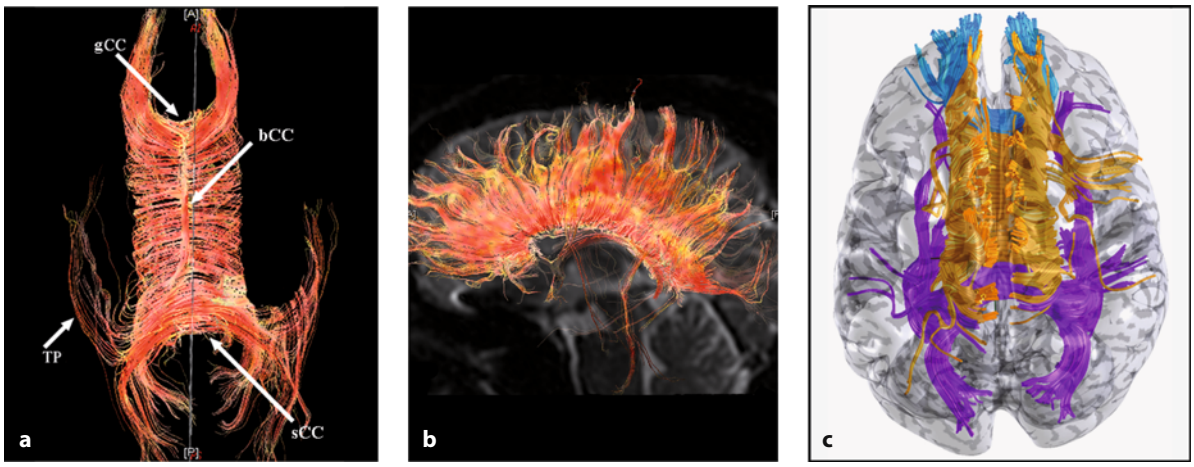

Figure 2.11 a–c

The corpus callosum is a broad thick plate of dense mylinated fibers that reciprocally interconnect broad regions of the cortex. The genu (gCC) contains fibers interconnecting rostral parts of the frontal lobes. Fibers from the remaining parts of the frontal lobe and the parietal lobe traverse the body of the corpus callosum (bCC). Fibers transversing the splenium relate regions of the temporal and occipital lobes. The tapetum (TP) is the extension into the hemisphere of the corpus callosum lying adjacent to the ventricular ependyma (Courtesy of White ML MD and Zhang Y MD, The University of Nebraska Medical Center, USA)

the cerebellum and medulla (Fig. 2.13). The ICP carries mostly afferent pathways from the spinal cord and conveys impulses from vestibular receptors, associated with balance coordination. The corpus medullare is a compact mass of cerebellar white matter imbedding four deep nuclei (dentate, fastigial, globose, and emboliform), continuous with the three cerebellar peduncles [34]. The corpus medullare splits in the roof of the fourth ventricle at an acute angle (fastigium) and forms the superior and inferior medullary vela.

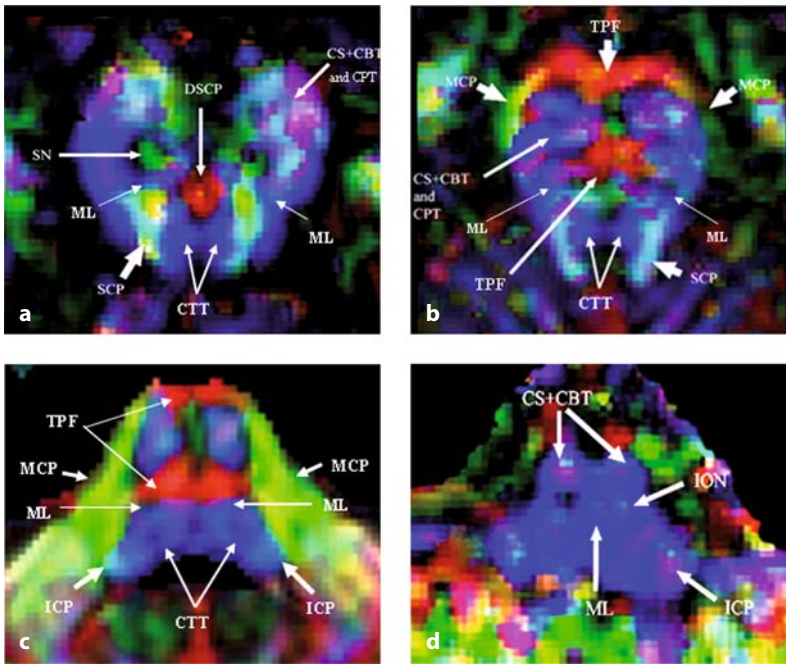

Figure 2.12 a–d

a The midbrain: The crus cerebri consists of corticopontine, corticobulbar and corticospinal fibers (CPT,CBT,CST). The tegmentum and crus cerebri are separated by the substantia nigra (SN). The superior cerebellar peduncle (SCP) and their decussation (DSCP, round red spot) are noted in the caudal midbrain tegmentum. The dorsal tegmental portion contains the central tegmental tract (CTT) and medial lemniscus (ML). **b c** The upper (**b**) and lower (**c**) pons: The ventral part of the pons contains CPT, CBT, CST, pontine nuclei, and transverse pontine fibers (TPF). The middle cerebellar peduncle (MCP) arises from pontine nuclei projecting to the cerebellar hemisphere. The inferior cerebellar peduncle is noted on each side of the lower part of the forth ventricle. **d** The medulla: The inferior olivary nuclei (ION), medullary pyramids (CST, CBT), medial leminiscus (ML) and ICP are demonstrated (Courtesy of White ML MD and Zhang Y MD, The University of Nebraska Medical Center, USA, and Courtesy of Salamon N MD, The University of California, Los Angelus, USA)

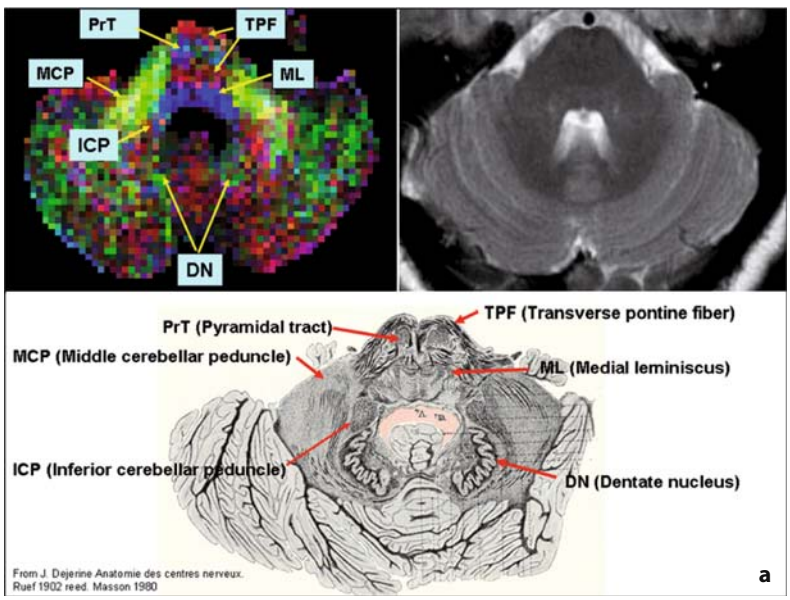

Figure 2.13 a–h

a-c Axial (**a**), Coronal (**b**), and Sagittal (**c**) images. The ventral part of the pons consists of pyramidal tracts (PrT), pontine nuclei, and transverse pontine fibers (TPF) projecting to the cerebellum. The medial leminiscus (ML) is large ascending fibers and terminates in the ventral posteriolateral nucleus of the thalamus. The middle cerebellar peduncle (MCP) consists of predominantly afferent fibers from TPF and most of them decussate and terminate as mossy fibers projecting to the cerebellar hemisphere. The inferior cerebellar peduncle (ICP), seen on each side of the lower part of the forth ventricle, connects the cerebellum and medulla

Figure 2.13 a–h

d-f Parasagittal images. The corpus medullare is a compact mass of cerebellar white matter imbedding 4 deep cerebellar nuclei (dentate, fastigial, globose, and emboliform), continuous with the three cerebellar peduncles. The superior cerebellar peduncle (SCP) is seen on each side of the upper part of the forth ventricle, decussates completely in the caudal midbrain tegmentum

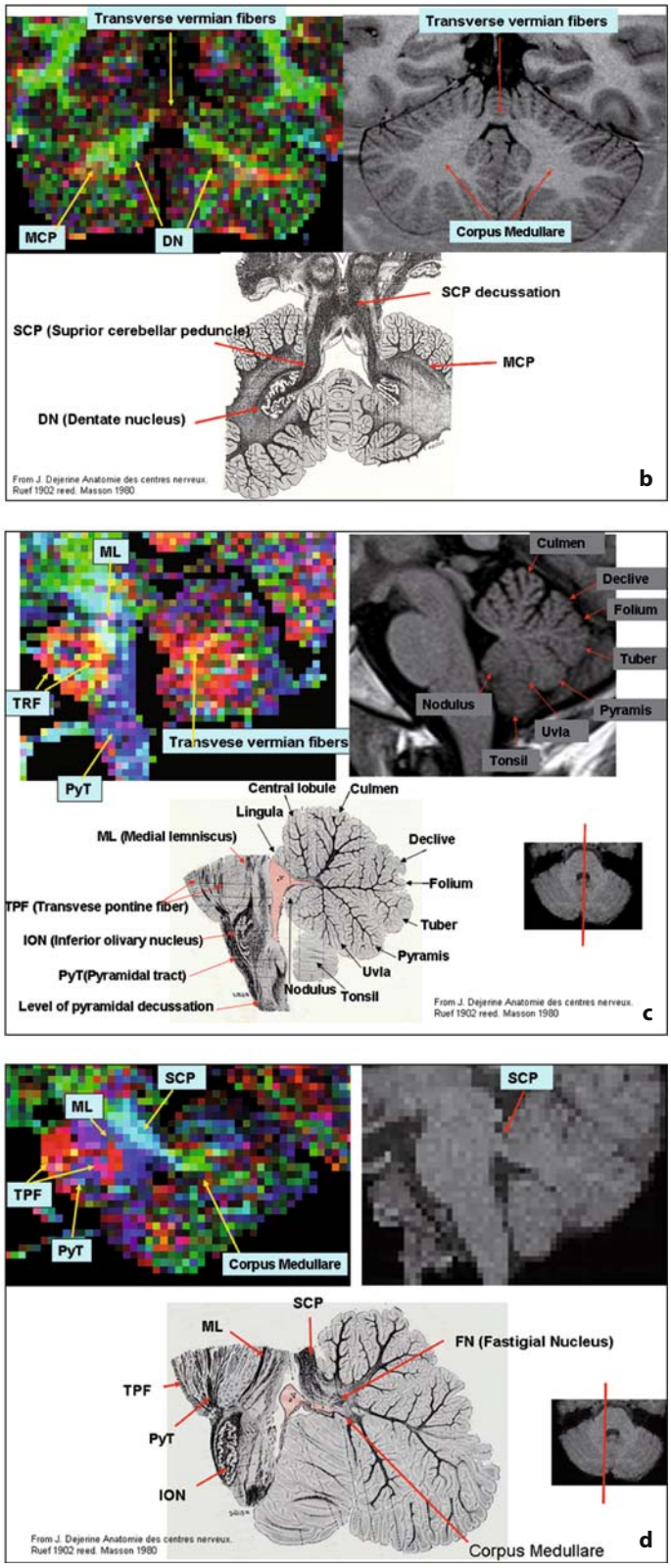

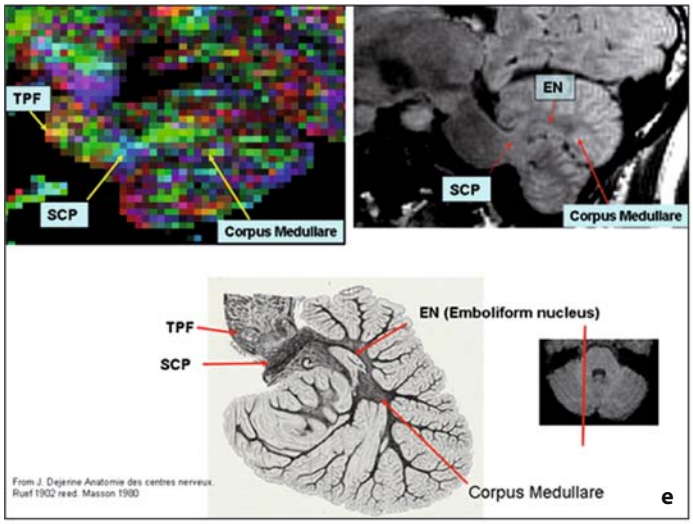

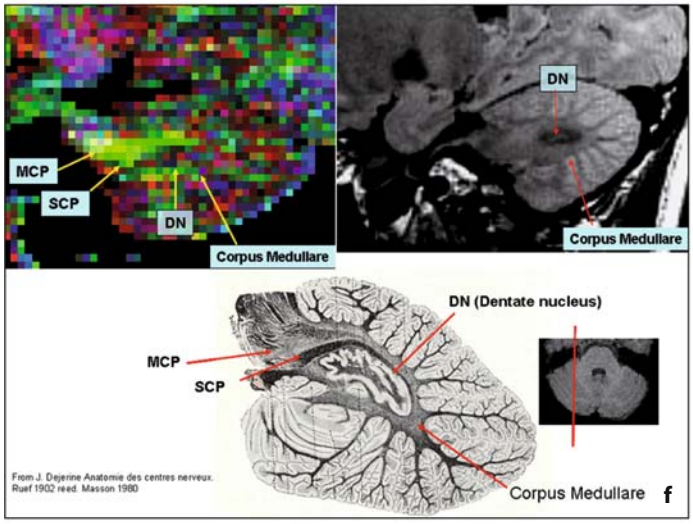

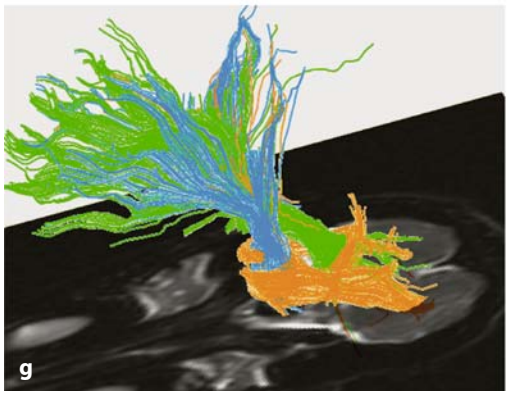

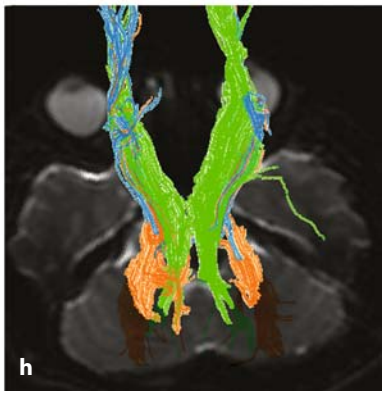

Figure 2.13 a–h

g, h Fiber tractography. SCP is predominantly efferent pathways arising from cerebellar cortex and deep cerebellar nuclei to thalamus and cerebral cortex (green). Pyramidal tracts (blue), and middle cerebellar peduncles and transverse pontine fibers (orange) are demonstrated (Courtesy of Salamon N MD, The University of California, Los Angelus, USA)

2.5 Conclusion

Good knowledge of the DW appearance of the normal adult and pediatric brain and variations is necessary to avoid misinterpretation. In children it is also important to match the findings with those of normal children of the same age. DT imaging is useful for understanding the normal white matter fiber tract anatomy.

References

1. Yoshiura T, Wu O, Sorensen AG (1999) Advanced MR techniques: diffusion MR imaging, perfusion MR imaging, and spectroscopy. Neuroimaging Clin N Am 9:439–453
2. Asao C, Hirai T, Yoshimatsu S, et al. (2007) Human cerebral cortices: signal variation on diffusion-weighted MR imaging. Neuroradiology 50:205-211
3. Chun T, Filippi CG, Zimmerman RD, Ulug AM (2000) Diffusion changes in the aging human brain. Am J Neuroradiol 21:1078–1083
4. Engelter ST, Provenzale JM, Petrella JR, DeLong DM, MacFall JR (2000) The effect of aging on the apparent diffusion coefficient of normal-appearing white matter. Am J Roentgenol 175:425–430
5. Helenius J, Soinne L, Perkio J (2002) Diffusion-weighted MR imaging in normal human brains in various age groups. Am J Neuroradiol 23:194–199
6. Gideon P, Thomsen C, Henriksen O (1994) Increased self-diffusion of brain water in normal aging. J Magn Reson Imaging 4:185–188
7. Nusbaum AO, Tang CY, Buchsbaum MS, Wei TC, Atlas SW (2001) Regional and global changes in cerebral diffusion with normal aging. Am J Neuroradiol 22:136–142
8. Abe O, Aoki S, Hayashi N, et al. (2002) Normal aging in the central nervous system: quantitative MR diffusion-tensor analysis. Neurobiol Aging 23:433–441
9. Kinoshita T, Moritani T, Hiwatashi A, et al. (2005) Clinically silent choroid plexus cyst: evaluation by diffusion-weighted MRI. Neuroradiology 47:251-255
10. Sakuma H, Nomura Y, Takeda K, et al. (1991) Adult and neonatal human brain: diffusional anisotropy and myelination with diffusion-weighted MR imaging. Radiology 180:229– 233
11. Morriss MC, Zimmerman RA, Bilaniuk LT, Hunter JV, Haselgrove JC (1999) Changes in brain water diffusion during childhood. Neuroradiology 41:929–934
12. Tanner SF, Ramenghi LA, Ridgway JP, et al. (2000) Quantitative comparison of intrabrain diffusion in adults and preterm and term neonates and infants. Am J Roentgenol 174:1643–1649
13. Neil JJ, Shiran SI, McKinstry RC, et al. (1998) Normal brain in human newborns: apparent diffusion coefficient and diffusion anisotropy measured by using diffusion tensor MR imaging. Radiology 209:57–66
14. Engelbrecht V, Scherer A, Rassek M, Witsack HJ, Modder U (2002) Diffusion-weighted MR imaging in the brain in children: findings in the normal brain and in the brain with white matter diseases. Radiology 222:410–418
15. Forbes KP, Pipe JG, Bird CR (2002) Changes in brain water diffusion during the 1st year of life. Radiology 222:405–409
16. Nucifora PGP, Verma R, Lee SK, Melhem ER (2007) Diffusion-tensor MR imaging and tractography: exploring brain microstructure and connectivity. Radiology 245:367-384
17. Assaf Y, Pasternak O (2008) Diffusion tensor imaging (DTI)-based white matter mapping in brain research: a review. J Mol Neurosci 34:51-61
18. Alexander AL, Lee JE, Lazar M, Field AS (2007) Diffusion tensor imaging of the brain. Neurotherapeutics 4:316-329
19. Jellison BJ, Field AS, Medow J, Lazar M, Salamat MS, Alexander AL (2004) Diffusion tensor imaging of cerebral white matter: a pictorial review of physics, fiber tract anatomy, and tumor imaging patterns. AJNR Am J Neuroradiol 25:356-369
20. Wakana S, Jiang H, Nagae-Poetscher LM, van Zijl PC, Mori S(2004) Fiber tract-based atlas of human white matter anatomy. Radiology 230:77-87
21. Mamata H, Mamata Y, Westin CF, Shenton ME, Kikinis R, Jolesz FA, Maier SE (2002) High-resolution line scan diffusion tensor MR imaging of white matter fiber tract anatomy. AJNR Am J Neuroradiol 23:67-75
22. Tamura H, Takahashi S, Kurihara N, Yamada S, Hatazawa J, Okudera T (2003) Practical visualization of internal structure of white matter for image interpretation: staining a spin-echo T2-weighted image with three echo-planar diffusion-weighted images. AJNR Am J Neuroradiol 24:401-409
23. Türe U, Yaşargil MG, Pait TG. Is there a superior occipitofrontal fasciculus? A microsurgical anatomic study. Neurosurgery. 1997 Jun;40(6):1226-32.
24. Kier EL, Staib LH, Davis LM, Bronen RA.MR imaging of the temporal stem: anatomic dissection tractography of the uncinate fasciculus, inferior occipitofrontal fasciculus, and Meyer's loop of the optic radiation. AJNR Am J Neuroradiol. 2004 May;25(5):677-91.
25. Schmahmann JD, Pandya DN (2006) Fiber pathways of the brain. Oxford University Press, Oxford, New York
26. Schmahmann JD, Pandya DN, Wang R, Dai G, D'Arceuil HE, de Crespigny AJ, Wedeen VJ (2007) Association fibre pathways of the brain: parallel observations from diffusion spectrum imaging and autoradiography. Brain 130:630-653
27. Schmahmann JD, Pandya DN (2007) The complex history of the fronto-occipital fasciculus. J Hist Neurosci 16:362-377
28. Utsunomiya H, Nakamura Y (2007) MR features of the developing perianterior horn structure including subcallosal fasciculus in infants and children. Neuroradiology 49:947-954
29. Aoki S, Iwata NK, Masutani Y, et al. (2005) Quantitative evaluation of the pyramidal tract segmented by diffusion tensor tractography: feasibility study in patients with amyotrophic lateral sclerosis. Radiat Med 23:195-199

30. Yamada K, Sakai K, Hoogenraad FG, Holthuizen R, Akazawa K, Ito H, Oouchi H, Matsushima S, Kubota T, Sasajima H, Mineura K, Nishimura T (2007) Multitensor tractography enables better depiction of motor pathways: initial clinical experience using diffusion-weighted MR imaging with standard b-value. AJNR Am J Neuroradiol 28:1668-1673
31. Taoka T, Sakamoto M, Nakagawa H, Nakase H, Iwasaki S, Takayama K, Taoka K, Hoshida T, Sakaki T, Kichikawa K (2008) Diffusion tensor tractography of the Meyer loop in cases of temporal lobe resection for temporal lobe epilepsy: correlation between postsurgical visual field defect and anterior limit of Meyer loop on tractography. AJNR Am J Neuroradiol 2008 [Epub ahead of print]
32. Kitajima M, Korogi Y, Takahashi M, Eto K (1996) MR signal intensity of the optic radiation. AJNR Am J Neuroradiol 17:1379-1383
33. Salamon N, Sicotte N, Alger J, Shattuck D, Perlman S, Sinha U, Schultze-Haakh H, Salamon G (2005) Analysis of the brain-stem white-matter tracts with diffusion tensor imaging. Neuroradiology 47:895-902
34. Salamon N, Sicotte N, Drain A, Frew A, Alger JR, Jen J, Perlman S, Salamon G (2007) White matter fiber tractography and color mapping of the normal human cerebellum with diffusion tensor imaging. J Neuroradiol 34:115-128

Pitfalls and Artifacts of DW Imaging

In collaboration with A. Hiwatashi and J. Zhong

3.1 Introduction

There are many inherent artifacts and pitfalls in diffusion-weighted (DW) imaging of the brain that are important to recognize to avoid misinterpretations.

3.2 Influence of ADC and T2 on the DW Appearance

Diffusion-weighted images are inherently T2 weighted and changes in T2 signal characteristics will thus influence the appearance of DW images independent of tissue diffusibility [1–16]. The effect of T2 prolongation, so-called "T2 shine-through", is well known. Less well known is the balance between apparent diffusion coefficient (ADC) and T2, sometimes called T2 washout. Also the effect of T2 shortening, or T2 blackout, and magnetic susceptibility effects will influence the DW appearance in many situations. This chapter will illustrate and discuss the effects of T2 and ADC on DW images.

3.2.1 Concepts

The signal intensity (SI) on DW images is influenced by T2, ADC, the b-factor, the spin density (SD) and the echo time (TE), and is calculated as follows:

$$SI=SI_{b=0}e^{-bADC}$$

However,

$$SI_{b=0}=kSD(1-e^{-TR/T1})e^{-TE/T2}$$

For TR >>T1

$$SI=kSDe^{-TE/T2}e^{-bADC}$$

where k is a constant, TR is repetition time, and $SI_{b=0}$ is the signal intensity on the spin-echo echo-planar image (b_0 image) [1, 2, 5, 7, 8, 10, 12, 16].

To evaluate the tissue T2 and ADC, we should pay attention to the images discussed below as well as isotropic DW images and b_0 images [3–5, 7, 8, 10, 11, 13–16].

3.2.2 Apparent Diffusion Coefficient Maps

To evaluate the diffusibility, ADC is calculated as:

$$ADC=-ln\ (SI/SI_{b=0})/b$$

Subsequently, increased ADC causes decreased SI on DW images, and decreased ADC causes increased SI on DW images [3–5, 7, 10, 15, 16].

3.2.3 Exponential Images

To remove the T2-weighted contrast, the DW image can be divided by the b_0 image to create an "exponential image" [4, 7, 10, 15].

The signal intensity (SIe_{DWI}) on the exponential image is calculated as:

$$SIe_{DWI}=SI/SI_{b=0}=e^{-bADC}$$

Therefore, this image can eliminate the effect of T2. Contrary to ADC maps, hyperintensity on exponential DW images means decreased ADC, and hypointensity means increased ADC.

3.3 Clinical Conditions

3.3.1 T2 Shine-through

This is a well-known phenomenon that causes hyperintensity on DW images by means of T2 prolongation [3–5, 7, 8, 10, 11, 15, 16]. If ADC is decreased at the same time, this can result in an accentuation of the hyperintensity on DW images (Figs. 3.1–3.3).

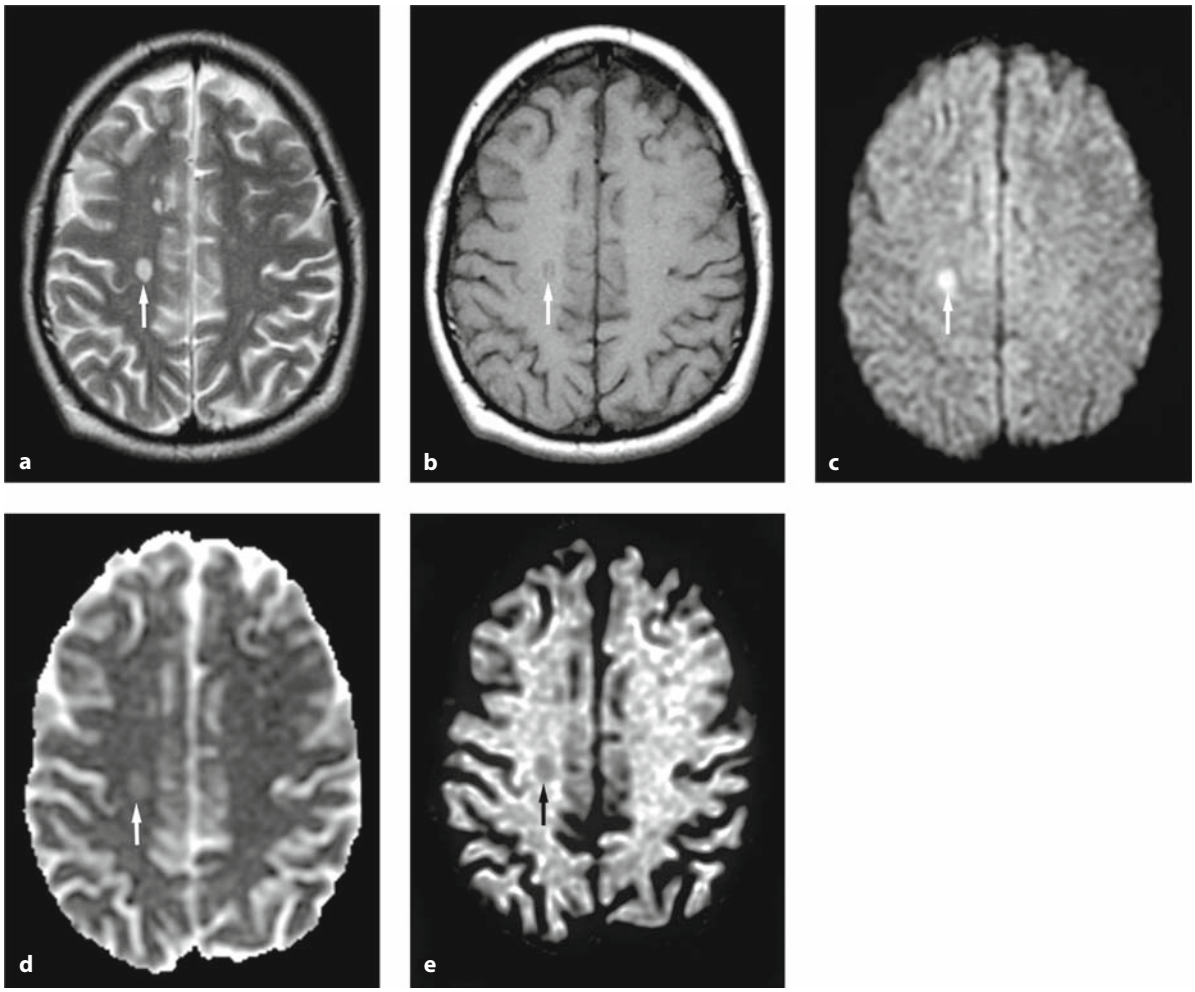

Figure 3.1 a–e

T2 shine-through in a 35-year-old female patient with multiple sclerosis and weakness of the lower extremities. **a** T2-weighted image shows several hyperintense lesions, with the largest in the right frontal lobe (*arrow*). **b** On T1-weighted image the lesion was hypointense (*arrow*) and did not enhance with contrast (not shown). **c** On DW image the lesion is hyperintense (*arrow*). **d** ADC map also shows hyperintensity in the lesion (1.2×10^{-3} mm^2/s; *arrow*). **e** Exponential image eliminates the T2 effect and shows the lesion to be hypointense (*arrow*). This confirms that the hyperintensity on DW image is due to a T2 shine-through effect

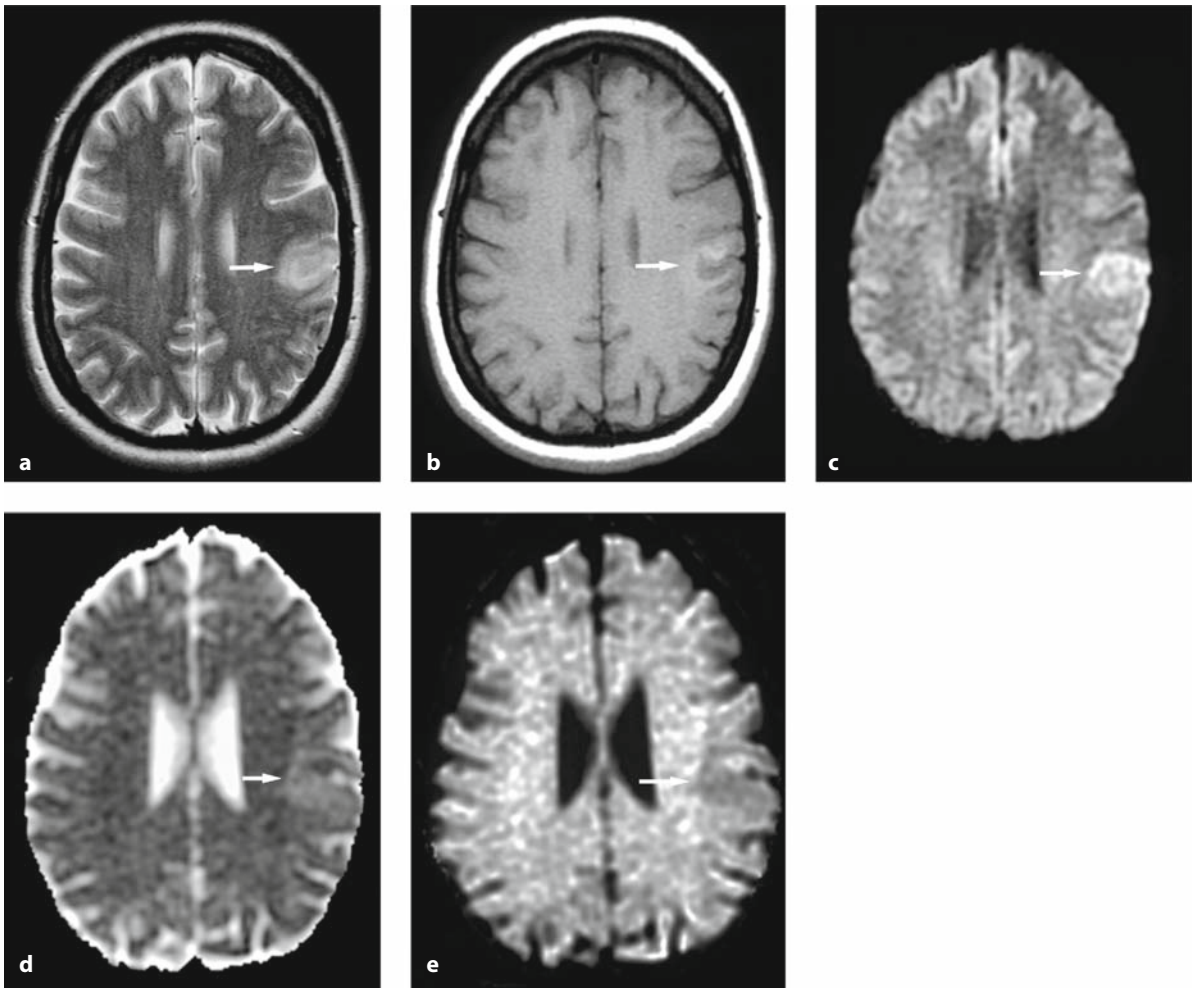

Figure 3.2 a–e

T2 shine-through in a 45-year-old female patient with seizures caused by an anaplastic astrocytoma. **a** T2-weighted image shows a hyperintense lesion in the left frontal lobe (*arrow*). **b** On T1-weighted image the lesion is hypointense with a peripheral hyperintense area (*arrow*). The lesion did not enhance with contrast (not shown). **c** DW image shows hyperintensity (*arrow*). **d** ADC map also shows hyperintensity in the lesion ($0.98–1.35\times10^{-3}$ mm^2/s; *arrow*). **e** Exponential image eliminates the T2 effect and shows the lesion to be hypointense (*arrow*). This confirms that the hyperintensity on the DW image is due to a T2 shine-through effect

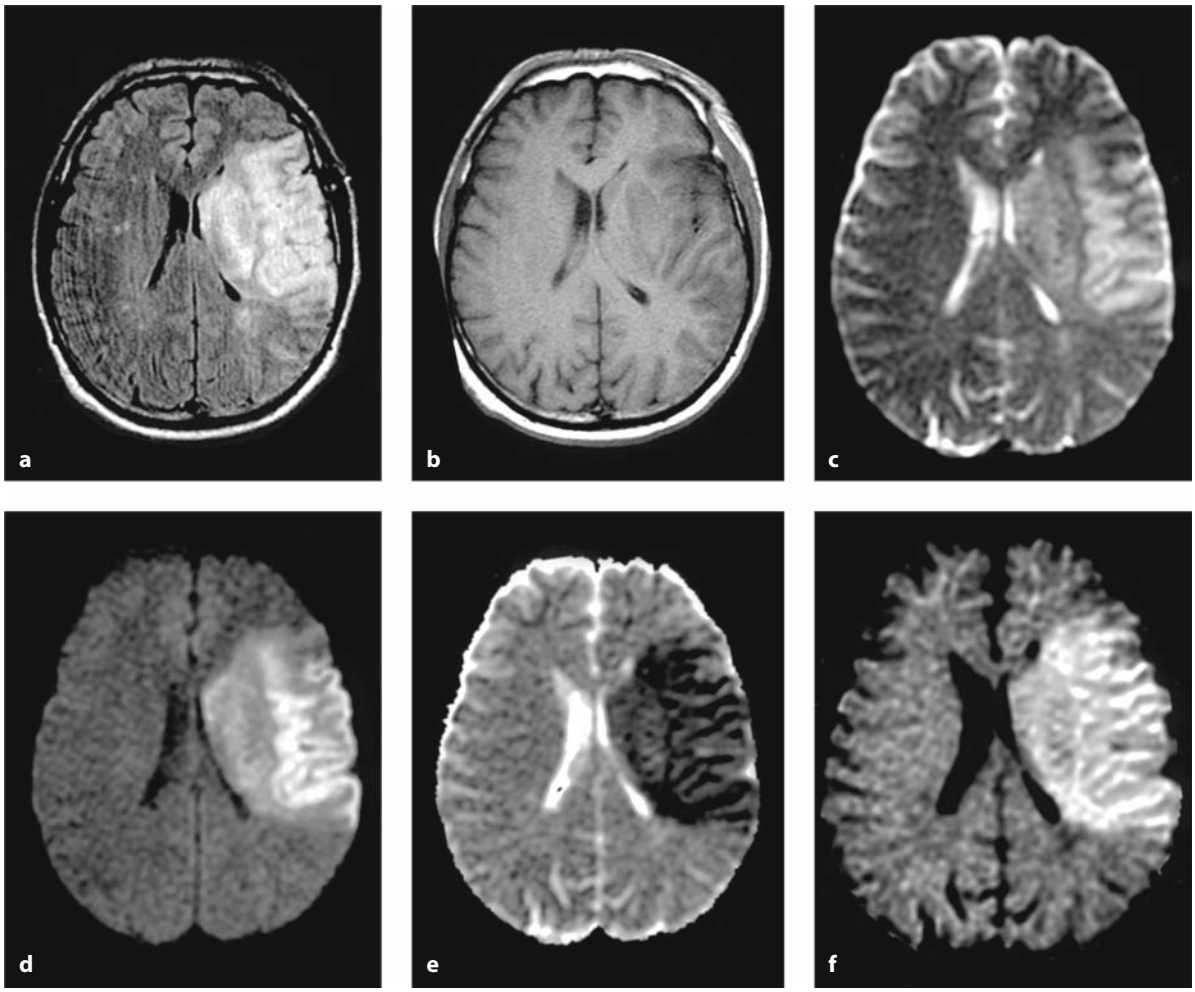

Figure 3.3 a–f

T2 shine-through and restricted diffusion in a 56-year-old male patient with right-sided weakness due to acute infarction. MR imaging was obtained 24 hours after the onset of symptoms. **a** FLAIR image shows a hyperintense lesion in the left middle cerebral artery territory. **b** On T1-weighted image the lesion is hypointense. **c** On T2-weighted image (b_0) the lesion is hyperintense. **d** DW image also shows hyperintensity in the lesion. **e** ADC map shows hypointensity in the lesion ($0.27–0.45\times10^{-3}$ mm^2/s). **f** On the exponential image, which eliminates the T2 effect, the lesion remains hyperintense. This confirms that the DW hyperintensity is due to both restricted diffusion and T2 prolongation

3.3.2 T2 Washout

This implies that isointensity on DW images is the result of a balance between hyperintensity on T2-weighted images and increased ADC [13, 14, 16]. This is often seen in vasogenic edema, where the combination of increased ADC and hyperintensity on T2-weighted images will result in isointensity on DW images (Fig. 3.4).

To the best of our knowledge there have been no systematic reports on pathological conditions with isointensity on DW images, caused by a balance of hypointensity on T2-weighted images and decreased ADC.

Figure 3.4 a–d

T2 washout in a 45-year-old female patient with hypertension, seizures and posterior reversible encephalopathy syndrome. **a** FLAIR image shows hyperintense lesions in the bilateral occipital lobe (*arrows*). **b** T2-weighted image (b_0) also shows hyperintensity of the lesions (*arrows*). **c** DW image shows mild hyperintensity in the lesions. **d** ADC map shows hyperintensity of the lesions (1.18–1.38×10^{-3} mm^2/s; *arrows*). With the strong T2 prolongation one would expect more hyperintensity on the DW image, but the T2 shine-through effect is reduced by the hyperintensity on the ADC, resulting in a balance between increased diffusibility and hyperintensity on the T2-weighted image (T2 wash-out)

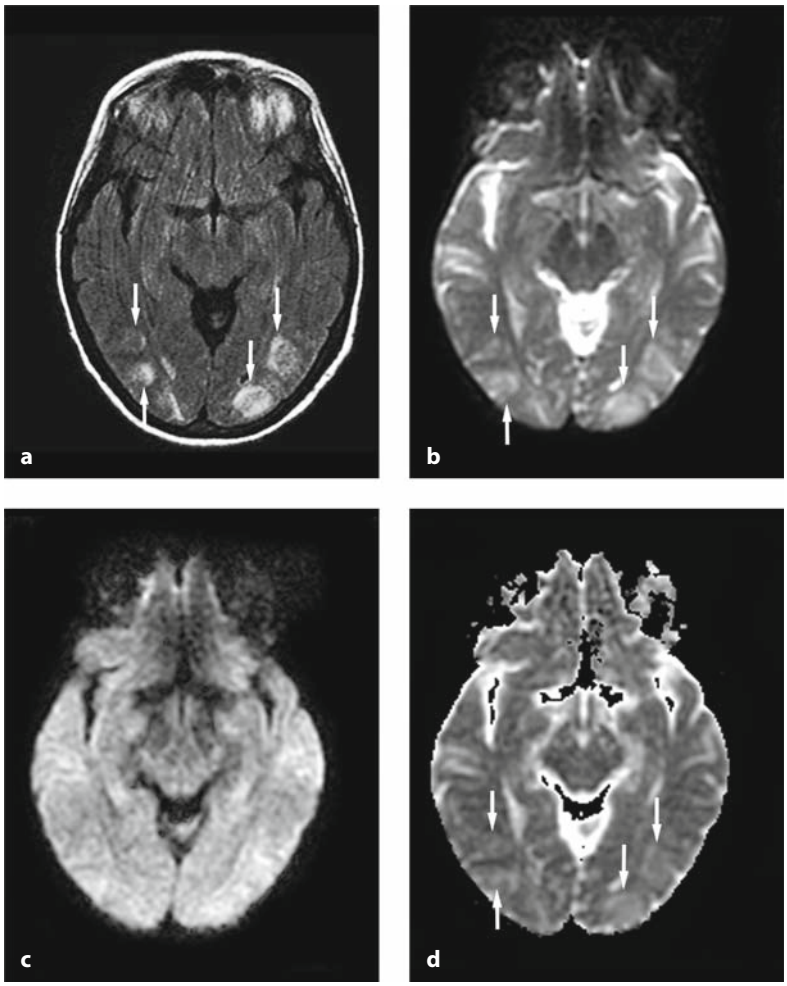

3.3.3 T2 Blackout

This indicates hypointensity on DW images caused by hypointensity on T2-weighted images and is typically seen in some hematomas [9,16]. Paramagnetic susceptibility artifacts may occur in this situation (Figs. 3.5 and 3.6).

3.4 Artifacts

Numerous artifacts can be generated during the acquisition of DW images. There are five main artifacts of single-shot DW echo-planar imaging:

1. Eddy current artifacts due to echo-planar imaging phase-encoding and readout gradients, and motion-probing gradient pulses for diffusion weighting
2. Susceptibility artifacts
3. N/2 ghosting artifacts
4. Chemical shift artifacts
5. Motion artifacts

We will discuss each artifact separately.

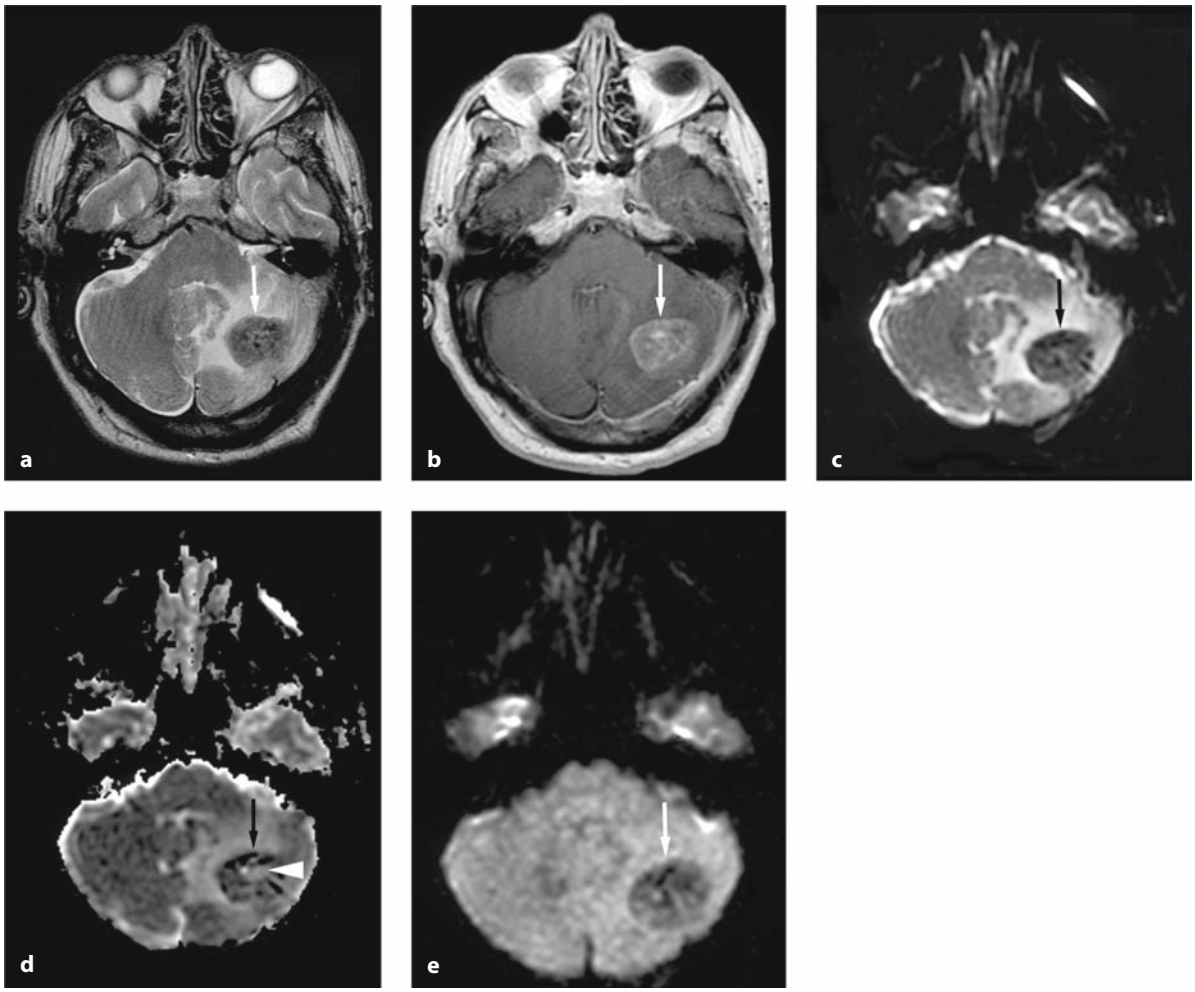

Figure 3.5 a–e

T2 blackout in lung cancer metastasis in a 62-year-old male patient with adenocarcinoma of the lung. **a** T2-weighted image shows a hypointense mass (*arrow*) with surrounding edema in the left cerebellar hemisphere. **b** Gadolinium-enhanced T1-weighted image shows heterogeneous enhancement of the mass (*arrow*). **c** T2-weighted image (b_0) also shows hypointensity in the lesion with surrounding hyperintense edema (*arrow*). **d** ADC map shows central hyperintensity ($1.63–2.35\times10^{-3}$ mm^2/s; *arrowhead*) and peripheral hypointensity ($1.13–1.38\times10^{-3}$ mm^2/s; *arrow*) of the mass. There is also hyperintensity of the surrounding tissue, consistent with vasogenic edema. **e** DW image shows heterogeneous hypointensity of the mass (*arrow*) and isointensity of the surrounding edema. The DW hypointensity of the mass (*arrow*) is due to the increased diffusibility and the hypointensity on the T2-weighted image (T2 blackout). The isointensity in the surrounding edema is due to the balance between increased diffusibility and hyperintensity on the T2-weighted image (T2 washout)

3.4.1 Eddy Current Artifacts

Eddy currents are electrical currents induced in a conductor by a changing magnetic field. Eddy currents can occur in patients and in the MR scanner itself, including cables or wires, gradient coils, cryoshields and radiofrequency shields [17]. Eddy currents are particularly severe when gradients are turned on and off quickly, as in echo-planar imaging pulse sequences. Gradient waveforms are distorted due to eddy currents, which results in image artifacts, including spatial blurring and misregistration. In single-shot DW

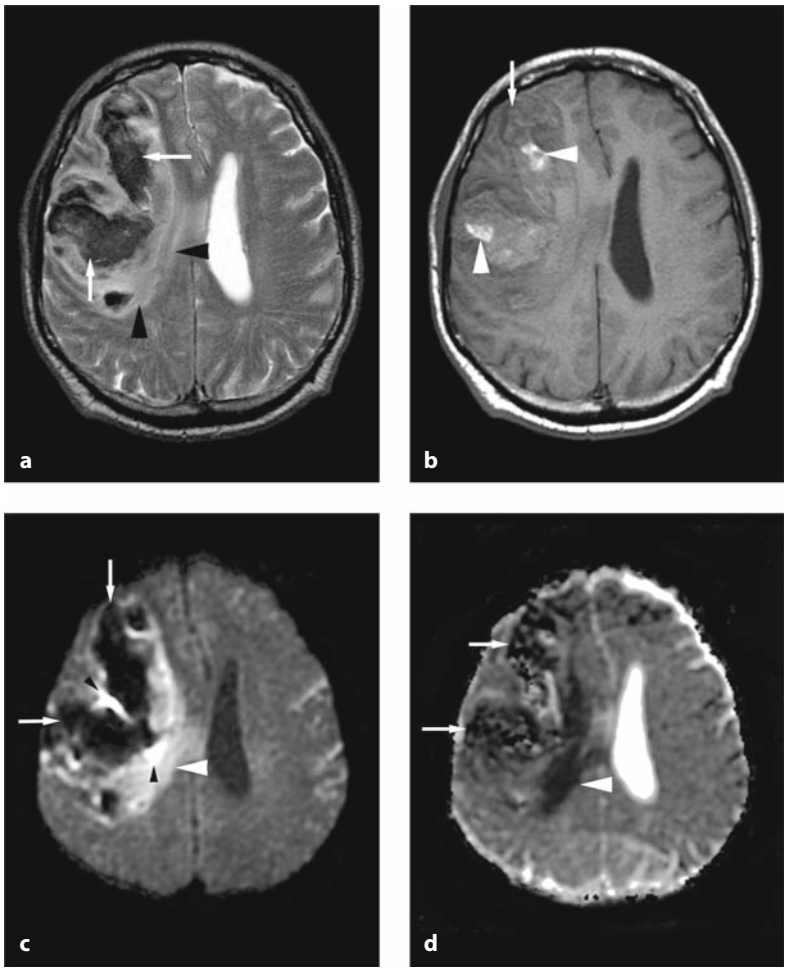

Figure 3.6 a–d

T2 blackout from susceptibility artifacts in acute hemorrhage (deoxyhemoglobin and intracellular met-hemoglobin) in a 74-year-old man with left-sided weakness. MR imaging was obtained 24 hours after the onset of symptoms. **a** T2-weighted image shows hypointense lesions in the right frontoparietal lobes (*arrows* deoxyhemoglobin and intracellular met-hemoglobin) with areas of surrounding hyperintensity consistent with edema (*arrowheads*). **b** T1-weighted image shows the heterogeneous lesion with hypointensity (*arrow* deoxyhemoglobin) and hyperintensity (*arrowheads* intracellular met-hemoglobin). **c** DW image shows hypointensity (*arrows* deoxy-hemoglobin and intracellular met-hemoglobin) and hyperintensity in the region of edema (*arrowhead*). The surrounding hyperintense rims (*small arrowheads*) are due to magnetic susceptibility artifacts. **d** ADC could not be calculated accurately in the T2 "dark" hematoma due to magnetic susceptibility artifacts (*arrows*). The surrounding areas of hypointensity (*arrowhead*) probably correspond to cytotoxic edema surrounding the hematoma. This example shows how T2 hypointensity from susceptibility effects can produce a complex appearance in and around cerebral hemorrhage

echo-planar imaging, eddy currents are due to both echo-planar imaging gradients and motion-probing gradients, which lead to image distortions (Fig. 3.7). Correction of image distortion is essential to calculate ADC values and especially to quantify anisotropy with diffusion tensor imaging.

Correction methods: (1) correction of distortion by using post-processing [18–21], (2) pre-emphasis or pre-compensation, purposely distorting the gradient-driving currents [22, 23], (3) shielded gradients, redesigning the magnet to incorporate shielding coils between the gradient coils and the main windings [24].

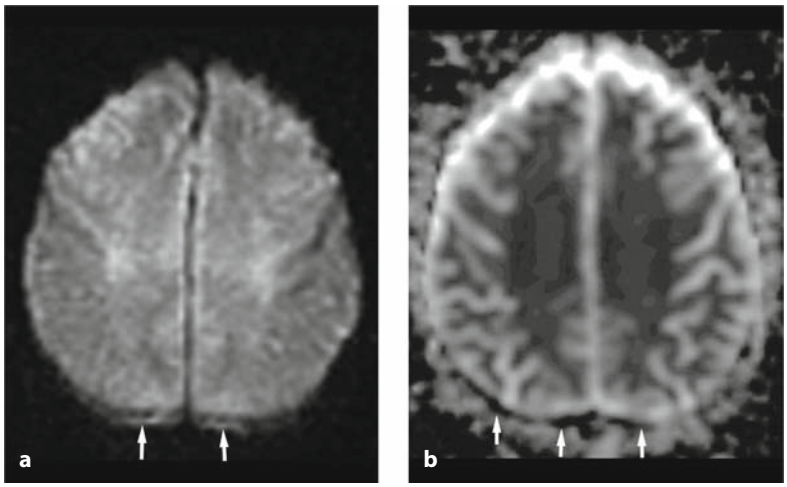

Figure 3.7 a, b

Misregistration due to eddy current artifact. a, b Misregistration artifact is noted in the occipital regions (*arrows*) on DW image (**a**) and the ADC map (**b**). Gradient waveforms are distorted due to eddy currents, which results in this misregistration

3.4.2 Susceptibility Artifacts

Single-shot echo-planar imaging is sensitive to susceptibility artifacts, especially frequency and phase errors due to paramagnetic susceptibility effects. These artifacts are seen near the skull base, especially near the air in paranasal sinuses and mastoid (Fig. 3.8). Susceptibility artifacts are more severe along the phase-encoding direction and phase encoding should thus be along the anterior–posterior direction for axial DW images. Coronal and sagittal DW images are helpful in detecting lesions in certain locations, such as the hippocampus and the brain stem, and to identify susceptibility artifacts (Fig. 3.9). Increased matrix size leads to elongation of the readout time, which causes even larger image distortions.

Correction methods: (1) multi-shot echo-planar imaging (to reduce the readout time, to enable high-resolution scanning) [25, 26], (2) line scan [27,28], (3) single-shot fast spin echo (SSFSE) [29, 30], (4) periodically rotated overlapping parallel lines with enhanced reconstruction (PROPELLER) [31, 32], (5) sensitive encoding (SENSE)/array spatial and sensitivity-encoding technique (ASSET), undersampling of k-space which enables effective band width and shortens readout time, providing thin section and high-resolution matrix [33].

3.4.3 N/2 Ghosting Artifact (Nyquist Ghost)

The N/2 ghosting artifact occurs when there are differences between the even and odd lines of the k-space. Phase error is due to hardware imperfections (eddy currents, imperfect timing of even and odd echo, imperfect gradients, and magnetic field inhomogeneity), which can be produced by on-off switching during readout gradients. The ghosts in this artifact are always shifted by half of the field of view in the phase-encoding direction (Fig. 3.10). This ghost can produce severe artifacts when ADC maps are calculated.

Correction methods: (1) reduce eddy currents, (2) adjust gradients and magnetic field homogeneity, (3) high b-value, (4) fluid-attenuated inverse-recovery (FLAIR) DW imaging (reduce cerebrospinal fluid signal) [33, 34].

3.4.4 Chemical Shift

In echo-planar DW imaging, chemical shift artifacts due to the different resonance frequencies in water and fat are produced along the phase-encoding direction, while they are along the frequency-encoding direction in conventional spin-echo type MR imaging. This artifact is more severe in echo-planar imaging than in conventional spin-echo type imaging. Effective fat suppression techniques, such as the chemical shift selective (CHESS) method and the spectral selective radiofrequency excitation method are necessary.

Correction methods: appropriate fat suppression techniques.

Figure 3.8

Susceptibility artifact. Susceptibility artifacts are seen near the air content of the mastoids (*arrows*). This is generally prominent in echo-planar sequences

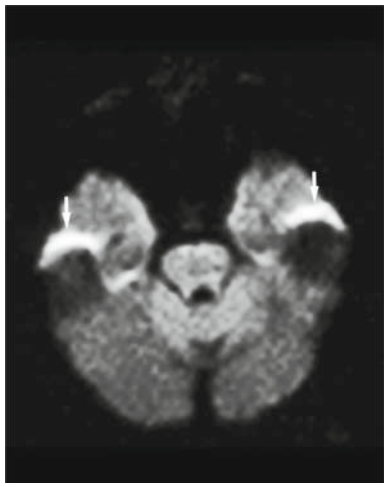

Figure 3.9 a–d

Susceptibility artifact in coronal and sagittal plane DW images. Coronal DW image (**a**) and the ADC map (**b**) are used to evaluate the hippocampus, but susceptibility artifacts distort the image near the mastoids. Sagittal DW image (**c**) and the ADC map (**d**) show a pontine infarct as hyperintense with decreased ADC (*arrowhead*). Susceptibility artifacts are caused by air in the ethmoid and sphenoid sinuses (*arrows*)

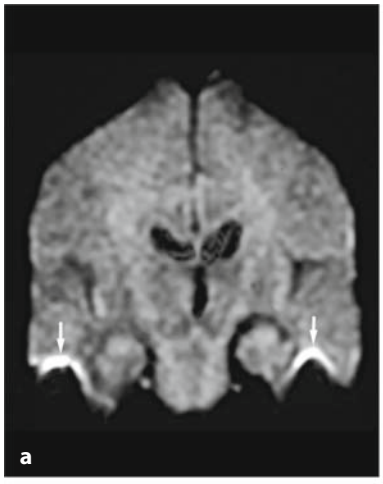

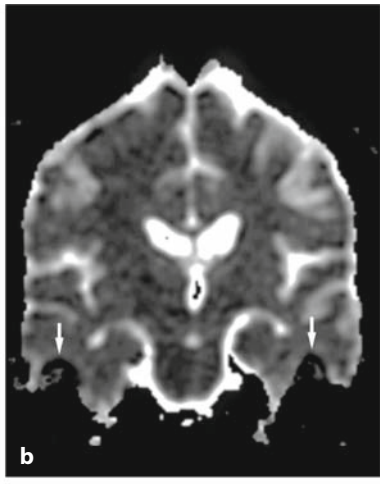

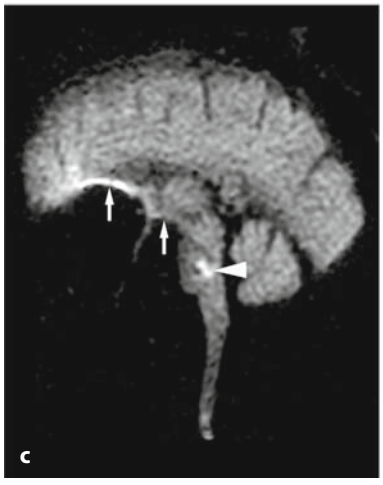

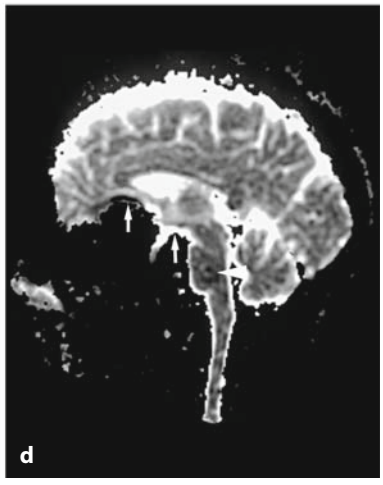

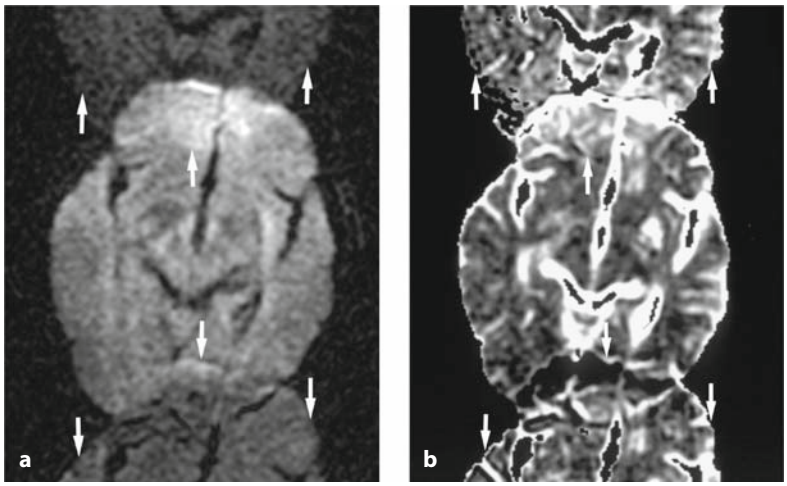

Figure 3.10 a, b

N/2 ghosting artifact. **a** DW image shows N/2 ghosting artifacts (*arrows*), which are always shifted by half of the field of view in the phase-encoding direction. **b** On the ADC map severe N/2 ghosting artifacts are also seen (*arrows*)

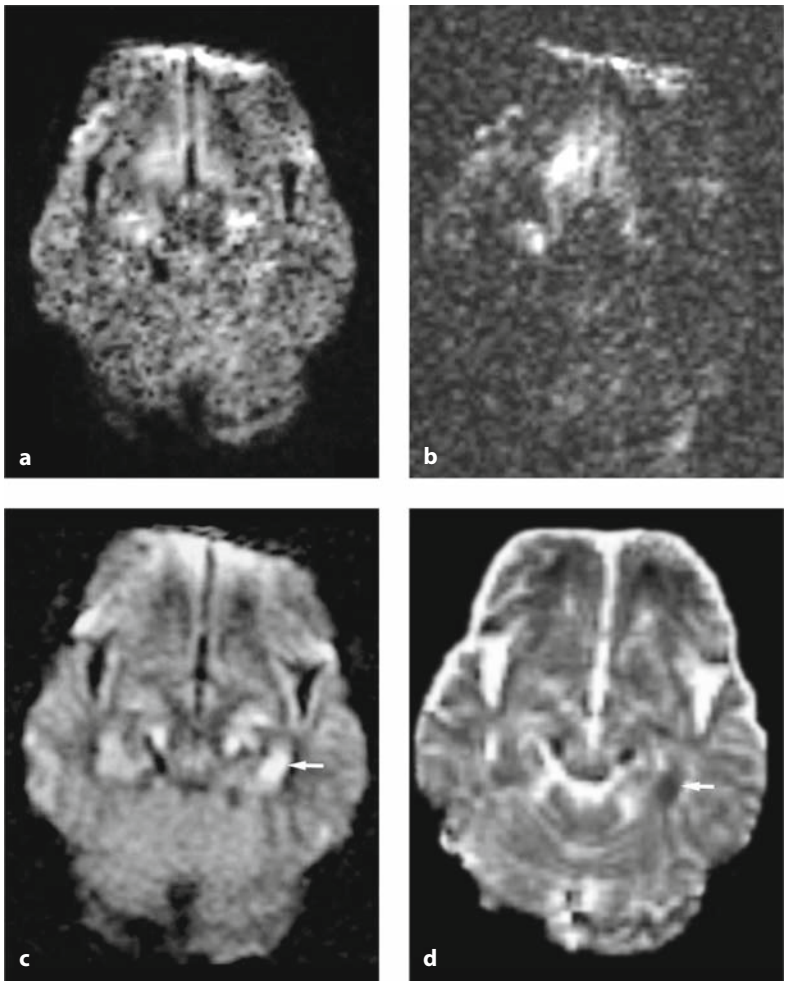

Figure 3.11 a–d

Motion artifacts due to head motion during the scan of a patient with status epilepticus. **a** It is difficult to evaluate the DW image because of severe motion artifacts. **b** In the raw data of the DW imaging, the *x* axis image is corrupted by head motion during the scan. **c** The *y* axis image is free from the artifacts. This image shows a hyperintense lesion in the left hippocampus (*arrow*). **d** ADC map of *y* axis image also shows decreased ADC of the lesion (transferred to a workstation for image processing, using a home-made code, which is based on the numerical computation software)

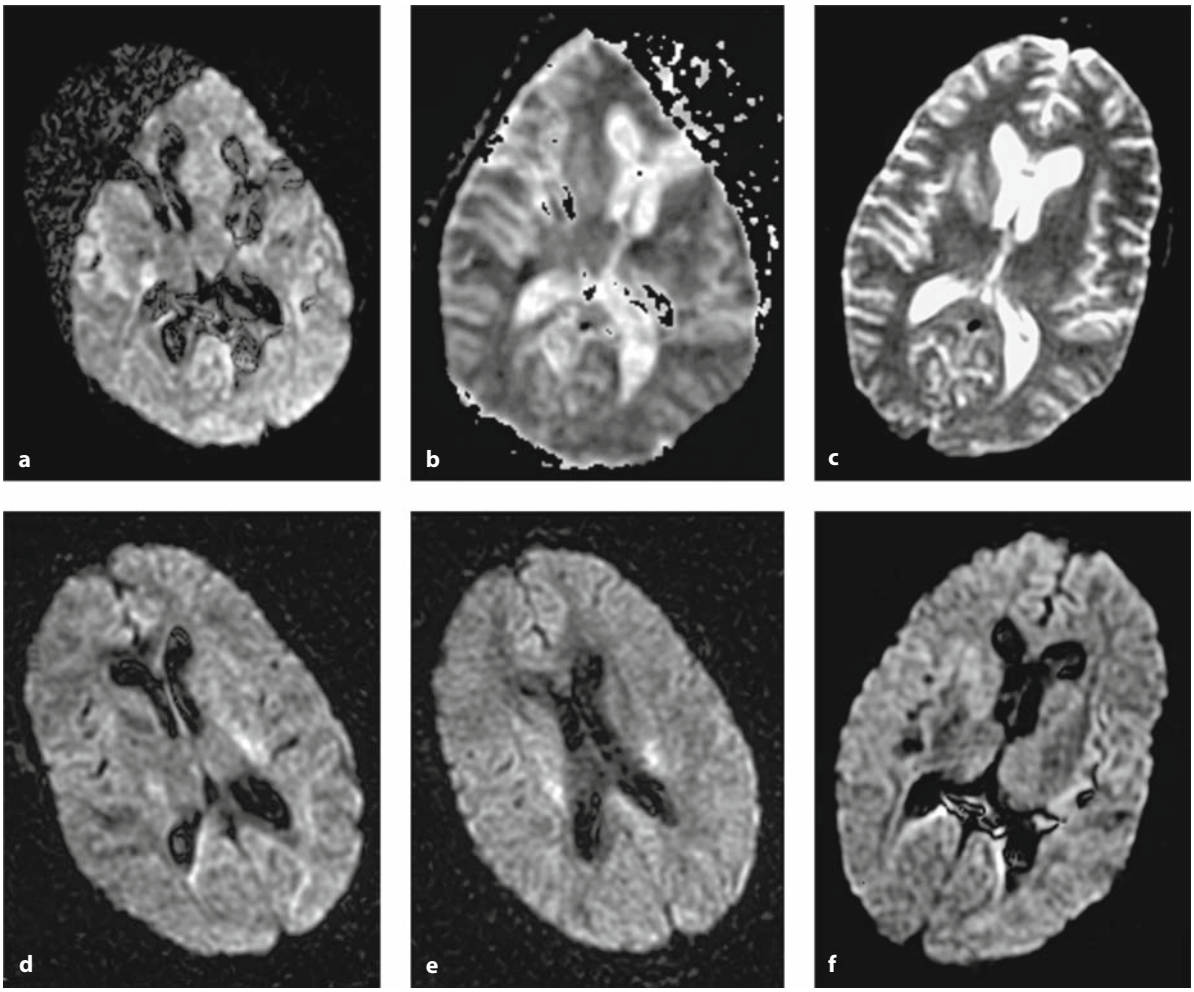

Figure 3.12 a–f

Motion artifacts due to head motion between the scans. Chronic infarcts in the right basal ganglia. **a** DW image has motion artifacts due to head motion between the scans. This image is composed of appears overlapping of b0, and *x, y,* and *z* axis images. **b** ADC map also shows severe motion artefacts. This map is composed of b0, *x, y,* and *z* axis images. **c** b0, **d** *x* axis, **e** *y* axis, **f** *z* axis. b0 and unidirectional images are all free from the artefacts

3.4.5 Motion Artifacts

The sources of motion artifacts include gross head motion, respiratory motions, cardiac-related pulsations and patient bed vibration due to gradient pulses. Single-shot DW echo-planar imaging has relatively low sensitivity to patient motion, because each image is acquired in about 100–300 ms and the total acquisition time is less than 40 s. If one of the *x, y, z* or b_0 images is corrupted by motion artifacts during a scan, or if patient head motion occurs between scans, the isotopic DW images and the ADC maps will have these artifacts (Figs. 3.11 and 3.12). In those cases, unidirectional and b_0 images from the raw data of DW imaging can be free from the motion artifacts and remain diagnostically useful. Long (tens of ms) gradient pulses to reach sufficient diffusion weighting often increase sensitivity to motion.

Correction methods: (1) For a fixed b-factor, use high-gradient amplitude but reduce gradient pulse duration to minimize the sensitivity to motion, (2)

post-processing to correct for phase error (Navigator method) [35–37], (3) elimination of phase-encode step (line scan method, projection reconstruction), (4) minimize time for phase error accumulation (single-shot echo-planar imaging, hybrid method with multishot echo-planar imaging), (5) SSFSE, (6) PROPELLER [38], (7) SENSE.

3.5 Conclusion

Diffusion-weighted images are inherently T2 weighted and the interpretation of signal intensity on DW images requires a correlation between b_0 images, ADC maps and exponential images to uncover the underlying pathophysiologic condition. It is also important to understand a variety of artifacts to avoid misinterpreting the DW images. Understanding inherent artifacts and how to reduce the artifacts on DW imaging will improve the quality and accuracy of DW imaging.

References

1. Stejkal EO, Tanner J (1965) Spin diffusion measurements: spin echoes in the presence of a time-dependent field gradient. J Chemical Phys 42:288–292
2. LeBihan D, Breton E, Lallemand D, Grenier P, Cabanis E, Laval-Jeantet (1986) MR imaging of intravoxel incoherent motions: application to diffusion and perfusion in neurologic disorders. Radiology 161:401–407
3. Warach S, Gaa J, Siewert B, Wielopolski P, Edelman RR (1995) Acute human stroke studied by whole brain echo planar diffusion-weighted magnetic resonance imaging. Ann Neurol 37:231–241
4. Provenzale JM, Engelter ST, Petrella JR, Smith JS, MacFall JR (1999) Use of MR exponential diffusion-weighted images to eradicate T2 "shine-through" effect. AJR Am J Roentgenol 172:537–539
5. Burdette JH, Elster AD, Ricci PE (1999) Acute cerebral infarction: quantification of spin-density and T2 shine-through phenomena on diffusion-weighted MR images. Radiology 212:333–339
6. Coley SC, Porter DA, Calamante F, Chong WK, Connelly A (1999) Quantitative MR diffusion mapping and cyclosporine-induced neurotoxicity. AJNR Am J Neuroradiol 20:1507–1510
7. Schaefer PW, Grant PE, Gonzalez RG (2000) Diffusion-weighted MR imaging of the brain. Radiology 217:331–345
8. Field A (2001) Diffusion and perfusion imaging. In: Elster AD, Burdette JH (eds). Questions and answers in magnetic resonance imaging. Mosby, St. Louis, Missouri pp 194–214
9. Maldjian JA, Listerud J, Moonis G, Siddiqi F (2001) Computing diffusion rates in T2-dark hematomas and areas of low T2 signal. AJNR Am J Neuroradiol 22:112–128
10. Engelter ST, Provenzale JM, Petrella JR, Alberts MJ, DeLong DM, MacFall JR (2001) Use of exponential diffusion imaging to determine the age of ischemic infarcts. J Neuroimaging 11:141–147
11. Chen S, Ikawa F, Kurisu K, Arita K, Takaba J, Kanou Y (2001) Quantitative MR evaluation of intracranial epidermoid tumors by fast fluid-attenuated inversion recovery imaging and echo-planar diffusion-weighted imaging. AJNR Am J Neuroradiol 22:1089–1096
12. Geijer B, Sundgren PC, Lindgren A, Brockstedt S, Stahlberg F, Holtas S (2001) The value of b required to avoid T2 shine-through from old lacunar infarcts in diffusion-weighted imaging. Neuroradiology 43:511–517
13. Casey S (2001) "T2 washout": an explanation for normal diffusion-weighted images despite abnormal apparent diffusion coefficient maps. AJNR Am J Neuroradiol 22:1450–1451
14. Provenzale JM, Petrella JR, Cruz LC Jr, Wong JC, Engelter S, Barboriak DP (2001) Quantitative assessment of diffusion abnormalities in posterior reversible encephalopathy syndrome. AJNR Am J Neuroradiol 22:1455–1461
15. Eastwood JD, Engelter ST, MacFall JF, Delong DM, Provenzale JM (2003) Quantitative assessment of the time course of infarct signal intensity on diffusion-weighted images. AJNR Am J Neuroradiol 24:680–687
16. Hiwatashi A, Kinoshita T, Moritani T, et al. (2003) Hypointensity on diffusion-weighted MRI related to T2 shortening and susceptibility effects. AJR Am J Roentgenol (in press)
17. Elster AD, Burdette JH (2001) Scanner hardware. In: Elster AD, Burdette JH (eds). Questions and answers in magnetic resonance imaging. Mosby, St. Louis, Missouri pp 54–71
18. Haselgrove JC, Moore JR (1996) Correction for distortion of echo-planar images used to calculate the apparent diffusion coefficient. Magn Reson Med 36:960–964
19. Horsfield MA (1999) Mapping eddy current induced fields for the correction of diffusion-weighted echo planar images. Magn Reson Imaging 17:1335–1345
20. Jezzard P, Barnett AS, Pierpaoli C (1998) Characterization of and correction for eddy current artifacts in echo planar diffusion imaging. Magn Reson Med 39:801–812
21. Calamante F, Porter DA, Gadian DG, Connelly A (1999) Correction for eddy current induced Bo shifts in diffusion-weighted echo-planar imaging. Magn Reson Med 41:95–102
22. Schmithorst VJ, Dardzinski BJ (2002) Automatic gradient preemphasis adjustment: a 15-minute journey to improved diffusion-weighted echo-planar imaging. Magn Reson Med 47:208–212
23. Papadakis NG, Martin KM, Pickard JD, Hall LD, Carpenter TA, Huang CL (2000) Gradient preemphasis calibration in diffusion-weighted echo-planar imaging. Magn Reson Med 44:616–624
24. Chapman BL (1999) Shielded gradients. And the general solution to the near field problem of electromagnet design. MAGMA 9:146–151
25. Robson MD, Anderson AW, Gore JC (1997) Diffusion-weighted multiple shot echo planar imaging of humans without navigation. Magn Reson Med 38:82–88

26. Brockstedt S, Moore JR, Thomsen C, Holtas S, Stahlberg F (2000) High-resolution diffusion imaging using phase-corrected segmented echo-planar imaging. Magn Reson Imaging 18:649–657
27. Maier SE, Gudbjartsson H, Patz S, et al. (1998) Line scan diffusion imaging: characterization in healthy subjects and stroke patients. AJR Am J Roentgenol 171:85–93
28. Robertson RL, Maier SE, Mulkern RV, Vajapayam S, Robson CD, Barnes PD (2000) MR line-scan diffusion imaging of the spinal cord in children. AJNR Am J Neuroradiol 21:1344–1348
29. Lovblad KO, Jakob PM, Chen Q, et al. (1998) Turbo spin-echo diffusion-weighted MR of ischemic stroke. Am J Neuroradiol 19:201–208
30. Alsop DC (1997) Phase insensitive preparation of single-shot RARE: application to diffusion imaging in humans. Magn Reson Med 38:527–533
31. Forbes KP, Pipe JG, Karis JP, Farthing V, Heiserman JE (2003) Brain imaging in the unsedated pediatric patient: comparison of periodically rotated overlapping parallel lines with enhanced reconstruction and single-shot fast spin-echo sequences. AJNR Am J Neuroradiol 24:794–798
32. Bammer R, Keeling SL, Augustin M, et al. (2001) Improved diffusion-weighted single-shot echo-planar imaging (EPI) in stroke using sensitivity encoding (SENSE). Magn Reson Med 46:548–554
33. Porter DA, Calamante F, Gadian DG, Connelly A (1999) The effect of residual Nyquist ghost in quantitative echo-planar diffusion imaging. Magn Reson Med 42:385–392
34. Bastin ME (2001) On the use of the FLAIR technique to improve the correction of eddy current induced artefacts in MR diffusion tensor imaging. Magn Reson Imaging 19:937–950
35. Anderson AW, Gore JC (1994) Analysis and correction of motion artifacts in diffusion weighted imaging. Magn Reson Med 32:379–387
36. Ordidge RJ, Helpern JA, Qing ZX, Knight RA, Nagesh V (1994) Correction of motional artifacts in diffusion-weighted MR images using navigator echoes. Magn Reson Imaging 12:455–460
37. Dietrich O, Heiland S, Benner T, Sartor K (2000) Reducing motion artefacts in diffusion-weighted MRI of the brain: efficacy of navigator echo correction and pulse triggering. Neuroradiology 42:85–91
38. Pipe JG (1999) Motion correction with PROPELLER MRI: application to head motion and free-breathing cardiac imaging. Magn Reson Med 42:963–969

Brain Edema

4.1 Characterization and Classification of Brain Edema

Brain edema is defined as accumulation of excess fluid in cells or in the extracellular space. Brain edema can be classified as cytotoxic (cellular), vasogenic [1] or interstitial. Cytotoxic and vasogenic edema usually coexist in pathological conditions such as infarction, hypoxic ischemic encephalopathy, trauma, and multiple sclerosis. The edema may primarily be either vasogenic or cytotoxic, but as the process evolves over time, the injury leads to a combination of cellular swelling and vascular damage. Interstitial edema occurs with hydrocephalus, water intoxication, or plasma hyposmolarity.

Conventional MR imaging does not always allow distinction between the different forms of edema. However, diffusion-weighted (DW) imaging, which is based on the microscopic movement of water molecules in brain tissue, can differentiate cytotoxic edema from vasogenic and interstitial edema [2].

4.2 Definition and Classification of Cytotoxic Edema

Cytotoxic or cellular edema is an abnormal uptake of fluid in the cytoplasm due to abnormal cellular osmoregulation. This kind of edema may accompany various processes that damage cells, such as ischemia, trauma, toxic metabolic disease, demyelination, and even the early phase of degeneration. Classification of the involved cell types may explain the pathophysiology and different prognosis of these conditions.

In normal brain tissues, the gray and white matters are mainly composed of neurons, glial cells, axons, and myelin sheaths (Fig. 4.1). In the gray matter, cytotoxic edema occurs mainly in neurons and glial cells (Fig. 4.2). In the white matter, however, cytotoxic edema occurs in glial cells, axons (axonal swelling) (Fig. 4.3) and myelin sheaths (intramyelinic edema) (Fig. 4.4) [1].

Figure 4.1

Normal brain tissue is mainly composed of neurons, glial cells (astrocytes or oligodendrocytes), axons, and myelin sheaths surrounded by an extracellular space

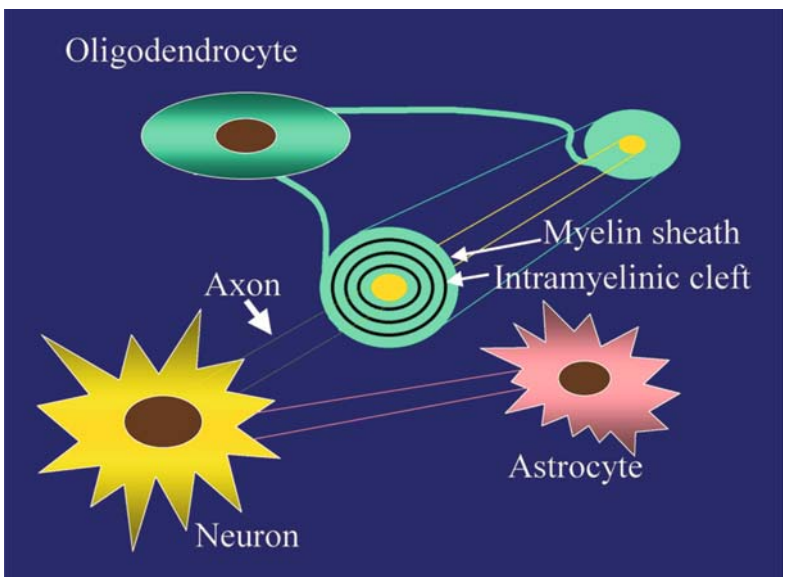

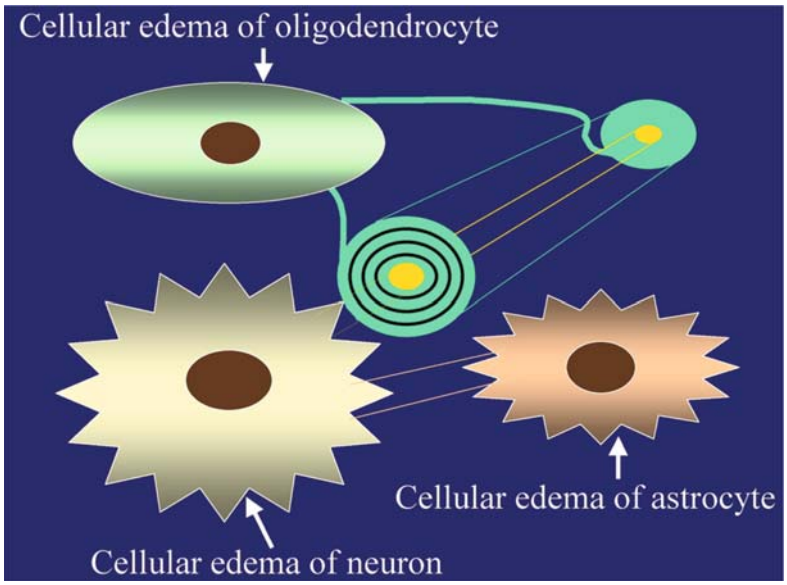

Figure 4.2

Cytotoxic edema occurs in neurons and glial cells (astrocytes and oligodendrocytes). These cells are vulnerable to ischemia. As cells increase in size, there is a shift of water from extracellular to intracellular compartments, which can occur without a net gain in water (compared with Fig. 4.1). Cytotoxic edema results in increased intracellular space and decreased extracellular space, which may cause a decrease in ADC

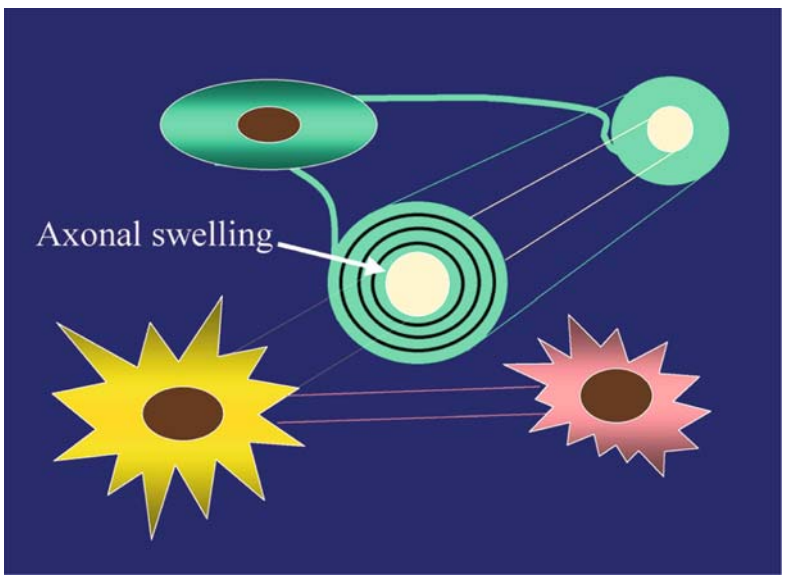

Figure 4.3

Cytotoxic edema can occur in axons

4.3 Pathophysiology of Cytotoxic Edema

4.3.1 Energy Failure

In ischemia or hypoxia, cytotoxic edema is mainly caused by energy failure [3]. The insult initiates substrate depletion, which leads to a decrease in intracellular ATP used for oxidative phosphorylation, and a failure of the sodium–potassium pump. This will cause an influx of sodium and calcium into the cells, subsequently increasing the osmotic gradient and the transport of water into the cells, resulting in cellular swelling. Moreover, in an attempt to produce

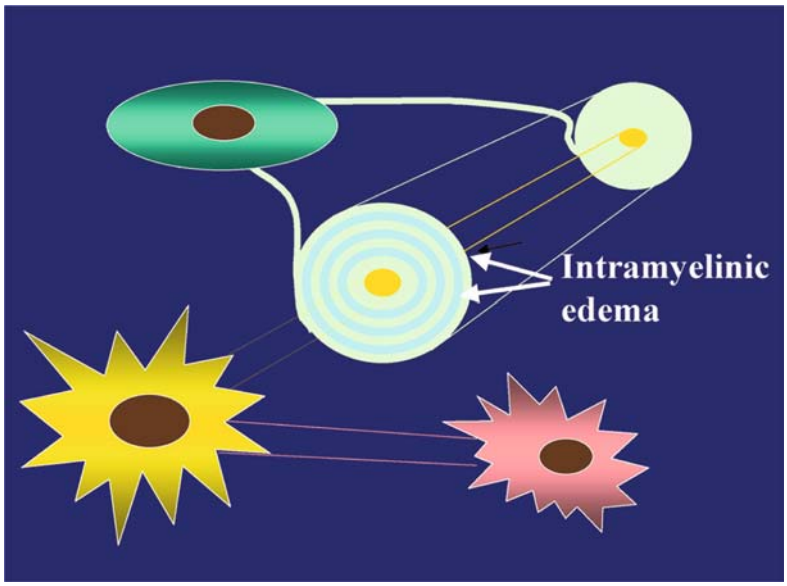

Figure 4.4
Cytotoxic edema can occur in myelin sheaths in which edema is found in either the myelin sheath itself or in the intramyelinic cleft

ATP, the cells switch from oxidative phosphorylation to anaerobic glycolysis, resulting in intracellular lactate formation. This will further increase the osmotic gradient across the cell membrane, which exacerbates the cytotoxic edema. Pathologically, injured neurons shrink and become esosinophilic due to increased density of dameged mitochondria. Astrocytes swelling (Alzheimer type II cells) is seen as a response to metabolic insults. The damaged neurons disintegrate and are removed by mauophages. With time, cortical atrophy and gliosis develop.

4.3.2 Excitotoxic Brain Injury

Energy failure is not the only mechanism responsible for the cytotoxic edema [3]. Membrane transporters can be triggered or inhibited by a range of excitatory neurotransmitters, such as glutamate and aspartate, but also other agents such as cytokines and free radicals [4]. Any cell, including neuron, glia, axon and myelin sheath can be a target of these toxic substances; however, reactive astrocytes play a significant role in cellular and tissue repair by detoxifying various noxious substances (such as glutamate, free radicals, ammonia and metals). Neuropathologic examination shows that the acutely reactive astrocytes have swollen cytoplasm and neurophil, consistent with cytotoxic edema [5].

High glutamate in the synaptic and extracellular space is one of the important mechanisms associated with cytotoxic edema of various diseases, including infarction, hypoxic ischemic encephalopathy, status epilepticus, and traumatic brain injury, such as diffuse axonal injury, contusion and shaken baby syndrome [6, 7]. Increased extracellular glutamate is a direct cause of excitotoxic brain injury. In acute excitotoxic injury, increased extracellular glutamate results from an increased release/leakage of glutamate or a decreased re-uptake (Figs. 4.5, 4.6)[8].

Neuronal glutamate is released from the pre-synaptic terminal into the synaptic cleft. The glutamate binding to N-methyl-D-aspartate (NMDA) receptors allows entry of Ca^{2+} into the post-synaptic neuron, which results in necrotic cell death or apoptosis. The glutamate binding to non-NMDA receptors allows entry of Na^{+} into the post-synaptic neuron, resulting in cytotoxic edema. Apoptosis is defined as a programmed cell death and is histologically characterized by fragmentation of DNA in the nucleus of the cell. Re-uptake of extracellular glutamate takes place at the pre-synaptic terminals and in adjacent glial cells, which may cause cytotoxic edema (acute phase of reactive astrocytosis).

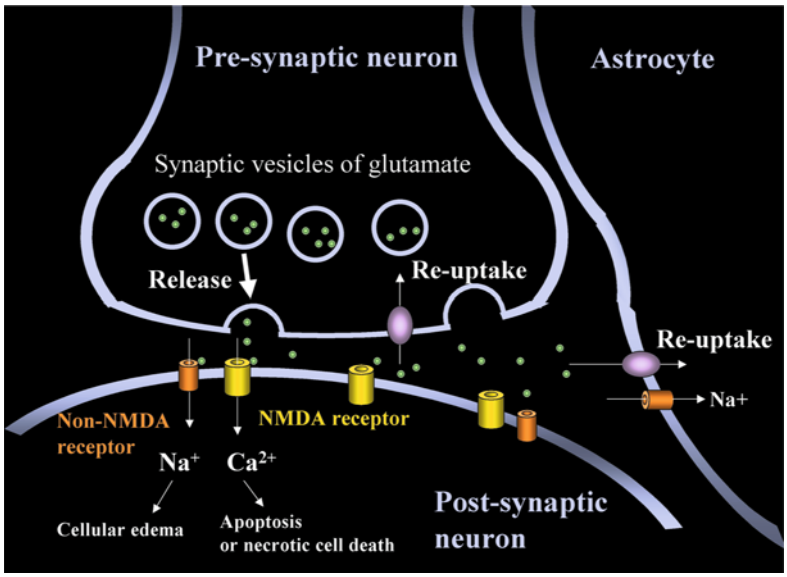

Figure 4.5

Excitotoxic mechanisms in the neuron and astrocyte. In the neuron, glutamate is released from the pre-synaptic terminal into the synaptic cleft. The glutamate binding to NMDA receptors allows entry of Ca^{2+} into the post-synaptic neuron, which can result in necrotic cell death or apoptosis. The glutamate binding to non-NMDA receptors allows entry of Na^{+} into the post-synaptic neuron, resulting in cytotoxic edema of the neuron. Re-uptake of extracellular glutamate takes place at the pre-synaptic terminals and in adjacent astrocytes. Similar mechanisms also cause cytotoxic edema in the astrocyte

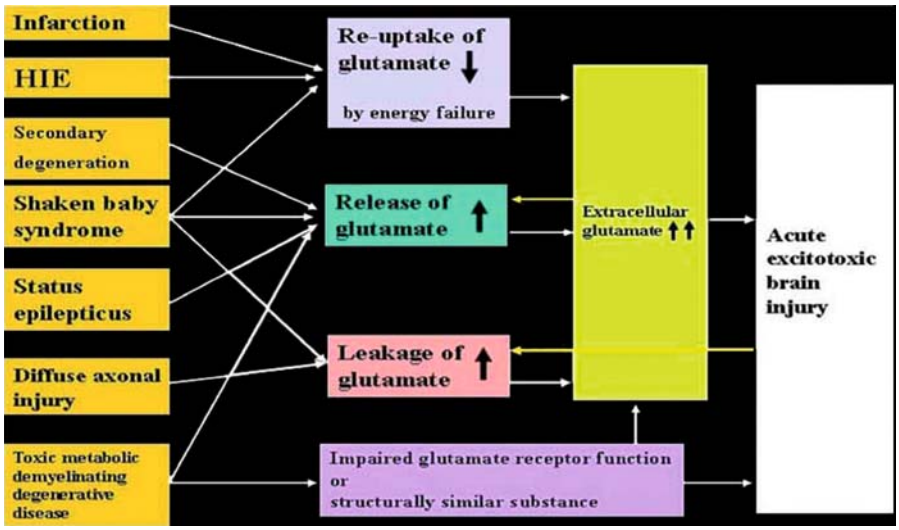

Figure 4.6

Acute excitotoxic brain injury in various diseases. Various diseases are associated with acute excitotoxic brain injury. The mechanisms are classified into: (1) decreased re-uptake, (2) increased release, (3) leakage due to disruption of axonal membranes, (4) others, including impaired glutamate receptor function, or substances structurally similar to glutamate. There are various combinations of mechanisms according to each disease process. There are two positive feedback loops (*yellow arrow*): (1) increased extracellular glutamate depolarizes adjacent neurons that release intracellular glutamate; (2) neuronal injury causes leakage of glutamate. This mechanism is self-propagating via neuron-glial cell units and via transaxonal or transynaptic routes along the fiber tracts. (From [8])

Acute excitotoxic injury can also be related to functional failure of the glutamate receptor and the presence of structurally similar substances to glutamate, such as hydroxyglutarate or glutarate, at the receptor sites. Excessive extracellular glutamate depolarizes injured adjacent glial cells or neurons and in turn causes release or leakage of glutamate. This mechanism is self-propagating through neuron-glial cell units, and transaxonal or transynaptic routes along the white matter fiber tracts [8].

Whatever the cause, cytotoxic edema can result in necrosis or delayed neuronal death, or degeneration similar to apoptosis with various amounts of reactive gliosis. Whether necrosis or apoptosis ensues, it may neurochemically depend on the levels of adenosine triphosphate or cytosol calcium ions that trigger protease and lipase production [9].

4.4 Diffusion-Weighted Imaging and Cytotoxic Edema

Cytotoxic edema characteristically shows hyperintensity on DW images associated with decreased apparent diffusion coefficient (ADC). The precise mechanisms underlying the reduction in ADC are unknown. The most common explanation is a shift of extracellular water to the intracellular space. However, the observed 40% reduction of ADC cannot be explained by an increase in intracellular water alone, even if all extracellular fluid went intracellular [10]. There must be a reduction in diffusivity of water molecules in the intracellular space which may be explained by the large number of intracellular organelles, that may act as obstacles for diffusion. A decrease in intracellular ADC could also be due to a decrease in the energy-dependent intracellular circulation or an increase in cytoplasmic viscosity from a swelling of intracellular organelles [11].

Tumors, hemorrhages, abscesses and coagulative necrosis also result in a decrease in ADC. The mechanisms underlying the reduction in ADC in those lesions are also unknown, but can be related to hypercellularity or hyperviscosity of the pathological tissue [12, 13].

4.4.1 Conditions that Cause Cytotoxic Edema, and Reversibility

Cytotoxic edema of neuron and glial cells usually accompany infarction [14–17], hypoxic ischemic encephalopathy [18, 19], traumatic brain injury [20, 21], status epilepticus [6, 22, 23], migraine [24, 25], encephalitis [26], and Creutzfeldt–Jakob disease [27, 28].

Neurons and glial cells are the cells most vulnerable to ischemia and hypoxia, but if the ischemia is severe, myelin sheaths and axons may also be affected [3]. These differences among cell types for cytotoxic edema can explain the different time courses of DW abnormalities between gray and white matter in cerebral infarction and hypoxic ischemic encephalopathy. In arterial infarction, the area of cytotoxic edema on DW imaging seems to be irreversibly damaged tissue, resulting in coagulative or liquefactive necrosis. However, mild decreased ADC in the ischemic penumbra can be reversible after intra-arterial or intravenous fibrinolytic therapy (Fig. 4.7). In transient ischemic attacks and venous infarctions, an initially abnormal signal on DW imaging has occasionally been reversed, partially or completely, on follow-up MR images. Hypoxic ischemic encephalopathy (Fig. 4.8) and traumatic brain injury are usually related to irreversible brain damage.

In status epilepticus (Fig. 4.9) and migraine (Fig. 4.10), cytotoxic edema is often partially or completely reversible. If severe, it may result in selective necrosis followed by brain atrophy or gliosis [6, 25]. A cytotoxic edema of reactive astrocytes in the acute phase can be responsible for the reversible signal abnormalities [6].

In Creutzfeldt–Jakob disease, the area of cytotoxic edema will eventually develop into prominent brain atrophy (Fig. 4.11). Axonal swelling can also accompany diffuse axonal injury (Fig 4.12) and the early phase of wallerian degeneration (Fig. 4.13) [29].

Intramyelinic edema may accompany the acute phase of multiple sclerosis (Fig. 4.14) [30, 31], toxic or metabolic leukoencephalopathy (Fig. 4.15) [32–34] and osmotic myelinolysis [35]. Partially or completely reversible lesions are also seen in these conditions.

A focal lesion in the splenium of the corpus callosum in epileptic patients or those with encephalitis/encephalopathy is often completely reversible (Fig. 4.16) [36-38].

The explanation for this reversibility may be an intramyelinic edema where the edema is often primarily located in the intramyelinic cleft [1].

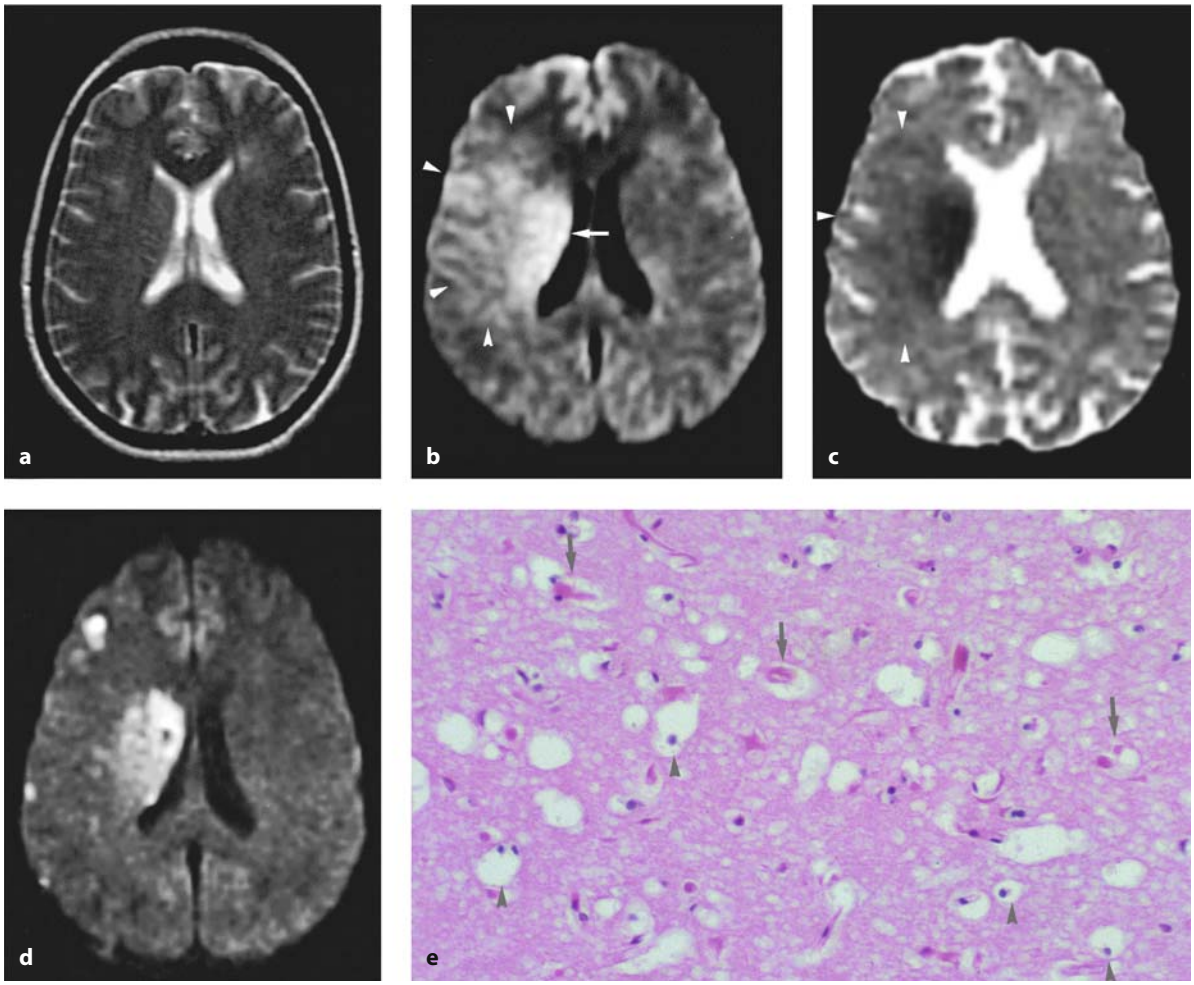

Figure 4.7 a–e

Hyperacute cerebral infarction (3 hrs after onset) in a 39-year-old woman with decreased consciousness. Her neurologic functions improved after intra-arterial thrombolytic therapy. **a** T2-weighted image appears normal. **b** DW image shows a hyperintense lesion in the right corona radiata (*arrow*) and a slightly hyperintense lesion in the right middle cerebral artery (MCA) territory, which may correspond to ischemic penumbra (*arrowheads*). **c** ADC map shows a definite decrease in ADC in the corona radiata and slightly decreased ADC in the right MCA territory (*arrowheads*). **d** On DW image after fibrinolytic therapy (3 days after onset), the hyperintense lesion in the cortical area is largely resolved, with remaining small, peripheral infarcts. Early cytotoxic edema with slightly decreased ADC does not always result in infarction. **e** Another case. Pathology of cytotoxic edema in the cortex in an acute stroke shows shrunken eosinophilic neurons which are anoxic (*arrows*) and swollen glial cells (*arrowheads*) (hematoxylin–eosin stain, original magnification ×200). (From [43])

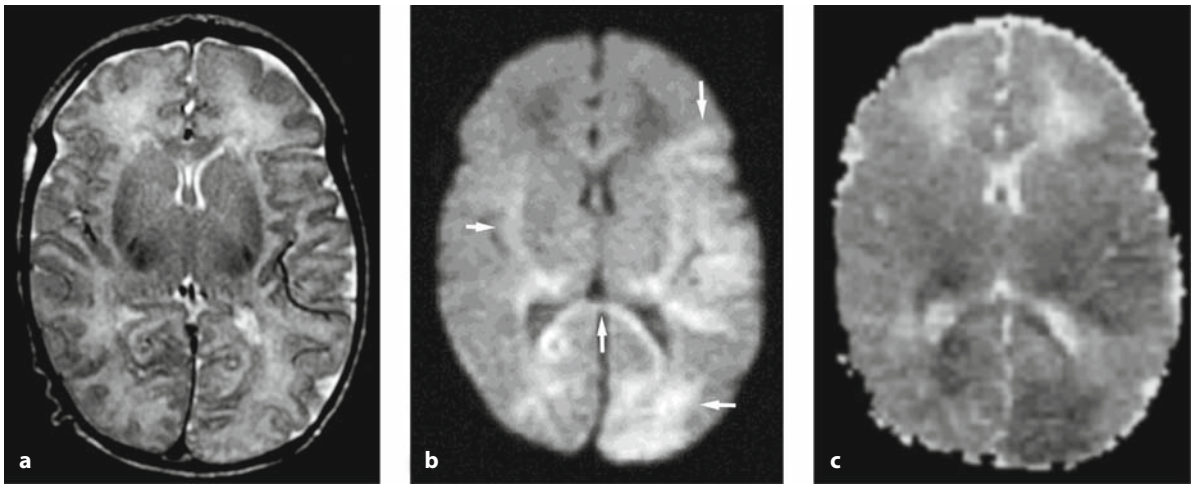

Figure 4.8 a–c

A 2-day-old term girl with hypoxic ischemic encephalopathy due to perinatal hypoxia–ischemia event. **a** T2-weighted image appears normal. **b** DW image shows hyperintense lesions in the temporo-occipital gray and white matter including the corpus callosum (*arrows*). Low intensity in bilateral frontal deep white matter (*arrowheads*) is a normal finding in a patient of this age. **c** ADC map shows these lesions as decreased ADC representing cytotoxic edema. Increased ADC in the frontal deep white matter is also a normal finding in a patient of this age. These ischemic lesions are more clearly seen on DW imaging than on the ADC map because DW imaging depicts subtle T2 contrast abnormalities (T2 shine-through effect) in addition to the contrast of diffusion restriction of these lesions

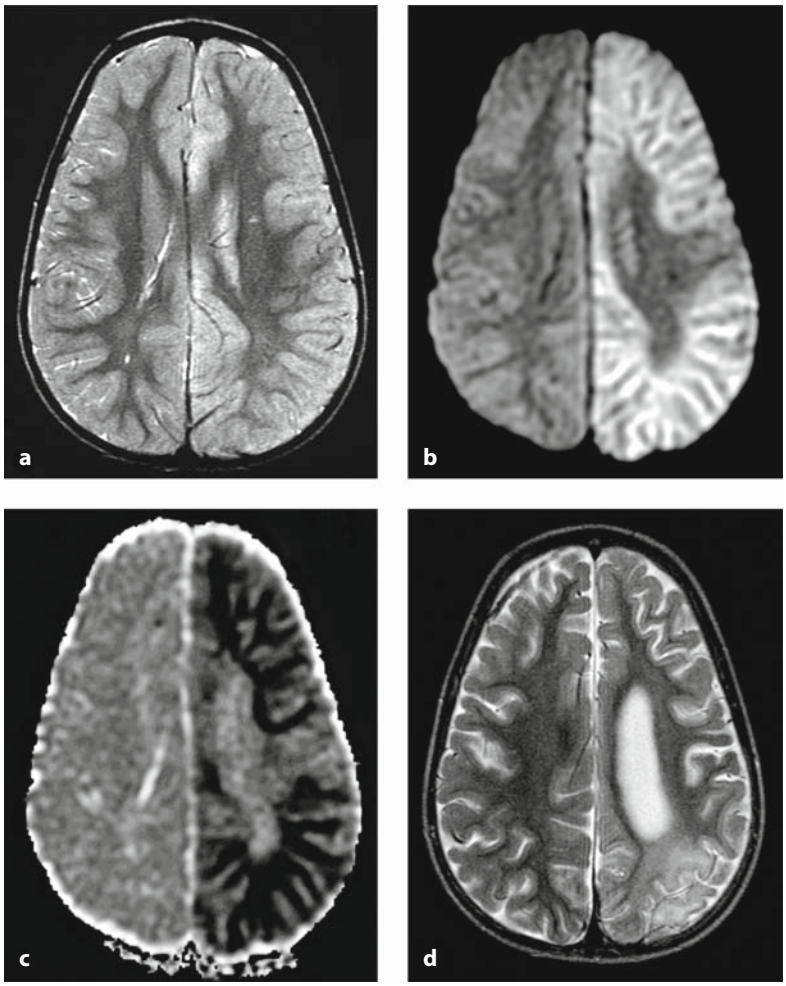

Figure 4.9 a–d

Status epilepticus in a 2-year-old girl 24 hours after onset. **a** T2-weighted image shows diffuse cortical hyperintensity in the entire left hemisphere cortex. **b** DW image shows diffuse hyperintensity mainly in the gray matter of the left hemisphere. **c** ADC map shows decreased ADC of these lesions. **d** Diffuse brain atrophy and hyperintense lesions in the left hemisphere are seen on a 5-month follow-up T2-weighted image

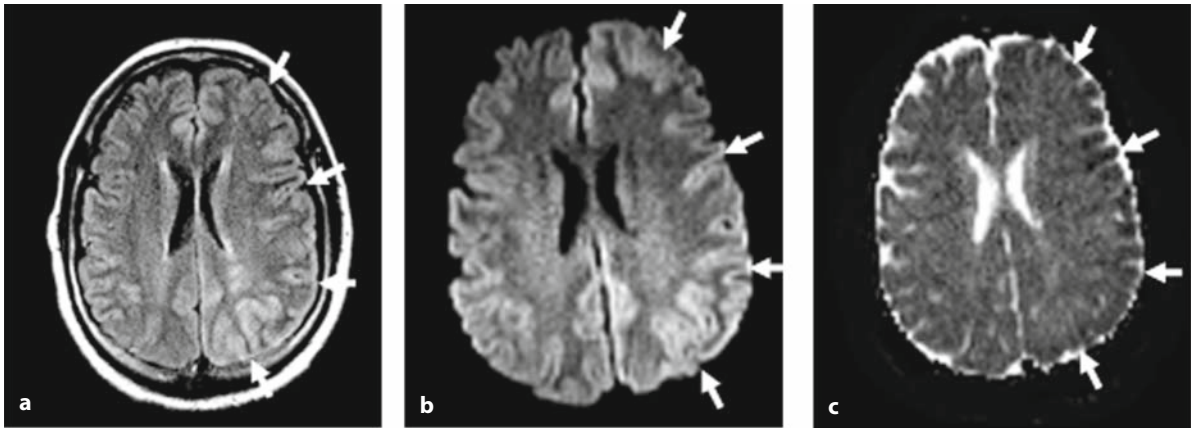

Figure 4.10 a–c

Migraine in a 37-year-old woman. **a** FLAIR image shows diffuse mild cortical hyperintensity in the left hemisphere (*arrows*). **b** DW image shows slightly increased intensity in the cortex (*arrows*). **c** ADC map shows decreased ADC of the lesions (*arrows*)

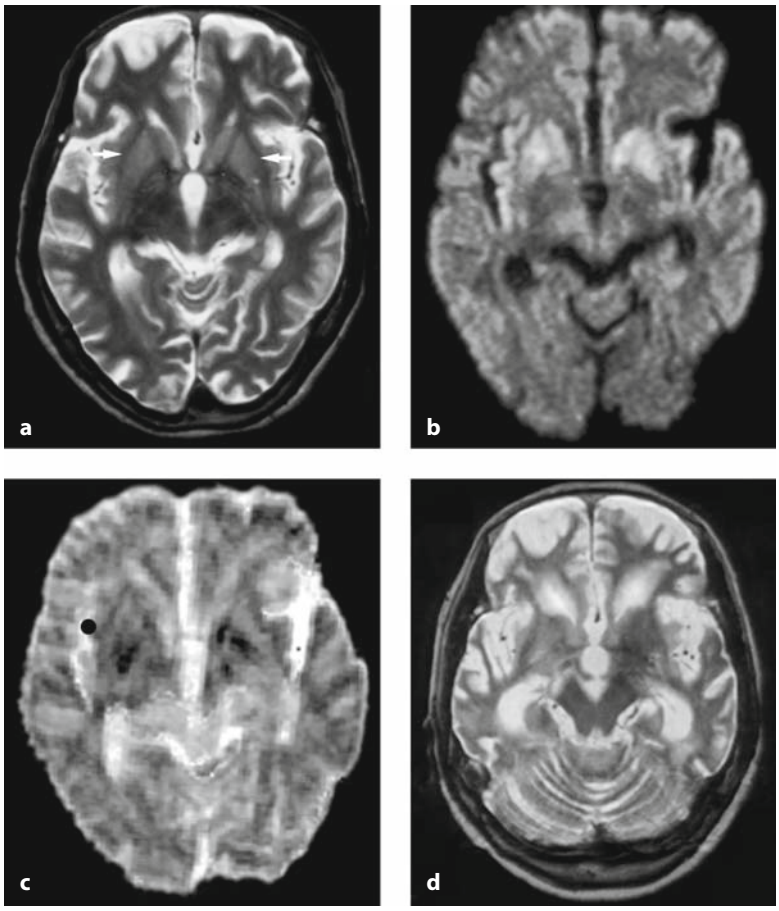

Figure 4.11 a–d

Creutzfeldt–Jakob disease in a 72-year-old woman with progressive dementia. **a** T2-weighted image demonstrates mildly increased signal bilaterally in the caudate nuclei and putamina (*arrows*). **b** DW image clearly demonstrates bilateral, symmetrical increase in signal intensity in the caudate nuclei and putamina. **c** ADC map shows these lesions as decreased ADC. **d** Four-month follow-up MR imaging shows prominent brain atrophy. (From [44])

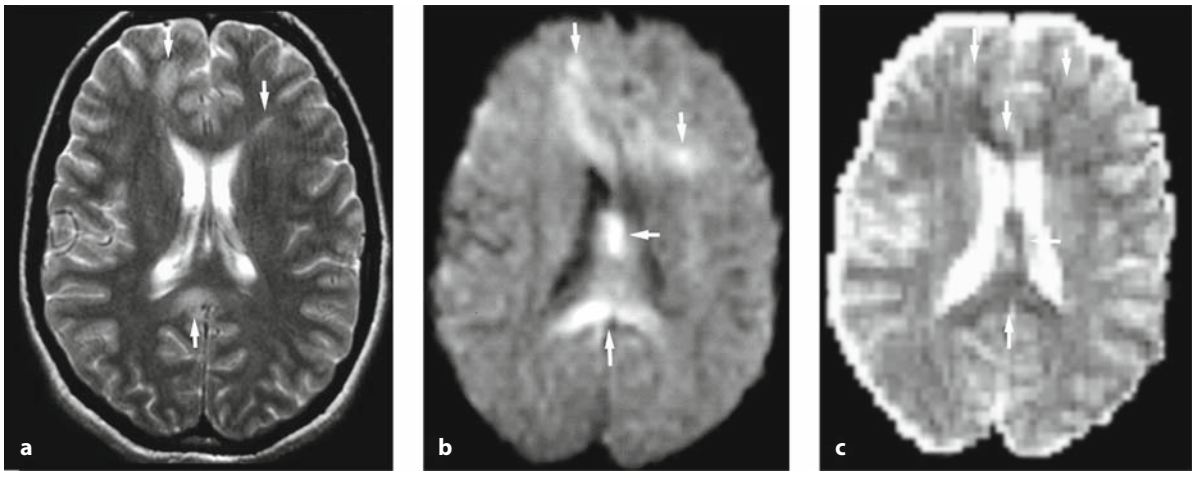

Figure 4.12 a–c

Diffuse axonal injury in an 18-year-old female patient 48 h after motor vehicle accident. **a** T2-weighted image shows mildly hyperintense lesions in the corpus callosum and the white matter of bilateral frontal lobes (*arrows*). **b** DW image demonstrates diffuse axonal injury as high signal intensity, representing cytotoxic edema (*arrows*). **c** ADC map shows decreased ADC lesions in the anterior to posterior corpus callosum and the frontal deep white matter (*arrows*). (From [44])

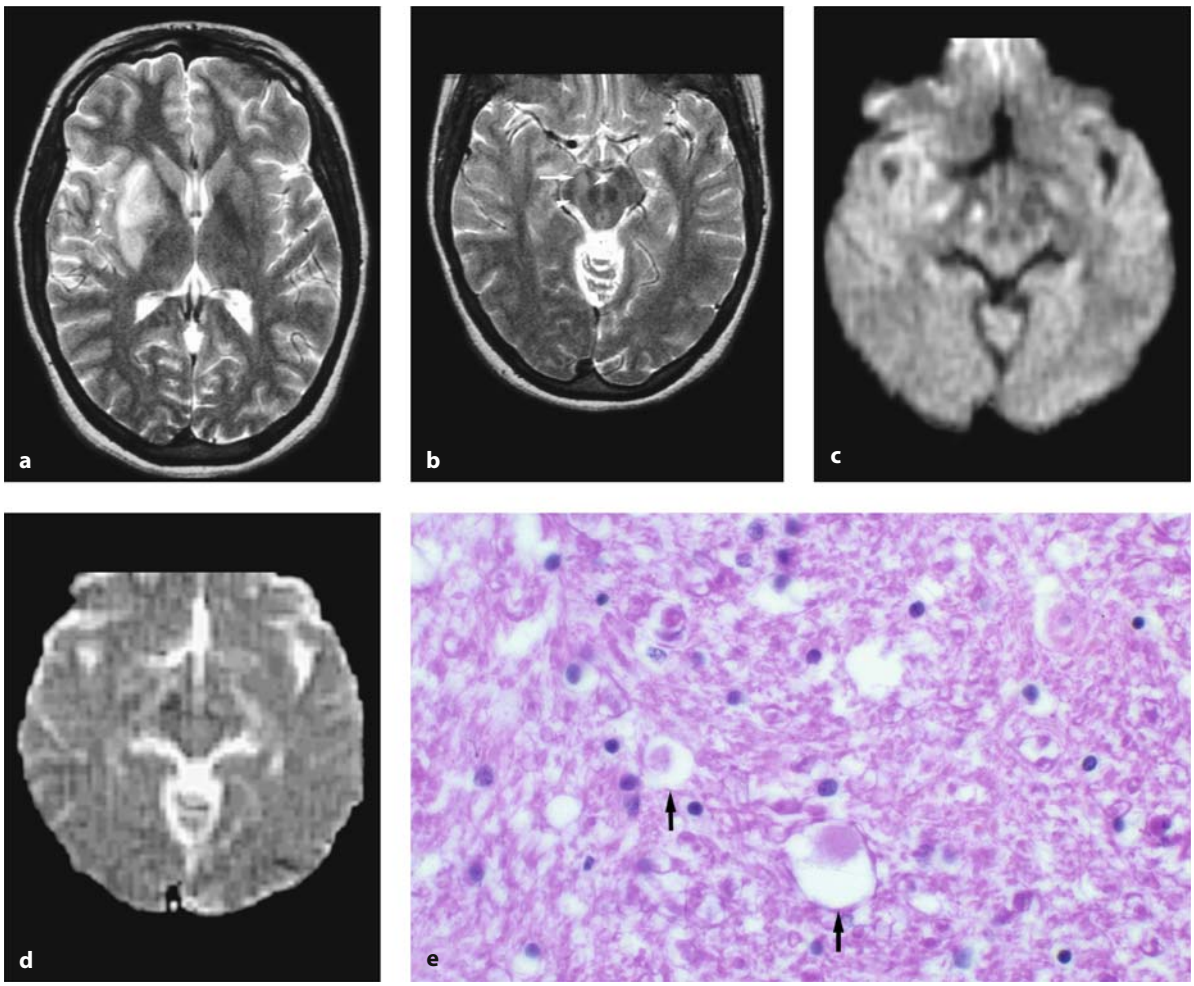

Figure 4.13 a–e

An early phase of wallerian degeneration in a 20-year-old woman with subacute infarction (72 h after onset). **a** T2-weighted image shows a hyperintense lesion involving the right basal ganglia, the posterior limb of the internal capsule and corona radiata, representing a subacute infarct. **b** T2-weighted image shows a hyperintense lesion along the ipsilateral corticospinal tract (*arrow*) and substantia nigra (*arrowheads*) in the cerebral peduncle, which represents wallerian and transneuronal degeneration secondary to the infarction in the right basal ganglia and corona radiata. **c, d** DW image shows a hyperintense spot in the right cerebral peduncle associated with decreased ADC, which may represent axonal swelling in the early phase of wallerian and transneuronal degeneration. **e** Another case of the early phase of wallerian degeneration. Histopathology shows axonal swelling as an enlarged axon in the corticospinal tract in the brain stem (*arrows*) (hematoxylin–eosin stain, original magnification ×200)

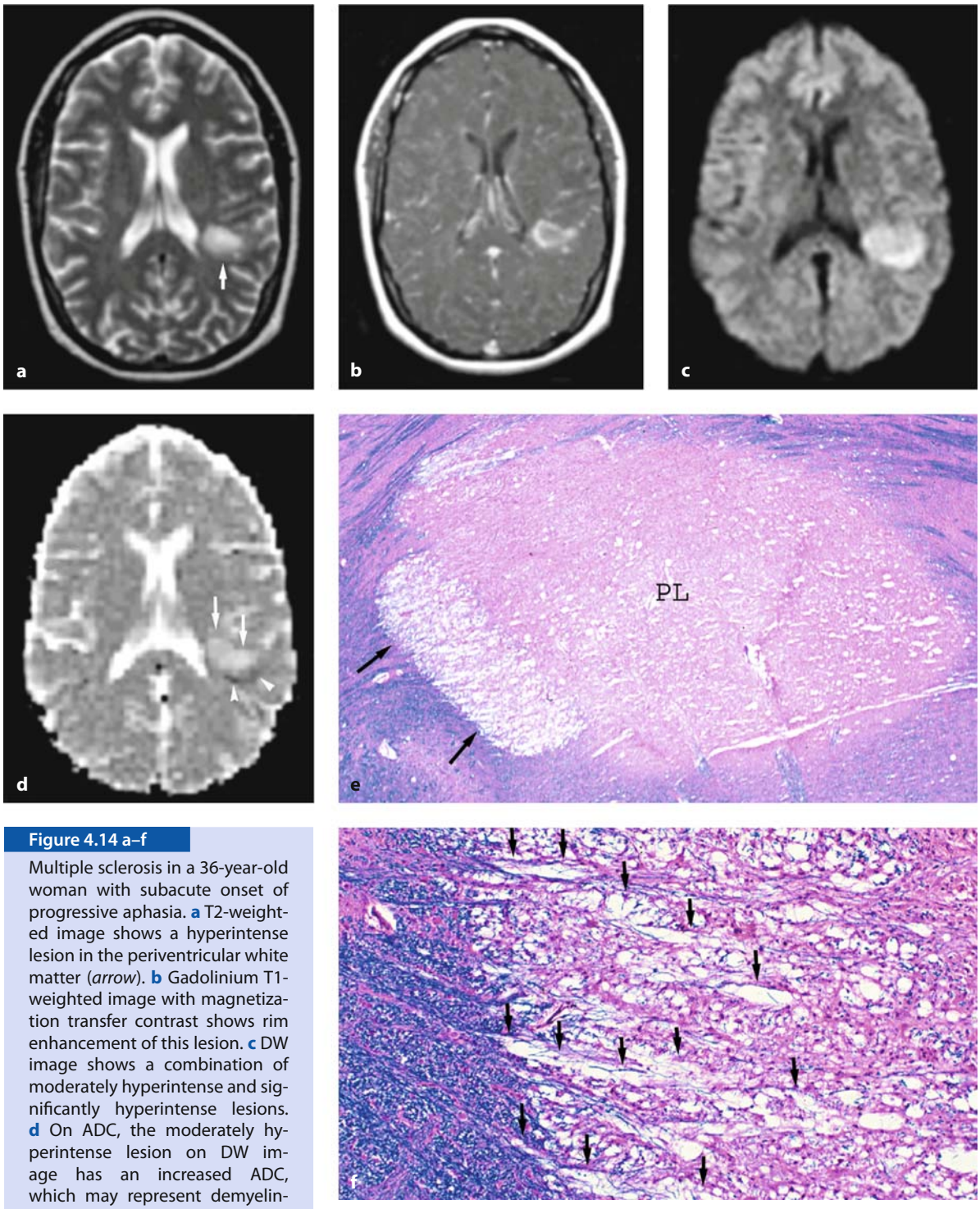

Figure 4.14 a–f

Multiple sclerosis in a 36-year-old woman with subacute onset of progressive aphasia. **a** T2-weighted image shows a hyperintense lesion in the periventricular white matter (*arrow*). **b** Gadolinium T1-weighted image with magnetization transfer contrast shows rim enhancement of this lesion. **c** DW image shows a combination of moderately hyperintense and significantly hyperintense lesions. **d** On ADC, the moderately hyperintense lesion on DW image has an increased ADC, which may represent demyelination (*arrows*), while the markedly hyperintense lesion on the DW image, with decreased ADC, may represent intramyelinic edema (*arrowheads*). **e** Another case. Histopathology shows that intramyelinic edema (*arrows*) is located in the periphery of a plaque (*PL*) (Luxol fast blue PAS stain, original magnification ×40). **f** Magnification of (**e**). Intramyelinic edema is seen along the myelin sheaths (*arrows*) (Luxol fast blue PAS stain, original magnification ×200). (From [43])

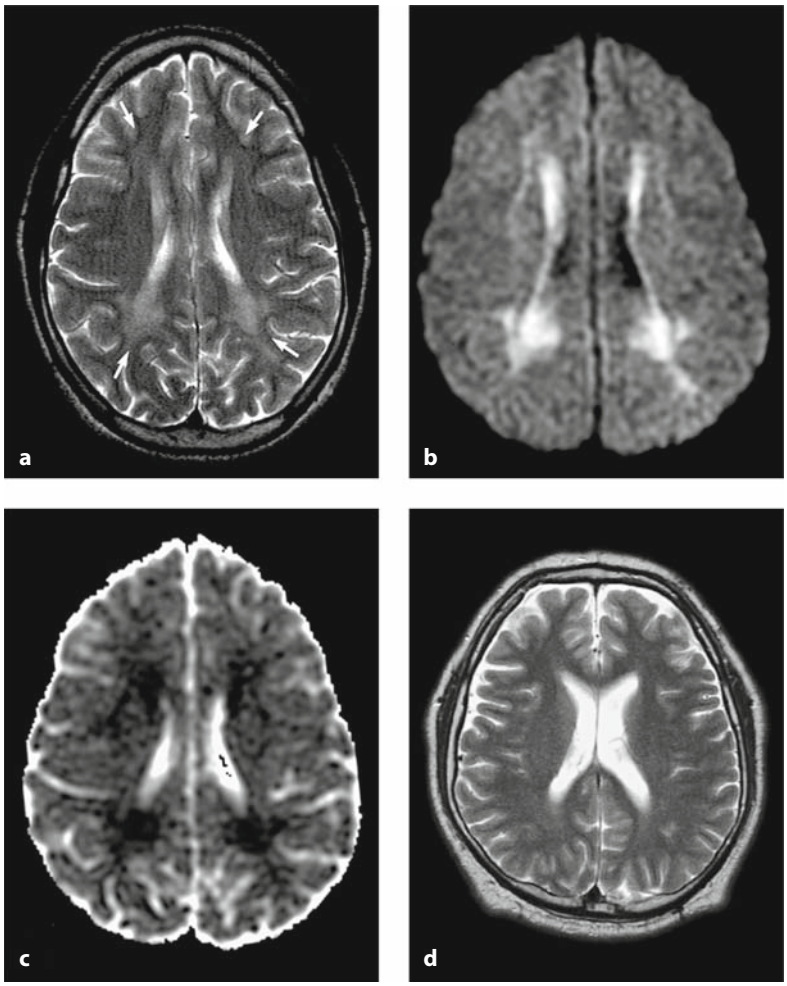

Figure 4.15 a–d

Phenylketonuria in a 36-year-old man. **a** T2-weighted image shows hyperintense lesions in the periventricular white matter (*arrows*). **b** DW image shows these lesions as hyperintense. **c** These hyperintense lesions have decreased ADC, representing cytotoxic edema, presumably intramyelinic edema. **d** Three-month follow-up MR imaging shows complete resolution of these lesions with clinical improvement

Figure 4.16 a–d

A focal lesion of the splenium of the corpus callosum in a 26-year-old woman. **a** T2-weighted image shows a hyperintense lesion in the splenium of the corpus callosum. **b** DW image shows this lesion as hyperintense. **c** This lesion has decreased ADC, representing cytotoxic edema, presumably intramyelinic edema which is usually completely reversible. **d** FA is relatively preserved

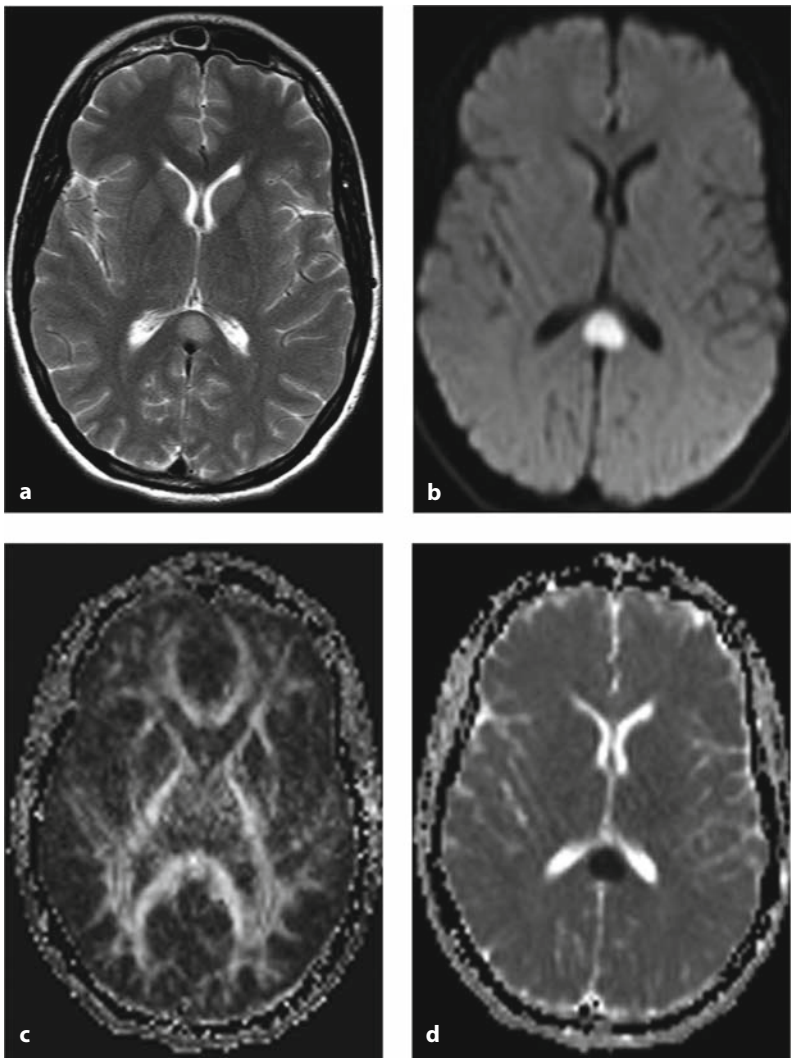

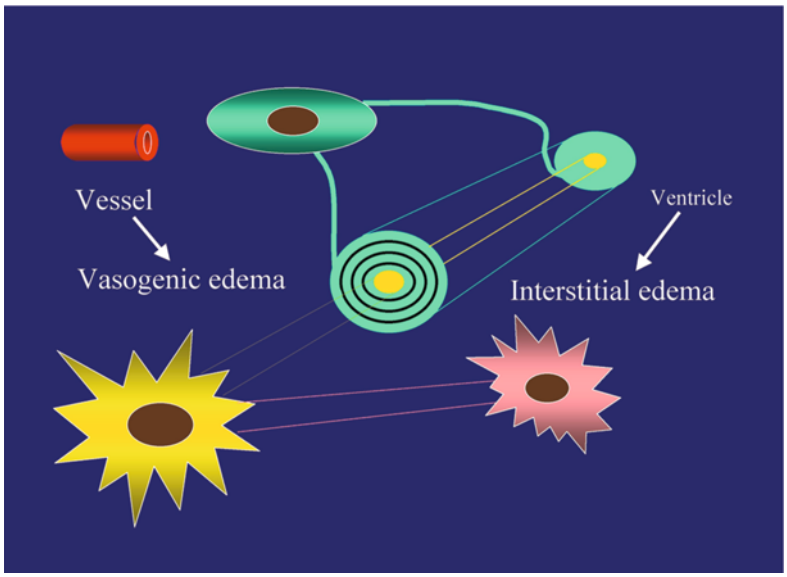

Figure 4.17

Vasogenic or interstitial edema. There is enlarged extracellular space as water shifts from the blood vessels and/or ventricles. Intracellular compartments are relatively preserved

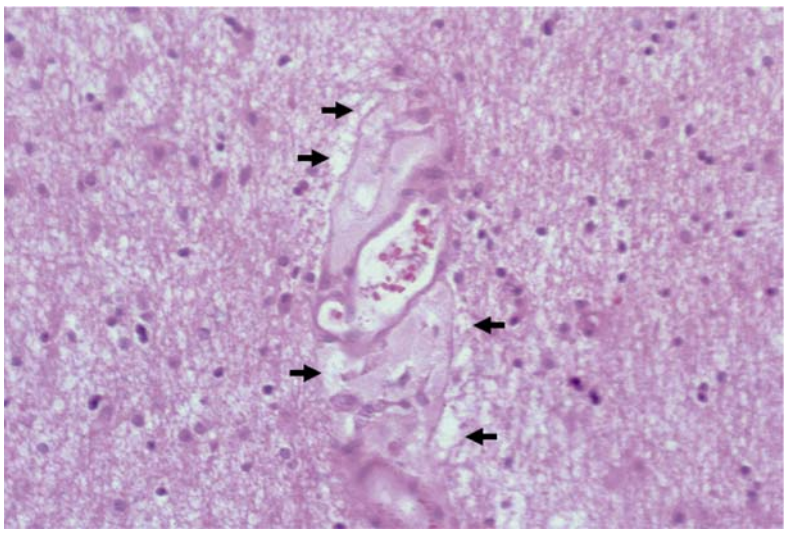

Figure 4.18

Vasogenic edema, as shown on this tissue stain of a trauma case (*arrows*), is the result of plasma leakage through the blood vessel walls. The increase in extracellular space osmolarity will result in a marked increase in extracellular water, i.e., vasogenic edema (hematoxylin–eosin stain, original magnification ×200). (From [43])

4.5 Vasogenic or Interstitial Edema

Vasogenic edema is characterized by dysfunction of the blood–brain barrier, allowing an abnormal passage of proteins, electrolytes and water into the extracellular compartments. Fluid leaving the capillaries enlarges the extracellular space, predominantly in the white matter. Osmotic and hydrostatic gradients will also cause interstitial edema, increasing the extracellular space as water shifts from blood vessels and/or ventricles. Intracellular components are relatively preserved (Fig. 4.17), although some swelling of myelin sheaths and astrogliosis may be seen histologically [3].

In vasogenic and interstitial edema, electron microscopy has shown an increase of interstitial spaces in white matter amounting to 1000 nm, versus 60 nm in normal white matter [39]. These enlarged extracellular spaces, with free water, may be the dominant source for the total brain water signal, resulting in increased ADC.

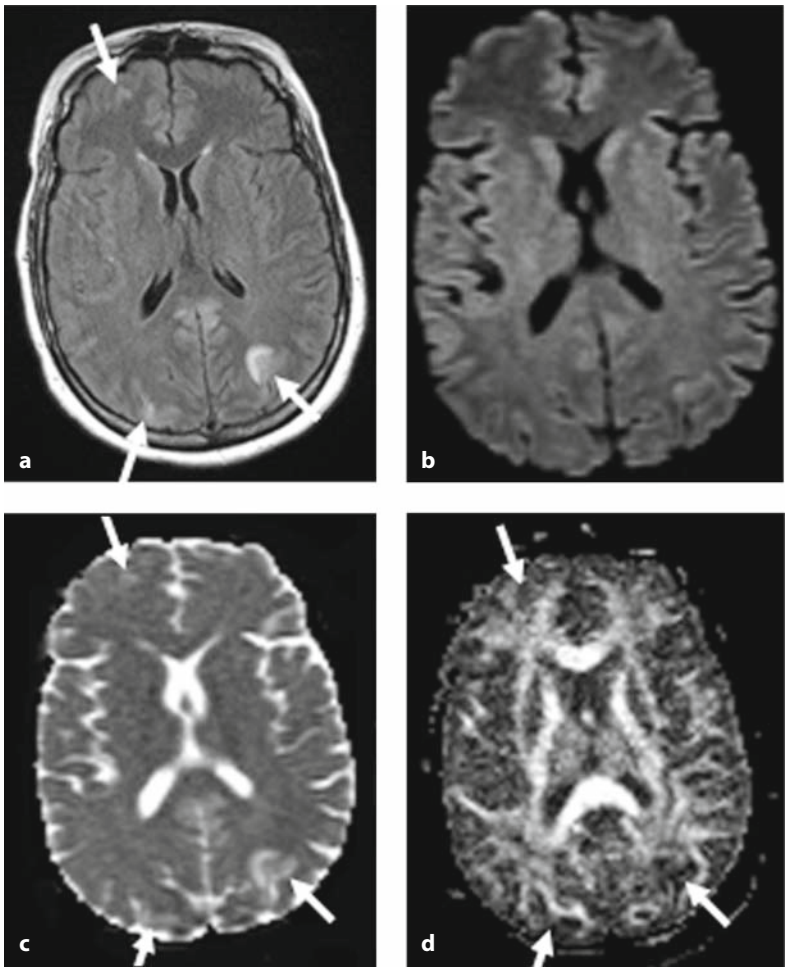

Figure 4.19 a–d

Posterior reversible encephalopathy syndrome (PRES) in a 42-year-old woman with hypertension after liver transplant. **a** FLAIR image shows multiple hyperintense lesions in the right frontal and bilateral parieto-occipital areas (*arrows*). **b** DW image reveals these lesions as isointense. **c** ADC map shows increased ADC consistent with the vasogenic edema seen in PRES (*arrows*). **d** FA map shows decreased FA in the area of the subcortical vasogenic edema (*arrows*)

4.5.1 Conditions That Cause Vasogenic Edema

Vasogenic edema is related to multiple pathological conditions. It typically occurs in the vicinity of brain tumors, intracerebral hematomas, infarctions, cerebral abscesses, contusions and in the reversible posterior leukoencephalopathy syndrome [40]. Venous ischemia at first shows a vasogenic edema due to venous congestion and a breakdown of the normal blood–brain barrier. Progressive venous ischemia results in reduced capillary perfusion pressure and cytotoxic edema [41].

Pathological specimens of vasogenic edema show leakage of plasma from the vessel and diffuse expansion of the extracellular space in the white matter (Fig. 4.18).

Diffusion-weighted images show low signal intensity, isointensity or slightly increased intensity, depending on T2 contrast, and an increase in ADC that reflects free water in the enlarged extracellular space (Figs. 4.19–4.21).

4.6 Diffusion Tensor Imaging and Edema

Diffusion tensor (DT) imaging measures the translation of extracellular water in the white matter tracts by directional evaluation of the water diffusivity (diffusion anisotropy) [42]. Fractional anisotropy (FA), a parameter derived from DT imaging computations, is sensitive for detecting extracellular edema (vasogenic and interstitial edema) in the white matter tracts (Fig. 4.19). DT imaging shows decreased FA in the area of vasogenic edema, while FA is relatively preserved in pure cytotoxic edema (Fig. 4.16).

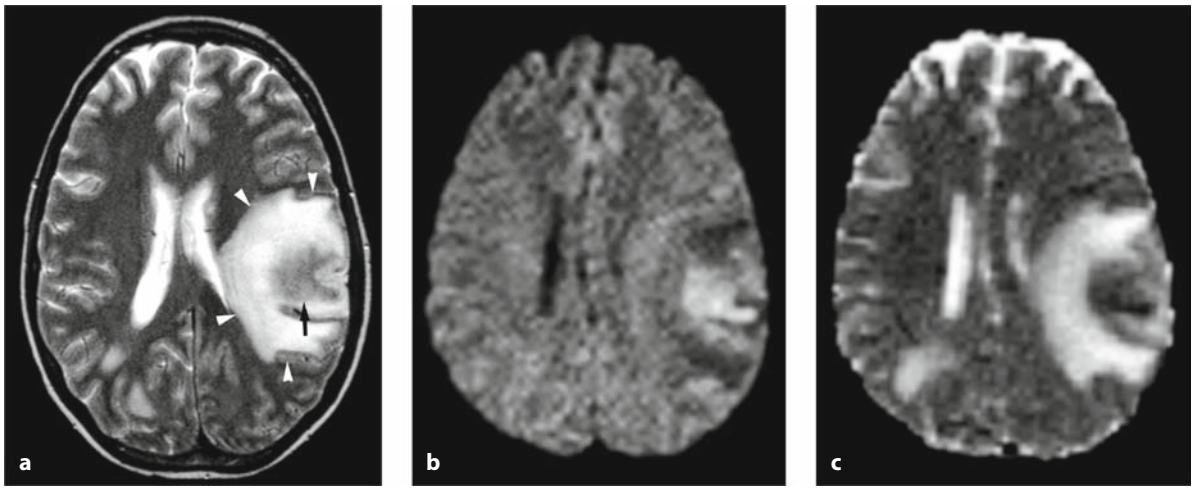

Figure 4.20 a–c

Cerebral toxoplasmosis and vasogenic edema in an 18-year-old female patient with headache. **a** T2-weighted image shows central necrosis as slightly hyperintense (*arrow*) and peripheral vasogenic edema as very hyperintense in the left hemisphere (*arrowheads*). Multiple lesions of toxoplasmosis are also seen in the right occipital and left periventricular areas. **b** DW image reveals vasogenic edema as hypointense, while the central necrosis shows hyperintensity on DW image. **c** ADC map shows increased ADC from the vasogenic edema. Decreased ADC of the central necrosis is probably due to hyperviscosity of the coagulative necrosis

4.6 Conclusion

4.6.1 Cytotoxic or Cellular Edema

Cytotoxic or cellular edema is hyperintense on DW images and associated with decreased ADC. It can occur in neurons, glial cells, axons (axonal swelling) and myelin sheaths (intramyelinic edema). Cytotoxic edema may be present not only in infarction/ischemia and trauma, but also in status epilepticus, the acute phase of multiple sclerosis, toxic or metabolic leukoencephalopathy, osmotic myelinolysis, encephalitis, and presumably in the early phase of transneuronal or wallerian degeneration and Creutzfeldt–Jakob disease. The differential diagnosis for hyperintense DW images also includes tumor, abscess and hemorrhage, conditions that also may have decreased ADC. The decreased ADC in these latter conditions may be due to hypercellularity and/or hyperviscosity rather than the cytotoxic edema.

4.6.2 Vasogenic Edema

Vasogenic edema has a variable appearance on DW images, with increased ADC. It is reversible but occasionally associated with cytotoxic edema, which usually is not reversible. DW images and ADC maps are useful for understanding MR images of various diseases with cytotoxic and/or vasogenic edema. These images are more sensitive than conventional MR imaging to determine the extent of edema in both gray and white matter.

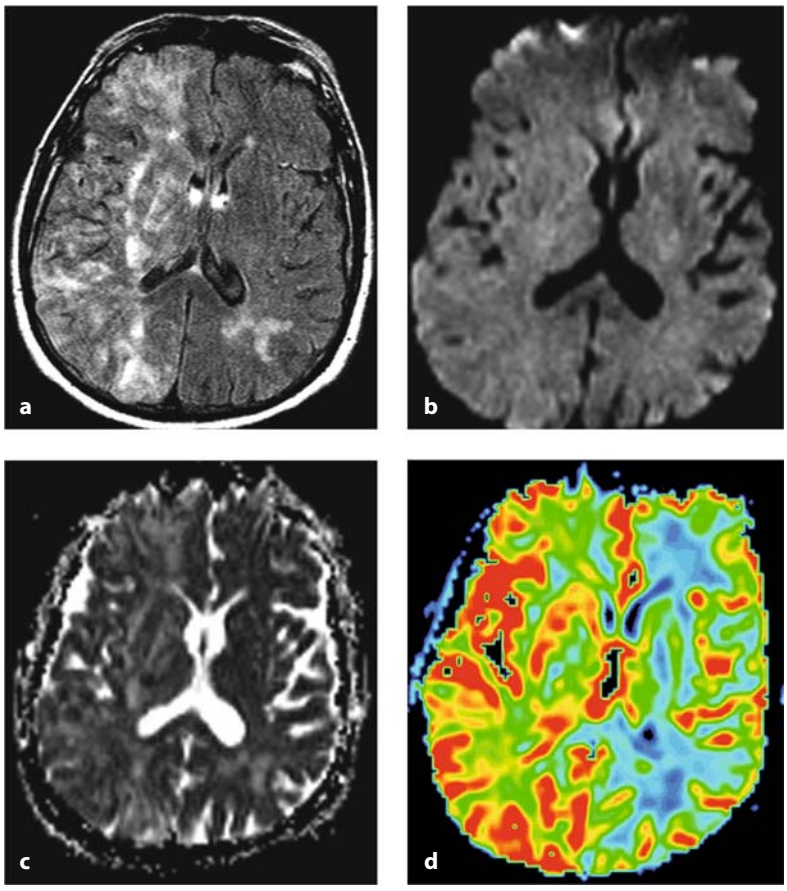

Figure 4.21 a–d

Hyperperfusion syndrome in a 72-year-old man after carotid endoatherectomy. **a** FLAIR image shows diffuse hyperintensity in the entire right hemisphere. **b** DW image reveals these areas as isointense. **c** ADC map shows increased ADC consistent with vasogenic edema. **d** Perfusion-weighted image (rCBV) shows increased cerebral blood volume in the entire right hemisphere

References

1. Milhorat TH (1992) Classification of the cerebral edemas with reference to hydrocephalus and pseudotumor cerebri. Child's Nerv Syst 8:301–306
2. Ebisu T, Naruse S, Horikawa Y, et al. (1993) Discrimination between different types of white matter edema with diffusion-weighted MR imaging. J Magn Res Imaging 3:863–868
3. Ironside JW, Pickard JD (2002) Raised intracranial pressure, oedema and hydrocephalus. In: Graham DI, Lantos PL (eds) Greenfield's neuropathology, 7th edn, pp 193–231
4. Lipton SA, Rosenberg PA (1994) Excitatory amino acids as a final common pathway for neurologic disorders. N Engl J Med 330:613–622
5. Chan S, et al. (1996) Reversible signal abnormalities in the hippocampus and neocortex after prolonged seizures. AJNR Am J Neuroradiol 17:1725–1731
6. Mark LP, Prost RW, Ulmer JL, et al. (2001) Pictorial review of glutamate excitotoxicity: fundamental concepts for neuroimaging. AJNR Am J Neuroradiol 22:1813–1824
7. Moritani T, Shrier D, Wang H, et al. (2002) Excitotoxic mechanism in pediatric brain. Neurographics Vol. 2, Article 1, http://foundation.asnr.org/neurographics/
8. Moritani T, Smoker WR, Sato Y, Numaguchi Y, Westesson PL (2005) Diffusion-weighted imaging of acute excitotoxic brain injury. AJNR Am J Neuroradiol 26:216-28
9. Sharp FR, Swanson RA, Honkaniemi J, et al. (1998) Neurochemistry and molecular biology. In: Barnett HJM, Mohr JP, Stein BM, et al. (eds) Stroke pathophysiology, diagnosis, and management, pp 54–56
10. Duong TO, Ackerman JJH, Ying HS, et al. (1998) Evaluation of extra- and intracellular apparent diffusion in normal and globally ischemic rat brain via 19F NMR. Magn Reson Med 40:1–13
11. van der Toorn A, Sykova EDRM, Vorisek I, et al. (1996) Dynamic changes in water ADC, energy metabolism, extracellular space volume, and tortuosity in neonatal rat brain during global ischemia. Magn Reson Med 36:52–56
12. Tien RD, Felsberg GJ, Friedman H, et al. (1993) MR imaging of high-grade cerebral gliomas: value of diffusion weighted echoplanar pulse sequence. AJR Am J Roentgenol 162:671–677

13. Desprechins B, Stadnik T, Koerts G, et al. (1999) Use of diffusion-weighted MR imaging in differential diagnosis between intracerebral necrotic tumors and cerebral abscesses. AJNR Am J Neuroradiol 20:1252–1257
14. Desmond PM, Lovell AC, Rawlinson AA, et al. (2001) The value of apparent diffusion coefficient maps in early cerebral ischemia. AJNR Am J Neuroradiol 22:1260–1267
15. Burdette JH, Ricci PE, Petitti N, et al. (1998) Cerebral infarction: Time course of signal intensity changes on diffusion-weighted MR images. AJR Am J Roentgenol 171: 791–795
16. Kamal AK, Segal AZ, Ulug AM (2002) Quantitative diffusion-weighted MR imaging in transient ischemic attacks. AJNR Am J Neuroradiol 23:1533–1538
17. Forbes KP, Pipe JG, Heiserman JE (2001) Evidence for cytotoxic edema in the pathogenesis of cerebral venous infarction. AJNR Am J Neuroradiol 22:450–455
18. Arbelaez A, Castillo M, Mukherji SK (1999) Diffusion-weighted MR imaging of global cerebral anoxia. AJNR Am J Neuroradiol 20:999–1007
19. Wolf RL, Zimmerman RA, Clancy R, et al. (2001) Quantitative apparent diffusion coefficient measurements in term neonates for early detection of hypoxic-ischemic brain injury: initial experience. Radiology 218:825–833
20. Barzo P, Marmarou A, Fatouros P, et al. (1997) Contribution of vasogenic and cellular edema to traumatic brain swelling measured by diffusion-weighted imaging. J Neurosurg 87:900–907
21. Liu AY, Maldjian JA, Bagley LJ, Sinson GP, et al. (1999) Traumatic brain injury: diffusion-weighted MR imaging findings. AJNR Am J Neuroradiol 20:1636–1641
22. Kim JA, Chung JI, Yoon PH, et al. (2001) Transient MR signal changes in patients with generalized tonicoclonic seizure or status epilepticus: periictal diffusion-weighted imaging. AJNR Am J Neuroradiol 22:1149–1160
23. Men S, Lee DH, Barron JR, et al. (2000) Selective neuronal necrosis associated with status epilepticus; MR findings. AJNR Am J Neuroradiol 21:1837–1840
24. Butteriss DJ, Ramesh V, Birchall D (2003) Serial MRI in a case of familial hemiplegic migraine. Neuroradiology 45:300-303
25. Liang Y, Scott TF (2007) Migrainous infarction with appearance of laminar necrosis on MRI. Clin Neurol Neurosurg 109:592-596
26. Tsuchiya K, Katase S, Yoshino A, et al. (1999) Diffusion-weighted MR imaging of encephalitis. AJR Am J Roentgenol 173:1097–1099
27. Demaerel P, Baert AL, Vanopdenbosch L, et al. (1997) Diffusion-weighted magnetic resonance imaging in Creutzfeldt–Jakob disease. Lancet 349:847–848
28. Bahn MM, Parchi P. (1999) Abnormal diffusion-weighted magnetic resonance images in Creutzfeldt–Jakob disease. Arch Neurol 56:577–583
29. Castillo M, Mukherji SK (1999) Early abnormalities related to postinfarction wallerian degeneration: evaluation with MR diffusion-weighted imaging. JCAT 23:1004–1007
30. Verity MA (1997) Toxic disorders. In: Graham DI, Lantos PL (eds) Greenfield's neuropathology, 6th edn, pp 755–811
31. Tievsky AL, Ptak T, Farkas J (1999) Investigation of apparent diffusion coefficient and diffusion tenser anisotropy in acute and chronic multiple sclerosis lesion. AJNR Am J Neuroradiol 20:1491–1499
32. Matsumoto S, Nishizawa S, Murakami M, et al. (1995) Carmofur-induced leukoencephalopathy: MRI. Neuroradiology 37:649–652
33. Phillips MD, McGraw P, Lowe MJ, et al. (2001) Diffusion-weighted imaging of white matter abnormalities in patients with phenylketonuria. AJNR Am J Neuroradiol 22:1583–1586
34. Sener RN (2002) Metachromatic leukodystrophy: diffusion MR imaging findings. AJNR Am J Neuroradiol 23:1424–1426
35. Cramer SC, Stegbauer KC, Schneider A, et al. (2001) Decreased diffusion in central pontine myelinolysis. AJNR Am J Neuroradiol 22:1476–1479
36. Maeda M, Shiroyama T, Tsukahara H, Shimono T, Aoki S, Takeda K (2003) Transient splenial lesion of the corpus callosum associated with antiepileptic drugs: evaluation by diffusion-weighted MR imaging. Eur Radiol 13:1902-1906
37. Tada H, Takanashi J, Barkovich AJ et al. (2004) Clinically mild encephalitis/encephalopathy with a reversible splenial lesion. Neurology 63:1854-1858
38. Maeda M, Tsukahara H, Terada H et al. (2006) Reversible splenial lesion with restricted diffusion in a wide spectrum of diseases and conditions. J Neuroradiol 33:229-236
39. Gonatas NK, Zimmerman HM, Levine S (1963) Ultrastructure of inflammation with edema in the rat brain. Am J Pathol 42:455–469
40. Mukherjee P, McKinstry RC (2001) Reversible posterior leukoencephalopathy syndrome: evaluation with diffusion-tensor MR imaging. Radiology 219:756–765
41. Keller E, Flancke S, Urbach H, et al. (1999) Diffusion- and perfusion-weighted magnetic resonance imaging in deep cerebral venous thrombosis. Stroke 30:1144–1146
42. Basser PJ, Pierpaoli C (1996) Microstructural and physiological features of tissues elucidated by quantitative-diffusion-tensor MRI. J Magn Reson 111:209-219
43. Moritani T, Shrier DA, Numaguchi Y, et al. (2000) Diffusion-weighted echo-planar MR imaging: clinical applications and pitfalls – a pictorial essay. Clin Imaging 24: 181–92
44. Moritani T (2002) Classification of brain edema. In: Aoki S, Abe O (eds), Koredewakaru Diffusion MRI. Shujunsha, Tokyo, pp 128–137

Infarction

In collaboration with Y. Ohgiya and R. de Guzman

5.1 Clinical Significance and Therapeutic Considerations for Brain Infarcts

Stroke is the third leading cause of death in the USA, and cerebral infarction is the most common cause of disability among adult Americans. Until recently these patients were mainly imaged with computed tomography (CT) to establish if the cause of stroke was ischemic or hemorrhagic. Treatment was above all aimed to reduce the risk for further embolic events.

The National Institute for Neurological Diseases and Stroke Trial [1] has demonstrated a clinical benefit for intravenous thrombolytic drug therapy in cases of acute stroke using CT. A subsequent trial showed better clinical outcomes of thrombolytic drug therapy in patients with acute infarction who were selected on the basis of imaging criteria including diffusion-weighted (DW) imaging [2].

5.1.1 Stroke Mimickers

There is a long list of conditions that mimic the symptoms of an acute ischemic stroke. The most common ones include intracranial hemorrhage, migraines, seizures, functional and metabolic disorders, and also vasogenic edema syndromes. It is important to visualize and verify that an ischemic lesion is indeed the cause of the clinical symptoms before therapy is initiated, as these non-ischemic stroke mimickers should not be treated with thrombolysis and such therapy could actually be harmful. Moreover, in older patients it is not uncommon to detect older lesions with prolonged T2 that are indistinguishable from acute lesions using conventional MR imaging.

5.1.2 Diffusion-Weighted Imaging

CT as well as conventional MR imaging have sensitivities below 50% with regard to detection of infarcts in the hyperacute stage, within 6 hours [3]. In recent years, DW imaging has been proven as the most sensitive MR imaging technique to diagnose hyperacute cerebral infarction, with a sensitivity of 88%–100% and a specificity of 86%–100% [4-7]. The detection of acute ischemic lesions is based on alterations in motion of water molecules [8, 9].

DW imaging techniques employ echo-planar sequences that are highly resistant to patient motion. DW imaging of the brain can usually be accomplished in less than 2 minutes. Other methods of diffusion imaging include single-shot fast spin-echo techniques, line scan DW imaging, and spiral DW MR imaging [10, 11].

The ischemic event results in restricted diffusion of the affected tissue, which can be seen as early as 30 minutes after ictus [12]. A few rare cases of false-negative DW imaging have been reported [13, 14]. These infarcts were seen on perfusion-weighted images and later on DW imaging [13, 14].

5.2 Diffusion-Weighted Imaging and Pathophysiology of Cerebral Infarction

The abnormal imaging finding of cerebral and cerebellar infarctions is an area of hyperintensity on DW imaging of the involved vascular territory. This hyperintensity is presumed to be caused by cytotoxic edema as a result of cessation of ATP production [15]. Under normal circumstances, ATP maintains the Na^+/K^+ pump activity and other intracellular energy-related processes. When the Na^+/K^+ pump is not functioning properly, an inability to remove excess water from the cells develops, resulting in intracellular edema [16]. With cellular swelling, there is a reduction in the volume of extracellular space. A decrease in the diffusion of low-molecular-weight tracer molecules has been demonstrated in animal models [17, 18], which suggests that the increased tortuosity of extracellular space pathways contributes to restricted diffusion in acute ischemia. The outcome of this on DW imaging is restriction of water diffusion, which results in a signal increase on DW imaging and a decrease in

diffusion shown as a reduced apparent diffusion coefficient (ADC) [19]. These findings in acute stroke usually represent irreversible damage of brain tissue, or infarction [20, 21].

5.3 Apparent Diffusion Coefficient

The actual diffusion coefficient cannot be measured by using DW imaging for a number of reasons [12]. When measuring molecular motion with DW imaging, the diffusion coefficient obtained from orthogonal DW images in all three planes is called the ADC. The ADC is used to determine whether the signal abnormality on DW images is caused by restricted diffusion or a T2 shine-through effect [22], as seen in subacute–chronic infarctions. ADC represents the degree of diffusibility of water molecules and aids in detecting subtle fluid changes in the hyperacute–acute stages of ischemic stroke. Reduced diffusion is seen as an area of low signal intensity on ADC maps.

5.3.1 Explanation for Restricted Diffusion

Several mechanisms have been proposed to explain the restricted diffusion in ischemia. These include cellular necrosis, shift of fluid from extra- to intracellular spaces causing a reduction in size and increase in tortuosity of the extracellular space, but there is also rather strong evidence that at least parts of these findings relate to a reduction in intracellular diffusion [23].

Regions of decreased or restricted diffusion are best seen on DW imaging, while ADC maps will verify the findings by eliminating the T2 shine-through effect as a cause of the increased signal intensity on DW imaging [12]. DW imaging and ADC can also show changes in diffusion that vary for the different stages of a stroke [24], and they can possibly distinguish between multiple strokes over time versus a single, progressive stroke by determining the time course of a cerebral infarction.

In animal models of ischemia, an ADC threshold for reversibility has been demonstrated [25, 26]. In humans, ADC values may also be of help in the future to assist in selecting patients with salvageable tissue within an ischemic penumbra for thrombolysis.

In older patients it is not uncommon to detect older lesions with prolonged T2 that are indistinguishable from acute lesions using conventional MR imaging. Acute infarctions are hyperintense on DW images and hypointense on ADC maps, whereas chronic foci are usually isointense on DW images and hyperintense on ADC maps [27].

Intermediate ADC values are noted in the ischemic penumbra, indicating tissue at risk of infarction [28]. An approach that is used more often to select patients who may benefit from thrombolysis is by comparing DW imaging and perfusion MR imaging to look for hypoperfused but not diffusion-restricted regions. The mismatch between DW imaging and perfusion demonstrates affected tissue that is still salvageable and not yet infarcted: the penumbra.

5.4 Time Course of Infarction

Infarctions may be classified as hyperacute (less than 6 hours from time of onset of symptoms), acute (6 hours to 3 days), subacute (3 days to 3 weeks), or chronic (3 weeks to 3 months), each having its characteristic signal abnormalities (Table 5.1).

5.4.1 Hyperacute (< 6 Hours)

One of the main clinical applications of DW imaging is to detect a hyperacute cerebral infarction. This information is critical, particularly in cases of territorial thromboembolic infarction, as thrombolytic therapy can be started within the golden period of 3 hours from onset of symptoms. Such treatment can result in early reperfusion and reduce the extension of the infarction [19, 29]. Diffusion restriction with reduced

Table 5.1 Time course of thromboembolic infarction of the middle cerebral artery [29]

	< 6 hours	3 days	7 days	30 days
T2	Isointense	Bright	Bright	Bright
DW imaging	Bright	Very bright	Bright	Isointense
ADC	Dark	Very dark	Dark	Bright

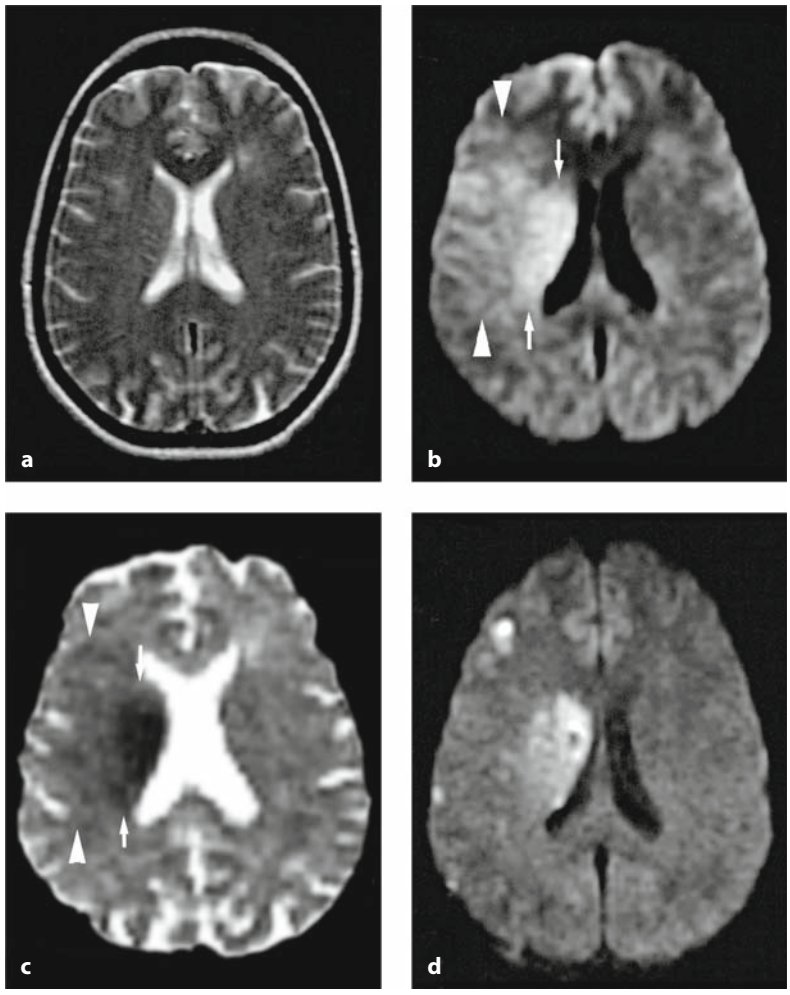

Figure 5.1 a–d

Hyperacute infarction (2 hours after onset) in a 39-year-old woman with decreased consciousness. The symptoms improved after intra-arterial fibrinolytic therapy. **a** T2-weighted image appears normal. **b** DW image shows a hyperintense lesion in the right corona radiata (*arrows*) and a slightly hyperintense lesion in the right middle cerebral artery (MCA) territory (*arrowheads*). **c** ADC map shows decreased ADC in the corona radiata (*arrows*) and slightly decreased ADC in the cortical area of the MCA territory (*arrowheads*). **d** On DW image after fibrinolytic therapy (3 days after onset), the hyperintense lesion in the cortical area mostly resolved with peripheral small infarcts. Early cytotoxic edema with mild decreased ADC does not always result in infarction after treatmentt

ADC has been observed as early as 30 minutes after the onset of ischemia, at a time when T2-weighted images still show a normal appearance. The DW signal intensity is increased during the hyperacute stage (<6 hours) (Fig. 5.1). DW signal intensity changes are generally considered to be permanent (and therefore reflect infarction) in clinical studies. However, some cases could be reversed with prompt treatment [30].

5.4.2 Acute (6 Hours to 3 Days)

Almost all acute (6 hours to 3 days) stroke patients examined within 24 hours of onset of symptoms show abnormal signal intensity on DW imaging [31]. At this stage the infarctions show a further increase in DW signal intensity and also a lower ADC than in the hyperacute stage (Fig. 5.2). The ADC continues to decrease and is most reduced at 8–32 hours, remaining markedly reduced for 3–5 days. In most patients, a secondary increase in the size of the DW imaging abnormality was seen within 1 week [32].

5.4.3 Subacute (3 Days to 3 Weeks)

As the infarct continues to evolve into the subacute stage (3 days to 3 weeks), there is pseudo-normalization of the ADC, most likely attributed to a combination of (a) persistence of cytotoxic edema, and (b) development of vasogenic edema and cell membrane disruption, which results in increased amounts of extracellular water. The hyperintensity on DW imaging usually decreases within 1–2 weeks [33], but is still

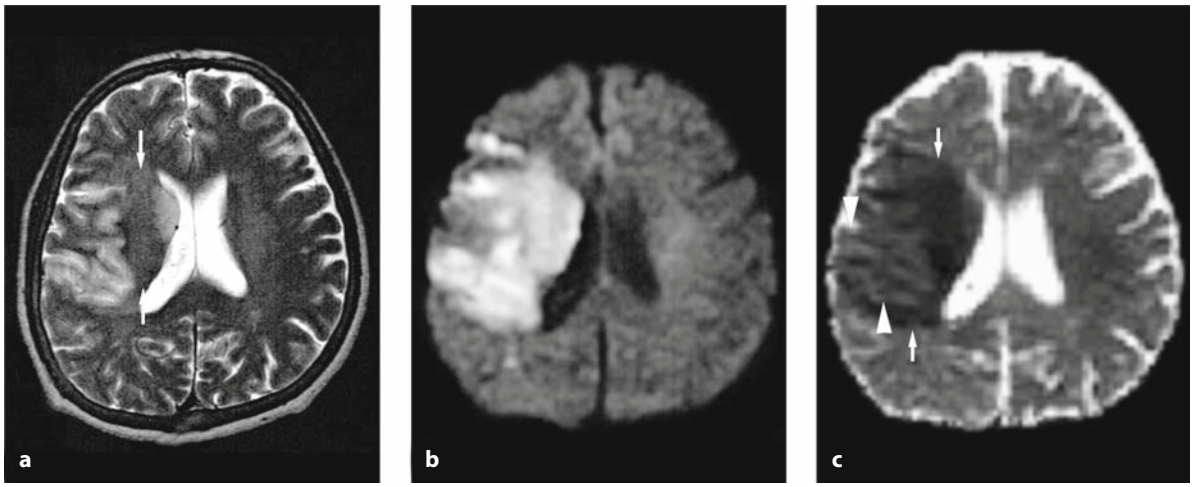

Figure 5.2 a–c

Acute infarction (24 hours after onset) in a 56-year-old man with left hemiparesis. **a** T2-weighted image shows hyperintense lesions preferentially involving the right posterior frontal cortex and the right caudate region, sparing the right corona radiata (*arrows*). This finding is consistent with a relatively greater involvement of gray matter in the early infarction. **b** DW image shows the entire right MCA territory as hyperintense. **c** Decreased ADC is seen in the right MCA territory (*arrows*). However, some cortical lesions seem to be isointense or have a slightly increased ADC (*arrowheads*). This may reflect relative vulnerability for brain tissue. Hyperintensity on DW image of these cortical lesions is due to a T2 shine-through effect. DW images and ADC maps are more sensitive than conventional MR imaging for showing both gray and white matter involvement. ADC maps precisely reflect diffusion restrictions of the lesion within the gray and white matter

slightly hyperintense, while ADC is usually normalized within 10 days [34, 35]. This time gap is thought to result from T2 shine-through effects on DW imaging in the late subacute infarction (Fig. 5.3).

5.4.4 Chronic (3 Weeks to 3 Months)

In the chronic stage (3 weeks to 3 months) of infarction, there is a more or less complete necrosis of the cells, and at this stage there is an increase in ADC with a bright signal on the ADC map. On T2-weighted images the infarction is seen as a bright signal and this, in combination with the increased ADC, will result in a decrease in the signal on DW imaging; the gliosis in the infarction is isointense with surrounding tissue (Fig. 5.4).

5.5 Diffusion-Weighted Imaging and ADC Characteristics of Gray and White Matter Ischemia

Diffusion-weighted imaging and ADC maps are more sensitive than conventional MR imaging in demonstrating both gray and white matter ischemia (Figs. 5.1, 5.2 and 5.3). Changes in ADC values in acute infarctions seem to be different for gray matter and white matter. Thus, there is a more prominent decrease in ADC in white matter than in gray matter. This decrease also remains for a longer period than in gray matter (Figs. 5.2 and 5.3). One of the explanations for these phenomena is that necrosis may be completed earlier in gray matter infarctions than in white matter infarctions. Another explanation is that the prominent and prolonged decrease in ADC in white matter may reflect cytotoxic edema in different cell types, such as myelin sheaths, axons and glial cells [23, 24, 34].

Fiebach et al. observed a decrease in the relative ADC up to 3 days after the stroke and an increase in relative ADC from the third to the tenth day [24]. The relative ADC increased slightly faster in gray matter

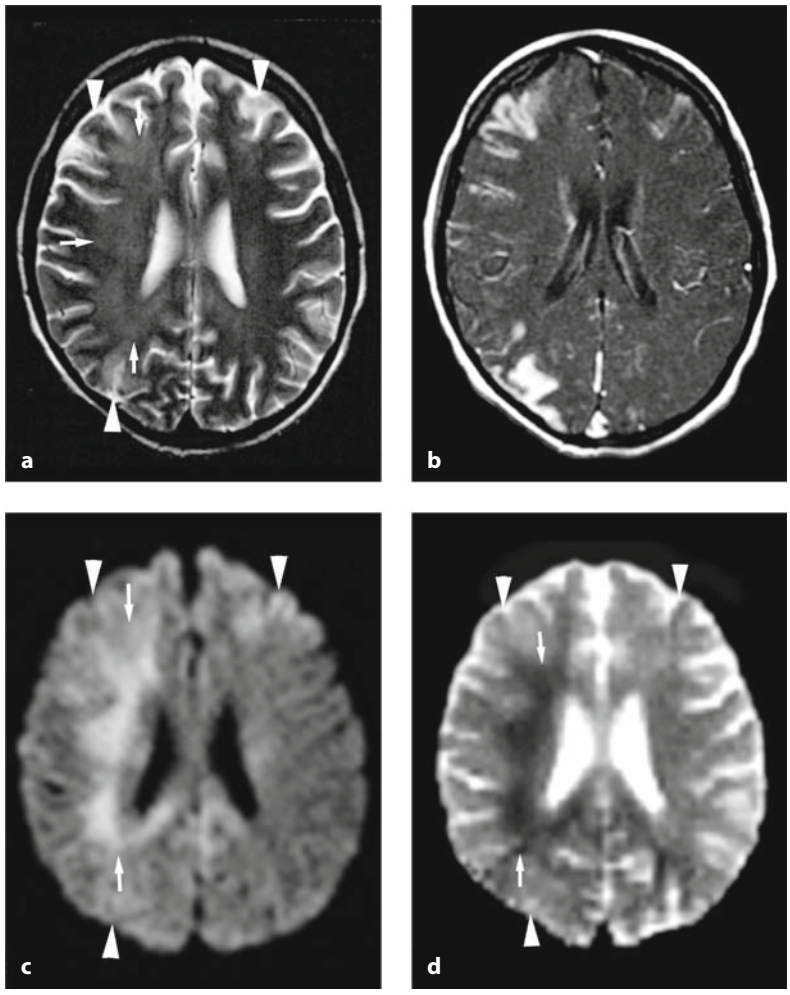

Figure 5.3 a–d

Subacute infarction (10 days after onset) in a 19-year-old woman with loss of consciousness due to cerebral embolism after cardiac surgery for endocarditis. **a** T2-weighted image shows hyperintense lesions in the gray (*arrowheads*) and white matter (*arrows*) in the right hemisphere and left frontal region. **b** Gadolinium T1-weighted image with magnetization transfer contrast shows gyral enhancement in the cortical lesions, representing subacute infarcts. **c** DW image also shows hyperintense lesions in the right deep white matter (*arrows*), and gray matter of both frontal and right parieto-occipital regions (*arrowheads*). **d** The ADC map shows decreased ADC in the right deep white matter lesion (*arrows*), and normal or slightly increased ADC in the gray matter lesions (*arrowheads*). The prolonged decreased ADC in the white matter may reflect edema of myelin sheaths or axons

than in white, which may be due to the variability between these two tissue types at any stage in the ischemic process, which leads to an altered diffusion. The observed diffusion contrast in gray and white matter could be caused by differences in the mismatch between blood supply and metabolic demand, the type and/or severity of the histopathologic response to ischemic injury (vulnerability) or mechanisms by which histopathologic changes lead to altered diffusion [36]. Regarding the histopathologic response, gray matter has traditionally been considered to be more vulnerable than white matter to early ischemia. More recent findings in experimental models of stroke have demonstrated that ischemic damage to white matter occurs earlier and with greater severity than previously appreciated [37]. However, if this is true for humans as well is to our knowledge, not yet established.

5.6 Reversibility and Treatment

Reversible ADC is rare but can be found in cases of transient ischemic attack in which imaging was performed within 4 hours, venous infarction, hemiplegic migraine and transient global amnesia. In these rare clinical settings, ischemia does not progress to complete necrosis but a minor subclinical, irreversible injury cannot be ruled out [23].

Clinically, the area of cytotoxic edema with bright DW signal seems to be irreversibly damaged resulting in permanent infarction. In early cerebral ischemia, mildly decreased ADC in the ischemic penumbra is indicative of viable tissue, but hypoperfused tissue at risk of infarction [38]. After intra-arterial or intravenous fibrinolytic therapy, or spontaneous lysis of

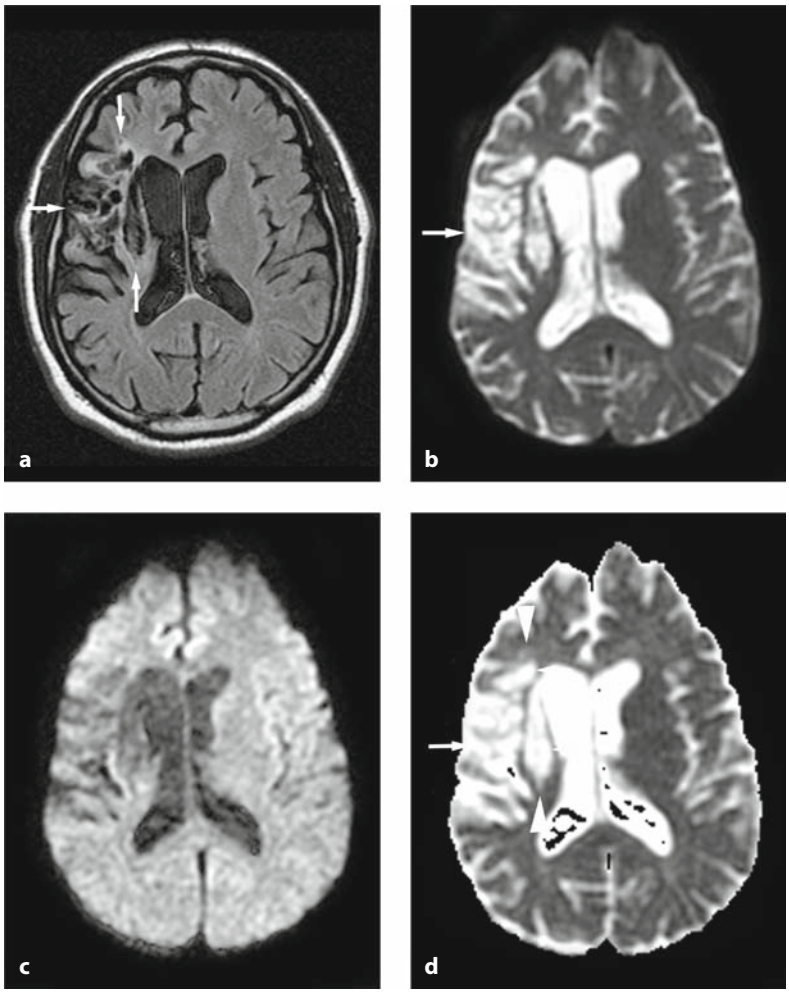

Figure 5.4 a–d

Chronic infarction (10 months after onset) in a 54-year-old man with numbness and weakness of the left lower extremity. **a** Fluid-attenuated inversion-recovery (FLAIR) image shows chronic infarction in the right MCA territory as a cystic lesion with low signal intensity (cystic necrosis) and peripheral mild hyperintensity (gliosis) with atrophy (*arrows*). **b** b_0 image shows the hyperintense cystic lesion (*arrow*). **c** DW image shows chronic infarction as hypointense cystic areas, and iso- or slightly hyperintense areas representing gliosis. **d** The ADC map shows marked increased ADC in the cystic necrosis (*arrow*), and slightly increased ADC in the gliotic periphery of the lesion (*arrowheads*)

a clot, abnormal signal in such areas is occasionally reversed, partially or completely (Figs. 5.4 and 5.5).

ADC normalization is not a rare event in acute stroke after thrombolytic therapy [39]. ADC normalization occurred predominantly in the basal ganglia and white matter after thrombolytic therapy in patients with more distal vessel occlusions. Early reperfusion is a prerequisite for ADC normalization. Tissue prone to ADC normalization is characterized by less severe initial ADC decreases.

5.7 Watershed Infarction

Watershed infarction may develop between two major vascular territories or within a single territory in the supraganglionic white matter, a border zone of the superficial and deep penetrating arterioles (Fig. 5.6). As mentioned above, thrombolytic therapy within the first 3 hours from acute onset of symptoms can be effective to limit the size of the infarct under those circumstances. This is, however, not the case in watershed infarctions, as the basic etiology for these lesions is a significant reduction in perfusion secondary to an overall decrease in cerebral blood flow with subsequent poor perfusion pressure distally [29, 40].

There is a difference in the evolution time of ADC between watershed and thromboembolic infarction, the latter having an earlier normalization (Table 5.2). However, T2 signal intensity is the same for both types of infarction. The reason for this difference most likely lies in the different pathophysiologic features and cerebral perfusion of the two stroke subtypes. It is important to note that strokes with different pathoge-

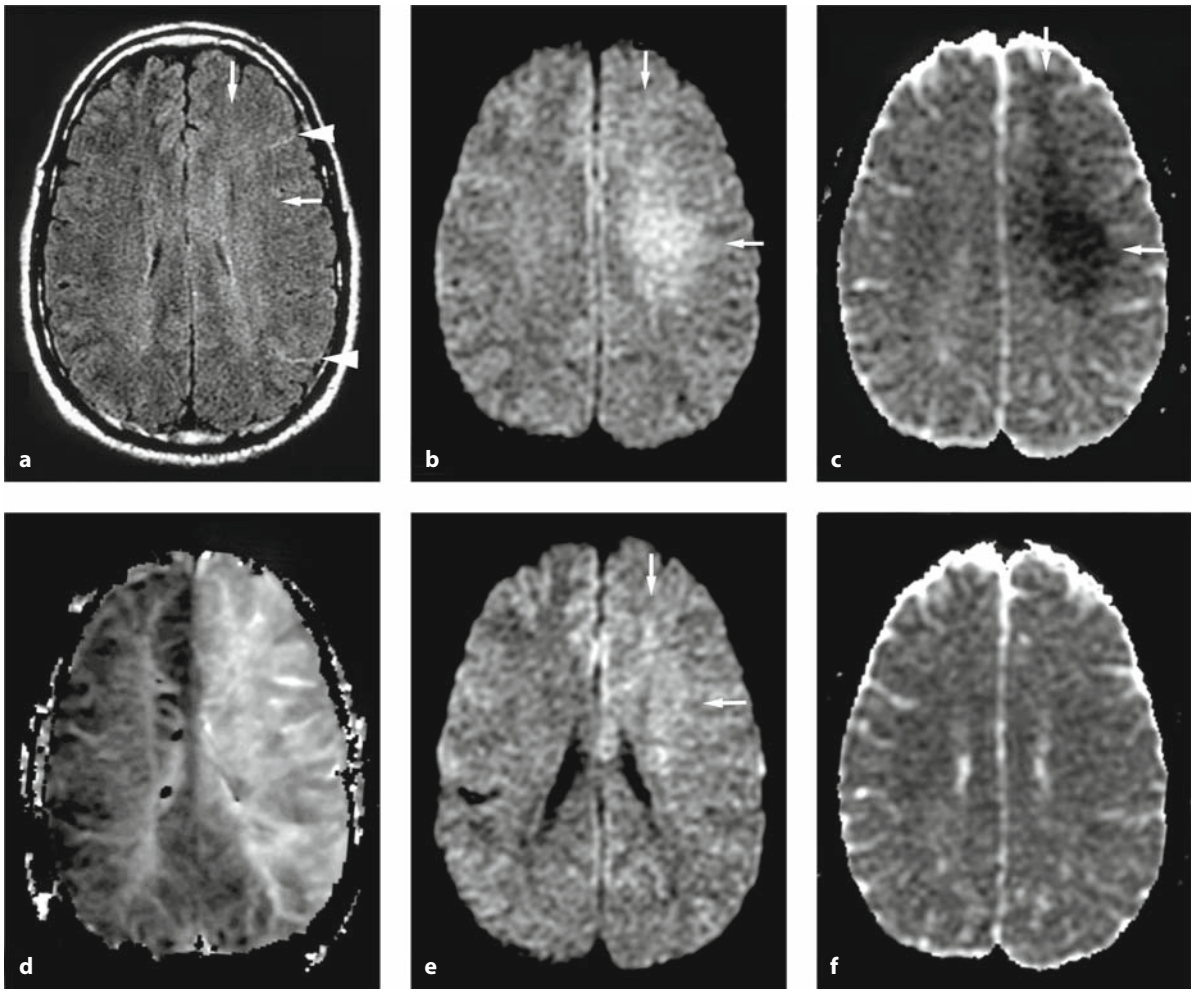

Figure 5.5 a–f

Reversible ischemia with cytotoxic edema (2 h from onset) in a 39-year-old man with left internal carotid artery dissection, presenting with right-sided weakness. **a** FLAIR image shows a subtle hyperintensity in the left frontoparietal white matter (*arrows*), and linear hyperintensity representing slow flow in the peripheral arteries (*arrowheads*). **b, c** DW image (**b**) shows a hyperintense lesion with decreased ADC (**c**) in the left frontoparietal white matter, representing cytotoxic edema (*arrows*). **d** Perfusion-weighted image shows increase in mean transit time of the entire left ACA and MCA territories. **e** Follow-up DW image 2 days later shows only a very subtle hyperintensity in the left frontal white matter (*arrows*). **f** ADC was normalized, which is in accordance with clinical improvement. Early ischemia with cytotoxic edema may have spontaneously resolved

netic, hemodynamic mechanisms may have different evolution in the ADC courses as well [29].

In fact, perfusion-weighted MR imaging demonstrated differences between territorial infarction and watershed infarction in the temporal changes of both relative cerebral blood volumes [40]. Patients with territorial infarction showed a progressively increasing pattern in relative cerebral blood volume from initial low values to peak high values at an early chronic stage. On the other hand, patients with watershed infarction showed consistently high relative cerebral blood volume throughout all stages.

5.8 Perfusion Versus Diffusion Imaging

Perfusion-weighted (PW) imaging may be more sensitive than DW imaging in the detection of a hyperacute cerebral infarction, but it currently entails extensive post-processing to create interpretable perfusion maps (Figs. 5.5 and 5.6). Moreover, MR perfusion determines the degree of blood flow reduction at the level of the cerebral microvasculature, but it will not tell if a hypoperfused area represents an area of infarction or severe hypoperfusion. Perfusion MR can, however, be matched with the infarcted area on DW images and can demonstrate the area of hypoperfusion outside the infarction – the so-called penumbra. This is the area where neural tissue is at risk

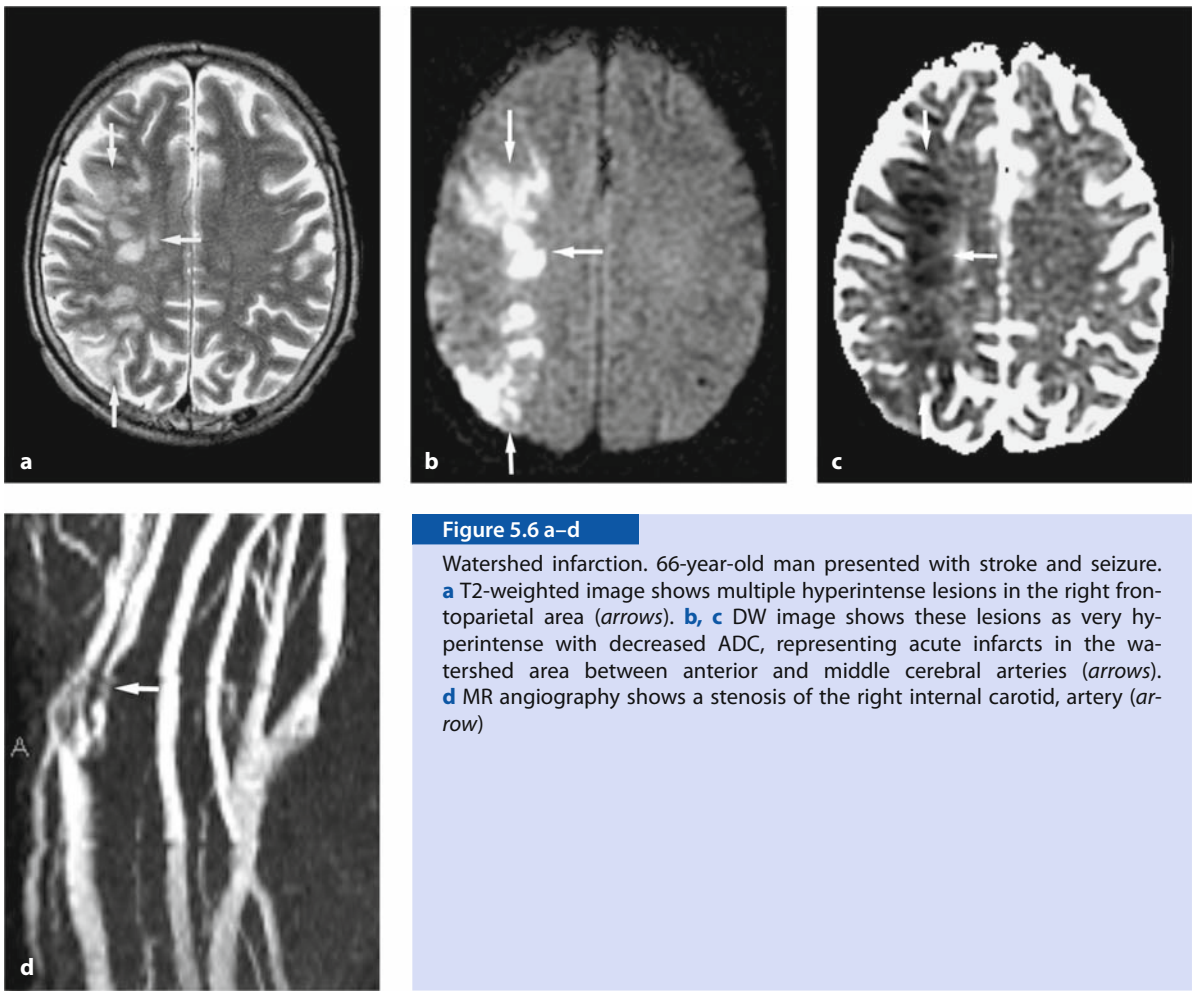

Figure 5.6 a–d

Watershed infarction. 66-year-old man presented with stroke and seizure. **a** T2-weighted image shows multiple hyperintense lesions in the right frontoparietal area (*arrows*). **b, c** DW image shows these lesions as very hyperintense with decreased ADC, representing acute infarcts in the watershed area between anterior and middle cerebral arteries (*arrows*). **d** MR angiography shows a stenosis of the right internal carotid, artery (*arrow*)

Table 5.2 Time course of watershed infarction of middle cerebral arterial territory [29]

	3 days	7 days	14 days	30 days
T2	Bright	Bright	Bright	Bright
DW imaging	Bright	Bright	Bright	Bright
ADC	Dark	Dark	Dark	Less dark

for infarction if perfusion is not re-established and ischemic penumbra is assumed to be salvageable by means of thrombolysis.

Most acute ischemic stroke patients arrive after the 3-hour time window for recombinant tissue plasminogen activator administration. Intravenous desmoteplase administered 3–9 hours after acute ischemic stroke in patients selected with perfusion/diffusion mismatch is associated with a higher rate of reperfusion and a better clinical outcome compared with placebo [2]. A wider time-to-treatment window may be achievable in patients selected by PW and DW imaging.

5.9 Venous Infarction

Cerebral venous sinus thrombosis accounts for only a small percentage of cerebral infarctions in general. Because of its non-specific presentation, cerebral venous sinus thrombosis can be difficult to diagnose. In about 50% of cases, cerebral venous sinus thrombosis results in cerebral venous infarction. This usually presents as a hemorrhagic infarction or focal edema in regions that are not typical for an arterial vascular distribution, usually occurring within the white matter or at the gray–white matter junction (Fig. 5.7).

5.9.1 Predisposing Factors

There are several predisposing factors for thrombus formation within the cerebral venous sinuses. These include pregnancy, infection, extrinsic compression or local invasion by tumor, dehydration, oral contraceptives, hypercoagulable state, trauma, drug abuse. It may also be idiopathic. Thrombus initially forms within the venous sinuses, eventually extending to the veins draining into the sinuses, leading to infarction.

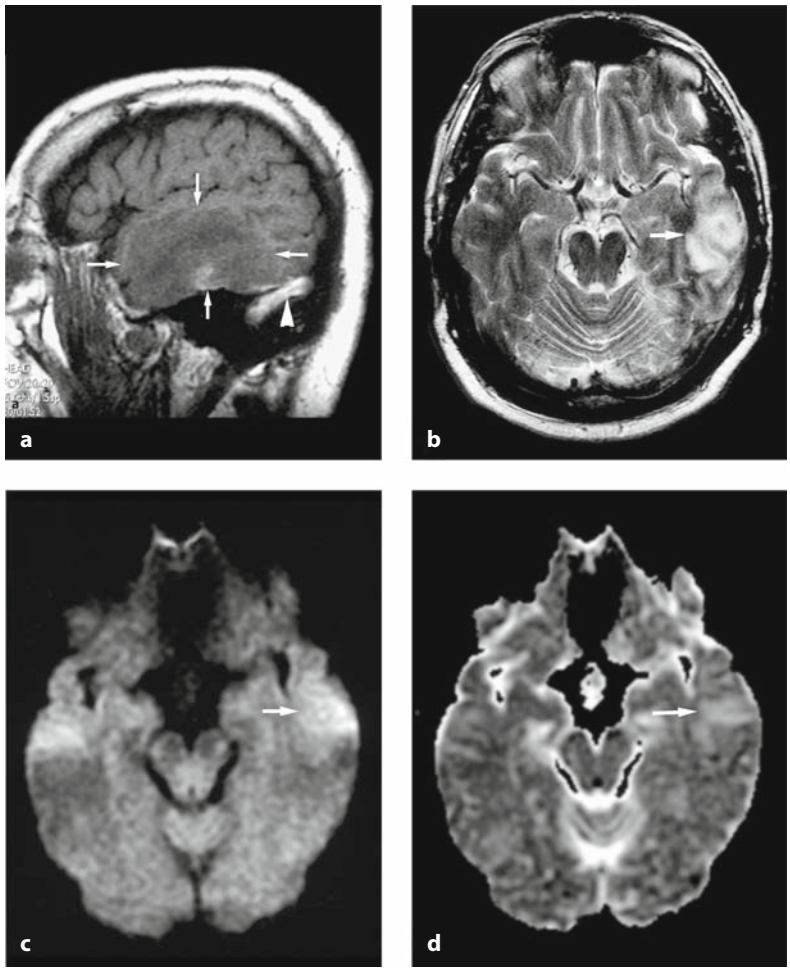

Figure 5.7 a–d

Venous infarction in a 57-year-old man with dysarthria. **a** Sagittal T1-weighted image shows a large area of hypointensity in the left temporal lobe (*arrows*) with a small area (hemorrhage). The hyperintensity in the left transverse sinus represents sinus thrombosis (*arrowhead*). **b** T2-weighted image shows a hyperintense lesion in the left temporal lobe (*arrow*). **c** DW image reveals this lesion as mildly hyperintense. **d** ADC is increased, representing vasogenic edema. On DW image, the lesion is overlapped with diamagnetic susceptibility artifacts from air in the mastoid cells

5.9.2 Pathophysiology and Imaging

The pathophysiological mechanisms that lead to cerebral venous infarction are unclear. It has been postulated that: (1) retrograde venous pressure may cause breakdown of the blood–brain barrier, with leakage of fluid (vasogenic edema) and hemorrhage into the extracellular space or, (2) retrograde venous pressure may cause a decrease in cerebral blood flow, causing tissue damage similar to that seen in arterial infarctions. Restricted water diffusion suggesting cytotoxic edema is found in patients with acute cerebral venous infarction [41, 42]. However, areas without diminishment in ADC may primarily represent vasogenic edema from venous hypertension [43] (Figs. 5.7 and 5.8). Complete or nearly complete resolution of edema in patients with cerebral venous thrombosis and diminished ADC values has also been reported [44].

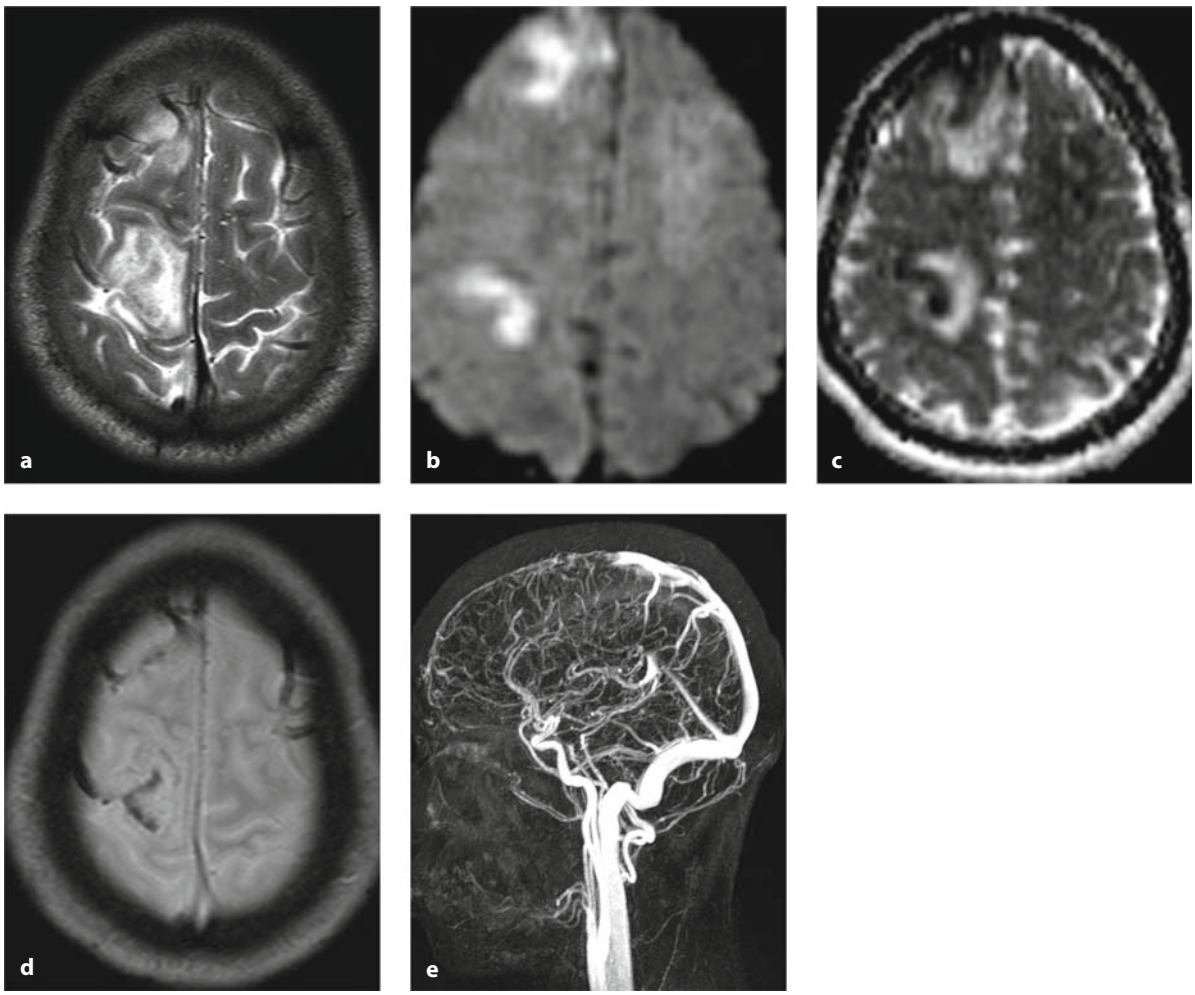

Figure 5.8 a–e

Acute-phase thrombosis with venous infarcts. A 23-year-old man with hypercoagulative state. **a** T2-weighted image shows hyperintense lesions in the right frontal lobe. It is difficult to detect the thrombi in the superior sagittal sinus and cortical veins. **b**, **c** DW image demonstrates hyperintense lesions with decreased ADC (cytotoxic edema) and surrounding increased ADC (vasogenic edema) consistent with venous infarcts. **d** On GRE hypointense thrombi in an arborizing fashion are clearly noted in the cortical veins in the bilateral frontal lobes. **e** Dynamic contrast 3D MR venogram shows nonvisualization of the anterior 2/3 of the superior sagittal sinus and the cortical veins

Gradient echo T2* images are very useful in the detection of acute- to subacute-phase thrombi as very low signals (deoxy- or intracellular methemoglobin), especially before T1-weighted images show high signals in the subacute-phase thrombi (Fig. 5.8). DW imaging shows subacute-phase thrombi as high signals with decreased ADC (Fig. 5.9). Diffusion restriction of the thrombi may be predictive of a low rate of recanalization [45].

Preferred imaging modalities when suspecting cerebral venous sinus thrombosis are conventional MR imaging including gradient echo T2* images combined with MR venography.

Figure 5.9 a–d

Subacute to chronic-phase thrombosis in the left jugular vein, transverse and sigmoid sinuses after decompression surgery for high jugular bulb in a 7 year-old boy. **a, b** T2- and T1-weighted images show subacute-phase thrombi (*arrows*) in the left transverse and sigmoid sinuses extending from the left jugular bulb as hyperintense. **c, d** DW image shows the subacute thrombi (*arrows*) as hyperintense with decreased ADC

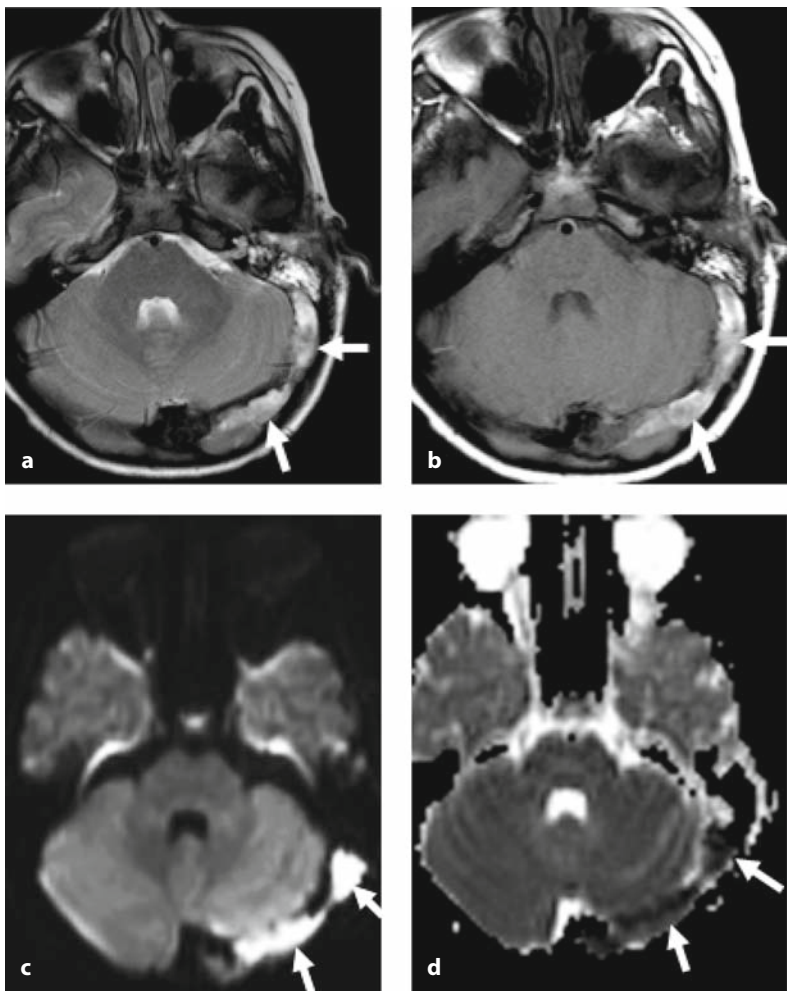

5.10 Small Vessel Infarcts

These are small infarcts measuring approximately 5–15 mm, usually seen in the basal ganglia, internal capsule, thalamus, pons and corona radiata. They account for about 20% of all infarctions and are secondary to an embolus, thrombus or atheromatous lesion within long, single, penetrating end arterioles.

These infarcts show increased signal in DW imaging with low ADC values (Fig. 5.10). However, unlike the usual time course of cerebral infarctions, they

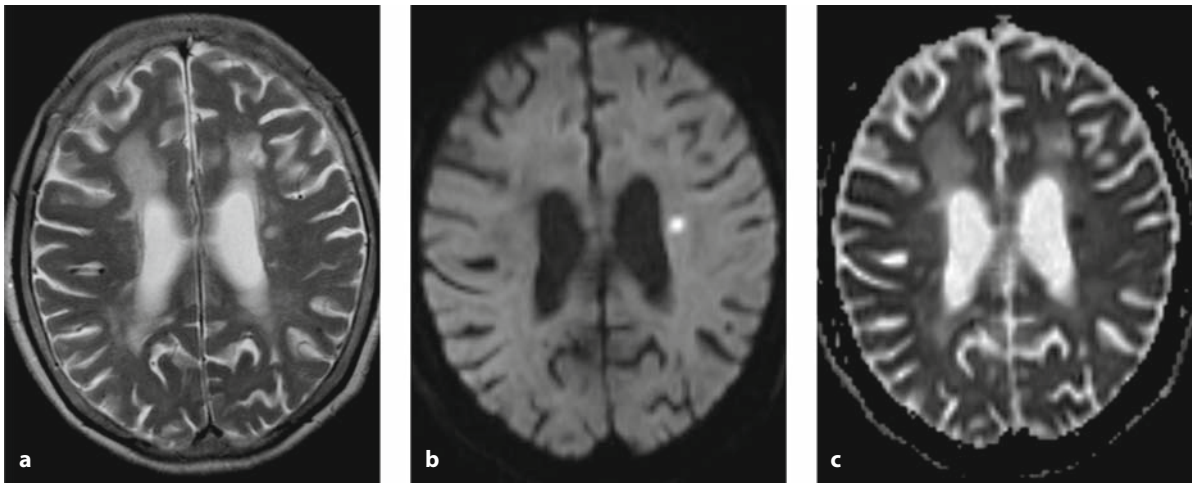

Figure 5.10 a–c

Small vessel infarction in a 74-year-old woman. **a** T2-weighted image shows periventricular hyperintensities; however, it is difficult to detect acute small infarction. **b** DW image clearly shows a small hyperintensity spot in the left white matter. **c** ADC is decreased, representing the acute phase of small vessel infarction

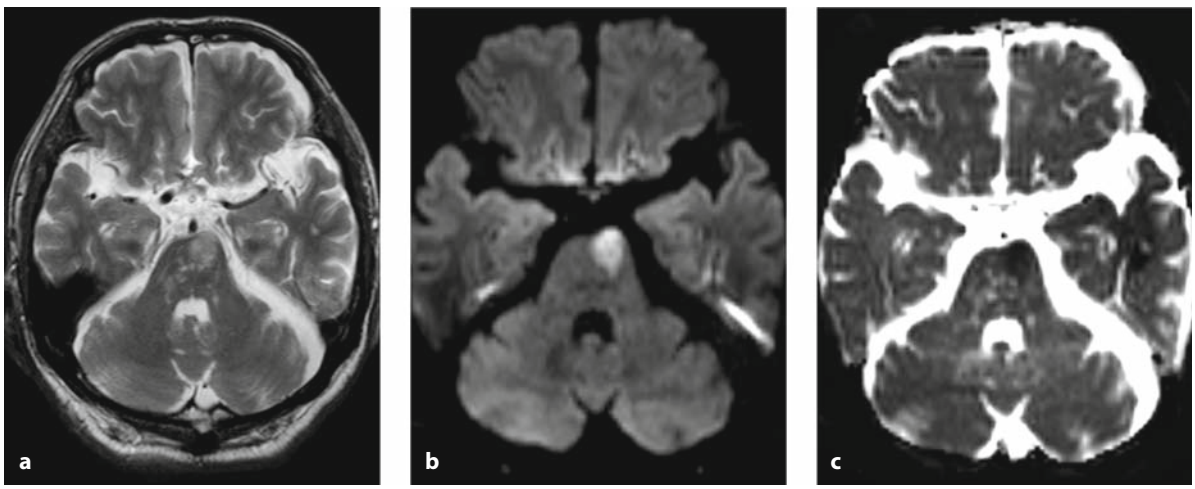

Figure 5.11 a–c

Brain stem infarction in an 85-year-old man with slurred speech and gait difficulties. **a** T2-weighted image show a hyperintense lesion in the left side of the pons. **b** DW image clearly shows a hyperintense lesion. **c** The ADC is decreased, representing acute infarction

may show a prolonged increase in DW imaging signal and decrease in ADC values, sometimes seen beyond 60 days after onset of symptoms [46, 47].

Differential diagnoses include widened perivascular spaces (Virchow–Robin spaces) and subependymal myelin pallor.

5.11 Brain Stem and Cerebellar Infarcts

Cerebellar infarction is caused by occlusion of one of the major posterior circulation branches, which include the superior cerebellar, the anterior and posterior inferior cerebellar arteries, and the basilar artery. The posterior inferior cerebellar artery (PICA) supplies the postero-inferior portions of the cerebellum and is the most commonly obstructed cerebellar artery. The size of the infarct is important because a large infarct may cause a significant mass effect on the fourth ventricle and lead to hydrocephalus as well as brain stem compression. PICA infarctions can also result in the so-called lateral medullary (Wallenberg) syndrome, manifested by ipsilateral Horner's syndrome, ataxia, dysphagia, vertigo, nystagmus, hiccups and contralateral numbness, diminished pain and temperature sensation. The brain stem and cerebellar infarcts behave similar to cerebral infarcts on DW imaging and ADC maps (Fig. 5.11).

Substantial image distortions are observed in the areas close to the base of the skull, which include areas in the posterior fossa. Some MR imaging techniques such as parallel MR imaging with SENSE and PROPELLER diffusion-weighted MR imaging reduce the susceptibility effect and image distortions. These techniques may improve detection of brain stem and cerebellar infarcts [48, 49].

5.12 Corpus Callosum Infarcts

Isolated corpus callosum infarction due to pericallosal artery disease is rare, but can present as an alien hand syndrome. These patients fail to recognize the ownership of one hand when placed in certain positions or situations [50]. Patients with corpus callosum infarcts can present with a variety of clinical signs and symptoms, which further complicates the diagnosis [51]. These lesions are readily detected by DW imaging and have signal characteristics similar to cerebral infarcts (Fig. 5.12).

5.13 Hemorrhagic Infarcts

About 40–50% of all stroke patients develop hemorrhagic transformation of their infarcts (Fig. 5.13, 5.14). This usually occurs during the first week after onset of symptoms. The cause may be a spontaneous lysis of an embolus, which took place at a time when en-

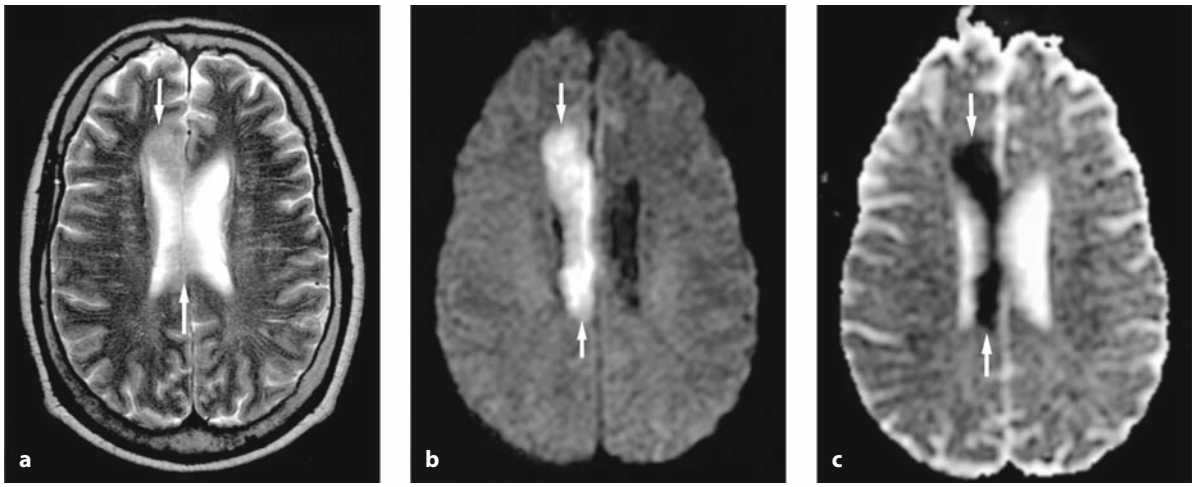

Figure 5.12 a–c

Corpus callosum infarction in a 64-year-old man with left-sided weakness. **a** T2-weighted image shows a hyperintense lesion in the anterior part and body of the corpus callosum extending into right frontal white matter (*arrows*). **b** DW image clearly shows this lesion as hyperintense (*arrows*). **c** ADC is decreased, representing acute infarction (*arrows*)

dothelial cells of the vessel had also been damaged by the ischemia, thus resulting in a breakthrough hemorrhage into the infarcted region. The incidence of hemorrhage is increased with use of thrombolytic therapy, as well as in the presence of certain clinical conditions, such as hypertension, embolic etiology, use of anticoagulant therapy and increasing stroke severity.

Studies have shown that neuroimaging can predict which lesions are prone to progress into a hemorrhagic infarction [52]. Thus, ischemic lesions with a significantly greater percentage of low ADC values have a higher risk for hemorrhagic transformation than lesions with a smaller proportion of low ADC [52].

The most feared complication of tissue plasminogen activator therapy for acute stroke patients is symptomatic intracerebral hemorrhage. Patients with large baseline DW image lesion volumes who achieve early reperfusion appear to be at greatest risk of symptomatic intracerebral hemorrhage after tissue plasminogen activator therapy [53].

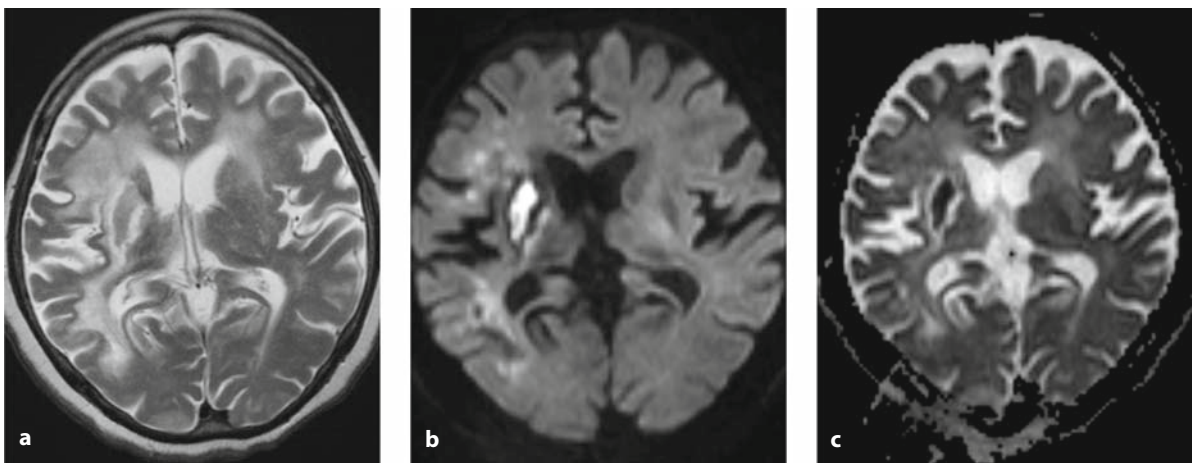

Figure 5.13 a–c

Hemorrhagic infarction in a 78-year-old woman with cardiogenic embolic-type acute infarction. **a** T2-weighted image shows a hyperintense area in the right white matter and hypointense lesions in right basal ganglia. **b** DW image shows hyperintense lesions in right basal ganglia, representing acute hemorrhagic infarction. **c** ADC is decreased with an area of hypointensity

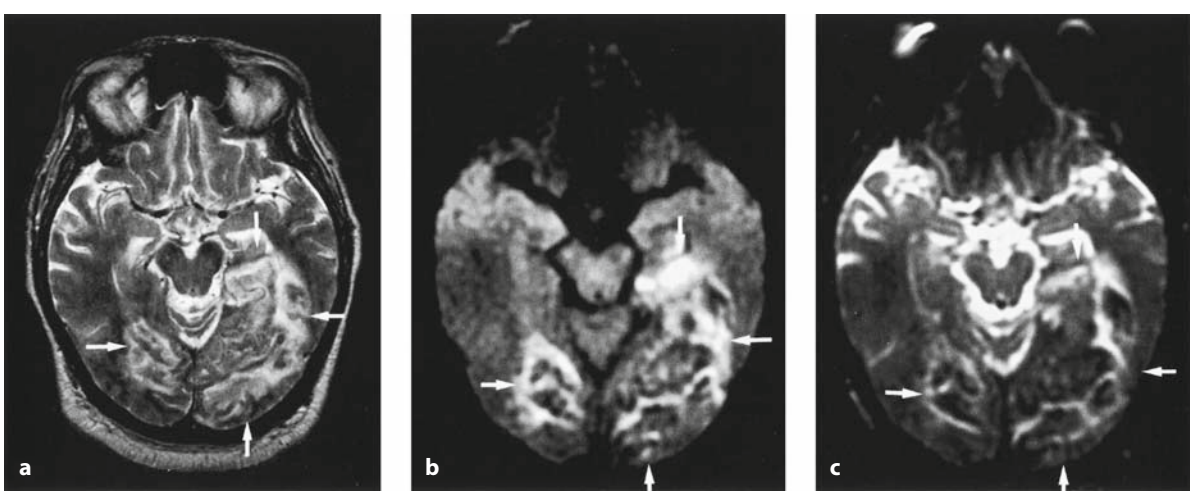

5.14 Diffusion Tensor Imaging

The success of DW imaging is rooted in the concept that during their random diffusion-driven displacements, molecules probe the tissue structure. As diffusion is a three-dimensional process, molecular mobility in tissues may be anisotropic. With diffusion tensor (DT) imaging, diffusion anisotropy effects can be extracted, providing more details on tissue microstructure [33].

Both reduced [54, 55] and normal-to-elevated [56, 57] anisotropy have been reported in acute infarcts less than 24 hours after the onset of symptoms. Some have proposed that increased diffusion anisotropy indicates continued structural integrity and tissue salvageability [56] and that increased anisotropic diffusion occurs as a result of fluid shift from the extracellular space to the intracellular space without membrane rupture [56]. Decreased diffusion anisotropy may signify the loss of cellular integrity with irreversible cellular injury.

Fiber tractography (FT) is a new method that can demonstrate the orientation and integrity of white matter fibers in vivo [58, 59, 60]; however, its clinical application is still under investigation. In stroke, FT may improve our understanding of the symptom progression and predict functional recovery [61-63] (Fig. 5.15, 5.16).

Figure 5.15

An acute infarct in the left corona radiate in a 51-year-old woman. A 3D tractography superimposed on an axial isotropic DW image (from left anterosuperior viewpoint). An acute infarct is shown in the left corona radiata. The corticospinal tract (*orange lines*) of the affected cerebral hemisphere appears to be just medial to, but not to run through, the infarct. (Courtesy of Aoki S MD, University of Tokyo, Japan)

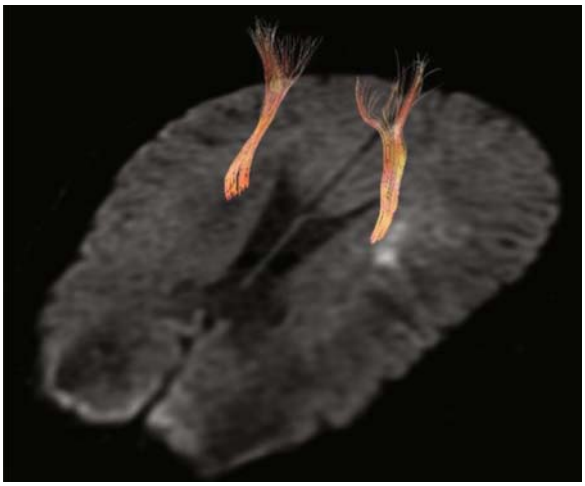

Figure 5.14 a–c

Hemorrhagic infarction in a 64-year-old man with mental status change. **a** T2-weighted image shows mixed hypher- and hypointense lesions in bilateral occipital lobes (*arrows*). **b** DW image shows these lesions as mixed hypher-, hypo-, and isointense, representing acute hemorrhagic infarction (*arrows*). **c** ADC is decreased with areas of DWI hyperintensity (*arrows*)

◄

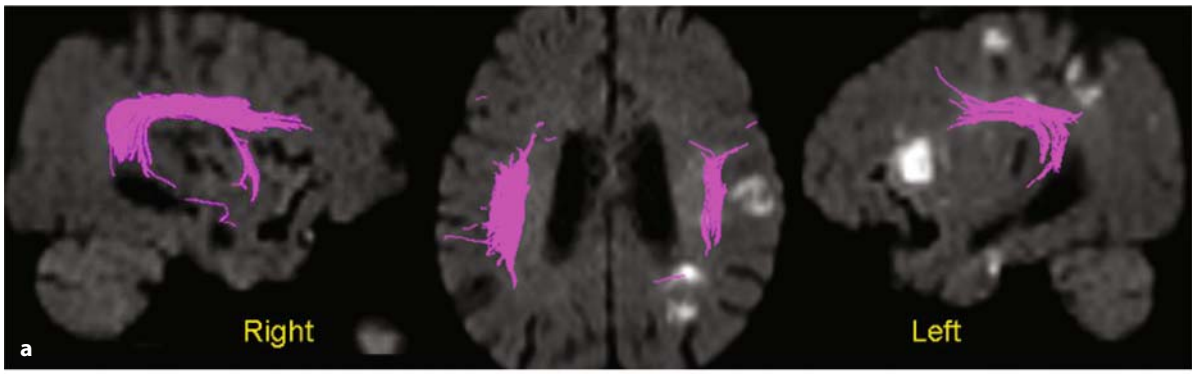

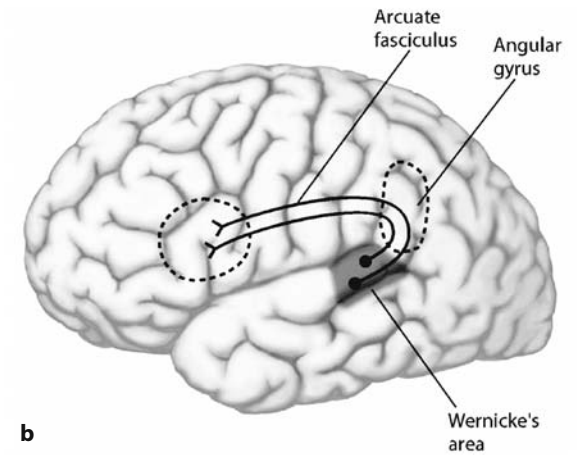

Figure 5.16 a, b

Acute left MCA infarcts in an 85-year-old woman with motor aphasia. **a** Sagittal and axial DW images are superimposed with fiber tractography show the relationship between infarcts and the arcuate fasciculus. **b** The arcuate fasciculus forms a curved shape along the angular gyrus, and connects the Wernicke area with the Broca area. (Courtesy of Yamada K MD, Kyoto Prefectural University of Medicine, Japan)

Kunimatsu et al. used FT to show the corticospinal tract in patients with acute or early subacute ischemic stroke involving the posterior limb of the internal capsule or corona radiata and to assess involvement of the tract [61]. Infarcts and the tract were shown simultaneously, providing information on their spatial relationships. In five of the eight patients, three-dimensional fiber tract maps showed the corticospinal tract in close proximity to the infarct but not passing through it. All these patients recovered well, with maximum improvement from the lowest score on manual muscle testing (MMT) up to the full score through rehabilitation. In the other three patients the corticospinal tract was shown running through the infarct; reduction in MMT did not improve favorably or last longer, other than in one patient. Three-dimensional white matter tractography can show spatial relationships between the corticospinal tract and an infarct. The authors concluded that FT might be helpful in prognosis of gross motor function.

5.15 High-b-Value Diffusion-Weighted Imaging

The b-values applied in the stroke diffusion studies were usually in the range of 800–1,500 s/mm^2. This range of b-values is considered reasonable based on contrast-to-noise ratio (CNR) estimates at gradient strengths of clinical MR instruments. MR technology has allowed higher b-values in recent years [64].

High-b-value DW imaging using a clinical MR imaging system has been applied and its clinical benefit has been discussed in the diagnosis of cerebral infarction. The initial application of DW imaging with high b-values of 2,500–3,000 s/mm^2 for acute or subacute infarction provided no apparent diagnostic advantages compared with those of usual images of b=1,000 s/mm^2 [65, 66].

However, the amount of diffusion weighting increases as the b-value increases [67]. Therefore, higher b-value DW imaging would be more advantageous in the diagnosis of hyperacute ischemic lesions in which mild diffusion changes can be present within the le-

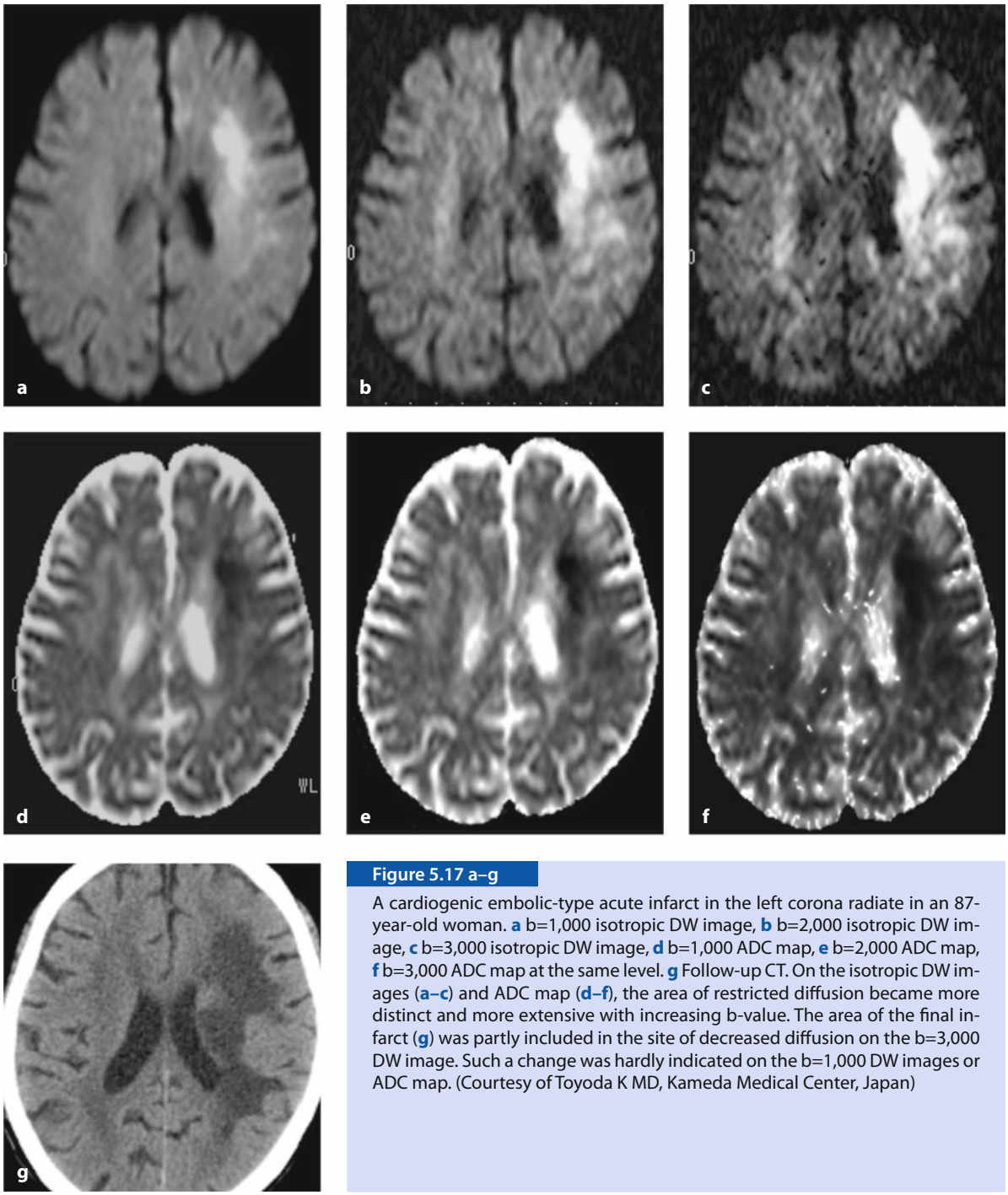

Figure 5.17 a–g

A cardiogenic embolic-type acute infarct in the left corona radiate in an 87-year-old woman. **a** b=1,000 isotropic DW image, **b** b=2,000 isotropic DW image, **c** b=3,000 isotropic DW image, **d** b=1,000 ADC map, **e** b=2,000 ADC map, **f** b=3,000 ADC map at the same level. **g** Follow-up CT. On the isotropic DW images (**a–c**) and ADC map (**d–f**), the area of restricted diffusion became more distinct and more extensive with increasing b-value. The area of the final infarct (**g**) was partly included in the site of decreased diffusion on the b=3,000 DW image. Such a change was hardly indicated on the b=1,000 DW images or ADC map. (Courtesy of Toyoda K MD, Kameda Medical Center, Japan)

sions than in the diagnosis of acute or subacute lesions. DW imaging at b=2,000 s/mm^2 was better than that at b=1,000 s/mm^2 for the detection and estimation of the extent of ischemia in patients with hyperacute ischemic stroke [68]. Toyoda et al. suggested that the size of the final infarction or irreversible cytotoxic edema was more predictable on high-b-value DW images than on the usual b=1,000 DW images (Fig. 5.17) [69].

5.16 Thin-Section Diffusion-Weighted Imaging

Conventional DW imaging uses 5–8-mm sections with a field of view of 20–40 cm and a matrix of 128–256, which produces in-plane resolution of 1–2×1–2 mm. Therefore, the in-plane resolution of DW imaging is higher than the section thickness. When a lesion is smaller than the section thickness and when it occupies only part of a voxel, the contrast relative to background tissue depends on both the signal intensity from the lesion and the proportion of the voxel that it occupies. Small, low-contrast lesions occupying only part of a voxel may go undetected. This phenomenon is known as partial volume effect [70, 71]. Nakamura et al. concluded that thin-section DW imaging with a 3-mm section thickness increased lesion conspicuity and improved the accuracy of stroke subtype diagnosis when comparing conventional 5-mm section DW imaging [72].

References

1. The National Institute of Neurological Disorders and Stroke rt-PA Stroke Study Group (1995) Tissue plasminogen activator for acute ischemic stroke. N Engl J Med 333:1581–1587
2. Hacke W (2005) The Desmoteplase in Acute Ischemic Stroke Trial (DIAS): a phase II MRI-based 9-hour window acute stroke thrombolysis trial with intravenous desmoteplase. Stroke 36:66–73
3. Mohr J, Biller J, Hial S, et al. (1995) Magnetic resonance versus computed tomographic imaging in acute stroke. Stroke 26:807-812
4. Moseley ME, Kucharczyk J, Mintorovitch J, et al. (1990) Diffusion-weighted MR imaging of acute stroke: correlation with T2- weighted and magnetic susceptibility-enhanced MR imaging in cats. AJNR Am. J. Neuroradiol 11:423-429
5. Marks MP, De Crespigny A, Lentz D, et al. (1996) Acute and chronic stroke: navigated spin-echo diffusion-weighted MR imaging. Radiology 199:403-408
6. Gonzalez RG, Schaefer PW, Buonanno FS, et al. (1999) Diffusion-weighted MR imaging: diagnostic accuracy in patients imaged within 6 hours of stroke symptom onset. Radiology 210:155-162
7. Lovblad K, Laubach H, Baird A, et al. (1998) Clinical experience with diffusion-weighted MR in patients with acute stroke. AJNR Am J Neuroradiol 19: 1061-1066
8. Chien D, Kwong KK, Gress DR, et al. (1992) MR diffusion imaging of cerebral infarction in humans. AJNR Am J Neuroradiol 13:1097-1102
9. Schaefer PW, Grant PE, Gonzalez RG (2000) Diffusion-weighted MR imaging of the brain. Radiology 217:331–345
10. Gudbjartsson H, Maier SE, Mulkern RV, et al. (1996) Line scan diffusion imaging. Magn Reson Med 36:509–519
11. de Crespigny AJ, Marks MP, Enzmann DR, et al. (1995) Navigated diffusion imaging of normal and ischemic human brain. Magn Reson Med 33:720–728
12. Schaefer PW, Grant PE, Gonzalez RG (2000) Diffusion-weighted MR imaging of the brain. Radiology 217:331–345
13. Lefkowitz D, LaBenz M, Nudo Sr, et al. (1999) Hyperacute ischemic stroke missed by diffusion-weighted imaging. AJNR Am J Neuroradiol 20:1871–1875
14. Wang PYK, Barker PB, Wityk RJ, et al. (1999) Diffusion-negative stroke: a report of two cases. AJNR Am J Neuroradiol 20:1876–1880
15. Benveniste H, Hedlund LW, Johnson GA (1992) Mechanism of detection of acute cerebral ischemia in rats by diffusion-weighted magnetic resonance microscopy. Stroke 23:746-754
16. Mintorovitch J, Yang GY, Shimizu H, et al. (1994) Diffusion-weighted magnetic resonance imaging of acute focal cerebral ischemia: comparison of signal intensity with changes in brain water and Na+,K(+)-ATPase activity. J Cereb Blood Flow Metab 14:332-336
17. Sykova E, Svoboda J, Polak J, et al. (1994) Extracellular volume fraction and diffusion characteristics during progressive ischemia and terminal anoxia in the spinal cord of the rat. J Cereb Blood Flow Metab 14:301-311
18. Niendorf T, Dijkhuizen R, Norris D, et al. (1996) Biexponential diffusion attenuation in various states of brain tissue: implications for diffusion weighted imaging. Magn Reson Med 36: 847-857
19. Provenzale JM, Sorensen AG (1999) Diffusion-weighted MR imaging in acute stroke: theoretic considerations and clinical applications. AJR Am J Radiol 173:1459–1467
20. Keller E, Flacke S, Urbach H, Schild H (1999) Diffusion- and perfusion-weighted magnetic resonance imaging in deep cerebral venous thrombosis. Stroke 30:1144–1146
21. Busza AL, Allen KL, King MD, et al. (1992) Diffusion-weighted imaging studies of cerebral ischemia in gerbils. Potential relevance to energy failure. Stroke 23: 1602 - 1612
22. Burdette JH, Elster AD, Ricci PE (1999) Acute cerebral infarction: quantification of spin-density and T2 shine-through phenomena on diffusion-weighted MR images. Radiology 212:333-339
23. Grant PE, He J, Halpern EF, Wu O, Schaefer PW, et al. (2001) Frequency and clinical context of decreased apparent diffusion coefficient reversal in the human brain. Radiology 221:43–50
24. Fiebach, JB, Jansen O, Schellinger PD, et al. (2002) Serial analysis of the apparent diffusion coefficient time course in human stroke. Neuroradiology 44:294–298
25. Hasegawa Y, Fisher M, Latour L, et al. (1994) MRI diffusion mapping of reversible and irreversible ischemic injury in focal brain ischemia. Neurology 44:1484-1490
26. Dardzinski B, Sotak C, Fisher M, et al. (1993) Apparent diffusion coefficient mapping of experimental focal cerebral ischemia using diffusion-weighted echo-planar imaging. Magn Reson Med 30:318-325
27. Singer M, Chong J, Lu D, et al. (1998) Diffusion-weighted MRI in acute subcortical infarction. Stroke 29:133-136

28. Desmond PM, Lovell AC, Rawlinson AA, et al. (2001) The value of apparent diffusion coefficient maps in early cerebral ischemia. AJNR Am J Neuroradiol 22:1260–1267
29. Huang IJ, Chen CY, Chung HW, et al. (2001) Time course of cerebral infarction in the middle cerebral arterial territory: deep watershed versus territorial subtypes on diffusion-weighted MR images. Radiology 221:35–42
30. Kidwell CS, Saver JL, Mattiello J, et al. (2000) Thrombolytic reversal of acute human cerebral ischemic injury shown by diffusion/perfusion magnetic resonance imaging. Ann Neurol 47:462-469
31. Burdette JH, Ricci PE, Petitti N, et al. (1998) Cerebral infarction: time course of signal intensity changes on diffusion-weighted MR images. Am J Radiol 171:791–795
32. Provenzale JM, Jahan R, Naidich TP, et al. (2003) Assessment of the patient with hyperacute stroke: imaging and therapy. Radiology 229:347-359
33. Mukherjee P, Bahn MM, McKinstry RC, et al. (2000) Differences between gray and white matter water diffusion in stroke: diffusion-tensor MR imaging in 12 patients. Radiology 215:211–220
34. Krueger K, Kugel H, Grond M, et al. (2000) Late resolution of diffusion-weighted MRI changes in a patient with prolonged reversible ischemic neurological deficit after thrombolytic therapy. Stroke 31:2715–2718
35. Burdette JH, Elster AD, Ricci PE (1999) Acute cerebral infarction: quantification of spin-density and T2 shine-through phenomena on diffusion-weighted MR images. Radiology 212:333-339
36. Fitzek C, Tintera J, Muller-Forell W, et al. (1998) Differentiation of recent and old cerebral infarcts by diffusion-weighted MRI. Neuroradiology 40:778–782
37. Pan Foni L, Garcia GH, Gutierreg JA (1996) Cerebral white matter is highly vulnerable to ischemia. Stroke 27:1641–1647
38. Kuroiwa T, Nagaoka T, Ueki M, et al. (1998) Different apparent diffusion coefficient: water content correlations of gray and white matter during early ischemia. Stroke 29:859–865
39. Fiehler J, Knudsen K, Kucinski T, et al. (2004) Predictors of apparent diffusion coefficient normalization in stroke patients. Stroke 35:514-519
40. Caplan LR, Mohr PJ, Kistler JP, Koroshetz W (1997) Should thrombolytic therapy be the first-line treatment for acute ischemic stroke? N Engl J Med 337:1309-1310
41. Yoshikawa T, Abe O, Tsuchiya K, et al. (2002) Diffusion-weighted magnetic resonance imaging of dural sinus thrombosis. Neuroradiology 44:481–488
42. Forbes KP, Pipe JG, Heiserman JE (2001) Evidence for cytotoxic edema in the pathogenesis of cerebral venous infarction. AJNR Am J Neuroradiol 22:450–455
43. Leach JL, Fortuna RB, Jones BV, et al. (2006) Imaging of cerebral venous thrombosis: current techniques, spectrum of findings, and diagnostic pitfalls. RadioGraphics 26:S19-S41
44. Ducreux D, Oppenheim C, Vandamme X, et al. (2001) Diffusion-weighted imaging patterns of brain damage associated with cerebral venous thrombosis. AJNR Am J Neuroradiol 22:261–268
45. Favrole P, Guichard JP, Crassard I, et al. (2004) Diffusion-weighted imaging of intravascular clots in cerebral venous thrombosis. Stroke 35:99-103
46. Geijer B, Lindgren A, Brockstedt S, et al. (2001) Persistent high-signal on diffusion-weighted MRI in the late stages of small cortical and lacunar ischemic lesions. Neuroradiology 43:115–122
47. Noguchi K, Nagayoshi T, Watanabe N, et al. (1998) Diffusion-weighted echo-planar MRI of lacunar infarcts. Neuroradiology 40:448-451
48. Kuhl CK, Gieseke J, von Falkenhausen M, et al. (2005) Sensitivity Encoding for Diffusion-weighted MR Imaging at 3.0 T: Intraindividual Comparative Study. Radiology 234:517-526
49. Forbes KP, Pipe JG, Karis JP, et al. (2002) Improved Image Quality and Detection of Acute Cerebral Infarction with PROPELLER Diffusion-weighted MR Imaging. Radiology 225:551-555
50. Suwanwela NC, Leelacheavasit N (2002) Isolated corpus callosal infarction secondary to pericallosal artery disease presenting as alien hand syndrome. J Neurosurg Psychiatry 72:533–536
51. Riedy G, Melhem ER. (2003) Acute infarct of the corpus callosum: appearance on diffusion-weighted MR imaging and MR spectroscopy. J Magn Reson Imaging 18:255-259
52. Tong DC, Adami A, Moseley ME, et al. (2000) Relationship between apparent diffusion coefficient and subsequent hemorrhagic transformation following acute ischemic stroke. Stroke 31:2378–2384
53. Lansberg MG, Thijs VN, Bammer R, et al. (2007) Risk Factors of symptomatic intracerebral hemorrhage after tPA therapy for acute stroke. Stroke 38:2275-2278
54. Sorensen AG, Wu O, Copen WA, et al (1999) Human acute cerebral ischemia: detection of changes in water diffusion anisotropy by using MR imaging. Radiology 212:785–792
55. Mukherjee P, Bahn MM, McKinstry RC, et al. (2000) Differences between gray matter and white matter water diffusion in stroke: diffusion-tensor MR imaging in 12 patients. Radiology 215:211-220
56. Yang Q, Tress BM, Barber PA, et al. (1999) Serial study of apparent diffusion coefficient and anisotropy in patients with acute stroke. Stroke 30:2382–2390
57. Ozsunard Y, Granta PE, Huismana TAGM, et al. (2004) Evolution of water diffusion and anisotropy in hyperacute stroke: significant correlation between fractional anisotropy and T2. AJNR Am J Neuroradiol 25:699-705
58. Bihan DL, Mangin JF, Poupon C, et al. (2001) Diffusion tensor imaging: concepts and applications. J Magn Reson Imaging 13:534-546
59. Stieltjes B, Kaufmann WE, van Zijl PC, et al. (2001) Diffusion tensor imaging and axonal tracking in the human brainstem. Neuroimage 14:723-735
60. Lee SK, Kim DI, Kim J, et al. (2005) Diffusion-tensor MR imaging and fiber tractography: a new method of describing aberrant fiber connections in developmental CNS anomalies. RadioGraphics 25:53-65
61. Kunimatsu A, Aoki S, Masutani Y. et al. (2003) Three-dimensional white matter tractography by diffusion tensor imaging in ischaemic stroke involving the corticospinal tract. Neuroradiology 45:532-535

62. Yamada K, Ito H, Nakamura H, et al. (2004) Stroke patients' evolving symptoms assessed by tractography. J Magn Reson Imaging 20:923-929
63. Konishi J, Yamada K, Kizu O, et al. (2005) MR tractography for the evaluation of functional recovery from lenticulostriate infarcts. Neurology 64:108-113
64. Yoshiura T, Wu O, Zaheer A, et al (2001) Highly-diffusion-sensitized MRI of brain: dissociation of gray and white matter. Magn Reson Med 45:734–740
65. Meyer JR, Gutierrez A, Mock B, et al (2000) High-b-value diffusion-weighted MR imaging of suspected brain infarction. Am J Neuroradiol 21:1821–1829
66. Burdette JH, Elster AD (2002) Diffusion-weighted imaging of cerebral infarctions: are higher B-values better? J Comut Assist Tomogr 26:622–627
67. Stejskal EO, Tanner JE (1965) Spin diffusion measurements: spin echoes in the presence of a time-dependent field gradient. J Chem Phys 42:288–292
68. Kim HJ, Choi CG, Lee DH, et al (2005) High-b-value diffusion-weighted MR imaging of hyperacute ischemic stroke at 1.5T. Am J Neuroradiol 26:208–215
69. Toyoda K, Kitai S, Ida M, et al (2007) Usefulness of high-b-value diffusion-weighted imaging in acute cerebral infarction. Eur Radiol 17:1212-1220
70. Molyneux PD, Tubridy N, Parker GJ, et al. (1998) The effect of section thickness on MR lesion detection and quantification in multiple sclerosis. AJNR Am J Neuroradiol 19:1715–1720
71. Bradley WG, Glenn BJ (1987) The effect of variation in slice thickness and interslice gap on MR lesion detection. AJNR Am J Neuroradiol 8:1057–1062
72. Nakamura H, Yamada K, Kizu O, et al. (2005) Effect of thin-section diffusion-weighted MR imaging on stroke diagnosis. AJNR Am J Neuroradiol 26:560-565

Intracranial Hemorrhage

In collaboration with A. Hiwatashi

6.1 Introduction

Intracranial hemorrhages are often characterized according to their location, such as intraparenchymal, subarachnoid, subdural, epidural and intraventricular hemorrhages. The etiology of these hemorrhages includes a variety of heterogeneous conditions, such as trauma, hypertension, infarction, infection, neoplasm, vascular malformations, vasculitis, vasculopathy, coagulopathy, and drugs. This chapter will describe diffusion-weighted (DW) imaging characteristics of intracranial hemorrhages in relation to their location and evolutionary stage.

6.2 Intraparenchymal Hemorrhages: Appearance and Evolution (Table 6.1)

The classic pattern for the temporal evolution of intracerebral hematomas on MR images at 1.5 T is well known [1–38]. However, determination of the age of a hemorrhage is often inaccurate because of variations between individual patients. The change in signal intensity over time depends on many factors, such as the oxygenation state of hemoglobin, the status of red blood cell membranes, hematocrit, proteins and clot formation [1–34, 37, 38]. Among these, the evolution of hemoglobin and the red cell membrane integrity are the most important [1–23, 25, 28, 30, 31, 33, 34].

The transition of oxy-hemoglobin to deoxy-hemoglobin and thereafter to met-hemoglobin depends primarily upon the oxygen tension in the vicinity of the lesion as well as inside the hematoma itself. In the hyperacute stage, oxy-hemoglobin will dominate initially, but transformation into deoxy-hemoglobin will soon take place and deoxy-hemoglobin will dominate after a few days – the acute hematoma [7, 11, 14, 19, 22, 23, 25, 28, 29, 33, 34]. Within a few days to a week, deoxy-hemoglobin will transform to met-hemoglobin [3, 4, 7, 10, 11, 14, 19, 22, 23, 28–30, 33, 34]. However, the rate of this oxidation to met-hemoglobin will depend on the oxygen tension in the tissue, which may further complicate the temporal pattern of expected signal changes. Initially, met-hemoglobin will be found within intact red blood cells (the early subacute stage), but when the red cell membranes start to rupture, met-hemoglobin will be found in the extracellular fluid space (the late subacute stage), which takes place about two weeks following hemorrhage [7, 11, 14, 19, 22, 23, 28, 29, 33, 34]. The final stage, the chronic stage, is the result of continuous phagocytation of the breakdown products of hemoglobin, ferritin and hemosiderin, which starts about one month following hemorrhage. The products, ferritin and hemosiderin, will remain within the phagocytic cells, which accumulate in the periphery of the hematoma, where they may remain for years, maybe indefinitely, as a marker of an old hemorrhage [6, 7, 11, 14, 17, 19–23, 27, 33, 34].

Table 6.1. Time course of intraparenchymal hematomas

	Hyperacute	Acute	Early Subaute	Late Subacute	Chronic
T2	Hyper	Dark	Dark	Bright	Bright with dark rim
T1	Hypo/iso	Hypo/iso	Bright	Bright	Hypo
DW	Bright	Dark	Dark	Bright	Hyper-hypo
ADC	Dark	NAC	NAC	Dark	Increase/NAC

NAC: no accurate calculation

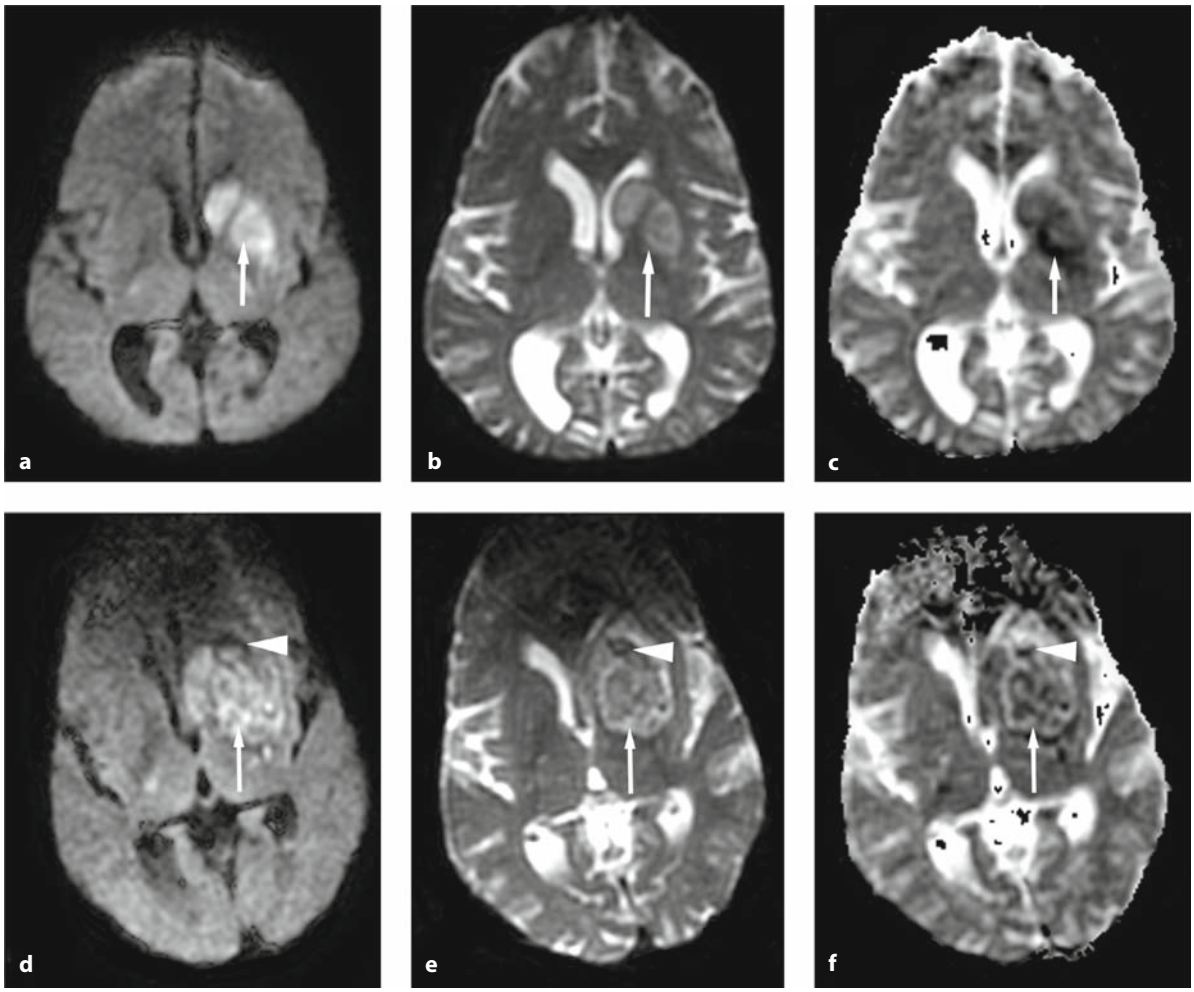

Figure 6.1 a–f

Acute infarction with hyperacute hemorrhage (oxy-hemoglobin/deoxy-hemoglobin). A 72-year-old woman suffered from a right-sided weakness. MR imaging 30 hours after the onset of symptoms (**a–c**) showed a lesion in the right basal ganglia (*arrow*) that is hyperintense on DW (**a**) and b_0 images (**b**). On the ADC map (**c**) the lesion is hypointense (*arrow*), indicating that this is a non-hemorrhagic acute infarction. During the end of the MR scanning, 30.5 hours after the onset of symptoms (**d–f**), the patient suddenly lost consciousness. The study was repeated, showing the increased size of the basal ganglia lesion. On the DW image (**d**) there is now a heterogeneous hyperintensity (*arrow*), consistent with oxy-hemoglobin. The b_0 image (**e**) also shows the lesion as heterogeneous, hyperintense (*arrow*), supporting oxy-hemoglobin. Note the new regions of hypointensity around the lesion (*arrowhead*), indicating deoxy-hemoglobin (**d–f**). The ADC map (**f**) shows the lesions as heterogeneously hypointense, consistent with oxy-hemoglobin (*arrow*). However, it is difficult to calculate the ADC due to the presence of paramagnetic deoxy-hemoglobin (*arrowhead*)

6.2.1 Hyperacute Hematoma

In the early stage of a hyperacute hematoma (Figs. 6.1 and 6.2), oxygenated hemoglobin within intact red blood cells is dominant. Oxy-hemoglobin is a diamagnetic substance and will, as such, generate an opposing magnetic field that reduces the applied magnetic field, as in most normal tissues in the body. Since there are no unpaired electrons in the iron of oxygenated hemoglobin, both longitudinal

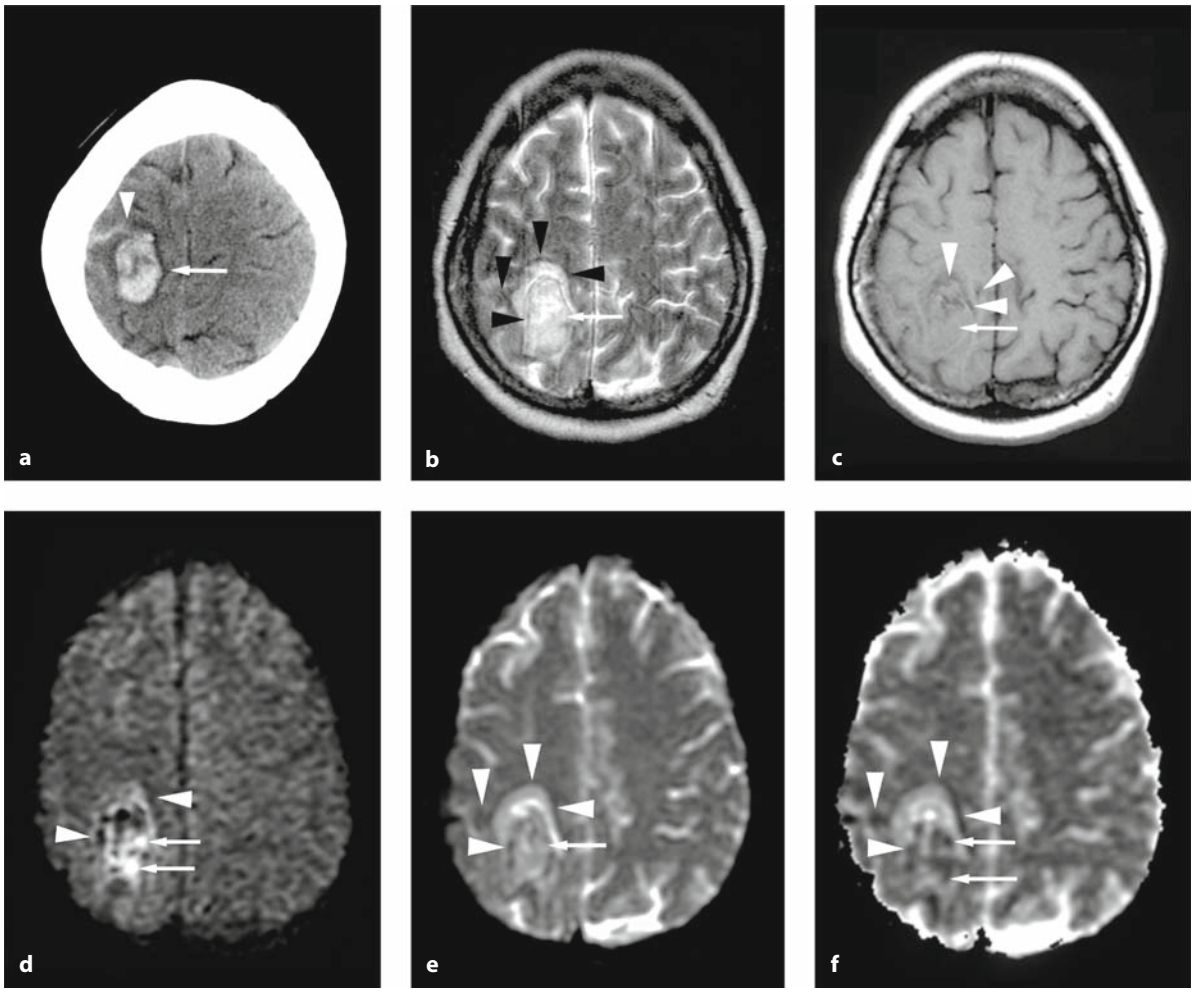

Figure 6.2 a–f

Hyperacute and chronic hemorrhage (oxy-hemoglobin/deoxy-hemoglobin, met-hemoglobin and hemosiderin/ferritin). A 40-year-old woman developed an acute left-sided weakness. A non-enhanced CT scan 6 hours after the onset of symptoms **(a)** shows a hyperdense lesion (*arrow*) in the right frontoparietal region associated with a small amount of subarachnoid hemorrhage (*arrowhead*). MR imaging 12 hours after the onset of symptoms **(b–h)** shows a heterogeneous lesion with areas of central hyperintensity on the T2-weighted image (**b**) (*arrow*; oxy-hemoglobin) with a peripheral hypointensity from the susceptibility influence of paramagnetic material (*arrowheads*; deoxy-hemoglobin). The T1-weighted image (**c**) shows the lesion as heterogeneous with areas of isointensity (*arrow*; oxy-hemoglobin) and hypointensity (*arrowheads*; deoxy-hemoglobin). Both the DW (**d**) and b_0 images (**e**) show the lesion as heterogeneous with areas of hyperintensity (*arrows*; oxy-hemoglobin) and hypointensity (*arrowheads*; deoxy-hemoglobin). The hypointensity is more prominent on these sequences than on the T2-weighted image (**b**). The ADC map (**f**) has a similar appearance of a heterogeneous lesion with areas of hypointensity (*arrows*; oxy-hemoglobin and *arrowheads*; deoxy-hemoglobin). As usual, when there is a strong susceptibility influence, it is difficult to calculate ADC

and transverse relaxation will be created by the so-called proton–proton, dipole–dipole interactions. At this stage, hematomas will have shorter relaxation times than water due to their protein content and will be slightly hypo- or iso-intense when compared with brain parenchyma on T1-weighted images. On T2-weighted images, oxy-hemoglobin will be seen as a slightly hyperintense region because of the high water content [7, 11, 14, 19, 22, 23, 25, 28, 29, 33, 34].

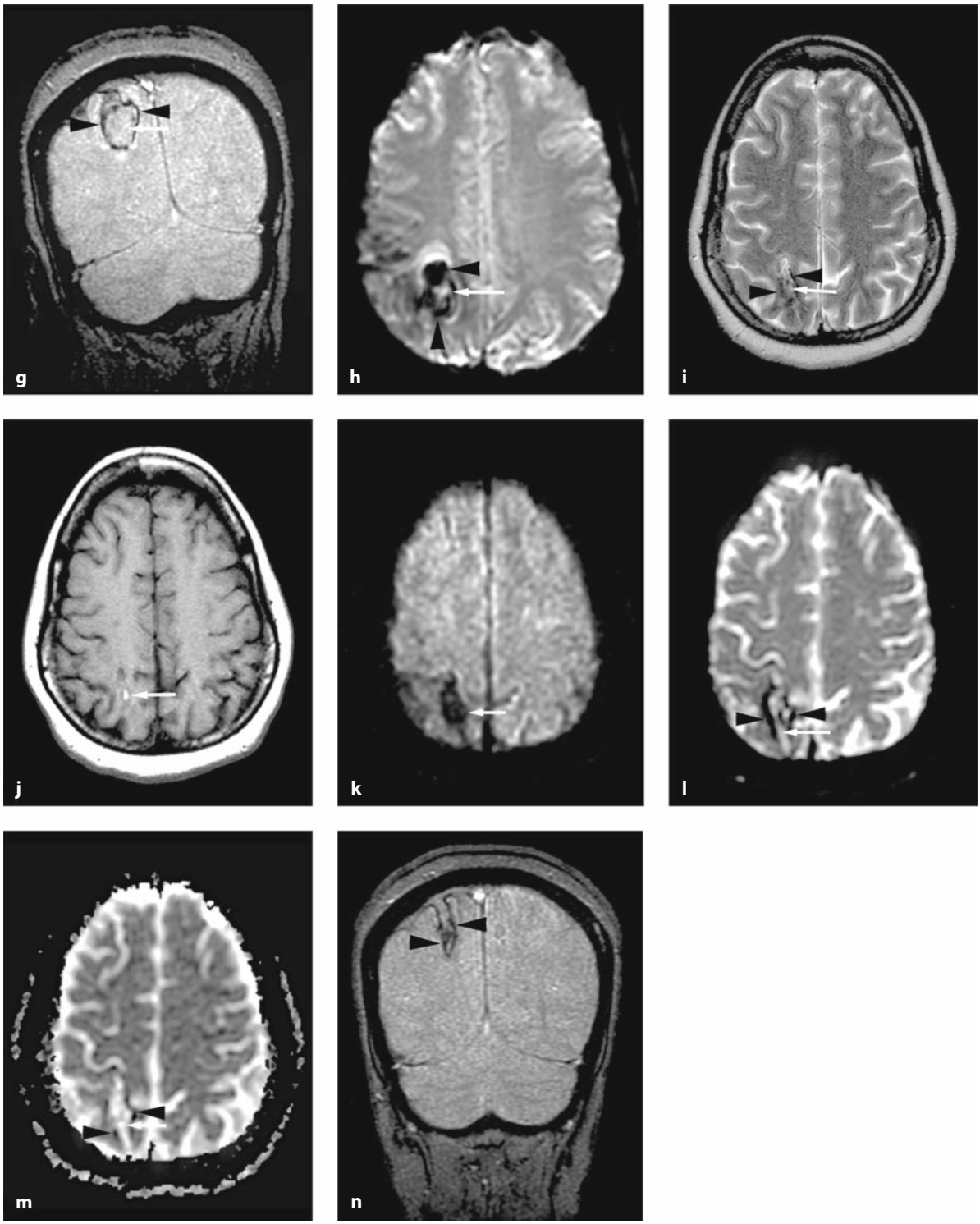
g
h
i
j
k
l
m
n

Figure 6.2 g–n

The coronal GRE image (**g**) and the GRE–echo-planar image (**h**) are more sensitive in depicting the susceptibility effect from deoxy-hemoglobin (*arrowheads*). The diamagnetic oxy-hemoglobin will, as expected, show an isointense signal (*arrow*), similar to the other sequences. Four months after the onset of symptoms **(i–n)**, the patient had a new MR examination. On a T2-weighted image (**i**), the lesion is still heterogeneous, but there are now areas of hyperintensity (extracellular met-hemoglobin; *arrow*) and hypointensity (*arrowheads*; hemosiderin/ferritin). The T1-weighted image (**j**) shows the heterogeneous lesion with areas of hyperintensity (*arrow*; extracellular met-hemoglobin) and hypointensity (hemosiderin/ferritin). The DW image (**k**) show the lesion as hypointense overall and the same is seen on the b_0 image (**l**), but this "T2-weighted" image has a small hyperintense zone in the center of the hematoma, probably due to extracellular met-hemoglobin (*arrow*). The hypointensity (*arrowheads*) on the b_0 image (**l**) is more pronounced than on the conventional T2-weighted image (**i**), demonstrating the higher sensitivity to susceptibility with this imaging sequence. The susceptibility effect will make it difficult to calculate ADC accurately, but the ADC map (**m**) will demonstrate the susceptibility from hemosiderin/ferritin as peripheral hypointense areas (*arrowheads*). In the center there are hyperintense areas (*arrow*), probably containing extracellular met-hemoglobin. The hypointensity on the DW image (**k**) is probably a combined effect of T2 shortening, magnetic susceptibility and increased diffusibility. A marked peripheral hypointensity from hemosiderin/ferritin will also be seen when a GRE technique (**n**) is used (*arrowheads*)

◄

Results of DW imaging of hematomas at this stage have not been well characterized. In our experience, however, a hyperacute intraparenchymal hemorrhage is hyperintense on DW images, with a decreased apparent diffusion coefficient (ADC). This is in accordance with observations of other authors [28, 33]. The possible causes for the decreased ADC are shrinkage of extracellular space due to clot retraction, changes in the concentration of hemoglobin and a high viscosity [13, 19, 22–24, 28, 33–35].

6.2.2 Acute Hematoma

Following hemorrhage there is normally a gradual oxygen desaturation of hemoglobin transforming oxy-hemoglobin into deoxy-hemoglobin (Fig. 6.3) [7, 11, 14, 19, 22, 23, 25, 28, 29, 33, 34]. The loss of oxygen will change the binding geometry of iron from a six-ligand system to a five-ligand system, leaving four unpaired electrons and making it paramagnetic. When exposed to a magnetic field, paramagnetic substances will enhance the applied field locally. This will influence image contrast by means of so-called magnetic susceptibility-induced relaxation, which only effects transverse relaxation (T2* effect). The susceptibility effects create local field inhomogeneities, with a rapid loss of transverse magnetization of protons within this region resulting in signal loss on T2-weighted images. Deoxy-hemoglobin will therefore demonstrate a marked hypointensity on T2-weighted images [1, 3, 7–9, 11–15, 19, 22–25, 30–34]. Besides the concentration of deoxy-hemoglobin, red blood cell concentration and/or clot formation may also contribute to this T2 hypointensity. Since this is an effect of magnetic susceptibility, gradient-echo (GRE) images will be more sensitive than DW- and T2-weighted images for the detection of acute, as well as chronic hematomas [19, 26, 27, 32]. The T1 relaxivity effect is related to dipole–dipole relaxation, in this case the dipoles of water and unpaired electrons of the paramagnetic center. This would normally result in a shortening of relaxation time; however, the molecular configuration of deoxy-hemoglobin will act as a shield for such a close approach of water molecules to the unpaired electrons of the paramagnetic, ferrous iron. The acute hematoma containing deoxy-hemoglobin will thus show an iso- to hypointense signal on T1-weighted images, similar to oxy-hemoglobin [5, 22, 23, 34].

Diffusion-weighted images of an acute hematoma show a marked hypointensity [28–31, 33], caused by the magnetic field inhomogeneity created by the paramagnetic deoxy-hemoglobin [6, 7, 14, 18, 22, 23, 25, 33]. Although the ADC has been reported to be decreased, accurate calculations are often difficult [28–30, 33, 36].

6.2.3 Early Subacute Hematoma

In the early stage of the subacute hematoma (Figs. 6.2 and 6.3), there is a decline in the energy state of the red blood cell and hemoglobin is oxidized to met-hemoglobin [3, 4, 7, 10, 11, 14, 19, 22, 23, 28–30, 33, 34]. In met-hemoglobin the iron is still bound to the heme moiety within the globin protein, but it is now in the ferric state with five unpaired electrons. This transformation normally starts in the periphery of the hemorrhage and gradually evolves to the center.

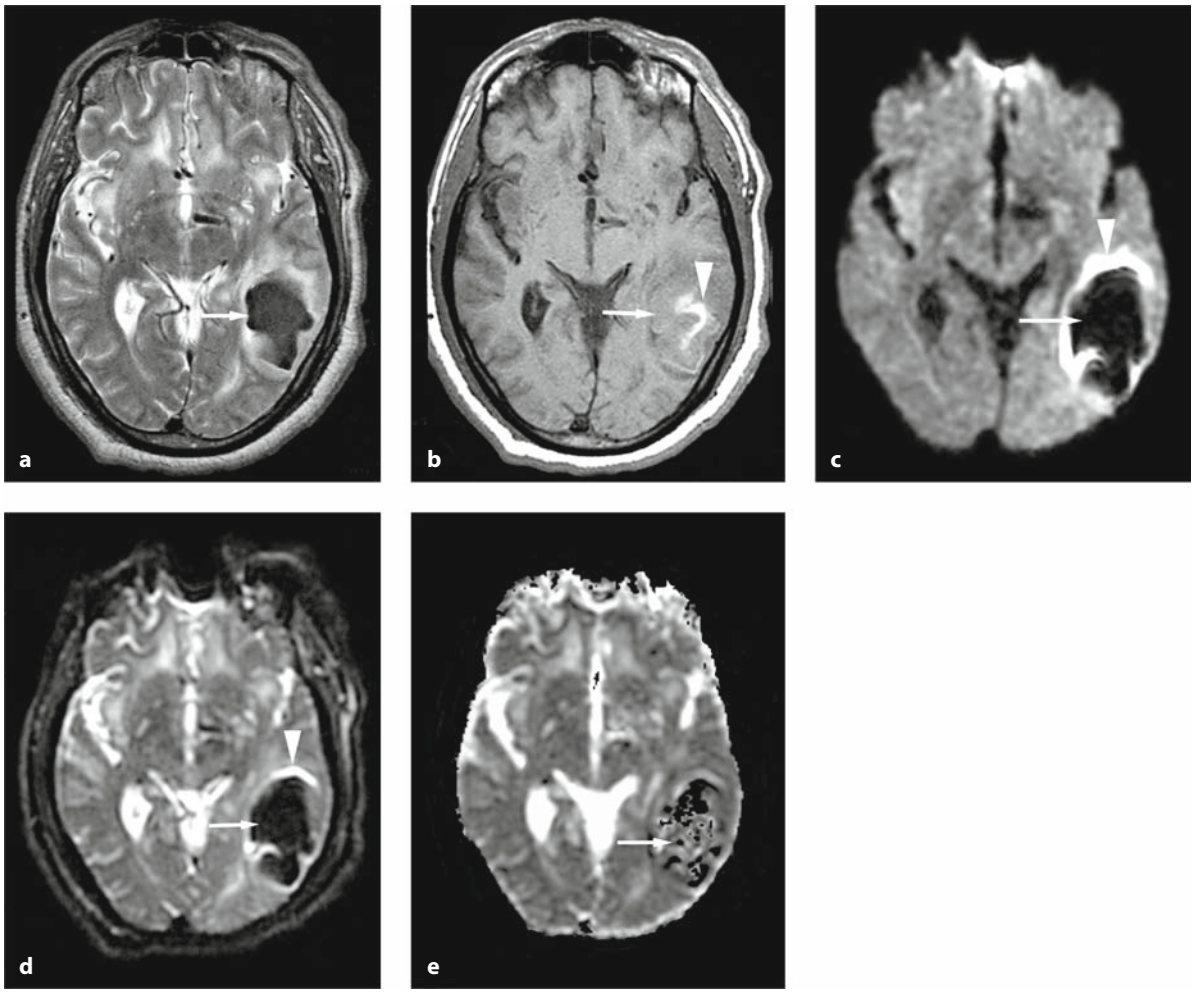

Figure 6.3 a–e

Acute to early subacute hemorrhage (deoxy-hemoglobin and intracellular met-hemoglobin). A 49-year-old man with headache and aphasia was referred for MR imaging 24 hours after the onset of symptoms (**a–e**). This study shows a left temporal lobe lesion that is hypointense on the T2-weighted image (**a**) (*arrow*; deoxy-hemoglobin and intracellular met-hemoglobin) with surrounding edema. On the T1-weighted image (**b**) the lesion is heterogeneous with areas of hypointensity (*arrow*; deoxyhemoglobin) and hyperintensity (*arrowhead*; intracellular met-hemoglobin). The DW image (**c**) demonstrates hypointensity (*arrow*; deoxy-hemoglobin and intracellular met-hemoglobin). The surrounding hyperintense rim (*arrowhead*) represents magnetic susceptibility artifact and perihematomal injury. This peripheral artifact is also seen around the hypointensity (*arrow*) created by deoxy-hemoglobin and intracellular met-hemoglobin on the b_0 image (**d**). ADC cannot be calculated accurately, which is easy to understand when looking at the extremely heterogeneous lesion depicted on the ADC map (**e**)

In the transition to met-hemoglobin, conformational changes will take place in the molecule and water protons will now have access to the unpaired electrons of iron in met-hemoglobin, creating a proton–electron, dipole–dipole interaction. Dipolar relaxation enhancement will then take place, making met-hemoglobin appear hyperintense on T1-weighted images. Met-hemoglobin, as a paramagnetic substance, will induce magnetic susceptibility relaxation affecting the transverse relaxation (T2* effect), which results in a marked hypointensity on T2-weighted images [3, 6, 7, 10, 14, 22–24, 28–31, 33, 34].

On DW imaging, intracellular met-hemoglobin shows hypointensity due to these paramagnetic susceptibility effects and ADC measurements are not reliable due to the susceptibility effects [28–30, 33].

6.2.4 Late Subacute Hematomas

The decline in energy state of the red blood cell will eventually damage the integrity of the red cell membrane, releasing the intracellular content to the extracellular fluid space (Figs. 6.2 and 6.4). Subsequently, there will be a dilution of the paramagnetic met-hemoglobin in extracellular fluid, reducing the susceptibility effect of met-hemoglobin [7, 11, 14, 19, 22, 23, 28, 29, 33, 34]. The signal intensity on T2-weighted images will thus relate to the water content, creating a hyperintense signal on T2-weighted images. Extracellular met-hemoglobin will, however, still have high signal intensity on T1-weighted images created by the same proton–electron, dipole–dipole relaxation as described in early subacute hematomas [5–7, 10, 14, 22, 23].

It has been reported that late subacute hematomas are hyperintense on DW imaging [28, 29]. The ADC value for late subacute hematoma is controversial. Ebisu et al. [24] reported decreased ADC in hematomas of hemorrhagic infarctions, whereas Atlas et al. reported ADC values higher than normal white matter in late subacute hematomas and suggested this was due to increased diffusibility [28]. Finally, Kang et al. reported decreased ADC in late subacute hematomas and thought this was due to high viscosity and cellularity [33]. It is important to differentiate late subacute hematomas from abscesses since both can show hyperintensity on DW images and decreased ADC. Late subacute hematomas are hyperintense on T1-weighted images but abscesses are usually hypointense.

6.2.5 Chronic Hematomas

Over time, met-hemoglobin will be resorbed or degraded and the effect on T1 enhancement will be reduced (Figs. 6.2 and 6.4). The high water content in the chronic stage will result in prolonged T1 as well as T2 relaxation. From the start of the hemorrhage there is a continuous phagocytation of heme proteins. Ferritin and hemosiderin, the final breakdown products of hemoglobin, will remain within the phagocytic cells, which accumulate in the periphery of the hematoma, where they may remain indefinitely as a marker of an old hemorrhage [6, 7, 11, 14, 17, 19–23, 27, 33, 34, 37, 38]. Ferritin and hemosiderin within these cells will have no access to water protons and thus there are no relaxivity effects. Magnetic susceptibility is the only factor influencing the signal, creating a marked signal loss on T2-weighted images. As mentioned earlier, the magnetic susceptibility effects are most prominent on T2*-weighted images [7, 17, 22, 23, 34].

Diffusion-weighted images also show hyperintensity in chronic hematomas [29, 33]. However, they can show hypointensity in late chronic hematomas. The ADC value has been reported to be increased, but sometimes decreased in early chronic hematomas probably due to the high viscosity. It is difficult to measure accurately due to magnetic susceptibility artifacts from the surrounding deposition of ferritin and hemosiderin [28–30, 33, 36]. Differentiation between early chronic hematomas and abscesses on MR imaging is difficult because both can show hyperintensity on DW images and iso- or hypointensity on T1-weighted images.

6.2.6 Perihematomal Edema and Injury

Morbidity and mortality are associated with hematoma enlargement and the development of perihematomal edema. Serum protein penetration from the clot into the surrounding white matter and blood-brain barrier breakdown have been proposed as mechanisms leading to edema formation in the extracellular compartment (vasogenic edema). There is a significant direct relationship between ADC elevation in the edema and the volume of hematoma [39].

A rim of decreased ADC (cytotoxic edema) outside the hematoma can be observed in the hyperacute or acute period. Mechanisms proposed as contributing factors to the perihematomal injury include ischemia resulting from mechanical compression and edema, or neurotoxicity resulting from breakdown products of blood or inflammation (Figs. 6.3, 6.5) [40, 41].

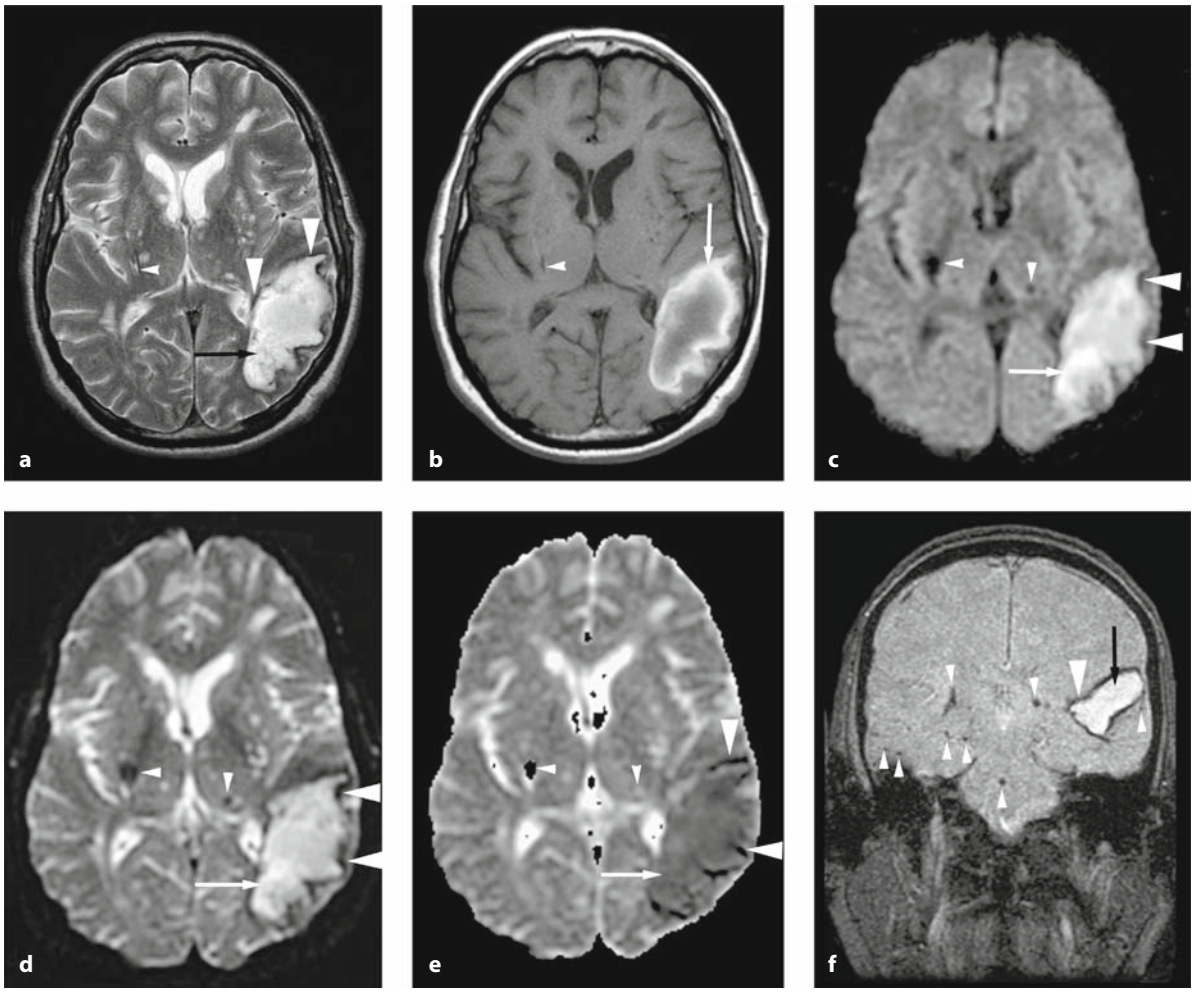

Figure 6.4 a–f

Late subacute-chronic hemorrhage (extracellular met-hemoglobin and hemosiderin/ferritin). A 52-year-old man with a history of chronic hypertension complained of headache and aphasia. MR examination 2 months after the onset of symptoms shows a left temporal lobe lesion that is hyperintense on the T2-weighted image (**a**) (*arrow*; extracellular met-hemoglobin) and surrounded by a hypointense rim (*arrowheads*; hemosiderin/ferritin). Another hypointense lesion is visualized in the right basal ganglia (*small arrowhead*; hemosiderin/ferritin), compatible with chronic hemorrhage secondary to hypertension. The T1-weighted image (**b**) shows the temporal lobe lesion as hyperintense (*arrow*; extracellular met-hemoglobin). The lesion in the right basal ganglia is also hypointense on this sequence (*small arrowhead*; hemosiderin/ferritin). On the DW image (**c**) the temporal lobe lesion is hyperintense (*arrow*; extracellular met-hemoglobin) with a hypointense rim (*arrowheads*; hemosiderin/ferritin). The basal ganglia lesion remains hypointense, but the signal void is more extensive than on the conventional T2-weighted image (**a**), since spin-echo type EPI does not compensate for signal loss due to local magnetic field inhomogeneities and is thus more sensitive than regular spin-echo imaging. This increased susceptibility sensitivity revealed a second, old hemorrhagic lesion in the left thalamus (small *arrowhead*; hemosiderin/ferritin). The b_0 image (**d**) also shows the hyperintense lesion (*arrow*; extracellular met-hemoglobin) with the hypointense rim (*arrowheads*; hemosiderin/ferritin) as well as the older lesions in the basal ganglia and thalamus (*small arrowheads*; hemosiderin/ferritin). On the ADC map (**e**) the temporal lesion is somewhat hypointense (*arrow*; extracellular met-hemoglobin) with a hypointense rim (*arrowheads*; hemosiderin/ferritin). The other lesions are also visualized (*small arrowheads*); however, ADC cannot be calculated. Finally, the coronal GRE image (**f**) shows the temporal lesion as hyperintense (*arrow*; extracellular met-hemoglobin) with a hypointense rim (*arrowhead*; hemosiderin/ferritin). The GRE sequence is the most sensitive and shows multiple small hypointense lesions (old hemorrhagic breakdown products) in the cerebral hemispheres and in the pons (*small arrowheads*; hemosiderin/ferritin)

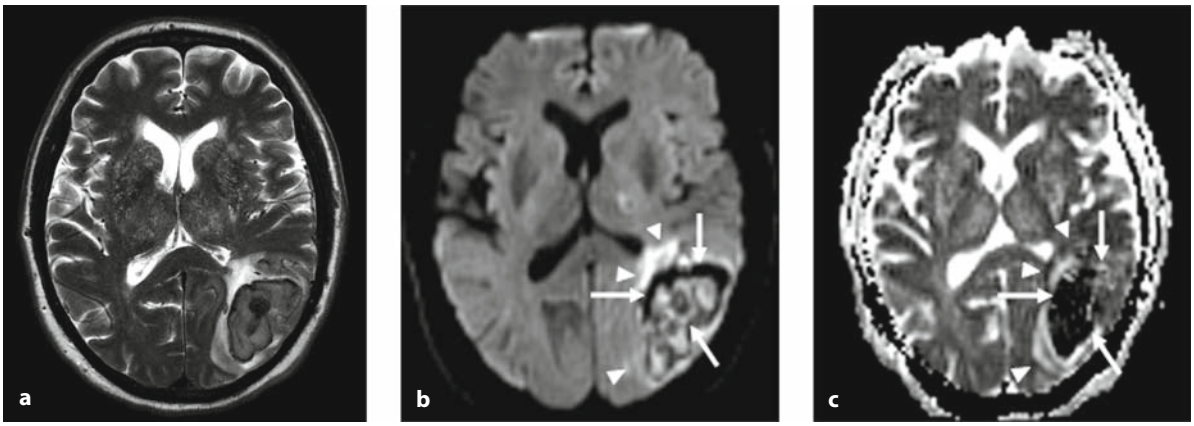

Figure 6.5 a–c

Perihematomal edema and injury. A 61-year-old man presented with headache. **a** T2-weighted image shows an acute hematoma as hypointense and the surrounding edema as hyperintense. **b** DW image shows the hematoma as mixed intense (*arrows*) and the edema as hyper- or isointense (*arrowheads*). **c** The ADC map shows most of the edema as increased ADC, which represents vasogenic edema (*arrows*). However, there is a peripheral decreased ADC rim that probably represents perihematomal injury (*arrowheads*)

6.3 Subarachnoid Hemorrhage

Computed tomography (CT) is still essential in the diagnosis of acute subarachnoid hemorrhages (Fig. 6.6), as the sensitivity and usefulness of MR imaging is controversial [4, 5, 9, 34, 42–48]. Fluid-attenuated inversion-recovery (FLAIR) imaging has a high sensitivity for subarachnoid hemorrhage [49–52]. However, the specificity is low because there are several other causes for the appearance of subarachnoid hemorrhage on FLAIR imaging, such as high proton concentration, mass effect, vascular disease, contrast medium and use of specific intravenous anesthetic agents [53–56].

It is often difficult to detect subarachnoid hemorrhage on DW images [31, 57]. Lin et al. detected subarachnoid hemorrhage in two of four cases on GRE imaging, but it could not be detected on b_0 images [31]. Wiesmann et al. reported that proton density and FLAIR images could detect subarachnoid hemorrhage, but T2-weighted and DW images could not [57].

However, DW images may be useful to visualize parenchymal injuries secondary to subarachnoid hemorrhage. Ischemic changes, probably related to subarachnoid hemorrhage, have shown hyperintensity on DW images in both clinical and animal studies [58–63]. This finding depends on the timing of imaging and the severity of injury.

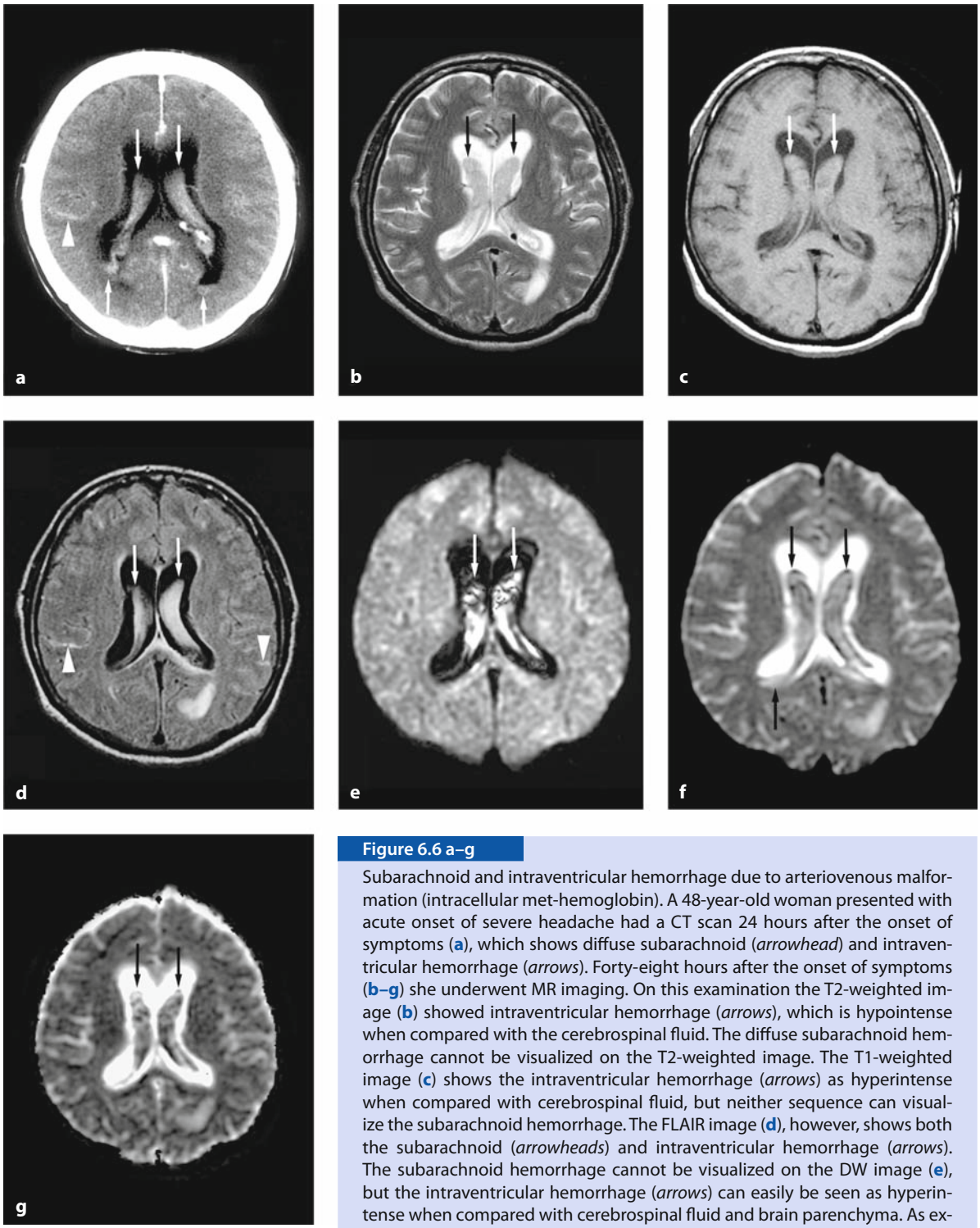

Figure 6.6 a–g

Subarachnoid and intraventricular hemorrhage due to arteriovenous malformation (intracellular met-hemoglobin). A 48-year-old woman presented with acute onset of severe headache had a CT scan 24 hours after the onset of symptoms (**a**), which shows diffuse subarachnoid (*arrowhead*) and intraventricular hemorrhage (*arrows*). Forty-eight hours after the onset of symptoms (**b–g**) she underwent MR imaging. On this examination the T2-weighted image (**b**) showed intraventricular hemorrhage (*arrows*), which is hypointense when compared with the cerebrospinal fluid. The diffuse subarachnoid hemorrhage cannot be visualized on the T2-weighted image. The T1-weighted image (**c**) shows the intraventricular hemorrhage (*arrows*) as hyperintense when compared with cerebrospinal fluid, but neither sequence can visualize the subarachnoid hemorrhage. The FLAIR image (**d**), however, shows both the subarachnoid (*arrowheads*) and intraventricular hemorrhage (*arrows*). The subarachnoid hemorrhage cannot be visualized on the DW image (**e**), but the intraventricular hemorrhage (*arrows*) can easily be seen as hyperintense when compared with cerebrospinal fluid and brain parenchyma. As expected, the subarachnoid hemorrhage cannot be demonstrated on either b_0 image (**f**) or ADC maps (**g**), but both sequences will depict the intraventricular hematoma as hypointense (*arrows*)

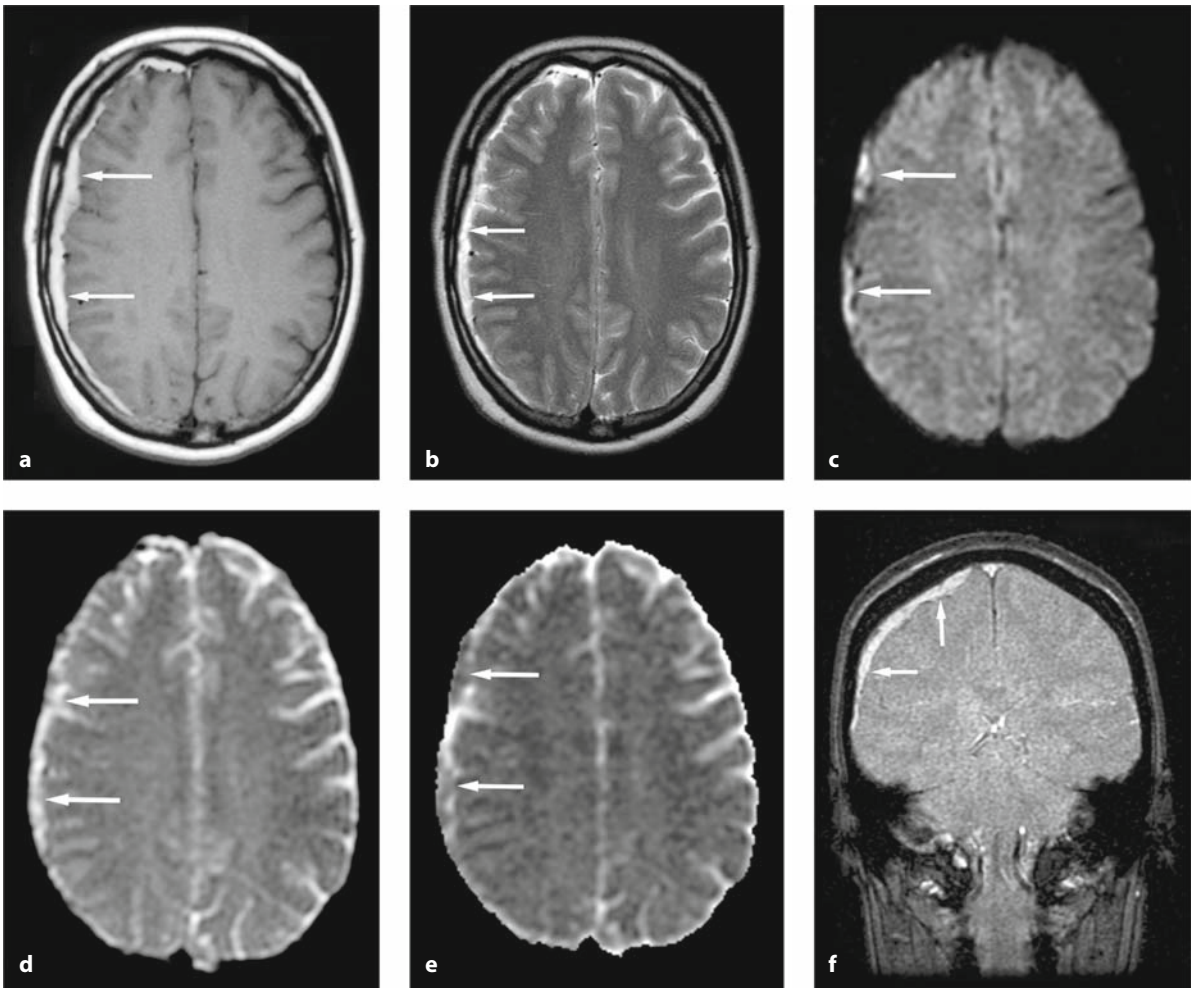

Figure 6.7 a–f

Subacute subdural hematoma (extracellular met-hemoglobin). A 49-year-old woman with headache following head trauma had an MR examination 2 weeks after the trauma, which shows right subdural hematoma as a hyperintense lesion (*arrows*) on the T1-weighted (**a**) and T2-weighted (**b**) images. The lesion was hyperintense on the DW (**c**) and the b_0 (**d**) images (*arrows*). On the ADC map (**e**) there are hypointense lesions (*arrows*), which correspond to the hyperintense lesions on the DW image (**c**). The coronal GRE image (**f**) shows the subdural hematoma to be hyperintense (*arrows*)

6.4 Subdural and Epidural Hematoma

Subdural and epidural hematomas (Fig. 6.7) are well demonstrated on T1- and T2-weighted images. In the acute and subacute stages, the evolution of signal intensity generally follows the one of intraparenchymal hematomas with a slower rate because of higher oxygen tension in the subdural or epidural space. In the chronic stage, MR images often show hyperintensity of the hematoma, which may be iso- to hypodense on CT [34, 64–70].

Diffusion-weighted imaging findings of subdural and epidural hematomas have not been well described. Lin et al. reported that all three lesions could be detected on b_0 images, but GRE images were better at detecting lesions [31]. The benefit of DW imaging is probably for the detection of underlying or associated parenchymal lesions [71, 72].

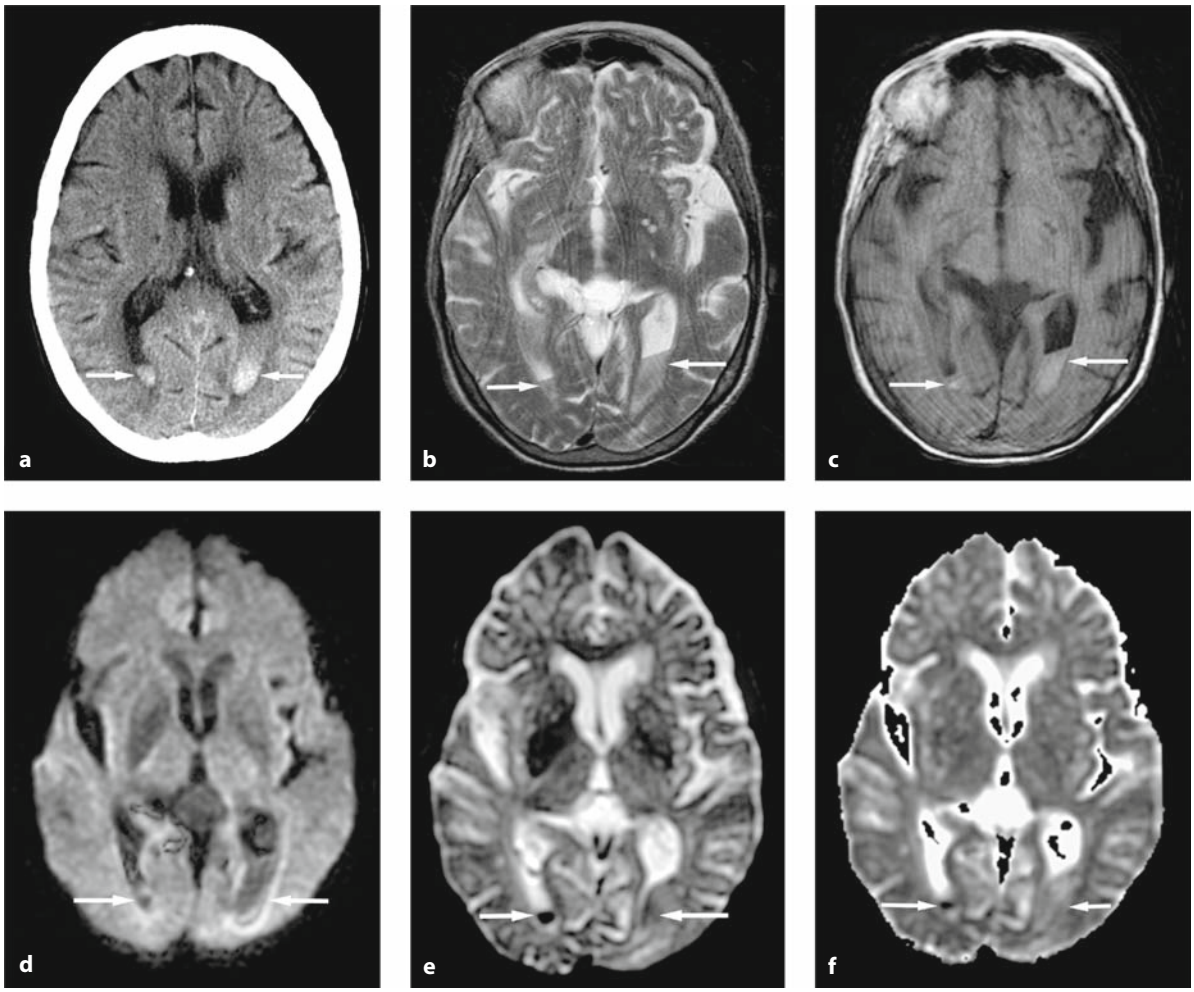

Figure 6.8 a–f

Intraventricular hemorrhage (intracellular met-hemoglobin). A 78-year-old woman with headache after thrombolytic therapy for femoral artery occlusion had a CT scan 6 hours after surgery (**a**). This shows intraventricular hemorrhage in the bilateral lateral ventricles (*arrows*). Three days after surgery (**b–f**), the T2-weighted image (**b**) shows hypointense lesions in the bilateral lateral ventricles with fluid–fluid levels (*arrows*) and the T1-weighted image (**c**) shows hyperintense lesions in the same distributions (*arrows*). The DW image (**d**) shows hypointense lesions (*arrows*) with surrounding hyperintensities. These are ascribed to magnetic susceptibility artifacts. The b_0 image (**e**) also shows hypointense lesions (*arrows*). These hypointensities are more prominent than on the T2-weighted images (**b**). The ADC map (**f**) shows hypointense lesions (*arrows*)

6.5 Intraventricular Hemorrhage

Intraventricular hemorrhages (Figs. 6.6 and 6.8) are well demonstrated on FLAIR, T1-, T2- and proton density-weighted images [34, 59, 73–75]. FLAIR has been reported to have the highest sensitivity for detection of intraventricular hematomas [74]. DW images can demonstrate intraventricular hemorrhages, but in general the GRE images have a higher sensitivity [31].

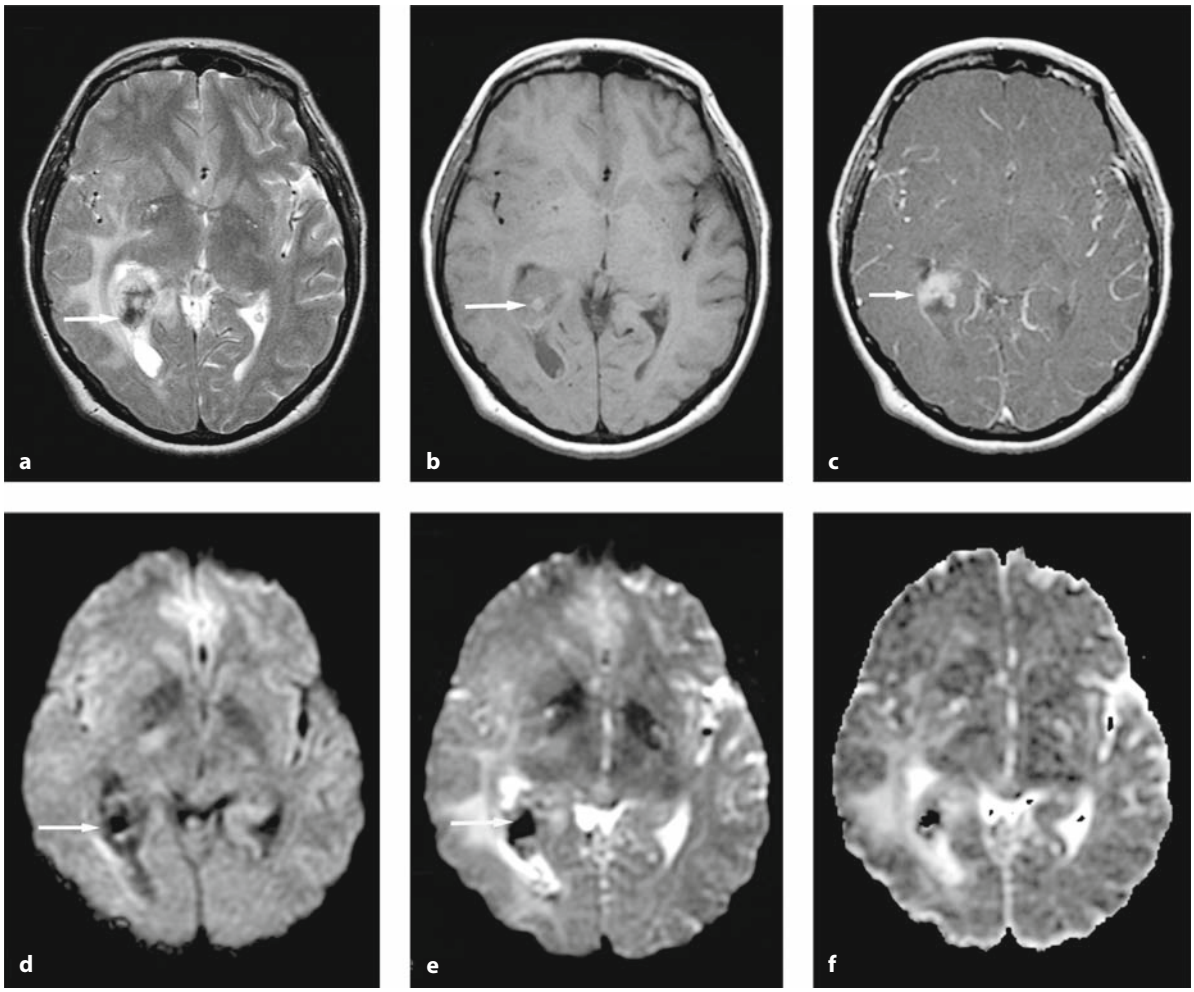

Figure 6.9 a–f

Hemorrhagic tumor. The T2-weighted MR image (**a**) in a 54-year-old woman with glioblastoma shows a mass lesion with heterogeneous intensity near the right lateral ventricle. The irregular hypointensities centrally in the lesion (*arrow*) indicate hemorrhage. The T1-weighted image (**b**) shows the heterogeneous hypointense to isointense mass, with a central area of higher signal intensity consistent with hemorrhage (*arrow*). The gadolinium-enhanced T1-weighted image (**c**) shows heterogeneous enhancement (*arrow*). On the DW image (**d**) the hemorrhage is heterogeneously hypointense (*arrow*). The b_0 image (**e**) shows the hemorrhage to be more hypointense (*arrow*) than on the T2-weighted image (**a**). The ADC (**f**) cannot be calculated due to magnetic susceptibility artifacts

6.6 Intratumoral Hemorrhage

Many primary brain tumors and metastases can bleed [34, 76–81]. The signal intensity of intratumoral hemorrhage (Fig. 6.9) tends to be more complex and its evolution tends to be delayed when compared with non-neoplastic hemorrhages [34, 81]. DW and b_0 images are useful to detect the hemorrhage in tumors [31].

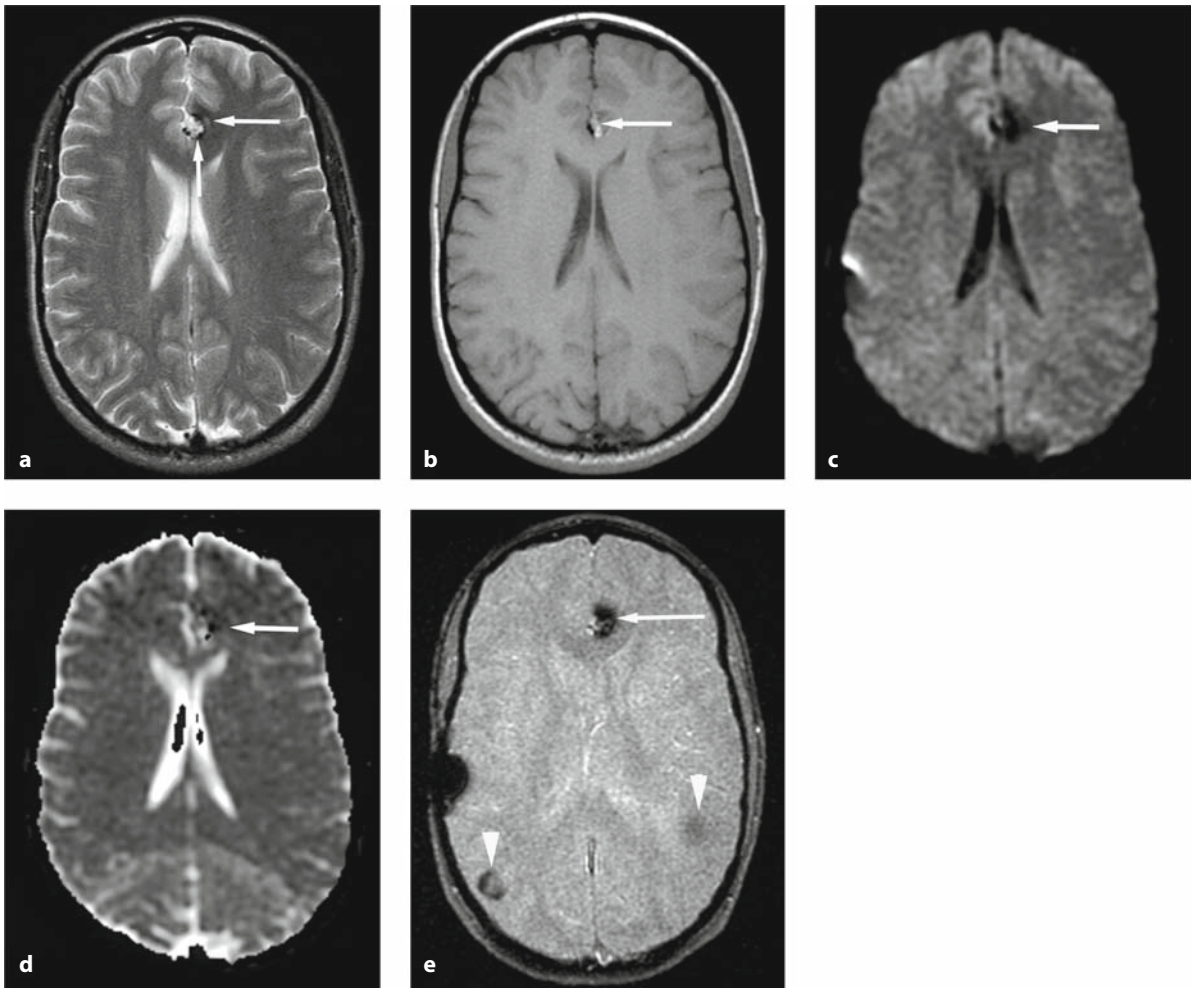

Figure 6.10 a–e

Multiple cavernous angiomas. The T2-weighted MR image (**a**) in a 30-year-old woman with seizures shows a hyperintense lesion in the left frontal lobe with a surrounding hypointense rim (*arrows*). This is a characteristic finding for a cavernous angioma. The lesion is hyperintense on the T1-weighted image (**b**) (*arrow*) and hypointense on the DW image (**c**) (*arrow*). The ADC map (**d**) shows heterogeneous intensity and the GRE image (**e**) shows marked hypointensity in the left frontal lobe (*arrow*). The hypointensities in the right and left temporo-occipital region (*arrowheads*) suggest multiple cavernous angiomas

6.7 Hemorrhage Related to Vascular Malformation

Vascular malformations can also cause intracranial hemorrhages (Fig. 6.10). Cavernous angioma is a vascular malformation that contains blood cavities surrounded by a single layer of endothelium [82–86]. MR imaging findings are well known and characterized as a central reticulated core with a peripheral rim of hypointensity due to the deposition of hemosiderin [82, 85, 86]. DW and b_0 images are useful for detecting hemorrhages related to vascular malformations.

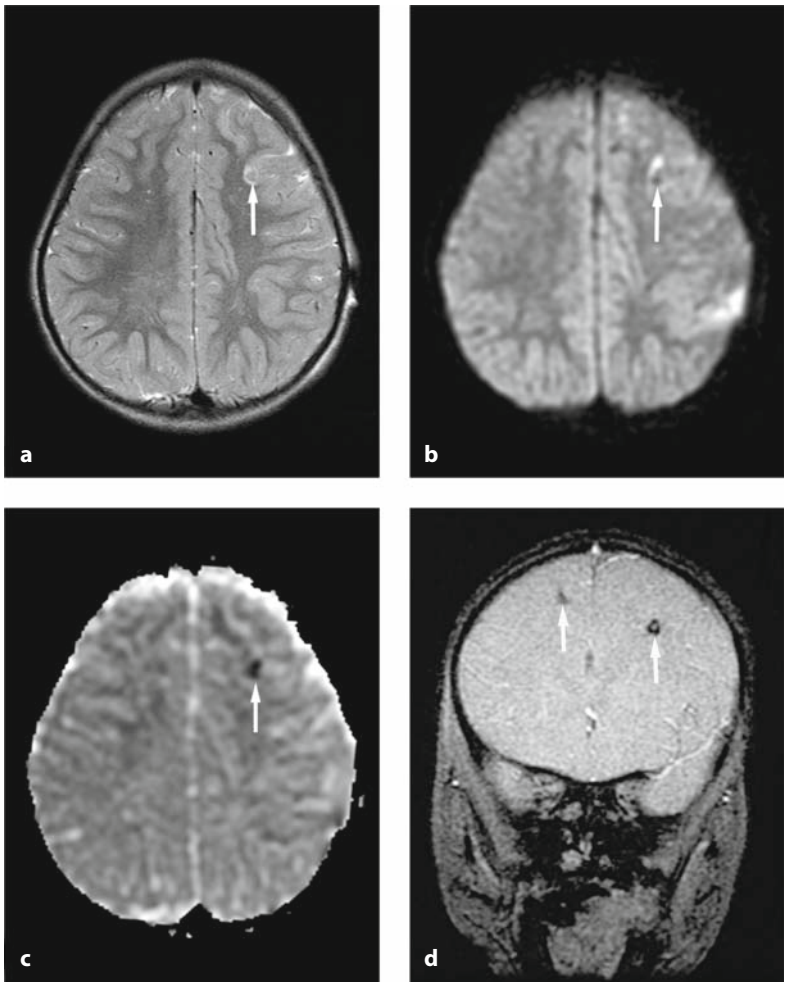

Figure 6.11 a–d

Trauma with hemorrhagic diffuse axonal injury. MR imaging of a 2-year-old girl 12 hours after a motor vehicle accident shows (**a**) a hyperintense lesion in the left frontal lobe on T2-weighted image (*arrow*). The corresponding area on the DW image (**b**) is hypointense with surrounding hyperintensity (*arrow*). The ADC map (**c**) shows hypointensity (*arrow*). The coronal GRE (**d**) image shows hypointense lesions in the bilateral frontal lobes (*arrows*)

6.8 Hemorrhage Related to Trauma

(see also Chap. 12)

Trauma is one of the most common causes of intracranial hemorrhages in younger patients (Fig. 6.11). MR imaging is valuable in detecting intracranial injuries. DW and b_0 images and an ADC map can be more sensitive than conventional MR images to detect whether the abnormality includes diffuse axonal injury [87].

6.9 Conclusions

Diffusion-weighted imaging is often of limited value for diagnosis and staging of intracranial hemorrhages because accurate ADC measurements are only possible in the hyperacute stage, which contains diamagnetic oxy-hemoglobin, and in the late subacute phase, which contains extracellular met-hemoglobin, whose paramagnetic susceptibility artifacts are diminished by the dilution of extracellular fluid. CT and routine MR imaging continue to be the mainstay in diagnosing and characterizing intracranial hemorrhages. A thorough understanding of DW imaging characteristics is important, however, in order to avoid misinterpretations and inaccurate conclusions.

References

1. Thulborn KR, Waterton JC, Matthews PM, Radda GK (1982) Oxygenation dependence of the transverse relaxation time of water protons in whole blood at high field. Biochim Biophys Acta 714:265–270
2. Fullerton GD, Potter JL, Dornbluth NC (1982) NMR relaxation of protons in tissues and other macromolecular water solutions. Magn Reson Imaging 1:209–226
3. Sipponen JT, Sepponen RE, Sivula A (1983) Nuclear magnetic resonance (NMR) imaging of intracerebral hemorrhage in the acute and resolving phases. J Comput Assist Tomogr 7:954–959
4. DeLaPaz RL, New PF, et al. (1984) NMR imaging of intracranial hemorrhage. J Comput Assist Tomogr 8:599–607
5. Bradley WG Jr, Schmidt PG (1985) Effect of methemoglobin formation on the MR appearance of subarachnoid hemorrhage. Radiology 156:99–103
6. Gomori JM, Grossman RI, Bilaniuk LT, Zimmerman RA, Goldberg HI (1985) High-field MR imaging of superficial siderosis of the central nervous system. J Comput Assist Tomogr 9:972–975
7. Gomori JM, Grossman RI, Goldberg HI, Zimmerman RA, Bilaniuk LT (1985) Intracranial hematomas: imaging by high-field MR. Radiology 157:87–93
8. Sipponen JT, Sepponen RE, Tanttu JI, Sivula A (1985) Intracranial hematomas studied by MR imaging at 0.17 and 0.02 T. J Comput Assist Tomogr 9:698–704
9. Grossman RI, Kemp SS, Ip CY, et al. (1986) Importance of oxygenation in the appearance of acute subarachnoid hemorrhage on high field magnetic resonance imaging. Acta Radiol Suppl 369:56–58
10. Di Chiro G, Brooks RA, Girton ME, et al. (1986) Sequential MR studies of intracerebral hematomas in monkeys. AJNR Am J Neuroradiol 7:193–199
11. Gomori JM, Grossman RI, Yu-Ip C, Asakura T (1987) NMR relaxation times of blood: dependence on field strength, oxidation state, and cell integrity. J Comput Assist Tomogr 11:684–690
12. Zimmerman RD, Heier LA, Snow RB, Liu DP, Kelly AB, Deck MD (1988) Acute intracranial hemorrhage: intensity changes on sequential MR scans at 0.5 T. AJR Am J Roentgenol 150:651–661
13. Hayman LA, Ford JJ, Taber KH, Saleem A, Round ME, Bryan RN (1988) T2 effect of hemoglobin concentration: assessment with in vitro MR spectroscopy. Radiology 168:489–491
14. Brooks RA, Di Chiro G, Patronas N (1989) MR imaging of cerebral hematomas at different field strengths: theory and applications. J Comput Assist Tomogr 13:194–206
15. Hayman LA, McArdle CB, Taber KH, et al. (1989) MR imaging of hyperacute intracranial hemorrhage in the cat. AJNR Am J Neuroradiol 10:681–686
16. Hayman LA, Taber KH, Ford JJ, et al. (1989) Effect of clot formation and retraction on spin-echo MR images of blood: an in vitro study. AJNR Am J Neuroradiol 10:1155–1158
17. Hardy PA, Kucharczyk W, Henkelman RM (1990) Cause of signal loss in MR images of old hemorrhagic lesions. Radiology 174:549–555
18. Bryant RG, Marill K, Blackmore C, Francis C (1990) Magnetic relaxation in blood and blood clots. Magn Reson Med 13:133–144
19. Clark RA, Watanabe AT, Bradley WG Jr, Roberts JD (1990) Acute hematomas: effects of deoxygenation, hematocrit, and fibrin-clot formation and retraction on T2 shortening. Radiology 175:201–206
20. Thulborn KR, Sorensen AG, Kowall NW, et al. (1990) The role of ferritin and hemosiderin in the MR appearance of cerebral hemorrhage: a histopathologic biochemical study in rats. AJNR Am J Neuroradiol 11:291–297
21. Bizzi A, Brooks RA, Brunetti A, et al. (1990) Role of iron and ferritin in MR imaging of the brain: a study in primates at different field strengths. Radiology 177:59–65
22. Bradley WG Jr (1993) MR appearance of hemorrhage in the brain. Radiology 189:15–26
23. Ekholm S (1996) Intracranial hemorrhages. Rivista di Neuroradiologia 9 (Suppl 1):17–21
24. Ebisu T, Tanaka C, Umeda M, et al. (1997) Hemorrhagic and nonhemorrhagic stroke: diagnosis with diffusion-weighted and T2-weighted echo-planar MR imaging. Radiology 203:823–828
25. Atlas SW, Thulborn KR (1998) MR detection of hyperacute parenchymal hemorrhage of the brain. AJNR Am J Neuroradiol 19:1471–1477
26. Liang L, Korogi Y, Sugahara T, et al. (1999) Detection of intracranial hemorrhage with susceptibility-weighted MR sequences. AJNR Am J Neuroradiol 20:1527–1534
27. Kinoshita T, Okudera T, Tamura H, Ogawa T, Hatazawa J (2000) Assessment of lacunar hemorrhage associated with hypertensive stroke by echo-planar gradient-echo T2*-weighted MRI. Stroke 31:1646–1650
28. Atlas SW, DuBois P, Singer MB, Lu D (2000) Diffusion measurements in intracranial hematomas: implications for MR imaging of acute stroke. AJNR Am J Neuroradiol 21:1190–1194
29. Schaefer PW, Grant PE, Gonzalez RG (2000) Diffusion-weighted MR imaging of the brain. Radiology 217:331–345
30. Maldjian JA, Listerud J, Moonis G, Siddiqi F (2001) Computing diffusion rates in T2-dark hematomas and areas of low T2 signal. AJNR Am J Neuroradiol 22:112–128
31. Lin DD, Filippi CG, Steever AB, Zimmerman RD (2001) Detection of intracranial hemorrhage: comparison between gradient-echo images and b(0) images obtained from diffusion-weighted echo-planar sequences. AJNR Am J Neuroradiol 22:1275–1281
32. Hermier M, Nighoghossian N, Derex L, et al. (2001) MRI of acute post-ischemic cerebral hemorrhage in stroke patients: diagnosis with T2*-weighted gradient-echo sequences. Neuroradiology 43:809–815
33. Kang BK, Na DG, Ryoo JW, Byun HS, Roh HG, Pyeun YS (2001) Diffusion-weighted MR imaging of intracerebral hemorrhage. Korean J Radiol 2:183–191
34. Atlas SW, Thulborn KR (2002) Intracranial hemorrhage. In: Magnetic resonance imaging of the brain and spine. Lippincott Williams & Wilkins, Philadelphia, pp 773–832
35. Latour LL, Svoboda K, Mitra PP, Sotak CH (1994) Time-dependent diffusion of water in a biological model system. Proc Natl Acad Sci USA 91:1229–1233

36. Does MD, Zhong J, Gore JC (1999) In vivo measurement of ADC change due to intravascular susceptibility variation. Magn Reson Med 41:236–240
37. Harrison PM, Fischbach FA, Hoy TG, Haggis GH (1967) Ferric oxyhydroxide core of ferritin. Nature 216:1188–1190
38. Munro HN, Linder MC (1978) Ferritin: structure, biosynthesis, and role in iron metabolism. Physiol Rev Apr;58(2):317–396
39. Carhuapoma JR, Barker PB, Hanley DF, Wang P, Beauchamp NJ (2002) Human brain hemorrhage: quantification of perihematoma edema by use of diffusion-weighted MR imaging. AJNR Am J Neuroradiol 23:1322-1326
40. Kidwell CS, Saver JL, Mattiello J, et al. (2001) Diffusion-perfusion MR evaluation of perihematomal injury in hyperacute intracerebral hemorrhage. Neurology 57:1611-1617
41. Forbes KP, Pipe JG, Heiserman JE (2003) Diffusion-weighted imaging provides support for secondary neuronal damage from intraparenchymal hematoma. Neuroradiology 45:363-367
42. Chakeres DW, Bryan RN (1986) Acute subarachnoid hemorrhage: in vitro comparison of magnetic resonance and computed tomography. AJNR Am J Neuroradiol 7:223–228
43. Jenkins A, Hadley DM, Teasdale GM, Condon B, Macpherson P, Patterson J (1988) Magnetic resonance imaging of acute subarachnoid hemorrhage. J Neurosurg 68:731–736
44. Satoh S, Kadoya S (1988) Magnetic resonance imaging of subarachnoid hemorrhage. Neuroradiology 30:361–366
45. Atlas SW (1993) MR imaging is highly sensitive for acute subarachnoid hemorrhage ... not! Radiology 186:319–322
46. Ogawa T, Uemura K (1993) MR imaging is highly sensitive for acute subarachnoid hemorrhage ... not! Reply. Radiology 186:323
47. Ogawa T, Inugami A, Shimosegawa E, et al. (1993) Subarachnoid hemorrhage: evaluation with MR imaging. Radiology 186:345–351
48. Griffiths PD, Wilkinson ID, Mitchell P, et al. (2002) Multimodality MR imaging depiction of hemodynamic changes and cerebral ischemia in subarachnoid hemorrhage. AJNR Am J Neuroradiol 22:1690–1697
49. Noguchi K, Ogawa T, Inugami A, Toyoshima H, Okudera T, Uemura K (1994) MR of acute subarachnoid hemorrhage: a preliminary report of fluid-attenuated inversion-recovery pulse sequences. AJNR Am J Neuroradiol 15:1940–1943
50. Noguchi K, Ogawa T, Inugami A, et al. (1995) Acute subarachnoid hemorrhage: MR imaging with fluid-attenuated inversion recovery pulse sequences. Radiology 196:773–777
51. Noguchi K, Ogawa T, Seto H, et al. (1997) Subacute and chronic subarachnoid hemorrhage: diagnosis with fluid-attenuated inversion-recovery MR imaging. Radiology 203(1):257–262
52. Noguchi K, Seto H, Kamisaki Y, Tomizawa G, Toyoshima S, Watanabe N (2000) Comparison of fluid-attenuated inversion-recovery MR imaging with CT in a simulated model of acute subarachnoid hemorrhage. AJNR Am J Neuroradiol 21:923–927
53. Melhem ER, Jara H, Eustace S (1997) Fluid-attenuated inversion recovery MR imaging: identification of protein concentration thresholds for CSF hyperintensity. AJR Am J Roentgenol 169:859–862
54. Singer MB, Atlas SW, Drayer BP (1998) Subarachnoid space disease: diagnosis with fluid-attenuated inversion-recovery MR imaging and comparison with gadolinium-enhanced spin-echo MR imaging – blinded reader study. Radiology 208:417–422
55. Dechambre SD, Duprez T, Grandin CB, Lecouvet FE, Peeters A, Cosnard G (2000) High signal in cerebrospinal fluid mimicking subarachnoid haemorrhage on FLAIR following acute stroke and intravenous contrast medium. Neuroradiology 42:608–611
56. Taoka T, Yuh WT, White ML, Quets JP, Maley JE, Ueda T (2001) Sulcal hyperintensity on fluid-attenuated inversion recovery mr images in patients without apparent cerebrospinal fluid abnormality. AJR Am J Roentgenol 176:519–524
57. Wiesmann M, Mayer TE, Yousry I, Medele R, Hamann GF, Bruckmann H (2002) Detection of hyperacute subarachnoid hemorrhage of the brain by using magnetic resonance imaging. J Neurosurg 96:684–689
58. Busch E, Beaulieu C, de Crespigny A, Moseley ME (1998) Diffusion MR imaging during acute subarachnoid hemorrhage in rats. Stroke 29:2155–2161
59. Rordorf G, Koroshetz WJ, Copen WA, et al. (1999) Diffusion- and perfusion-weighted imaging in vasospasm after subarachnoid hemorrhage. Stroke 30:599–605
60. Domingo Z, Bradley JK, Blamire AM, Brindle K, Styles P, Rajagopalan B (2000) Diffusion weighted imaging and magnetic resonance spectroscopy in a low flow ischaemia model due to endothelin induced vasospasm. NMR Biomed 13:154–162
61. Condette-Auliac S, Bracard S, Anxionnat R, et al. (2001) Vasospasm after subarachnoid hemorrhage: interest in diffusion-weighted MR imaging. Stroke 32:1818–1824
62. Hadeishi H, Suzuki A, Yasui N, Hatazawa J, Shimosegawa E (2002) Diffusion-weighted magnetic resonance imaging in patients with subarachnoid hemorrhage. Neurosurgery 50:741–747
63. Leclerc X, Fichten A, Gauvrit JY, et al. (2002) Symptomatic vasospasm after subarachnoid haemorrhage: assessment of brain damage by diffusion and perfusion-weighted MRI and single-photon emission computed tomography. Neuroradiology 44:610–616
64. Fobben ES, Grossman RI, Atlas SW, Hackney DB, Goldberg HI, Zimmerman RA, Bilaniuk LT (1989) MR characteristics of subdural hematomas and hygromas at 1.5 T. AJR Am J Roentgenol 153:589–595
65. Ebisu T, Naruse S, Horikawa Y, Tanaka C, Higuchi T (1989) Nonacute subdural hematoma: fundamental interpretation of MR images based on biochemical and in vitro MR analysis. Radiology 171:449–453
66. Wilms G, Marchal G, Geusens E, et al. (1992) Isodense subdural haematomas on CT: MRI findings. Neuroradiology 34:497–499
67. Ashikaga R, Araki Y, Ishida O (1997) MRI of head injury using FLAIR. Neuroradiology 39:239–242

68. Williams VL, Hogg JP (2000) Magnetic resonance imaging of chronic subdural hematoma. Neurosurg Clin N Am Jul;11(3):491–498
69. Tsui EY, Fai Ma K, Cheung YK, Chan JH, Yuen MK (2000) Rapid spontaneous resolution and redistribution of acute subdural hematoma in a patient with chronic alcoholism: a case report. Eur J Radiol 36:53-57
70. Lee Y, Lee KS, Hwang DH, Lee IJ, Kim HB, Lee JY (2001) MR imaging of shaken baby syndrome manifested as chronic subdural hematoma. Korean J Radiol 2:171–174
71. Biousse V, Suh DY, Newman NJ, Davis PC, Mapstone T, Lambert SR (2002) Diffusion-weighted magnetic resonance imaging in Shaken Baby Syndrome. Am J Ophthalmol Feb;133(2):249–255
72. Mesiwala AH, Goodkin R (2002) Reversible ischemia detected by diffusion-weighted magnetic resonance imaging. Case illustration. J Neurosurg 97:230
73. Bakshi R, Kamran S, Kinkel PR, et al. (1999) MRI in cerebral intraventricular hemorrhage: analysis of 50 consecutive cases. Neuroradiology 41:401–409
74. Bakshi R, Kamran S, Kinkel PR, et al. (1999) Fluid-attenuated inversion-recovery MR imaging in acute and subacute cerebral intraventricular hemorrhage. AJNR Am J Neuroradiol 20:629–636
75. Nakai Y, Hyodo A, Yanaka K, Nose T (2002) Fatal cerebral infarction after intraventricular hemorrhage in a pregnant patient with moyamoya disease. J Clin Neurosci 9:456–458
76. Scott M (1975) Spontaneous intracerebral hematoma caused by cerebral neoplasms. Report of eight verified cases. J Neurosurg 42:338–342
77. Mandybur TI (1977) Intracranial hemorrhage caused by metastatic tumors. Neurology 27:650–655
78. Little JR, Dial B, Belanger G, Carpenter S (1979) Brain hemorrhage from intracranial tumor. Stroke 10:283–288
79. Zimmerman RA, Bilaniuk LT (1980) Computed tomography of acute intratumoral hemorrhage. Radiology 135:355–359
80. Leeds NE, Elkin CM, Zimmerman RD (1984) Gliomas of the brain. Semin Roentgenol 19:27–43
81. Atlas SW, Grossman RI, Gomori JM, et al. (1987) Hemorrhagic intracranial malignant neoplasms: spin-echo MR imaging. Radiology 164:71–77
82. Brunereau L, Labauge P, Tournier-Lasserve E, Laberge S, Levy C, Houtteville JP (2000) Familial form of intracranial cavernous angioma: MR imaging findings in 51 families. French Society of Neurosurgery. Radiology 214:209–216
83. Tagle P, Huete I, Mendez J, del Villar S (1986) Intracranial cavernous angioma: presentation and management. J Neurosurg 64:720–723
84. Zabramski JM, Wascher TM, Spetzler RF, et al. (1994) The natural history of familial cavernous malformations: results of an ongoing study. J Neurosurg 80:422–432
85. Gomori JM, Grossman RI, Goldberg HI, Hackney DB, Zimmerman RA, Bilaniuk LT (1986) Occult cerebral vascular malformations: high-field MR imaging. Radiology 158:707–713
86. Sigal R, Krief O, Houtteville JP, Halimi P, Doyon D, Pariente D (1990) Occult cerebrovascular malformations: follow-up with MR imaging. Radiology 176:815–819
87. Liu AY, Maldjian JA, Bagley LJ, Sinson GP, Grossman RI (1999) Traumatic brain injury: diffusion-weighted MR imaging findings. AJNR Am J Neuroradiol 20:1636–1641

Vasculopathy and Vasculitis

7.1 Definition

Vasculopathy is a general term used to describe any disease affecting blood vessels [1]. It includes vascular abnormalities caused by degenerative, metabolic and inflammatory conditions, embolic diseases, coagulative disorders, and functional disorders such as posterior reversible encephalopathy syndrome. The etiology of vasculopathy is generally unknown and the condition is frequently not pathologically proven. Vasculitis, on the other hand, is a more specific term and is defined as inflammation of the wall of a blood vessel [2]. However, the term vasculopathy is also used for "vasculitis" that has not been pathologically established.

7.2 Clinical Presentation

Vasculitis and vasculopathy of the central nervous system (CNS) often have similar clinical and radiological characteristics. Both result in ischemia, which can be reversible or develop into infarction. The reversibility of a lesion is related to the size and location of vessels involved and the severity of ischemia. Diffusion-weighted (DW) imaging has been useful in the early detection of cytotoxic edema in hyperacute or acute infarctions and can distinguish cytotoxic edema from vasogenic edema and chronic infarctions [3]. Some specific types of vasculitis or vasculopathy demonstrate primarily vasogenic edema [4–8].

7.3 Treatment

Vasculitis and vasculopathy of the CNS caused by an abnormal immune reaction are often treated with immunosuppressant agents. If, on the other hand, the vascular changes are caused by thrombosis or embolism, they are treated with anticoagulants. Prompt characterization of the nature of CNS vasculitis and vasculopathy, by imaging and/or biopsy, is thus necessary to institute appropriate management.

7.4 Vasculitis of the CNS

The term vasculitis encompasses a heterogeneous group of multisystemic disorders characterized pathologically by inflammation and necrosis of the blood vessel wall. Cerebral ischemia, which may result in focal infarction, is the major neurological manifestation of CNS vasculitis. The clinical manifestations include headache, transient ischemic attacks (TIAs), altered mental status, seizures, cranial nerve palsies and localized neurologic deficits.

7.4.1 Characterization of CNS Vasculitis

Vasculitis of the CNS is characterized by the size of the affected vessel, as illustrated in Fig. 7.1 [2]. Determining size and location of the predominantly affected vessels is useful to obtain an optimal tissue biopsy and establish appropriate treatment [9]. Large artery vasculitis usually responds well to steroids alone, while small and medium-sized vessel vasculitis respond better to a combination of cytotoxic agents and steroids. Therefore, a clear understanding of the size of the vessels involved and the pathophysiologic mechanisms are useful for the treatment decision [10, 11].

Digital subtraction catheter angiography and brain biopsy are the diagnostic foundations in establishing the diagnosis. However, angiography has a false-negative rate of 20–30%, as small arteries with a diameter of less than 100–200 μm are beyond the limit of resolution of digital subtraction angiography [2]. Good-quality MR angiography can demonstrate stenosis or occlusion of large to middle-sized arteries, but the resolution is not sufficient to detect abnormalities of small arteries. MR imaging, on the other hand, is sensitive to detect gray and white matter lesions in CNS vasculitis, but the appearance of these lesions is usually not specific [12].

Whether the lesions on MR imaging are reversible or irreversible depends on the severity of ischemia and seems to be related to size and location of the ves-

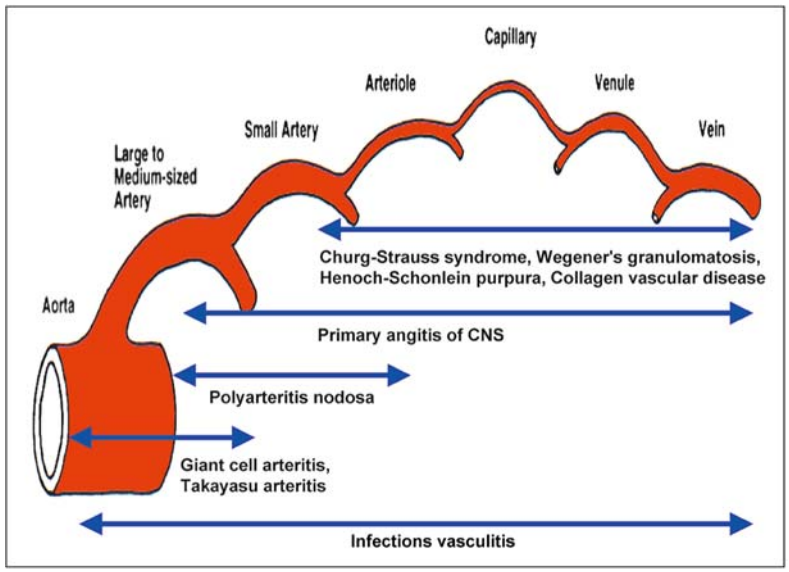

Figure 7.1
Classification of CNS vasculitis. (Modified from [10])

sels involved. Occlusion or stenosis involving large, medium or small arteries mainly results in infarction, whereas lesions involving arterioles, capillaries, venules or veins predominantly cause vasogenic edema. DW imaging can be useful to differentiate an acute or subacute infarction from vasogenic edema, which is important both for choice of treatment and to predict the long-term prognosis.

Multifocal and multiphasic ischemia are some of the characteristic sequelae of CNS vasculitis. DW imaging can differentiate the phases of cerebral infarction as hyperacute, acute, subacute or chronic. The hyperacute phase of an infarction usually has a decreased apparent diffusion coefficient (ADC) and a normal or subtle increase in signal intensity on T2-weighted or fluid-attenuated inversion-recovery (FLAIR) images. The acute phase has a decreased ADC with hyperintensity on T2-weighted images. In the subacute phase, ADC values are normalized; in the chronic phase, DW imaging shows hypointensity with increased ADC. Diffuse increase in water diffusion in the normal-appearing brain with CNS vasculitis is also observed [13].

7.4.2 Primary Angitis of the Central Nervous System

Primary angitis (angiitis) of the central nervous system (PACNS) is a non-infectious granulomatous angitis, pathologically characterized by infiltration of the vessel walls with lymphocytes, histiocytes, and/or multinucleated giant cells, with a variable degree of fibrinoid necrosis [14]. PACNS is usually seen in young adult and middle age groups (mean age 46.2 years) [15]. PACNS in association with amyloid angiopathy has been reported and in older patients [16, 17]. The pathogenesis is probably related to T cell-mediated inflammation. PACNS tends to affect small to medium-sized vessels of the brain parenchyma and meninges, but can affect vessels of any size. Angiography typically shows a "string-of-beads" appearance, which is usually seen in PACNS involving medium-sized arteries, but it has a false-negative rate of 20–30% [18]. Brain and meningeal biopsies are diagnostic in only 50–72% of patients with PACNS.

Magnetic resonance imaging findings in PACNS are highly variable, ranging from multiphasic cerebral infarction, vasogenic edema and gliosis, to hemorrhage and leptomeningeal enhancement [19, 20]. The lesions caused by occlusion of large or medium-sized arteries affect the cortical or deep gray matter which may result in multiple infarcts. If the vessels involved are small, MR imaging may show discrete or diffuse lesions in the deep or subcortical white matter with leptomeningeal enhancement. On follow-up MR imaging, the lesions may change with regard to number and size, and they may even disappear. DW imaging is useful in differentiating an acute or subacute infarction from reversible vasogenic edema (Figs. 7.2, 7.3), and can demonstrate multiphasic infarctions (Fig. 7.4). Prompt diagnosis is important, as PACNS

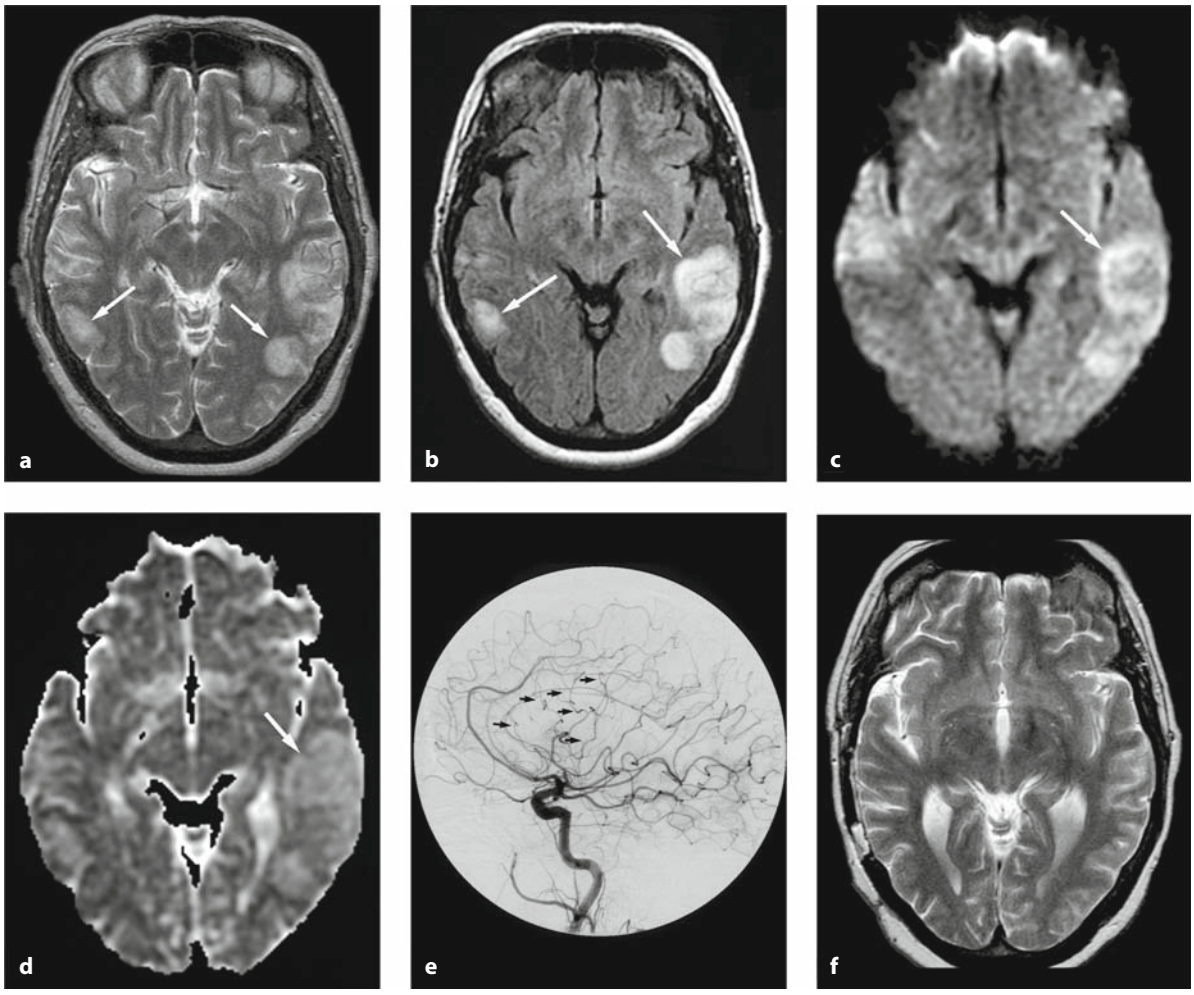

Figure 7.2 a–f

Primary angiitis of central nervous system (proven by biopsy) in a 60-year-old woman with dizziness and speech difficulties. **a** T2-weighted image shows hyperintense lesions in the bilateral tempo-occipital cortices (*arrows*). **b** FLAIR image shows hyperintense lesions in the bilateral tempo-occipital cortices (*arrows*). **c** DW image shows slightly high signal in the lesions (*arrow*) with increased ADC (**d**), mainly representing vasogenic edema (*arrow*). **e** DSA shows multiple focal stenoses of distal branches of left middle cerebral arteries (*arrows*). **f** Two-month follow-up T2-weighted image shows no infarction in the bilateral tempo-occipital areas. (From [69])

is often fatal if not treated with aggressive immunosuppression [21]. PACNS involving small vessels tends to be responsive to immunosuppressive drugs, but often there is relapse. PACNS involving medium-sized vessels tends to have isolated episodes with paucity of relapses [22].

7.4.3 Giant Cell (Temporal) Arteritis

The criteria of the American College of Rheumatology for the diagnosis of giant cell arteritis (Fig. 7.5) include at least three of the following: (1) age at disease onset >50 years, (2) new onset of headache, (3) claudication of jaw or tongue, (4) tenderness of the temporal artery on palpation or decreased pulsation,

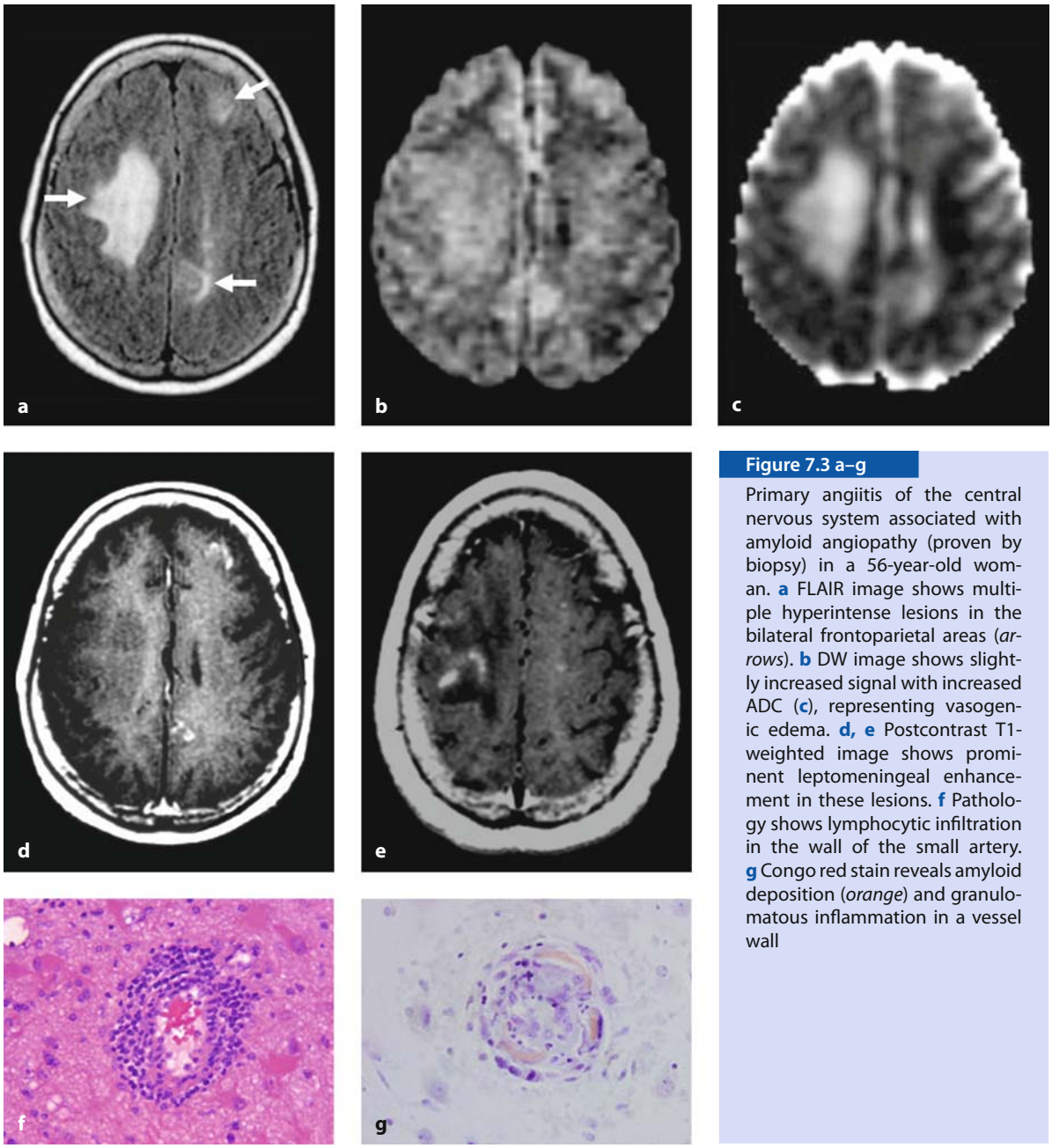

Figure 7.3 a–g

Primary angiitis of the central nervous system associated with amyloid angiopathy (proven by biopsy) in a 56-year-old woman. **a** FLAIR image shows multiple hyperintense lesions in the bilateral frontoparietal areas (*arrows*). **b** DW image shows slightly increased signal with increased ADC (**c**), representing vasogenic edema. **d, e** Postcontrast T1-weighted image shows prominent leptomeningeal enhancement in these lesions. **f** Pathology shows lymphocytic infiltration in the wall of the small artery. **g** Congo red stain reveals amyloid deposition (*orange*) and granulomatous inflammation in a vessel wall

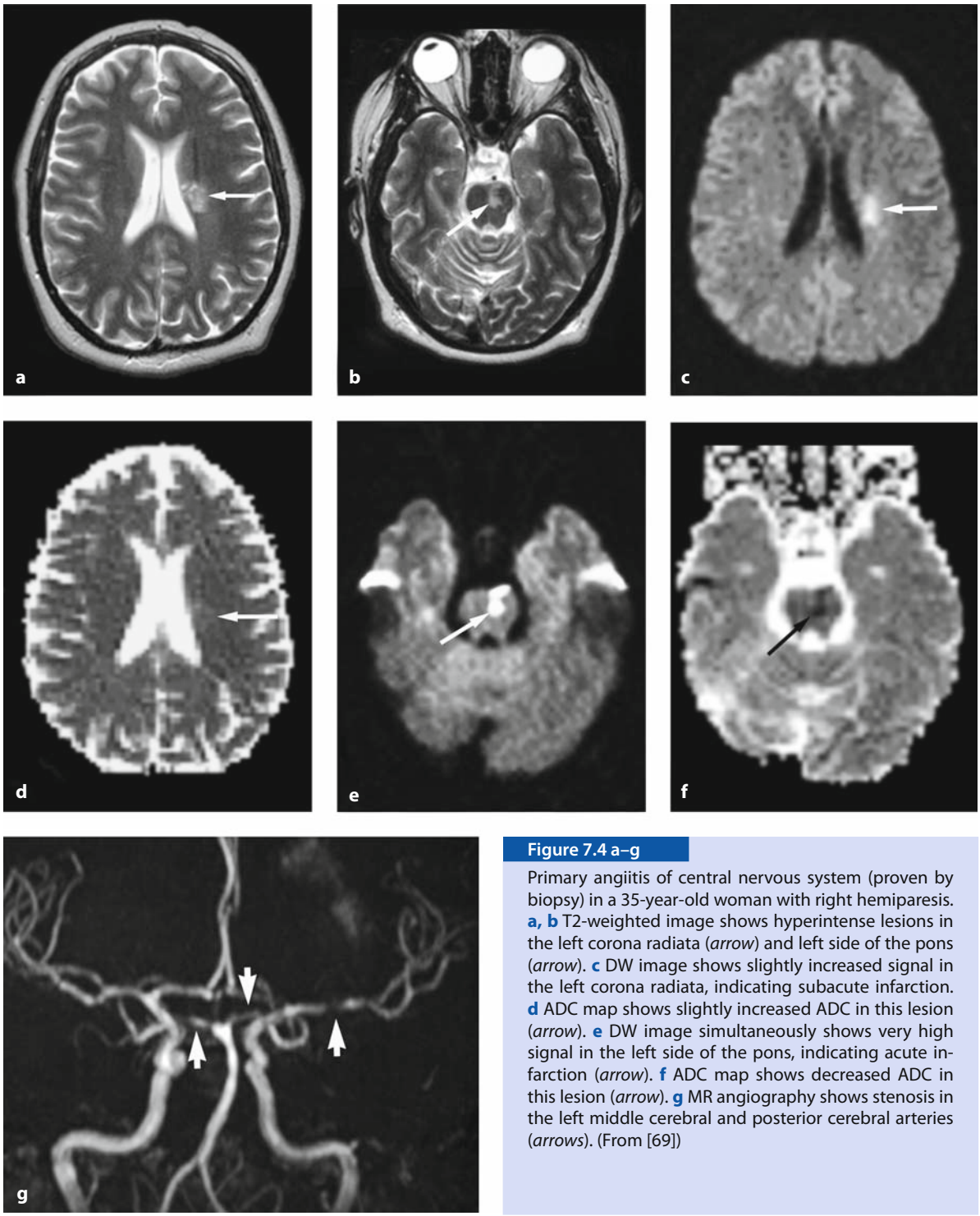

Figure 7.4 a–g

Primary angiitis of central nervous system (proven by biopsy) in a 35-year-old woman with right hemiparesis. **a, b** T2-weighted image shows hyperintense lesions in the left corona radiata (*arrow*) and left side of the pons (*arrow*). **c** DW image shows slightly increased signal in the left corona radiata, indicating subacute infarction. **d** ADC map shows slightly increased ADC in this lesion (*arrow*). **e** DW image simultaneously shows very high signal in the left side of the pons, indicating acute infarction (*arrow*). **f** ADC map shows decreased ADC in this lesion (*arrow*). **g** MR angiography shows stenosis in the left middle cerebral and posterior cerebral arteries (*arrows*). (From [69])

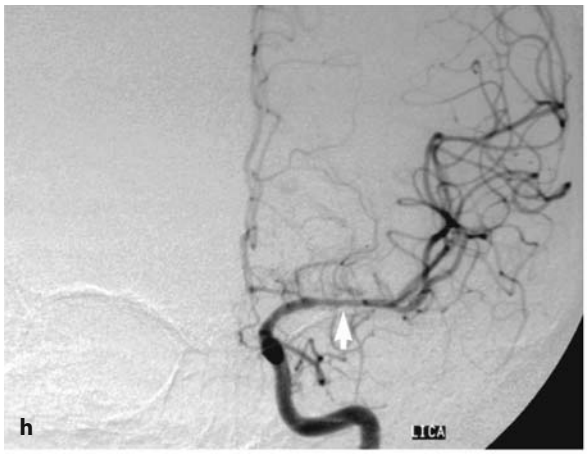

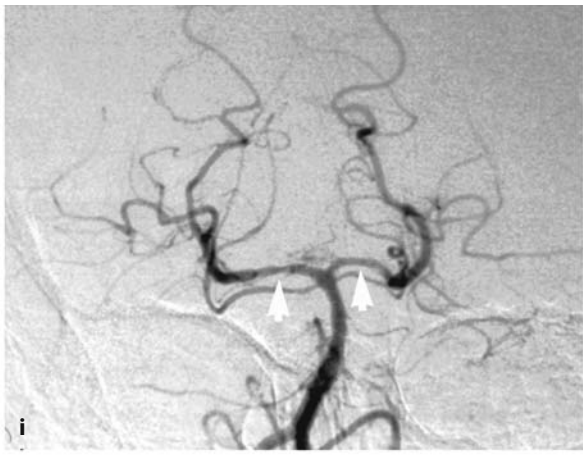

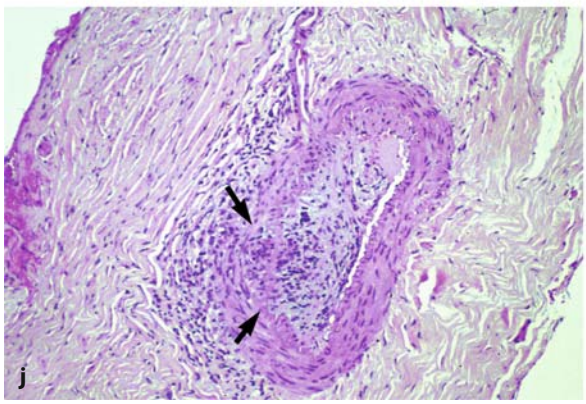

Figure 7.4 h–j

h, i Digital subtraction angiography (DSA) confirms the stenosis in the left middle cerebral (*arrow*) and posterior cerebral arteries, consistent with PACNS involving medium-sized arteries (*arrows*). **j** Pathological specimen by meningeal biopsy shows infiltration of the vessel wall with lymphocytes, multinucleated giant cells, and intramural granulomatous inflammation (*arrows*). (From [69])

(5) erythrocyte sedimentation ratio >50 mm/h and (6) temporal artery biopsy showing vasculitis with multinucleated giant cells.

Giant cell arteritis is probably a T cell-mediated vasculitis and it can affect medium to large arteries. The superficial temporal, vertebral and ophthalmic arteries are more commonly involved than the internal carotid arteries, while the intracranial arteries are rarely involved (Fig. 7.5) [23]. Abrupt and irreversible visual loss is the most dramatic complication of giant cell arteritis, while TIA and stroke are rare (7%), but when present most often involve the vertebrobasilar territory. Steroids are effective, and giant cell arteritis is usually self-limited and rarely fatal.

7.4.4 Takayasu's Arteritis (Aortitis Syndrome)

Takayasu's arteritis (Fig. 7.6) is a primary arteritis of unknown cause but probably also related to T cell-mediated inflammation. Takayasu's arteritis commonly affects large vessels including the aorta and its major branches to the arms and the head. It is more commonly seen in Asia and usually affects young women [24]. Pulseless upper extremities and hypertension are the common clues to suggest the diagnosis. Most patients are treated with steroids alone to reduce the inflammation. The prognosis is relatively good and 90% of patients are still alive after 10 years. TIA or stroke is rare but can occasionally occur in severe cases with significant stenosis of arteries supplying the CNS (Fig. 7.6).

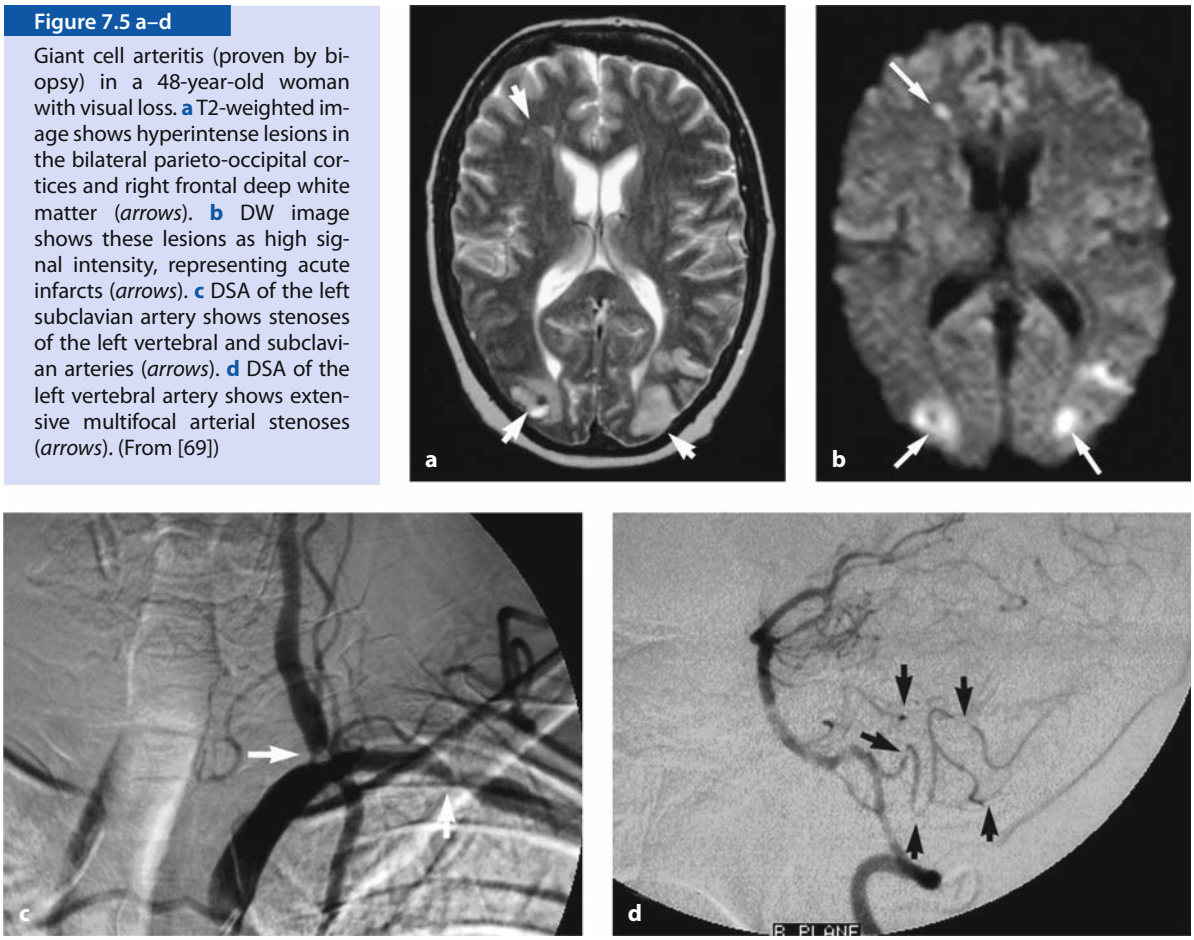

Figure 7.5 a–d

Giant cell arteritis (proven by biopsy) in a 48-year-old woman with visual loss. **a** T2-weighted image shows hyperintense lesions in the bilateral parieto-occipital cortices and right frontal deep white matter (*arrows*). **b** DW image shows these lesions as high signal intensity, representing acute infarcts (*arrows*). **c** DSA of the left subclavian artery shows stenoses of the left vertebral and subclavian arteries (*arrows*). **d** DSA of the left vertebral artery shows extensive multifocal arterial stenoses (*arrows*). (From [69])

7.4.5 Polyarteritis Nodosa

The criteria of the American College of Rheumatology for the diagnosis of polyarteritis nodosa include at least three of the following: (1) weight loss >4 kg, (2) livedo reticularis, (3) testicular pain or tenderness, (4) myalgias, weakness or leg tenderness, (5) mono- or polyneuropathy, (6) hypertension, (7) elevated blood creatinine or blood urea nitrogen, (8) hepatitis B antigen or antibodies in the serum, (9) aneurysm or occlusion of the visceral arteries and (10) granulocytes in small or medium-sized arteries on vessel wall biopsy. Neurologic abnormalities occur in 25–50% of cases. Ischemic stroke can result from vasculitis, severe hypertension or embolism secondary to cardiac involvement [25]. The treatment usually requires both cytotoxic agents and steroids.

7.4.6 Churg–Strauss Disease

This is an antineutrophil cytoplasmic autoantibody-mediated vasculitis, defined by at least four of the following: (1) asthma, (2) history of allergy, (3) eosinophilia (>10%), (4) mono- or polyneuropathy, (5) migratory or transitory pulmonary infiltrates and (6) sinusitis. A biopsy of affected organs, including small arteries, arterioles or venules shows a vasculitis with extravascular eosinophils, which confirms the diagnosis. Neurological involvement occurs in 62% of cases, including stroke and intracerebral hemorrhage (Fig. 7.7) [26, 27]. Steroids usually stabilize this condition, but treatment with cyclophosphamide may be required. A normal angiogram does not exclude this form of vasculitis, as affected vessels are often smaller than the resolution of angiography.

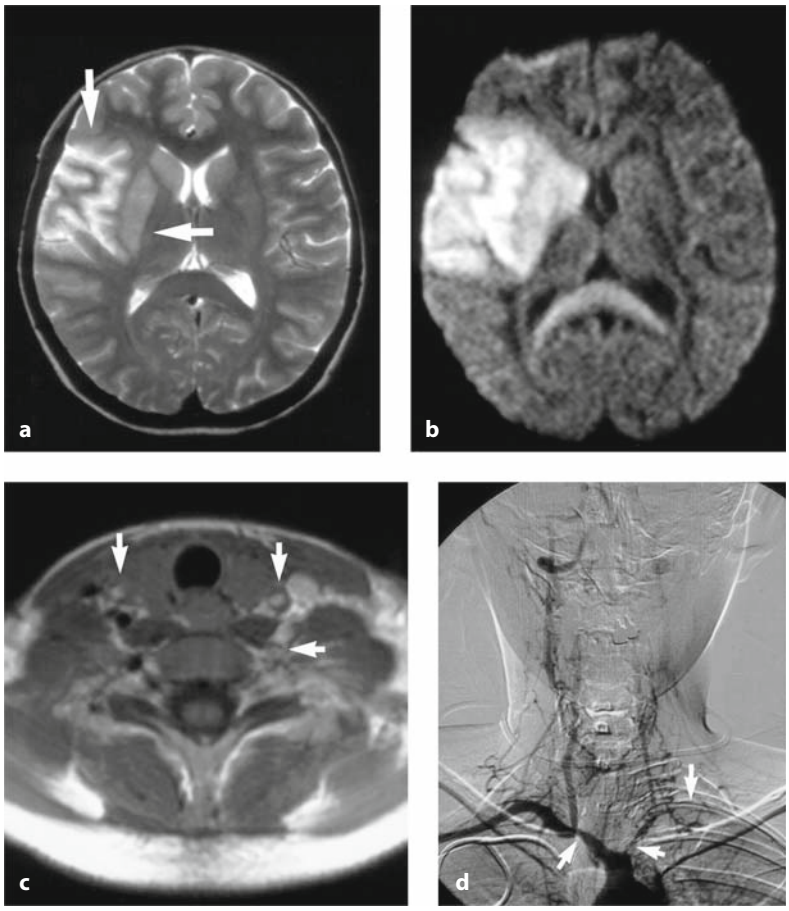

Figure 7.6 a–d

Takayasu's arteritis in an 18-year-old woman with left hemiparesis. **a** T2-weighted image shows a hyperintense lesion in the right basal ganglia and temporal lobe (*arrows*). **b** DW image shows a very high signal lesion, indicating an acute infarct. **c** T1-weighted axial image shows occlusion of internal carotid arteries bilaterally and the left vertebral artery, with thickening of the wall and thrombosis (*arrows*). **d** DSA shows occlusion of both carotid arteries, and stenosis of the brachiocephalic and left subclavian arteries (*arrows*)

7.4.7 Other Small Vessel Vasculitis

The incidence of neurological symptoms in Wegener's granulomatosis varies from 11 to 54%, but cerebral or meningeal involvement is uncommon, occurring in 2-8% of cases (Fig. 7.8) [28]. Involvement of the CNS in other forms of small vessel vasculitis (microscopic polyangitis, Henoch–Schönlein purpura, essential cryoglobulinemia and hypersensitivity vasculitis) is rare. In the case of Henoch–Schönlein purpura, MR imaging can show reversibility of lesions [7].

Figure 7.7 a, b

Churg–Strauss disease in a 65-year-old man with seizures. **a** T2-weighted image shows multiple hyperintense lesions in both corona radiata and right parieto-occipital area, the latter with a hemosiderin rim, representing old hemorrhage (*arrow*). **b** DW image shows a hyperintense lesion (*arrow*) in the left corona radiata, representing an acute infarct. An old hemorrhage shows hypointensity (*arrowhead*) on DW image. MR angiography and DSA revealed no abnormalities (not shown). (From [69])

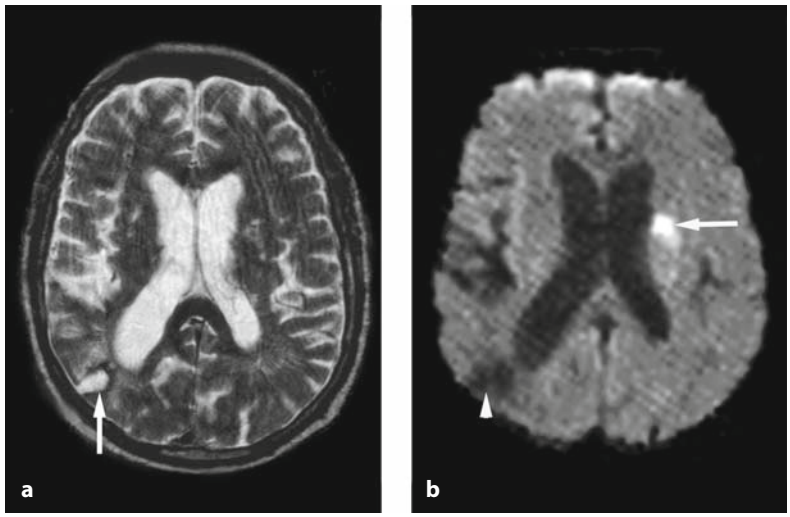

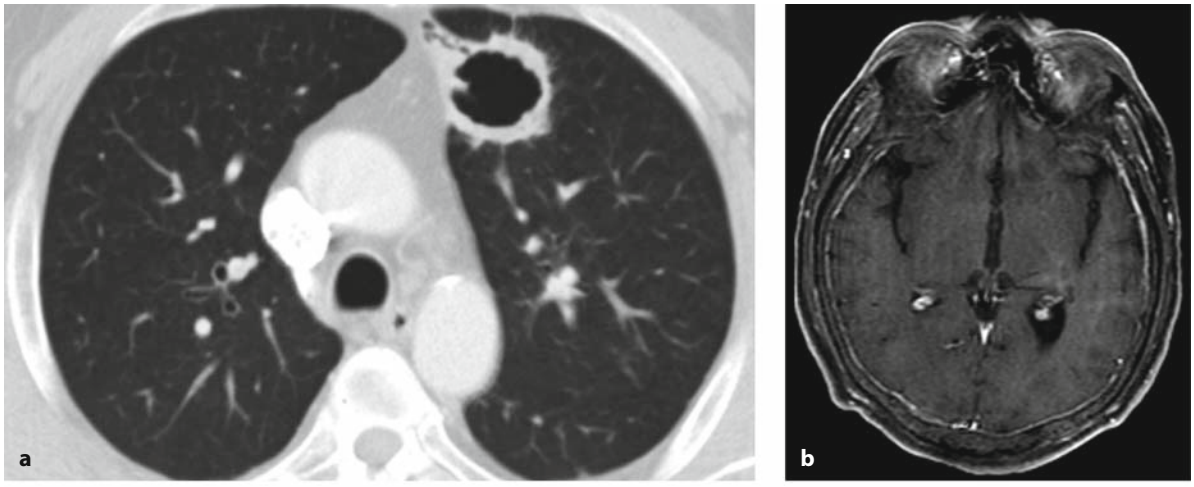

Figure 7.8 a–d

Wegener's granulomatosis in a 50-year-old man. **a** Chest CT shows a cavitary lesion in the left lung. **b** Postcontrast T1-weighted image shows diffuse dural enhancement. **c** DW image shows a hyperintense lesion (*arrow*) in the left temporal lobe, representing an acute infarct. **d** Decreased ADC in the ischemic lesion is noted

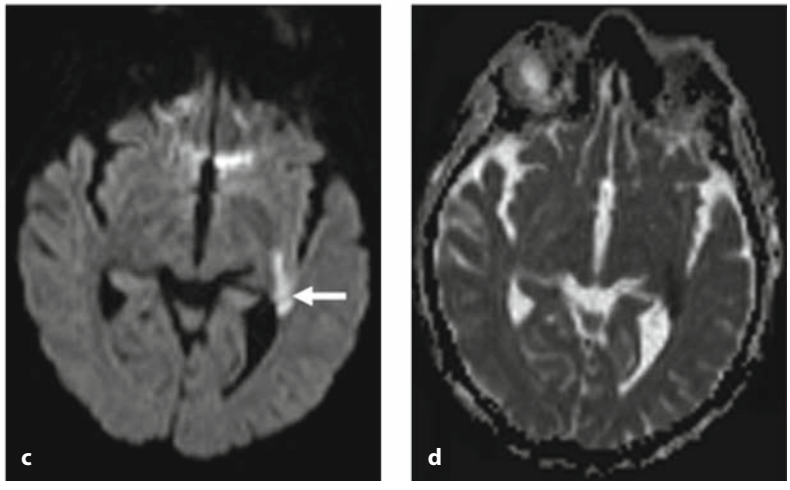

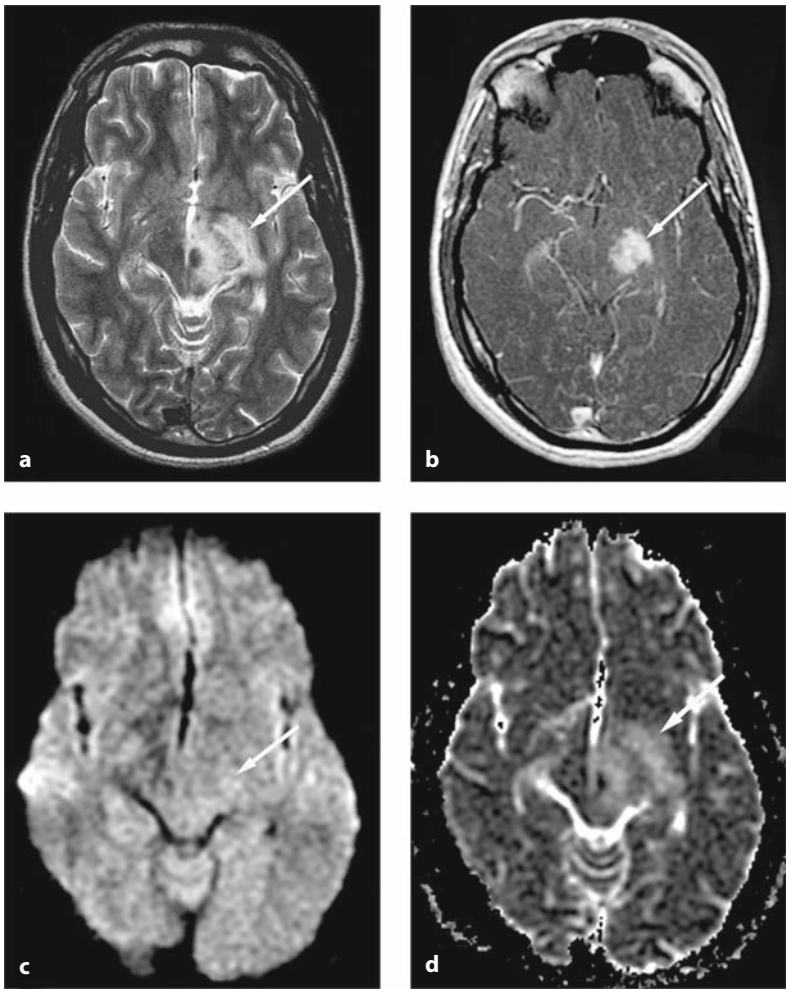

Figure 7.9 a–d

Neuro-Behçet's disease in a 24-year-old man. **a** T2-weighted image shows a hyperintense lesion in the left midbrain extending into the left temporal lobe, with enlargement of the left cerebral peduncle (*arrow*). **b** Gadolinium-enhanced T1-weighted image shows enhancement in this lesion (*arrow*). **c** DW image shows a hyperintense lesion with increased signal intensity in the left cerebral peduncle, probably representing vasogenic edema (*arrow*). **d** ADC map shows increased ADC in this lesion (*arrow*). (From [70])

7.4.8 Collagen Vascular Diseases

Behçet's disease is a multisystem vasculitis of unknown origin. It is most common in Middle Eastern and Mediterranean countries. CNS involvement has been described in 4–49% of cases [6]. The parenchymal distribution of lesions in Behçet's disease, especially at the mesodiencephalic junction (46%) supports small vessel vasculitis involving both the arterial and venous system; mainly venules. Occasionally, these lesions are reversible on MR images that mainly represent vasogenic edema. This is why DW imaging is useful in distinguishing them from infarction (Fig. 7.9). The treatment is usually a combination of cytotoxic agents and steroids. In other types of collagen diseases, such as scleroderma or rheumatoid arthritis, involvement of the CNS is very rare.

7.4.9 Infectious Vasculitis

Infections can cause vasculitis both by direct invasion of the vessel walls and by an immune-mediated response to the pathogens. Bacterial, fungal

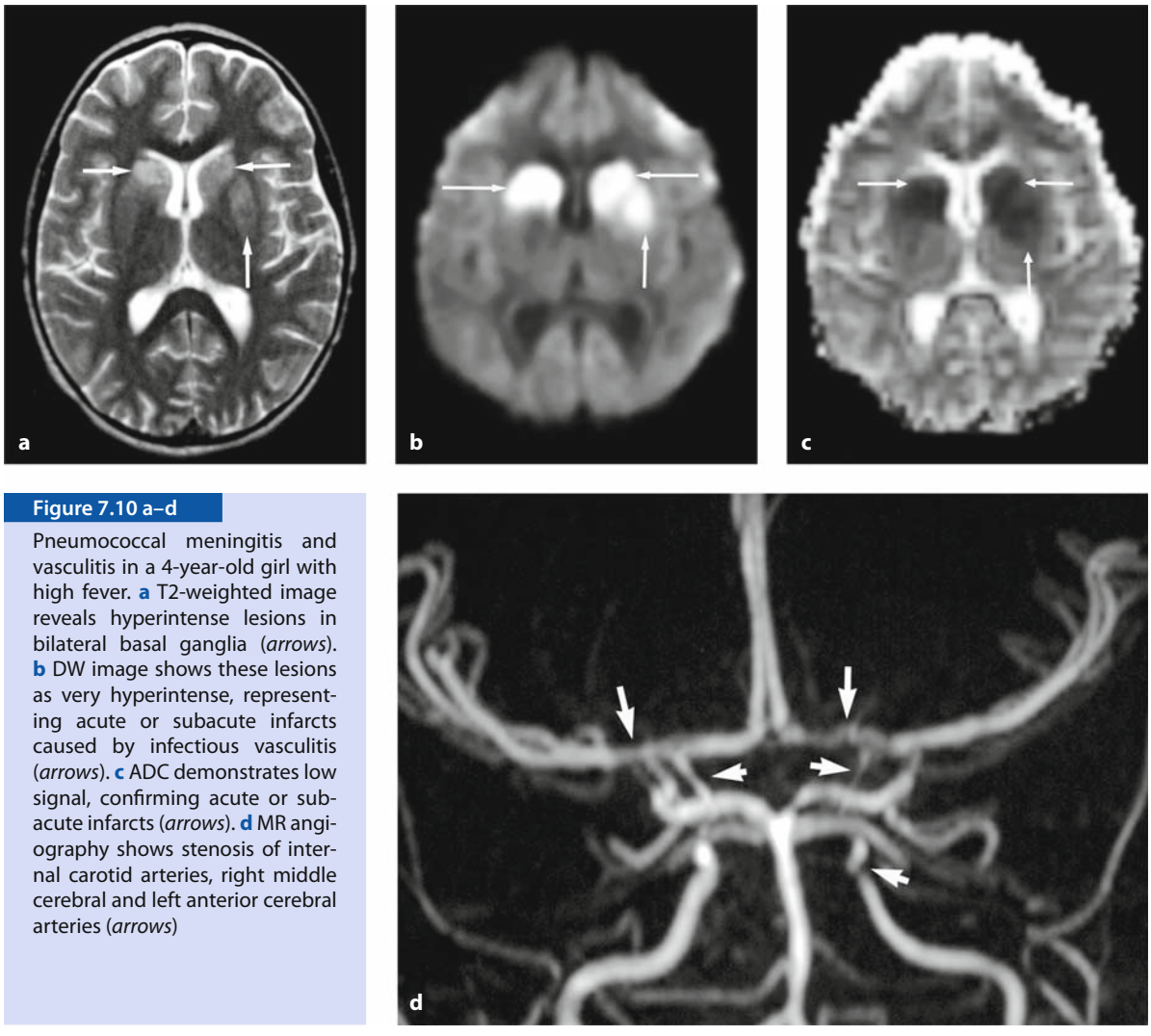

Figure 7.10 a–d

Pneumococcal meningitis and vasculitis in a 4-year-old girl with high fever. **a** T2-weighted image reveals hyperintense lesions in bilateral basal ganglia (*arrows*). **b** DW image shows these lesions as very hyperintense, representing acute or subacute infarcts caused by infectious vasculitis (*arrows*). **c** ADC demonstrates low signal, confirming acute or subacute infarcts (*arrows*). **d** MR angiography shows stenosis of internal carotid arteries, right middle cerebral and left anterior cerebral arteries (*arrows*)

and some viral infections (e.g. herpes virus) result in a vasculitis such a direct involvement of the vessel walls usually results in ischemia with or without subsequent infarction (Fig. 7.10) [2, 29]. Vasculitis with aseptic meningitis is probably related to an immunologic reaction, which can show reversible lesions. Aspergillus infiltrates and destroys the internal elastic lamina of major cerebral arteries, which results in infarction, abscess formation and hemorrhage [30] (Fig. 7.11). Infection of the infarcted tissue may be aggressive, and direct extension into the surrounding brain may progress quickly.

7.4.10 Drug-Induced Vasculitis, Including Illicit Drugs

Some drugs, such as chemotherapeutic agents (e.g. sulfonamide, thiouracil) and illicit drugs (e.g. cocaine), can cause vasculitis [31]. Stroke can occur soon after administration of illicit drugs by an intravenous, oral or nasal route. Cocaine, heroin, amphetamine and other sympathomimetic drugs are most commonly implicated. The diagnosis of "vasculitis" depends on the pathological findings, not on the angiographic findings, which are usually non-specific

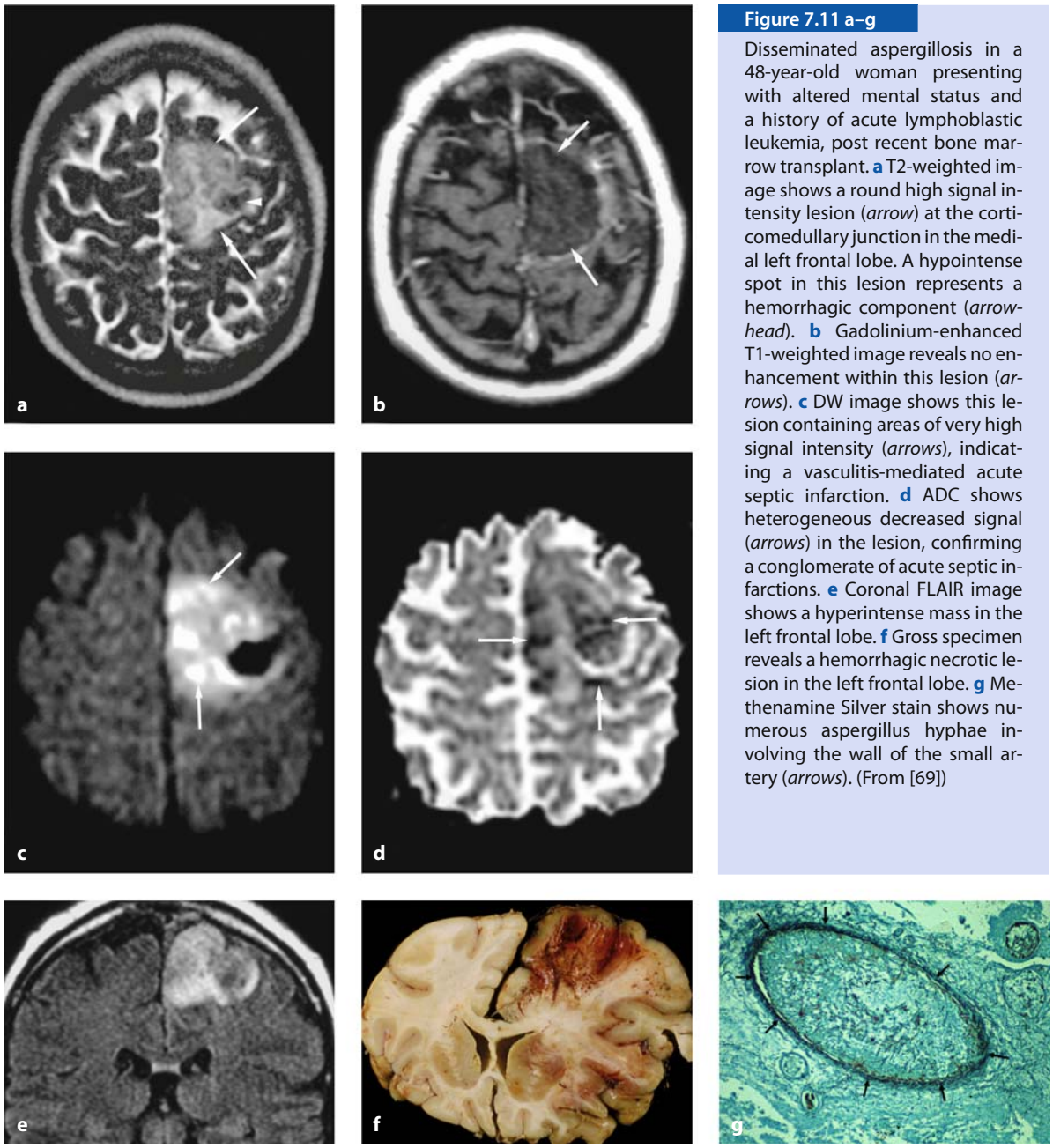

Figure 7.11 a–g

Disseminated aspergillosis in a 48-year-old woman presenting with altered mental status and a history of acute lymphoblastic leukemia, post recent bone marrow transplant. **a** T2-weighted image shows a round high signal intensity lesion (*arrow*) at the corticomedullary junction in the medial left frontal lobe. A hypointense spot in this lesion represents a hemorrhagic component (*arrowhead*). **b** Gadolinium-enhanced T1-weighted image reveals no enhancement within this lesion (*arrows*). **c** DW image shows this lesion containing areas of very high signal intensity (*arrows*), indicating a vasculitis-mediated acute septic infarction. **d** ADC shows heterogeneous decreased signal (*arrows*) in the lesion, confirming a conglomerate of acute septic infarctions. **e** Coronal FLAIR image shows a hyperintense mass in the left frontal lobe. **f** Gross specimen reveals a hemorrhagic necrotic lesion in the left frontal lobe. **g** Methenamine Silver stain shows numerous aspergillus hyphae involving the wall of the small artery (*arrows*). (From [69])

and may simply indicate vasospasm induced by these drugs.

Cocaine use has emerged as an important cause of cerebrovascular events in young adults [32]. Vasculitic changes can be present on angiography, but the significance of these changes has been debated. However, elevated sedimentation rate and biopsy changes of vasculitis have been documented. MR angiography may reveal irregularity of the intracerebral vessels and DW imaging is useful for the detection of acute ischemic changes (Fig. 7.12).

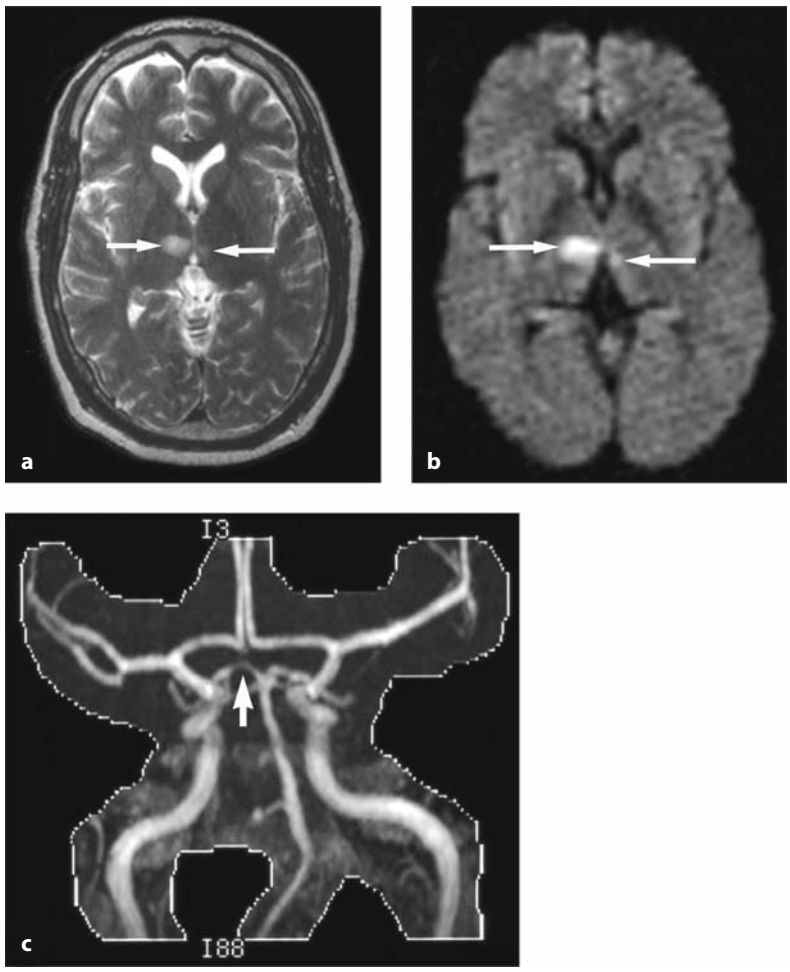

Figure 7.12 a–c

Cocaine-induced vasculopathy in a 41-year-old man with dysarthria. **a** T2-weighted image shows bilateral hyperintense lesions in medial thalami (*arrows*). **b** DW image shows the lesion in the right thalamus as hyperintense, indicating an acute infarct. **c** MR angiography shows stenosis of the right posterior cerebral artery (*arrow*). Biopsy was not performed and therefore the term cocaine-induced vasculopathy was used. (From [69])

7.5 Vasculopathy of the CNS

Vasculopathy is caused by a wide variety of underlying conditions such as degenerative, metabolic, inflammatory, embolic, coagulative and functional disorders [1]. This presentation focuses on vasculopathies that mimic vasculitis, but have no inflammation in the wall of the blood vessel (Fig. 7.13).

7.5.1 Systemic Lupus Erythematosus

Involvement of the CNS occurs in 14–75% of patients with systemic lupus erythematosus (SLE) [4]. Pathologically, microinfarcts and small vessel vasculopathy are the most common. Vasculopathy affects predominantly the arterioles and capillaries, resulting in vessel tortuosity, vascular hyalinization, endothelial proliferation and perivascular inflammation or gliosis. True vasculitis is very rare (0–7%). This vasculopathy may be related to both acute inflammation and ischemia [33]. In recent reports, the mechanism of the SLE vasculopathy has been attributed to intravascular activation of a complement, which leads to adhesion between neutrophils and/or platelets and endothelium, resulting in leukothrombosis in the microvasculature (Shwartzman phenomenon) [34].

In this vasculopathy, despite widespread microvascular occlusions, parenchymal damage is minimal and potentially reversible. Sibbit et al. reported that up to 38% of CNS lesions in SLE were potentially reversible on MR imaging [35]. MR angiography and conventional angiography may provide additional information concerning vascular abnormalities. DW imaging shows primarily two patterns of parenchymal

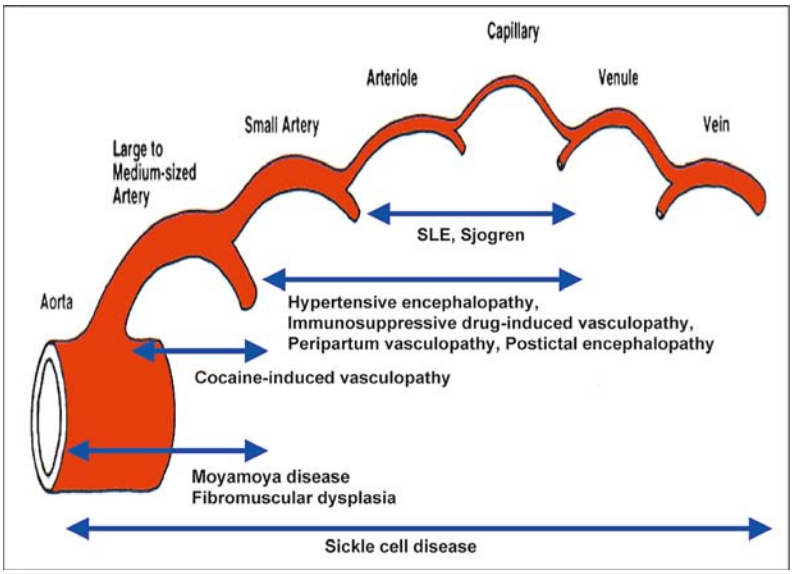

Figure 7.13

Spectrum of CNS vasculopathy. (Modified from [10])

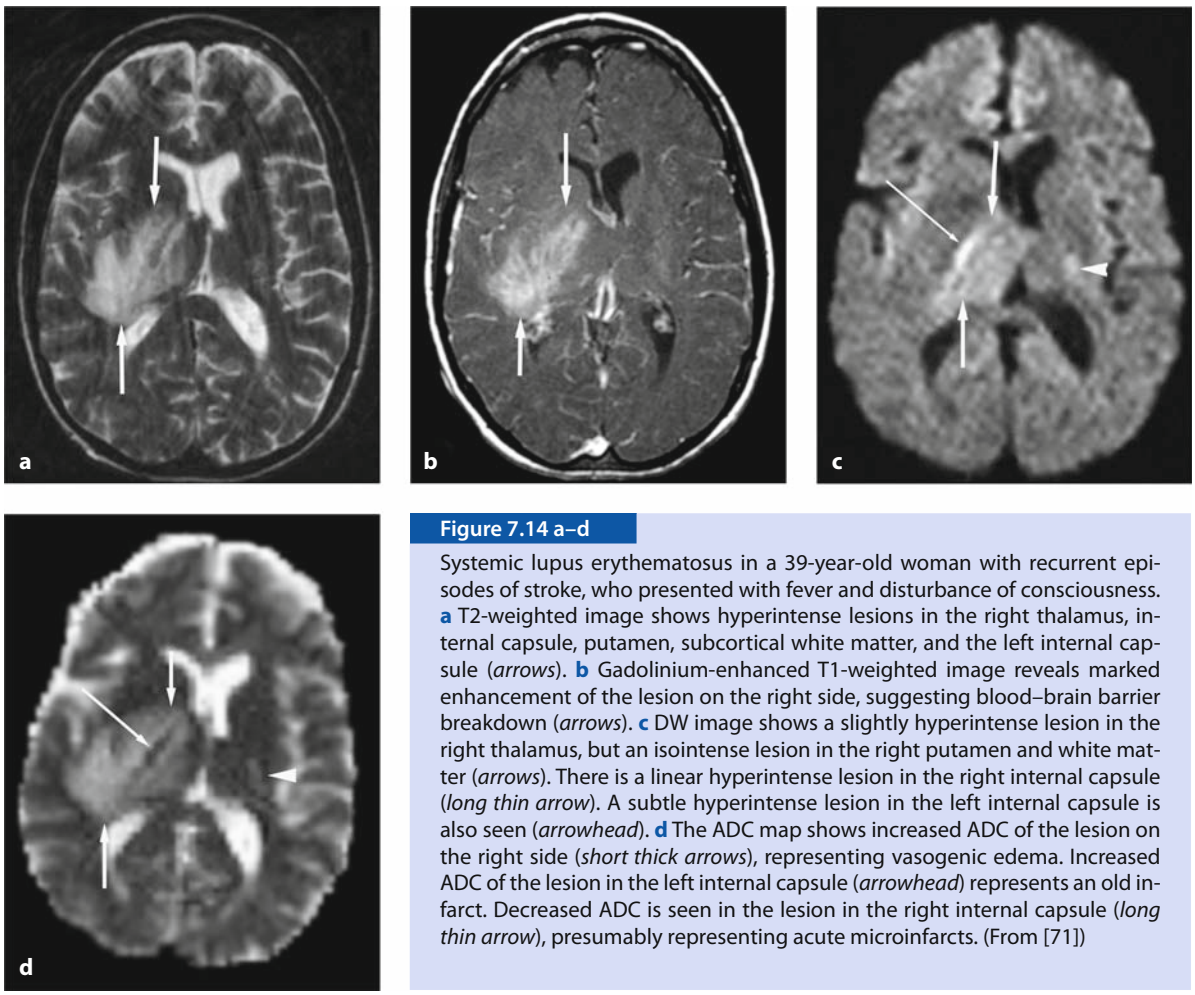

Figure 7.14 a–d

Systemic lupus erythematosus in a 39-year-old woman with recurrent episodes of stroke, who presented with fever and disturbance of consciousness. **a** T2-weighted image shows hyperintense lesions in the right thalamus, internal capsule, putamen, subcortical white matter, and the left internal capsule (*arrows*). **b** Gadolinium-enhanced T1-weighted image reveals marked enhancement of the lesion on the right side, suggesting blood–brain barrier breakdown (*arrows*). **c** DW image shows a slightly hyperintense lesion in the right thalamus, but an isointense lesion in the right putamen and white matter (*arrows*). There is a linear hyperintense lesion in the right internal capsule (*long thin arrow*). A subtle hyperintense lesion in the left internal capsule is also seen (*arrowhead*). **d** The ADC map shows increased ADC of the lesion on the right side (*short thick arrows*), representing vasogenic edema. Increased ADC of the lesion in the left internal capsule (*arrowhead*) represents an old infarct. Decreased ADC is seen in the lesion in the right internal capsule (*long thin arrow*), presumably representing acute microinfarcts. (From [71])

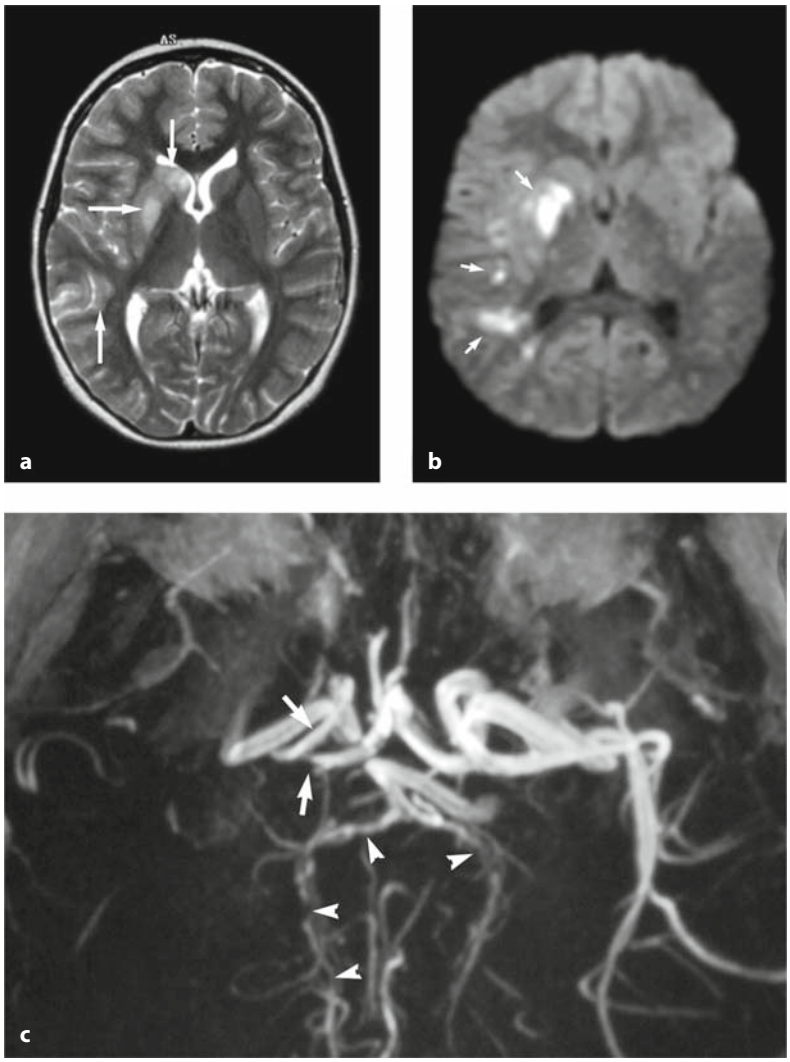

Figure 7.15 a–c

Probable Moyamoya disease in a 7-year-old girl with left hemiparesis. **a** T2-weighted image shows lesions with mildly increased signal in the right basal ganglia and parieto-occipital cortex (*arrows*). **b** DW image clearly shows these lesions as high signal intensity, representing acute infarcts (*arrows*). **c** MR angiography shows occlusion of the right middle cerebral artery, and stenosis of the right internal carotid artery (*arrows*) and bilateral posterior cerebral arteries (*arrowheads*)

lesions with acute or subacute CNS symptoms: one is an acute or subacute infarction, and the other is vasogenic edema with or without microinfarcts (Fig. 7.14) [5]. CNS involvement in SLE is also due to associated uremia, hypertension, infection, Libman–Sacks endocarditis, and corticosteroid or immunosuppressive therapy.

7.5.2 Moyamoya Disease

Moyamoya disease is a rare, non-inflammatory vasculopathy of the intracranial vessels of unknown cause, which is found predominantly in East Asia. It has a bimodal age presentation, the first in childhood (first decade) and the second in adults (fourth decade). Endothelial thickening, the main pathological finding, leads to chronic progressive arterial stenosis of the circle of Willis and eventually to infarctions. In the adult form, the presenting symptom is often intracranial hemorrhage, usually intraparenchymal. The stenosis or occlusion of the supraclinoid portion of the internal carotid artery should be bilateral, but unilateral lesions can be included as "probable" cases of Moyamoya disease. DW imaging is useful in evaluating cerebral ischemia in Moyamoya disease (Fig. 7.15) [36].

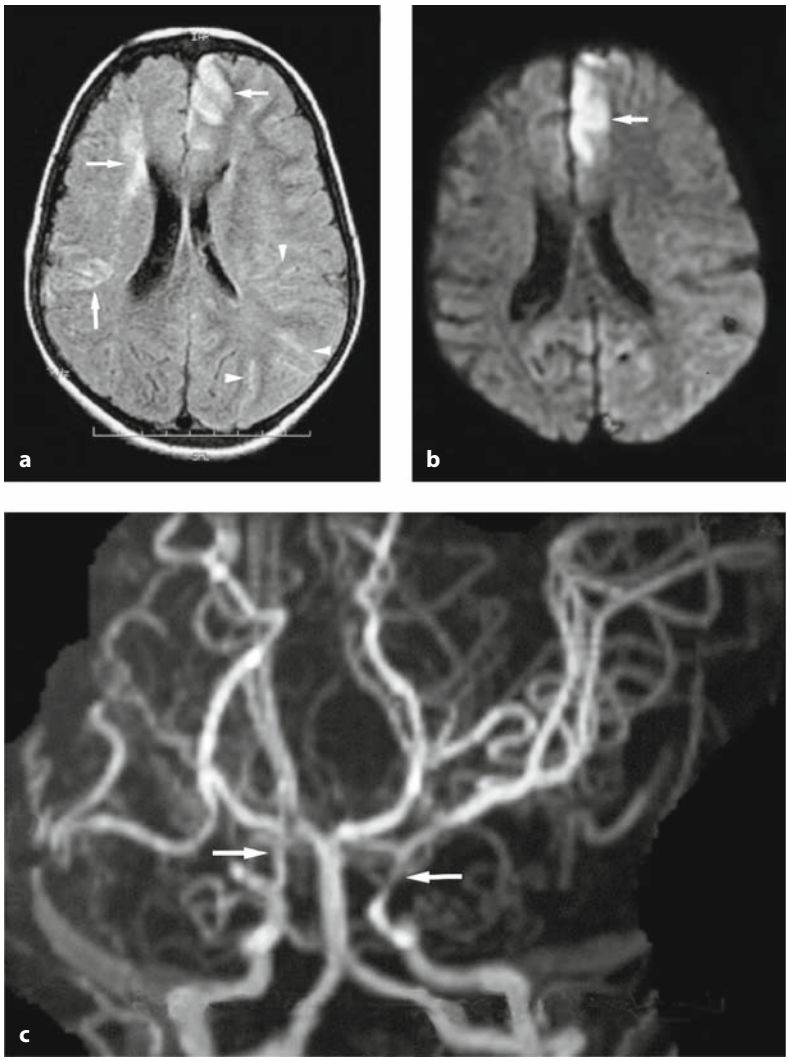

Figure 7.16 a–c

Sickle cell disease. 3-year-old boy presented with right side weakness as a recurrent stroke. He has been non-compliant to transfusion therapy. **a** FLAIR image shows multiple hyperintense lesions in the left frontal and right frontotemporal regions (*arrows*). FLAIR image also shows multiple curvilinear hyperintensities along the peripheral vessels that probably reflects the slow flow in the collateral circulation (*arrowheads*). **b** DW image shows the left frontal lesion as very hyperintense representing an acute infarct (*arrow*). **c** MR angiography shows bilateral stenoses of internal carotid, and middle and anterior cerebral arteries (*arrows*). (From [38])

7.5.3 Sickle Cell Disease

About 5–8% of patients with sickle cell disease develop symptomatic cerebrovascular disease. The risk of stroke is greatest during thrombotic crises and during the first 15 years of life [37]. Approximately 75% of strokes are the result of an occlusion of the large arteries at the base of the brain. Cortical and white matter watershed ischemia is common. This vasculopathy can be similar to Moyamoya disease. Occlusion of small vessel branches, which leads to ischemia of deep white matter, accounts for 25% of the cerebral infarctions in sickle cell disease. These lesions are thought to be related to peripheral vaso-occlusive events in which the arteriole or postcapillary venule is the major site of sickle cell adhesion [37]. If progression is associated with neurologic dysfunction, strong consideration should be given to place the patient on a long-term transfusion program. DW imaging is useful in detecting active ischemic changes and in differentiating them from chronic ischemic changes (Fig. 7.16) [38].

7.5.4 Posterior Reversible Encephalopathy Syndrome

Posterior reversible encephalopathy syndrome is a remarkably heterogeneous group of disorders, related to hypertensive encephalopathy, severe preeclampsia/eclampsia, immunosuppressive drug or interferon neurotoxicity, uremia and thrombotic thrombocytopenic purpura [39]. The clinical symptoms are headache, altered mental status, seizures and visual loss. Posterior reversible encephalopathy syndrome is due to dysfunction of a cerebrovascular autoregulatory system, and a vasculopathy of small vessels, the arterioles. Brain perfusion is maintained by the autoregulatory system of the small arteries and arterioles that have myogenic and neurogenic components. Since the vertebrobasilar system and the posterior cerebral arteries are sparsely innervated by sympathetic nerves, the occipital lobes and other posterior brain regions are more susceptible to a breakthrough of the autoregulation in case of a sudden elevation of the systemic blood pressure. Endothelial damage, which can attenuate the myogenic response of the autoregulatory system, is hypothesized to be the cause of the posterior reversible encephalopathy syndrome.

Other names for the posterior reversible encephalopathy syndrome are reversible posterior leukoencephalopathy syndrome, or posterior leuko-encephalopathy syndrome [40, 41]. The lesion can also involve the cerebral cortex and another name for posterior reversible encephalopathy syndrome is occipital parietal encephalopathy [42]. Similar lesions can also be seen in the frontal lobes, basal ganglia, brain stem and cerebellum [43-45]. In addition, the posterior reversible encephalopathy syndrome may not be entirely reversible, as infarction and hemorrhage may develop.

7.5.5 Hypertensive Encephalopathy

The primary cause of hypertensive encephalopathy is thought to be fluid extravasation through the interstitium, resulting from overdistension of distal small cerebral vessels (breakthrough of autoregulation) causing vasogenic edema [46]. Ischemic processes can be triggered by the vasospasm of the cerebral arteriole in response to a severe increase in blood pressure (overregulation), which often results in infarctions. Hypertensive encephalopathy is a clinical syndrome in which morphological and clinical phenomena are not correlated to each other. However, plasma proteins, including fibrin, are deposited in the walls of small arteries (hypertensive vasculopathy). This process leads to destruction of smooth muscle cells (fibrinoid necrosis).

The most common affected area is the bilateral parieto-occipital subcortical white matter. However, these lesions can occur in the gray matter as well and also involve the frontal lobes, basal ganglia, thalamus, cerebellum and brain stem. They are potentially reversible; however, if left untreated, permanent neurologic deficits or even death may occur as a result of ensuing cerebral infarction or hemorrhage. The prognosis probably depends on the extent of cytotoxic edema, which may be seen in severe cases. DW imaging can distinguish irreversible ischemic changes from reversible conditions with vasogenic edema alone (Fig. 7.17) [46].

7.5.6 Preeclampsia/Eclampsia

Preeclampsia is characterized by hypertension, abnormal peripheral edema, and proteinuria that can progress to eclampsia, which also involves seizures. Although CNS changes in severe preeclampsia and eclampsia represent a form of hypertensive encephalopathy, they also occur in normotensive individuals. The precise pathogenesis remains unclear. However, endothelial dysfunction due to circulating endothelial toxins or antibodies against the endothelium can be the primary cause [47]. MR findings in patients with severe preeclampsia/eclampsia are often similar to those with hypertensive encephalopathy. However, intracranial hemorrhage and infarction (Fig. 7.18) are common [48]. Bilateral external capsule or basal ganglia lesions are also common [49]. DW imaging can discriminate a cytotoxic edema from vasogenic edema [50].

Hemolysis, elevated liver enzymes and low platelets (HELLP syndrome) is a thrombotic microangiopathic vasculopathy in pregnancy. Fatalities are attributable to intracranial hemorrhage, which may occur either in isolation or as part of the HELLP syndrome. The DW imaging findings are similar to those in eclampsia/preeclampsia.

7.5.7 Immunosuppressive Drug-Induced Vasculopathy

Cyclosporine, tacrolimus (FK506) and interferon-α are effective immunosuppressive agents for the treatment of organ transplant rejection. Previous theories regarding the mechanism of neurotoxicity include neuropeptide-mediated ischemia and high-pressure failure

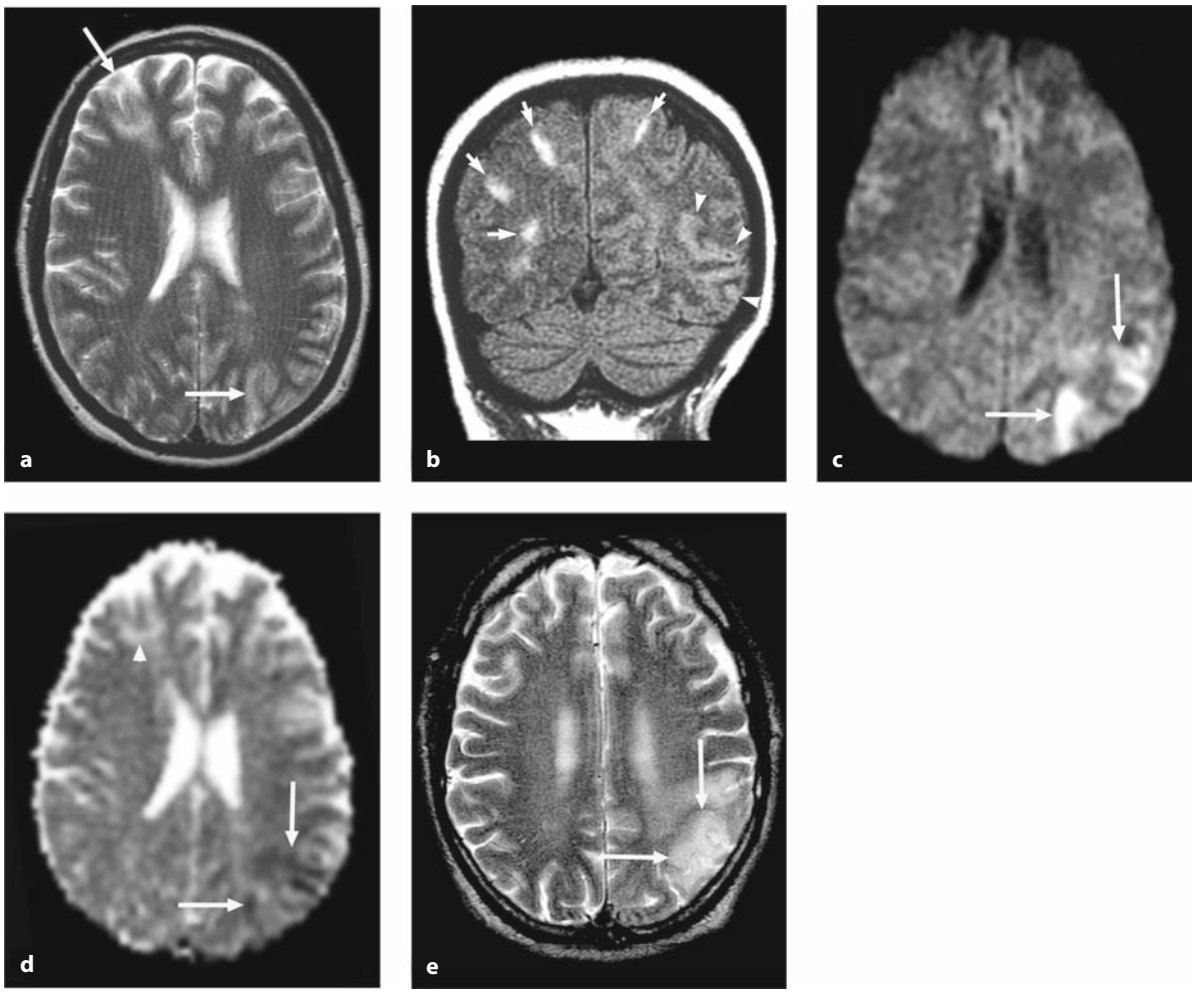

Figure 7.17 a–e

Hypertensive encephalopathy in a 41-year-old woman with hypertensive crisis with pheochromocytoma. **a** T2-weighted image shows hyperintense lesions in the right frontal lobe and left temporo-parieto-occipital area (*arrows*). **b** Coronal FLAIR image shows multiple hyperintense lesions in the subcortical white matter (*arrows*) and slightly hyperintense lesions (*arrowheads*) in the left parieto-occipital area. **c** DW image shows the lesion in the left side as hyperintense (*arrows*) and the subcortical lesions as isointense. **d** ADC map reveals decreased ADC of the lesion on the left side, representing acute infarcts (*arrows*). Subcortical lesions show slightly increased or normal ADC, representing vasogenic edema (*arrowhead*). **e** Three-month follow-up MR imaging shows hyperintense lesions in the left parieto-occipital area, representing old infarcts (*arrows*). The lesion in the right frontal lobe is not detected. (From [69])

of cerebral autoregulation [51]. Neurotoxicity usually coexists with hypertensive crisis; however, it also occurs in normotensive individuals. These drugs have profound effects directly on the endothelium and cause release of potent vasoconstrictors such as endothelin. Disruption of the blood–brain barrier with possible focal loss of vascular autoregulation causes extravasation of fluid, which leads to vasogenic edema.

Magnetic resonance imaging shows signal changes within the cortex and subcortical white matter in the occipital, posterior temporal, parietal and frontal lobes (Fig. 7.19). Non-transplant patients or those with total body irradiation develop white matter le-

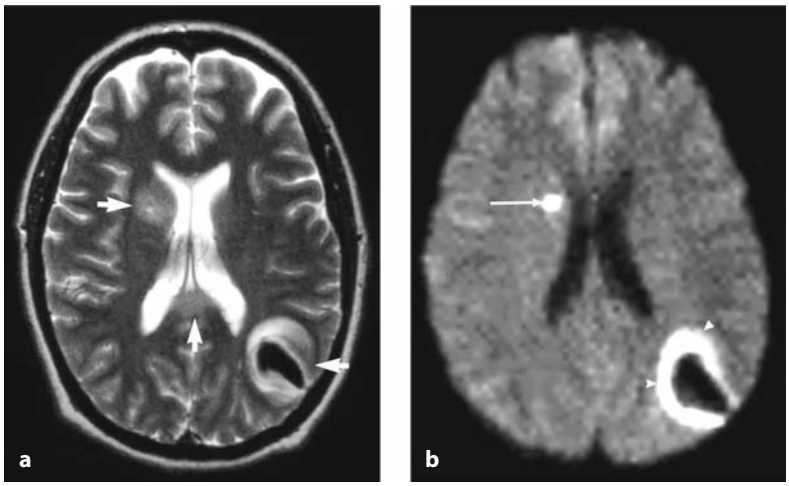

Figure 7.18 a, b

Eclampsia in a 30-year-old woman with seizures. **a** T2-weighted image shows high signal intensity lesions in the right corona radiata, posterior corpus callosum and left parieto-occipital region (*arrows*). The lesion in the left parieto-occipital region has a central, very low signal intensity, representing hemorrhage. **b** On DW image, a small infarct in the right corona radiata (*arrow*) and a hemorrhagic infarct in the left parieto-occipital region (*arrowheads*) are shown as hyperintense associated with decreased ADC (not shown). The lesion in the posterior corpus callosum represents vasogenic edema

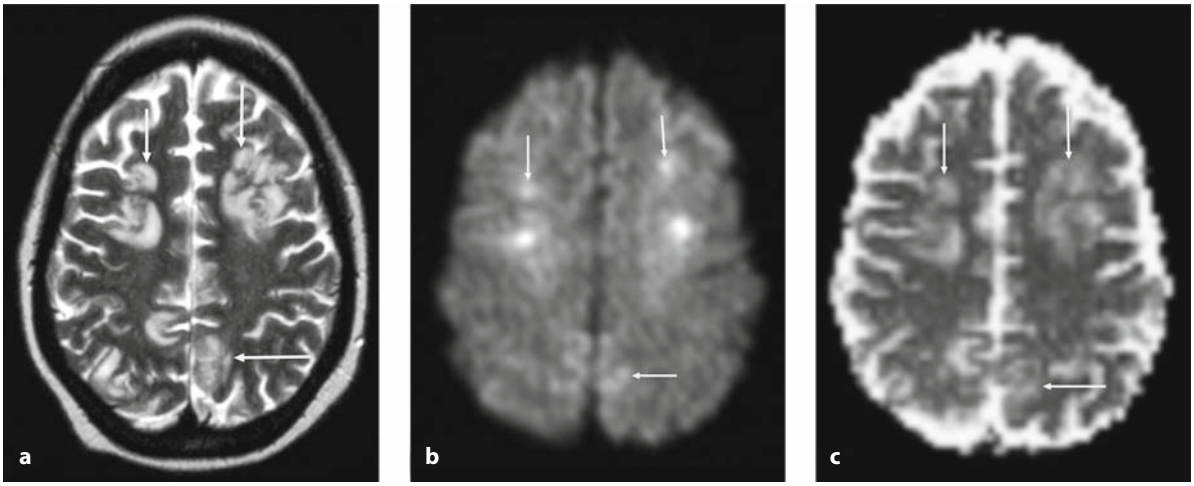

Figure 7.19 a–c

Tacrolimus neurotoxicity in a 42-year old woman with confusion after liver transplantation. **a** T2-weighted image shows high signal intensity lesions in the bilateral fronto-parieto-occipital subcortical white matter (*arrows*). **b** On DW image, these lesions show slightly hyperintense or isointense signal intensity (*arrows*). **c** ADC map shows increased ADC, which with hyperintense lesions (*arrows*) on DW image indicates T2 shine-through effect. These lesions had resolved on follow-up MR imaging (not shown)

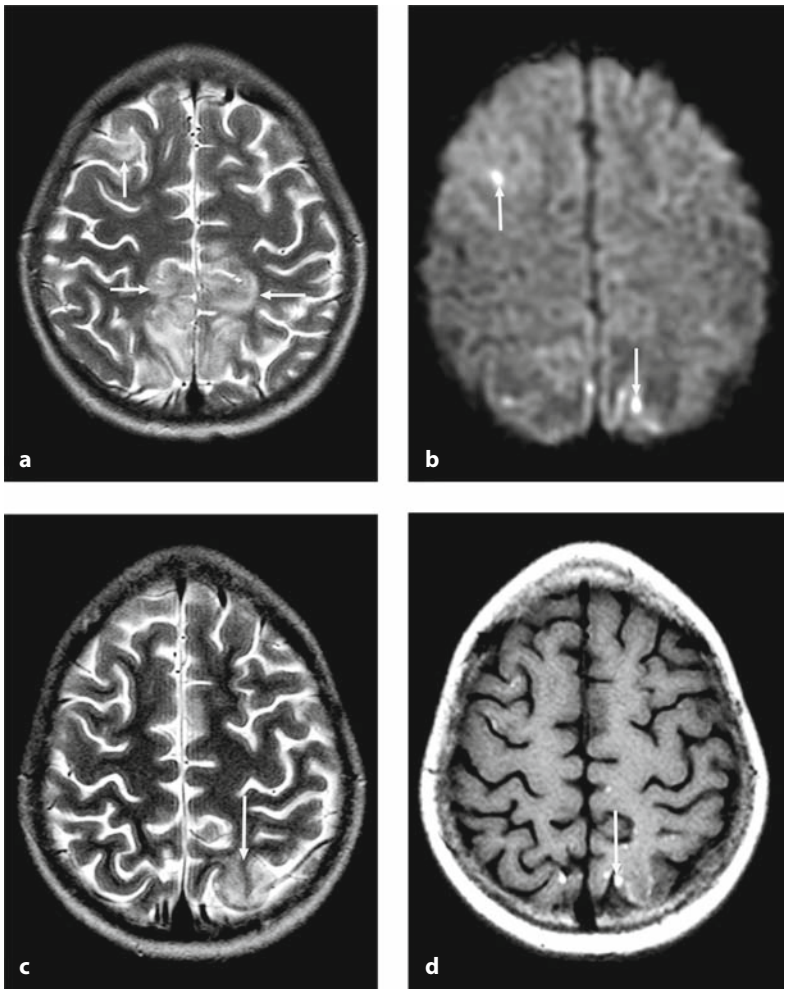

Figure 7.20 a–d

Uremic encephalopathy in a 10-year-old girl with seizure. She improved after dialysis. **a** T2-weighted image shows hyperintense lesions in bilateral parietal and right frontal subcortical white matter and cortex (*arrows*). **b** DW image reveals punctate foci of high signal within T2 high signal area (*arrow*) in the right frontal lobe and an additional bright lesion in the left parietal lobe. **c** Follow-up T2-weighted image obtained 5 days later shows incomplete resolution of left parietal high signal area (*arrow*). **d** T1-weighted image reveals punctate foci of high signal corresponding to a high signal area on the initial DW image (*arrow*). (From [53])

sions, whereas those conditioned with chemotherapy develop mixed cortical and white matter lesions [52].

7.5.8 Uremic Encephalopathy and Hemolytic Uremic Syndrome

Uremic encephalopathy is the name given to a brain syndrome that occurs in patients with renal failure. The pathogenesis is unknown, but it has been hypothesized that it may be caused by various toxins associated with uremia (elevated parathyroid hormone level, hypercalcemia, and other metabolic abnormalities) [53]. MR imaging usually shows reversible bilateral symmetric white matter lesions. The lesions can also involve the basal ganglia or cortex. DW imaging usually shows iso- or slightly hyperintense lesions with increased ADC, mainly representing vasogenic edema (Fig. 7.20). Follow-up MR imaging can show cortical laminar necrosis on T1-weighted images.

Hemolytic uremic syndrome is defined as a multiorgan disease characterized by the triad of microangiopathic hemolytic anemia, thrombocytopenia and uremia. CNS complications are commonly seen (20–50%) [54]. Hemolytic uremic syndrome caused by O-157 *Escherichia coli* enterocolitis can potentially result in fatal CNS complications in infants and children. MR imaging sometimes shows irreversible lesions in the basal ganglia or cortex, representing infarction or cortical laminar necrosis. DW imaging can show these lesions as hyperintense with decreased ADC (Fig. 7.21).

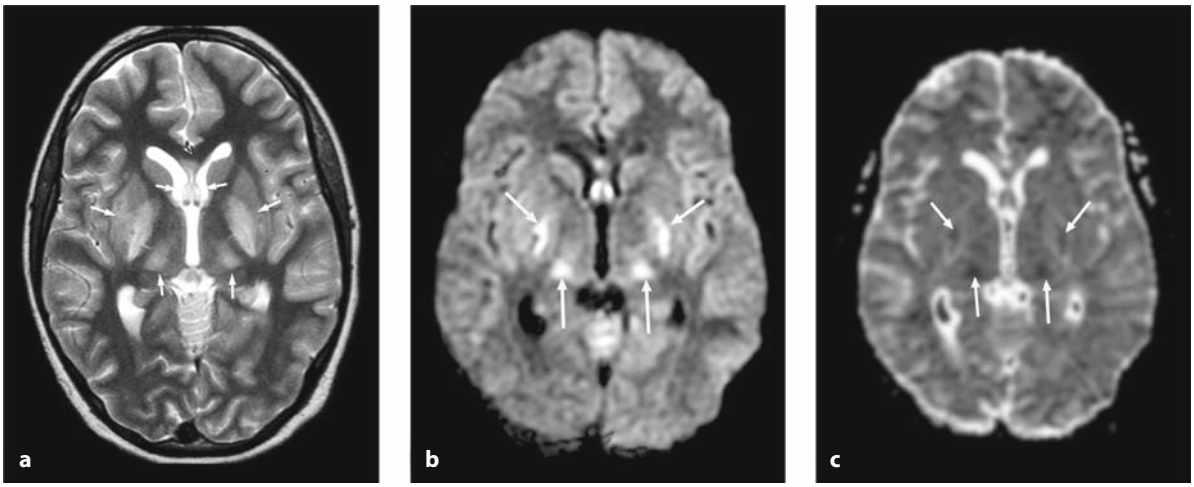

Figure 7.21 a–c

Hemolytic uremic syndrome in a 12-year-old girl with bloody diarrhea. **a** T2-weighted image shows high signal intensity lesions in the bilateral basal ganglia, thalami and fornices (*arrows*). **b** DW image shows these lesions as hyperintense (*arrows*). **c** ADC map shows these lesions as decreased ADC (*arrows*)

7.5.9 Thrombotic Thrombocytopenic Purpura

Thrombotic thrombocytopenic purpura is a multisystem vasculopathy characterized by microangiopathic hemolytic anemia, thrombocytopenia, renal involvement, fluctuating neurologic manifestations and fever [55]. Neuropathology shows hyaline thrombosis and occlusion of capillaries and arterioles without surrounding inflammatory reaction, which results in infarcts and petechial hemorrhages. MR findings are variable, ranging from punctate white matter lesions to posterior reversible encephalopathy syndrome, multifocal gray matter edema, infarction and hemorrhage. DW imaging can differentiate between these lesions (Fig. 7.22), which is important since some of the lesions seen on T2-weighted images may disappear following treatment with plasma exchange [56].

7.5.10 Cerebral Amyloid Angiopathy

Cerebral amyloid angiopathy is characterized by deposition of homogeneous eosinophilic material in the media and adventitia of arterioles and small and medium-sized vessels of the cortex, subcortex, and leptomeninges [57]. The usual neurologic presentation includes spontaneous hemorrhage, transient ischemic attack-like symptoms, and dementia. Up to 90% of elderly patients with Alzheimer disease have changes of amyloid angiopathy at autopsy. Histologically, β-amyloid deposits stained with

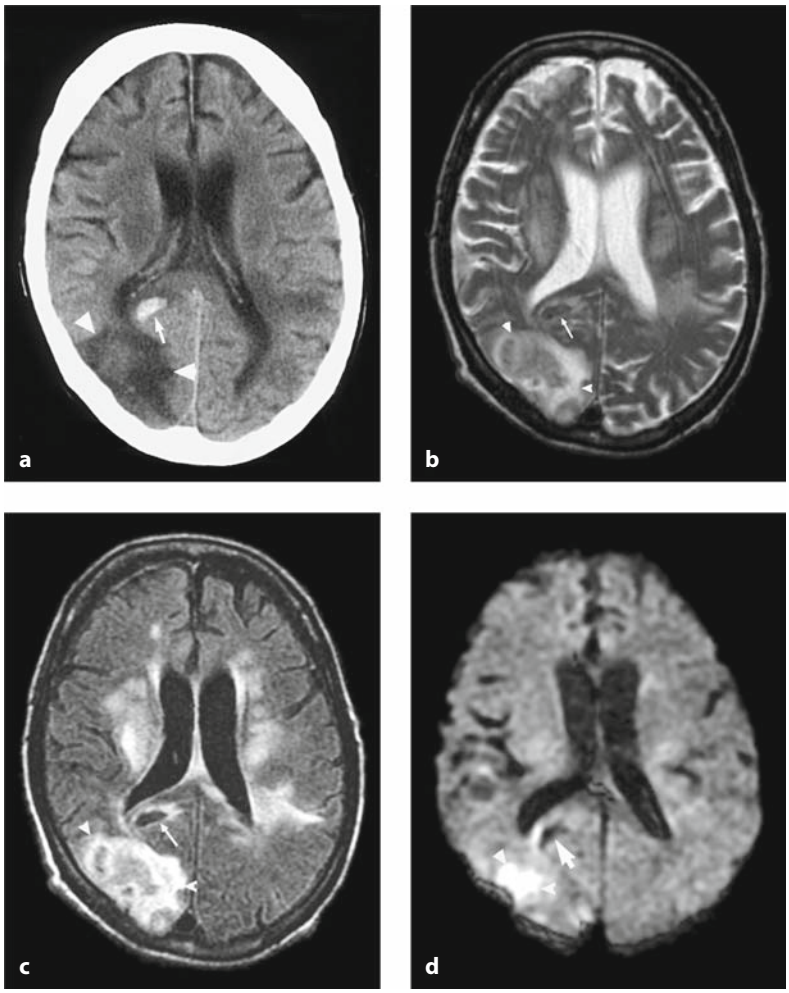

Figure 7.22 a–d

Thrombotic thrombocytopenic purpura in a 53-year-old woman with altered mental status and seizures. **a** Computed tomography shows a hemorrhage in the right parieto-occipital area (*arrow*) and a wedged-shaped area of low density more peripherally in the right occipito-parietal area (*arrowheads*). **b** T2-weighted and **c** FLAIR images show corresponding hyperintense lesions in the deep white matter and right occipito-parietal area (*arrowheads*). Hemorrhage is seen as a hypointense lesion (*arrow*). **d** On DW image, deep white matter lesions are isointense, mainly representing vasogenic edema, while a cortical lesion in the right occipito-parietal area is hyperintense, representing acute infarction (*arrowheads*). Hemorrhage is hypointense with a hyperintense rim (*arrow*)

Congo red show classic yellow-green birefringence under polarized light.

Gradient echo T2*-weighted imaging is sensitive for detecting microangiopathy-related microbleeds, which are not often detected on T2-weighted fast spin-echo images. Susceptibility-weighted imaging is the most sensitive for the detection of microbleeds [58] (Fig. 7.23). DW images and the b0 image can show such microbleeds as low signal intensity spots.

Two imaging patterns of leukoencephalopathy in association with amyloid angiopathy have been reported in the literature [57, 59-61]: (1) chronic ischemic change pattern in the white matter, and (2) white matter edema pattern with subacute cognitive decline. In the latter pattern, perivascular inflamma-

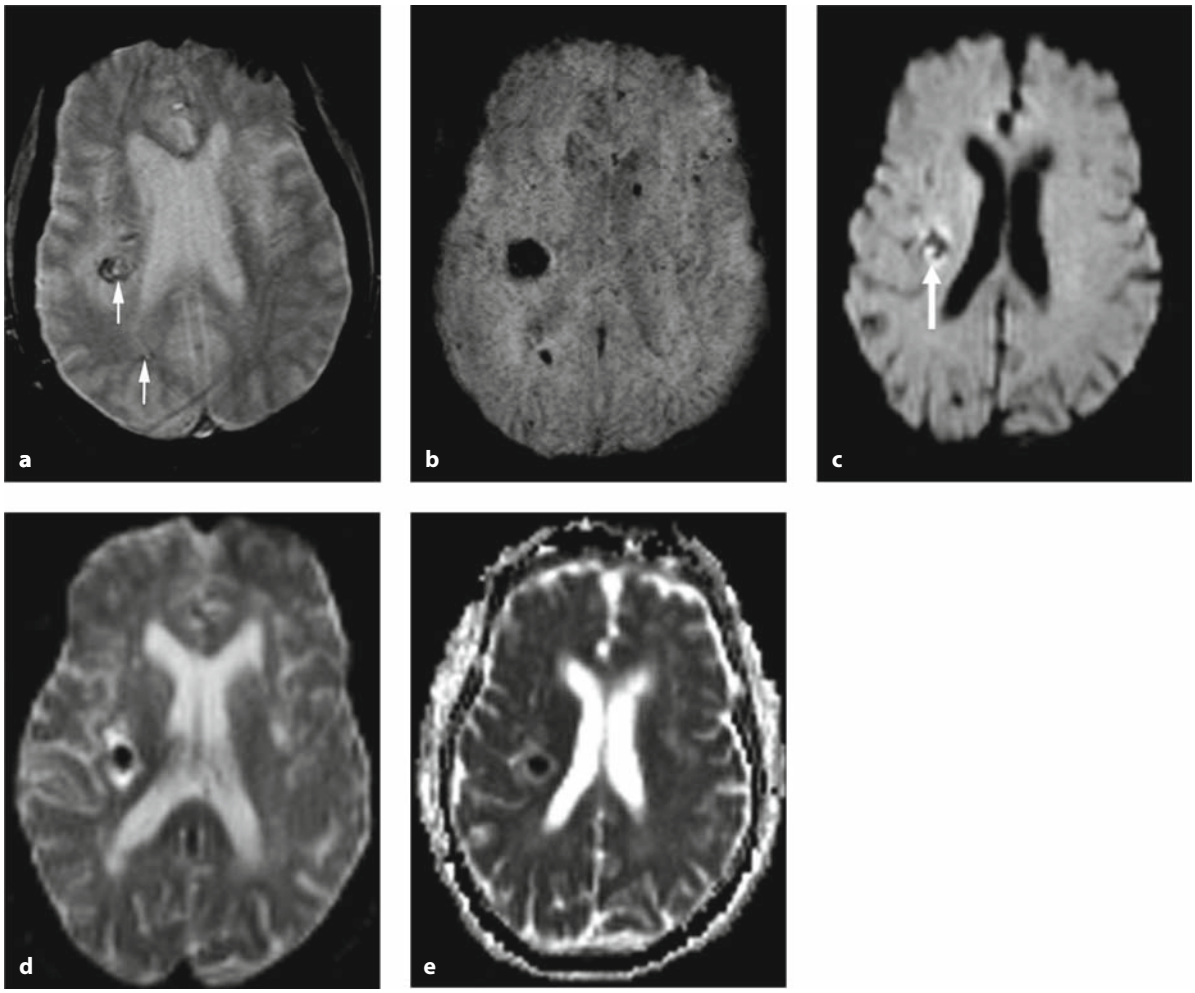

Figure 7.23 a–e

Cerebral amyloid angiopathy in a 68-year-old woman (autopsy proven). **a** Gradient echo T2*-weighted image shows low signal intensity lesions representing microbleeds in the right temporo-parietal white matter (*arrows*). **b** Susceptibility-weighted image demonstrates numerous low signal spots in both hemispheres. Susceptibility-weighted image is more sensitive for detecting microbleeds than gradient echo T2*-weighted image. **c, d** DW image (**c**) and b0 image (**d**) show the microbleed in the right temporo-parietal white matter as a hypointensity spot (*arrow*). The detection of the microhemorrhage is less conspicuous than on the T2* and susceptibility-weighted image. **e** The ADC cannot be calculated accurately due to the susceptibility artifact

tion secondary to β-amyloid-induced vasculopathy, cerebral amyloid inflammatory vasculopathy has been proposed [60]. DW imaging shows the leukoencephalopathy as isointense with increased ADC consistent with extracellular edema (Fig. 7.24). The leukoencephalopathy has responded to immunosuppressive therapy with at least partial resolution at imaging [61].

7.5.11 Susac Syndrome

Susac syndrome is characterized by acute or subacute encephalopathy, sensorineural hearing loss, and occlusion of the retinal artery branch caused by microangiopathy involving the brain, cochlea, and retina [62, 63]. There is a female predominance of 3:1 and the age ranges from 16 to 58 years. The pathogenesis

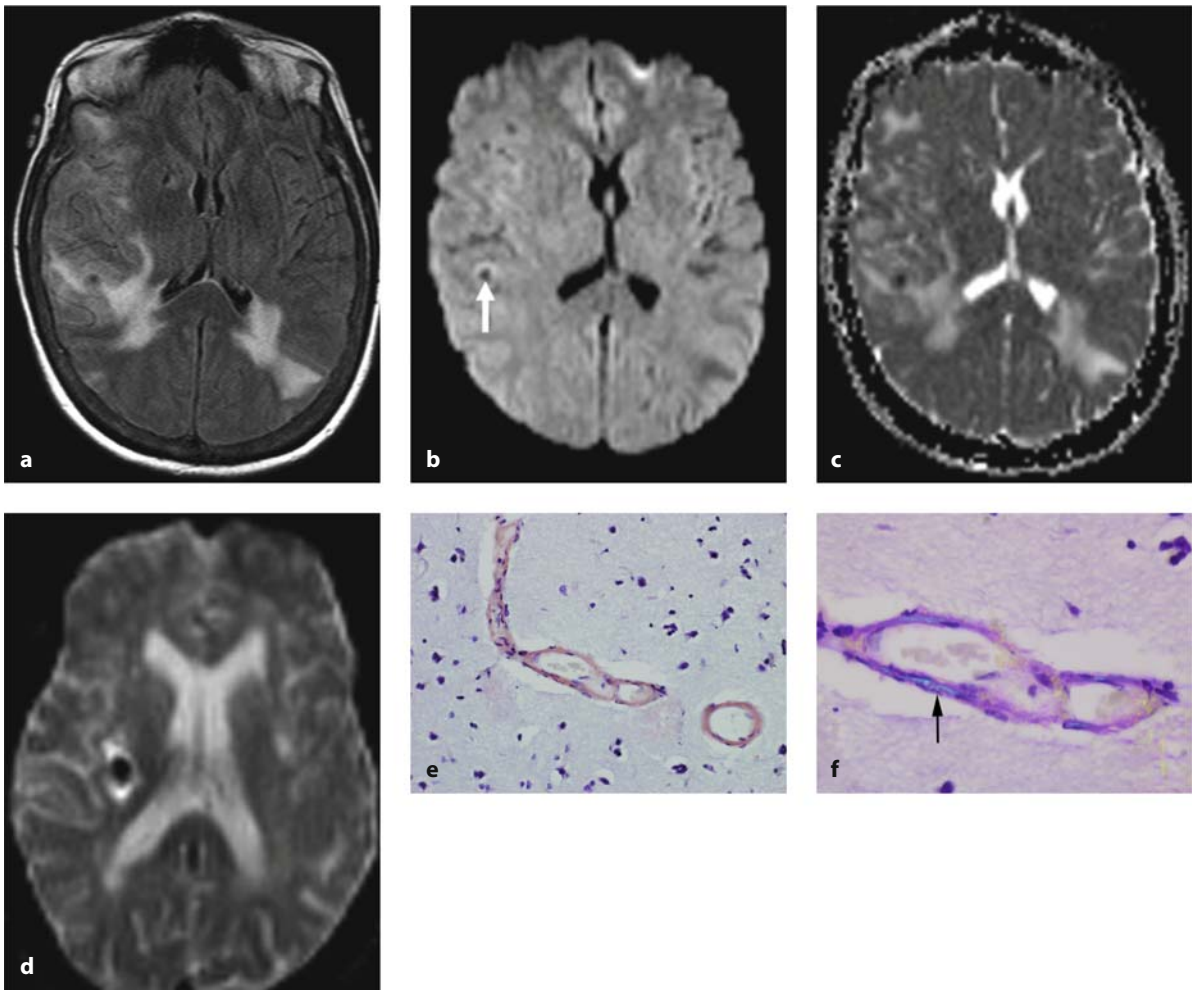

Figure 7.24 a–f

Cerebral amyloid angiopathy with leukoencephalopathy in a 54-year-old woman (biopsy proven). **a** FLAIR image shows white matter hyperintensity in the right fronto-temporal and left temporo-occipital regions. A microhemorrhage is noted as a low signal spot in the right temporo-parietal white matter. **b**, **c** DW image shows the white matter lesions as isointense associated with increased ADC consistent with vasogenic edema (**d**). DW image also demonstrates the microbleed as a low signal spot (*arrow*). **e** Congo red stain shows β-amyloid deposits along the wall of the arteriole. **f** Congo red stain viewed with polarized light shows the classic yellow-green birefringence of the β-amyloid deposits (*arrow*)

is unknown. The basic histologic feature is microinfarctions. T2-weighted and FLAIR images typically show small and multifocal hyperintense lesions, which are sometimes similar to multiple sclerosis plaques. The lesions are predominantly supratentorial, with a predilection for the corpus callosum (100%) and deep gray matter (basal ganglia and thalamus)(70%), although they can be seen in the cerebellum and brain stem. The lesions frequently enhance during the acute stage (70%) and leptomeningeal enhancement is occasionally seen (30%). DW imaging shows some lesions as hyperintense with decreased ADC, and others with increased ADC (Fig. 7.25) [64]. DW imaging can also depict diffuse abnormalities in the nonlesional white matter. The disease may have a self-limited course but patients usually have residual cognitive and visual/hearing disability.

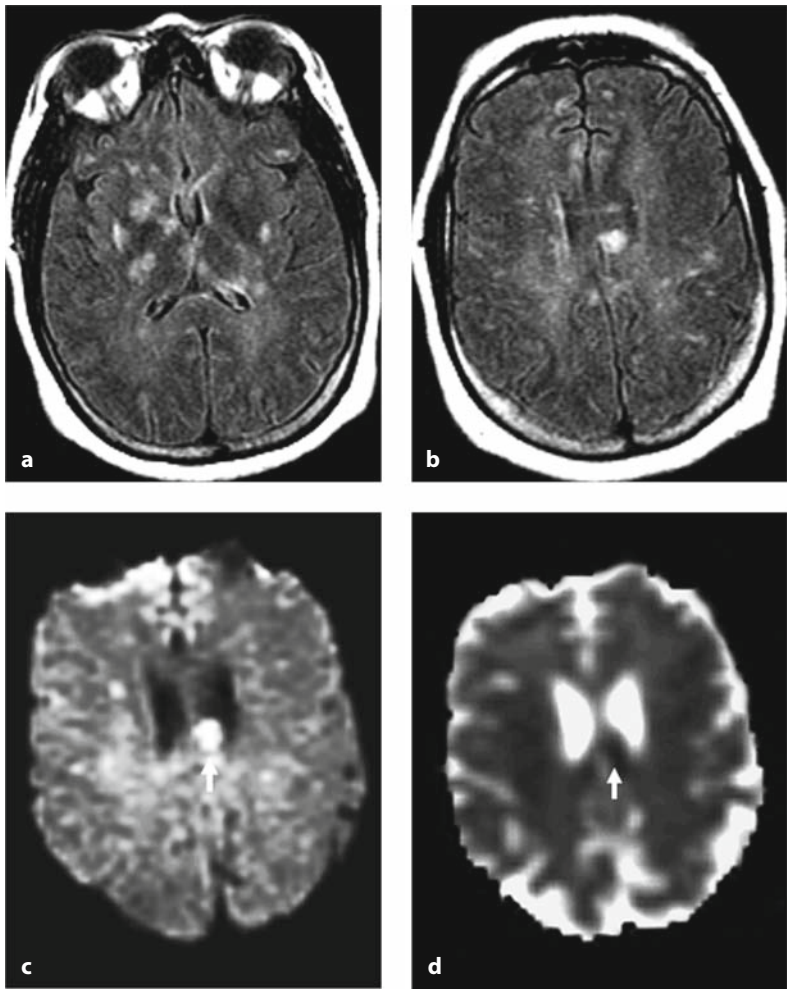

Figure 7.25 a–d

Susac syndrome in a 49-year-old woman with recurrent neurologic deficits, hearing loss, and retinal artery branch occlusions. **a, b** FLAIR image shows multiple small high signal intensity lesions in the bilateral basal ganglia, thalami, and corpus callosum. A diffuse, mild white matter hyperintensity is also noted. **c** DW image shows these small multiple lesions as hyperintensity, especially in the corpus callosum (*arrow*). **d** ADC map shows a callosal lesion as decreased ADC (*arrow*). Diffusely increased ADC is also noted in deep white matter

7.5.12 Hypereosinophilic Syndrome

Hypereosinophilic syndrome (HES) is characterized by an eosinophil count of more than 1,500/μL for more than 6 months and multiorgan involvement without other causes of eosinophilia and in the absence of eosinophil blast cells in the marrow or blood. The three subtypes are myeloproliferative, lymphocytic, and idiopathic. 65% of HES patients have neurologic involvement, including three major types: peripheral polyneuropathy, encephalopathy, and central nervous system (CNS) thromboemboli infarction. The locations of the infarctions are distributed particularly in the border zone or distal fields of the major cerebral arteries (Fig. 7.26). The specific mechanism of hypereosinophilia-induced brain infarctions remains unclear. For patients with cardiac involvement, microembolism in the CNS may be secondary to intracardiac thrombus formation

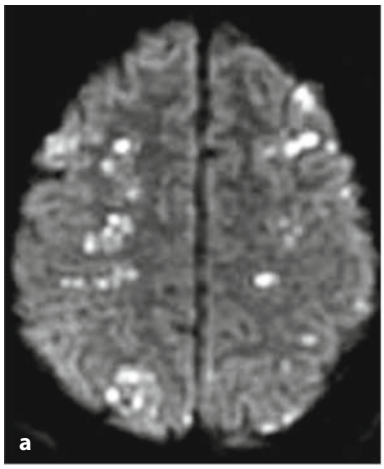

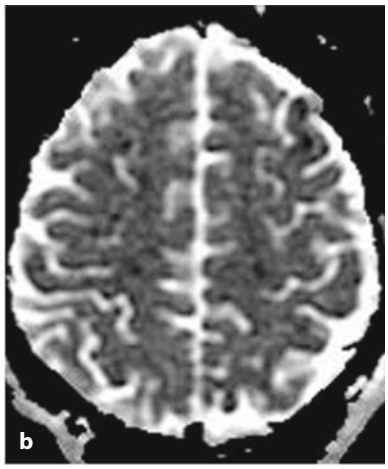

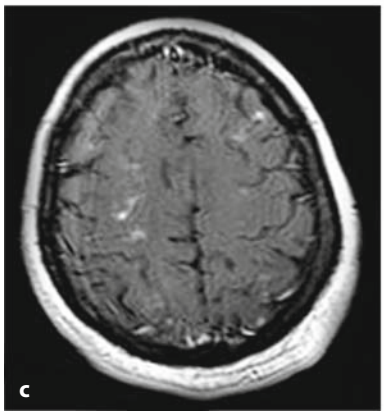

Figure 7.26 a–c
Hypereosinophilic syndrome without evident cardiac abnormality. **a**, **b** DW image shows multiple hyperintense foci associated with the decreased ADC in bilateral watershed areas. **c** Postcontrast T1-weighted image shows multiple enhancing foci consistent with acute- to subacute-phase infarcts

due to endomyocardial fibrosis and eosinophilic infiltration. However, small and multiple infarcts in the border zone may also occur in HES patients without demonstrable cardiac disease. It has been postulated in these cases that local thrombus formation from a hyperviscous, hypercoaguable state or distant microthromboemboli within the vessels of the CNS may be the underlying mechanisms.

7.6 Conclusion

Diffusion-weighted imaging is useful in patients with CNS vasculitis and vasculopathy to detect acute infarctions and to differentiate diseases that show cytotoxic edema from those with vasogenic edema. Overall, lesions demonstrating cytotoxic edema are usually irreversible and those with vasogenic edema are often reversible. Thus, DW imaging is an important tool to establish a prognosis and to determine the best treatment.

References

1. Berlit P (1994) The spectrum of vasculopathies in the differential diagnosis of vasculitis. Semin Neurol 14:370–379
2. Lie JT (1997) Classification and histopathologic spectrum of central nervous system vasculitis. Neurologic Clinics 15:805–819
3. Ebisu T, Naruse S, Horikawa Y, Ueda S, Tanaka C, Uto M, Umeda M, Higuchi T (1993) Discrimination between different types of white matter edema with diffusion-weighted MR imaging. J Magn Res Imaging 3:863–868
4. Aisen AM, Gabrielsen TO, McCune WJ (1985) MR imaging of systemic lupus erythematosus involving the brain. AJR Am J Roentgenol 144:1027–1031
5. Moritani T, Shrier DA, Numaguchi Y, Takahashi C, Yano T, Nakai K, Zhong J, Wang HZ, Shibata DK, Naselli SM (2001) Diffusion-weighted MR imaging of CNS involvement in systemic lupus erythematosus. Academic Radiology 8:741–753
6. Kocer N, Islak C, Siva A, Saip S, Akman C, Kantarci O, Hamuryudan V (1999) CNS involvement in neuro-Behçet syndrome: an MR study. AJNR Am J Neuroradiol 20:1015–1024
7. Woolfenden AR, Hukin J, Poskitt KJ, Connolly MB (1998) Encephalopathy complicating Henoch–Schonlein purpura: reversible MRI changes. Pediatr Neurol 19:74–77
8. Hinchey J, Chaves C, Appignani B, Breen J, Pao L, Wang A, Pessin MS, Lamy C, Mas JL, Caplan LR (1996) A reversible posterior leukoencephalopathy syndrome. N Engl J Med 334:494–500
9. Parisi JE, Moore PM (1994) The role of biopsy in vasculitis of the central nervous system. Semin Neurol 14:341–347
10. Jennette JC, Falk RJ, Milling DM (1994) Pathogenesis of vasculitis. Semin Neurol 14:291–299
11. Valente RM, Conn DL (1994) Current therapies for systemic vasculitis. Semin Neurol 14:380–386

12. Pomper MG, Miller TJ, Stone JH, et al. (1999) CNS vasculitis in autoimmune disease: MR imaging findings and correlation with angiography. AJNR Am J Neuroradiol 20:75–85
13. White ML, Hadley WL, Zhang Y, Dogar MA (2007) Analysis of central nervous system vasculitis with diffusion-weighted imaging and apparent diffusion coefficient mapping of the normal-appearing brain. AJNR Am J Neuroradiol 5:933-937
14. Lie JT (1994) Primary (granulomatous) angiitis of the central nervous system: a clinicopathologic analysis of 15 new cases and a review of the literature. Hum Pathol 23:164–171
15. Watts RA, Lane SE, Bentham G, Scott DG (2000) Epidemiology of systemic vasculitis: a ten-year study in the United Kingdom. Arthritis Rheum 43:414-419
16. Schwab P, Lidov HG, Schwartz RB, Anderson RJ. (2003) Cerebral amyloid angiopathy associated with primary angiitis of the central nervous system: report of 2 cases and review of the literature. Arthritis Rheum 49:421-427
17 Scolding NJ, Joseph F, Kirby PA, Mazanti I, Gray F, Mikol J, Ellison D, Hilton DA, Williams TL, MacKenzie JM, Xuereb JH, Love S (2005) Abeta-related angiitis: primary angiitis of the central nervous system associated with cerebral amyloid angiopathy. Brain 128:500-515
18. Harris KG, Tran DD, Sickels WJ, Cornell SH, Yuh WT (1994) Diagnosing intracranial vasculitis: the role of MR and angiography. AJNR Am J Neuroradiol 15:317–330
19. Campi A, Benndorf G, Filippi M, Reganati P, Martinelli V, Terreni MR (2001) Primary angiitis of the central nervous system: serial MRI of brain and spinal cord. Neuroradiology 43:599–607
20. Ay H, Sahin G, Saatci I, Soylemezoglu F, Saribas O (2002) Primary angiitis of the central nervous system and silent cortical hemorrhages. AJNR Am J Neuroradiol 23:1561–1563
21. Moore P (1989) Diagnosis and management of isolated angitis of the central nervous system. Neurology 39:167–173
22. MacLaren K, Gillespie J, Shrestha S, Neary D, Ballardie FW (2005) Primary angiitis of the central nervous system: emerging variants. QJM 98:643-654
23. Brack A, Martinez-tabada V, Stanson A, et al. (1999) Disease pattern in cranial and large-vessel giant cell arteritis. Arthritis Rheum 42:311–317
24. Yamada I, Nakagawa T, Himeno Y, et al. (1998) Takayasu arteritis: evaluation of the thoracic aorta with CT angiography. Radiology 209:103–109
25. Provenzale JM, Allen NB (1996) Neurologic findings in polyarteritis nodosa. AJNR Am J Neuroradiol 17:1119–1126
26. Sehgal M, Swanson JW, DeRemee RA, et al. (1995) Neurologic manifestations of Churg-Strauss syndrome. Mayo Clin Proc 70:337–341
27. Liou HH, Liu HM, Chiang IP, et al. (1997) Churg-Strauss syndrome presented as multiple intracerebral hemorrhage. Lupus 6:279–282
28. Murphy JM, Gomez-Anson FB, Gillard JH, et al. (1999) Wegener granulomatosis: MR imaging findings in brain and meninges. Radiology 213:794–799
29. Castillo M (1994) Magnetic resonance imaging of meningitis and its complications. Top Magn Reson Imaging 6:53–58
30. DeLone DR, Goldstein RA, Petermann G, et al. (1999) Disseminated aspergillosis involving the brain: distribution and imaging characteristics. AJNR Am J Neuroradiol 20:1597–1604
31. Lexa FJ (1995) Drug-induced disorders of the central nervous system. Semin Roentgenol 30:7–17
32. Gradon JD, Wityk R (1995) Diagnosis of probable cocaine-induced cerebral vasculitis by magnetic resonance angiography. South Med J 88:1264–1266
33. Hess DC (1997) Cerebral lupus vasculopathy. Mechanism and clinical relevance. Ann NY Acad Sci 823:154–168
34. Belmont HM, Abramson SB, Lie JT (1996) Pathology and pathogenesis of vascular injury in systemic lupus erythematosus. Interactions of inflammatory cells and activated endothelium. Arthritis Rheum 39:9–22
35. Sibbit WL, Sibbit RR, Griffey RH, et al. (1989) Magnetic resonance and computed tomographic imaging in the evaluation of acute neuropsychiatric disease in systemic lupus erythematosus. Ann Rheum Dis 48:1014–1022
36. Yamada I, Himeno Y, Nagaoka T, et al. (1999) Moyamoya disease: evaluation with diffusion-weighted and perfusion echo-planar MR imaging. Radiology 212:340–347
37. Moran CJ, Siegel MJ, DeBaun MR (1998) Sickle cell disease: imaging of cerebrovascular complications. Radiology 206:311–321
38. Moritani T, Numaguchi Y, Lerner NB, et al. (2004) Sickle cell cerebrovascular disease: usual and unusual findings on MR imaging and MR angiography. Clin Imaging 28:261-270
39. Casey SO, Sampaio RC, Michel E, et al. (1998) Posterior reversible encephalopathy syndrome: utility of fluid-attenuated inversion recovery MR imaging in the detection of cortical and subcortical lesions. AJNR Am J Neuroradiol 21:1199–1206
40. Hinchey J, Chaves C, Appignani B, et al. (1996) A reversible posterior leukoencephalopathy syndrome. N Engl J Med 334:494–500
41. Ay H, Buonanno FS, Schaefer PW, Le DA, et al. (1998) Posterior leukoencephalopathy without severe hypertension: utility of diffusion-weighted MRI. Neurology 51:1369–1376
42. Pavlakis SG, Frank Y, Kalina P, et al. (1997) Occipital-parietal encephalopathy: a new name for an old syndrome. Pediatr Neurol 16:145–148
43. Kinoshita T, Moritani T, Shrier DA, et al. (2003) Diffusion-weighted MR imaging of posterior reversible leukoencephalopathy syndrome. A pictorial essay. Clin Imaging 27: 307–315
44. McKinney AM, Short J, Truwit CL, McKinney ZJ, Kozak OS, SantaCruz KS, Teksam M (2007) Posterior reversible encephalopathy syndrome: incidence of atypical regions of involvement and imaging findings. AJR Am J Roentgenol 189:904-912
45. Bartynski WS, Boardman JF (2007) Distinct imaging patterns and lesion distribution in posterior reversible encephalopathy syndrome. AJNR Am J Neuroradiol 28:1320-1327

46. Schwartz RB, Mulkern RV, Gudbjartsson H, et al. (1998) Diffusion-weighted MR imaging in hypertensive encephalopathy: clues to pathogenesis. AJNR Am J Neuroradiol 19:859–862
47. Schwartz RB, Feske SK, Polak JF, et al. (2000) Preeclampsia-eclampsia: clinical and neuroradiographic correlates and insights into the pathogenesis of hypertensive encephalopathy. Radiology 217:371–376
48. Ursell MR, Marras CL, Farb R, et al. (1998) Recurrent intracranial hemorrhage due to postpartum cerebral angiopathy: implications for management. Stroke 29:1995–1998
49. Digre KB, Varner MW, Osborn AG, et al. (1993) Cranial magnetic resonance in severe preeclampsia vs eclampsia. Arch Neurol 50:399–406
50. Schaefer PW, Mulkern RV, Gudbjartsson H, et al. (1997) Diffusion-weighted imaging discriminates between cytotoxic and vasogenic edema in a patient with eclampsia. Stroke 28:1082–1085
51. Coley SC, Porter DA, Calamante F, et al. (1999) Quantitative MR diffusion mapping and cyclosporine-induced neurotoxicity. AJNR Am J Neuroradiol 20:1507–1510
52. Bartynski WS, Zeigler Z, Spearman MP, Lin L, Shadduck RK, Lister J (2001) Etiology of cortical and white matter lesions in cyclosporin-A and FK-506 neurotoxicity. AJNR Am J Neuroradiol 22:1901–1914
53. Okada J, Yoshikawa K, Matsuo H, et al. (1991) Reversible MRI and CT findings in uremic encephalopathy. Neuroradiology 33:524–526
54. Schmidt S, Gudinchet F, Meagher-Villemure K, et al. (2001) Brain involvement in haemolytic-uraemic syndrome: MRI features of coagulative necrosis. Neuroradiology Jul;43(7):581–585
55. Bakshi R, Shaikh ZA, Bates VE, et al. (1999) Thrombotic thrombocytopenic purpura: brain CT and MRI findings in 12 patients. Neurology 52:1285–1288
56. D'Aprile P, Farchi G, Pagliarulo R, et al. (1994) Thrombotic thrombocytopenic purpura: MR demonstration of reversible brain abnormalities. AJNR Am J Neuroradiol 15:19–20
57. Chao CP, Kotsenas AL, Broderick DF (2006) Cerebral amyloid angiopathy: CT and MR imaging findings. Radiographics 26:1517-31
58. Fazekas F, Kleinert R, Roob G, et al. (1999) Histopathologic analysis of foci of signal loss on gradient-echo T2*-weighted MR images in patients with spontaneous intracerebral hemorrhage: evidence of microangiopathy-related microbleeds. AJNR Am J Neuroradiol 20:637–42
59. Haacke EM, DelProposto ZS, Chaturvedi S, Sehgal V, Tenzer M, Neelavalli J, Kido D (2007) Imaging cerebral amyloid angiopathy with susceptibility-weighted imaging. AJNR Am J Neuroradiol 28:316-317
60. Kinnecom C, Lev MH, Wendell L, Smith EE, Rosand J, Frosch MP, Greenberg SM (2007) Course of cerebral amyloid angiopathy-related inflammation. Neurology 68:1411-1416
61. Harkness KA, Coles A, Pohl U, Xuereb JH, Baron JC, Lennox GG (2004) Rapidly reversible dementia in cerebral amyloid inflammatory vasculopathy. Eur J Neurol 11:59-62
62. Oh U, Gupta R, Krakauer JW, Khandji AG, Chin SS, Elkind MS (2004) Reversible leukoencephalopathy associated with cerebral amyloid angiopathy. Neurology 62:494-497
63. Susac JO, Hardman JM, Selhorst JB (1979) Microangiopathy of the brain and retina. Neurology 29:313-316
64. White ML, Zhang Y, Smoker WR (2004) Evolution of lesions in Susac syndrome at serial MR imaging with diffusion-weighted imaging and apparent diffusion coefficient values. AJNR Am J Neuroradiol 25:706-713
65. McMillan HJ, Johnston DL, Doja A. Watershed infarction due to acute hypereosinophilia. Neurology. 2008;70(1):80-2.
66. Kwon SU, Kim JC, Kim JS. Sequential magnetic resonance imaging findings in hypereosinophilia-induced encephalopathy. J Neurol. 2001;248(4):279-84
67. Sarazin M, Caumes E, Cohen A, Amarenco P. Sarazin M, Caumes E, Cohen A, Amarenco P. Multiple microembolic borderzone brain infarctions and endomyocardial fibrosis in idiopathic hypereosinophilic syndrome and in Schistosoma mansoni infestation.J Neurol Neurosurg Psychiatry. 2004; 75(2):305-7.
68. Battineni ML, Galetta SL, Oh J, Lango M, Brooks JJ, Schuster SJ, Loevner LA. Idiopathic hypereosinophilic syndrome with skull base involvement. AJNR Am J Neuroradiol. 2007;28(5):971-3.
69. Moritani T, Hiwatashi A, Shrier DA, et al. (2004) CNS vasculitis and vasculopathy Efficacy and usefulness of diffusion-weighted echo-planar MR imaging. Clin Imaging 28:173-186
70. Hiwatashi A, Garber T, Moritani T, Kinoshita T, Westesson P-L (2003) Diffusion-weighted MR Imaging of neuro_ Behcet disease: a case report. Neuroradiology 45: 468–471
71. Moritani T, Shrier DA, Numaguchi Y, et al. (2001) Diffusion-weighted MR imaging of CNS involvement in systemic lupus erythematosus. Academic Radiology 8: 741–753

Epilepsy

8.1 Definition

Epilepsy is a chronic brain disorder, which has a wide spectrum of underlying causes. It is characterized by recurrent seizures due to excessive discharge of cerebral neurons (epileptic seizures) and is associated with a variety of clinical and laboratory manifestations [1]. Epileptic seizures are defined as the clinical manifestation of abnormal excessive neuronal activity in cerebral gray matter.

8.2 Classification

The international classification of epileptic seizures is useful to describe the patients' symptoms, but this is often only the first step in the diagnostic process (Table 8.1) [2]. If the clinical characteristics are associated with a recognizable group of features, such as age of onset, genetic background and course, they may constitute an epileptic syndrome. The international classification of the epilepsy and epileptic syndromes classifies epilepsy as localized or generalized, and idiopathic, cryptogenic or symptomatic (Table 8.2) [2].

Table 8.1 Classification of epileptic seizures (from [2])

1. Partial (focal, local) seizures
   - Simple partial seizures
   - Complex partial seizures
   - Partial seizures evolving to secondary generalized seizures
2. Generalized seizures (convulsive or non-convulsive
   - Absence seizures
   - Myoclonic seizures
   - Clonic seizures
   - Tonic seizures
   - Tonic–clonic seizures
   - Atonic seizures
3. Unclassified epileptic seizures

Table 8.2 Classification of epilepsies and epileptic syndromes (modified from [2])

1. Localization-related epilepsies and syndromes
   - Idiopathic with age-related onset
   - Symptomatic (temporal, frontal, parietal or occipital epilepsy)
   - Cryptogenic
2. Generalized epilepsies and syndromes
   - Idiopathic with age-related onset
   - Cryptogenic or symptomatic (West syndrome, Lennox–Gestaut syndrome)
   - Symptomatic (early myoclonic encephalopathy, specific syndromes)
3. Epilepsies and syndromes undetermined as to whether they are focal or generalized
   - Neonatal seizures
4. Special syndromes
   - Febrile convulsions
   - Drug-induced seizures
   - Eclampsia
   - Chronic progressive epilepsia partialis continua of childhood

However, most generalized seizures eventually occur secondary to partial or localized seizures because generalized seizures are often improved after corpus callosotomy.

Idiopathic epilepsies are the most common and occur in otherwise normal children who have underlying genetic etiology with age-related, specific seizures and classic EEG patterns. Most of these are turning out to be channelopathies (calcium, sodium, potassium, Ach receptor, GABA receptor). Symptomatic epilepsies are those in which seizures are related to abnormalities that are clearly defined by imaging, metabolic, and genetic testing. In cryptogenic epilepsies the underlying etiology is suspected to be symptomatic, but the seizures are not specifically age-related without classic EEG pattern.

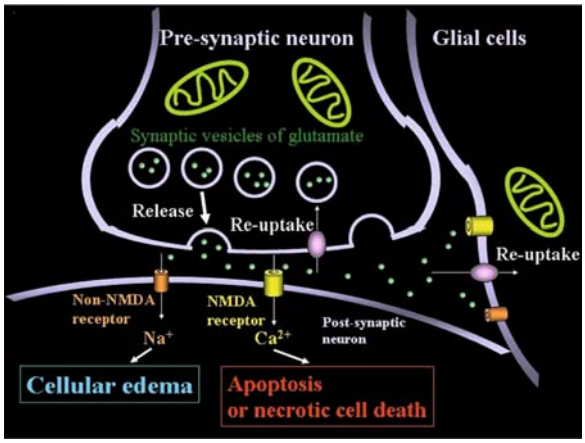

Figure 8.1

Excitotoxic mechanisms in the neuron and astrocyte. In the neuron, glutamate is released from the pre-synaptic terminal into the synaptic cleft. The glutamate binding to NMDA receptors allows entry of Ca^{2+} into the post-synaptic neuron, which can result in necrotic cell death or apoptosis. The glutamate binding to non-NMDA receptors allows entry of Na^{+} into the post-synaptic neuron, resulting in cytotoxic edema of the neuron. Re-uptake of extracellular glutamate takes place at the pre-synaptic terminals and in adjacent astrocytes. Similar mechanisms also cause cytotoxic edema in the astrocyte

8.3 Mechanisms and Pathophysiology of Epilepsy

The fundamental mechanisms of epilepsy can be studied at the basic level of the molecular environment of the cell. This involves cellular systems such as membrane channels, neuronal systems, cell populations and cell-to-cell interactions.

Several neurotransmitter systems are important for the mechanisms of epilepsy [3]. Glutamate is an excitatory synaptic transmitter in cerebral cortex and hippocampus. The primary receptors are divided into two groups: N-methyl-D-aspartate (NMDA) receptors and non-NMDA receptors [4]. Excessive release of glutamate activates the NMDA receptor, depolarizes the postsynaptic terminals, and induces changes in membrane function and ionic homeostasis. NMDA receptors, which have a high density in the hippocampus and other parts of the limbic system, can be related to regions that are susceptible to excitotoxic damage (Fig. 8.1) [5, 6]. In some models of epileptogenesis it has been possible to block bursts of discharges by NMDA channel antagonists [7].

Another neurotransmitter related to epilepsy is gamma-aminobutyric acid (GABA), which is an inhibitor of discharges. Loss of GABAergic inhibition can generate epileptiform activity, which is believed to be important in chronic epilepsy [3].

The onset of epileptiform activity presupposes that an epileptic focus must exist where the seizure originates. The epileptic focus almost always exists in the cortex usually near structural brain abnormalities such as an anomaly or tumor, but it could be located far from the focus or even in the contralateral side. The epileptic focus may exist in a discrete group of neurons, such as the CA1 pyramidal cells in the hippocampus, or over a larger region, including hippocampus and entorhinal cortex [5]. The seizure attack is associated with abnormal discharges in populations of synchronously active neurons. The spread of the seizure may be associated with an accumulation of extracellular substances, such as potassium ions or excitotoxic amines, and electrical gating mechanisms among neurons.

8.4 Imaging of Epilepsy

8.4.1 Magnetic Resonance Imaging of Epilepsy

MR imaging is widely used to evaluate patients with seizures and can detect structural brain abnormalities that may give rise to the epileptic disorder, e.g. stroke, anoxic injury, ulegyria, trauma, tumor, infections, demyelination, arteriovenous malformation, Sturge-Weber syndrome, and congenital anomalies (focal cortical dysplasia, microdysgenesis, tuberous sclerosis, polymicrogyria, hemimegalencephaly, gray matter heterotopia). The most common cause of seizures in patients older than 45 years is stroke [8]. Intracranial tumors are often associated with epileptic seizures, and trauma is the most common cause of seizures in patients aged 15–24 years [9]. Up to 5% of epilepsy cases have a history of central nervous system infections [10]. MR imaging is performed for preoperative planning in epilepsy (anteromedial lobectomy, multiple subpial transection, corpus callosotomy, hemispherotomy etc.).

MR imaging has become useful for the diagnosis of temporal lobe epilepsy, especially mesial temporal (hippocampal) sclerosis [11–15]. "Mesial" means the "proximal" site of the temporal stem. Brain tumors, congenital anomalies such as microdysgenesis, cortical dysplasias, and polymicrogyria, or other lesions sometimes coexist with mesial temporal sclerosis (dual pathology).

Most seizure activity resolves within a few minutes without persistent neurologic deficits. However, transient hemiparesis (Todd's paralysis), sensory loss, Jacksonian march, persistent altered mental status, or aphasia occasionally occurs in epilepsy. MR imaging can show secondary effects of seizures on the brain [16–27]. Mesial temporal sclerosis may occur as a primary lesion and may also arise as a lesion secondary to status epilepticus [20, 22].

Variable MR findings have been reported in the brain in the ictal or postictal stage [16–27]. These findings include transient increase in T2 signal and swelling of the cerebral cortex, subcortical white matter and medial temporal lobe (including hippocampus), thalamus (anterior, medial dorsal thalamic nuclei, pulvinar), fornix, claustrum and cerebellar hemispheres (Figs. 8.2-8.11). The distribution of lesions with temporal lobe epilepsy on MR imaging is related to transneuronal degeneration via the circuit of Papetz [28, 29]. The circuit of Papetz starts in the hippocampus connected to the mamillary body through the fornix. Via synapses in the mamillary body, the mamillothalamic tract connects to the anterior thalamic nucleus. The thalamocingulate fiber projects into the cingulate gyrus via synapses. The circuit is completed by the transfer of impulses from

Figure 8.2 a–d

Postictal encephalopathy following partial seizure evolving to generalized seizure in a 60-year-old woman. **a** T2-weighted and **b** FLAIR images 24 h after seizures show hyperintense lesions (*arrows*) in the right fronto-parietal cortex. **c** DW image and **d** ADC map show these lesions as isointense, probably representing mild vasogenic edema. These lesions were resolved on the 20-day follow-up MR imaging (not shown)

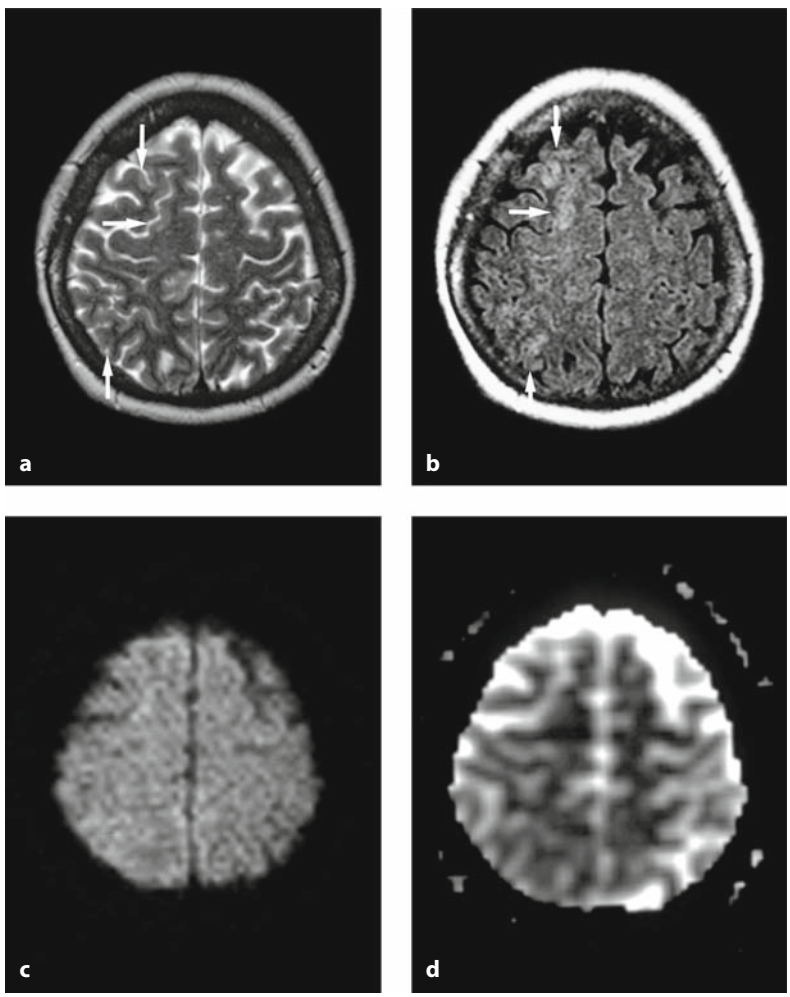

the cingulum to the hippocampus through the parahippocampal gyrus.

The medial pulvinar of the thalamus has rich and reciprocal connections with the temporal lobe cortex and is involved in the maintenance and propagation of epileptic seizures (corticothalamic coupling or thalamocortical synchrony through epileptogenic network) (Figs. 8.8, 8.9)[30, 31]. Cortical or subcortical lesions can be uni- or bilateral and they are predominantly found in the fronto-parietal regions. Whether periictal lesions are reversible or irreversible on MR imaging seems to depend on the duration and/or severity of the seizures.

8.4.2 Diffusion-Weighted Imaging in Epilepsy

On routine MR imaging, signal alterations related to ictal or postictal status can be misdiagnosed as infarctions, tumorous conditions, inflammatory diseases or demyelinating diseases. This may occur because routine MR sequences will not separate vasogenic edema

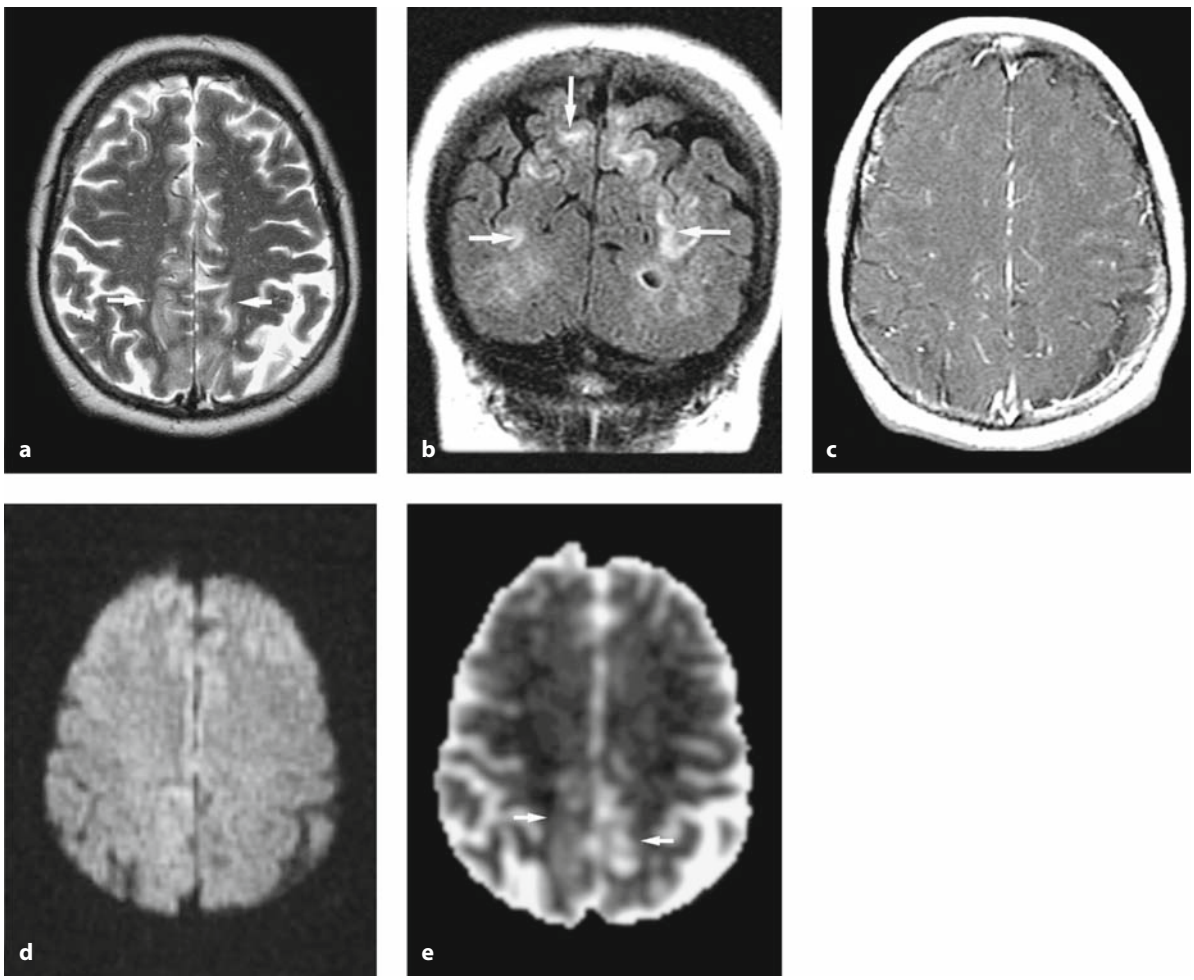

Figure 8.3 a–e

Postictal encephalopathy lesion following partial seizure in a 64-year-old woman with generalized seizure secondary to hyperglycemia. **a** T2-weighted image 24 h after seizures shows hyperintense lesions in bilateral medial fronto-parietal cortex (*arrows*). **b** Coronal FLAIR image also shows cortical and subcortical hyperintense lesions (*arrows*). **c** Gadolinium-enhanced T1-weighted image shows no abnormal enhancement. **d** DW image shows these lesions as isointense with increased ADC (**e**) (*arrows*), representing vasogenic edema

from cytotoxic edema. Such misdiagnoses may result in unnecessary invasive treatment. Diffusion-weighted (DW) imaging is helpful in evaluating epilepsy, as it will detect cytotoxic edema and can differentiate between cytotoxic and vasogenic edema in ictal and postictal lesions of the brain (peri–or postical encephalopathy.

8.4.3 Ictal Stage to Periictal Stage

During ictus there is an increase in metabolism (oxygen and glucose) in the seizure focus. This hypermetabolic state results in consumptive hypoxia, hypercarbia and lactic acidosis, which impair vascular autoregulation in the affected areas of cortex, leading to vasogenic edema and disruption of the blood–brain barrier [23]. If the seizures are not too prolonged, the periictal brain lesions will only show transient T2 hyperintensity, mainly representing vasogenic edema. However, if the seizures

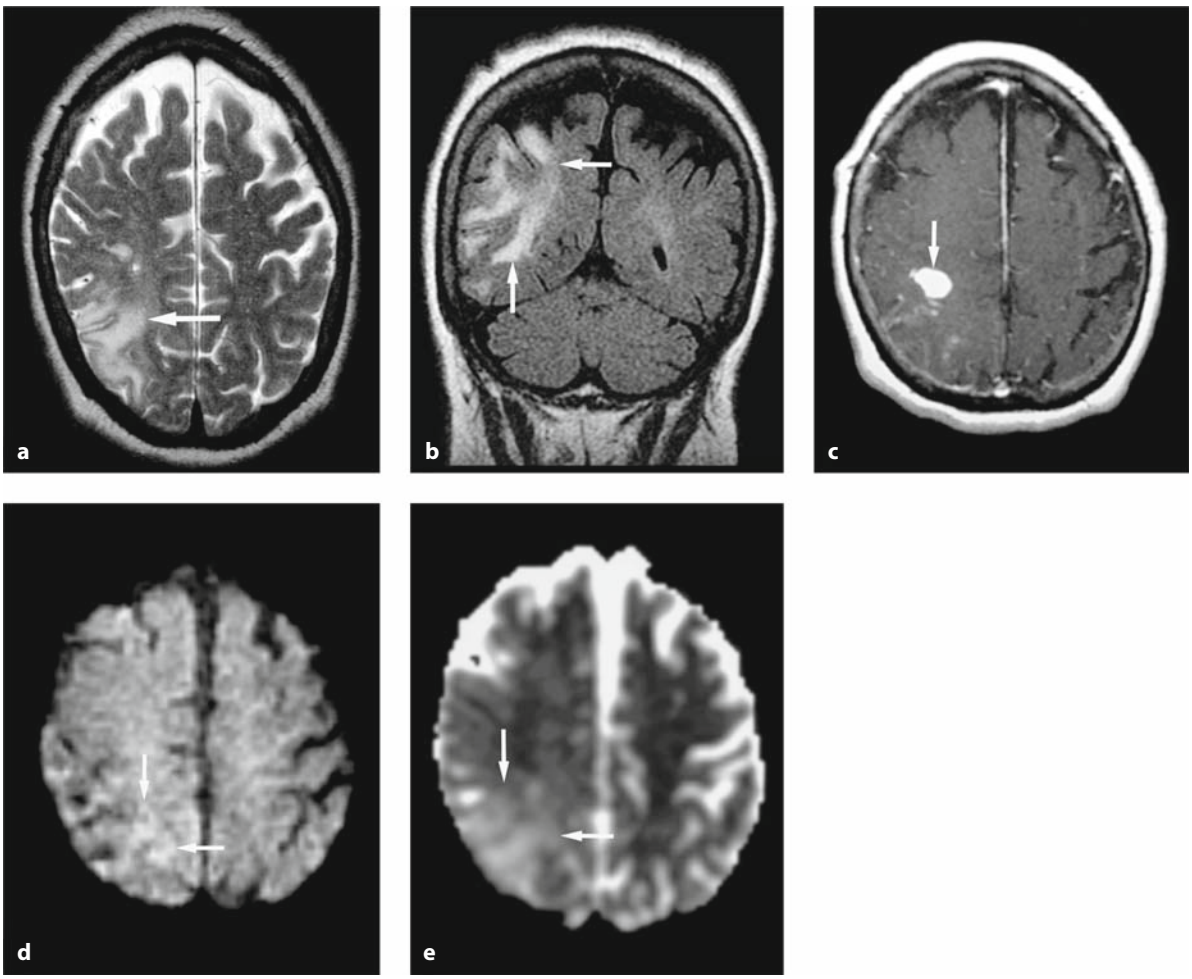

Figure 8.4 a–e

Postictal encephalopathy following partial seizures with or without secondary generalization in a 75-year-old woman. **a** T2-weighted image at 4 days after seizures shows hyperintense lesions in the right fronto-parietal region (*arrow*). **b** Coronal FLAIR image shows cortical and subcortical hyperintense lesions (*arrows*). **c** Gadolinium-enhanced T1-weighted image shows a dense enhancing nodule (*arrow*) and leptomeningeal enhancement. **d** DW image shows these lesions as isointense to slightly hyperintense (*arrows*), with increased ADC (*arrows*) (**e**). Brain biopsy was performed and proved the lesions to be acute ischemic changes

are severe or prolonged, cytotoxic edema can develop, which usually results in cortical and/or subcortical white matter hyperintensity on DW imaging associated with decreased ADC. This is often seen in patients with generalized tonic–clonic seizure or status epilepticus (Figs. 8.5–8.8). Whether these lesions show enhancement or not depends on the degree of blood–brain barrier disruption (Figs. 8.3 and 8.4).

Vasogenic edema in periictal brain lesions has variable signal intensity on DW imaging, which is associated with an increase in ADC (Figs. 8.2-8.4). As mentioned above, DW imaging is useful in detecting and differentiating cytotoxic from vasogenic edema.

8.4.4 Status Epilepticus

Status epilepticus is defined as continuous seizure activity that lasts longer than 30 minutes, or two or more sequential seizures that together last longer than

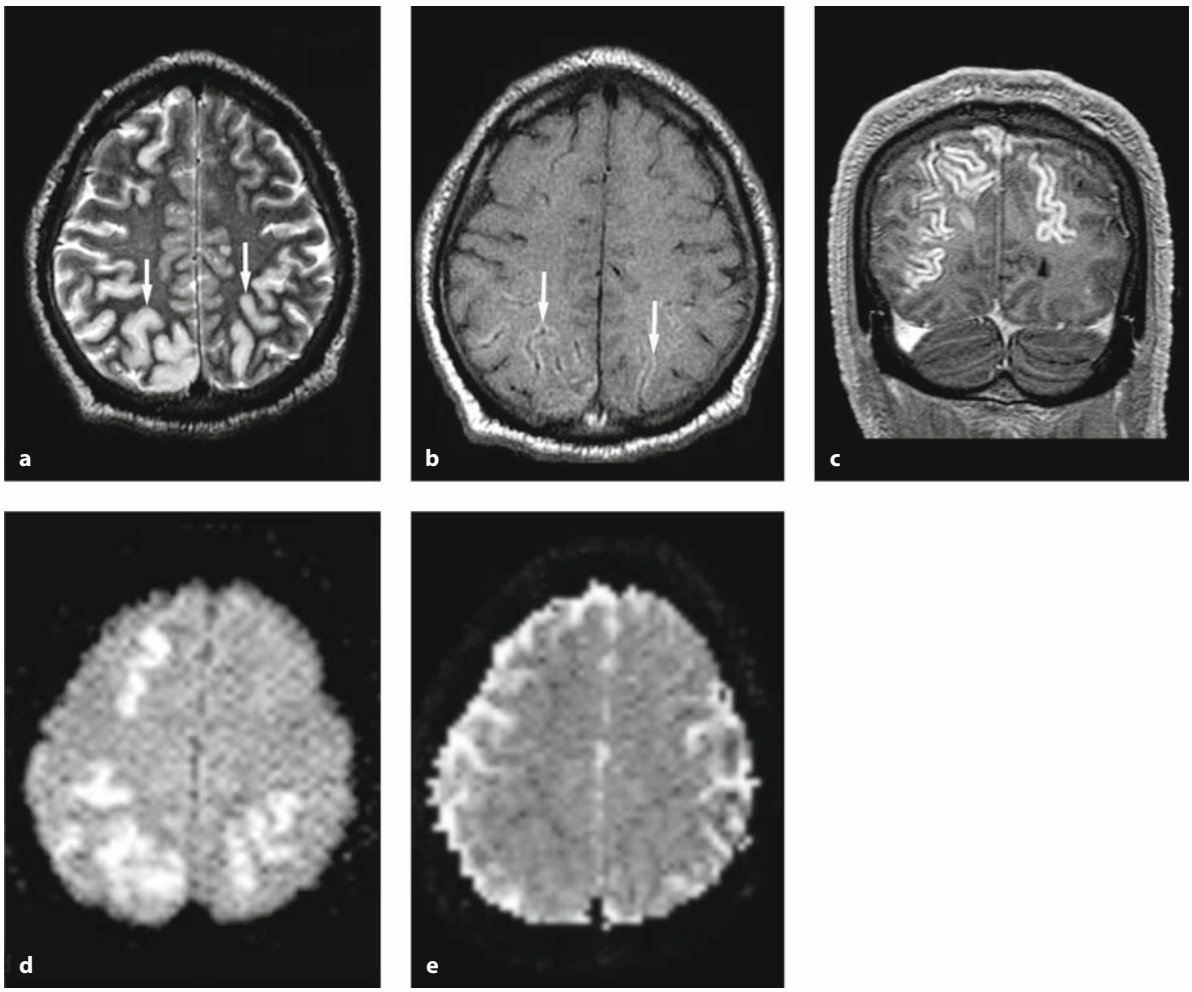

Figure 8.5 a–e

Postictal encephalpathy following generalized tonic–clonic seizure in a 42-year-old man with alcohol withdrawal. **a** T2-weighted image shows hyperintense lesions (*arrows*) in bilateral fronto-parietal cortex. **b** T1-weighted image 8 days after the seizure shows gyriform high signal intensity in these lesions, representing cortical laminar necrosis (*arrows*). **c** Coronal gadolinium-enhanced T1-weighted image shows gyriform enhancement of these lesions. **d** DW image shows corresponding regions of hyperintensity. **e** ADC map shows almost normal ADC values of these lesions, suggesting a subacute phase of ischemia

30 minutes and without full recovery of consciousness between the seizure attacks [33]. This is a serious event and should be treated aggressively, as the mortality associated with status epilepticus is about 8% in children and 30% in adults [33, 34].

In status epilepticus, neuronal injury is thought to result primarily from an excitotoxic mechanism mediated by intrinsic neuronal seizure activity. This is supported by the effect of kainic acid (an excitotoxic analog of glutamate), as shown in animal studies [35, 36]. Neuronal seizure activity will increase the release of glutamate from the pre-synaptic terminal of neuronal axons. The released glutamate crosses the synaptic cleft to bind to NMDA receptors of the postsynaptic neurons, resulting in cytotoxic edema. Cytotoxic edema is also seen in the astrocytes as an acute phase of reactive astrocytosis [22].

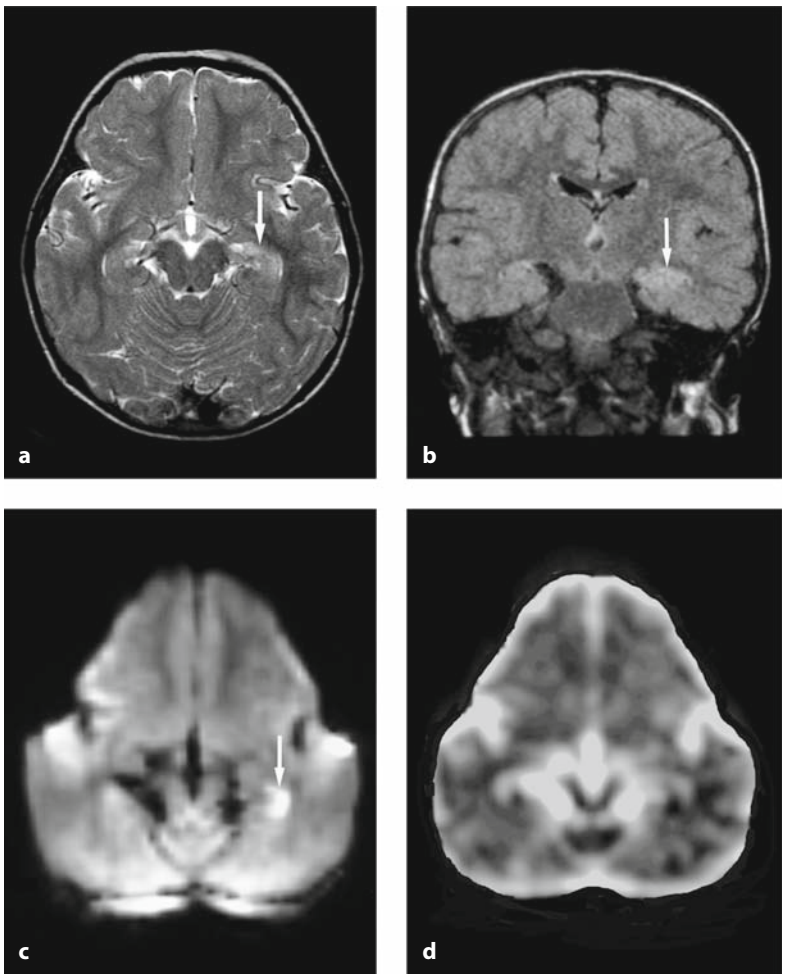

Figure 8.6 a–d

Hippocampal lesion following generalized tonic–clonic seizure in a 2-year-old girl with febrile seizure leading to generalized tonic–clonic seizure. **a** T2-weighted and **b** FLAIR images 3 days after seizure show hyperintensity in the left hippocampus (*arrows*). **c** DW image shows increased signal in the left hippocampus (*arrows*) associated with normal or slightly decreased ADC (**d**), suggesting a subacute phase of the postictal hippocampal lesion

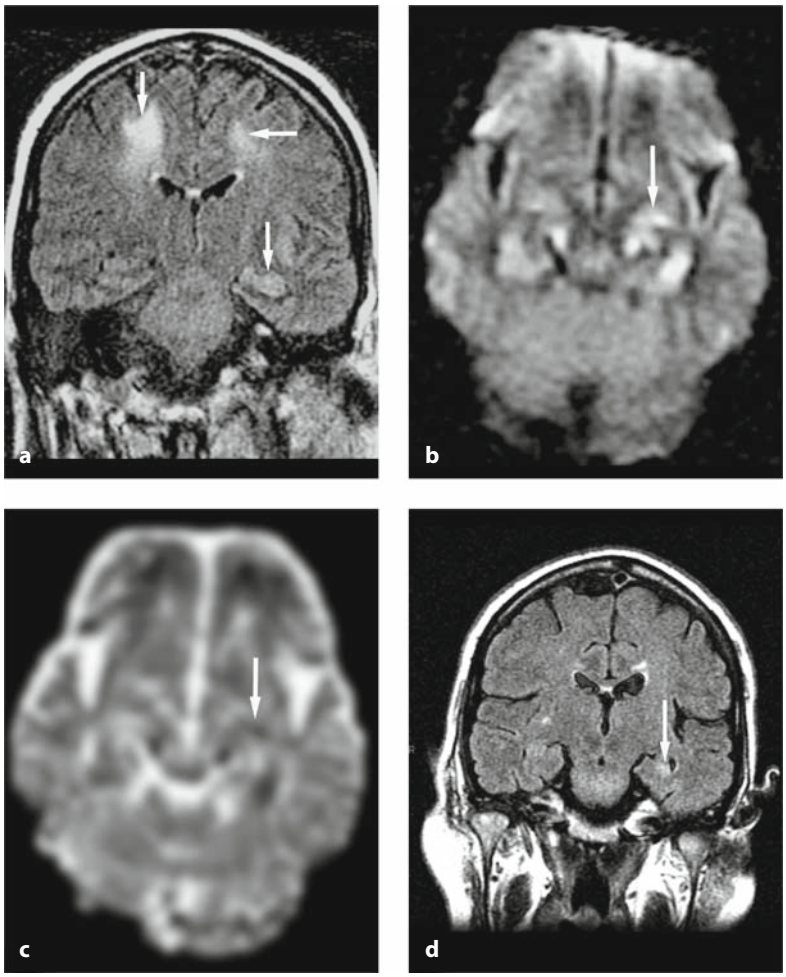

Figure 8.7 a–d

Hippocampal lesion following status epilepticus in a 55-year-old man with prolonged seizures associated with tacrolimus toxicity. **a** FLAIR image at 2 days after seizure shows high signal areas in the bilateral frontal deep white matter and the left hippocampus (*arrows*). **b** DW image (*y axis*) shows high signal in the left hippocampus (*arrow*). **c** ADC (*y axis*) shows low signal intensity (*arrow*) consistent with cytotoxic edema. **d** Seven-month follow-up coronal FLAIR image shows the resolution of white matter changes and residual high signal intensity with atrophy in the left hippocampus (*arrow*)

8.4.5 Cytotoxic Edema in Status Epilepticus

Cytotoxic edema following status epilepticus can be at least partially reversible [23], as compared to cerebral ischemia, where these changes are usually irreversible. In cerebral ischemia, a significant compromise of blood supply leads to irreversible failure of energy metabolism. In sustained seizures, there is an increased cerebral metabolism with an increase in cerebral blood flow. This will maintain the energy state of the neuron provided there is sufficient oxygen supply.

The parts of the human brain that are most vulnerable include parts of the hippocampus (the CA1 and CA3 segments, and the hilus), amygdala, pyriform cortex, thalamus, cerebellum, and cerebral cortex. NMDA receptors are predominantly located in the CA1 of the hippocampus and layers 3 and 4 in the cerebral cortex [37, 38]. The Purkinje cell loss of the cerebellum, seen in severe epilepsy, may be explained by an increased demand for inhibition, resulting in GABA depletion and subsequent influx of calcium into neurons [39]. Unilateral hemispheric involvement is occasionally seen in status epilepticus.

Transient and reversible MR signal changes have been reported in patients following status epilepticus [17, 20–24]. On the other hand, other lesions have been proven irreversible, resulting in selective neuronal necrosis, gliosis and delayed neuronal death with subsequent atrophy [25–27] (Figs. 8.7 and 8.8). Following status epilepticus, there has also been reported acute neuronal loss in the hippocampus accompanied by intense astrocytic reactions, called mesial temporal gliosis. This is pathologically different from mesial temporal sclerosis [17, 40, 41] (Fig. 8.7). However, these lesions may be the first step in

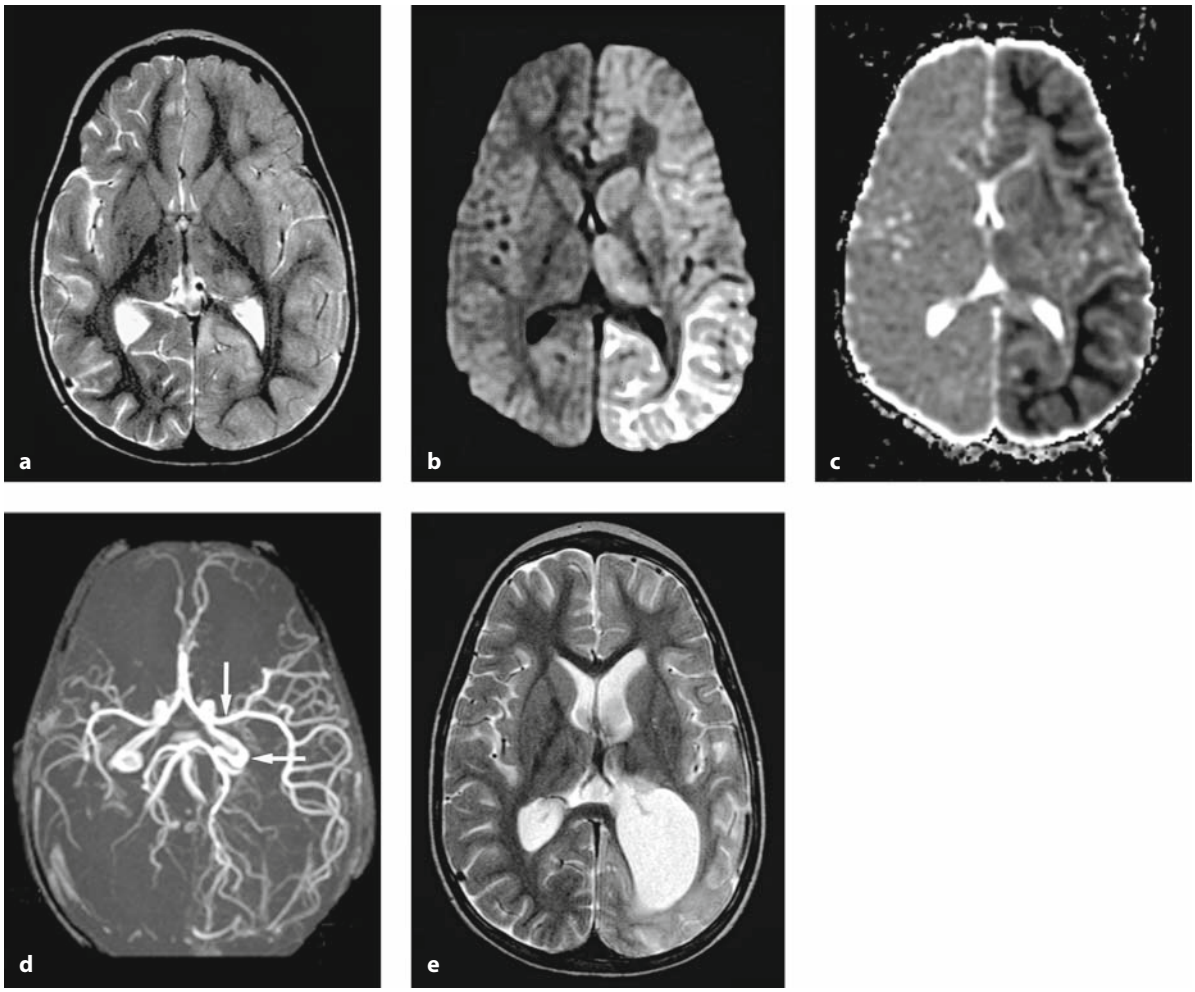

Figure 8.8 a–e

Hemiplegic hemiconvulsion epilepsy syndrome in a 2-year-old girl with partial status epilepticus involving the right face and hand. **a** T2-weighted image 24 h after seizure shows diffuse cortical hyperintense lesions in the entire left cerebral hemisphere, including the basal ganglia, and thalamus (anterior and medial area, pulvinar). **b** DW image shows diffuse left-sided cortical and subcortical hyperintense lesions with decreased ADC (**c**), representing cytotoxic edema. **d** MR angiography reveals dilatation of the left middle cerebral and posterior cerebral artery branches (*arrows*), representing hyperperfusion. **e** Diffuse atrophy with ventricular dilatation and hyperintense lesions in the left hemisphere seen on 5-month follow-up T2-weighted image

the development of mesial temporal sclerosis [20, 22]. Increased apparent diffusion coefficient (ADC) in the hippocampus has been reported in mesial temporal sclerosis [32].

Diffusion-weighted imaging and ADC maps are more sensitive than conventional MR imaging to show both gray and white matter involvement, and discriminate between cytotoxic and vasogenic edema following status epilepticus [23]. In experimental status epilepticus models, ADC decrease was first seen at about 3 hours and lasted until 48 hours after the onset of seizures, after which time it normalized or even increased [42–47]. The definite time course of DW imaging changes in humans is unknown, but areas of

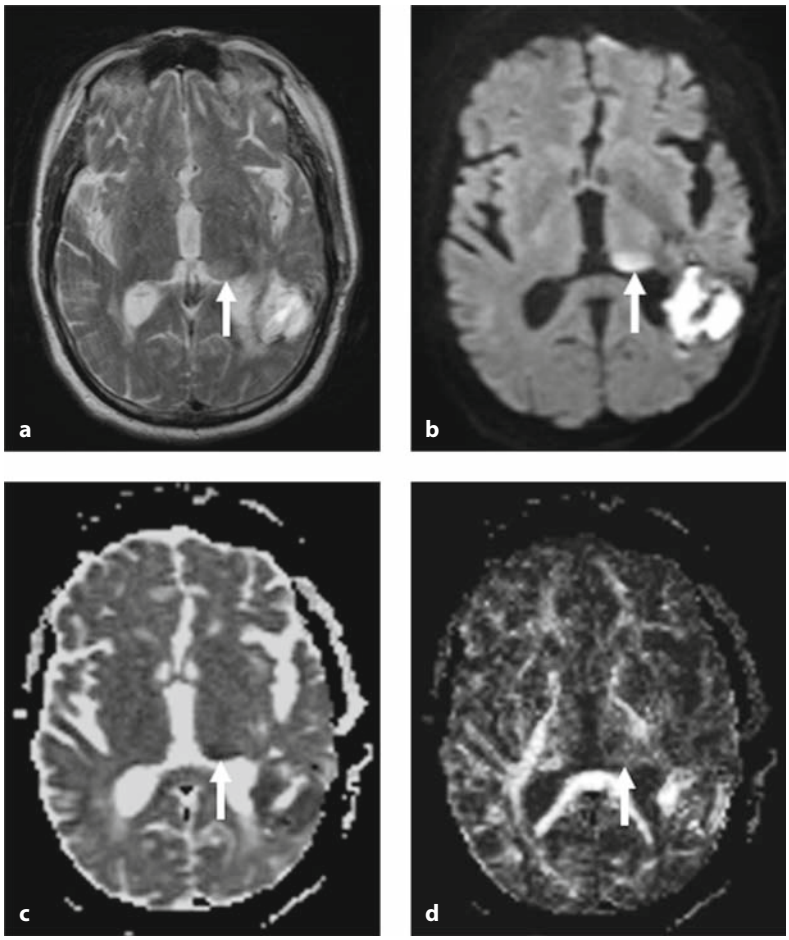

Figure 8.9 a–d

Posticta l lesion involving the pulvinar of the thalamus with intraparenchymal hemorrhage in a 65-year-old man. **a** T2-weighted image shows a subacute phase hemorrhage in the left temporoparietal cortex. Mild hyperintensity is noted in the ipsilateral pulvinar of the thalamus (*arrow*). **b–d** DW image shows the left pulvinar lesion as hyperintense associated with decreased ADC (**c**) and slightly decreased FA (**d**) (*arrows*). The hemorrhage is very high on the DW image with decreased ADC (**c**) and partially increased FA (**d**). (Courtesy of Gurol E, MD, The University of Iowa Hospitals and Clinics, USA)

signal abnormalities on DW imaging and ADC are seen in cytotoxic edema following status epilepticus, although they are sometimes reversible, as mentioned above [23].

8.4.6 Other Imaging Techniques for Epilepsy

Several other newer MR imaging techniques have been used in epilepsy. These include MR angiography [20], perfusion-weighted imaging [24], single-photon emission computed tomography (SPECT) [48], xenon CT [49] and positron emission tomography (PET) [50]. MR perfusion may provide information on the periictal phase in epileptic patients (Figs. 8.10 and 8.11) [51]. Diffusion tensor tractography demonstrates the relationship between the lesion and fiber tracts such as the corticospinal tract, uncinate fasciculus, and optic radiation, which is useful in preoperative planning (Figs. 8.12 and 8.13). MR spectroscopy can show metabolic changes such as decreased *N*-acetyl aspartate (NAA), and increased lactate and glutamate/glutamine peaks [52].

8.5 Hemiconvulsion–Hemiplegia Epilepsy Syndrome and Rasmussen Encephalitis

Hemiconvulsion–hemiplegia epilepsy (HHE) syndrome is one of the recognized sequelae of convulsive status epilepticus in infancy and early childhood: (1) less than 4 years of age; (2) prolonged seizures with unilateral predominance; and (3) sequelae of hemiconvulsion and hemiparesis [53, 54]. MR imaging shows signal abnormalities in the entire hemisphere. DW imaging shows diffuse cytotoxic edema confined

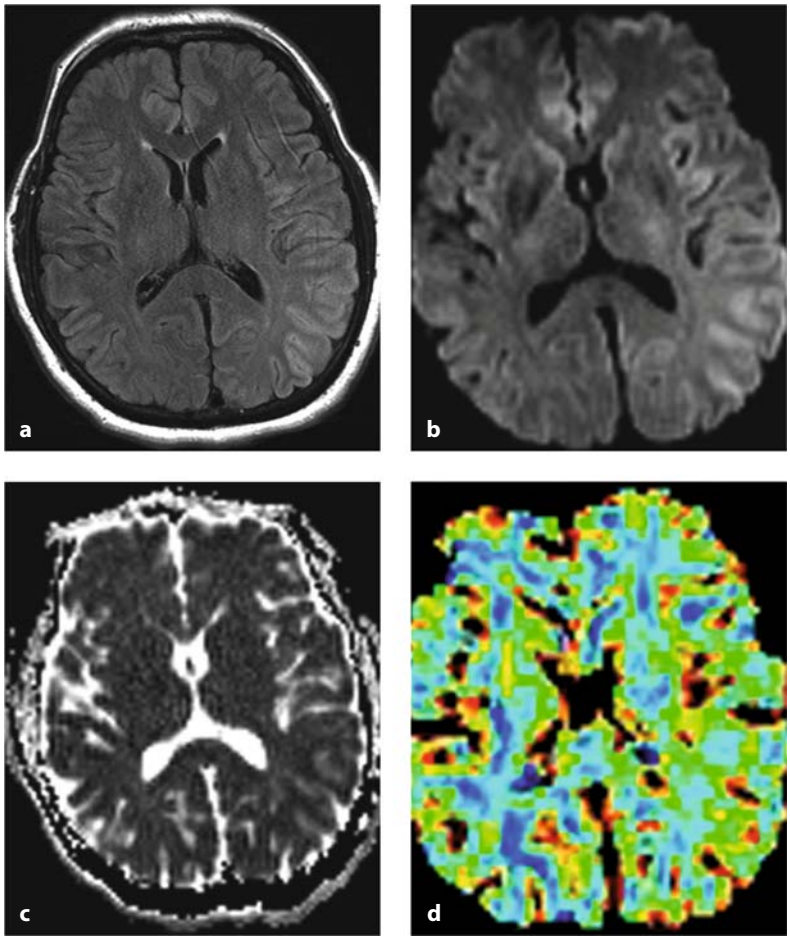

Figure 8.10 a–d

Postictal encephalopathy in a 45-year-old man. **a** FLAIR image shows mild hyperintensity in the left temporoparietal cortices. b, c DW image shows the lesion as hyperintense associated with slightly decreased ADC (**c**). **d** MR perfusion demonstrates slightly increased cerebral blood volume in the left temporoparietal area

to one hemisphere (Fig. 8.8). Epilepsia partialis continua or Rasmussen encephalitis is excluded on clinical grounds.

Rasmussen encephalitis, characterized by seizures, progressive hemiplegia, and psychomotor deterioration, is a chronic progressive inflammation of unknown etiology. Epilepsia partialis continua is the most common pattern of seizures. Glutamate receptor (GluR3) autoimmunity, associated with persistent viral infection, has recently been proposed as a cause [55]. Diagnosis is confirmed by pathology, showing laminar spongiform degeneration, perivascular T-cell lymphocyte cuffing, neuronal loss, gliosis, and microglial nodules. MR imaging shows T2 prolongation and progressive atrophy in the affected regions of the brain often involving the holohemisphere including the basal ganglia [56, 57]. DW imaging usually shows increased ADC values in the hemispheric lesion, but may show partially restricted diffusion areas [58, 59].

8.6 Limbic Encephalitis

Limbic encephalitis is initially described as a paraneoplastic syndrome characterized by an acute or subacute onset of confusion, temporal lobe seizures, short-term memory loss, and psychiatric symptoms [60, 61]. Limbic encephalitis is now known to be a relatively frequent autoimmune encephalitis [62]. It is associated with various antibodies including paraneoplastic antibodies (Hu, Yo, Ri, Ma1,Ma2, Cv2/CR MP5, Tr, amphiphysin, NMDA receptor) and non-paraneoplastic voltage-gated potassium channel (VGKC) antibodies, among others [63,64,65]. Neuropathologic features are dominant T-cell infil-

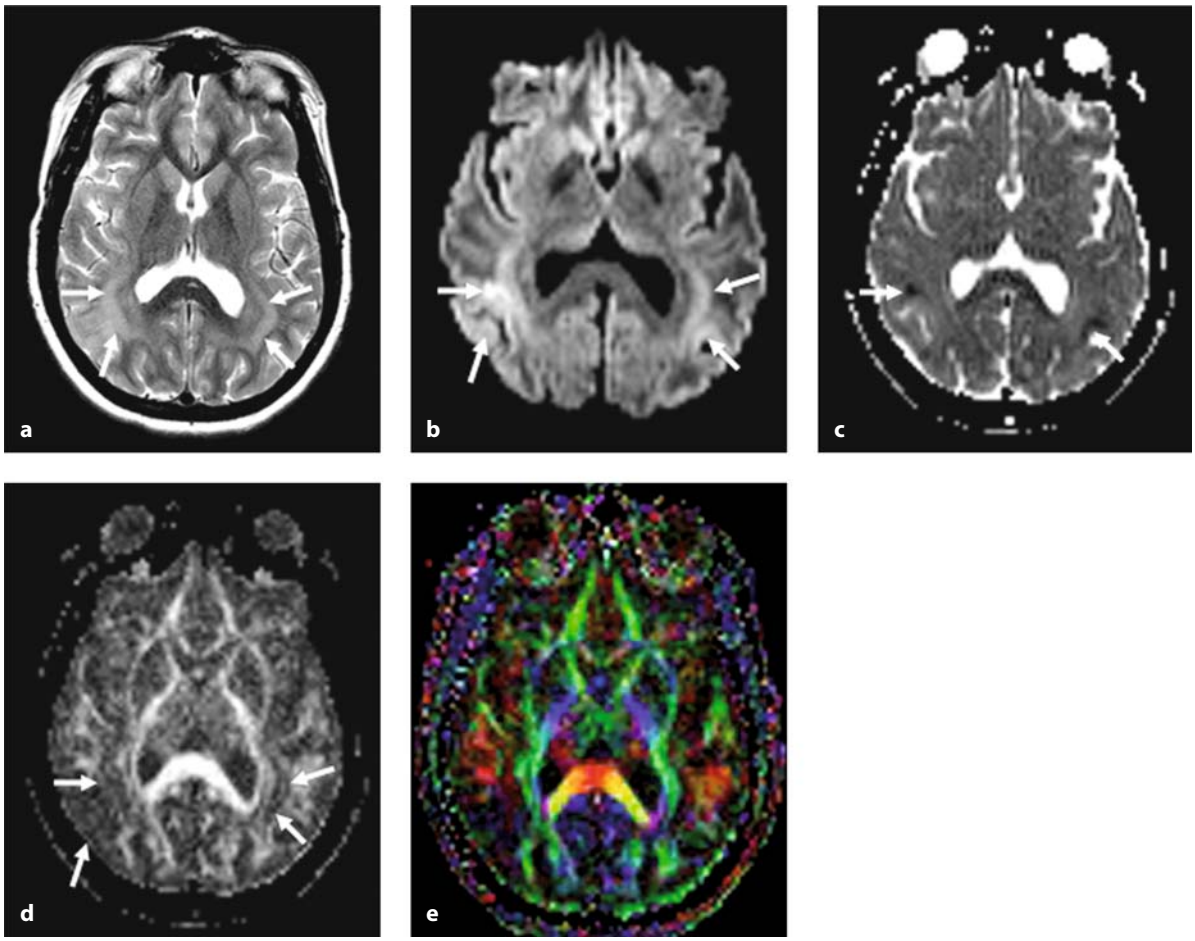

Figure 8.11 a–e

Band type heterotopia with postictal encephalopathy in a 21-year-old man. **a** T2-weighted image shows typical band type heterotopia (*arrows*) and mild hyperintensity in the right temporoparietal cortex. **b, c** DW image shows hyperintense lesions in the temporoparietal cortices and heterotopic gray matter bilaterally (*arrows*) with partially decreased ADC (*arrows*). **d, e** DT imaging with FA and color map demonstrate the band type heterotopia and the edema as decreased anisotropy (*arrows*). f MR perfusion shows preserved perfusion in the cortex and heterotopic gray matter

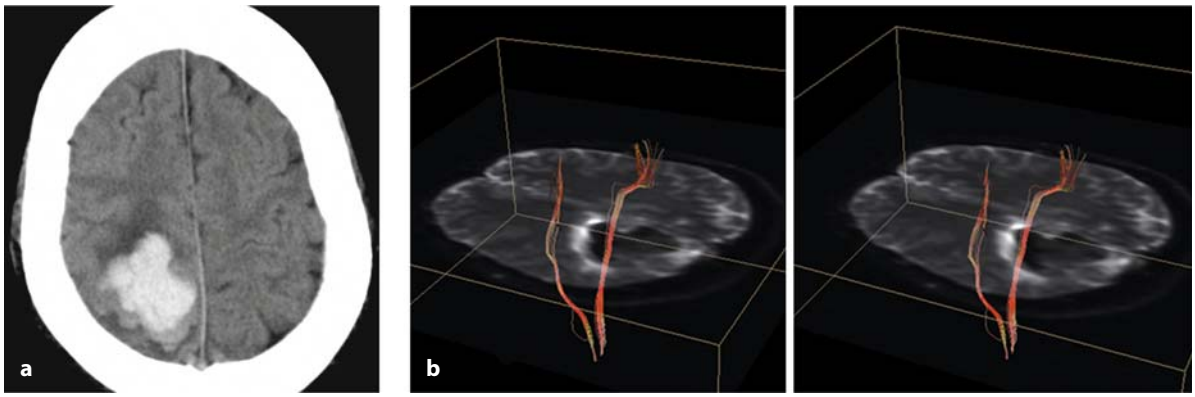

Figure 8.12 a, b

Arteriovenous malformation and subcortical hemorrhage in a 33-year-old man. **a** CT shows a subcortical hemorrhage with edema adjacent to the right central sulcus. **b** DT imaging tractography images (stereo view) demonstrate the relationship between the hematoma and corticospinal tract, which is useful for the preoperative planning. (Courtesy of Taoka T. MD, Nara Medical University, Japan)

Figure 8.13 a, b

Glioma in the hippocampus in a 66-year-old woman. **a** Coronal T2-weighted image show a focal hyperintense mass lesion in the right hippocampus (*arrow*). **b** DT imaging tractography images (stereo view) demonstrate the relationship between the tumor and unscinate faciculus (*yellow*) and optic radiation (*green*). The unscinate faciculus and optic radiation appear to be kissing at the temporal stem. (Courtesy of Taoka T. MD, Nara Medical University, Japan)

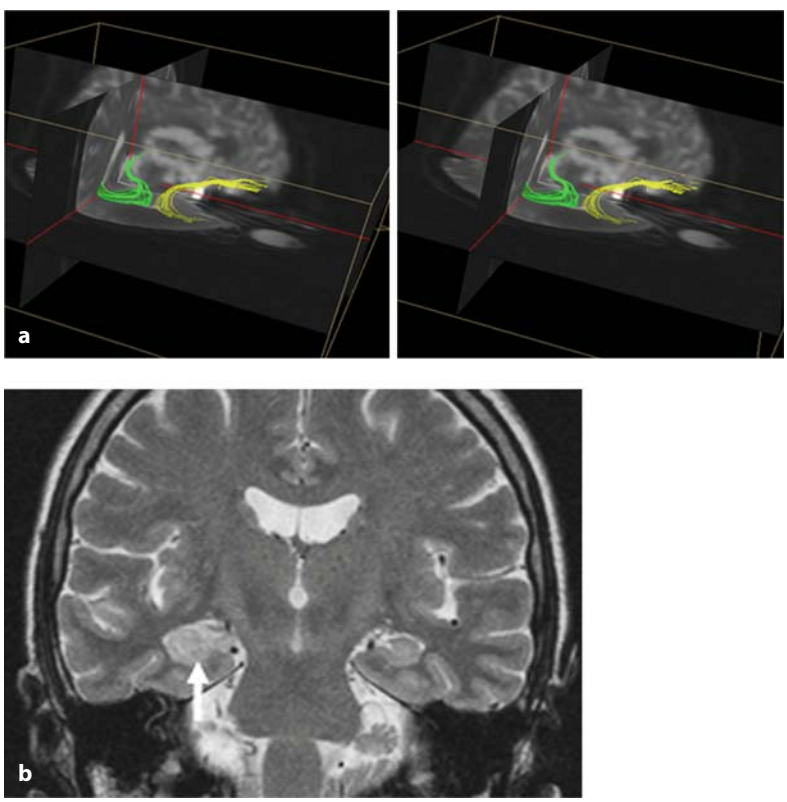

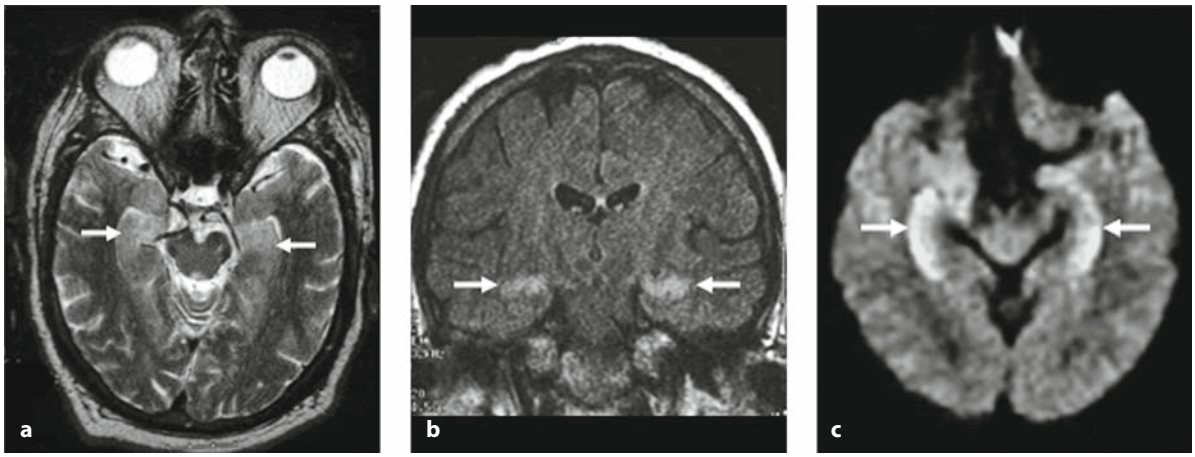

Figure 8.14 a–c

Limbic encephalitis (non-paraneoplastic) in a 45-year-old woman. **a** T2-weighted and **b** coronal FLAIR show hyperintense lesions in the bilateral hippocampi (*arrow*). **c** DW image shows these lesions as hyperintense (*arrows*) associated with slightly increased ADC (not shown)

tration, neuronal loss, activated microglia, neuronophagia, and reactive astrocytosis.

MR imaging contributes to the diagnosis by showing T2 and FLAIR high signal and swelling in the medial temporal lobe which is more often bilateral than unilateral. Contrast enhancement is very rare. Significant atrophy is visible approximately 1 year after symptom onset [61]. Extralimbic involvement (pyriform cortex, insula etc.) is occasionally seen. DW imaging shows hyperintensity in the medial temporal lobe with slightly increased ADC (Fig. 8.14) [66]. Paraneoplastic limbic encephalitis is treated with tumor removal and immunotherapy. Limbic encephalitides related to cell membrane antigen (NMDA receptor, VGKC, unknown neuropil antigens) are more sensitive to immunotherapy (IVIg, plasma exchange, corticosteroids, cyclophosphamide, rituximab) than those with intracellular antigens [67].

8.7 Focal Lesion in the Splenium of the Corpus Callosum in Epileptic Patients

The cause of the focal lesion sometimes seen in the splenium of the corpus callosum is not known. It has been speculated to represent transient focal edema, related to the transhemispheric connection and secondary generalized seizure activity [68]. Interhemispheric propagation of the seizure activity is via the splenial callosal fibers. The splenium contains decussating fibers originating in the temporal lobe, which are likely to be involved in a secondarily generalized seizure. The lesion may be related to toxic effects of antiepileptic drugs such as dilantin, carbamazepine and vigabatrin [69]. Abrupt withdrawal and dose reduction of antiepileptic drugs may contribute to the transient edema, mediated by the influence of these drugs on fluid balance systems, namely arginine–vasopressin [70]. However, reversible splenial lesions are apparent in a wide spectrum of diseases and conditions, including infectious encephalitis/meningitis /encephalopathy, alcoholism and malnutrition, hypoglycemia, osmotic myelinolysis, trauma, other medications (5-FU, metronidazole, IVIg), systemic lupus erythematosus, and leptomeningeal malignancy [71-78]. The cause of the reversible splenial lesions should be related to more integrated mechanisms such as CNS cytokinopathy and excitotoxic mechanisms [6, 79, 80].

Conventional MR imaging shows a non-hemorrhagic, hyperintense lesion on T2-weighted and FLAIR images, which is slightly hypointense on T1-weighted images (Figs. 8.15, 8.16). There is no enhancement after administration of intravenous gadolinium. DW imaging shows an acute, hyperintense lesion in the

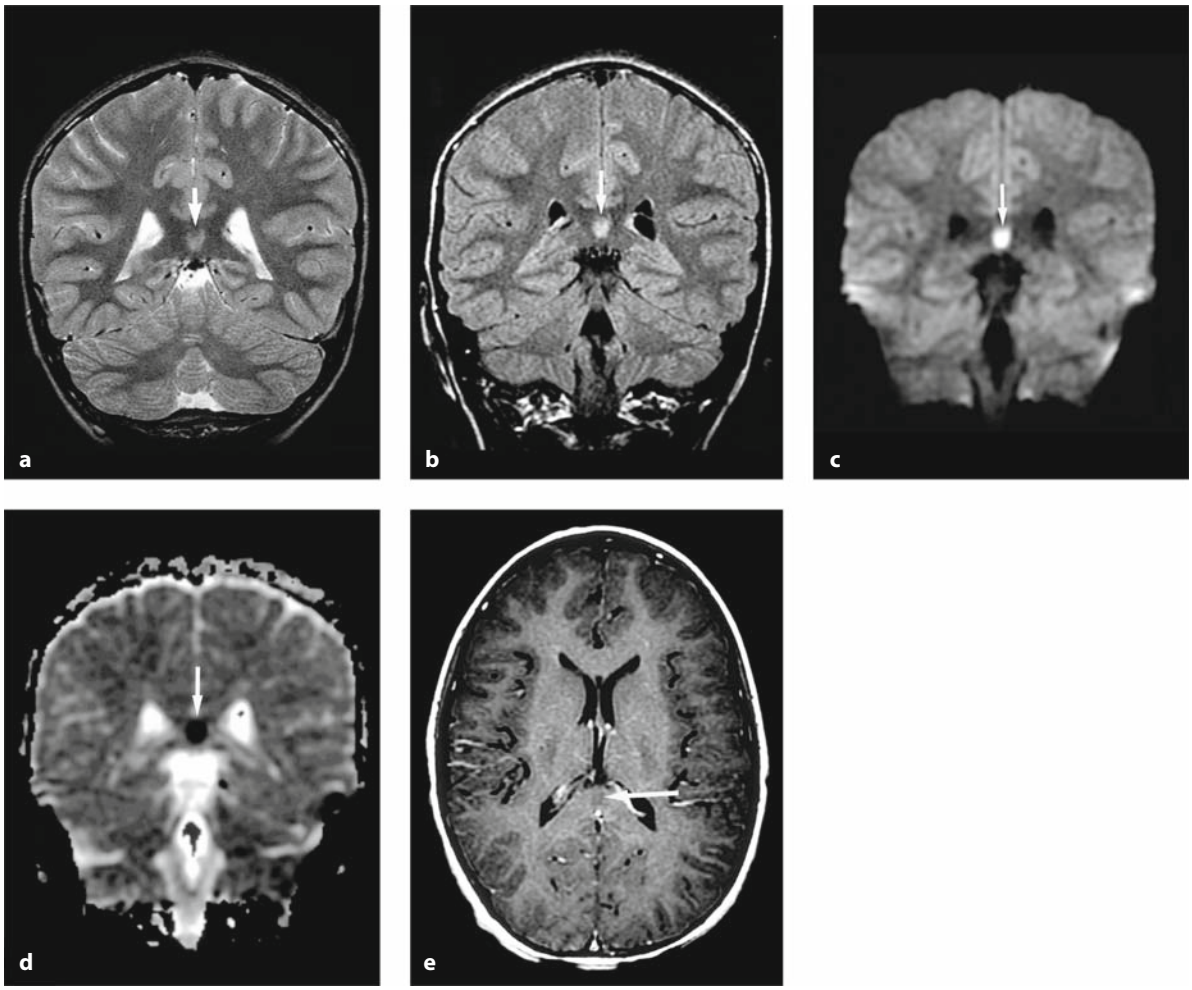

Figure 8.15 a–e

Focal lesion in the splenium of the corpus callosum in epilepsy in a 9-year-old patient presenting with intractable partial seizures since the age of 4 years. **a** Coronal T2-weighted and **b** FLAIR images 3 days after seizure show a small round hyperintense lesion in the central portion of the splenium of the corpus callosum (*arrow*). **c** Coronal DW image shows this lesion (*arrow*) as hyperintense associated with decreased ADC (**d**). **e** Gadolinium-enhanced T1-weighted image reveals mild hypointense lesion with no abnormal enhancement (*arrow*)

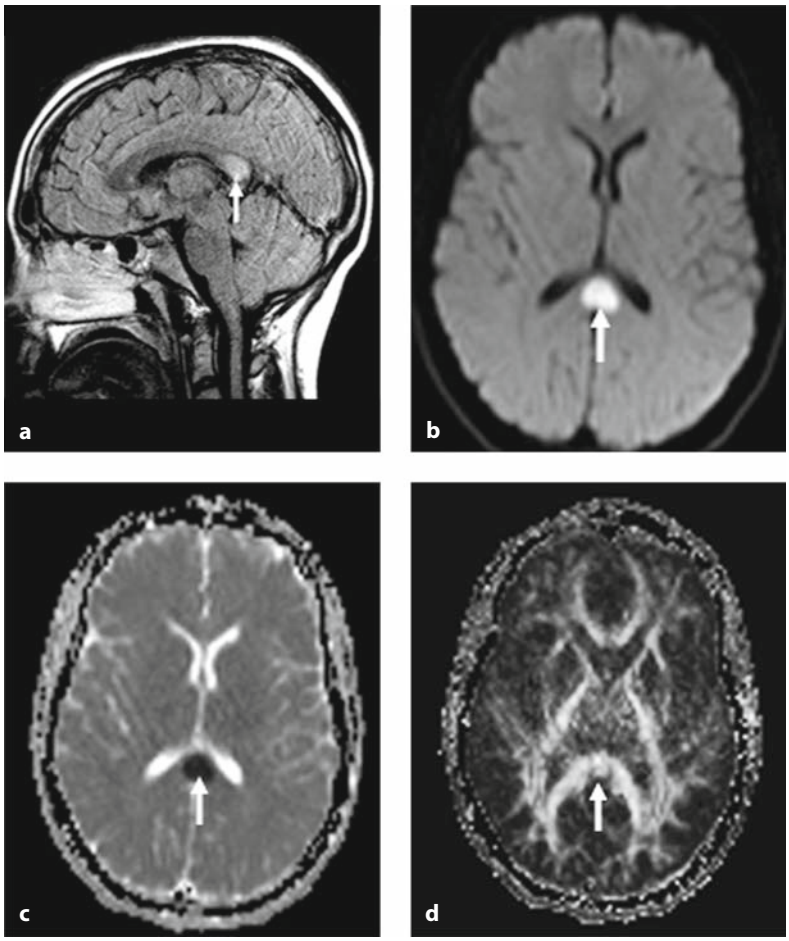

Figure 8.16 a–d

Focal lesion in the splenium of the corpus callosum with intractable epilepsy in a 25-year-old patient. **a** Sagittal FLAIR image shows hyperintense lesion in the splenium of the corpus callosum (*arrow*). **b-d** DW image shows an oval-shaped splenium lesion as hyperintense associated with decreased ADC (**c**) and preserved normal FA values (**d**) (*arrow*)

splenium of the corpus callosum, with decreased ADC. Fractional anisotropy (FA) map shows preserved FA values in the lesion (Fig 8.16). These findings indicate that the lesion represents a cytotoxic edema in myelinated tracts (intramyelinic edema) in the corpus callosum, which can be a reversible lesion.

8.7 Conclusion

Routine MR imaging is widely used to evaluate various primary brain diseases that cause seizures. These include stroke, anoxic injury, trauma, tumor, infections, demyelination, congenital anomaly and many others. The typical MR finding in a seizure patient is an area of T2 hyperintensity, often located in the cerebral cortex, subcortical white matter, hippocampus, thalamus and/or cerebellum. DW imaging can provide additional information concerning the brain edema and tell whether it is primarily cytotoxic or vasogenic. This is important since cytotoxic edema following seizures indicates a more serious injury and, although often reversible, may result in brain atrophy and necrosis.

References

1. Gestaut H (1973) Dictionary of epilepsy, part 1: definitions. Geneva: World Health Organization
2. Commission on Classification and Terminology of the International League Against Epilepsy (1989) Proposal for revised classification of epilepsies and epileptic syndromes. Epilepsia 30:389–399
3. Wasterlain CG, et al. (1993) Pathophysiological mechanisms of brain damage from status epilepticus. Epilepsia 34(Suppl 1):S37–S53
4. Rothman SM, et al. (1987) Excitotoxicity and NMDA receptor. Trends Neurosci 10:301–304

5. Babb TL, Lieb JP, Brown WJ, Pretorius J, Crand PH (1984) Distribution of pyramidal cell density and hyperexcitability in the epileptic human hippocampal formation. Epilepsia 25:721–728
6. Moritani T, Smoker WR, Sato Y, Numaguchi Y, Westesson PL (2005) Diffusion-weighted imaging of acute excitotoxic brain injury. AJNR Am J Neuroradiol 26:216-28
7. Herron CE, Williamson R, Collingridge GL (1985) A selective N-methyl-D-aspartate antagonist depresses epileptiform activity in rat hippocampal slices. Neurosci Lett 61:255–260
8. Aminoff MJ, Simon RP, Wiedemann E (1980) Status epilepticus. Causes, clinical features and consequences in 98 patients. Am J Med 69:657–666
9. Annegers JF, Hauser WA, Lee JR, Rocca WA (1995) Incidence of acute symptomatic seizures in Rochester, Minnesota, 1935–1984. Epilepsia 36:327–333
10. Durack DT, Whitly RJ, Scheld WM (1991) Approach to the patient with central nervous system infection. In: Sheld WM (eds). Infections of the central nervous system. New York: Raven Press, pp 41–86
11. Maertens PM, Machen BC, Williams JP, Evans O, Bebin J, Bassam B, Lum GB (1987) Magnetic resonance imaging of mesial temporal sclerosis: case reports. J Comput Tomogr 11:136–139
12. Heinz ER, Crain BJ, Radtke RA, Burger PC, Friedman AH, Djang WT, Wilkinson WE (1990) MR imaging in patients with temporal lobe seizures: correlation of results with pathologic findings. AJNR Am J Neuroradiol 11:827–832
13. Meiners LC, van Gils A, Jansen GH, de Kort G, Witkamp TD, Ramos LM, Valk J, Debets RM, van Huffelen AC, van Veelen CW, et al (1994) Temporal lobe epilepsy: the various MR appearances of histologically proven mesial temporal sclerosis. AJNR Am J Neuroradiol 15:1547–1555
14. Jack CR Jr, Rydberg CH, Krecke KN, Trenerry MR, Parisi JE, Rydberg JN, Cascino GD, Riederer SJ (1996) Mesial temporal sclerosis: diagnosis with fluid-attenuated inversion-recovery versus spin-echo MR imaging. Radiology 199:367–373
15. Lee DH, Gao FQ, Rogers JM, Gulka I, Mackenzie IR, Parrent AG, Kubu CS, Munoz DG, McLachlan RS, Blume WT, Girvin JP (1998) MR in temporal lobe epilepsy: analysis with pathologic confirmation. AJNR Am J Neuroradiol 19:19–27
16. Silverstein AM, Alexander JA (1998) Acute postictal cerebral imaging. AJNR Am J Neuroradiol 20:1485–1488
17. Chan S, et al. (1996) Reversible signal abnormalities in the hippocampus and neocortex after prolonged seizures. AJNR Am J Neuroradiol 17:1725–1731
18. Horowitz SW, et al. (1992) Complex partial seizure-induced transient MR enhancement. J Comput Assist Tomogr 16:814–816
19. Kassem-Moussa H, et al. (2000) Early diffusion-weighted MR imaging abnormalities in sustained seizure activity. AJR Am J Roentgenol 174:1304–1306
20. Cox JE, Mathews VP, Santos CC, Elster AD (1995) Seizure-induced transient hippocampal abnormalities on MR: correlation with positron emission tomography and electroencephalography. AJNR Am J Neuroradiol 16:1736–1738
21. Lansberg MG, et al. (1999) MRI abnormalities associated with partial status epilepticus. Neurology 52:1021–1027
22. Tien RD, Felsberg GJ (1995) The hippocampus in status epilepticus: demonstration of signal intensity and morphologic changes with sequential fast spin-echo MR imaging. Radiology 194:249–256
23. Kim JA, Chung JI, Yoon PH, et al. (2001) Transient MR signal changes in patients with generalized tonicoclonic seizure or status epilepticus: periictal diffusion-weighted imaging. AJNR Am J Neuroradiol 22:1149–1160
24. Flacke S, Wullner U, Keller E, Hamzei F, Urbach H (2000) Reversible changes in echo planar perfusion- and diffusion-weighted MRI in status epilepticus. Neuroradiology 42:92–95
25. Men S, et al. (2000) Selective neuronal necrosis associated with status epilepticus: MR findings. AJNR Am J Neuroradiol 21:1837–1840
26. Soffer D, Melamed E, Assaf Y, et al. (1986) Hemispheric brain damage in unilateral status epilepticus. Ann Neurol 20:737–740
27. Walker MT, et al. (1999) Profound neocortical atrophy after prolonged, continuous status epilepticus. AJR Am J Roentgenol 173:1712–1713
28. Kodama F, Ogawa T, Sugihara S, Kamba M, Kohaya N, Kondo S, Kinoshita T (2003) Transneuronal degeneration in patients with temporal lobe epilepsy: evaluation by MR imaging. Eur Radiol 13:2180-2185
29. Oikawa H, Sasaki M, Tamakawa Y, Kamei A (2001) The circuit of Papez in mesial temporal sclerosis: MRI. Neuroradiology 43:205-210
30. Rosenberg DS, Mauguière F, Demarquay G, Ryvlin P, Isnard J, Fischer C, Guénot M, Magnin M (2006) Involvement of medial pulvinar thalamic nucleus in human temporal lobe seizures. Epilepsia 47:98-107
31. Kimiwada T, Juhász C, Makki M, Muzik O, Chugani DC, Asano E, Chugani HT (2006) Hippocampal and thalamic diffusion abnormalities in children with temporal lobe epilepsy. Epilepsia 47:167-175
32. Yoo SY, Chang KH, Song IC, Han MH, Kwon BJ, Lee SH, Yu IK, Chun CK (2002) Apparent diffusion coefficient value of the hippocampus in patients with hippocampal sclerosis and in healthy volunteers. AJNR Am J Neuroradiol 23:809–812
33. Dodson WE, DeLorenzo RJ, Pedley TA, et al. (1993) Treatment of convulsive status epilepticus. Recommendations of the Epilepsy Foundation of America's Working Group on Status Epilepticus. JAMA 270:854–859
34. Hauser WA (1990) Status epilepticus: epidemiologic considerations. Neurology 40(5 Suppl 2):9–13
35. Sperk G, Lassmann H, Baran H, Kish SJ, Seitelberger F, Hornykiewicz O (1983) Kainic acid induced seizures: neurochemical and histopathological changes. Neuroscience 10:1301–1315
36. Siesjo BK, Wieloch T (1986) Epileptic brain damage: pathophysiology and neurochemical pathology. Adv Neurol 44:813–847
37. DeGiorgio CM, Tomiyasu U, Gott PS, Treiman DM (1992) Hippocampal pyramidal cell loss in human status epilepticus. Epilepsia 33:23–27

38. Ingvar M, Morgan PF, Auer RN (1988) The nature and timing of excitotoxic neuronal necrosis in the cerebral cortex, hippocampus and thalamus due to flurothyl-induced status epilepticus. Acta Neuropathol (Berl) 75:362–369
39. Dam AM, Dam M (1991) Neuropathology. In: Dam M, Gram L (eds) Comprehensive epileptology. New York: Raven Press, pp 43–55
40. Bruton CJ (1988) The neuropathology of temporal lobe epilepsy. New York: Oxford University Press
41. Corsellis JAN, Bruton CJ (1983) Neuropathology of status epilepticus in humans. In: Delgado-Escuta AV, Wasterlain CG, Treiman DM, Porter RJ (eds) Advances in neurology: status epilepticus. New York: Raven Press, 34:129–139
42. Zhong J, Petroff OA, Prichard JW, Gore JC (1993) Changes in water diffusion and relaxation properties of rat cerebrum during status epilepticus. Magn Reson Med 30:241–246
43. Zhong J, Petroff OA, Prichard JW, Gore JC (1995) Barbiturate-reversible reduction of water diffusion coefficient in flurothyl-induced status epilepticus in rats. Magn Reson Med 33:253–256
44. Righini A, Pierpaoli C, Alger JR, Di Chiro G (1994) Brain parenchyma apparent diffusion coefficient alterations associated with experimental complex partial status epilepticus. Magn Reson Imaging 12:865–871
45. Nakasu Y, Nakasu S, Morikawa S, Uemura S, Inubushi T, Handa J (1995) Diffusion-weighted MR in experimental sustained seizures elicited with kainic acid. AJNR Am J Neuroradiol 16:1185–1192
46. Christopher JW, et al (2000) Rapid alterations in diffusion-weighted images with anatomic correlates in a rodent model of status epilepticus. AJNR Am J Neuroradiol 21:1841–1852
47. Wang Y, et al. (1996) Postictal alteration of sodium content and apparent diffusion coefficient in epileptic rat brain induced by kainic acid. Epilepsia 37:1000–1006
48. Wichert-Ana L, Velasco TR, Terra-Bustamante VC, et al. (2001) Typical and atypical perfusion patterns in periictal SPECT of patients with unilateral temporal lobe epilepsy. Epilepsia 42:660–666
49. Johnson DW, Hogg JP, Dasheiff R, Yonas H, Pentheny S, Jumao-as A (1993) Xenon/CT cerebral blood flow studies during continuous depth electrode monitoring in epilepsy patients. AJNR Am J Neuroradiol 14:245–252
50. Theodore WH (1999) Cerebral blood flow and glucose metabolism in human epilepsy. Adv Neurol 79:873–881
51. Szabo K, Poepel A, Pohlmann-Eden B, Hirsch J, Back T, Sedlaczek O, Hennerici M, Gass A (2005) Diffusion-weighted and perfusion MRI demonstrates parenchymal changes in complex partial status epilepticus. Brain 128:1369-1376
52. Fazekas F, Kapeller P, Schmidt R, Stollberger R, Varosanec S, Offenbacher H, Fazekas G, Lechner H (1995) Magnetic resonance imaging and spectroscopy findings after focal status epilepticus. Epilepsia 36:946–949
53. Salih MA, Kabiraj M, Al-Jarallah AS, El Desouki M, Othman S, Palkar VA (1997) Hemiconvulsion-hemiplegia-epilepsy syndrome. A clinical, electroencephalographic and neuroradiological study. Childs Nerv Syst 13:257–263
54. Freeman JL, Coleman LT, Smith LJ, Shield LK (2002) Hemiconvulsion-hemiplegia-epilepsy syndrome: characteristic early magnetic resonance imaging findings. J Child Neurol 17:10–16
55. Whitney KD, McNamara JO (2000) GluR3 autoantibodies destroy neural cells in a complement-dependent manner modulated by complement regulatory proteins. J Neurosci 20:7307-7316
56. Geller E, Faerber EN, Legido A, Melvin JJ, Hunter JV, Wang Z, de Chadarevian JP. (1998) Rasmussen encephalitis: complementary role of multitechnique neuroimaging. AJNR Am J Neuroradiol 19:445-449
57. Chiapparini L, Granata T, Farina L, Ciceri E, Erbetta A, Ragona F, Freri E, Fusco L, Gobbi G, Capovilla G, Tassi L, Giordano L, Viri M, Dalla Bernardina B, Spreafico R, Savoiardo M (2003) Diagnostic imaging in 13 cases of Rasmussen's encephalitis: can early MRI suggest the diagnosis? Neuroradiology 45:171-183
58. Sener RN.(2003) Diffusion MRI and spectroscopy in Rasmussen's encephalitis. Eur Radiol 13:2186-2191
59. Arias M, Dapena D, Arias-Rivas S, Sesar A, Vázquez F, Prieto A, Suárez-Peñaranda JM (2006) Rasmussen encephalitis in the sixth decade: magnetic resonance image evolution and immunoglobulin response. Eur Neurol 56:236-239
60. Graus F, Saiz A (2008) Limbic encephalitis: an expanding concept. Neurology 70:500-501
61. Urbach H, Soeder BM, Jeub M, Klockgether T, Meyer B, Bien CG (2006) Serial MRI of limbic encephalitis. Neuroradiology 48:380-386
62. Irani S, Lang B (2008) Autoantibody-mediated disorders of the central nervous system. Autoimmunity 41:55-65
63. Iizuka T, Sakai F, Ide T, Monzen T, Yoshii S, Iigaya M, Suzuki K, Lynch DR, Suzuki N, Hata T, Dalmau J (2008) Anti-NMDA receptor encephalitis in Japan: long-term outcome without tumor removal. Neurology 70:504-511
64. Mochizuki Y, Mizutani T, Isozaki E, Ohtake T, Takahashi Y (2006) Acute limbic encephalitis: a new entity? Neurosci Lett 394:5-8
65. Asaoka K, Shoji H, Nishizaka S, Ayabe M, Abe T, Ohori N, Ichiyama T, Eizuru Y (2004) Non-herpetic acute limbic encephalitis: cerebrospinal fluid cytokines and magnetic resonance imaging findings. Intern Med 43:42-48
66. Sener RN. (2002) MRI and diffusion MRI in nonparaneoplastic limbic encephalitis. Comput Med Imaging Graph 26:339-342
67. Tüzün E, Dalmau J (2007)Limbic encephalitis and variants: classification, diagnosis and treatment. Neurologist 13:261-271
68. Cohen-Gadol AA, Britton JW, Jack CR Jr, Friedman JA, Marsh WR (2002) Transient postictal magnetic resonance imaging abnormality of the corpus callosum in a patient with epilepsy. Case report and review of the literature. J Neurosurg 97:714–717
69. Kim SS, Chang KH, Kim ST, Suh DC, Cheon JE, Jeong SW, Han MH, Lee SK (1999) Focal lesion in the splenium of the corpus callosum in epileptic patients: antiepileptic drug toxicity? AJNR Am J Neuroradiol 20:125–129

70. Polster T, Hoppe M, Ebner A (2001) Transient lesion in the splenium of the corpus callosum: three further cases in epileptic patients and a pathophysiological hypothesis. J Neurol Neurosurg Psychiatry 70: 459–463
71. Maeda M, Tsukahara H, Terada H, Nakaji S, Nakamura H, Oba H, Igarashi O, Arasaki K, Machida T, Takeda K, Takanashi JI (2006)Reversible splenial lesion with restricted diffusion in a wide spectrum of diseases and conditions. J Neuroradiol 33:229-236
72. Takanashi J, Barkovich AJ, Shiihara T, Tada H, Kawatani M, Tsukahara H, Kikuchi M, Maeda M (2006) Widening spectrum of a reversible splenial lesion with transiently reduced diffusion. AJNR Am J Neuroradiol 27:836-838
73. Kim JH, Choi JY, Koh SB, Lee Y (2007) Reversible splenial abnormality in hypoglycemic encephalopathy. Neuroradiology 49:217-222
74. Doherty MJ, Jayadev S, Watson NF, Konchada RS, Hallam DK (2005)Clinical implications of splenium magnetic resonance imaging signal changes. Arch Neurol 62:433-437
75. Conti M, Salis A, Urigo C, Canalis L, Frau S, Canalis GC (2007) Transient focal lesion in the splenium of the corpus callosum: MR imaging with an attempt to clinical-physiopathological explanation and review of the literature. Radiol Med (Torino) 112:921-935
76. da Rocha AJ, Reis F, Gama HP, da Silva CJ, Braga FT, Maia AC Jr, Cendes F (2006) Focal transient lesion in the splenium of the corpus callosum in three non-epileptic patients. Neuroradiology 48:731-735
77. Cecil KM, Halsted MJ, Schapiro M, Dinopoulos A, Jones BV (2002) Reversible MR imaging and MR spectroscopy abnormalities in association with metronidazole therapy. J Comput Assist Tomogr 26:948-951
78. Appenzeller S, Faria A, Marini R, Costallat LT, Cendes F (2006) Focal transient lesions of the corpus callosum in systemic lupus erythematosus. Clin Rheumatol 25:568-571
79. Tada H, Takanashi J, Barkovich AJ, Oba H, Maeda M, Tsukahara H, Suzuki M, Yamamoto T, Shimono T, Ichiyama T, Taoka T, Sohma O, Yoshikawa H, Kohno Y (2004) Clinically mild encephalitis/encephalopathy with a reversible splenial lesion. Neurology 63:1854-1858
80. Bulakbasi N, Kocaoglu M, Tayfun C, Ucoz T (2006) Transient splenial lesion of the corpus callosum in clinically mild influenza-associated encephalitis/encephalopathy. AJNR Am J Neuroradiol 27:1983-1986

Demyelinating and Degenerative Disease

9.1 Demyelinating Disease

Demyelination is divided into two types: primary and secondary. Primary demyelination is defined as the abnormality or dysfunction of the oligodendrocytes. Secondary demyelination is defined as changes of the myelin secondary to neuronal or axonal degeneration associated with ischemia, infection, or metabolic/toxic disease. Demyelinating disease usually refers to the primary demyelination, which pathologically represents perivenous demyelination and inflammatory cell infiltration. Idiopathic inflammatory–demyelinating diseases comprises the spectrum of demyelinating diseases based on purely clinical considerations, including monophasic, multiphasic, and progressive disorders from a localized form to multifocal or diffuse variants [1, 2].

9.1.1 Multiple Sclerosis

Multiple sclerosis (MS) is the most common demyelinating disease characterized by relapses and remissions of neurological disturbances. It is classified according to the clinical course: (1) relapsing-remitting (80%), (2) primary progressive (10%), (3) secondary progressive (10%) [1]. MS plaques are usually well-demarcated round-to-oval and frequently show finger-like extension in the periphery that follow the path of a small or medium-sized vessel (Dawson's finger), which was observed by Dr. Dawson (neuropathologist) in 1916 [3]. Corticosteroids and plasmapheresis are used for the acute exacerbation of MS, while interferon-β prevents the relapse and progression of MS.

MR imaging has become important for the diagnosis of MS, which is integrated with clinical and paraclinical diagnostic methods as in McDonald's new criteria [4]. Axial T2-weighted and fluid-attenuated inversion-recovery (FLAIR) images show well-demarcated round-to-oval lesions along the white matter tract. These MR sequences are sensitive for depicting focal lesions, but sometimes lack histopathologic specificity. Other lesions such as inflammation, edema, reactive gliosis, axonal loss, and secondary demyelination sometimes have a similar appearance [5]. On sagittal FLAIR images, subcallosal striations and ependymal "dot-dash" signs have been reported as relatively specific early findings of MS (Fig. 9.1) [6, 7]. Enhancement in the MS plaque on post-contrast T1-weighted images is related to the activity of the plaque, which histologically represents inflammation and breakdown of the blood-brain barrier. Hypointense T1 lesions in MS are usually caused by matrix destruction and loss of axons [8]. The T1 hypointense MS lesion usually has a low magnetization transfer ratio (MTR), and correlates better with clinical disability than proton density/T2 lesions [9]. Decreased MTR is also observed in normal-appearing white matter in MS patients [10].

MS plaques can show hyper-, iso-, or hypointensity on diffusion-weighted (DW) images, with increased ADC, in contrast-enhancing active plaques (Figs. 9.1, 9.2) and chronic plaques alike (Fig. 9.3). An enhancing portion of the MS plaques tends to have mildly increased ADC, representing prominent inflammation and blood-brain barrier breakdown with mild demyelination, while the non-enhancing portions tend to have more increased ADC, representing scarring with mild inflammation and myelin loss [11, 12]. ADC values of MS plaques seem to be related to the severity of MS. The ADC values in secondary-progressive MS are higher than those in relapsing-remitting MS [13].

In some cases of the acute or subacute phase of MS, decreased ADC is observed in plaques (Figs. 9.4 and 9.5) [14]. The decreased ADC is presumably due to intramyelinic edema with inflammatory cell infiltration and accumulation of myelin breakdown products (cytotoxic plaque). The decreased ADC area can be located in the periphery of a plaque. Intramyelinic edema occurs in the myelin sheath itself and/or in the intramyelinic cleft. Some of the intramyelinic edema is completely reversible.

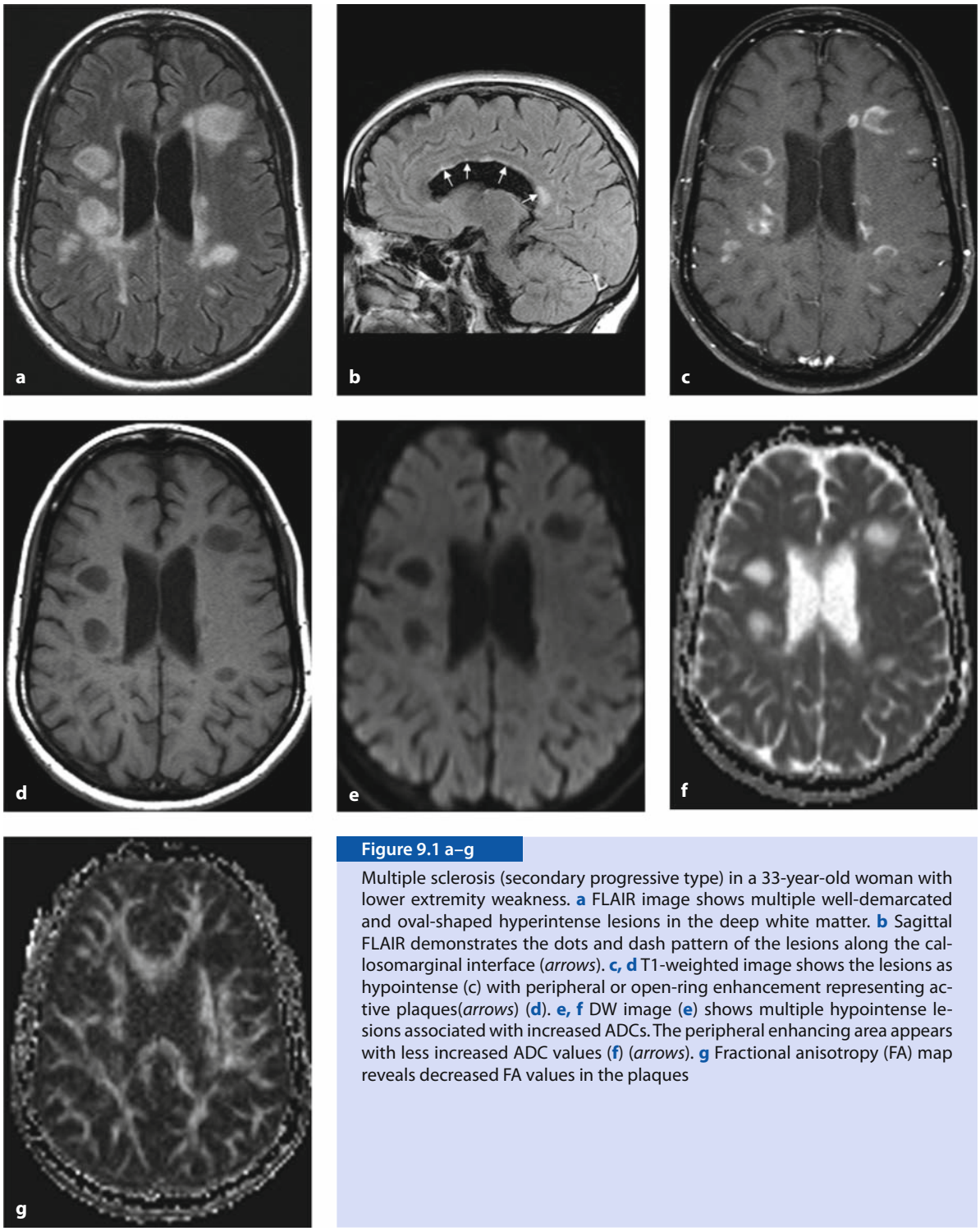

Figure 9.1 a–g

Multiple sclerosis (secondary progressive type) in a 33-year-old woman with lower extremity weakness. **a** FLAIR image shows multiple well-demarcated and oval-shaped hyperintense lesions in the deep white matter. **b** Sagittal FLAIR demonstrates the dots and dash pattern of the lesions along the callosomarginal interface (*arrows*). **c, d** T1-weighted image shows the lesions as hypointense (c) with peripheral or open-ring enhancement representing active plaques(*arrows*) (**d**). **e, f** DW image (**e**) shows multiple hypointense lesions associated with increased ADCs. The peripheral enhancing area appears with less increased ADC values (**f**) (*arrows*). **g** Fractional anisotropy (FA) map reveals decreased FA values in the plaques

Figure 9.2 a–d

Multiple sclerosis (active plaque) in a 28-year-old man presenting with visual problems. **a** T2-weighted image shows a round hyperintense lesion in the right frontotemporal region (*arrow*). **b** Gadolinium T1-weighted image shows mild enhancement of this lesion, representing an active plaque. **c, d** DW image shows a hyperintense lesion associated with increased ADC (*arrow*), which represents T2 shine-through

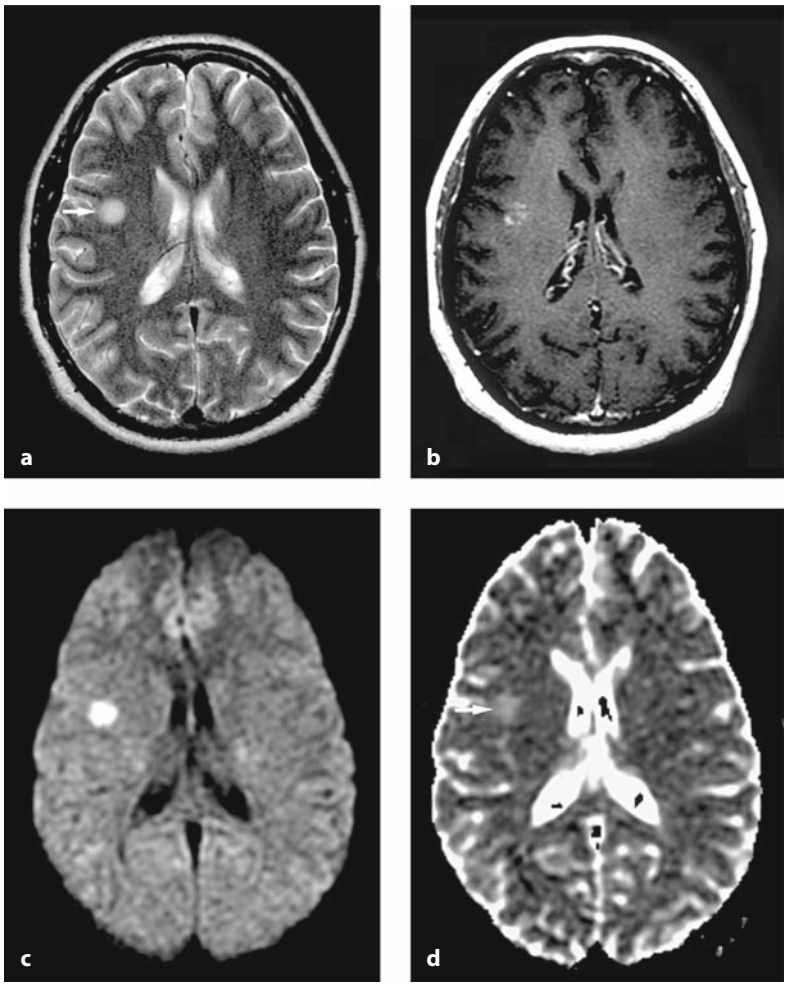

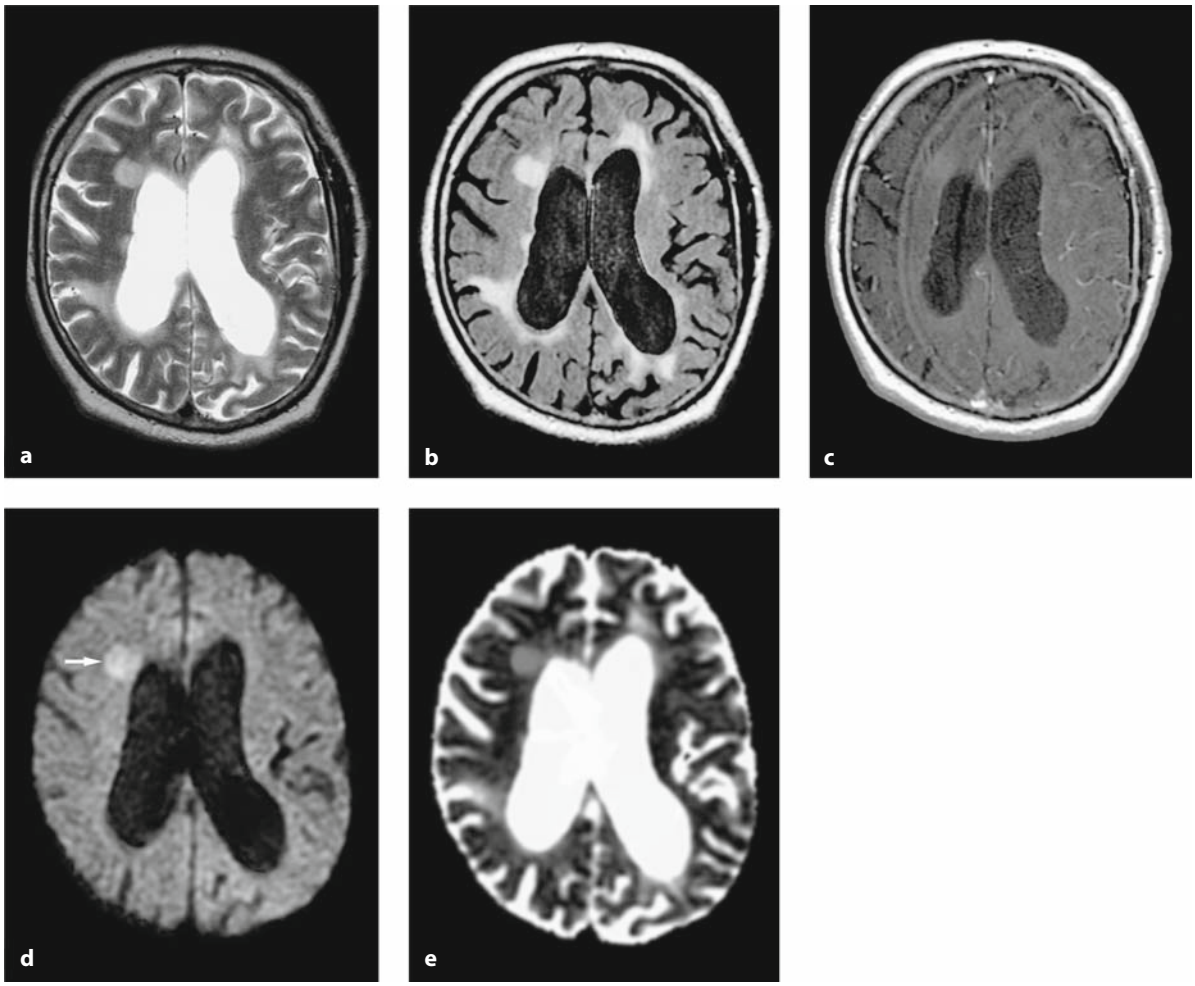

Figure 9.3 a–e

Multiple sclerosis (chronic plaque) in a 59-year-old man with a long history of recurrent seizures. T2-weighted (**a**) and FLAIR (**b**) images show multiple periventricular hyperintense lesions with ex-vacuo ventricular dilatation. **c** On gadolinium T1-weighted image with magnetization transfer contrast, there is no enhancement of these lesions, representing relatively chronic plaques. **d** DW image shows a right frontal lesion as mildly hyperintense (*arrow*). **e** ADC is increased (T2 shine-through) and the other periventricular lesions are isointense with increased ADC (T2 washout)

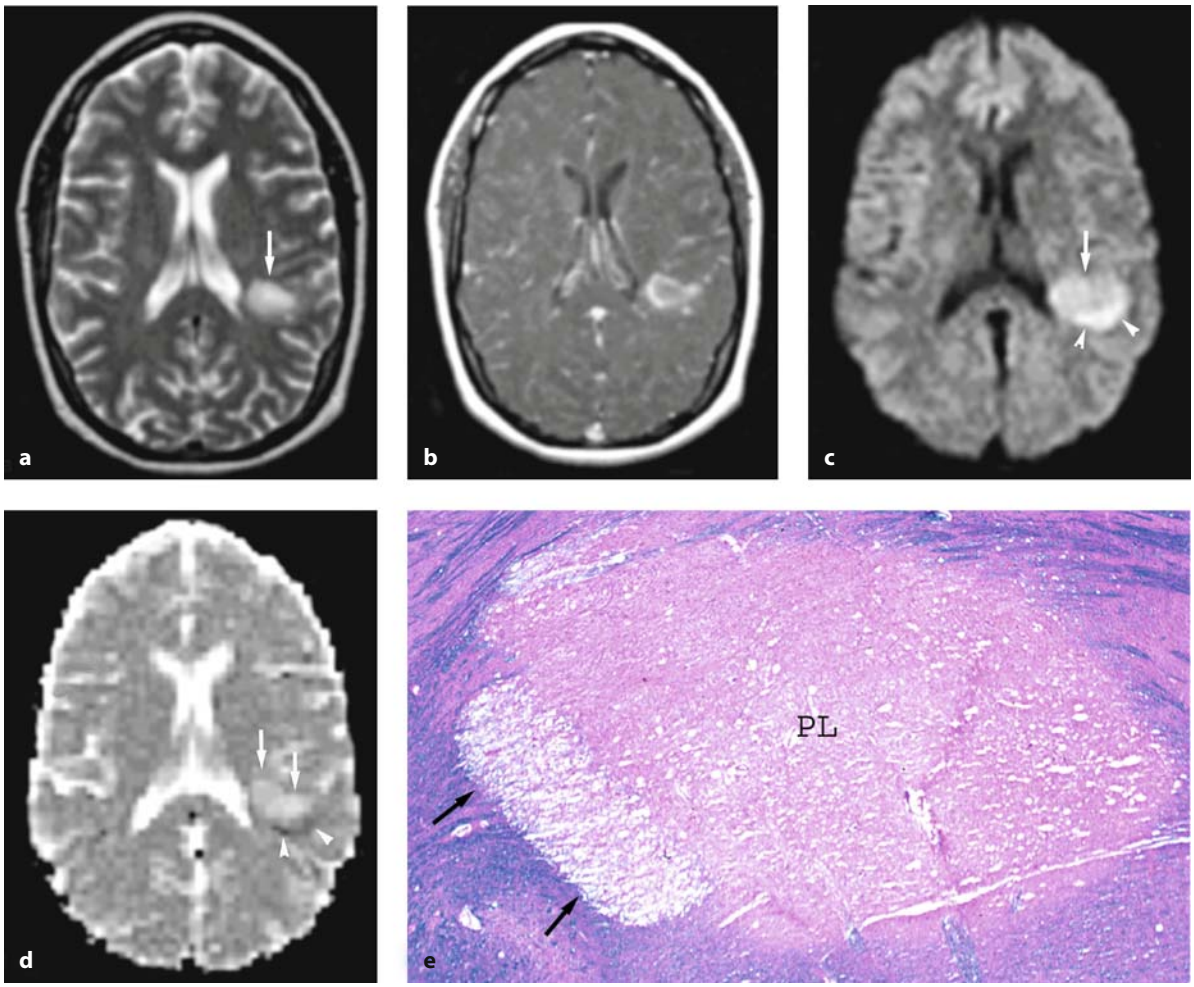

Figure 9.4 a–e

Multiple sclerosis (active plaque) in a 36-year-old woman presenting with subacute onset of progressive aphasia. **a** T2-weighted image shows an oval-shaped, hyperintense lesion in the left periventricular white matter (*arrow*). **b** Gadolinium T1-weighted image with magnetization transfer contrast shows rim enhancement of this lesion. **c** DW image shows combination of a moderately hyperintense (*arrow*) and a significantly hyperintense lesion (*arrowheads*). **d** The moderately hyperintense lesion on DW image with increased ADC may represent demyelination (*arrows*), and the very hyperintense lesion on DW image with decreased ADC may represent intramyelinic edema (*arrowheads*). **e** Histopathology of another case shows that intramyelinic edema (*arrows*) is located in the periphery of a plaque (*PL*) (Luxol fast blue PAS stain, original magnification ×40). (From [90])

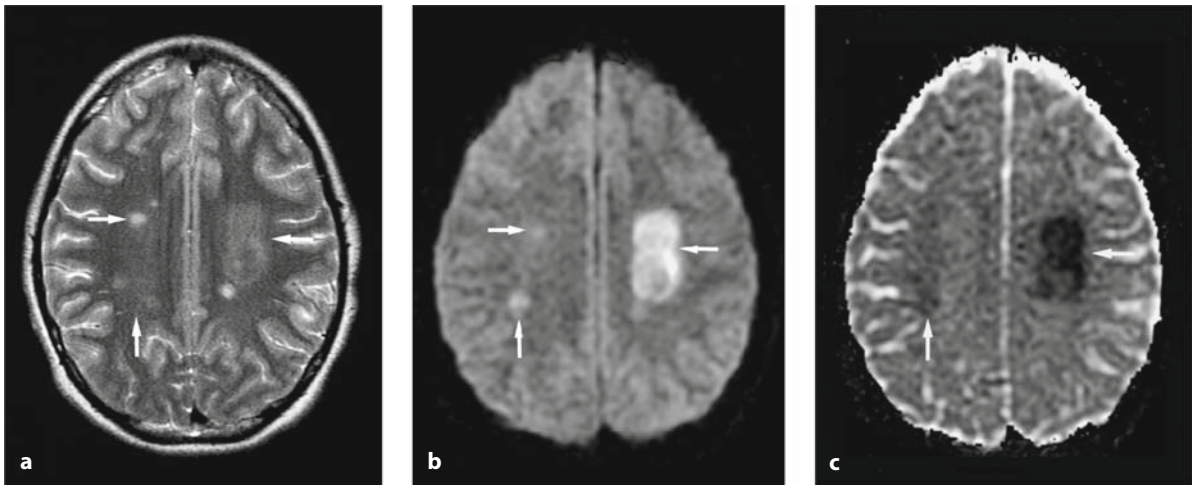

Figure 9.5 a–c

Multiple sclerosis (acute plaque) in a 13-year-old girl who presented with acute-onset right-sided weakness and dysarthria. **a** T2-weighted image shows multiple hyperintense lesions in the bilateral centrum semiovale (*arrows*). **b** DW image shows some lesions as hyperintense (*arrows*). **c** ADC is decreased representing acute cytotoxic plaques (*arrows*)

MS plaques are reported to have decreased anisotropy [11, 15] (Fig. 9.1). The increased ADC and decreased fractional anisotropy (FA) in MS plaques are thought to be related to an increase in the extracellular space due to demyelination, perivascular inflammation with vasogenic edema, gliosis, and axonal loss.

Increased ADC and decreased FA values can be seen in normal-appearing white matter of MS patients. This is clearly different from healthy control subjects, where these abnormalities are not seen [15-17]. The ADC and FA abnormalities may represent occult small MS plaques, gliosis, or Wallerian degeneration. Increased ADC and FA are observed in cortical lesions in MS [18].

9.1.1.1 Baló's Concentric Sclerosis

Baló's concentric sclerosis is a rare demyelination disease and a variant of multiple sclerosis [1, 19-21]. In 1927, Baló described the case of a young student who died rapidly after the onset [22]. Post-mortem examination showed large lesions with concentric layers or a lamellar pattern, representing alternating bands of partial preservation of myelin and myelin loss. Baló named this particular form "leukoencephalitis periaxialis concentrica." It often has an acute monophasic course and is more common in individuals of Asian descent, suggesting a special genetic predisposition. Baló-like lesions can occasionally be seen during an exacerbation of relapsing and remitting MS with a nonfatal course [1].

MR imaging shows a multilayered appearance, mostly hyperintense on T2-weighted images, and it shows a variable degree of enhancement. DW images show hyperintensity with a reduced ADC in the acute phase of Baló's concentric sclerosis and Baló-like lesions (Fig. 9.6) [23-25]. Follow-up DW imaging shows increased ADC in the chronic lesion. Corticosteroids are effective for treatment.

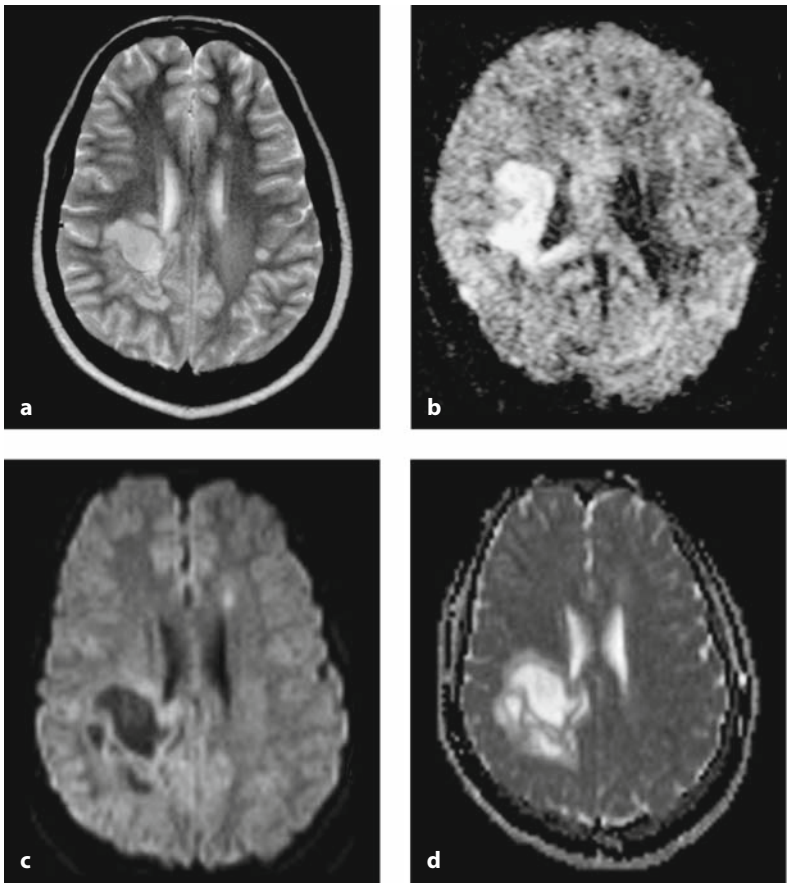

Figure 9.6 a–d

Baló's concentric sclerosis in a 17-year-old female patient who presented with stroke-like symptoms. **a** T2-weighted image shows a large hyperintense mass with a multilayered appearance in the right posterior periventricular and deep white matter. **b** DW image shows the lesions as very hyperintense. The ADC map was not obtained at this time. **c, d** A 2-month follow-up DW image shows the lesion as hypointense with increased ADC

9.1.1.2 Myelinoclastic Diffuse Sclerosis (Schilder's Disease)

Myelinoclastic diffuse sclerosis, also known as inflammatory diffuse sclerosis and Schilder's disease, is a rare primary demyelination disorder and is now considered to be a variant of MS [1, 26, 27]. In 1912, Schilder described the case of a 14-year-old girl with mental deterioration who died after 19 weeks. An autopsy revealed large areas of sharply demarcated plaques of demyelination in both hemispheres. Schilder named this specific form "encephalitis periaxialis diffusa" [28]. The characteristic pathological features are demyelination of the white matter, lymphocytic perivascular infiltrates, and microglial proliferation.

MR imaging shows large T2 hyperintense lesions with irregular or smooth enhancing rims in the deep and subcortical white matter. The "open-ring" imaging sign is characteristic of tumefactive demyelination and is useful in differentiating it from a neoplasm or abscess [29]. The enhancement is shaped like an open-ring or a crescent circumscribed to the white matter, but the enhancement is not identified to the cortical side. DW imaging shows a thin, smooth, hyperintense rim with decreased ADC, and surrounding hypointense areas with increased ADC (Fig. 9.7)

9.1.2 Acute Disseminated Encephalomyelitis

Acute disseminated encephalomyelitis (ADEM) is an immune-mediated inflammatory disorder of the CNS, usually triggered by an inflammatory response to viral infections or vaccinations [30]. The neurologic picture of ADEM commonly reflects a multifocal but usually monophasic involvement, while MS is characterized by recurrent episodes in both time and space. ADEM lesions tend to resolve, partially or completely, and new lesion formation rarely occurs

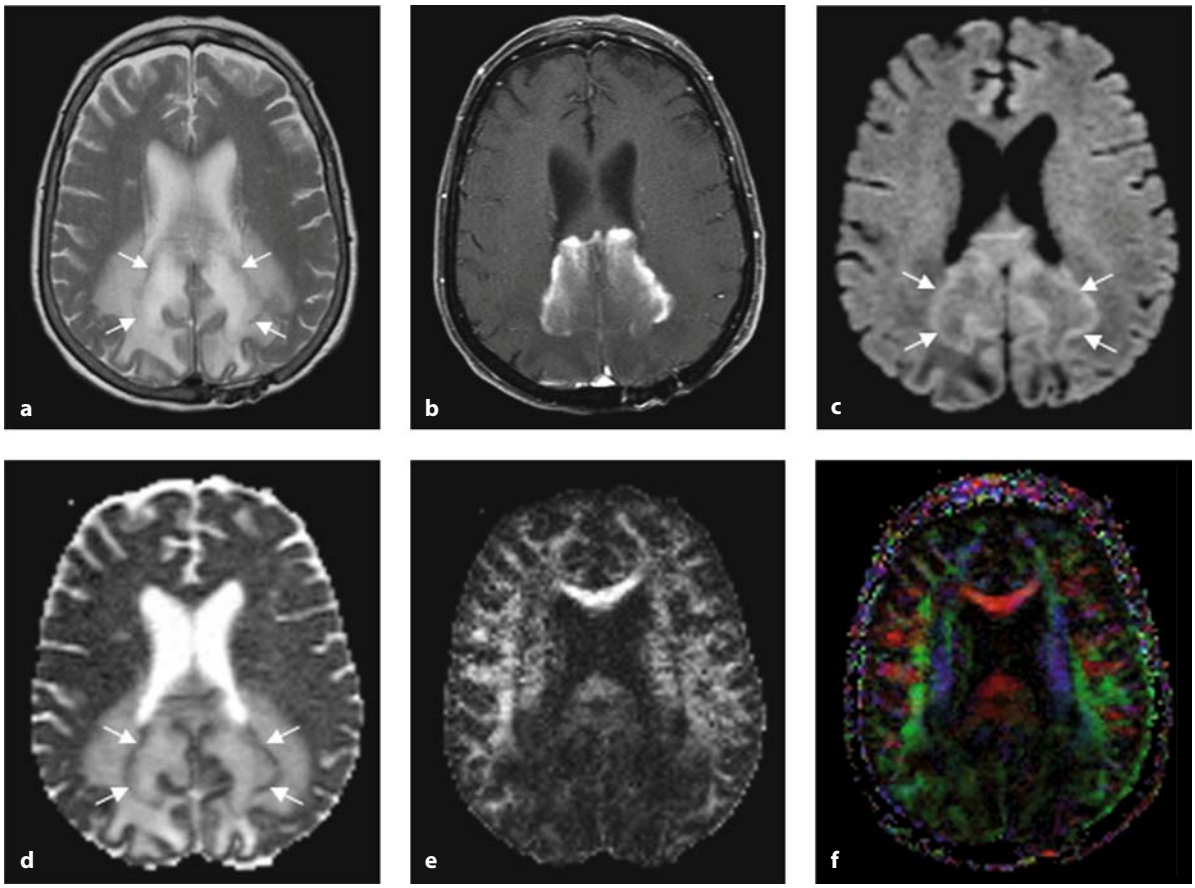

Figure 9.7 a–f

Myelinoclastic diffuse sclerosis in an 80-year-old woman with confusion. **a** T2-weighted image shows symmetric large hyperintense lesions with slightly low signal curvilinear areas (*arrows*) involving the posterior corpus callosum and occipital white matter bilaterally. **b** Post-contrast T1-weighted image shows symmetric irregular enhancement along the curvilinear T2 low signal areas. **c, d** DW image shows the curvilinear areas as isointense with iso ADC, corresponding to active demyelination (*arrows*). The surrounding areas are mildly hypointense on DW imaging with increased ADC, which probably represents vasogenic edema and demyelination. **e, f** FA and color maps show decreased anisotropy in both areas

(5-8%) [30]. Inflammatory demyelinating lesions are observed in the supratentorial and infratentorial white matter, brain stem, spinal cord, and also in the thalami and basal ganglia, especially in children. Involvement of the subcortical white matter is nearly a constant finding, which helps to distinguish ADEM from MS. Pathologic findings include perivenous demyelination, infiltration of lymphocytes and macrophages, hyperemia, edema, endothelial swelling, and hemorrhage.

MR imaging shows ill-defined T2 and FLAIR hyperintense lesions asymmetrically distributed in the white and gray matter. The incidence of gadolinium enhancing lesions on T1-weighted sequences is quite variable, depending on the stage of inflammation. Magnetization transfer ratio and ADC values in normal-appearing white matter of ADEM patients are similar to those of healthy control subjects [31]. DW imaging usually shows hyperintense lesions with increased ADC in the white matter due to expanded

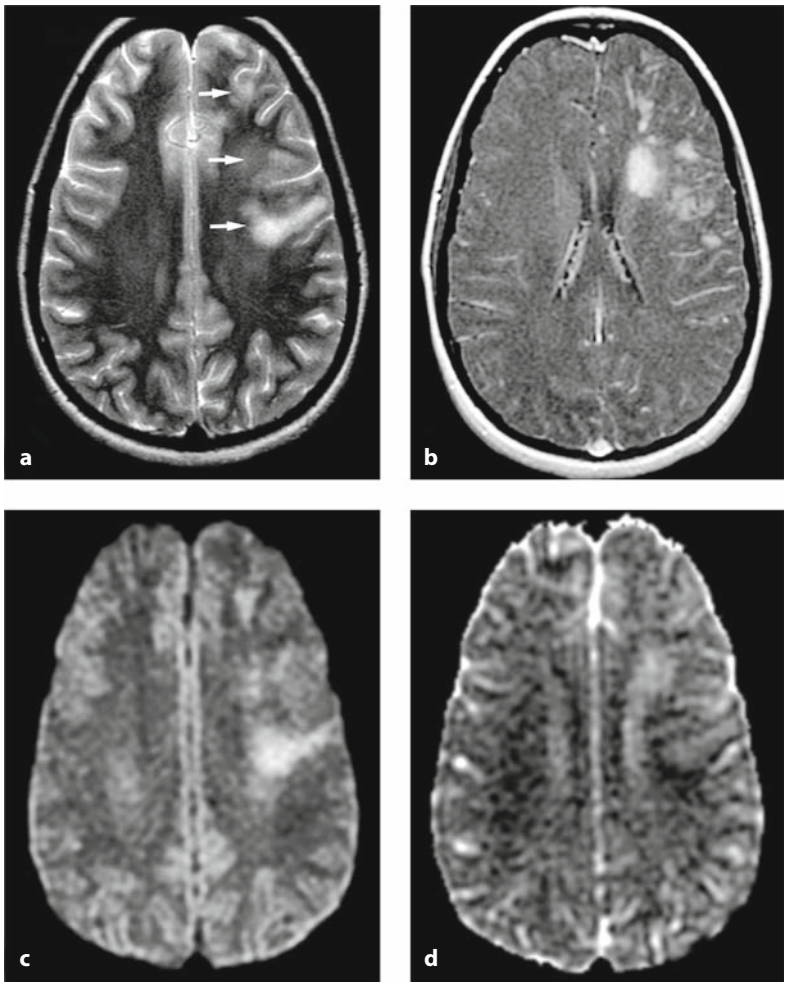

Figure 9.8 a–d

Acute disseminated encephalomyelitis in a 15-year-old male patient presenting with right hemiparesis. **a** T2-weighted image shows multiple ill-defined, hyperintense lesions in the left frontal lobe (*arrows*) **b** Gadolinium T1-weighted image with magnetization transfer contrast shows inhomogeneous enhancement of these lesions. **c** DW image shows left frontal lesions as hyperintense due to T2 shine-through. **d** ADC is increased

extracellular space with axonal loss, demyelination and vasogenic edema [32] (Fig. 9.8). However, in the acute stage, ADEM lesions can show decreased ADC, presumably due to intramyelinic edema (Fig. 9.9) [33, 34].

9.1.2.1 Acute Hemorrhagic Leukoencephalitis

Acute hemorrhagic leukoencephalitis (AHL; Hurst encephalitis) is an acute, rapidly progressive, and frequently fulminant inflammatory hemorrhagic demyelination, considered a hyperacute form of the maximum variant of ADEM [2, 30]. It is usually triggered by upper respiratory tract infections. MR imaging shows large white matter lesions with the surrounding edema [35]. DW imaging shows restricted diffusion in

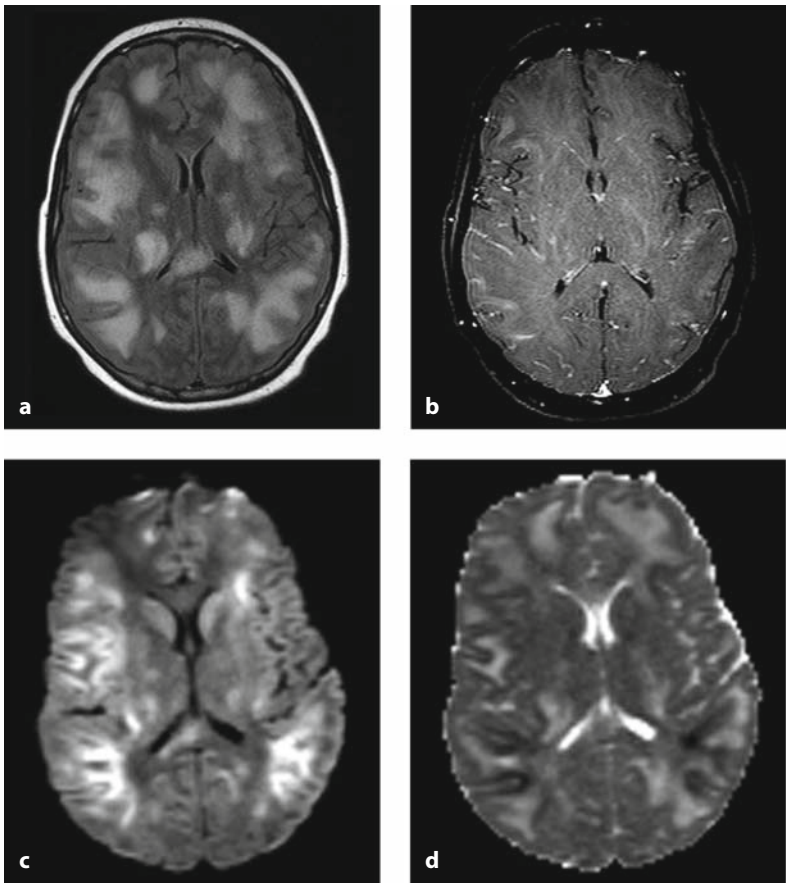

Figure 9.9 a–d

Acute disseminated encephalomyelitis in an 11-year-old boy with altered mental status. **a** FLAIR image shows multiple ill-defined, hyperintense lesions in the white matter, corpus callosum and basal ganglia, and thalami. **b** Post-contrast T1-weighted image shows mild enhancement in subcortical white matter lesions. **c, d** DW image shows multiple hyperintense lesions with increased ADC and partially decreased ADC in the peripheral area of the lesions, which probably represents a combination of vasogenic and cytotoxic edema with demyelination

the affected areas of the brain and hemorrhage, probably due to acute vasculitis with subsequent vessel occlusion (Fig. 9.10) [30, 36]. Death from brain edema is common within a week. Early and aggressive treatment is necessary using steroids, immunoglobulin, cyclophosphamide, and plasma exchange.

9.1.3 Progressive Multifocal Leukoencephalopathy

Progressive multifocal leukoencephalopathy (PML) is a fatal demyelinating disease of the central nervous system, occurring in immunocompromised patients

Figure 9.10 a–d

Acute hemorrhagic leukoencephalitis in a 48-year-old woman with altered mental status. **a** T2-weighted image shows multiple hyperintense lesions in the anterior and posterior white matter bilaterally. **b** T1-weighted image shows a hyperintense area in the left occipital lobe consistent with intracerebral hemorrhage (*arrows*). **c** DW image shows the lesions as mildly low or isosignal intensity areas with multiple very hyperintense foci consistent with a combination of vasogenic and cytotoxic edema. **d** DSA shows multiple stenosis in the anterior and middle cerebral arteries (*arrows*). This patient died within 1 week

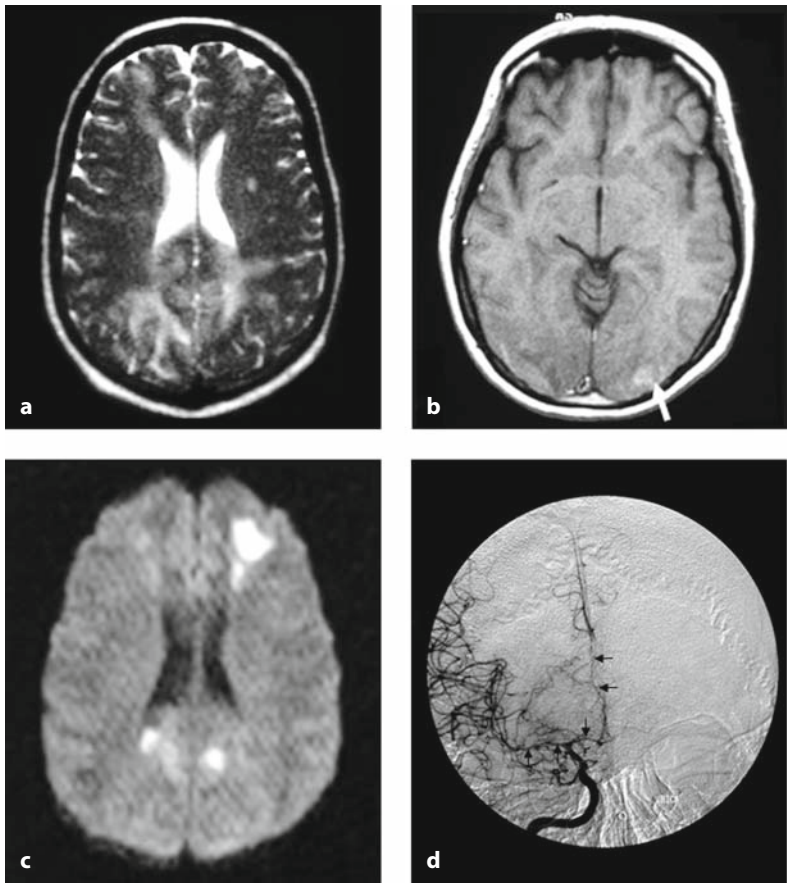

such as those with HIV infection or other conditions associated with impaired T-cell function [37]. Demyelination in PML results from the lytic infection of oligodendrocytes by JC papovavirus, spreading to adjacent oligodendrocytes. Diagnosis is established by the detection of JC virus DNA in the CSF.

MR imaging shows T2 and FLAIR hyperintensity white matter lesions, often extending to subcortical U-fibers. The degree of contrast enhancement of the lesion depends on the patient's immunological state. DW imaging usually shows mildly hyperintense lesions with increased ADC, which may have central

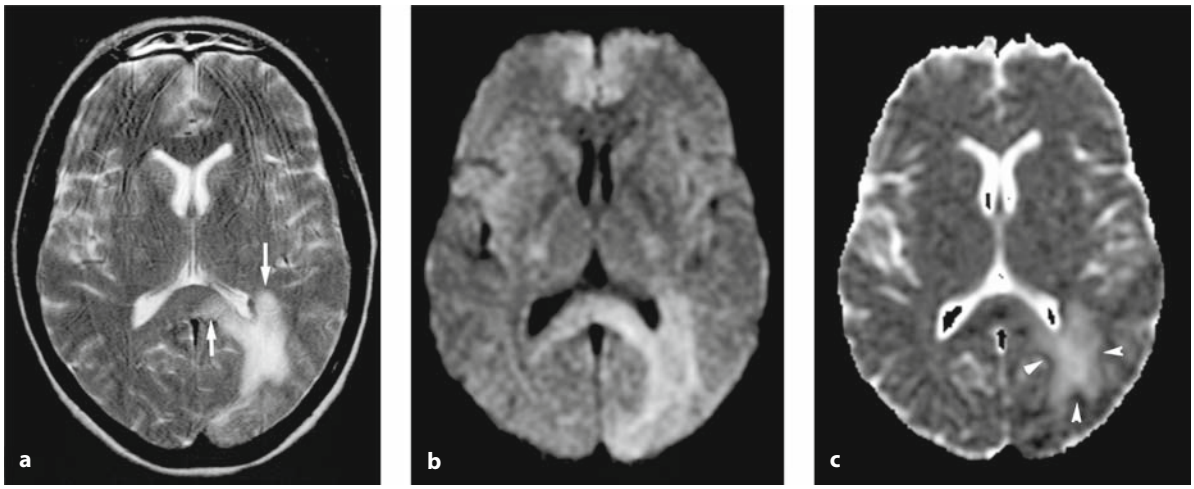

Figure 9.11 a–c

Progressive multifocal leukoencephalopathy in a 50-year-old woman presenting with right hemianopsia after chemotherapy for chronic lymphocytic leukemia. **a** T2-weighted image shows a hyperintense lesion in the left occipital white matter extending into the posterior corpus callosum (*arrows*). **b** DW image shows the lesion as hyperintense due to T2 shine-through. **c** ADC is increased. The peripheral area of the lesion seems to have relatively decreased ADC (*arrowheads*)

iso- or hypointense area. It occasionally shows hyperintensity with decreased ADC, especially at the margin of the lesion, reflecting different stages of the disease (Figs. 9.11, 9.12). These findings probably represent a concentric, centripetal process of tissue injury with central areas of necrosis surrounded by a progressing rim of active tissue injury with cytotoxic edema [38]. The peripheral hyperintensity rim on DW images with decreased ADC may represent JC virus-infected, swollen oligodendrocytes with viral intranuclear inclusions [37, 39, 40]. On diffusion-tensor (DT) imaging, the area of decreased fractional anisotropy (FA) is observed in PML, which represents abnormal microstructural integrity of the myelin sheath. This change may be observed earlier than the increased ADC which represents secondary diffuse cell loss (Fig. 9.12) [38].

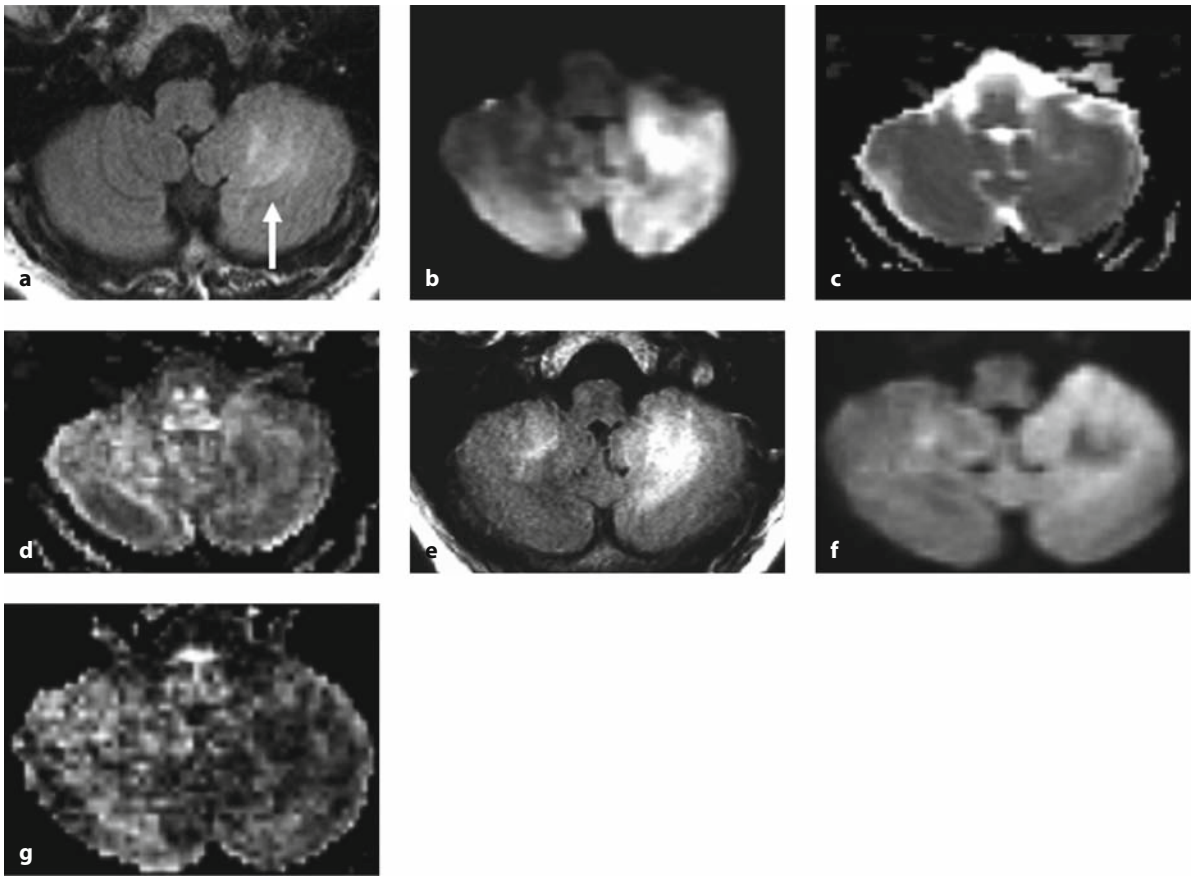

Figure 9.12 a–g

Progressive multifocal leukoencephalopathy (PML) in a 48-year-old man. **a** FLAIR image shows a hyperintense lesion in the left cerebellum (*arrow*). **b, c** DW imaging shows the lesion as hyperintense with iso or slightly increased ADC values, which suggests the early active phase of demyelination in PML. **d** FA is slightly decreased in this lesion. **e** Follow-up FLAIR image after 19 days shows increased size of the left cerebellar lesion extending to the right cerebellum. **f** DW image shows the left cerebellar lesion as mildly hyperintense with a central hypointensity, suggesting vasogenic edema, demyelination, and necrosis. **g** FA map showed a significantly enlarged area of decreased FA in the left cerebellum suggesting ongoing tissue damage. (Courtesy of Gurol E., MD, The University of Iowa, Hospitals and Clinics, USA)

9.2 Degenerative Disease

Neurodegeneration represents the process of neuronal cell death in which the cause is often unknown. Histologically, it is characterized by neuronal loss associated with variable gliosis due to one of the mechanisms of non-necrotic, often apoptotic cell death. There are primary degeneration and secondary degeneration. During the process of neuronal cell death, neuronal and axonal swelling and swelled reactive gliosis are observed in some degenerative disease processes. This presumably causes water diffusion restriction on DW imaging. Diffusion-tensor imaging is sensitive in detecting and quantifying subtle changes of the microstructure integrity and the extracellular space in the neurodegeneration.

9.2.1 Secondary Degeneration (Wallerian, Transneuronal, and Retrograde Degeneration)

There are three major types of secondary degenerations: (1) Wallerian degeneration (antegrade), (2) transneuronal/trans-synaptic degeneration (antegrade or retrograde), and (3) retrograde degeneration (Fig. 9.13)[41].

Wallerian degeneration is an antegrade degeneration of the axons and myelin sheath resulting from injury of the proximal portion of the axons or cell bodies. It is most commonly recognized in the corticospinal tract secondary to middle cerebral artery infarction. Wallerian degeneration can also be seen in corticobulbar and corticopontine tracts, the corpus callosum, and middle cerebral peduncles [42, 43]. Energy depletion in layer 5 neurons may lead to failure of ion channel activ-

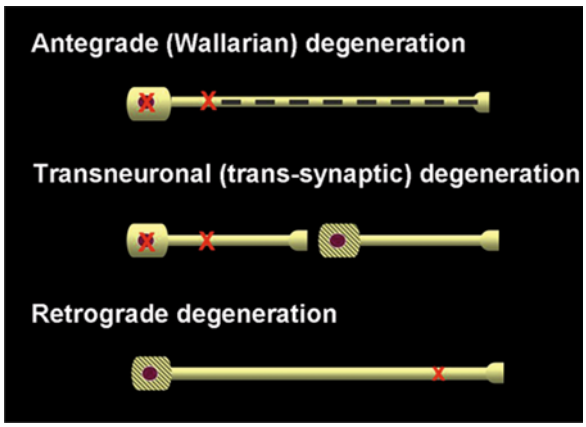

Figure 9.13

Three major types of secondary degenerations. (1) Wallerian degeneration; an antegrade degeneration of the axons and myelin sheath resulting from injury of the proximal portion of the axons or cell bodies. (2) Transneuronal/trans-synaptic degeneration (antegrade type); a degeneration of the distal neuron via the synapse resulting from injury of the proximal portion of the axons or cell bodies. (3) Retrograde degeneration; a degeneration of the proximal neuron resulting from injury of the distal portion of the axons

ity in the axolemma [44]. This results in axonal swelling followed by disintegration of the intraaxonal organelles. This in turn is followed by collapse of the myelin sheaths and ensuing gliosis. DW imaging shows the acute phase of wallerian degeneration as hyperintense associated with decreased ADC, presumably representing axonal and reactive astrocytic swelling [45, 46] (Fig. 9.14). DW high signals can be observed after more than 24 hours following the associated territorial infarction [47]. In DT imaging, diffusion fractional anisotropy is reduced in the corticospinal tract, and may correlate with impairment of motor function [48, 49](Fig. 9.15). DT imaging is more sensitive than DW imaging in detecting chronic Wallerian degeneration [50].

Transneuronal (trans-synaptic) degeneration in the substantia nigra can occur secondary to striatal infarction [51]. There are fiber connections originating in the caudate and putamen projecting over the substantia nigra (striatonigral pathway) [52]. Loss of inhibitory GABAergic output from the ischemic lesion can induce a postsynaptic long-term potentiation or a continuous excitatory state in the substantia nigra, resulting in neuronal swelling and cell death [53]. DW imaging shows hyperintensity associated with decreased ADC in the substantia nigra (Fig. 9.14) [54]. The decreased ADC of these lesions is thought to represent cellular edema of astrocytes or neurons in the substantia nigra. Astrocytic swelling, which is related to this degeneration, has been reported in an experimental study [55]. Diffusion abnormalities in the striatum or thalamus secondary to external capsular hemorrhage have also been reported, which are presumably related to antegrade transneuronal degeneration of the striatum (corticostriat fibers) and

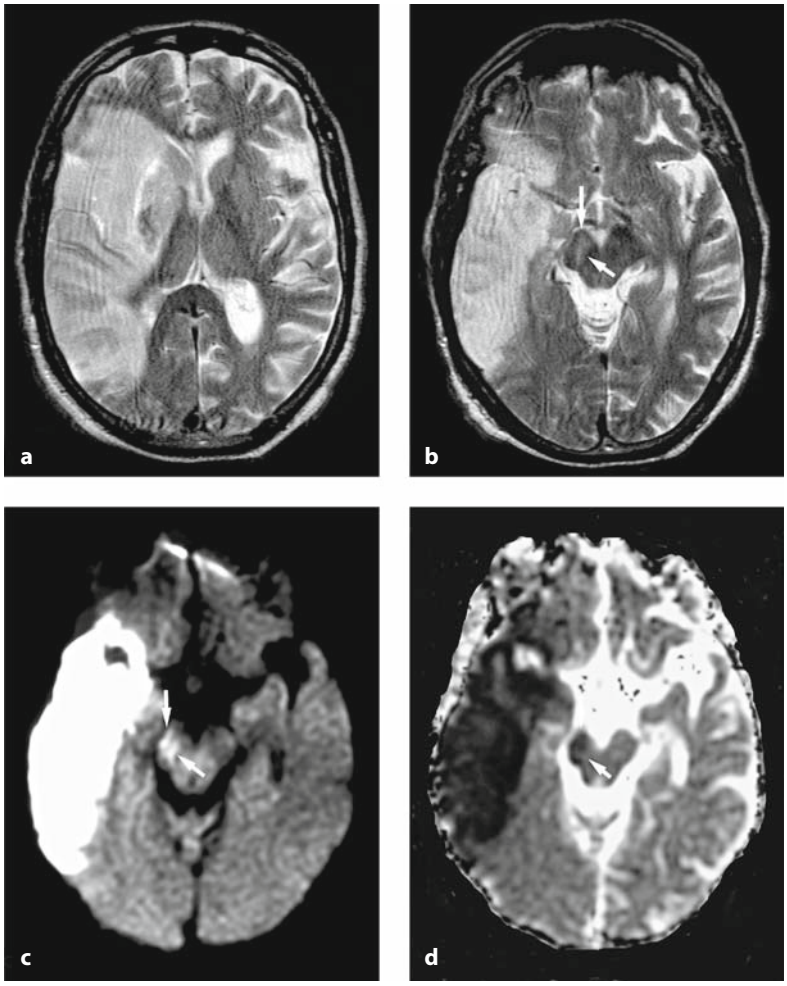

Figure 9.14 a–d

Wallerian and transneuronal degeneration (acute phase) in a 76-year-old man with a large infarct in the right middle cerebral artery (MCA) territory (6 days after onset). **a** T2-weighted image shows a right MCA infarct as hyperintense, including the left putamen. **b** T2-weighted image at the level of the midbrain reveals slightly a hyperintense lesion in the right cerebral peduncle including the substantia nigra (*arrows*), as well as a right MCA infarct in the temporal area. **c** DW image shows a hyperintense lesion (*arrows*). **d** ADC is decreased involving both the right cerebral peduncle and the right substantia nigra (*arrow*)

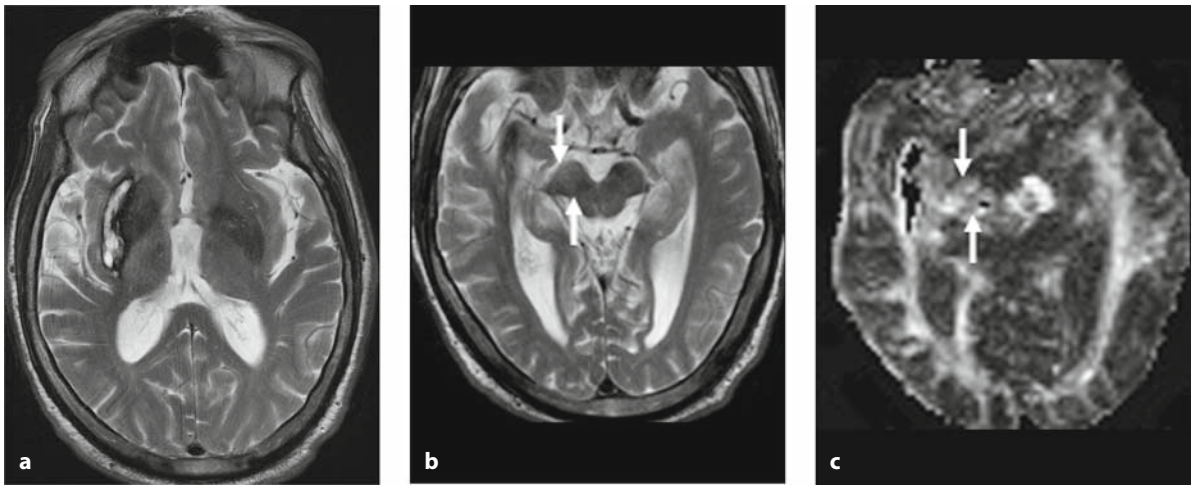

Figure 9.15 a–c

Wallerian and transneuronal degeneration in a 78-year-old woman with right chronic putaminal hemorrhage. **a** T2-weighted image shows a right old putaminal hemorrhage as hypointense. **b** T2-weighted image at the level of the midbrain reveals mild hyperintense lesion in the right cerebral peduncle, including the substantia nigra (*arrows*). **c** FA map shows decreased anisotropy in the right cerebral peduncle(*arrows*)

retrograde transneuronal degeneration of the thalamus (thalamostriate fibers)[56].

Retrograde thalamic degeneration is usually seen in anterior and dorsomedial nuclei secondary to ipsilateral large infarction or hemorrhage. It is thought to be a retrograde degeneration through the thalamocortical pathway [41, 54, 55]. DW imaging shows hyperintensity in the thalamic nuclei (Fig. 9.16).

9.2.2 Creutzfeldt–Jakob Disease

Creutzfeldt–Jakob disease (CJD) is one of the prion diseases characterized by rapidly progressive degenerative dementia, myoclonus and ataxia. However, the initial clinical symptom is sometimes non-specific and variable such as visual disturbance (Heidenhain variant), deafness, and hemiparesis [57, 58]. The cause of neurodegeneration is thought to be an accumulation of an abnormal form of human prion protein (infectious proteinaceous scrapie particles, PrP^{Sc}). CJD has been reclassified as an infectious disease. There are four forms: sporadic, iatrogenic, familial and variant [59]. Iatrogenic cases include contaminated neurosurgical instruments, administration of human growth hormone, cadaver-derived gonadotrophin, and dura matter (Fig. 9.17) and corneal grafts [60]. Histological features include spongiform degeneration of the gray matter, characterized by clustered, 5–25 micrometer large prion protein-containing vacuoles in the neuronal and glial elements, and neuronal loss, presumably due to apoptosis and gemistocytic astrocytosis [61].

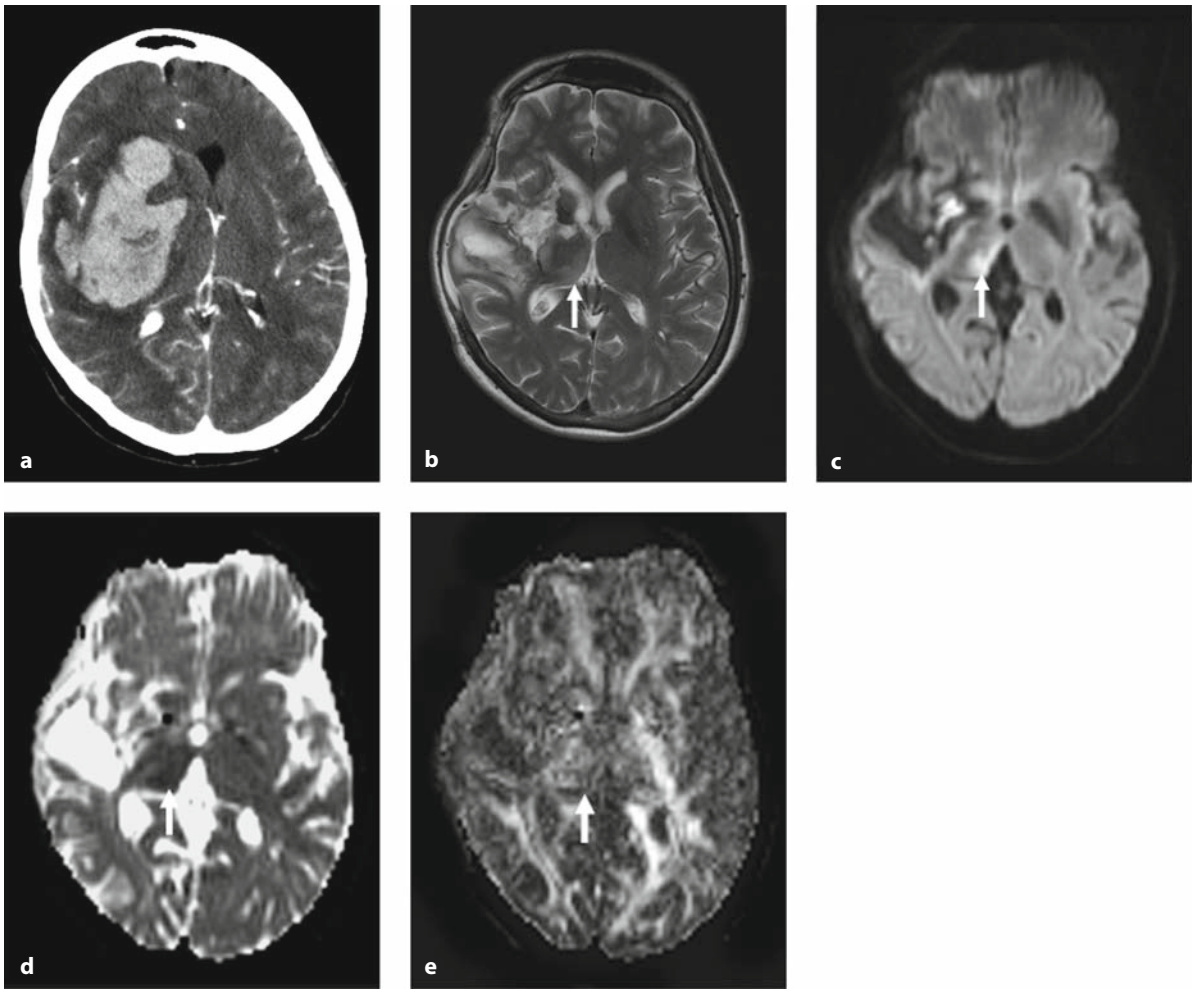

Figure 9.16 a–e

Retrograde degeneration in the dorsomedial thalamus in a 56-year-old woman with right large putaminal hemorrhage. **a** Postcontrast CT shows a large hematoma in the right putamen extending into the frontotemporal region with edema and a mass effect. **b** The 2-month follow-up T2-weighted image shows a high signal intensity in the dorsomedial thalamus (*arrow*). Right craniectomy and extensive encephalomalacia are also noted. **c, d** DW image shows a hyperintense lesion with decreased ADC in the right dorsomedial thalamus (*arrow*). **e** FA map shows decreased anisotropy in the right internal capsule and dorsomedial thalamus (*arrow*). (Courtesy of Lee HK, MD, The University of Iowa Hospitals and Clinics, USA)

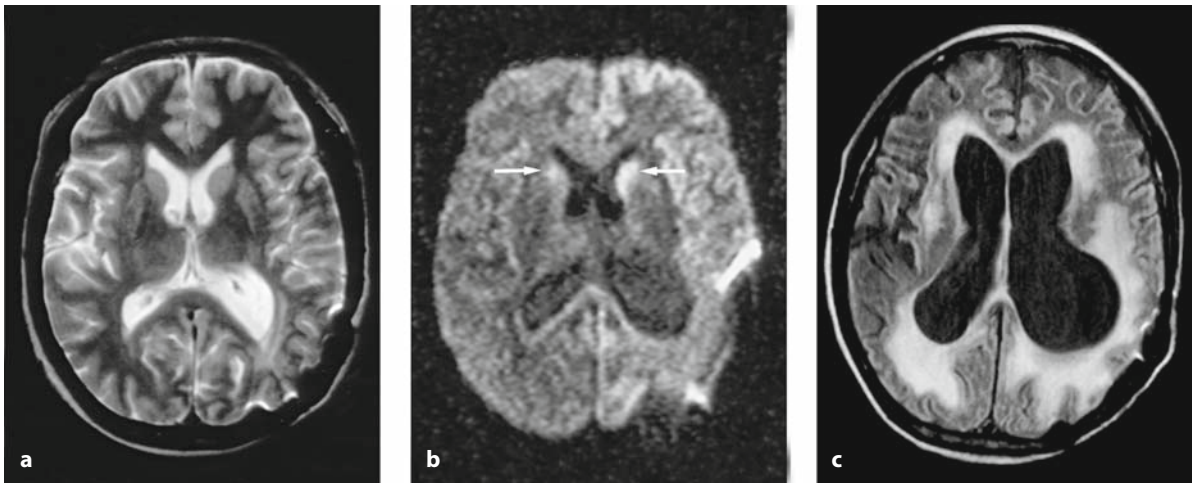

Figure 9.17 a–c

Creutzfeldt–Jakob disease in a 57-year-old woman with progressive dementia 10 years after surgery using cadaver dura matter. **a** T2-weighted image shows postoperative change in the left temporo-occipital region with mild ventricular dilatation. **b** DW image reveals bilateral hyperintensity in the caudate nuclei (*arrows*) and mild increased signal diffusely in the left hemisphere. **c** A 4-month follow-up FLAIR image shows extensive white matter hyperintensity and diffuse atrophy

Periodic synchronous discharge on electroencephalography (EEG) and the detection of 14-3-3 protein in the CSF support the clinical diagnosis of CJD.

T2-weighted and FLAIR images show very subtle hyperintense lesions in the cerebral cortex and bilateral basal ganglia in patients with CJD, usually seen 2-5 months after the onset of symptoms. The lesions often involve bilateral thalami (pulvinar sign) and periaqueductal areas in patients with variant CJD [62, 63], but this finding is also seen in sporadic CJD [64] (Fig. 9.18) Cerebral white matter T2 hyperintensity is considered to be primary degeneration, and first occurs in the periventricular area 4-5 months after the onset and rapidly extends to the deep and subcortical white matter during the following several months [65]. DW imaging is the most sensitive in detecting early findings in CJD, and should be included in the clinical diagnostic criteria [66-70] (Figs. 9.16-9.19). The cortical involvement is usually asymmetric, which does not correspond to the arterial territory. Bilateral basal ganglia or thalamic involvement is usually symmetric, but can be asymmetric (Fig. 9.19). The lesions are hyperintense on DW images and often associated with decreased ADC [67, 69–75]. Electron microscopy shows these vacuoles as focal swelling of neuritic processes, both axonal and dendritic swelling (cellular edema), which may cause decreased ADC [75]. In the late stages, abnormal hyperintense signals

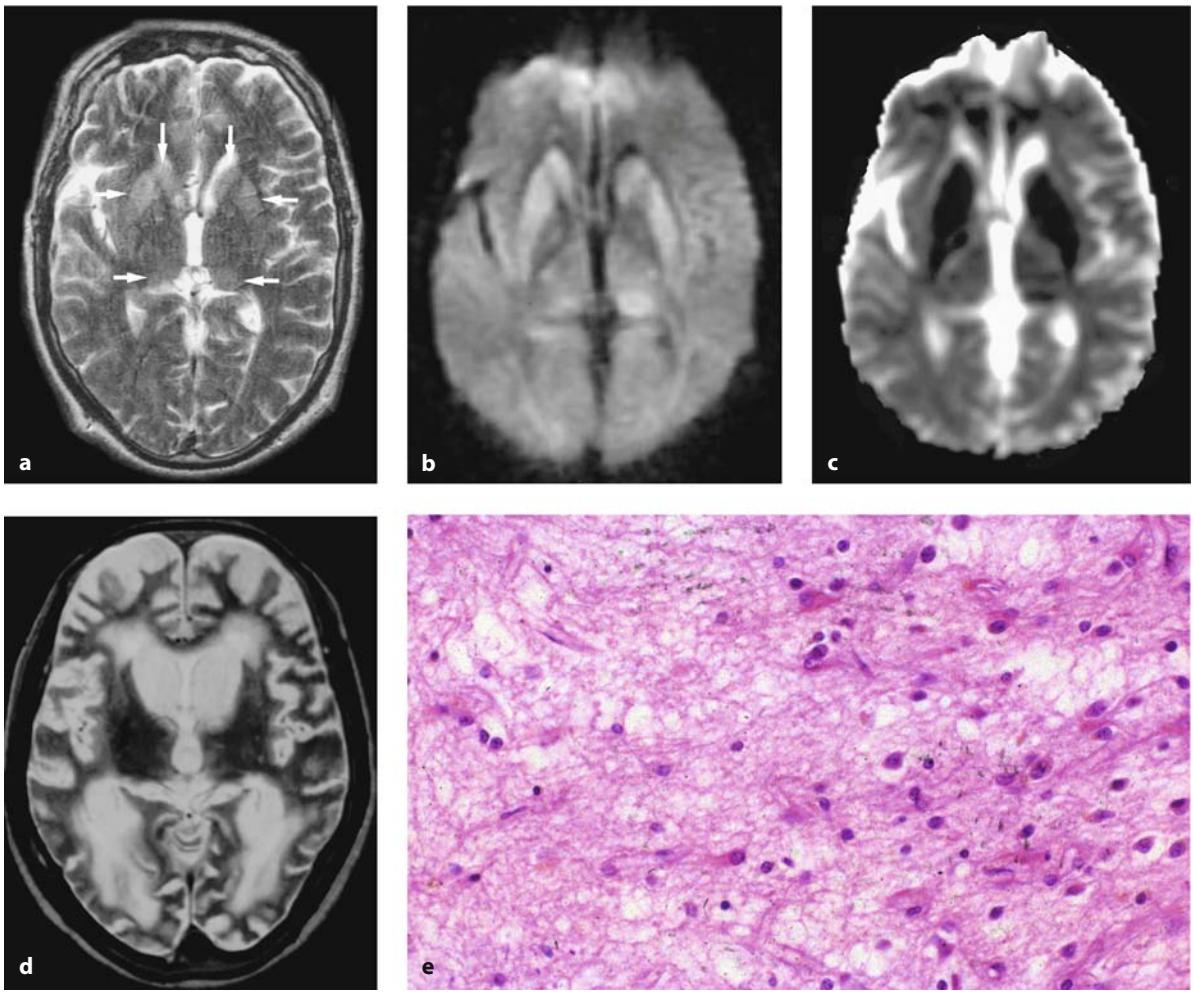

Figure 9.18 a–e

Creutzfeldt–Jakob disease in a 51-year-old man with progressive dementia. **a** T2-weighted image demonstrates mild hyperintensity bilaterally in the caudate nuclei, putamina and pulvinar of the thalami (*arrows*). **b** DW image clearly demonstrates these lesions as hyperintense. **c** ADC is decreased. **d** A 6-month follow-up T2-weighted image shows prominent diffuse atrophy and white matter hyperintensity. **e** Pathological specimen of another case shows spongiform degeneration and reactive astrocytosis. (Courtesy of Ukisu R, MD, Showa University, School of Medicine, Japan)

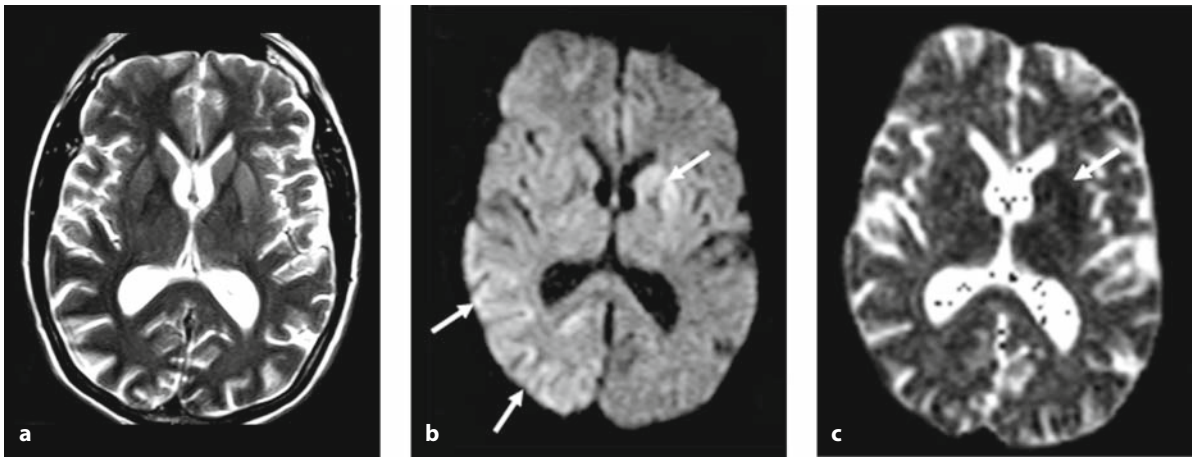

Figure 9.19 a–c

Creutzfeldt–Jakob disease in a 58-year-old woman with altered mental status and visual symptoms (Heidenhain variant). **a** T2-weighted image shows questionable hyperintensities in the basal ganglia bilaterally. **b** DW image demonstrates hyperintensities only in the left basal ganglia (*arrows*). Hyperintense lesions are also noted in the right temporo-occipital cortices, which does not correspond to a single vascular territory (*arrows*). **c** ADC is partially decreased in these lesions (*arrows*)

disappear with prominent brain atrophy, histologically representing neuronal loss and marked fibrillary gliosis [76].

9.2.3 Amyotrophic Lateral Sclerosis

Amyotrophic lateral sclerosis (ALS) is a progressive neurodegenerative disease affecting both upper and lower motor neurons. It often affects middle-aged patients and is characterized by progressive muscle weakness, limb and truncal atrophy associated with bulbar signs and symptoms. The disease progression is relentless and half of the patients are dead within 3 years. Degeneration of upper motor neurons usually starts in the primary motor cortex and secondary degeneration of motor fibers and gliosis occurs along the corticospinal tract.

MR images of ALS are characterized by high T2 signal along the large myelinated pyramidal tract fibers in the posterior limb of the internal capsule and cerebral peduncles. On DW imaging there are typically increased ADC and decreased fractional anisotropy in the corticospinal tracts [77]. Diffusion tensor imaging is useful in analyzing the extent and severity of axonal degeneration quantitatively in ALS (Fig. 9.20) [78-82]. Diffusion tensor tractography can be used for segmentation of white matter tracts, the corticospinal tract (CST), and corticobulbar tract (CBT) (Fig. 9.21), which may enable one to differentiate clinical subtypes of ALS. FA values along the corticobulbar tract of bulbar-onset type are significantly lower than that of limb-onset type [78].

9.2.4 Other Degenerative Diseases

The accumulation of tau (microtubule-associated protein) and synuclein (protein regulating synaptic plasticity) is the hallmark of distinct neurodegenerative disorders classified as tauopathies and synucleinopathies [83]. Tauopathies include Alzheimer's disease, Pick's disease, corticobasal degeneration, progressive supranuclear palsy, argyrophilic grain disease, and frontotemporal dementia. Synucleinopathies include Parkinson's disease, Lewy body disease, and multiple system atrophy (MSA).

Multiple system atrophy is a sporadic progressive adult-onset neurodegenerative disorder characterized by parkinsonism (80%), and pyramidal, autonomic, and cerebellar dysfunction in varying combinations. Pathologic features are cell loss, gliosis, and glial cytoplasmic inclusions in the affected structures.

Figure 9.20 a–d

Amyotrophic lateral sclerosis in a 27-year-old man with progressive weakness and dysphagia. **a** Coronal spin-echo T2-weighted image shows bilateral symmetrical hyperintensity along the corticospinal tract (*arrows*), extending into the white matter of the motor area. **b** DW image shows mild hyperintensity in bilateral corticospinal tracts. **c** ADC is increased (*arrows*). Hyperintensity and distortion in the frontal region is due to susceptibility artifact from air in the frontal sinuses. **d** Coronal diffusion tensor image with color mapping reveals decreased anisotropy along bilateral corticospinal tracts

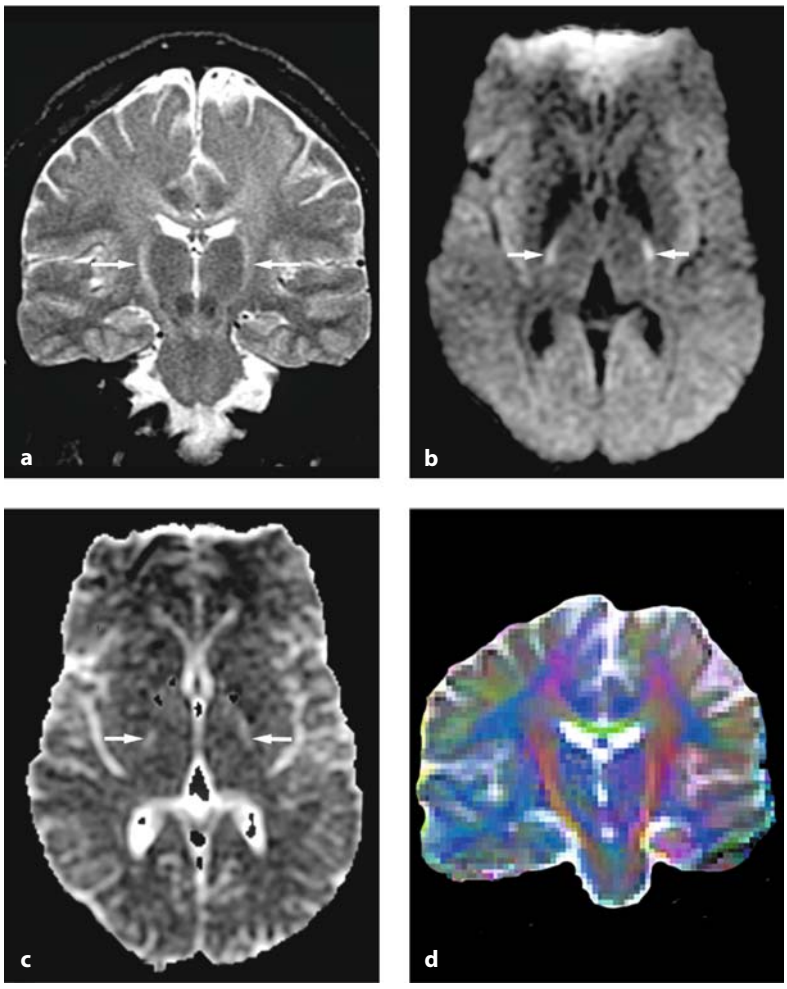

Figure 9.21

Tract-specific analysis of amyotrophic lateral sclerosis. (Courtesy of Aoki S, MD, The University of Tokyo, Japan)

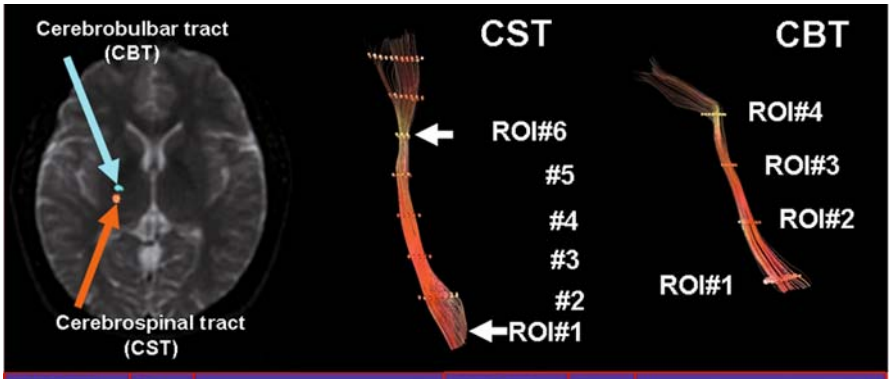

DTT-CST	FA	p	DTT-CBT	FA	p
Limb-onset	0.594	p<0.05 (vs Normal)	Limb-onset	0.558	p<0.01 (vs Bulbar)
Bulbar-onset	0.574	p<0.01 (vs Normal)	Bulbar-onset	0.509	p<0.01 (vs Normal, vs Limb)
Normal	0.629		Normal	0.561	

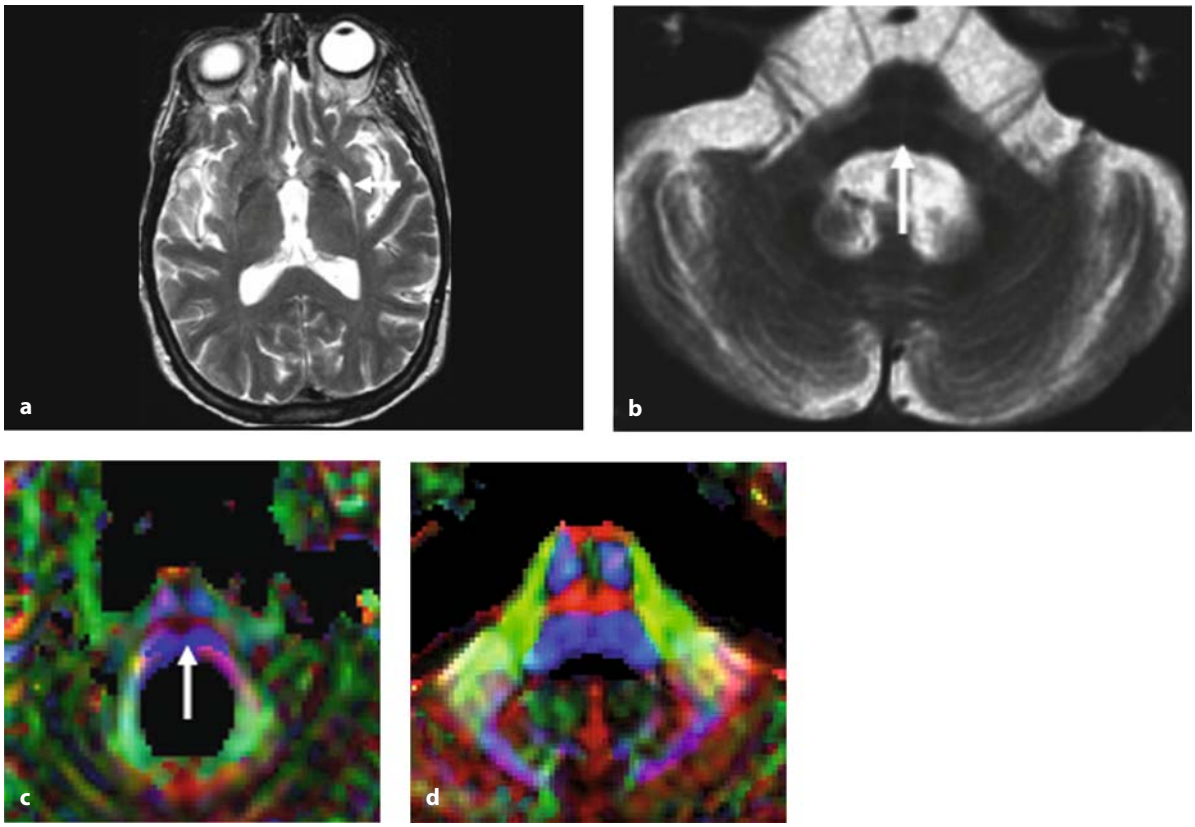

Figure 9.22 a–d

Multiple system atrophy in a 56-year-old man with ataxia and Shy-Drager syndrome. **a, b** T2-weighted image shows hyperintense lateral putaminal rim (*arrow*) and atrophy of the middle cerebral peduncles and pons (hot cross bun sign; *arrow*). **c** Color DT imaging shows decreased anisotropy and atrophy in the middle cerebral peduncles and pons (hot cross bun sign; *arrow*). **d** The same level of the color DT imaging map in a normal patient as a comparison. (Courtesy of Salamon N, MD, The University of California, Los Angeles, USA)

MR imaging findings include a T2 hyperintense rim in the outer margin of the putamen, putaminal T2 hypointensity and atrophy, T2 hyperintensity in the pons, middle cerebellar peduncle, and cerebellum [84]. The pontine cruciform hyperintensity (hot cross bun sign) represents degeneration of transverse pontocerebellar fibers. Increased ADC and decreased FA values are observed in the middle cerebral peduncle, basis pontis, and internal capsule [85, 86]. FA values in the middle cerebellar peduncle are negatively correlated with ataxia severity [86]. The color map shows selective atrophy and decreased anisotropy in the transverse pontine fibers and the middle cerebellar peduncles (Fig. 9.22).

Progressive supranuclear palsy (PSP) is clinically characterized by parkinsonism with supranuclear ophthalmoplegia. Atrophy of the midbrain is a typical neuropathologic feature. The appearance of the brainstem and the volumetry on midsagittal MR images provide an important diagnostic clue [87]. The shapes of the midbrain tegmentum (bird's head) and the pons (bird's body) look like a lateral view of a standing penguin (penguin silhouette sign)[87]. In PSP, increased ADC and decreased FA are observed in the decussation of the superior cerebellar peduncles (Fig. 9.23) [88]. Diffusion tensor tractography shows a selective degeneration of the superior cerebellar peduncle with a reduction of cortical projection fibers in all patients with PSP [89].

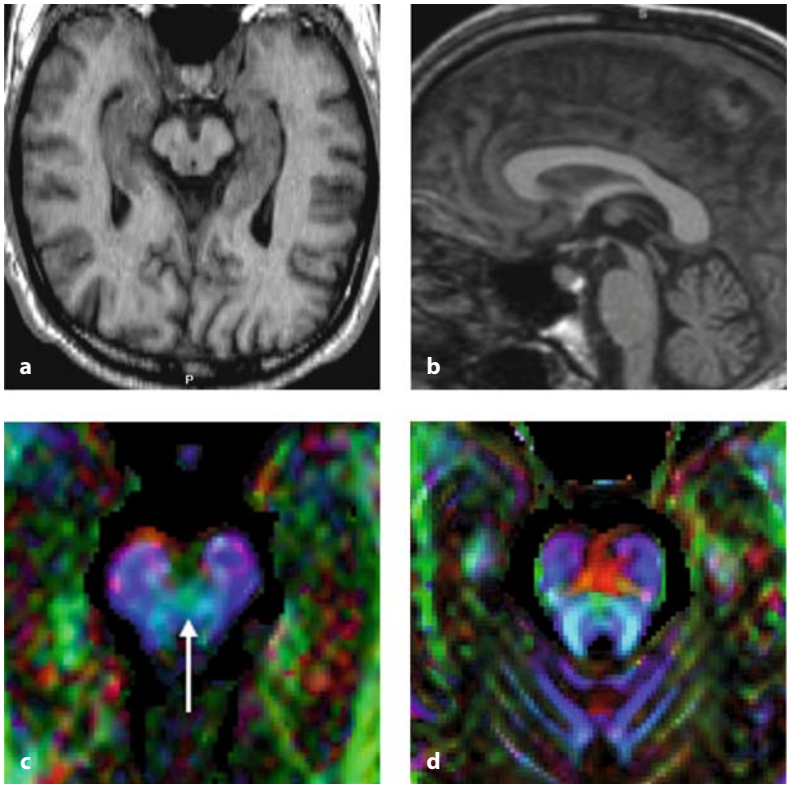

Figure 9.23 a–d

Progressive supranuclear palsy in a 60-year-old male. The patient has signs of 4 to 5 years' development of basal ganglia cerebellar and upper motor neuron dysfunction with some cognitive impairment and most recently onset of a supranuclear vertical gaze palsy. **a** Axial T1-weighted image shows atrophy in the midbrain. **b** Sagittal T1-weighted image shows a characteristic atrophy of the midbrain (penguin silhouette sign). **c, d** Color DTI image shows decreased anisotropy and atrophy in the midbrain. No red color is identified in the superior cerebellar peduncle decussation, compared with the color DTI map at the same level in a normal patient. (Courtesy of Salamon N, MD, The University of California, Los Angeles, USA)

9.3 Conclusion

Magnetic resonance imaging with diffusion-weighted and tensor imaging including ADC and FA maps, and fiber tractography are useful in characterizing demyelinating and degenerative lesions of the brain. These imaging techniques can increase specificity and improve our understanding of the pathophysiology of these diseases.

References

1. Poser CM, Brinar VV (2004) The nature of multiple sclerosis. Clin Neurol Neurosurg 106:159-171
2. Cañellas AR, Gols AR, Izquierdo JR, Subirana MT, Gairin XM (2007) Idiopathic inflammatory-demyelinating diseases of the central nervous system. Neuroradiology 49:393-409
3. Dawson J (1916) The histology of disseminated sclerosis. Transactions of the Royal Society of Edinburgh 50:517-5740
4. McDonald WI, Compston A, Edan G, Goodkin D, Hartung HP, Lublin FD, McFarland HF, Paty DW, Polman CH, Reingold SC, Sandberg-Wollheim M, Sibley W, Thompson A, van den Noort S, Weinshenker BY, Wolinsky JS (2001) Recommended diagnostic criteria for multiple sclerosis: guidelines from the International Panel on the diagnosis of multiple sclerosis. Ann Neurol 50:121-127
5. Filippi M, Inglese M (2001) Overview of diffusion-weighted magnetic resonance studies in multiple sclerosis. J Neurol Sci 186 Suppl 1:S37–S43
6. Lisanti CJ, Asbach P, Bradley WG Jr. (2005) The ependymal "Dot-Dash" sign: an MR imaging finding of early multiple sclerosis. AJNR Am J Neuroradiol 26:2033-2036
7. Palmer S, Bradley WG, Chen DY, Patel S (1999) Subcallosal striations: early findings of multiple sclerosis on sagittal, thin-section, fast FLAIR MR images. Radiology 210:149-153
8. van Walderveen MA, Lycklama A Nijeholt GJ, et al. (2001) Hypointense lesions on T1-weighted spin-echo magnetic resonance imaging: relation to clinical characteristics in subgroups of patients with multiple sclerosis. Arch Neurol 58:76–81
9. Loevner LA, Grossman RI, McGowan JC, Ramer KN, Cohen JA (1995) Characterization of multiple sclerosis plaques with T1-weighted MR and quantitative magnetization transfer. AJNR Am J Neuroradiol 16:1473–1479

10. Loevner LA, Grossman RI, Cohen JA, Lexa FJ, Kessler D, Kolson DL (1995) Microscopic disease in normal-appearing white matter on conventional MR images in patients with multiple sclerosis: assessment with magnetization-transfer measurements. Radiology 196:511–515
11. Tievsky AL, Ptak T, Farkas J (1999) Investigation of apparent diffusion coefficient and diffusion tensor anisotropy in acute and chronic multiple sclerosis lesion. Am J Neuroradiol 20:1491–1499
12. Roychowdhury S, Maldjian JA, Grossman RI (2000) Multiple sclerosis: comparison of trace apparent diffusion coefficients with MR enhancement pattern of lesions. AJNR Am J Neuroradiol 21:869–874
13. Castriota Scanderbeg A, Tomaiuolo F, Sabatini U, Nocentini U, Grasso MG, Caltagirone C (2000) Demyelinating plaques in relapsing-remitting and secondary-progressive multiple sclerosis: assessment with diffusion MR imaging. Am J Neuroradiol 21:862–868
14. Rovira A, Pericot I, Alonso J, Rio J, Grive E, Montalban X (2002) Serial diffusion-weighted MR imaging and proton MR spectroscopy of acute large demyelinating brain lesions: case report. Am J Neuroradiol 23:989–994
15. Horsfield MA, Larsson HB, Jones DK, Gass A (1998) Diffusion magnetic resonance imaging in multiple sclerosis. J Neurol Neurosurg Psychiatry 64 Suppl 1:S80–S84
16. Guo AC, MacFall JR, Provenzale JM (2002) Multiple sclerosis: diffusion tensor MR imaging for evaluation of normal-appearing white matter. Radiology 222:729–736
17. Gallo A, Rovaris M, Riva R, Ghezzi A, Benedetti B, Martinelli V, Falini A, Comi G, Filippi M (2005) Diffusion-tensor magnetic resonance imaging detects normal-appearing white matter damage unrelated to short-term disease activity in patients at the earliest clinical stage of multiple sclerosis. Arch Neurol 62:803-808
18. Poonawalla AH, Hasan KM, Gupta RK, Ahn CW, Nelson F, Wolinsky JS, Narayana PA (2008) Diffusion-tensor MR imaging of cortical lesions in multiple sclerosis: initial findings. Radiology 246:880-886
19. Karaarslan E, Altintas A, Senol U, Yeni N, Dincer A, Bayindir C, Karaagac N, Siva A (2002) Baló's concentric sclerosis: clinical and radiologic features of five cases. AJNR Am J Neuroradiol 22:1362-1367
20. Capello E, Mancardi GL (2004) Marburg type and Balò's concentric sclerosis: rare and acute variants of multiple sclerosis. Neurol Sci 25[Suppl 4]:S361-363
21. Caracciolo JT, Murtagh RD, Rojiani AM, Murtagh FR (2001) Pathognomonic MR imaging findings in Balo concentric sclerosis. AJNR Am J Neuroradiol 22:292-293
22. Baló J (1927) A leukoenkephalitis periaxialis concentricaról. Magyar Orv Arch 28:108-124
23. Ball T, Malik O, Roncaroli F, Quest RA, Aviv RI (2007) Apparent diffusion coefficient changes and lesion evolution in Balo's type demyelination-correlation with histopathology. Clin Radiol 62:498-503
24. Wiendl H, Weissert R, Herrlinger U, Krapf H, Küker W (2005) Diffusion abnormality in Balo's concentric sclerosis: clues for the pathogenesis. Eur Neurol 53:42-44
25. Kavanagh EC, Heran MK, Fenton DM, Lapointe JS, Nugent RA, Graeb DA (2006) Diffusion-weighted imaging findings in Balo concentric sclerosis. Br J Radiol 79:e28-31
26. Obara S, Takeshima H, Awa R, Yonezawa H, Oyoshi T, Nagayama T, Hirano H, Niiro M, Kuratsu J (2003) Tumefactive myelinoclastic diffuse sclerosis--case report. Neurol Med Chir (Tokyo) 43:563-566
27. Miyamoto N, Kagohashi M, Nishioka K, Fujishima K, Kitada T, Tomita Y, Mori K, Maeda M, Wada R, Matsumoto M, Mori H, Mizuno Y, Okuma Y (2006) An autopsy case of Schilder's variant of multiple sclerosis (Schilder's disease). Eur Neurol 55:103-107
28. Schilder P (1912) Zur kenntnis der sogenannten diffusen Sklerose. Z Ges Neurol Psychiatr 10:1-60
29. Masdeu JC, Quinto C, Olivera C, Tenner M, Leslie D, Visintainer P (2000) Open-ring imaging sign: highly specific for atypical brain demyelination. Neurology 54:1427-1433
30. Tenembaum S, Chitnis T, Ness J, Hahn JS (2007) International Pediatric MS Study Group. Acute disseminated encephalomyelitis. Neurology 68 [16 Suppl 2]:S23-36
31. Inglese M, Salvi F, Iannucci G, Mancardi GL, Mascalchi M, Filippi M (2002) Magnetization transfer and diffusion tensor MR imaging of acute disseminated encephalomyelitis. Am J Neuroradiol 23:267–272
32. Harada M, Hisaoka S, Mori K, Yoneda K, Noda S, Nishitani H (2000) Differences in water diffusion and lactate production in two different types of postinfectious encephalopathy. J Magn Reson Imaging 11:559–563
33. Bernarding J, Braun J, Koennecke HC (2002) Diffusion- and perfusion-weighted MR imaging in a patient with acute demyelinating encephalomyelitis (ADEM). J Magn Reson Imaging 15:96–100
34. Balasubramanya KS, Kovoor JM, Jayakumar PN, Ravishankar S, Kamble RB, Panicker J, Nagaraja D (2007) Diffusion-weighted imaging and proton MR spectroscopy in the characterization of acute disseminated encephalomyelitis. Neuroradiology 49:177-183
35. Gibbs WN, Kreidie MA, Kim RC, Hasso AN (2005) Acute hemorrhagic leukoencephalitis: neuroimaging features and neuropathologic diagnosis. J Comput Assist Tomogr 29:689-693
36. Mader I, Wolff M, Niemann G, Küker W (2004) Acute haemorrhagic encephalomyelitis (AHEM): MRI findings. Neuropediatrics 35:143-146
37. Mader I, Herrlinger U, Klose U, Schmidt F, Küker W (2003) Progressive multifocal leukoencephalopathy: analysis of lesion development with diffusion-weighted MRI. Neuroradiology 45:717-121
38. Huisman TA, Boltshauser E, Martin E, Nadal D (2005) Diffusion tensor imaging in progressive multifocal leukoencephalopathy: early predictor for demyelination? AJNR Am J Neuroradiol 26:2153-2156
39. Ohta K, Obara K, Sakauchi M, Obara K, Takane H, Yogo Y (2001) Lesion extension detected by diffusion-weighted magnetic resonance imaging in progressive multifocal leukoencephalopathy. J Neurol 248:809–811
40. Küker W, Mader I, Nägele T, Uhl M, Adolph C, Klose U, Herrlinger U (2006) Progressive multifocal leukoencephalopathy: value of diffusion-weighted and contrast-enhanced magnetic resonance imaging for diagnosis and treatment control. Eur J Neurol 13:819-826

41. Yamada K, Patel U, Shrier DA, Tanaka H, Chang JK, Numaguchi Y (1998) MR imaging of CNS tractopathy: wallerian and transneuronal degeneration. AJR Am J Roentgenol 171:813-818
42. Gupta RK, Saksena S, Hasan KM, Agarwal A, Haris M, Pandey CM, Narayana PA (2006) Focal Wallerian degeneration of the corpus callosum in large middle cerebral artery stroke: serial diffusion tensor imaging. J Magn Reson Imaging 24:549-555
43. O'uchi T (1998) Wallerian degeneration of the pontocerebellar tracts after pontine hemorrhage. Int J Neuroradiol 4:171-177
44. Mazumdar A, Mukherjee P, Miller JH, Malde H, McKinstry RC (2003) Diffusion-weighted imaging of acute corticospinal tract injury preceding Wallerian degeneration in the maturing human brain. AJNR Am J Neuroradiol 24:1057-1066
45. Castillo M, Mukheriji SK (1999) Early abnormalities related to postinfarction wallerian degeneration: evaluation with MR diffusion-weighted imaging. JCAT 23:1004–1007
46. Kang DW, Chu K, Yoon BW, Song IC, Chang KH, Roh JK (2000) Diffusion-weighted imaging in wallerian degeneration. J Neurol Sci 178:167–169
47. Pierpaoli C, Barnett A, Pajevic S, Chen R, Penix LR, Virta A, Basser P (2001) Water diffusion changes in Wallerian degeneration and their dependence on white matter architecture. Neuroimage 13:1174-1185
48. Thomalla G, Glauche V, Weiller C, Röther J (2005) Time course of wallerian degeneration after ischaemic stroke revealed by diffusion tensor imaging. J Neurol Neurosurg Psychiatry 76:266-268
49. Thomalla G, Glauche V, Koch MA, Beaulieu C, Weiller C, Röther J (2004) Diffusion tensor imaging detects early Wallerian degeneration of the pyramidal tract after ischemic stroke. Neuroimage 22:1767-1774
50. Werring DJ, Toosy AT, Clark CA, Parker GJ, Barker GJ, Miller DH, Thompson AJ (2000) Diffusion tensor imaging can detect and quantify corticospinal tract degeneration after stroke. J Neurol Neurosurg Psychiatry 69:269-272
51. Ogawa T, Okudera T, Inugami A, et al. (1997) Degeneration of the ipsilateral substantia nigra after striatal infarction: evaluation with MR imaging. Radiology 204:847–851
52. Abe O, Nakane M, Aoki S, Hayashi N, Masumoto T, Kunimatsu A, Mori H, Tamura A, Ohtomo K (2003) MR imaging of postischemic neuronal death in the substantia nigra and thalamus following middle cerebral artery occlusion in rats. NMR Biomed 16:152-159
52. Kinoshita T, Moritani T, Shrier DA, et al. (2002) Secondary degeneration of the Substantia Nigra and Corticospinal tract after hemorrhagic middle cerebral artery infarction; Diffusion-weighted MR findings. Magnetic Resonance in Medical Sciences 1: 175–198
53. Nakase M, Tamura A, Miyasaka N, et al. (2001) Astrocytic swelling in the ipsilateral substantia niagra after occlusion of the middle cerebral artery in rats. Am J Neuroradiol 22:660–663
54. Ogawa T, Yoshida Y, Okudera T, Noguchi K, Kado H, Uemura K (1997) Secondary thalamic degeneration after cerebral infarction in the middle cerebral artery distribution: evaluation with MR imaging. Radiology 204:255-262
55. Nakane M, Tamura A, Sasaki Y, Teraoka A (2002) MRI of secondary changes in the thalamus following a cerebral infarct. Neuroradiology 44:915-920
56. Moon WJ, Na DG, Kim SS, Ryoo JW, Chung EC (2005) Diffusion abnormality of deep gray matter in external capsular hemorrhage. AJNR Am J Neuroradiol 26:229-35
57. Cataldi ML, Restivo O, Reggio E, Restivo DA, Reggio A (2000) Deafness: an unusual onset of genetic Creutzfeldt-Jakob disease. Neurol Sci 21:53-55
58. Tsuji Y, Kanamori H, Murakami G, Yokode M, Mezaki T, Doh-ura K, Taniguchi K, Matsubayashi K, Fukuyama H, Kita T, Tanaka M (2004) Heidenhain variant of Creutzfeldt-Jakob disease: diffusion-weighted MRI and PET characteristics. J Neuroimaging 14:63-66
59. Johnson RT, Gibbs CJ Jr (1998) Creutzfeldt–Jakob disease and related transmissible spongiform encephalopathies. N Engl J Med 339:1994–2004
60. Brown P, Preece M, Brandel JP, et al. (2000) Iatrogenic Creutzfeldt–Jakob disease at the millennium. Neurology 55:1075–1081
61. Lucassen PJ, Williams A, Chung WCJ, et al. (1995) Detection of apoptosis in murine scrapie. Neuroscience Letters 198:185–188
62. Zeidler M, Sellar RJ, Collie DA, et al. (2000) The pulvinar sign on magnetic resonance imaging in variant Creutzfeldt–Jakob disease. Lancet 355:1412–1418
63. Molloy S, O'Laoide R, Brett F, Farrell M (2000) The "pulvinar" sign in variant Creutzfeldt–Jakob disease. Am J Roentgenol 175:555–556
64. Haik S, Brandel JP, Oppenheim C, et al. (2002) Sporadic CJD clinically mimicking variant CJD with bilateral increased signal in the pulvinar. Neurology 58:148–149
65. Matsusue E, Kinoshita T, Sugihara S, Fujii S, Ogawa T, Ohama E (2004) White matter lesions in panencephalopathic type of Creutzfeldt-Jakob disease: MR imaging and pathologic correlations. AJNR Am J Neuroradiol 25:910-918
66. Shiga Y, Miyazawa K, Sato S, Fukushima R, Shibuya S, Sato Y, Konno H, Doh-ura K, Mugikura S, Tamura H, Higano S, Takahashi S, Itoyama Y (2004) Diffusion-weighted MRI abnormalities as an early diagnostic marker for Creutzfeldt-Jakob disease. Neurology 63:443-449
67. Young GS, Geschwind MD, Fischbein NJ, Martindale JL, Henry RG, Liu S, Lu Y, Wong S, Liu H, Miller BL, Dillon WP (2005) Diffusion-weighted and fluid-attenuated inversion recovery imaging in Creutzfeldt-Jakob disease: high sensitivity and specificity for diagnosis. AJNR Am J Neuroradiol 26:1551-1162
68. Kallenberg K, Schulz-Schaeffer WJ, Jastrow U, Poser S, Meissner B, Tschampa HJ, Zerr I, Knauth M (2006) Creutzfeldt-Jakob disease: comparative analysis of MR imaging sequences. AJNR Am J Neuroradiol 27:1459-1462
69. Ukisu R, Kushihashi T, Tanaka E, Baba M, Usui N, Fujisawa H, Takenaka H (2006) Diffusion-weighted MR imaging of early-stage Creutzfeldt-Jakob disease: typical and atypical manifestations. Radiographics 26 [Suppl 1]:S191-204
70. Ukisu R, Kushihashi T, Kitanosono T, Fujisawa H, Takenaka H, Ohgiya Y, Gokan T, Munechika H (2005) Serial diffusion-weighted MRI of Creutzfeldt-Jakob disease. AJR Am J Roentgenol 184:560-566

71. Demaerel P, Baert AL, Vanopdenbosch, et al. (1997) Diffusion-weighted magnetic resonance imaging in Creutzfeldt–Jakob disease. Lancet 349:847–848
72. Bahn MM, Parchi P (1999) Abnormal diffusion-weighted magnetic resonance images in Creutzfedlt–Jakob disease. Arch Neurol 56:577–583
73. Mittal S, Farmer P, Kalina P, Kingsley PB, Halperin J (2002) Correlation of diffusion-weighted magnetic resonance imaging with neuropathology in Creutzfeldt–Jakob disease. Arch Neurol 59:128–134
74. Murata T, Shiga Y, Higano S, Takahashi S, Mugikura S (2002) Conspicuity and evolution of lesions in Creutzfeldt–Jakob disease at diffusion-weighted imaging. AJNR Am J Neuroradiol 23:1164–1172
75. Dearmond MA, Kretzschmar HA, Prusiner SB (2002) Prion diseases. In: Graham DI, Lantos PL (eds) Greenfield's neuropathology, 7th edn, pp 273–323
76. Matoba M, Tonami H, Miyaji H, Yokota H, Yamamoto I (2001) Creutzfeldt–Jakob disease: serial changes on diffusion-weighted MRI. J Comput Assist Tomogr 25:274–277
77. Ellis CM, Simmons A, Jones DK, et al. (1999) Diffusion tensor MRI assesses corticospinal tract damage in ALS. Neurology 53:1051–1058
78. Aoki S, Iwata NK, Masutani Y, Yoshida M, Abe O, Ugawa Y, Masumoto T, Mori H, Hayashi N, Kabasawa H, Kwak S, Takahashi S, Tsuji S, Ohtomo K (2005) Quantitative evaluation of the pyramidal tract segmented by diffusion tensor tractography: feasibility study in patients with amyotrophic lateral sclerosis. Radiat Med 23:195-199
79. Wang S, Poptani H, Bilello M, Wu X, Woo JH, Elman LB, McCluskey LF, Krejza J, Melhem ER (2006) Diffusion tensor imaging in amyotrophic lateral sclerosis: volumetric analysis of the corticospinal tract. AJNR Am J Neuroradiol 27:1234-1238
80. Iwata NK, Aoki S, Okabe S, Arai N, Terao Y, Kwak S, Abe O, Kanazawa I, Tsuji S, Ugawa Y (2008) Evaluation of corticospinal tracts in ALS with diffusion tensor MRI and brainstem stimulation. Neurology 70:528-532
81. Abe O, Yamada H, Masutani Y, Aoki S, Kunimatsu A, Yamasue H, Fukuda R, Kasai K, Hayashi N, Masumoto T, Mori H, Soma T, Ohtomo K (2004) Amyotrophic lateral sclerosis: diffusion tensor tractography and voxel-based analysis. NMR Biomed 17:411-416
82. Graham JM, Papadakis N, Evans J, Widjaja E, Romanowski CA, Paley MN, Wallis LI, Wilkinson ID, Shaw PJ, Griffiths PD (2004) Diffusion tensor imaging for the assessment of upper motor neuron integrity in ALS. Neurology 63:2111-2119
83. Ingelsson M, Ramasamy K, Russ C, Freeman SH, Orne J, Raju S, Matsui T, Growdon JH, Frosch MP, Ghetti B, Brown RH, Irizarry MC, Hyman BT (2007) Increase in the relative expression of tau with four microtubule binding repeat regions in frontotemporal lobar degeneration and progressive supranuclear palsy brains. Acta Neuropathol 114:471-479
84. Ngai S, Tang YM, Du L, Stuckey S (2006) Hyperintensity of the middle cerebellar peduncles on fluid-attenuated inversion recovery imaging: variation with age and implications for the diagnosis of multiple system atrophy. AJNR Am J Neuroradiol 27:2146-2148
85. Taoka T, Kin T, Nakagawa H, Hirano M, Sakamoto M, Wada T, Takayama K, Wuttikul C, Iwasaki S, Ueno S, Kichikawa K (2007) Diffusivity and diffusion anisotropy of cerebellar peduncles in cases of spinocerebellar degenerative disease. Neuroimage 37:387-393
86. Shiga K, Yamada K, Yoshikawa K, Mizuno T, Nishimura T, Nakagawa M (2005) Local tissue anisotropy decreases in cerebellopetal fibers and pyramidal tract in multiple system atrophy. J Neurol 252:589-596
87. Oba H, Yagishita A, Terada H, Barkovich AJ, Kutomi K, Yamauchi T, Furui S, Shimizu T, Uchigata M, Matsumura K, Sonoo M, Sakai M, Takada K, Harasawa A, Takeshita K, Kohtake H, Tanaka H, Suzuki S (2005) New and reliable MRI diagnosis for progressive supranuclear palsy. Neurology 64:2050-2055
88. Blain CR, Barker GJ, Jarosz JM, Coyle NA, Landau S, Brown RG, Chaudhuri KR, Simmons A, Jones DK, Williams SC, Leigh PN (2006) Measuring brain stem and cerebellar damage in parkinsonian syndromes using diffusion tensor MRI. Neurology 67:2199-2205
89. Nilsson C, Markenroth Bloch K, Brockstedt S, Lätt J, Widner H, Larsson EM (2007) Tracking the neurodegeneration of parkinsonian disorders--a pilot study. Neuroradiology 49:111-119
90. Moritani T (2002) Classification of brain edema. In Aoki S, Abe O eds Koredewakaru Diffusion MRI, Tokyo: Shujunsha. pp 128–137

Toxic and Metabolic Disease

Computed tomography (CT) of patients with toxic and metabolic disease is generally non-specific, showing decreased attenuation of lesions in the white matter. Routine MR imaging is informative, but usually also non-specific, with T2 prolongation of those lesions. The white matter is often diffusely and symmetrically involved, as are the basal ganglia and/or brain stem. Diffusion-weighted (DW) imaging can add to the diagnostic information and improve the understanding of the pathophysiology of various white matter abnormalities, such as dysmyelination and demyelination in toxic and metabolic diseases.

10.1 Toxic Disease

10.1.1 Chemotherapy-Induced Leukoencephalopathy

Intrathecal or intravenous methotrexate, with or without radiation therapy, can cause diffuse white matter changes [1]. There are two types of methotrexate-related leukoencephalopathy: (1) disseminated necrotizing leukoencephalopathy (DNL) and (2) mild leukoencephalopathy [2]. DNL indicates a rapidly deteriorating clinical course, with irreversible extensive white matter damage. Mild leukoencephalopathy is usually transient.

MR imaging findings are different in these two types. In DNL, MR imaging shows multifocal T2 and FLAIR hyperintensities in the white matter with small irregular low-signal foci and contrast enhancement on T1-weighted images. DW imaging shows slightly increased ADC in the center of the lesion and increased ADC in the perilesional vasogenic edema [3] (Fig. 10.1) In mild leukoencephalopathy MR imaging shows diffuse T2 hyperintensity in the white matter. DW imaging shows the diffuse white matter as hyperintense with decreased apparent diffusion coefficient (ADC), even before conventional MR imaging can detect the lesions (Fig. 10.2). Pathologically the white matter lesion represents intramyelinic edema.

High-dose chemotherapy including carmustine (BCNU), cyclophosphamide, cisplatin, 5-fluorouracil (5-FU) and carmofur can also cause diffuse white matter disease. The lesions are hyperintense on T2-weighted images as well as on DW images, and ADC is decreased [4–6] (Fig. 10.3). Chemotherapeutic agents such as 5-FU and carmofur can have direct toxic effects on myelin, which causes intramyelinic edema [7]. Chemotherapy-associated leukoencephalopathy can be fatal and early diagnosis and discontinuation of the offending drug is therefore necessary.

10.1.2 Heroin-Induced Spongiform Leukoencephalopathy

The inhalation of black-market heroin vapors (pyrolysate) as well as intravenous consumption of heroin can lead to toxic leukoencephalopathy [8]. The leukoencephalopathy is pathologically characterized by spongiform degeneration of the white matter as a result of fluid accumulation within the myelin sheaths (intramyelinic edema). Electron microscopy shows vacuoles between the myelin lamellae by splitting of the intraperiod lines [9]. CT and MR imaging show abnormalities in the cerebral and cerebellar white matter, cerebral peduncles, corticospinal tracts, lemniscus medialis and solitary tracts [10]. The accumulation of restricted fluid between the layers of myelin lamellae may cause hyperintensity on DW imaging with decreased ADC [11] (Fig. 10.4). Because the myelin itself and the blood–brain barrier are intact in cases of less severe heroin-induced leukoencephalopathy, one may expect the changes in the DW signal to be reversible on follow-up MR imaging [12].

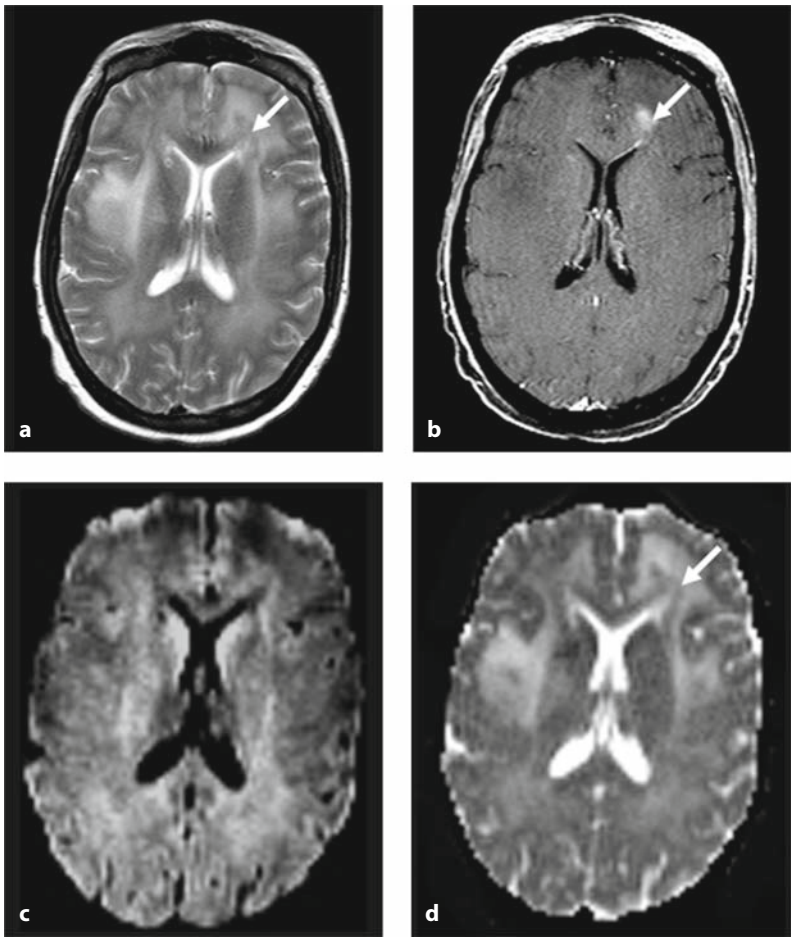

Figure 10.1 a–d

Disseminated necrotizing leukoencephalopathy in a 43-year-old woman with leptomeningeal metastasis from breast carcinoma treated with methotrexate and radiation. **a** T2-weighted image shows multifocal hyperintensities in the deep white matter with small irregular low signal foci in the left frontal area (*arrow*). **b** Post-contrast T1-weighted image reveals enhancement in the foci (*arrow*) in the left frontal white matter consistent with a necrosis. **c, d** DW image shows mild hyperintensity in the white matter lesions associated with diffuse increased ADC and mild increased ADCs in the left frontal foci, consistent with diffuse vasogenic edema and necrotic foci (*arrow*) (Courtesy of Policeni B, MD, The University of Iowa Hospitals and Clinics, USA)

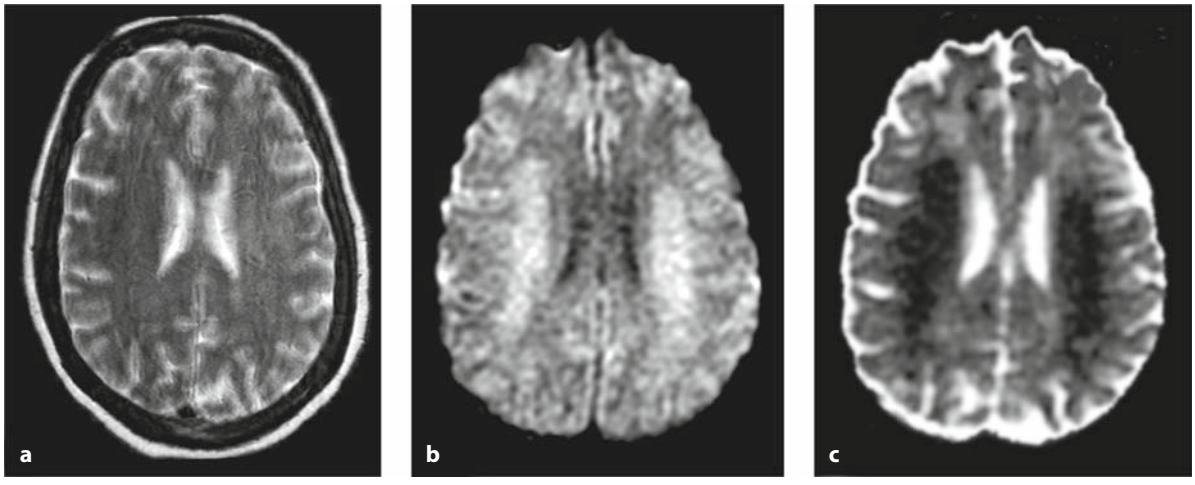

Figure 10.2 a–c

Methotrexate leukoencephalopathy (high dose) in a 50-year-old woman. **a** T2-weighted image does not demonstrate an appreciable abnormality in the white matter. **b** DW image shows diffuse hyperintensity in the bilateral corona radiata extending into the central semiovale. **c** ADC map shows diffuse white matter lesions as decreased ADC, which represents pure intramyelinic edema

Figure 10.2 d

d Pathology shows spongiform change representing intramyelinic edema (*arrows*) diffusely in white matter. Astrocytes are relatively spared (hematoxylin–eosin stain, original magnification ×200)

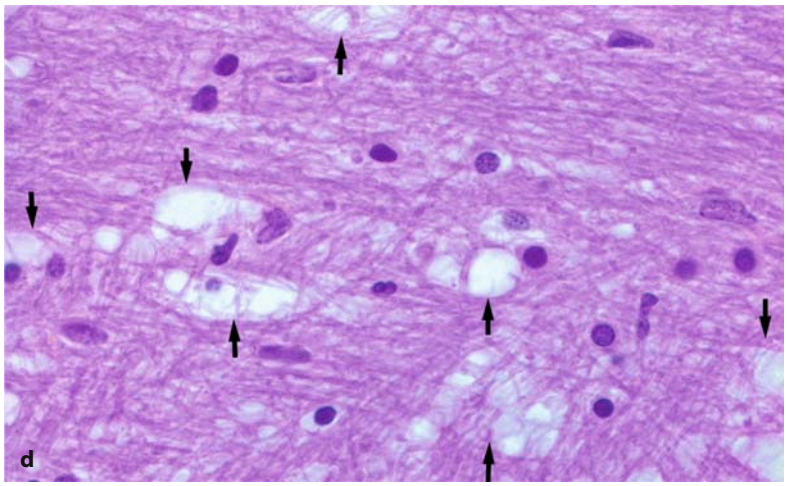

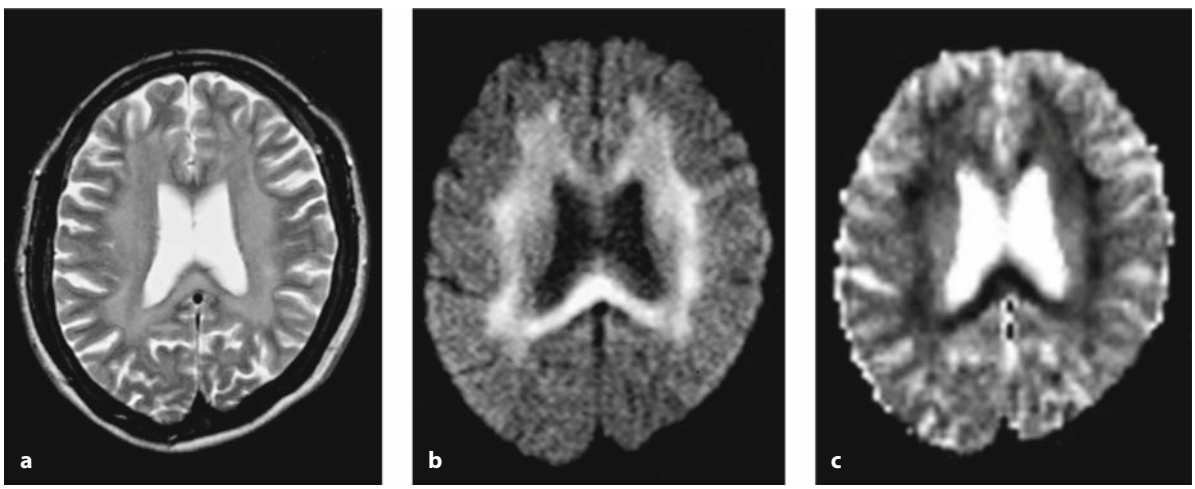

Figure 10.3 a–c

Carmofur leukoencephalopathy in a 58-year-old woman. **a** T2-weighted image shows diffuse hyperintensity in the periventricular white matter including the corpus callosum. **b, c** DW image shows these lesions as hyperintense with decreased ADC, presumably related to intramyelinic edema

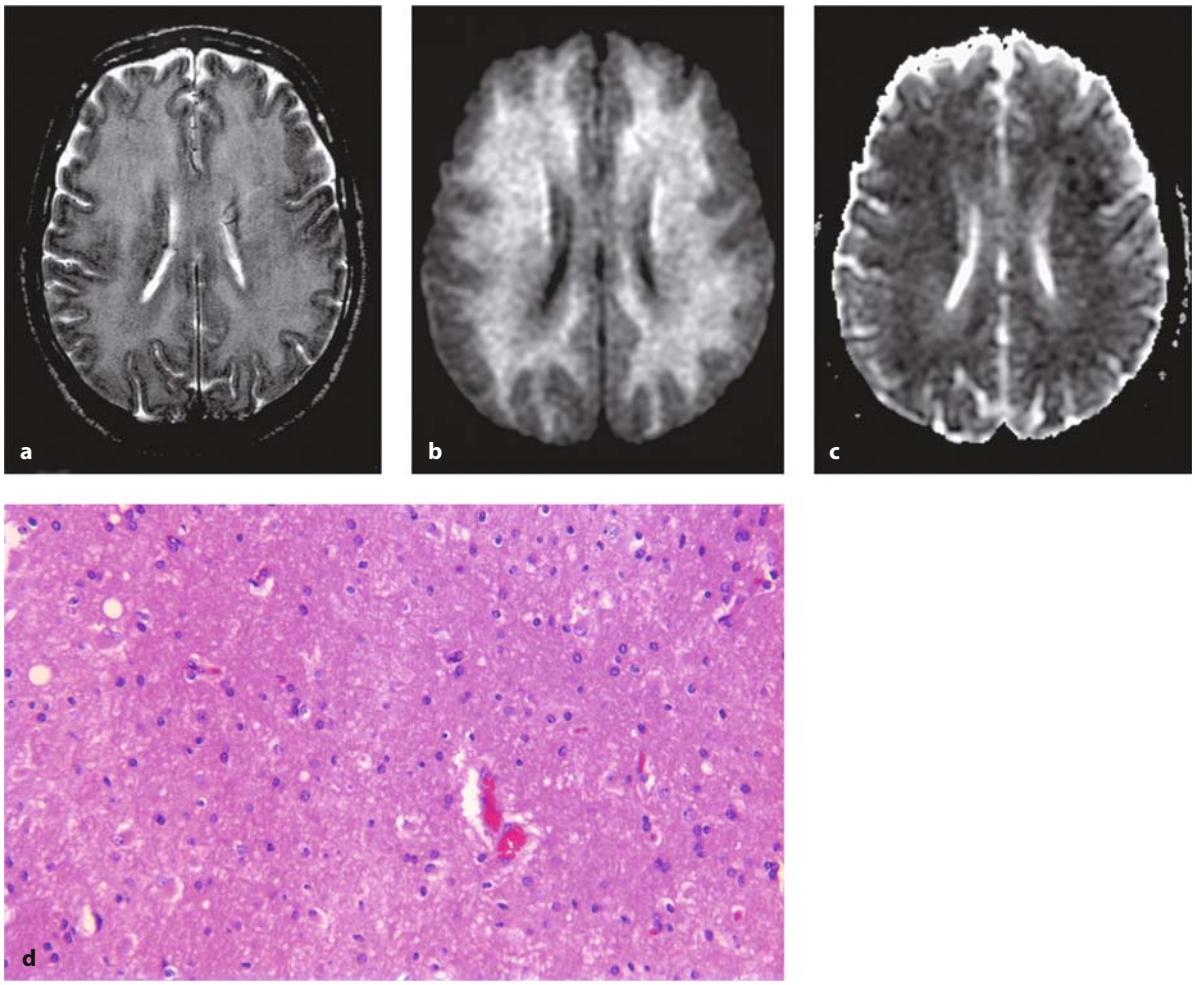

Figure 10.4 a–d

Heroin-induced leukoencephalopathy in a 55-year-old man. **a** T2-weighted image shows diffuse hyperintensity in the white matter including U fibers. **b, c** DW image shows these lesions as diffusely hyperintense with mildly decreased ADC. **d** Pathology shows intramyelinic edema and reactive astrogliosis, consistent with the subacute phase of heroin induced leukoencephalopathy (hematoxylin–eosin stain, original magnification ×200)

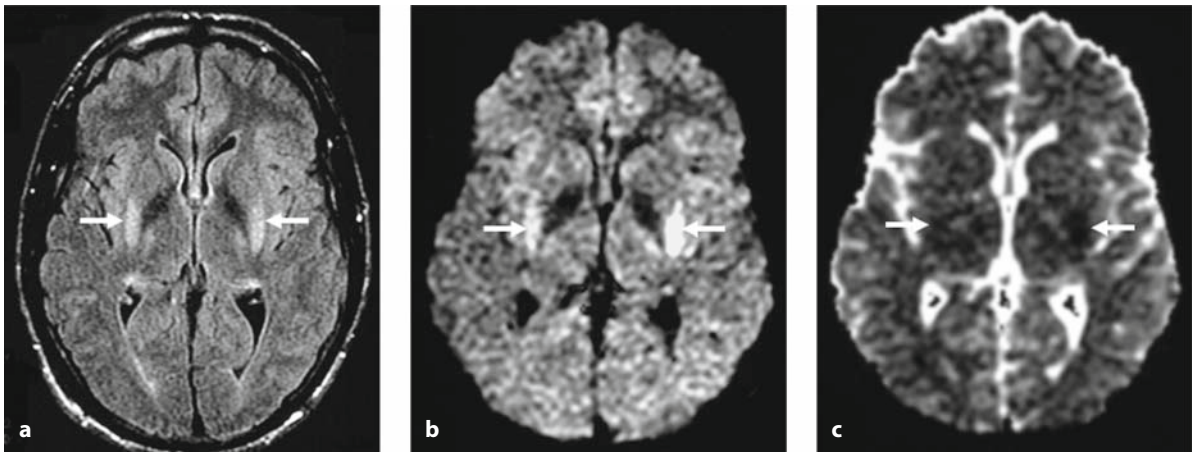

Figure 10.5 a–c

Hypoxic ischemic encephalopathy in an 18-year-old male patient after hanging himself. **a** FLAIR image shows hyperintensity in the posterior part of the putamina bilaterally. **b, c** DW image shows these lesions as hyperintense with the decreased ADC

10.1.3 Cocaine, Phencyclidine Hydrochloride, Amphetamines and Related Catecholaminergics

Cocaine, phencyclidine hydrochloride, amphetamines and related catecholaminergics can cause hemorrhage or infarction due to vasculitis, vasculopathy, or acute hypertensive effects [1]. DW imaging can be useful for the detection of these lesions (see also Chap. 7).

10.1.4 Hypoxic–Ischemic Encephalopathy

Hypoxic-ischemic encephalopathy (HIE) is the result of decreased global perfusion or oxygenation. The distribution of HIE varies according to the duration, degree, and abruptness of the hypoxic and/or ischemic insults, basal blood flow, and metabolic activity in the areas of ischemia, temperature, and serum glucose levels [13-15]. Hypoxia basically causes cardiac decompensation within minutes, resulting in global hypoperfusion and ischemic brain injury. However, pure anoxic encephalopathy may exist in some patients who are found early after the insult or who have suffered less severe anoxia [16]. In pure anoxia, cerebral blood flow is preserved allowing effective supply of nutrients and removal of toxic products such as lactic acid. Neurons tolerate pure anoxia for a longer duration than ischemia. Coma and other clinical findings can result from synaptic dysfunction.

DW imaging often depicts acute or subacute ischemic lesions when conventional MR imaging and CT scans show only subtle abnormalities [17]. Layers 3, 4, and 5 of the cortex, watershed zones, and the hippocampi (cornu ammonis 1 zone) are sensitive to ischemia. Cortical laminar necrosis is observed as hyperintensity on T2-weighted, FLAIR images(variably seen as early as 1 day after injury), and on T1-weighted images from the subacute to chronic phase of HIE. DW imaging often depicts acute or subacute ischemic lesions when MR imaging and CT scans are still normal or show only subtle abnormalities [18]. DW hyperintensity throughout the cerebral cortex suggests devastating diffuse hypoxic-ischemic necrosis, whereas a pattern of basal ganglia or thalamus suggests primary hypoxic injury or mild HIE (Figs. 10.5, 10.6). The prognosis of HIE depends on the extension of the cytotoxic edema, which is usually irreversible. DW imaging is helpful in establishing both the diagnosis and prognosis, but also in the management of HIE [19, 20]. High-b-value DW imaging with long TE improves accuracy in the early detection of the HIE lesions [21].

10.1.5 Brain Death

Brain death is defined as the irreversible cessation of all function of the entire brain [22]. Brain death criteria that most countries have commonly accepted are: deep unresponsive coma; absence of brain stem function and reflexes; positive apnea test despite pCO_2 greater than 60 mmHg. The irreversibility of such criteria must be confirmed. Brain electrical activity (EEG, brain stem evoked potentials) may be inaccurate in comatose patients with drug-induced hypothermia or intoxication. The absence of cerebral blood flow is accepted as a confirmatory sign of brain death.

Conventional angiography was considered the gold standard until the 1990s, but it is an invasive method and may damage transplantable organs.

MR imaging and MR angiography have been reported as reliable methods in demonstrating absence of cerebral blood flow and determining brain death [22-24]. MR findings in brain death include: (1) central and tonsillar herniation, (2) absent intracranial vascular flow void, (3) poor gray matter/white matter differentiation, (4) no intracranial contrast enhancement, (5) carotid artery enhancement (intravascular enhancement sign), and (6) prominent nasal and scalp enhancement (MR hot nose sign) [24]. MR angiograms show no intracranial flow above the supraclinoid carotid arteries. This is presumably due to the increased intracranial pressure. DW imaging shows diffuse hyperintense areas in the gray and white matter including the brain stem (Fig. 10.7). A massive drop in ADC values in the hemispheres has been reported (<50% of normal values) [25]. The ADC value of the white matter is significantly lower than that of the gray matter [26]. Severe ADC reduction in gray and white matter probably reflects global irreversible pathological changes. These ADC changes may also be related to the brain temperature and a decrease in brain temperature of 1.5°C corresponds to an ADC decrease of 0.02×10^{-3} mm^2/s [27].

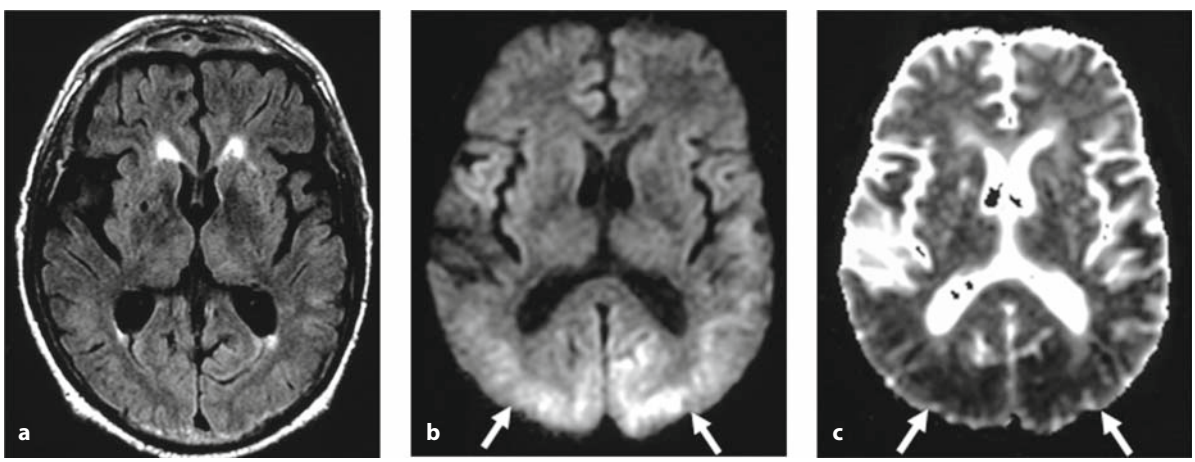

Figure 10.6 a–c

Hypoxic ischemic encephalopathy in an 83-year-old man with a cardiac arrest. **a** It is difficult to detect the abnormalities on the FLAIR image. **b, c** DW image shows extensive diffuse hyperintense lesions in the temporo-occipital cortices bilaterally (*arrows*) with the decreased ADC

10.1.6 Hypoglycemia and Hyperglycemia

Glucose is the main energy substrate of the brain. Hypoglycemia is caused by overuse of insulin, oral hypoglycemic agents, insulinoma, sepsis, renal or hepatic failure, or Addison disease. Neurologic signs of hypoglycemia are non-specific including weakness, confusion, seizures, and coma. Sequelae of hypoglycemic coma are rare, but if so they includes profound memory loss, persistent vegetative state, and death in 2-4% of cases.

MR imaging shows lesions that involve the cerebral cortex, particularly the temporal lobe, hippocampus, and basal ganglia [28]. The most severely affected patients manifest basal ganglia involvement. DW imaging shows hyperintense lesions with decreased ADC similar to hypoxic–ischemic encephalopathy (Fig. 10.8) [28, 29]. Reversible lesions on DW imaging have also been reported, which often involves the bilateral internal capsules, corona radiata, and corpus callosum [29-31]. This pattern may be the result of a different pathophysiologic process such as a release of excitatory amino acids into the extracellular space [32].

Hyperglycemia can disrupt the blood-brain barrier and produce a decreased cerebral blood flow, intracellular acidosis, accumulation of extracellular glutamate, and decreased activity of GABAergic neurons. Hemichorea-hemiballismus associated with hyperglycemia is characterized by hyperintensities in the striatum on T1-weighted images and CT studies. The process is either unilateral or bilateral. The T1 high signal is probably related to manganese (Mn) accumulations accompanied by Mn superoxide dismutase and glutamine synthetase with rich protein contents in the reactive swollen astrocytes (gemistocytes) [33-35]. DW imaging has been reported to detect early ischemic damage as areas of heterogeneous signal intensity with decreased ADC (Fig. 10.9) [33, 34, 36]. Diabetic ketoacidosis with prolonged hyperglycemia

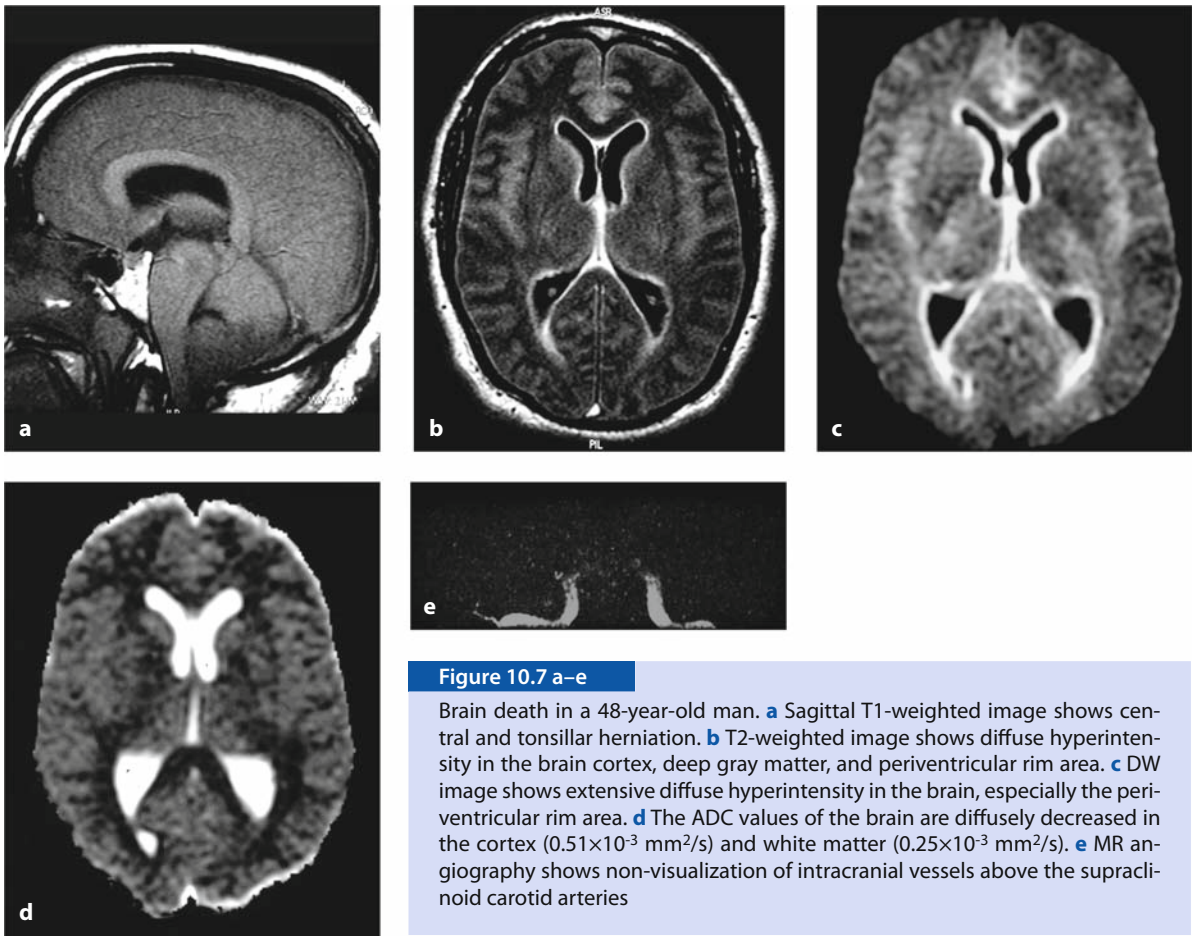

Figure 10.7 a–e

Brain death in a 48-year-old man. **a** Sagittal T1-weighted image shows central and tonsillar herniation. **b** T2-weighted image shows diffuse hyperintensity in the brain cortex, deep gray matter, and periventricular rim area. **c** DW image shows extensive diffuse hyperintensity in the brain, especially the periventricular rim area. **d** The ADC values of the brain are diffusely decreased in the cortex (0.51×10^{-3} mm^2/s) and white matter (0.25×10^{-3} mm^2/s). **e** MR angiography shows non-visualization of intracranial vessels above the supraclinoid carotid arteries

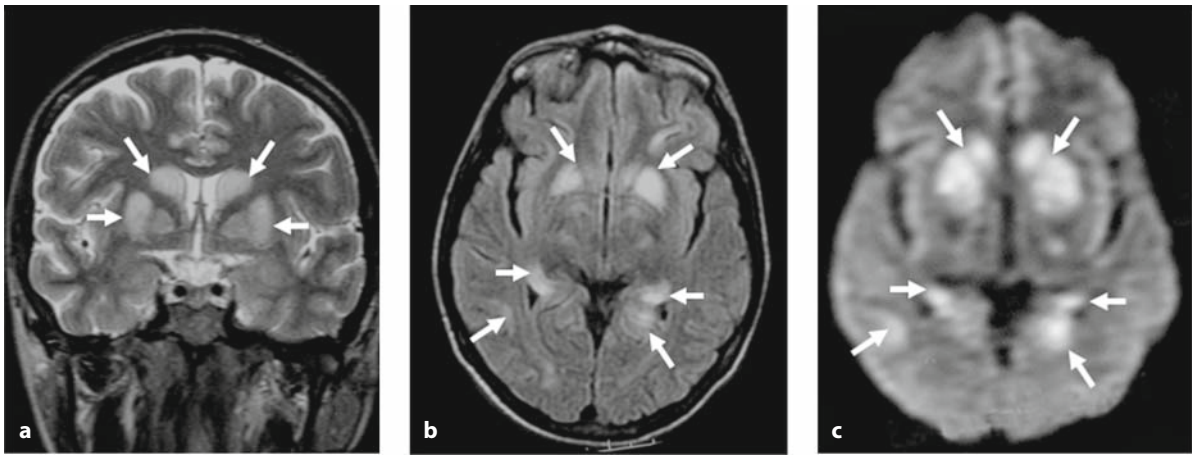

Figure 10.8 a–c

Hypoglycemic encephalopathy in a 53-year-old man. **a, b** Coronal T2-weighted and axial FLAIR images show symmetric hyperintense lesions in the basal ganglia, hippocampi, and temporo-occipital lobes (*arrows*). **c** DW image shows these areas as hyperintensity lesions (*arrows*)

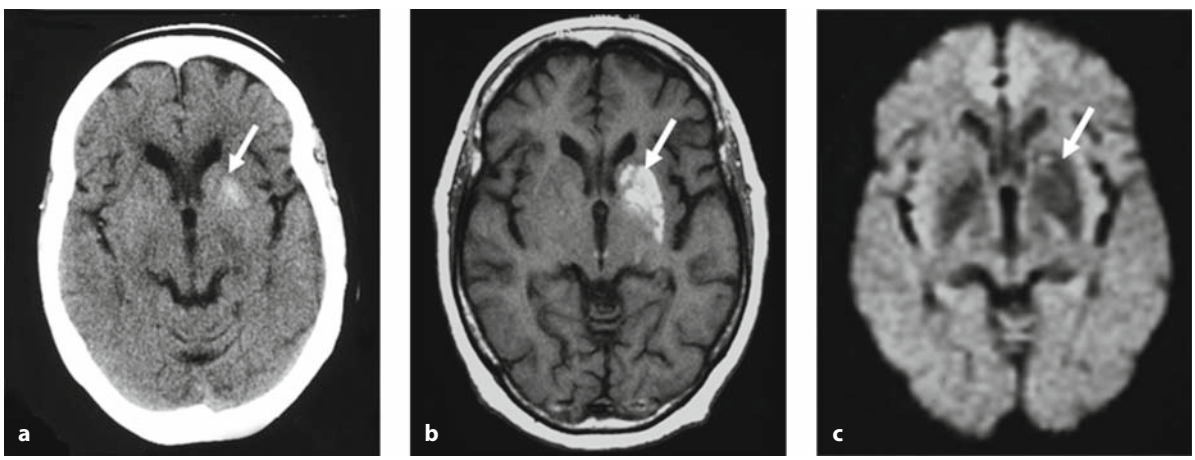

Figure 10.9 a–c

Hemichorea-hemiballismus associated with hyperglycemia in a 69-year-old woman with type 2 diabetes. **a** CT shows high density areas in the left caudate head and anterior part of the putamen (*arrow*). **b** T1-weighted image shows hyperintensity in the left entire striatum (*arrows*). **c** DW image shows these lesions as low signal intensity with an isointense area in the left caudate head (*arrows*)

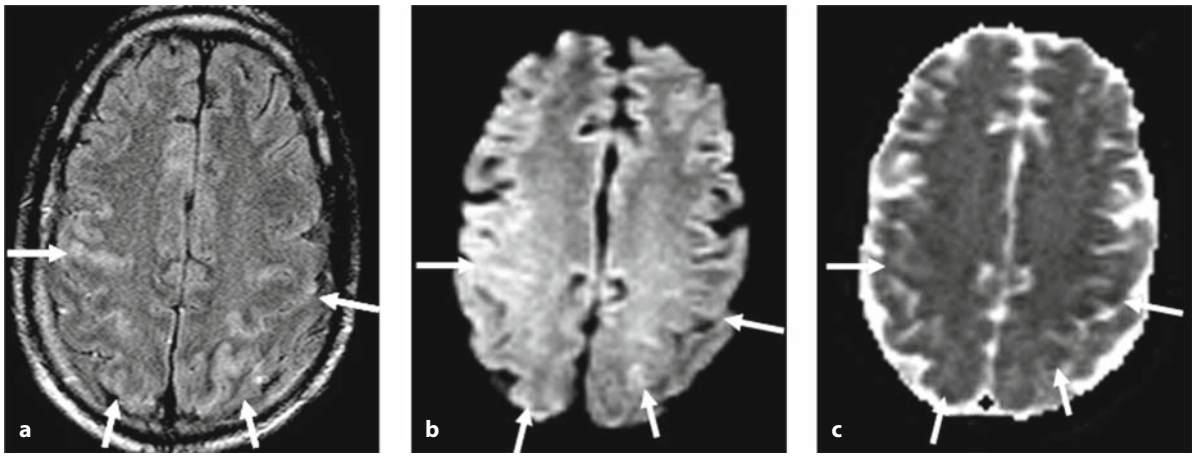

Figure 10.10 a–c

Diabetic ketoacidosis with type 1 diabetes in a 28-year-old man (blood sugar 1,500 mg/dl). **a** FLAIR image show symmetric hyperintense lesions in the parietal cortices bilaterally. **b, c** DW image shows these areas as hyperintense with mild decreased ADC

may cause subtle FLAIR and diffusion abnormalities in the cortex associated with elevations in glucose, myoinositol, taurine, and ketones in MR spectroscopy (Fig. 10.10) [37]

10.1.6 Carbon Monoxide Intoxication

The affinity of carbon monoxide (CO) for hemoglobin is approximately 250 times that of oxygen. The carboxyhemoglobin reduces the oxygen-carrying capacity of blood, causing tissue hypoxia. CO also inhibits the mitochondrial electron transport enzyme system and activates polymorphonuclear leukocytes, which causes brain lipid peroxydation and myelin breakdown. The globus pallidus is the most common site of this involvement. The putamen, caudate nucleus, thalamus, hippocampus, and substantia nigra are also occasionally involved [38]. The globus pallidus and the pars reticulata of the substantia nigra contain the highest iron content in the brain. CO directly binds heme-iron in these areas, which is the cause of the histotoxicity and selective vulnerability of the pallidoreticularis [39]. DW imaging shows hyperintensity with decreased ADC in these lesions in the acute phase (Fig. 10.11).

Cerebral white matter involvement is common and usually presented as delayed anoxic encephalopathy. It is usually seen in the late subacute phase after recovery from the acute stage of CO poisoning (lucid interval usually 2-3 weeks). DW imaging shows diffuse hyperintensity with decreased ADC in the periventricular white matter and centrum semiovale [40, 41].

10.1.7 Delayed Postanoxic Encephalopathy

Delayed postanoxic encephalopathy is a rare condition in which patients appear to make a complete clinical recovery after an episode of anoxia or hypoxia and then develop progressive neuropsychiat-

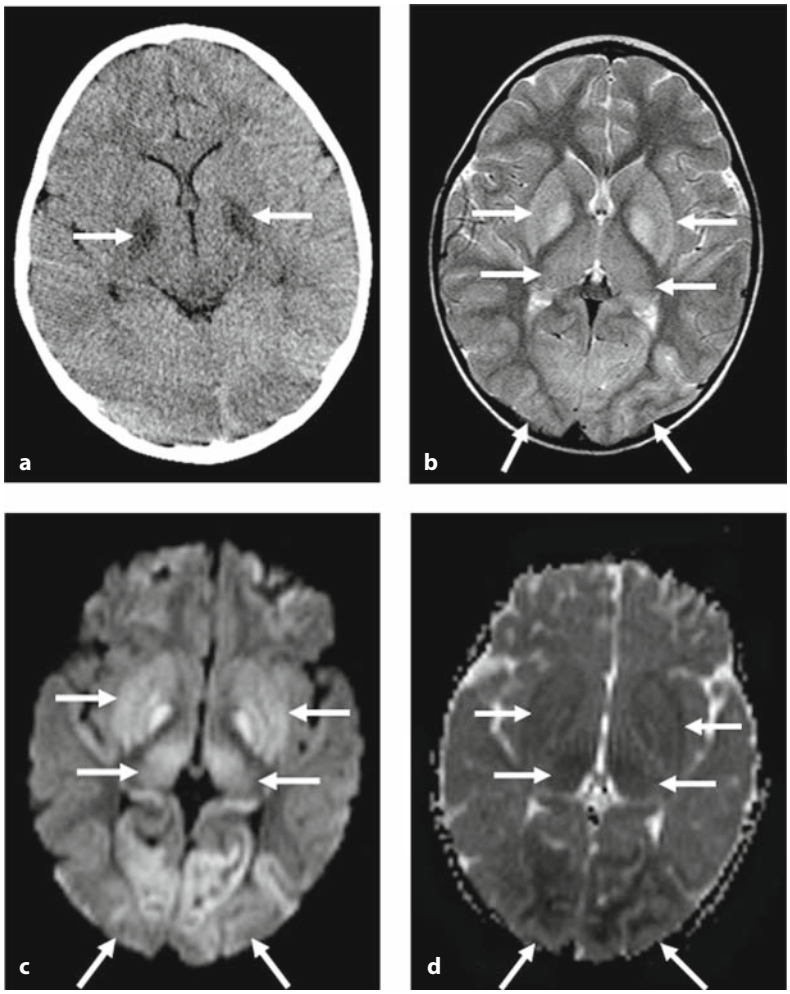

Figure 10.11 a–d

Carbon monoxide poisoning in a 4-year-old boy. **a** CT shows symmetric low-density areas in the globi pallidi. **b** T2-weighted imaging shows symmetric extensive hyperintense lesions in the basal ganglia, thalami, hippocampi, and posterior cerebral cortices. **c, d** DW image shows these areas as hyperintense with decreased ADC

ric symptoms and/or neurological deficits [42]. The incidence has been reported to range from 1 to 28 per 1,000 suffering from hypoxic or anoxic events. It is most commonly associated with CO poisoning (13 cases among 20,000 patients), but has also been reported after hypoxic events related to childbirth, surgery and anesthesia, drug overdose, exposure to toxins, anaphylaxis, seizures, cyanosis, and strangulation. The prognosis is variable from a full recovery to permanent neurologic sequelae, personality changes, and death. The pathogenesis is presumably related to programmed cell death/apoptosis of the oligodendrocytes triggered by hypoxia.

DW imaging shows diffuse hyperintensity with decreased ADC in the periventricular white matter and centrum semiovale, pathologically consistent with cytotoxic edema in the myelin sheath (intramyelinic edema) (Fig. 10.12).

10.1.8 Central Pontine Myelinolysis and Extrapontine Myelinolysis

Central pontine myelinolysis (CPM) and extrapontine myelinolysis (EPM) represent destruction of myelin sheaths in characteristic places within the brain stem and cerebrum. The most common location is the central part of the basis pontis, followed by a combined type with central and extrapontine areas of myelinolysis. Isolated EPM is rare [43]. The basal ganglia, caudate nucleus, thalamus, geniculate bodies, internal and external capsules, corpus callosum, cerebellum, cerebellar peduncle, and gray–white matter junction are possible sites of EPM [44-47]. The synonyms include osmotic myelinolysis and osmotic demyelination syndrome. Symptoms include acute confusional state, pseudobulbar affect, stupor, coma, and occasionally locked-in syndrome, intermingled with

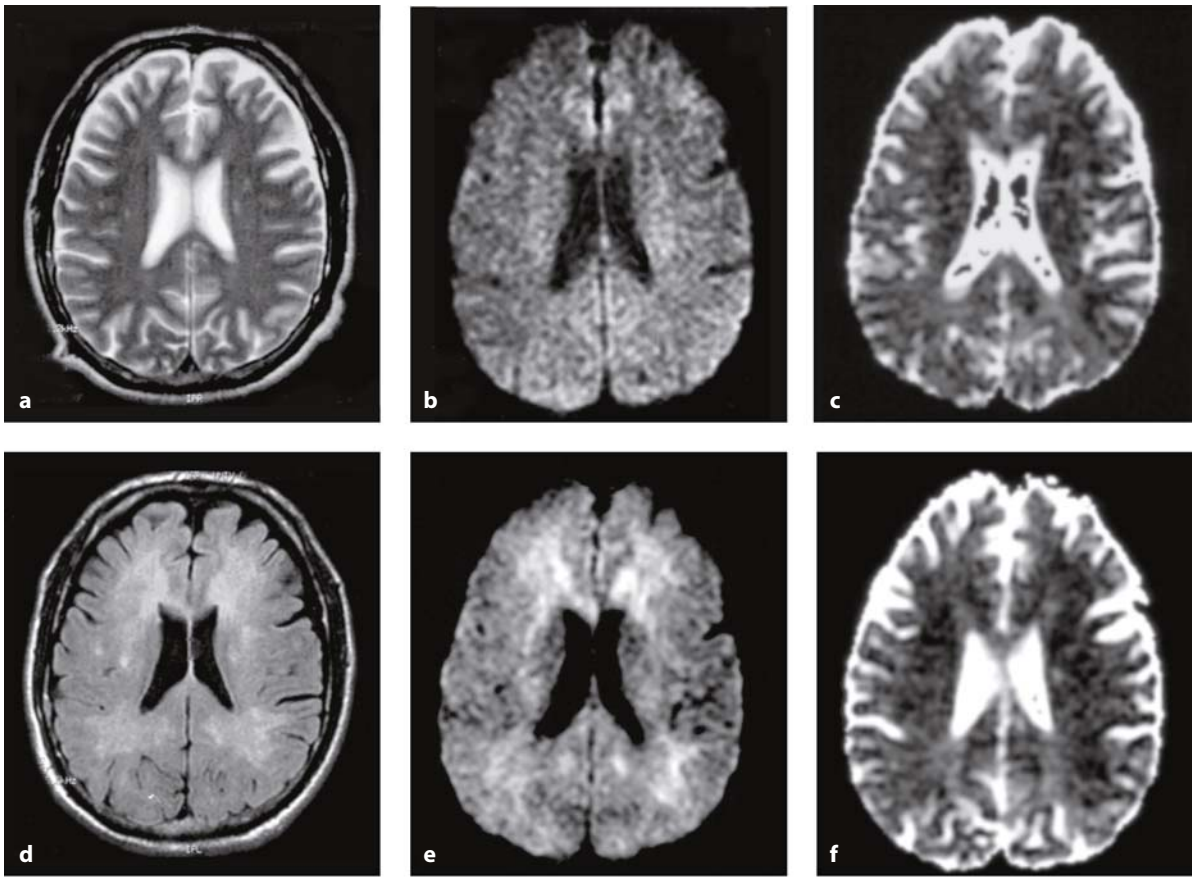

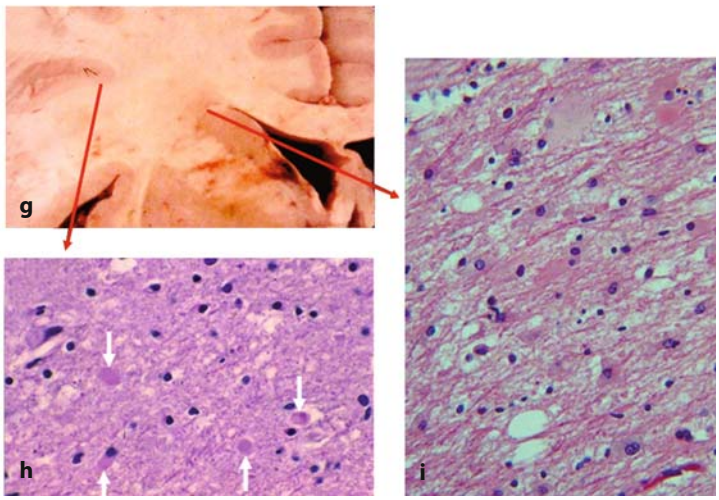

Figure 10.12 a–i

Delayed postanoxic encephalopathy in a 53-year-old man with progressive mental status changes for 3-4 days. There was a history of narcotic overdose 2 weeks earlier. **a** T2-weighted image shows no abnormal signal intensity in the brain. **b, c** DW image shows very subtle hyperintensity with mild decreased ADC in the corona radiata. **d** Follow-up MR imaging was performed 14 days after the onset. FLAIR image shows high signal intensity in the deep white matter bilaterally. **e** DW images revealed diffuse hyperintensity with decreased ADC. **f** He continued to deteriorate and died about 20 days later, 46 days after the overdose. Autopsy was performed. **g–i** Pathology shows myelin discoloration in the periventricular white matter and caudate lobe. Pathology shows neuronal axonal spheroids (*arrows*) in the gray matter (**h**) and varying degrees of myelin loss with some spongy changes in the white matter, reflecting intramyelinic edema in the deep white matter (**i**)

prominent motor manifestations of flaccid evolving to spastic quadriparesis, dysarthria, and dysphagia [48-50].

Pathological findings show destruction of myelin sheaths, though the nerve cells and axons are relatively spared. The underlying etiology and pathogenesis are unknown, but the hypotheses include osmotic endothelial injury, microglia-derived cytokines, excessive brain dehydration, and metabolic compromise [51]. Organic osmolytes, including glutamate, glutamine, betamine, or taurine, have been implicated in the pathogenesis of myelinolysis [52]. The most common osmotic insult is a rapid correction of hyponatremia. However, CPM and EPM can also occur

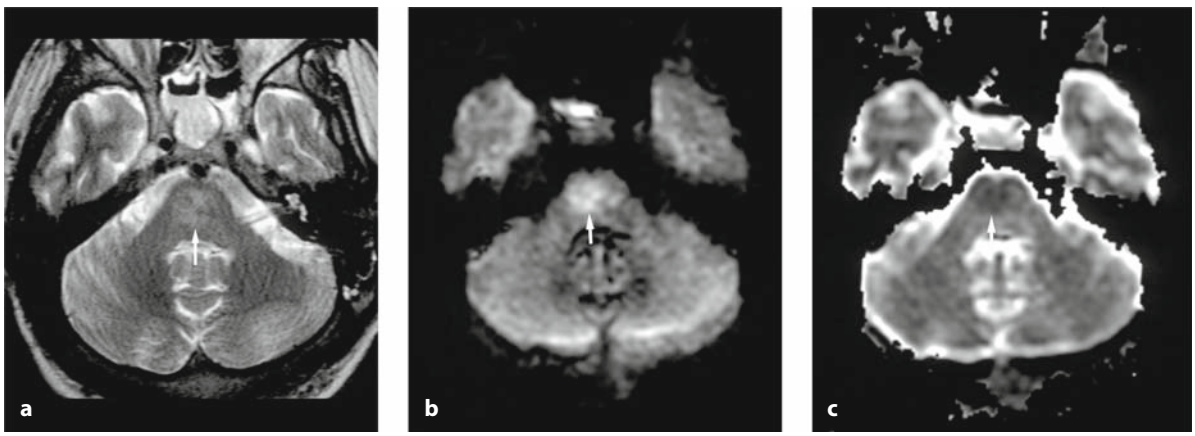

Figure 10.13 a–c

Central pontine myelinolysis in a 33-year-old man. **a** T2-weighted image shows a hyperintense lesion in the center of the pons (*arrow*). **b, c** DW image shows this lesion as hyperintense with decreased ADC

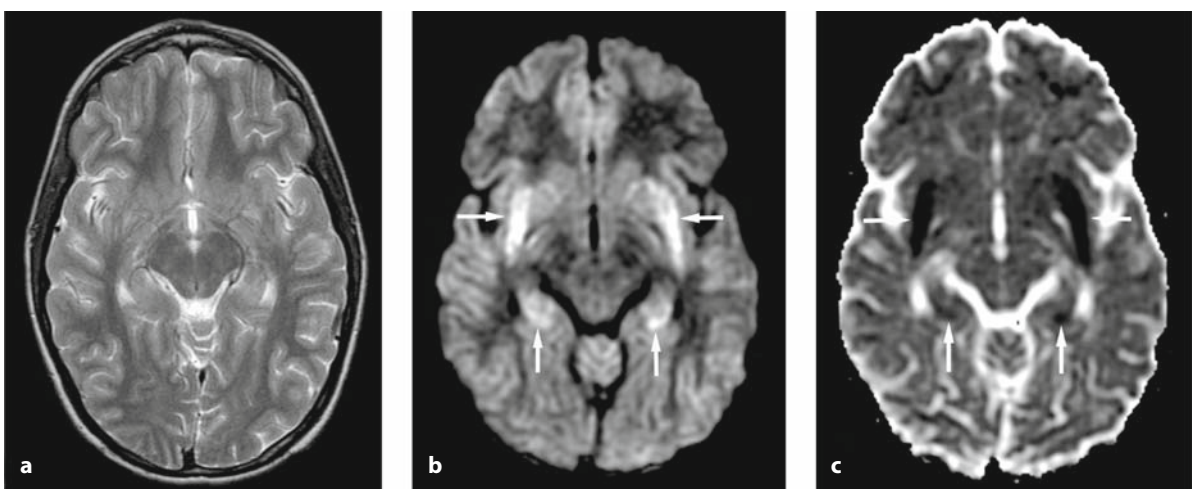

Figure 10.14 a–c

Extrapontine myelinolysis in an 11-year-old boy. **a** T2-weighted image shows no appreciable abnormality in the external capsules and hippocampi. **b, c** DW image demonstrates bilateral symmetrical hyperintense lesions with decreased ADC in the external capsules and hippocampi (*arrows*), representing cytotoxic edema

in normo- or hypernatremic states in patients with chronic alcoholism, post-liver transplantation, malnutrition, burn, hyperemesis gravidarum, and AIDS [53–55].

MR imaging has a fundamental role in the diagnosis and discloses hyperintense lesions on T2-weighted images, with or without enhancement on gadolinium-enhanced T1-weighted images. DW imaging can be useful in detecting the lesions in the early phase as hyperintense with decreased ADC, which represents cytotoxic edema (Figs. 10.13-10.15) [56]. Cytotoxic edema in CPM and EPM occur not only in myelin sheaths, but also in neurons, axons and astrocytes [57]. The clinical outcome of CPM and EPM is highly variable, and both fatal and clinically reversible cases may be associated with this kind of cytotoxic edema.

10.1.9 Wernicke Encephalopathy

Thiamine (vitamin B1) deficiency can cause Wernicke encephalopathy, characterized by confusion, ataxia, and abnormal eye movements, but is not always present. It is frequently associated with chronic alcohol abuse. Nonalcoholic Wernicke encephalopathy, which is uncommon, includes many other conditions such as tumors and bypass surgery of gastrointestinal tract, gastroplasty, pancreatitis, psychogenic refusal of food,

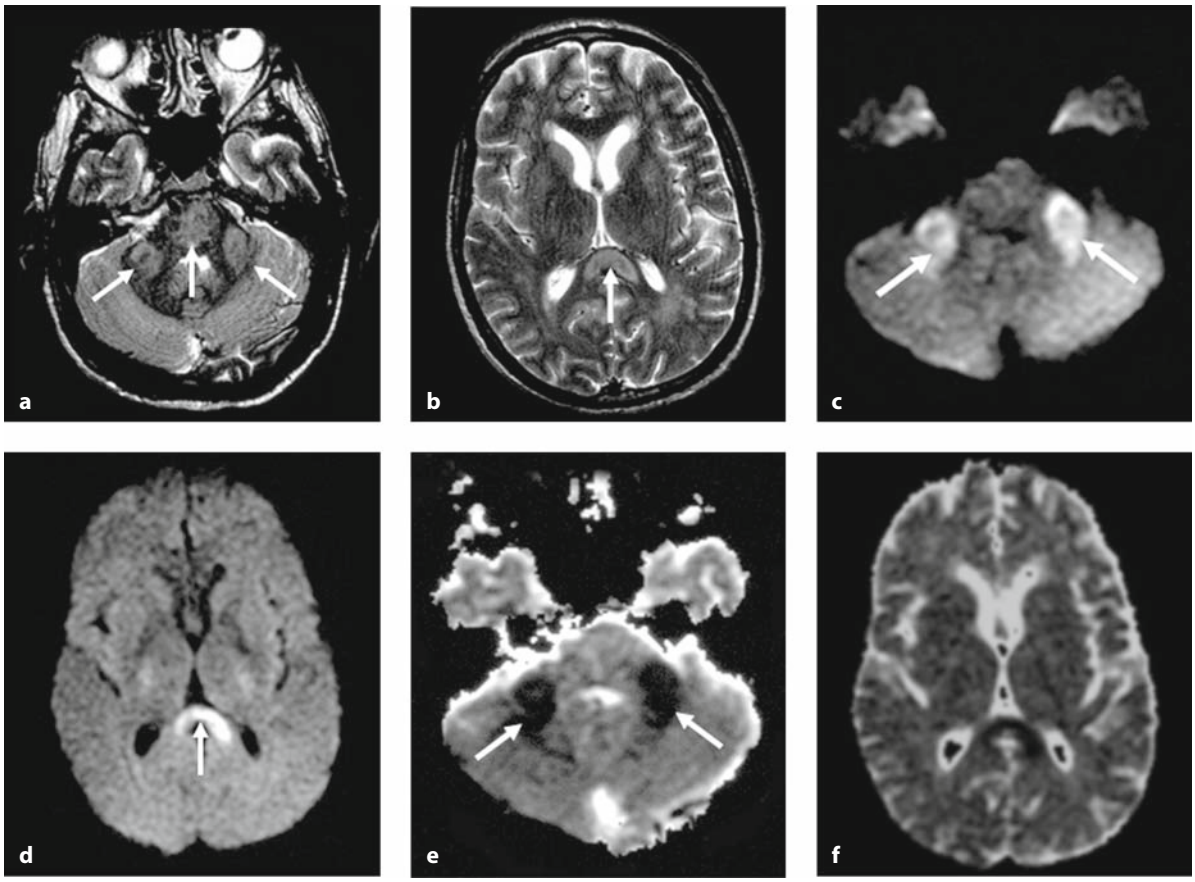

Figure 10.15 a–f

Central pontine and cerebellar peduncle myelinolysis in a 54-year-old man with slurred speech and confusion. **a, b** T2-weighted image shows hyperintense lesions in the center of the pons, middle cerebellar peduncles (**a**), and corpus callosum (**b**) (*arrows*). **c-f,** DW image shows the lesions in the middle cerebellar peduncles and corpus callosum as hyperintense with decreased ADC, and the pontine lesion as isointense with increased ADC (*arrows*)

anorexia nervosa, voluntary food starvation, parental therapy, hyperemesis gravidarum, prolonged infectious-febrile disease, chronic uremia, dialysis, HIV infection, and thyrotoxicosis [58-60]. Without thiamine, the Krebs and pentose phosphate cycles cannot metabolize glucose [61, 62]. The enzymatic inactivity leads to accumulation of intracellular glutamate. Cellular homeostasis will soon fail resulting in release of glutamate into the extracellular space (NMDA receptor mediated excitotoxicity), and the midline gray matter degenerates. Thiamine is also essential in maintaining osmotic gradients across cell membranes. Pathologic features are edema, spongy degeneration of the neurophil, swelling of capillary endothelial cells and astrocytes, necrosis, and decreased myelination. The lesions are commonly seen in the mamillary bodies (57-75%), thalamic and hypothalamic nuclei, periaqueductal gray matter, tectal plate, walls of the third and floor of the fourth ventricle, and less commonly in the caudate, frontal, and parietal cortex, pons, dorsal medulla, red nuclei, corpus callosum, cerebellum, and dentate nuclei [58, 63-65].

MR imaging shows symmetrical hyperintense lesions of these areas on FLAIR and T2-weighted images. They may or may not show enhancement on T1-weighted images following contrast agent injection, depending on local disruption of the blood-brain barrier [58, 66]. Mamillary body involvement and en-

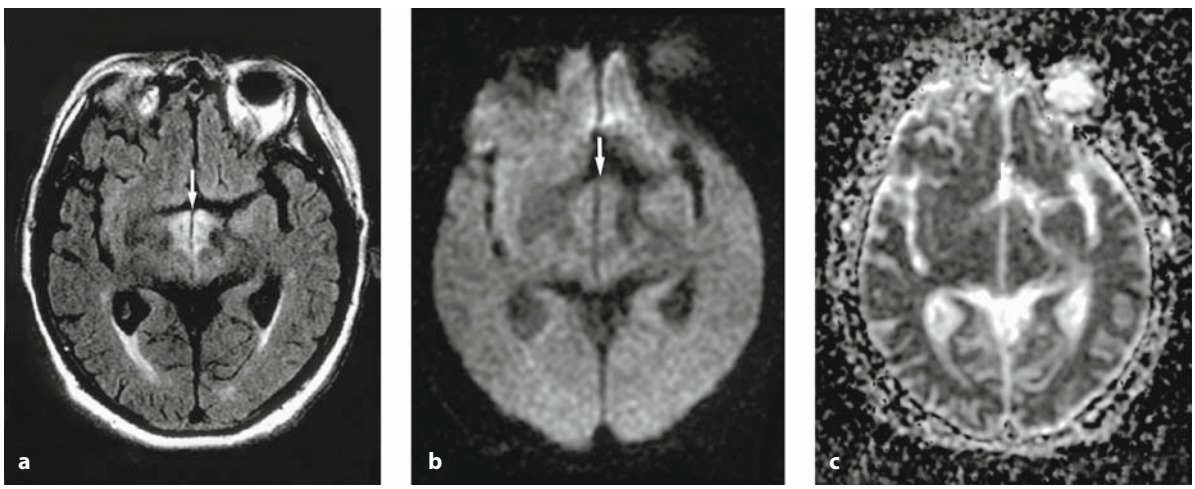

Figure 10.16 a–c

Wernicke encephalopathy with alcohol abuse in a 75-year-old man. **a** FLAIR shows a symmetrical hyperintense lesion in the hypothalamus (*arrow*). **b, c** DW image shows isointense lesions with increased ADC in the hypothalamus, which may represent vasogenic edema (*arrow*)

hancement are often seen in Wernicke encephalopathy with alcohol abuse but are less frequent in non-alcoholic Wernicke encephalopathy [58-60]. With intravenous thiamine treatment, these lesions may dissipate. DW imaging shows these lesions as hyperintense with decreased or increased ADC. Lesions with decreased ADC are thought to represent cytotoxic edema of neurons or astrocytes, while lesions with increased ADC may represent vasogenic edema (Figs. 10.16, 10.17) [67–72]. Both types of lesion can be reversible [71, 72]. The important differential diagnosis of symmetric lesions in the medial thalami includes ischemia due to occlusion of the artery of Percheron and deep cerebral vein thrombosis.

10.1.10 Marchiafava–Bignami Disease

Marchiafava–Bignami disease is a fatal disorder characterized by demyelination of the corpus callosum, often associated with chronic alcoholism [73]. The genu of the corpus callosum is more frequently involved, but the degeneration can extend throughout the entire corpus callosum. Occasionally, optic chiasm and the visual tracts, putamen, anterior commissure, cerebellar peduncles, cortical gray matter and U-fibers may be involved. Clinical signs include seizures, impairment of consciousness, and signs of interhemispheric disconnection, but they are nonspecific.

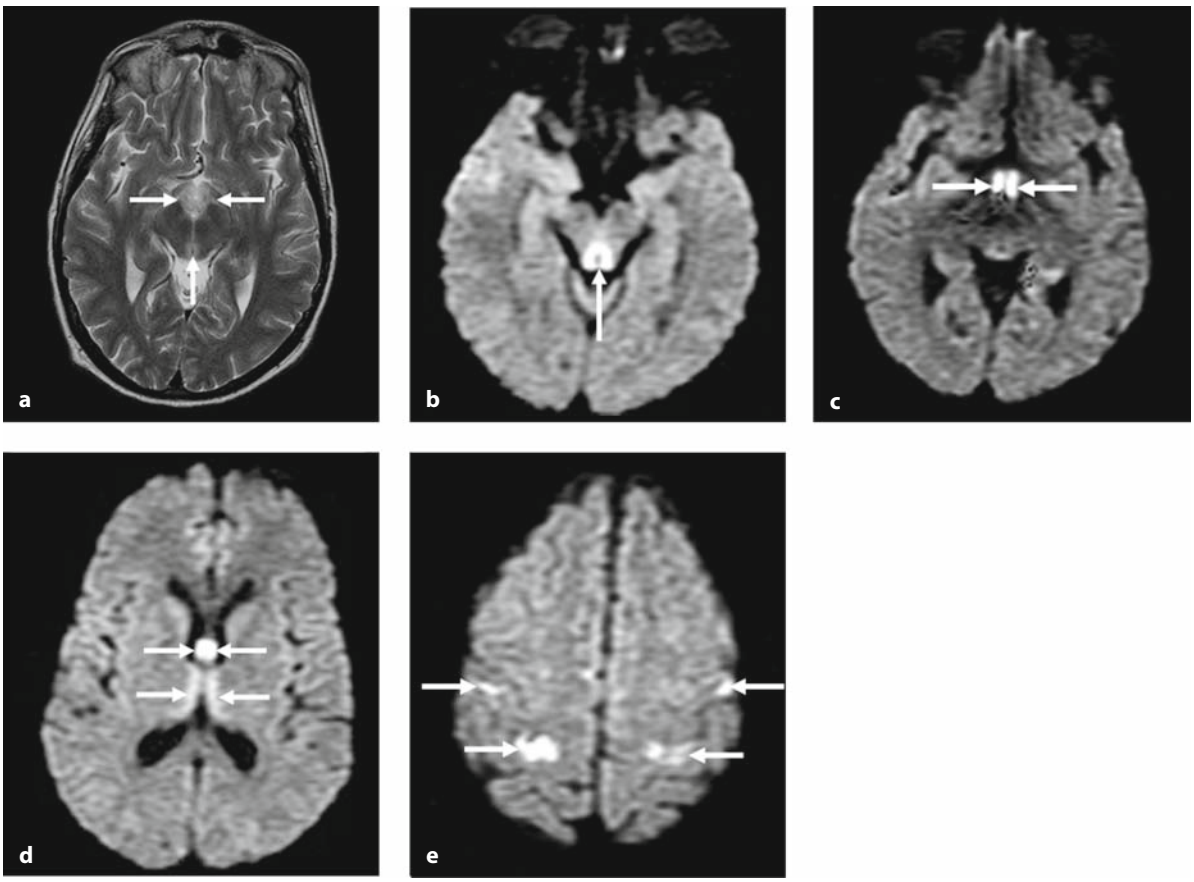

Figure 10.17 a–e

Wernicke encephalopathy with thyrotoxicosis in a 36-year-old man. **a** T2-weighted image shows symmetric hyperintense lesions in the mamillary bodies, hypothalami, and periaqueductal region (*arrows*). **b-e** DW imaging shows hyperintense lesions in the hypothalami, midbrain tectum, periaqueductal region, medial thalami, fornices, and pre- and postcentral gyri (*arrows*), associated with partially decreased ADC (not shown)

The corpus callosum appears hypoattenuated on CT and hyperintense on T2-weighted and fluid-attenuated inversion-recovery (FLAIR) images, which is essential to confirm the diagnosis. These lesions can be partially reversible with treatment [74]. DW imaging shows lesions in the early phase as hyperintense with decreased ADC [75] representing cytotoxic edema, mainly in the myelin sheaths (intramyelinic edema). In the subacute phase, the lesions are hyperintense on DW imaging with increased ADC representing demyelination or necrosis (Fig. 10.18).

10.1.11 Steroid-Responsive Encephalopathy Associated with Autoimmune Thyroiditis (Hashimoto's Encephalopathy)

Steroid-responsive encephalopathy associated with autoimmune thyroiditis (SREAT), often termed Hashimoto's encephalopathy, is characterized by subacute relapsing-remitting neurologic and neuropsychiatric symptoms and increased titers of antithyroid antibodies (thyroperoxidase antibody, formerly known as antimicrosomal antibody) in the serum

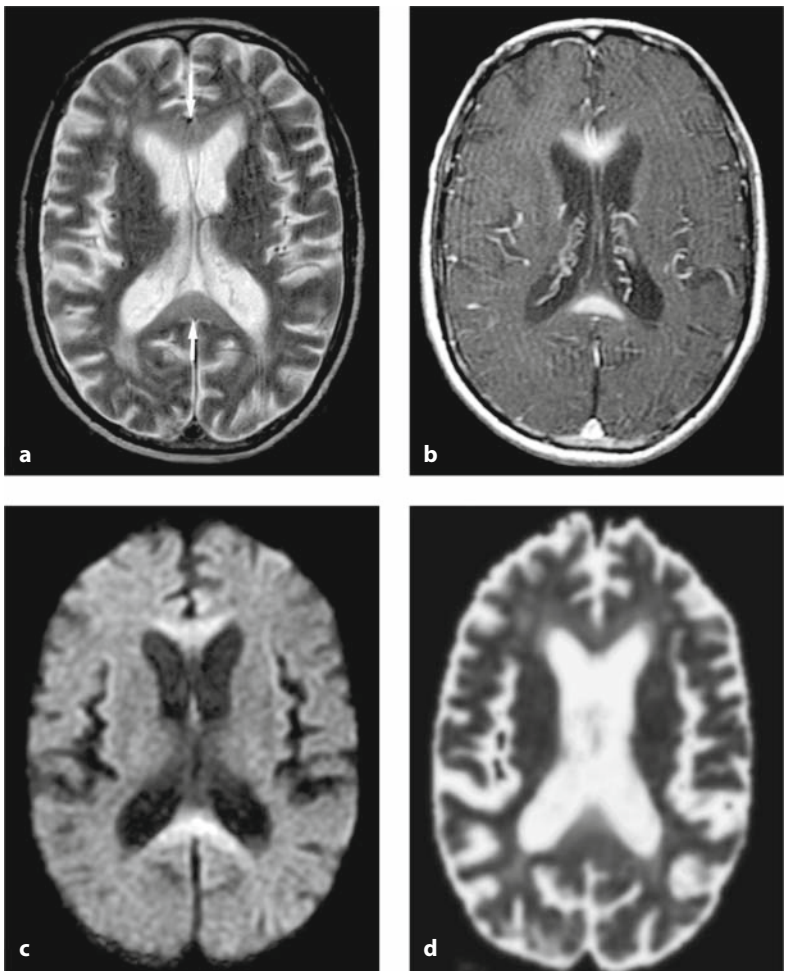

Figure 10.18 a–d

Marchiafava–Bignami disease in a 58-year-old man. **a** T2-weighted image shows hyperintensity in the anterior and posterior corpus callosum (*arrows*) and in the periventricular white matter. **b** Gadolinium-enhanced T1-weighted image with magnetization transfer contrast reveals enhancing lesions in the anterior and posterior corpus callosum. **c, d** DW image shows hyperintense lesions with increased ADC in the corpus callosum, representing demyelination and necrosis in the subacute phase

and CSF [76]. SREAT has a variety of clinical presentations including stroke-like symptoms, seizure, tremor, mental status changes, delirium, hallucination, and dementia. It is often misdiagnosed initially due to non-specific symptoms. The pathogenesis is largely debated. Current hypotheses encompass autoimmune encephalopathies (an immunological reaction to antineuronal antibodies against brain-thyroid antigens), autoimmune vasculitis, direct toxic effect by excessive thyrotropin-releasing hormone, global hypoperfusion, edema, and primary demyelination [76-83]. Since the disease responds to steroids very well, it is important for early diagnosis in conjunction with MR imaging, which can minimize the adverse outcome.

Recently reported MR imaging findings include diffuse white matter lesions [84], nucleus accumben, part of the ventral striate nucleus [85], hippocampal and medulla lesions, as well as cerebellar atrophy [86, 87]. DW imaging shows diffuse white matter lesions as isointense with the increased ADC values (Fig. 10.19)

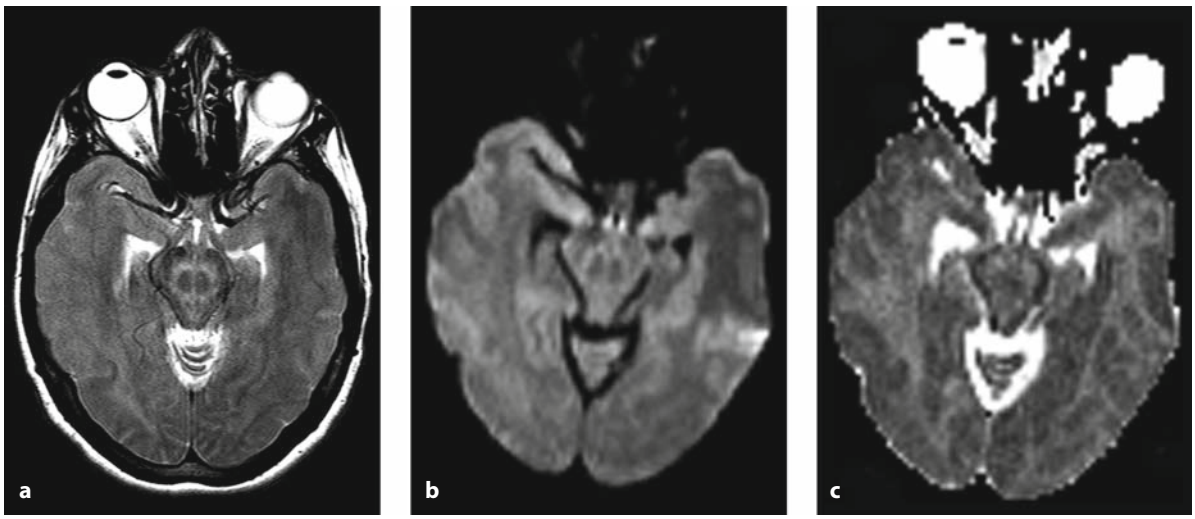

Figure 10.19 a–c

Hashimoto's encephalopathy in a 43-year-old woman with hypothyroidism. **a** T2-weighted image shows brain swelling and diffuse white matter hyperintensity. **b, c** DW imaging shows diffuse white matter hyperintensity with increased ADC consistent with vasogenic edema. Follow-up MR imaging showed improved swelling and edema (Courtesy of Yang L, MD, The University of Iowa Hospitals and Clinics, USA)

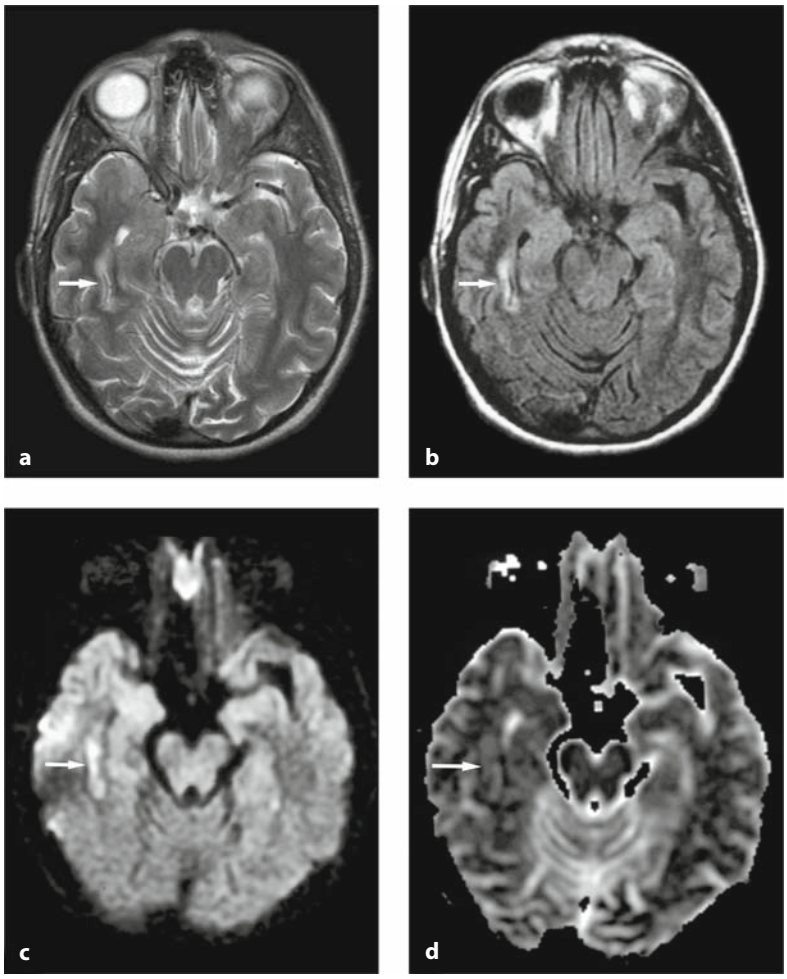

Figure 10.20 a–d

Mitochondrial encephalopathy with lactic acidosis and stroke (MELAS) in a 27-year-old woman. **a, b** T2-weighted and FLAIR images show a hyperintense lesion in the right temporal lobe (*arrow*). **c, d** DW image shows this lesion as hyperintense with increased ADC (*arrow*), mainly representing vasogenic edema

10.2 Metabolic Disease

10.2.1 Mitochondrial Encephalopathy

Mitochondrial encephalopathies are a heterogeneous group of disorders affecting primarily the central nervous system and skeletal muscles. Two main hypotheses attempt to explain the cerebral lesions: (1) metabolic damage of the endothelium, which leads to small-vessel occlusion and secondary neuronal death and (2) mitochondrial dysfunction, which results in anaerobic metabolism and neuronal death from acidosis [88].

T2-weighted images occasionally show increased signal intensity in the gray and white matter, which

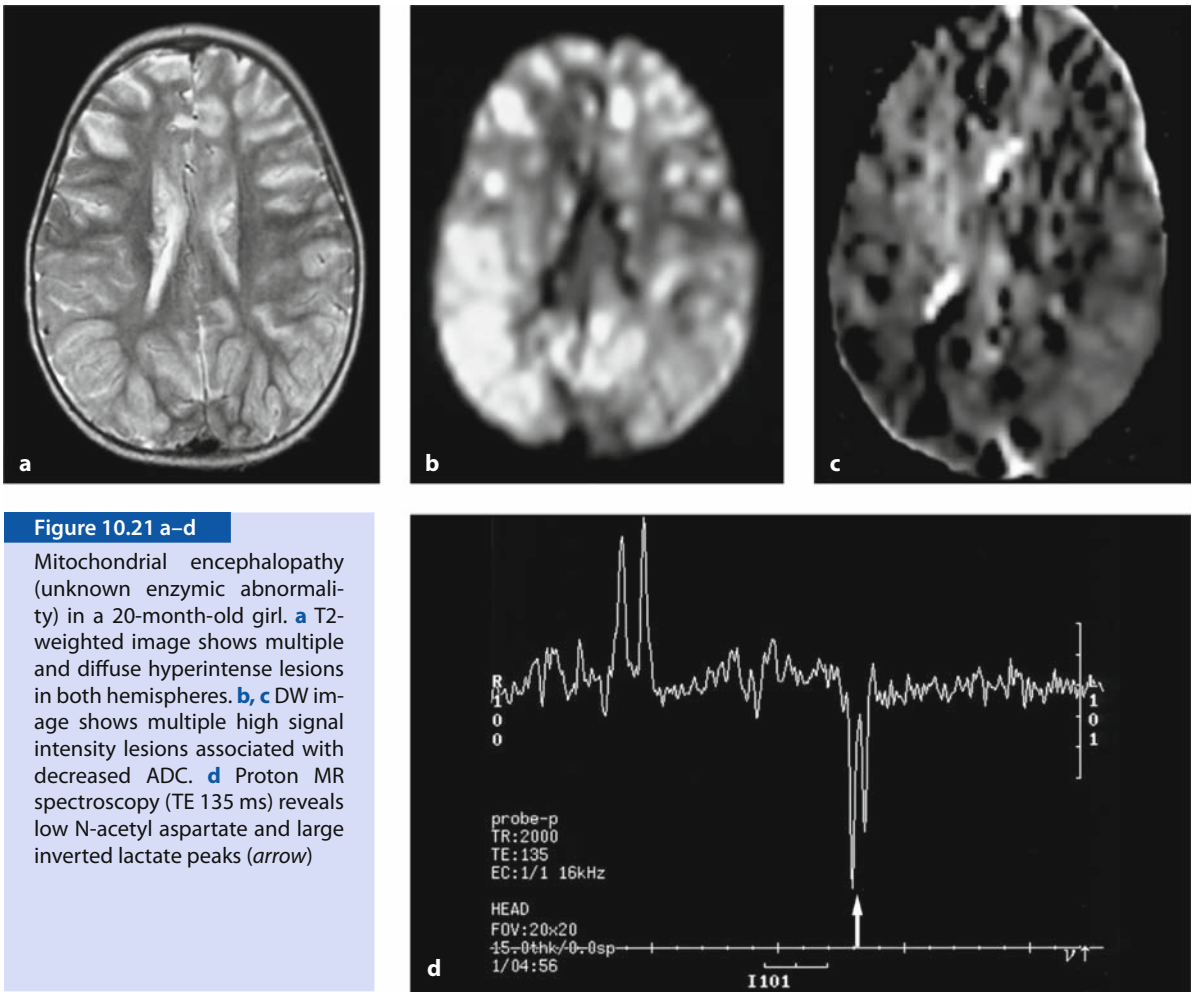

Figure 10.21 a–d

Mitochondrial encephalopathy (unknown enzymic abnormality) in a 20-month-old girl. **a** T2-weighted image shows multiple and diffuse hyperintense lesions in both hemispheres. **b, c** DW image shows multiple high signal intensity lesions associated with decreased ADC. **d** Proton MR spectroscopy (TE 135 ms) reveals low N-acetyl aspartate and large inverted lactate peaks (*arrow*)

usually does not follow vascular territories. Proton MR spectroscopy is useful in the diagnosis by detecting elevated lactate peak. DW imaging often shows the stroke-like lesions in mitochondrial encephalomyopathy, lactic acidosis and stroke–like episodes (MELAS) as hyperintense. They have increased or normal ADC, which presumably represents vasogenic edema [89–91] (Fig. 10.20). However, decreased ADC in these lesions representing cytotoxic edema can be observed [92–94] (Fig. 10.21).

10.2.2 Phenylketonuria

Phenylketonuria is an autosomal recessive disorder caused by a deficiency of phenylalanine hydroxylase. It is the most common congenital disorder of amino acid metabolism. Untreated patients typically develop mental retardation, seizures, growth retardation, hyper-reflexia, eczematous dermatitis, and hyperpigmentation. Pathologic findings include delayed or defective myelination, diffuse white matter vacuolation, demyelination, and gliosis [95].

Magnetic resonance imaging shows hyperintense lesions on T2-weighted images in the periventricular parietal and occipital regions, and in more severe cases extending to the frontal and subcortical white matter [96]. DW imaging shows these lesions as hyperintense with decreased ADC, which presumably represents intramyelinic edema and astrocytic swelling [97] (Fig. 10.22). These lesions can be completely reversible on follow-up MR imaging when dietary control has been instituted.

10.2.3 Other Metabolic Diseases and Leukodystrophies

Diffusion-weighted imaging is thought to be useful to differentiate between demyelinating and dysmyelinating disorders [98, 99]. Decreased ADC in the white matter has been reported in Canavan disease [100] (Chap. 14), adrenoleukodystrophy [101], metachromatic leukodystrophy [102], L-2 hydroxyglutaric aciduria [103] (Fig. 10.23), and infantile neuronal dystrophy [104]. The cause of the decrease in ADC in these diseases seems to be intramyelinic edema [105], or axonal swelling associated with impaired myelin sheaths or axons. On the other hand, increased or normal ADC in the white matter is seen on Pelizaeus–Merzbacher disease [106] (Chap. 14), Krabbe disease, van de Knaap disease (Fig. 10.24) and leukoencephalopathy with vanishing white matter (Chap. 14). Diffusion tensor MR imaging can be useful in differential diagnosis of leukodystrophies [98, 101, 107].

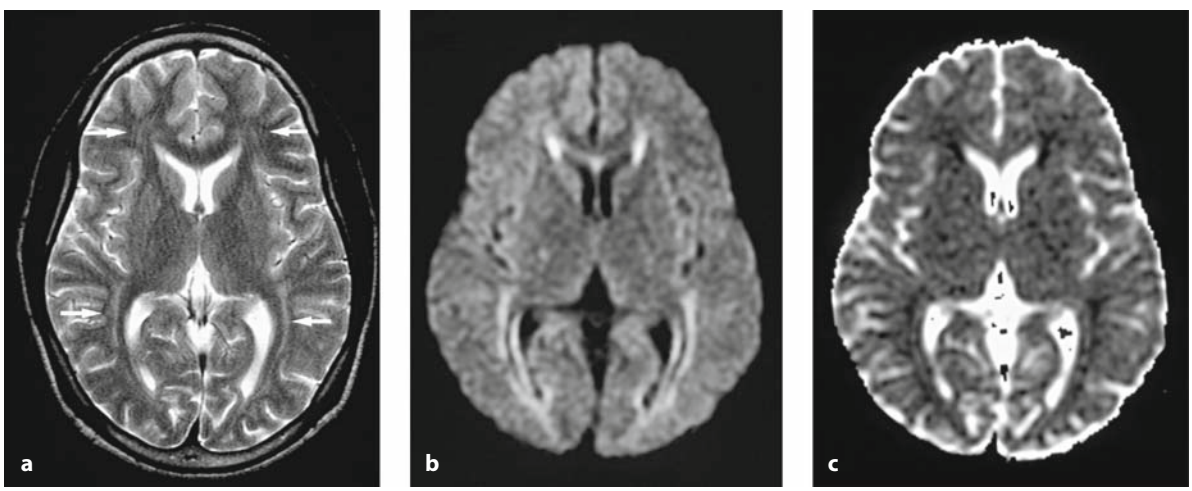

Figure 10.22 a–c

Phenylketonuria in a 36-year-old man. **a** T2-weighted image shows hyperintense lesions in the periventricular white matter (*arrows*). **b, c** DW image shows these lesions as hyperintense with decreased ADC, presumably representing intramyelinic edema

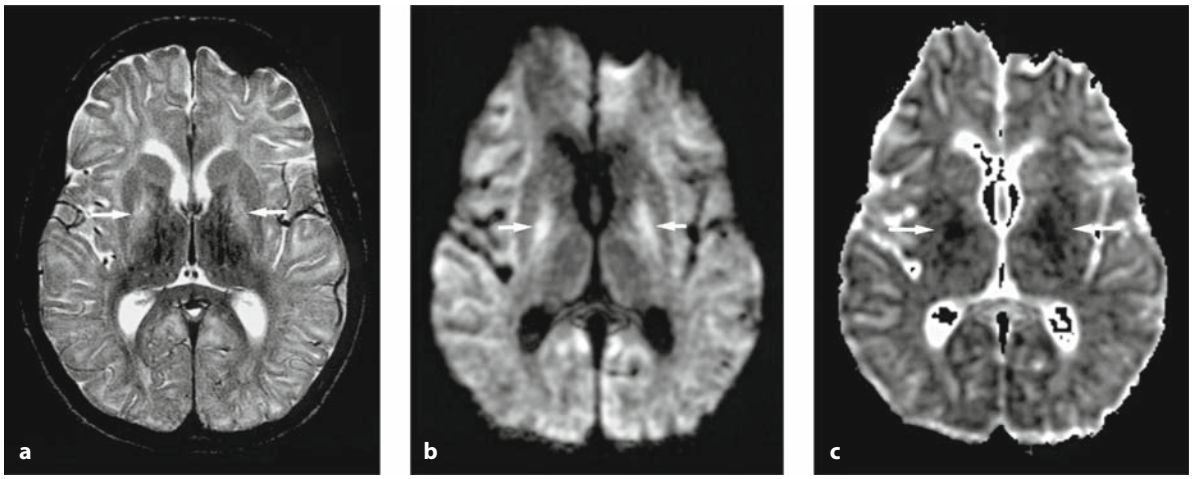

Figure 10.23 a–c

L-2-Hydroxyglutaric aciduria in a 13-year-old boy. **a** T2-weighted image shows symmetrical hyperintense lesions in bilateral globus pallidum (*arrows*) and diffusely in the white matter. **b, c** DW image shows these lesions as hyperintense; however, ADC is mildly decreased in the globus pallidum (*arrows*), and mildly increased in the white matter

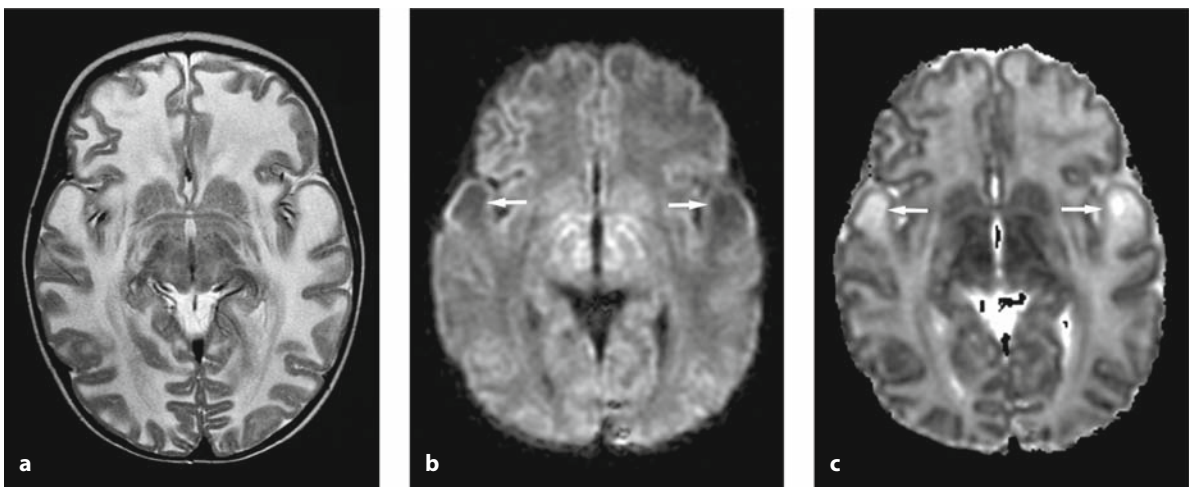

Figure 10.24 a–c

Van der Knaap disease in a 10-month-old boy with megalencephaly. **a** T2-weighted image shows diffuse hyperintensity in the white matter. **b, c** DW image shows diffuse hypointensity with increased ADC, especially prominent in symmetrical subcortical cysts in the temporal lobes (*arrows*)

References

1. Lexa FJ (1995) Drug-induced disorders of the central nervous system. Seminars in Roentgenol 30:7–17
2. Oka M, Terae S, Kobayashi R, Sawamura Y, Kudoh K, Tha KK, Yoshida M, Kaneda M, Suzuki Y, Miyasaka K (2003) MRI in methotrexate-related leukoencephalopathy: Disseminated necrotising leukoencephalopathy in comparison with mild leukoencephalopathy. Neuroradiology 45:493-497
3. Raghavendra S, Nair MD, Chemmanam T, Krishnamoorthy T, Radhakrishnan VV, Kuruvilla A (2007) Disseminated necrotizing leukoencephalopathy following low-dose oral methotrexate. Eur J Neurol 14:309-314
4. Brown MS, Stemmer SM, Simon JH, et al. (1998) White matter disease induced by high-dose chemotherapy: longitudinal study with MR imaging and proton spectroscopy. AJNR Am J Neuroradiol 19:217–221
5. Fujikawa A, Tsuchiya K, Katase S, Kurosaki Y, Hachiya J (2001) Diffusion-weighted MR imaging of Carmofur-induced leukoencephalopathy. Eur Radiol 11:2602–2606
6. Tha KK, Terae S, Sugiura M, et al. (2002) Diffusion-weighted magnetic resonance imaging in early stage of 5-fluorouracil-induced leukoencephalopathy. Acta Neurol Scand 106:379–386
7. Matsumoto S, Nishizawa S, Murakami S, et al. (1995) Carmofur-induced leukoencephalopathy: MRI. Neuroradiology 37:649–652
8. Maschke M, Fehlings T, Kastrup O, Wilhelm HW, Leonhardt G (1999) Toxic leukoencephalopathy after intravenous consumption of heroin and cocaine with unexpected clinical recovery. J Neurol 246:850–851
9. Wolters EC, van Wijngaarden GK, Stam FC, et al (1982) Leucoencephalopathy after inhaling "heroin" pyrolysate. Lancet 2:1233–1237
10. Tan TP, Algra PR, Valk J, Wolters EC (1994) Toxic leukoencephalopathy after inhalation of poisoned heroin: MR findings. Am J Neuroradiol 15:175–178
11. Chen CY, Lee KW, Lee CC, Chin SC, Chung HW, Zimmerman RA (2000) Heroin-induced spongiform leukoencephalopathy: value of diffusion MR imaging. J Comput Assist Tomogr 24:735–737
12. Barnett MH, Miller LA, Reddel SW, Davies L (2001) Reversible delayed leukoencephalopathy following intravenous heroin overdose. J Clin Neurosci 8:165–167
13. Busto R, Dietrich WD, Globus MY, Ginsberg MD (1989) The importance of brain temperature in cerebral ischemic injury. Stroke 20:1113-1114
14. Siesjö BK, Katsura K, Mellergård P, Ekholm A, Lundgren J, Smith ML (1993) Acidosis-related brain damage. Prog Brain Res 96:23-48
15. Longstreth WT Jr, Diehr P, Cobb LA, Hanson RW, Blair AD (1986) Neurologic outcome and blood glucose levels during out-of-hospital cardiopulmonary resuscitation. Neurology 36:1186-1191
16. Singhal AB, Topcuoglu MA, Koroshetz WJ (2002) Diffusion MRI in three types of anoxic encephalopathy. J Neurol Sci 196:37-40
17. McKinney AM, Teksam M, Felice R, Casey SO, Cranford R, Truwit CL, Kieffer S (2004) Diffusion-weighted imaging in the setting of diffuse cortical laminar necrosis and hypoxic-ischemic encephalopathy. AJNR Am J Neuroradiol 25:1659-1665
18. Arbelaez A, Castillo M, Mukherji SK (1999) Diffusion-weighted MR imaging of global cerebral anoxia. AJNR Am J Neuroradiol 20:999-1007
19. Wijdicks EF, Campeau NG, Miller GM (2001) MR imaging in comatose survivors of cardiac resuscitation. AJNR Am J Neuroradiol 22:1561-1565
20. Els T, Kassubek J, Kubalek R, Klisch J (2004) Diffusion-weighted MRI during early global cerebral hypoxia: a predictor for clinical outcome? Acta Neurol Scand 110:361-367
21. Tha KK, Terae S, Yamamoto T, Kudo K, Takahashi C, Oka M, Uegaki S, Miyasaka K (2005) Early detection of global cerebral anoxia: improved accuracy by high-b-value diffusion-weighted imaging with long echo time. AJNR Am J Neuroradiol 26:1487-1497
22. Karantanas AH, Hadjigeorgiou GM, Paterakis K, Sfiras D, Komnos A (2002) Contribution of MRI and MR angiography in early diagnosis of brain death. Eur Radiol 12:2710-2726
23. Ishii K, Onuma T, Kinoshita T, Shiina G, Kameyama M, Shimosegawa Y (1996) Brain death: MR and MR angiography. AJNR Am J Neuroradiol 17:731-735
24. Orrison WW Jr, Champlin AM, Kesterson OL, Hartshorne MF, King JN (1994) MR 'hot nose sign' and 'intravascular enhancement sign' in brain death. AJNR Am J Neuroradiol 15:913-916
25. Lövblad KO, Bassetti C (2000) Diffusion-weighted magnetic resonance imaging in brain death. Stroke 31:539-542
26. Nakahara M, Ericson K, Bellander BM (2001) Diffusion-weighted MR and apparent diffusion coefficient in the evaluation of severe brain injury. Acta Radiol 42:365-369
27. Hasegawa Y, Latour LL, Sotak CH, Dardzinski BJ, Fisher M (1994) Temperature dependent change of apparent diffusion coefficient of water in normal and ischemic brain of rats. J Cereb Blood Flow Metab 14:383-390
28. Finelli PF (2001) Diffusion-weighted MR in hypoglycemic coma. Neurology 57:933
29. Lo L, Tan AC, Umapathi T, Lim CC (2006) Diffusion-weighted MR imaging in early diagnosis and prognosis of hypoglycemia. AJNR Am J Neuroradiol 27:1222-1224
30. Aoki T, Sato T, Hasegawa K, Ishizaki R, Saiki M (2004) Reversible hyperintensity lesion on diffusion-weighted MRI in hypoglycemic coma. Neurology 63:392-393
31. Albayram S, Ozer H, Gokdemir S, Gulsen F, Kiziltan G, Kocer N, Islak C (2006) Reversible reduction of apparent diffusion coefficient values in bilateral internal capsules in transient hypoglycemia-induced hemiparesis. AJNR Am J Neuroradiol 27:1760-1762
32. Auer RN (2004) Hypoglycemic brain damage. Metab Brain Dis 19:169-175
33. Shan DE (2005) An explanation for putaminal CT, MR, and diffusion abnormalities secondary to nonketotic hyperglycemia. AJNR Am J Neuroradiol 26:194; author reply 194-195

34. Chu K, Kang DW, Kim DE, Park SH, Roh JK (2002) Diffusion-weighted and gradient echo magnetic resonance findings of hemichorea-hemiballismus associated with diabetic hyperglycemia: a hyperviscosity syndrome? Arch Neurol 59:448-452
35. Fujioka M, Taoka T, Matsuo Y, Mishima K, Ogoshi K, Kondo Y, Tsuda M, Fujiwara M, Asano T, Sakaki T, Miyasaki A, Park D, Siesjö BK (2003) Magnetic resonance imaging shows delayed ischemic striatal neurodegeneration. Ann Neurol 54:732-747. Erratum in Ann Neurol 55:148-149
36. Wintermark M, Fischbein NJ, Mukherjee P, Yuh EL, Dillon WP (2004) Unilateral putaminal CT, MR, and diffusion abnormalities secondary to nonketotic hyperglycemia in the setting of acute neurologic symptoms mimicking stroke. AJNR Am J Neuroradiol 25:975-976
37. Cameron FJ, Kean MJ, Wellard RM, Werther GA, Neil JJ, Inder TE (2005) Insights into the acute cerebral metabolic changes associated with childhood diabetes. Diabet Med 22:648-653
38. Lo CP, Chen SY, Lee KW, Chen WL, Chen CY, Hsueh CJ, Huang GS (2007) Brain injury after acute carbon monoxide poisoning: early and late complications. AJR Am J Roentgenol 189:W205-211
39. Kinoshita T, Sugihara S, Matsusue E, Fujii S, Ametani M, Ogawa T (2005) Pallidoreticular damage in acute carbon monoxide poisoning: diffusion-weighted MR imaging findings. AJNR Am J Neuroradiol 26:1845-1848
40. Murata T, Kimura H, Kado H, Omori M, Onizuka J, Takahashi T, Itoh H, Wada Y (2001) Neuronal damage in the interval form of CO poisoning determined by serial diffusion weighted magnetic resonance imaging plus 1H-magnetic resonance spectroscopy. J Neurol Neurosurg Psychiatry 71:250-253
41. Kim JH, Chang KH, Song IC, Kim KH, Kwon BJ, Kim HC, Kim JH, Han MH (2003) Delayed encephalopathy of acute carbon monoxide intoxication: diffusivity of cerebral white matter lesions. AJNR Am J Neuroradiol 24:1592-1597
42. Custodio CM, Basford JR (2004) Delayed postanoxic encephalopathy: a case report and literature review. Arch Phys Med Rehabil 85:502-505
43. Gocht A, Colmant HJ (1987) Central pontine and extrapontine myelinolysis: a report of 58 cases. Clin Neuropathol 6:262–270
44. Huq S, Wong M, Chan H, Crimmins D (2007) Osmotic demyelination syndromes: central and extrapontine myelinolysis. J Clin Neurosci 14:684-688
45. Hagiwara K, Okada Y, Shida N, Yamashita Y (2008) Extensive central and extrapontine myelinolysis in a case of chronic alcoholism without hyponatremia: a case report with analysis of serial MR findings. Intern Med 47:431-435
46. Kim J, Song T, Park S, Choi IS (2007) Cerebellar peduncular myelinolysis in a patient receiving hemodialysis. J Neurol Sci 253:66-68
47. Mangat KS, Sherlala K (2002) Cerebellar peduncle myelinolysis: case report. Neuroradiology 44:768-769
48. Sterns RH, Riggs JE, Schochet SS Jr (1986) Osmotic demyelination syndrome following correction of hyponatremia. N Engl J Med 314:1535–1542
49. Ho VB, Fitz CR, Yoder CC, Geyer CA (1993) Resolving MR features in osmotic myelinolysis (central pontine and extrapontine myelinolysis. Am J Neuroradiol 14:163–167
50. Kleinschmidt-Demasters BK, Rojiani AM, Filley CM (2006) Central and extrapontine myelinolysis: then...and now. J Neuropathol Exp Neurol 65:1-11
51. Norenberg MD (1983) A hypothesis of osmotic endothelial injury. A pathogenetic mechanism in central pontine myelinolysis. Arch Neurol 40:66–69
52. Lien YH (1995) Role of organic osmolytes in myelinolysis. A topographic study in rats after rapid correction of hyponatremia. J Clin Invest 95:1579-1586
53. Mascalchi M, Cincotta M, Piazzini M (1993) Case report: MRI demonstration of pontine and thalamic myelinolysis in a normonatremic alcoholic. Clin Radiol 47:137–138
54. Rodriguez J, Benito-Leon J, Molina JA, Ramos A, Bermejo F (1998) Central pontine myelinolysis associated with cyclosporin in liver transplantation. Neurologia 13:437–440
55. Miller RF, Harrison MJ, Hall-Craggs MA, Scaravilli F (1998) Central pontine myelinolysis in AIDS. Acta Neuropathol 96:537–540
56. Cramer SC, Stegbauer KC, Schneider A, Mukai J, Maravilla KR (2001) Decreased diffusion in central pontine myelinolysis. AJNR Am J Neuroradiol 22:1476–1479
57. Anderson AW, Zhong J, Petroff OA, et al (1996) Effects of osmotically driven cell volume changes on diffusion-weighted imaging of the rat optic nerve. Magn Reson Med 35:162–167
58. Zuccoli G, Gallucci M, Capellades J, Regnicolo L, Tumiati B, Giadás TC, Bottari W, Mandrioli J, Bertolini M (2007) Wernicke encephalopathy: MR findings at clinical presentation in twenty-six alcoholic and nonalcoholic patients. AJNR Am J Neuroradiol 28:1328-1331
59. Zhong C, Jin L, Fei G (2005) MR Imaging of nonalcoholic Wernicke encephalopathy: a follow-up study. AJNR Am J Neuroradiol 26:2301-2305
60. Fei GQ, Zhong C, Jin L, Wang J, Zhang Y, Zheng X, Zhang Y, Hong Z (2008) Clinical characteristics and MR imaging features of nonalcoholic Wernicke encephalopathy. AJNR Am J Neuroradiol;29:164-169
61. Victor M, Adams RD, Collins GH (1971) The Wernicke-Korsakoff syndrome. A clinical and pathological study of 245 patients, 82 with post-mortem examinations. Contemp Neurol Ser 7:1–206
62. Chu K, Kang DW, Kim HJ, Lee YS, Park SH (2002) Diffusion-weighted imaging abnormalities in wernicke encephalopathy: reversible cytotoxic edema? Arch Neurol 59:123–127
63. Bae SJ, Lee HK, Lee JH, Choi CG, Suh DC (2001) Wernicke's encephalopathy: atypical manifestation at MR imaging. AJNR Am J Neuroradiol 22:1480-1482
64. Loh Y, Watson WD, Verma A, Krapiva P (2005) Restricted diffusion of the splenium in acute Wernicke's encephalopathy. J Neuroimaging 15:373-375
65. Morcos Z (2003) Diffusion abnormalities and Wernicke encephalopathy. Neurology 60:727-728

66. Antunez E, Estruch R, Cardenal C, Nicolas JM, Fernandez-Sola J, Urbano-Marquez A (1998) Usefulness of CT and MR imaging in the diagnosis of acute Wernicke's encephalopathy. AJR Am J Roentgenol 171:1131–1137
67. Oka M, Terae S, Kobayashi R, et al. (2001) Diffusion-weighted MR findings in a reversible case of acute Wernicke encephalopathy. Acta Neurol Scand 104:178–181
68. Doherty MJ, Watson NF, Uchino K, Hallam DK, Cramer SC (2002) Diffusion abnormalities in patients with Wernicke encephalopathy. Neurology 58:655–657
69. Bergui M, Bradac GB, Zhong J (2003) Diffusion abnormalities and Wernicke encephalopathy. Neurology 60:727-728; author reply 727-728
70. White ML, Zhang Y, Andrew LG, Hadley WL (2005) MR imaging with diffusion-weighted imaging in acute and chronic Wernicke encephalopathy. AJNR Am J Neuroradiol 26:2306-2310
71. Rugilo CA, Roca MC, Zurru MC, Gatto EM (2003) Diffusion abnormalities and Wernicke encephalopathy. Neurology 60:727–728; author reply 727–728
72 Bergui M, Bradac GB, Zhong JJ, Barbero PA, Durelli L (2001) Diffusion-weighted MR in reversible wernicke encephalopathy. Neuroradiology 43:969-972
73. Gambini A, Falini A, Moiola L, Comi G, Scotti G (2003) Marchiafava-Bignami disease: longitudinal MR imaging and MR spectroscopy study. Am J Neuroradiol 24:249–253
74. Gass A, Birtsch G, Olster M, Schwartz A, Hennerici MG (1998) Marchiafava-Bignami disease: reversibility of neuroimaging abnormality. J Comput Assist Tomogr 22:503–504
75. Inagaki T, Saito K (2000) A case of Marchiafava-Bignami disease demonstrated by MR diffusion-weighted image. No To Shinkei 52:633–637
76. Castillo P, Woodruff B, Caselli R, Vernino S, Lucchinetti C, Swanson J, Noseworthy J, Aksamit A, Carter J, Sirven J, Hunder G, Fatourechi V, Mokri B, Drubach D, Pittock S, Lennon V, Boeve B (2006) Steroid-responsive encephalopathy associated with autoimmune thyroiditis. Arch Neurol 63:197-202
77. Tamagno G, Federspil G, Murialdo G (2006) Clinical and diagnostic aspects of encephalopathy associated with autoimmune thyroid disease (or Hashimoto's encephalopathy). Intern Emerg Med 1:15-23
78. Irani S, Lang B (2008) Autoantibody-mediated disorders of the central nervous system. Autoimmunity 41:55-65
79. Sánchez Contreras A, Rojas SA, Manosalva A, Méndez Patarroyo PA, Lorenzana P, Restrepo JF, Iglesias-Gamarra A, Rondon F (2004) Hashimoto encephalopathy (autoimmune encephalitis). J Clin Rheumatol 10:339-343
80. Nolte KW, Unbehaun A, Sieker H, Kloss TM, Paulus W (2000) Hashimoto encephalopathy: a brainstem vasculitis? Neurology 54:769
81. Oide T, Tokuda T, Yazaki M, Watarai M, Mitsuhashi S, Kaneko K, Hashimoto T, Ohara S, Ikeda S (2004) Anti-neuronal autoantibody in Hashimoto's encephalopathy: neuropathological, immunohistochemical, and biochemical analysis of two patients. J Neurol Sci 217:7-12
82. Takahashi S, Mitamura R, Itoh Y, Suzuki N, Okuno A (1994) Hashimoto encephalopathy: Etiologic considerations. Pediatr Neurol 11:328-331
83. Mahad DJ, Staugaitis S, Ruggieri P, et al. (2005) Steroid-responsive encephalopathy associated with autoimmune thyroiditis and primary CNS demyelination. J Neurol Sci 228:305
84. Creutzfeldt C, haberle R (2005) Hashimoto encephalopathy: a do-not-miss in the differential diagnosis of dementia. J Neurol 252:125-1287
85. Mancardi MM, Fazzini F, Rossi A, Gaggero R (2005) Hashimoto's encephalopathy with selective involvement of the nucleus accumbens: a case report. Neuropediatrics 36:218-220
86. Song Y M, Seo D W, Chang G Y (2004) MR findings in Hashimoto encephalopathy. Am J Neuroradiol 25:807-808
87. McCabe DJH, Burket T, Connolly S, Hutchinson M (2000) Amnesic syndrome with bilateral mesial temporal lobe involvement in Hashimoto encephalopathy. Neurology 54:737
88. Oppenheim C, Galanaud D, Samson Y, et al. (2000) Can diffusion weighted magnetic resonance imaging help differentiate stroke from stroke-like events in MELAS? J Neurol Neurosurg Psychiatry 69:248–250
89. Yoneda M, Maeda M, Kimura H, Fujii A, Katayama K, Kuriyama M (1999) Vasogenic edema on MELAS: a serial study with diffusion-weighted MR imaging. Neurology 53: 2182–2184
90. Yonemura K, Hasegawa Y, Kimura K, Minematsu K, Yamaguchi T (2001) Diffusion-weighted MR imaging in a case of mitochondrial myopathy, encephalopathy, lactic acidosis, and strokelike episodes. AJNR Am J Neuroradiol 22:269–272
91. Ohshita T, Oka M, Imon Y, et al. (2000) Serial diffusion-weighted imaging in MELAS. Neuroradiology 42:651–656
92. Kim HS, Kim DI, Lee BI, et al. (2001) Diffusion-weighted image and MR spectroscopic analysis of a case of MELAS with repeated attacks. Yonsei Med J 42:128–133
93. Majoie CB, Akkerman EM, Blank C, Barth PG, Poll-The BT, den Heeten GJ (2002) Mitochondrial encephalomyopathy: comparison of conventional MR imaging with diffusion-weighted and diffusion tensor imaging: case report. AJNR Am J Neuroradiol 23:813–816
94. Flemming K, Ulmer S, Duisberg B, Hahn A, Jansen O (2002) MR spectroscopic findings in a case of Alpers-Huttenlocher syndrome. AJNR Am J Neuroradiol 23:1421–1423
95. Huttenlocher PR (2000) The neuropathology of phenylketonuria: human and animal studies. Eur J Pediatr Suppl 2: S102–S106
96. Pearsen KD, Gean-Marton AD, Levy HL, Davis KR (1990) Phenylketonuria: MR imaging of the brain with clinical correlation. Radiology 177:437–440
97. Phillips MD, McGraw P, Lowe MJ, Mathews VP, Hainline BE (2001) Diffusion-weighted imaging of white matter abnormalities in patients with phenylketonuria. AJNR Am J Neuroradiol 22:1583–1586
98. Ono J, Harada K, Mano T, Sakurai K, Okada S (1997) Differentiation of dys- and demyelination using diffusional anisotropy. Pediatr Neurol 16:63–66

99. Engelbrecht V, Scherer A, Rassek M, Witsack HJ, Modder U (2002) Diffusion-weighted MR imaging in the brain in children: findings in the normal brain and in the brain with white matter diseases. Radiology 222:410–418
100. Sener RN (2003) Canavan disease: diffusion magnetic resonance imaging findings. J Comput Assist Tomogr 27:30–33
101. Eichler FS, Itoh R, Barker PB, et al. (2002) Proton MR spectroscopic and diffusion tensor brain MR imaging in X-linked adrenoleukodystrophy: initial experience. Radiology 225:245–252
102. Sener RN (2002) Metachromatic leukodystrophy: diffusion MR imaging findings. AJNR Am J Neuroradiol 23:1424–1426
103. Sener RN (2003) L-2 hydroxyglutaric aciduria: proton magnetic resonance spectroscopy and diffusion magnetic resonance imaging findings. J Comput Assis Tomo 27:38–43
104. Sener RN (2003) Diffusion magnetic resonance imaging in infantile neuroaxonal dystrophy. J Comput Assis Tomo 27:34–37
105. Ellison D, Love S (1998) Toxic injury of the CNS. In: Neuropathology, 1st edn, section 8, chapter 25. Barcelona, Mosby, pp 25.1–25.22
106. Ono J, Harada K, Sakurai K, et al. (1994) MR diffusion imaging in Pelizaeus-Merzbacher disease. Brain Dev 16:219–223
107. Guo AC, Petrella JR, Kurtzberg J, Provenzale JM (2001) Evaluation of white matter anisotropy in Krabbe disease with diffusion tensor MR imaging: initial experience. Radiology 218:809–815

Infectious Diseases

11.1 Overview of Brain Infections

Infections of the brain are caused by bacteria, virus, fungi or parasites. Bacterial infections are often related to septic emboli and extracranial infections spreading intracranially and intra-axially. This can result in cerebritis and brain abscesses. Viral infections are more diffuse and cause encephalitis and vasculitis. Toxoplasmosis, which is the most common parasitic infection of the brain, causes encephalitis and abscesses, while disseminated aspergillosis causes vasculitis-mediated infarctions resulting in extensive cerebritis and/or abscess formation.

The pathophysiology and the imaging findings vary greatly depending on the organism causing the infection. Diffusion-weighted (DW) imaging is useful for the diagnosis of infectious conditions of the brain by means of differentiating vasogenic edema from cytotoxic edema [1]. DW imaging can also separate abscesses from cystic and necrotic tumors [2–6].

11.2 Bacterial Brain Abscess and Cerebritis

Bacterial brain abscesses are potentially fatal, but can often be medically and surgically treated if detected early. Symptoms are often non-specific and vague, and imaging is therefore necessary for detection and characterization.

A brain abscess begins as a focal area of microvascular injury, usually at the gray–white matter junction or deeper in the white matter. Pathologically the initial stage of a brain abscess is a focal area of cerebritis or presuppurative encephalitis. This is characterized by early necrosis of the cerebral parenchyma, vascular congestion, petechial hemorrhage, neutrophil infiltration and vasogenic edema [7–9]. DW imaging shows a variety of signal characteristics in the area of the cerebritis with mildly increased or decreased ADC, presumably depending on the degree of inflammatory cell infiltration and types of edema (cytotoxic or vasogenic, Figs. 11.3, 11.10).

Late cerebritis is characterized by a necrotic and purulent center. This evolves into frank abscess formation, which is characterized by central pus, inflammatory granulation tissue and a fibrous capsule. The pus usually consists of both dead and viable neutrophils, necrosis, and bacteria. Even in the chronic phase of an abscess, neutrophils and necrosis can still be found (Fig. 11.1).

The early phase of the brain abscess has a homogeneous, bright signal on DW imaging associated with decreased apparent diffusion coefficient (ADC) (Figs. 11.2 and 11.3). The late phase of an abscess can still show hyperintensity on DW images, but ADC values are partially increased (Fig. 11.1) [10]. A possible explanation for the high signal on DW imaging is restriction of water mobility due to the high viscosity of coagulative necrosis and the prominence of polynucleated neutrophils in the pus. DW imaging is superior to conventional MR imaging in evaluating the success or failure of abscess therapy [11].

A brain abscess cavity shows regions of increased fractional anisotropy (FA) values with restricted mean diffusivity (Fig. 11.3) [12]. Geometrical analysis shows that a planar shape of the diffusion tensor is more frequently observed in the abscess than that in the normal white matter tract in which the diffusion tensor is predominantly of a linear shape. This phenomenon presumably reflects adherent inflammatory cells, tangled up with each other, inside the abscess cavity [13].

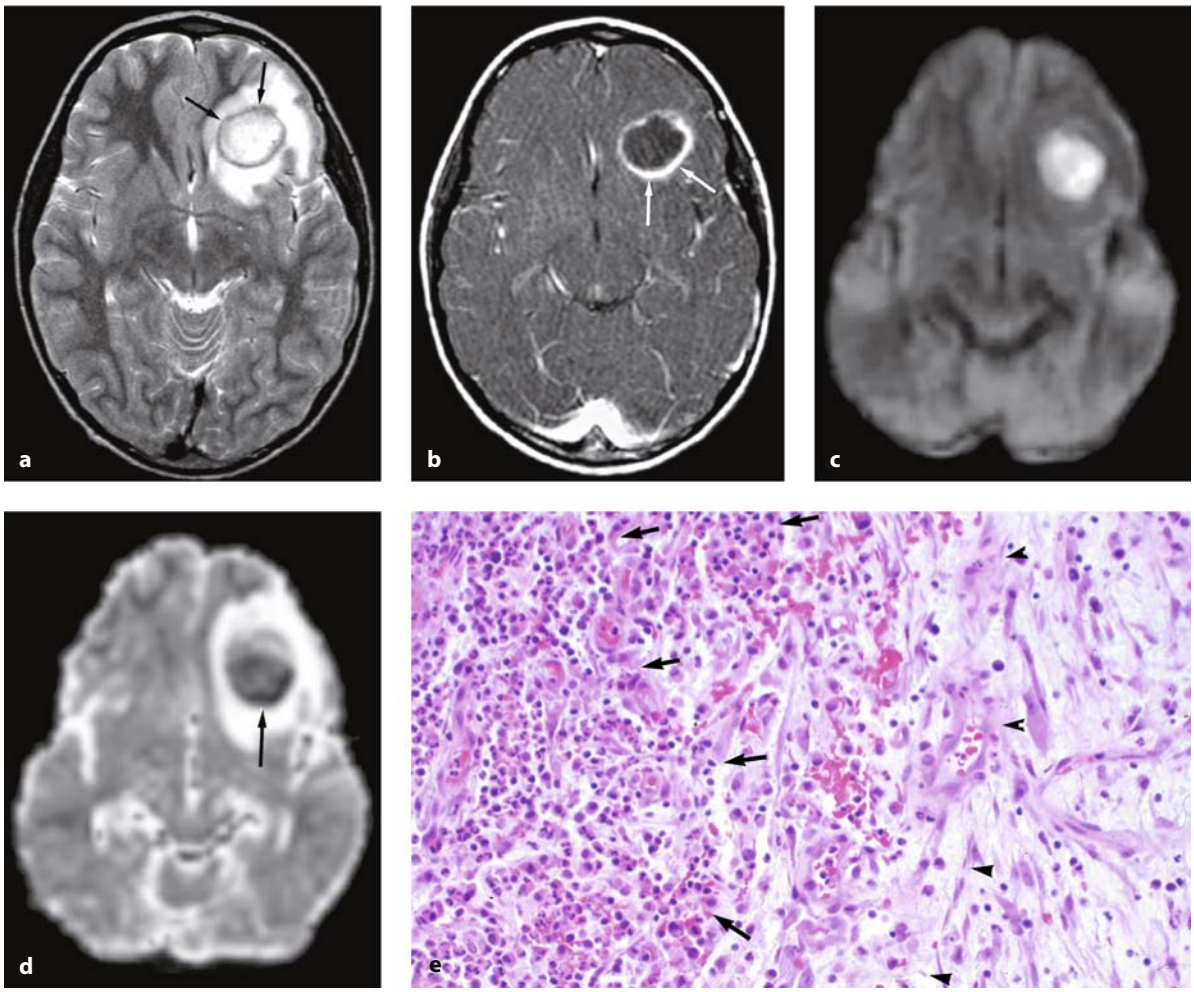

Figure 11.1 a–e

Streptococcal brain abscess in a 7-year-old boy presenting with a week-long severe headache. **a** T2-weighted image shows a central hyperintense mass lesion with low signal rim (*black arrows*) and peripheral edema in the left frontal lobe. **b** Gadolinium-enhanced T1-weighted image with magnetization transfer contrast shows this mass with ring enhancement. **c** DW image shows a central cystic component as hyperintense. **d** ADC map shows a fluid-fluid level and partially decreased ADC of this component, which is sometimes observed in the late phase of the abscess. **e** Pathology shows numerous neutrophils (*arrows*) in the center of the abscess with sourrounding granulation tissue and organizing fibrous capsule. In the pus and granulomatous fibrous capsules (*arrowheads*) in a chronic abscess

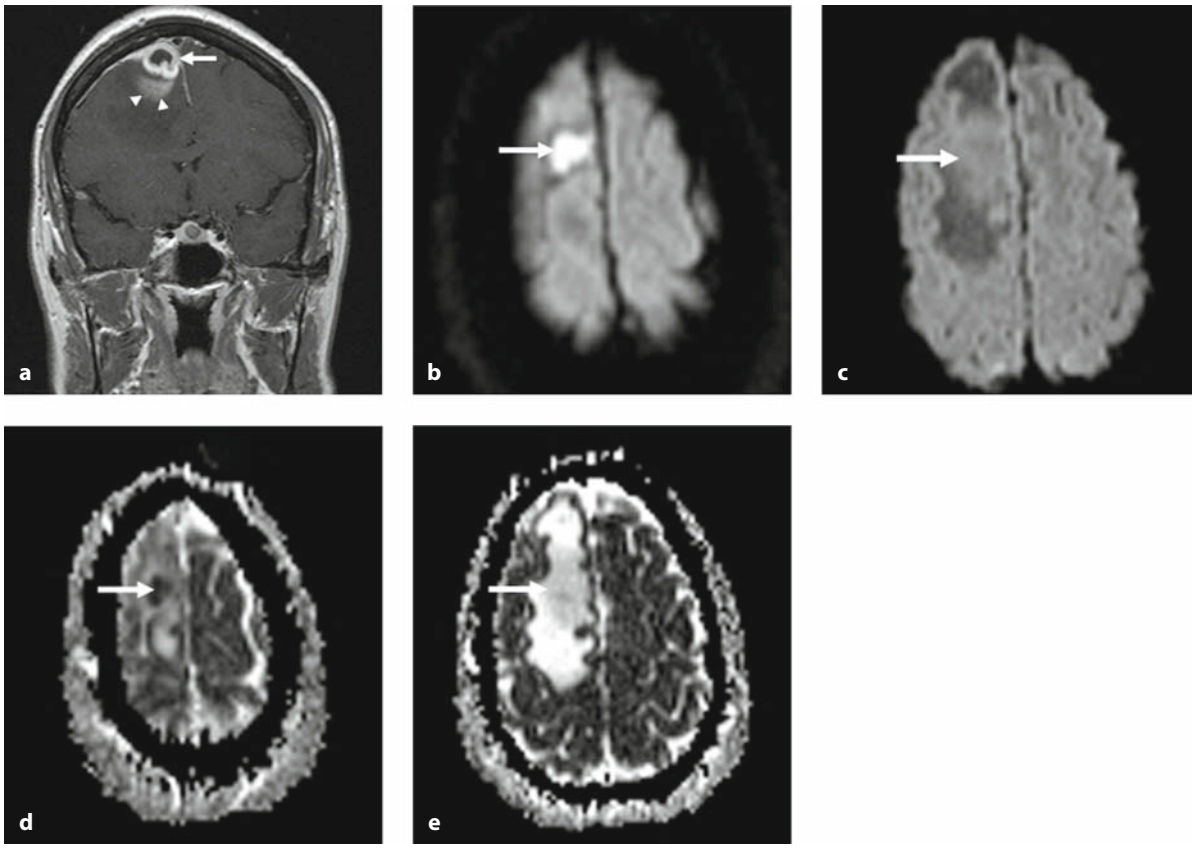

Figure 11.2 a–e

Streptococcal brain abscess in a 48-year-old woman presenting with headache. **a** Gadolinium-enhanced coronal T1-weighted image shows a ring-enhancing mass (*arrow*) and enhancement (*arrowheads*) in the surrounding edema, consistent with abscess and cerebritis. There is an incidental finding of a Rathke's cleft cyst in the pituitary gland. **b**, **c** DW image shows an abscess as hyperintense (*arrow*) (**b**) and cerebritis as isointense (*arrow*) (**c**). **d, e** ADC map shows the abscess as decreased ADC (*arrow*) (**d**) and the cerebritis as mildly increased ADC (*arrow*) which is lower than the surrounding edema (**e**)

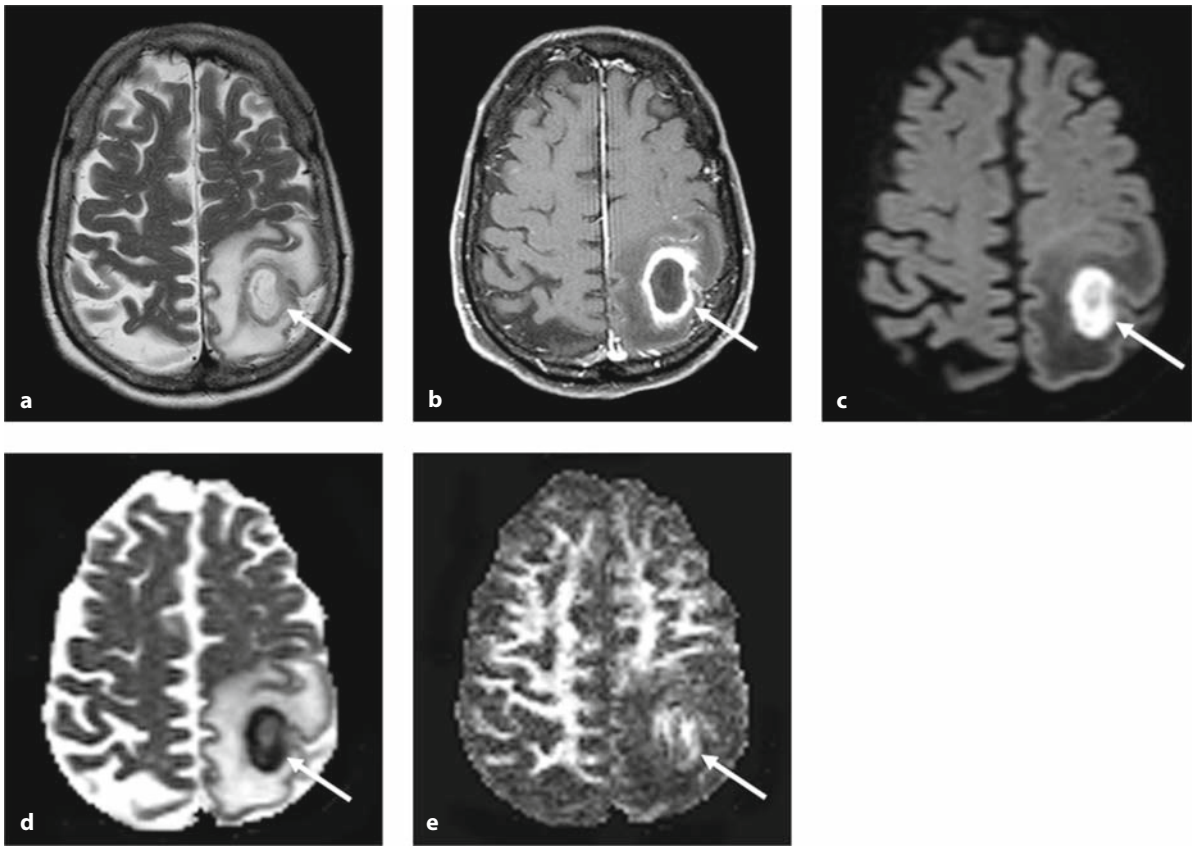

Figure 11.3 a–e

Brain abscess with mixed anaerobe bacteria in an 86-year-old woman presenting with right upper and lower extremity weakness and seizures. **a** T2-weighted image shows a central hyperintense mass with low-signal rim and peripheral edema in the left frontoparietal region (*arrow*). **b** Gadolinium-enhanced T1-weighted image shows this mass with ring enhancement (*arrow*). **c** DW image shows a central cystic component as hyperintense. **d** ADC map shows decreased ADC of this component (*arrow*). **e** FA map shows increased FA values in the abscess (*arrow*)

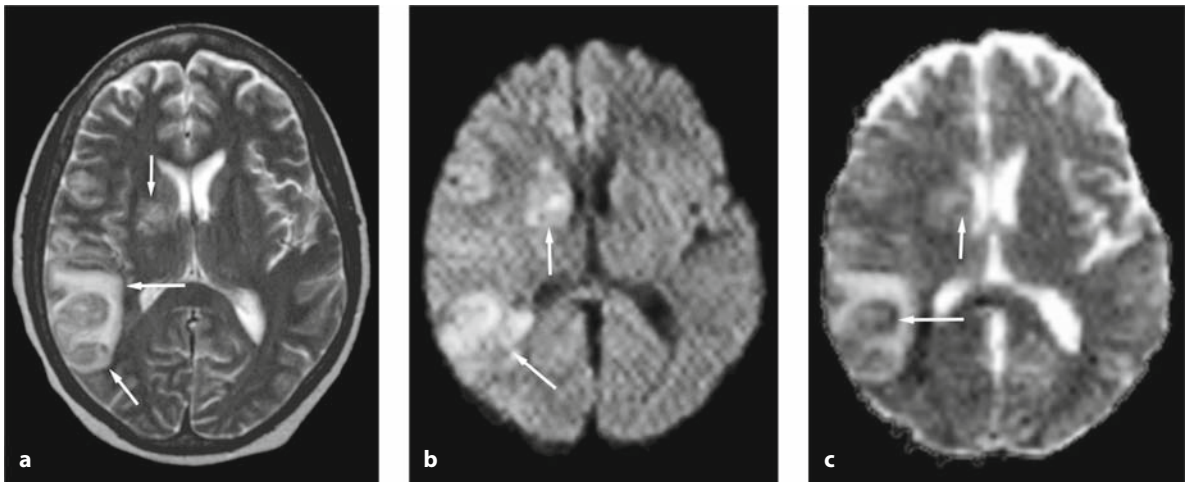

Figure 11.4 a–c

Septic emboli from staphylococcus endocarditis in a 44-year-old woman presenting with left hemiparesis of 3 days' duration. **a** T2-weighted image shows hyperintense lesions in the right basal ganglia and posteriorly in the middle cerebral artery territory (*arrows*). **b** DW image shows these lesions as hyperintense (*arrows*). **c** ADC map shows these lesions as decreased ADC, mainly representing infarcts (*arrows*)

11.3 Septic Emboli

The main risk factors for brain abscesses are bacterial endocarditis and chronic suppurative intrathoracic infections [14]. If septic emboli of sufficient size are lodged in an intracerebral arterial vessel, infarction can occur. Infarctions are bright on DW imaging, with decreased ADC (Fig. 11.4). Septic infarctions usually occur in the distal cortical branch territories, while small septic emboli are characteristically found in the cortical-white matter junction. It can take a few weeks and up to several months for septic emboli to develop into an abscess. Serial DW imaging is therefore often useful in patients at risk for septic encephalopathy. By means of repeated DW imaging, it is possible to identify the initial infarction and the subsequent cerebritis/abscess evolution [15]. This allows for early treatment.

11.4 Brain Abscess Caused by Unusual Bacteria

The classical finding in a brain abscess is a cystic lesion with marked enhancement following contrast medium injection. On DW imaging, the cystic area shows a high signal and ADC is reduced. However, the characteristics of brain abscess appear to be related to the type of organism and the immunity of the host. Thus, in an immunodeficient patient with sepsis, multiple micro-abscesses are often observed. Multiple micro-abscesses may involve basal ganglia bilaterally and mimic small infarcts (Fig. 11.5) [16].

Listeria monocytogenes is a facultative intracellular nonspore-forming gram-positive bacillus. Listeria infection, usually seen in immunocompromised hosts, is often associated with extensive parenchymal involvement, especially in the brain stem and basal ganglia [17]. The ability to cross the meninges and blood-brain barrier is thought to be the result of endothelial cell or macrophage phagocytosis of the organisms, which use the host-cell contractile system to migrate to and grow within the brain. A central small abscess may be seen as high signal on DW imaging with decreased ADC with the surrounding vasogenic edema (Fig. 11.6).

Nocardia asteroides is an aerobic acid-fast branching gram-positive bacterium. Nocardia infection is under-reported and often goes unrecognized. Nocardia brain abscesses have mortality rates three times higher than usual bacterial brain abscesses. It may be curable with long-term trimethoprim-sulfamethoxazole. Immunodeficiency makes the prognosis poorer than in immunocompetent patients [18, 19]. DW imaging shows some lesions as low ADC and others as iso ADC (Fig. 11.7).

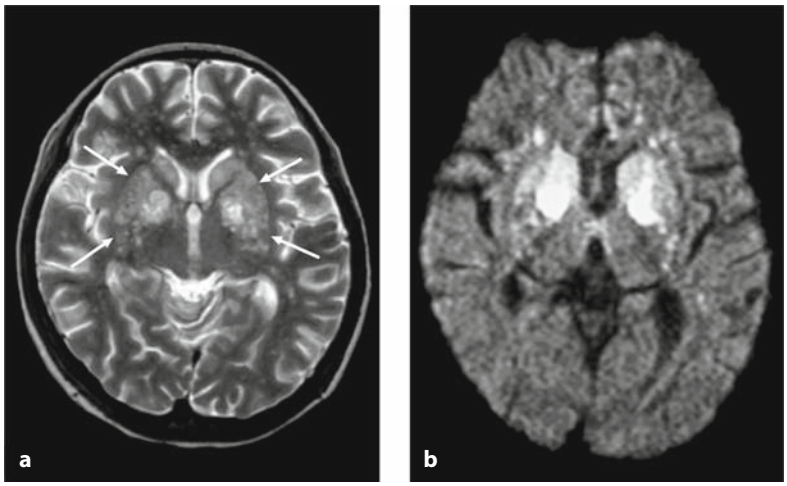

Figure 11.5 a, b

Brain abscesses due to gram-negative rod bacteria in a 28-year-old woman with Crohn's disease and long-term steroid use presenting with headache. Blood culture showed gram-negative rods. **a** T2-weighted image shows multiple small hyperintense lesions in bilateral basal ganglia (*arrows*) and white matter. **b** DW image shows these lesions as very hyperintense with decreased ADC (not shown). This finding mimics multiple small infarcts but it represents multiple small abscesses

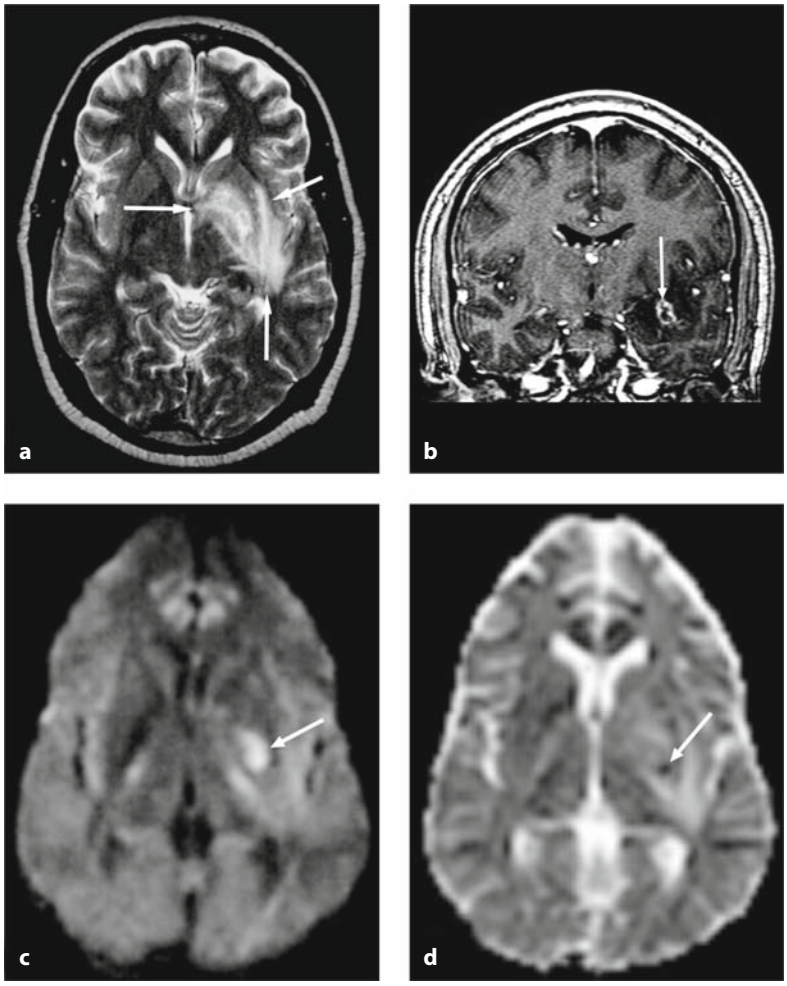

Figure 11.6 a–d

Listeria meningoencephalitis after bone marrow transplantation for chronic myeloblastic leukemia in a 31-year-old man presenting with a 2-day history of severe headache. **a** T2-weighted image shows hyperintense lesions in the left basal ganglia, internal capsule and white matter in the temporal lobe, representing encephalitis (*arrows*). **b** Coronal gadolinium-enhanced T1-weighted image shows an irregular ring-enhancing lesion (*arrow*). **c** DW image shows a central cystic component as hyperintense with decreased ADC (**d**) (*arrow*), representing an abscess

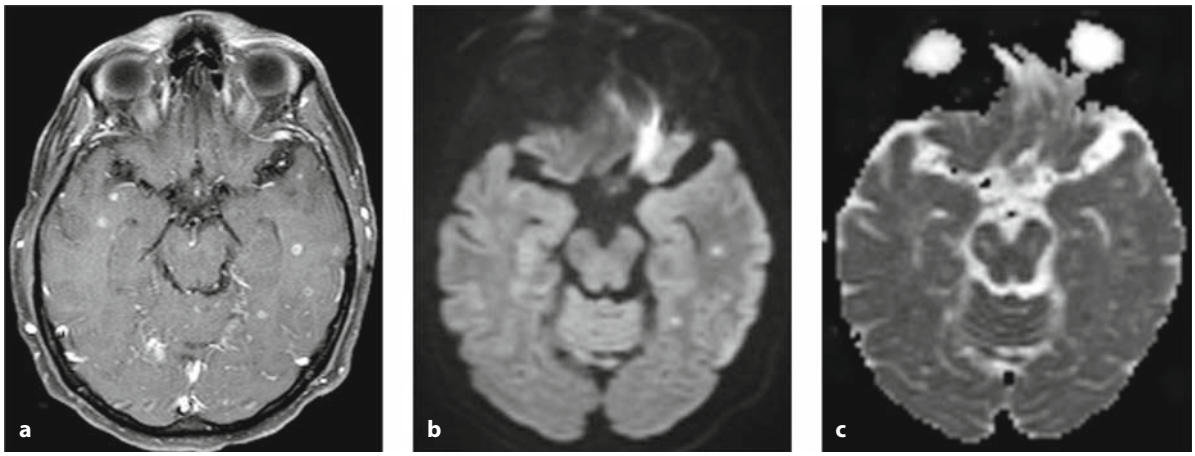

Figure 11.7 a–c

Nocardia abscess in a 50-year-old man with alcohol abuse. **a** Gadolinium-enhanced T1-weighted image shows multiple small ring-enhancing lesions in the bilateral temporo-occipital lobes. **b, c** DW image shows these lesions as hyperintense with decreased ADC (**c**), representing small abscesses

A tuberculous abscess has been reported to be seen as hyperintensity with low ADC, probably due to the presence of intact inflammatory cells in the pus [20, 21]. The diffusion abnormality of the caseous necrosis may be variable depending on the degree of liquefaction [22].

11.4.1 Differential Diagnosis

DW imaging can discriminate brain abscesses from cystic or necrotic tumors, which is often difficult with conventional MR imaging (Fig. 11.8) [2–6]. Cystic and necrotic components of the tumor are usually dark on DW images associated with increased ADC. However, there are exceptions; central necrosis of a primary tumor or metastasis can occasionally show the same characteristics with hyperintensity on DW imaging with iso or low ADC values (Fig. 11.9) [23–25]. Sterile and coagulative necrosis, hemorrhage and viscous mucinous components are possible causes for this finding. The sensitivity and specificity in differentiating cystic/necrotic neoplasms from bacterial abscesses are reported as 85% and 95%, respectively, at the threshold of 1.39 ADC ratio (dividing the ADC values of the non-enhancing portion of the mass by those of contralateral normal-appearing white matter) [23].

Pure coagulative necrosis typically develops after radiofrequency thalamotomy [27]. The lesion often shows hyperintensity on DW imaging, with decreased ADC (Fig. 11.10). Although imaging characteristics are very similar to those of an abscess, the history of the patient and the symptomatology can usually help to differentiate post-surgical lesions from abscesses.

11.5 Bacterial Abscess in the Extra-Axial Space

Infections can enter the extra-axial spaces by a variety of mechanisms, including direct spread from an adjacent focus, retrograde septic thrombophlebitis, hematogenous seeding and sequela of purulent leptomeningitis [28]. Abscesses can occur in epidural (Fig. 11.11), subdural (Fig. 11.12), subarachnoid (Fig. 11.13), or intraventricular spaces (Fig. 11.14) [29, 30]. Wherever they occur, DW imaging shows pus in the abscess as hyperintense, with relatively low ADC values. An exception to the rule can be found in some cases of extra-axial pus collections where the ADC value varies from low to high. Regions of increased ADC presumably represent dilution of the pus with the cerebrospinal fluid or exudate.

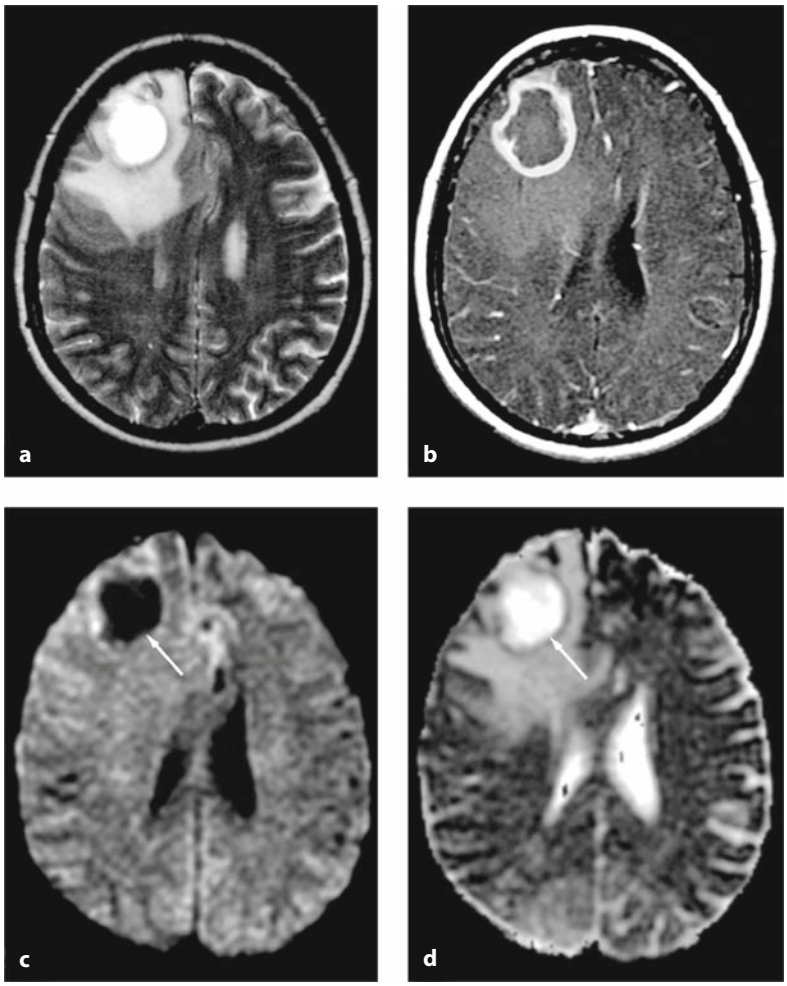

Figure 11.8 a–d

Glioblastoma in a 69-year-old woman. **a** T2-weighted image shows a central hyperintense mass lesion with low signal rim and peripheral edema in the right frontal lobe. **b** Gadolinium-enhanced T1-weighted image with magnetization transfer contrast shows this mass with irregular ring enhancement. **c** DW image shows a central cystic component as hypointense (*arrow*). **d** ADC map shows increased ADC of this cystic component (*arrow*)

Figure 11.10 a–c

Coagulative necrosis 4 weeks after radiofrequency thalamotomy for essential tremor in a 70-year-old man. **a** T2-weighted image shows a hyperintense lesion with mild peripheral edema in the left thalamus (*arrow*). **b** DW image shows a central cystic component as hyperintense. **c** ADC map shows this component as decreased ADC, probably representing coagulative necrosis. This lesion was decreased in size on follow-up MR imaging without antibiotic treatment

►

Figure 11.9 a–d

Brain metastasis from adenocarcinoma of the lung in a 44-year-old man. **a** T2-weighted image shows multiple mass lesions and peripheral edema in the left parieto-occipital lobe. **b** Gadolinium-enhanced T1-weighted image with magnetization transfer contrast shows these lesions with irregular ring enhancement (*arrows*). **c** DW image shows central cystic components as hyperintense (*arrows*). **d** ADC map shows relative low ADC values of cystic components, presumably representing coagulative necrosis or mucinous substance (*arrows*)

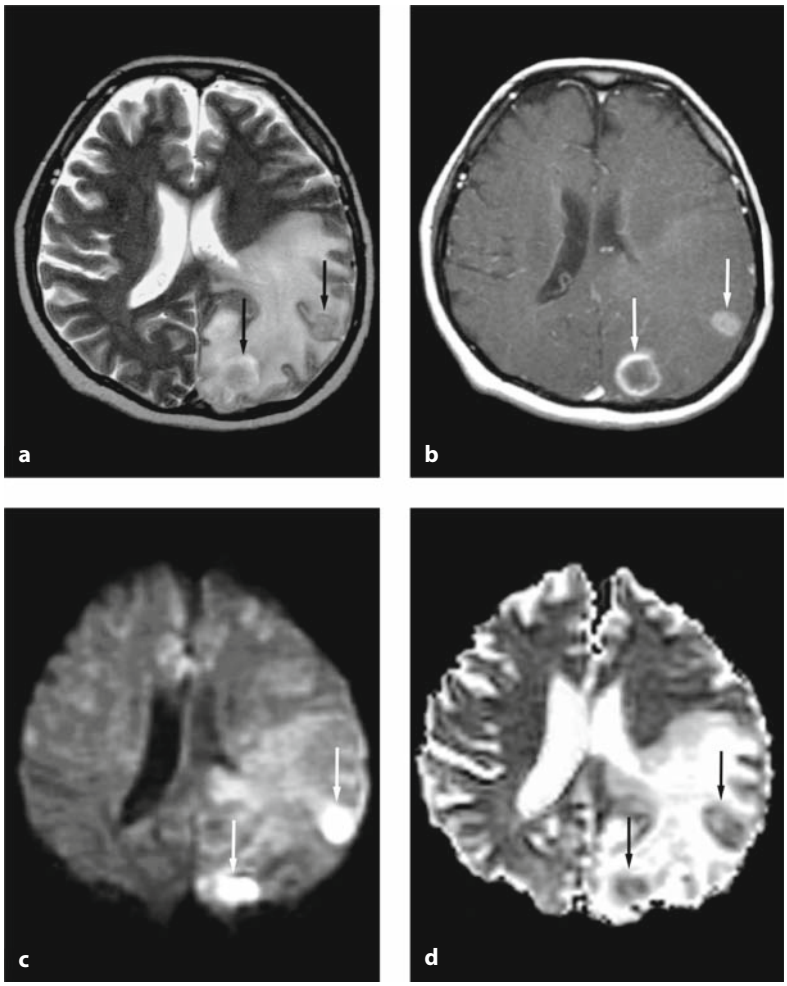

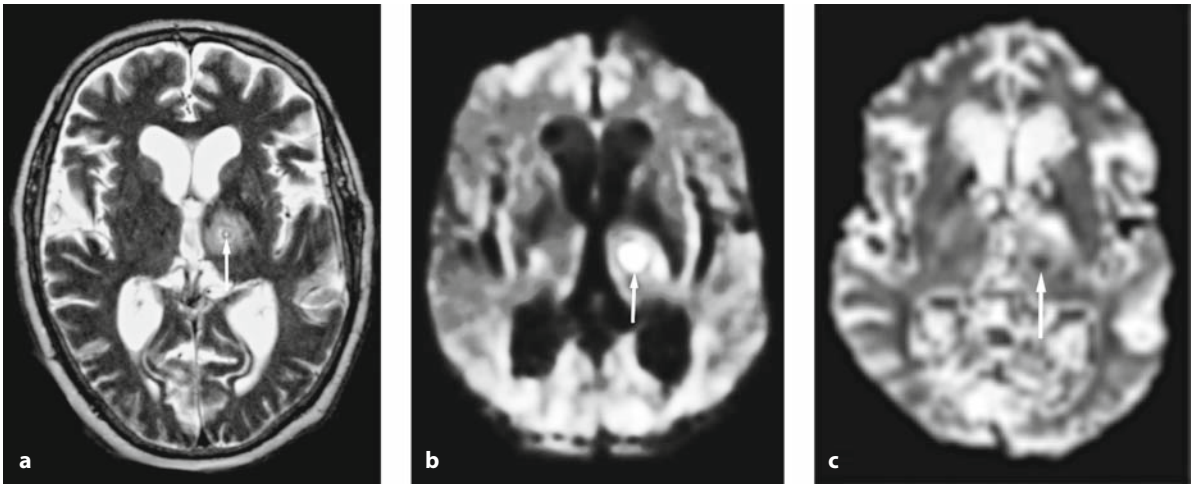

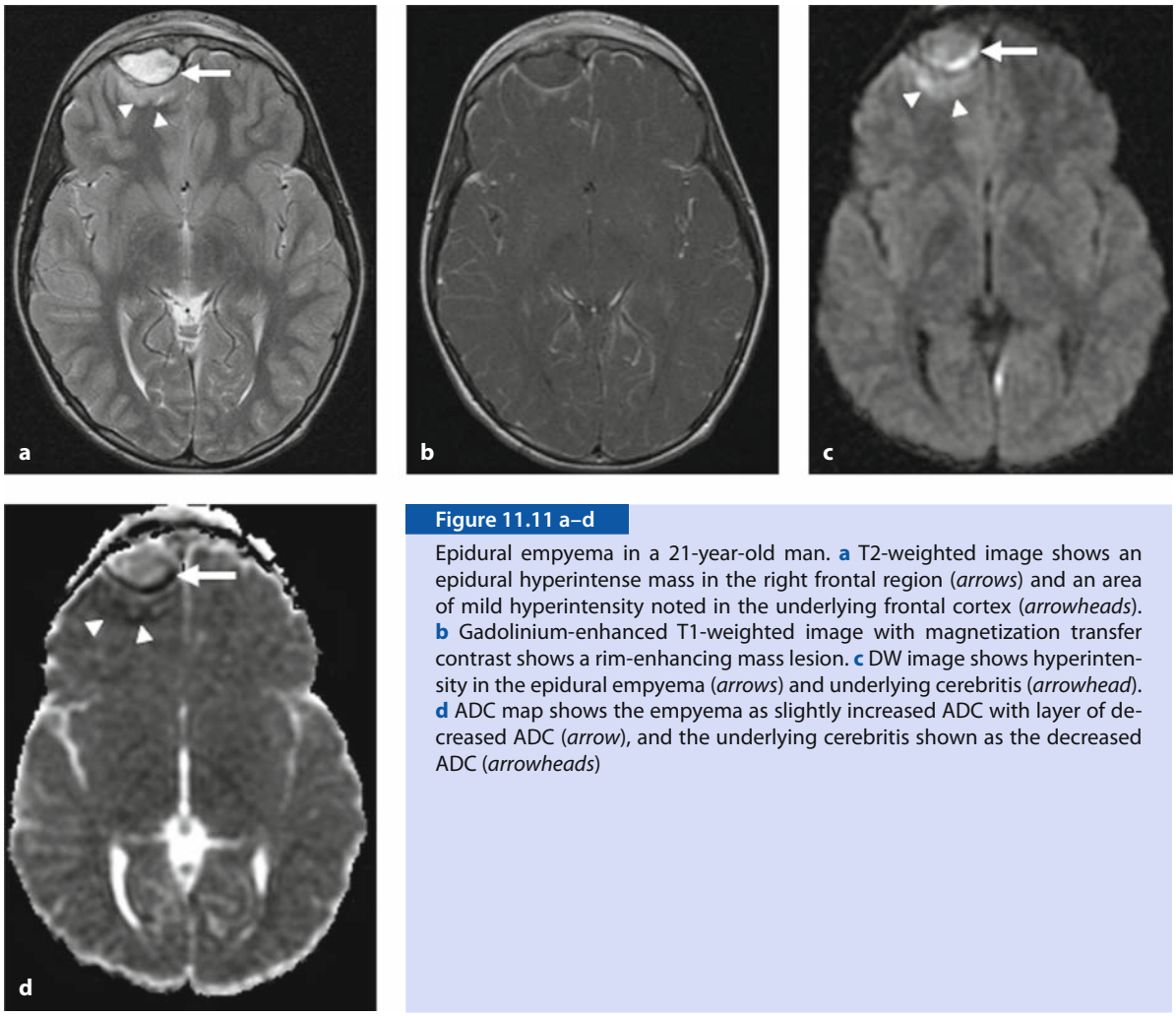

Figure 11.11 a–d

Epidural empyema in a 21-year-old man. **a** T2-weighted image shows an epidural hyperintense mass in the right frontal region (*arrows*) and an area of mild hyperintensity noted in the underlying frontal cortex (*arrowheads*). **b** Gadolinium-enhanced T1-weighted image with magnetization transfer contrast shows a rim-enhancing mass lesion. **c** DW image shows hyperintensity in the epidural empyema (*arrows*) and underlying cerebritis (*arrowhead*). **d** ADC map shows the empyema as slightly increased ADC with layer of decreased ADC (*arrow*), and the underlying cerebritis shown as the decreased ADC (*arrowheads*)

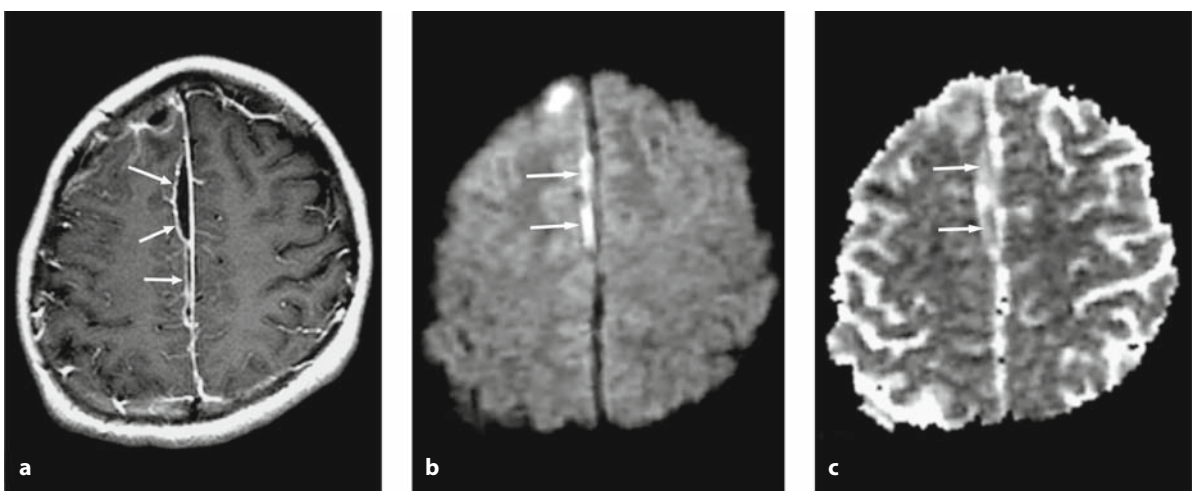

Figure 11.13 a–d

Purulent leptomeningitis in a 77-year-old man. Pneumococcus was proven by CSF examination. **a** Coronal fluid-attenuated inversion-recovery image shows hyperintense lesions in subarachnoid space in the right fronto- parietal region (*arrow*). **b** Gadolinium-enhanced T1-weighted image with magnetization transfer contrast shows irregular enhancement of these lesions (*arrows*). **c** DW image shows these lesions as hyperintense, representing purulent leptomeningitis (*arrows*). **d** ADC map shows these lesions as decreased ADC (*arrows*)

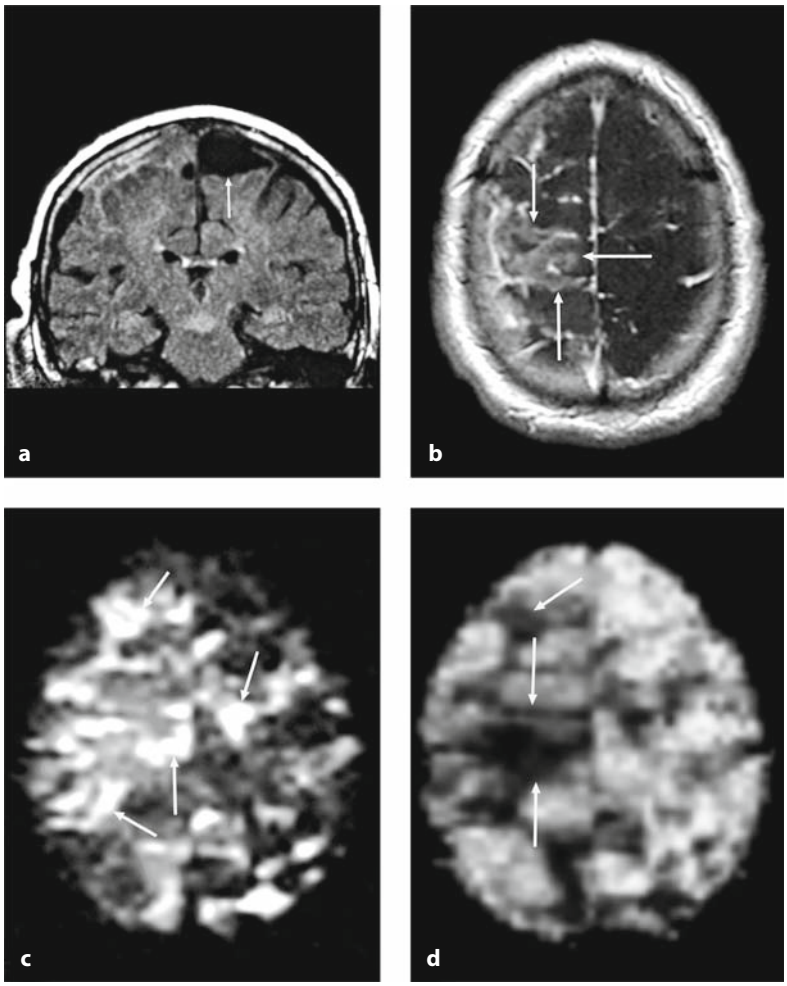

Figure 11.12 a–c

Subdural empyema in a 16-year-old male patient. **a** Gadolinium-enhanced T1-weighted image with magnetization transfer contrast shows rim-enhancing lesions along the falx (*arrows*). Mild meningeal enhancement is also seen. **b** DW image shows these lesions as hyperintense, representing subdural abscesses (*arrows*). **c** ADC map shows these lesions as relatively decreased ADC (*arrows*) compared with CSF. (Courtesy of Morikawa M MD, Nagasaki University, School of Medicine, Japan)

◄

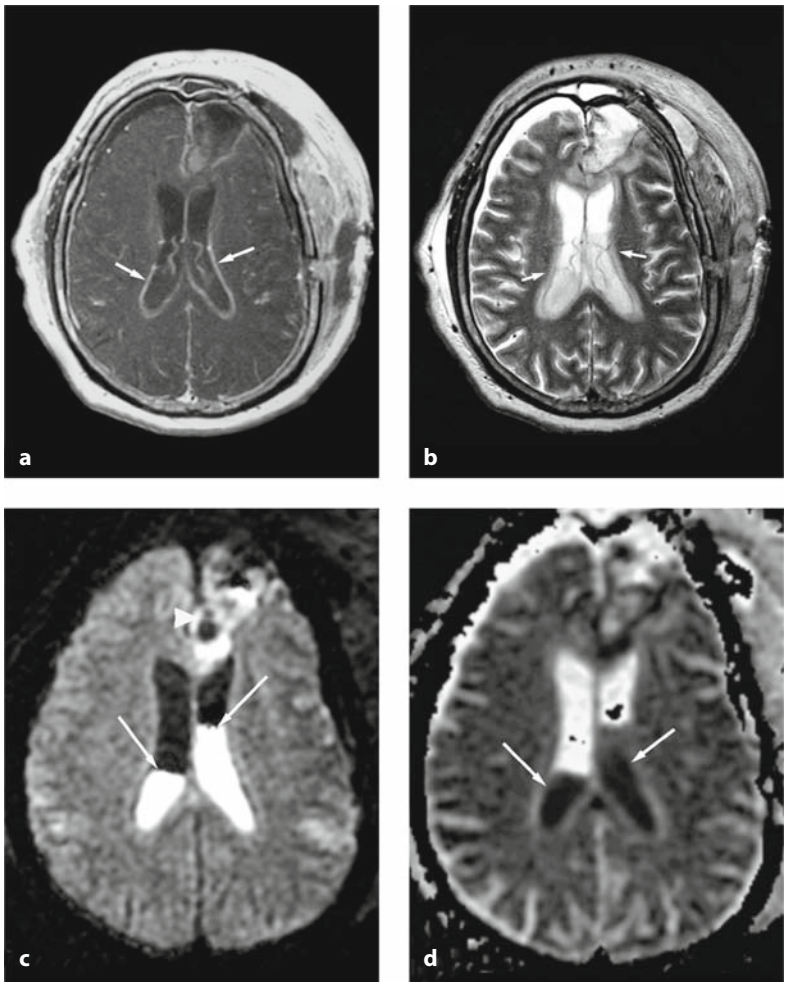

Figure 11.14 a–d

Purulent ventriculitis after surgery in a 60-year-old man. **a** Gadolinium-enhanced T1-weighted image with magnetization transfer contrast shows linear enhancement along the ventricle (*arrows*). There are postsurgical changes in the left frontal lobe and extracranially on the left. **b** T2-weighted image shows a fluid–fluid level in bilateral lateral ventricles (*arrows*) and postoperative changes in the left frontal lobe (*arrowhead*). **c** DW image shows the fluid (*arrows*) as hyperintense, representing purulent ventriculitis, and postoperative changes in the left frontal lobe (*arrowhead*). **d** ADC map shows these lesions as decreased ADC

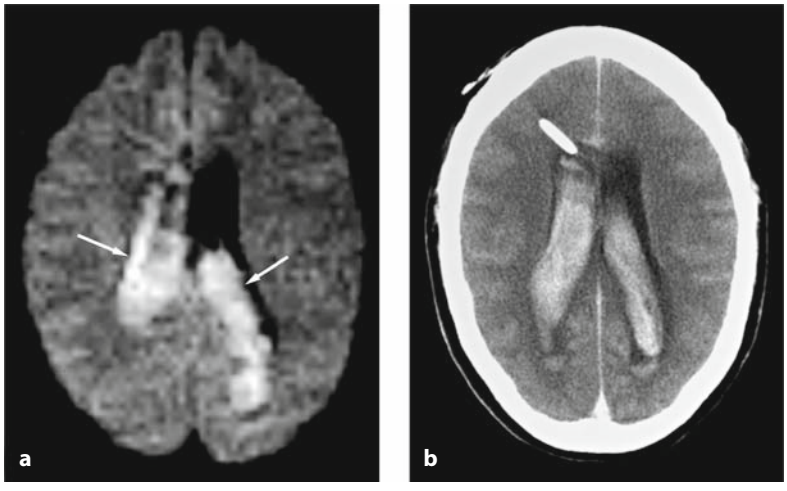

Figure 11.15 a, b

Intraventricular hemorrhage due to arteriovenous malformation in a 29-year-old man. **a** DW image shows hyperintense lesions (*arrows*) with decreased ADC (not shown), similar to the finding seen in purulent intraventriculitis. **b** Computed tomography shows the high density of intraventricular hemorrhage

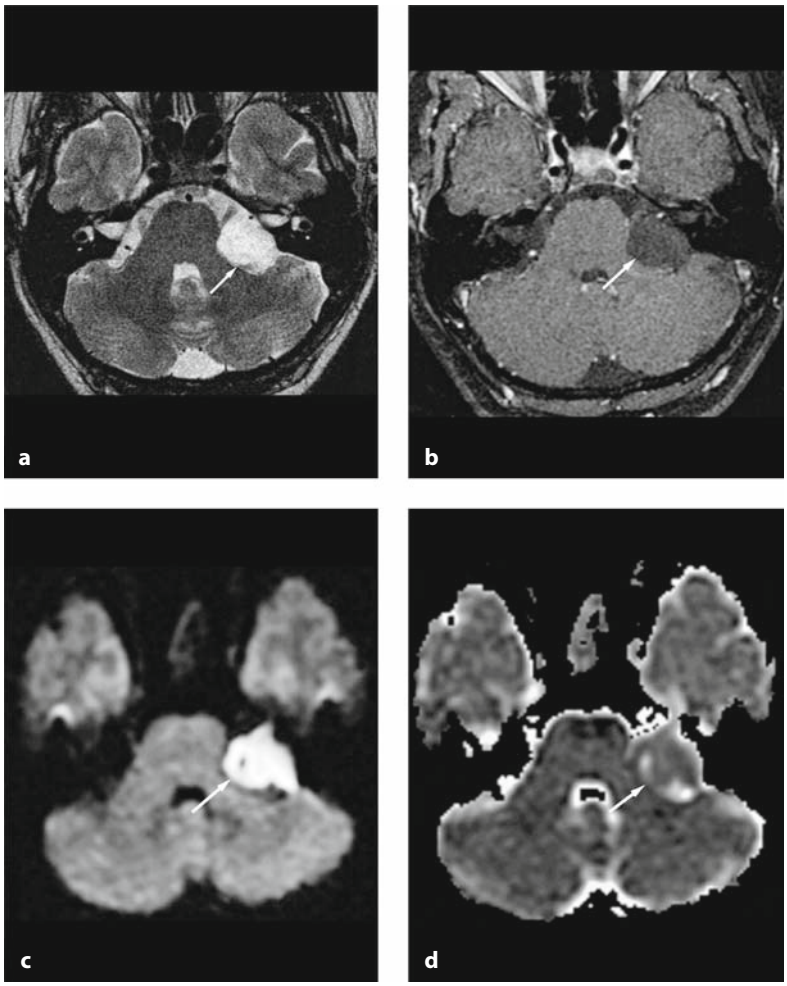

Figure 11.16 a–d

Epidermoid in a 29-year-old man. **a** T2-weighted image shows a hyperintense mass (*arrow*) in the left cerebello-pontine angle. **b** Gadolinium-enhanced T1 weight- ed image with magnetization transfer contrast shows the lesion (*arrow*) as hypointense with no enhancement. **c** DW image shows this lesion (*arrow*) as hyperintense. **d** ADC map shows almost similar ADC value to the cerebellar parenchyma

11.5.1 Differential Diagnosis

Hematomas and epidermoids occasionally have imaging characteristics similar to those of an extra-axial abscess on DW imaging. The hematomas often show hyperintensity with decreased ADC, probably because of the hypercellularity or hyperviscosity (Fig. 11.15) [31, 32]. Epidermoids also show an extra-axial hyperintense lesion on DW imaging (Fig. 11.16) caused by high viscosity keratohyalin-containing materials, which are arranged in layers, as in an onion bulb. ADC maps usually show slightly increased ADC as compared with normal brain parenchyma [33].

11.6 Bacterial Vasculitis

Cerebral infarctions secondary to meningitis are well documented in the pediatric age group. Thus, *Streptococcus* B meningitis in neonates can result in infarction, a condition that is rare in adults. The blood–brain/blood–cerebrospinal fluid (CSF) barrier and the mechanical integrity of meninges are immature in young infants, which may explain the preponderance for these changes to occur in babies and young infants [34]. Both arteries and veins can be involved by infection via the perivascular space. Pial arteriolar occlusion causes infarction of the subpial cortex (Fig. 11.17). Although vasculitic changes occur early, they only become prominent resulting in an infarction by the second to third week after onset of the meningeal infection. DW imaging is useful in early detection of the infarction, which is bright on DW imaging, with low ADC.

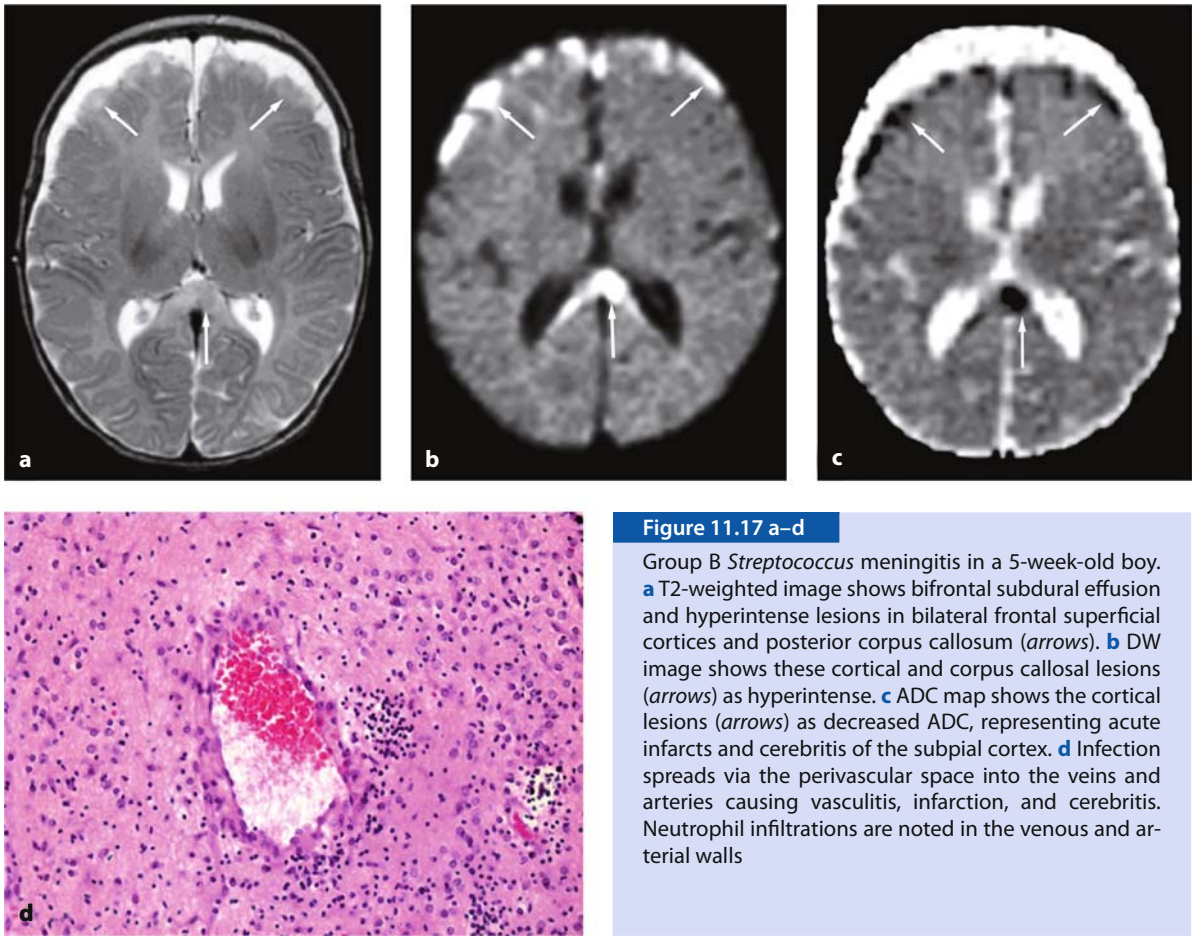

Figure 11.17 a–d

Group B *Streptococcus* meningitis in a 5-week-old boy. **a** T2-weighted image shows bifrontal subdural effusion and hyperintense lesions in bilateral frontal superficial cortices and posterior corpus callosum (*arrows*). **b** DW image shows these cortical and corpus callosal lesions (*arrows*) as hyperintense. **c** ADC map shows the cortical lesions (*arrows*) as decreased ADC, representing acute infarcts and cerebritis of the subpial cortex. **d** Infection spreads via the perivascular space into the veins and arteries causing vasculitis, infarction, and cerebritis. Neutrophil infiltrations are noted in the venous and arterial walls

11.7 Toxoplasmosis

Toxoplasma abscesses consist of ischemic necrosis of the brain tissue associated with sclerosing endoarteritis and a variety of inflammatory reactions. Toxoplasma abscesses are more commonly seen in immunocompromised patients, such as patients with acquired immunodeficiency syndrome (AIDS). In fact, toxoplasma abscesses in AIDS patients were once so common that they were morphologically grouped into three subtypes: (1) poorly circumscribed areas of necrosis (necrotizing abscess), (2) a central area of coagulative necrosis surrounded by macrophages and organism (organizing abscess), and (3) well-demarcated cystic spaces (chronic abscess) [35]. Central necrosis in toxoplasma abscesses does not contain as many inflammatory cells as regular bacterial abscesses.

DW imaging of a toxoplasma abscess has been reported to show no water restriction in the core of the rim-enhancing area, which is helpful in differentiating them from bacterial abscesses and possibly lymphomas (Figs. 11.18, 11.20) [36, 37]. However, there are exceptions; DW imaging may show a variety of signal characteristics (Fig. 11.19) [38]. Abscesses with different characteristics are occasionally seen in the same patient. This probably reflects the different pathologic/morphologic subtypes such as coagulative or liquefactive necrosis (Fig. 11.19).

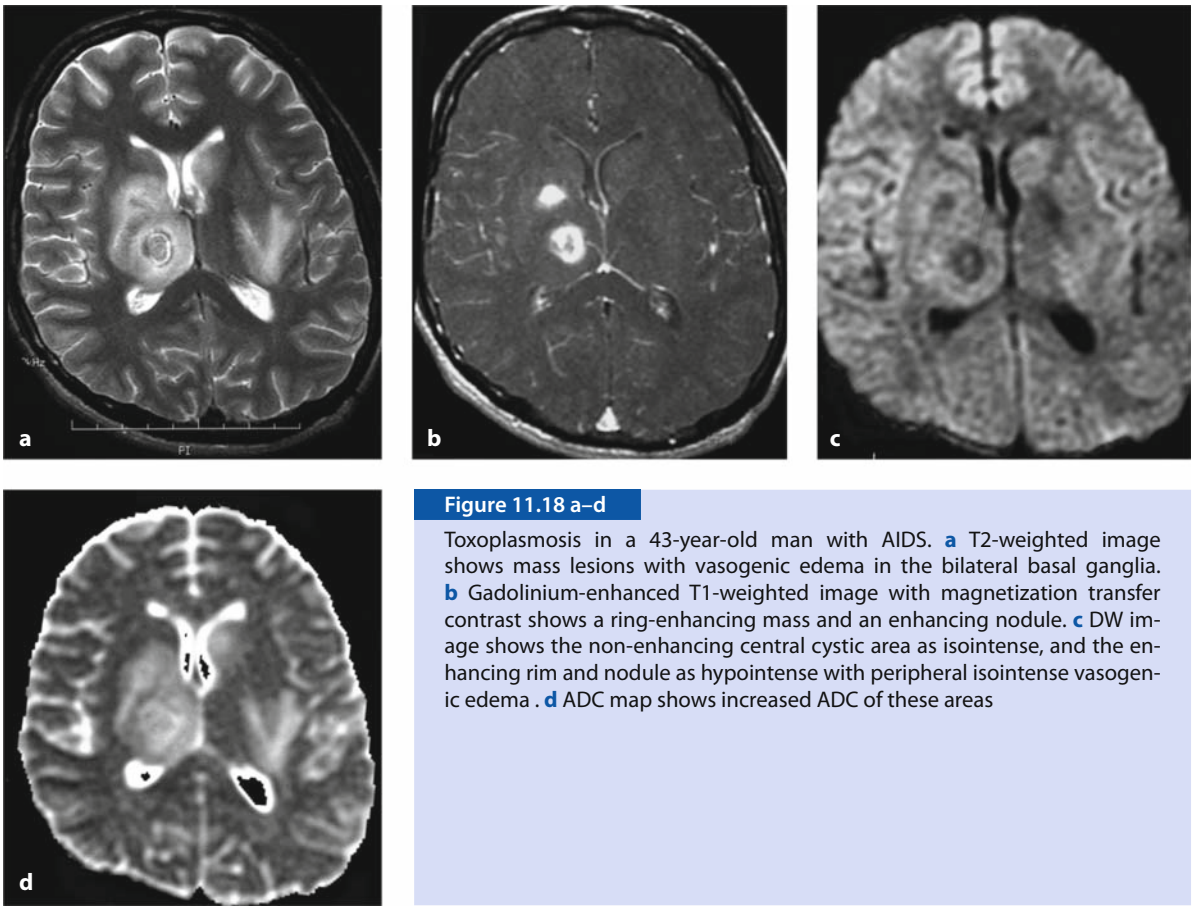

Figure 11.18 a–d

Toxoplasmosis in a 43-year-old man with AIDS. **a** T2-weighted image shows mass lesions with vasogenic edema in the bilateral basal ganglia. **b** Gadolinium-enhanced T1-weighted image with magnetization transfer contrast shows a ring-enhancing mass and an enhancing nodule. **c** DW image shows the non-enhancing central cystic area as isointense, and the enhancing rim and nodule as hypointense with peripheral isointense vasogenic edema . **d** ADC map shows increased ADC of these areas

11.7.1 Differential Diagnosis

The main differential diagnosis is lymphoma. In AIDS patients, central nervous system lymphoma is often associated with central necrosis. This is occasionally liquefactive, presumably related to hypoxia or apoptosis of tumor cells. The enhancing portion of the lesion usually shows hyperintensity on DW imaging, with relatively low ADC due to hypercellularity of lymphomas (Fig. 11.20). A central necrosis typically shows hypointensity on DW imaging with increased ADC [38]. However, a non-enhancing central core may show relatively lower ADC values than those in toxoplasmosis, reflecting the hypercellularity of lymphoma, especially in AIDS patients [36].

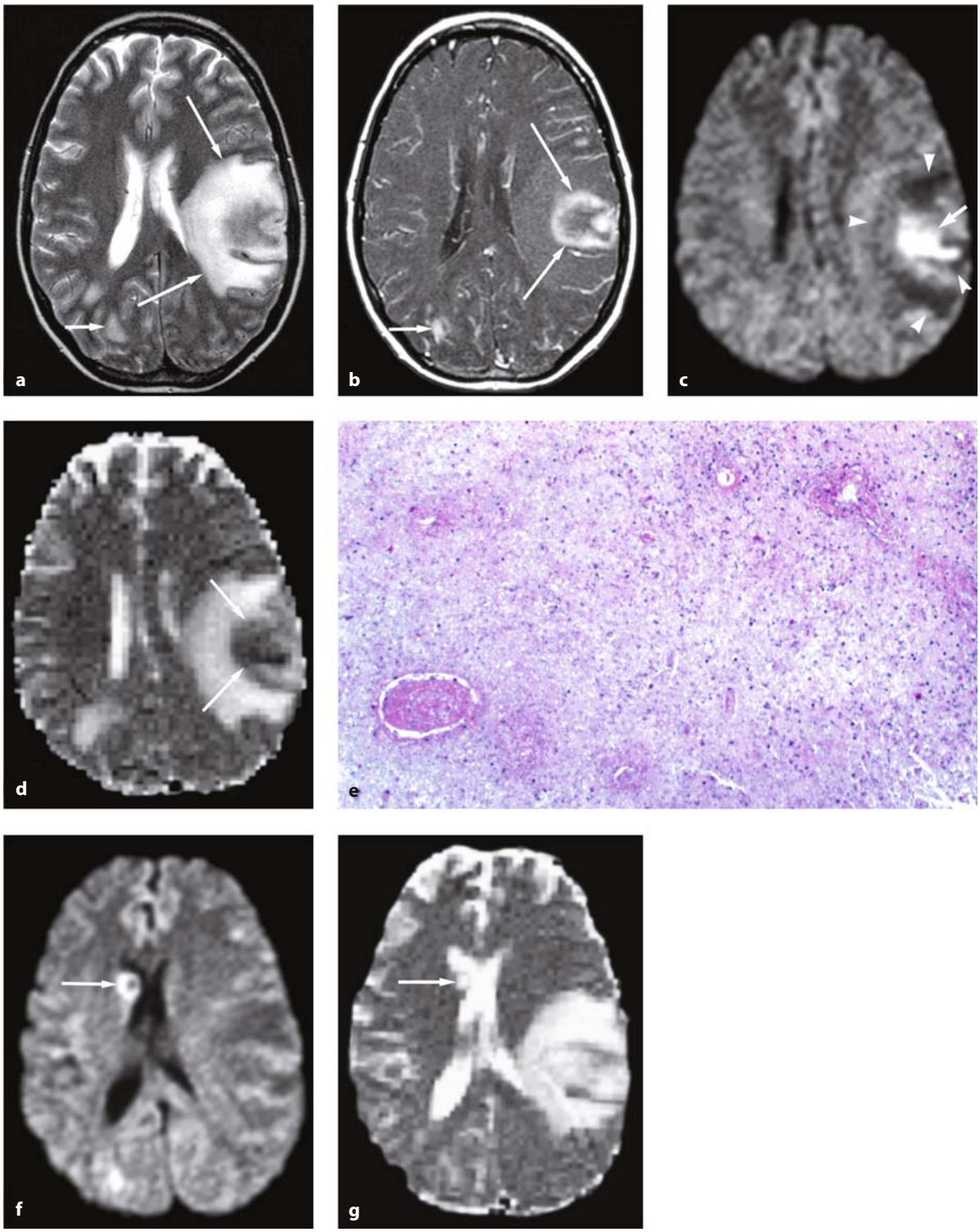
a
b
c
d
e
f
g

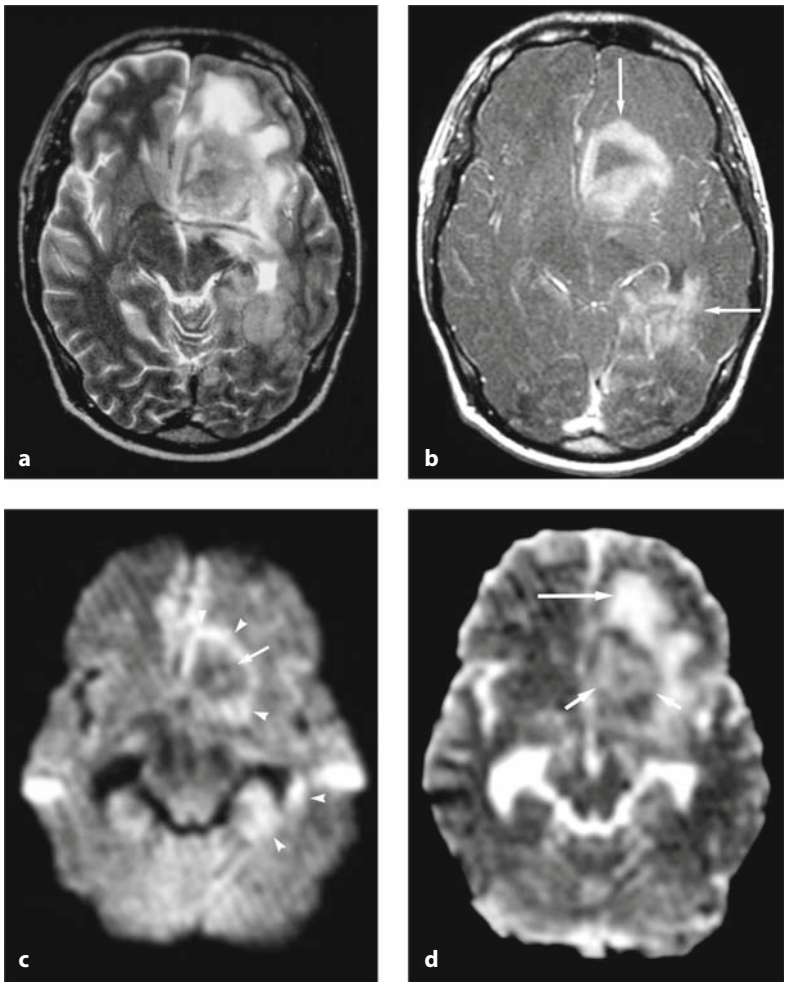

Figure 11.20 a–d

AIDS-related lymphoma in a 23-year-old man. **a** T2-weighted image shows a necrotic mass in the left frontal lobe extending into the temporo-occipital lobe. **b** Gadolinium-enhanced T1-weighted image magnetization transfer contrast shows these lesions (*arrows*) with irregular ring enhancement. **c** DW image shows enhancing solid components as hyperintensity (*arrowheads*), and a necrotic component as hypointensity (*arrow*). **d** ADC map shows central necrosis as increased ADC (*arrow*) and the solid components (*arrowheads*) as relatively low ADC compared to the central necrosis

Figure 11.19 a–g

Toxoplasmosis in an 18-year-old female patient with acute myeloblastic leukemia. **a** T2-weighted image shows a mass lesion with vasogenic edema in the left fronto-temporal region (*long arrows*). Hyperintense lesions are also seen in the right occipital area (*short arrow*). **b** Gadolinium-enhanced T1-weighted image with magnetization transfer contrast shows a ring-enhancing mass (*long arrows*) and an enhancing nodule (*short arrow*). **c** DW image shows the non-enhancing cystic central area as hyperintense (*arrow*), and the enhancing rim and peripheral vasogenic edema as hypointense (*arrowheads*). **d** ADC map shows decreased ADC of this cystic component (*arrows*). **e** Biopsy specimen shows coagulative necrosis of this cystic component (hematoxylin–eosin stain). **f**, **g** DW image shows a small cystic lesion (*arrow*) as hypointense with increased ADC (**g**) in the right caudate nucleus (*arrow*), which may indicate the different phase of toxoplasma abscess. Left fronto-temporal mass and multiple hyperintense nodules are also seen

◂

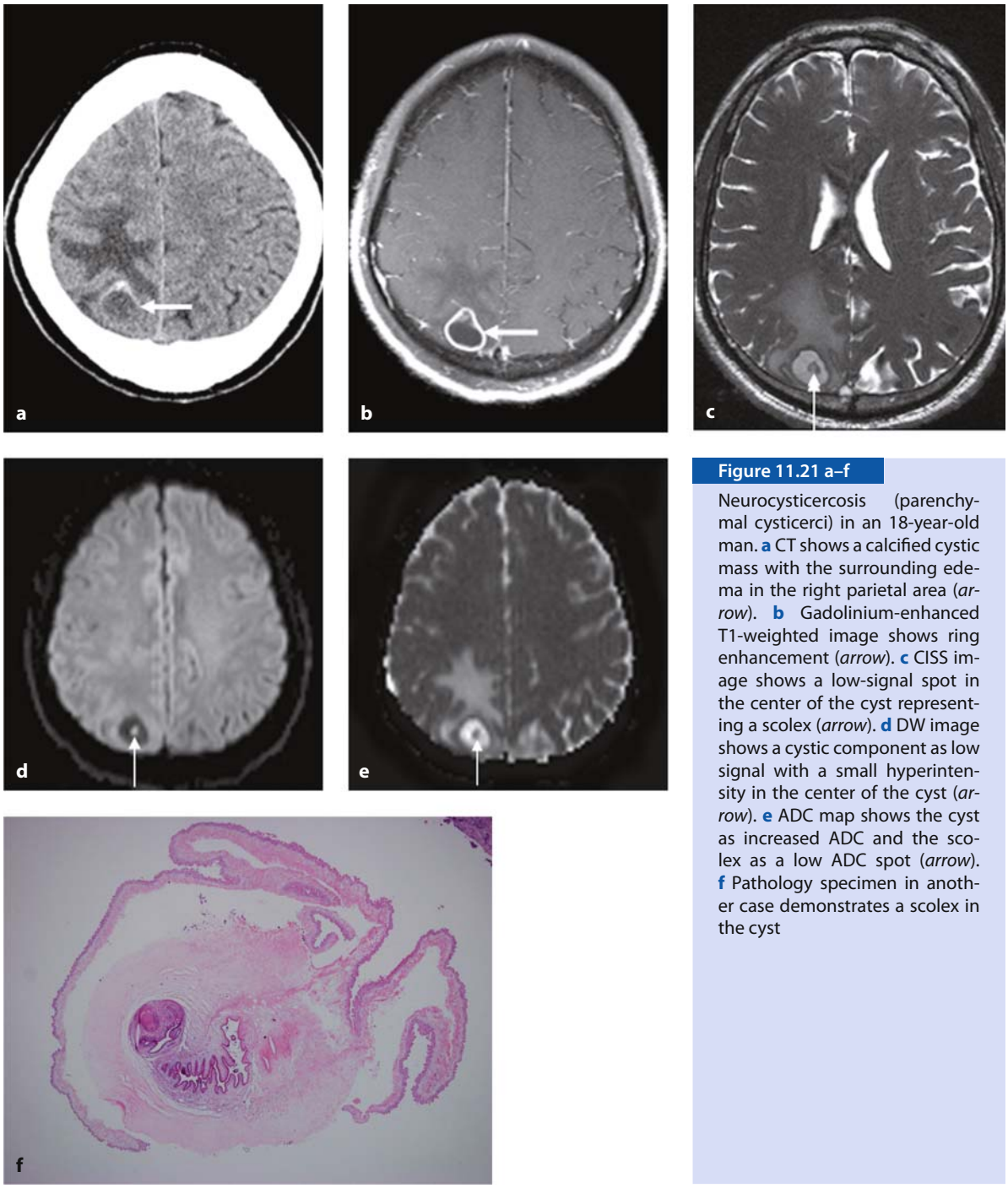

Figure 11.21 a–f

Neurocysticercosis (parenchymal cysticerci) in an 18-year-old man. **a** CT shows a calcified cystic mass with the surrounding edema in the right parietal area (*arrow*). **b** Gadolinium-enhanced T1-weighted image shows ring enhancement (*arrow*). **c** CISS image shows a low-signal spot in the center of the cyst representing a scolex (*arrow*). **d** DW image shows a cystic component as low signal with a small hyperintensity in the center of the cyst (*arrow*). **e** ADC map shows the cyst as increased ADC and the scolex as a low ADC spot (*arrow*). **f** Pathology specimen in another case demonstrates a scolex in the cyst

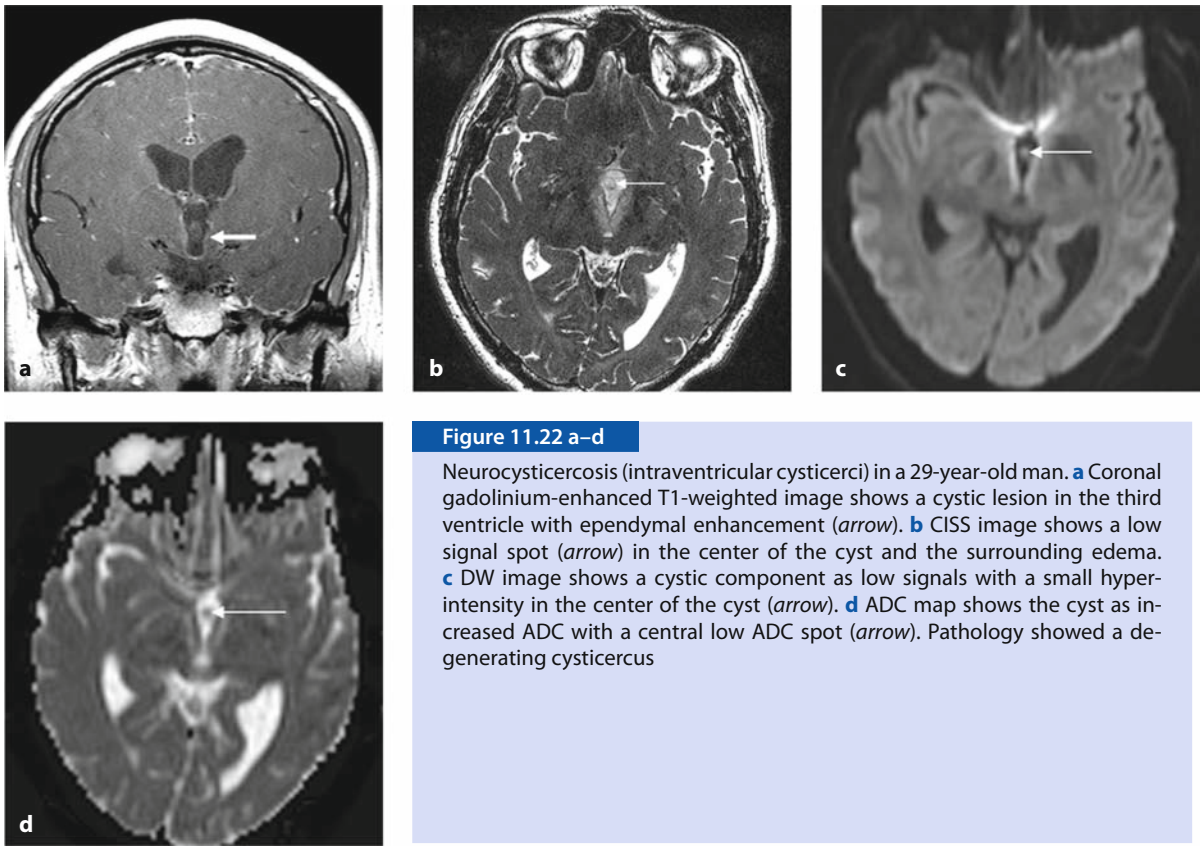

Figure 11.22 a–d

Neurocysticercosis (intraventricular cysticerci) in a 29-year-old man. **a** Coronal gadolinium-enhanced T1-weighted image shows a cystic lesion in the third ventricle with ependymal enhancement (*arrow*). **b** CISS image shows a low signal spot (*arrow*) in the center of the cyst and the surrounding edema. **c** DW image shows a cystic component as low signals with a small hyperintensity in the center of the cyst (*arrow*). **d** ADC map shows the cyst as increased ADC with a central low ADC spot (*arrow*). Pathology showed a degenerating cysticercus

11.8 Neurocysticercosis

Cysticercosis is the most common parasitic infection of the central nervous system and it is caused by *Taenia solium*. Pathologically, there are four forms: (1) parenchymal cysticerci (Fig. 11.21), (2) leptomeningitis, (3)intraventricular cysticerci (Fig. 11.22), and (4) racemose cysts. DW imaging shows cystic lesions in neurocysticercosis as low signal intensity with high ADC values, which is useful in differentiating them from bacterial or tuberculous abscess [21]. The scolex may be detectable as a hyperintense nodule on DW imaging (Fig. 11.21) [39].

11.9 Fungal Infection

Aspergillosis is the most common intracranial fungal infection, commonly seen in immunocompromised patients. In disseminated aspergillosis, *Aspergillus* infiltrates and destroys the internal elastic lamina of cerebral arteries and causes vasculitis [40]. This leads initially to acute infarction or hemorrhage. Most of the process extends into the surrounding tissue as cerebritis and may evolve into an abscess. Infection of already infarcted brain tissue is often aggressive with rapid progression. MR imaging shows round lesions often involving the basal ganglia and gray-white matter junction with absence or minimal peripheral enhancement. Ring or parenchymal enhancement of the lesion can be seen in less severely immunocompromised patients. DW imaging is useful for early detection of this vasculopathy-mediated septic infarction and abscess (Fig. 11.23) [20, 41, 42]. The mortality rate is estimated between 85 and 100%. New antifungal therapies (triazole) have made effective treatment possible.

Rhinocerebral mucormycosis often occurs in diabetic patients, especially with diabetic ketoacidosis, which is an excellent medium for this fungus in an environment of elevated glucose and acidic pH [43]. DW imaging shows the lesion as restricted water diffusion typically located in the inferior frontal lobe [44] (Fig. 11.24). Cryptococcus infection shows enhancing or non-enhancing lesions involving the basal ganglia, meninges, and ventricles. The cystic lesions are isosignal to CSF on T2-weighted and DW images (Fig. 11.25) [45].

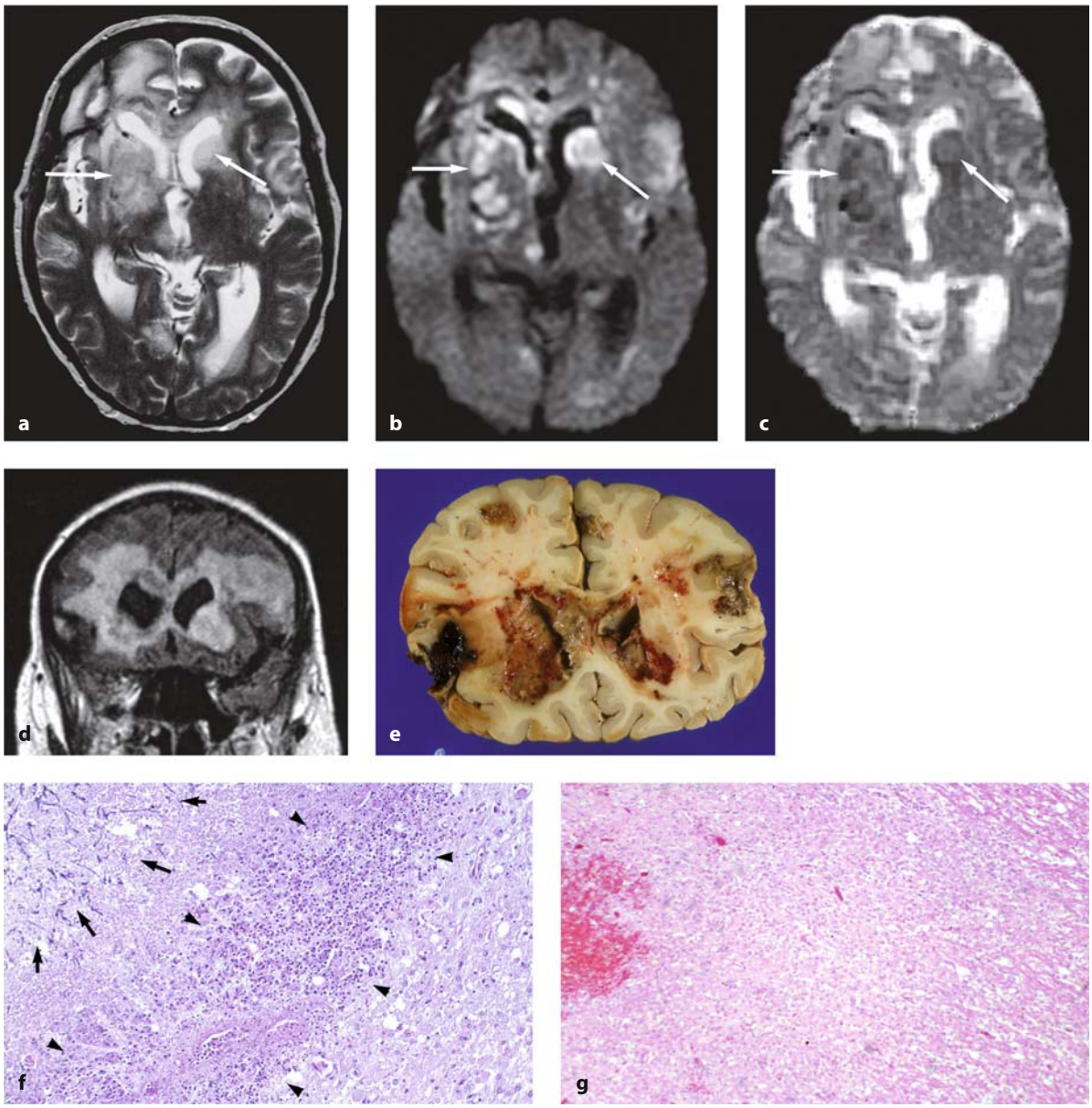

Figure 11.23 a–g

Disseminated aspergillosis in a 55-year-old woman with fever and mental status change. She had hepatitis C and underwent liver transplantation. **a** T2-weighted image shows multiple hyperintense round lesions (*arrows*) in bilateral basal ganglia, right thalamus, and cerebral white matter and cortex. Subdural hematoma is also seen in the right frontal region. **b** DW image shows these lesions as very high signal intensity (*arrows*), representing infarction, hemorrhage and abscess. **c** ADC maps show decreased ADC in these lesions (*arrows*). **d** Coronal FLAIR image shows extensive hyperintense lesions in the frontal lobes. **e** Brain specimen with the same slice of the FLAIR image demonstrates extensive hemorrhagic necrotic lesions. **f** Pathological specimen of the right thalamus shows *Aspergillus* hyphae (*arrows*) and infiltration of neutrophils and macrophages (*arrowheads*) in an abscess (hematoxylin–eosin stain). **g** Pathological specimen of left frontal area shows necrosis due to vasculitis-mediated acute septic infarction and hemorrhage (hematoxylin–eosin stain)

Figure 11.24 a–d

Rhinocerebral mucormycosis in a 48-year-old man with diabetes mellitus type 1 and ketoacidosis. **a** FLAIR image shows postoperative changes of invasive fungal infection in the right orbit and paranasal sinus. **b** DW image shows hyperintense lesions in the bilateral frontal bases. **c** Decreased ADCs of these lesions are noted, consistent with cerebritis. **d** On a 1-week follow-up MR image, the lesions extend into the frontal lobes and basal ganglia shown as hyperintense lesions on the FLAIR image

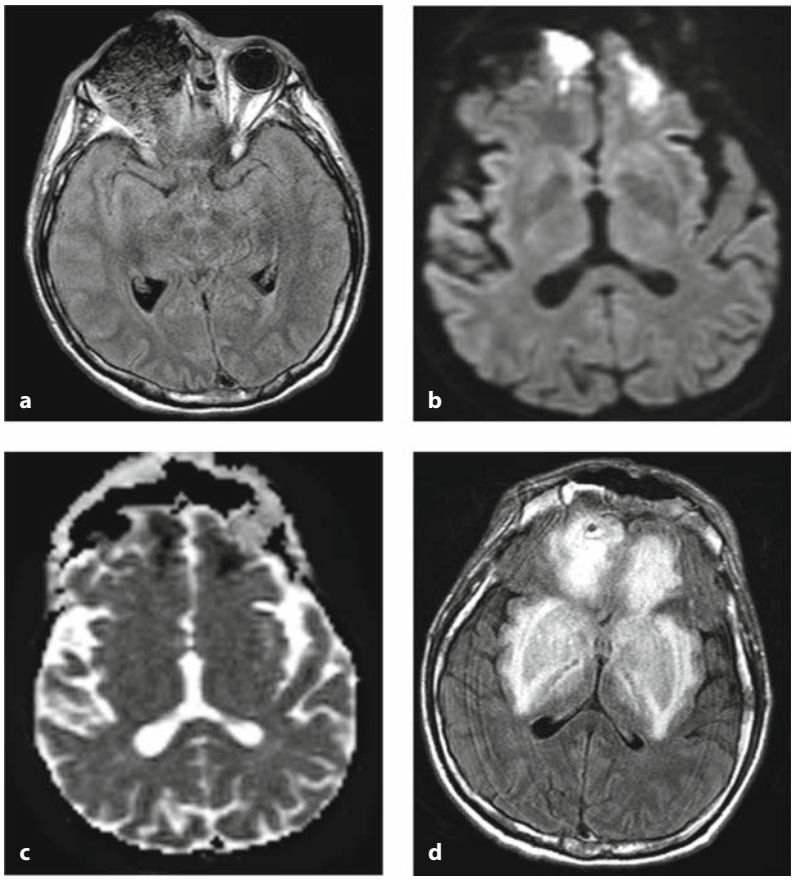

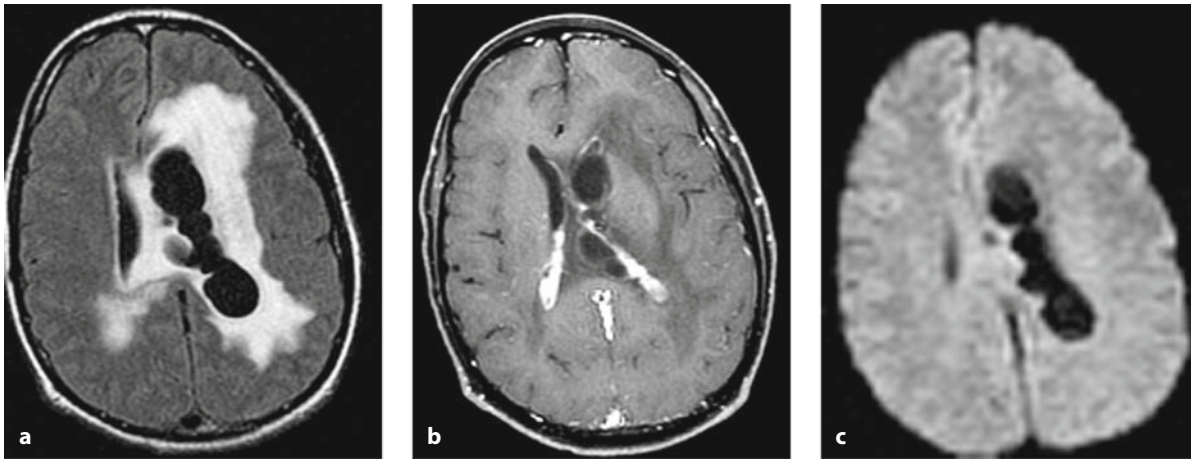

Figure 11.25 a–c

Cryptococcus ependymitis and choroid plexitis in a 40-year-old man with AIDS. **a** FLAIR image shows multiloculated cystic lesions in the lateral ventricles with extensive periventricular and deep white matter edema. **b** Gadolinium-enhanced T1-weighted image shows thin-wall-enhancing intraventricular cystic lesions and ependymal enhancement. **c** DW image shows the cystic lesions as hypointense with increased ADC (not shown)

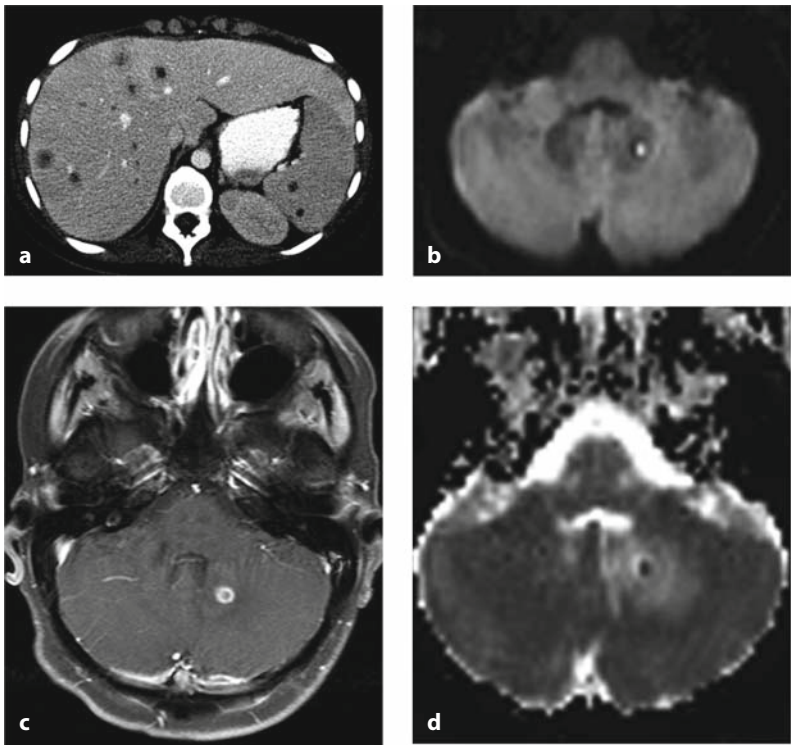

Figure 11.26 a–d

Cerebral candidiasis in a 17-year-old girl with pre-B-cell acute lymphoblastic leukemia and fungal sepsis. **a** Contrast-enhanced abdominal CT shows multiple abscesses in the liver and spleen. **b** Gadolinium-enhanced T1-weighted image shows a small ring-enhancing lesion in the left cerebellum. **c** DW image shows very small hyperintensity representing a small abscess. **d** ADC map shows decreased ADC in the abscess

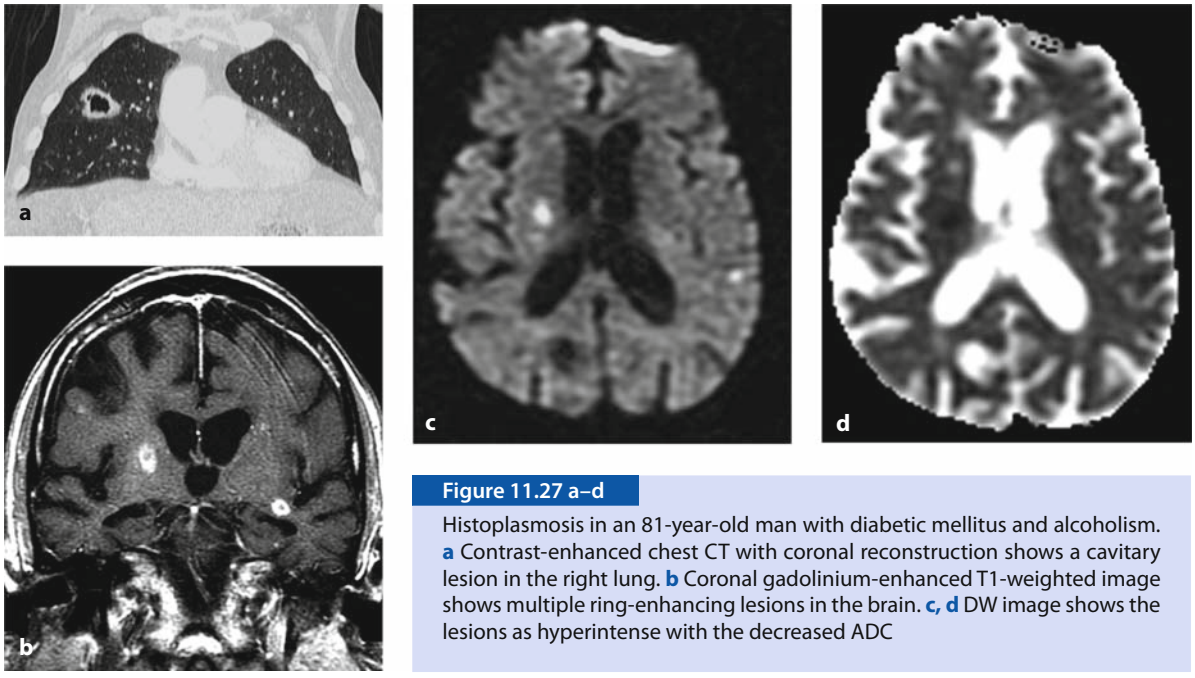

Figure 11.27 a–d

Histoplasmosis in an 81-year-old man with diabetic mellitus and alcoholism. **a** Contrast-enhanced chest CT with coronal reconstruction shows a cavitary lesion in the right lung. **b** Coronal gadolinium-enhanced T1-weighted image shows multiple ring-enhancing lesions in the brain. **c, d** DW image shows the lesions as hyperintense with the decreased ADC

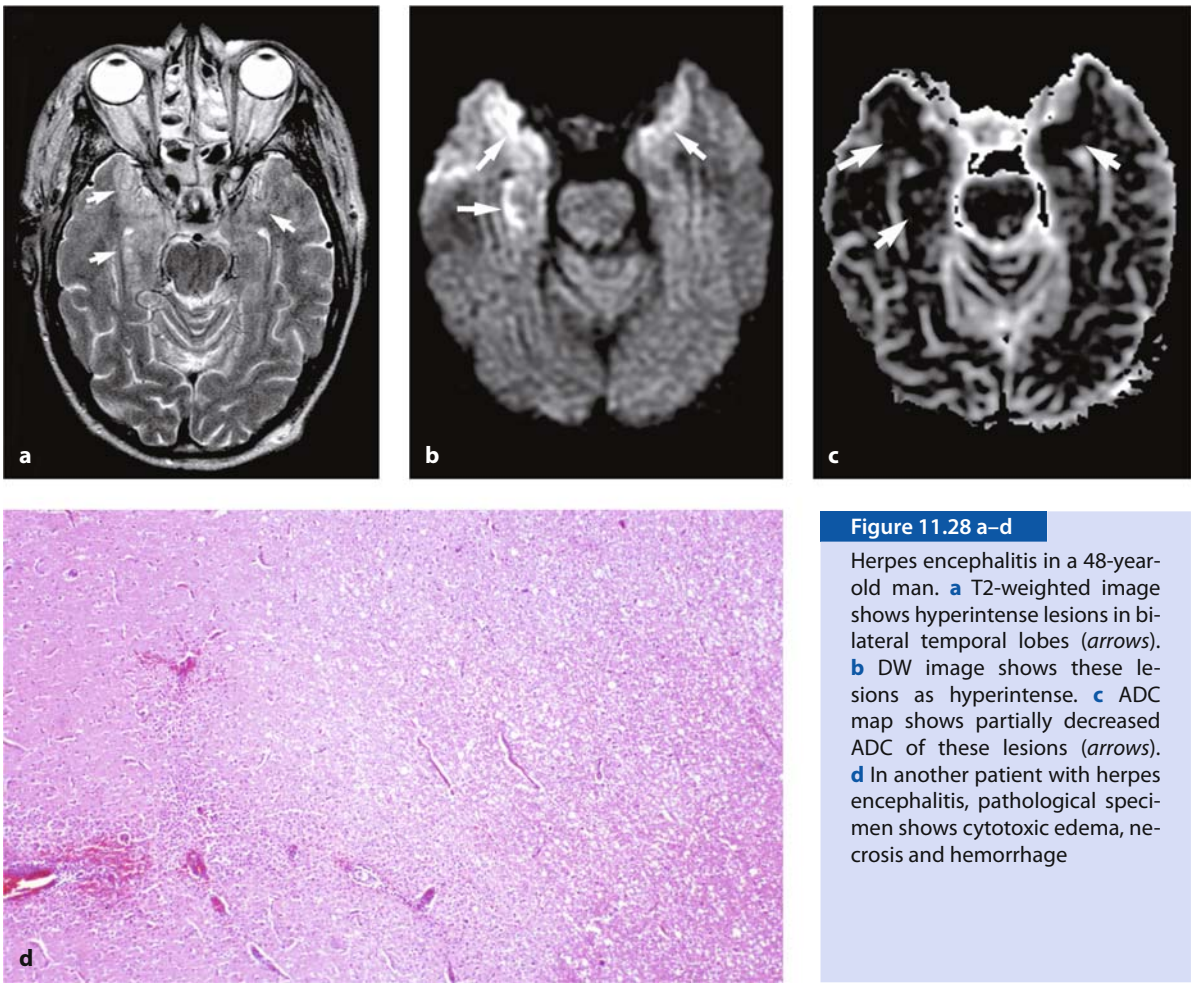

Figure 11.28 a–d

Herpes encephalitis in a 48-year-old man. **a** T2-weighted image shows hyperintense lesions in bilateral temporal lobes (*arrows*). **b** DW image shows these lesions as hyperintense. **c** ADC map shows partially decreased ADC of these lesions (*arrows*). **d** In another patient with herpes encephalitis, pathological specimen shows cytotoxic edema, necrosis and hemorrhage

Cerebral candidiasis usually appears as ring-enhancing or non-enhancing microabscess, measuring less than 3 mm (Fig. 11.26) [41]. Histoplasmosis may show ring-enhancing lesions on the brain MR images. DW imaging may show various signals depending on the presence of inflammatory cells and the type of necrosis, i.e., coagulative or liquefactive (Fig. 11.27) [46].

11.10 Herpes Encephalitis

Herpes simplex encephalitis is the most common cause of sporadic fatal encephalitis, accounting for 10-20% of encephalitic viral infections. Pathologically, herpes encephalitis has both cytotoxic and vasogenic edema associated with massive tissue necrosis and petechial or even confluent hemorrhage, typically in the limbic system and the insular cortex. Restricted diffusion of herpes encephalitides is attributed to direct cytotoxicity that results in neuronal swelling. DW imaging is more sensitive than conventional MR imaging in detecting early changes of herpes encephalitis (Fig. 11.28) [47-51]. This is important for early diagnosis, as treatment with acyclovir reduces mortality at 18 months from 70 to 30%. Herpes encephalitis often affects the temporal lobes, which occasionally can make the detection of lesions in the middle cranial fossa difficult on DW imaging because of susceptibility artifacts.

Human herpesvirus-6 (HHV6) is a ubiquitous neurotropic virus latent in most adults, also known to be the cause of exanthem subitum or roseola infantum [52, 53]. HHV-6-associated encephalitis/encephalopathy has been increasingly recognized as a serious complication in immunocompromised patients. MR imaging often shows mesial temporal lobe abnormalities. Abnormal high signal intensity with

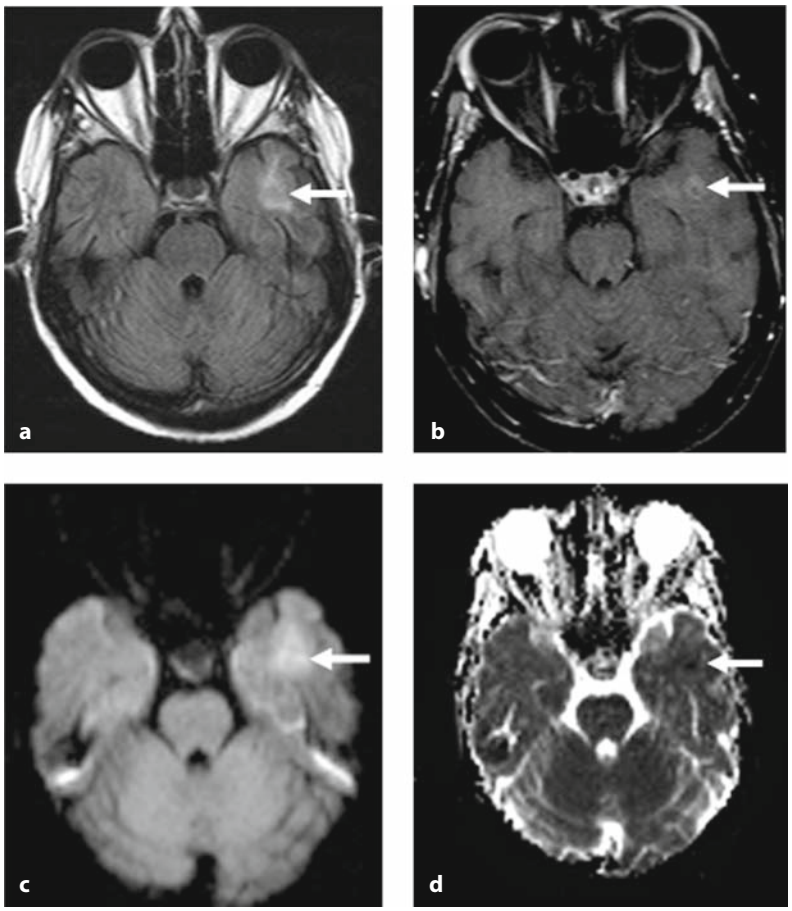

Figure 11.29 a–d

Human herpesvirus-6 encephalitis in a 28-year-old woman with acute lymphoblastic leukemia after allogeneic stem cell transplant. **a** FLAIR image shows a hyperintense lesion in the left temporal lobe. **b** Gadolinium-enhanced T1-weighted image shows mild enhancement in the lesion. **c** DW image shows the lesion as hyperintense. **d** ADC map shows decreased ADC of the lesion

ADC reduction is observed to be consistent with cytotoxic edema (Fig. 11.29). In transplantation, acyclovir is routinely administered but not effective against HHV-6 because of the lack of virus-specific thymidine kinase. Ganciclovir and foscarnet can be effective in therapy.

11.11 Brain Stem Encephalitis

Brain stem encephalitis, mesenrhombencephalitis, is a rare life-threatening inflammatory disorder involving the brain stem and cerebellum. It was initially described by Bickerstaff and Cloake in 1951 [54]. The etiology is frequently undetermined but thought to be an immune-mediated process. It often follows viral infection (herpes simplex virus, influenza A, enterovirus 71, adenovirus). In some cases, bacteria (Listeria, Mycoplasma, Legionella) and parasites or paraneoplastic syndromes have been implicated. MR imaging shows a T2- and FLAIR-hyperintense lesion in the brain stem, and enhancement in the lesion can be seen post-contrast on T1-weighted images [55]. DW imaging shows hyperintensity in the lesion with decreased or increased ADC, depending on whether there is cytotoxic or vasogenic edema (Fig. 11.30) [56].

11.12 West Nile Encephalitis

West Nile virus (WNV) is a single-stranded RNA flavivirus, and part of the Japanese encephalitis serocomplex. It is transmitted by Culex species mosquitoes. WNV can infect birds, humans, horses, dogs, cats, bats, chipmunks, skunks, squirrels, and rabbits.

Four other transmissions have been reported: (1) transfusion, (2) transplanted organ, (3) transplacental, and (4) breast feeding. The incubation period is around 3-14 days. One in 150 patients with WNV develops meningoencephalitis. The clinical symptoms include fever, headache, altered mental status, tremor, and flaccid paralysis and poliomyelitis associated

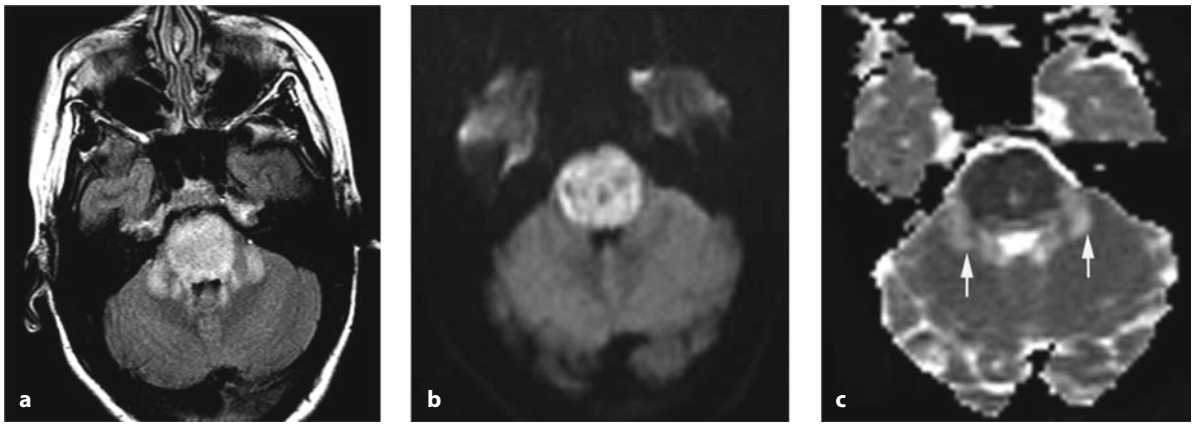

Figure 11.30 a–c

Brain stem encephalitis in a 29-year-old woman diagnosed with a viral syndrome. **a** FLAIR image shows hyperintense lesions diffusely in the pons and bilateral middle cerebellar peduncles. **b, c** DW image shows the diffuse pontine lesion as hyperintense with decreased ADC which represents cytotoxic edema, and the bilateral middle cerebellar peduncles as isointense with increased ADC representing vasogenic edema (*arrows*)

with spinal cord involvement. The diagnosis is based on detection of a WNV IgM antibody in the CSF. MR imaging shows mild hyperintense lesions on T2 and FLAIR studies in the basal ganglia, thalami, mesial temporal lobe, white matter, cerebellum, brain stem, especially the substantia nigra and medulla, and the spinal cord with or without enhancement (Fig. 11.31). Leptomeningeal enhancement and FLAIR hyperintensity in the CSF can also be seen. However, 30% of cases have normal MR images. DW imaging shows these parenchymal lesions as hyperintense with reduced ADC [57-61]. Pathology demonstrates lymphocytic neutropholis, perivascular lymphocytic cuffing, microglial nodules, spongiotic changes, and necrosis (Fig. 11.31). Treatment is conservative with IV fluid and respiratory support. Interferon-α2b or ribavirin may be used.

11.13 Cerebral Malaria

Malaria has infected humans for over 50,000 years. There are 300-500 million cases per year and 2 million people die of the disease (90% in Africa). It is transmitted by Anopheles mosquitoes. Cerebral malaria (2% of cases) is responsible for most malaria deaths, and Plasmodium falciparum (tropical malaria) is the most common parasite. The diagnosis of malaria is based on a blood smear which shows ring-stage trophozoites. If malaria load in the blood smear is more than 10%, about 50% of the patients die. Moreover, 15-25% of patients with cerebral malaria die despite treatment. Two main mechanisms have been suggested in cerebral malaria: (1) Infected RBCs adhered to the endothelium cause blockage of the capillaries, and (2) cerebral toxicity by cytokines [62].

CT is normal in 30-50% of cases. MR imaging demonstrates diffuse cytotoxic or vasogenic cerebral edema (70%) or infarcts in the white matter, especially involving the corpus callosum, basal ganglia, thalami, brain stem, and cerebellum [63]. DW imaging shows these areas as hyperintense with reduced ADC (Fig. 11.32) [64]. Diffuse petechial hemorrhages in the cortex and subcortical white matter are well visualized on gradient T2*-weighted images.

11.14 Human Immunodeficiency Virus Infection

The pathological hallmark of human immunodeficiency virus (HIV) encephalopathy is multinucleated giant cells in the white matter [65]. MR imaging typically shows diffuse periventricular white matter lesions, but brain stem and basal ganglia can also be involved. DW imaging usually shows mild hyperintensity with increased ADC which is secondary to a T2 shine through effect (Fig. 11.33).

Cerebral infarction in HIV patients is common and has been seen on MR imaging in up to 18% of the patients [66]. The infarctions are caused by opportunistic infections, drug use and primary HIV vasculitis. AIDS-related bilateral basal ganglia lesions are re-

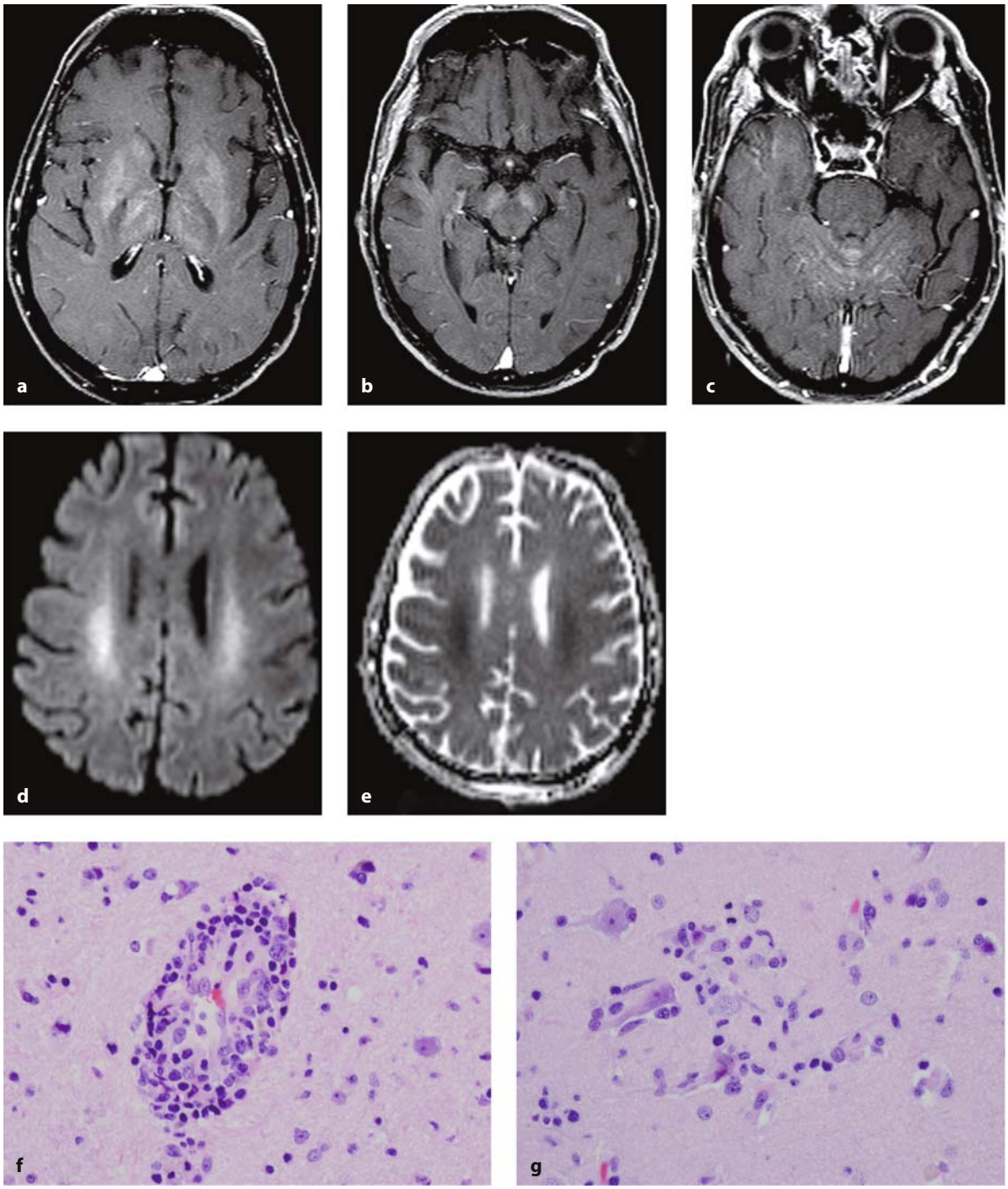

Figure 11.31 a–g

West Nile encephalitis in a 56-year-old man with fever and tremors with a history of renal transplant. **a-c** Gadolinium-enhanced T1-weighted image shows symmetric mild enhancement in the basal ganglia, thalami, and substantia nigra, and leptomeningeal enhancement in the posterior fossa. **d, e** DW image shows diffuse symmetric hyperintense lesions with decreased ADC only in the deep white matter. **f, g** Pathological specimens of the brain biopsy show perivascular lymphocytic cuffing (**f**) and microglial nodules (**g**)

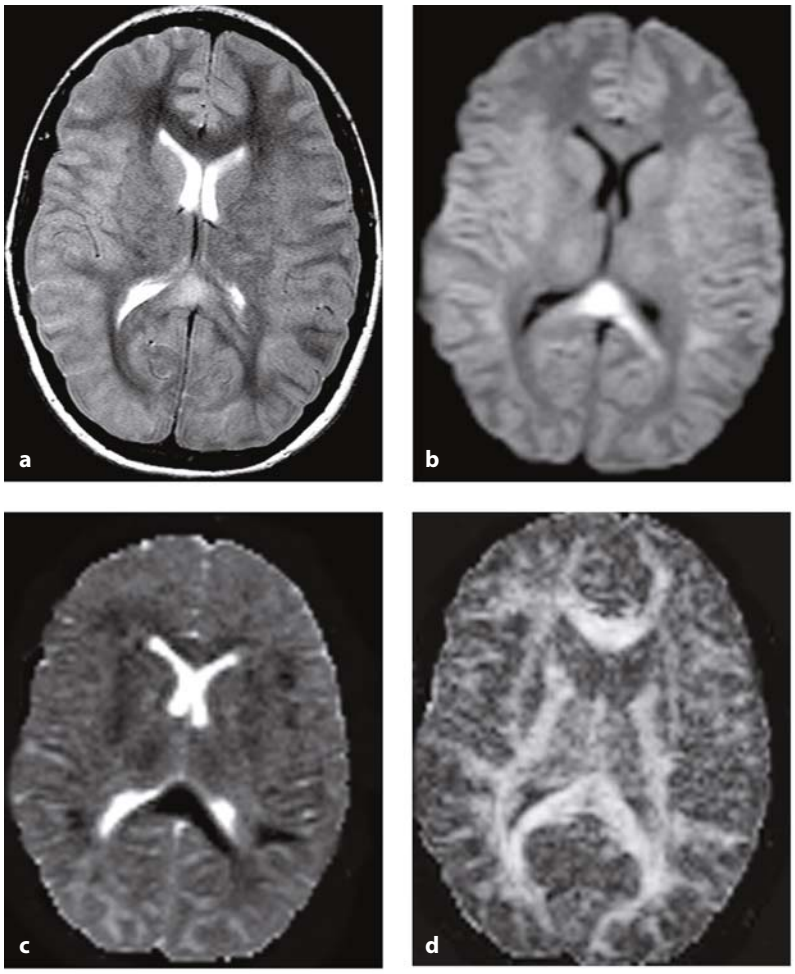

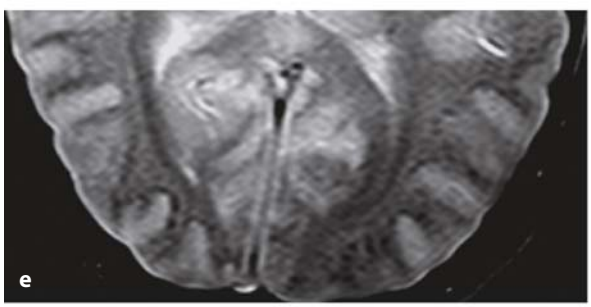

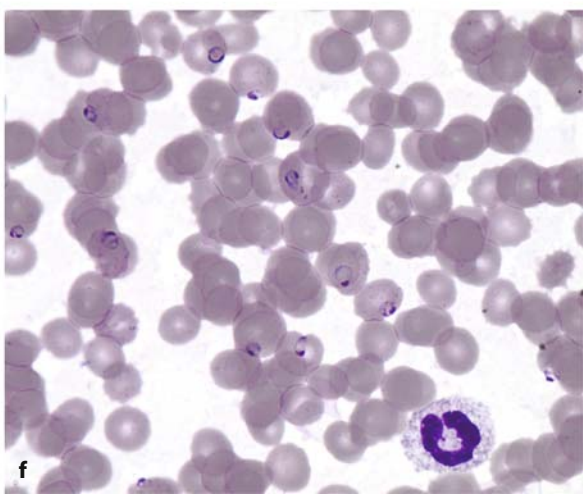

Figure 11.32 a–f

Cerebral malaria in a 19-year-old female patient with headache, fever, and jaundice. **a** T2-weighted image shows diffuse hyperintensity and swelling in the brain, especially of the gray matter and the splenium of the corpus callosum. **b** DW image shows hyperintense lesions in the white matter, thalami, basal ganglia, and the splenium of the corpus callosum. **c** ADC map shows these areas as decreased ADC consistent with cytotoxic edema. **d** Fractional anisotropy is preserved in these areas. **e** Gradient T2*-weighted image shows petechial hemorrhage in the cortico-white matter junction post mortem (Courtesy of Kim J MD, The University of Iowa Hospitals and Clinics, USA). **f** Blood smear shows ring-stage trophozoites

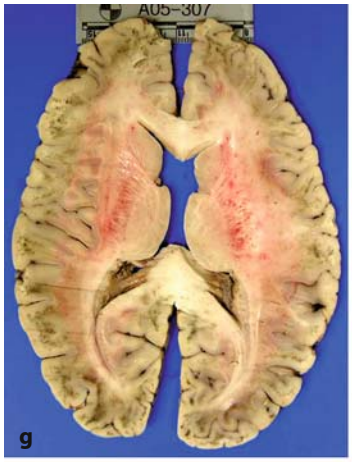

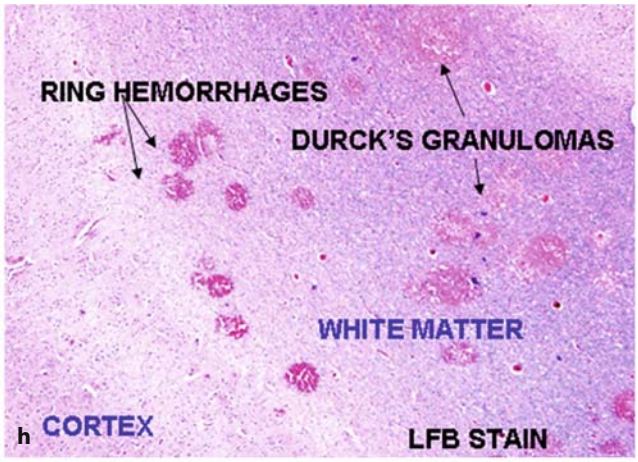

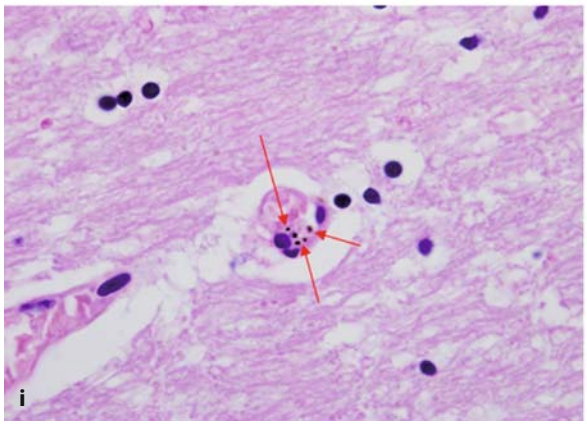

Figure 11.32 g–i

g Pathological specimen shows diffuse brain edema and petechial hemorrhage in the cortico-white matter junction (*arrows*). **h** Luxol Fast Blue stain shows ring hemorrhage at the cortico-white matter junction and Durck's granulomas in the white matter. **i** Malarial trophoziotes and hematoidin pigment are noted in the red blood cell in the capillary (*arrows*)

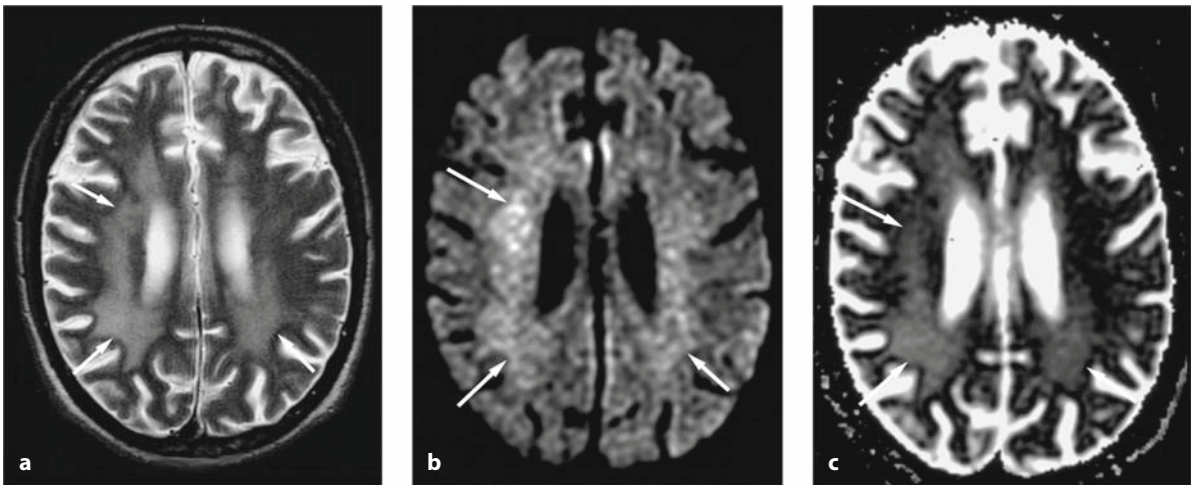

Figure 11.33 a–c

HIV encephalopathy in a 60-year-old man. **a** T2-weighted image shows periventricular hyperintense lesions (*arrows*). **b** DW image shows these lesions as mild hyperintensity (*arrows*). **c** ADC map shows these lesions as increased ADC. Mild hyperintensity on DW imaging is due to T2 shine-through effect (*arrows*)

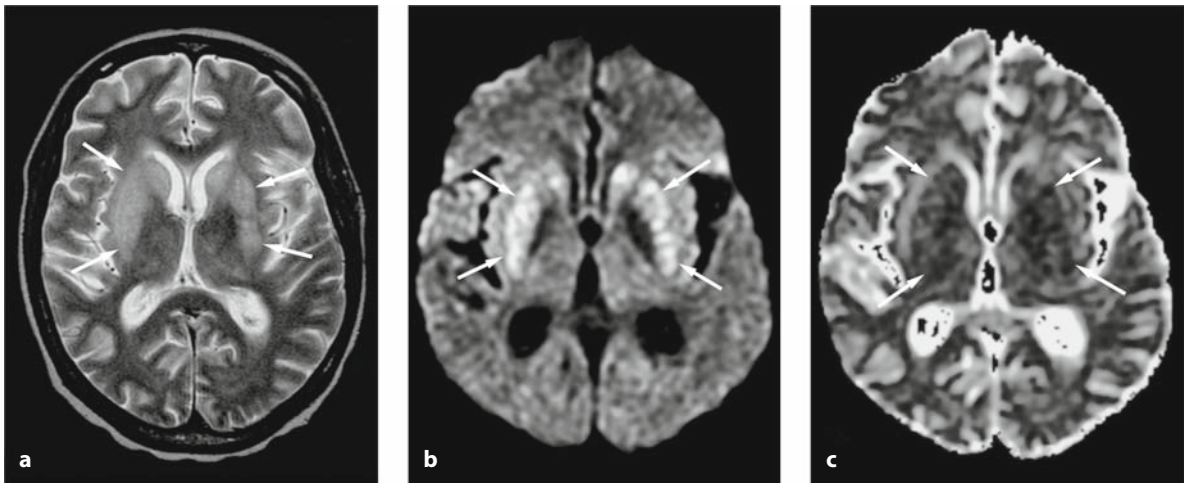

Figure 11.34 a–c

AIDS-related bilateral basal ganglia lesions in a 38-year-old woman with multiple small infarcts. **a** T2-weighted image shows hyperintense lesions in bilateral caudate nuclei and putamina (*arrows*). **b** DW image demonstrates these lesions as numerous hyperintense spots, probably representing microinfarcts associated with HIV infection and/or drug abuse (*arrows*). **c** ADC map shows these lesions as partially decreased ADC (*arrows*)

ported to be numerous microinfarcts on postmortem neuropathological examination [67]. DW imaging can show numerous hyperintense lesions in bilateral basal ganglia, presumably representing microinfarcts (Fig. 11.34).

References

1. Ebisu T, Naruse S, Horikawa Y, et al. (1993) Discrimination between different types of white matter edema with diffusion-weighted MR imaging. JMRI 3:863–868
2. Ebisu T, Tanaka C, Umeda M, et al. (1996) Discrimination of brain abscess from necrotic or cystic tumors by diffusion-weighted echo planar imaging. Magn Reson Imaging 14:1113–1116
3. Kim YJ, Chang KH, Song IC, et al. (1998) Brain abscess and necrotic or cystic brain tumor: discrimination with signal intensity on diffusion-weighted MR imaging. AJR Am J Roentgenol 171:1487–1490
4. Desprechins B, Stadnik T, Koerts G, et al. (1999) Use of diffusion-weighted MR imaging in differential diagnosis between intracerebral necrotic tumors and cerebral abscesses. AJNR Am J Neuroradiol 20:1252–1257
5. Noguchi K, Watanabe N, Nagayashi T, et al. (1999) Role of diffusion-weighted echo-planar MRI in distinguishing between brain abscess and tumor: a preliminary report. Neuroradiology 41:171–174
6. Castillo M (1999) Imaging brain abscess with diffusion-weighted and other sequences. AJNR Am J Neuroradiol 20:1193–1194
7. Gray F, Nordmann P (1997) Bacterial infections. In: Graham DI, Lantos PL (eds) Greenfield's neuropathology, vol 2, 6th edn, pp 114–129
8. Falcone S, Post MJD (2000) Encephalitis, cerebritis, and brain abscess: pathophysiology and imaging findings. Neuroimaging Clin North Am 10:333–353
9. Hatta S, Mochizuki H, Kuru Y, et al. (1994) Serial neurological studies in focal cerebritis. Neuroradiology 36:285–288
10. Ketelslegers E, Duprez T, Ghariani S, et al. (2000) Time dependence of serial diffusion-weighted imaging features in a case of pyogenic brain abscess. JCAT 24:478–481
11. Cartes-Zumelzu FW, Stavrou I, Castillo M, Eisenhuber E, Knosp E, Thurnher MM (2004) Diffusion-weighted imaging in the assessment of brain abscesses therapy. AJNR Am J Neuroradiol 25:1310-1317
12. Gupta RK, Hasan KM, Mishra AM, et al. (2005) High fractional anisotropy in brain abscesses versus other cystic intracranial lesions. AJNR Am J Neuroradiol 26:1107-1114
13. Kumar M, Gupta RK, Nath K, Rathore RK, et al. (2008) Can we differentiate true white matter fibers from pseudofibers inside a brain abscess cavity using geometrical diffusion tensor imaging metrics? NMR Biomed 21:581-588
14. Bakshi R, Wright PD, Kinkel PR, et al. (1999) Cranial magnetic resonance imaging findings in bacterial endocarditis: the neuroimaging spectrum of septic brain embolization demonstrated in twelve patients. J Neuroimaging 9:78–84

15. Höllinger P, Zürcher R, Schroth G, et al. (2000) Diffusion magnetic resonance imaging findings in cerebritis and brain abscess in a patient with septic encephalopathy. J Neurol 247:232–234
16. Nagase T, Wada S, Nakamura R, et al. (1995) Magnetic resonance imaging of multiple brain abscesses of bilateral basal ganglia. Intern Med 34:554–558
17. Southwick FS, Purich DL (1996) Intracellular pathogenesis of listeriosis. New Eng J Med 334:770–776
18. Fleetwood IG, Embil JM, Ross IB (2000) Nocardia asteroides cerebral abscess in immunocompetent hosts: report of three cases and review of surgical recommendations. Surg Neurol 53:605-610
19. Shin JH, Lee HK (2003) Nocardial brain abscess in a renal transplant recipient. Clin Imaging 27:321-324
20. Luthra G, Parihar A, Nath K, et al. (2007) Comparative evaluation of fungal, tubercular, and pyogenic brain abscesses with conventional and diffusion MR imaging and proton MR spectroscopy. AJNR Am J Neuroradiol 28:1332-1338
21. Gupta RK, Prakash M, Mishra AM, Husain M, Prasad KN, Husain N (2005) Role of diffusion weighted imaging in differentiation of intracranial tuberculoma and tuberculous abscess from cysticercus granulomas-a report of more than 100 lesions. Eur J Radiol 55:384-392
22. Sadeghi N, Rorive S, Lefranc F (2003) Intracranial tuberculoma: is diffusion-weighted imaging useful in the diagnosis? Eur Radiol 13:2049-2050
23. Holtås S, Geijer B, Strömblad LG, et al. (2000) A ring-enhancing metastasis with central high signal on diffusion-weighted imaging and low apparent diffusion coefficients. Neuroradiology 42:824–827
24. Hartman M, Jansen O, Heiland S, et al. (2001) Restricted diffusion within ring enhancement is not pathognomonic for brain abscess. AJNR Am J Neuroradiol 22:1738–1742
25. Tung GA, Evangelista P, Rogg JM, et al. (2001) Diffusion-weighted MR imaging of rim-enhancing brain masses: is markedly decreased water diffusion specific for brain abscess? AJR Am J Roentgenol 177:709–712
26. Fertikh D, Krejza J, Cunqueiro A, Danish S, Alokaili R, Melhem ER (2007) Discrimination of capsular stage brain abscesses from necrotic or cystic neoplasms using diffusion-weighted magnetic resonance imaging. J Neurosurg 106:76-81
27. Fredman DP, Goldman HW, Flanders AE (1997) MR imaging of stereotaxic palidotomy and thalamotomy. AJR Am J Roentgenol 169:894–896
28. Ackerman LL, Traynelis VC (1999) Dural space infection: cranial subdural empyema and cranial epidural abscess. In: Osenbach RK, Zeidman SM, (eds) Infections in neurological surgery. Philadelphia: Lippincott-Raven, pp 85–99
29. Ramsay DW (2000) Diffusion-weighted imaging of cerebral abscess and subdural empyema. AJNR Am J Neuroradiol 21:1172
30. Rana S, Albayram S, Lin DDM, et al. (2002) Diffusion-weighted imaging and apparent diffusion coefficient maps in a case of intracerebral abscess with ventricular extension. AJNR Am J Neuroradiol 23:109–112
31. Ebisu T, Tanaka C, Umeda M, et al. (1997) Hemorrhagic and nonhemorrhagic stroke: diagnosis with diffusion-weighted and T2-weighted echo-planar MR imaging. Radiology 203:823–828
32. Atlas SW, Dubois P, Singer MB, et al. (2000) Diffusion measurements in intracranial hematomas: implications for MR imaging of acute stroke. AJNR Am J Neuroradiol 21:1190–1194
33. Tsuruda JS, et al. (1990) Diffusion-weighted MR imaging of the brain: value of differentiating between extraaxial cysts and epidermoid tumors. AJNR Am J Neuroradiol 11:925–931
34. Moodley M, Bullock MR (1985) Severe neurological sequelae of childhood bacterial meningitis. S Afr Med J 68:566–570
35. Navia BA, Petito CK, Gold JWM, et al. (1986) Cerebral toxoplasmosis complicating the acquired immune deficiency syndrome: clinical and neurological findings in 27 patients. Ann Neurol 19:224–238
36. Camacho DL, Smith JK, Castillo M (2003) Differentiation of toxoplasmosis and lymphoma in AIDS patients by using apparent diffusion coefficients. AJNR Am J Neuroradiol 24:633-637
37. Chong-Han CH, Cortez SC, Tung GA (2003) Diffusion-weighted MRI of cerebral toxoplasma abscess. AJR Am J Roentgenol 181:1711-1714
38. Schroeder PC, Post MJ, Oschatz E, Stadler A, Bruce-Gregorios J, Thurnher MM (2006) Analysis of the utility of diffusion-weighted MRI and apparent diffusion coefficient values in distinguishing central nervous system toxoplasmosis from lymphoma. Neuroradiology 48:715-720
39. do Amaral LL, Ferreira RM, da Rocha AJ, Ferreira NP (2005) Neurocysticercosis: evaluation with advanced magnetic resonance techniques and atypical forms. Top Magn Reson Imaging 16:127-144
40. DeLone DR, Goldstein RA, Petermann G, et al. (1999) Disseminated aspergillosis involving the brain: distribution and imaging characteristics. AJNR Am J Neuroradiol 20:1597–1604
41. Charlot M, Pialat JB, Obadia N, et al. (2007) Diffusion-weighted imaging in brain aspergillosis. Eur J Neurol 14:912-916
42. Gaviani P, Schwartz RB, Hedley-Whyte ET, et al. (2005) Diffusion-weighted imaging of fungal cerebral infection. AJNR Am J Neuroradiol 26:1115-1121
43. Simmons JH, Zeitler PS, Fenton LZ, Abzug MJ, Fiallo-Scharer RV, Klingensmith GJ (2005) Rhinocerebral mucormycosis complicated by internal carotid artery thrombosis in a pediatric patient with type 1 diabetes mellitus: a case report and review of the literature. Pediatr Diabetes 6:234-238
44. Tung GA, Rogg JM (2003) Diffusion-weighted imaging of cerebritis. AJNR Am J Neuroradiol 24:1110-1113
45. Ho TL, Lee HJ, Lee KW, Chen WL (2005) Diffusion-weighted and conventional magnetic resonance imaging in cerebral cryptococcoma. Acta Radiol 46:411-414

46. Smith JS, Quiñones-Hinojosa A, Phillips JJ, Bollen AW, McDermott MW, Cha S (2006) Limitations of diffusion-weighted imaging in distinguishing between a brain tumor and a central nervous system histoplasmoma. J Neurooncol 79:217-218
47. Sener RN (2001) Herpes simplex encephalitis: diffusion MR imaging findings. Comput Med Imaging Graph 25:391–397
48. Tsuchiya K, Katase S, Yoshino A, et al. (1999) Diffusion-weighted MR imaging of encephalitis. AJR Am J Roentgenol 173:1097–1099
49. Obeid M, Franklin J, Shrestha S, Johnson L, Quattromani F, Hurst D (2007) Diffusion-weighted imaging findings on MRI as the sole radiographic findings in a child with proven herpes simplex encephalitis. Pediatr Radiol 37:1159-1162
50. Küker W, Nägele T, Schmidt F, Heckl S, Herrlinger U (2004) Diffusion-weighted MRI in herpes simplex encephalitis: a report of three cases. Neuroradiology 46:122-125
51. Heiner L, Demaerel P (2003) Diffusion-weighted MR imaging findings in a patient with herpes simplex encephalitis. Eur J Radiol 45:195-198
52. Noguchi T, Mihara F, Yoshiura T, et al. (2006) MR imaging of human herpesvirus-6 encephalopathy after hematopoietic stem cell transplantation in adults. AJNR Am J Neuroradiol 27:2191-2195
53. Gorniak RJ, Young GS, Wiese DE, Marty FM, Schwartz RB (2006) MR imaging of human herpesvirus-6-associated encephalitis in 4 patients with anterograde amnesia after allogeneic hematopoietic stem-cell transplantation. AJNR Am J Neuroradiol 27:887-891
54. Wasenko JJ, Park BJ, Jubelt B, et al. (2002) Magnetic resonance imaging of mesenrhombencephalitis. Clin Imaging 26:237-242
55. Soo MS, Tien RD, Gray L, Andrews PI, Friedman H (1993) Mesenrhombencephalitis: MR findings in nine patients. AJR Am J Roentgenol 160:1089-1093
56. Weidauer S, Ziemann U, Thomalske C, Gaa J, Lanfermann H, Zanella FE (2003) Vasogenic edema in Bickerstaff's brainstem encephalitis: a serial MRI study. Neurology 61:836-838
57. Ali M, Safriel Y, Sohi J, Llave A, Weathers S (2005) West Nile virus infection: MR imaging findings in the nervous system. AJNR Am J Neuroradiol 26:289-297
58. Petropoulou KA, Gordon SM, Prayson RA, Ruggierri PM (2005) West Nile virus meningoencephalitis: MR imaging findings. AJNR Am J Neuroradiol 26:1986-1995
59. Kraushaar G, Patel R, Stoneham GW (2005) West Nile Virus: a case report with flaccid paralysis and cervical spinal cord: MR imaging findings. AJNR Am J Neuroradiol 26:26-29
60. Zak IT, Altinok D, Merline JR, Chander S, Kish KK (2005) West Nile virus infection. AJR Am J Roentgenol 184:957-961
61. Rosas H, Wippold FJ 2nd. (2003) West Nile virus: case report with MR imaging findings. AJNR Am J Neuroradiol 24:1376-1378
62. Cordoliani YS, Sarrazin JL, Felten D, Caumes E, Lévêque C, Fisch A (1998) MR of cerebral malaria. AJNR Am J Neuroradiol 19:871-874
63. Patankar TF, Karnad DR, Shetty PG, Desai AP, Prasad SR (2002) Adult cerebral malaria: prognostic importance of imaging findings and correlation with postmortem findings. Radiology 224:811-816
64. Sakai O, Barest GD (2005) Diffusion-weighted imaging of cerebral malaria. J Neuroimaging. 15:278-280
65. Flowers CH, Mafee MF, Crowell R, et al. (1990) Encephalopathy in AIDS patients: evaluation with MR imaging. AJNR Am J Neuroradiol 11:1235–1245
66. Connor MD, Lammie GA, Bell JE, et al. (2000) Cerebral infarction in adult AIDS patients: observations from the Edinburgh HIV autopsy cohort. Stroke 31:2117–2126
67. Meltzer CC, Wells SW, Becher MW, et al. (1998) AIDS-related MR hyperintensity of the basal ganglia. AJNR Am J Neuroradiol 19:83–89

Trauma

12.1 Introduction

Head injuries are the most common cause of death and permanent disability in the early decades of life. They vary widely in their etiology, pathophysiology, clinical presentation, and optimal treatment strategies. Traumatic brain injuries are classified in two main categories: focal and diffuse brain injuries [1]. Focal brain injuries usually result from direct impact force to the head, like cerebral contusions and epidural hematomas. Diffuse brain injuries are caused by sudden changes in movement of the head, usually rotational accelerations, which result in a variety of injuries, ranging from a brief cerebral concussion to extensive diffuse axonal injuries (DAI).

Computed tomography (CT) is imperative in patients with focal and diffuse injuries, especially when hemodynamically or neurologically unstable [2]. However, CT is often false negative or underestimates contusions shortly after trauma, and DAIs are often not detected. Conventional MR imaging has higher detection sensitivity with regard to these lesions because of its greater sensitivity for edema [3].

Once it was thought that edema following traumatic brain injury was vasogenic, but recent experimental studies using diffusion-weighted (DW) imaging have shown that edema after head trauma consists of both vasogenic and cytotoxic edema [4–9]. Since DW imaging is also very sensitive in detecting small lesions of cytotoxic edema and can differentiate cytotoxic from vasogenic edema, it has become especially useful in the evaluation and staging of patients with DAI.

12.2 Diffuse Axonal Injury

Diffuse axonal injury (traumatic axonal injury) results from a diffuse shearing-strain deformation causing change in shape of brain tissue from unequal movement of adjacent tissues that differ in density and rigidity [1]. Patients with DAI, more often than with other types of primary brain injuries show severe impairment of consciousness at impact.

Pathologically, injury related to DAI is always more extensive microscopically than at gross examination [10]. Microscopically, shearing injuries initially produce multiple, characteristic axonal bulbs, or retraction balls, as well as numerous foci of perivascular hemorrhages.

The origin behind cytotoxic edema in DAI seems to be related to an excitotoxic mechanism, in particular glutamate [1, 11, 12]. Damage at the node of Ranvier will result in a traumatic defect in the axonal membrane (Fig. 12.1). This defect causes excessive

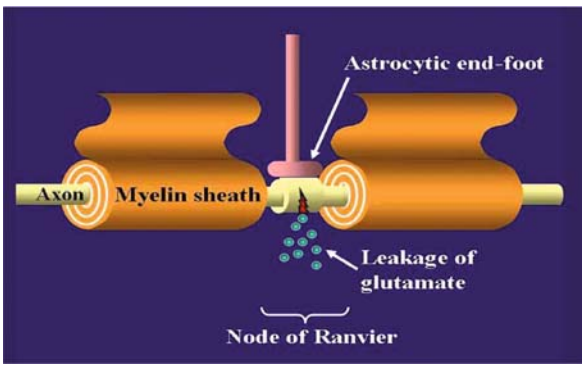

Figure 12.1
Leakage of glutamate in diffuse axonal injury. Diffuse axonal injury is presumably due to the leakage of glutamate at the node of Ranvier. The astrocytic end-foot is located on the axon at the node of Ranvier and may protect the axons. (From [40])

neurotransmitter release with increase in intracellular calcium ions, as in brain ischemia, which leads to axonal and glial cell swelling (cytotoxic or neurotoxic edema). These changes can eventually lead to axonal degeneration or necrosis with microglial and astrocytic reactive changes. Accumulation of hemosiderin-laden macrophages is also seen in the chronic phase.

12.2.1 Location

Common locations of DAI are at the gray–white matter junctions (Fig. 12.2), in the corpus callosum (Fig. 12.3) and at the dorsolateral aspect of the upper brain stem (Fig. 12.4). DAI may be confined to the white matter of the frontal and temporal lobes in mild head trauma [13]. With more severe rotational acceleration, lesions are also seen in the lobar white matter as well as in the posterior half of the corpus callosum. In cases with even greater trauma, lesions will also be found in the anterior corpus callosum, and the dorsolateral aspects of the midbrain and upper pons. Occasionally, DAI lesions occur in the parietal and occipital lobes, internal and external capsules (Fig. 12.3), basal ganglia (Fig. 12.5), thalamus (Fig. 12.3), fornix (Fig. 12.6), septum pellucidum, and cerebellum (Fig. 12.7). Intraventricular hemorrhage can accompany these findings. They have the same mechanical origin and are due to disruption of the subependymal plexus of capillaries and veins that lie along the ventricular surface of the corpus callosum, fornix, and septum pellucidum [14].

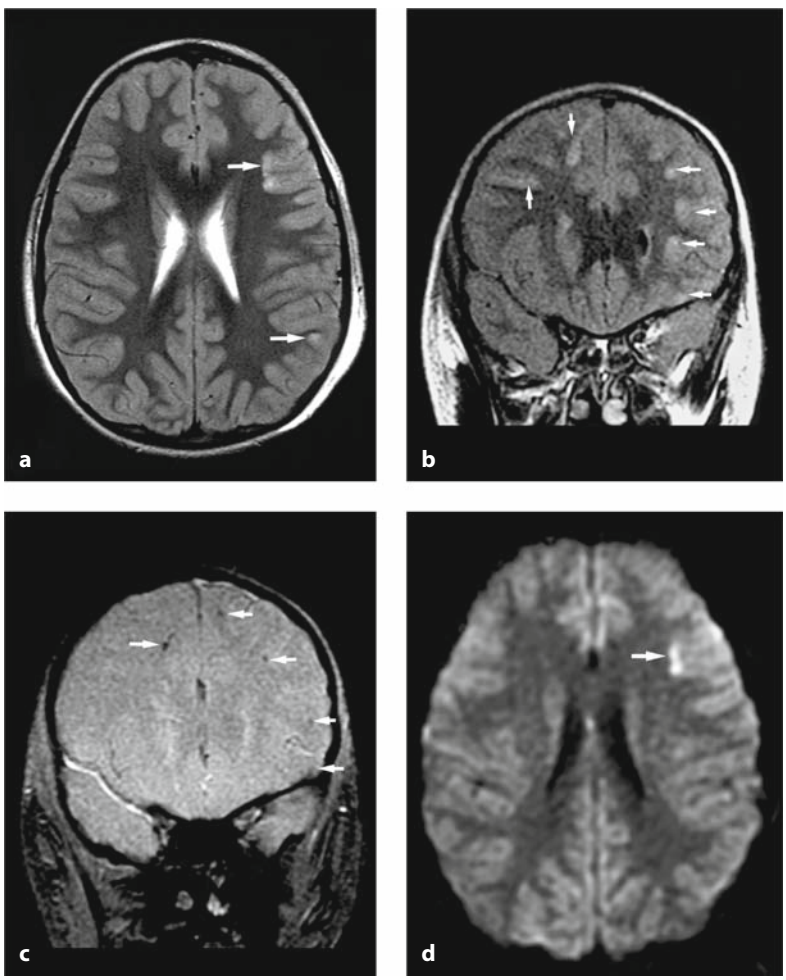

Figure 12.2 a–d

Diffuse axonal injury in gray–white matter junction in a 7-year-old boy after a motor vehicle accident. **a, b** T2-weighted and coronal FLAIR images show multiple hyperintense lesions in the gray–white matter junction of bilateral frontoparietal lobes (*arrows*). **c** Coronal GRE image shows multiple small hemorrhages as low signal in these lesions (*arrows*). **d** DW image demonstrates diffuse axonal injury as high signal intensity (*arrow*) with decreased ADC (not shown), representing cytotoxic edema

Figure 12.3 a–d

Diffuse axonal injury in the corpus callosum, internal capsule and thalamus in a 29-year-old woman after a motor vehicle accident. **a, b** T2-weighted and FLAIR images show multiple hyperintense lesions in the anterior and posterior corpus callosum, internal capsules and left thalamus (*arrows*). **c, d** DW image demonstrates these lesions as high signal intensity with decreased ADC (*arrows*)

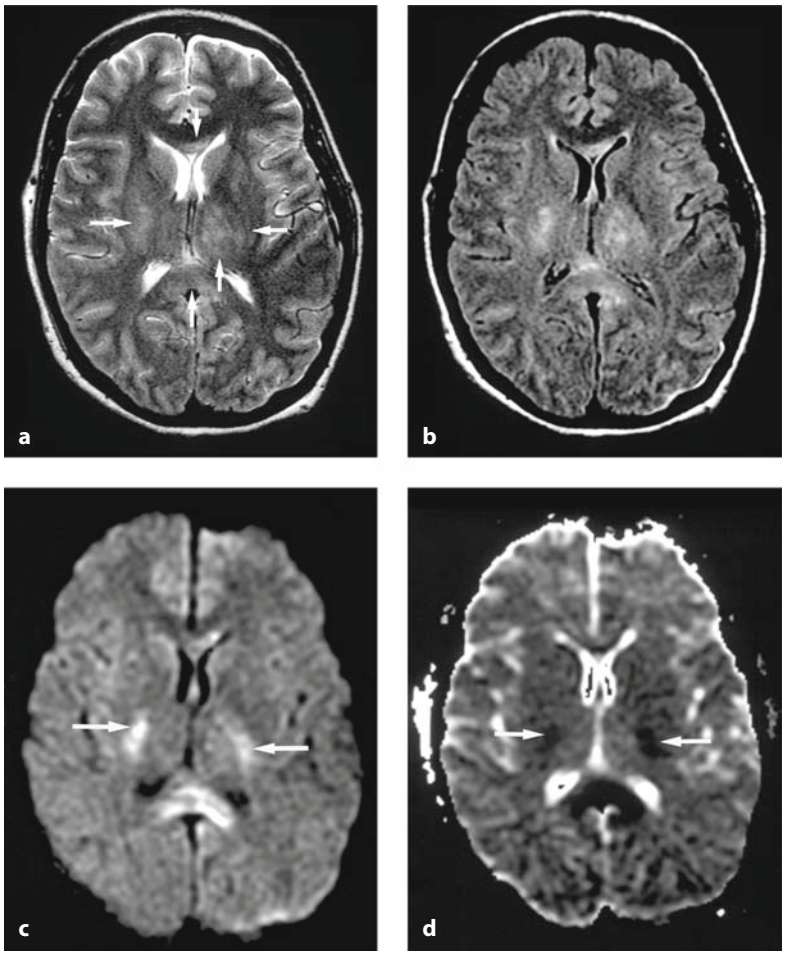

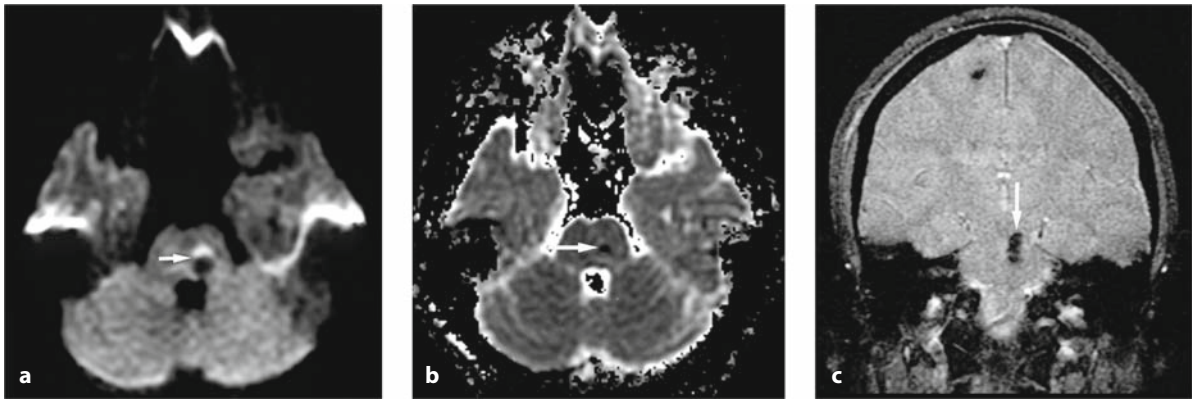

Figure 12.4 a–c

Diffuse axonal injury in the brain stem in a 28-year-old man after a motor vehicle accident. **a** DW image shows a hypointense lesion with a hyperintense rim in the dorsolateral aspect of the midbrain, representing a hemorrhagic lesion of diffuse axonal injury (*arrow*). **b** ADC map shows decreased ADC of this lesion (*arrow*). This might be due to a paramagnetic susceptibility artifact. **c** Coronal GRE image clearly shows hemorrhagic lesions as hypointense in the brain stem (*arrow*) and in the right frontoparietal region

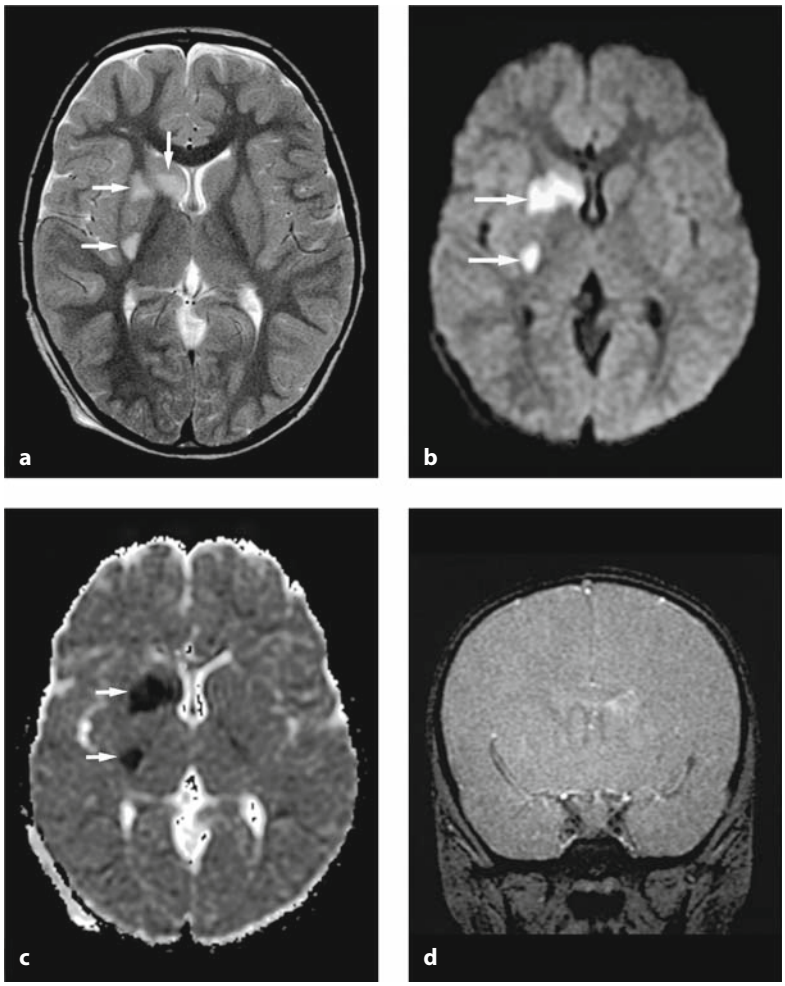

Figure 12.5 a–d

Diffuse axonal injury in the basal ganglia in a 3-year-old boy after a motor vehicle accident. **a** T2-weighted image shows hyperintense lesions in the right lentiform and caudate nucleus (*arrows*). **b, c** DW imaging shows these lesions as hyperintense with decreased ADC (*arrows*). **d** Coronal GRE image clearly shows no hemorrhagic foci in these lesions

12.2.2 Computed Tomography and MR Imaging

Few DAI lesions are visible with CT. Only large lesions or those that are grossly hemorrhagic are seen. MR imaging has been proven to be more sensitive for detection as well as for characterization of DAI lesions [2]. Conventional MR imaging shows multiple, small, deeply situated elliptical lesions that spare the overlying cortex. Fluid-attenuated inversion-recovery (FLAIR) images are more sensitive than T2-weighted images to detect small hyperintense lesions adjacent to the cerebrospinal fluid, such as in the fornix and septum pellucidum [15]. These lesions are, moreover, often accompanied by small, petechial hemorrhages. They occur in 10–30% of all DAI lesions [16] and are best appreciated on T2*-weighted gradient-echo (GRE) images because of their susceptibility effects [17]. However, even these MR imaging sequences are thought to underestimate the true extent of DAI.

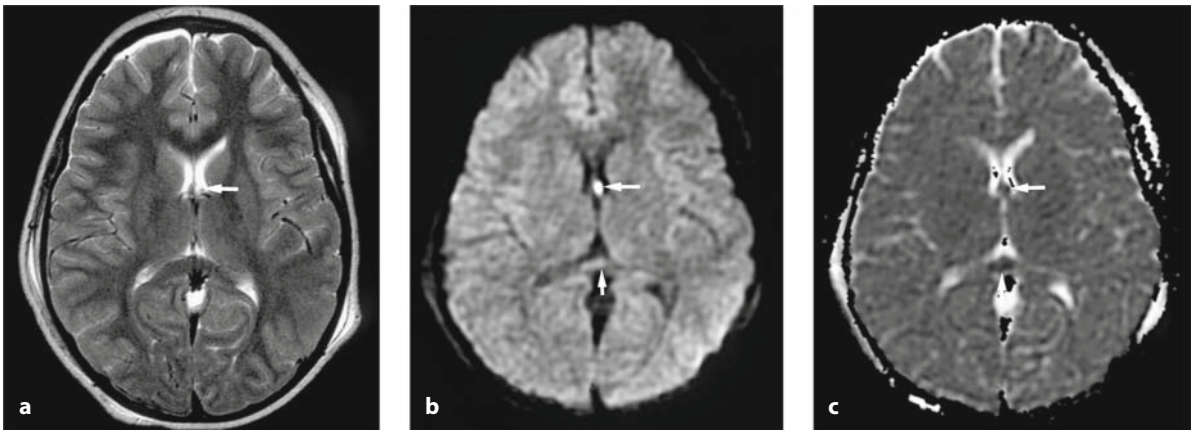

Figure 12.6 a–c

Diffuse axonal injury in the fornix of an 11-year-old girl after a motor vehicle accident. **a** On T2-weighted image, it is difficult to detect a small hyperintense lesion in the fornix (*arrow*). **b, c** DW image shows the lesion in the fornix and posterior corpus callosum as hyperintense with decreased ADC (*arrows*)

12.2.3 Diffusion-Weighted Imaging

Diffusion-weighted imaging measures a unique physiologic parameter, movement of water in the tissue, which allows for identification of DAI lesions that may not be visible on T2/FLAIR or T2*-weighted GRE images [18]. DAI lesions on DW imaging are hyperintense and associated with decreased apparent diffusion coefficient (ADC) [19–24]. The precise mechanisms underlying the diffusion changes associated with DAI are unknown. Cytotoxic edema, which seems to be the cause of reduced ADC in ischemic brain injury, can also occur in the early phase of DAI. However, reduced ADC is presumably due to the development of retraction balls and concomitant cytoskeletal collapse along the severed axons [22]. The time course of the ADC abnormality seems to be different from that of ischemic brain injury. Prolonged decrease in ADC, over 2 weeks, has occasionally been observed in DAI [19], and cytotoxic edema in the corpus callosum can be partially reversible on follow-up imaging using T2-weighted sequences [23]. Axonal and glial cell swelling in DAI is thought to be mainly due to excitotoxic mechanisms that essentially propagates through the white matter tracts. It can also be a slower or reversible form of cellular swelling than that seen in ischemic brain injuries [6]. Hemorrhagic components, which often accompany these brain injuries, will affect the signal intensity on DW images. Volume and number of lesions on DW images reportedly correlate with the prognosis [25].

12.2.4 Diffusion-Tensor Imaging

Diffusion-tensor (DT) imaging measures the translation of extracellular water in the white matter tracts by directional evaluation of the water diffusivity (diffusion anisotropy) [26]. Fractional anisotropy (FA), a parameter derived from DT imaging computations, is sensitive for detection of the extracellular edema in the white matter tracts. FA and fiber tracking possibly access the fiber connectivity [27, 28]. DT imaging can show two different pattern of the early phase of DAI:

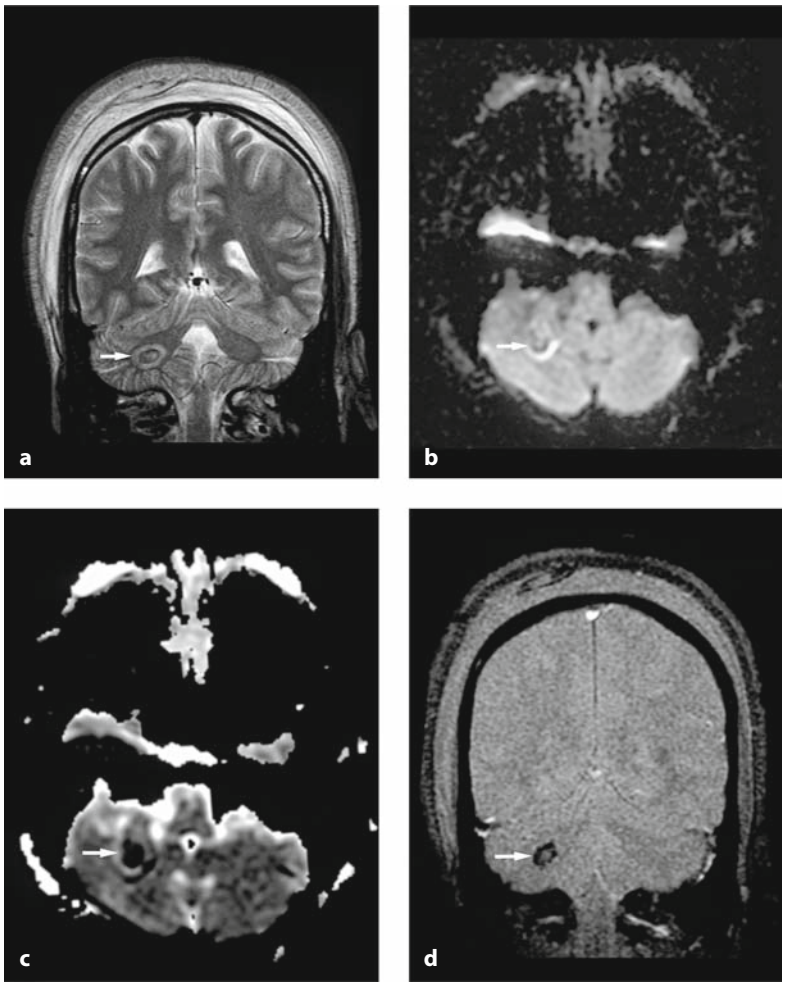

Figure 12.7 a–d

Diffuse axonal injury in the cerebellum of an 18-year-old male patient after a motor vehicle accident. **a** T2-weighted image shows a hypo- intense lesion in the right middle cerebellar peduncle (*arrow*). **b** DW image shows a hypointense lesion with a hyperintense rim, representing a hemorrhagic lesion (*arrow*). **c** ADC map reveals decreased ADC in this lesion (*arrow*). This may be due to a paramagnetic susceptibility artifact. **d** Coronal GRE image clearly demonstrates hemorrhagic lesions as hypointense (*arrow*)

(1) decreased FA with decreased or isointense ADC which represents mixed intra- and extracellular edema and broken fibers, and (2) normal FA with decreased ADC which represents pure cytotoxic edema and presumably preserved fiber connectivity (Fig. 12.8). In the late phase of DAI, decreased FA and increased ADC are observed. DT imaging is thought to be useful in the early detection of DAI and a prognostic measure of subsequent brain damage [29].

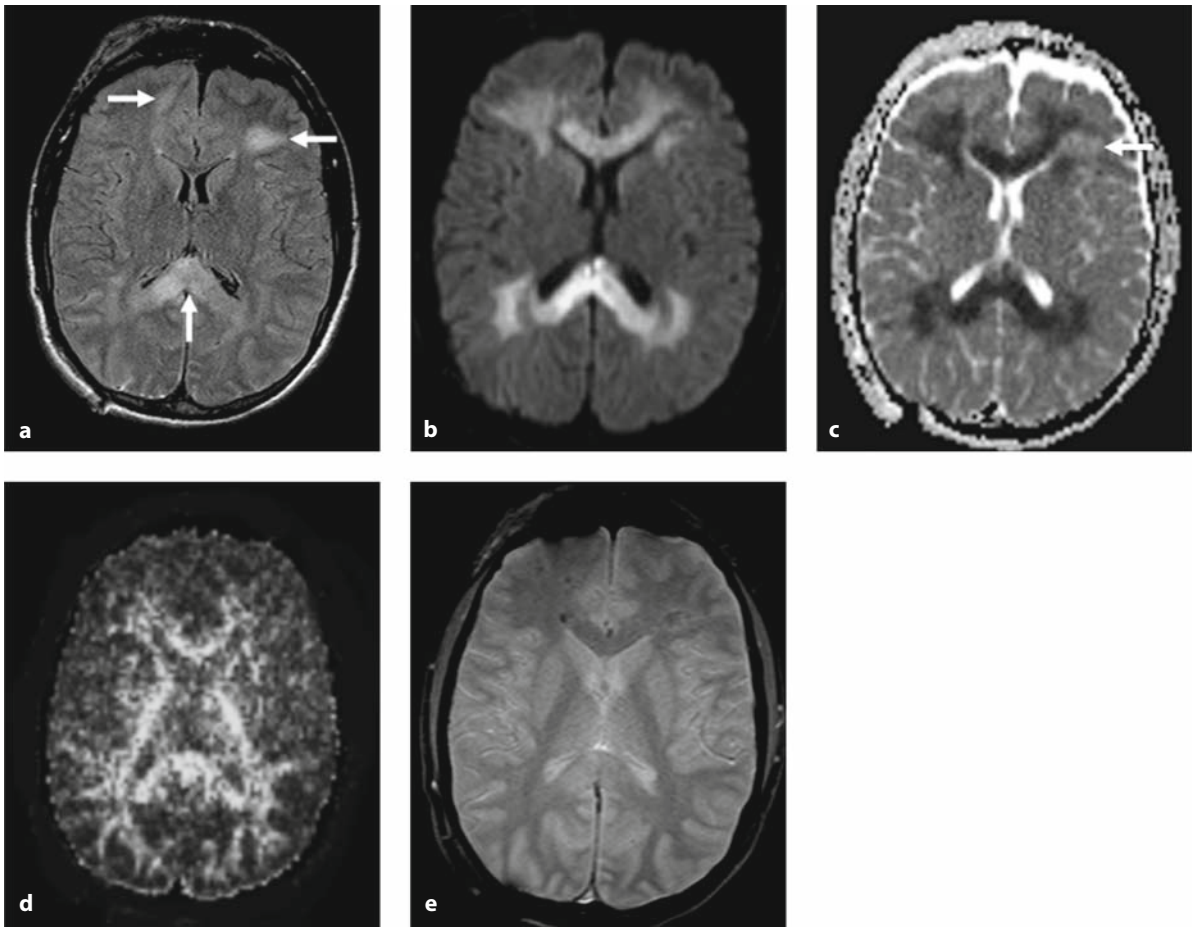

Figure 12.8 a–e

Diffuse axonal injury in a 24-year-old man after a motor vehicle accident. **a** FLAIR image shows multiple asymmetric hyperintense lesions in the bilateral frontal white matter and the corpus callosum (*arrows*). **b** DW image shows diffuse hyperintense lesion in the deep white matter and the corpus callosum. **c** ADC map reveals decreased ADC in the deep white matter and the corpus callosum. The left frontal lesion seen on FLAIR image has iso- to slightly increased ADC (*arrow*). **d** FA is preserved in most of the diffuse white matter abnormalities suggestive of a pure cytotoxic edema. Decreased FAs are observed in the lesions in the bilateral frontal white matter and splenium of the corpus callosum seen on the FLAIR image. **e** GRE image demonstrates hemorrhagic foci in the frontal white matter

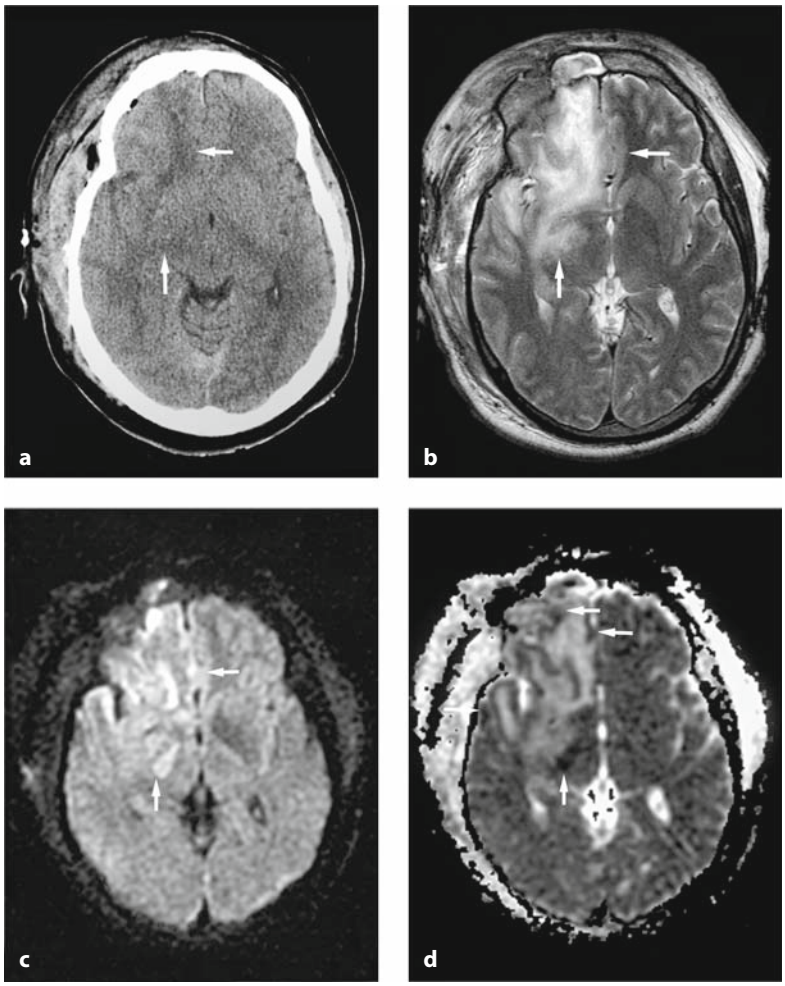

Figure 12.9 a–d

Brain contusion in the frontal lobe in a 37-year-old man after a motor vehicle accident. **a** On CT obtained after evacuation of epidural hematoma, it is difficult to delineate the extent of a mass lesion in the right frontal lobe (*arrows*). **b** T2-weighted image delineates the extent of the edematous brain contusion (*arrows*). **c** DW image shows heterogeneous signal intensity in these lesions, representing mixed vasogenic and cytotoxic edema with hemorrhagic necrotic tissues (*arrows*). **d** ADC map reveals mixed increase and relative decrease of ADC (*arrows*) in these lesions

12.3 Brain Contusion

Brain contusions are defined as traumatic injuries to the cortical surface of the brain [1]. They are caused by direct contact between the skull and the brain parenchyma. Compared with DAI, contusions tend to be larger, more superficial, more ill defined and more likely to contain areas of hemorrhage. Cytotoxic edema in brain contusions is also related to excitotoxic mechanisms [30].

12.3.1 Location

Common locations of brain contusions are in the temporal and frontal lobes, especially along their anterior, lateral, and inferior surfaces (Fig. 12.9). The parietal occipital lobes, hippocampus (Fig. 12.10), cerebellar hemisphere, vermis and cerebellar tonsils (Fig. 12.11) are less frequently involved [2].

12.3.2 Computed Tomography and MR Imaging

Contusions are often difficult to identify on CT obtained shortly after trauma unless they are large or contain areas of hemorrhage [2]. Initial CT will often show only faint areas of low attenuation, sometimes mixed with a few tiny areas of petechial hemorrhage. MR imaging is considerably more sensitive than CT for early detection and evaluation of their extent.

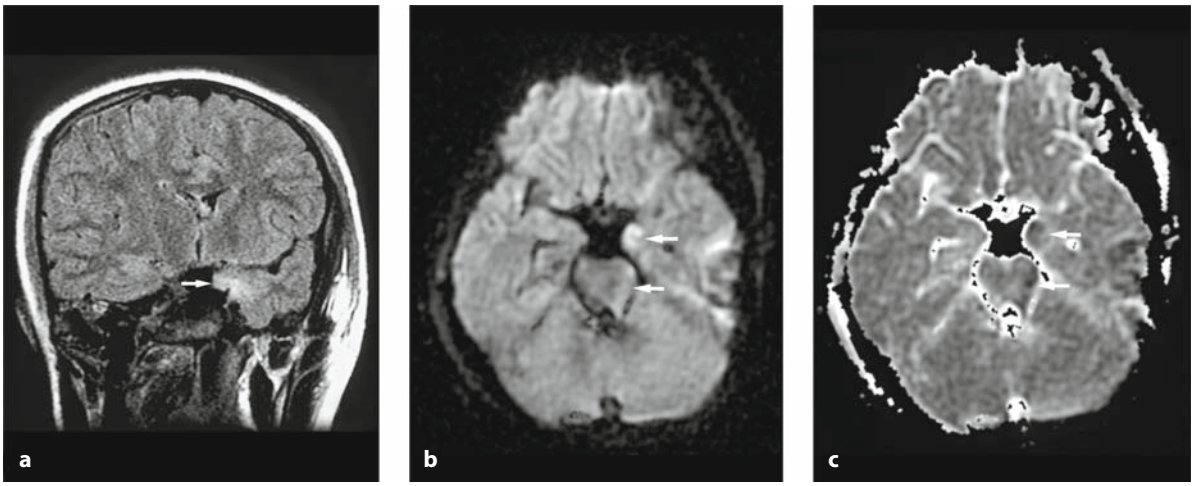

Figure 12.10 a–c

Brain contusion in the hippocampus in an 11-year-old girl after a motor vehicle accident. **a** FLAIR image shows a hyperintense lesion in the left hippocampus (*arrow*). **b** DW image shows this lesion as hyperintense. **c** ADC is decreased in the left hippocampus and left side of the brain stem (*arrows*), representing mainly cytotoxic edema

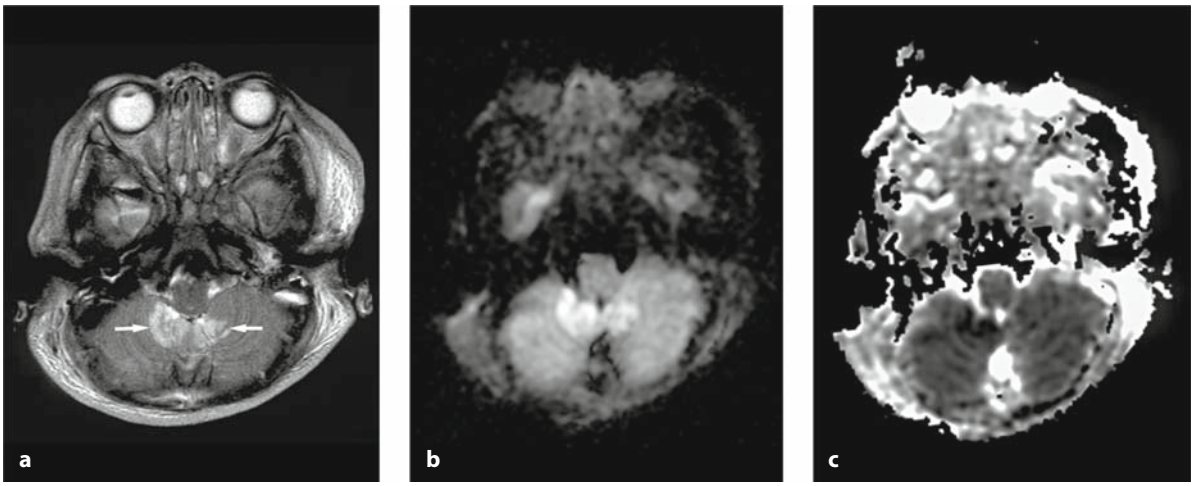

Figure 12.11 a–c

Brain contusion in the cerebellar tonsil in an 11-year-old girl after a motor vehicle accident. **a** T2-weighted image shows hyperintense lesions in the cerebellar tonsils (*arrows*). **b** DW image shows this lesion as hyperintense. **c** ADC is partially decreased

12.3.3 Diffusion-Weighted Imaging Findings

Brain contusions are sometimes associated with a non-hemorrhagic mass effect, which progresses rapidly after the trauma. Edema in brain contusions is heterogeneous, composed of cytotoxic and vasogenic edema [31], which can be demonstrated by DW imaging. Kawamata et al. reported a specific DW imaging finding of brain contusions [32, 33]. On DW imaging, the contusion is shown as a low intensity core, with increased ADC, surrounded by a rim of a high intensity, with decreased ADC. This suggests that intra- and extracellular components undergo disintegration and homogenization within the central area, whereas cellular swelling is predominant in the peripheral area.

12.4 Hemorrhage Related to Trauma

Traumatic hemorrhages result from injury to a cerebral vessel (artery, vein or capillary) [2]. Subdural hematomas originate from disruption of the bridging cortical veins, which are vulnerable to rapid stretching. Epidural hematoma can have either an arterial or a venous sinus origin, typically associated with a skull fracture. Traumatic intracerebral hematomas result from a shear-strain injury involving arteries, veins or capillaries. Traumatic subarachnoid hemorrhage is usually seen after severe head trauma and may as such accompany brain contusion or DAI. Hemorrhages can also represent a disruption of intracranial arteries, especially arteries of the vertebrobasilar system.

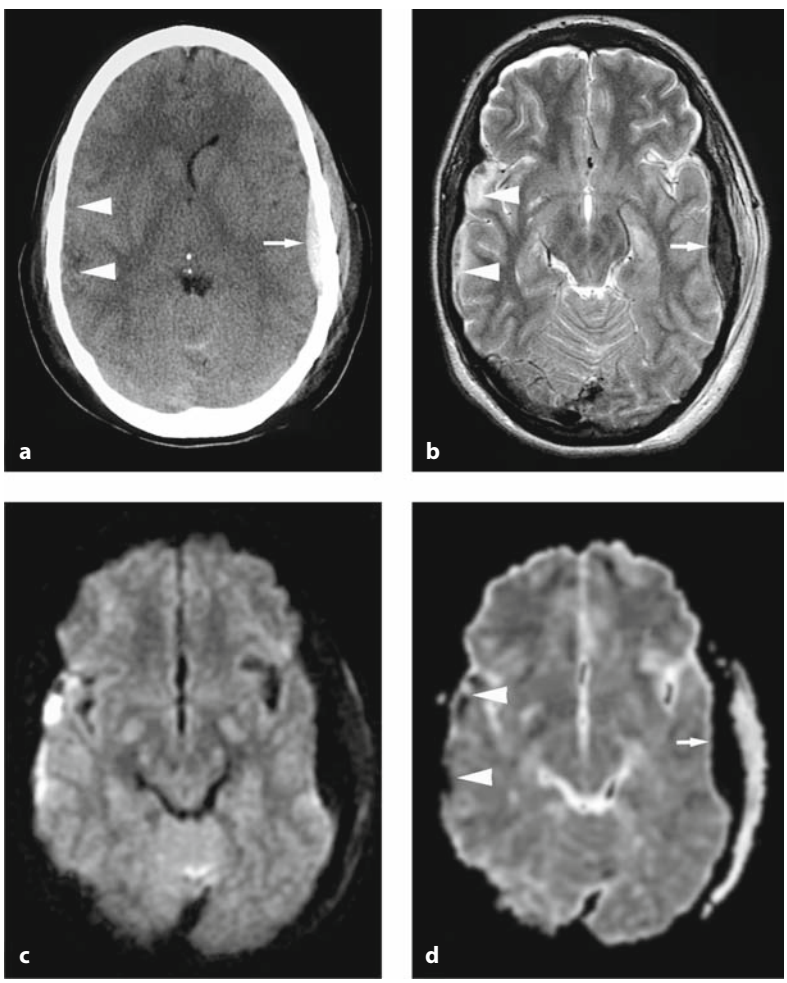

Figure 12.12 a–d

Epidural and subdural hematoma in a 26-year-old man after a motor vehicle accident. **a** CT shows a left epidural hematoma (*arrow*) but it is difficult to depict the isodense small subdural hematoma in the right side (*arrowheads*). **b** T2-weighted image shows the left epidural hematoma (*arrow*) as a hypointense lesion and the right subdural hematoma as partially hypointense lesions (*arrowheads*). **c** DW image shows the epidural hematoma as very hypointense due to deoxy-hemoglobin, and the subdural hematoma as very hyperintense presumably due to high viscosity or hypercellularity of hematoma. **d** ADC map shows hypointensity due to loss of pixels with background masking in the left epidural hematoma (*arrow*). ADC map also shows decreased ADC in the right subdural hematoma (*arrowheads*)

12.4.1 Computed Tomography and MR Imaging

Computed tomography is the modality of choice for the initial evaluation of traumatic brain hemorrhages, as it is a fast examination technique, is widely available, has no contraindications and relatively accurately depicts most hematomas that need immediate intervention [2].

Magnetic resonance imaging is usually not the primary imaging technique and findings will then depend on the stage of degradation of the hemoglobin at the time of examination. However, in most instances MR imaging is extremely helpful to detect hematomas, especially along the vertex and skull base, and can in certain questionable cases differentiate between subdural and epidural hematomas [2]. T2*-weighted GRE and FLAIR images seem to be more sensitive to detect hemorrhage than conventional spin-echo imaging [34–37].

12.4.2 Diffusion-Weighted Imaging

Diffusion-weighted imaging findings of subdural and epidural hematomas have not been well described in the literature. Depending on the age of the hematoma, DW imaging will vary in signal intensity (Fig. 12.12). Gradient-echo sequences are better in detecting hematomas, including subdural and epidural hematomas, than DW imaging [38]. Although often difficult to detect [38, 39], DW imaging can occasionally depict a subarachnoid hemorrhage as a hyperintense signal (Fig. 12.13). The benefit of DW imaging is probably for

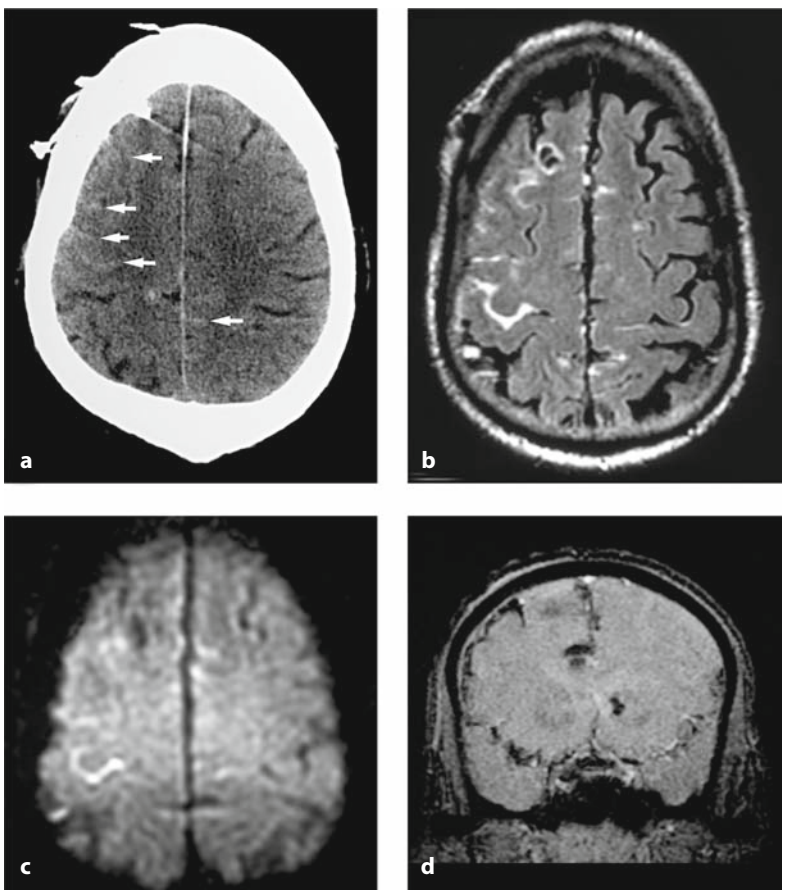

Figure 12.13 a–d

Subarachnoid hemorrhage in a 68-year-old man with ruptured aneurysm of the right middle cerebral artery bifurcation. **a** Postoperative CT shows subtle high density of subarachnoid space in the right frontoparietal area (arrows). **b** FLAIR image shows subarachnoid hemorrhage as hyperintensity. **c** DW image also shows subarachnoid hemorrhage as hyperintensity with mildly increased ADC (not shown). **d** Coronal GRE shows the hemorrhage as low signal intensity

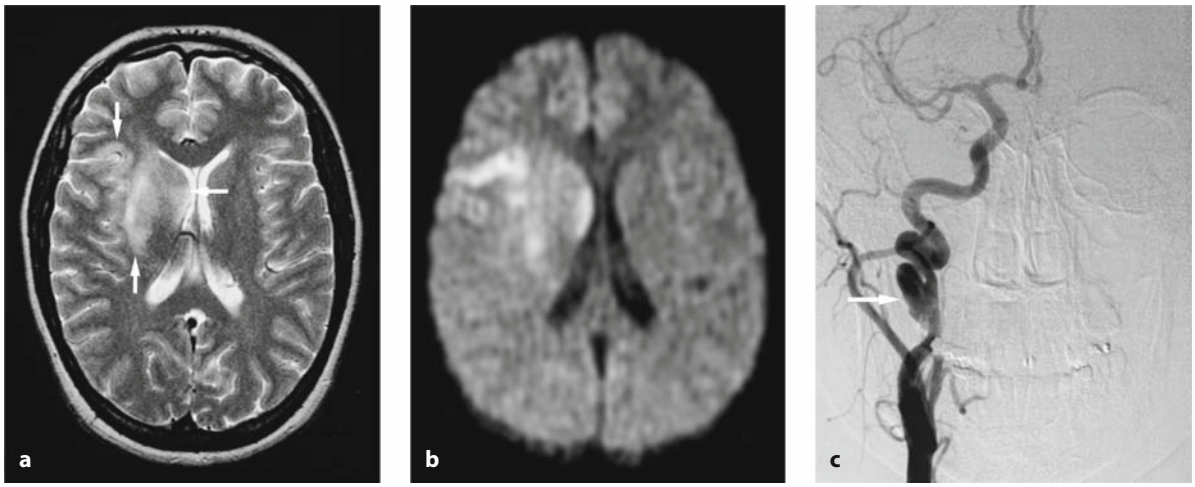

Figure 12.14 a–c

Cerebral infarction after carotid artery dissection with pseudoaneurysm in a 20-year-old female patient after a motor vehicle accident. **a** T2-weighted image shows hyperintense lesions in the right middle cerebral artery territory including the right basal ganglia (arrows). **b** DW image also shows these lesions as hyperintense with decreased ADC (not shown), representing acute infarction. **c** Conventional angiogram shows pseudoaneurysm of the right carotid artery (*arrow*)

the detection of underlying or associated parenchymal lesions. For example, subarachnoid hemorrhage will often cause vasospasm of the intracranial arteries, which can result in brain ischemia. Mass effect secondary to subdural or epidural hematomas, which is closely related to morbidity and mortality, is due to a combination of the hematoma, underlying parenchymal edema and diffuse cerebral swelling.

12.5 Vascular Injuries

Traumatic arterial and venous injuries (dissections, lacerations, occlusions, pseudoaneurysm, arteriovenous fistulas) are more prevalent than generally believed [2]. Many asymptomatic lesions probably escape detection, and others are recognized several days to months after the injury (Fig. 12.14). CT is useful to detect skull base fractures and CT angiography may help to evaluate the vascular injuries. However, a combination of MR imaging and MR angiography is probably the most efficacious way to screen high-risk patients for traumatic vascular injuries, especially if combined with DW imaging, which is very sensitive to detect small and early ischemic lesions secondary to traumatic vascular injuries. Still, one has to acknowledge that conventional angiography continues to be the gold standard in the evaluation of known or suspected traumatic arterial lesions.

References

1. Gennarelli TA (1993) Mechanisms of brain injury. J Emerg Med 11 Suppl 1:5–11
2. Gentry LR (1994) Imaging of closed head injury. Radiology 191:1–17
3. Kelly AB, Zimmerman RD, Snow RB, Gandy SE, Heier LA, Deck MD (1988) Head trauma: comparison of MR and CT-experience in 100 patients. AJNR Am J Neuroradiol 9:699–708
4. Alsop DC, Murai H, Detre JA, McIntosh TK, Smith DH (1996) Detection of acute pathologic changes following experimental traumatic brain injury using diffusion-weighted magnetic resonance imaging. J Neurotrauma 13:515–521
5. Hanstock CC, Faden AI, Bendall MR, Vink R (1994) Diffusion-weighted characterization, edema, diffusion aging differentiates ischemic tissue from traumatized tissue. Stroke 25:843–848
6. Barzo P, Marmarou A, Fatouros P, Hayasaki K, Corwin F (1997) Contribution of vasogenic and cellular edema to traumatic brain swelling measured by diffusion-weighted imaging. J Neurosurg 87:900–907
7. Ito J, Marmarou A, Barzo P, Fatouros P, Corwin F (1996) Characterization of edema by diffusion-weighted imaging in experimental traumatic brain injury. J Neurosurg 84:97–103

8. Albensi BC, Knoblach SM, Chew BG, O'Reilly MP, Faden AI, Pekar JJ (2000) Diffusion and high resolution MRI of traumatic brain injury in rats: time course and correlation with histology. Exp Neurol 162:61–72
9. Assaf Y, Beit-Yannai E, Shohami E, Berman E, Cohen Y (1997) Diffusion- and T2-weighted MRI of closed-head injury in rats: a time course study and correlation with histology. Magn Reson Imaging 15:77–85
10. Gennarelli TA, Graham DI (1998) Neuropathology of the head injuries. Semin Clin Neuropsychiatry 3:160–175
11. Faden AI, Demediuk P, Panter SS, Vink R (1989) The role of excitatory amino acids and NMDA receptors in traumatic brain injury. Science 244:798–800
12. Katayama Y, Becker DP, Tamura T, Ikezaki K (1990) Cellular swelling during cerebral ischaemia demonstrated by microdialysis in vivo: preliminary data indicating the role of excitatory amino acids. Acta Neurochir Suppl (Wien) 51:183–185
13. Mittl RL, Grossman RI, Hiehle JF, Hurst RW, Kauder DR, Gennarelli TA, Alburger GW (1994) Prevalence of MR evidence of diffuse axonal injury in patients with mild head injury and normal head CT findings. AJNR Am J Neuroradiol 15:1583–1589
14. Gentry LR, Thompson B, Godersky JC (1988) Trauma to the corpus callosum: MR features. Am J Neuroradiol 9:1129– 1138
15. Ashikaga R, Araki Y, Ishida O (1997) MRI of head injury using FLAIR. Neuroradiology 39:239–242
16. Yanagawa Y, Tsushima Y, Tokumaru A, Un-no Y, Sakamoto T, Okada Y, Nawashiro H, Shima K (2000) A quantitative analysis of head injury using T2*-weighted gradient-echo imaging. J Trauma 49:272–277
17. Huisman TA, Sorensen AG, Hergan K, Gonzalez RG, Schaefer PW (2003) Diffusion-weighted imaging for the evaluation of diffuse axonal injury in closed head injury. J Comput Assist Tomo 27:5–11
18. Kinoshita T, Moritani T, Hiwatashi A, et al. (2005) Conspicuity of diffuse axonal injury lesions on diffusion-weighted MR imaging. Eur J Radiol 56:5-11
19. Liu AY, Maldjian JA, Bagley LJ, Sinson GP, et al. (1999) Traumatic brain injury: diffusion-weighted MR imaging findings. AJNR Am J Neuroradiol 20:1636–1641
20. Rugg-Gunn FJ, Symms MR, Barker GJ, Greenwood R, Duncan JS (2001) Diffusion imaging shows abnormalities after blunt head trauma when conventional magnetic resonance imaging is normal. J Neurol Neurosurg Psychiatry 70:530–533
21. Hergan K, Schaefer PW, Sorensen AG, Gonzalez RG, Huisman TA (2002) Diffusion-weighted MRI in diffuse axonal injury of the brain. Eur Radiol 12:2536–2541
22. Arfanakis K, Haughton VM, Carew JD, Rogers BP, Dempsey RJ, Meyerand ME (2002) Diffusion tensor MR imaging in diffuse axonal injury. AJNR Am J Neuroradiol 23:794–802
23. Takayama H, Kobayashi M, Sugishita M, Mihara B (2000) Diffusion-weighted imaging demonstrates transient cytotoxic edema involving the corpus callosum in a patient with diffuse brain injury. Clin Neurol Neurosurg 102:135–139
25. Schaefer PW, Huisman TA, Sorensen AG, Gonzalez RG, Schwamm LH (2004) Diffusion-weighted MR imaging in closed head injury: high correlation with initial Glasgow coma scale score and score on modified Rankin scale at discharge. Radiology 233:58-66
26. Basser PJ, Pierpaoli C (1996) Microstructural and physiological features of tissues elucidated by quantitative-diffusion-tensor MRI. J Magn Reson 111:209-219
27. Ducreux D, Huynh I, Fillard P, et al. (2005) Brain MR diffusion tensor imaging and fibre tracking to differentiate between two diffuse axonal injuries. Neuroradiology 47:604-608
28. Naganawa S, Sato C, Ishihra S, et al. (2004) Serial evaluation of diffusion tensor brain fiber tracking in a patient with severe diffuse axonal injury. AJNR Am J Neuroradiol 25:1553-1556
29. Inglese M, Makani S, Johnson G, et al. (2005) Diffuse axonal injury in mild traumatic brain injury: a diffusion tensor imaging study. J Neurosurg 103:298-303
30. Maeda T, Katayama Y, Kawamata T, Yamamoto T (1998) Mechanisms of excitatory amino acid release in contused brain tissue: effects of hypothermia and in situ administration of CO2+ on extracellular levels of glutamate. J Neurotrauma 15:655–664
31. Umeda M, Yamaki T, Tanaka C, et al. (1996) Analysis of brain edema in experimental cerebral contusion using diffusion weighted MRI and ADC value. Neurotraumatology 19:79–83
32. Kawamata T, Katayama Y, Mori T, Aoyama N, Tsubokawa T (2002) Mechanisms of the mass effect of cerebral contusion: ICP monitoring and diffusion MRI study. Acta Neurochir Suppl 81:281–283
33. Kawamata T, Katayama Y, Aoyama N, Mori T (2000) Heterogeneous mechanisms of early edema formation in cerebral contusion: diffusion MRI and ADC mapping study. Acta Neurochir Suppl 76:9–12
34. Melhem ER, Jara H, Eustace S (1997) Fluid-attenuated inversion recovery MR imaging: identification of protein concentration thresholds for CSF hyperintensity. Am J Roentgenol 169:859–862
35. Singer MB, Atlas SW, Drayer BP (1998) Subarachnoid space disease: diagnosis with fluid-attenuated inversion-recovery MR imaging and comparison with gadolinium-enhanced spin-echo MR imaging–blinded reader study. Radiology 208:417–422
36. Dechambre SD, Duprez T, Grandin CB, Lecouvet FE, Peeters A, Cosnard G (2000) High signal in cerebrospinal fluid mimicking subarachnoid haemorrhage on FLAIR following acute stroke and intravenous contrast medium. Neuroradiology 42:608–611
37. Taoka T, Yuh WT, White ML, Quets JP, Maley JE, Ueda T (2001) Sulcal hyperintensity on fluid-attenuated inversion recovery MR images in patients without apparent cerebrospinal fluid abnormality. AJR Am J Roentgenol 176: 519–524
38. Lin DD, Filippi CG, Steever AB, Zimmerman RD (2001) Detection of intracranial hemorrhage: comparison between gradient-echo images and b0 images obtained from diffusion-weighted echo-planar sequences. AJNR Am J Neuroradiol 22:1275–1281

39. Wiesmann M, Mayer TE, Yousry I, Medele R, Hamann GF, Bruckmann H (2002) Detection of hyperacute subarachnoid hemorrhage of the brain by using magnetic resonance imaging. J Neurosurg 96:684–689

40. Moritani T, Smoker WR, Sato Y, Numaguchi Y, Westesson PL (2005) Diffusion-weighted imaging of acute excitotoxic brain injury. AJNR Am J Neuroradiol 26:216-28

Brain Neoplasms

13.1 Introduction

Routine MR imaging is the most sensitive method of detecting tumors of the brain. It is, however, not specific enough to determine the histologic nature of most tumors. Diffusion-weighted (DW) imaging can differentiate between tumor and infection and can provide information about tumor cellularity, thereby helping in the characterization and grading of brain tumors. This chapter will demonstrate DW imaging characteristics of intracranial tumors. The newly revised World Health Organization classification (WHO 2007) [1] of tumors has introduced a number of substantial changes compared with the previous edition. These changes include additions and shifts of entities as well as alterations in diagnostic criteria for a better understanding of neoplastic behavior (Table 13.1).

Table 13.1 The 2007 WHO classification of tumors of the central nervous system and of grade 1-4 (modified from [35])

Tumors of Neurepithelial Tissue
Astrocytic Tumors
Pilocytic astrocytoma 1
Pilomyxoid astrocytoma 2
Subependymal giant cell astrocytoma 1
Pleomorphic xanthoastrocytoma 2
Diffuse astrocytoma 2
Fibrillary astrocytoma
Gemistocytic astrocytoma
Protoplasmic astrocytoma
Anaplastic astrocytoma 3
Glioblastoma 4
Giant cell glioblastoma
Gliosarcoma
Gliomatosis cerebri
Oligodendroglial Tumors
Oligodendroglioma 2
Anaplastic oligodendroglioma 3
Oligoastrocytic Tumors
Oligoastrocytoma 2
Anaplastic oligoastrocytoma 3
Ependymal Tumors
Subependymoma 1
Myxopapillary ependymoma 1
Ependymoma 2 – Cellular – Papillary – Clear cell – Tanycytic
Anaplastic ependymoma 3
Choroid Plexus Tumors
Choroid plexus papilloma 1
Atypical choroid plexus papilloma 2
Choroid plexus carcinoma 3
Other Neuroepithelial Tumors
Astroblastoma
Chordoid glioma of the third ventricle 2
Angiocentric glioma 1
Neuronal and Mixed Neuroglial Tumors
Dysplastic gangliocytoma of cerebellum (Lhermitte-Duclos)
Desmoplastic infantile astrocytoma/ganglioglioma 1
Dysembryoplastic neuroepithelial tumor 1
Gangliocytoma 1
Ganglioglioma 1
Anaplastic ganglioglioma 3
Central neurocytoma 2
Extraventricular neurocytoma 2

Cerebellar liponeurocytoma 2

Papillary glioneuronal tumor 1

Rosette-forming glioneuronal tumor of the fourth ventricle 1

Paraganglioma

Tumors of the Pineal Region

Pineocytoma 1

Pineal parenchymal tumor of intermediate differentiation 2, 3

Pineoblastoma 4

Papillary tumor of the pineal Region 2, 3

Embryonal Tmors

Medulloblastoma 4
- Desmoplastic/nodular medulloblastoma
- Medulloblastoma with extensive nodularity
- Anaplastic medulloblastoma
- Large cell medulloblastoma

CNS primitive neuroectodermal tumor 4

CNS Neuroblastoma

CNS Ganglioneuroblastoma

Medulloepithelioma

Ependymoblastoma

Atypical teratoid/rhabdoid tumor 4

Tumors of Cranial and Paraspinal Nerves

Schwannoma (neurilemoma, neurinoma) 1
- Cellular
- Plexiform
- Melanotic
- Neurofibroma 1
- Plexiform

Perineurioma 1–3

Malignant perineurioma

Malignant peripheral nerve sheath tumor (MPNST) 2–4
- Epithelioid MPNST
- MPNST with mesenchymal differentiation
- Melanotic MPNST
- MPNST with glandular differentiation

Tumors of the Menings

Tumors of Meningothelial Cells

Meningioma
- Meningothelial 1
- Fibrous (fibroblastic) 1
- Transitional (mixed) 1
- Psammomatous 1
- Angiomatous 1
- Microcystic 1
- Secretory 1
- Lymphoplasmacyte-rich 1
- Metaplastic 1
- Chordoid 2
- Clear cell 2
- Atypical 2
- Papillary 3
- Rhabdoid 3
- Anaplastic (malignant) 3

Mesenchymal Tumors

Lipoma

Angiolipoma

Hibernoma

Liposarcoma

Solitary fibrous tumor

Fibrosarcoma

Malignant fibrous histiocytoma

Leiomyoma

Leiomyosarcoma

Rhabdomyoma

Rhabdomyosarcoma

Chondroma

Chondrosarcoma

Osteoma

Osteosarcoma

Osteochondroma

Hemangioma

Epithelioid hemangioendothelioma

Hemangiopericytoma 2

Anaplastic hemangiopericytoma 3

Angiosarcoma

Kaposi sarcoma

Ewing sarcoma - PNET

Primary Melanocytic Lesions

Diffuse melanocytosis

Melanocytoma

Malignant melanoma

Meningeal melanomatosis

Other Neoplasms Related to the Meninges

Hemangioblastoma 1

Lymphomas and Hemopoietic Neoplasms
Malignant lymphomas
Plasmacytoma
Granulocytic sarcoma
Germ Cell Tumors
Germinoma
Embryonal carcinoma
Yolk sac tumor
Choriocarcinoma
Teratoma – Mature – Immature – Teratoma with malignant transformation
Mixed germ cell tumor

Tumors of the Sellar Region
Craniopharyngioma 1 – Adamantinomatous – Papillary
Granular cell tumor 1
Pituicytoma 1
Spindle cell oncocytoma of the adenohypophysis 1
Metastatic Tumors

13.2 Gliomas

Gliomas are classified as tumors of neuroepithelial tissue (Table 13.1). The signal intensity of gliomas on DW images is variable and depends mainly on their T2 and apparent diffusion coefficient (ADC) values [2–23]. Thus, some gliomas are hyperintense on DW images with decreased ADC, which generally reflects high tumor cellularity and reduced volume of the extracellular space. Other gliomas have normal or increased ADC, and if the DW signal is high, it is due to a T2 shine-through effect.

Significant differences have been reported between the ADC values of low- and high-grade gliomas [9, 13]. High ADC values of low-grade gliomas probably reflect relatively lower cellularity, a lower nuclear-to-cytoplasm ratio, and the presence of tumor-cell-associated extracellular matrix that includes glycosaminoglycans and fibrous proteins (collagen, elastin, fibronectin, laminin) [24]. The solid components of low-grade astrocytomas (Figs. 13.1-13.3),

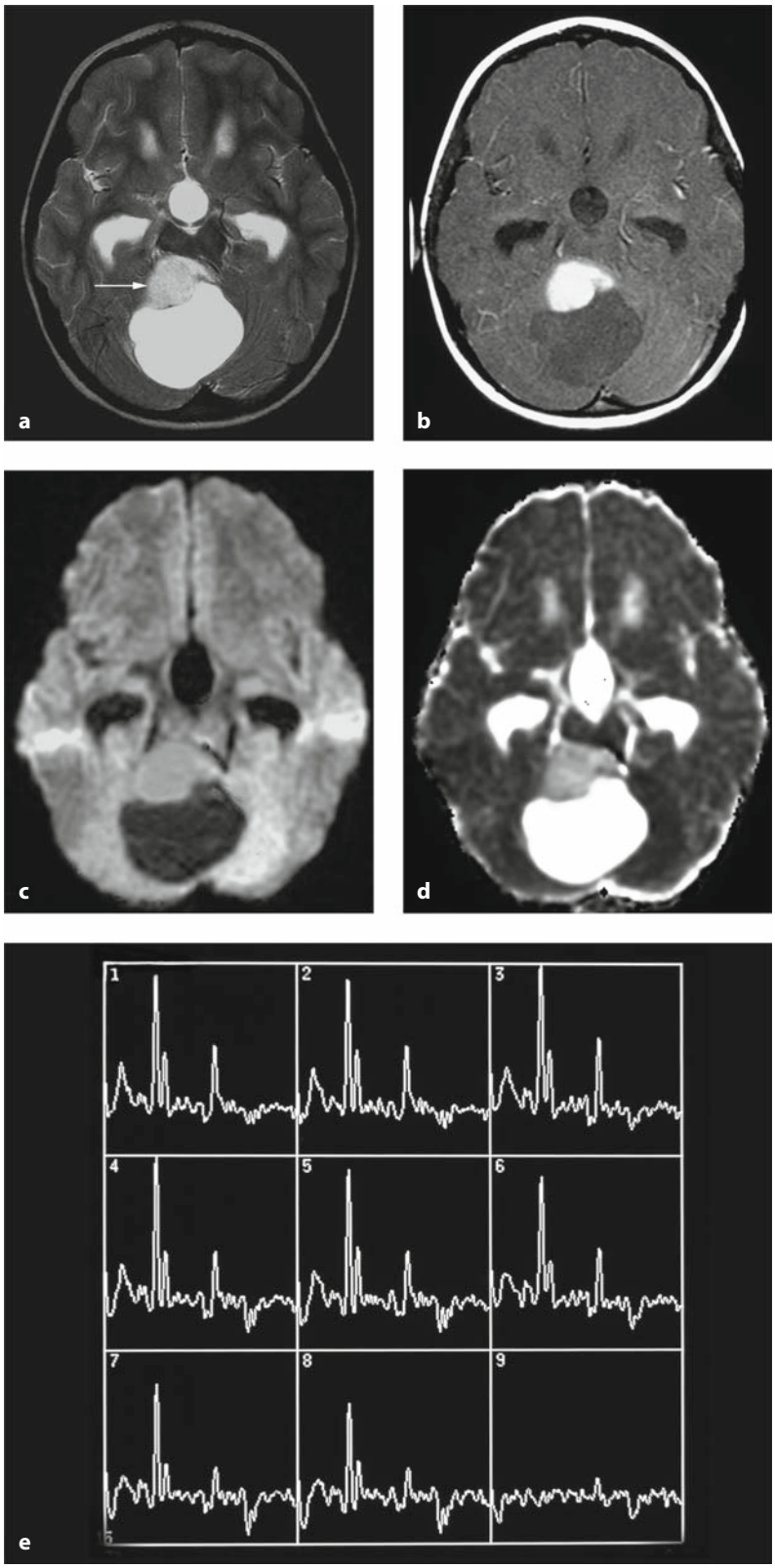

Figure 13.1 a–e

Juvenile pilocytic astrocytoma in a 10-year-old boy. **a** T2-weighted image shows a hyperintense cystic mass in the cerebellum and hydrocephalus. There is a mural nodule (*arrow*) in the tumor. **b** Gadolinium-enhanced T1-weighted image shows enhancement in the nodule. **c** DW image shows hypointensity in the cystic component and isointensity in the nodule. **d** ADC map shows hyperintensity in the cystic component and hyperintensity in the nodule ($1.41\text{-}1.67\times10^{-3}$ mm^2/s) of the mass. **e** A high choline/NAA ratio and lactate peak are observed despite the benign histology of this tumor

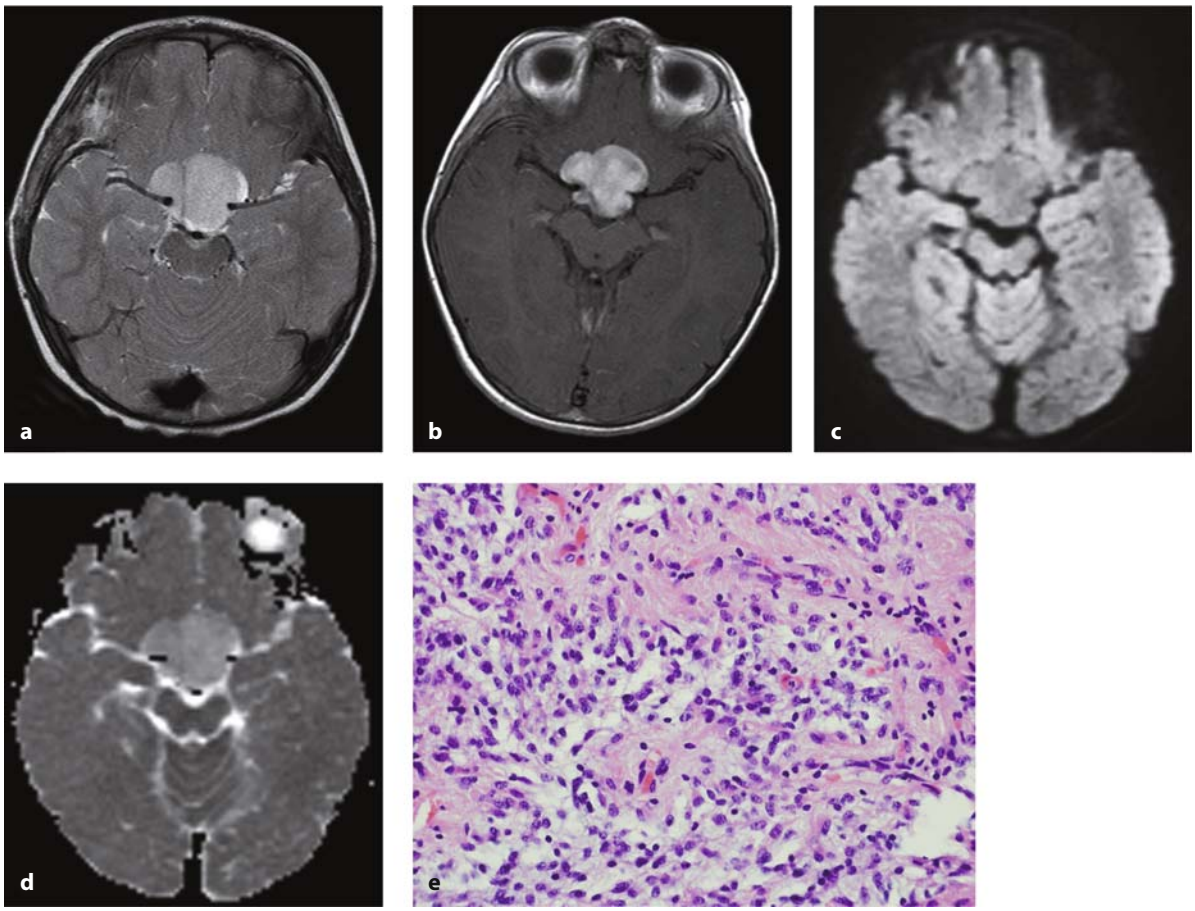

Figure 13.2 a–e

Hypothalamic pilocytic astrocytoma in a 5-year-old boy with headache. **a** T2-weighted image shows a hyperintense mass in the hypothalamus. **b** Gadolinium-enhanced T1-weighted image shows enhancement in the mass. **c** DW image shows isointensity. **d** ADC map shows hyperintensity in the mass (1.53×10^{-3} mm^2/s). **e** Pathology shows intermediate cellularity and abundant extracellular matrix (Rosenthal fibers and microcystic changes)

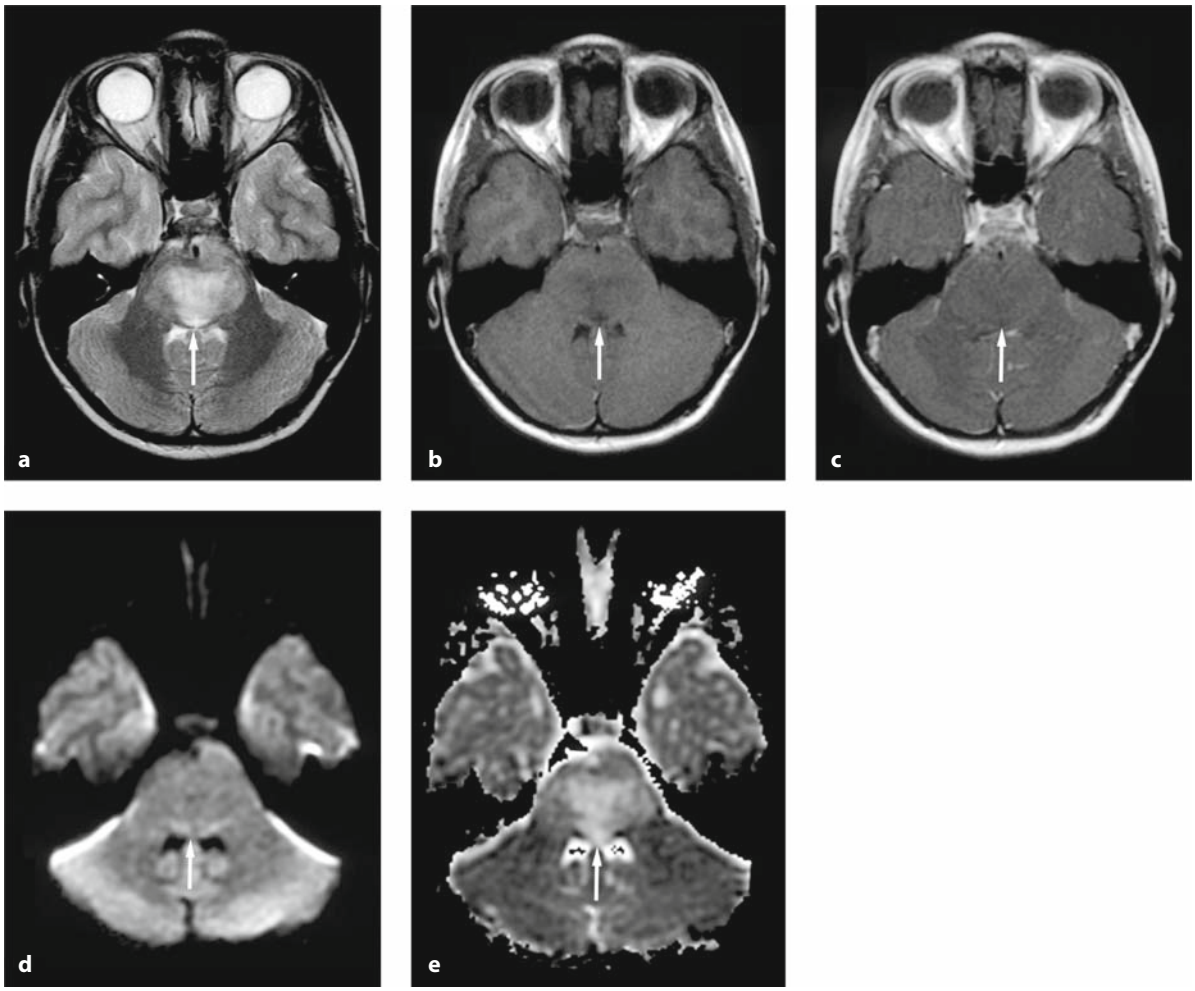

Figure 13.3 a–e

Brain stem glioma in an 8-year-old girl with headache. **a** T2-weighted image shows a hyperintense lesion (*arrow*) with surrounding edema in pons. **b** T1-weighted image shows the hypointense lesion (*arrow*). **c** Gadolinium-enhanced T1-weighted image shows no significant enhancement. **d** DW image shows isointensity in the lesion (*arrow*). **e** ADC map shows hyperintensity in the lesion ($0.85–1.17\times10^{-3}$ mm^2/s; *arrow*). The isointensity on the DW image is caused by a balance between increased T2 and ADC

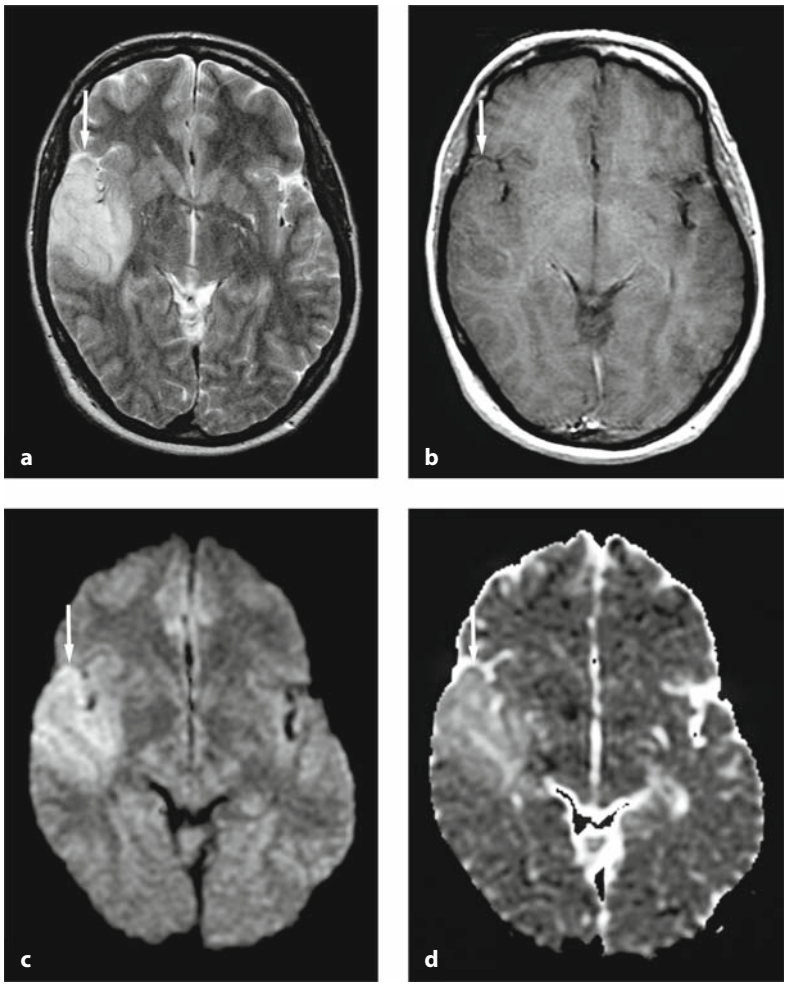

Figure 13.4 a–d

Low-grade oligoastrocytoma in a 48-year-old woman with seizures. **a** T2-weighted image shows a hyperintense lesion in the right temporal lobe (*arrow*). **b** Gadolinium-enhanced T1-weighted image shows a slightly hypointense lesion and no enhancement (*arrow*). **c** DW image shows hyperintensity (*arrow*). **d** ADC map shows hyperintensity in the lesion (0.98–1.19×10^{-3} mm^2/s; *arrow*)

oligoastrocytomas (Fig. 13.4), oligodendrogliomas (Fig. 13.5), ependymomas, and subependymomas (Fig. 13.6) generally show slightly low, iso-, or slightly high signal intensity on DW images associated with increased ADC. The ADC value in pilocytic astrocytomas is often higher than 1.5 × 10^{-3} mm^2/s (Figs. 13.1, 13.2) [25]. This finding is useful in the differential diagnosis because MR spectroscopy shows a high choline/NAA and lactate peak despite the benign histology of pilocytic astrocytomas [26]. Low-grade astrocytomas and oligodendrogliomas have a high concentration of glycosaminoglycans, which is highly hydrophilic causing the shift of water molecules in the extracellular matrix [24]. However, some low-grade neoplasms can show up as hyperintense on DW images with relatively low ADC values probably

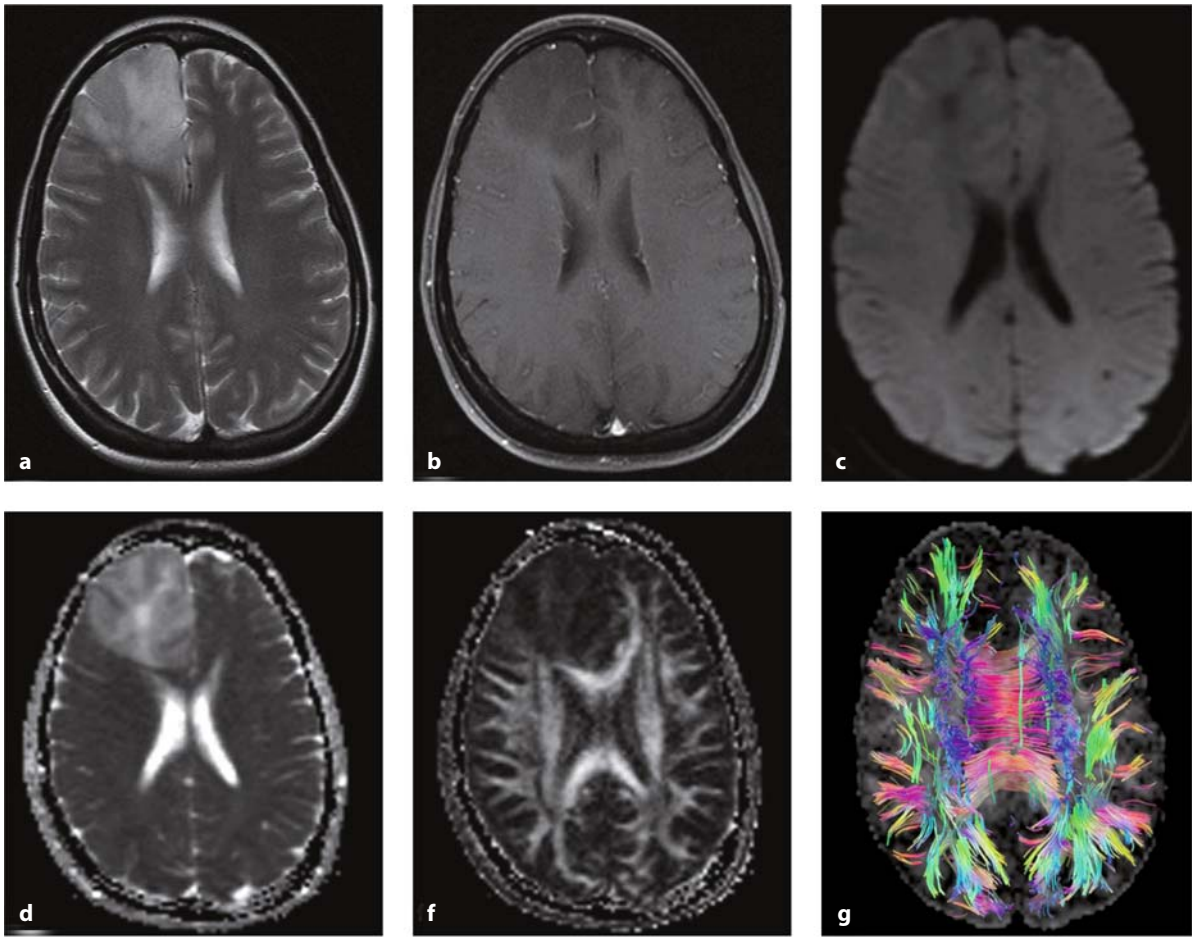

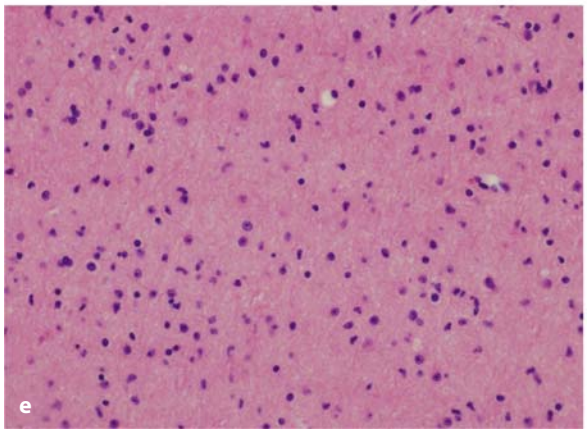

Figure 13.5 a–g

Low-grade oligodendroglioma in a 40-year-old woman. **a** T2-weighted image shows a hyperintense mass lesion in the right frontal lobe. **b** Gadolinium-enhanced T1-weighted image with fat saturation shows a slight hypointense lesion and no enhancement. **c** DW image shows iso- and slight hypointensity. **d** ADC map shows hyperintensity in the lesion ($0.82–1.53\times10^{-3}$ mm^2/s). **e** Pathology shows low cellularity and fibrillary background. **f** FA map shows decreased anisotropy in the right frontal mass but white matter structure is identified in the mass. **g** White matter fiber tracts in the tumor are relatively preserved on the DT fiber tractography (Courtesy of Kim J MD, The University of Iowa Hospitals and Clinics, USA)

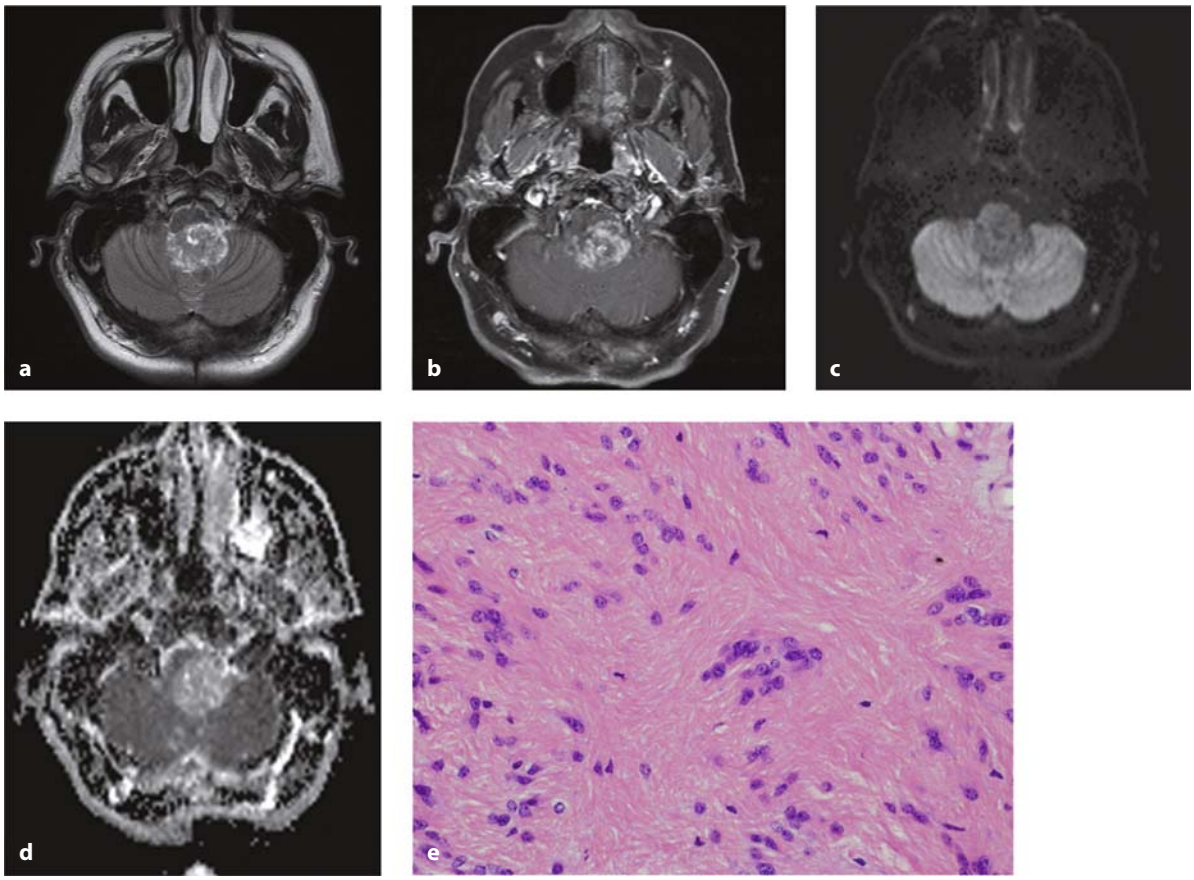

Figure 13.6 a–e

Low-grade subependymoma in a 49-year-old man. **a** T2-weighted image shows a hyperintense mass lesion in the 4th ventricle. **b** Gadolinium-enhanced T1-weighted image with fat saturation shows heterogeneous enhancement. **c** DW image shows slight hypointensity. **d** ADC map shows hyperintensity in the lesion ($0.96–1.30\times10^{-3}$ mm^2/s). **e** Pathology specimen shows low cellularity and abundant fibrillary background

due to the hypercellularity, which includes pleomorphic xanthoastrocytoma (Fig. 13.7), ganglioglioma, and neurocytoma.

The periphery of low-grade gliomas contains preserved white matter fiber tracts, while these fiber tracts are disarranged in high-grade gliomas [27] (Figs. 13.5, 13.14, 13.18).

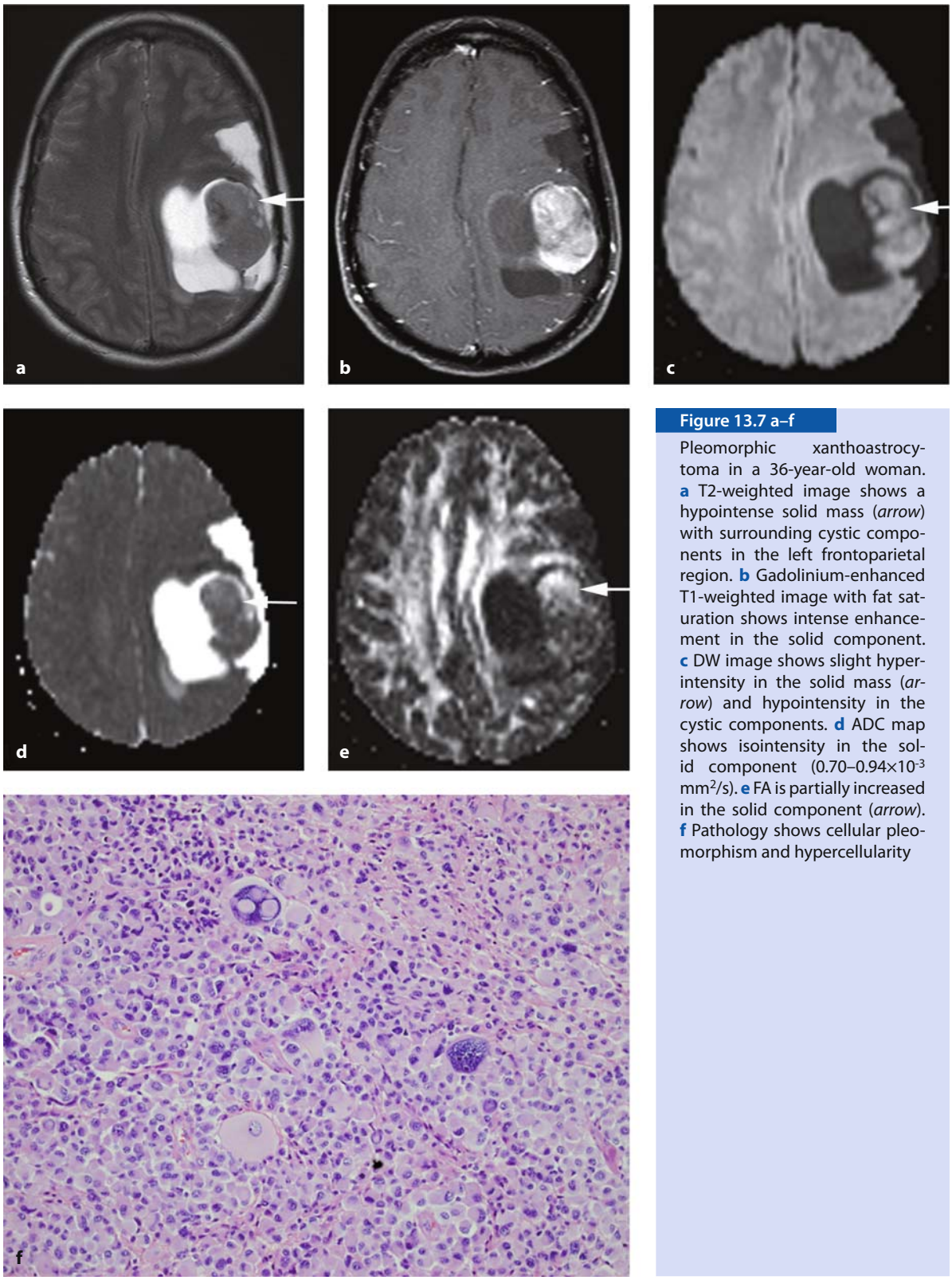

Figure 13.7 a–f

Pleomorphic xanthoastrocytoma in a 36-year-old woman. **a** T2-weighted image shows a hypointense solid mass (*arrow*) with surrounding cystic components in the left frontoparietal region. **b** Gadolinium-enhanced T1-weighted image with fat saturation shows intense enhancement in the solid component. **c** DW image shows slight hyperintensity in the solid mass (*arrow*) and hypointensity in the cystic components. **d** ADC map shows isointensity in the solid component ($0.70–0.94\times10^{-3}$ mm^2/s). **e** FA is partially increased in the solid component (*arrow*). **f** Pathology shows cellular pleomorphism and hypercellularity

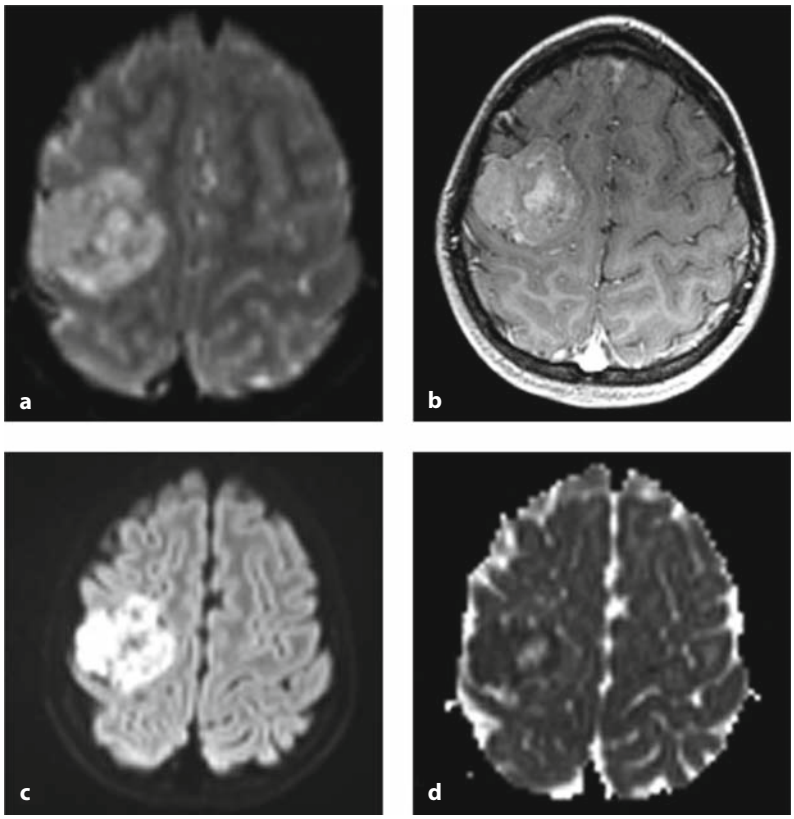

Figure 13.8 a–d

Anaplastic ependymoma in a 7-year-old boy. **a** T2-weighted (b0) image shows a hyperintense solid mass in the right frontal area. **b** Gadolinium-enhanced T1-weighted image shows heterogeneous enhancement. **c** DW image shows hyperintensity in the solid mass. **d** ADC map shows hypointensity (0.50-0.64×10^{-3} mm^2/s) with hyperintensity (1.44×10^{-3} mm^2/s) in a central necrotic area

13.2.1 High-Grade Gliomas and Differential Diagnosis on DW Imaging

High-grade gliomas include anaplastic glioma (anaplastic astrocytoma, anaplastic oligodendroglioma, anaplastic oligoastrocytoma, anaplastic ependymoma) and glioblastoma (GBM) (Figs. 13.8-13.14). It has been reported that high-grade gliomas typically are hyperintense on DW images with decreased ADC [4, 9–11, 13, 14, 20]. High tumor cellularity is probably the major determinant of the decreased ADC values in high-grade brain tumors [4, 9, 13, 19]. Other studies have suggested that ADC correlates not only with tumor cellularity, but also with total nuclear area and tumor grade [9, 13, 14, 18, 20], with high-grade tumors having high cellular density and decreased ADC. Other studies have correlated areas of decreased ADC and found it to be associated with increased choline on MR spectroscopy. Choline is a marker for cell membrane turnover [8, 10]. Minimal ADC values in high-grade astrocytomas are negatively correlated with the Ki-67 labeling index and related to posttreatment prognosis [28]. FA may be better than ADC for assessment and delineation of the different degrees of pathologic changes in gliomas [29].

Although there is a general principle of high-grade gliomas having high DW signal with decreased ADC, there are still controversies regarding how well DW imaging can differentiate between high-grade primary brain tumors, lymphoma and metastasis. Krabbe et al. reported that both the contrast-enhancing portions and the peritumoral edema of metastasis have higher ADC than high-grade gliomas [7]. In the individual case the distinction between metastasis and high-grade glioma is often difficult to make, as some high-grade gliomas also have high ADC [19, 30]. For lymphomas, Guo et al. reported that ADC was generally lower than in high-grade gliomas. This could be useful to differentiate the two [17], but in the clinical situation there is often overlap between lymphoma and high-grade glioma. In our experience, the ADC of lymphoma ranges between 0.51 and 0.71×10^{-3} mm^2/s, whereas that of high-grade gliomas ranges between 0.58 and 0.89×10^{-3} mm^2/s. Lymphomas tend

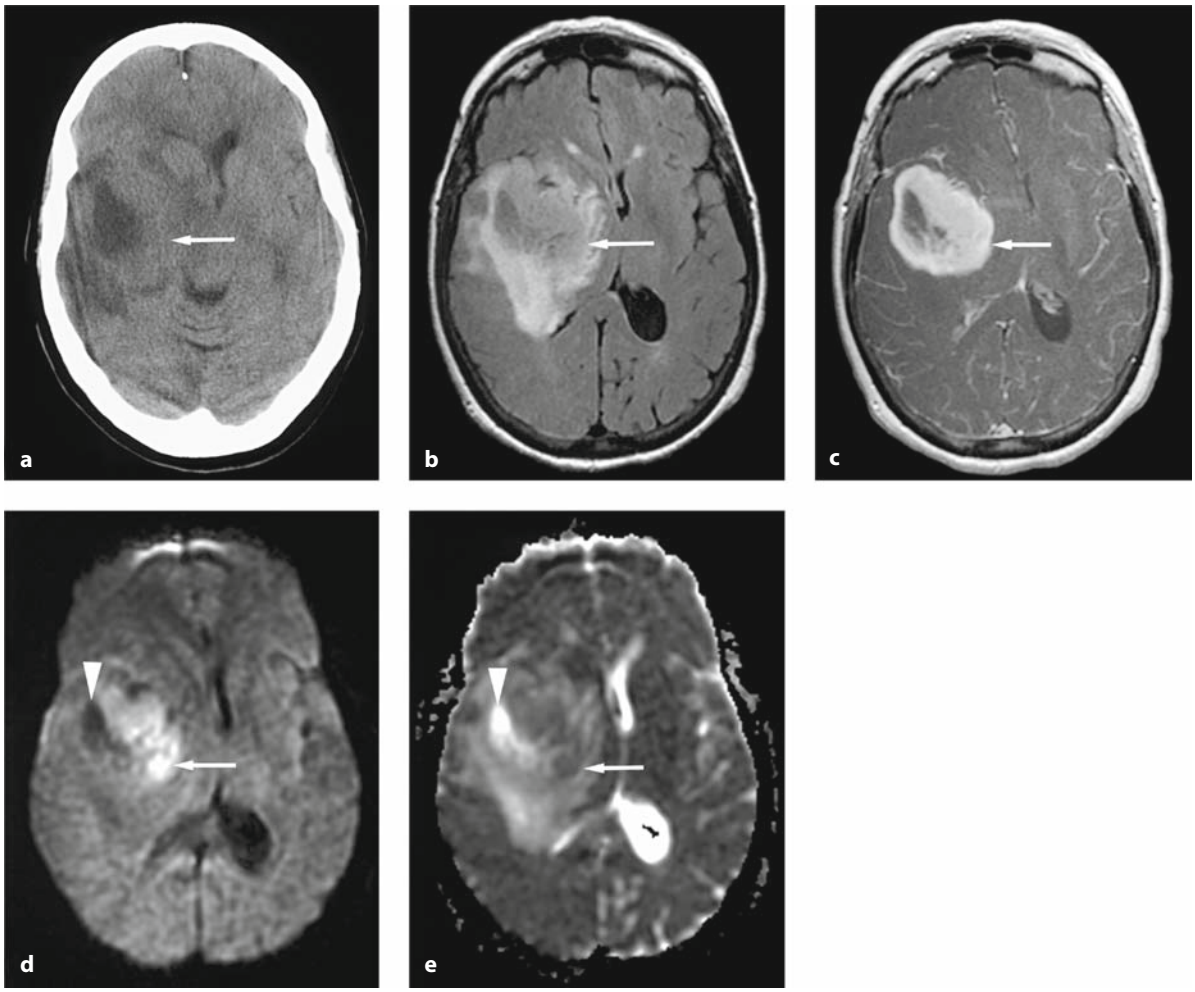

Figure 13.9 a–e

Glioblastoma in a 69-year-old woman with left-side weakness. **a** Unenhanced CT image shows a heterogeneous iso- to hypodense lesion in the right temporal lobe (*arrow*). **b** Fluid-attenuated inversion-recovery image shows the heterogeneous hyperintense lesion in the right temporal lobe (*arrow*). **c** Gadolinium-enhanced T1-weighted image shows heterogeneous enhancement in the mass (*arrow*). **d** DW image shows hyperintensity in the enhancing portion of the mass (*arrow*) and hypointensity in the cystic/necrotic portion of the mass (*arrowhead*). **e** ADC map shows heterogeneous hypointensity ($0.74–0.85\times10^{-3}$ mm^2/s; *arrow*) in the enhancing portion of the mass compared to the surrounding vasogenic edema. Cystic/necrotic portion of the mass (*arrowhead*) is hyperintense. These findings may correspond to the high cellularity of the enhancing tumor and increased diffusivity of the cystic/necrotic portion

to have lower ADC values because of a higher nuclear to cytoplasmic ratio [17]. The FA and ADC values of primary cerebral lymphoma are significantly lower than those of GBM [31] These are general principles, but in practical clinical work it is sometimes difficult to distinguish between lymphomas, metastasis and high-grade gliomas, even with the most sophisticated ADC maps [5, 11–14, 19].

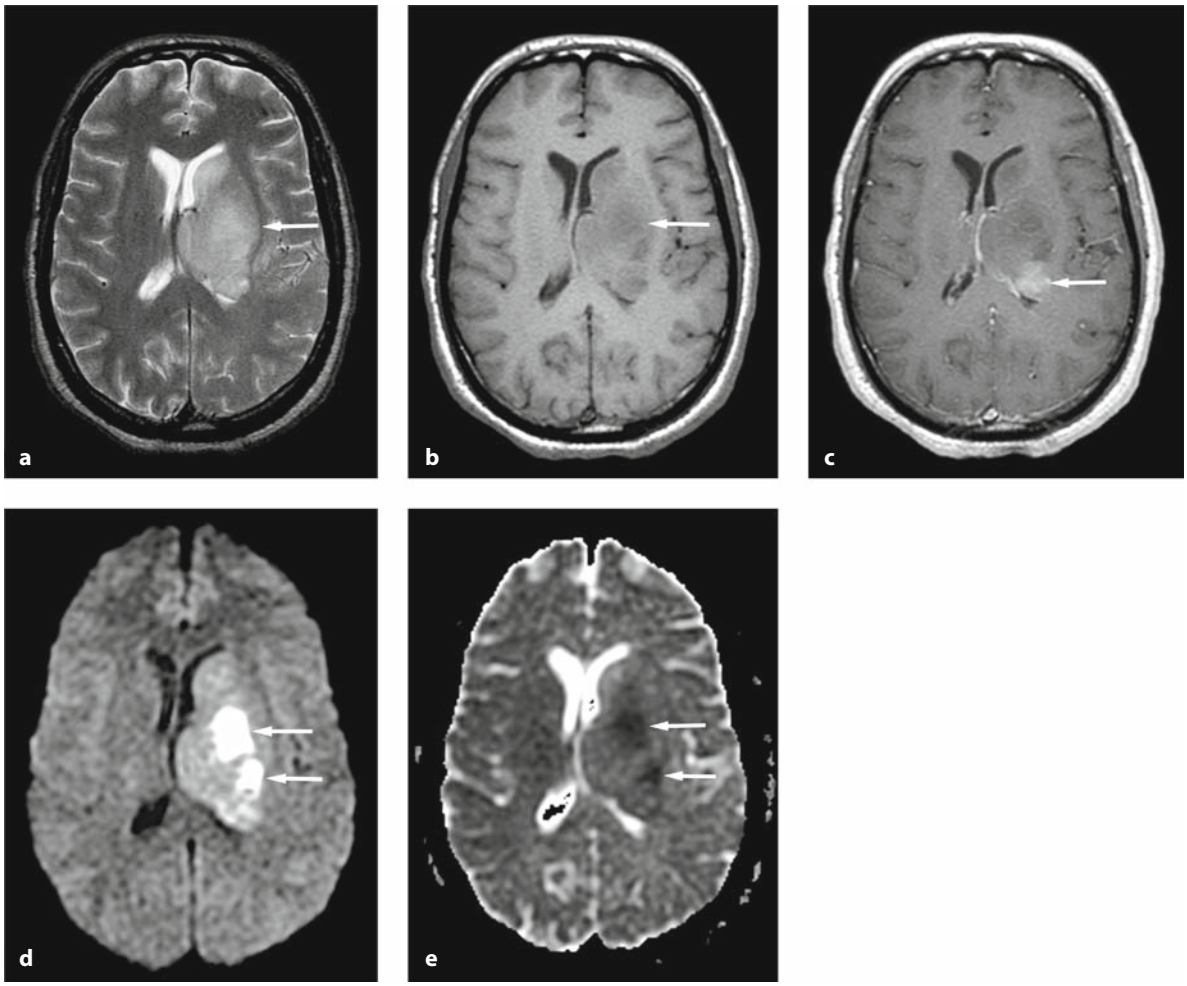

Figure 13.10 a–e

Glioblastoma in a 51-year-old woman with right-side weakness. **a** T2-weighted image shows a hyperintense mass in the left basal ganglia and thalamus (*arrow*). **b** T1-weighted image shows hypointensity in the lesion (*arrow*). **c** Gadolinium-enhanced T1-weighted image shows heterogeneous enhancement in the posterior portion of the tumor (*arrow*). **d** DW image shows hyperintensities (*arrows*). The areas of marked hyperintensity on the DW image does not show contrast enhancement in this patient. **e** ADC map shows heterogeneous hypointensity in the lesion (0.58–0.89×10^{-3} mm^2/s; *arrows*)

13.2.2 Glioblastoma

Glioblastoma (GBM) is the most common primary brain tumor in adults. Despite advances in microneurosurgery, radiation therapy, chemotherapy, and advances in imaging, only 10% of patients will survive 3 years following diagnosis [32]. Recent molecular and genetic approaches have provided dramatic insights into glioma biology, including genetic alterations in tumorigenesis and molecular mechanisms of angiogenesis.

GBM develops de novo (primary GBM) or by transformation from low-grade or anaplastic tumors (secondary GBM) [33-35]. Primary and secondary GBM evolves through different tumorigenesis pathways. Primary GBM usually occurs among older patients

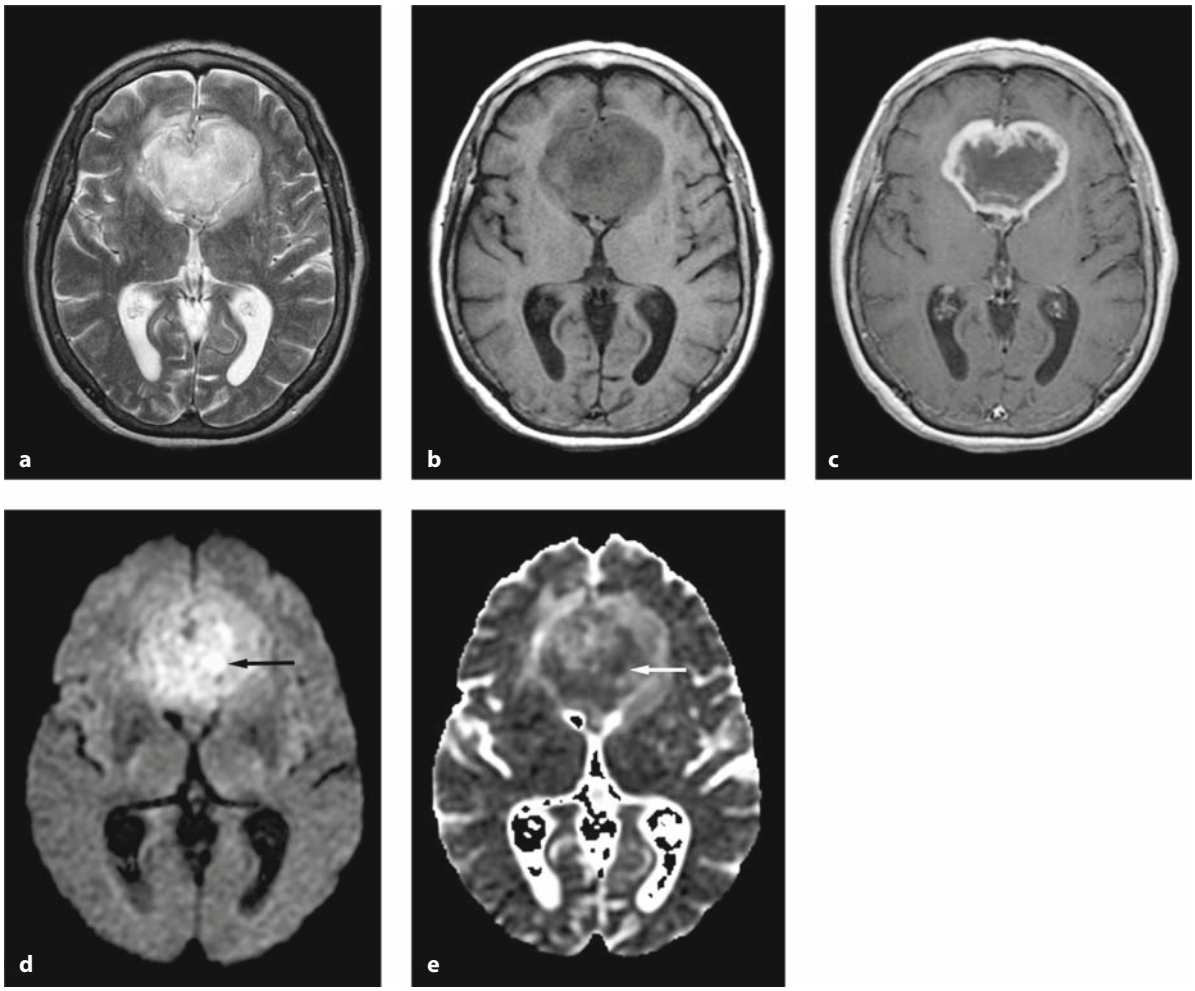

Figure 13.11 a–e

Glioblastoma in an 80-year-old woman with personality changes. **a** T2-weighted image shows a hyperintense mass, which involves the genu of corpus callosum (butterfly tumor). **b** T1-weighted image shows hypointensity in the lesion. **c** Gadolinium-enhanced T1-weighted image shows irregular ring-like enhancement of the tumor. **d** DW image shows hyperintensity (*arrow*). **e** ADC map shows heterogeneous intensity in the mass. Note the hypointensity in the center of the lesion (0.65×10^{-3} mm^2/s; *arrow*). These findings may correspond to the cellularity of the tumor

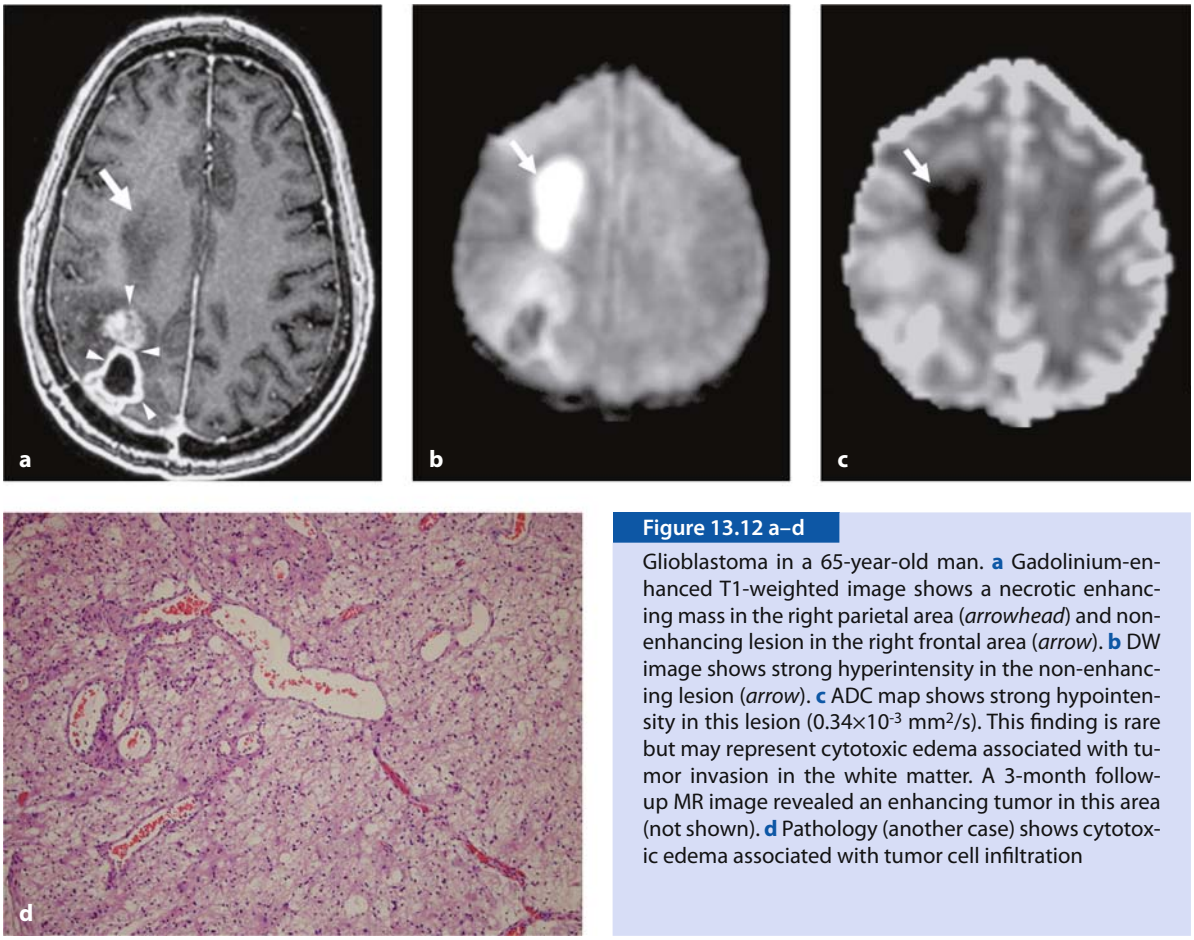

Figure 13.12 a–d

Glioblastoma in a 65-year-old man. **a** Gadolinium-enhanced T1-weighted image shows a necrotic enhancing mass in the right parietal area (*arrowhead*) and non-enhancing lesion in the right frontal area (*arrow*). **b** DW image shows strong hyperintensity in the non-enhancing lesion (*arrow*). **c** ADC map shows strong hypointensity in this lesion (0.34×10^{-3} mm^2/s). This finding is rare but may represent cytotoxic edema associated with tumor invasion in the white matter. A 3-month follow-up MR image revealed an enhancing tumor in this area (not shown). **d** Pathology (another case) shows cytotoxic edema associated with tumor cell infiltration

(mean age 55 years). It is characterized by epidermal growth factor receptor (*EGFR*) overexpression (60%) / amplification (40%) in chromosome 7p, and other chromosome abnormalities (*PTEN in chromosome 10q, MDM2 mutations, p16 deletion in chromosome 9p21, LOH in chromosome 10*) (Fig. 13.15). GBM cells are often small and undifferentiated. The prognosis of primary GBM is worse than that of secondary GBM.

Secondary GBM more frequently occurs among younger patients (mean age 40 years), and results from histologic progression of lower-grade diffuse or anaplastic astrocytomas (Fig. 13.13). It contains *TP53* mutations (65%) and subsequent allelic loss of chromosome 19q and 10q. Secondary GBM is transformed from anaplastic astrocytoma or astrocytic components in anaplastic oligoastrocytoma/oligodendroglioma (*LOH, p16, DCC, PTEN, EGFR*) (Fig. 13.15), although other possibilities have been suggested in the literature [32, 34]. The latter is described as "GBM with oligodendroglial component" (GBMO) in which loss of heterozygosity (LOH) on 1p and 19q, known as common makers of oligodendroglial tumors, is more frequently observed than in the standard GBM (Fig. 13.15) GBMO has a relatively better prognosis and responds to radiation and chemotherapy [32, 34, 36].

Solid components of GBM are typically hyperintense on DW images with slightly decreased or slightly increased ADC (Figs. 13.9-13.13). Cystic necrotic components of GBM are usually hypointense on DW images with increased ADC (Fig. 13.9). One of the important differential diagnoses is brain abscess in which cystic components are usually hyperintense on DW images with decreased ADC. Hypercellularity of solid tumors is the major determinant of the decreased ADC values. Background vasogenic edema and micronecrosis affect the DW imaging signal intensity and ADC values. Decreased ADC can be observed in the cystic component or non-enhancing portion of GBM. The causes of the decreased ADC are: (1) tumor cell infiltration (hypercellularity), (2)

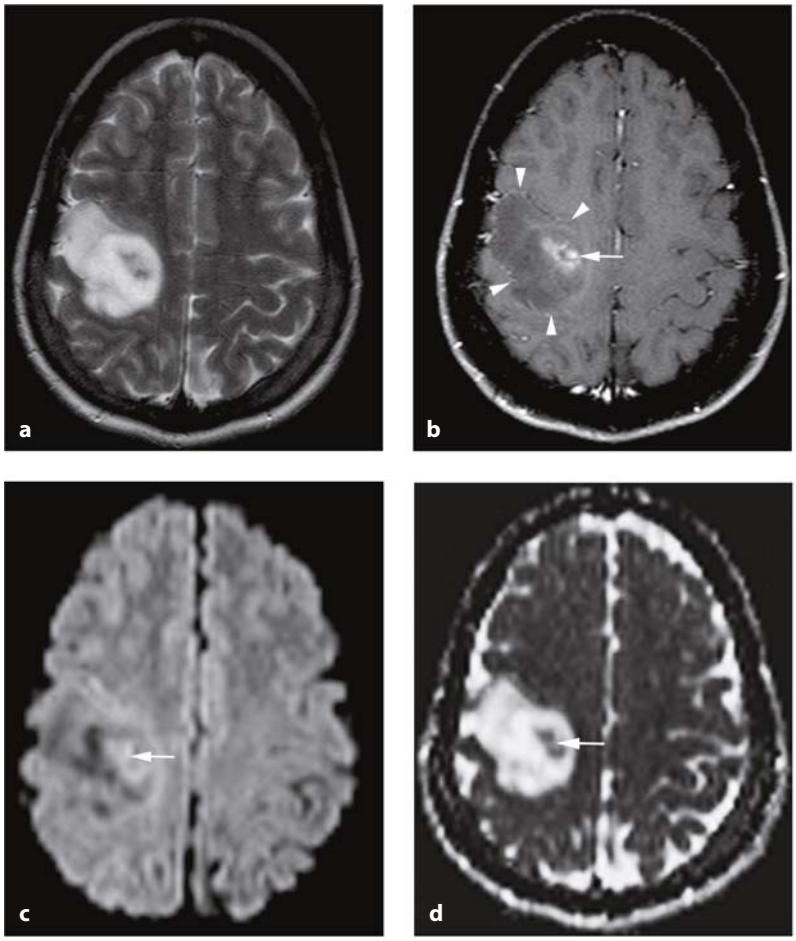

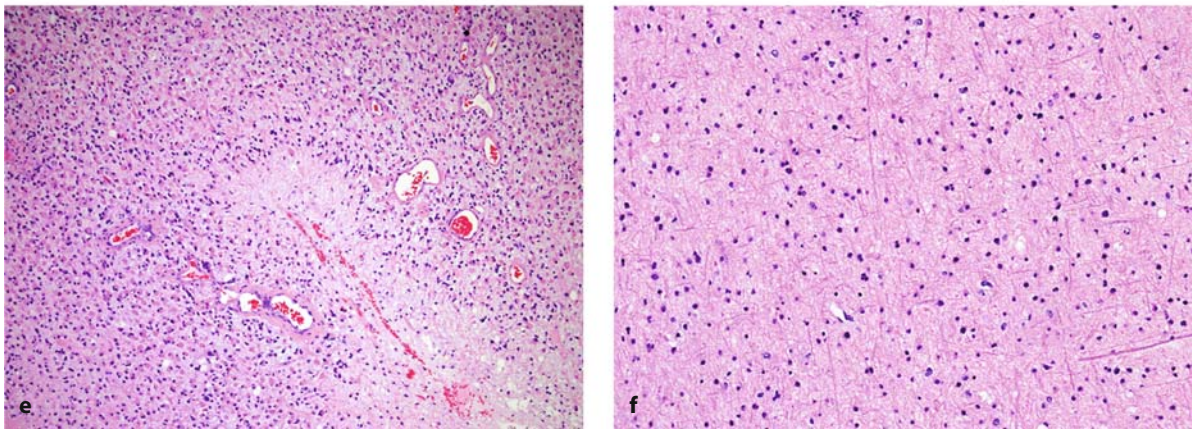

Figure 13.13 a–f

Glioblastoma secondary to anaplastic astrocytoma in a 37-year-old man. **a** T2-weighted image shows a hyperintense mass in the right frontal lobe. **b** Gadolinium-enhanced T1-weighted image with fat saturation shows a necrotic enhancing lesion (*arrow*) within a non-enhancing mass (*arrowheads*). **c** DW image shows mild hyperintensity in the enhancing lesion (*arrow*). **d** The enhancing lesion has a lower ADC (0.97×10^{-3} mm^2/s) than the surrounding non-enhancing mass (1.20×10^{-3} mm^2/s) (*arrow*). **e** Pathology of the enhancing lesion shows hypercellularity, pleomorphism, endothelial proliferation, and necrosis consistent with glioblastoma multiforme. **f** Pathology of surrounding non-enhancing mass shows intermediate cellularity and pleomorphism consistent with anaplastic astrocytoma

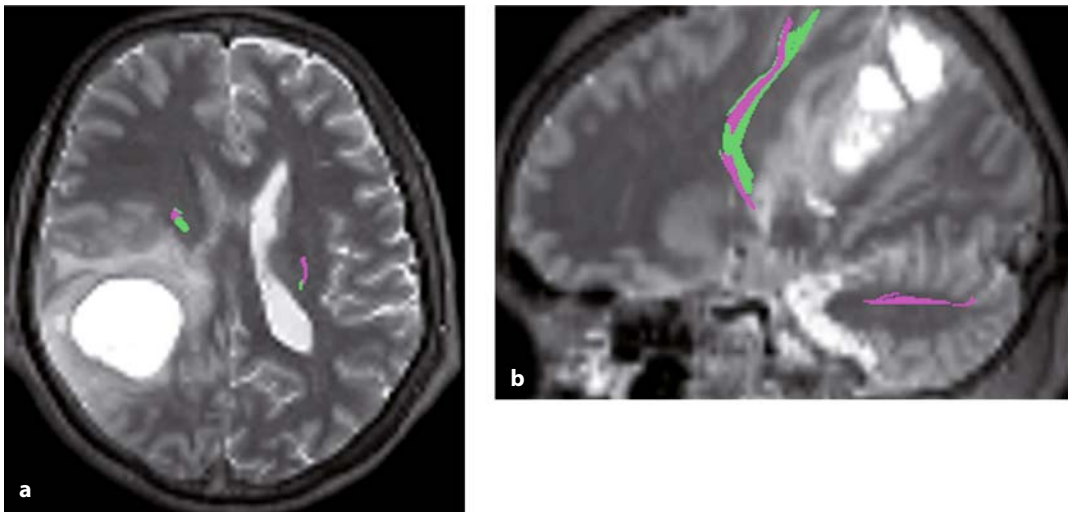

Figure 13.14 a, b

Glioblastoma in a 58–year-old woman. **a, b** Diffusion tensor fiber tractography shows the displacement of the corticospinal tract (motor; *red*) and the corticothalamic tract (sensory; *green*) (Courtesy of Yamada K MD, Kyoto Prefectural University of Medicine, Japan)

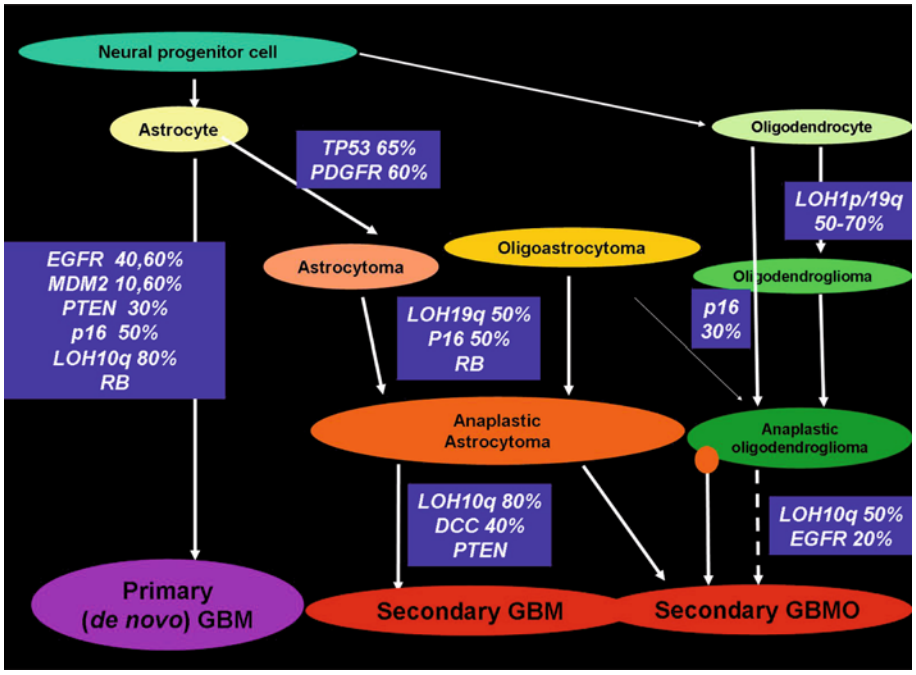

Figure 13.15

Glioblastoma (*GBM*) develops de novo (primary) or by transformation from low-grade or anaplastic tumor (secondary). Primary GBM and secondary GBM or GBMO (with oligodendroglial component) evolve through different tumorigenesis pathways

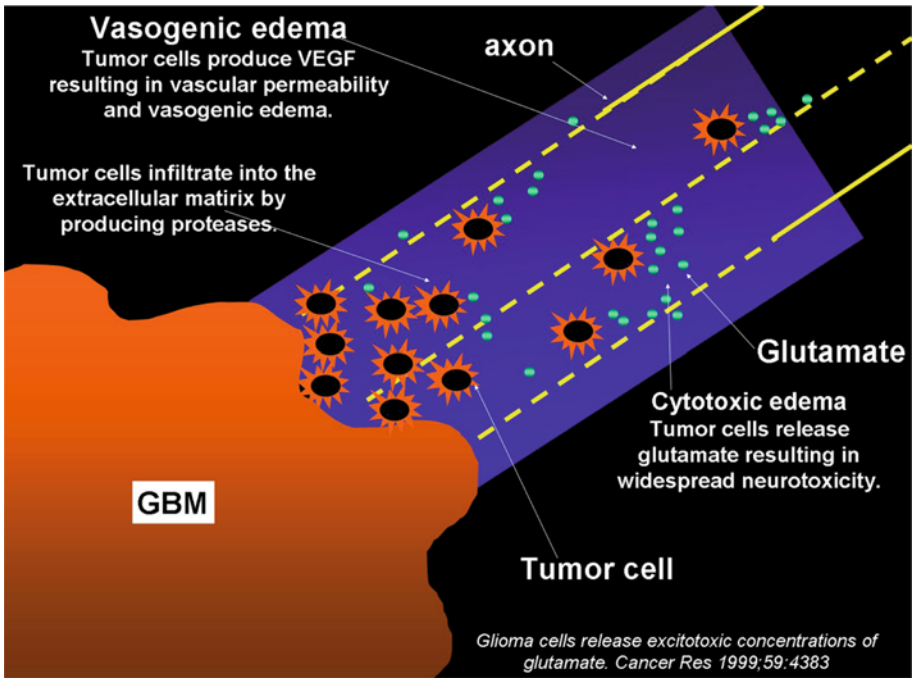

Figure 13.16

In glioblastoma (*GBM*), tumor cells produce proteases and infiltrate into the extracellular space in the white matter. Tumor cells produce vascular endothelial growth factor (*VEGF*) resulting in increased vascular permeability and in vasogenic edema. Tumor cells also release glutamate resulting in surrounding neurotoxicity that facilitates infiltration of the tumor cells. This may cause the cytotoxic edema in peritumoral areas and rarely in the white matter tumor infiltration

tumoral hemorrhage, (3) tumor cell edema or coagulative necrosis resulting from tumoral ischemia, and (4) cytotoxic edema due to excitotoxic injury (high concentrations of excitotoxic amines such as glutamate released by GBM cells) (Figs. 13.9-13.12, 13.16, 13.17) [37, 38].

The narrow rim of increased FA and decreased ADC observed at the edge of GBM is caused by compressed white matter fibers or peripheral cellular infiltration and associated cytotoxic edema (Fig. 13.18) [39, 40]. Tumor cells invade and change white matter fiber structures by widening, displacing, and disrupting the fiber bundles [41, 42] (Fig. 13.14). Fiber tractography can be useful for preoperative planning and intraoperative image-guided surgery [43, 44].

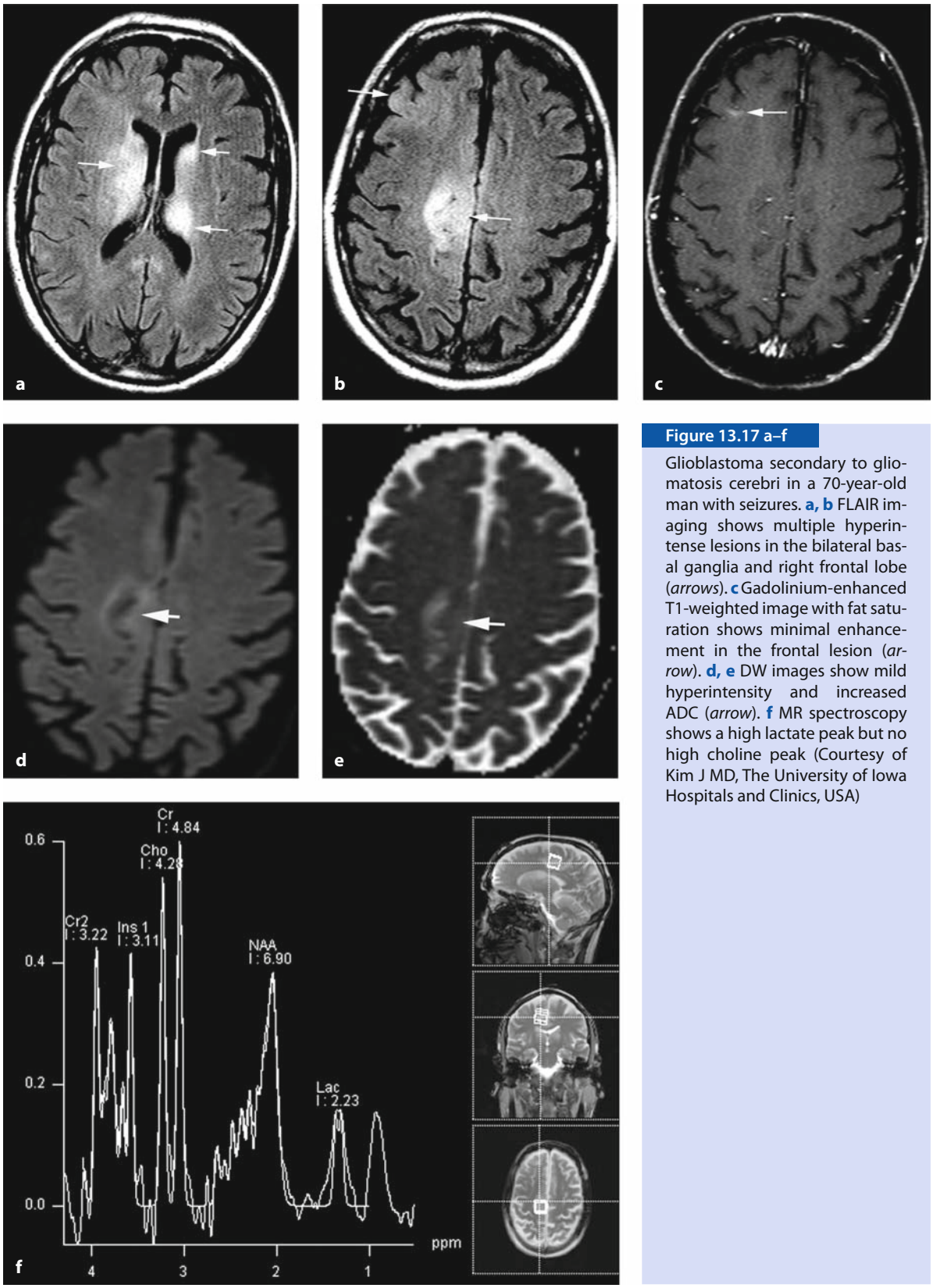

Figure 13.17 a–f

Glioblastoma secondary to gliomatosis cerebri in a 70-year-old man with seizures. **a, b** FLAIR imaging shows multiple hyperintense lesions in the bilateral basal ganglia and right frontal lobe (*arrows*). **c** Gadolinium-enhanced T1-weighted image with fat saturation shows minimal enhancement in the frontal lesion (*arrow*). **d, e** DW images show mild hyperintensity and increased ADC (*arrow*). **f** MR spectroscopy shows a high lactate peak but no high choline peak (Courtesy of Kim J MD, The University of Iowa Hospitals and Clinics, USA)

Figure 13.17 g–j

g One-month follow-up MR image shows multiple enhancing masses in the right frontal area. **h**, **i** DW imaging shows peripheral and peritumoral hyperintensity associated with decreased ADC (*arrowheads*). **j** MR spectroscopy shows not only a high lactate peak but also high choline and glutamate/glutamine peaks (*arrow*)

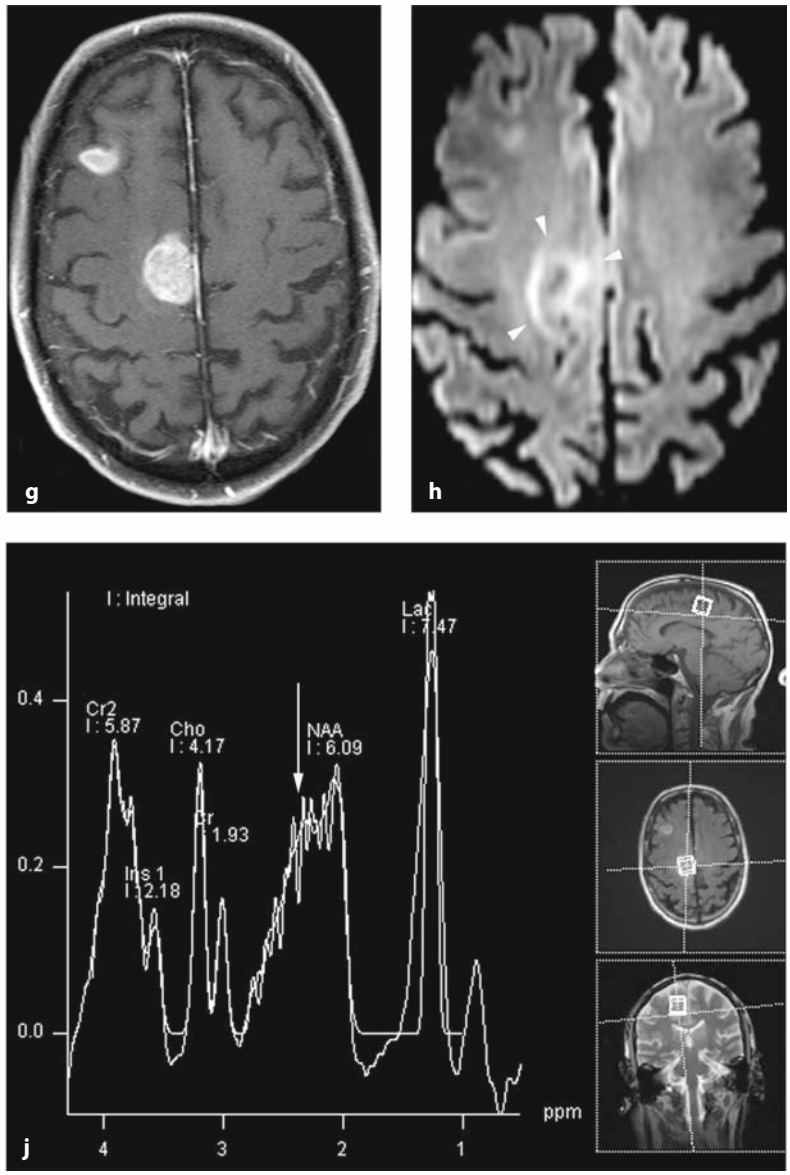

13.2.3 Gliomatosis Cerebri

The WHO 2007 guidelines redefine gliomatosis cerebri as a diffuse glioma growth pattern, infiltrating at least two lobes, most commonly a presentation form of diffuse astrocytoma, occasionally oligodendroglioma or mixed glioma. Previously it was an unique entity (*sui generis*) and defined as a malignant-grade neuroepithelial neoplasm of uncertain origin [45]. Genetic abnormalities are often detected in the p53 or Rb gene. Pathologically, features differentiating gliomatosis cerebri from multiple gliomas are continuity of cellular infiltration and lack of clear distinction from adjacent normal brain tissue. Pathologically, myelin sheaths are destroyed but axons and neurons are relatively preserved. If GBM occurs in gliomatosis cerebri, it can present as multiple enhancing mass lesions (Fig. 13.17). It is often difficult to differentiate multicentric GBMs from multifocal GBMs associated with gliomatosis cerebri based on MR imaging [46]. Diffusion tensor fiber tractography shows the fiber tracking passing through the tumor in gliomatosis cerebri (Fig. 13.18) [47].

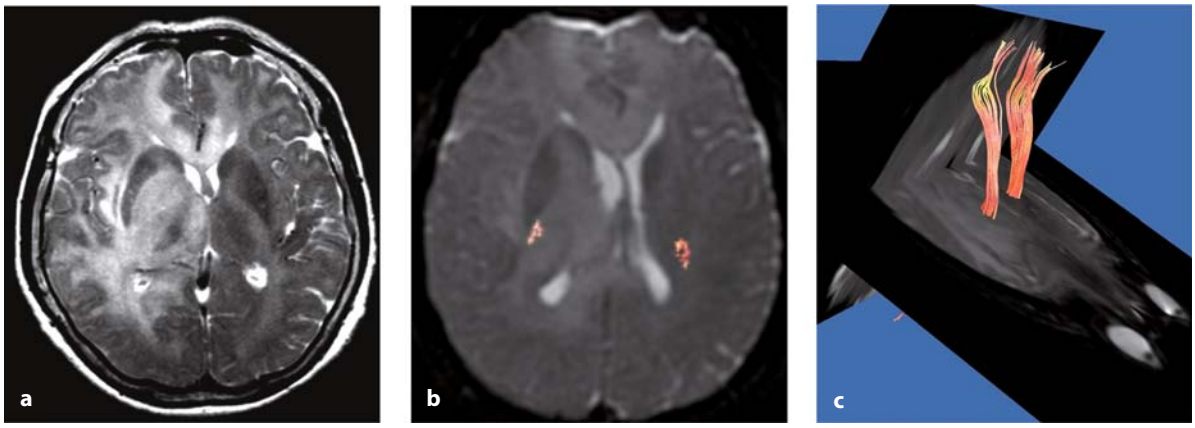

Figure 13.18 a–c

Gliomatosis cerebri in a 73-year-old woman. **a** T2-weighted image shows extensive, asymmetric white matter hyperintensity bilaterally. **b**, **c** Diffusion tensor fiber tractography shows only minimal shift of the pyramidal tracts. (Courtesy of Aoki S MD, University of Tokyo, Japan). (From [47])

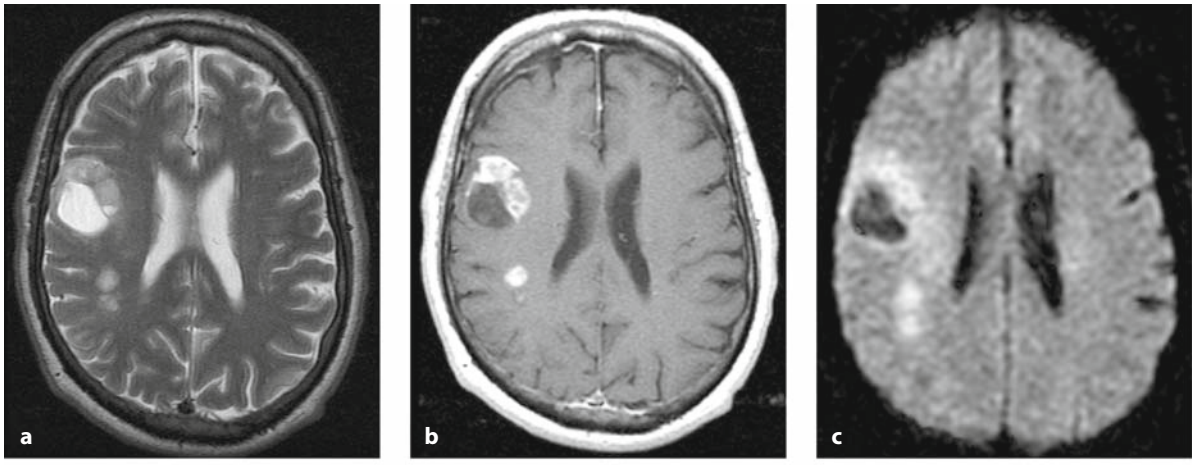

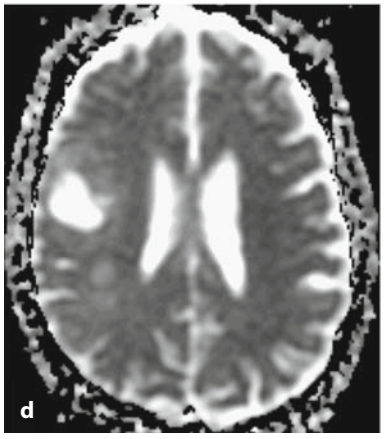

Figure 13.19 a–d

Gliosarcoma (de novo). A 74 year-old man presenting with a focal motor seizure. **a** T2-weighted image shows a cystic/necrotic tumor in the right frontal lobe. **b** On gadolinium-enhanced T1-weighted image, the tumor shows peripheral and irregular solid enhancement. A solid part is attached to a dural surface. There is another smaller enhancing nodule posterior to this mass. **c**, **d** On DW imaging, the solid part of the tumor shows increased signal intensity with mildly elevated ADC

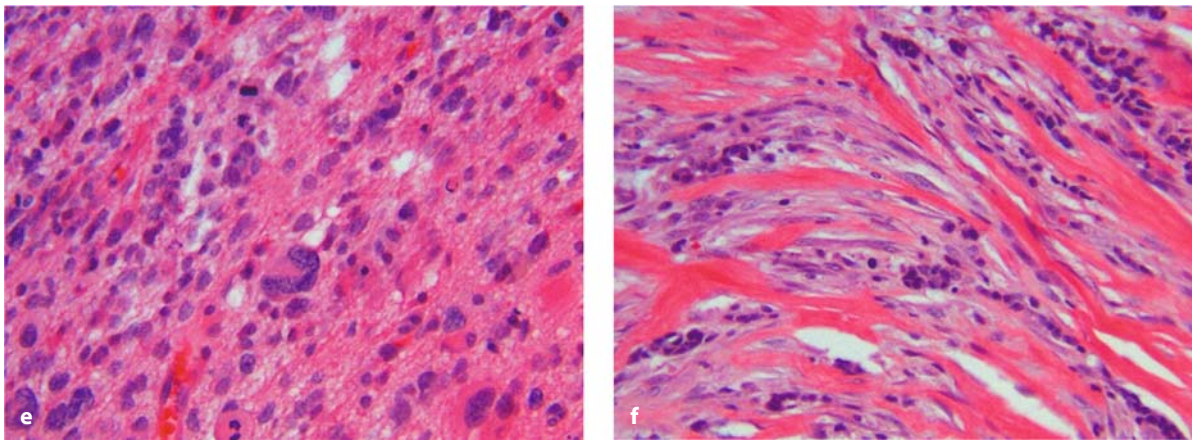

Figure 13.19 e, f

The tumor has a biphasic histologic pattern with areas displaying astrocytic (**e**) and sarcomatous (**f**) differentiation. (Courtesy of Oka M MD, University of Rochester Medical Center, USA)

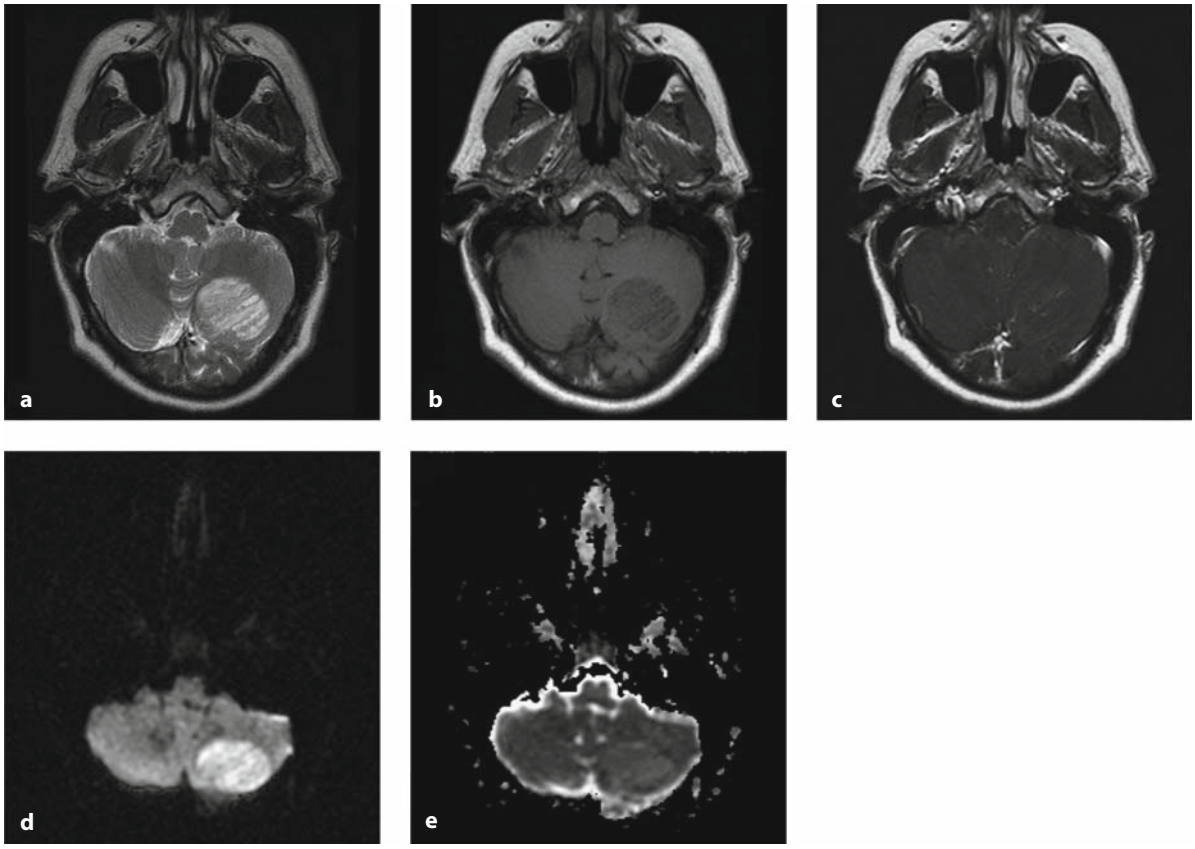

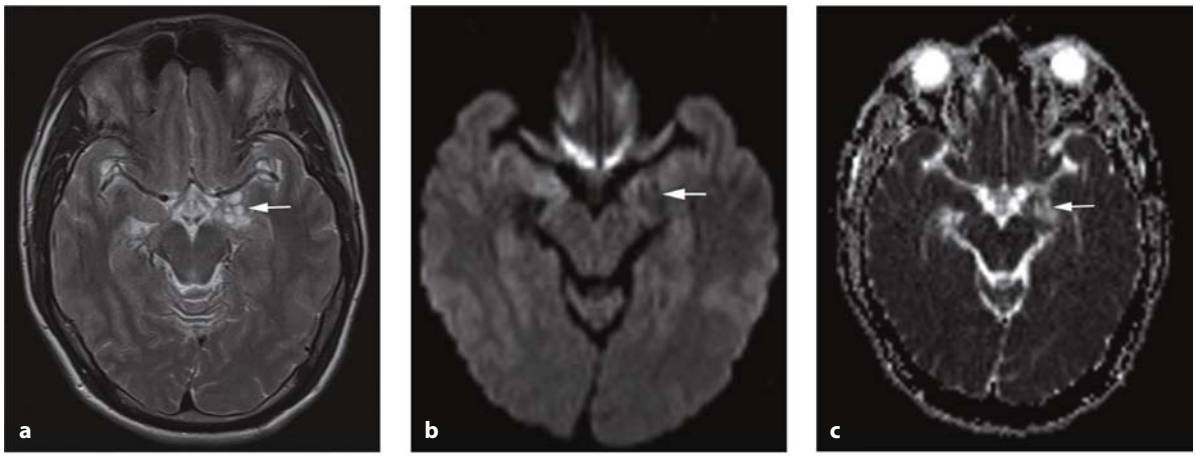

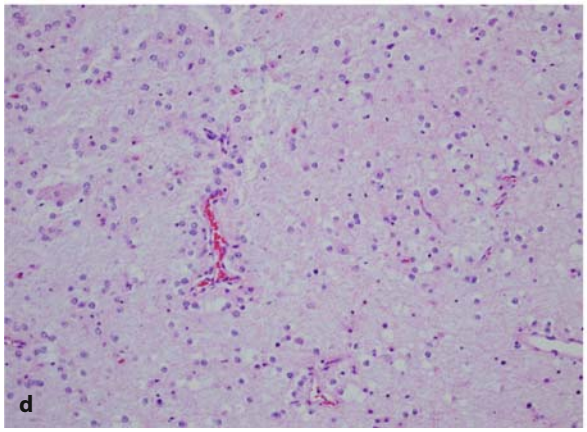

Figure 13.21 a–d

Dysembryoplastic neuroepithelial tumor in 32-year-old man with seizures. **a** T2-weighted image shows multicystic lesions in the medial temporal lobe with no edema (*arrow*). **b**, **c** DW imaging shows hypointense lesions with high ADC values (1.87-2.34×10^{-3} mm^2/s) (*arrow*). **d** Pathology shows oligodendroglial–like cells, thin vessels, scattered neurons, and myxoid matrix

13.2.4 Gliosarcoma

Gliosarcoma is a subtype of GBM characterized by neoplastic glial cells and sarcomatous components. It is rare (1.8-8.0 % of GBMs, M>F). The age distribution and survival characteristics of gliosarcomas are similar to typical GBMs. The exact origin of the sarcoma cells in gliosarcomas remains obscure. Macroscopically, gliosarcomas tend to have a hard consistency and are usually well-delineated from the surrounding tissue. In contrast, the typical GBM usually infiltrates surrounding white and gray matter. Gliosarcomas can either arise de novo (Fig. 13.19) or secondary to irradiation of GBM or anaplastic gliomas. Dwyer et al. reported that gliosarcomas tend to abut a dural surface but they may be indistinguishable from the typical GBM on MR imaging including DW imaging [48].

Figure 13.20 a–e

Lhermitte-Duclos disease in a 48-year-old woman. **a**, **b** T1- and T2-wighted images show a well-circumscribed mass with a striated pattern. **c** Gadolinium-enhanced T1-weighted image shows minimal vascular enhancement in the mass. **d**, **e** DW imaging shows a hyperintense mass associated with slightly increased ADC that may reflect an increased number and size of ganglion cells replacing the granular and Purkinje cell layers. (Courtesy of Nakamura H MD, Kitanosono T MD, University of Rochester Medical Center, USA)

◂

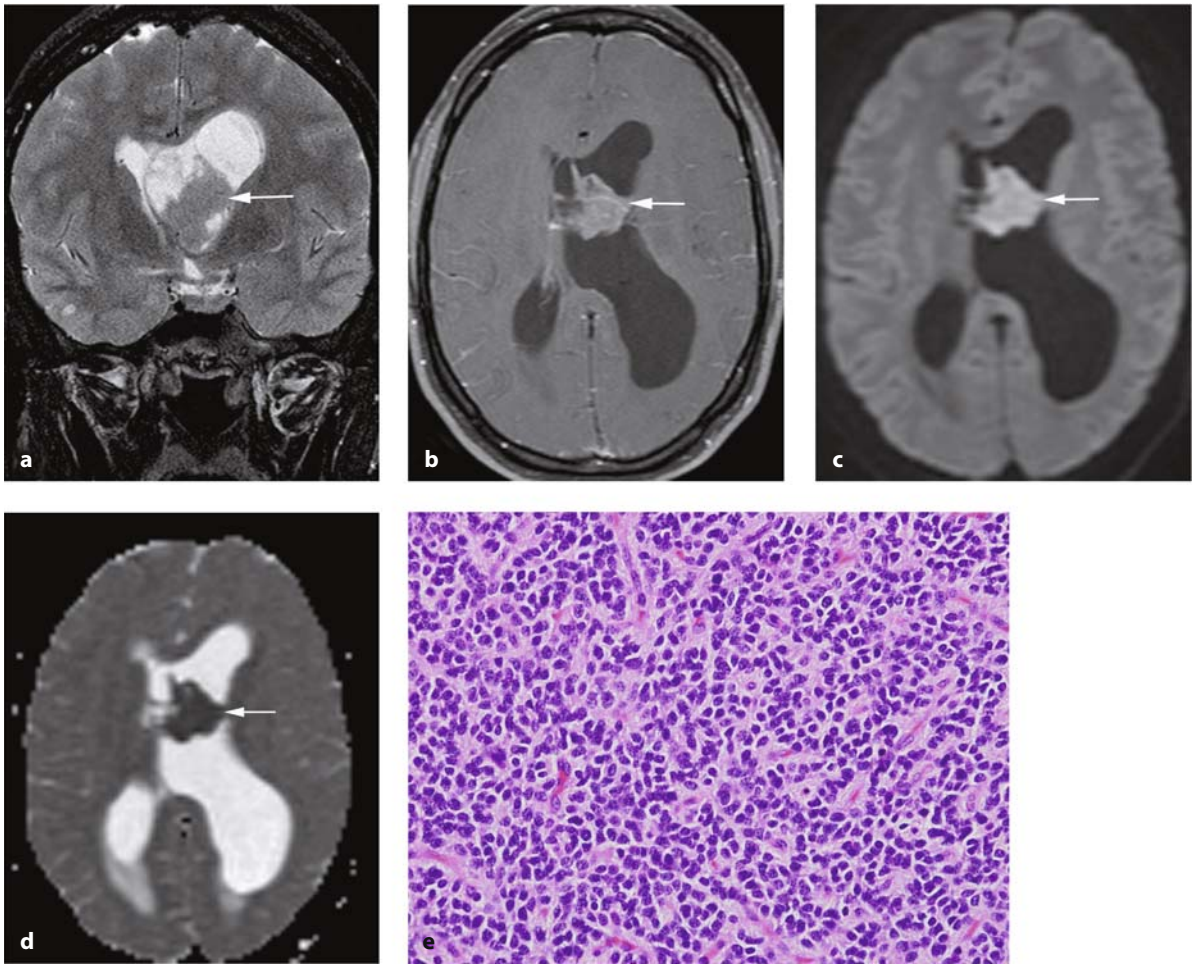

Figure 13.22 a–e

Central neurocytoma in 32-year-old woman. **a** Coronal T2-weighted image shows isointense intraventricular mass with cystic components involving the septum pellucidum (*arrow*). **b** Gadolinium-enhanced T1-weighted image with fat saturation shows heterogeneous enhancement in the mass (*arrow*). **c**, **d** DW imaging shows a hyperintense mass associated with decreased ADC (0.54×10^{-3} mm^2/s) that may reflect the hypercellularity of the central neurocytoma (*arrow*). **e** Pathology shows hypercellularity composed of small well-differentiated neurons with uniform nuclei

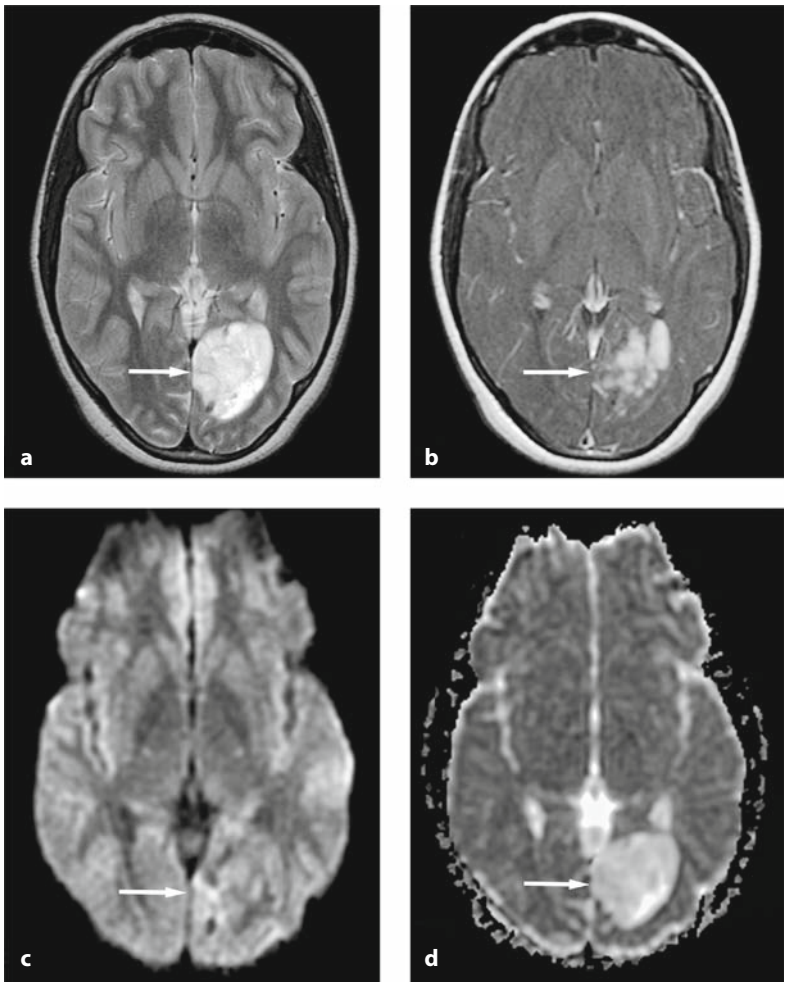

Figure 13.23 a–d

Ganglioglioma in a 12-year-old girl with seizures. **a** T2-weighted image shows a hyperintense lesion in the right occipital lobe (*arrow*). **b** Gadolinium-enhanced T1-weighted image shows heterogeneous enhancement (*arrow*). **c** DW image shows heterogeneous mild hyperintensity in the lesion (*arrow*). **d** ADC map shows hyperintensity in the lesion (0.98–1.35×10^{-3} mm^2/s; *arrow*)

13.2.5 Peritumoral Infiltration

The value of DW imaging for the delineation of peritumoral invasion in primary brain tumors is controversial. Some authors have suggested that ADC is useful to determine the extent of tumor invasion [4, 20], but most of the recent studies have shown that it is not possible to determine accurately the degree of peritumoral infiltration by DW imaging and ADC mapping [5, 11–13, 19, 20]. The poor delineation is probably due to the conjoined effects of T2 and ADC on DW images. For tumors that are biologically different, such as glioblastomas and meningiomas, it has been reported that ADC, T1 and fractional anisotropy of the enhancing tumor and its peritumoral edema are markedly different [16]. In GBM, tumor cells produce proteases and infiltrate into the extracellular space in the white matter. Tumor cells produce vascular endothelial growth factor (VEGF) resulting in increased vascular permeability and vasogenic edema. Tumor cells also release glutamate resulting in surrounding neurotoxicity that facilitates infiltration by the tumor cells. This may cause the cytotoxic edema in peritumoral areas and in white matter infiltrations (Figs. 13.12, 13.16, 13.17).

Diffusion-tensor (DT) imaging may distinguish presumed tumor-infiltrated edema from purely vasogenic edema [29, 39, 49]. However, reliable differentiation between infiltration and vasogenic edema is not yet possible on the basis of DT imaging [40]. FA values in peritumoral normal-appearing white matter are higher in meningiomas than in gliomas [39].

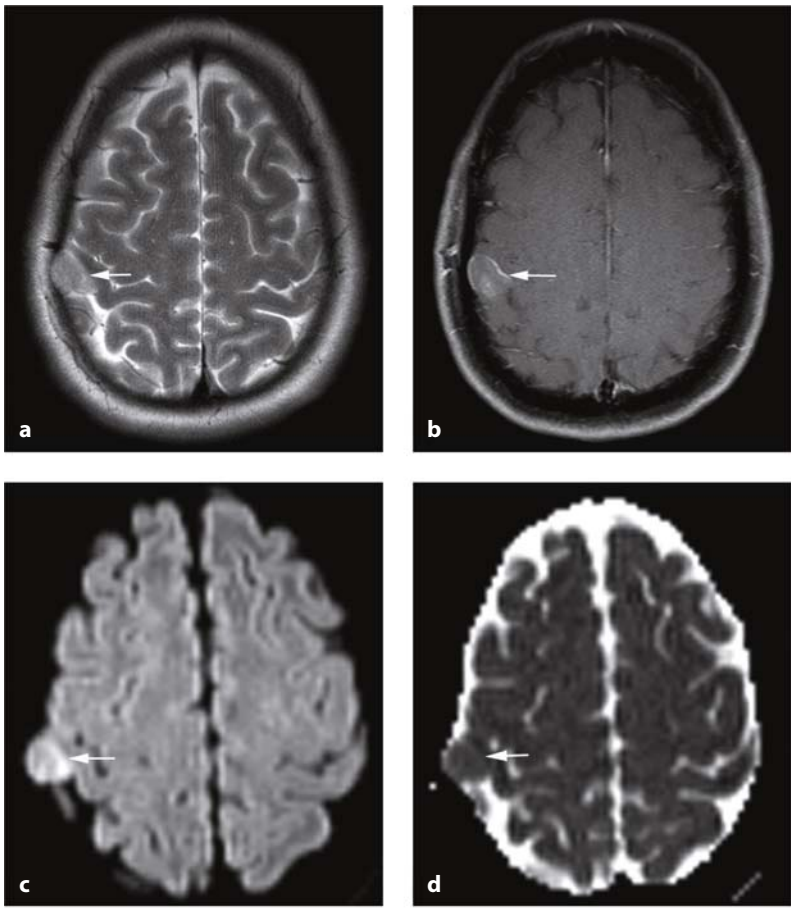

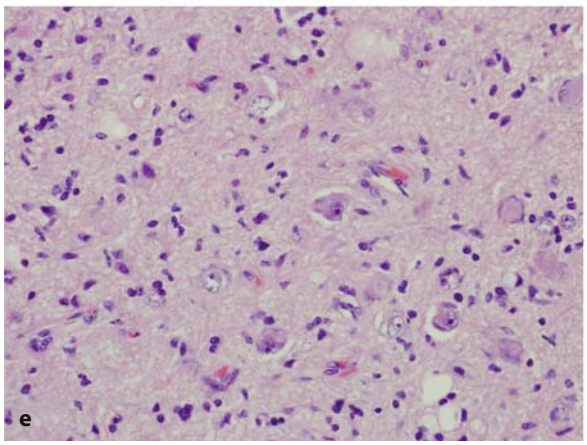

Figure 13.24 a–e

Ganglioglioma in a 31-year-old man with seizures. **a** T2-weighted image shows a well-defined mildly hyperintense lesion in the right parietal cortex (*arrow*). **b** Gadolinium-enhanced T1-weighted image with fat saturation shows heterogeneous enhancement (*arrow*). **c** DW image shows hyperintensity in the lesion. **d** ADC map shows isointensity in the lesion ($0.76–0.88\times10^{-3}mm^2/s$; *arrow*). **e** Pathology shows intermediate cellularity composed of ganglion cells and neoplastic astrocytes

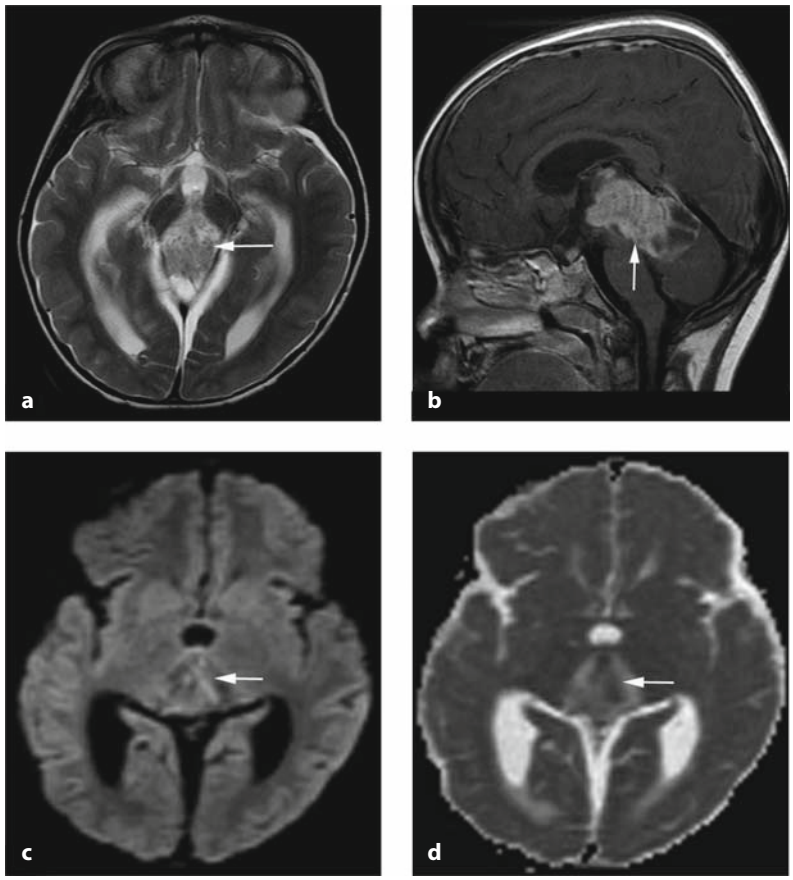

Figure 13.25 a–d

Pinealoblastoma in a 4-year-old boy. **a** T2-weighted image shows a mildly hyperintense lesion in the pineal region (*arrow*). **b** Gadolinium-enhanced sagittal T1-weighted image shows a heterogeneously enhancing mass with cystic components in the pineal region (*arrow*). **c** DW image shows isointensity or mild hyperintensity in the solid portion of the lesion (*arrow*). **d** ADC map shows isointensity or slight hyperintensity in the solid portion of the lesion ($0.74–1.05\times10^{-3}$ mm^2/s; *arrow*)

13.2.6 Treatment Response

DW imaging has been attempted to follow response to treatment and disease progress. For example, animal studies have shown a tendency to an increase in ADC during treatment, followed by a return to the pretreatment level during recurrent tumor growth [21–23]. There are no published human studies, but the preliminary reports have confirmed the observations in animals.

13.2.7 Choroid Plexus Tumors

(see Chap. 14, Figs. 14.13–14.15)

Choroid plexus papilloma (WHO grade 1) is a benign intraventricular papillary neoplasm derived from the choroid plexus epithelium and can be cured by surgery. Choroid plexus carcinoma (WHO grade 3) is a malignant neoplasm showing brisk mitotic activity, increased cellularity, blurring of the papillary pattern, necrosis, and frequent invasion of brain parenchyma. Choroid plexus carcinoma is more heterogeneously enhanced on MR images. DW imaging shows hyperintense with decreased ADC due to the hypercellularity. The WHO has introduced an additional entity with intermediate features, designated 'atypical choroid plexus papilloma' (WHO grade 2), which is primarily distinguished from choroid plexus papilloma by increased mitotic activity. Curative surgery is still possible but the probability of recurrence appears to be significantly higher.

13.3 Neuronal and Mixed Neuronal-Glial Tumors

Lhermitte-Duclos disease or dysplastic gangliocytoma of the cerebellum is a rare condition of uncertain pathogenesis with features of both benign neoplasm and malformation (distortion of normal cerebellar laminar cytoarchitecture). The histopathological

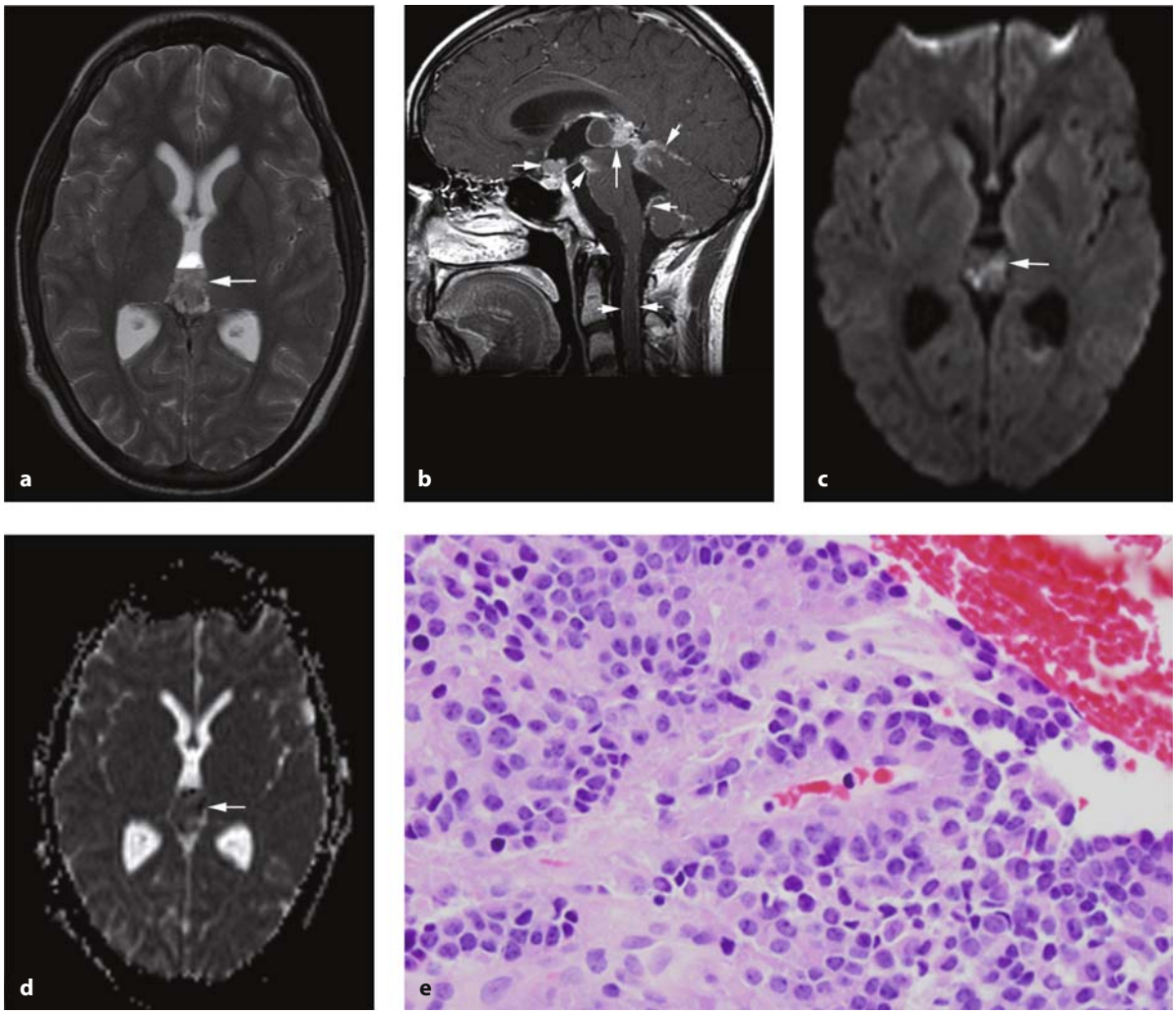

Figure 13.26 a–e

Papillary tumor of the pineal region in an 18-year-old male patient. **a** T2-weighted image shows a well-defined mildly hyperintense lesion with a cystic component and fluid-fluid level (*arrow*). **b** Gadolinium-enhanced sagittal T1-weighted image shows heterogeneously enhancing lesions in the pineal and suprasellar regions and leptomeningeal enhancement along the cerebellum and spinal cord due to tumor dissemination (*arrows*). **c** DW image shows a hyperintense lesion (*arrow*). **d** ADC map shows isointensity in the lesion ($0.70–0.85\times10^{-3}$ mm^2/s; *arrow*). **e** Micropathology specimen shows hypercellularity with a papillary growth pattern of plump epithelial-like cells and hemorrhage. Nuclei were uniform. (Courtesy of Sato TS, University of Iowa Carver College of Medicine, USA). (From [58])

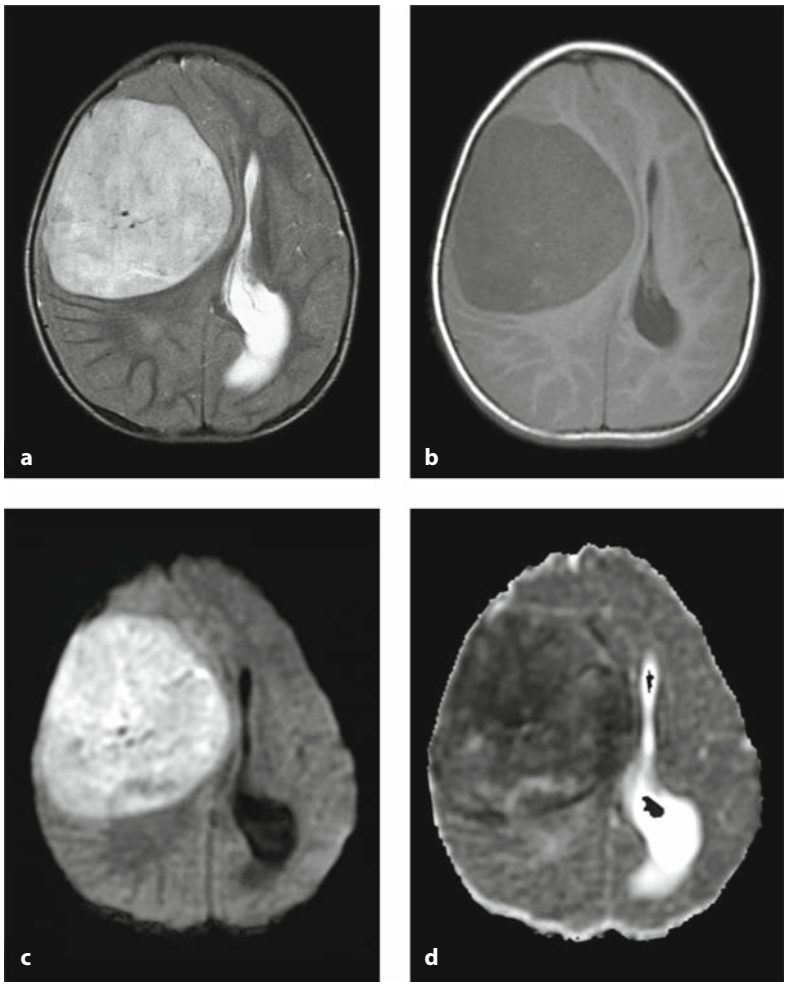

Figure 13.27 a–d

Primitive neuroectodermal tumor in a 20-month-old girl with lethargy and nausea. **a** T2-weighted image shows a well-demarcated and heterogeneous intense mass in the right frontal lobe. **b** T1-weighted image shows heterogeneous hypointensity in the lesion. **c** DW image shows hyperintensity. **d** ADC map shows heterogeneous hypointensity (0.54–0.74×10^{-3} mm^2/s) in the lesion, which may represent hypercellularity

characteristics include widening of molecular layers occupied by abnormal ganglion cells, absence of the Purkinje cell layer, and hypertrophy of the granular cell, with atrophy of the cerebellar white matter. It is associated with Cowden disease. MR imaging typically shows a well-circumscribed non-enhancing mass with a unique striated pattern (Fig. 13.20) [50, 51]. DW imaging shows a hyperintense lesion associated with slightly increased or decreased ADC, which reflects the hypercellularity; it also shows increased number and size of ganglion cells replacing the granular and Purkinje cell layers.

Dysembryoplastic neuroepithelial tumor (DNT) is classified as a mixed neuronal-glial tumor. DNT often has adjacent cortical involvement that is responsible for the epileptogenic activity. Oligodendroglial-like cells, thin vasculature, hanging neurons, and myxoid matrix are required features. In addition there may be oligodendroglial-like nodules, ganglioglioma, astrocytoma and cortical dysplasia. DNT is typically hypointense on T1-weighted images and hyperintense on T2-weighted images with no edema and absence of nodular enhancement [52]. DW imaging shows DNT as a hypointense lesion with significantly higher ADC values (>2×10^{-3} mm^2/s) compared with those of low-grade glial tumors (0.96×10^{-3} mm^2/s to 1.92×10^{-3} mm^2/s) (Fig. 13.21) [20, 53].

Central neurocytoma occurs predominantly in young adults and involves the lateral and third ventricles closely related to the septum pellucidum. Cystic components and calcifications are common. Microscopy shows a honeycomb architecture with small, uniform, round cells with central nuclei. MR imaging shows a well-defined heterogeneous T1 hypointense and T2 hyperintense mass with heterogeneous enhancement. DW imaging shows a hyperin-

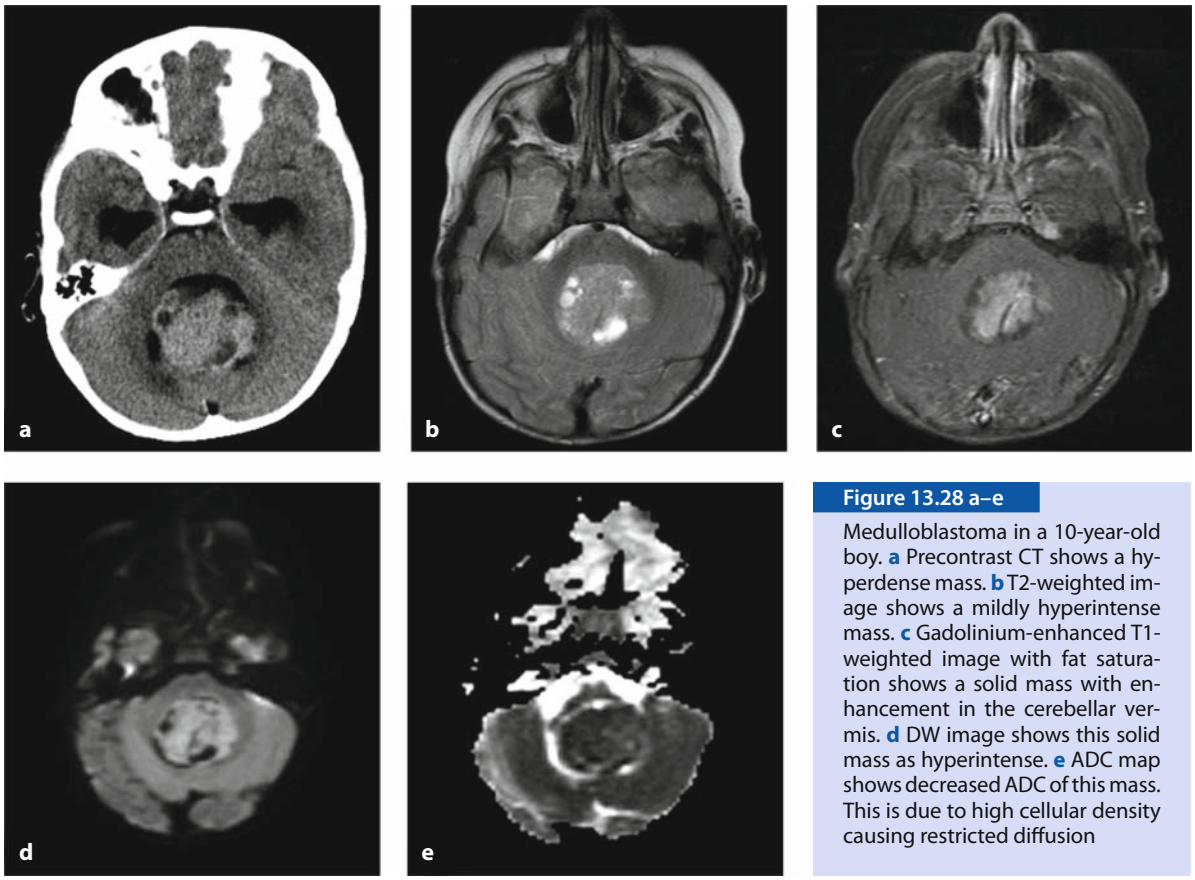

Figure 13.28 a–e

Medulloblastoma in a 10-year-old boy. **a** Precontrast CT shows a hyperdense mass. **b** T2-weighted image shows a mildly hyperintense mass. **c** Gadolinium-enhanced T1-weighted image with fat saturation shows a solid mass with enhancement in the cerebellar vermis. **d** DW image shows this solid mass as hyperintense. **e** ADC map shows decreased ADC of this mass. This is due to high cellular density causing restricted diffusion

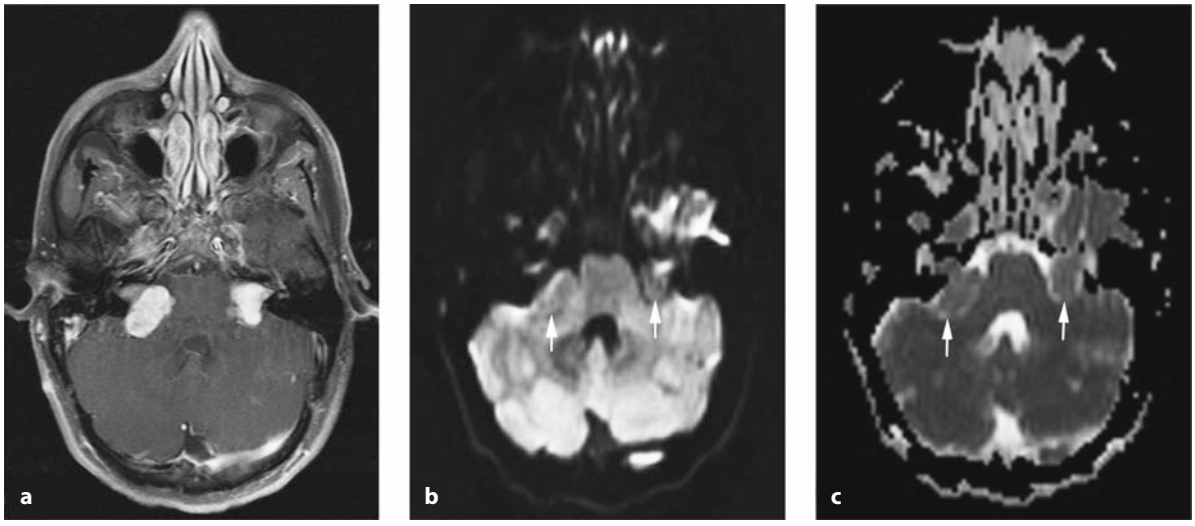

Figure 13.29 a–c

Bilateral vestibular schwannomas with neurofibromatosis type 2 in an 18-year-old male patient. **a** Gadolinium-enhanced T1-weighted image with fat saturation shows homogeneously enhancing masses in bilateral cerebellopontine angles. **b, c** DW image shows isointensity with increased ADCs ($0.96–1.22\times10^{-3}$ mm^2/s; *arrows*)

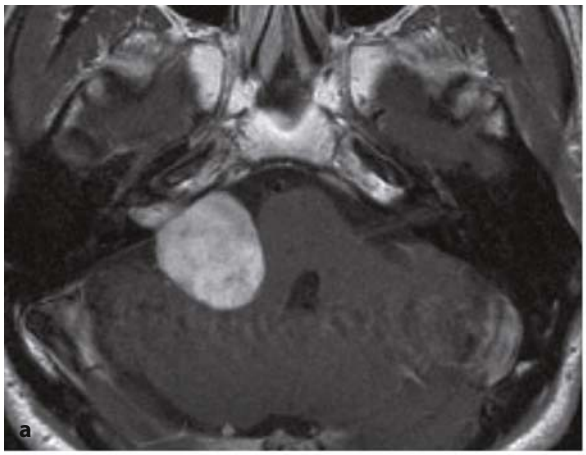

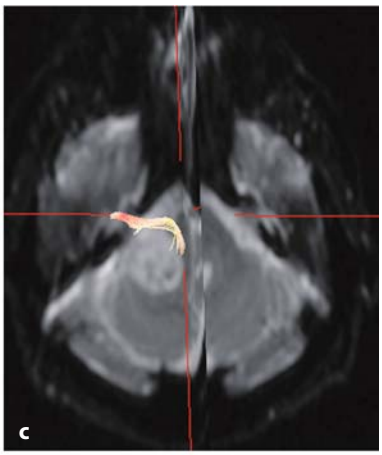

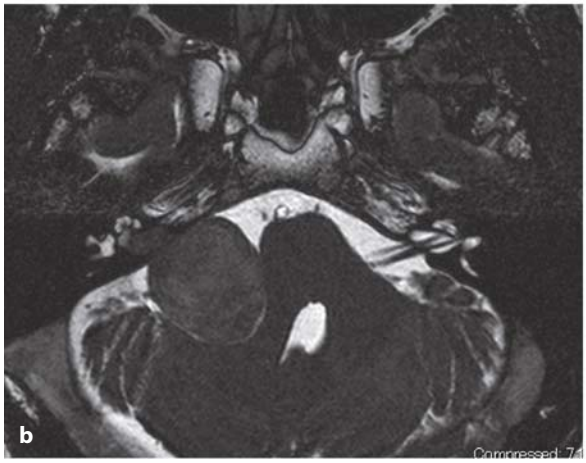

Figure 13.30 a–c

Vestibular schwannoma in a 39-year-old man. **a** Gadolinium-enhanced T1-weighted image shows a homogeneously enhancing mass in the right cerebellopontine angle and internal auditory canal. **b** CISS image cannot separate a hypointense tumor and the facial nerve. **c** DTI fiber tractography clearly shows the facial nerve located anterior to the vestibular schwannoma, which provides important preoperative information. (Courtesy of Taoka T MD, Nara Medical University, Japan)

tense lesion with lower ADC values (0.65-0.95×10^{-3} mm^2/s) compared with those of astrocytomas and nonastrocytic gliomas (Fig. 13.22) [53, 54]. The decreased ADC values probably reflect hypercellularity of the central neurocytoma.

Ganglioglioma is the most common tumor involving the temporal lobe. Histologically, it is a mixed tumor composed of relatively mature glial cells and ganglionic cells in varying proportions [55]. MR imaging shows a T1 hypointense and T2 hyperintense mass with or without cystic components. DW imaging shows a hyperintense mass with slightly decreased or increased ADC values, probably depending on the cellular components (Figs. 13.23, 13.24).

13.4 Tumors of Pineal Region

Three types of pineal region tumors are classified: pineocytomas, pineoblastoma, and papillary tumor of the pineal region. Increased ICP, hydrocephalus, papilledema, and Parinaud syndrome are common clinical symptoms. Pineoblastoma can be associated with congenital retinoblastoma, so-called trilateral retinoblastoma. Pineoblastomas tend to have a lobular pattern and occupy the quadrigeminal cistern [56]. T1-weighted imaging shows pinealoblastoma as hypointense with homogeneous or heterogeneous enhancement. DW imaging usually shows it as hyperintense associated with iso- or slightly decreased ADC, probably reflecting the cellularity (Fig. 13.25). Papillary tumors of the pineal region are well-circumscribed masses of the pineal region, commonly with a cystic component (Fig. 13.26). The proposed cell of origin is the ependymocyte located in the subcommissural organ. The prognosis of papillary tumors of the pineal region is usually worse and less sensitive to treatment than pineoblastoma. T1-hyperintensity in the tumor has been reported due to protein, glycoprotein, or other T1-shortening substances produced by tumor cells [57, 58].

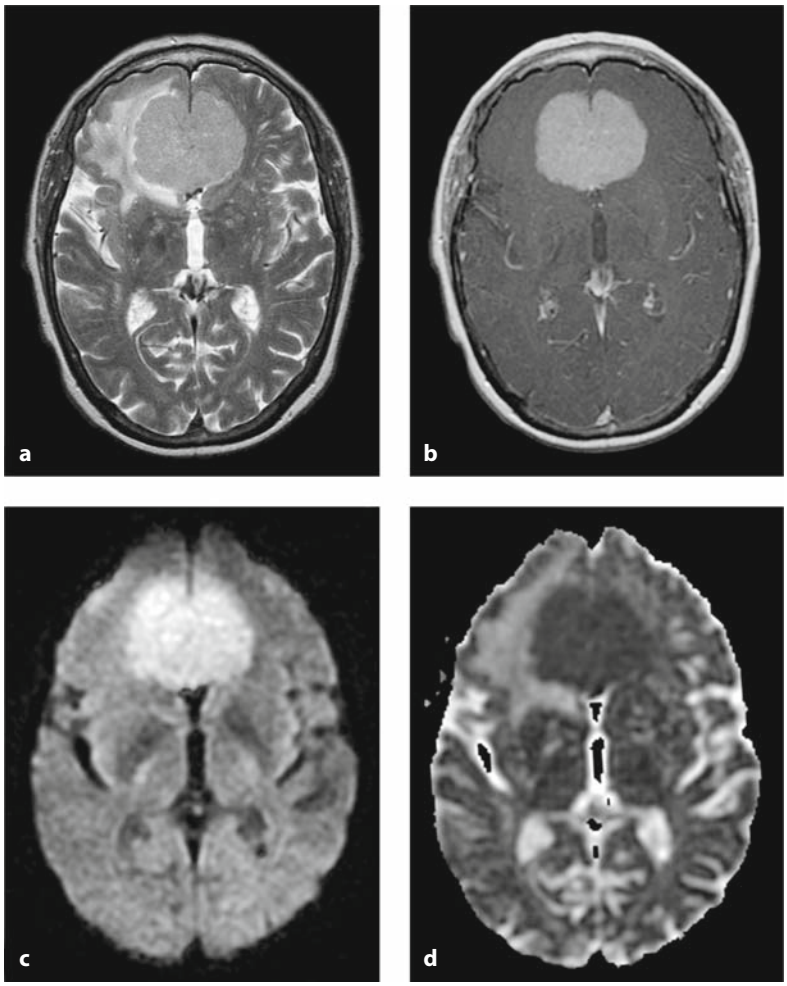

Figure 13.31 a–d

Benign meningioma (meningothelial meningioma) in a 72-year-old woman with a visual disturbance. **a** T2-weighted image shows a slightly hyperintense mass near the frontal aspect of the falx. **b** Gadolinium-enhanced T1-weighted image shows homogeneous enhancement. **c** DW image shows hyperintensity in the lesion. **d** ADC map shows mild hypointensity ($0.73–0.78\times10^{-3}$ mm^2/s)

13.5 Embryonal Tumors – Medulloblastoma and Primitive Neuroectodermal Tumors

Primitive neuroectodermal tumors (Fig. 13.27) are a group of histologically similar tumors that occur mostly in children. They include embryonal, largely undifferentiated tumors, such as medulloblastoma (Fig. 13.28), neuroblastoma, pineoblastoma (Fig. 13.25), ependymoblastoma, medulloepithelioma, and atypical teratoid-rhabdoid tumor (Chap. 14, Fig. 14.20). These tumors have a high cellular density and are typically hyperintense on DW images, with decreased ADC [53, 58–61]. The hyperintensity on DW images and decreased ADC is caused by their dense cellularity and high nuclear to cytoplasmic ratio. Atypical teratoid-rhabdoid tumor is another hypercellular CNS tumor in children and has more malignant biological behavior and is less sensitive to therapy [61]. Cerebellopontine angle involvement and intratumoral hemorrhage are more common than in medulloblastoma. Atypical teratoid-rhabdoid tumor is hyperintense on DW images with decreased ADC values, similar to medulloblastoma ($0.47\text{-}0.83\times10^{-3}$ mm^2/s) [53, 61].

13.6 Tumors of Cranial Nerves

There are three types of nerve sheath tumors: schwannoma, neurofibroma, and malignant nerve sheath tumor. Schwannoma comprises approximately 8% of all intracranial tumors. Cystic degeneration

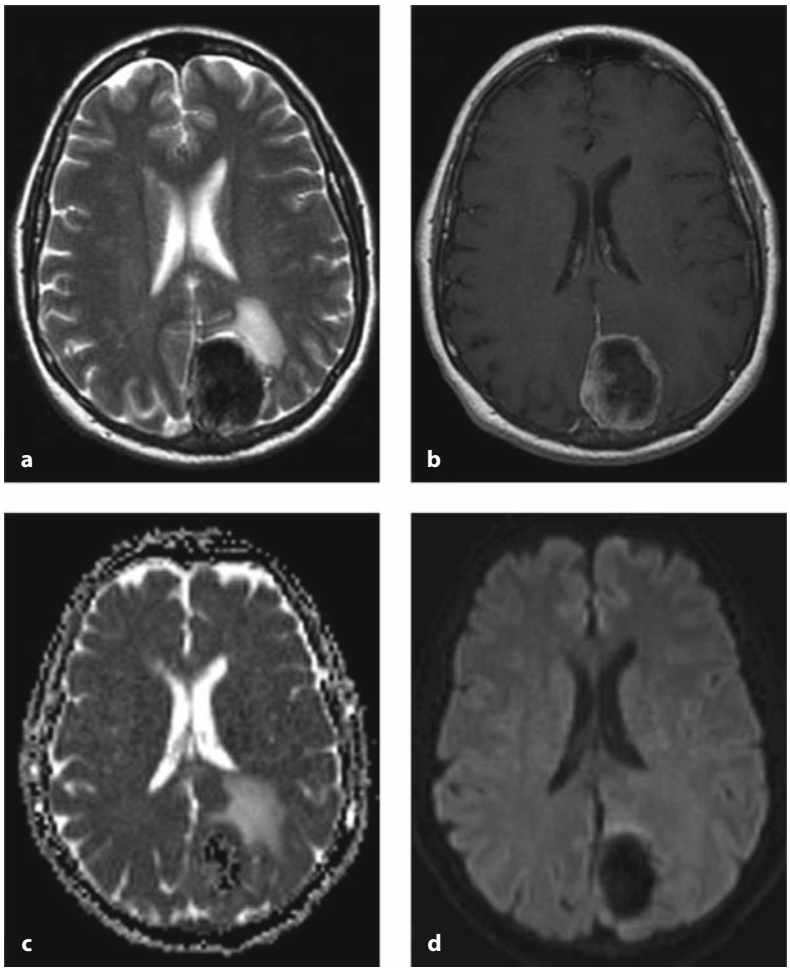

Figure 13.32 a–d

Meningioma (psammomatous meningioma) in a 56-year-old woman. **a** T2-weighted image shows a hypointense mass in the left medial occipital region with vasogenic edema. **b** Gadolinium-enhanced T1-weighted image shows a hypointense mass with peripheral enhancement. **c** DW image shows hypointensity in the lesion. **d** ADC map is not calculated accurately due to susceptibility artifacts from the dense calcification

is common (5.7-24%), and may be accompanied by hemorrhage (5%). Histologically, schwannoma is composed of two types of tissues: Antoni type A is more cellular with palisading nuclei creating membrane-like structures, while Antoni type B is less cellular associated with degenerative changes and hemorrhage.

Vestibular schwannoma is the most common intracranial Schwann cell tumor. Bilateral vestibular schwannomas are one of the diagnostic criteria for neurofibromatosis type 2. DW imaging can be useful for the differential diagnosis of cerebellopontine angle tumors [62]. The ADC values of schwannoma are significantly higher than those of meningioma [53]. The higher ADC values in schwannoma probably reflect the lower cellularity (Fig. 13.29). Identifying the compressed facial nerve in cases of vestibular schwannoma is important so as to avoid complications during surgical removal. Diffusion tensor fiber tractography is useful for identifying the facial nerve displacement preoperatively (Fig. 13.30) [63].

13.7 Tumors of the Meningothelial Cells – Meningiomas

Meningioma is the most common extraaxial brain tumor, comprising 15% of all intracranial tumors. Histologically, 10% are atypical or malignant. Tumor recurrence is 30%–40% in atypical/malignant meningioma, while it is 7%–20% in typical meningioma. There are 15 histologic subtypes identified in the WHO classification: nine are considered grade 1 (meningothelial, fibrous, transitional, psammomatous, angiomatous,

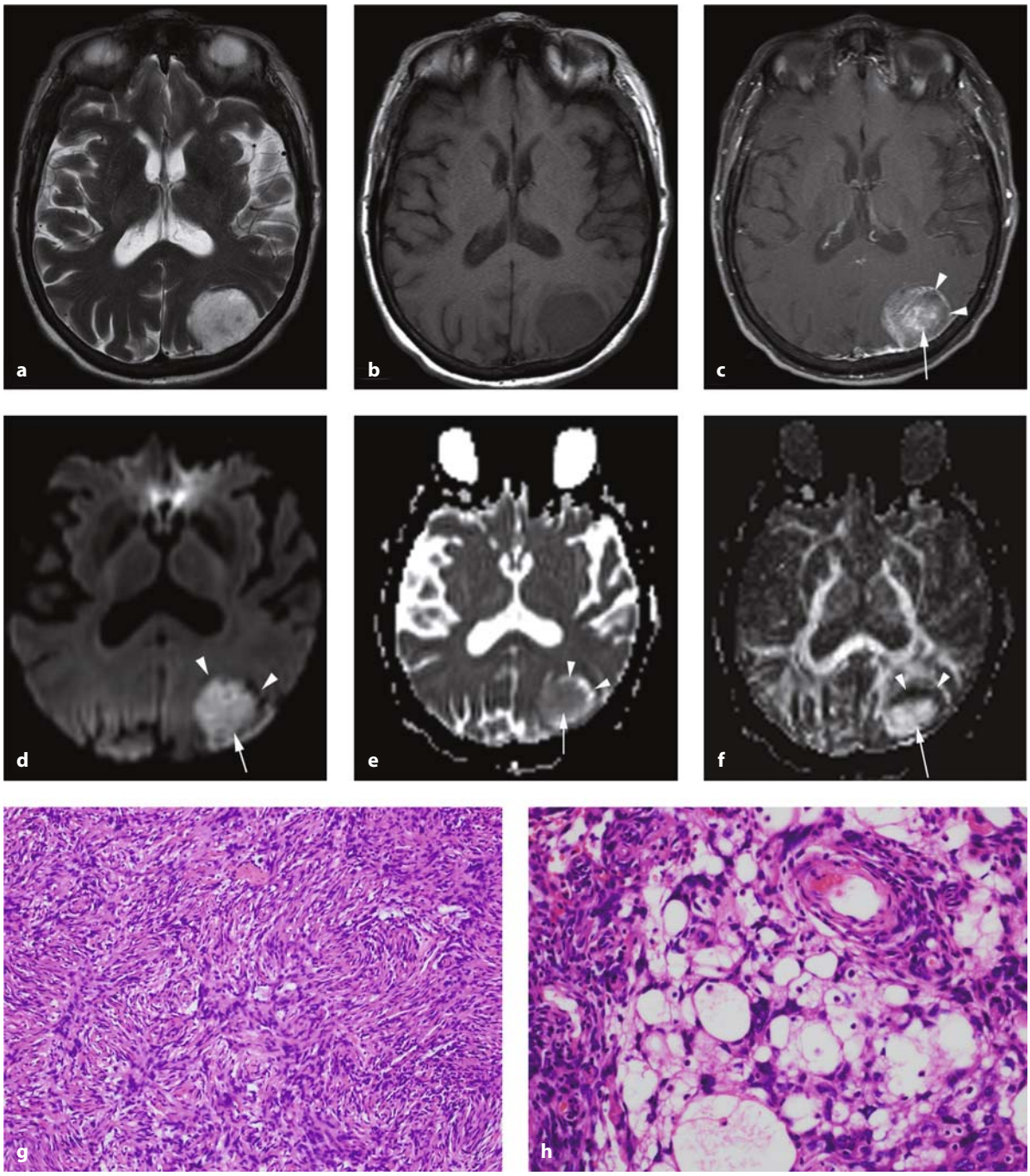

Figure 13.33 a–h

Meningioma (microcystic meningioma) in a 68-year-old woman. **a** T2-weighted image shows a hyperintense mass in the left occipital region with no vasogenic edema. **b** T1-weighted image shows a hypointense mass in the left occipital region. **c** Gadolinium-enhanced T1-weighted image with fat saturation shows a central heterogeneously enhancing mass (*arrow*) and peripheral microcystic components (*arrowheads*). **d** DW image shows a hypointense mass (*arrow*) with peripheral hypointensity (*arrowheads*). **e** ADC map shows iso- or slight hypointensity centrally (*arrow*) with peripheral hyperintensity in the microcystic components (*arrowheads*). **f** FA map shows increased anisotropy in the central solid portion (*arrow*) and decreased anisotropy in the peripheral microcystic areas (*arrowheads*). **g** Pathology of the central portion shows spindle-shaped tumor cells. **h** Pathology of the peripheral portion shows microcystic components

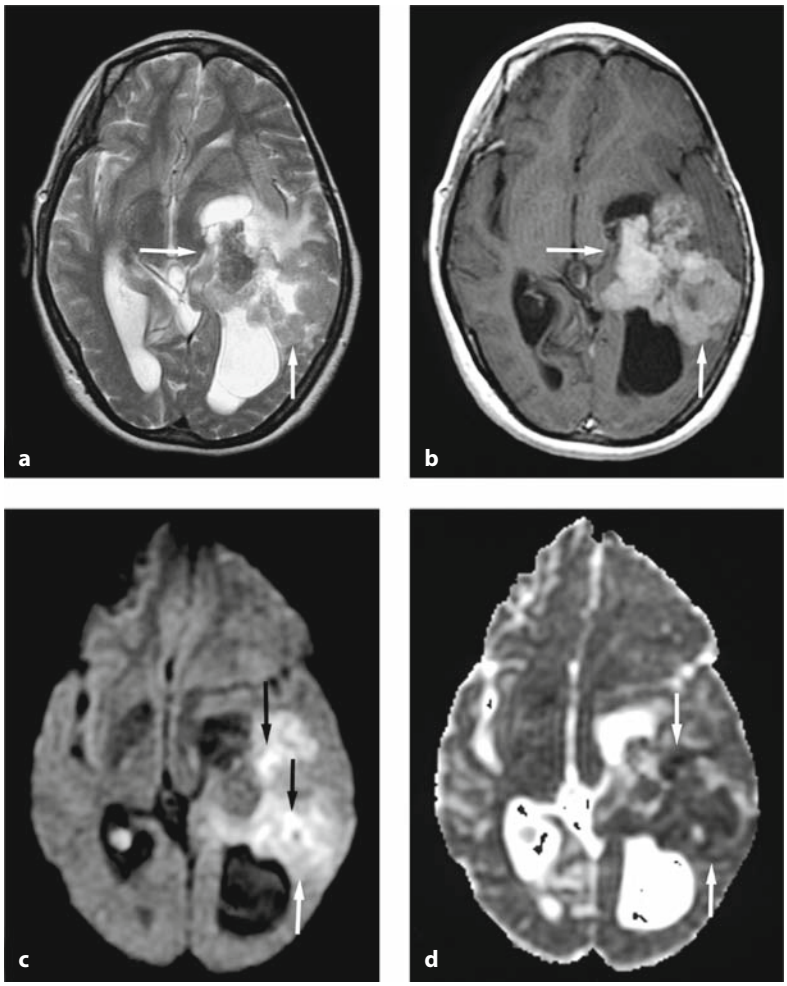

Figure 13.34 a–d

Atypical meningioma in a 45-year-old female patient with headache. **a** T2-weighted image shows a heterogeneous intense mass in the temporal lobe (*arrows*). **b** Gadolinium-enhanced T1-weighted image shows heterogeneous enhancement (*arrows*). **c** DW image shows heterogeneous hyperintensity (*arrows*). **d** ADC map shows hypointensity, especially in the right side of the mass (0.51×10^{-3} mm^2/s; *arrows*)

microcystic, secretory, lymphoplasmacyte-rich, metaplastic), three as grade 2 (chordoid, clear cell, atypical), and three as grade 3 (papillary, rhabdoid, anaplastic). Cysts associated with meningioma are seen in 4%-10% of all meningiomas [64]. Peritumoral edema is seen in 40%-60% of cases, presumably related to vasogenic edema substances such as vascular endothelial growth factor or vascular permeability factor with intratumoral congestion [65, 66].

Typical MR imaging findings, including extraaxial T1 and T2 isointense solid mass with homogeneous enhancement and dural tail sign, are seen in 85% of cases. The signal characteristics of meningiomas on DW images are variable [12, 13, 19, 67, 68]. Most benign meningiomas are isointense on DW images and ADC maps, but some are slightly hyperintense on both DW images and ADC maps (Fig. 13.31). In meningioma, mixed histological subtypes are often observed in the same tumor. Fibroblastic, transitional, and calcified psammomatous meningioma can be hypointense on both T2-weighted [69] and DW images (Fig. 13.32). FA values in fibroblastic-type meningioma or fibrous components in meningiomas are higher than other histological subtypes presumably due to the fascicular arrangement of long spindle-shaped tumor cells (Fig. 13.33) [70]. Microcystic meningiomas or components can be hypodense on CT images, hypointense on T1-weighted images, and hyperintense on T2-weighted images [71]. Microcystic meningiomas can have high ADC values (Fig. 13.33).

Malignant or atypical meningioma usually has increased signal intensity on DW images and lower intratumoral ADC values than typical meningioma due to the higher tumor cellularity [13, 19, 53, 67, 72]. However, other factors, such as multifocal areas of necrosis, numerous abnormal mitoses and cytologic

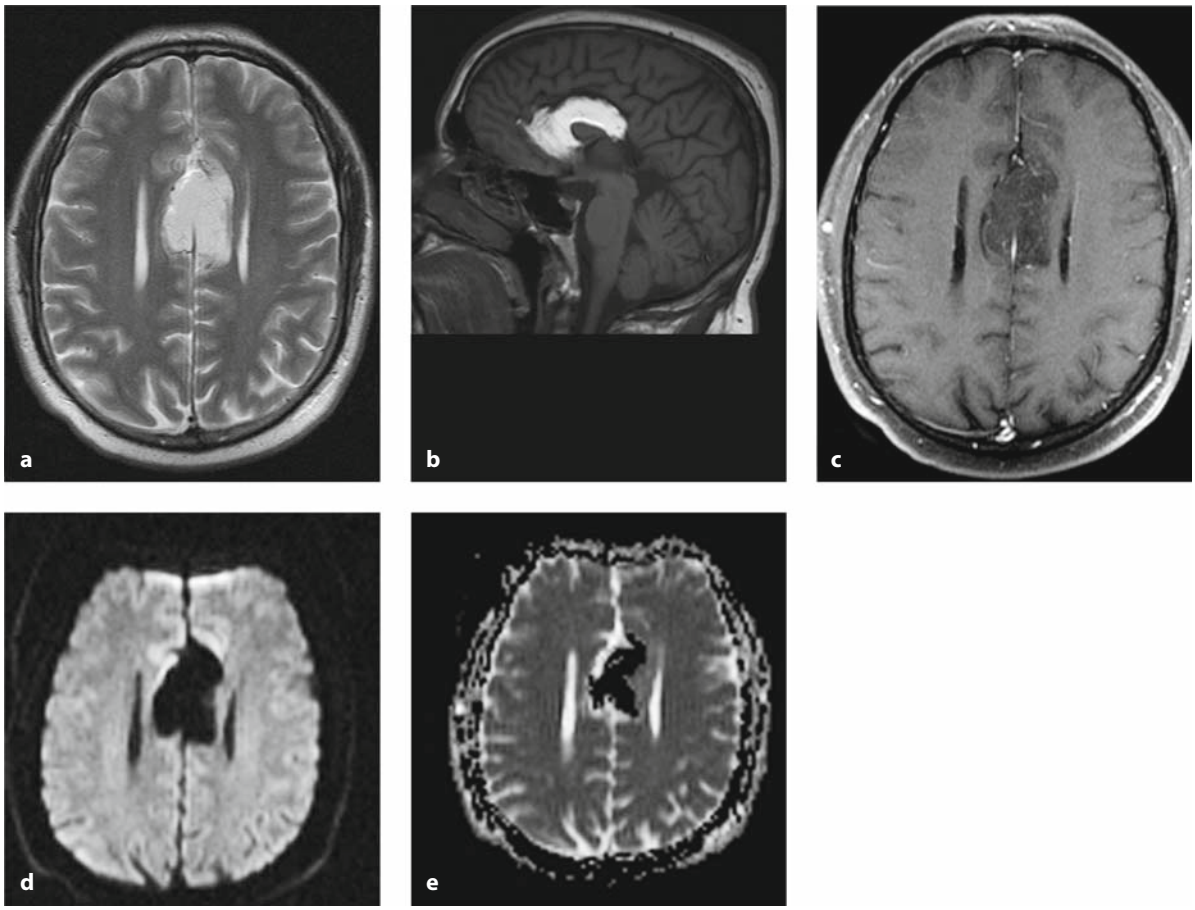

Figure 13.35 a–e

Lipoma in a 43-year-old woman. **a** T2-weighted image shows a hyperintense mass in the corpus callosum. **b** Sagittal T1-weighted image shows a well-demarcated very hyperintense mass along the corpus callosum. **c** Gadolinium-enhanced T1-weighted image with fat saturation shows a suppression of T1 hyperintensity of fat signals with no enhancement. **d** DW image shows the lipoma as hypointense due to the inherent fat saturation. **e** Accurate calculation of ADC values is difficult because of the fat saturation on both the DW and b0 images

pleomorphism may also cause the high DW signal in atypical and malignant meningiomas (Fig. 13.34). The ADC values are similar in most of the histological subtypes [13, 53].

13.8 Mesenchymal Tumors

Lipoma is a congenital abnormality associated with persistence of the meninx primitiva. Locations of lipoma include the corpus callosum, pericallosal interhemispheric fissure, quadrigeminal plate, suprasellar cistern, cerebellopontine cistern, sylvian fissure, cerebellar vermis, and lamina terminalis. Lipoma is hyperintense on T1-weighted images, and is suppressed on fat-saturation images. DW imaging uses the same chemical fat-saturation technique as fat-saturated T1-weighted images (Fig. 13.35).

Hemangiopericytoma, previously considered as "angioblastic" meningioma, is now a distinct clinicopathologic entity and a rare aggressive neoplasm derived from vascular pericytes. The peak incidence is at 30–50 years. Calcifications and hyperostosis are

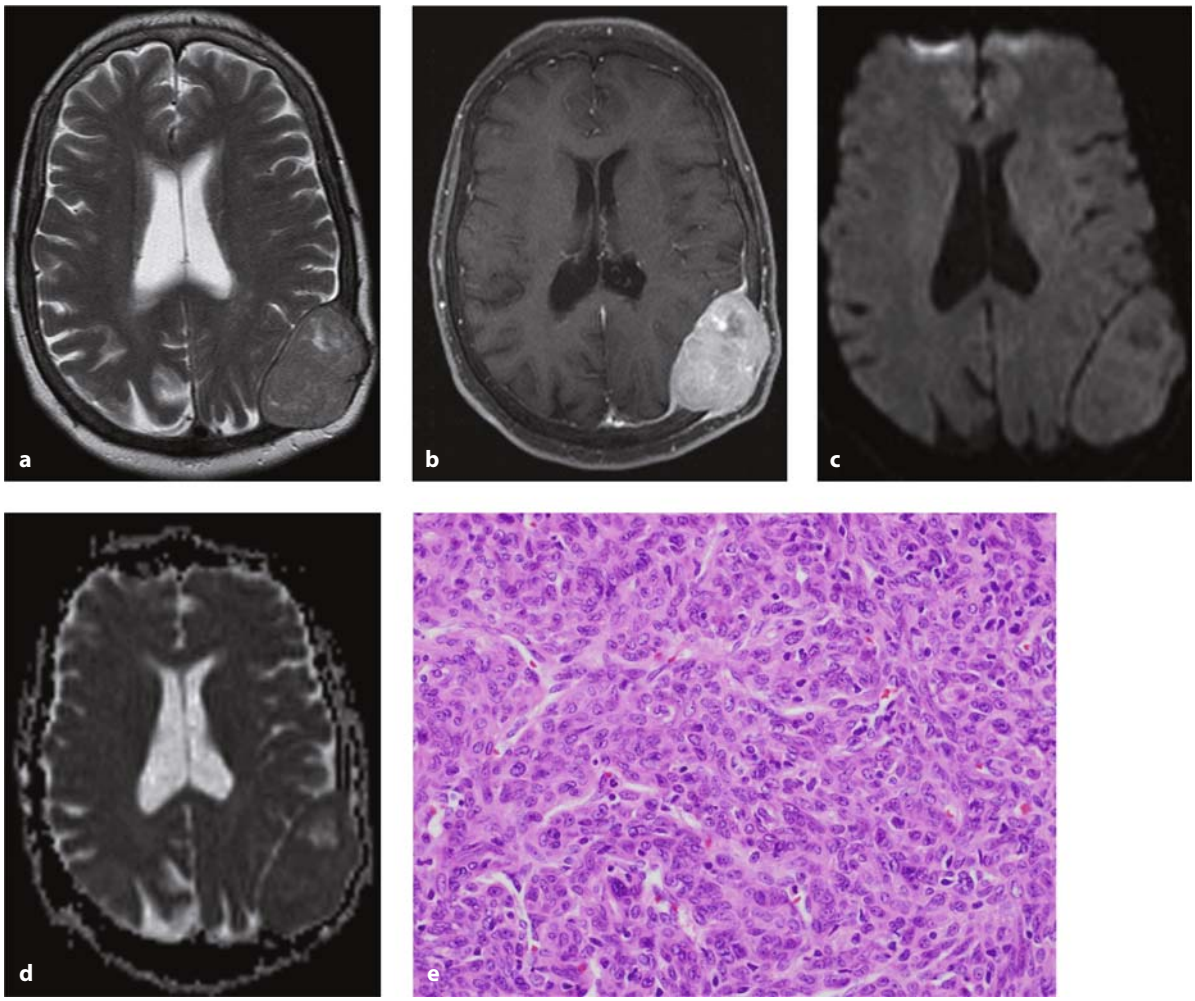

Figure 13.36 a–e

Hemangiopericytoma in a 50-year-old man. **a** T2-weighted image shows an extraaxial hyperintense mass involving the left parietal skull and scalp. **b** Gadolinium-enhanced T1-weighted image with fat saturation shows homogeneous enhancement with the dural tail. No adjacent hyperostosis or sclerotic changes are noted. **c** DW image shows mild hyperintensity. **d** ADC map shows decreased ADC of this mass. **e** Micropathology specimen shows hypercellularity, dense interstitium, and dilated thin-walled vessels

not common. MR and DW signal characteristics are similar to meningioma (Fig. 13.36).

Hemangioblastoma is the most common infratentorial neoplasm in adults. It is associated with von-Hippel-Lindau disease in 20% of cases. Histologically it is characterized by a network of capillary-like channels, separated by trabeculae or islands of stromal cells. Intratumoral hemorrhage and cyst formation are common. Vascular flow voids in and around the tumor can be a clue to the diagnosis. DW imaging usually shows the solid portion of hemangioblastoma as low signal with increased ADC, presumably due to rich vascular spaces (Fig. 13.37) [73]. Metastatic renal cell carcinoma is an important diffrential diagnosis

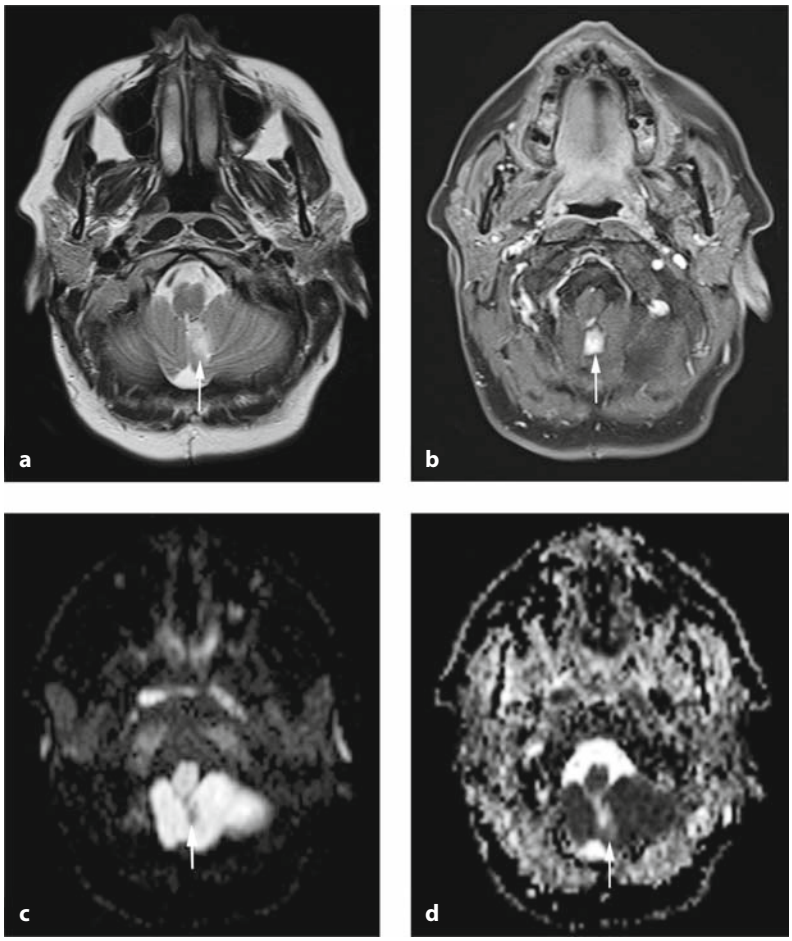

Figure 13.37 a–d

Hemangioblastoma in a 41-year-old woman. **a** T2-weighted image shows a hyperintense mass in the cerebellar vermis (*arrow*). **b** Gadolinium-enhanced T1-weighted image with fat saturation shows intense homogeneous enhancement (*arrow*). **c** DW image shows hyperintensity of the lesion (*arrow*). **d** ADC map shows increased ADC of the lesion presumably due to rich vascular spaces (*arrow*)

which is usually hyperintense on DW images with lower ADC values.

13.9 Lymphoma and Hematopoietic Neoplasm

Primary lymphomas of the central nervous system are rare malignant tumors, accounting for less than 1% of all brain tumors. However, the incidence has been increasing subsequent to the spread of the acquired immunodeficiency syndrome [19, 74–77]. A majority of lymphomas are iso- or hypointense on T2-weighted images [19]. Most lymphomas show homogeneous enhancement in immunocompetent patients, but in immunosuppressed patients a rim enhancement is a more common finding [19, 74–76]. The enhancing components of lymphomas are generally hyperintense on DW images (Figs. 13.38, 13.39). [17, 19, 77]. The ADC of lymphomas is often lower than that

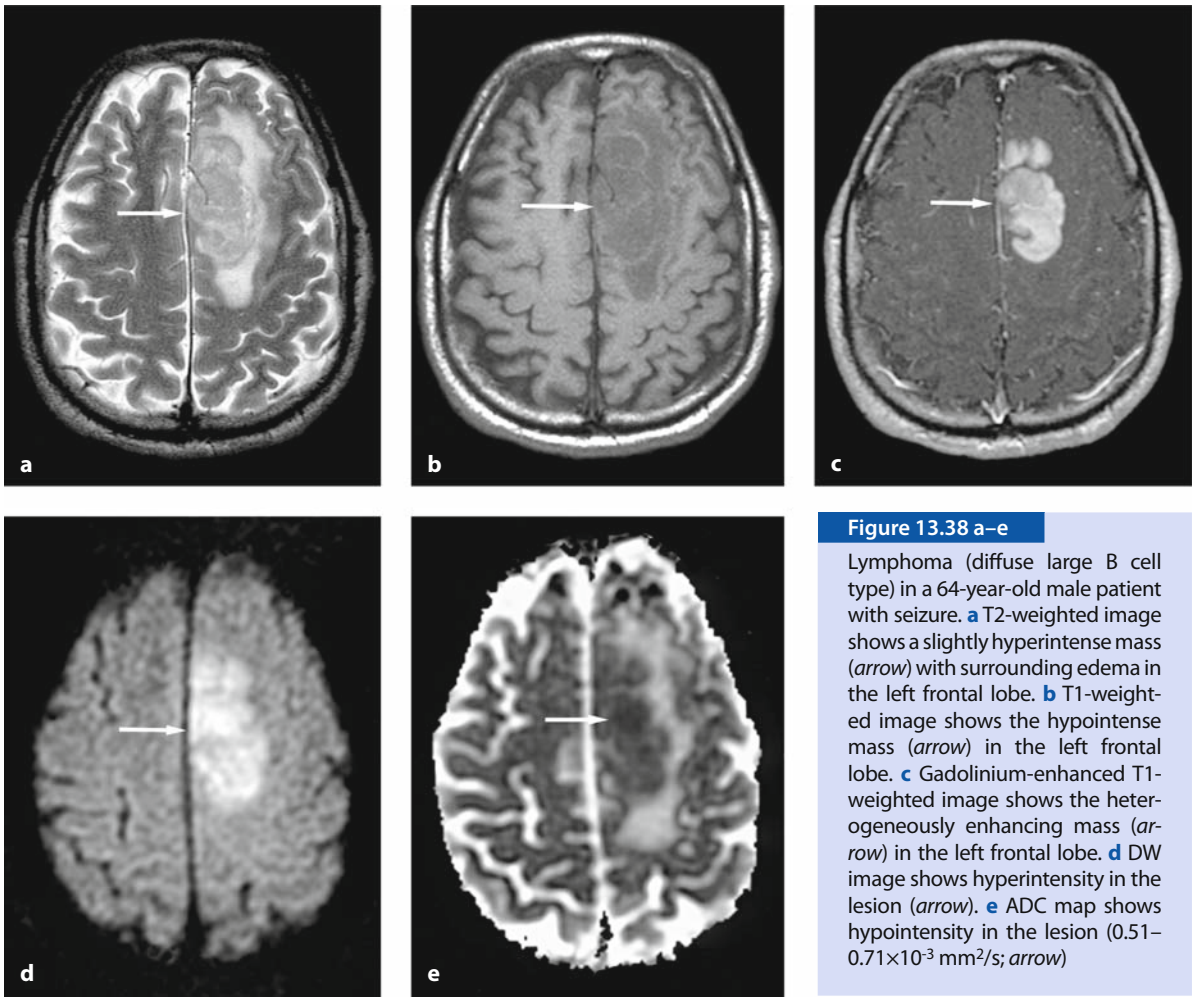

Figure 13.38 a–e

Lymphoma (diffuse large B cell type) in a 64-year-old male patient with seizure. **a** T2-weighted image shows a slightly hyperintense mass (*arrow*) with surrounding edema in the left frontal lobe. **b** T1-weighted image shows the hypointense mass (*arrow*) in the left frontal lobe. **c** Gadolinium-enhanced T1-weighted image shows the heterogeneously enhancing mass (*arrow*) in the left frontal lobe. **d** DW image shows hyperintensity in the lesion (*arrow*). **e** ADC map shows hypointensity in the lesion (0.51–0.71×10^{-3} mm^2/s; *arrow*)

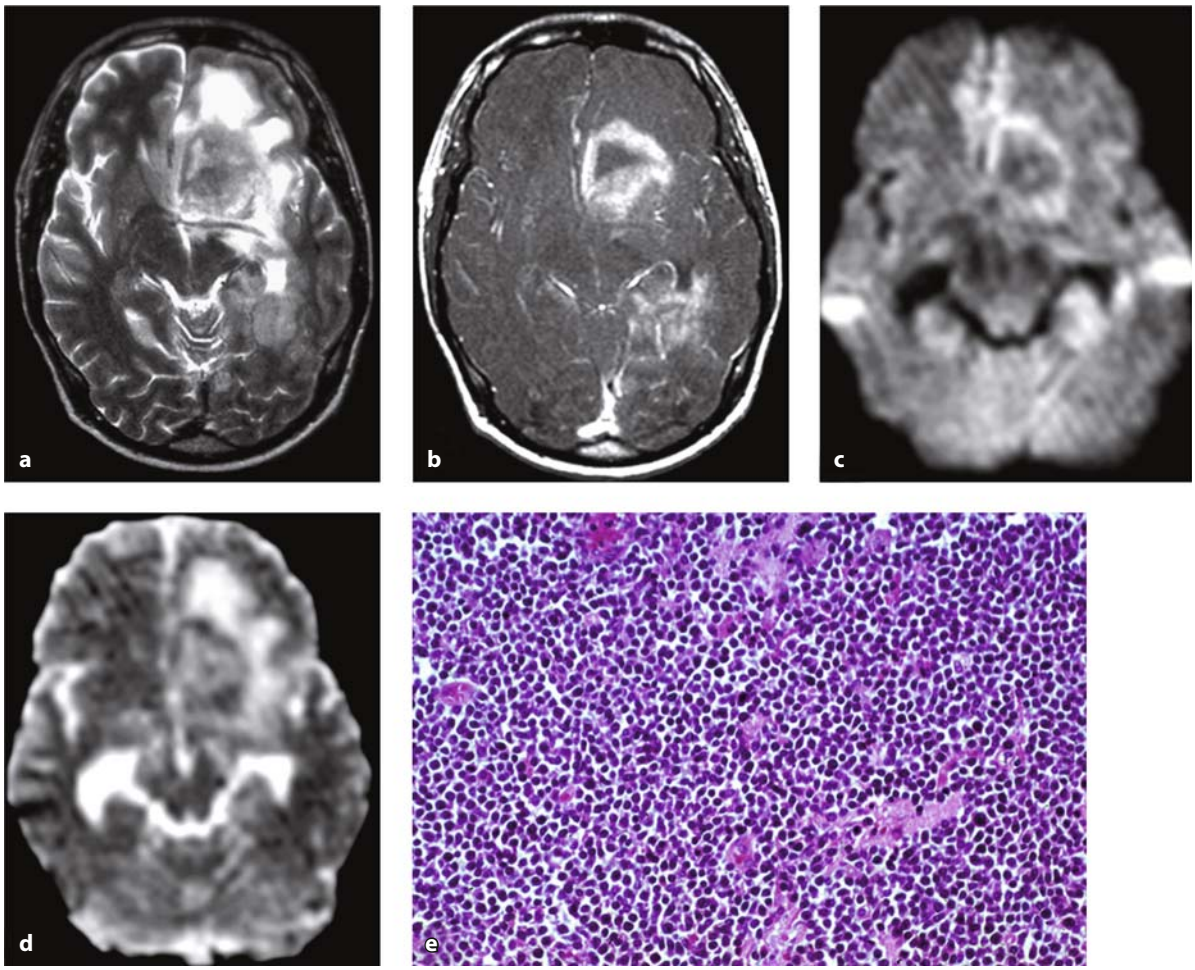

Figure 13.39 a–e

AIDS-related lymphoma in a 23-year-old man. **a** T2-weighted image shows iso- or mildly hyperintense masses in the left periventricular region with vasogenic edema. **b** Gadolinium-enhanced T1-weighted image shows ring or heterogeneous enhancement. **c** DW image shows hyperintensity in the solid portion of the lesions. **d** ADC map shows partially decreased ADC of the solid portion of the mass. **e** Pathology shows a diffuse infiltrate of fairly uniform, large cells with little cytoplasm

in high-grade gliomas [17]. As mentioned above, this corresponds to the hypercellularity and might help in differentiating between lymphomas and high-grade gliomas [17].

Central nervous system post-transplant lymphoproliferative disorder (CNS-PTLD) is seen in the brain of 2%-7% of post-transplant patients in autopsy series [78]. CNS-PTLD is a spectrum of disease ranging from Epstein-Barr virus-driven polyclonal proliferation to malignant lymphoma. Histologically, transmural invasion of blood vessel walls by tumor cells and necrosis are common features. Multiple necrotic ring enhancing lesions are the most common findings on CT and MR imaging. DW imaging shows hyperintensity in the ring enhancing solid portion and hypointensity in the central necrosis (Fig. 13.40).

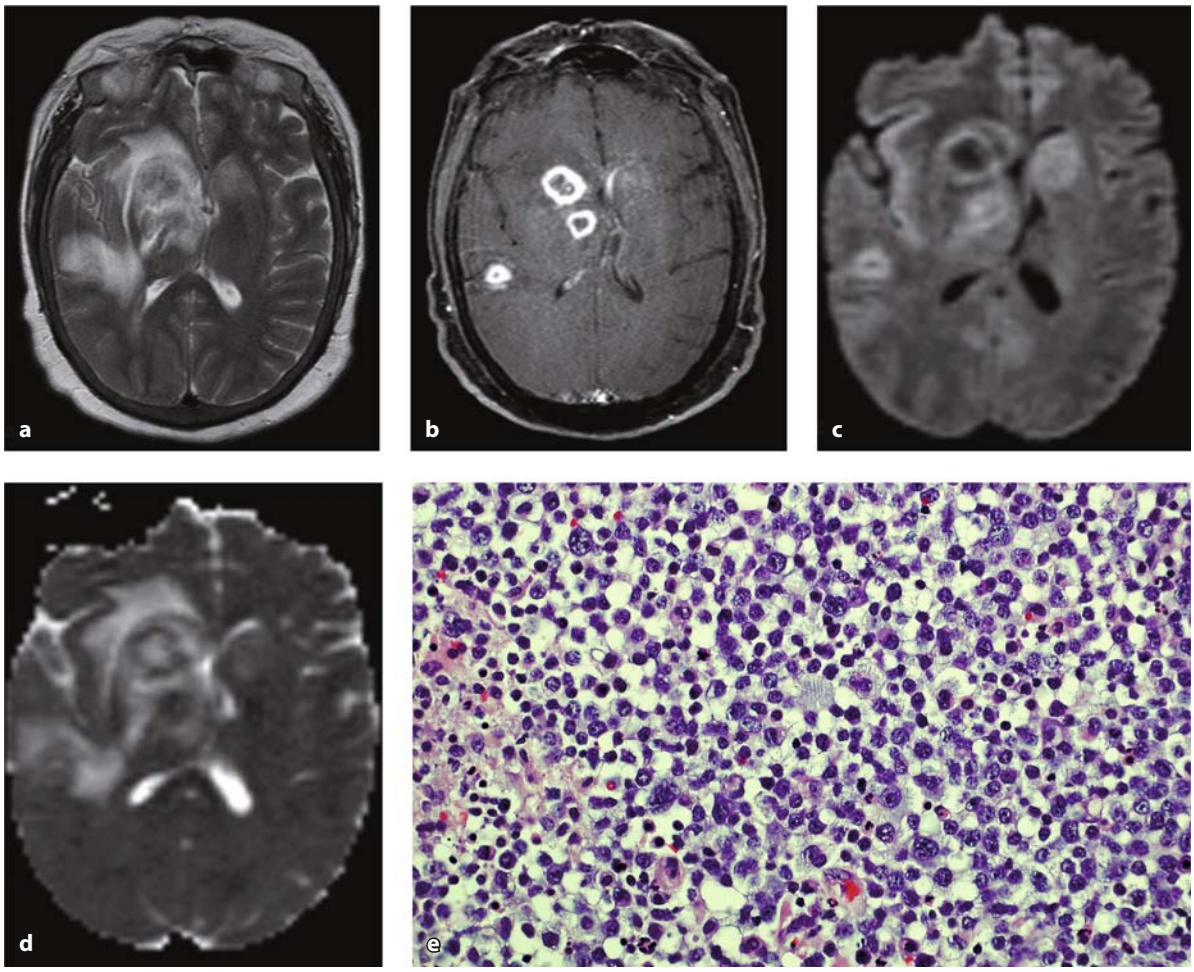

Figure 13.40 a–e

Post-transplant lymphoproliferative disease in a 54-year-old man after renal transplantation. **a** T2-weighted image shows iso- or mildly hyperintense masses in the left periventricular region with vasogenic edema. **b** Gadolinium-enhanced T1-weighted image shows ring or heterogeneous enhancement. **c** DW image shows hyperintense in the ring enhancing solid portion and hypointense in the central necrosis. **d** ADC map shows partially decreased ADC of the solid portion of the mass. **e** Pathology shows a hypercellular mixed lymphoid infiltrate with mitosis and nuclear pleomorphism. (Courtesy of Sergei S MD, PhD, Department of Pathology, The University of Iowa Hospitals and Clinics, USA)

Granulocytic sarcoma (chloroma) is a focal solid mass consisting of immature granulocytes. It often occurs in myelogenous leukemia, but may arise in acute lymphoblastic leukemia and other myeloproliferative and myelodysplastic disorders [79, 80]. The term "chloroma" is derived from the green color of the tumor on gross examination due to the high level of myeloperoxidase, which is not always seen in granulocytic sarcomas. In intracranial granulocytic sarcoma, leukemic cells from the bone marrow invade the periosteum via haversian canals, infiltrate the dural and subarachnoid spaces through the arachnoidal vein, and infiltrate the brain parenchyma with destruction of the pial-glial barrier. Typically, the lesion is iso- or slightly hypointense on T1- and hyperintense on T2-weighted images with homogeneous enhancement. DW imaging shows hyperintensity associated with decreased ADC (Fig. 13.41) [81].

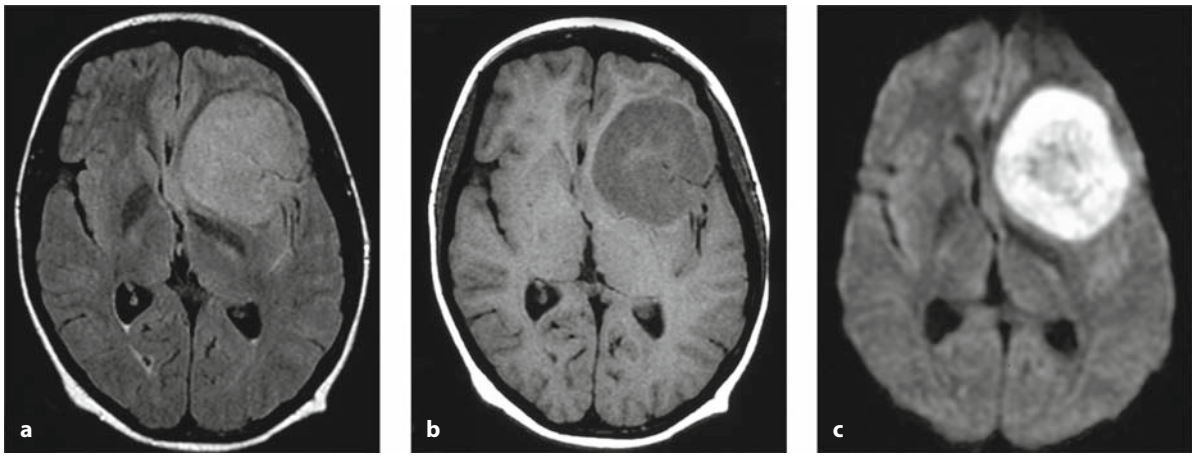

Figure 13.41 a–c

Granulocytic sarcoma in a 42-year-old man with acute myelogenous leukemia. **a** FLAIR image shows a mildly hyperintense mass in the left frontal region. **b** T1-weighted image shows a hypointense mass. **c** DW image shows a markedly hyperintense mass with decreased ADC (not shown)

13.10 Germ Cell Tumors

Germ cell tumors account for 0.5%–3% of primary intracranial tumors and 12% of primary intracranial tumors in children [82]. The five histological types are germinoma, embryonal carcinoma, yolk-sac tumor, choriocarcinoma, teratoma, and a number of tumors contain a mixture of histological types. Pineal and neurohypophyseal regions are common (76%–90%) and synchronous occurrence has been reported. A significant number arises in the basal ganglia and thalami (4%–14%). MR imaging usually shows an iso- or hyperintense mass on T1- and T2-weighted images with homogeneous or heterogeneous enhancement. Associated cysts are common. Ipsilateral cerebral, brain stem, and basal ganglia atrophy has been reported in patients with basal ganglia germinoma, probably due to tumor involvement of fiber tracts and secondary Wallerian, retrograde, and transsynaptic degenerations [83–85]. DW imaging shows the solid potion as hyperintense with decreased ADC probably due to the hypercellularity (Fig. 13.42).

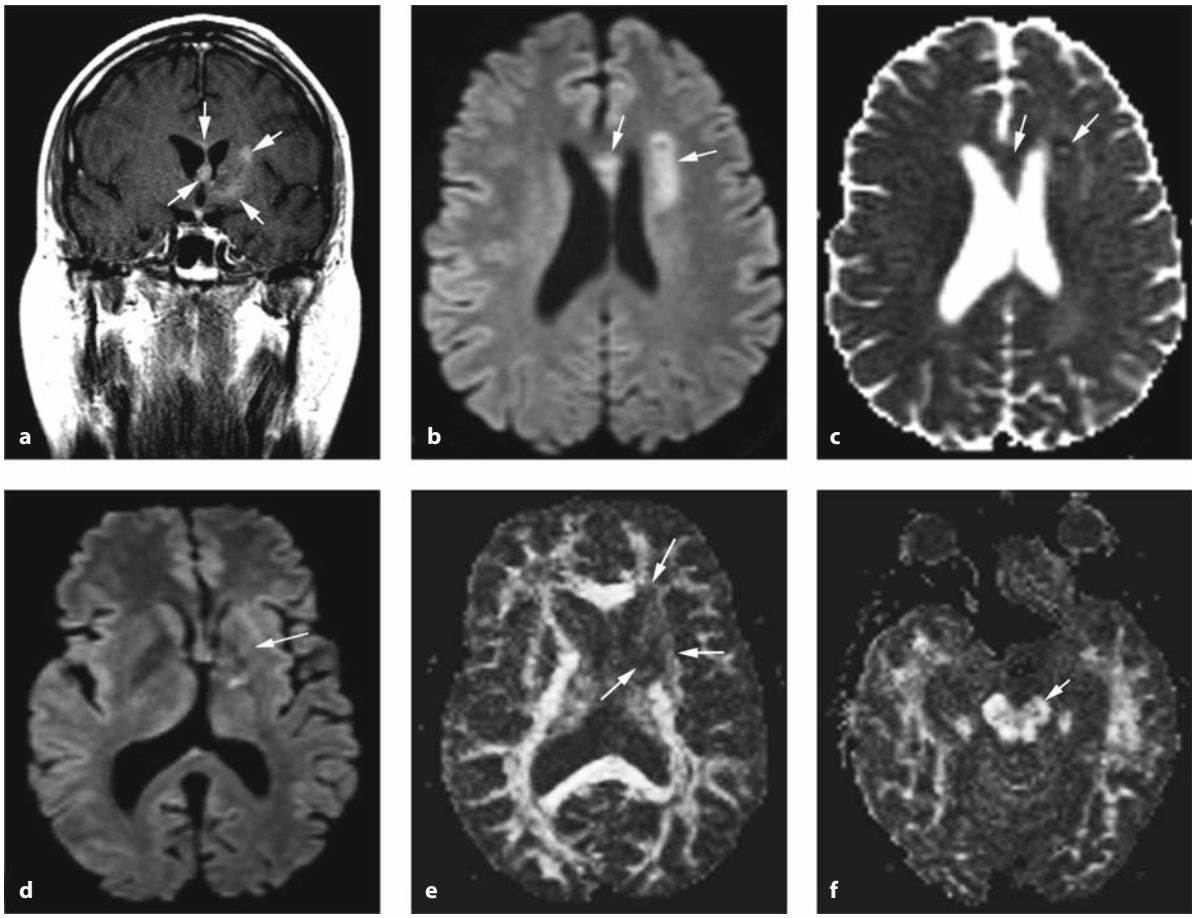

Figure 13.42 a–f

Germinoma in a 32-year-old man. **a** Gadolinium-enhanced coronal T1-weighted image shows enhancing lesions in the left basal ganglia, septum pellucidum, and corpus callosum (*arrows*). **b**, **c** DW image shows hyperintensity in the lesions with decreased ADC (*arrows*). **d** The left basal ganglia appears atrophic (*arrow*) compared to the other side, presumably due to the tumor involvement of fiber tracts and secondary degeneration. **e** FA map shows decreased anisotropy in the anterior limb and genu of internal capsules (*arrows*). Corticostriatal fibers (external capsule, subcallosal fasciculus of Muratoff) may also be involved (*arrows*). **f** Fractional anisotropy in the left cerebral peduncle is decreased, which represents Wallerian degeneration (*arrow*)

13.11 Epidermoid Cysts and Arachnoid Cysts

Epidermoid cysts are benign neoplasms of ectodermal origin with stratified squamous epithelium and keratinaceous debris [14, 86–93]. On T1- and T2-weighted images, intracranial epidermoids often have similar signal intensity to the cerebrospinal fluid (CSF). On FLAIR images, they are inhomogeneously hyperintense relative to the CSF [94]. DW imaging is highly sensitive in detecting intracranial epidermoids, which are shown as hyperintense. The ADC of epidermoid tumors has been reported to be much lower than that of the CSF and equal to or higher than that of brain parenchyma (Figs. 13.43, 13.44) [86–88, 90–93, 95]. Therefore, the hyperintensity of epidermoid tumors on DW images is mainly caused by a T2 shine-through effect. DT imaging may show increased anisotropy on FA maps. DW imaging is useful in detecting postoperative residual tumors and delineating their borders.

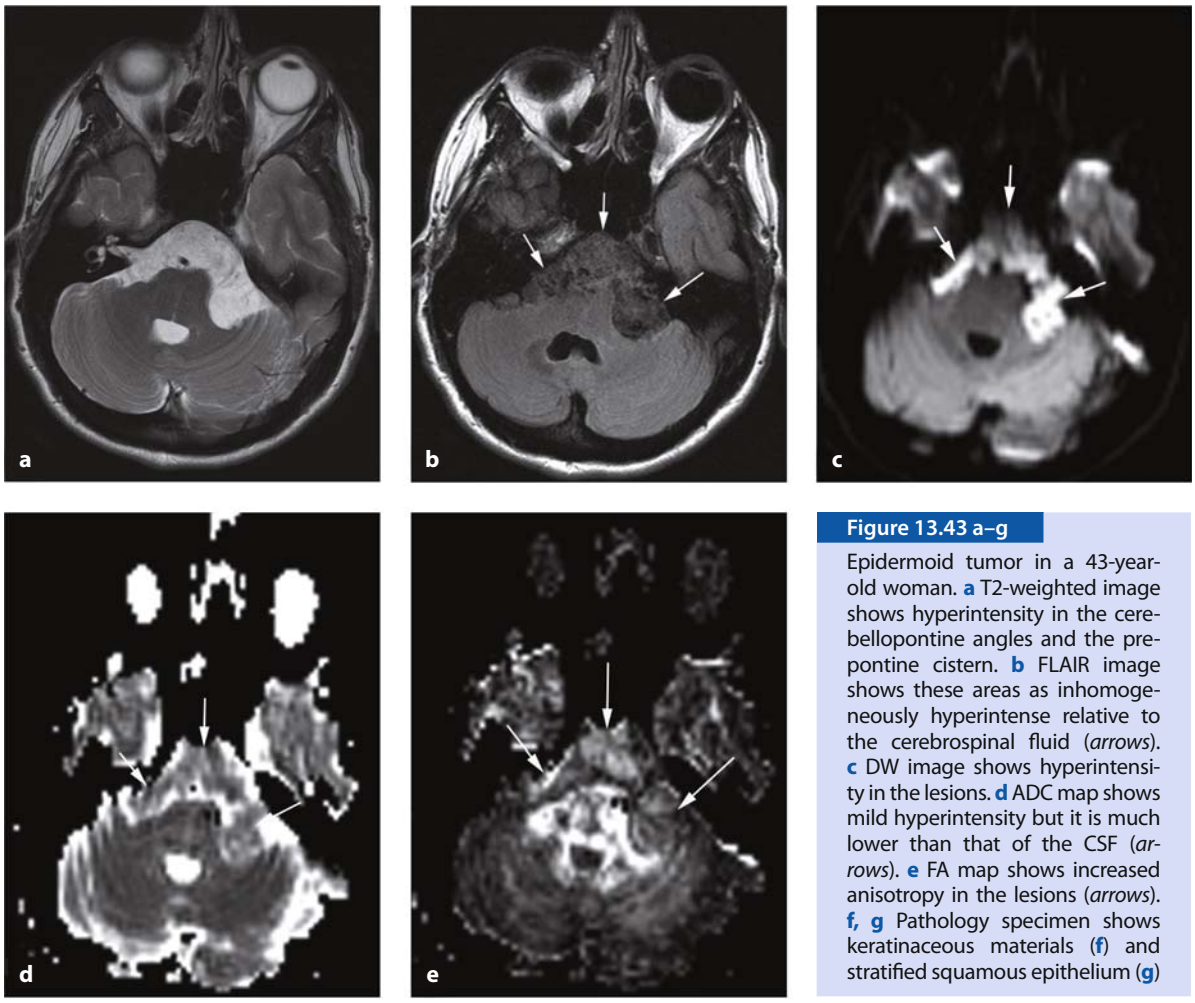

Figure 13.43 a–g

Epidermoid tumor in a 43-year-old woman. **a** T2-weighted image shows hyperintensity in the cerebellopontine angles and the prepontine cistern. **b** FLAIR image shows these areas as inhomogeneously hyperintense relative to the cerebrospinal fluid (*arrows*). **c** DW image shows hyperintensity in the lesions. **d** ADC map shows mild hyperintensity but it is much lower than that of the CSF (*arrows*). **e** FA map shows increased anisotropy in the lesions (*arrows*). **f, g** Pathology specimen shows keratinaceous materials (**f**) and stratified squamous epithelium (**g**)

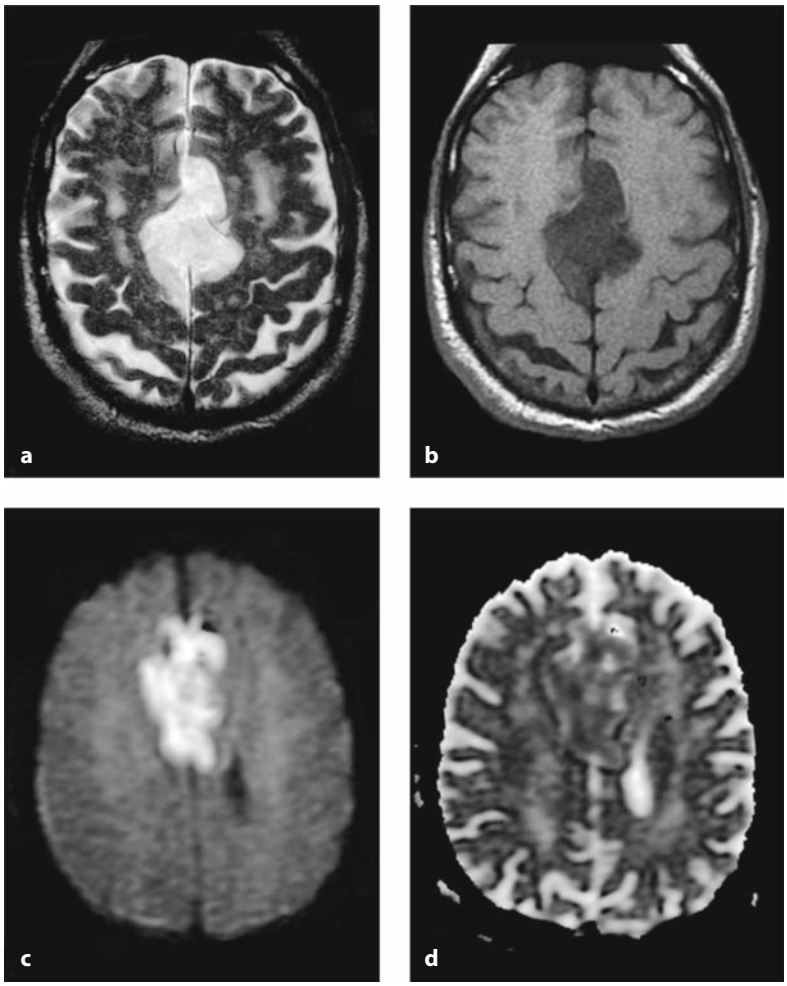

Figure 13.44 a–d

Epidermoid tumor in a 9-year-old girl without symptoms. **a** T2-weighted image shows a hyperintense mass near the falx. **b** T1-weighted image shows the hypointense lesion. **c** DW image shows hyperintensity in the lesion, which is caused by both increased T2 and restricted diffusivity. **d** ADC map shows heterogeneous iso- or hypointensity in the lesion, consistent with restricted diffusion similar to that of the brain parenchyma

Arachnoid cysts have a similar appearance on routine MR imaging as epidermoid tumors, but it is well known that DW imaging can distinguish the two [86–93]. Arachnoid cysts are hypointense on DW images as a result of free diffusion and in general their DW signal characteristics are similar to those of cerebrospinal fluid (Fig. 13.45).

13.12 Tumors of the Sella Region – Craniopharyngiomas, Rathke's Cleft Cysts, Pituitary Adenoma

Craniopharyngioma is a benign tumor comprising 3% of all intracranial tumors, originating from the neuroepithelium in the craniopharyngeal duct (Rathke's cleft/pouch). It typically shows a combination of contrast enhancement, cyst formation and calcifications. MR imaging shows the cystic components of craniopharyngioma as T1 hyper- or hypointense and T2 hyperintense, probably depending on the protein concentrations (4,000-12,000 mg/dl) [96]. DW imaging usually shows a hypointense mass lesion with increased ADC (Fig. 13.46). Sener et al. reported hyperintensity on DW images, with increased ADC, corresponding to an increased diffusivity in the tumor and a T2 shine-through effect [97].

Rathke's cleft cysts are benign epithelium-lined intrasellar cysts arising from the remnant of Rathke's pouch. MR imaging shows various signals in Rathke's cleft cysts depending on the protein concentration [96]. T1 hypo- and T2 hyperintense cysts contain CSF-like fluids. T1 hyper- and T2 hypointense cysts contain creamy yellow or white gelatinous fluid.

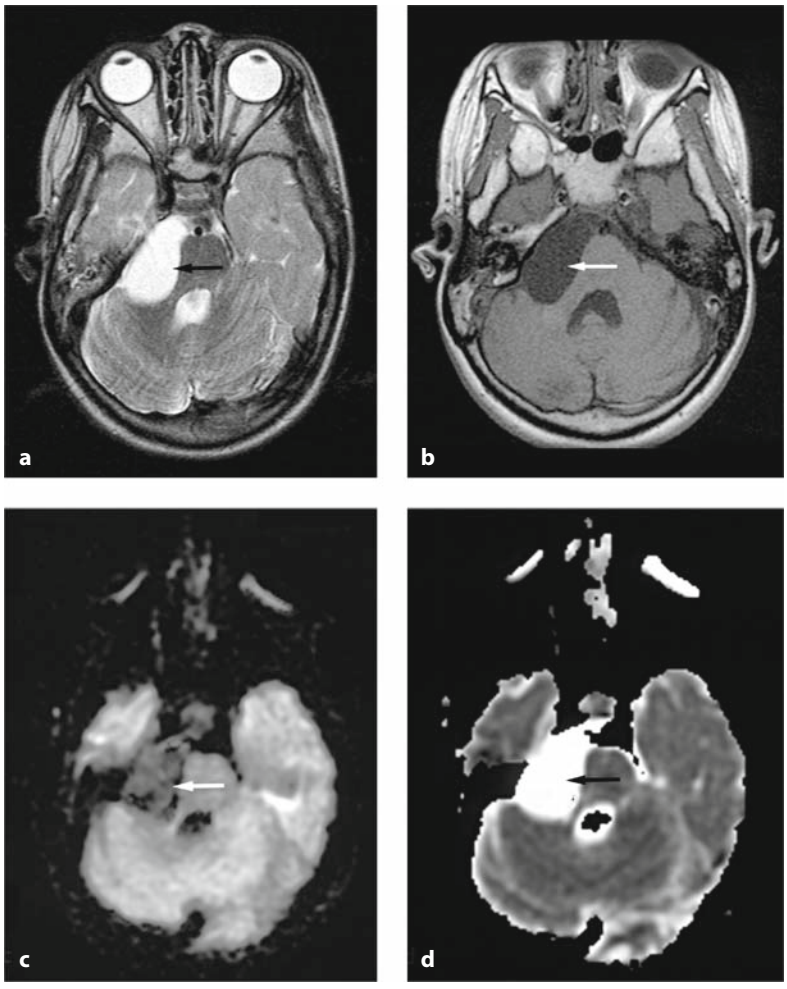

Figure 13.45 a–d

Arachnoid cyst in a 9-year-old girl with developmental delay. **a** T2-weighted image shows a large hyperintense lesion in the right cerebellopontine angle (*arrow*). **b** T1-weighted image shows hypointensity in the lesion (*arrow*). **c** DW image shows hypointensity (*arrow*). **d** ADC map shows hyperintensity in the lesion due to increased diffusivity (3.07–3.12×10^{-3} mm^2/s; *arrow*)

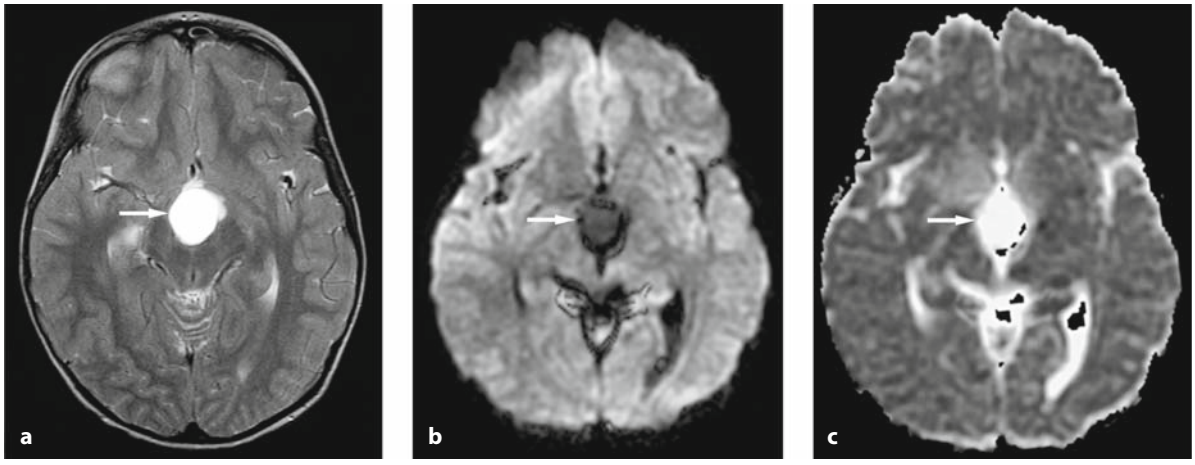

Figure 13.46 a–c

Craniopharyngioma in an 8-year-old boy with panhypopituitarism. **a** T2-weighted image shows a hyperintense mass (*arrow*) in the suprasellar region. **b** DW image shows hypointensity in the mass (*arrow*). **c** ADC map shows hyperintensity (2.25–2.38×10^{-3} mm^2/s; *arrow*)

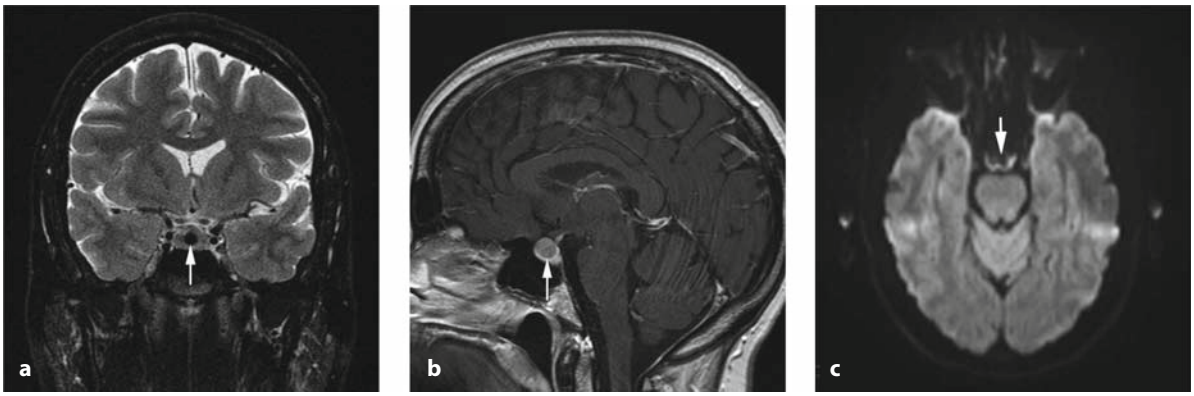

Figure 13.47 a–c

Rathke's cleft cyst in a 35-year-old woman. **a** Coronal T2-weighted image with fat saturation shows a hypointense lesion in the pituitary gland (*arrow*). **b** Postcontrast sagittal T1-weighted image shows a non-enhancing hyperintense lesion in the pituitary fossa (*arrow*). **c** DW image shows hypointensity in the lesion (*arrow*)

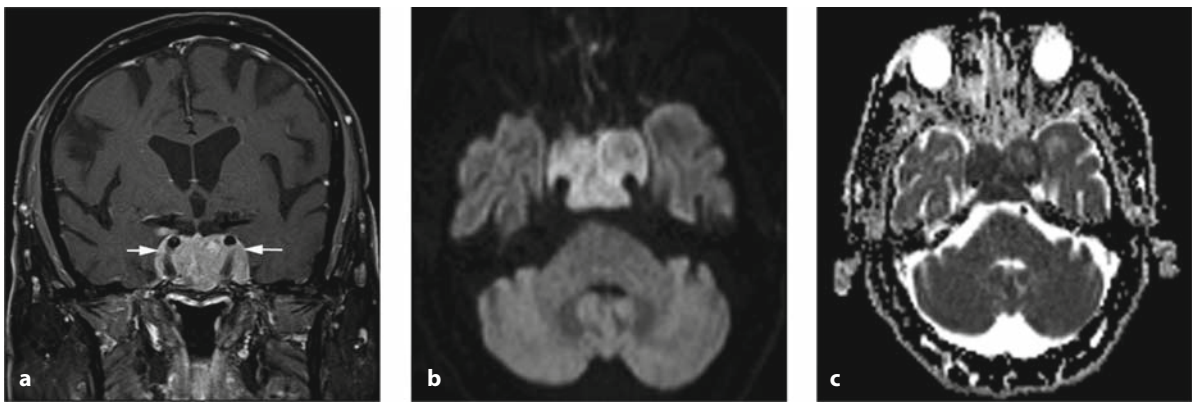

Figure 13.48 a–c

Pituitary adenoma in a 62-year-old female patient. **a** Gadolinium-enhanced coronal T1-weighted image shows a homogeneously enhancing mass in the pituitary fossa involving the bilateral cavernous sinuses (*arrows*). **b**, **c** DW image shows hypointensity in the lesion and decreased ADC ($0.46–0.77\times10^{-3}$ mm^2/s)

A protein concentration of more than 8,000 mg/dl causes the T1 hyperintensity, while a concentration of more than 15,000 mg/dl causes the T2 hypointensity. DW imaging usually shows a hypointense lesion (Fig. 13.47) [98].

Pituitary adenomas account for 10%-15% of all intracranial tumors, being five times more common than craniopharyngioma and Rathke's cleft cysts. MR imaging typically shows hypointensity on T1-weighted images, with heterogeneous hyperintensity on T2-weighted images and enhancement. DW imaging shows a hyperintense mass with ADC values ($0.84\pm0.3\times10^{-3}$ mm^2/s) (Fig. 13.48) [99]. There is a significant correlation between ADC values and tumor consistency of pituitary adenomas. Pituitary apoplexy results from hemorrhage and/or infarction of the pituitary gland. The DW signals and ADC values probably depend on the phase of hemorrhage and/or infarction in the pituitary gland or the pituitary adenoma (Fig. 13.49) [98, 100].

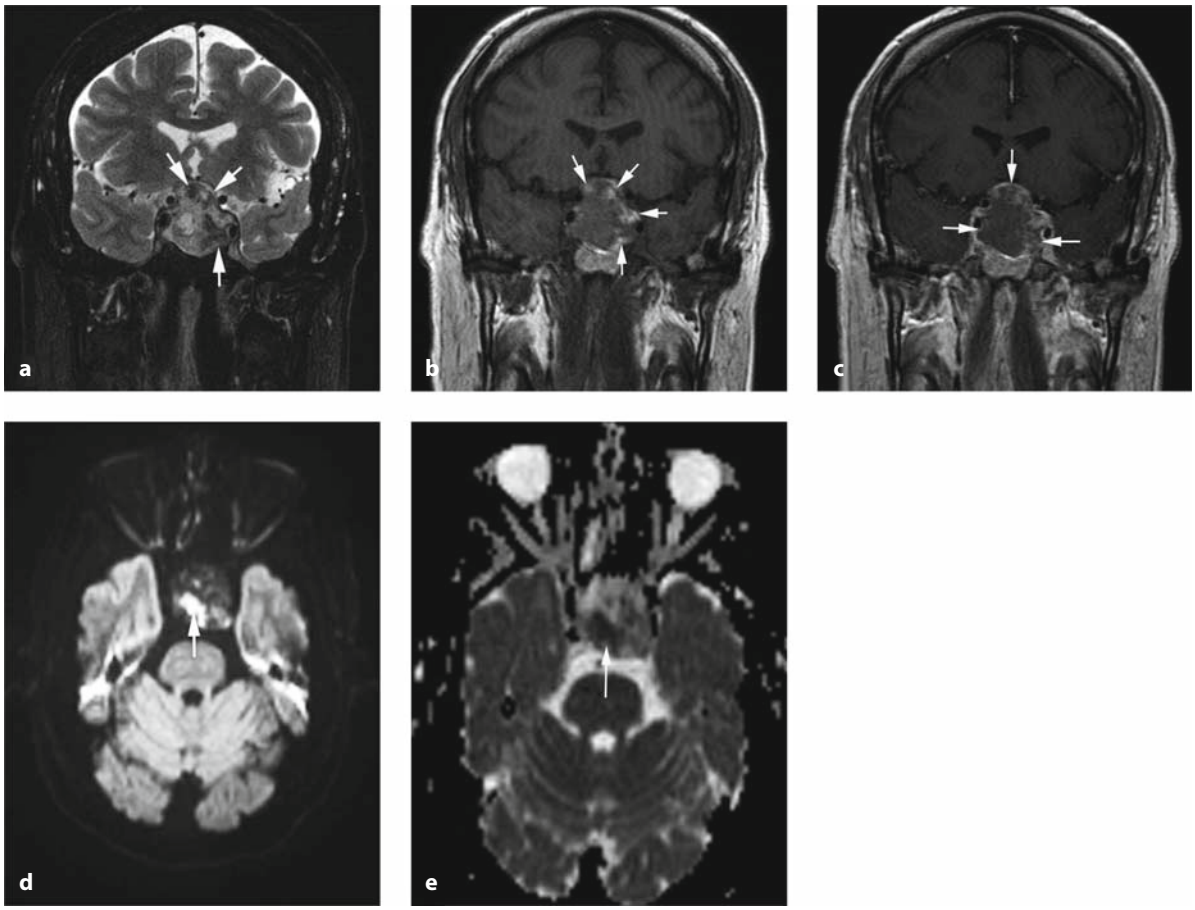

Figure 13.49 a–e

Pituitary apoplexy (pathologically proven) in a 29-year-old woman. **a** Coronal T2-weighted image shows a large heterogeneous mass in the pituitary fossa. Hypointense areas represent hemorrhagic components (*arrows*). **b** Precontrast coronal T1-weighted image shows a hypointense mass in the pituitary fossa and cavernous sinuses with T1 hyperintense hemorrhagic components (*arrows*). **c** Gadolinium-enhanced coronal T1-weighted image shows a necrotic hypointense mass with partial enhancement (*arrows*). **d**, **e** DW image shows hypointensity with increased ADC in the necrosis and hyperintensity with decreased ADC in the hemorrhagic component (*arrow*)

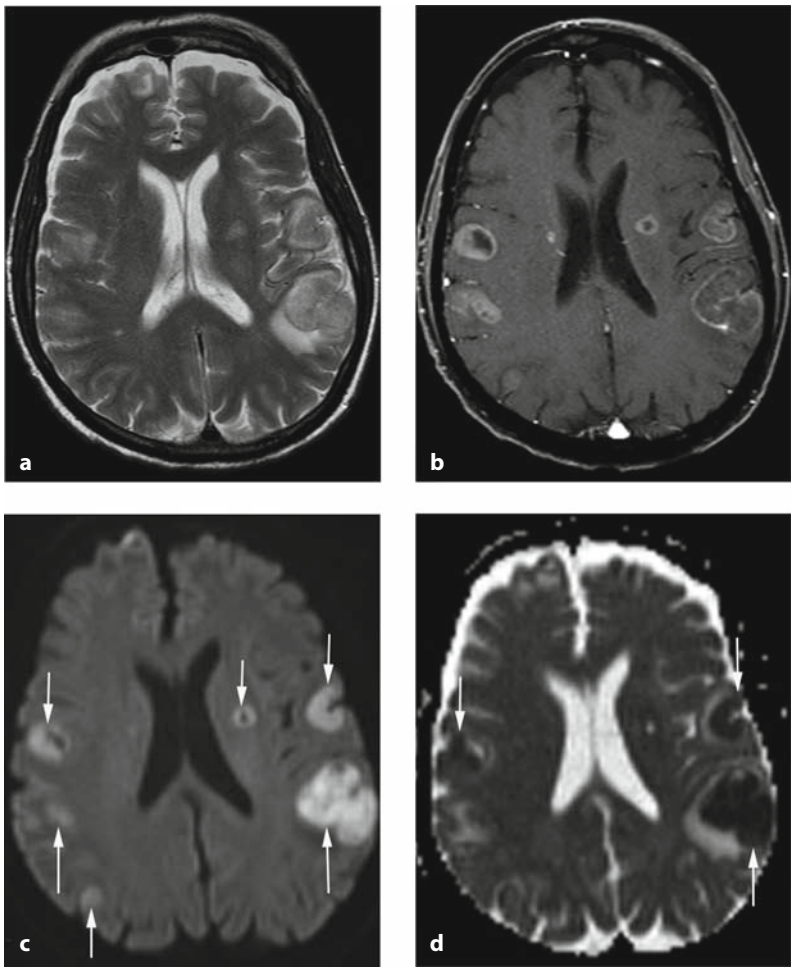

Figure 13.50 a–d

Metastasis (small cell lung carcinoma) in a 65-year-old male patient. **a** T2-weighted image shows multiple hyperintense mass lesions and edema in the bilateral hemispheres. **b** Gadolinium-enhanced T1-weighted image shows multiple inhomogeneously enhancing mass lesions. **c** DW image shows hyperintensity in the solid enhancing portion of the mass lesions (*arrows*). **d** ADC map shows marked decreased ADC (0.32–0.59×10^{-3} mm^2/s) in the solid portion of the lesions (*arrows*)

13.13 Metastatic Tumors

Brain metastasis accounts for about one-third of all intracranial tumors. While most metastases are multiple, up to 30% are solitary. MR imaging shows hypointensity on T1-weighted images, variable signal intensity on T2-weighted images, and enhancement. T2 hypointensity in brain metastatic lesions is often seen in well-differentiated adenocarcinoma [101].

The signal intensity of non-necrotic components of metastases on DW images is variable and depends on their T2 and ADC [3, 7, 12, 13, 19, 20, 30, 92, 101–109]. DW imaging findings of solid components of metastasis are similar to those of gliomas, probably reflecting the cellularity of the primary tumor. The cellularity is a major determinant of their DW signal intensity [7, 12, 19, 92]. Brain metastasis from small cell carcinoma often shows hyperintensity on DW images and decreased ADC probably due to the hypercellularity (Fig. 13.50). The common signal intensity of necrotic/cystic components of cerebral metastases may relate to an increase in free water, showing hypointensity on DW images and increased ADC. However, in the presence of extracellular met-hemoglobin and/or increased viscosity due to coagulative necrosis or mucin, DW images can show hyperintensity with decreased ADC (Figs. 13.51, 13.52) [19, 102–109]. This situation is rare, but it should be considered as one differential diagnosis of pyogenic abscesses.

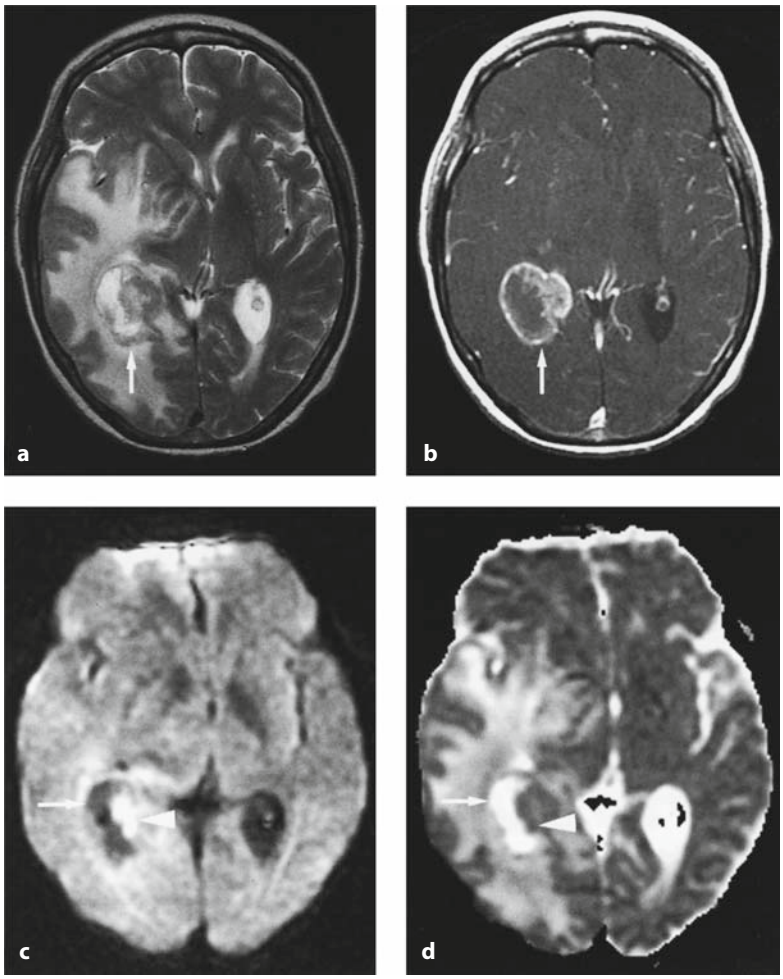

Figure 13.51 a–d

Metastasis (squamous cell lung carcinoma) in a 59-year-old female patient with adenocarcinoma of the lung. **a** T2-weighted image shows heterogeneous intensity of a mass (*arrow*) with surrounding edema in the right temporal lobe. **b** Gadolinium-enhanced T1-weighted image shows heterogeneous ring-like enhancement (*arrow*). **c** DW image shows hyperintensity in the solid portion (*arrowhead*) and hypointensity in the cystic/necrotic portion (*arrow*). **d** ADC map shows hypointensity in the solid portion ($0.97–1.00\times10^{-3}$ mm^2/s; *arrowhead*) and hyperintensity in the cystic portion ($2.21–2.35\times10^{-3}$ mm^2/s; *arrow*). Increased ADC is also seen in the surrounding vasogenic edema

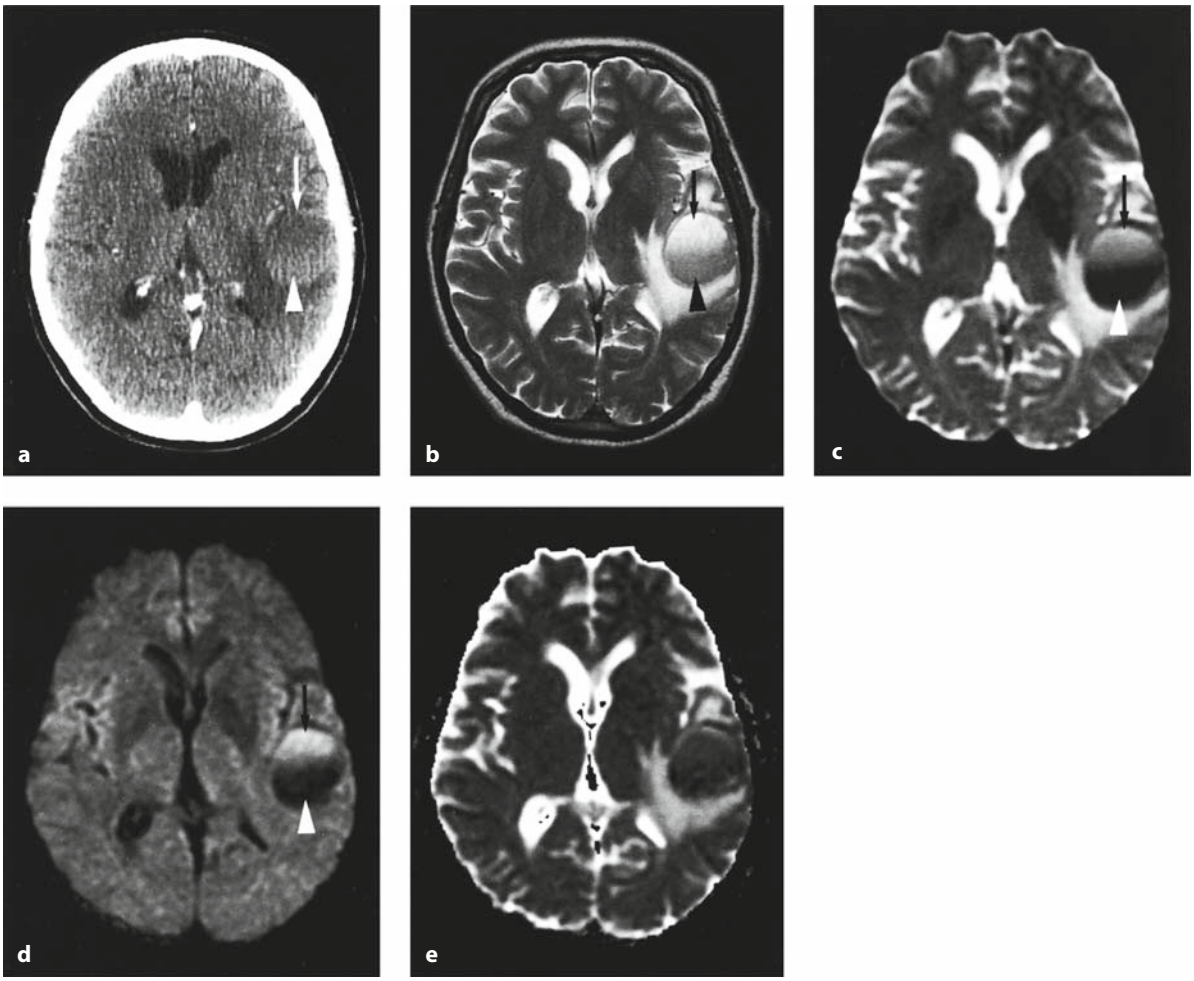

Figure 13.52 a–e

Metastasis (melanoma) in a 56-year-old man. **a** Postcontrast computed tomography shows a heterogeneous density mass, which shows hypodensity (*arrow*) in the anterior portions and hyperdensity (*arrowhead*) in the posterior portions. **b** T2-weighted image shows the heterogeneous intense mass, which contains anterior hyperintense portion (*arrow*) and posterior hypointense portion (*arrowhead*) with surrounding edema in the left temporal lobe. **c** b_0 image also shows anterior hyperintense portion (*arrow*) and posterior hypointense portion (*arrowhead*). **d** DW image again shows anterior hyperintense portion (*arrow*) and posterior hypointense portion (*arrowhead*). **e** ADC map shows iso- to hypointensity in the lesion. The accurate calculation of ADC in the hemorrhage is difficult

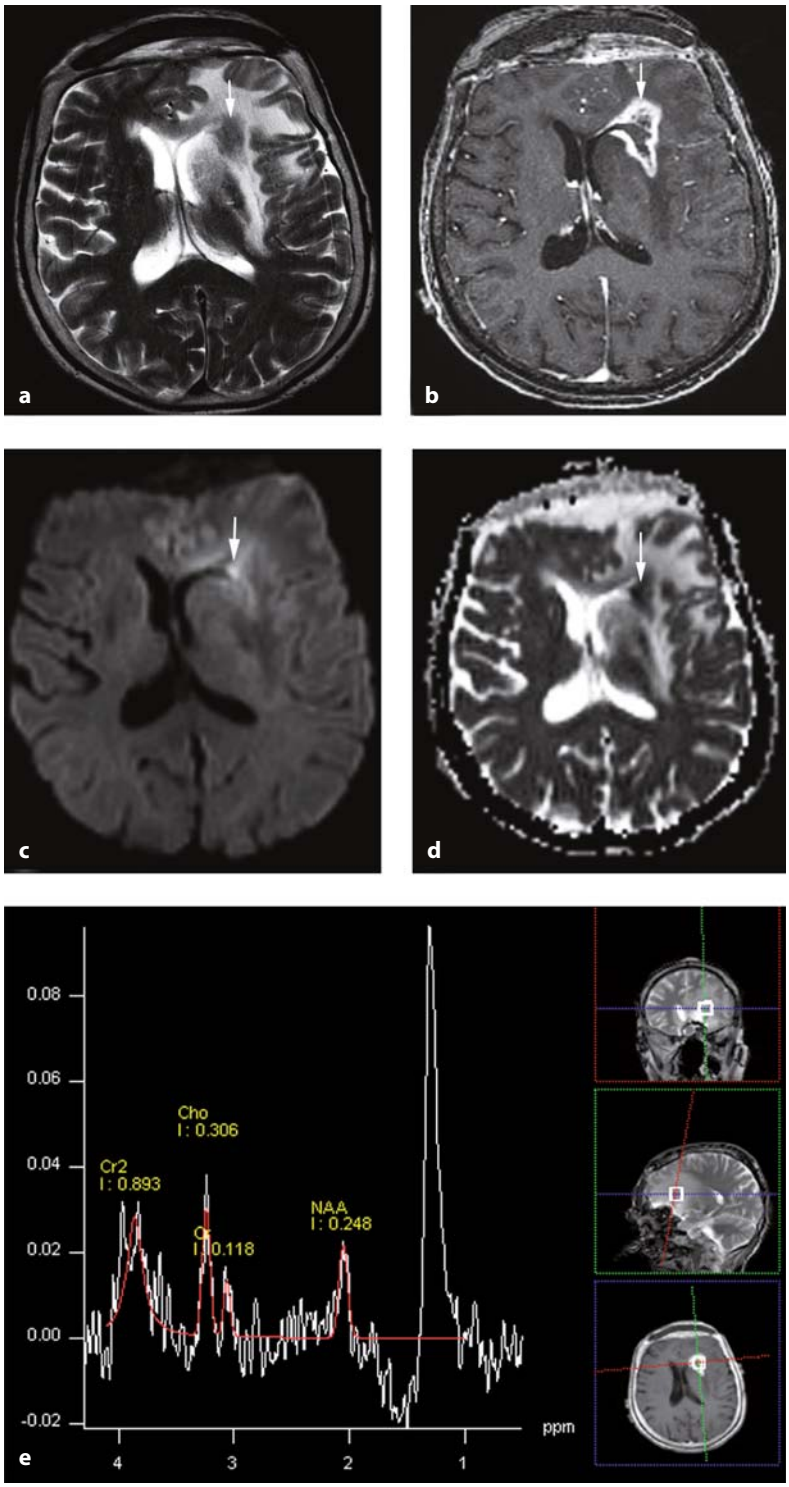

Figure 13.53 a–e

Radiation necrosis after the resection of olfactory neuroblastoma in a 65-year-old man. **a** T2-weighted image shows a mildly hyperintense necrotic area with surrounding edema in the left frontal deep white matter (*arrow*). Postoperative changes are seen in the frontal skull. **b** Gadolinium-enhanced T1-weighted image shows a necrotic enhancing mass lesion in the left frontal deep white matter (*arrow*). **c** DW image shows a central hyperintensity in the necrotic portion of the lesion (*arrow*). **d** ADC map shows iso- or hypointensity ($0.51–0.82\times10^{-3}$ mm^2/s) in the necrotic portion of the lesion (*arrow*). **e** MR spectroscopy (TE 135) shows a large lipid peak. A Cho/NAA ratio is less than 2.0. (Courtesy of Capizzano A MD, The University of Iowa Hospitals and Clinics, USA)

Figure 13.53 f

f Pathology shows a coagulative neuosis

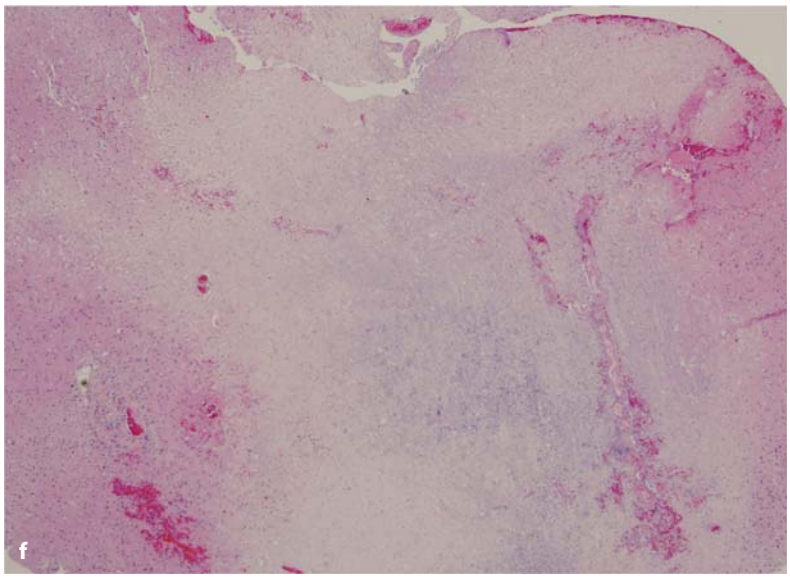

13.14 Radiation Necrosis

Radiation necrosis may occur several weeks to years after radiation, most commonly seen after 6-24 months. The early detection of recurrent tumors and the identification of radiation necrosis are important for adequate treatment. With conventional CT and MR imaging it is often difficult to differentiate between residual/recurrent tumors and radiation necrosis. ^{18}Fluorodeoxyglucose-PET (sensitivity 62%-86%, specificity 50%-94%) or ^{11}C methionine-PET (sensitivity 100%, specificity 60%), ^{201}Tl SPECT (sensitivity 92%), CT perfusion (sensitivity 94%, specificity 87%), MR perfusion, and MR spectroscopy are valuable in distinguishing between tumor recurrence and radiation necrosis [110-115]. The Cho/NAA and Cho/Cr ratios are higher in tumor recurrence than in radiation necrosis [116, 117]. DW imaging of radiation necrosis has been reported. ADC values are significantly higher in radiation necrosis than in tumor recurrence or normal brain tissue [110, 118, 119]. The maximum ADC is significantly higher in radiation necrosis than in tumor recurrence [120]. However, in some cases, radiation necrosis has shown restricted diffusion on ADC maps, which is not surprising given the potential role of ischemia in the occurrence of radiation necrosis (Fig. 13.53) [121].

13.15 Conclusion

Diffusion-weighted imaging can provide valuable information about tumor cellularity and the extracellular matrix, and help in the characterization and grading of tumors of the brain. Diffusion-tensor imaging adds some information about the tumor characteristics and peritumoral infiltration. In most situations, it is difficult to differentiate between specific tumors and to determine tumor infiltration. Fiber tractography can be useful for preoperative planning and intraoperative image-guided surgery.

References

1. Louis DN, Ohgaki H, Wiestler OD, Cavenee WK, Burger PC, Jouvet A, Scheithauer BW, Kleihues P (2007) The 2007 WHO classification of tumours of the central nervous system. Acta Neuropathol 114:97–109
2. LeBihan D, Breton E, Lallemand D, Grenier P, Cabanis E, Laval-Jeantet M (1986) MR imaging of intravoxel incoherent motions: application to diffusion and perfusion in neurologic disorders. Radiology 161:401–407
3. Hajnal JV, Doran M, Hall AS, et al. (1991) MR imaging of anisotropically restricted diffusion of water in the nervous system: technical, anatomic, and pathologic considerations. J Comput Assist Tomogr 15:1–18
4. Tien RD, Felsberg GJ, Friedman H, Brown M, MacFall J (1994) MR imaging of high-grade cerebral gliomas: value of diffusion-weighted echoplanar pulse sequences. AJR Am J Roentgenol 162:671–677

5. Eis M, Els T, Hoehn-Berlage M, Hossmann KA (1994) Quantitative diffusion MR imaging of cerebral tumor and edema. Acta Neurochir Suppl (Wien) 60:344–346
6. Brunberg JA, Chenevert TL, McKeever PE, et al. (1995) In vivo MR determination of water diffusion coefficients and diffusion anisotropy: correlation with structural alteration in gliomas of the cerebral hemispheres. AJNR Am J Neuroradiol 16:361–371
7. Krabbe K, Gideon P, Wagn P, Hansen U, Thomsen C, Madsen F (1997) MR diffusion imaging of human intracranial tumours. Neuroradiology 39:483–489
8. Gupta RK, Sinha U, Cloughesy TF, Alger JR (1999) Inverse correlation between choline magnetic resonance spectroscopy signal intensity and the apparent diffusion coefficient in human glioma. Magn Reson Med 41:2–7
9. Sugahara T, Korogi Y, Kochi M, et al. (1999) Usefulness of diffusion-weighted MRI with echo-planar technique in the evaluation of cellularity in gliomas. J Magn Reson Imaging 9:53–60
10. Gupta RK, Cloughesy TF, Sinha U, et al. (2000) Relationships between choline magnetic resonance spectroscopy, apparent diffusion coefficient and quantitative histopathology in human glioma. J Neurooncol 50:215–226
11. Castillo M, Smith JK, Kwock L, Wilber K (2001) Apparent diffusion coefficients in the evaluation of high-grade cerebral gliomas. AJNR Am J Neuroradiol 22:60–64
12. Stadnik TW, Chaskis C, Michotte A, et al. (2001) Diffusion-weighted MR imaging of intracerebral masses: comparison with conventional MR imaging and histologic findings. AJNR Am J Neuroradiol 22:969–976
13. Kono K, Inoue Y, Nakayama K, et al. (2001) The role of diffusion-weighted imaging in patients with brain tumors. AJNR Am J Neuroradiol 22:1081–1088
14. Gauvain KM, McKinstry RC, Mukherjee P, et al. (2001) Evaluating pediatric brain tumor cellularity with diffusion-tensor imaging. AJR Am J Roentgenol 177:449–454
15. Sinha S, Bastin ME, Whittle IR, Wardlaw JM (2002) Diffusion tensor MR imaging of high-grade cerebral gliomas. AJNR Am J Neuroradiol 23:520–527
16. Bastin ME, Sinha S, Whittle IR, Wardlaw JM (2002) Measurements of water diffusion and T1 values in peritumoural oedematous brain. Neuroreport 13:1335–1340
17. Guo AC, Cummings TJ, Dash RC, Provenzale JM (2002) Lymphomas and high-grade astrocytomas: comparison of water diffusibility and histologic characteristics. Radiology 224:177–183
18. Yang D, Korogi Y, Sugahara T, et al. (2002) Cerebral gliomas: prospective comparison of multivoxel 2D chemical-shift imaging proton MR spectroscopy, echoplanar perfusion and diffusion-weighted MRI. Neuroradiology 44:656–666
19. Stadnik TW, Demaerel P, Luypaert RR, et al. (2003) Imaging tutorial: differential diagnosis of bright lesions on diffusion-weighted MR images. Radiographics 23:E7–7
20. Bulakbasi N, Kocaoglu M, Ors F, Tayfun C, Ucoz T (2003) Combination of single-voxel proton MR spectroscopy and apparent diffusion coefficient calculation in the evaluation of common brain tumors. AJNR Am J Neuroradiol 24:225–233
21. Chenevert TL, McKeever PE, Ross BD (1997) Monitoring early response of experimental brain tumors to therapy using diffusion magnetic resonance imaging. Clin Cancer Res 3:1457–1466
22. Chenevert TL, Stegman LD, Taylor JM, et al. (2000) Diffusion magnetic resonance imaging: an early surrogate marker of therapeutic efficacy in brain tumors. J Natl Cancer Inst 92:2029–2036
23. Mardor Y, Roth Y, Lidar Z, et al. (2001) Monitoring response to convection-enhanced taxol delivery in brain tumor patients using diffusion-weighted magnetic resonance imaging. Cancer Res 61:4971–4973
24. Sadeghi N, Camby I, Goldman S, Gabius HJ, Balériaux D, Salmon I, Decaesteckere C, Kiss R, Metens T (2003) Effect of hydrophilic components of the extracellular matrix on quantifiable diffusion-weighted imaging of human gliomas: preliminary results of correlating apparent diffusion coefficient values and hyaluronan expression level. AJR Am J Roentgenol 181:235–241
25. Murakami R, Hirai T, Kitajima M, Fukuoka H, Toya R, Nakamura H, Kuratsu J, Yamashita Y (2008) Magnetic resonance imaging of pilocytic astrocytomas: usefulness of the minimum apparent diffusion coefficient (ADC) value for differentiation from high-grade gliomas. Acta Radiol 49:462–467
26. Hwang JH, Egnaczyk GF, Ballard E, Dunn RS, Holland SK, Ball WS Jr. (1998) Proton MR spectroscopic characteristics of pediatric pilocytic astrocytomas. AJNR Am J Neuroradiol 19:535–540
27. Goebell E, Paustenbach S, Vaeterlein O, Ding XQ, Heese O, Fiehler J, Kucinski T, Hagel C, Westphal M, Zeumer H (2006) Low grade and anaplastic gliomas: differences in architecture evaluated with diffusion-tensor MR imaging. Radiology 239:217–222
28. Higano S, Yun X, Kumabe T, Watanabe M, Mugikura S, Umetsu A, Sato A, Yamada T, Takahashi S (2006) Malignant astrocytic tumors: clinical importance of apparent diffusion coefficient in prediction of grade and prognosis. Radiology 241:839–846
29. Stadlbauer A, Ganslandt O, Buslei R, Hammen T, Gruber S, Moser E, Buchfelder M, Salomonowitz E, Nimsky C (2006) Gliomas: histopathologic evaluation of changes in directionality and magnitude of water diffusion at diffusion-tensor MR imaging. Radiology 240:803–810
30. Tung GA, Evangelista P, Rogg JM, Duncan JA 3rd (2001) Diffusion-weighted MR imaging of rim-enhancing brain masses: is markedly decreased water diffusion specific for brain abscess? AJR Am J Roentgenol 177:709–712
31. Toh CH, Castillo M, Wong AM, Wei KC, Wong HF, Ng SH, Wan YL (2008) Primary cerebral lymphoma and glioblastoma multiforme: differences in diffusion characteristics evaluated with diffusion tensor imaging. AJNR Am J Neuroradiol 29:471–475
32. Behin A, Hoang-Xuan K, Carpentier AF, Delattre JY (2003) Primary brain tumours in adults. Lancet 361:323–331
33. Kleihues P, Ohgaki H (1999) Primary and secondary glioblastomas: from concept to clinical diagnosis. Neuro Oncol 1:44–51

34. Preusser M, Haberler C, Hainfellner JA (2006) Malignant glioma: neuropathology and neurobiology. Wien Med Wochenschr 156:332–337
35. Kleihues P, Louis DN, Scheithauer BW, Rorke LB, Reifenberger G, Burger PC, Cavenee WK (2002) The WHO classification of tumors of the nervous system. J Neuropathol Exp Neurol 61:215–225
36. Vordermark D, Ruprecht K, Rieckmann P, Roggendorf W, Vince GH, Warmuth-Metz M, Kölbl O, Flentje M (2006) Glioblastoma multiforme with oligodendroglial component (GBMO): favorable outcome after post-operative radiotherapy and chemotherapy with nimustine (ACNU) and teniposide (VM26). BMC Cancer 6:247
37. Ye ZC, Sontheimer H (1999) Glioma cells release excitotoxic concentrations of glutamate. Cancer Res 59:4383–4391
38. Moritani T, Smoker WR, Sato Y, Numaguchi Y, Westesson PL (2005) Diffusion-weighted imaging of acute excitotoxic brain injury. AJNR Am J Neuroradiol 26:216–228
39. Provenzale JM, McGraw P, Mhatre P, Guo AC, Delong D (2004) Peritumoral brain regions in gliomas and meningiomas: investigation with isotropic diffusion-weighted MR imaging and diffusion-tensor MR imaging. Radiology 232:451–460
40. Tropine A, Vucurevic G, Delani P, Boor S, Hopf N, Bohl J, Stoeter P (2004) Contribution of diffusion tensor imaging to delineation of gliomas and glioblastomas. J Magn Reson Imaging 20:905–912
41. Yamada K, Kizu O, Mori S, Ito H, Nakamura H, Yuen S, Kubota T, Tanaka O, Akada W, Sasajima H, Mineura K, Nishimura T (2003) Brain fiber tracking with clinically feasible diffusion-tensor MR imaging: initial experience. Radiology 227:295–301
42. Stadlbauer A, Nimsky C, Buslei R, Salomonowitz E, Hammen T, Buchfelder M, Moser E, Ernst-Stecken A, Ganslandt O (2007) Diffusion tensor imaging and optimized fiber tracking in glioma patients: Histopathologic evaluation of tumor-invaded white matter structures. Neuroimage 34:949-956
43. Nimsky C, Ganslandt O, Hastreiter P, Wang R, Benner T, Sorensen AG, Fahlbusch R (2005) Preoperative and intraoperative diffusion tensor imaging-based fiber tracking in glioma surgery. Neurosurgery 56:130–137
44. Kinoshita M, Yamada K, Hashimoto N, Kato A, Izumoto S, Baba T, Maruno M, Nishimura T, Yoshimine T (2005) Fiber-tracking does not accurately estimate size of fiber bundle in pathological condition: initial neurosurgical experience using neuronavigation and subcortical white matter stimulation. Neuroimage 25:424–429
45. Yu A, Li K, Li H (2006) Value of diagnosis and differential diagnosis of MRI and MR spectroscopy in gliomatosis cerebri. Eur J Radiol 59:216–221
46. Lafitte F, Morel-Precetti S, Martin-Duverneuil N, Guermazi A, Brunet E, Heran F, Chiras J (2001) Multiple glioblastomas: CT and MR features. Eur Radiol 11:131–136
47. Akai H, Mori H, Aoki S, Masutani Y, Kawahara N, Shibahara J, Ohtomo K (2005) Diffusion tensor tractography of gliomatosis cerebri: fiber tracking through the tumor. J Comput Assist Tomogr 29:127–129
48. Dwyer KW, Naul LG, Hise JH (1996) Gliosarcoma: MR features. J Comput Assist Tomogr 20:719–723
49. Lu S, Ahn D, Johnson G, Law M, Zagzag D, Grossman RI (2004) Diffusion-tensor MR imaging of intracranial neoplasia and associated peritumoral edema: introduction of the tumor infiltration index. Radiology 232:221–228
50. Moonis G, Ibrahim M, Melhem ER (2004) Diffusion-weighted MRI in Lhermitte-Duclos disease: report of two cases. Neuroradiology 46:351–354
51. Thomas B, Krishnamoorthy T, Radhakrishnan VV, Kesavadas C (2007) Advanced MR imaging in Lhermitte-Duclos disease: moving closer to pathology and pathophysiology. Neuroradiology 49:733–738
52. Bulakbasi N, Kocaoglu M, Sanal TH, Tayfun C (2007) Dysembryoplastic neuroepithelial tumors: proton MR spectroscopy, diffusion and perfusion characteristics. Neuroradiology 49:805–812
53. Yamasaki F, Kurisu K, Satoh K, Arita K, Sugiyama K, Ohtaki M, Takaba J, Tominaga A, Hanaya R, Yoshioka H, Hama S, Ito Y, Kajiwara Y, Yahara K, Saito T, Thohar MA (2005) Apparent diffusion coefficient of human brain tumors at MR imaging. Radiology 235:985–991
54. Kocaoglu M, Ors F, Bulakbasi N, Onguru O, Ulutin C, Secer HI (2008) Central neurocytoma: proton MR spectroscopy and diffusion weighted MR imaging findings. Magn Reson Imaging, Sep 10 [Epub ahead of print]
55. Zhang D, Henning TD, Zou LG, Hu LB, Wen L, Feng XY, Dai SH, Wang WX, Sun QR, Zhang ZG (2008) Intracranial ganglioglioma: clinicopathological and MRI findings in 16 patients. Clin Radiol 63:80–91
56. Cuccia V, Rodríguez F, Palma F, Zuccaro G (2006) Pinealoblastomas in children. Childs Nerv Syst 22:577–585
57. Chang AH, Fuller GN, Debnam JM, Karis JP, Coons SW, Ross JS, Dean BL (2008) MR imaging of papillary tumor of the pineal region. AJNR Am J Neuroradiol 29:187–189
58. Sato T, Kirby PA, Buatti JM, Moritani T (2009) Papillary tumor of the pineal region: Report of a rapidly progressive tumor with possible multicentric origin. Pediatr Radiol 39:188–190
57. Kotsenas AL, Roth TC, Manness WK, Faerber EN (1999) Abnormal diffusion-weighted MRI in medulloblastoma: does it reflect small cell histology? Pediatr Radiol 29:524–526
58. Klisch J, Husstedt H, Hennings S, von Velthoven V, Pagenstecher A, Schumacher M (2000) Supratentorial primitive neuroectodermal tumours: diffusion-weighted MRI. Neuroradiology 42:393–398
59. Wilke M, Eidenschink A, Muller-Weihrich S, Auer DP (2001) MR diffusion imaging and 1H spectroscopy in a child with medulloblastoma. A case report. Acta Radiol 42:39–42
60. Erdem E, Zimmerman RA, Haselgrove JC, Bilaniuk LT, Hunter JV (2001) Diffusion-weighted imaging and fluid attenuated inversion recovery imaging in the evaluation of primitive neuroectodermal tumors. Neuroradiology 43:927–933
61. Koral K, Gargan L, Bowers DC, Gimi B, Timmons CF, Weprin B, Rollins NK (2008) Imaging characteristics of atypical teratoid-rhabdoid tumor in children compared with medulloblastoma. AJR Am J Roentgenol 190:809–814

62. Sener RN (2003) Diffusion magnetic resonance imaging of solid vestibular schwannomas. J Comput Assist Tomogr 27:249–252
63. Taoka T, Hirabayashi H, Nakagawa H, Sakamoto M, Myochin K, Hirohashi S, Iwasaki S, Sakaki T, Kichikawa K (2006) Displacement of the facial nerve course by vestibular schwannoma: preoperative visualization using diffusion tensor tractography. J Magn Reson Imaging 24:1005–1010
64. Nauta HJ, Tucker WS, Horsey WJ, Bilbao JM, Gonsalves C (1979) Xanthochromic cysts associated with meningioma. J Neurol Neurosurg Psychiatry 42:529–535
65. Tanaka M, Imhof HG, Schucknecht B, Kollias S, Yonekawa Y, Valavanis A (2006) Correlation between the efferent venous drainage of the tumor and peritumoral edema in intracranial meningiomas: superselective angiographic analysis of 25 cases. J Neurosurg 104:382–388
66. Paek SH, Kim CY, Kim YY, Park IA, Kim MS, Kim DG, Jung HW (2002) Correlation of clinical and biological parameters with peritumoral edema in meningioma. J Neurooncol 60:235–245
67. Filippi CG, Edgar MA, Ulug AM, Prowda JC, Heier LA, Zimmerman RD (2001) Appearance of meningiomas on diffusion-weighted images: correlating diffusion constants with histopathologic findings. AJNR Am J Neuroradiol 22:65–72
68. Bitzer M, Klose U, Geist-Barth B (2002) Alterations in diffusion and perfusion in the pathogenesis of peritumoral brain edema in meningiomas. Eur Radiol 12:2062–2076
69. Maiuri F, Iaconetta G, de Divitiis O, Cirillo S, Di Salle F, De Caro ML (1999) Intracranial meningiomas: correlations between MR imaging and histology. Eur J Radiol 31:69–75
70. Tropine A, Dellani PD, Glaser M, Bohl J, Plöner T, Vucurevic G, Perneczky A, Stoeter P (2007) Differentiation of fibroblastic meningiomas from other benign subtypes using diffusion tensor imaging. J Magn Reson Imaging 25:703–708
71. Paek SH, Kim SH, Chang KH, Park CK, Kim JE, Kim DG, Park SH, Jung HW (2005) Microcystic meningiomas: radiological characteristics of 16 cases. Acta Neurochir (Wien) 147:965–972
71. Hakyemez B, Yildirim N, Gokalp G, Erdogan C, Parlak M. (2006) The contribution of diffusion-weighted MR imaging to distinguishing typical from atypical meningiomas. Neuroradiology 48:513–520
73. Quadery FA, Okamoto K (2003) Diffusion-weighted MRI of haemangioblastomas and other cerebellar tumours. Neuroradiology 45:212–219
74. Jack CR Jr, Reese DF, Scheithauer BW (1986) Radiographic findings in 32 cases of primary CNS lymphoma. AJR Am J Roentgenol 146:271–276
75. Hochberg FH, Miller DC (1988) Primary central nervous system lymphoma. J Neurosurg 68:835–853
76. Poon T, Matoso I, Tchertkoff V, Weitzner I Jr, Gade M (1989) CT features of primary cerebral lymphoma in AIDS and non-AIDS patients. J Comput Assist Tomogr 13:6–9
77. Chang L, Ernst T (1997) MR spectroscopy and diffusion-weighted MR imaging in focal brain lesions in AIDS. Neuroimaging Clin N Am 7:409–426
78. Castellano-Sanchez AA, Li S, Qian J, Lagoo A, Weir E, Brat DJ (2004) Primary central nervous system posttransplant lymphoproliferative disorders. Am J Clin Pathol 121:246–253
79. Ahn JY, Kwon SO, Shin MS, Kang SH, Kim YR (2002) Meningeal chloroma (granulocytic sarcoma) in acute lymphoblastic leukemia mimicking a falx meningioma. J Neurooncol 60:31–35
80. Parker K, Hardjasudarma M, McClellan RL, Fowler MR, Milner JW (1996) MR features of an intracerebellar chloroma. AJNR 17:1592–1594
81. Hakyemez B, Yildirim N, Taskapilioglu O, Erdogan C, Aker S, Yilmazlar S, Parlak M (2007) Intracranial myeloid sarcoma: conventional and advanced MRI findings. Br J Radiol 80:e109–112
82. Liang L, Korogi Y, Sugahara T, Ikushima I, Shigematsu Y, Okuda T, Takahashi M, Kochi M, Ushio Y. (2002) MRI of intracranial germ-cell tumours. Neuroradiology 44:382–388
83. Higano S, Takahashi S, Ishii K, Matsumoto K, Ikeda H, Sakamoto K (1994) Germinoma originating in the basal ganglia and thalamus: MR and CT evaluation. AJNR Am J Neuroradiol 15:1435–1441
84. Ozelame RV, Shroff M, Wood B, Bouffet E, Bartels U, Drake JM, Hawkins C, Blaser S (2006) Basal ganglia germinoma in children with associated ipsilateral cerebral and brain stem hemiatrophy. Pediatr Radiol 36:325–330
85. Okamoto K, Ito J, Ishikawa K, Morii K, Yamada M, Takahashi N, Tokiguchi S, Furusawa T, Sakai K (2002) Atrophy of the basal ganglia as the initial diagnostic sign of germinoma in the basal ganglia. Neuroradiology 44:389–394
86. Tsuruda JS, Chew WM, Moseley ME, Norman D (1990) Diffusion-weighted MR imaging of the brain: value of differentiating between extraaxial cysts and epidermoid tumors. AJNR Am J Neuroradiol 11:925–931
87. Tsuruda JS, Chew WM, Moseley ME, Norman D (1991) Diffusion-weighted MR imaging of extraaxial tumors. Magn Reson Med 19:316–320
88. Maeda M, Kawamura Y, Tamagawa Y (1992) Intravoxel incoherent motion (IVIM) MRI in intracranial, extraaxial tumors and cysts. J Comput Assist Tomogr 16:514–518
89. Laing AD, Mitchell PJ, Wallace D (1999) Diffusion-weighted magnetic resonance imaging of intracranial epidermoid tumours. Australas Radiol 43:16–19
90. Dechambre S, Duprez T, Lecouvet F, Raftopoulos C, Gosnard G (1999) Diffusion-weighted MRI postoperative assessment of an epidermoid tumour in the cerebellopontine angle. Neuroradiology 41:829–831
91. Chen S, Ikawa F, Kurisu K, Arita K, Takaba J, Kanou Y (2001) Quantitative MR evaluation of intracranial epidermoid tumors by fast fluid-attenuated inversion recovery imaging and echo-planar diffusion-weighted imaging. AJNR Am J Neuroradiol 22:1089–1096
92. Bergui M, Zhong J, Bradac GB, Sales S (2001) Diffusion-weighted images of intracranial cyst-like lesions. Neuroradiology 43:824–829

93. Annet L, Duprez T, Grandin C, Dooms G, Collard A, Cosnard G (2002) Apparent diffusion coefficient measurements within intracranial epidermoid cysts in six patients. Neuroradiology 44:326–328
94. Hakyemez B, Aksoy U, Yildiz H, Ergin N (2005) Intracranial epidermoid cysts: diffusion-weighted, FLAIR and conventional MR findings. Eur J Radiol 54:214–220
95. Hu XY, Hu CH, Fang XM, Cui L, Zhang QH (2008) Intraparenchymal epidermoid cysts in the brain: diagnostic value of MR diffusion-weighted imaging. Clin Radiol 63:813–818
96. Hayashi Y, Tachibana O, Muramatsu N, Tsuchiya H, Tada M, Arakawa Y, Suzuki M, Yamashita J (1999) Rathke cleft cyst: MR and biomedical analysis of cyst content. J Comput Assist Tomogr 23:34–38
97. Sener RN, Dzelzite S, Migals A (2002) Huge craniopharyngioma: diffusion MRI and contrast-enhanced FLAIR imaging. Comput Med Imaging Graph 26:199–203
98. Kunii N, Abe T, Kawamo M, Tanioka D, Izumiyama H, Moritani T (2007) Rathke's cleft cysts: differentiation from other cystic lesions in the pituitary fossa by use of single-shot fast spin-echo diffusion-weighted MR imaging. Acta Neurochir (Wien) 149:759–769
99. Pierallini A, Caramia F, Falcone C, Tinelli E, Paonessa A, Ciddio AB, Fiorelli M, Bianco F, Natalizi S, Ferrante L, Bozzao L (2006) Pituitary macroadenomas: preoperative evaluation of consistency with diffusion-weighted MR imaging–initial experience. Radiology 239:223–231
100. Rogg JM, Tung GA, Anderson G, Cortez S (2002) Pituitary apoplexy: early detection with diffusion-weighted MR imaging. AJNR Am J Neuroradiol 23:1240–1245
101. Hayashida Y, Hirai T, Morishita S, Kitajima M, Murakami R, Korogi Y, Makino K, Nakamura H, Ikushima I, Yamura M, Kochi M, Kuratsu JI, Yamashita Y (2006) Diffusion-weighted imaging of metastatic brain tumors: comparison with histologic type and tumor cellularity. AJNR Am J Neuroradiol 27:1419–1425
102. Noguchi K, Watanabe N, Nagayoshi T, et al. (1999) Role of diffusion-weighted echo-planar MRI in distinguishing between brain abscess and tumour: a preliminary report. Neuroradiology 41:171–174
103. Park SH, Chang KH, Song IC, Kim YJ, Kim SH, Han MH (2000) Diffusion-weighted MRI in cystic or necrotic intracranial lesions. Neuroradiology 42:716–721
104. Holtas S, Geijer B, Stromblad LG, Maly-Sundgren P, Burtscher IM (2000) A ring-enhancing metastasis with central high signal on diffusion-weighted imaging and low apparent diffusion coefficients. Neuroradiology 42:824–827
105. Hartmann M, Jansen O, Heiland S, Sommer C, Munkel K, Sartor K (2001) Restricted diffusion within ring enhancement is not pathognomonic for brain abscess. AJNR Am J Neuroradiol 22:1738–1742
106. Geijer B, Holtas S (2002) Diffusion-weighted imaging of brain metastases: their potential to be misinterpreted as focal ischaemic lesions. Neuroradiology 44:568–573
107. Chang SC, Lai PH, Chen WL, et al. (2002) Diffusion-weighted MRI features of brain abscess and cystic or necrotic brain tumors: comparison with conventional MRI. Clin Imaging 26:227–236
108. Lai PH, Ho JT, Chen WL, Hsu SS, Wang JS, Pan HB, Yang CF (2002) Brain abscess and necrotic brain tumor: discrimination with proton MR spectroscopy and diffusion-weighted imaging. AJNR Am J Neuroradiol 23:1369–1377
109. Guzman R, Barth A, Lovblad KO, et al. (2002) Use of diffusion-weighted magnetic resonance imaging in differentiating purulent brain processes from cystic brain tumors. J Neurosurg 97:1101–1107
110. Hein PA, Eskey CJ, Dunn JF, Hug EB (2004) Diffusion-weighted imaging in the follow-up of treated high-grade gliomas: tumor recurrence versus radiation injury. AJNR Am J Neuroradiol 25:201–209
111. Stokkel M, Stevens H, Taphoorn M, Van Rijk P (1999) Differentiation between recurrent brain tumour and post-radiation necrosis: the value of 201Tl SPET versus 18F-FDG PET using a dual-headed coincidence camera–a pilot study. Nucl Med Commun 20:411–417
112. Tsuyuguchi N, Takami T, Sunada I, Iwai Y, Yamanaka K, Tanaka K, Nishikawa M, Ohata K, Torii K, Morino M, Nishio A, Hara M (2004) Methionine positron emission tomography for differentiation of recurrent brain tumor and radiation necrosis after stereotactic radiosurgery–in malignant glioma. Ann Nucl Med 18:291–296
113. Jain R, Scarpace L, Ellika S, Schultz LR, Rock JP, Rosenblum ML, Patel SC, Lee TY, Mikkelsen T (2007) First-pass perfusion computed tomography: initial experience in differentiating recurrent brain tumors from radiation effects and radiation necrosis. Neurosurgery 61:778–786
114. Sugahara T, Korogi Y, Tomiguchi S, Shigematsu Y, Ikushima I, Kira T, Liang L, Ushio Y, Takahashi M (2000) Posttherapeutic intraaxial brain tumor: the value of perfusion-sensitive contrast-enhanced MR imaging for differentiating tumor recurrence from nonneoplastic contrast-enhancing tissue. AJNR Am J Neuroradiol 21:901–909
115. Provenzale JM, Mukundan S, Barboriak DP (2006) Diffusion-weighted and perfusion MR imaging for brain tumor characterization and assessment of treatment response. Radiology 239:632–649
116. Rock JP, Scarpace L, Hearshen D, Gutierrez J, Fisher JL, Rosenblum M, Mikkelsen T (2004) Associations among magnetic resonance spectroscopy, apparent diffusion coefficients, and image-guided histopathology with special attention to radiation necrosis. Neurosurgery 54:1111–1117; discussion 1117–1119
117. Schlemmer HP, Bachert P, Henze M, Buslei R, Herfarth KK, Debus J, van Kaick G (2002) Differentiation of radiation necrosis from tumor progression using proton magnetic resonance spectroscopy. Neuroradiology 44:216–222
118. Zeng QS, Li CF, Liu H, Zhen JH, Feng DC (2007) Distinction between recurrent glioma and radiation injury using magnetic resonance spectroscopy in combination with diffusion-weighted imaging. Int J Radiat Oncol Biol Phys 68:151–158
119. Chan YL, Yeung DK, Leung SF, Chan PN (2003) Diffusion-weighted magnetic resonance imaging in radiation-induced cerebral necrosis. Apparent diffusion coefficient in lesion components. J Comput Assist Tomogr 27:674–680

120. Asao C, Korogi Y, Kitajima M, Hirai T, Baba Y, Makino K, Kochi M, Morishita S, Yamashita Y (2005) Diffusion-weighted imaging of radiation-induced brain injury for differentiation from tumor recurrence. AJNR Am J Neuroradiol 26:1455–1460

121. Biousse V, Newman NJ, Hunter SB, Hudgins PA (2003) Diffusion weighted imaging in radiation necrosis. J Neurol Neurosurg Psychiatry 74:382–384

Pediatrics

14.1 Water Content of the Pediatric Brain

The water content of the pediatric brain is considerably higher than that of the adult brain. This makes it more difficult to diagnose ischemic and other lesions in pediatric patients using computed tomography (CT) and MR imaging. Diffusion-weighted (DW) imaging is sensitive to alteration in diffusion of water molecules, and this technique can help overcome some of these difficulties [1]. DW imaging is primarily useful for detecting and characterizing ischemic lesions, but also for evaluation of myelinization by demonstrating anisotropy of the white matter earlier than conventional MR imaging [2, 3].

14.2 Normal Structures

Diffusion-weighted imaging characteristics of a normal brain in young infants are different from those in adults [4]. Apparent diffusion coefficient (ADC) values in both gray and white matter of newborns are considerably higher than in adults. This reflects the high water content of the pediatric brain [5]. For the same reason, the deep white matter in the newborn normally shows hypointensity on DW imaging associated with increased ADC (Fig. 14.1). With increasing age, there is a relative decrease in water content of a pediatric brain (Fig. 14.2). This is more evident in the white matter than in the gray matter. The decrease in water content is caused by myelinization replacing water during normal white matter development [2].

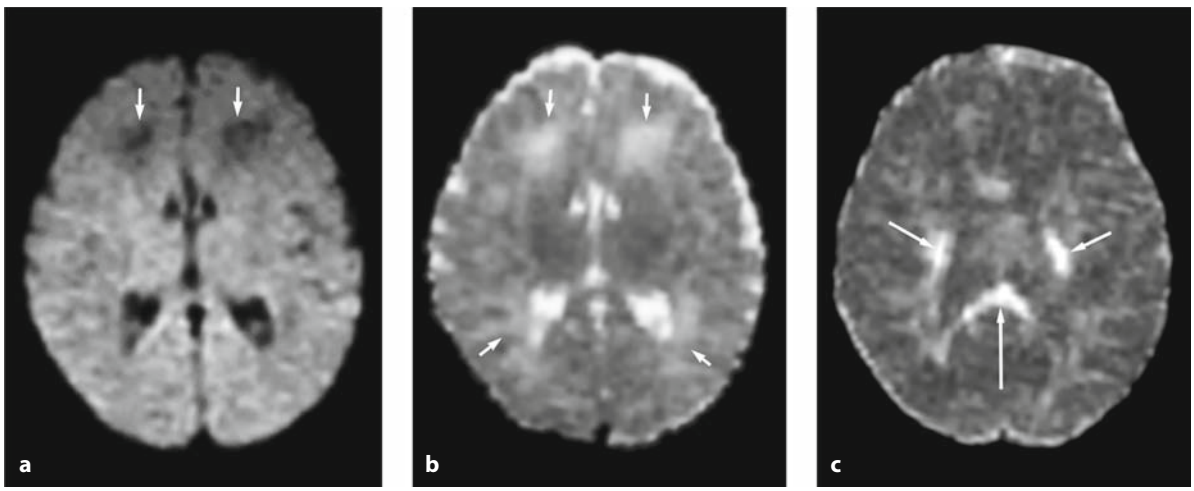

Figure 14.1 a–c

Normal pediatric DW imaging in a 2-day-old boy. **a** Low signal intensity and **b** increased ADC in the deep white matter are normal in this age group (*arrows*). **c** Fractional anisotropy map demonstrates anisotropy along the anterior and posterior limbs of the internal capsules (*arrows*), the corpus callosum (*long arrow*), and the temporo-parieto-occipital white matter earlier than regular T1- and T2-weighted images

14.3 Diffusion Tensor Imaging and Anisotropy

Normally anisotropy is much less evident in the immature brain than in the adult. One exception is corpus callosum, where anisotropy is already visible by diffusion imaging as early as the 28th gestational week. This occurs although the corpus callosum is composed of non-myelinated fibers. The phenomenon has been called premyelination anisotropy [3]. The anisotropic effect in the immature brain is thought to be related to structural changes of the axonal membrane. Anisotropy in the white matter of newborns and infants is lower than in adults (Figs. 14.1, 14.2). The anisotropic pattern can vary depending on the irregularity of axonal orientation as well as the degree of myelination. Structural and functional alterations of the axons and oligodendrocytes that may affect diffusion anisotropy include an increase of the axonal diameter, increase in the concentration of the microtubule-associated proteins and microperoxysome, activity of Na+/K+-ATPase, and ion fluxes secondary to action potentials [6].

Diffusion tensor (DT) imaging is useful for evaluating the myelination and premyelination states of the infant brain. Data of fractional anisotropy (FA) and ADC values have been reported in utero, in newborns (preterm, term), infants, and early childhood [7-17]. FA and ADC values dramatically change during the in utero period (32 weeks) in the pyramidal tract and the corpus callosum [7] and in the first 3 months of life. In the first 3 months, the early rate of ADC decrease is twice as great for peripheral white matter than deep white matter, while the rate of FA increase is half as great for peripheral white matter than deep white matter [12]. DT imaging allows earlier detection of specific anatomic microstructural abnormalities in infants at risk for neurological abnormalities and disability [9].

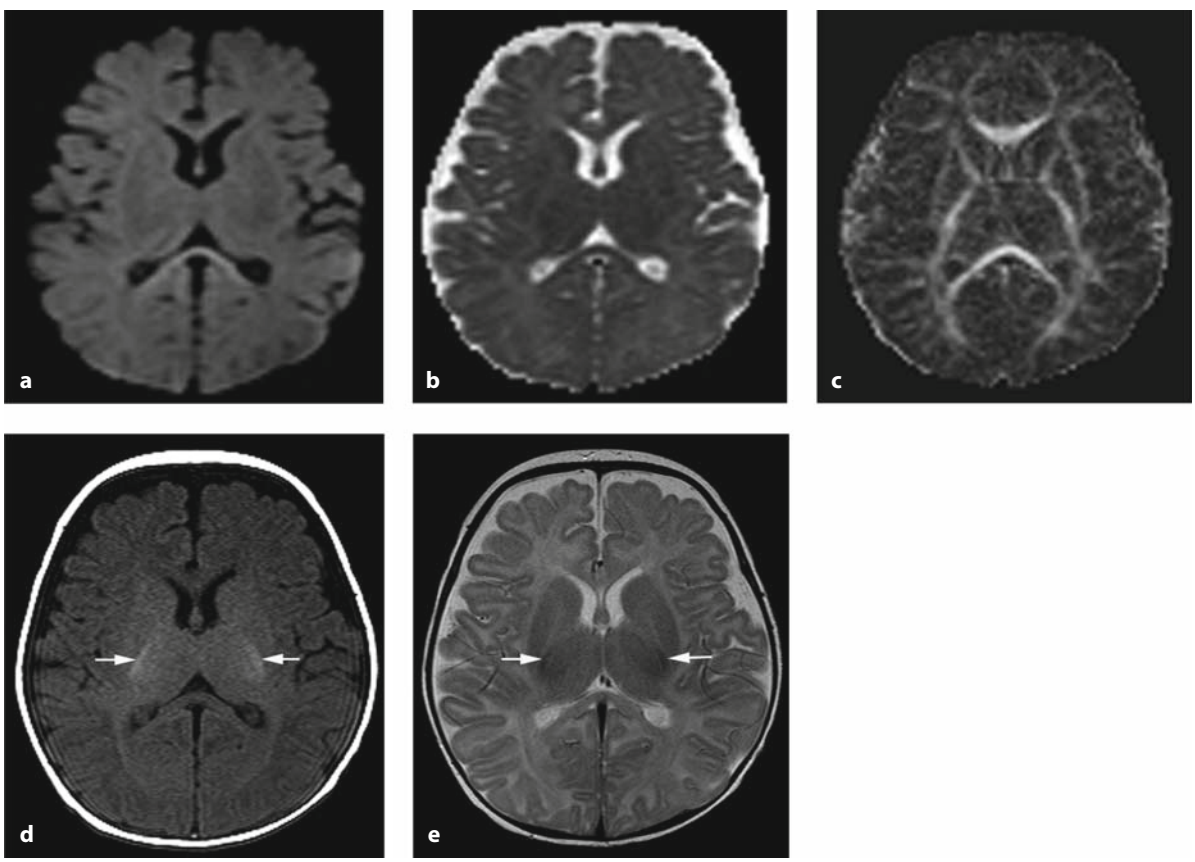

14.4 Infarction and Ischemia

Ischemic infarctions in children are uncommon when compared with adults and they have different etiologies. They can be caused by thrombosis, embolism, arterial dissection, vasculitis, Moyamoya disease, sickle cell disease, child abuse, etc. (Figs. 14.3–14.6) [18, 19]. Hyperacute and acute infarctions are characterized by cytotoxic edema. Vasogenic edema occurs later and is typically seen in the subacute phase. DW imaging is useful for early detection of infarction in children, but also to differentiate between acute/subacute infarctions and chronic infarctions or ischemic gliosis.

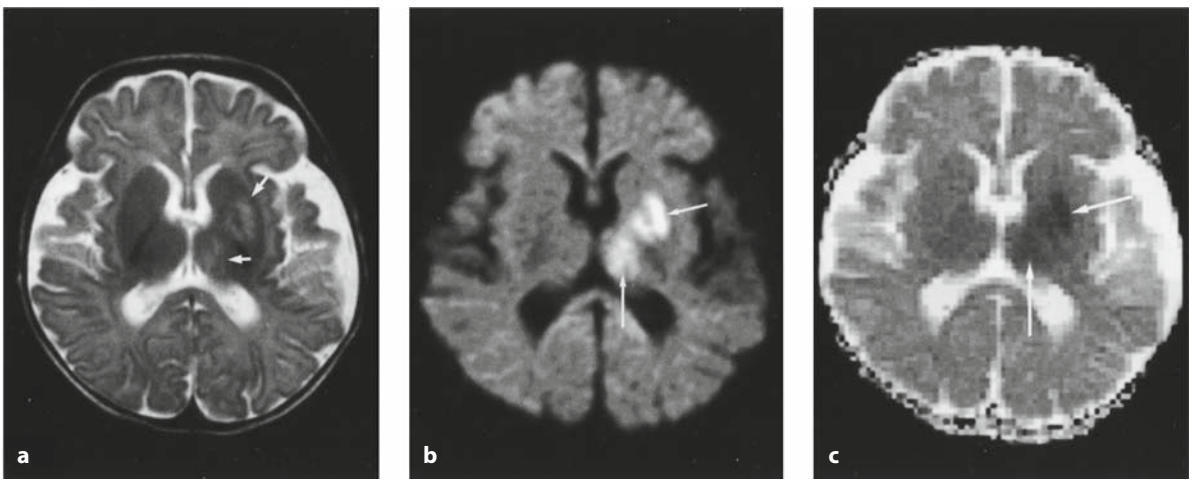

Figure 14.3 a–c

Cerebral infarction due to embolism in a 3-month-old boy. He had Down syndrome and ventricular septal defect. **a** T2-weighted image shows mild high signal lesions in the left putamen and thalamus (*arrows*). **b** DW image shows these lesions as high signal intensity (*arrows*). **c** ADC is decreased (*arrows*), consistent with acute infarcts

Figure 14.2 a–e

Normal MR image in a 2-month-old girl. **a, b** The low signal intensity on DW imaging and increased ADC in the deep white matter are no longer visualized in this age group. The ADC values in the gray matter and corpus callosum appear slightly lower than in the other white matter. **c** Fractional anisotropy map demonstrates anisotropy noted not only in the corpus callosum and internal capsules but also the entire white matter including U-fibers. **d, e** T1- and T2-weighted images show myelination mainly in the posterior limb of the internal capsules (*arrows*)

◀

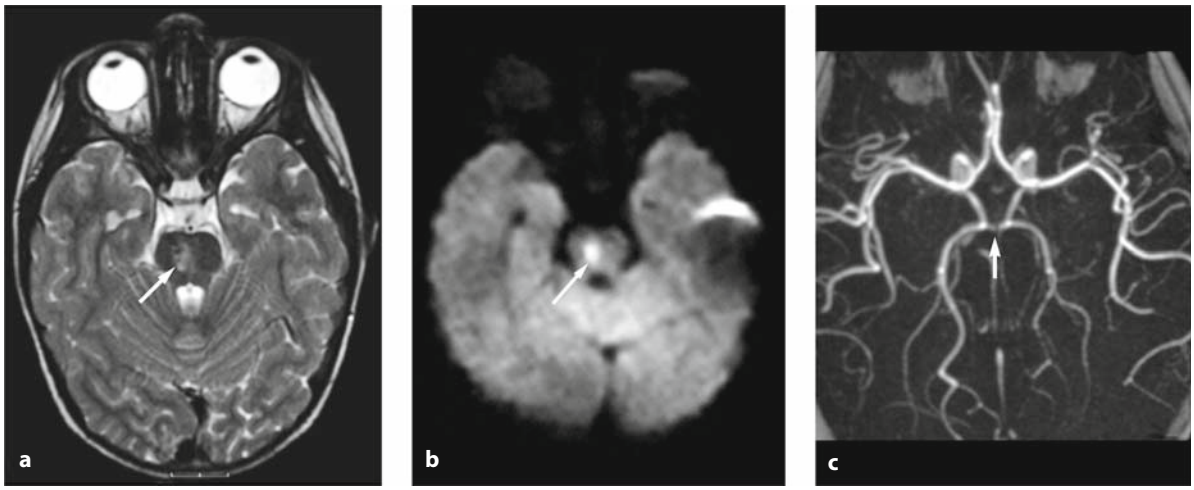

Figure 14.4 a–c

Dissection of the vertebrobasilar arteries and infarction in a 4-year-old girl. **a** T2-weighted image shows high signal lesion in the right medial side of the pons (*arrow*). **b** DW image shows this lesion as hyperintense with decreased ADC (not shown), representing an acute infarct (*arrow*). **c** On MR angiography the vertebrobasilar arteries are absent due to dissection of the vertebrobasilar arteries (*arrow*). The posterior cerebral arteries are supplied from the anterior circulation

14.4.1 Moyamoya Disease

Moyamoya disease is a chronic cerebrovascular occlusive disease of unknown origin that occurs predominantly in East Asia. In children it is characterized by progressive arterial stenosis with cerebral infarctions. The stenosis involves primarily the circle of Willis and the supraclinoid portion of the internal carotid arteries. Typically the internal carotid arteries are occluded bilaterally. In so-called "probable" Moyamoya disease, there is unilateral occlusion of one of the carotid arteries in its supraclinoid portion. DW imaging is useful for early detection of cerebral ischemia in this disease (Fig. 14.5) [18].

14.4.2 Sickle Cell Disease

About 5%–8% of patients with sickle cell disease develop symptomatic cerebrovascular disease [19]. The risk of stroke is greatest during thrombotic crises and during the first 15 years of life. Stenosis or occlusion of both large and small vessels can cause cerebral infarction. Sickle cell disease results in vasculopathy, which in many respects is similar to Moyamoya disease. Cortical and white matter watershed ischemia is common; however, patients with sickle cell disease often also demonstrate multiple ischemic white matter lesions. These lesions can occur in spite of normal MR angiography and conventional angiography (Fig. 14.6) [20]. They are thought to be due to small vessel ischemia similar to what is seen in small vessel disease of older patients.

Figure 14.6 a–c

Sickle cell disease in a 4-year-old boy presenting with severe headache. **a** T2-weighted image shows multiple high signal spots in the white matter (*arrows*). **b** DW image shows some of these spots as very high signal intensity, representing small acute infarcts (*arrows*). **c** ADC map shows decreased ADC of these lesions consistent with small ischemic lesions (*arrows*). (From [45])

►

Figure 14.5 a–c

"Probable" Moyamoya disease in a 7-year-old girl. **a** T2-weighted image shows mild high signal lesions in the right basal ganglia. **b** DW image shows ischemic lesions not only in the basal ganglia but also in the parieto-occipital region as high signal, representing acute infarcts (*arrows*). **c** MR angiography shows occlusion of the right middle cerebral artery and stenosis of the right internal carotid artery (*arrows*) and bilateral posterior cerebral arteries (*arrowheads*)

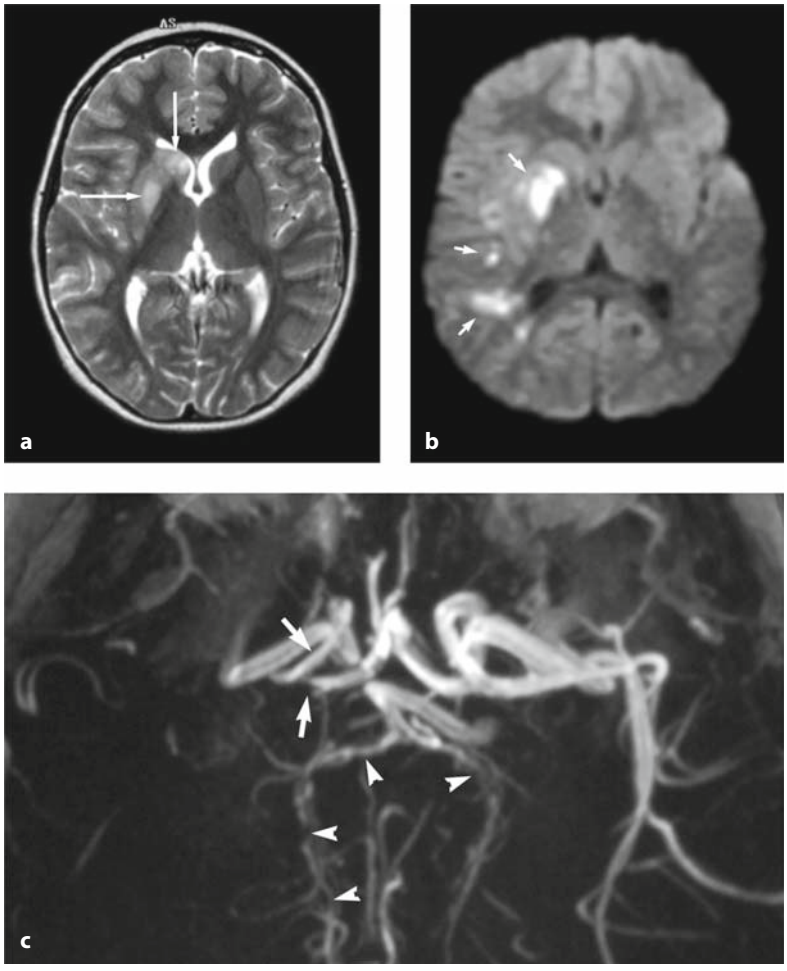

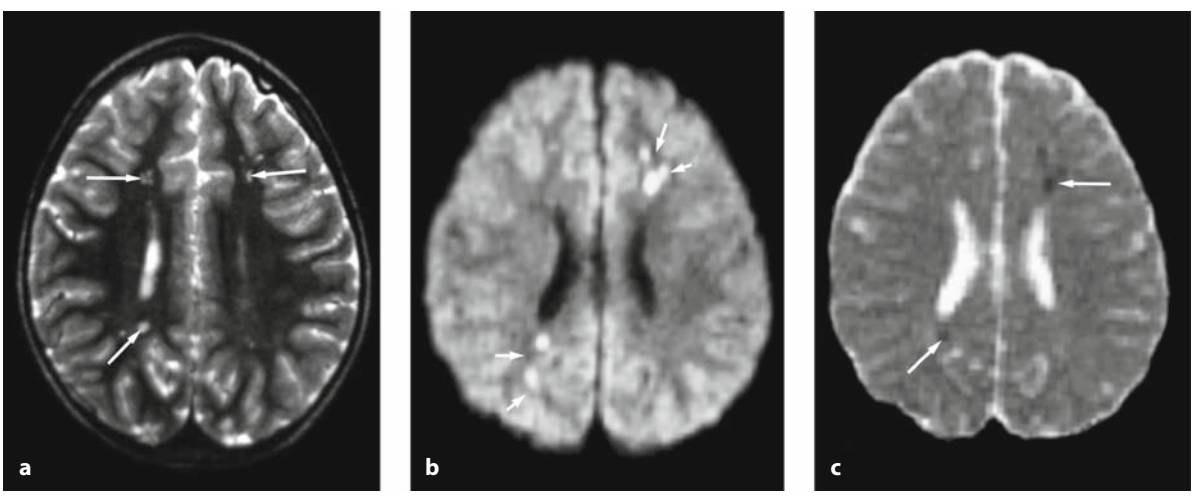

14.4.3 Cerebral Venous Sinus Thrombosis

Cerebral venous sinus thrombosis and venous infarction/hemorrhage are common in children. Risk factors include infections, perinatal complications, hematologic disorders, nephritic syndrome, malignancy, and collagen vascular disease among others. Parasagittal infarction/hemorrhage is seen in superior sagittal sinus thrombosis, temporal lobe involvement is associated with transverse sinus and vein of Labbe thrombosis, and thalamic or basal ganglia involvement is associated with deep vein thrombosis (Fig. 14.7). Reduced venous outflow due to venous sinus occlusion causes leakage of fluid (vasogenic edema) and hemorrhage into the extracellular space. If adequate venous collaterals are not established, subsequent venous infarction will occur. Gradient-echo T2*-weighted imaging is very useful in the detection of acute- to subacute-phase thrombi as very low signals, especially before T1-weighted imaging shows high signals in the subacute-phase thrombi. DW imaging shows subacute-phase thrombi as high signals with decreased ADC. Accelerated myelination has been reported in association with cerebral venous thrombosis in neonates [21].

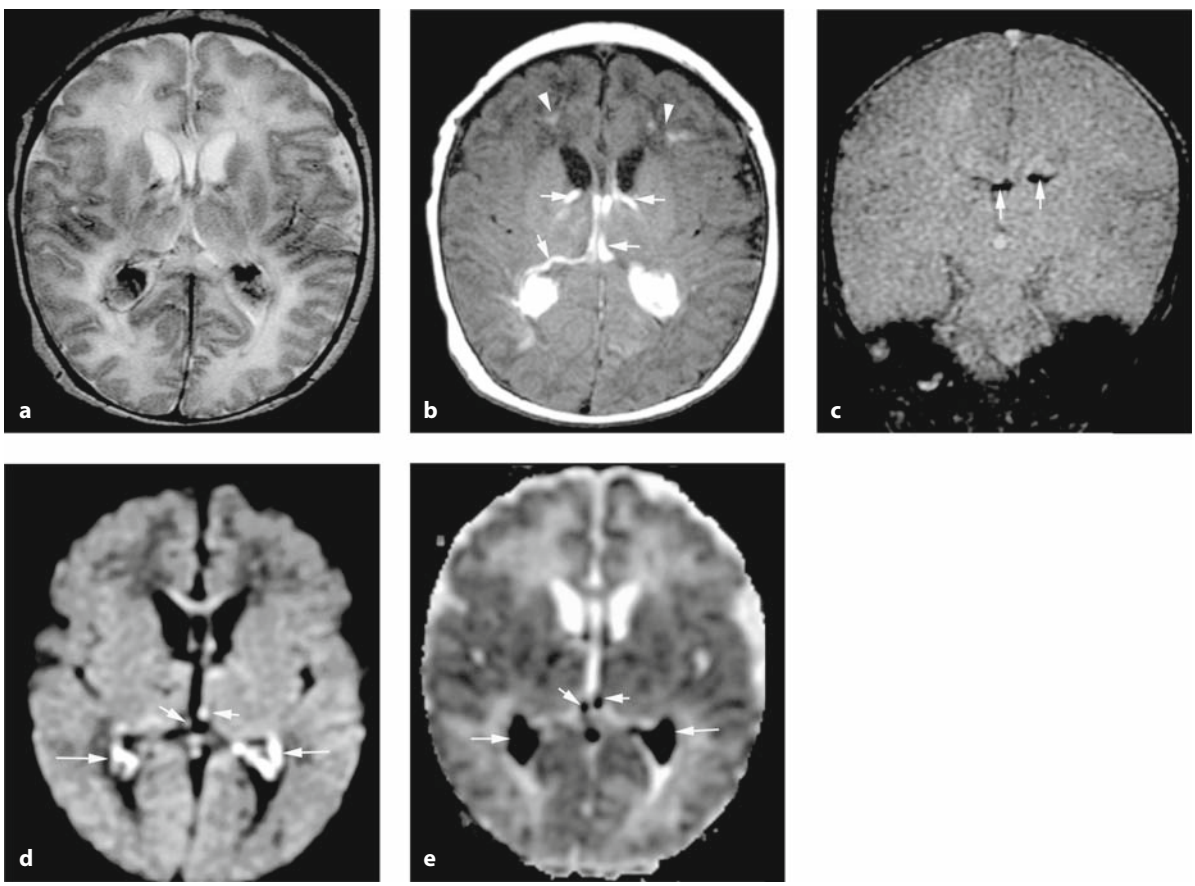

Figure 14.7 a–e

Cerebral venous sinus thrombosis in a 5-day-old boy with bacterial meningitis. **a, b** Hemorrhage in the choroid plexi is hyperintense on T1- and hypointense on T2-weighted image. Precontrast T1-weighted image shows thrombi in the bilateral internal cerebral veins and branches as hyperintense (*arrows*). Small T1 hyperintense petechial hemorrhage is seen in the bilateral frontal white matter related to venous ischemia (*arrowheads*). **c** Coronal gradient-echo image demonstrates the thrombi as hypointense (*arrows*). **d, e** DW imaging shows vasogenic edema in the bilateral frontal white matter as hypointense with increased ADC, and the venous thrombi and hemorrhage in the choroid plexi as hyperintense with decreased ADC (*arrows*)

14.4.4 Vein of Galen Malformations

Vein of Galen malformation is thought to result from the development of an arteriovenous connection between the primitive choroidal vessels and median prosencephalic vein of Markowski. There are two main types: (1) the choroidal type (90%) characterized by numerous feeders occurring in neonates, (2) the mural type characterized by fewer feeders occurring in infants. Progressive stenosis of the jugular bulbs complicates the course in many cases. Ischemia can occur as arterial or venous type, associated with steal phenomena of the arteriovenous shunt and the treatment. Pre- and posttreatment evaluations of the extent of ischemic brain injury are important for providing information on likely neurological and developmental sequelae (Fig. 14.8) [22].

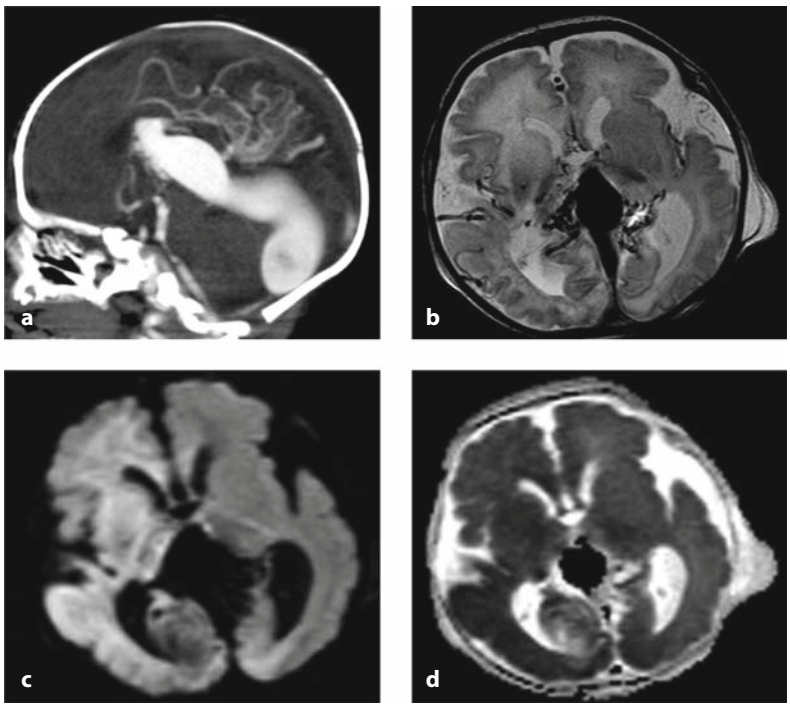

Figure 14.8 a–d

Vein of Galen malformation in a 10-day-old boy. **a** Postcontrast CT shows a dilated venous structure with multiple feeders. **b** T2-weighted image shows the vein of Galen malformation and dilated feeding arteries. Hyperintensity in the right frontal white matter suggests the presence of ischemia. **c, d** DW imaging shows cytotoxic edema in the entire right hemisphere and the left occipital lobe associated with decreased ADC

14.4.5 Hypoxic Ischemic Encephalopathy

Hypoxic ischemic encephalopathy is the result of decreased global perfusion or oxygenation. It is generally due to neonatal anoxia, hypoglycemia, suffocation, cardiac arrest, or child abuse. Whether produced by ischemia, anoxia, or hypoglycemia, it is remarkably similar to infarcted brain in its appearance histologically. The distribution of hypoxic ischemic encephalopathy varies according to the duration, degree, and abruptness of the hypoxic and/or ischemic insults, basal blood flow, and metabolic activity in the areas of ischemia, temperature, and serum glucose levels.

Diffusion-weighted imaging often depicts acute or subacute ischemic lesions when MR imaging and CT scans are normal or show only subtle abnormalities (Figs. 14.9, 14.10) [23–28]. The distribution of the lesions in the putamen, thalamus, and perirolandic cerebral cortex is related to intrinsic vulnerability of these areas to energy failure. One potentially important link among these areas is their interconnection by excitatory circuits. Thus, overactivity in these excitatory pathways could propagate to other locations through synaptic connections. The corticospinal tract, corpus callosum, and deep gray matter can be secondarily involved through these pathways, also known as secondary Wallerian and transsynaptic degenerations [29]. Diffuse hyperintensity on DW imaging with decreased ADC in the corpus callosum, and along the pyramidal tract in the internal capsules and the brain stem is occasionally seen. This is presumably due to cytotoxic edema of the glial cells, axons and myelin sheaths [30].

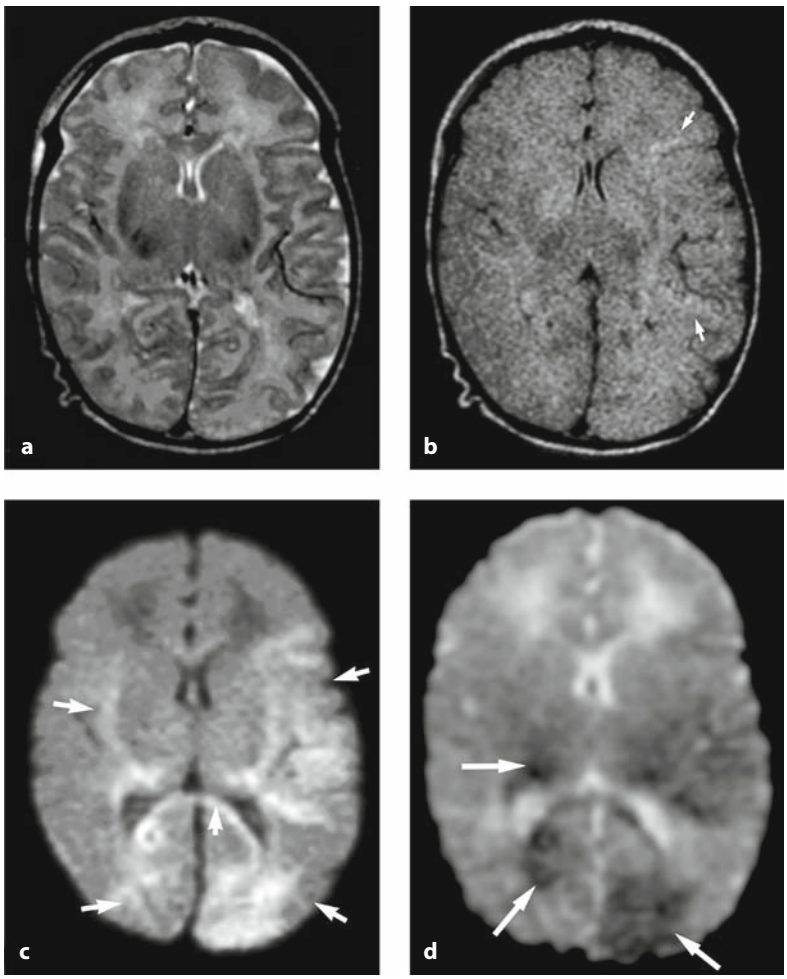

Figure 14.9 a–d

Hypoxic ischemic encephalopathy secondary to intrauterine cerebrovascular accident in a 2-day-old term girl. **a** T2-weighted image appears normal. **b** Fluid attenuated inversion-recovery (FLAIR) image shows slightly high signal in the white matter (*arrows*). **c** DW image shows bilateral hyperintense lesions in the temporo-occipital cortices, white matter and corpus callosum (*arrows*), representing ischemic lesion and cytotoxic edema. **d** ADC map shows corresponding decreased ADC values

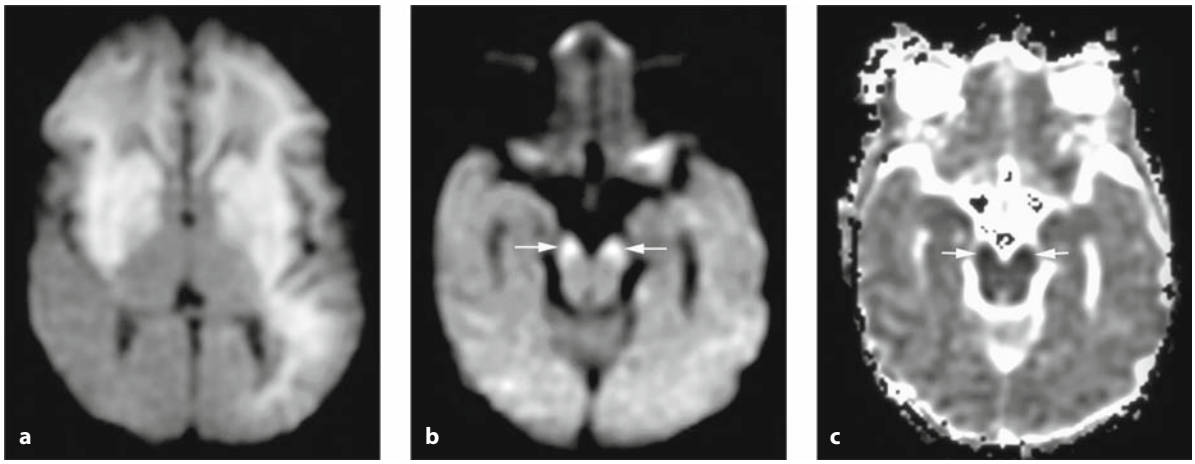

Figure 14.10 a–c

Hypoxic ischemic encephalopathy in a 10-day-old boy. **a** DW image shows extensive hyperintense lesions involving the fronto-temporo-parietal white matter, internal capsules and basal ganglia bilaterally. **b, c** DW image shows hyperintense lesions with decreased ADC in the bilateral cerebral peduncles probably including both corticospinal tracts (*arrows*). These findings represent the early phase of wallerian degenerations

The prognosis of hypoxic ischemic encephalopathy depends on the extension of the cytotoxic edema, which is seen as hyperintensity on DW imaging. Hypoxic ischemic injury with cytotoxic edema is usually irreversible. DW imaging is helpful in establishing both the diagnosis and the prognosis, but also in the management of hypoxic ischemic encephalopathy. Abnormal ADC and FA values may help in early and more accurate assessment of microstructural damage in hypoxic ischemic encephalopathy that may have predictive value for long-term neurofunctional outcome in neonates [31].

14.5 Trauma

14.5.1 Nonaccidental Head Injury

Nonaccidental head injury (NAHI), shaking baby (impact) syndrome, is most commonly seen among children under 3 years of age with the majority of cases occurring during the first year. In the USA, there are an estimated 3,000 deaths per year from NAHI. Because of anatomic and developmental differences in the brain and skull of young children, the mechanisms and types of brain injury are distinctly different from those seen in older children and adults. Young infants have a relatively large head, weak neck muscles, and thin calvarial bones separated by soft membranous sutures and fontanelles, making them extremely vulnerable to traumatic injuries (deformation-mediated impact, shearing stress). Unmyelinated white matter is also vulnerable to such traumatic injuries and hypoxia [32].

In experimental studies of acute subdural hematomas in the infant rat, the glutamate concentration in the extracellular fluid of cortex was increased more than seven times over the basal level [33]. The postnatal period of brain development is particularly vulnerable to excitotoxic injury. Excitatory amino acid receptors are abundant in the cortex during the first 2 years of life. The high rate of generation of synapses (synaptogenesis) results in an overexpression of the receptor. NMDA receptors dominate in the immature brain when synaptic transmission is weak and extremely plastic. Experimental studies show that too many or too few NMDA receptors can be threatening to developing neurons. During maturation, non-NMDA receptors, alpha-amino-3-hydroxy-5-methyl-5-isoxazolepropionate (AMPA) receptors and kainic receptors, predominate. This suggests that the primary increased release of glutamate from the presynaptic terminal following traumatic stimuli and the primary decreased re-uptake of glutamate from the synapse following hypoxic or ischemic events are related to brain parenchymal injuries [29].

The clinical presentation of NAHI is nonspecific. NAHI is suspected when retinal hemorrhage is present (75%-90%), or when the magnitude of the injuries demonstrated clinically or on neuroimaging is discrepant with the history provided. Histologic similarities have been observed in child abuse victims and infants with hypoxic ischemic encephalopathy. However, a history of apnea suggesting hypoxic–ischemic injury was only found in 57% (16/28) of the child abuse cases [34]. In a neuropathology study it was noted that diffuse axonal injuries were rare among child abuse victims, only seen in three out of 53 cases [35].

Subdural hematomas are the most common associated intracranial pathology in NAHI. The distribution of parenchymal injuries is usually not related to the vascular territories. Some parenchymal lesions are located subjacent to subdural hematomas but other parenchymal lesions are not related to the location and size of subdural hematomas on CT and MR imaging (Figs. 14.11, 14.12). It can be difficult to detect brain parenchyma injuries on CT as well as on routine MR imaging.

Diffusion-weighted imaging has a significant role in recognizing the extent of brain parenchymal injury. The parenchymal lesions can be unexpectedly extensive and caution is needed to window DW imaging optimally (Fig. 14.13). Quantifying the ADC value is especially useful to detect extensive parenchyma abnormalities. The severity of abnormality in DW imaging correlates with the patient's outcome [36]. MR spectroscopy can also evaluate the severity of trauma, as this will show decreased *N*-acetyl aspartate (NAA) (decreased neuronal activity), increased lactate (metabolic acidosis) and increased glutamate/glutamine (Gx) (increased extracellular glutamate); the degree of these changes seems to be related to the severity of brain damage (Figs. 14.11, 14.12) [37]. Gx levels peak early after injury and then fall rapidly. This grading may become important in the future since neuroprotective effects have been reported with several kinds of selective glutamate receptor antagonists in animal studies [38–40].

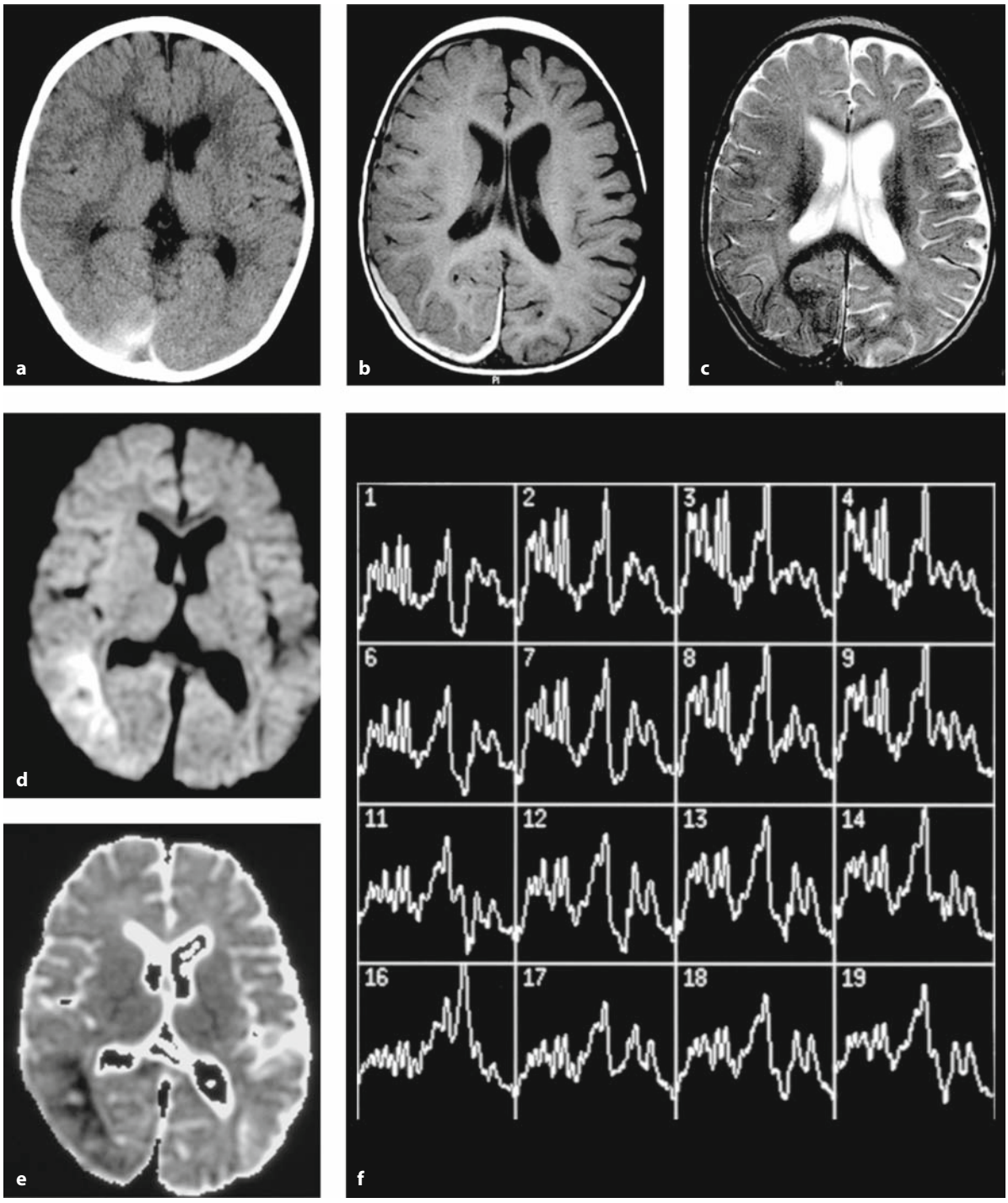

Figure 14.11 a–f

Nonaccidental head injury in a 9-month-old boy. **a–c** CT and T1- and T2-weighted images show an acute subdural hematoma in the right parieto-occipital region. CT and conventional MR images show no apparent parenchymal lesions. **d, e** DW image shows a hyperintense lesion in the right parieto-occipital region subjacent to the subdural hematoma. **f** Multivoxel MR spectroscopy (TE 30 ms) shows increased glutamate/glutamine and lipid/lactate peaks

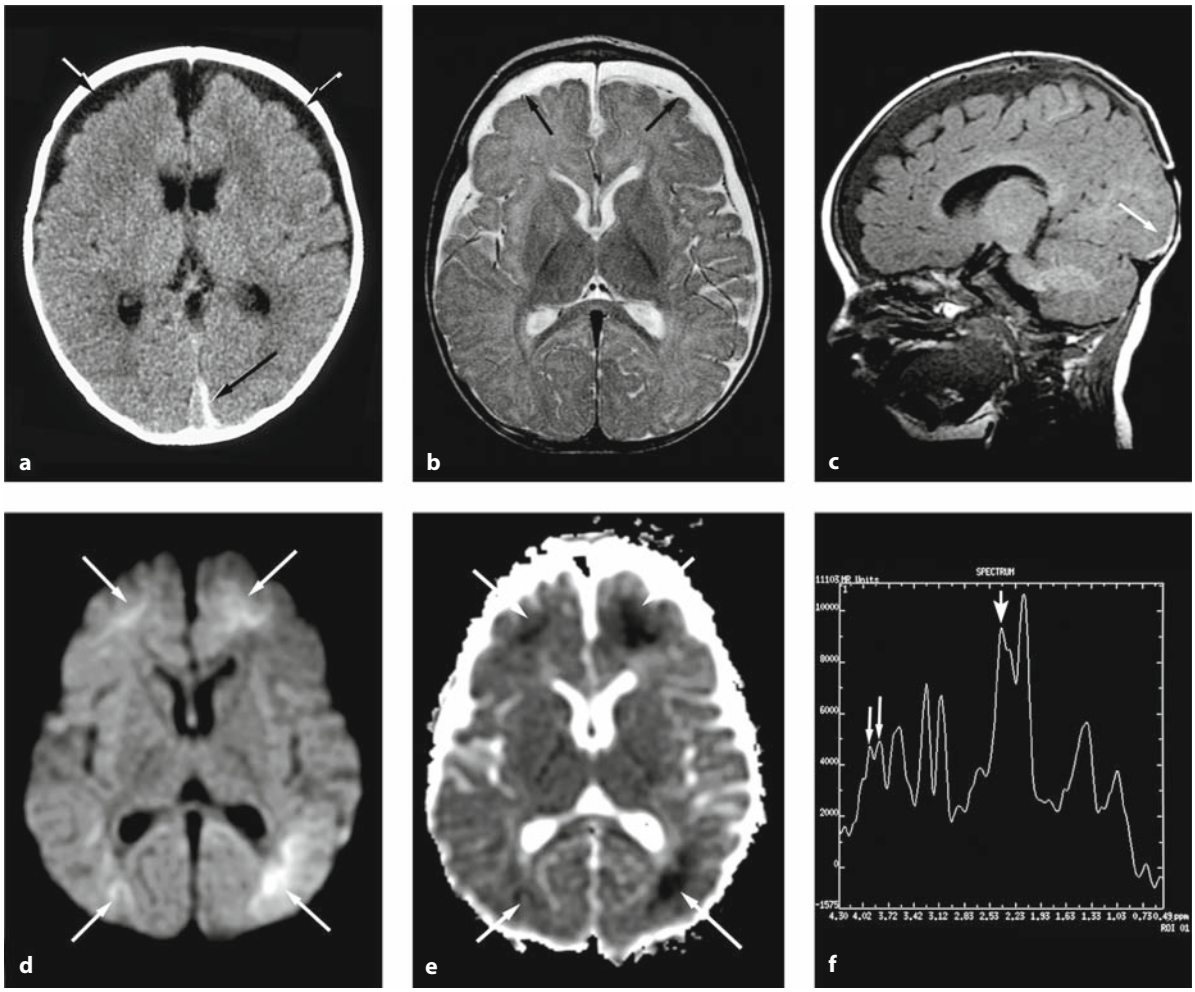

Figure 14.12 a–f

Nonaccidental head injury in a 6-month-old boy. **a** CT shows high density area representing acute subdural hematoma in the left occipital region (*long arrow*), and bilateral subdural fluid collections in the frontal region (*short arrows*). **b** T2-weighted image also shows bilateral subdural fluid collection and no apparent abnormalities in the brain parenchyma. **c** Sagittal T1-weighted image shows acute subdural hematoma as small linear hyperintensity in the occipital area (*arrow*). **d**, **e** DW image shows the extent of parenchymal abnormality as hyperintense lesions with decreased ADC in bilateral fronto-parieto-occipital white matter (*arrows*). The distribution of the parenchymal lesion is not related to that of the subdural hematomas and is rather similar to that of hypoxic–ischemic encephalopathy. **f** MR spectroscopy (TE 30 ms) shows an increased glutamate/glutamine peak (*arrow*) that may represent increased glutamate release or decreased glutamate re-uptake

Figure 14.13 a–d

Nonaccidental head injury in a 2-month-old boy. **a** T2-weighted image shows intracranial hemorrhages with shearing injury (*arrows*) and bilateral chronic subdural hematomas in the bilateral occipital regions. **b** DW image shows diffusely increased signal in both hemispheres (*arrows*) with sparing of only the right frontal area. **c** DW image filmed with incorrect window and level setting, suggesting wrongly that the low signal in the right frontal area is abnormal (*arrows*), when indeed this is the only normal portion of the brain. Correct window and levels are critical, as is comparison with findings on other sequences. **d** ADC values are decreased (0.31×10^{-3}/mm^2/s) in the diffuse parenchymal abnormalities (*arrows*)

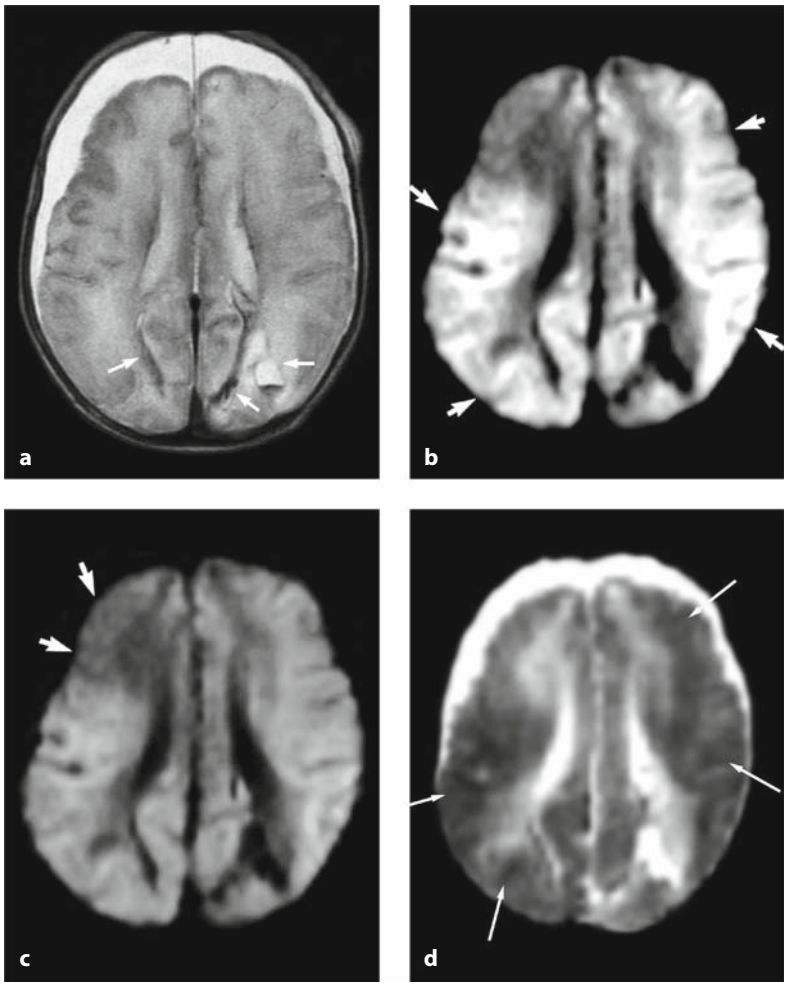

14.5.2 Diffuse Axonal Injury and Brain Contusion

It was once considered that edema following brain contusion or diffuse axonal injury (DAI) was vasogenic. Experimental studies using DW imaging have shown that edematous regions following injury consist of both vasogenic and cytotoxic edema [41, 42]. DAI usually occurs in older children. DAI is related to excitotoxic mechanisms, particularly glutamate and NMDA receptors. Axonal damage often occur at the node of Ranvier (a short interval between processes of oligodendrocytes), resulting in a traumatic defect in the axonal membrane. DW imaging shows diffuse axonal injury as hyperintense, presumably due to cytotoxic edema (Fig. 14.14). It should be noted, however, that hemorrhagic components often accompany these brain injuries, which will affect the signal intensity on DW imaging. Brain contusions near the skull base are also often overlooked on DW imaging due to susceptibility artifacts.

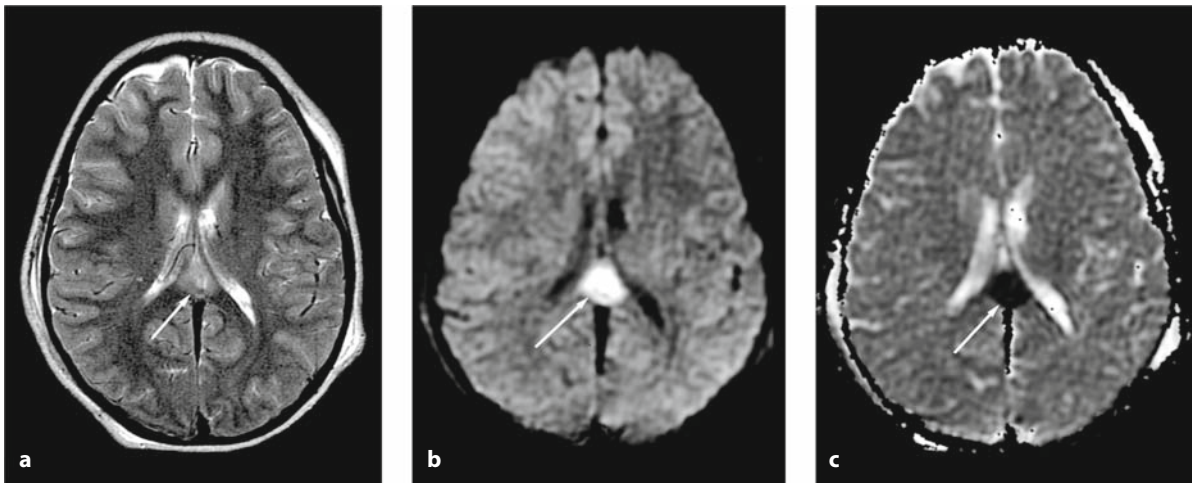

Figure 14.14 a–c

Diffuse axonal injury in an 11-year-old boy injured in a motor vehicle accident. **a** T2-weighted image shows a mildly hyperintense lesion in the corpus callosum (*arrow*). **b** DW image demonstrates this lesion as hyperintense (*arrow*). **c** ADC map shows decreased ADC of this lesion (*arrow*), probably representing cytotoxic edema associated with diffuse axonal injury

14.6 Infections

14.6.1 Encephalitis

Diffusion-weighted imaging can detect early encephalitic changes [43] and is generally more sensitive than conventional MR imaging. Herpes encephalitis demonstrates pathologically severe edema including both cytotoxic and vasogenic edema and massive tissue necrosis with petechial or confluent hemorrhage.

Herpes simplex type 1 encephalitis in older children and adults usually involves the medial temporal lobe, inferior frontal lobes and insula (Fig. 14.15). Neonatal herpes simplex type 2 encephalitis involves the cortex and white matter extensively (Fig. 14.16). Widespread brain lesions in neonatal herpes encephalopathy are presumably related to the vulnerability to excitatory amines in the neonatal brain. The early detection by DW imaging is valuable for early institution of treatment.

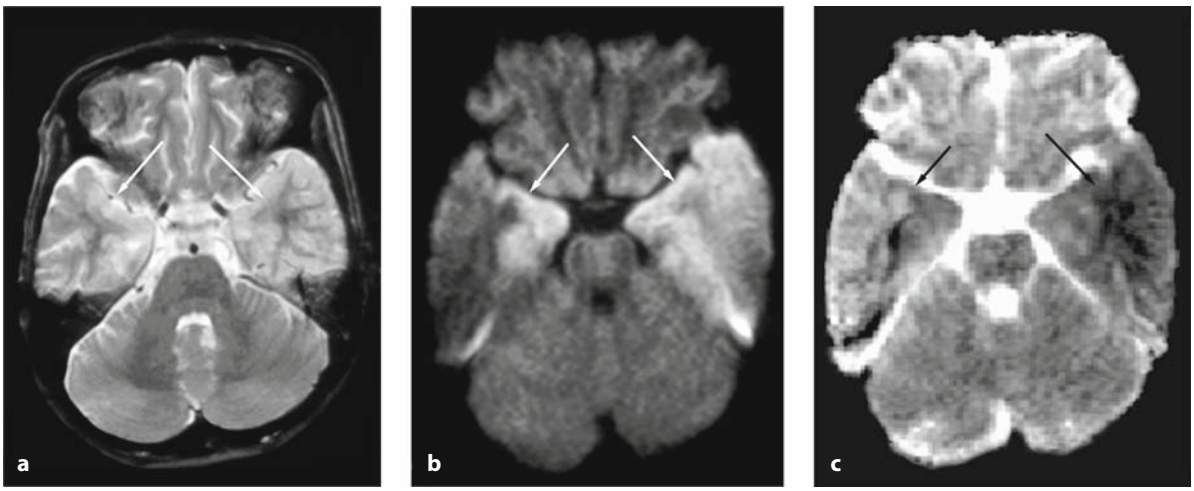

Figure 14.15 a–c

Herpes simplex type 1 encephalitis in an 11-year-old boy. **a** T2-weighted image shows hyperintense lesions in bilateral temporal lobes (*arrows*). **b** DW image clearly shows these lesions as hyperintense (*arrows*). **c** ADC map shows decreased ADC of these lesions (*arrows*)

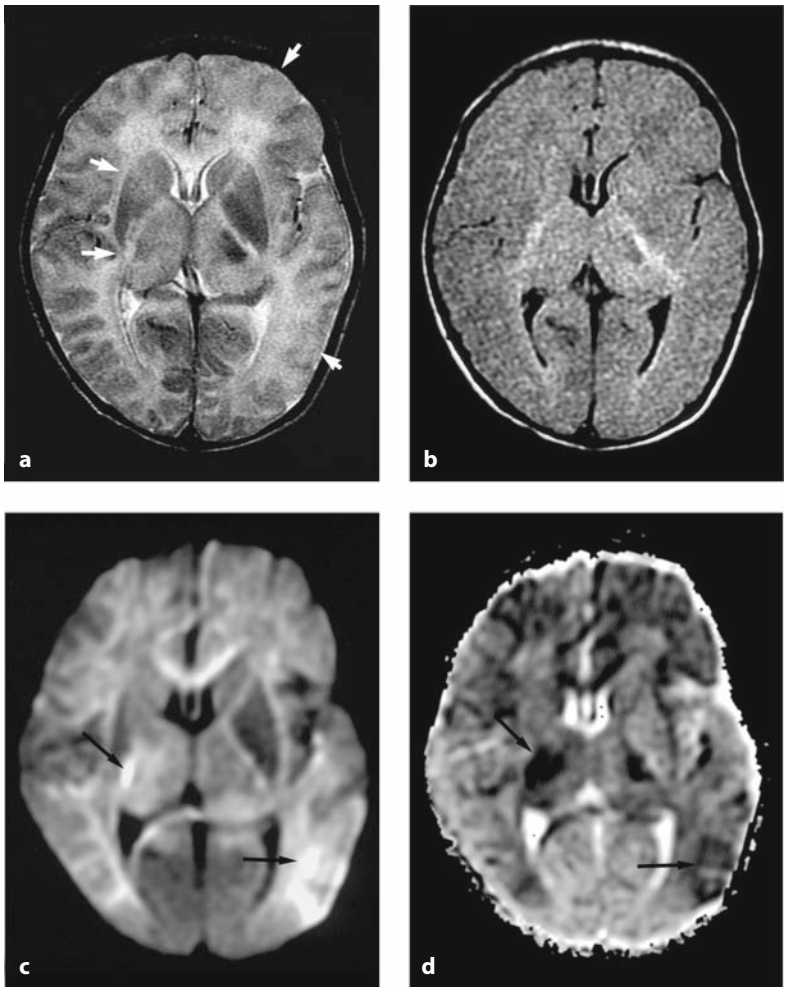

Figure 14.16 a–d

Herpes simplex type 2 encephalitis in a 2-week-old girl. **a** T2-weighted images show asymmetric hyperintense lesions in the thalami and right basal ganglia and cerebral cortices (*arrows*). The precise extent of the lesions is difficult to determine. **b** FLAIR image appears normal. **c, d** DW image shows asymmetric but extensive hyperintense lesions (*arrows*) with decreased ADC in the thalamus and gray and white matter of both hemispheres

14.6.2 Brain Abscess

Abscesses in the brain are potentially fatal, but may be successfully treated by early medical or surgical intervention. DW imaging can discriminate a brain abscess from a cystic or necrotic tumor, which is often difficult with conventional MR imaging [44]. The brain abscess shows very high signal on DW imaging associated with decreased ADC (Fig. 14.17). Pus usually consists of both dead and still viable neutrophils, along with necrotic tissue and bacteria, as well as exuded plasma. A possible explanation for the high signal on DW imaging is limited water mobility, presumably due to the high viscosity of continuous coagulative necrosis and hypercellularity of neutrophils in the pus. Systemic candidal infection occurs in 3%-5% of very low-birth-weight neonates and infants and is often associated with morbidity and mortality. Central nervous system candidiasis is a serious complication but it is often not identified until postmortem examination. Ultrasound and MR imaging are useful for the diagnosis [45]. DW imaging can show multiple candidal microabscesses as hyperintense with decreased ADC (Fig. 14.18).

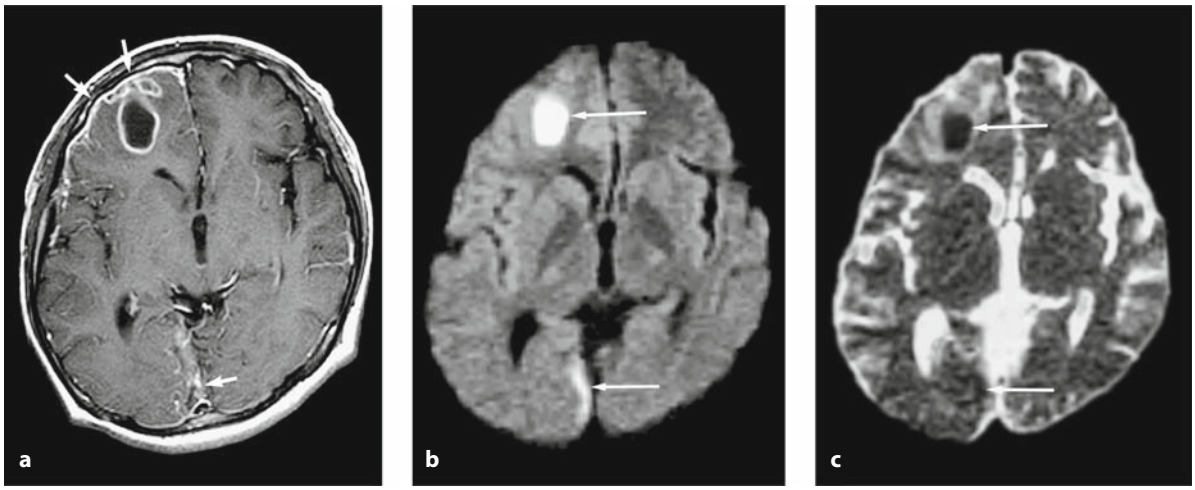

Figure 14.17 a–c

Brain abscess and subdural abscess in a 16-year-old boy with high fever and headache. **a** Gadolinium-enhanced T1-weighted image shows thin-walled ring or rim-enhancing lesions with pachymeningeal enhancement in the right frontal lobe and right medial occipital region (*arrows*). **b** DW image shows cystic components of the right frontal and occipital lesion as very hyperintense (*arrows*). **c** ADC map shows decreased ADC in these cystic components (*arrows*). (Courtesy of Morikawa M. MD, Nagasaki University, School of Medicine, Japan)

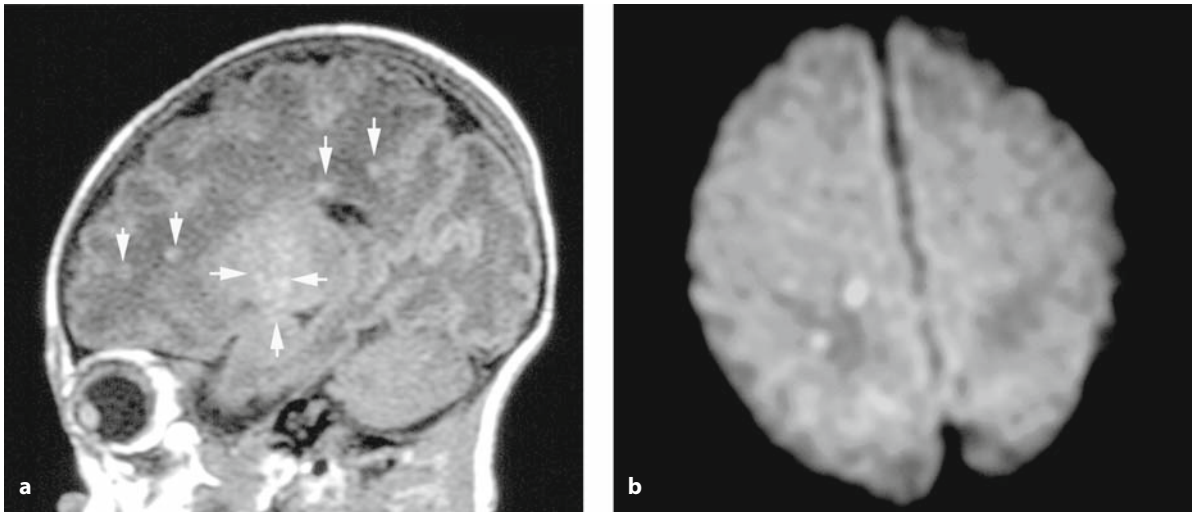

Figure 14.18 a, b

Central nervous system candidiasis in a 4-day-old very-low-birth-weight neonate. **a** Precontrast sagittal T1-weighted image shows multiple small nodular or ring-shaped lesions in the white matter and basal ganglia (*arrows*). **b** DW imaging shows multiple small hyperintense lesions consistent with candidal microabscesses

14.7 Brain Tumor

The signal intensity on DW imaging and the ADC values of brain tumors are variable and related to the architecture of the tumor. Medulloblastoma (Fig. 14.19), cerebral neuroblastone primitive neuroectodermal tumor (Chap. 13, Fig. 13.28), atypical teratoid-rhabdoid tumor (Fig. 14.20), desmoplastic infantile ganglioglioma (Fig. 14.21), choroid plexus carcinoma (Fig. 14.26), lymphoma, germ cell tumor, granulocytic sarcoma, and some of other primary and metastatic tumors can show high signal intensity on DW imaging associated with decreased ADC [46–52] (see Chap. 13). The decreased ADC values, in either benign or malignant tumors, are caused by increased intracellular water, hypercellularity and/or decreased extracellular water in tumor interstitium. Other brain tumors such as pilocytic astrocytoma (Fig. 14.22; Chap. 13, Figs. 13.1, 13.2) and other low grade gliomas (Fig. 14.23) show hyperintensity on DW imaging associated with increased ADC, indicating a T2 shine-through effect. The characteristics on DW imaging and ADC maps have been reported to be correlated with the histological grade in pediatric brain tumors [53]. ADC values are useful in differentiating posterior fossa tumors in pediatric patients (pilocytic astrocytoma $>1.4\times10^{-3}$ mm^2/s, medulloblastoma $<0.9\times10^{-3}$ mm^2/s, specificity 100 %) [54].

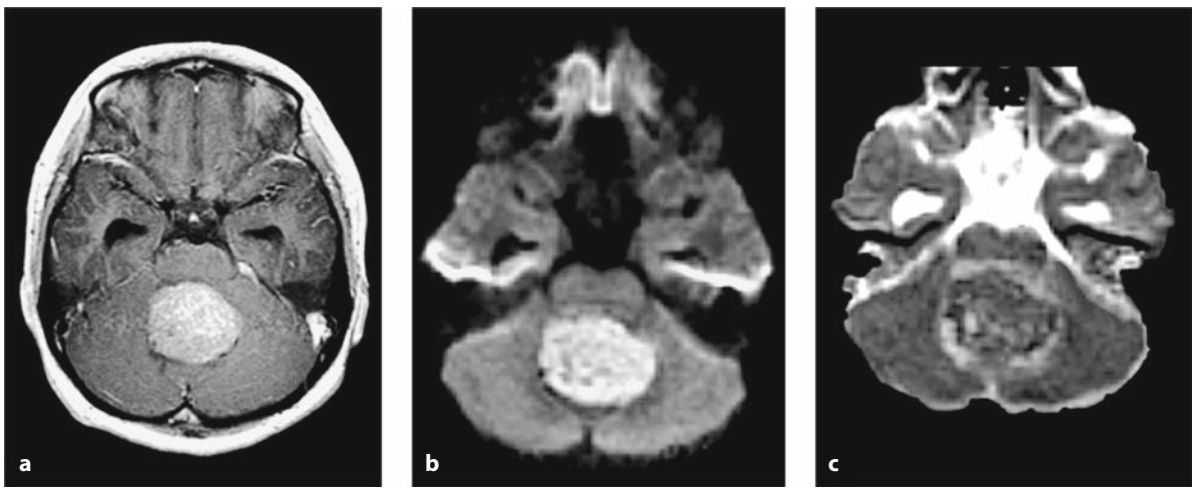

Figure 14.19 a–c

Medulloblastoma in a 10-year-old boy. **a** Gadolinium-enhanced T1-weighted image shows a solid mass with enhancement in the cerebellar vermis. **b** DW image shows this solid mass as hyperintense. **c** ADC map shows decreased ADC of this mass. This is due to high cellular density causing restricted diffusion. (Courtesy of Morikawa M., MD, Nagasaki University, School of Medicine, Japan)

Figure 14.20 a–d

Atypical teratoid-rhabdoid tumor in a 14-month-old boy. **a** T2-weighted image shows a heterogeneous mass lesion with surrounding edema in the right frontal white matter. **b** Gadolinium-enhanced T1-weighted image shows a heterogeneously enhancing mass. **c** DW image shows an iso- or slightly hyperintense mass. **d** ADC map shows partially decreased ADC in this mass (*arrow*)

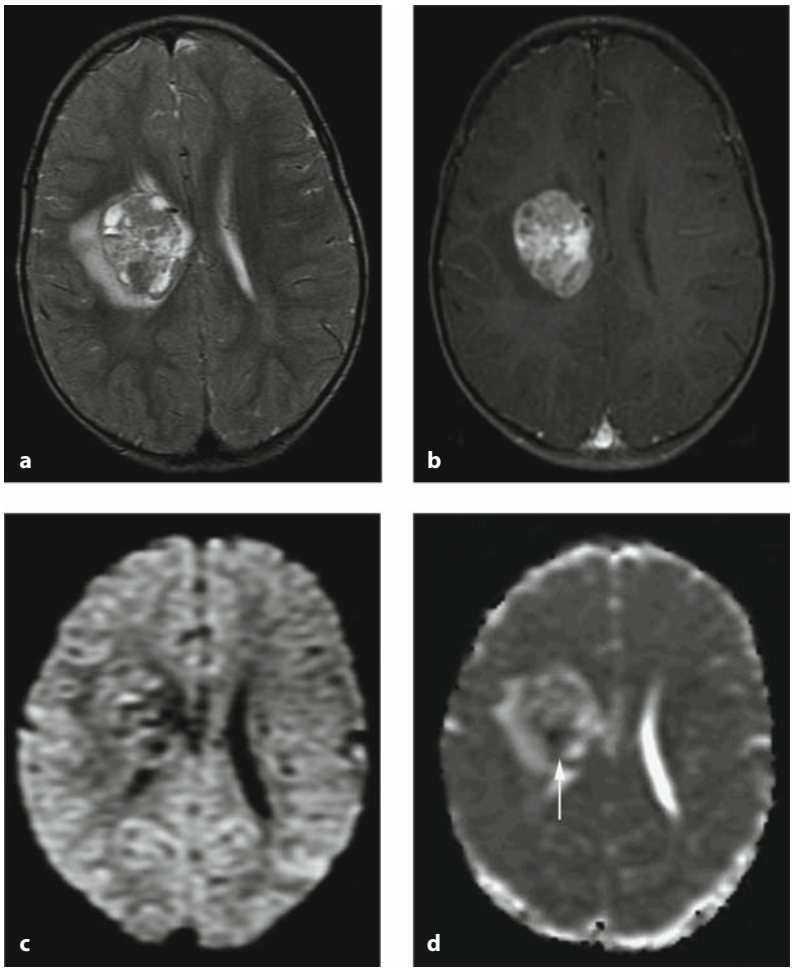

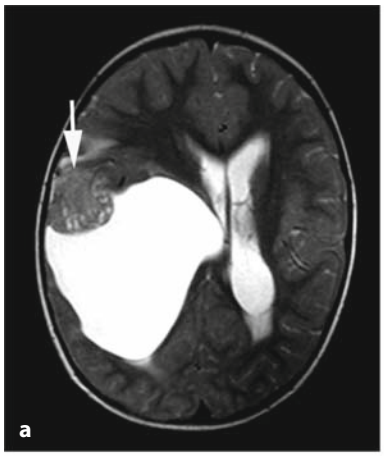

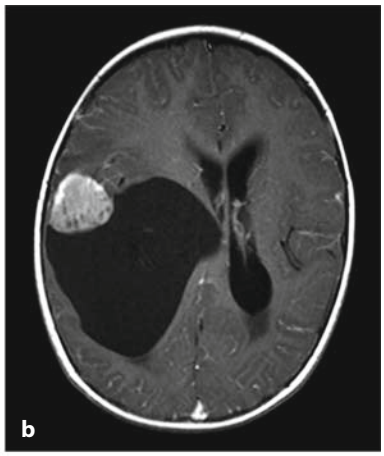

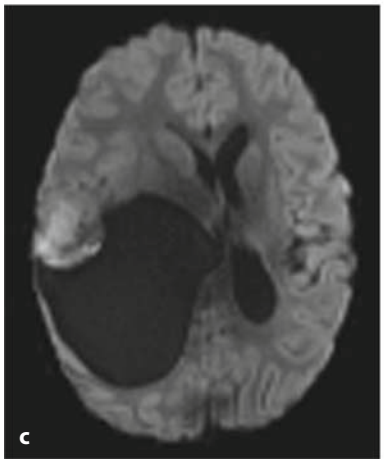

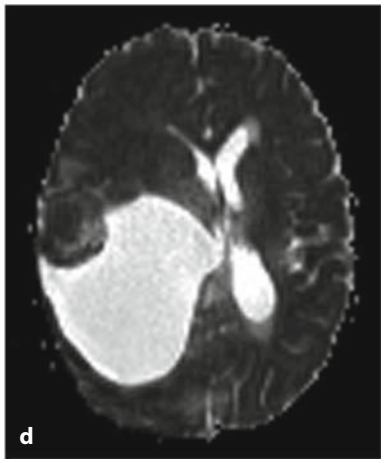

Figure 14.21 a–d

Desmoplastic infantile ganglioglioma in a 5-year-old girl. **a** T2-weighted image shows an isointense solid mass (*arrow*) with a large cystic component. **b** Gadolinium-enhanced T1-weighted image shows a homogeneous enhancement in the solid portion of the mass. **c, d** DW imaging shows hyperintensity with partially decreased ADC in the solid portion of the mass

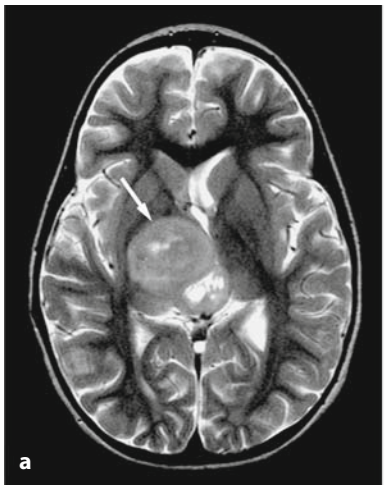

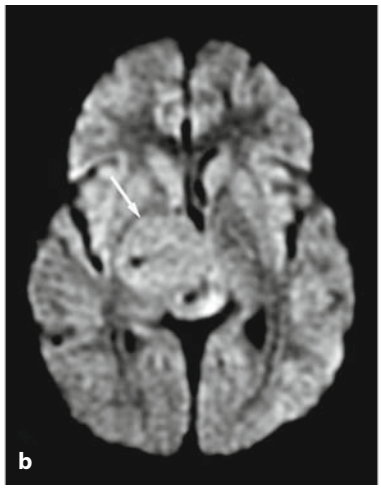

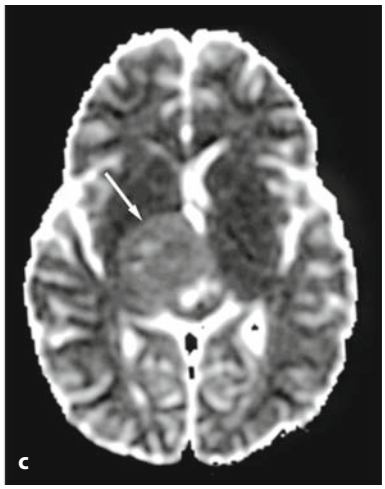

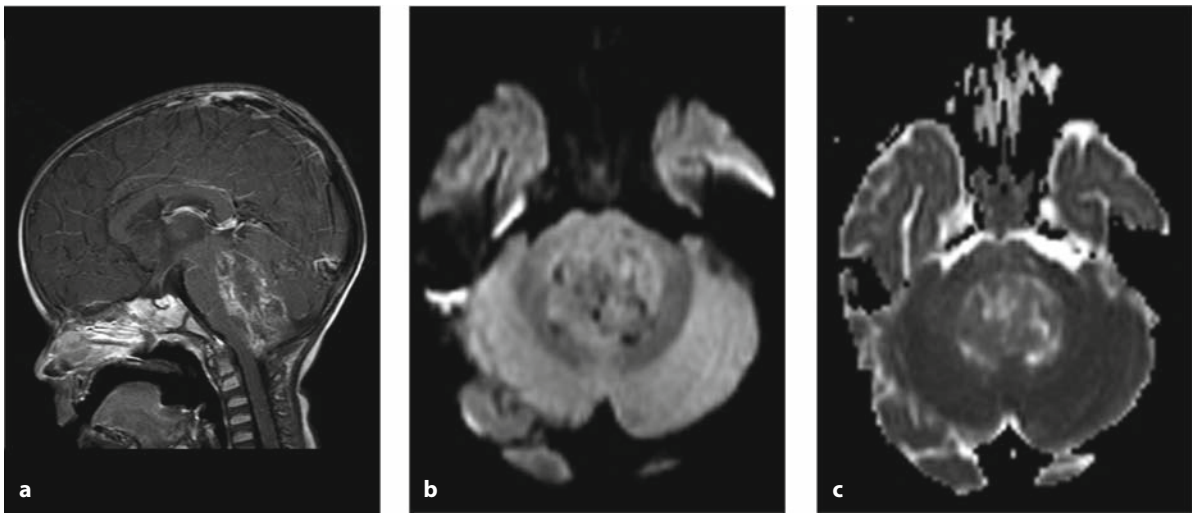

Figure 14.23 a–c

Ependymoma in a 3-year-old boy. **a** Gadolinium-enhanced T1-weighted image shows a heterogeneously enhancing mass in the fourth ventricle extending into the cisterns through the foramen of Magendie and Luschka (plastic ependymoma). **b, c** DW imaging shows isointensity with heterogeneously increased ADC in the mass

Atypical teratoid-rhabdoid tumor is a hypercellular CNS tumor in children; it has a more malignant biological behavior and is less sensitive to therapy than medulloblastoma [52, 55]. Cerebellopontine angle involvement and intratumoral hemorrhage are more common than in medulloblastoma. Atypical teratoid-rhabdoid tumor has been reported to be hyperintense on DW images with decreased ADC similar to medulloblastoma (Fig. 14.20) [52].

Choroid plexus papilloma (WHO grade 1) is a benign intraventricular papillary neoplasm derived from the choroid plexus epithelium and can be cured by surgery. The typical MR findings are of a homogeneous lobulated mass with papillary-appearance and with uniform intense enhancement. The WHO has introduced an additional entity with intermediate features, designated 'atypical choroid plexus papilloma' (WHO grade 2), which is primarily distinguished from the choroid plexus papilloma by increased mitotic activity. Curative surgery is still possible but the probability of recurrence appears to be significantly higher. Choroid plexus carcinoma (WHO grade 3) is a malignant neoplasm with mitotic activity, increased cellularity, blurring of the papillary pattern, necrosis, and frequent invasion of brain parenchyma. Five-year survival rates have been reported to range between 26% and 43%. The typical MR findings are a more heterogeneous signal mass with irregular enhancing margins and edema in the adjacent brain [56]. DW imaging shows choroid plexus tumors as iso- or hyperintense with the slightly increased or decreased ADC depending on the cellularity (Figs. 14.24–14.26).

Figure 14.22 a–c

Pilocytic astrocytoma in a 4-year-old girl. **a** T2-weighted images show a hyperintense mass lesion in the right thalamus (*arrow*). **b** DW image shows this solid mass as hyperintense (*arrow*). **c** ADC map shows slightly increased ADC of this mass. Hyperintensity on DW imaging is due to T2 signal effect, which is called T2 shine-through effect

◄

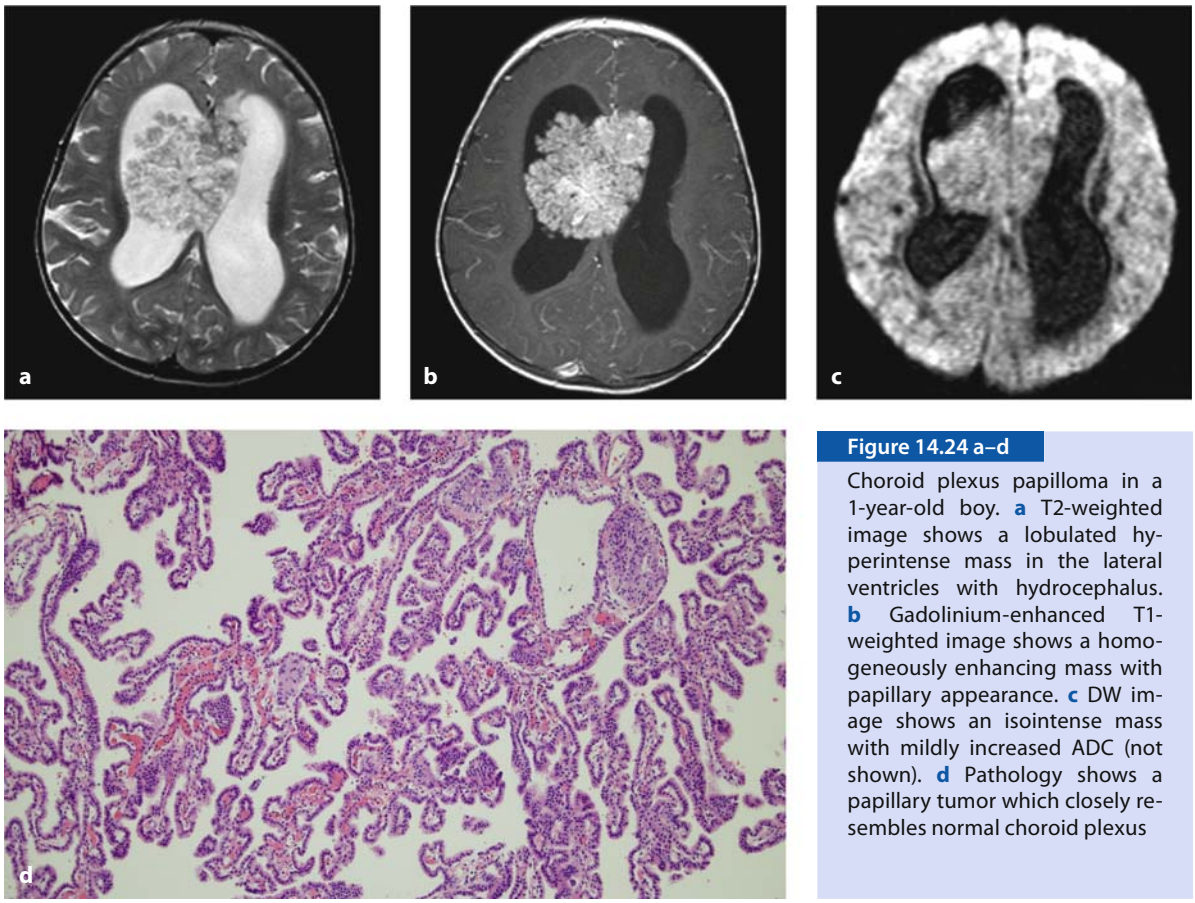

Figure 14.24 a–d

Choroid plexus papilloma in a 1-year-old boy. **a** T2-weighted image shows a lobulated hyperintense mass in the lateral ventricles with hydrocephalus. **b** Gadolinium-enhanced T1-weighted image shows a homogeneously enhancing mass with papillary appearance. **c** DW image shows an isointense mass with mildly increased ADC (not shown). **d** Pathology shows a papillary tumor which closely resembles normal choroid plexus

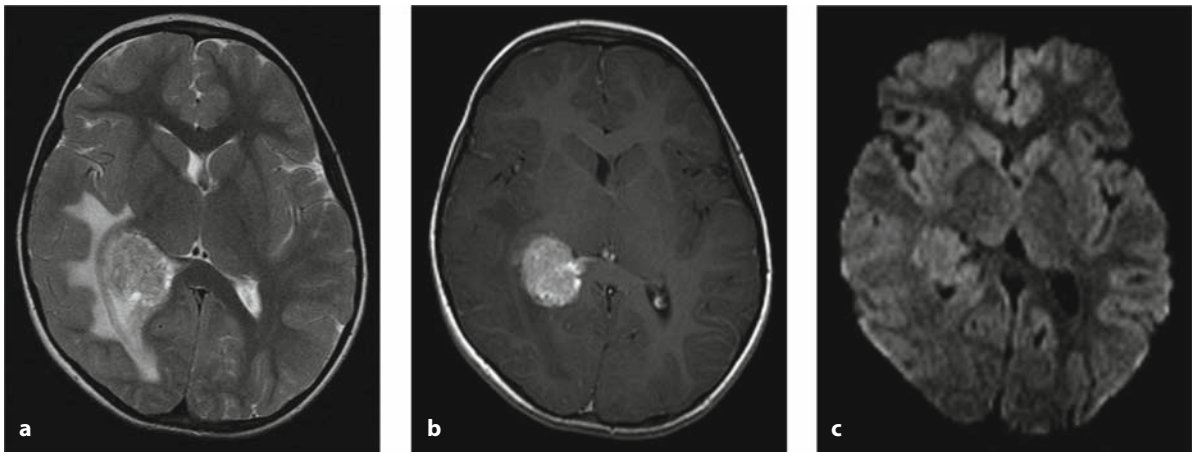

Figure 14.25 a–c

Atypical choroid plexus papilloma in a 6-year-old girl. **a** T2-weighted image shows a hyperintense mass in the occipital horn with surrounding edema suggesting brain parenchymal invasion. **b** Gadolinium-enhanced T1-weighted image shows heterogeneous enhancement of the mass. **c, d** DW image shows hyperintensity with slightly increased ADC in the mass. **e** Two-year follow-up MR image shows dissemination and a recurrent tumor

Figure 14.25 d, e

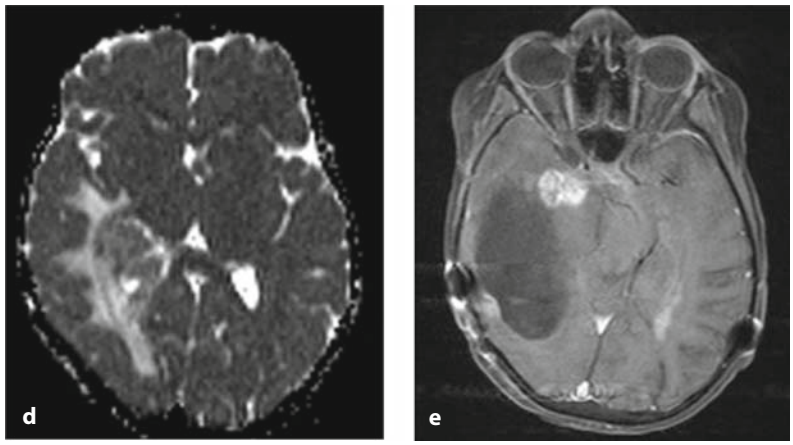

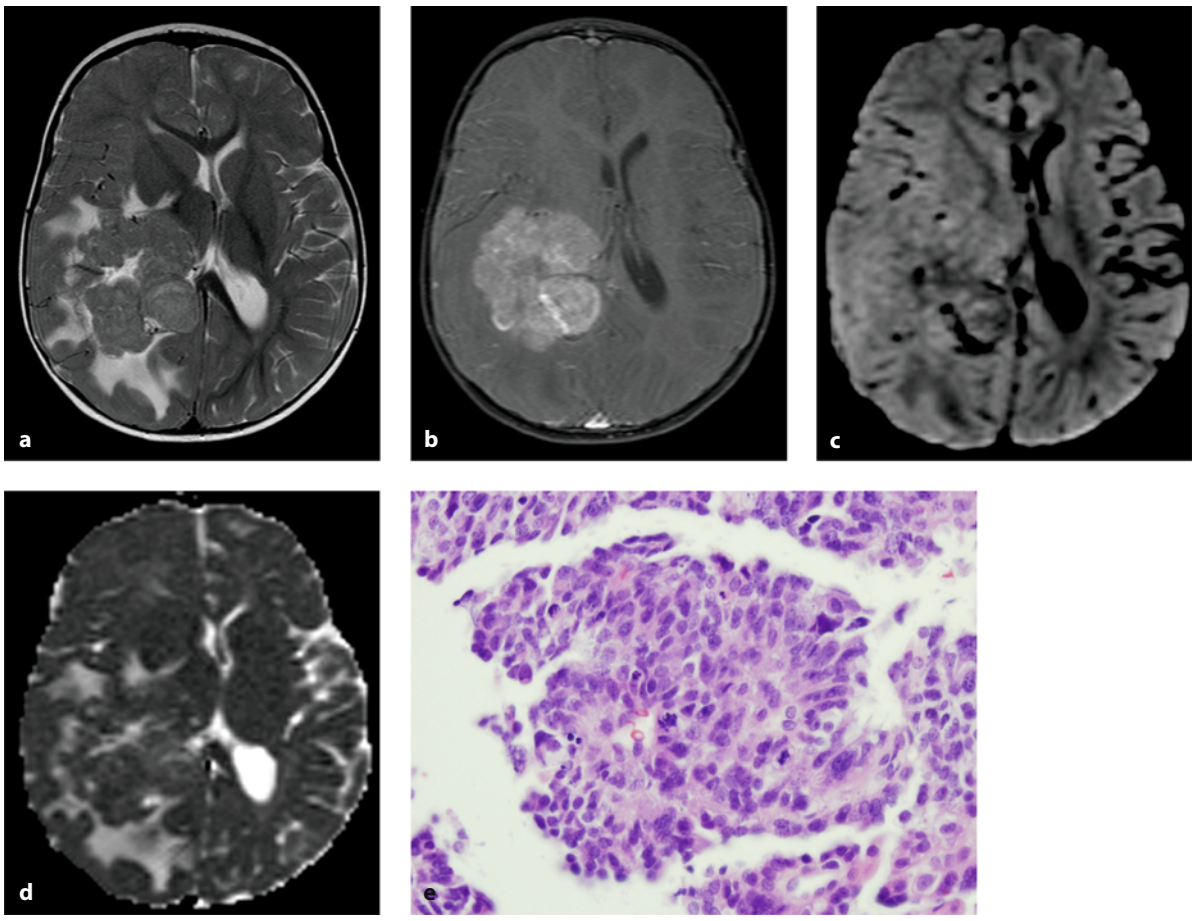

Figure 14.26 a–e

Choroid plexus carcinoma in a 2-year-old girl. **a** T2-weighted image shows an isointense solid mass with necrosis. **b** Gadolinium-enhanced T1-weighted image shows a heterogeneous enhancement in the mass. **c, d** DW image shows isointense with partially decreased ADC in the mass. **e** Pathology shows increased pleomorphic cellularity, mitosis, and blurring of the papillary pattern

14.8 Encephalopathies

14.8.1 Hypertensive Encephalopathy

Hypertensive encephalopathy occurs most often secondary to renal diseases in children. It also occurs in children treated for myeloproliferative disorders [57]. In children, convulsions are often accompanied by severe headache and restlessness. The most common abnormality on MR imaging is bilateral high signal intensity in parieto-occipital subcortical white matter. These lesions can also occur in the frontal lobes and gray matter, including basal ganglia, thalamus, cerebellum and brain stem. The mechanism of the disease is thought to be vasogenic edema from failure of autoregulation and/or a cytotoxic edema triggered by severe vasospasm. DW imaging can distinguish irreversible ischemic changes from reversible conditions with vasogenic edema (Fig. 14.27) [58].

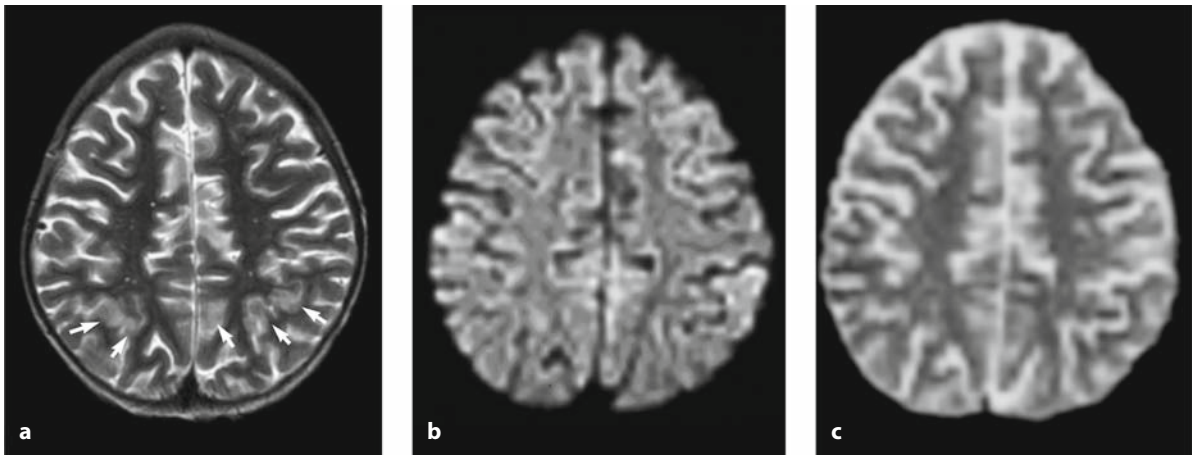

Figure 14.27 a–c

Hypertensive encephalopathy in a 5-year-old girl with acute lymphoblastic leukemia during chemotherapy presenting with seizure. **a** T2-weighted image shows hyperintense lesions in bilateral parieto-occipital cortex (*arrows*). This high signal seems to be due to subtle vasogenic edema rather than frank ischemia. **b, c** DW image and ADC map show no apparent abnormal signal intensities

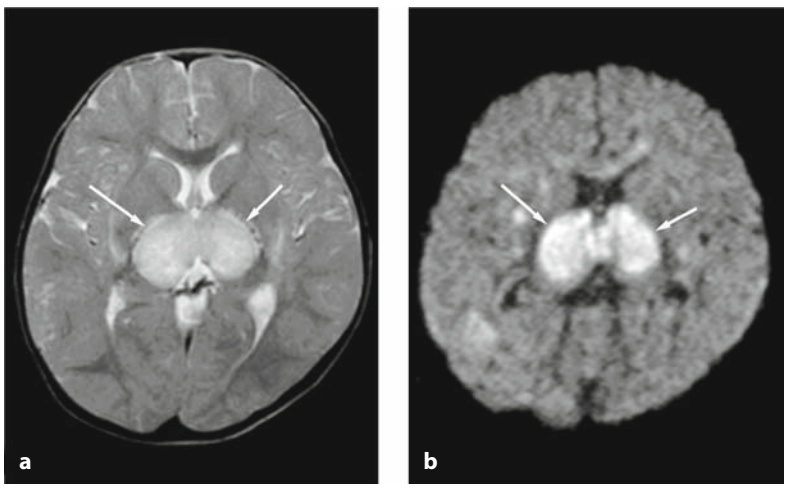

Figure 14.28 a, b

Acute necrotizing encephalopathy in a 1-year-old boy with seizure. **a** T2-weighted image shows multiple hyperintense lesions in bilateral thalami and right temporo-occipital region (*arrows*). **b** DW image also shows these lesions (*arrows*) as hyperintense associated with decreased ADC (not shown). (Courtesy of Ida M, MD, Ebara Municipal Hospital, Japan)

14.8.2 Acute Necrotizing Encephalopathy

Acute necrotizing encephalopathy is acute encephalopathy with bilateral thalamotegmental involvement that occurs in infants and children. It is a clinicopathological entity recently separated from acute encephalopathy of unknown etiology. It may be associated with a cytokine storm after viral infections. It frequently occurs in East Asia but has also been identified in other parts of the world. The hallmark of acute necrotizing encephalopathy is multiple, bilateral symmetric brain lesions showing necrosis, petechial hemorrhage, and cytotoxic edema without inflammatory cell infiltration [59]. The prognosis is generally poor. DW imaging shows multiple symmetric hyperintense lesions with decreased ADC mainly seen in the bilateral thalami, the bilateral brain stem tegmenta, and the cerebral white matter (Fig. 14.28) [60].

14.8.3 Focal Lesion in the Splenium of the Corpus Callosum with Meningoencephalitis/Encephalopathy

Symmetric cytotoxic edema in the corpus callosum with or without white matter involvement can be seen in meningoencephalitis/encephalopathy associated with viral (rota, Epstein-Barr, influenza) and bacterial (staphylococcus, streptococcus, legionnaire, hemolytic uremic syndrome) infections [61-64]. Similar corpus callosum lesions are seen in patients with seizures, antiepileptic medication, other medications (5-FU, metronidazole, IVIg), alcoholism and malnutrition, hypoglycemia, osmotic myelinolysis, trauma, systemic lupus erythematosus, and leptomeningeal malignancy [61, 65-70]. The pathogenesis remains unknown. Influx of inflammatory materials, intramyelinic edema, inflammatory cytokine (interleukin-6) released from virus-stimulated glial cells, cellular fluid mechanism in the arginine-vasopressin fluid balance systems, and toxin-mediated immune activation causing endothelial injury have been suggested. DW imaging shows a symmetric round or oval hyperintense lesion with decreased ADC in the splenium of the corpus callosum, which may extend along the callosal fiber laterally and sometimes may extend into the entire corpus callosum and white matter (Fig. 14.29).

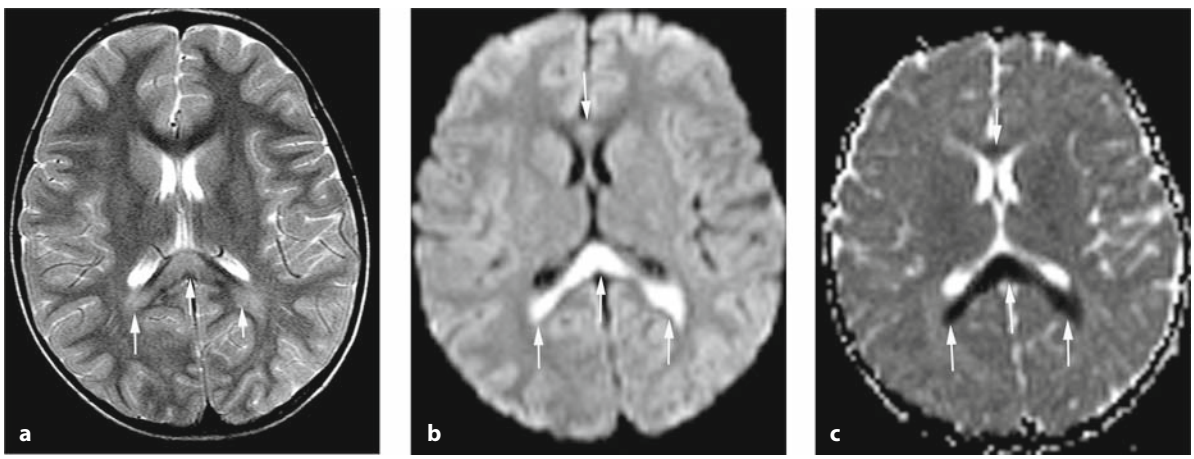

Figure 14.29 a–c

Corpus callosum lesions associated with Rota virus encephalopathy in a 3-year-old boy. **a** T2-weighted image shows a symmetric hyperintense lesion in the splenium of the corpus callosum that extends along the callosal fibers bilaterally (*arrows*). **b, c** DW imaging shows symmetric hyperintense lesions with decreased ADC in the posterior and anterior corpus callosum (*arrows*)

14.9 Demyelinating Disease and Toxic Disease

14.9.1 Acute Disseminated Encephalomyelitis and Multiple Sclerosis

Acute disseminated encephalomyelitis (ADEM) is more frequent than multiple sclerosis in children. ADEM is usually monophasic but relapses in patients initially diagnosed with ADEM, and conversion to multiple sclerosis has been reported [71, 72]. If these relapses represent part of the same acute monophasic immune process, the term "multiphasic ADEM" is used. If, however, relapses occur, disseminating with respect to site and time, this supports the diagnosis of multiple sclerosis.

On MR images, ADEM lesions tend to be in the subcortical white matter, while multiple sclerosis lesions tend to be situated both in the subcortical and periventricular white matter. Cortical and deep gray matter lesions are more frequent in ADEM. ADEM lesions tend to be poorly marginated, whereas multiple sclerosis lesions have more clearly defined margins. ADEM lesions are characterized in the acute stage by restricted diffusion (ADC values: $0.56\pm0.16\times10^{-3}$ mm^2/s) and subacute stage by increased diffusion ($1.24\pm0.13\times10^{-3}$ mm^2/s) (Fig. 14.30) [73].

Multiple sclerosis in pediatric patients is relatively rare but may have been underreported. It is estimated that 0.3%-2% of all patients with multiple sclerosis present during childhood [74]. The incidence of tumefactive plaques and posterior fossa plaques may be higher. Hyperintense plaques on DW imaging with decreased ADC have been reported to be rare even in the active enhancing multiple sclerosis plaques [75]. When present, a possible explanation for the hyperintense, cytotoxic multiple sclerosis plaques is intramyelinic edema (Fig. 14.31).

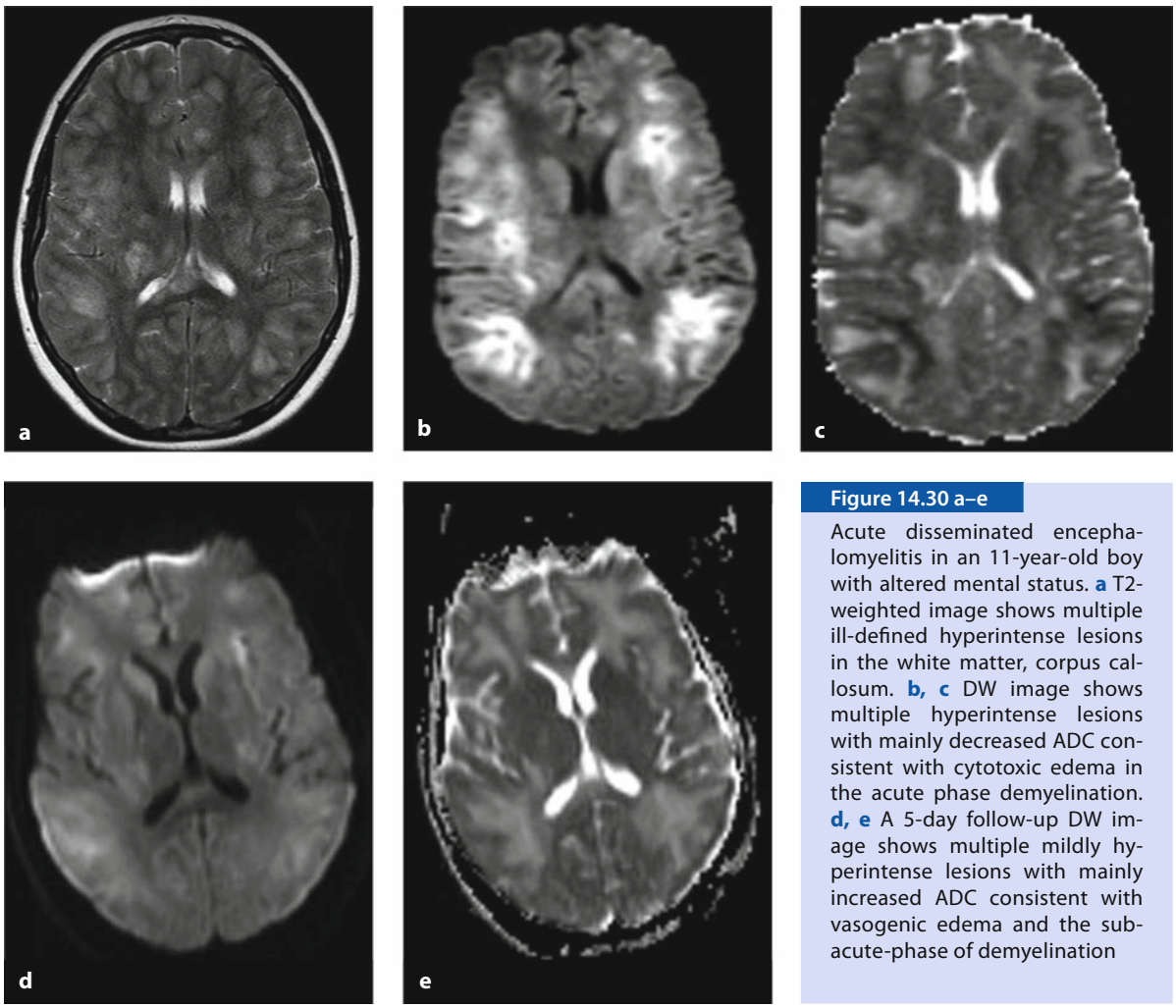

Figure 14.30 a–e

Acute disseminated encephalomyelitis in an 11-year-old boy with altered mental status. **a** T2-weighted image shows multiple ill-defined hyperintense lesions in the white matter, corpus callosum. **b, c** DW image shows multiple hyperintense lesions with mainly decreased ADC consistent with cytotoxic edema in the acute phase demyelination. **d, e** A 5-day follow-up DW image shows multiple mildly hyperintense lesions with mainly increased ADC consistent with vasogenic edema and the subacute-phase of demyelination

14.9.2 Osmotic Myelinolysis

Osmotic myelinolysis also occurs in pediatric patients. Central pontine myelinolysis (CPM) and extrapontine myelinolysis (EPM) represent destruction of myelin sheaths in characteristic places within the brain stem and cerebrum. Organic osmolytes, including glutamate, glutamine, betamine, or taurine, have been implicated in the pathogenesis of myelinolysis induced by rapid correction of severe hyponatremia [76]. Pathological findings include destruction of myelin sheaths, although the nerve cells and axons are relatively spared. DW imaging can detect the lesions in the early phase as hyperintense with decreased ADC, which represents cytotoxic edema (Fig. 14.32; Chap. 10, Fig. 10.14).

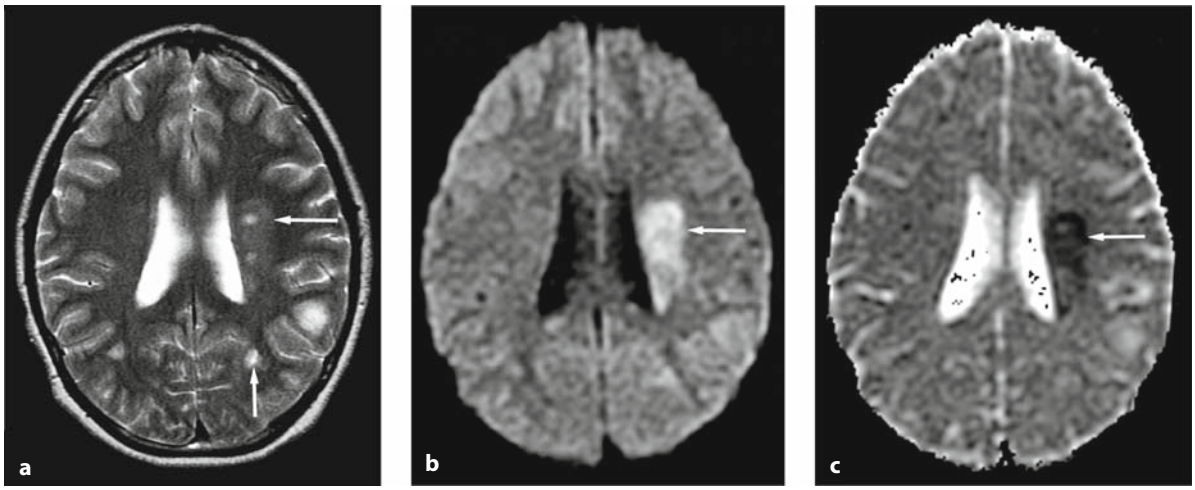

Figure 14.31 a–c

Acute multiple sclerosis in a 13-year-old girl. **a** T2-weighted image shows multiple hyperintense lesions in the periventricular and subcortical white matter (*arrows*). **b, c** DW image shows a hyperintense plaque with decreased ADC (*arrows*) in the left corona radiata. This is a cytotoxic plaque, presumably mainly composed of intramyelinic edema

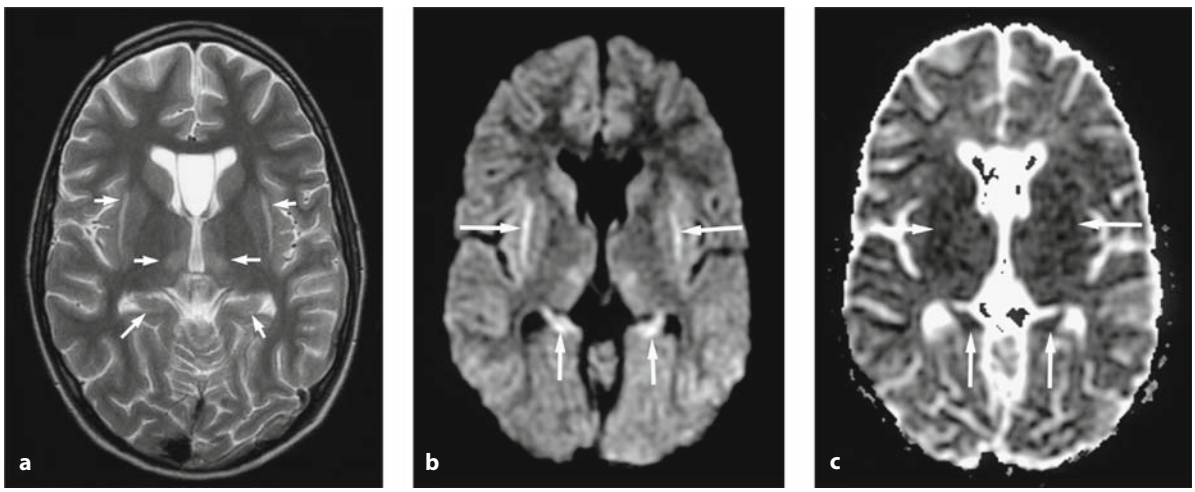

Figure 14.32 a–c

Osmotic myelinolysis (extrapontine myelinolysis) in an 11-year-old boy. **a** T2-weighted image shows symmetrical multiple slightly hyperintense lesions in the external capsules, hippocampi and medial thalami (*arrows*). **b, c** DW image shows these lesions (*arrows*) as hyperintense with decreased ADC, representing cytotoxic edema

14.10 Congenital Dysmyelination and Demyelination (Leukodystrophies)

Leukodystrophies comprise a wide spectrum of inherited neurodegenerative disorders affecting white matter, while the term leukoencephalopathy is applied to all white matter disease. Myelin is formed from the processes of oligodendrocytes and is composed of multiple layers of proteins (myelin basic protein and proteolipid protein) and lipids (cholesterol, phospholipids, and glycolipids: galactocerebroside and sulfatide).

Pathology shows delayed myelination (hypomyelination, amyelination), dysmyelination, demyelination, or a combination of these. The loss of myelin in leukodystrophies results in increased water and hyperintensity on T2-weighted images. DW imaging can discriminate intramyelinic edema (restricted diffusion) from vasogenic edema, gliosis, and spongiosis/vacuolation. DT imaging is useful in evaluating myelination and premyelination states. DW imaging and DT imaging are useful in differentiating between white matter diseases in pediatric patients.

14.10.1 Lysosomal Disorders

The lysosome is an organelle containing acid hydrolases responsible for digestion of degraded cellular constituents.

Metachromatic leukodystrophy is an autosomal recessive disorder caused by a deficiency of lysosomal enzyme arylsulfatase A (chromosome 22), resulting in the accumulation of sulfatides that are important constituents of the myelin sheath. A tigroid white matter pattern on MR imaging is due to the relative sparing of myelin around the medullary veins. Subcortical U-fibers are spared until late in the disease. DW imaging shows periventricular hyperintensity with decreased ADC in the active stage of the disease (Fig. 14.33) [77-79].

Krabbe disease (globoid cell leukodystrophy) is an autosomal recessive disorder caused by a deficiency of galactosylceramidase (14q21 to q31). The accumulation of galactocerebroside and galactosylsphingosine is toxic to oligodendrocytes. DW imaging may show hyperintensity in the subcortical white matter, caudate head, and internal capsule with decreased ADC in the early stage of the disease. As the disease progresses, the lesions show iso- or hypointensity [79].

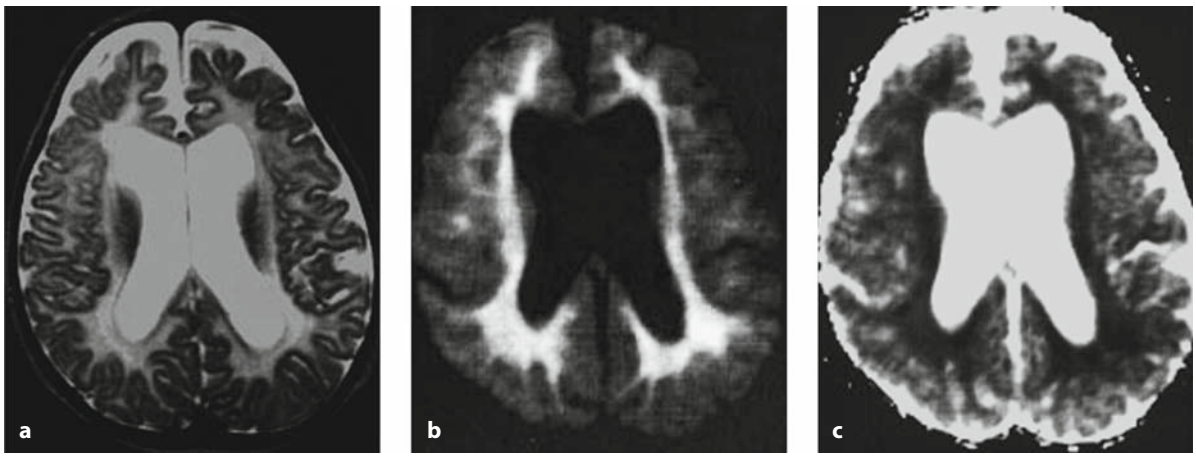

Figure 14.33 a–c

Metachromatic leukodystrophy in a 10-month-old boy with developmental delay. **a** T2-weighted image shows diffuse deep white matter hyperintensity. **b, c** DW imaging shows periventricular hyperintensity with decreased ADC in the active stage of the disease. Subcortical U-fibers are relatively spared. (Courtesy of Sener R N., MD, Department of Radiology, Ege University Hospital, Turkey). (From [78])

DT images are more sensitive than T2-weighted images for detecting white matter abnormalities [80].

Mucopolysaccharidoses are a genetically heterogeneous group of inborn errors of lysosomal glycosaminoglycan (dermatan, heparan, keratan, or chondroitin sulfate) metabolism. The major neuronal storage materials are a secondary accumulation of gangliosides. Multiple cystic areas in the white matter and basal ganglia correspond to enlarged perivascular spaces with loosely packed fibrous tissues that are the sequelae of glycosaminoglycan extraction [81]. DW imaging shows the lesions as iso- or hypointense with increased ADC (Fig. 14.34).

In GM1 (beta-galactosidase, 3p21) and GM2 (Tay-Sachs hexosamidase A, 15q23-24, and Sandhoff diseases, hexosamidase A and B, 5q13) gangliosidoses, the accumulation of gangliosides in the cytoplasm of neurons results in extensive neuronal loss and white matter degeneration. Diffuse white matter T2 hyperintensity is seen. Thalamic T2 hypointensity with relatively reduced diffusion can be seen in Tay-Sachs disease [82].

Figure 14.34 a–d

Mucopolysaccharidosis (Hurler-Sheie 1H/S) in an 18-year-old man. **a** T2-weighted image shows multiple cystic areas in the white matter, thalami, and basal ganglia corresponding to enlarged perivascular spaces. **b, c** DW imaging shows hypointensity with increased ADC in these lesions. **d** Sagittal T1-weighted image shows thickening of the dura causing a canal stenosis at the craniovertebral junction (*arrow*)

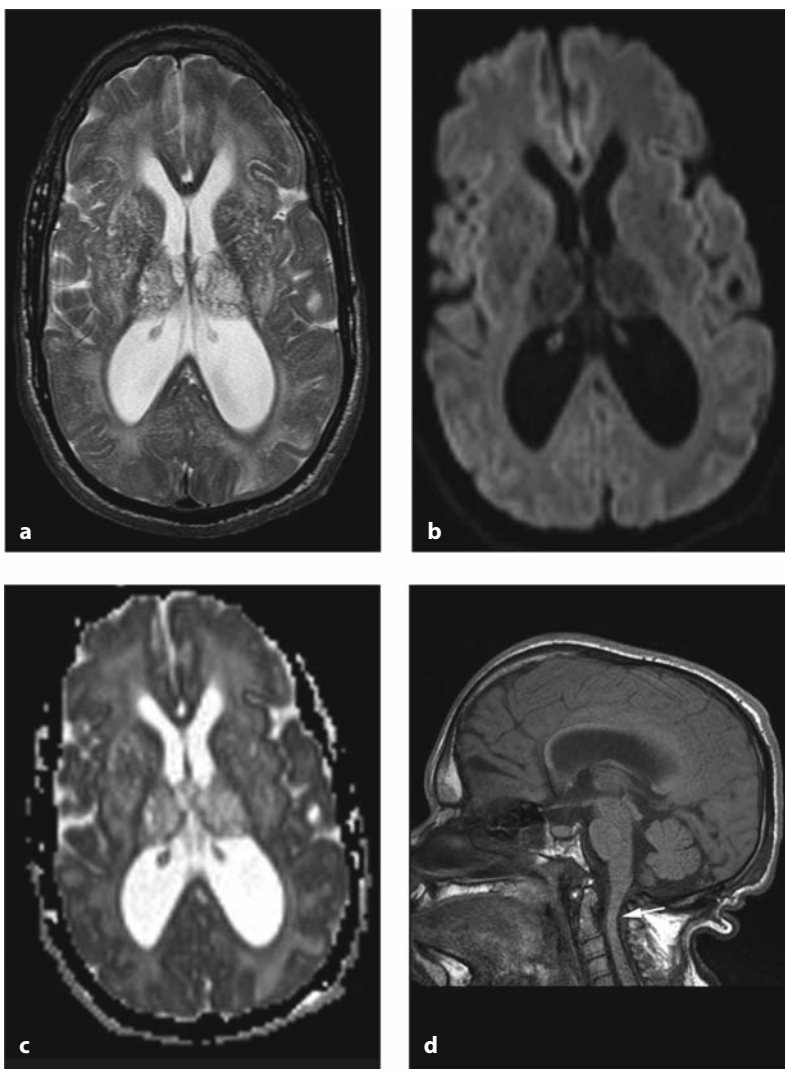

14.10.2 Peroxisome Disorders

The peroxisome is an organelle that is largely located in oligodendrocytes and is involved in oxidation of very long-chain and branched-chain fatty acids. It is indispensable in myelin maintenance.

Zellweger syndrome (cerebrohepatorenal syndrome) is an autosomal recessive severe peroxisome biogenesis disorder caused by multiple enzyme defects. MR imaging shows diffuse white matter hyperintensity with abnormal severe gyration in perisylvian and perirolandic regions. DW imaging shows extensive mild hypointensity with increased ADC corresponding to hypomyelination [79].

X-linked adrenoleukodystrophy (Xq28) is caused by a deficiency of acyl-CoA synthetase. MR imaging shows the white matter involvement with posterior predominance in 80% and frontal predominance in 15% of cases. The peripheral zone of the lesion is enhanced corresponding to the leading edge of inflammation. DW imaging can depicts two or three different zones: (1) A central burn-out zone (gliosis) is hypointense; (2) An immune-mediated inflammatory zone may have relatively restricted diffusion; (3) The most peripheral demyelinating zone is minimally hyperintense with increased ADC (Fig. 14.35) [79, 83].

14.10.3 Mitochondrial Disorders

Mitochondria not only produce energy with the synthesis of adenosine triphosphate (ATP) through the electron transport chain (respiratory chain) but are also involved in oxidation of fatty acids, pyruvate, ketone, and amino acids. These associated diverse enzymes are encoded by the mitochondrial DNA (mtDNA) and/or the nuclear DNA (nDNA). The spectrum of mitochondrial diseases encompasses various mitochondrial syndromes and isolated enzymic deficiencies: (1) mtDNA mutations (mitochondrial encephalomyopathy, my lactic acidosis and stroke-like episodes: MELAS; myoclonic epilepsy with ragged-red fibers: MERRF; Leigh syndrome; Leber hereditary optic neuropathy: LHON; neuropathy, ataxia, retinitis pigmentosa: NARP; chronic progressive external ophthalmoplegia: CPEO; Kearns-Sayre syndrome, etc.), (2) nDNA mutations producing deletion or depletion of mtDNA (Leigh syndrome, Alpers disease, myo-neuro-gastrointestinal encephalopathy: MNGIE, glutaric aciduria, pyruvate dehydrogenase or carboxylase deficiency, etc.) [84].

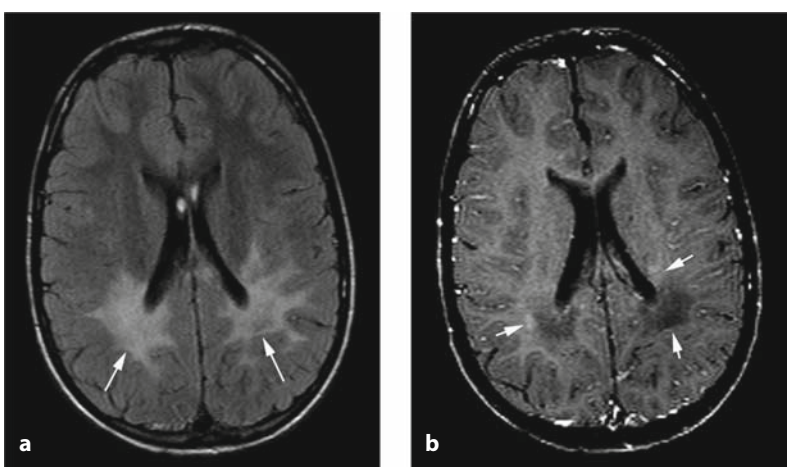

Figure 14.35 a, b

Adrenoleukodystrophy in an 8-year-old boy. **a** FLAIR image shows the posterior predominant white matter involvement (*arrows*). **b** Gadolinium-enhanced T1-weighted image shows minimal peripheral enhancement (*arrow*).

Figure 14.35 c, d

c, d DW imaging shows a central hypointensity with increased ADC (*arrows*) and peripheral mild hyperintensity with mildly increased ADC (*arrowheads*). (Courtesy of Lee A MD The University of Iowa Hospitals and Clinics, USA)

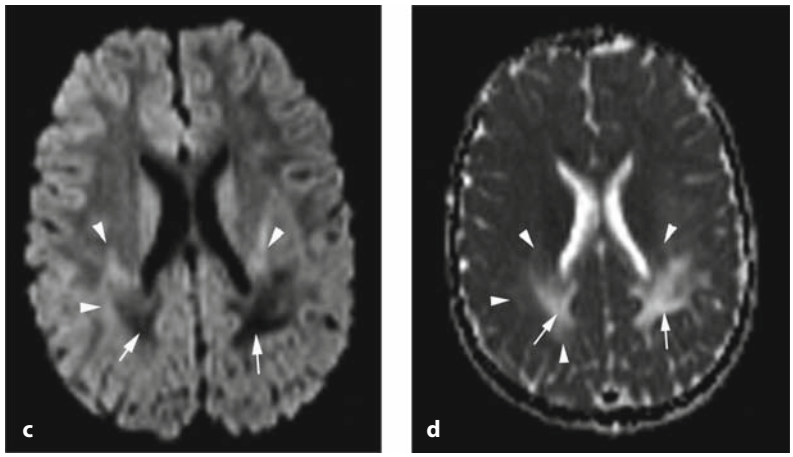

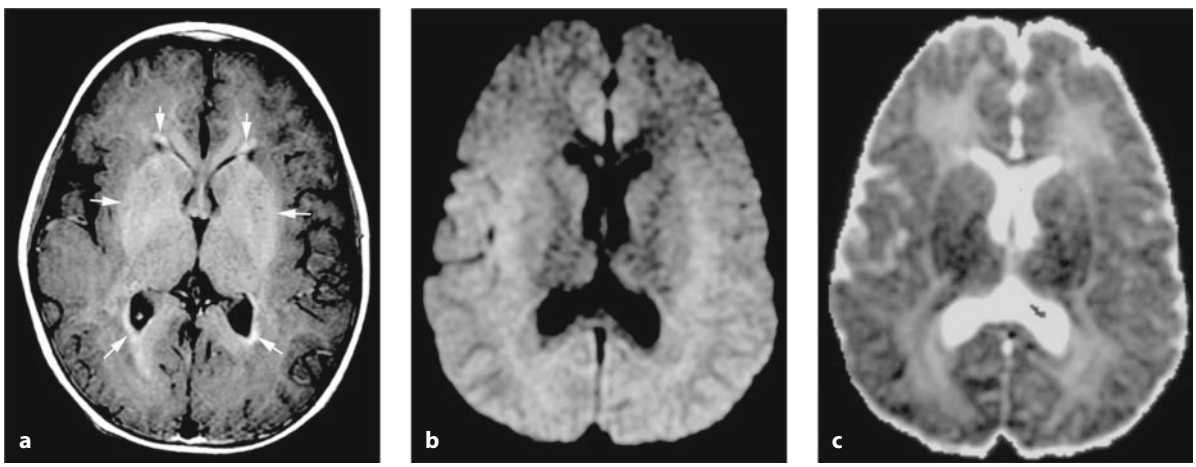

Figure 14.36 a–c

Myo-neuro-gastrointestinal encephalopathy (MNGIE) in an 11-year-old boy. **a** Gadolinium-enhanced T1-weighted image shows minimal enhancement in the basal ganglia and periventricular white matter (*arrows*). **b, c** DW imaging shows diffuse white matter isointensity with increased ADC

Mitochondrial encephalopathies can show various patterns of central nervous system involvement. These include multiple infarcts in the cortex, white matter, and basal ganglia, which do not usually follow vascular territories. Other features of mitochondrial encephalopathy are spongiform leukoencephalopathy due to splitting of the myelin lamellae, demyelination with intramyelinic edema, and atrophy [85, 86]. Either energy depletion or oxidative damage involves oligodendrocytes. DW imaging often shows the stroke-like lesions in MELAS as hyperintense. They have increased or normal ADC, which presumably represents vasogenic edema (Chap. 10, Fig. 10.20; Fig. 14.36) [87-90]. However, decreased ADC in the lesions representing cytotoxic edema can be observed in MELAS and other mitochondrial encephalopathies (Figs. 14.37, 14.38) [91-93].

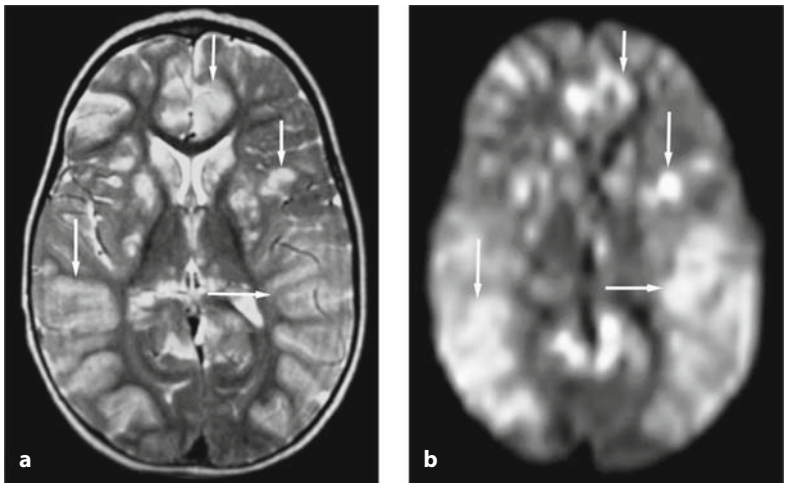

Figure 14.37 a, b

Mitochondrial enaphalopathy (unknown enzyme abnormality) in a 20-month-old girl with seizures. **a** T2-weighted image shows multiple high signal lesions in bilateral basal ganglia and fronto-parieto-occipital cortex not corresponding to a vascular territory (*arrows*). **b** DW image shows multiple high signal intensity lesions associated with decreased ADC (*not shown*)

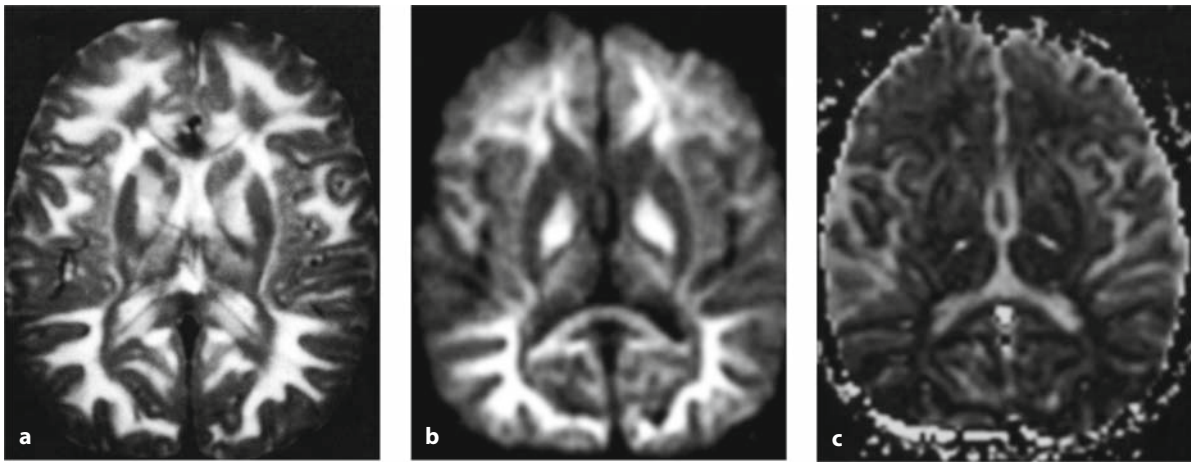

Figure 14.38 a–c

Kearns-Sayre syndrome in an 18-year-old woman. **a** T2-weighted image shows diffuse high signal intensity in bilateral basal ganglia, thalami, and the white matter. **b, c** DW image shows hyperintensity associated with decreased ADC. (Courtesy of Sacher M, MD, Department of Radiology, Mount Sinai Medical Center, USA). (From [93])

14.10.4 Other Metabolic Encephalopathies and Leukoencephalopathies

Many kinds of metabolic encephalopathies/leukoencephalopathies can show hyperintense lesions associated with decreased ADC on DW imaging, which include phenylketonuria (Fig. 14.39), maple syrup urine disease, L-2 hydroxyglutaric aciduria (Chap. 10, Fig. 10.23), HMG-coenzyme A lyase deficiency, Canavan's disease (Fig. 14.40), non-ketotic hyperglycinemia, hyperhomocysteinemia, tyrosinemia, citrullinemia, hyperammonemic encephalopathy secondary to urea cycle disorders (Fig. 14.41), propionic aciduria, and infantile neuronal dystrophy [94-104].

One possible explanation for the hyperintense lesion is intramyelinic edema, which is one form of cytotoxic edema selectively occurring in myelin sheaths. Some organic acid disorders are characterized by an accumulation of organic acids that share structural similarities with the excitotoxic amino acid glutamate (D-2.l-2,3 hydroxyglutarate, glutarate) [29]. In urea cycle disorders, high levels of ammonia result in the conversion of large amounts of glutamate to gluta-

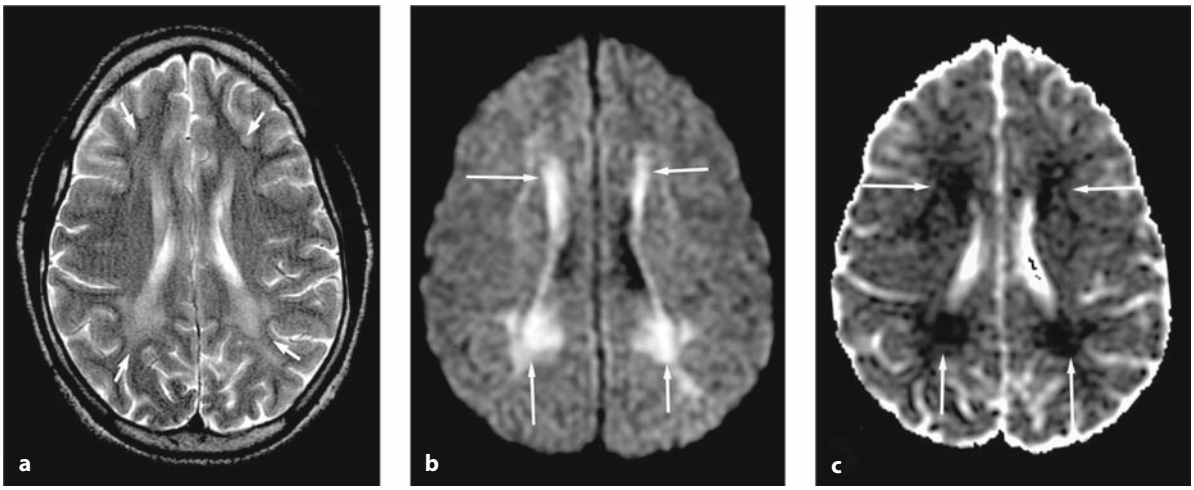

Figure 14.39 a–c

Phenylketonuria in a 36-year-old man. **a** T2-weighted image shows hyperintense lesions in the periventricular white matter (*arrows*). **b** DW image shows these lesions as hyperintense (*arrows*). **c** These hyperintense lesions have decreased ADC representing cytotoxic edema, especially intramyelinic edema (*arrows*)

Figure 14.40 a, b

Canavan disease. A 15-month-old boy presented with delayed psychomotor development, seizures, and spasticity. **a** T2-weighted image reveals high signal in peripheral white matter, globi pallidi and thalami. Note diffuse atrophy and thinning of the cortex. **b** DW image shows high signal changes in the peripheral white matter and globi pallidi with mildly decreased ADC partially (not shown). (Courtesy of Sener RN, MD, Department of Radiology, Ege University Hospital, Turkey). (From [97])

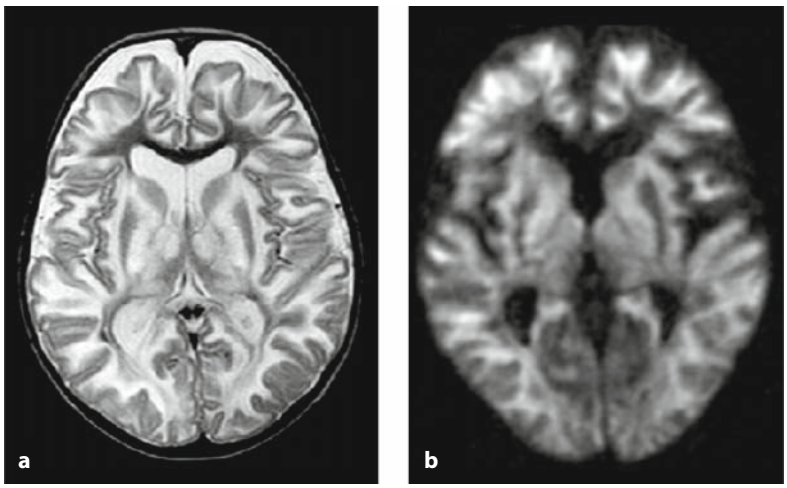

mine by glutamine synthetase, which may cause astrocyte swelling and brain edema [103].

Phenylketonuria is an autosomal recessive disorder caused by a deficiency of phenylalanine hydroxylase. l-phenylalanine impairs glutamate receptor function and thus contributes to brain dysfunction in phenylketonuria. Pathologic findings include delayed or defective myelination, intramyelinic edema, diffuse white matter vacuolation, demyelination, and gliosis. DW imaging shows these lesions as hyperintense with decreased ADC, probably the result of intramyelinic edema and/or astrocytic swelling, presumably due to acute excitotoxic injury [29] (Fig. 14.39). With appropriate dietary control, these MR abnormalities can completely resolve.

Canavan disease is an autosomal recessive disorder caused by mutations in the gene of aspartoacylase, which leads to an abnormal accumulation of *N*-acetyl-aspartate (NAA) in the brain, especially in oligodendrocytes, associated with macrocephaly. Pathology shows astroglial swelling, intramyelinic edema and swollen mitochondria. DW imaging reveals restricted diffusion in the white matter without any focal predominance (Fig. 14.40) [96-98].

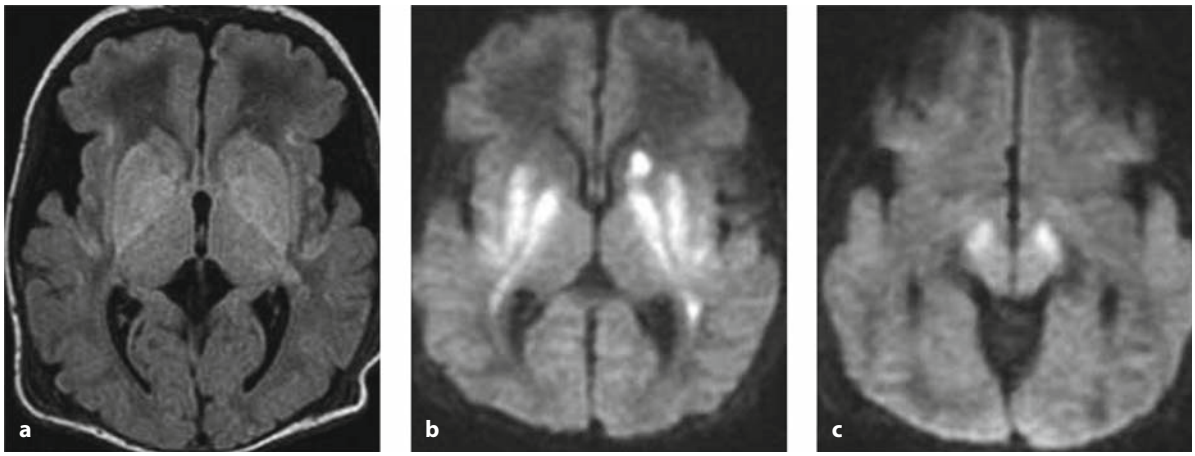

Figure 14.41 a–c

Hyperammonemic encephalopathy secondary to urea cycle disorders in a 9-day-old male infant. **a** FLAIR image reveals mild hyperintensity in the basal ganglia and internal capsules. **b**, **c** DW imaging shows symmetric hyperintense lesions in the basal ganglia, internal capsules, and cerebral peduncles with decreased ADC (not shown)

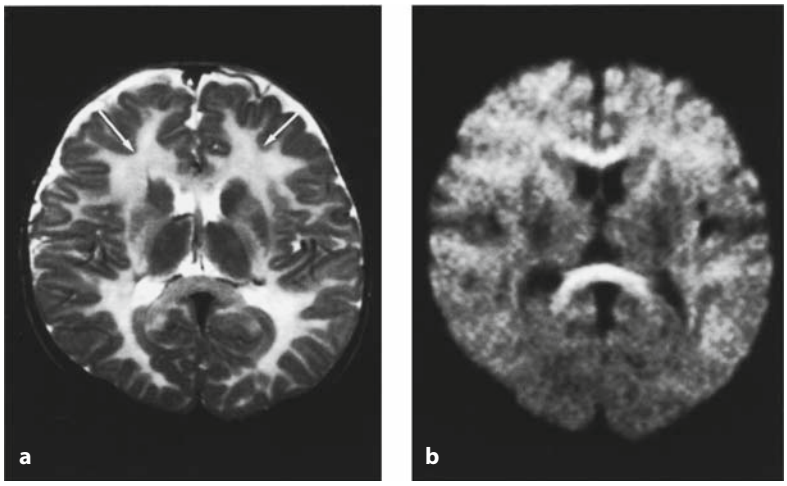

Figure 14.42 a, b

Pelizaeus–Merzbacher disease in a 7-month-old boy with developmental delay. **a** T2-weighted image shows diffuse white matter hyperintensity extending into the U-fibers due to hypo- or amyelination (*arrows*). **b** DW image (*z axis*) demonstrates isointensity in the white matter and essentially normal anisotropy in the corpus callosum. ADC values are diffusely slightly increased in the white matter (not shown). (From [119])

14.10.5 Miscellaneous Leukoencephalopathy

Alexander disease (Fibrinoid leukodystrophy) is a sporadic leukodystrophy associated with macrocephaly. The cause appears to be mutations in the glial fibrillary acidic protein (GFAP) gene (chromosome 17q21). Rosenthal fibers are intracytoplasmic proteinaceous inclusions from aggregation of GFAP proteins. Pathologically, there is widespread myelin deficiency, cystic degeneration, and cavitation. MR imaging shows frontal predominant white matter changes with gadolinium enhancement in the deep white matter and basal ganglia. DW imaging shows diffuse hypointensity in the white matter and increased ADC [105].

Van der Knaap disease, also known as megalencephalic leukodystrophy with subcortical cysts or leukoencephalopathy with macrocephaly and mild clinical course, is an autosomal recessive disorder caused by chromosome 22 mutations that encode a

membrane protein. Megalencephaly occurs during the second year of life associated with slowly progressive dysarthria, ataxia, and seizures. Pathology reveals a vacuolating myelinopathy in which the outer layer of myelin sheaths is affected. Subcortical cysts are seen in the frontal and temporal lobes. DW imaging shows diffuse hypointensity in the white matter and in the subcortical cysts associated with increased ADC (Chap. 10, Fig. 10.24) [79].

Pelizaeus–Merzbacher disease is an X-linked leukodystrophy due to a defect of proteolipid protein (PLP gene Xq22). It pathologically shows hypo- or amyelination and spares the axon. MR imaging shows total absence of myelination (connatal type) or arrested myelination (classical form). Despite hypo- or amyelination in Pelizaeus–Merzbacher disease, DW imaging shows normal diffusional anisotropy in the white matter (Fig. 14.42) [106]. This finding suggests that anisotropy is primarily related to structural changes of the axonal membrane in the immature brain.

Leukoencephalopathy with vanishing white matter (childhood ataxia with diffuse CNS hypomyelination) is an autosomal recessive disorder with chronic progression and additional episodes of rapid deterioration, provoked by fever and minor head trauma. This leukoencephalopathy is a primary axonopathy, with myelin being secondarily affected. Mutations are identified in the eukaryotic translation initiation factor (eIF2B), which is essential for the initiation of translation of RNA into protein and is involved under circumstances of stress. Increased cerebrospinal glycine may be secondary to excitotoxic brain damage. Pathology shows axonal loss, hypomyelination, demyelination, and gliosis, primarily in subcortical white matter. In the late stage, there are extensive cystic degenerations of the white matter associated with reactive changes. Typical MR imaging findings are diffuse white matter signal hyperintensity on T2-weighted images similar to CSF intensity with additional lesions in the central tegmental tracts and basis pontis. MR spectroscopy shows mildly increased lactate and glucose peaks with decreased NAA, choline, and creatine peaks. DW imaging shows low signal intensity, presumably representing cystic degeneration (Fig. 14.43) [79].

14.11 Congenital Anomaly

14.11.1 Sturge-Weber Syndrome

Sturge-Weber syndrome (encephalotrigeminal angiomatosis) is a congenital, sporadic disorder of unknown cause. Impaired venous drainage, due to leptomeningeal angiomatosis, results in impaired arterial blood flow to the subjacent brain. The subjacent brain tissue is atrophic and displays neuronal loss, astrogliosis, dysgenetic cortex, and calcification in the cortical and subcortical layers. MR imaging is the most sensitive imaging study demonstrating the precise extent and distribution of the leptomeningeal angiomatosis that is the hallmark of the diagnosis. Bilateral involvement occurs in 10%-20% of cases. Decreased T2 signal intensity in the subcortical white matter underlying the area of leptomeningeal angiomatosis reflects areas of calcification, cerebral blood oxygenation effect, and abnormal hypermyelination or accelerated myelination. The axon controls the formation and thickness of myelin. If ischemia occurs in the cortex, it could interfere with normal neuronal function and lead to premature axonal release of a myelinogenic trophic factor [107]. Increased FA and decreased ADC values in the white matter subjacent to the leptomeningeal angiomatosis in neonatal Sturge-Weber syndrome probably reflect such abnormal hypermyelination (Fig. 14.44) [108].

14.11.2 Hemimegalencephaly

Abnormally accelerated myelination has been reported in hemimegalencephaly [109]. Pathologically, neuronal maturation and increase in size of the axons occur earlier than in normal brain, which may lead to advanced myelination. Restricted diffusion has been reported in hemimegalencephaly on prenatal DW imaging [110]. This finding probably results from a combination of abnormally advanced myelination and increased cellularity (immature-appearing neurons) related to excessive prenatal neurogenesis and heterotopia (Fig. 14.45) [111]. Increased FA values are also observed in the areas of the abnormal advanced myelination. Aberrant midsagittal fiber tracts are observed in 57% of cases (15/26 patients) with hemimegalencephaly on MR and DT imaging [112]. DT imaging shows the fibers passing anteroposteriorly between the two anterior horns of the lateral ventricles (Fig. 14.45).

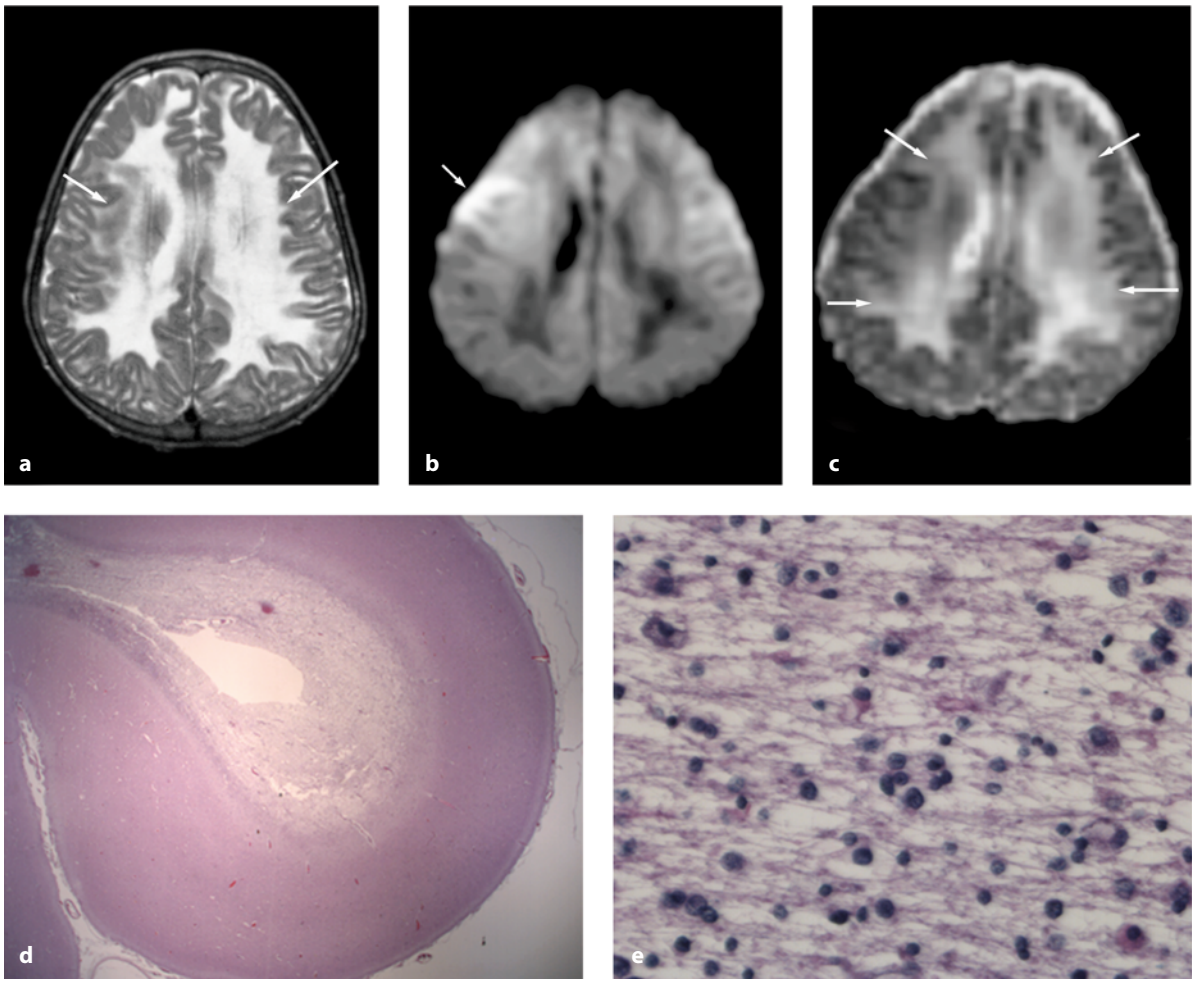

Figure 14.43 a–e

Vanishing white matter disease in an 8-year-old boy with progressive leukoencephalopathy. **a** T2-weighted image shows diffuse white matter hyperintensity extending into the U-fibers (*arrows*). **b** DW image demonstrates diffuse low signal intensity in the white matter. **c** ADC map shows diffusely increased ADC in the white matter due to cystic changes (*arrows*). **d, e** Pathology specimens show cystic degeneration and reactive astrogliosis involving in the subcortical white matter

14.11.3 Polymicrogyria, Focal Cortical Dysplasia, and Tuberous Sclerosis

Polymicrogyria is characterized by the abnormal arrangement of cortical layers and excessive folding of the cortical ribbon. Decreased FA and normal ADC are observed in the subcortical white matter the underlying polymicrogyric cortex [113].

Focal cortical dysplasia was first described by Taylor and is characterized by the presence of cytomegalic neurons, grotesque and balloon cells, and hypomyelination. DT imaging might show decreased FA and increased ADC within the region of dysplastic brain (Fig. 14.46) [114, 115]. Decreased fiber connection between the deep white matter and the dysplastic cortex and the aberrant white matter tract can be detected with fiber tractography.

In tuberous sclerosis, epileptogenic tubers may have a significant increase in ADC [116]. DT imaging demonstrates a decrease in anisotropy in normal-appearing white matter that may be associated with changes in myelin packing of axonal fibers disrupted by astrogliosis and myelination defects [117].

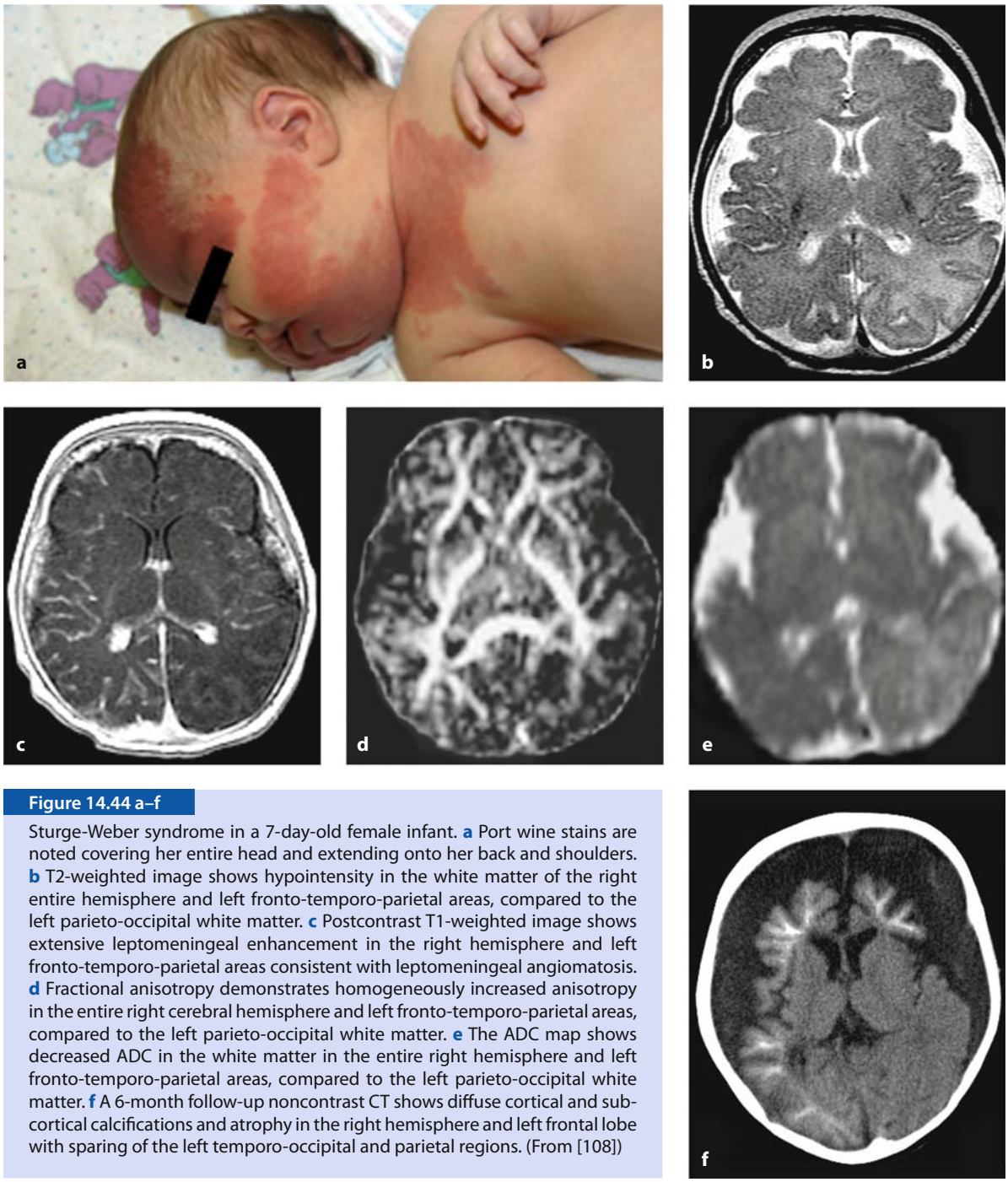

Figure 14.44 a–f

Sturge-Weber syndrome in a 7-day-old female infant. **a** Port wine stains are noted covering her entire head and extending onto her back and shoulders. **b** T2-weighted image shows hypointensity in the white matter of the right entire hemisphere and left fronto-temporo-parietal areas, compared to the left parieto-occipital white matter. **c** Postcontrast T1-weighted image shows extensive leptomeningeal enhancement in the right hemisphere and left fronto-temporo-parietal areas consistent with leptomeningeal angiomatosis. **d** Fractional anisotropy demonstrates homogeneously increased anisotropy in the entire right cerebral hemisphere and left fronto-temporo-parietal areas, compared to the left parieto-occipital white matter. **e** The ADC map shows decreased ADC in the white matter in the entire right hemisphere and left fronto-temporo-parietal areas, compared to the left parieto-occipital white matter. **f** A 6-month follow-up noncontrast CT shows diffuse cortical and subcortical calcifications and atrophy in the right hemisphere and left frontal lobe with sparing of the left temporo-occipital and parietal regions. (From [108])

14.11.4 Corpus Callosum Agenesis/Dysgenesis

Corpus callosum agenesis/dysgenesis occurs as a result of the failure of association fibers to decussate to the contralateral hemisphere via the callosal precursor due to a lack of induction by the massa commissuralis. Diffusion tensor fiber tractography demonstrates the arrangement of fiber tracts forming Probst bundles(Fig. 14.47), the rudimentary cingulum, and the dysplastic fornices [115, 118]. If the development

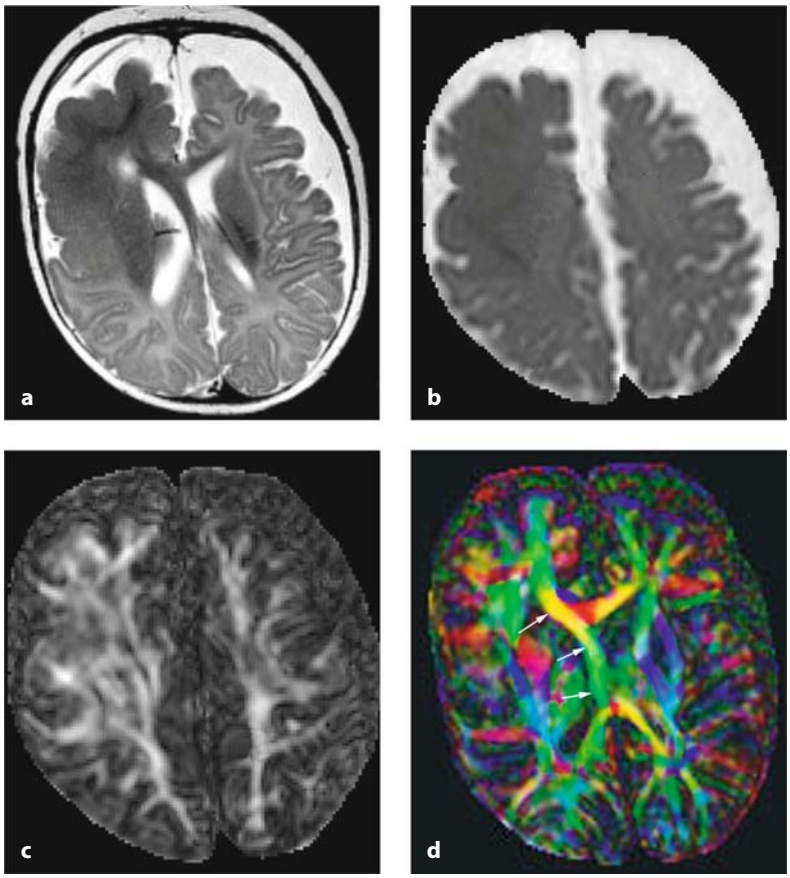

Figure 14.45 a–d

Hemimegalencephaly in a 4-month-old boy with infantile spasm. **a** T2-weighted image shows hypointense areas in the right frontal cortex and white matter which probably represents abnormally advanced myelination associated with hemimegalencephaly. **b, c** DT imaging shows increased FA and slightly decreased ADC suggesting accentuated myelination in the right hemisphere. **d** DT imaging color map shows aberrant midsagittal fiber tracts passing anteroposteriorly through between the two anterior horns of the lateral ventricles (*arrows*). (Courtesy of Salamon N, MD, The University of California, Los Angeles, USA)

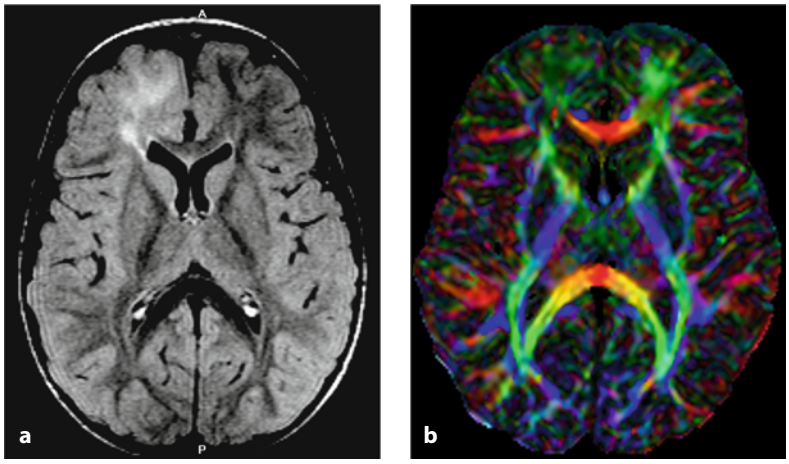

Figure 14.46 a, b

Cortical dysplasia in a 5-year-old boy with right frontal spikes. **a** FLAIR image shows cortical thickening and white matter hyperintensity in the right frontal lobe. **b** DT imaging color map shows decreased anisotropy in the right frontal abnormal area which may represent decreased fiber connection between deep white matter and dysplastic cortex. (Courtesy of Salamon N, MD, The University of California, Los Angeles, USA)

of the association fibers is impaired by some insult such as cortical dysplasia, formation of the Probst bundle is impaired (Fig. 14.48). On DT imaging fiber tractography, the fibers from the prefrontal area run on the inner side of the Probst bundle and form the genu of the corpus callosum, while fibers from the

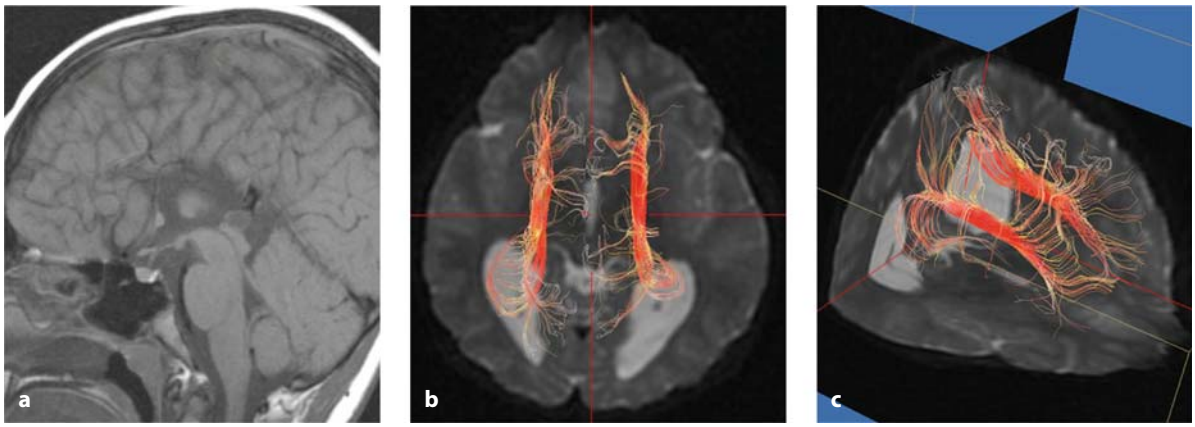

Figure 14.47 a–c

Corpus callosum agenesis in a 10-year old boy. **a** Sagittal T1-weighted image shows agenesis of the corpus callosum. **b**, **c** DT imaging fiber tractography demonstrates the arrangement of fiber tracts forming Probst bundles (*orange*). (Courtesy of Mori H, MD, and Aoki S, MD, The University of Tokyo, Japan)

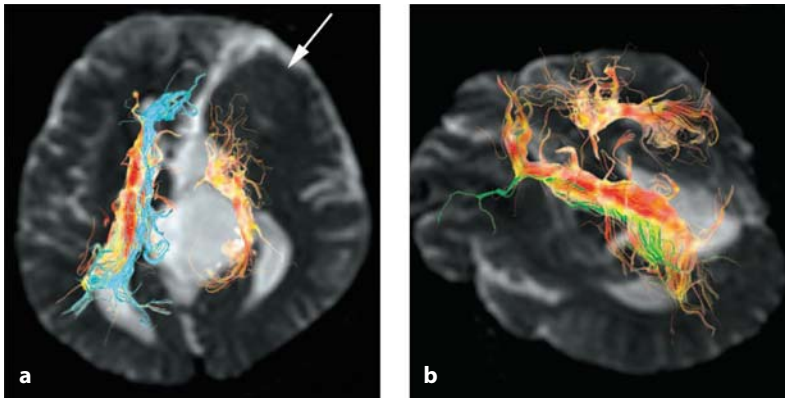

Figure 14.48 a, b

Complete callosal agenesis and cortical dysplasia in the left frontal lobe in a 34-year-old man. **a** DT imaging fiber tractography (Two-ROI method) shows that while the Probst bundle in the right hemisphere is well-developed, that in the left hemisphere is poorly developed. Cortical dysplasia is shown in the left frontal lobe (*arrow*). The fibers from the right prefrontal area run along the innermost side of the Probst bundle (*blue lines*). **b** The fibers from the right orbital gyrus run along the outermost side in Probst bundle (*green lines*). (Courtesy of Utsunomiya H, MD, Fukuoka University, Japan). (From [118])

caudal region of the frontal lobe run along the more lateral side and form the body of the corpus callosum. The fibers from the orbital gyri that form the rostrum of the corpus callosum run along the outermost side of the Probst bundle [118]. These findings support that the growth of the corpus callosum is primarily anteroposterior, with the genu forming first, followed by the body, splenium, and rostrum.

14.11.5 Other Anomalies

DT imaging fiber tractography findings have been reported in holoprosencephaly, lissencephaly, Joubert syndrome, and posterior fossa malformations [114, 115].

14.12 Conclusion

Diffusion-weighted imaging plays an important role in the diagnosis of various pathological conditions in the pediatric brain, which has a high water content . DW imaging can also depict acute or subacute ischemic changes in children when conventional MR imaging or CT is normal or shows only subtle abnormalities. DW imaging is useful in differentiating white matter diseases and in differentiating between tumor and abscess. The calculation of ADC maps or fractional anisotropic images is quantitative and demonstrates the water content or anisotropy more precisely than DW imaging. The recognition of imaging pitfalls is important for optimal interpretation of DW imaging. Diffusion tensor imaging (fractional anisotropy map, fiber tractography) is a useful tool for the evaluation of myelination and microstructural changes of the white matter, and for the demonstration of the white matter tract anatomy in various diseases in pediatric patients.

References

1. Roley HA, Grant PE, Roberts TPL (1999) Diffusion MR imaging. Theory and applications. Neuroimaging Clin N Am 9:343–361
2. Neil JJ, Shiran SI, McKinstry RC, et al. (1998) Normal brain in human newborns: apparent diffusion coefficient and diffusion anisotropy measured by using diffusion tensor MR imaging. Radiology 209:57–66
3. Wimberger DM, Roberts TP, Barkobich AJ, et al. (1995) Identification of "premyelination" by diffusion-weighted MRI. JCAT 19:28–33
4. Tanner SF, Ramenghi LA, Ridgway JP, et al. (2000) Quantitative comparison of intrabrain diffusion in adults and preterm and term neonates and infants. AJR Am J Roentgenol 174:1643–1649
5. Morris MC, Zimmerman RA, Bilaniuk LT, et al. (1999) Changes in brain water diffusion during childhood. Neuroradiology 41:929–934
6. Prayer D, Barkovich AJ, Kirschner DA, Prayer LM, Roberts TP, Kucharczyk J, Moseley ME (2001) Visualization of nonstructural changes in early white matter development on diffusion-weighted MR images: evidence supporting premyelination anisotropy. AJNR Am J Neuroradiol 22:1572–1576
7. Bui T, Daire JL, Chalard F, Zaccaria I, Alberti C, Elmaleh M, Garel C, Luton D, Blanc N, Sebag G. (2006) Microstructural development of human brain assessed in utero by diffusion tensor imaging. Pediatr Radiol 36:1133–1140
8. Counsell SJ, Shen Y, Boardman JP, Larkman DJ, Kapellou O, Ward P, Allsop JM, Cowan FM, Hajnal JV, Edwards AD, Rutherford MA (2006) Axial and radial diffusivity in preterm infants who have diffuse white matter changes on magnetic resonance imaging at term-equivalent age. Pediatrics 117:376–386
9. Arzoumanian Y, Mirmiran M, Barnes PD, Woolley K, Ariagno RL, Moseley ME, Fleisher BE, Atlas SW (2003) Diffusion tensor brain imaging findings at term-equivalent age may predict neurologic abnormalities in low birth weight preterm infants. AJNR Am J Neuroradiol 24:1646–1653
10. Neil JJ, Shiran SI, McKinstry RC, Schefft GL, Snyder AZ, Almli CR, Akbudak E, Aronovitz JA, Miller JP, Lee BC, Conturo TE. (1998) Normal brain in human newborns: apparent diffusion coefficient and diffusion anisotropy measured by using diffusion tensor MR imaging. Radiology 209:57–66
11. Forbes KP, Pipe JG, Bird CR (2002) Changes in brain water diffusion during the 1st year of life. Radiology 222:405–409
12. Provenzale JM, Liang L, DeLong D, White LE (2007) Diffusion tensor imaging assessment of brain white matter maturation during the first postnatal year. AJR Am J Roentgenol 189:476–486
13. McGraw P, Liang L, Provenzale JM (2002) Evaluation of normal age-related changes in anisotropy during infancy and childhood as shown by diffusion tensor imaging. AJR Am J Roentgenol 179:1515–1522
14. Hermoye L, Saint-Martin C, Cosnard G, Lee SK, Kim J, Nassogne MC, Menten R, Clapuyt P, Donohue PK, Hua K, Wakana S, Jiang H, van Zijl PC, Mori S (2006) Pediatric diffusion tensor imaging: normal database and observation of the white matter maturation in early childhood. Neuroimage 29:493–504
15. Boujraf S, Luypaert R, Shabana W, De Meirleir L, Sourbron S, Osteaux M (2002) Study of pediatric brain development using magnetic resonance imaging of anisotropic diffusion. Magn Reson Imaging 20:327–336
16. Evans AC; Brain Development Cooperative Group (2006) The NIH MRI study of normal brain development. Neuroimage 30:184–202
17. Filippi CG, Lin DD, Tsiouris AJ, Watts R, Packard AM, Heier LA, Uluğ AM (2003) Diffusion-tensor MR imaging in children with developmental delay: preliminary findings. Radiology 229:44–50
18. Yamada I, Himeno Y, Nagaoka T, et al. (1999) Moyamoya disease: evaluation with diffusion-weighted and perfusion echo-planar MR imaging. Radiology 212:340–347
19. Moran CJ, Siegel MJ, DeBaun MR (1998) Sickle cell disease: imaging of cerebrovascular complications. Radiology 206:311–321
20. Moritani T, Numaguchi Y, Lerner NB, et al. (2004) Sickle Cell Cerebrovascular Disease: usual and unusual findings on MR Imaging and MR Angiography, Clin Imaging 28:173–86

21. Porto L, Kieslich M, Yan B, Zanella FE, Lanfermann H. (2006) Accelerated myelination associated with venous congestion. Eur Radiol 16:922–926
22. Barkovich JA (2005) Pediatric Neuroimaging, 4th edn. Lippincott Williams & Wilkins, Philadelphia, pp. 875–884
23. Phillips MD, Zimmerman RA (1999) Diffusion imaging in pediatric hypoxic ischemia injury. Neuroimaging Clin N Am 9:41–52
24. Robertson RL, Ben-Sira L, Barnes PD, et al. (1999) MR line-scan diffusion-weighted imaging of term neonates with perinatal brain ischemia. AJNR Am J Neuroradiol 20:1658–1670
25. Johnson AJ, Lee BC, Lin W (1999) Echoplanar diffusion-weighted imaging in neonates and infants with suspected hypoxic-ischemic injury: correlation with patient outcome. AJR Am J Roentgenol 172:219–226
26. Inder T, Huppi PS, Zientara GP, et al. (1999) Early detection of periventricular leukomalacia by diffusion-weighted magnetic resonance imaging techniques. J Pediatr 134:631–634
27. Forbes KP, Pipe JG, Bird R (2000) Neonatal hypoxic-ischemic encephalopathy: detection with diffusion-weighted MR imaging. AJNR Am J Neuroradiol 21:1490–6
28. Wolf RL, Zimmerman RA, Clancy R, Haselgrove JH (2001) Quantitative apparent diffusion coefficient measurements in term neonates for early detection of hypoxic-ischemic brain injury: initial experience. Radiology 218:825–33
29. Moritani T, Smoker WR, Sato Y, Numaguchi Y, Westesson PL (2005) Diffusion-weighted imaging of acute excitotoxic brain injury. AJNR Am J Neuroradiol 26:216–228
30. Rumpel H, Nedelcu J, Aguzzi A, et al. (1997) Late glial swelling after acute cerebral hypoxic-ischemia in the neonatal rat: a combined magnetic resonance and histochemical study. Pediatr Res 42:54–59
31. Malik GK, Trivedi R, Gupta RK, Hasan KM, Hasan M, Gupta A, Pandey CM, Narayana PA (2006) Serial quantitative diffusion tensor MRI of the term neonates with hypoxic-ischemic encephalopathy (HIE). Neuropediatrics 37:337–343
32. Chen CY, Zimmerman RA, Rorke LB (1999) Neoroimaging in child abuse: a mechanism-based approach. Neuroradiology 41:711–722
33. Bullock R, Butcher SP, Chen MH, et al. (1991) Correlation of the extracellular glutamate concentration with extent of blood flow reduction after subdural hematoma in the rat. J Neurosurg 74:794–802
34. Johnson DL, Boal D, Baule R. (1995) Role of apnea in non-accidental head injury. Pediatr Neurosurg 23:305–310
35. Geddes JF, Hackshaw AK, Vowles GH, et al. (2001) Neuropathology of inflicted head injury in children. Patterns of brain damage. Brain 124:1290–1298
36. Suh DY, Davis PC, Hopkins KL, et al. (2001) Nonaccidental pediatric head injury: diffusion-weighted imaging findings. Neurosurgery 49:309–320
37. Holshouser BA, Ashwal S, Luh G, et al. (1997) Proton MR spectroscopy after central nervous system injury: outcome prediction in neonates, infants, and children. Radiology 202:487–496
38. Duhaime AC, Gennarelli LM, Boardman C (1996) Neuroprotection by dextromethorphan in acute experimental subdural hematoma in the rat. J Neurotrauma 13:79–84
39. Ikonomidou C, Qin Y, Labruyere J, Kirby C, et al. (1996) Prevention of trauma-induced neurodegeneration in infant rat brain. Pediatr Reseach 39:1020–1027
40. Smith SL, Hall ED (1998) Tirilazad widens the therapeutic window for riluzole-induced attenuation of progressive cortical degeneration in an infant rat model of the shaken baby syndrome. J Neurotrauma 15:707–719
41. Barzo P, Marmarou A, Fatouros P, et al. (1997) Contribution of vasogenic and cellular edema to traumatic brain swelling measured by diffusion-weighted imaging. J Neurosurg 87:900–907
42. Liu AY, Maldjian JA, Bagley LJ, Sinson GP, et al. (1999) Traumatic brain injury: diffusion-weighted MR imaging findings. AJNR Am J Neuroradiol 20:1636–1641
43. Tsuchiya K, Katase S, Yoshino A, et al. (1999) Diffusion-weighted MR imaging of encephalitis. AJR Am J Roentgenol 173:1097–1099
44 Ebisu T, Tanaka C, Umeda M, et al. (1996) Discrimination of brain abscess from necrotic or cystic tumors by diffusion-weighted echo planar imaging. Magn Reson Imaging 14:1113–1116
45. Huang CC, Chen CY, Yang HB, Wang SM, Chang YC, Liu CC (1998) Central nervous system candidiasis in very low-birth-weight premature neonates and infants: US characteristics and histopathologic and MR imaging correlates in five patients. Radiology 209:49–56
46. Kotsenas AL, Roth TC, Manness WK, et al. (1999) Abnormal diffusion-weighted MRI in medulloblastoma: does it reflect small cell histology? Pediatr Radiol 29:524–526
47. Wilke M, Eidenschink A, Muller-Weihrich S, Auer DP (2001) MR diffusion imaging and 1H spectroscopy in a child with medulloblastoma. A case report. Acta Radiol 42:39–42
48. Erdem E, Zimmerman RA, Haselgrove JC, Bilaniuk LT, Hunter JV (2001) Diffusion-weighted imaging and fluid attenuated inversion recovery imaging in the evaluation of primitive neuroectodermal tumors. Neuroradiology 43:927–933
49. Klisch J, Husstedt H, Hennings S, von Velthoven V, Pagenstecher A, Schumacher M (2000) Supratentorial primitive neuroectodermal tumours: diffusion-weighted MRI. Neuroradiology 42:393–398
50. Tien RD, Felsberg GJ, Friedman H, et al. (1993) MR imaging of high-grade cerebral gliomas: value of diffusion-weighted echoplanar pulse sequence. AJR Am J Roentgenol 162:671–677
51. Guo AC, Cummings TJ, Dash RC, Provenzale JM (2002) Lymphomas and high-grade astrocytomas: comparison of water diffusibility and histologic characteristics. Radiology 224:177–183
52. Koral K, Gargan L, Bowers DC, Gimi B, Timmons CF, Weprin B, Rollins NK (2008) Imaging characteristics of atypical teratoid-rhabdoid tumor in children compared with medulloblastoma. AJR Am J Roentgenol 190:809–814

53. Kan P, Liu JK, Hedlund G, Brockmeyer DL, Walker ML, Kestle JR (2006) The role of diffusion-weighted magnetic resonance imaging in pediatric brain tumors. Childs Nerv Syst 22:1435–1439
54. Rumboldt Z, Camacho DL, Lake D, Welsh CT, Castillo M (2006) Apparent diffusion coefficients for differentiation of cerebellar tumors in children. AJNR Am J Neuroradiol 27:1362–1369
55. Meyers SP, Khademian ZP, Biegel JA, Chuang SH, Korones DN, Zimmerman RA (2006) Primary intracranial atypical teratoid/rhabdoid tumors of infancy and childhood: MRI features and patient outcomes. AJNR Am J Neuroradiol 27:962–971
56. Meyers SP, Khademian ZP, Chuang SH, Pollack IF, Korones DN, Zimmerman RA (2004) Choroid plexus carcinomas in children: MRI features and patient outcomes. Neuroradiology 46:770–780
57. Cooney MJ, Bradly WG, Symko SC, et al. (2000) Hypertensive encephalopathy: complication in children treated for myeloproliferative disorders: report of three cases. Radiology 214:711–716
58. Schwartz RB, Mulkern RV, Gudbjartsson H, et al. (1998) Diffusion-weighted MR imaging in hypertensive encephalopathy: clues to pathogenesis. AJNR Am J Neuroradiol 19:859–862
59. Yagishita A, Nakano I, Ushioda T, Otsuki N, Hasegawa A (1995) Acute encephalopathy with bilateral thalamotegmental involvement in infants and children: imaging and pathology findings. AJNR Am J Neuroradiol 16:439–447
60. Albayram S, Bilgi Z, Selcuk H, Selcuk D, Cam H, Koçer N, Islak C (2004) Diffusion-weighted MR imaging findings of acute necrotizing encephalopathy. AJNR Am J Neuroradiol 25:792–797
61. Maeda M, Tsukahara H, Terada H, Nakaji S, Nakamura H, Oba H, Igarashi O, Arasaki K, Machida T, Takeda K, Takanashi JI. (2006) Reversible splenial lesion with restricted diffusion in a wide spectrum of diseases and conditions. J Neuroradiol 33:229–236
62. Takanashi J, Barkovich AJ, Shiihara T, Tada H, Kawatani M, Tsukahara H, Kikuchi M, Maeda M. (2006) Widening spectrum of a reversible splenial lesion with transiently reduced diffusion. AJNR Am J Neuroradiol 27:836–838
63. Tada H, Takanashi J, Barkovich AJ, Oba H, Maeda M, Tsukahara H, Suzuki M, Yamamoto T, Shimono T, Ichiyama T, Taoka T, Sohma O, Yoshikawa H, Kohno Y (2004) Clinically mild encephalitis/encephalopathy with a reversible splenial lesion. Neurology 63:1854–1858
64. Bulakbasi N, Kocaoglu M, Tayfun C, Ucoz T. (2006) Transient splenial lesion of the corpus callosum in clinically mild influenza-associated encephalitis/encephalopathy. AJNR Am J Neuroradiol 27:1983-6http://www.ncbi.nlm.nih.gov/pubmed/17032879?ordinalpos=9&itool=EntrezSystem2.PEntrez.Pubmed.Pubmed_ResultsPanel.Pubmed_RVDocSum
65. Kim JH, Choi JY, Koh SB, Lee Y (2007) Reversible splenial abnormality in hypoglycemic encephalopathy. Neuroradiology 49:217–222
66. Doherty MJ, Jayadev S, Watson NF, Konchada RS, Hallam DK (2005) Clinical implications of splenium magnetic resonance imaging signal changes. Arch Neurol 62:433–437
67. Conti M, Salis A, Urigo C, Canalis L, Frau S, Canalis GC (2007) Transient focal lesion in the splenium of the corpus callosum: MR imaging with an attempt to clinical-physiopathological explanation and review of the literature. Radiol Med (Torino) 112:921–935
68. da Rocha AJ, Reis F, Gama HP, da Silva CJ, Braga FT, Maia AC Jr, Cendes F (2006) Focal transient lesion in the splenium of the corpus callosum in three non-epileptic patients. Neuroradiology 48:731–735
69. Cecil KM, Halsted MJ, Schapiro M, Dinopoulos A, Jones BV. (2002) Reversible MR imaging and MR spectroscopy abnormalities in association with metronidazole therapy. J Comput Assist Tomogr 26:948–951
70. Appenzeller S, Faria A, Marini R, Costallat LT, Cendes F. (2006) Focal transient lesions of the corpus callosum in systemic lupus erythematosus. Clin Rheumatol 25:568–571
71. Mikaeloff Y, Adamsbaum C, Husson B, Vallée L, Ponsot G, Confavreux C, Tardieu M, Suissa S; KIDMUS Study Group on Radiology (2004) MRI prognostic factors for relapse after acute CNS inflammatory demyelination in childhood. Brain 127(Pt 9):1942–1947
72. Dale RC, de Sousa C, Chong WK, Cox TC, Harding B, Neville BG (2000) Acute disseminated encephalomyelitis, multiphasic disseminated encephalomyelitis and multiple sclerosis in children. Brain 123 Pt 12:2407–2
73. Balasubramanya KS, Kovoor JM, Jayakumar PN, Ravishankar S, Kamble RB, Panicker J, Nagaraja D (2007) Diffusion-weighted imaging and proton MR spectroscopy in the characterization of acute disseminated encephalomyelitis. Neuroradiology 49(2):177–83
74. Barkovich JA (2005) Pediatric Neuroimaging, 4th edn. Lippincott Williams & Wilkins, Philadelphia, pp. 110–112
75. Rovira A, Pericot I, Alonso J, Rio J, et al. (2002) Serial diffusion-weighted MR imaging and proton MR spectroscopy of acute large demyelinating brain lesions: case report. AJNR Am J Neuroradiol Jun-Jul; 23:989–994
76. Cramer SC, Stegbauer KC, Schneider A, et al. (2001) Decreased diffusion in central pontine myelinolysis. AJNR Am J Neuroradiol Sep; 22:1476–1479
77. Ono J, Harada K, Mano T, et al. (1997) Differentiation of dys- and demyelination using diffusion anisotropy. Pediatr Neurol 16:63–66
78. Sener RN (2002) Metachromatic leukodystrophy: diffusion MR imaging findings. AJNR Am J Neuroradiol 23:1424–1426
79. Patay Z (2005) Diffusion-weighted MR imaging in leukodystrophies. Eur Radiol 15:2284–2303
80. Guo AC, Petrella JR, Kurtzberg J, Provenzale JM (2001) Evaluation of white matter anisotropy in Krabbe disease with diffusion tensor MR imaging: initial experience. Radiology 218:809–815
81. Suzuki K, Suzuki K (2002) Lysosomal diseases. In Graham DI, Lantos PL (eds) Greenfield's neuropathology, 7th edn. Arnold, London, New York, New Delhi, pp. 684–685
82. Barkovich, *op. cit*., pp.160–161
83. Eichler FS, Itoh R, Barker PB, et al. (2002) Proton MR spectroscopic and diffusion tensor brain MR imaging in X-linked adrenoleukodystrophy; initial experience. Radiology 225:245–252

84. Powers JM, De Vino DC (2002) Peroxisomal and mitochondrial disorders. In Graham DI, Landos PL (eds) Greenfield's neuropathology, 7th edn. Arnold, London, New York, New Delhi, pp. 758–765
85. Ellison D, Love S (1998) Toxic injury of the CNS. In: Neuropathology, 1st edn. London: Mosby 25:5
86. Lerman-Sagie T, Leshinsky-Silver E, Watemberg N, Luckman Y, Lev D (2005) White matter involvement in mitochondrial diseases. Mol Genet Metab 93:179–189
87. Yonemura K, Hasegawa Y, Kimura K, Minematsu K, Yamaguchi T (2001) Diffusion-weighted MR imaging in a case of mitochondrial myopathy, encephalopathy, lactic acidosis, and strokelike episodes. AJNR Am J Neuroradiol 22:269–272
88. Yoneda M, Maeda M, Kimura H, Fujii A, Katayama K, Kuriyama M (1999) Vasogenic edema on MELAS: a serial study with diffusion-weighted MR imaging. Neurology 53:2182–2184
89. Oppenheim C, Galanaud D, Samson Y, Sahel M, Dormont D, Wechsler B, Marsault C (2000) Can diffusion weighted magnetic resonance imaging help differentiate stroke from stroke-like events in MELAS? J Neurol Neurosurg Psychiatry 69:248–250
90. Ito H, Mori K, Harada M, Minato M, Naito E, Takeuchi M, Kuroda Y, Kagami S (2008) Serial brain imaging analysis of stroke-like episodes in MELAS. Brain Dev 30:483–488
91. Wang XY, Noguchi K, Takashima S, Hayashi N, Ogawa S, Seto H (2003) Serial diffusion-weighted imaging in a patient with MELAS and presumed cytotoxic oedema. Neuroradiology 45:640–643
92. Sakai Y, Kira R, Torisu H, Ihara K, Yoshiura T, Hara T (2006) Persistent diffusion abnormalities in the brain stem of three children with mitochondrial diseases. AJNR Am J Neuroradiol 27:1924–1926
93. Sacher M, Fatterpekar GM, Edelstein S, Sansaricq C, Naidich TP (2005) MRI findings in an atypical case of Kearns-Sayre syndrome: a case report. Neuroradiology 47:241–244
94. Kono K, Okano Y, Nakayama K, Hase Y, Minamikawa S, Ozawa N, Yokote H, Inoue Y (2005) Diffusion-weighted MR imaging in patients with phenylketonuria: relationship between serum phenylalanine levels and ADC values in cerebral white matter. Radiology 236:630–636
95. Sakai M, Inoue Y, Oba H, Ishiguro A, Sekiguchi K, Tsukune Y, Mitomo M, Nakamura H (2005) Age dependence of diffusion-weighted magnetic resonance imaging findings in maple syrup urine disease encephalopathy. J Comput Assist Tomogr 29:524–527
96. Srikanth SG, Chandrashekar HS, Nagarajan K, Jayakumar PN (2007) Restricted diffusion in Canavan disease. Childs Nerv Syst 23:465–468
97. Sener RN (2003) Canavan disease: diffusion magnetic resonance imaging findings. J Comput Assist Tomogr 27:30–33
98. Janson CG, McPhee SW, Francis J, Shera D, Assadi M, Freese A, Hurh P, Haselgrove J, Wang DJ, Bilaniuk L, Leone P (2006) Natural history of Canavan disease revealed by proton magnetic resonance spectroscopy (1H-MRS) and diffusion-weighted MRI. Neuropediatrics 37:209–221
99. Sener RN (2003) L-2 hydroxyglutaric aciduria: proton magnetic resonance spectroscopy and diffusion magnetic resonance imaging findings. J Comput Assist Tomogr 27:38–43
100. Sener RN (2005) Tyrosinemia: computed tomography, magnetic resonance imaging, diffusion magnetic resonance imaging, and proton spectroscopy findings in the brain. J Comput Assist Tomogr 29:323–325
101. Sener RN (2004) Diffusion magnetic resonance imaging patterns in metabolic and toxic brain disorders. Acta Radiol 45:561–570
102. Au WL, Lim TC, Seow DC, Koh PL, Loh NK, Lim MS, Tan IK, Yee WC (2003) Serial diffusion-weighted magnetic resonance imaging in adult-onset citrullinaemia. J Neurol Sci 209:101–104
103. Takanashi J, Barkovich AJ, Cheng SF, Kostiner D, Baker JC, Packman S (2003) Brain MR imaging in acute hyperammonemic encephalopathy arising from late-onset ornithine transcarbamylase deficiency. AJNR Am J Neuroradiol 24:390–393
104. Sener RN (2003) Diffusion magnetic resonance imaging in infantile neuroaxonal dystrophy. J Comput Assis Tomogr 27:34–37
105. Barkovich, *op. cit*., pp. 131–134
106. Ono J, Harada K, Sakurai K, et al. (1994) MR diffusion imaging in Pelizaeus-Merzbacher disease. Brain Dev 16:219–223
107. Kennedy C, Grave GD, Jehle JW, Sokoloff L (1970) Blood flow to white matter during maturation of the brain. Neurology 20:613–618
108. Moritani T, Kim J, Sato Y, Bonthius D, Smoker WR (2008) Abnormal hypermyelination in a neonate with Sturge-Weber syndrome demonstrated on diffusion-tensor imaging. J Magn Reson Imaging 27:617–620
109. Yagishita A, Arai N, Tamagawa K, Oda M (1998) Hemimegalencephaly: signal changes suggesting abnormal myelination on MRI. Neuroradiology 40:734–738
110 Agid R, Lieberman S, Nadjari M, Gomori JM (2006) Prenatal MR diffusion-weighted imaging in a fetus with hemimegalencephaly. Pediatr Radiol 36:138–140
111. Salamon N, Andres M, Chute DJ, Nguyen ST, Chang JW, Huynh MN, Chandra PS, Andre VM, Cepeda C, Levine MS, Leite JP, Neder L, Vinters HV, Mathern GW (2006) Contralateral hemimicrencephaly and clinical-pathological correlations in children with hemimegalencephaly. Brain 129(Pt 2):352–365
112. Sato N, Ota M, Yagishita A, Miki Y, Takahashi T, Adachi Y, Nakata Y, Sugai K, Sasaki M (2008) Aberrant midsagittal fiber tracts in patients with hemimegalencephaly. AJNR Am J Neuroradiol 29:823–827
113. Trivedi R, Gupta RK, Hasan KM, Hou P, Prasad KN, Narayana PA (2006) Diffusion tensor imaging in polymicrogyria: a report of three cases. Neuroradiology 48:422–427
114. Lee SK, Kim DI, Kim J, Kim DJ, Kim HD, Kim DS, Mori S (2005) Diffusion-tensor MR imaging and fiber tractography: a new method of describing aberrant fiber connections in developmental CNS anomalies. Radiographics 25:53–65
115. Rollins NK (2007) Clinical applications of diffusion tensor imaging and tractography in children. Pediatr Radiol 37:769–780

116. Jansen FE, Braun KP, van Nieuwenhuizen O, Huiskamp G, Vincken KL, van Huffelen AC, van der Grond J (2003) Diffusion-weighted magnetic resonance imaging and identification of the epileptogenic tuber in patients with tuberous sclerosis. Arch Neurol 60:1580–1584
117. Makki MI, Chugani DC, Janisse J, Chugani HT (2007) Characteristics of abnormal diffusivity in normal-appearing white matter investigated with diffusion tensor MR imaging in tuberous sclerosis complex. AJNR Am J Neuroradiol 28:1662–1667
118. Utsunomiya H, Yamashita S, Takano K, Okazaki M (2006) Arrangement of fiber tracts forming Probst bundle in complete callosal agenesis: report of two cases with an evaluation by diffusion tensor tractography. Acta Radiol 47:1063–1066
119. Moritani T, Shrier DA, Numaguchi Y, et al. (2000) Diffusion-weighted echo-planar MR imaging: clinical applications and pitfalls – a pictorial essay. Clin Imaging 24:181–192

Scalp and Skull Lesions

In collaboration with Jack Kademian

15.1 Introduction

Diffusion-weighted (DW) imaging has recently been included as a standard magnetic resonance (MR) sequence of the brain. The use of DW imaging in the evaluation of brain pathology has been extensively studied. The imaging findings of scalp and skull lesions are often nonspecific and include various benign and malignant pathological conditions. DW imaging demonstrates characteristics unique to certain etiologies, such as cholesteatomas, epidermoids, abscesses, hypercellular tumors, and diffuse leukemic bone marrow infiltration, which assists in developing the differential diagnosis. DW imaging in the evaluation of scalp and skull lesions has lagged behind somewhat because of the technical limitations involved in imaging bone, air, and soft tissue interfaces. However, the DW imaging with its inherent fat saturation enhances the conspicuity of the scalp and skull lesions with nulling of the scalp fat.

15.2 Benign Processes and Tumors

15.2.1 Cholesteatomas

Cholesteatomas are classified as congenital (2%–5%) or acquired (95%–98%), and represent a sac lined with stratified squamous epithelium with keratin debris [1–11]. The acquired forms of cholesteatoma arise at the pars flaccida or the pars tensa of the tympanic membrane. The pars flaccida cholesteatoma extends into Prussak's space (bounded by the pars flaccida laterally, the lateral mallear ligament superiorly, the short process of the malleus inferiorly, and the neck of the malleus medially) with erosions primarily involving the scutum, ossicles, or lateral epitympanic wall [1–3, 12, 13]. The pars tensa cholesteatoma erodes into the posterior tympanic cavity and can involve the sinus tympani, facial recess, ossicles, aditus ad antrum, or mastoid [3]. Histopathologically, cholesteatoma is identical to an epidermoid cyst [3].

In suspected cases of cholesteatoma, noncontrast high-resolution computed tomography (CT) is the initial test of choice to evaluate for a middle ear mass with associated erosions. MR imaging can be used in selected cases for further characterization [14]. On standard MR sequences, cholesteatomas are usually hypointense on T1-weighted images and hyperintense on T2-weighted images [3]. Some cholesteatomas may be of intermediate or high intensity on T1-weighted images [15]. Postcontrast gadolinium imaging demonstrates lack of enhancement except for a thin peripheral rim [3, 16, 17].

One of the major treatments for cholesteatoma is canal wall up tympanoplasty. However, a second-look surgery is often required 6–18 months after the original surgery to evaluate for residual cholesteatoma [17–19]. Nonenhancing residual cholesteatoma on postcontrast images can be confused with relatively poorly vascularized scar tissue. Improved specificity on postcontrast images can be obtained with delayed (30–45 min) imaging [17].

Studied have shown the utility of DW imaging in the diagnosis of cholesteatoma [14, 16, 20–25] (Fig. 15.1). In a study by Fitzek et al., 13 of 15 patients with cholesteatomas demonstrated bright signal on single-shot spin echo echoplanar DW imaging [16]. Of the two false-negative findings in this study, one was an epitympanic retraction pocket (an early stage of the disease without production of significant cholesteatoma mass) and one in which the cholesteatoma mass spontaneously extruded into the external auditory canal. In a study by Vercruysse et al., 100 patients were evaluated with DW imaging to detect the presence of primary acquired cholesteatoma or residual cholesteatoma [14]. Increased signal on DW images was found in 89% of the cases of primary cholesteatoma, but only one of seven cases of residual cholesteatoma. The false-negatives seen with primary cholesteatomas demonstrated atelectatic retraction cholesteatoma or partially evacuated cholesteatoma with limited keratin accumulation. No false-positive results were found in the group of primary acquired cholesteatomas. In the second group of patients in which DW imaging

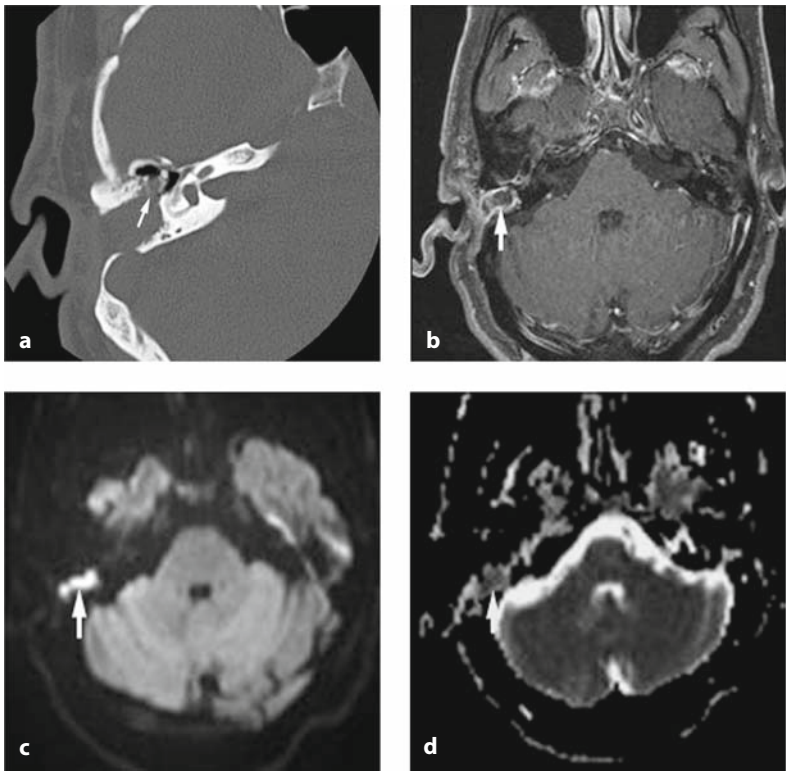

Figure 15.1 a–d

Recurrent cholesteatoma in a 45-year-old man. **a** CT shows right mastoidectomy and soft tissue density in the Prussak space with bony erosions (*arrow*). **b** Postcontrast T1-weighted image with fat saturation shows a recurrent cholesteatoma as hypointense with a characteristic rim enhancement (*arrow*). **c, d** DW image shows a hyperintense lesion with isointense ADC (0.82×10^{-3}mm^2/s) in the right mastoid representing a recurrent cholesteatoma (*arrow*)

was used to evaluate for residual cholesteatoma prior to second-look surgery, DW imaging was not found to be useful. However, all false-negative findings in this group of residual cholesteatomas were less than 4 mm in diameter. They concluded that the limitation in the detection of cholesteatoma on DW imaging was the size of lesion (4–5 mm) combined with low spatial resolution, thick slices, and air–bone artifacts. Other groups have also found size limitations in the 4–5 mm range [22, 25].

The calculated apparent diffusion coefficients (ADCs) for cholesteatomas in this study demonstrated no diffusion restriction. For 20 patients, the average ADC value was 0.844 (10^{-3} mm^2/s) and gray matter 0.837 (10^{-3} mm^2/s). The authors concluded that this supported the hypothesis that the hyperintensity on DW images is primarily due to T2 shine-through effect. Other groups have also supported this hypothesis [16, 21, 24].

15.2.2 Subcutaneous and Intracranial Epidermoid Cysts

Subcutaneous epidermoid cysts are asymptomatic, slowly enlarging, dome-shaped lesions that are frequently seen in the neck and face and often arise from a ruptured pilosebaceous follicle [26]. Subcutaneous epidermoid cysts are also known as epidermal cysts, keratin cysts, epithelial cysts, or sebaceous cysts. Pathologically, subcutaneous epidermoid cysts and intracranial epidermoid cysts are thought to be identical. Intracranial epidermoid cysts are also known as primary cholesteatomas [27].

In a study of 24 patients by Hong et al., the signal intensities of ruptured and unruptured subcutaneous epidermal cysts were described as well as enhancement patterns [28]. Unruptured cysts demonstrated thin, smooth rim cyst wall enhancement. Ruptured cysts had thick, irregular rim cyst wall enhancement, fuzzy enhancement in the surrounding subcutaneous tissue, and thin, smooth cyst wall enhancement.

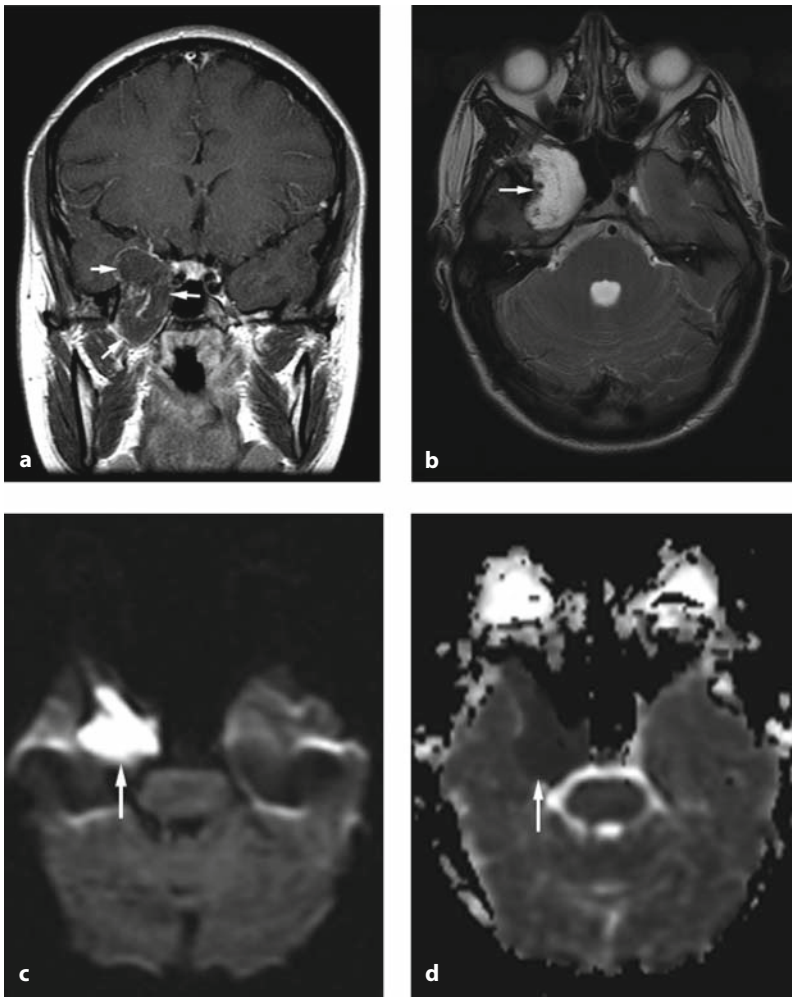

Figure 15.2 a–d

Epidermoid cyst in a 20-year-old woman. **a** Postcontrast coronal T1-weighted image shows a hypointense mass with rim enhancement in the right sphenoid bone and cavernous sinus (*arrows*). **b** T2-weighted image shows the mass as hyperintense (*arrow*). **c, d** DW images clearly show an epidermoid as hyperintense with decreased ADC ($0.57–0.62\times10^{-3}mm^2/s$) (*arrow*). (Courtesy of Jain V MD, The University of Iowa, Hospitals and Clinics, USA)

In an MR imaging study of five cases of epidermoid cysts in the extremities by Shibata et al., the cysts had slightly high signal intensity on T1-weighted imaging in three of five cases and isosignal intensity in two cases [29]. On T2-weighted images, all were of high signal intensity. Irregular areas of low signal intensity was seen on both T1- and T2-weighted images. There was no enhancement in the cysts.

In a study by Suzuki et al., using line scan DW imaging, unruptured subcutaneous epidermal cysts in the head were compared with intracranial epidermoid cysts [30] (Figs. 15.2–15.4). Signal intensity of subcutaneous epidermal cysts was low to mildly high on T1-weighted images (relative to muscle) and variable on T2-weighted images (nine high signal intensity, three low signal intensity, and two mixed signal intensity). This differed from intracranial epidermoid cysts, which were low on T1-weighted images and high on T2-weighted images. The subcutaneous epidermal cysts demonstrated no enhancement or thin and smooth rim enhancement.

The measured ADC of intracranial epidermoid cysts was significantly higher than subcutaneous epidermal cysts (1.06×10-3 mm2/s versus 0.81×10-3 mm2/ s). The authors hypothesize that the higher ADC for intracranial epidermoid cysts may be due to CSF interstices extending into the cysts. The authors also note the difficulty in measuring the ADC of

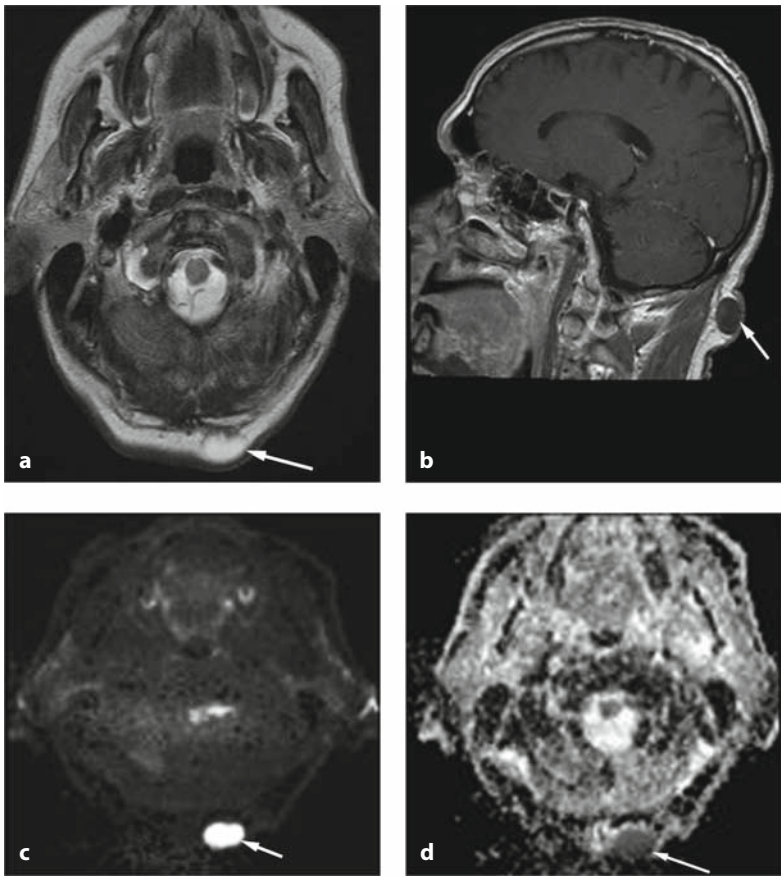

Figure 15.3 a–d

Epidermoid cyst in a 55-year-old man. **a** T2-weighted image shows an oval hyperintense lesion in the occipital scalp (*arrow*). **b** Postcontrast sagittal T1-weighted image shows an non enhancing hypointense mass(arrow). **c, d** DW imaging clearly shows an epidermoid as a hyperintense lesion associated with isointense ADC (0.97–1.10 $10^{-3}mm^2/s$) (*arrow*), which may correspond to stratified keratinaceous debris and squamous epithelium

head and neck legions using echoplanar DW imaging because of the susceptibility artifacts. They propose that line-scan DW imaging, or other DW imaging techniques with decreased sensitivity to susceptibility artifacts, should be used to evaluate head and neck lesions.

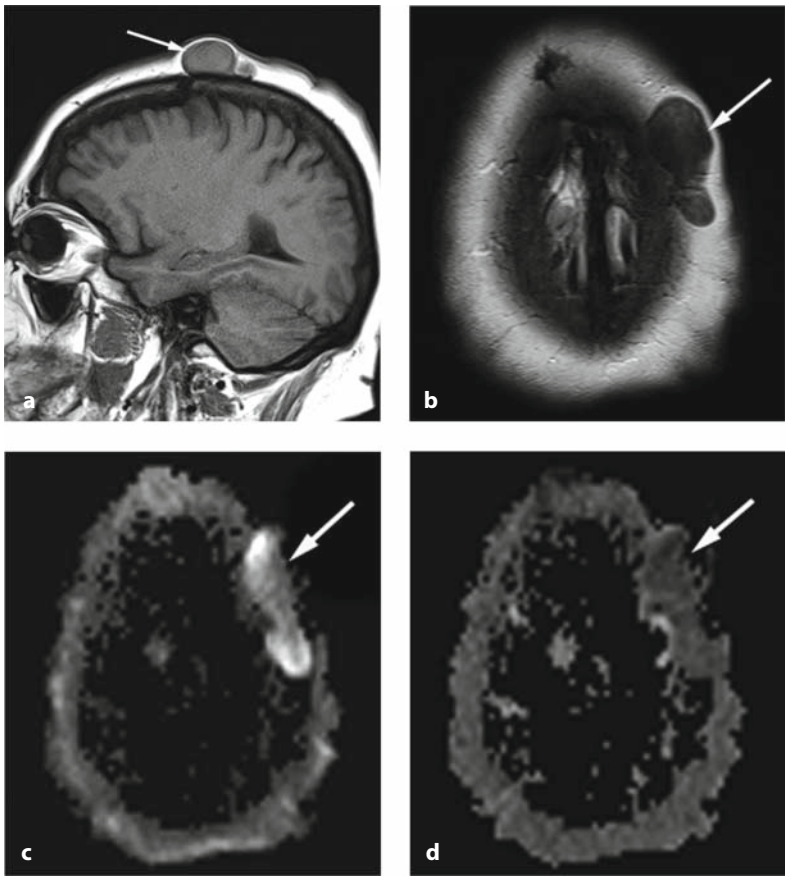

Figure 15.4 a–d

Epidermoid cyst in a 48-year-old woman **a** Precontrast sagittal T1-weighted image shows an oval iso- or slightly hyperintense lesion in the frontoparietal scalp (*arrow*). **b** T2-weighted image shows this lesion as hypointense (*arrow*). **c, d** DW images show the lesion as hyperintense associated with slightly low or isointense ADC ($0.67–0.93\times10^{-3}mm^2/s$) (*arrow*), which may correspond to stratified keratinaceous debris and squamous epithelium with less water contents

15.2.3 Cholesterol Granuloma

Cholesterol granulomas have a characteristically high signal on T1-weighted images due to a blood product (extracellular methohemoglobin) and have a central high signal on T2-weighted images with peripheral decreased signal from hemosiderin deposition [3]. A case of cholesterol granuloma with increased signal on DW images has been reported [31]. DW signals are usually mildly hyperintense with a high ADC value. However, ADC maps can show a heterogeneous lesion, which presumably depends on the viscosity of blood products in a cholesterol granuloma (Figs. 15.5, 15.6).

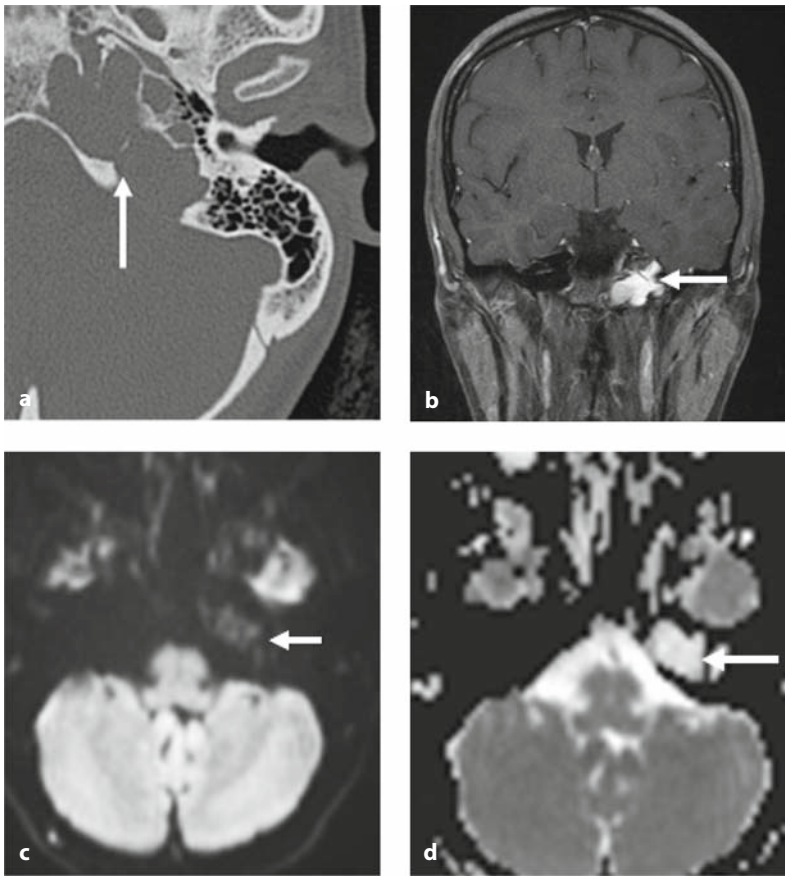

Figure 15.5 a–d

Cholesterol granuloma in a 35-year-old man. **a** CT shows a soft tissue density mass in the left petrous apex (*arrow*). **b** Postcontrast coronal T1-weighted image with fat saturation shows a nonenhancing mass as homogeneously hyperintense consistent with a cholesterol granuloma (*arrow*). **c, d** DW imaging shows a cholesterol granuloma as a mildly hyperintense lesion with increased ADC (2.32×10^{-3}mm^2/s) (*arrow*)

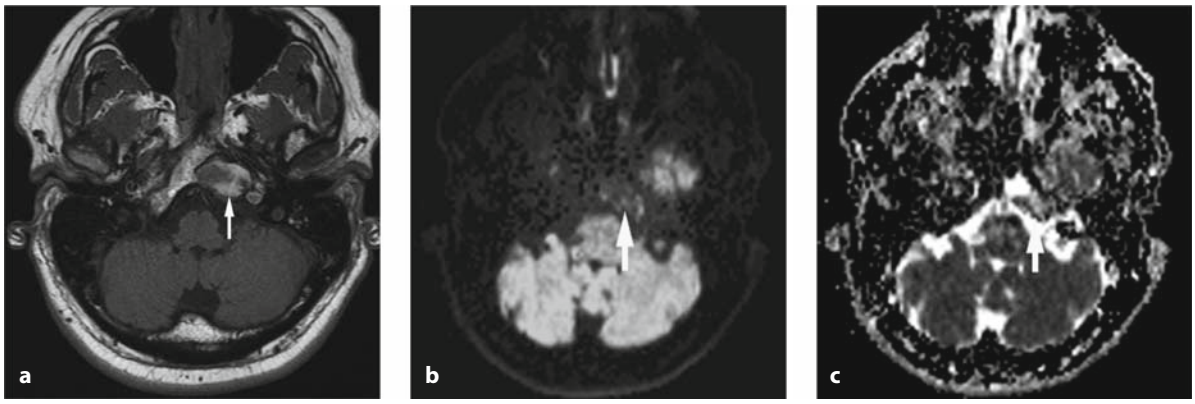

Figure 15.6 a–c

Cholesterol granuloma in a 55-year-old woman. **a** T1-weighted image shows the mass as partially hyperintense consistent with a cholesterol granuloma (*arrow*). **b, c** DW imaging shows a cholesterol granuloma as a mildly hyperintense lesion with variable ADC values ($0.82–2.45\times10^{-3}$mm^2/s) (*arrow*)

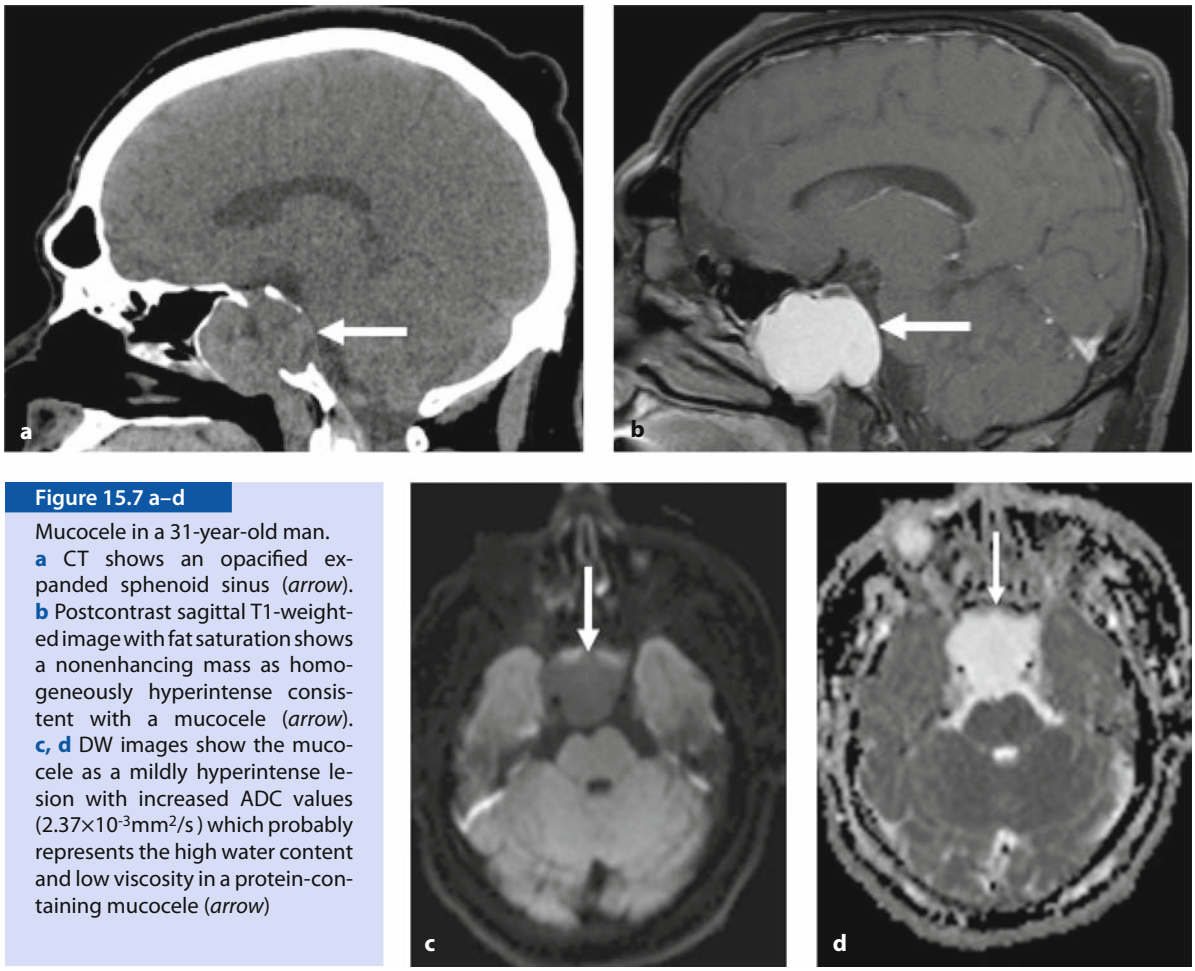

Figure 15.7 a–d

Mucocele in a 31-year-old man. **a** CT shows an opacified expanded sphenoid sinus (*arrow*). **b** Postcontrast sagittal T1-weighted image with fat saturation shows a nonenhancing mass as homogeneously hyperintense consistent with a mucocele (*arrow*). **c, d** DW images show the mucocele as a mildly hyperintense lesion with increased ADC values (2.37×10^{-3}mm^2/s) which probably represents the high water content and low viscosity in a protein-containing mucocele (*arrow*)

15.2.4 Mucocele

A mucocele is an opacified expanded sinus that is the result of chronic ostial obstruction [3]. MR signal characteristics depend on the concentration of mucus and protein. A high water content results in low T1 signal and high T2 signal, whereas high protein content results in high T1 signal and low signal on T2 with inspissated mucus. White et al. reported a case of an ethmoid sinus mucocele with slightly low signal on DW imaging with increased ADC [32]. DW signals and the ADC values in a mucocele are variable depending on the viscosity of the fluid in a mucocele (Figs. 15.7, 15.8).

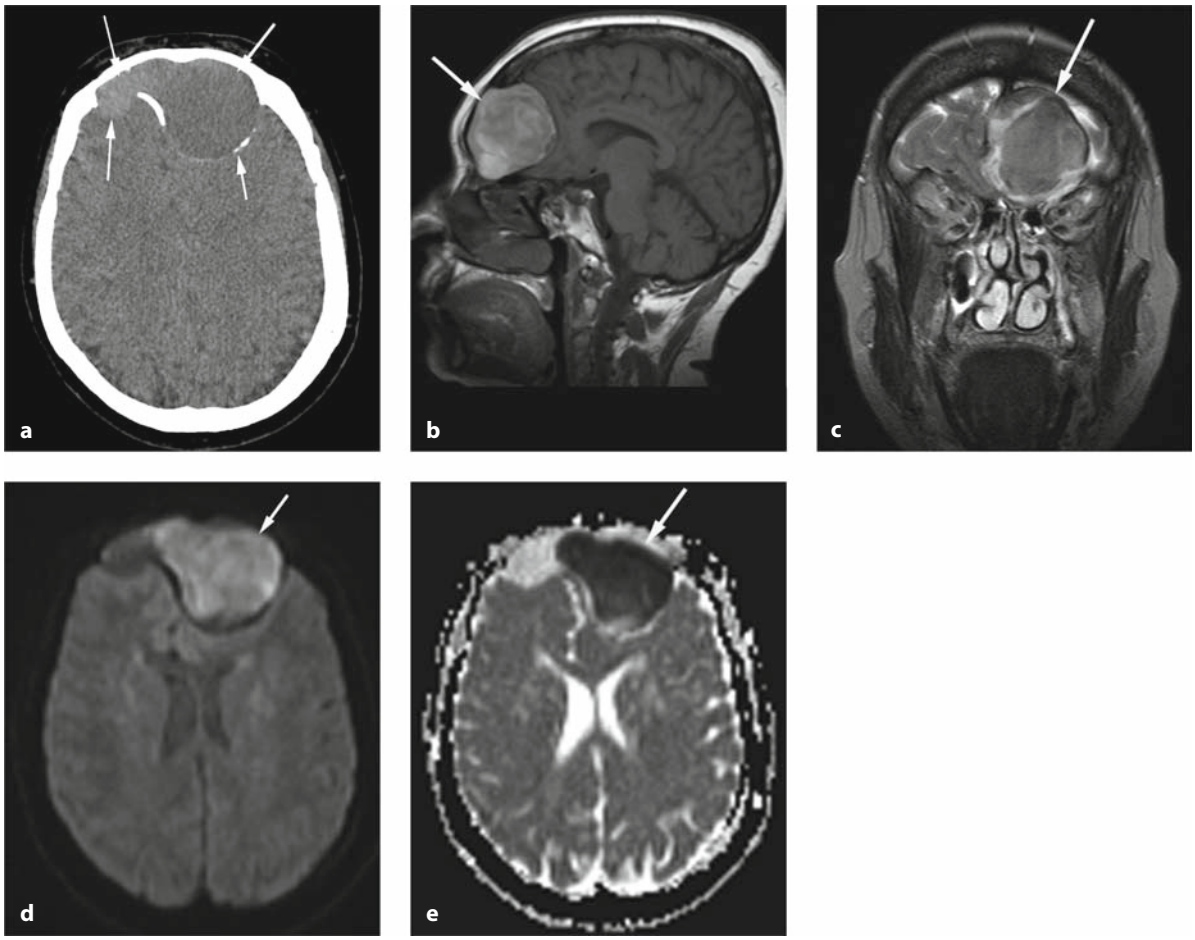

Figure 15.8 a–e

Mucocele in a 45-year-old woman. **a** CT shows an exponsile slightly hypen- and insointense mass with calcifications of the wall originating from the frontal sinus (*arrows*). **b** Precontrast sagittal T1-weighted image shows the mass as hyperintense (*arrow*). **c** Coronal T2-weighted image shows the mass as isointense consistent with a mucocele (*arrow*). **d, e** DW image shows most of the lesion as hyperintense with decreased ADC values (0,30–0,51x10^{-3} mm^2/s), which probably represents the high viscosity in a highly protein-containing mucocele (*arrow*). (Courtesy of Policeni B MD The University of Iowa Hospitals and Clinics)

15.2.5 Fibrous Dysplasia and Paget's Disease

Fibrous dysplasia is a disorder of unknown etiology characterized by abnormal development of fibroblasts and replacement of normal bone by dysplastic fibro-osseous tissues. The radiologic findings are divided into three types: pagetoid, sclerotic, and cyst-like. CT demonstrates fibrous dysplasia best. CT findings include an increase bone thickness, homogeneous radiodensity, and loss of trabecular pattern (ground-glass appearance). MR imaging shows a low-to-intermediate signal intensity with moderate to marked enhancement. Hayashida et al. used quantitative spin echo DW imaging to study 20 bone lesions (eight solitary bone cysts, five fibrous dysplasia, and seven chondrosarcomas) [33]. DW imaging shows mild hyperintensity in fibrous dysplasia associated with increased ADC (Fig. 15.9). They found that the mean ADC values of benign tumors and chondrosarcomas were not significantly different, whereas the mean ADC value of simple bone cysts was significantly higher than either fibrous dysplasia or chondrosarcoma.

Figure 15.9 a–d

Fibrous dysplasia in a 39-year-old woman. **a** Postcontrast sagittal T1-weighted image shows an inhomogeneously enhancing mass in the skull base (arrow). **b, c** DW imaging reveals minimally hyperintense mass in the skull base with increased ADC (1.32–1.97×10-3mm2/s) (arrow). **d** CT shows enlarged medullary space and typical ground-glass appearance of a fibrous dysplasia (*arrow*)

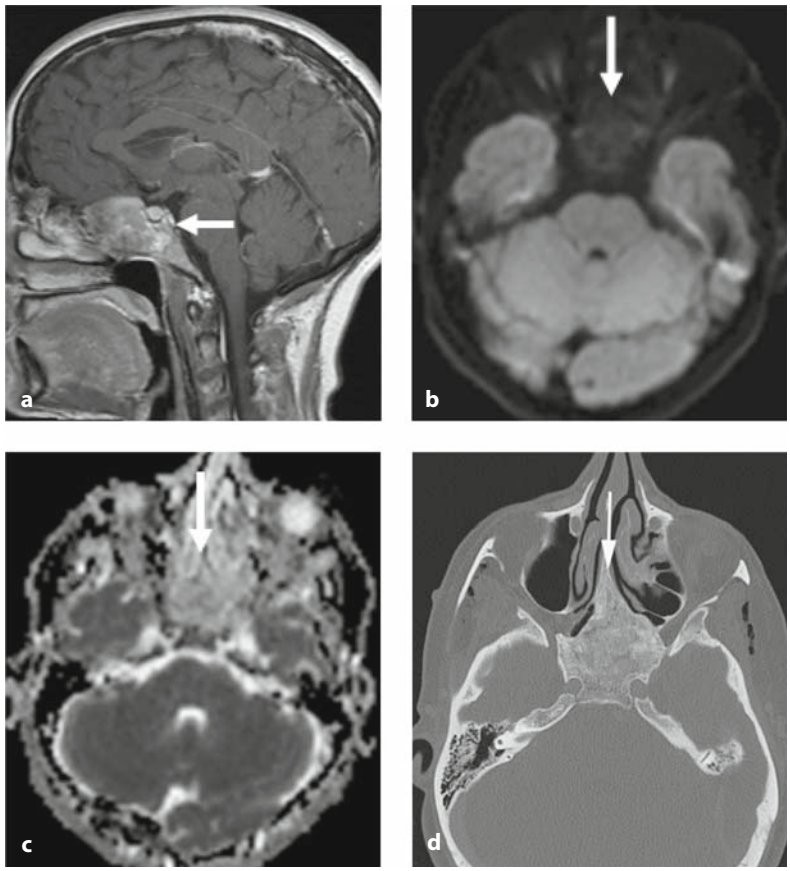

Figure 15.10 a, b

Paget's disease in a 45-year-old man. **a** CT shows diffuse bone thickening with a heterogeneous lytic and sclerotic bone density (cotton-wool appearance). **b** Postcontrast T1-weighted image with fat saturation shows a heterogeneous enhancement in the frontal skull

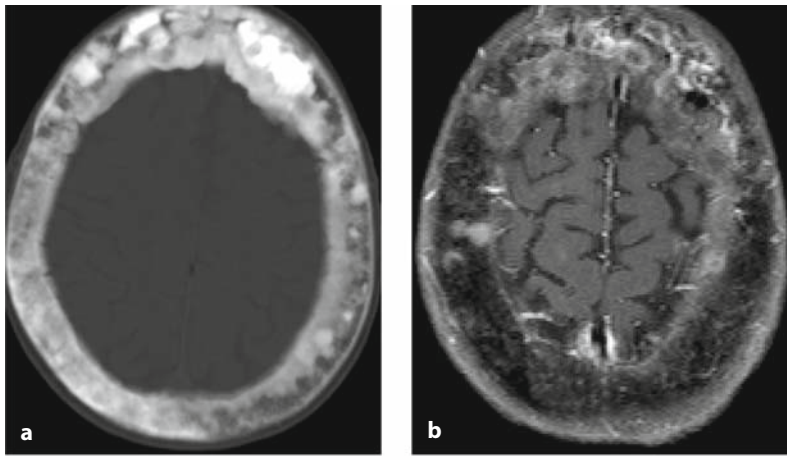

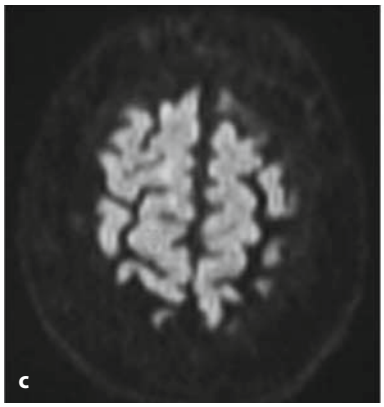

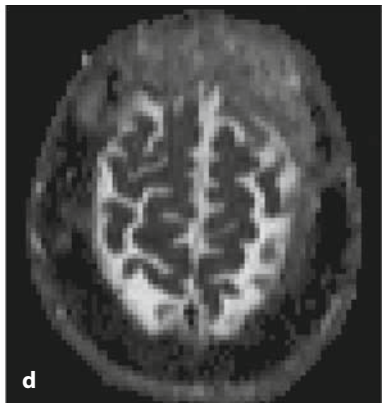

Figure 15.10 c, d

c, d DW imaging shows diffuse minimal hyperintensity in the skull associated with mildly increased ADC ($0.94–1.45\times10^{-3}mm^2/s$) in the frontal thickened skull

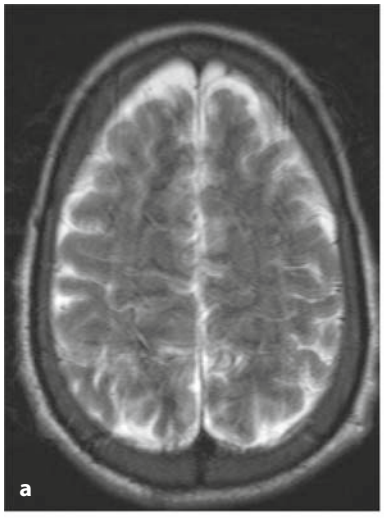

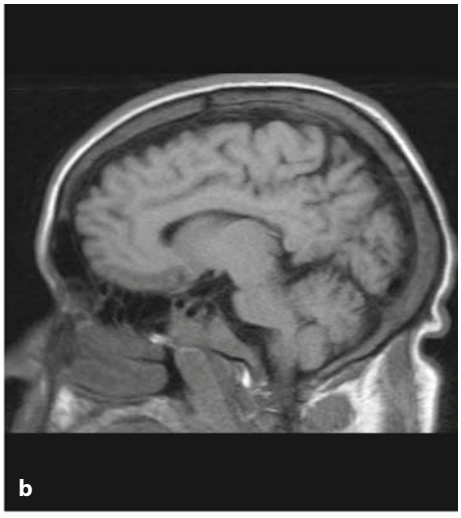

Figure 15.11 a–d

Sickle cell disease in a 22-year-old man. **a, b** Axial T2 and sagittal T1-weighted images show diffuse bone thickening of the skull. **c, d** DW imaging shows diffuse homogeneous hyperintensity (*arrows*) associated with mildly decreased ADC in the skull which corresponds to bone marrow hyperplasia

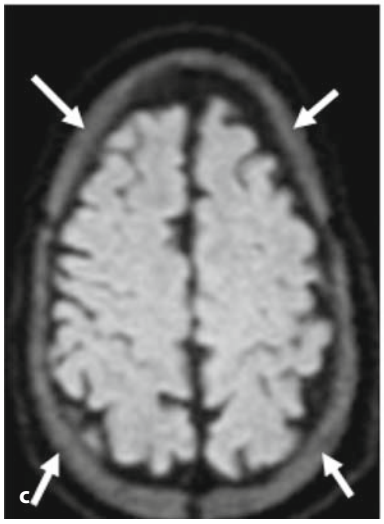

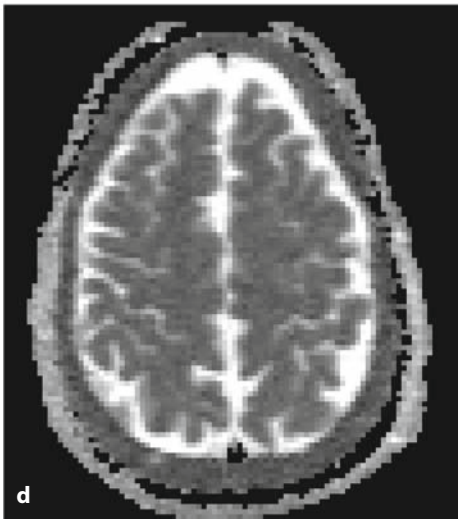

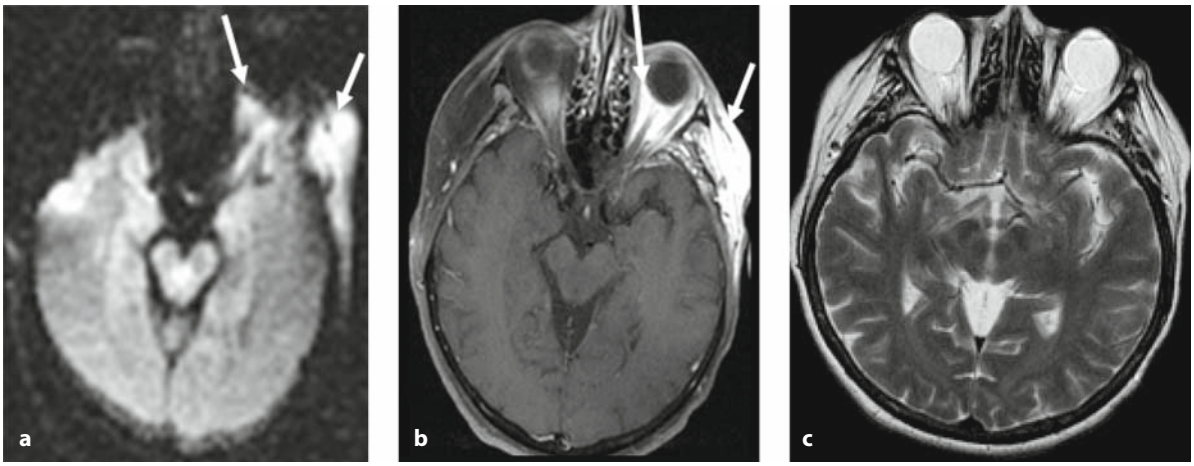

Figure 15.12 a–c

Artifacts similar to scalp mass lesion on DW imaging. **a** DW imaging shows high signal in the left periorbital and retro-orbital areas similar to lesions (*arrows*). **b** Postcontrast T1-weighted image with fat saturation shows an inadequate suppression of fat signals in exactly the same areas (*arrows*), which is due to susceptibility effects from metal of the tooth. **c** T2-weighted image shows no lesion in the areas

Paget's disease is a process of unknown cause in which osteoclastic activity is abnormal. The histopathology is divided into four phases: osteolytic, mixed, osteoblastic, and remodeled. The mixture of phases results in a heterogeneous lytic and sclerotic bone density (cotton-wool appearance) on CT. MR findings are variable. Contrast enhancement reflects the hypervascular nature of the process. DW imaging shows diffuse minimal hyperintensity in the skull associated with mildly increased ADC, which may reflect intermediate cellularity in the bone marrow spaces (Fig. 15.10). Diffuse bone marrow disease is characterized by diffuse fat replacement in the bone marrow on MR imaging [34, 35]. Bone marrow hyperplasia is seen in hematologic disorders such as sickle cell disease, thalassemia, and aplastic anemia (Fig. 15.11).

15.2.6 Artifacts, Other Benign Lesions, and Differential Diagnoses

DW imaging uses a fat suppression technique (chemical fat saturation) that is used in conventional MR imaging (fat sat T1- and T2-weighted images). Inadequate fat suppression due to a susceptibility artifact causes a hyperintensity on DW imaging which is sometimes similar to a scalp lesion (Fig. 15.12). A scalp lipoma is seen as a very hypointense lesion because of suppressed fat signals on DW imaging (Fig. 15.13). Benign lymphadenopathy and lymphoid tissues in tonsils (adenoids) can show hyperintensity on DW imaging associated with relatively low ADC values [36–38]. Intraosseous meningioma can show hyperintensity with decreased ADC (Fig. 15.14).

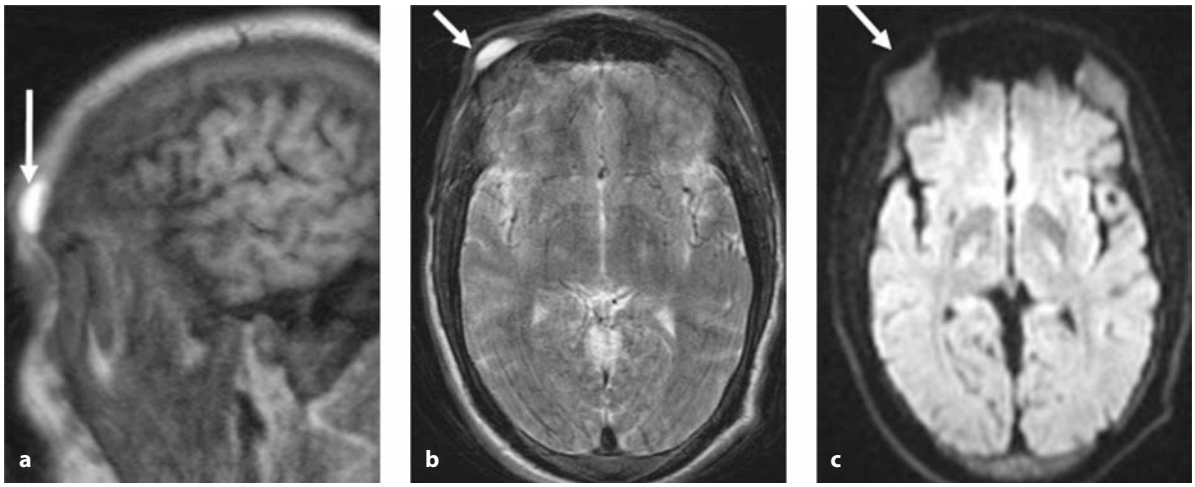

Figure 15.13 a–c

Lipoma in a 22-year-old man. **a, b** T1- and T2-weighted images show a hyperintense lesion in the right frontal scalp consistent with a lipoma (*arrow*). **c** DW imaging shows suppressed fat signal in the lipoma (*arrow*). This patient also has sickle cell disease. The thickened skull with increased DW imaging signal reflects red bone marrow hyperplasia

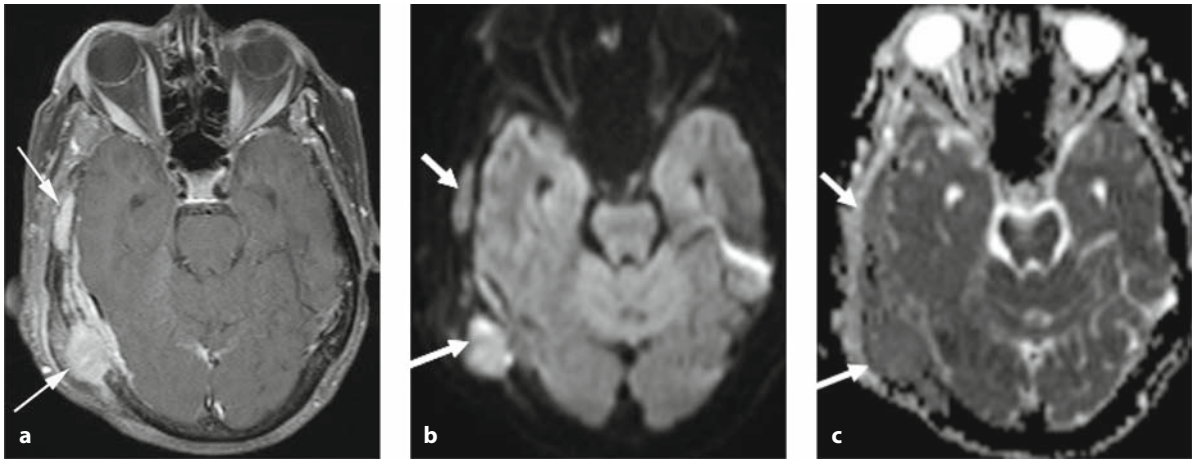

Figure 15.14 a–c

Intraosseous meningioma in a 57-year-old woman. **a** Postcontrast T1-weighted image with fat saturation demonstrates homogeneously enhancing masses with dural enhancement in the right temporo-occipital region (*arrows*). **b, c** DW imaging shows multiple hyperintense mass lesions with the isointense ADC ($0.77–0.89\times10^{-3}mm^2/s$), related to cellularity of meningioma (*arrows*)

Figure 15.15 a–d

Subgaleal hematoma in a 35-year-old man. **a** CT shows an occipitoparietal subgaleal hematoma and a left parafalcine subdural hematoma (*arrows*). **b** T2-weighted image shows iso- and low signal areas in the subgaleal and subdural hematomas (*arrows*). **c, d** DW imaging shows a slightly hyperintense hematoma with a low signal in the center area of the subgaleal hematoma associated with decreased ADC values (*arrows*). DW signals of hematomas are variable depending on the phase

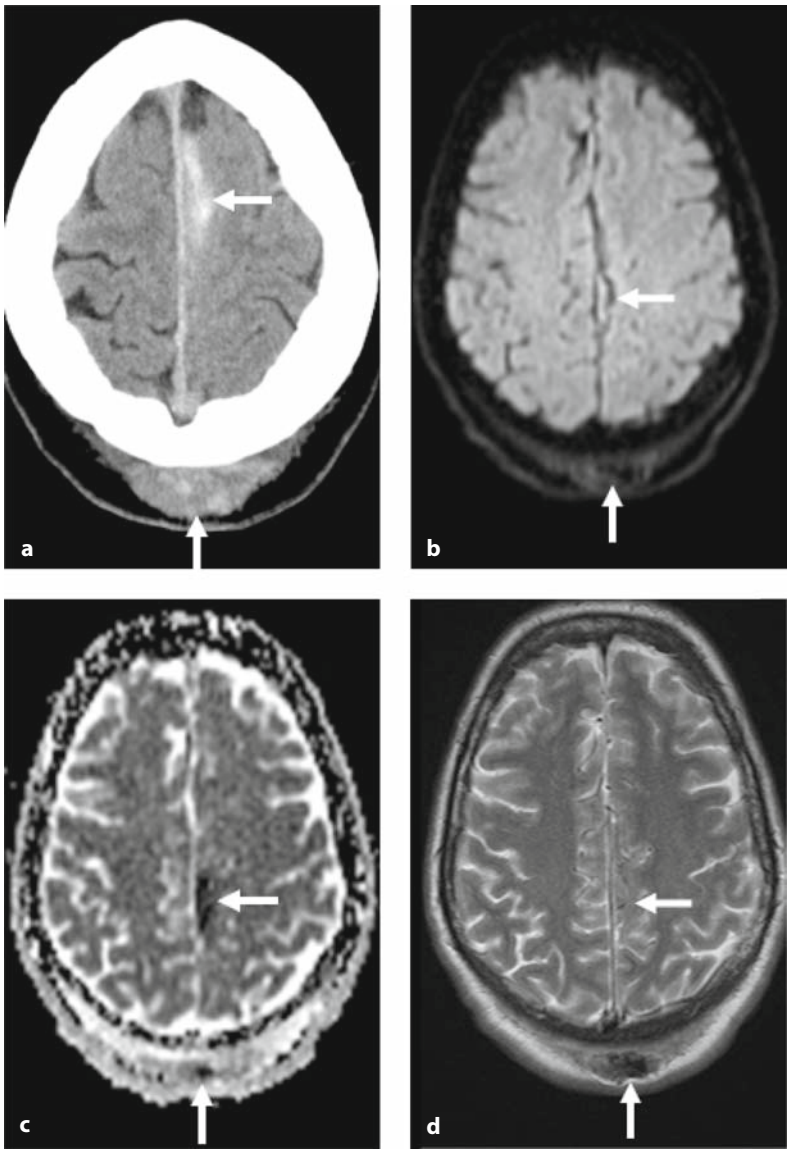

Scalp or subgaleal hematomas can have various DW signals and ADC values depending on the phase of the hematomas (Fig. 15.15). Caution is needed when differentiating them from pus collection, abscess, or tumors. Mild hyperintense lesions on DW imaging associated with increased ADC include scalp or intraosseous hemangiomas and Langerhans' cell histiocytosis (Figs. 15.16, 15.17) and neurogenic tumors (schwannoma, neurofibroma) (Figs. 15.18, 15.19).

In a study by Sener using echo-planar DW imaging, six vestibular schwannomas were found to be isointense to brain parenchyma on b=1,000 s/mm^2

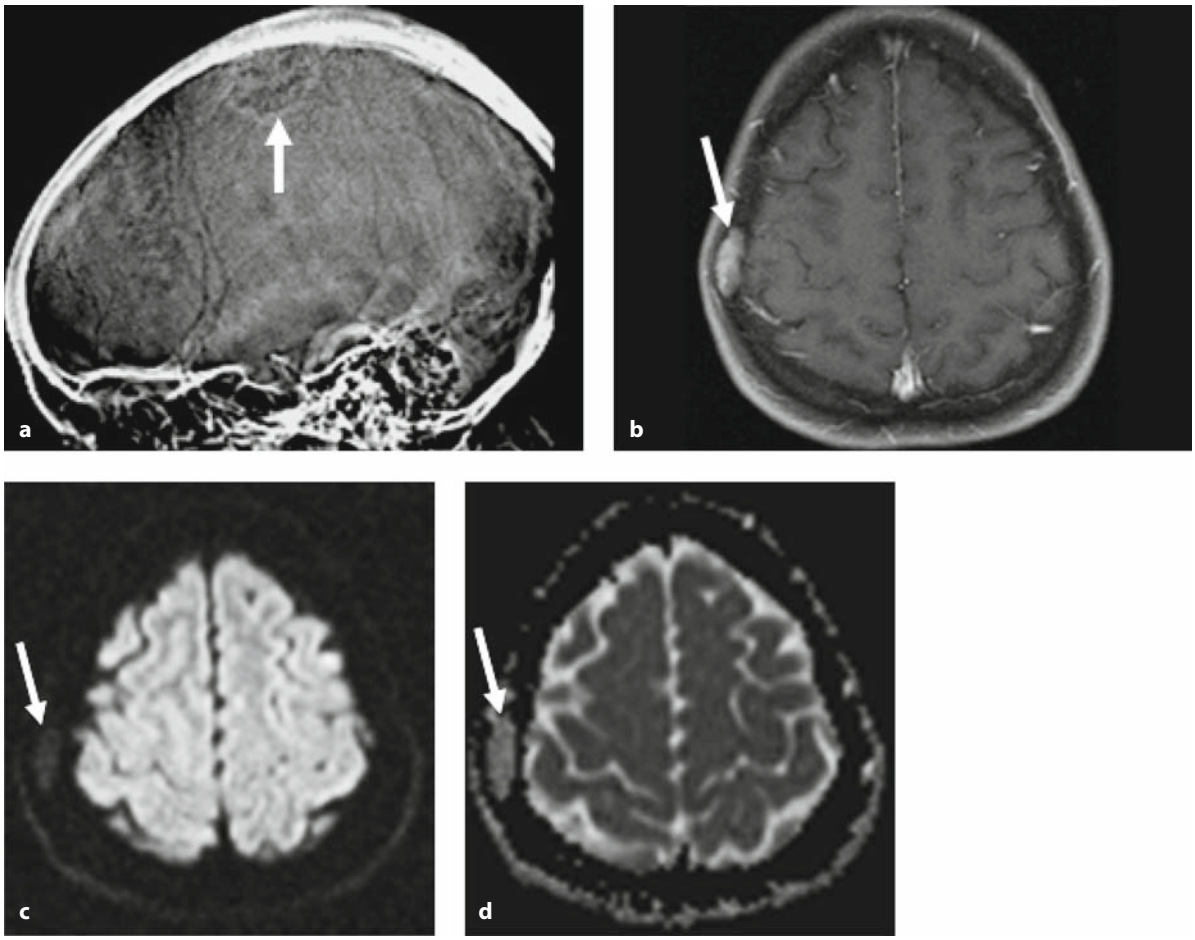

Figure 15.16 a–d

Intraosseous hemangioma in a 26-year-old man. **a** CT scanogram shows a calvarial lesion with sclerotic margins consistent with an intraosseous hemangioma (*arrow*). **b** Postcontrast T1-weighted image with fat saturation shows homogeneous enhancement (*arrow*). **c, d** DW imaging shows a slightly hyperintense lesion associated with slightly increased ADC ($1.37–1.48 \times 10^{-3} mm^2/s$) in the right parietal skull (*arrow*)

images, but with ADC values significantly higher than parenchyma (schwannoma range $1.14–1.72 \times 10^{-3}$ mm^2/s with mean value $1.42 \pm 0.17 \times 10^{-3}$ mm^2/s; parenchyma range $0.64–0.98 \times 10^{-3}$ mm^2/s with average value $0.80 \pm 0.11 \times 10^{-3}$ mm^2/s) [39]. The lesions studied were predominantly solid with minimal cystic degeneration. Srinivasan et al., using 3-T single-shot spin-echo echo-planar DW imaging, found a range of ADC values for six schwannomas (range $0.739–2.080 \times 10^{-3}$ mm^2/s; four vestibular schwannomas, one jugular foramen schwannoma, and one mandibular nerve schwannoma) [40]. They hypothesized differences could be due to differences in the internal architecture of the lesions. Maeda et al., using line-scan DW imaging, found that myxoid containing soft tissue tumors had significantly higher ADC values than non-myxoid soft tissue tumors [41]. Relatively low ADC values ($0.45–0.60 \times 10^{-3}$ mm^2/s) with increased signal on DW images were reported in a case of malignant oculomotor schwannoma [42].

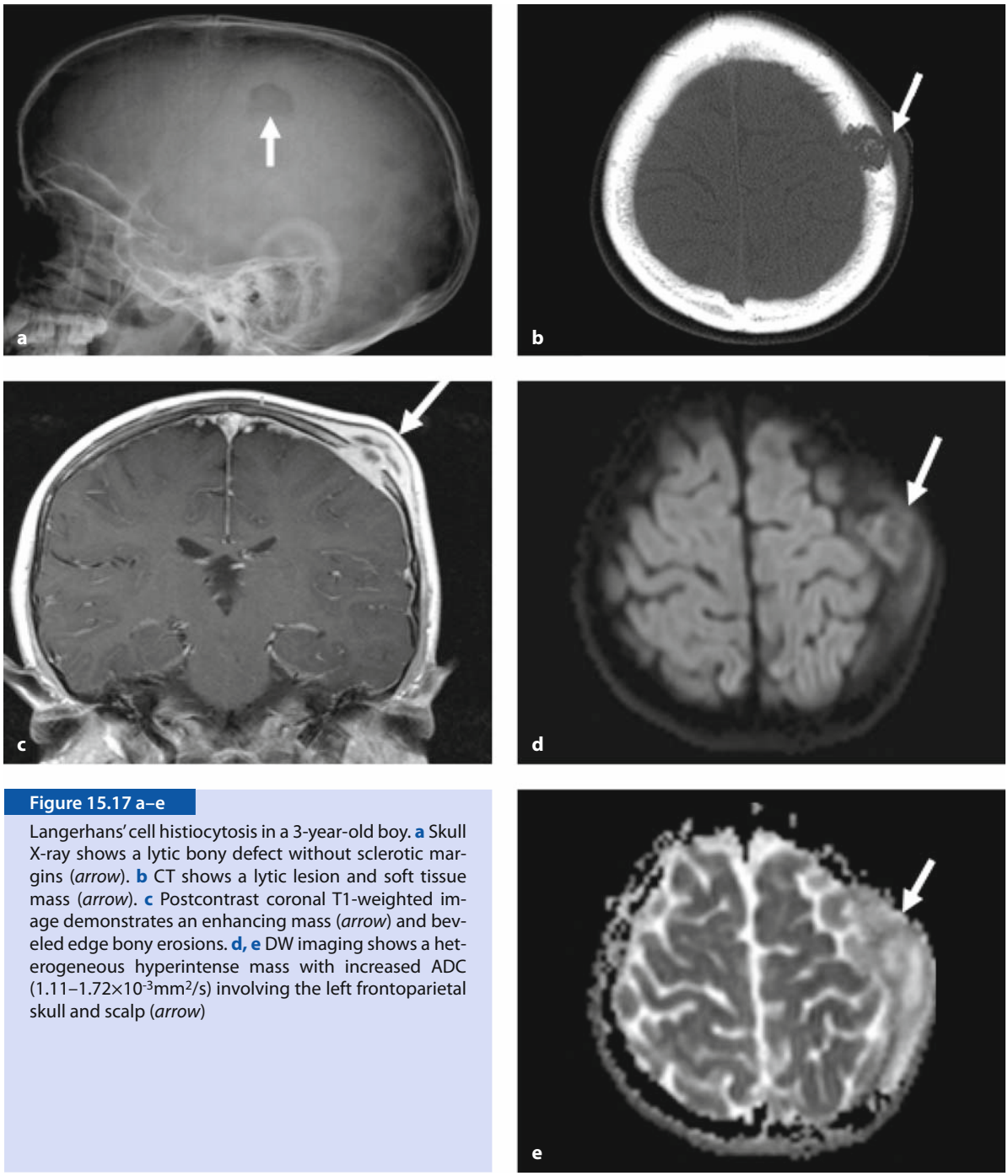

Figure 15.17 a–e

Langerhans' cell histiocytosis in a 3-year-old boy. **a** Skull X-ray shows a lytic bony defect without sclerotic margins (*arrow*). **b** CT shows a lytic lesion and soft tissue mass (*arrow*). **c** Postcontrast coronal T1-weighted image demonstrates an enhancing mass (*arrow*) and beveled edge bony erosions. **d, e** DW imaging shows a heterogeneous hyperintense mass with increased ADC ($1.11–1.72\times10^{-3}mm^2/s$) involving the left frontoparietal skull and scalp (*arrow*)

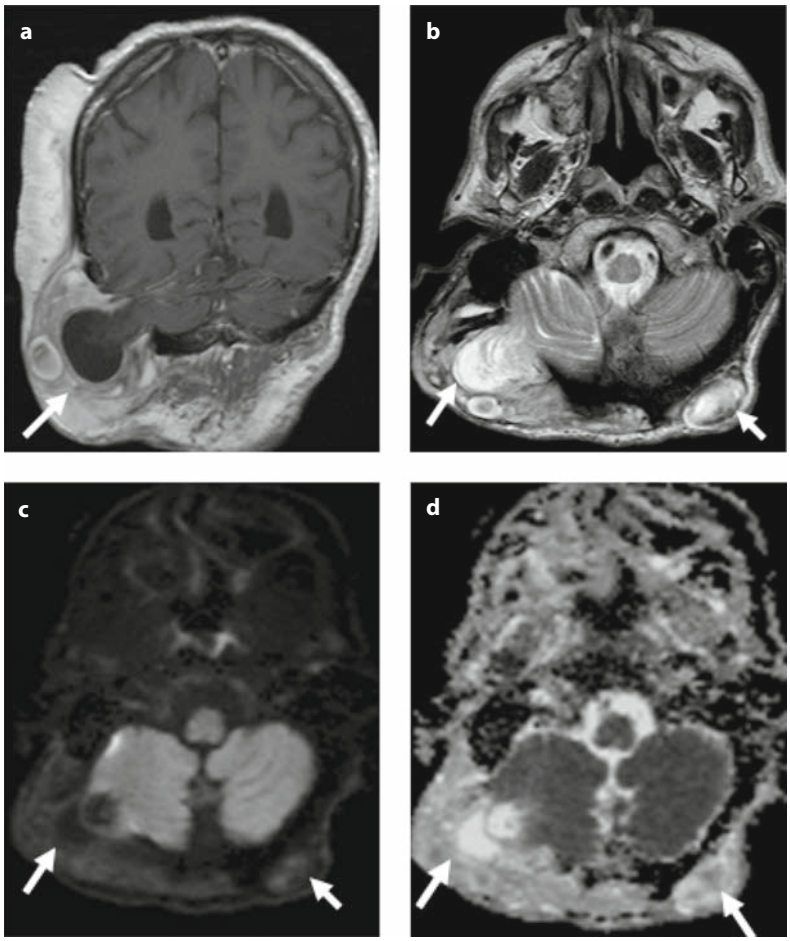

Figure 15.18 a–d

Neurofibromatosis type 1 in a 20-year-old man. **a, b** Postcontrast coronal T1- and axial T2-weighted images show multiple diffuse plexiform neurofibromatosis, a meningoencephalocele, and bony defect in the right occipital bone (*arrows*). **c, d** DW imaging shows multiple plexiform neurofibromas as slightly hyperintense with increased ADC ($1.63–2.11\times10^{-3}mm^2/s$) (*arrows*)

15.3 Infection (Abscess and Pus Collection), Mastoiditis, Malignant Otitis Externa

Acute otomastoiditis and acute coalescent otomastoiditis are defined as acute infections of the middle ear and mastoid air cells without destruction of mastoid septations in acute otomastoiditis and with destruction of septations in acute coalescent otomastoiditis with development of intramastoid empyema. MR imaging demonstrates isointense debris on T1-weighted images, hyperintense debris on T2-weighted images, and diffuse enhancement on postcontrast images. Postcontrast imaging also allows for characterization of focal abscess. An associated cholesteatoma will demonstrate relative decreased signal on T2-weighted images.

Bezold's abscess, first described in 1908, is considered as a neck abscess spreading from the tip of the mastoid, extending deep to the sternocleidomastoid muscle, and may extend into the posterior cervical and perivertebral spaces. Unlike coalescent mastoiditis, Bezold's abscess lies inferior to the tip of the mastoid process and does not extend superiorly to the lateral aspect of the mastoid process [43]. Coalescent mastoiditis with subperiosteal abscess is caused by an extension of infection via an eroded lateral mastoid cortex [43]. Distinguishing these entities is important because the surgical treatment is different (Bezold's abscess requires mastoidectomy and abscess drain-

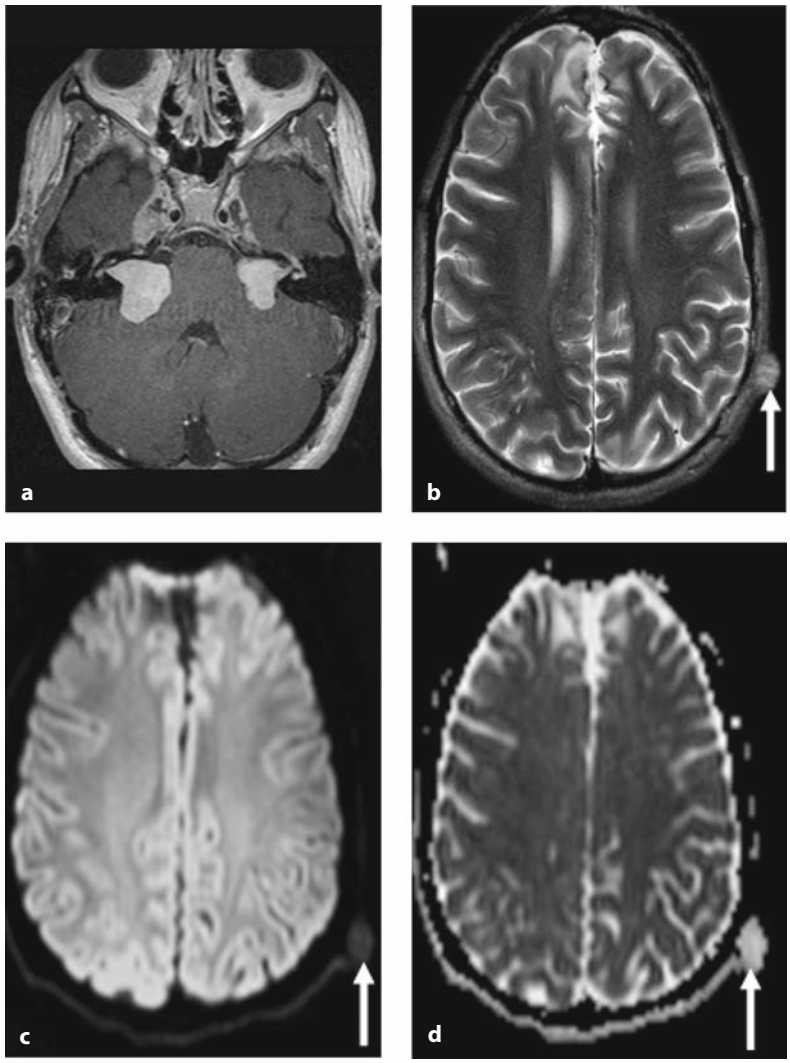

Figure 15.19 a–d

Neurofibromatosis type 2 and schwannoma in a 32-year-old woman. **a** Postcontrast T1-weighted image shows homogeneously enhancing vestibular schwannomas bilaterally. **b** T2-weighted image shows a round hyperintense lesion in the left parietal scalp (*arrow*). **c, d** DW imaging shows a subtle hyperintense lesion associated with increased ADC (1.82–2.02×$10^{-3}$$mm^2$/s) which may represent a mucoid degeneration of a schwannoma

age). DW imaging clearly shows the extent of the abscess (Fig. 15.20).

Malignant external otitis or necrotizing external otitis is an infection of the bony/cartilaginous external auditory canal with bone erosion and associated cellulitis/abscess formation. The adjacent soft tissue is also involved. On T2-weighted images, diffuse increased signal is seen with cellulitis and focal increased signal with abscess. Postcontrast T1-weighted images demonstrate diffuse enhancement with cellulitis and typical rim enhancement with abscess [44]. DW imaging shows the abscess or pus collection as hyperintense (Fig. 15.21).

Pott's puffy tumor is a subperiosteal abscess with progressive frontal bone osteomyelitis. It is a potentially life-threatening complication of frontal sinusitis [45–51]. It was originally described by Sir Percival Pott around 1760. Rare etiologies include trauma, dental sepsis, fibrous dysplasia, and malignancy. The subperiosteal abscess erodes the outer table of the frontal bone with associated soft tissue swelling, i.e., the puffy tumor. DW imaging shows the abscess as hyperintense with decreased ADC (Fig. 15.22). Surgical intervention (abscess drainage and debridement of the osteomyelitic bone) and antibiotic therapy prevent further suppurative complications.

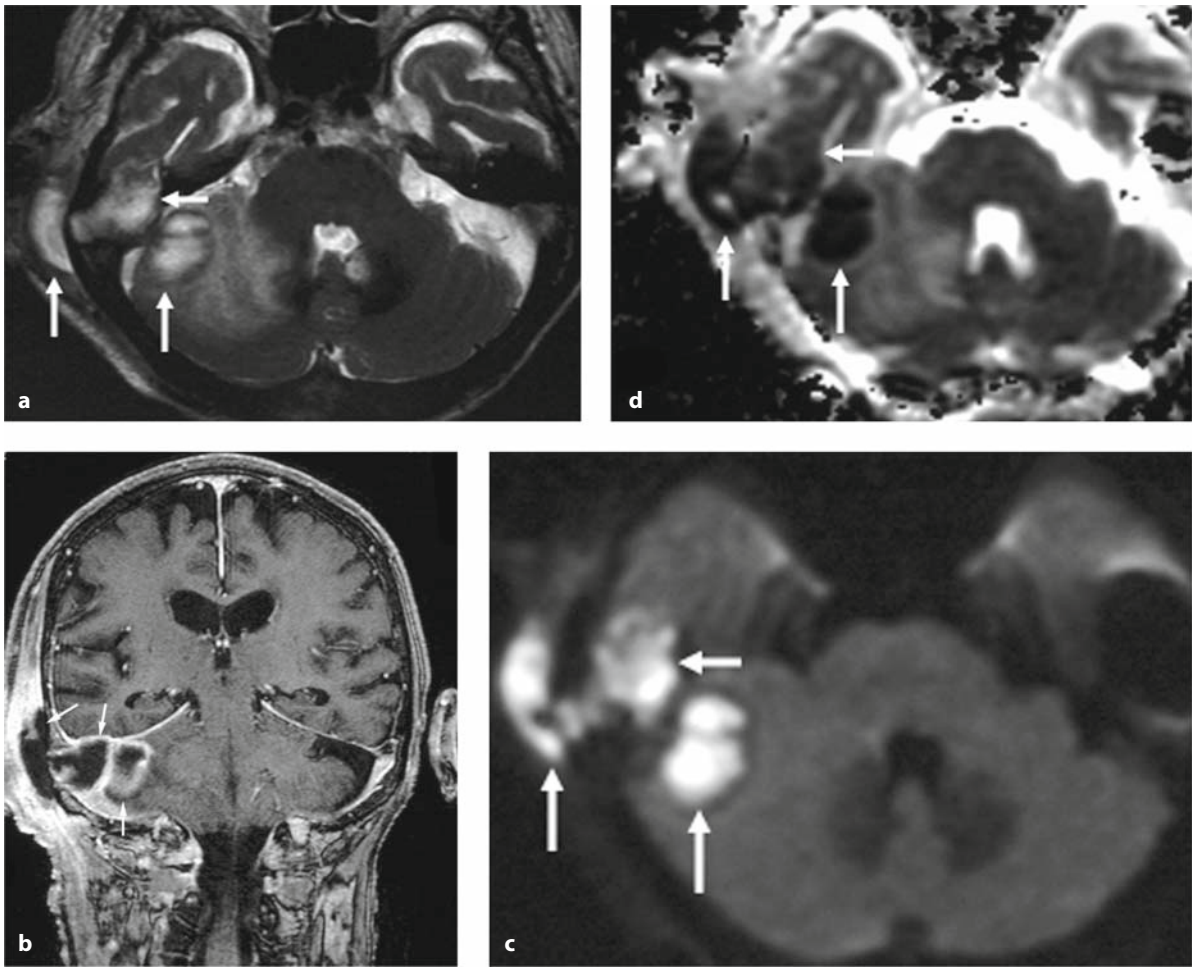

Figure 15.20 a–d

Coalescent mastoiditis with perimastoid abscess and brain abscess in a 50-year-old man. **a** T2-weighted image shows right mastoid, perimastoid, and brain abscesses as hyperintense lesions (*arrows*). **b** Postcontrast sagittal T1-weighted image shows these abscesses as hypointense with rim enhancement (*arrows*). There is a communication between the mastoid abscess and perimastoid abscess with an erosion of lateral wall of the mastoid and soft tissue swelling. **c, d** DW image shows the abscesses as very hyperintense with decreased ADC ($0.35\text{-}0.46\times10^{-3}mm^2/s$) (*arrows*)

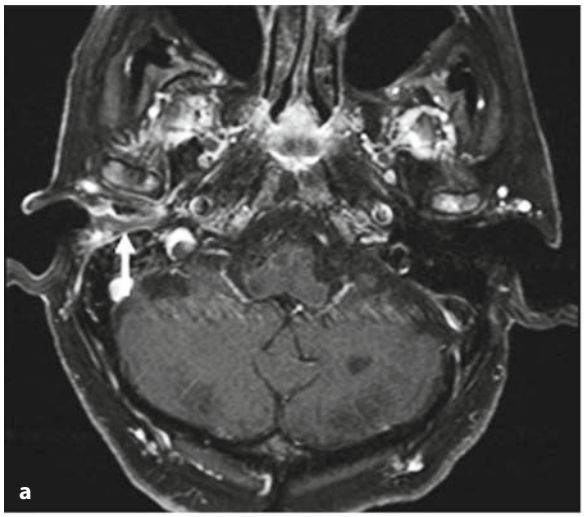

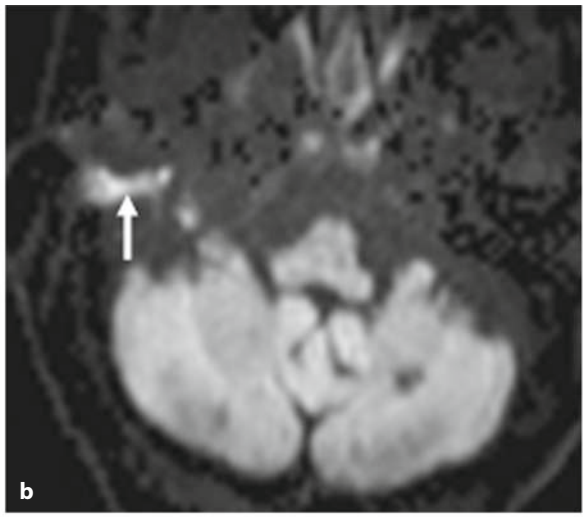

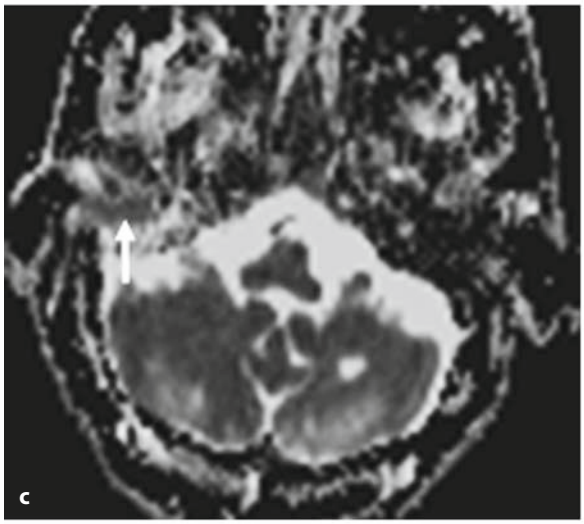

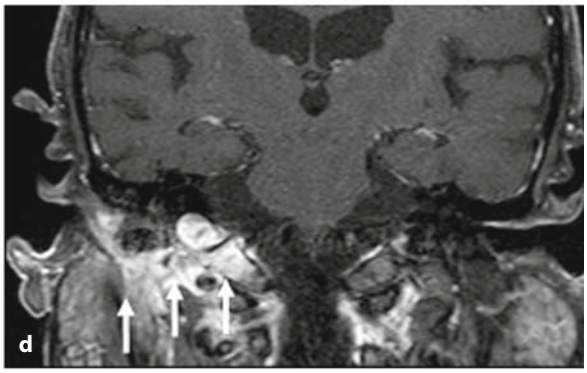

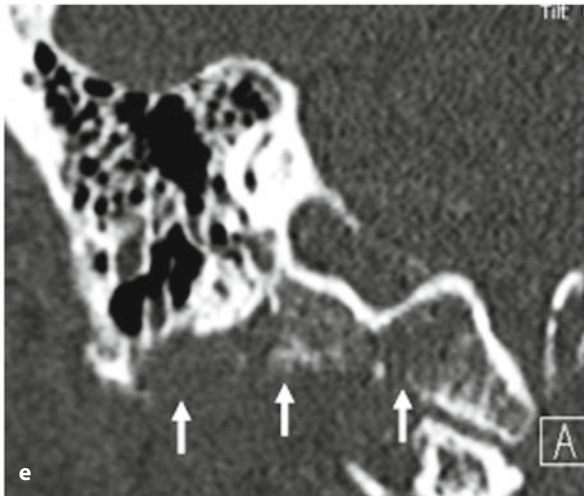

Figure 15.21 a–e

Malignant otitis externa in a 65-year-old man with type 2 diabetes mellitus. **a** Postcontrast axial T1-weighted image with fat saturation shows a rim enhancing fluid collection in the right external auditory canal (*arrow*). **b, c** DW image shows hyperintensity in the right external auditory canal with mildly decreased ADC representing pus collections (*arrow*). **d** Postcontrast coronal T1-weighted image with fat saturation shows extensive enhancement in the soft tissue and bone marrow consistent with cellulitis and osteomyelitis (*arrows*) **e** Coronal CT shows osseous destructions of the inferior aspect of the right petrous bone and clivus (*arrows*)

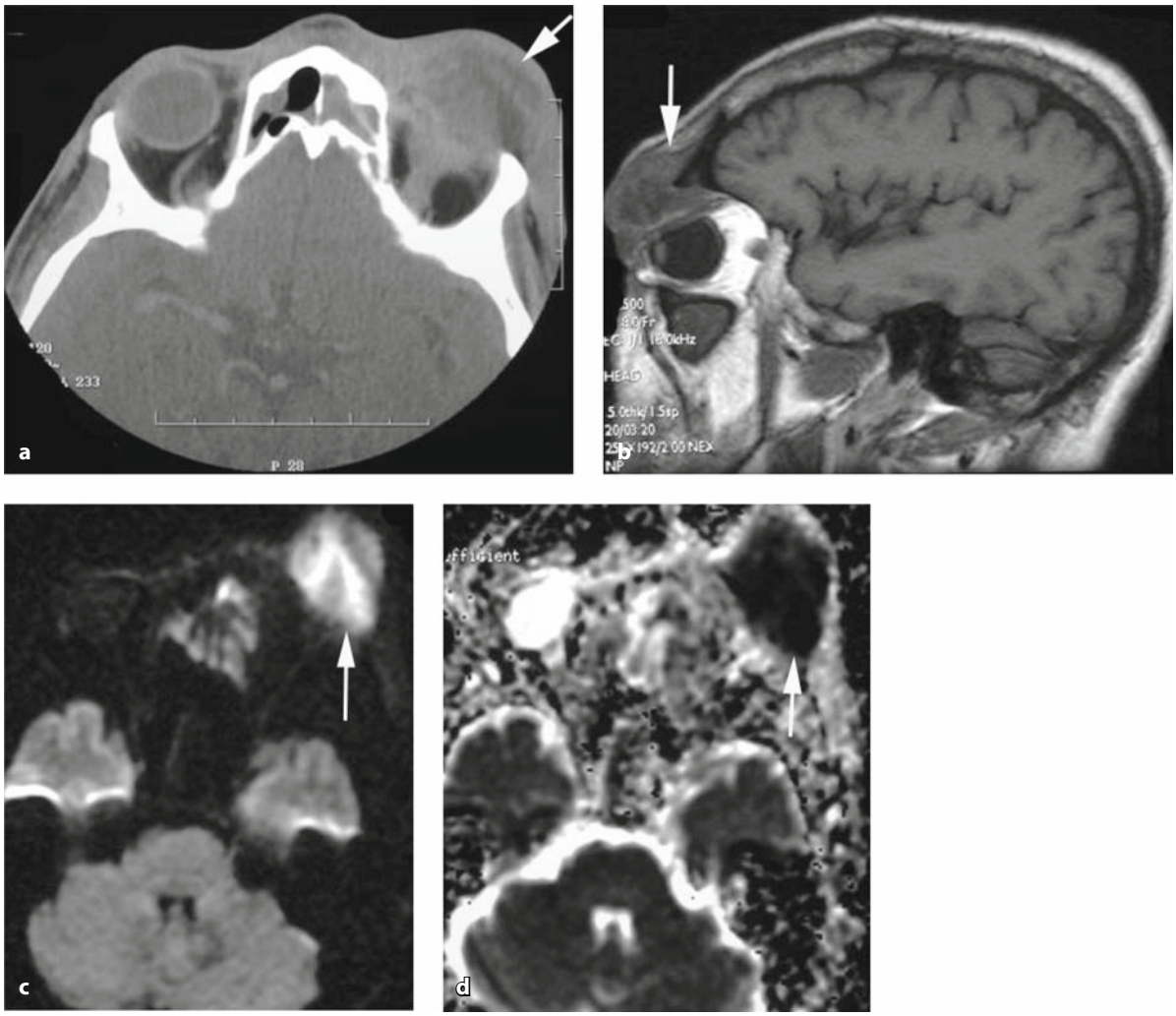

Figure 15.22 a–d

Pott's puffy tumor (subperiosteal abscess) in a 71-year-old man. **a** CT shows a left periorbital mass and soft tissue swelling (*arrow*). **b** Precontrast sagittal T1-weighted image demonstrates a heterogeneously hypointense mass located in the subperiosteal space (*arrow*). **c, d** DW image shows the subperiosteal abscess as very hyperintense associated with very decreased ADC (0.26–0.48×$10^{-3}$$mm^2$/s), which is a characteristic of pus collections and abscess formations (*arrow*)

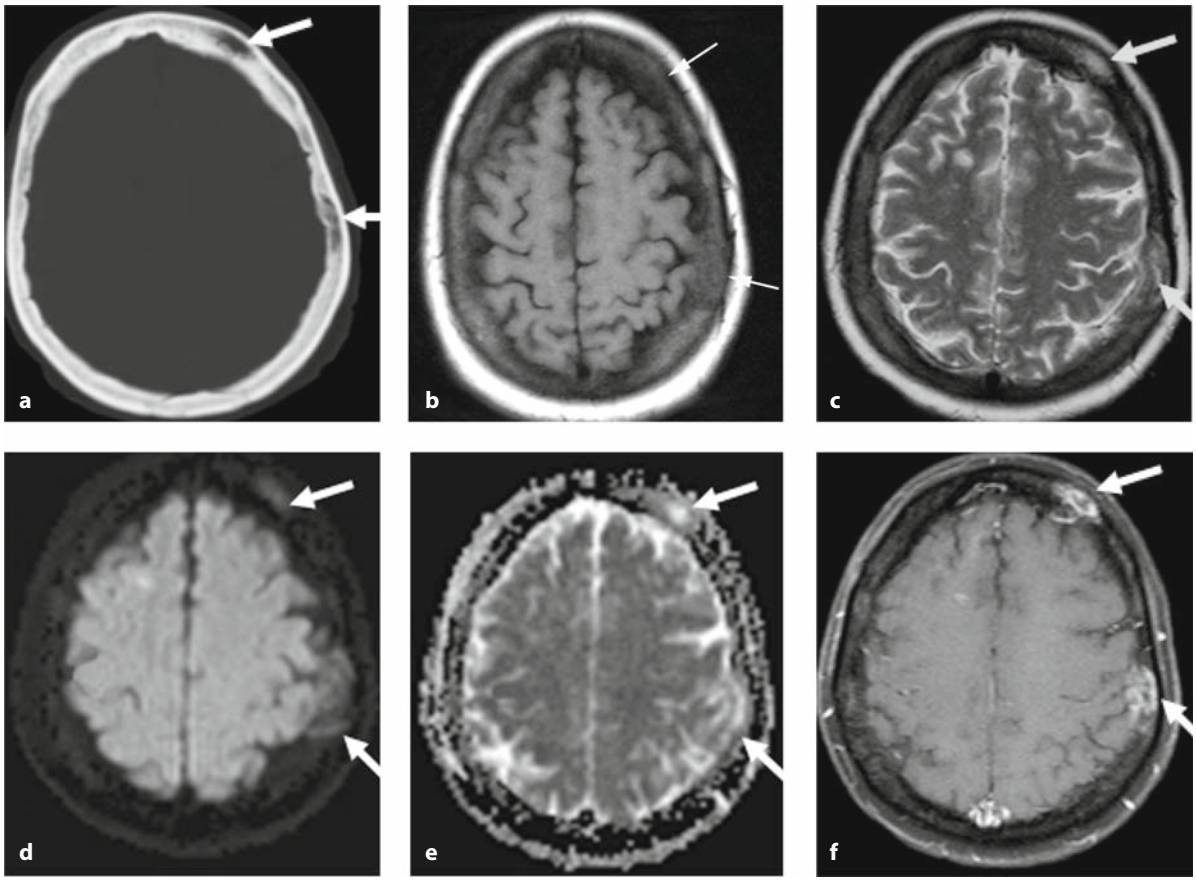

Figure 15.23 a–f

Bone metastasis from breast carcinoma in a 38-year-old woman. **a** CT shows permeative lytic lesions in the left calvarium (*arrows*). **b** Precontrast sagittal T1-weighted image shows the lesions as isointense (*arrows*). **c** T2-weighted image shows the lesions as slightly hyperintense (*arrows*). **d, e** DW image clearly shows the lesions as hyperintense and associated with increased ADC in the skull (intermediate cellularity and necrosis) (*arrows*). **f** Postcontrast with fat saturation T1-weighted image demonstrates necrotic enhancing bone metastases (*arrows*)

15.4 Malignant Tumor

15.4.1 Metastases and Leukemic Infiltration

Potentially, DW imaging may provide information to allow better discrimination of soft tissue or osseous metastatic lesions. DW imaging characteristics of benign and malignant lesions can overlap.

Moon et al., using DW imaging with sensitivity encoding (SENSE), a parallel imaging technique that reduces susceptibility artifacts in the skull base, studied 13 patients with 20 cranial bone marrow metastases, and found that DW images of metastases demonstrated better lesion conspicuousness than T1-weighted images and b0 images on a qualitative basis [52]. On a quantitative basis, lesion contrast was best shown on b0 images. All metastatic lesions in the study demonstrated increased signal on DW images and b0 images compared to normal bone marrow.

In a study by Nemeth et al., the authors found DW imaging improved the detection of skull metastatic disease over conventional MR imaging [53]. Detection of focal breast cancer and lung cancer metastatic dis-

ease was improved by 20% and 36.3%, respectively. However, the fat saturation technique was not used for conventional T2- and postcontrast T1-weighted images. Postcontrast T1-weighted images with fat saturation and DW imaging probably demonstrate better lesion conspicuousness than other conventional MR sequences (Figs. 15.23–15.29). DW imaging also shows diffuse scalp, bone, and extraaxial metastasis as hyperintense (Figs. 15.27, 15.28). When the primary lesion is prostate cancer or when the skull metastatic disease is diffuse, DW imaging may offer no advantages over conventional MR imaging [53].

The signal intensity on DW images and the ADC values in the bone metastasis mainly depend on the tumor cellularity, extracellular matrix, and necrosis. Metastasis from hypercellular tumors such as Ewing sarcoma, neuroblastoma, and small cell carcinoma can show significant hyperintensity on DW images associated with decreased ADC (Figs. 15.26–15.28). Intermediate cellular metastasis shows hyperintensity on DW imaging with mildly increased ADC (T2 shine-through) (Figs. 15.23, 15.24, 15.29). The area of necrosis usually shows hypointensity on DW imaging with increased ADC (Figs. 15.23, 15.28). The area of

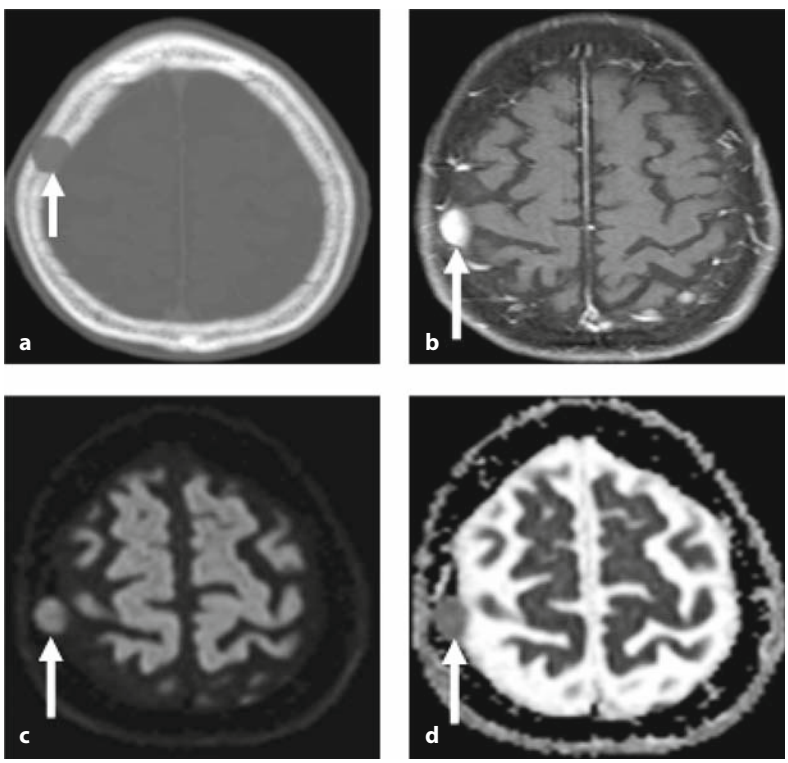

Figure 15.24 a–d

Bone metastasis from renal cell carcinoma in a 64 year-old man. **a** CT shows a lytic bone metastasis from renal cell carcinoma in the skull (*arrow*). **b** Postcontrast T1-weighted image with fat saturation demonstrates a well-defined intensely enhancing lesion (*arrow*). **c, d** DW imaging shows the lesion as hyperintense associated with slightly increased ADC values (*arrow*)

sclerotic bone metastasis may be difficult to detect on DW imaging because of the lack of mobile protons and diamagnetic susceptibility artifact from sclerotic osseous tissue mixed with the tumor cells (Figs. 15.25, 15.28). Some authors have advised caution when interpreting ADC values in the bone marrow because of the high lipid marrow component and its possible effect on DW signals and ADC values [54, 55].

DW imaging can be useful for evaluating the therapeutic response of leukemic infiltration (Fig. 15.29) [56, 57]. Moon et al displayed the DW images in an inverted gray–white scale in the evaluation of bone metastasis or bone marrow infiltration, similar to that used in bone scans, for their qualitative analysis [52]. They felt this allowed easier comparison with bone scans and PET images.

Figure 15.25 a–d

Bone metastasis from breast carcinoma in a 45-year-old woman. **a** CT shows a large soft tissue density mass involving the right frontal skull and scalp with underlying sclerotic bony changes (*arrow*). **b** Postcontrast T1-weighted image with fat saturation shows a heterogeneously enhancing necrotic mass and dural enhancement (*arrows*). **c** DW imaging shows a large mass with central low and peripheral iso- or high signal intensity associated with central high and peripheral low ADC values (*arrow*). **d** The area of sclerotic bone metastasis may be difficult to detect on DW imaging because of the lack of mobile protons in the sclerotic bone changes surrounding tumor cells

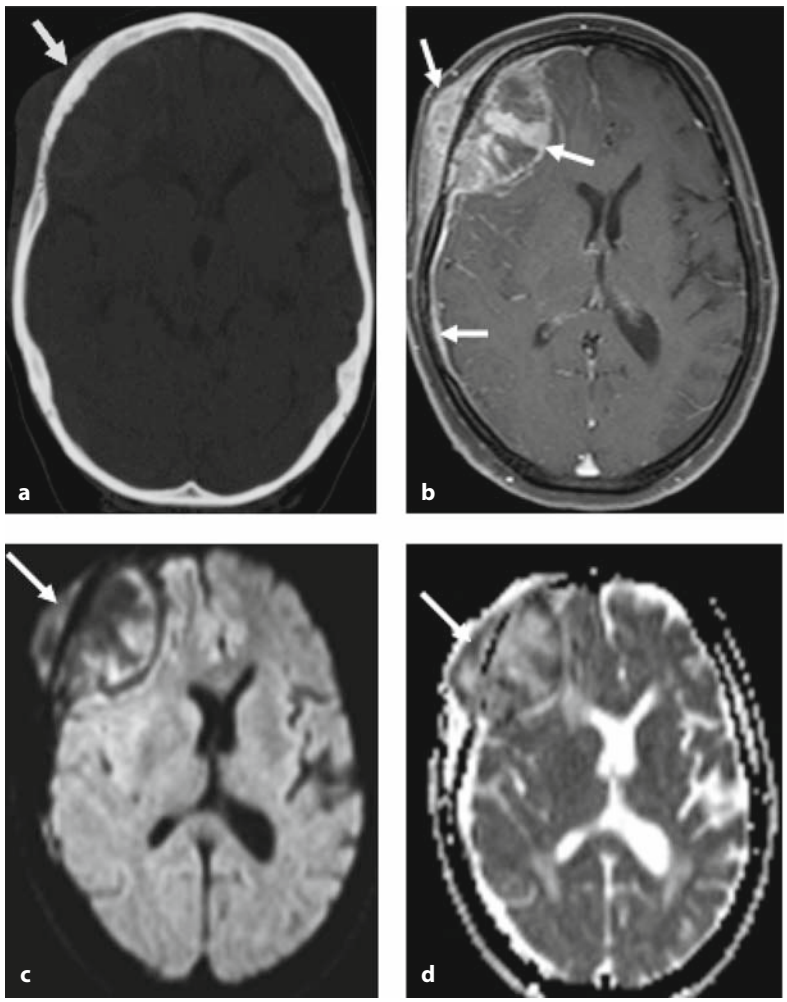

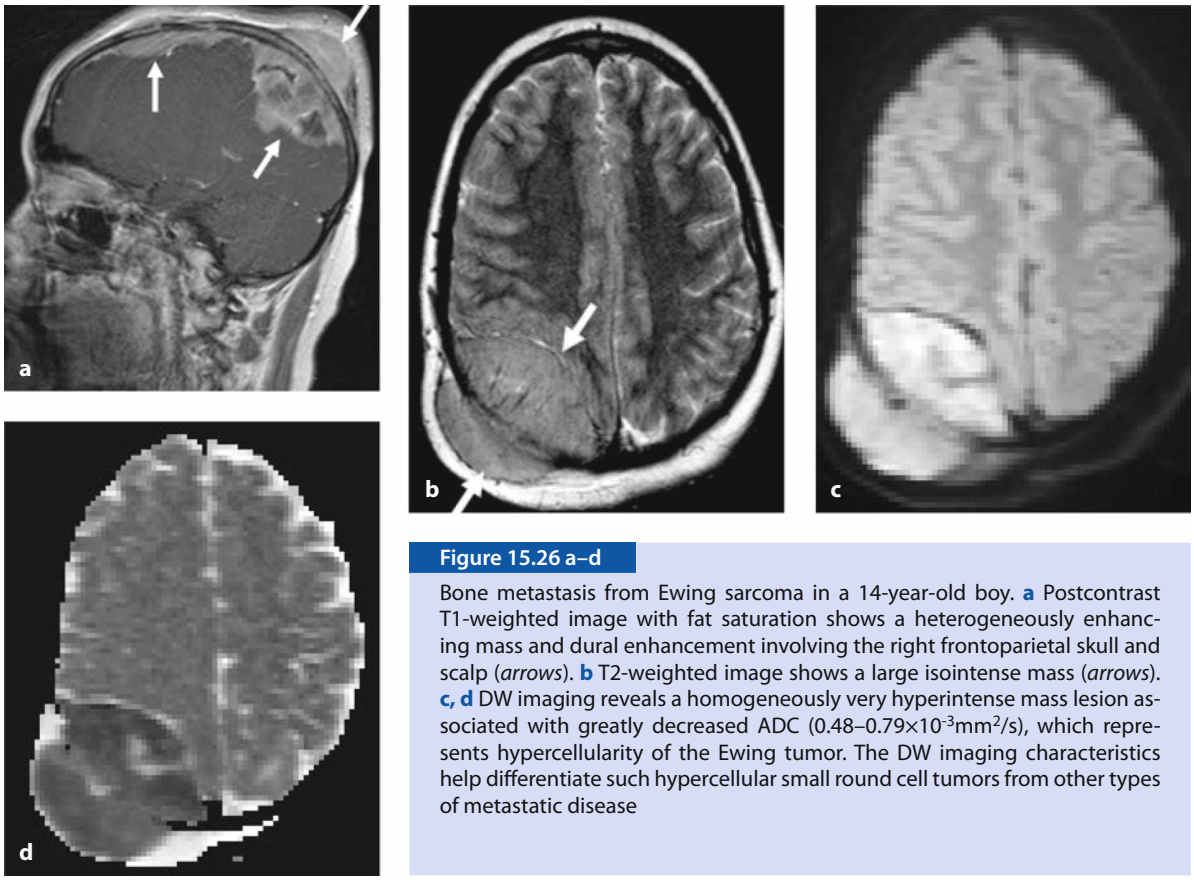

Figure 15.26 a–d

Bone metastasis from Ewing sarcoma in a 14-year-old boy. **a** Postcontrast T1-weighted image with fat saturation shows a heterogeneously enhancing mass and dural enhancement involving the right frontoparietal skull and scalp (*arrows*). **b** T2-weighted image shows a large isointense mass (*arrows*). **c, d** DW imaging reveals a homogeneously very hyperintense mass lesion associated with greatly decreased ADC ($0.48–0.79\times10^{-3}mm^2/s$), which represents hypercellularity of the Ewing tumor. The DW imaging characteristics help differentiate such hypercellular small round cell tumors from other types of metastatic disease

Figure 15.27 a–d

Bone metastasis from neuroblastoma in a 15-year-old boy. **a** T2-weighted image shows multiple hyperintense mass lesions along the right fronto-parieto-occipital skull and dura (*arrows*). **b** Postcontrast T1-weighted image with fat saturation shows heterogeneously enhancement and dural enhancement (right more than left) (*arrows*). **c, d** DW imaging reveals irregular dural-based hyperintense mass in the right frontoparietal region with decreased ADC ($0.52–0.89\times10^{-3}mm^2/s$) corresponding to the hypercellularity of neuroblastoma (*arrows*)

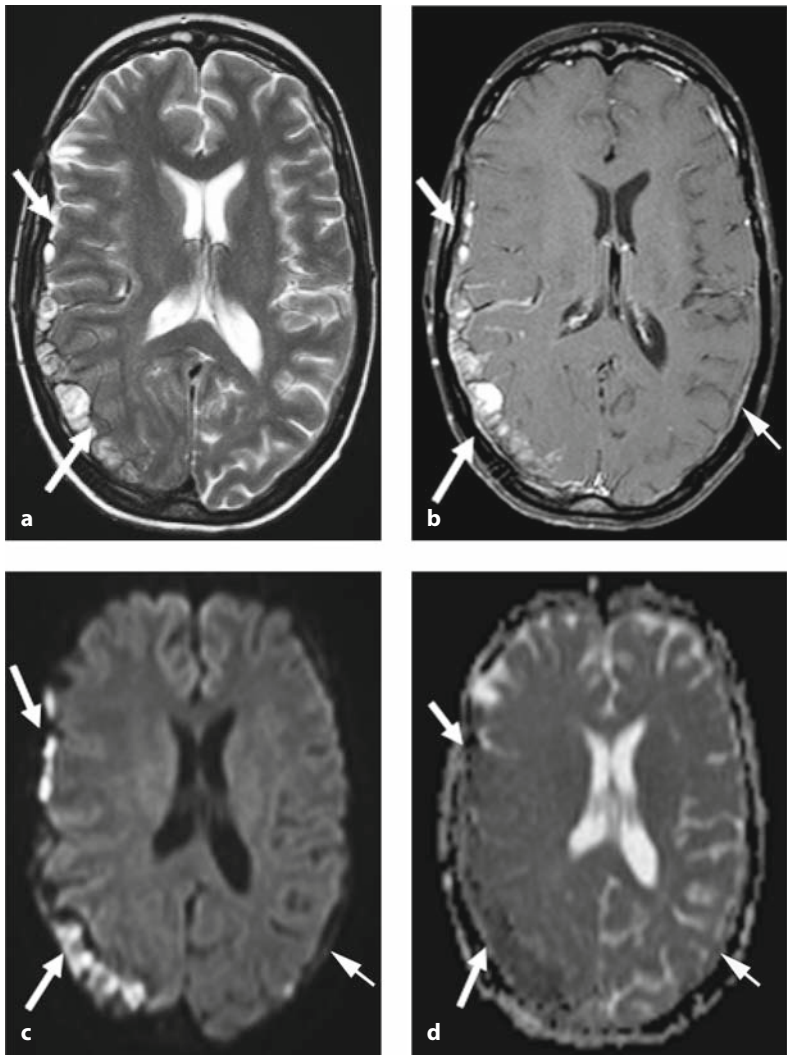

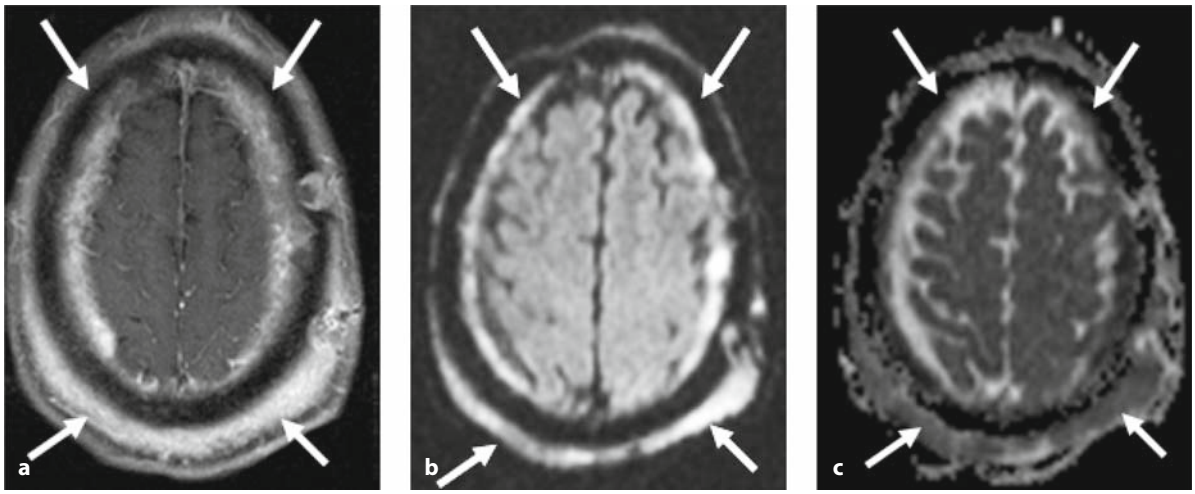

Figure 15.28 a–c

Diffuse bone, dural, and scalp metastasis from prostate carcinoma in an 89-year-old man. **a** Postcontrast T1-weighted image with fat saturation shows diffuse marked enhancement in the dura and scalp (*arrows*). Diffuse sclerotic bony changes are noted in the skull. **b, c** DW imaging shows diffuse hyperintense lesions in the dura and scalp associated with decreased ADC (*arrows*). Diffuse sclerotic bone metastases are seen as low signal intensity on DW images. It is difficult to calculate the ADC value of the bone marrow infiltration accurately

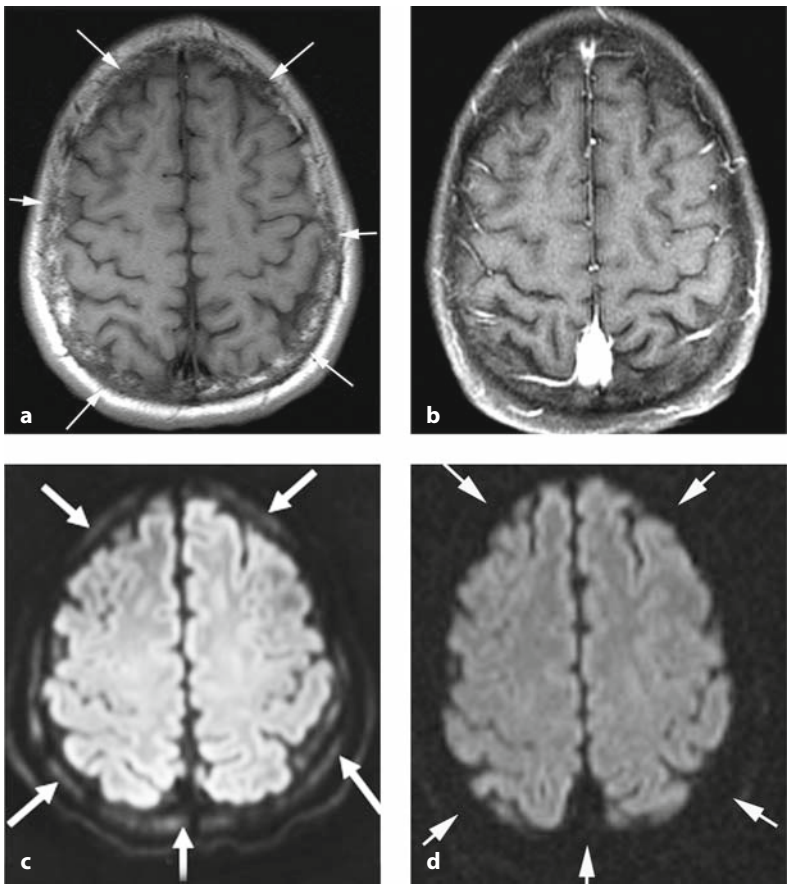

Figure 15.29 a–d

Leukemia in a 23-year-old woman. **a, b** Pre- and postcontrast T1-weighted images show diffuse heterogeneous signals in the bone marrow of the skull (*arrows*). **c** DW image shows diffuse hyperintense lesions in the skull which probably represents leukemic infiltrations (*arrow*). **d** After the course of chemotherapy, the DW imaging abnormalities have disappeared (*arrow*)

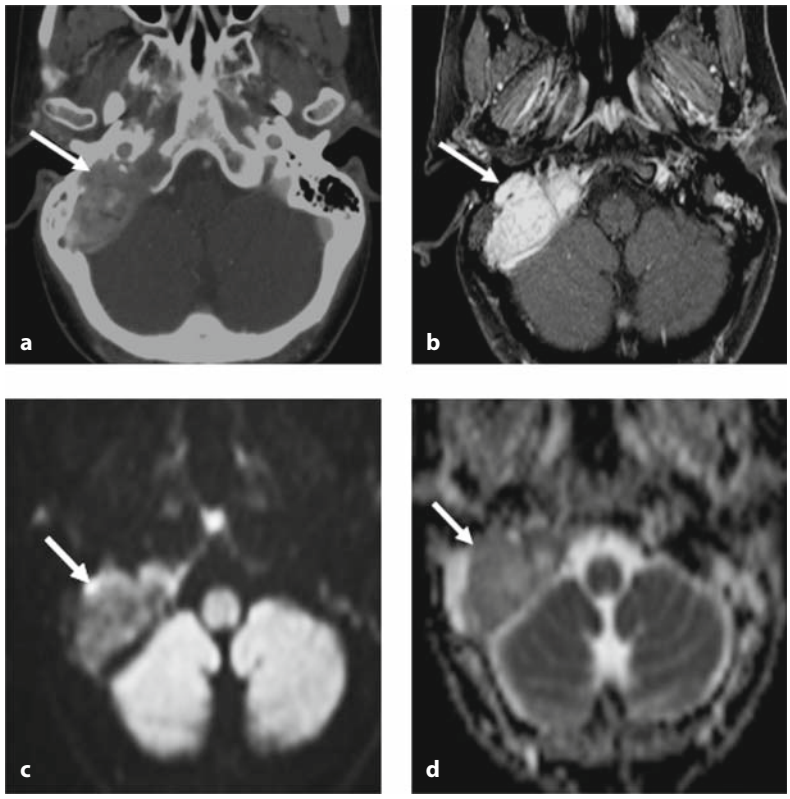

Figure 15.30 a–d

Mastoid bone metastasis from breast carcinoma in a 58-year-old woman. **a** CT shows a lytic bone destruction in the right petrous bone (*arrows*). **b** Postcontrast T1-weighted image with fat saturation shows intense homogeneous enhancement in the mass (*arrows*). **c, d** DW imaging shows a hyperintense mass with mildly increased ADC (0.96–1.66×10^{-3}mm^2/s) in the right mastoid (*arrows*), which probably corresponds to the intermediate cellularity of the tumor

15.4.2 Squamous Cell Carcinoma and Lymphoma in Head and Neck Area

In a study using echo-planar DW imaging by Wang et al., the mean ADC of malignant lymphomas was lower than that of carcinomas [58] (lymphoma 0.66±0.17×10^{-3} mm^2/s versus carcinomas 1.13±0.43×10^{-3} mm^2/s) (Figs. 15.30–15.32). They also found the ADC of lymphoma and carcinoma to be significantly lower than that of benign solid tumors or benign cystic lesions [58] (benign solid tumors 1.56±0.51×10^{-3} mm^2/s; mean ADC of benign cystic lesions 2.05±0.62×10^{-3} mm^2/s).

In order to reduce susceptibility artifacts commonly seen with echo-planar DW imaging in the evaluation of head and neck lesions, Maeda et al. used line-scan DW imaging to study squamous cell carcinomas and malignant lymphomas [59]. They found ADC values to be significantly lower in lymphomas than in squamous cell carcinomas (lymphoma 0.65±0.09×10^{-3} mm^2/s versus squamous cell carcinoma 0.96±0.11×10^{-3} mm^2/s).

King et al. also found a threshold value that helped differentiate squamous cell carcinoma from lymphoma [60]. They found that an ADC value greater than 0.824×10^{-3} mm^2/s could identify squamous cell carcinoma, and an ADC value less than 0.767×10^{-3} mm^2/s could identify lymphoma with a specificity of 100%. Sensitivity for squamous cell carcinoma was 94% and for lymphoma 88%. However, when evaluated in conjunction with nasopharyngeal carcinoma, the determination of a threshold value with high sensitivity and specificity was problematic because of overlapping ADC values. Using 3-T DW imaging, Srinivasan et al. found malignant head and neck lesions to have significantly lower ADC values than benign lesions [61]. White et al., despite moderately overlapping values, also found the mean ADC values for malignant lesions to be significantly lower than for benign lesions [32].

Sumi et al. found that metastatic lymph nodes with moderately differentiated carcinomas had significantly higher ADC values than those of poorly differentiated carcinoma and approximated those of malignant lymphoma [62]. Abdel Razek et al. found the mean ADC of metastatic and lymphomatous nodes to be significantly lower than benign nodes [36]. Additionally, they found two patients with benign nodes (sarcoid and cat scratch disease) with relatively low ADC values.

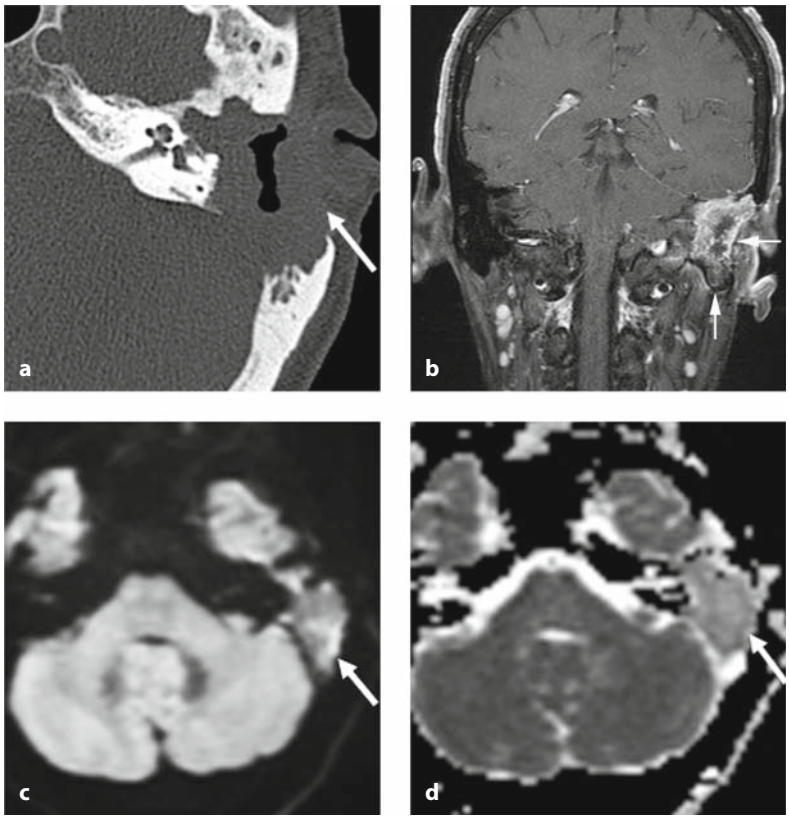

Figure 15.31 a–d

Primary squamous cell carcinoma in the middle ear in a 64-year-old man. **a** CT shows a soft tissue density mass with bone destruction in the left mastoid and middle ear cavity (*arrow*). **b** Postcontrast T1-weighted image with fat saturation shows heterogeneously enhancing necrotic mass (*arrow*). **c, d** DW imaging shows hyperintensity in the left mastoid and middle ear cavity with mildly increased ADC ($1.03–1.46\times10^{-3}$mm^2/s) (*arrow*), which probably corresponds to the intermediate cellularity and necrosis in squamous cell carcinoma

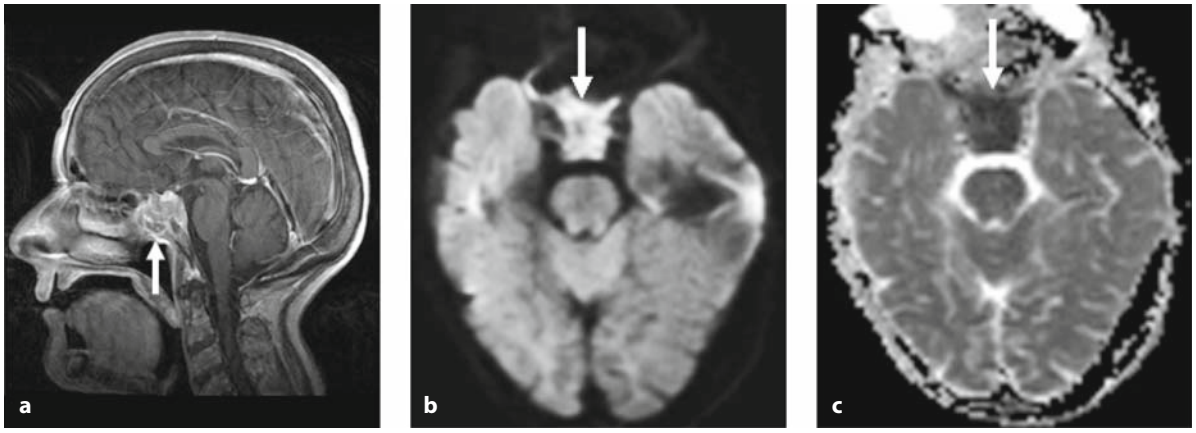

Figure 15.32 a–c

Malignant lymphoma in a 74-year-old woman. **a** Postcontrast sagittal T1-weighted image shows an inhomogeneously enhancing mass in the skull base (*arrow*). **b, c** DW imaging reveals a homogeneously very hyperintense mass in the skull base with decreased ADC ($0.46–0.62\times10^{-3}$mm^2/s) (*arrow*), which corresponds to hypercellularity of the lymphoma

15.5 Conclusion

DW imaging demonstrates benign and malignant scalp and skull lesions well, even if the lesion is very small or diffuse, because of the significant contrast in the surrounding scalp and skull structures with fat saturation techniques. DW imaging with ADC maps demonstrates characteristics unique to certain etiologies, particularly abscesses, hypercellular tumors, and epidermoids.

References

1. Som PM, Curtin HD (2003) Head and Neck Imaging, 4th edn. Mosby, St. Louis, MO, pp 1184–1191
2. Swartz JD, Harnsberger HR (1998) Imaging of the Temporal Bone, 3rd edn. Thieme, New York, pp 85–107
3. Harnsberger HR et al (2004) Diagnostic Imaging Head and Neck. Amirsys, Salt Lake City, UT:
4. Chakeres DW, Spiegel PK(1984) A systematic technique for comprehensive evaluation of the temporal bone by computed tomography. Radiology 146:97–106
5. Ritter FN (1977) Complications of cholesteatoma. In McCabe BF, Sade J, Abramson M (eds) Cholesteatoma. First International Conference. Aesculapius, Birmingham, AL, pp 430–437
6. Schuknecht HF, Gulya AJ (1986) Anatomy of the Temporal Bone with Surgical Implications. Lea & Febiger, Philadelphia
7. Storrs LA (1983) Complications after surgery for otosclerosis. Laryngoscope 93:265–267
8. Schuknecht HF (1993) Pathology of the Ear, 2nd edn. Lea & Febiger, Philadelphia
9. Moran WB Jr. (1980) Cholesteatoma. In: English GM (ed). Otolaryngology. Harper & Row, New York, NY
10. Swartz JD, Harnsberger HR, Mukherji SK (1998) The temporal bone. Contemporary diagnostic dilemmas. Radiol Clin North Am 36:819–853
11. Swartz JD (1984) Cholesteatomas of the middle ear: diagnosis, etiology and complications. Radiol Clin North Am 22:15–35
12. Harnsberger HR (1995) Handbook of Head and Neck Imaging, 2nd edn. Mosby, St. Louis, MO, pp 444–446
13. Gunlock MG, Gentry LR (1998) Anatomy of the temporal bone. Neuroimaging Clin N Am 8:195–209
14. Vercruysse JP, De Foer B, Pouillon M, Somers T, Casselman J, Offeciers E (2006) The value of diffusion-weighted MR imaging in the diagnosis of primary acquired and residual cholesteatoma: a surgical verified study of 100 patients. Eur Radiol 16:1461–1467
15. Jackler RK, Parker DA (1992) Radiographic differential diagnosis of petrous apex lesions. Am J Otol 13:561–574
16. Fitzek C, Mewes T, Fitzek S, Mentzel HJ, Hunsche S, Stoeter P (2002) Diffusion-weighted MRI of cholesteatomas of the petrous bone. J Magn Reson Imaging 15:636–641
17. Williams MT, Ayache D, Alberti C, Héran F, Lafitte F, Elmaleh-Bergès M, Piekarski JD (2003) Detection of postoperative residual cholesteatoma with delayed contrast-enhanced MR imaging: initial findings. Eur Radiol 13:169–174
18. Baylor College of Medicine. Department of Otolaryngology-Head and Neck Surgery Website. Chronic Otitis Media and Cholesteatoma. http://www.bcm.edu/oto/jsolab/tm_me_mastoid/chron_om_cholesteatoma.htm
19. Shelton C, Sheehy JL (1990) Tympanoplasty: review of 400 staged cases. Laryngoscope 100:679–681
20. Yoshida T, Ito K, Adachi N, Yamasoba T, Kondo K, Kaga K (2005) Cholesteatoma of the petrous bone: the crucial role of diffusion-weighted MRI. Eur Arch Otorhinolaryngol 262:440–441
21. De Foer B, Vercruysse JP, Pilet B, Michiels J, Vertriest R, Pouillon M, Somers T, Casselman JW, Offeciers E (2006) Single-shot, turbo spin-echo, diffusion-weighted Imaging versus spin-echo-planar, diffusion-weighted imaging in the detection of acquired middle ear cholesteatoma. AJNR Am J Neuroradiol 27:1480–1482
22. Aikele P, Kittner T, Offergeld C, Kaftan H, Hüttenbrink KB, Laniado M (2003) Diffusion-weighted MR imaging of cholesteatoma in pediatric and adult patients who have undergone middle ear surgery. AJR Am J Roentgenol 181:261–265
23. Dubrulle F, Souillard R, Chechin D, Vaneecloo FM, Desaulty A, Vincent C (2006) Diffusion-weighted MR imaging sequence in the detection of postoperative recurrent cholesteatoma. Radiology 238:604–610
24. Maheshwari S, Mukherji SK (2002) Diffusion-weighted imaging for differentiating recurrent cholesteatoma from granulation tissue after mastoidectomy: case report. AJNR Am J Neuroradiol 23:847–849
25. Stasolla A, Magliulo G, Parrotto D, Luppi G, Marini M (2004) Detection of postoperative relapsing/residual cholesteatomas with diffusion-weighted echo-planar magnetic resonance imaging. Otol Neuroltol 25:879–884
26. Zuber TJ (2002) Minimal excision technique for epidermoid (sebaceous) cysts. Am Fam Physician 65:1409-1412, 1417–1418, 1420
27. Warakaulle DR, Anslow P (2003) Differential diagnosis of intracranial lesions with high signal on T1 or Low signal on T2-weighted MRI. Clin Radiol 58:922–933
28. Hong SH, Chung HW, Choi JY, Koh YH, Choi JA, Kang HS (2006) MRI findings of subcutaneous epidermal cysts: emphasis on the presence of rupture. AJR Am J Roentgenol 186:961–966
29. Shibata T, Hatori M, Satoh T, Ehara S, Kokubun S (2003) Magnetic resonance imaging features of epidermoid cyst in the extremities. Arch Orthop Trauma Surg 123:239–241
30. Suzuki C, Maeda M, Matsumine A, Matsubara T, Taki W, Maier SE, Takeda K. (2007) Apparent diffusion coefficient of subcutaneous epidermal cysts in the head and neck: comparison with intracranial epidermoid cysts. Acad Radiol 14:1020–1028
31. Kosling S, Bootz F (2001) CT and MR imaging after middle ear surgery. Eur J Radiol 40:113–118

32. White ML, Zhang Y, Robinson RA (2006) Evaluating tumors and tumorlike lesions of the nasal cavity, the paranasal sinuses, and the adjacent skull base with diffusion-weighted MRI. J Comput Assist Tomogr 30:490–495
33. Hayashida Y, Hirai T, Yakushiji T, Katahira K, Shimomura O, Imuta M, Nakaura T, Utsunomiya D, Awai K, Yamashita Y (2006) Evaluation of diffusion-weighted imaging for the differential diagnosis of poorly contrast-enhanced and T2-prolonged bone masses: Initial experience. J Magn Reson Imaging 23:377–382
34. Vanel D, Dromain C, Tardivon A (2000) MRI of bone marrow disorders. Eur Radiol 10:224–229
35. Katsuya T, Inoue T, Ishizaka H, Aoki J, Endo K (2000) Dynamic contrast-enhanced MR imaging of the water fraction of normal bone marrow and diffuse bone marrow disease. Radiat Med 18:291–729
36. Abdel Razek AA, Soliman NY, Elkhamary S, Alsharaway MK, Tawfik A (2006) Role of diffusion-weighted MR imaging in cervical lymphadenopathy. Eur Radiol 16:1468–1477
37. Koç O, Paksoy Y, Erayman I, Kivrak AS, Arbag H (2007) Role of diffusion weighted MR in the discrimination diagnosis of the cystic and/or necrotic head and neck lesions. Eur J Radiol 62:205–213
38. Holzapfel K, Duetsch S, Fauser C, Eiber M, Rummeny EJ, Gaa J (2008) Value of diffusion-weighted MR imaging in the differentiation between benign and malignant cervical lymph nodes. Eur J Radiol Nov 6. [Epub ahead of print]
39. Sener RN (2003) Diffusion Magnetic Resonance Imaging of Solid Vestibular Schwannomas. J Comput Assist Tomogr 27:249–252
40. Srinivasan A, Dvorak R, et al. (2008) Differentiation of Benign and Malignant Pathology in the Head and Neck Using 3T Apparent Diffusion Coefficient Values: Early Experience. AJNR Am J Neuroradiol 29:40–44
41. Maeda M, Matsumine A, Kato H, Kusuzaki K, Maier SE, Uchida A, Takeda K (2007) Soft-tissue tumors evaluated by line-scan diffusion-weighted imaging: influence of myxoid matrix on the apparent diffusion coefficient. J Magn Reson Imaging 25:1199–1204
42. Sener RN (2006) Malignant oculomotor schwannoma: diffusion MR imaging. J Neuroradiol 33:270–272
43. Castillo M, Albernaz VS, Mukherji SK, Smith MM (1998) Imaging of Bezold's abscess. AJR Am J Roentgenol 171:1491–1495
44. Karantanas AH, Karantzas G, Katsiva V, Proikas K, Sandris V (2003) CT and MRI in malignant external otitis: a report of four cases. Comput Med Imaging Graph 27:27–34
45. Clark JR, Lim JK, Poole M (1999) Pott's puffy tumour: a clinical variant. Aust N Z J Surg 69:759–762
46. McDermott C, O'Sullivan R, McMahon G (2007) An Unusual Cause of Headache: Pott's Puffy Tumour. Eur J Emerg Med 14:170–173
47. Tattersall R, Tattersall R (2002) Pott's puffy tumour. Lancet 359:1060–1063
48. Kaabia N, Abdelkafi M, Bellara I, Khalifa M, Bahri F, Letaief A (2007) Pott's puffy tumor. A Case report. Med Mal Infect 37:350–353
49. Feder HM Jr, Cates KL, Cementina AM (1987) Pott Puffy Tumor: A serious occult infection. Pediatrics 79:625–629
50. Altman KW, Austin MB, Tom LW, Knox GW (1997) Complications of frontal sinusitis in adolescents: case presentations and treatment options. Int J Pediatr Otorhinolaryngol 41:9–20
51. Babu RP, Todor R, Kasoff SS (1996) Pott's puffy tumor: the forgotten entity. J Neurosurg 84:110–112
52. Moon W-J, Lee MH, and Chung EC (2007) Diffusion-weighted imaging with sensitivity encoding (SENSE) for detecting cranial bone marrow metastases: comparison with T1-weighted images. Korean J Radiol 8:185–191
53. Nemeth AJ, Henson JW, Mullins ME, Gonzalez RG, Schaefer PW (2007) Improved detection of skull metastasis with diffusion-weighted MR imaging. AJNR Am J Neuroradiol 28:1088–1092
54. Mulkern RV, Schwartz, RB (2003) In Re: characterization of benign and metastatic vertebral compression fractures with quantitative diffusion MR imaging. AJNR Am J Neuroradiol 24:1489–1490
55. Herneth AM, Friedrich K, Weidekamm C, Schibany N, Krestan C, Czerny C, Kainberger F (2005) Diffusion weighted imaging of bone marrow pathologies. Eur J Radiol 55:74–83
56. Ballon D, Dyke J, Schwartz LH, Lis E, Schneider E, Lauto A, Jakubowski AA (2000) Bone marrow segmentation in leukemia using diffusion and T (2) weighted echo planar magnetic resonance imaging. NMR Biomed 13:321–328
57. Ballon D, Watts R, Dyke JP, Lis E, Morris MJ, Scher HI, Uluğ AM, Jakubowski AA (2004) Imaging therapeutic response in human bone marrow using rapid whole-body MRI. Magn Reson Med 52:1234–1238
58. Wang J, Takashima S, Takayama F, Kawakami S, Saito A, Matsushita T, Momose M, Ishiyama T (2001) Head and neck lesions: characterization with diffusion-weighted echo-planar MR Imaging. Radiology 220:621–630
59. Maeda M, Kato H, Sakuma H, Maier SE, Takeda K (2005) Usefulness of the apparent diffusion coefficient in line scan diffusion-weighted imaging for distinguishing between squamous cell carcinomas and malignant lymphomas of the head and neck. AJNR Am J Neuroradiol 26:1186–1192
60. King AD, Ahuja AT, Yeung DK, Fong DK, Lee YY, Lei KI, Tse GM (2007) Malignant cervical lymphadenopathy: diagnostic accuracy of diffusion-weighted MR imaging. Radiology 245:806–813
61. Srinivasan A, Dvorak R, Perni K, Rohrer S, Mukherji SK (2008) Differentiation of Benign and Malignant Pathology in the Head and Neck Using 3T Apparent Diffusion Coefficient Values: Early Experience. AJNR Am J Neuroradiol 29:40–44
62. Sumi M, Sakihama N, Sumi T, Morikawa M, Uetani M, Kabasawa H, Shigeno K, Hayashi K, Takahashi H, Nakamura T (2003) Discrimination of Metastatic Cervical Lymph Nodes with Diffusion-Weighted MR Imaging in Patients with Head and Neck Cancer. AJNR Am J Neuroradiol 24:1627–1634

How to Use This Book

In collaboration with A. Hiwatashi

Most textbooks related to imaging are organized into chapters based on the disease or the conditions that are described. This traditional way of organizing an imaging book, namely, from the disease to the images, provides a firm structure and allows the author or editor to present all the imaging characteristics of a specific disease condition with its typical, atypical, and specific features in one place. This book is no different and is also organized in this traditional way.

For the clinician using the book as an aid to solve a clinical case, this traditional approach is not practical. To match the imaging characteristics of your specific clinical case you essentially have to go through the entire book to find all the images that match the imaging features of your specific patient. To overcome this problem of a disease-oriented imaging book, we developed this chapter: here we turned the organization around, proceeding from the images to the disease/diagnosis. In this chapter we have prepared the material based on the imaging characteristics and grouped all conditions with similar imaging features together in seven tables. We used DW imaging, ADC, and T2 characteristics to create seven tables with conditions that appeared similar on MR imaging.

The clinician can go directly to this chapter, determine if the lesion in question has a high, intermediate, or low DW imaging signal intensity and then determine the same with regard to the ADC and T2 characteristics. He or she can then go to the table in Chaper 16 that lists conditions with these imaging features. Each table is essentially a list of differential diagnoses for conditions with similar imaging characteristics. When combined with the knowledge of patient symptomatology and demographic criteria, the radiologist will be able to narrow the differential diagnosis to a few conditions.

These tables take into account that the same condition may have variable imaging characteristics; for this reason, several conditions are listed in more than one table. Moreover, within the tables there are variations as to the degree of a specific imaging feature, which allows the clinician to match his/her clinical case to the best table and condition. Chapter 16 makes direct reference to other chapters of the book, where a full description is then provided.

Table 16.1

Differential diagnoses for lesions with a **high diffusion** signal associated with **low ADC** and **isointense T2** signal

Diagnoses	Reference images		
	DWI high	ADC low	T2WI iso
Infarction/hypoxia/trauma			
Nonaccidental head injury	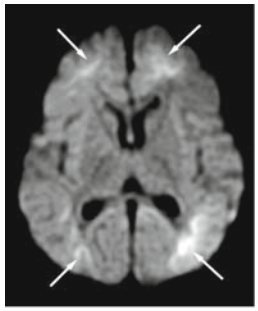 Fig. 14.12 d	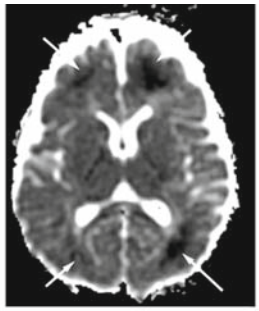 Fig. 14.12 e	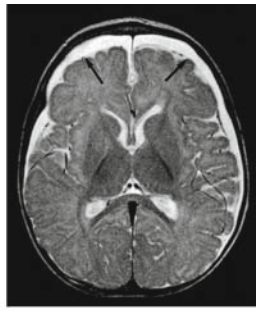 Fig. 14.12 b
Hyperacute infarction	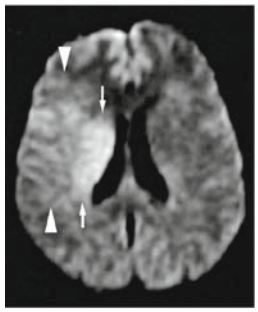 Fig. 5.1 b	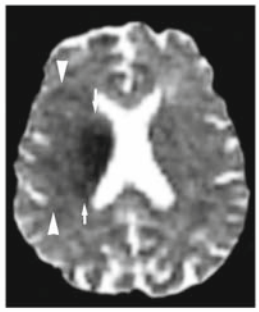 Fig. 5.1 c	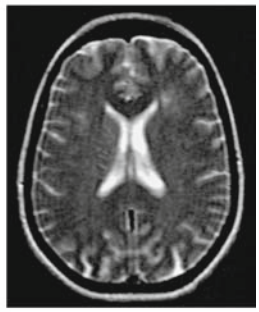 Fig. 5.1 a
Hypoxic ischemic encephalopathy	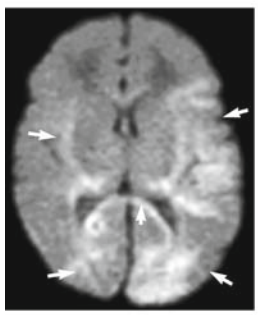 Fig. 14.9 c	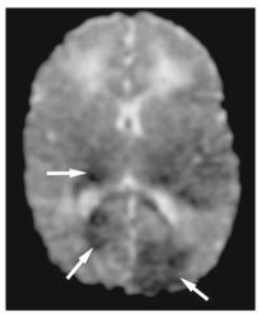 Fig. 14.9 d	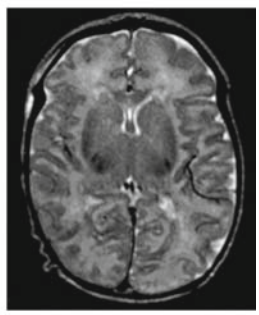 Fig. 14.9 a
Toxic/metabolic			
Methotrexate leukoencephalopathy	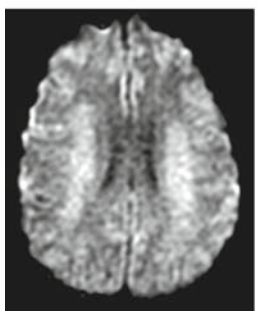 Fig. 10.2 b	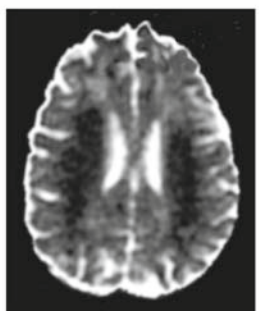 Fig. 10.2 c	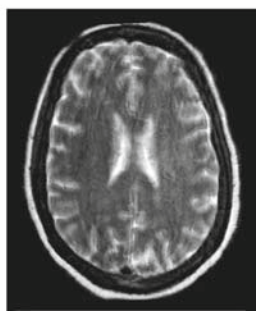 Fig. 10.2 a

Table 16.2

Differential diagnoses for lesions with a **high diffusion** signal associated with **iso-high ADC** and a **high intense T2** signal

Diagnoses	Reference images		
	DWI high	ADC iso-high	T2 high
Degeneration			
Amyotrophic lateral sclerosis (ALS)	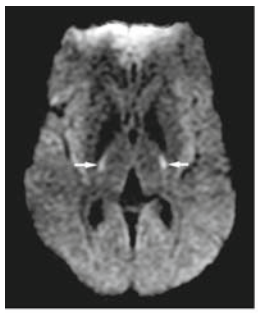 Fig. 9.20 b	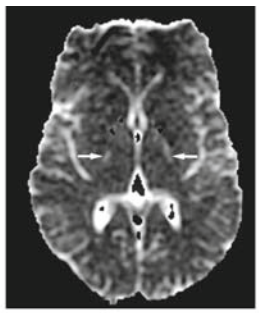 Fig. 9.20 c	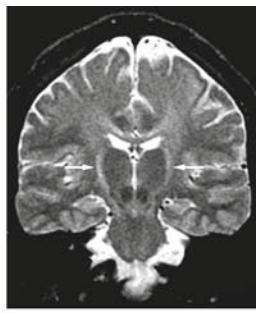 Fig. 9.20 a
Demyelination			
Acute disseminated encephalomyelitis (ADEM)	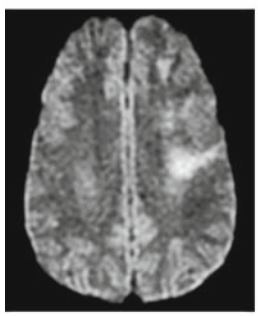 Fig. 9.8 c	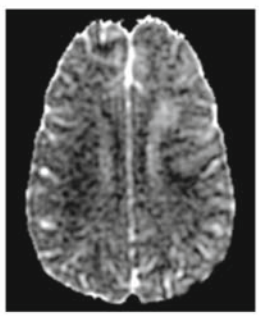 Fig. 9.8 d	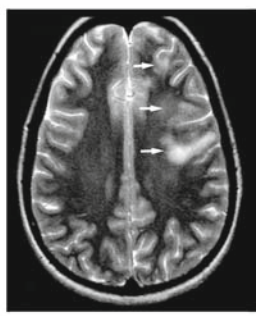 Fig. 9.8 a
Multiple sclerosis (MS)	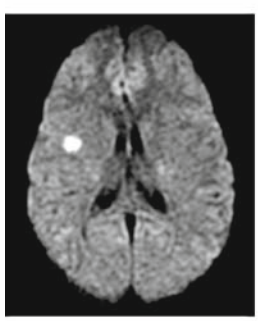 Fig. 9.2 c	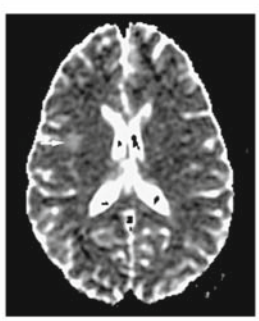 Fig. 9.2 d	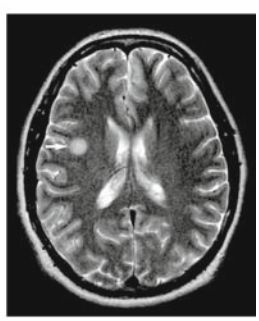 Fig. 9.2 a
Progressive multiple leukoencephalopathy (PML)	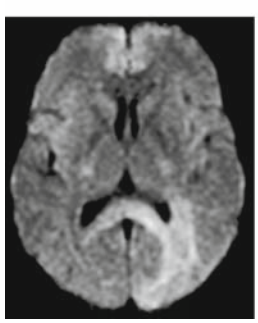 Fig. 9.11 b	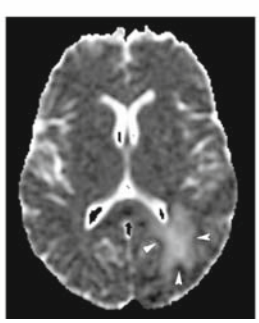 Fig. 9.11 c	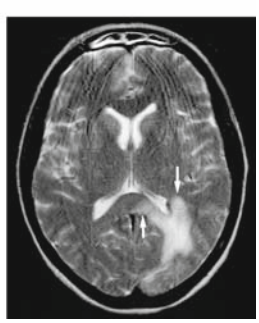 Fig. 9.11 a

Table 16.2

Differential diagnoses for lesions with a **high diffusion** signal associated with **iso-high ADC** and a **high intense T2** signal

Diagnoses	Reference images		
	DWI high	ADC iso-high	T2 high
Epilepsy			
Postictal encephalopathy	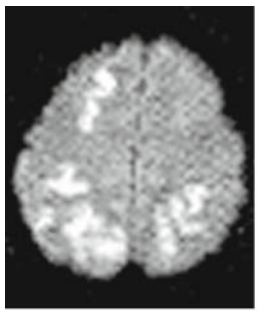 Fig. 8.5 d	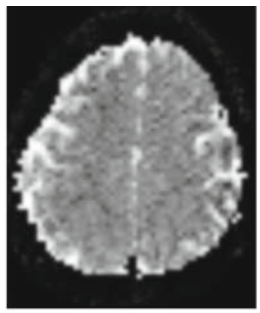 Fig. 8.5 e	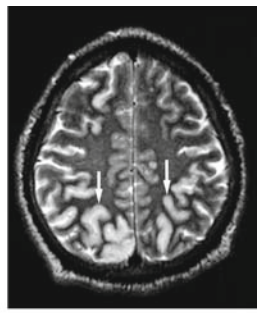 Fig. 8.5 a
Infarction			
Venous infarction	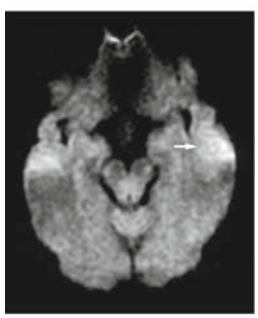 Fig. 5.7 c	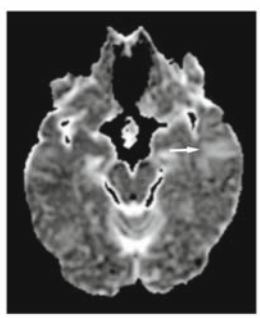 Fig. 5.7 d	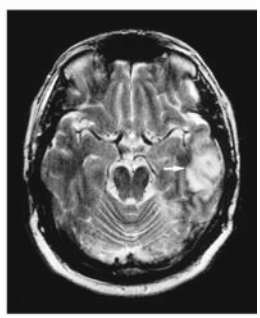 Fig. 5.7 b
Infection			
Human immunodeficiency virus (HIV) encephalopathy	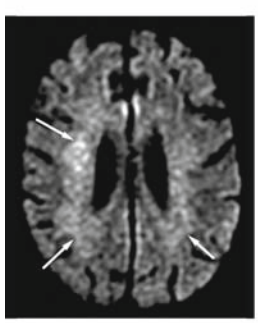 Fig. 11.33 b	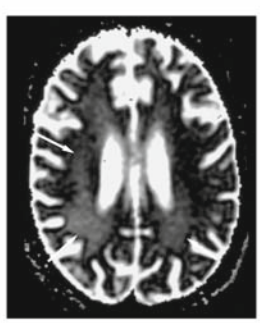 Fig. 11.33 c	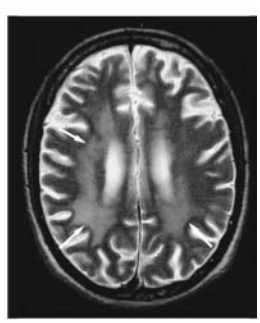 Fig. 11.33 a
Toxic/metabolic			
Marchiafava-Bignami disease	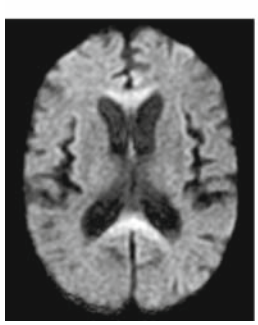 Fig. 10.18 c	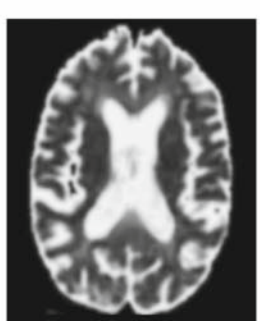 Fig. 10.18 d	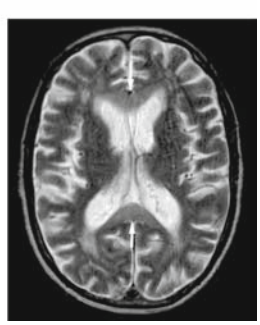 Fig. 10.18 a

Table 16.2

Differential diagnoses for lesions with a **high diffusion** signal associated with **iso-high ADC** and a **high intense T2** signal

Diagnoses	Reference images		
	DWI high	ADC iso-high	T2 high
Mitochondrial encephalopathy, lactic acidosis and stroke-like episodes (MELAS)	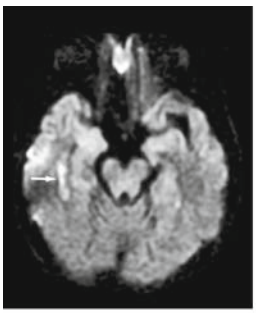 Fig. 10.20 c	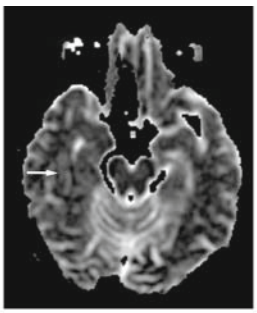 Fig. 10.20 d	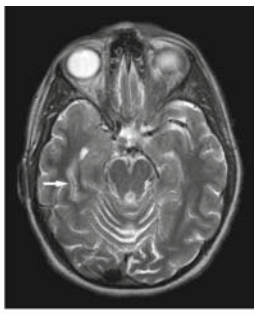 Fig. 10.20 a
Tumor			
Epidermoid	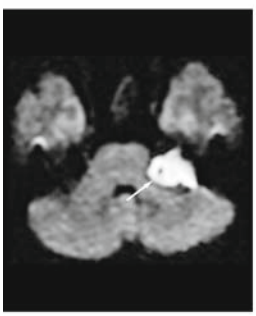 Fig. 11.16 c	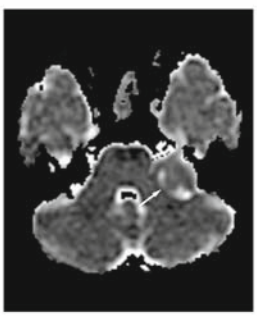 Fig. 11.16 d	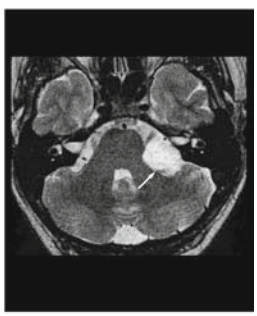 Fig. 11.16 a
Brain stem glioma	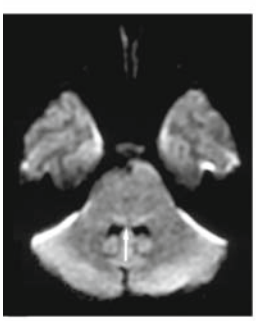 Fig. 13.3 d	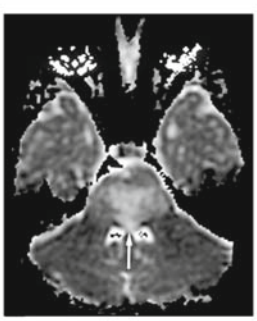 Fig. 13.3 e	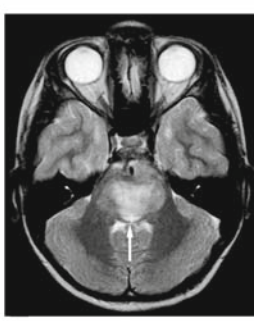 Fig. 13.3 a
Anaplastic astrocytoma	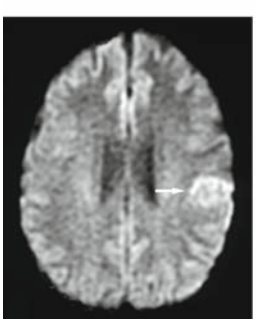 Fig. 3.2 c	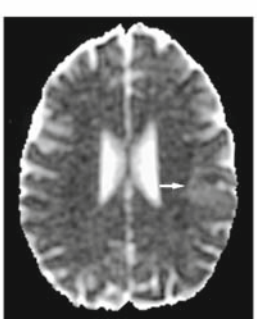 Fig. 3.2 d	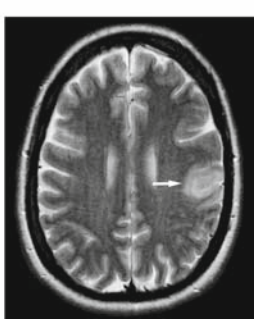 Fig. 3.2 a

Table 16.2

Differential diagnoses for lesions with a **high diffusion** signal associated with **iso-high ADC** and a **high intense T2** signal

Diagnoses	Reference images		
	DWI high	ADC iso-high	T2 high
Low-grade oligoastrocytoma	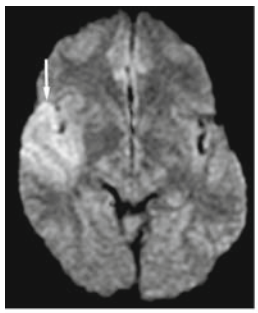 Fig. 13.4 c	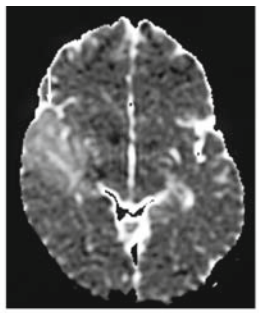 Fig. 13.4 d	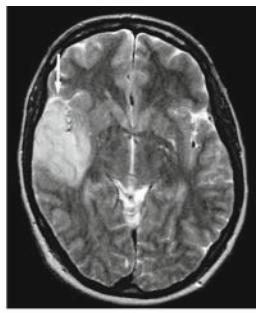 Fig. 13.4 a
Ganglioglioma	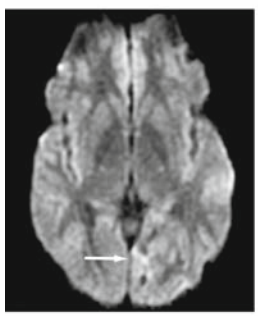 Fig. 13.23 c	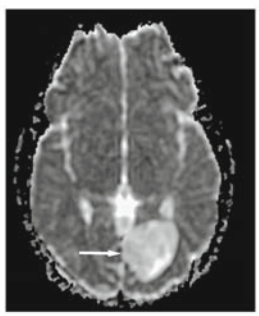 Fig. 13.23 d	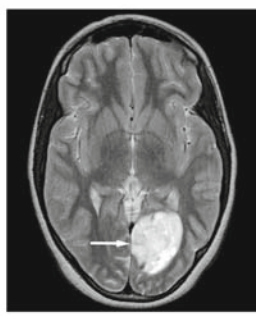 Fig. 13.23 a
Pilocytic astrocytoma	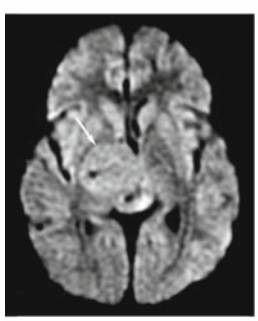 Fig. 14.22 b	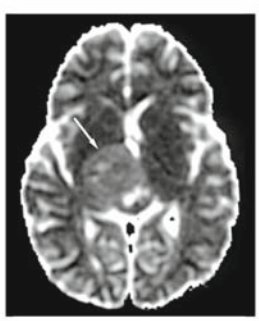 Fig. 14.22 c	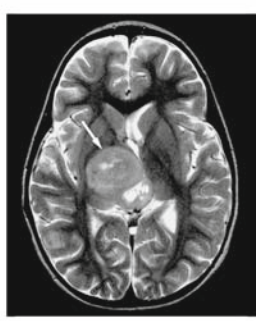 Fig. 14.22 a
Vasculitis/vasculopathy			
Primary angiitis of central nervous system (PACNS)	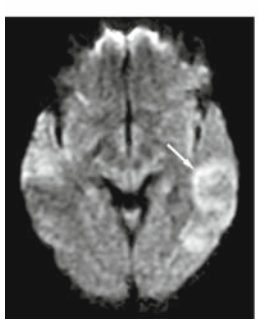 Fig. 7.2 c	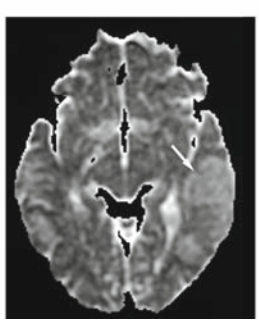 Fig. 7.2 d	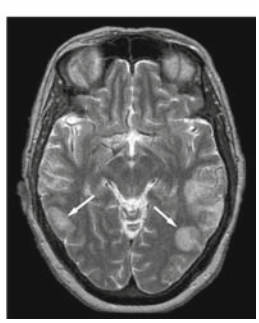 Fig. 7.2 a

Table 16.2

Differential diagnoses for lesions with a **high diffusion** signal associated with **iso-high ADC** and a **high intense T2** signal

Diagnoses	Reference images		
	DWI high	ADC iso-high	T2 high
Neuro-Behçet's disease	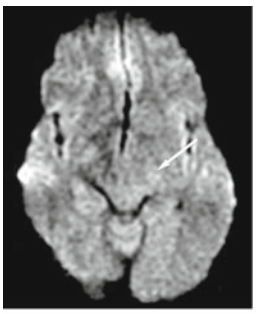	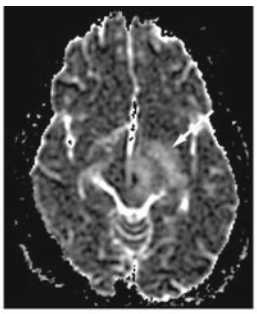	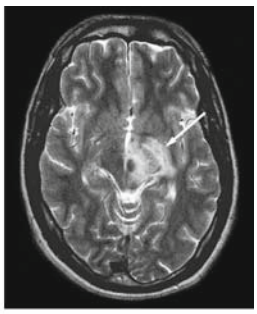
	Fig. 7.9 c	Fig. 7.9 d	Fig. 7.9 a
Tacrolimus neurotoxicity (PRES)	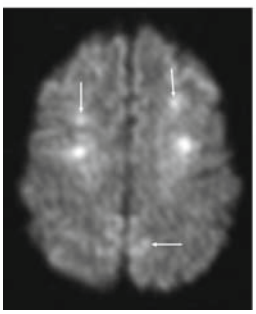	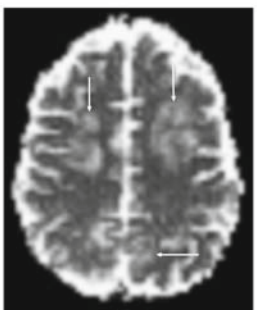	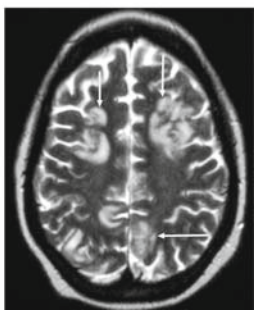
	Fig. 7.19 b	Fig. 7.19 c	Fig. 7.19 a

Table 16.3

Differential diagnoses for lesions with a **high diffusion** signal associated with a **low ADC** and **high intense T2** signal

Diagnoses	Reference images		
	DWI high	ADC low	T2 high
Degeneration			
Wallerian degeneration	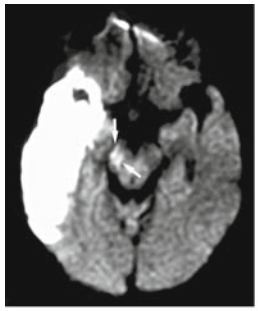 Fig. 9.14 c	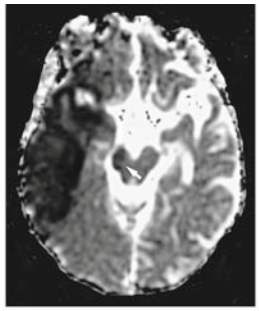 Fig. 9.14 d	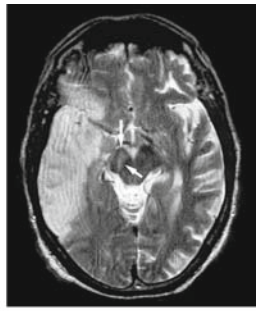 Fig. 9.14 b
Demyelination			
Multiple sclerosis (cytotoxic plague)	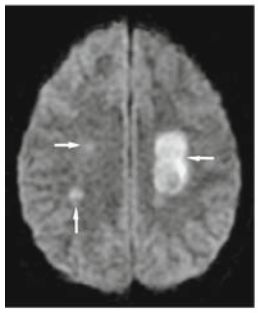 Fig. 9.5 b	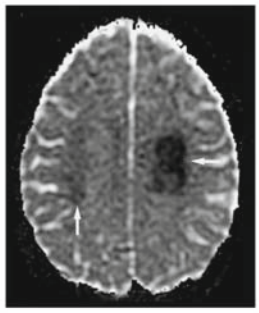 Fig. 9.5 c	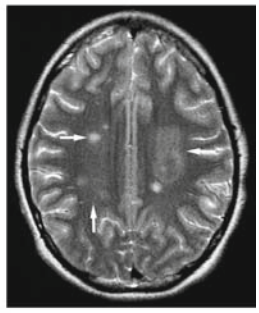 Fig. 9.5 a
Epilepsy			
Status epileptics	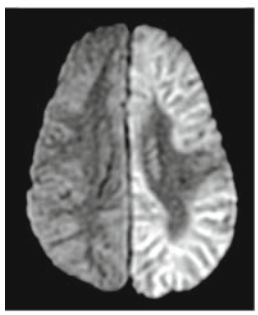 Fig. 4.9 b	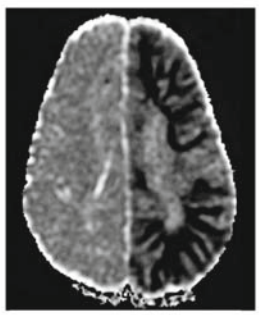 Fig. 4.9 c	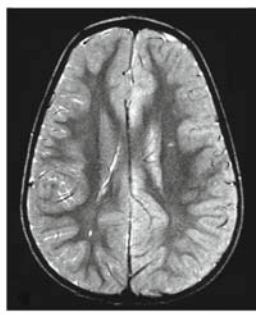 Fig. 4.9 a
Postictal encephalopathy	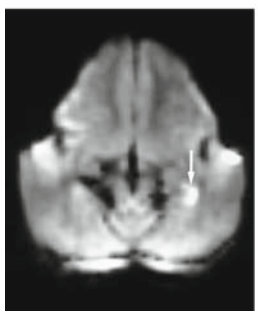 Fig. 8.6 c	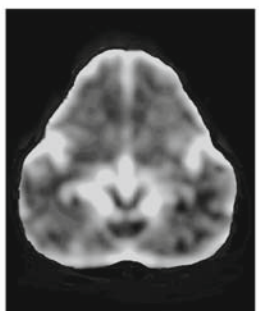 Fig. 8.6 d	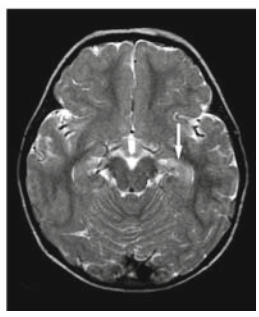 Fig. 8.6 a

Table 16.3

Differential diagnoses for lesions with a **high diffusion** signal associated with a **low ADC** and **high intense T2** signal

Diagnoses	Reference images		
	DWI high	ADC iso-high	T2 high
Hematoma			
Late subacute hematoma (Extracellular methemoglobin)	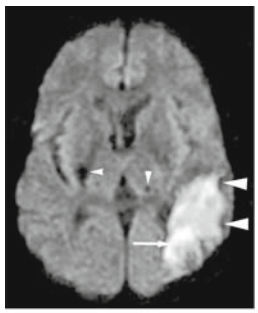 Fig. 6.4 c	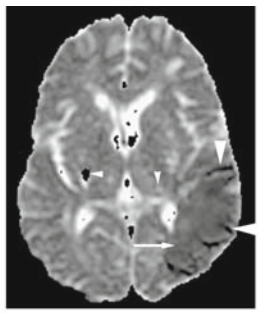 Fig. 6.4 e	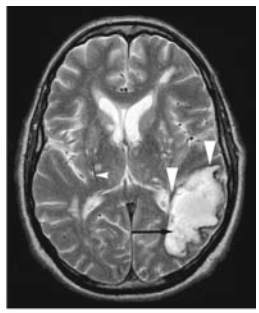 Fig. 6.4 a
Subdural hematoma (SDH)	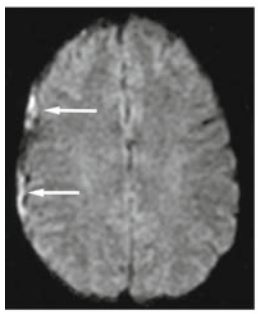 Fig. 6.7 c	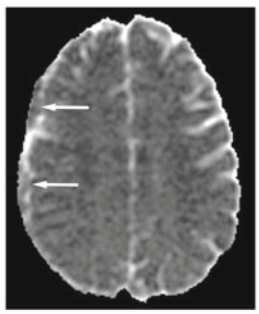 Fig. 6.7 e	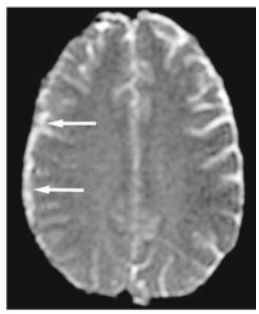 Fig. 6.7 d
Infarction/Ischemia			
Hyperacute reversible ischemia (2 h)	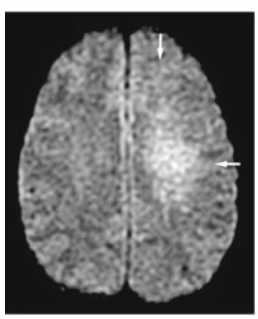 Fig. 5.5 b	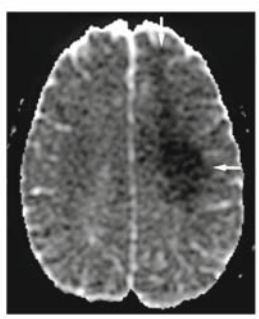 Fig. 5.5 c	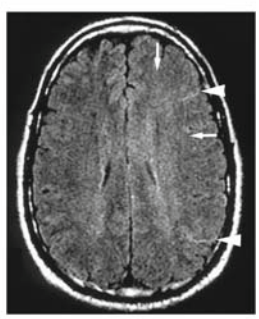 Fig. 5.5 a
Acute infarction (24 h)	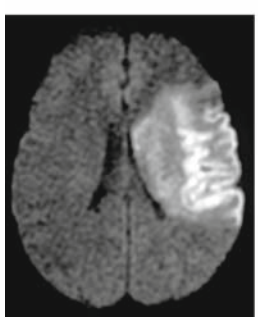 Fig. 3.3 d	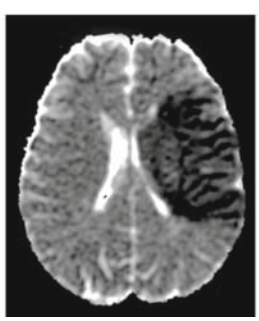 Fig. 3.3 e	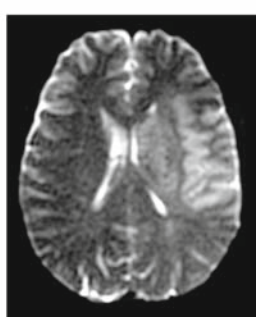 Fig. 3.3 c

Table 16.3

Differential diagnoses for lesions with a **high diffusion** signal associated with a **low ADC** and **high intense T2** signal

Diagnoses	Reference images		
	DWI high	ADC low	T2 high
Subacute infarction (10 day)	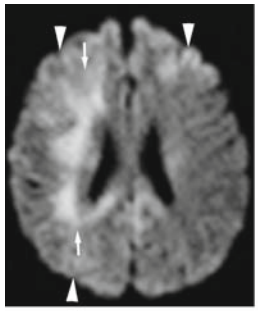 Fig. 5.3 c	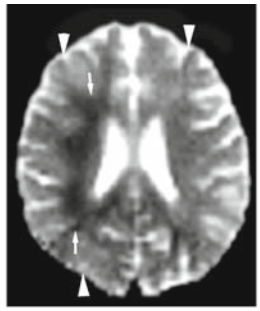 Fig. 5.3 d	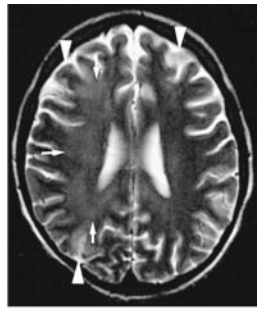 Fig. 5.3 a
Infection			
Abscess	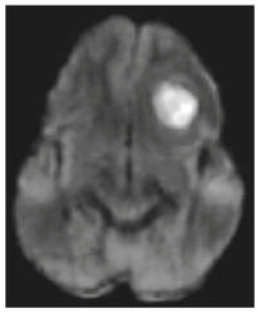 Fig. 11.1 c	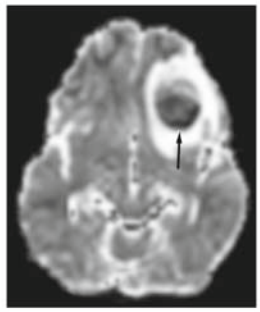 Fig. 11.1 d	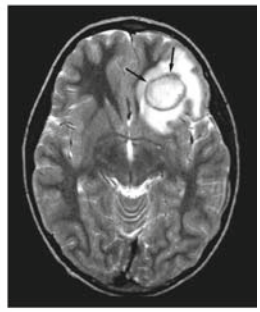 Fig. 11.1 a
Septic emboli	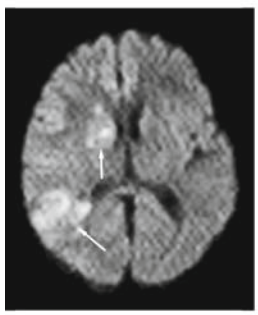 Fig. 11.4 b	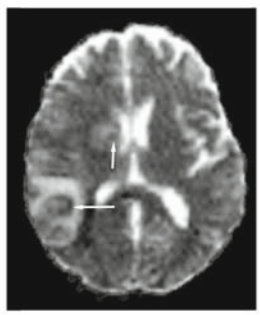 Fig. 11.4 c	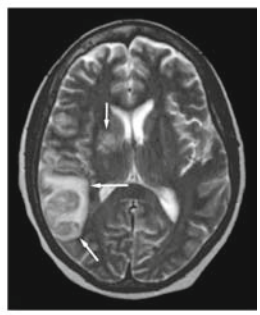 Fig. 11.4 a
Ventriculitis	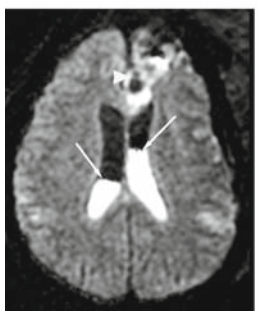 Fig. 11.14 c	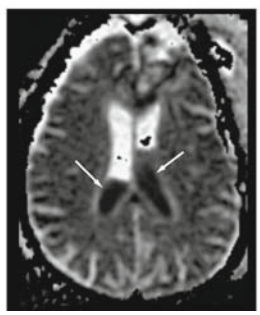 Fig. 11.14 d	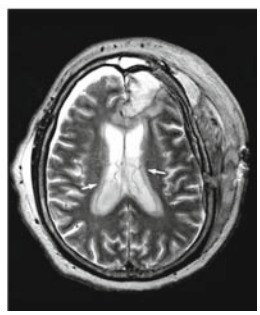 Fig. 11.14 b

Table 16.3

Differential diagnoses for lesions with a **high diffusion** signal associated with a **low ADC** and **high intense T2** signal

Diagnoses	Reference images		
	DWI high	ADC iso-high	T2 high
Acquired immunodeficiency syndrome (AIDS)	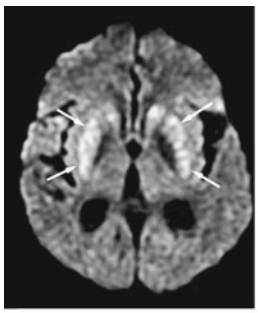 Fig. 11.34 b	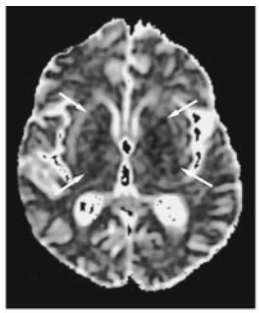 Fig. 11.34 c	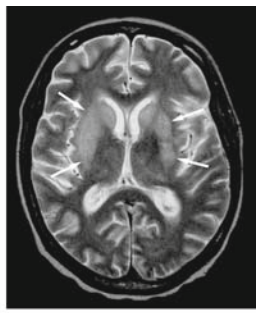 Fig. 11.34 a
Aspergillosis (disseminated)	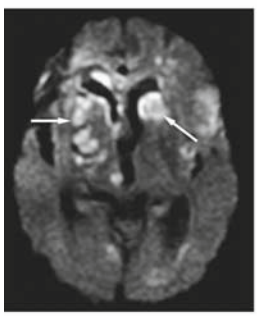 Fig. 11.23 b	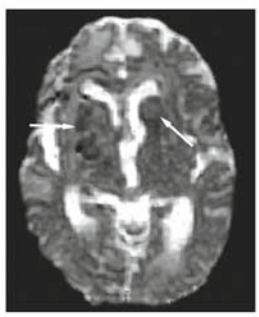 Fig. 11.23 c	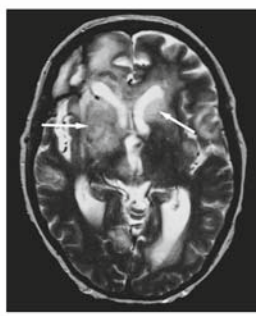 Fig. 11.23 a
Creutzfeldt-Jakob disease (CJD)	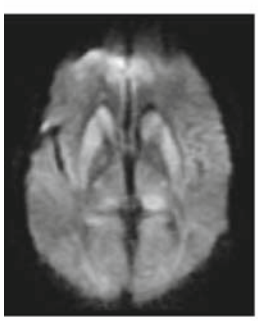 Fig. 9.18 b	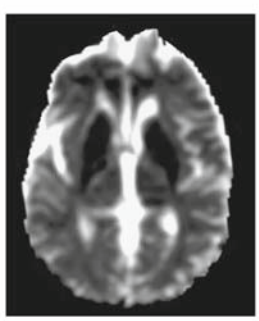 Fig. 9.18 c	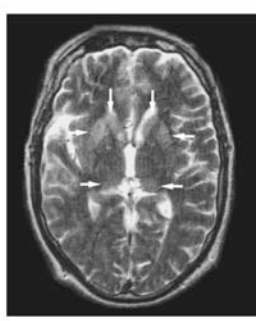 Fig. 9.18 a
Group B Streptococcus meningitis	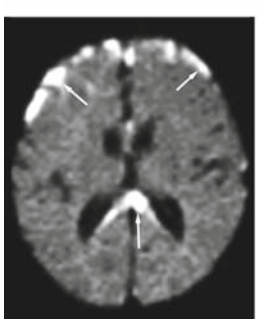 Fig. 11.17 b	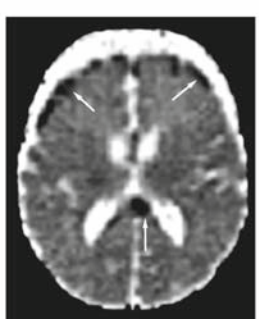 Fig. 11.17 c	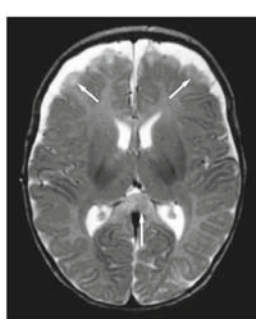 Fig. 11.17 a

Table 16.3

Differential diagnoses for lesions with a **high diffusion** signal associated with a **low ADC** and **high intense T2** signal

Diagnoses	Reference images		
	DWI high	ADC low	T2 high
Herpes simplex virus encephalitis	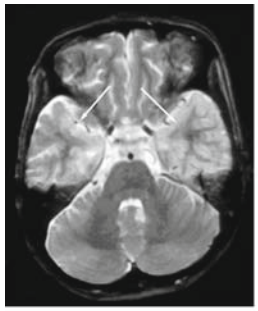 Fig. 14.15 b	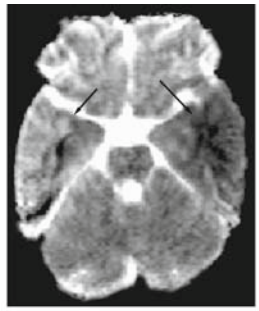 Fig. 14.15 c	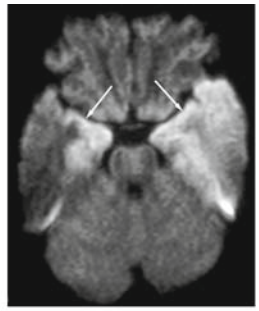 Fig. 14.15 a
Toxoplasmosis (exceptional case)	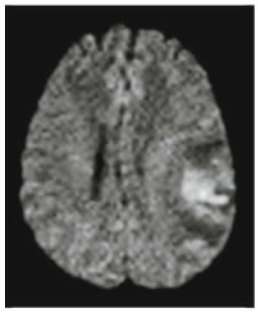 Fig. 4.20 d	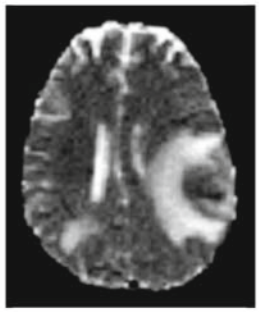 Fig. 4.20 c	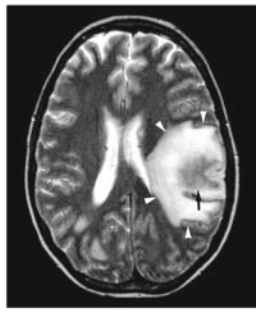 Fig. 4.20 a
Toxic/metabolic			
Carmofur leukoencephalopathy	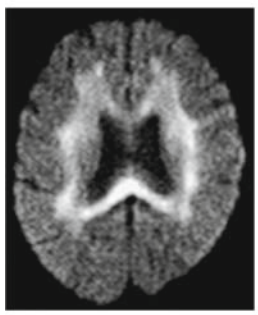 Fig. 10.3 b	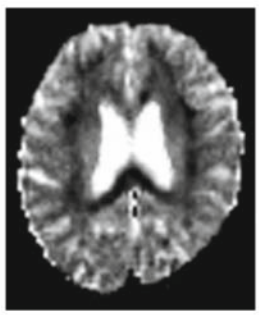 Fig. 10.3 c	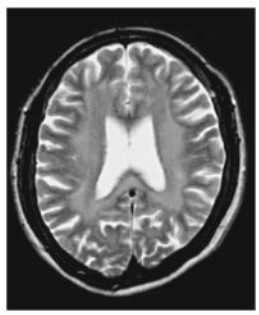 Fig. 10.3 a
Heroin-induced leukoencephalopathy	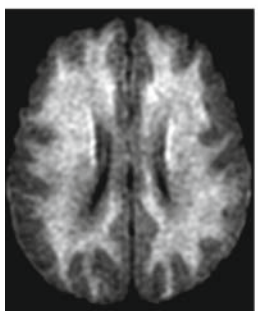 Fig. 10.4 b	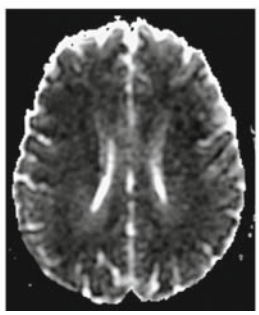 Fig. 10.4 c	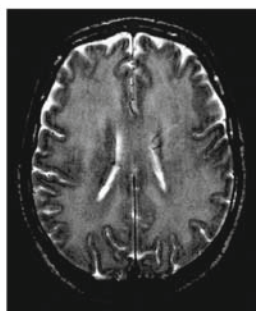 Fig. 10.4 a

Table 16.3

Differential diagnoses for lesions with a **high diffusion** signal associated with a **low ADC** and **high intense T2** signal

Diagnoses	Reference images		
	DWI high	ADC iso-high	T2 high
Central pontine myelinolysis (CPM)	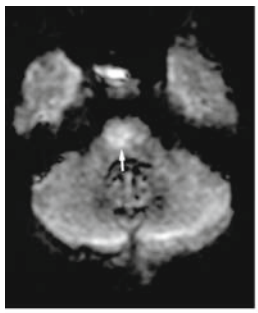 Fig. 10.13 b	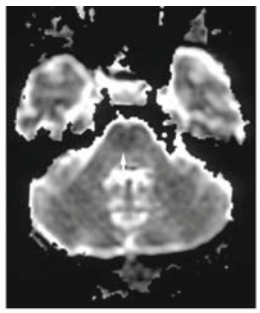 Fig. 10.13 c	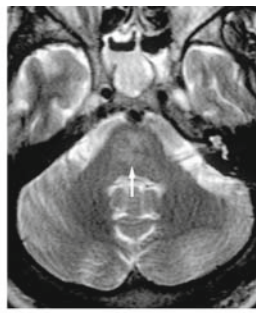 Fig. 10.13 a
Extrapontine myelinolysis (EPM)	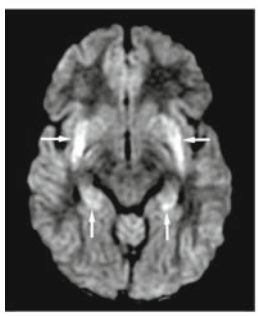 Fig. 10.14 b	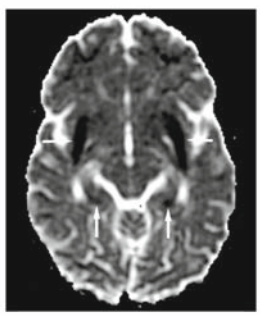 Fig. 10.14 c	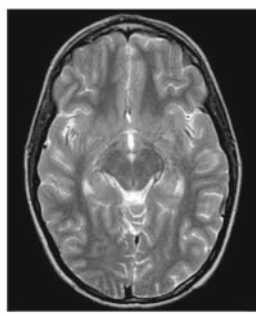 Fig. 10.14 a
L-2-hydroxyglutaric aciduria	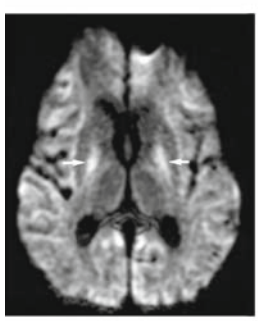 Fig. 10.23 b	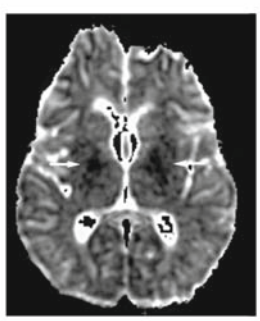 Fig. 10.23 c	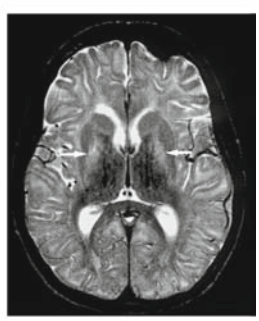 Fig. 10.23 a
Mitochondrial encephalopathy (unknown metabolic abnormality)	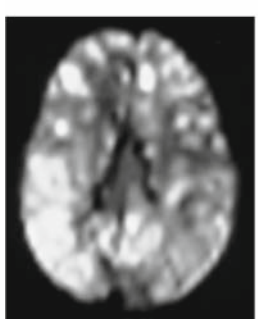 Fig. 10.21 b	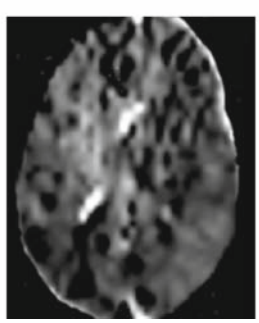 Fig. 10.21 c	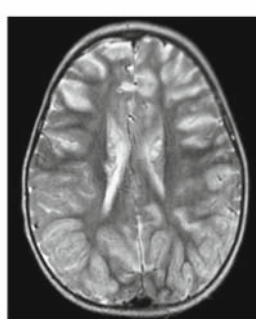 Fig. 10.21 a

Table 16.3

Differential diagnoses for lesions with a **high diffusion** signal associated with a **low ADC** and **high intense T2** signal

Diagnoses	Reference images		
	DWI high	ADC low	T2 high
Phenylketonuria (PKU)	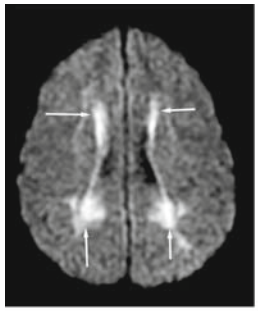 Fig. 14.39 b	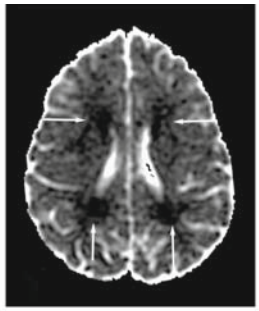 Fig. 14.39 c	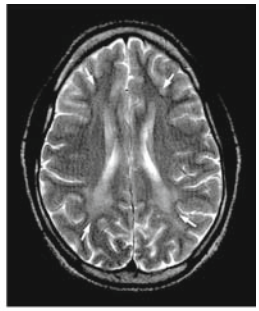 Fig. 14.39 a
Trauma			
Non accidental head injury	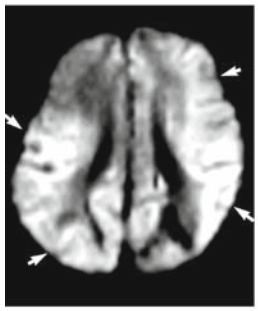 Fig. 14.13 b	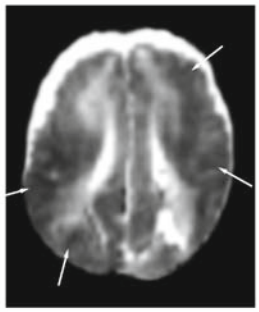 Fig. 14.13 d	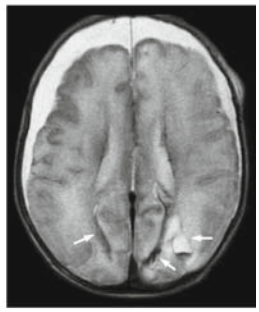 Fig. 14.13 a
Contusion	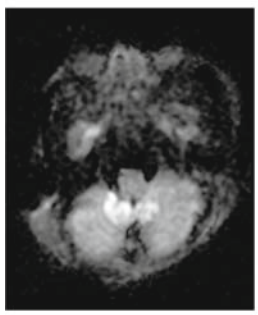 Fig. 12.11 b	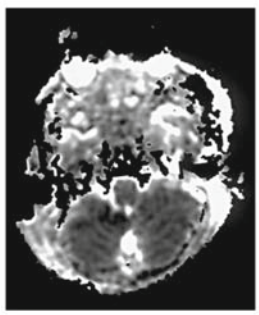 Fig. 12.11 c	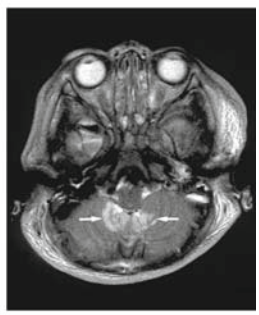 Fig. 12.11 a
Diffuse axonal injury (DAI)	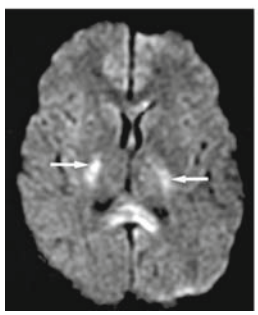 Fig. 12.3 c	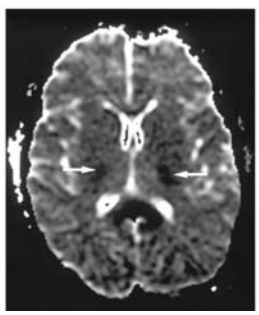 Fig. 12.3 d	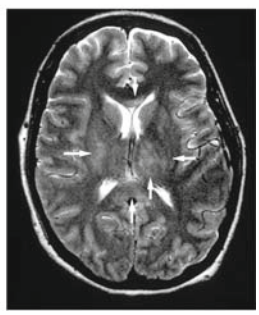 Fig. 12.3 a

Table 16.3

Differential diagnoses for lesions with a **high diffusion** signal associated with a **low ADC** and **high intense T2** signal

Diagnoses	Reference images		
	DWI high	ADC iso-high	T2 high
Tumor			
Glioblastoma (solid)	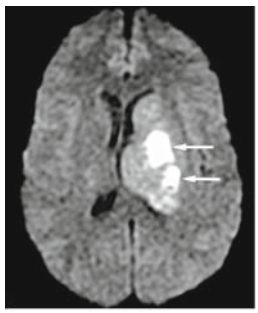 Fig. 13.10 d	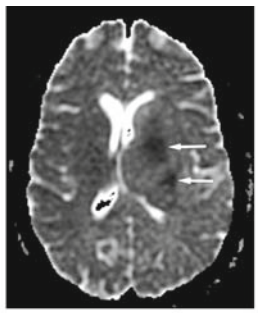 Fig. 13.10 e	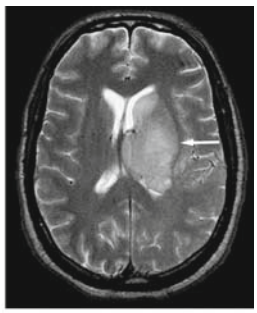 Fig. 13.10 a
Lymphoma	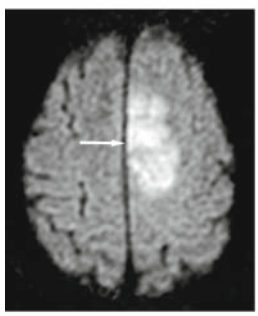 Fig. 13.38 d	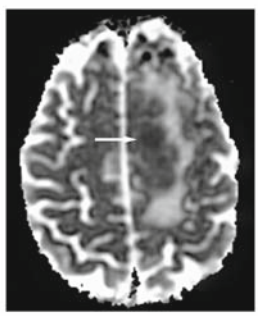 Fig. 13.38 e	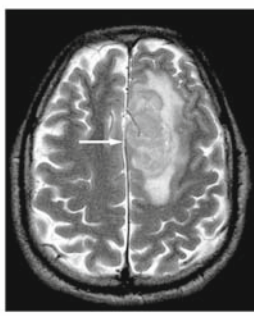 Fig. 13.38 a
Meningioma (syncytial)	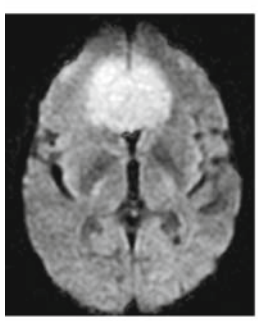 Fig. 13.31 c	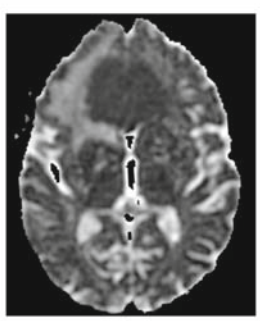 Fig. 13.31 d	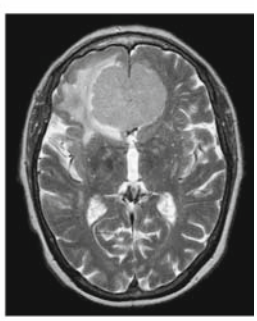 Fig. 13.31 a
Meningioma (atypical)	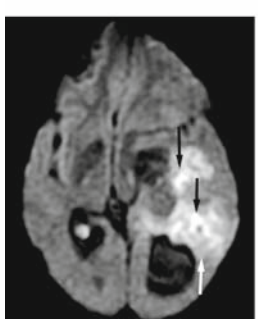 Fig. 13.34 c	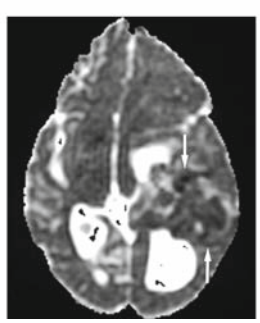 Fig. 13.34 d	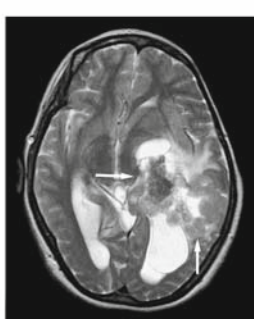 Fig. 13.34 a

Table 16.3

Differential diagnoses for lesions with a **high diffusion** signal associated with a **low ADC** and **high intense T2** signal

Diagnoses	Reference images		
	DWI high	ADC low	T2 high
Metastasis (lung)	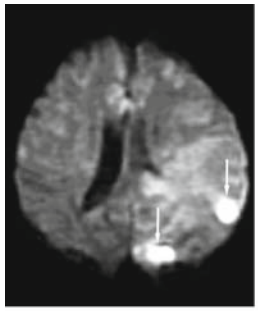 Fig. 11.9 c	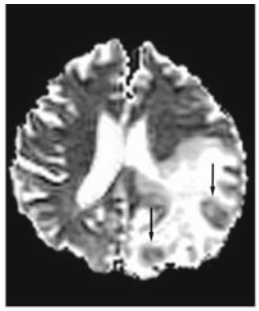 Fig. 11.9 d	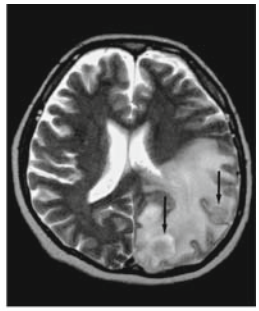 Fig. 11.9 a
Primitive neuroectodermal tumor (PNET)	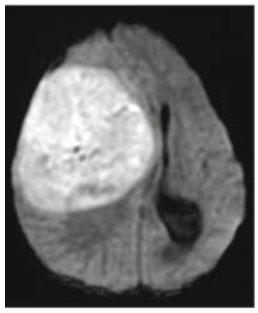 Fig. 13.27 c	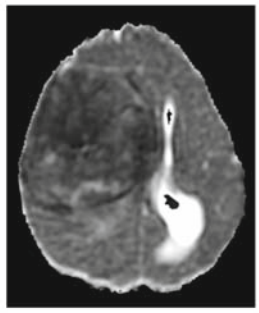 Fig. 13.27 d	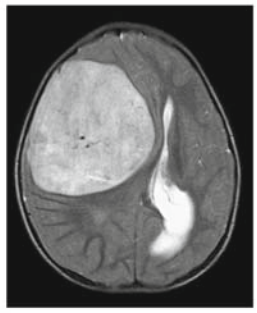 Fig. 13.27 a
Radiofrequency thalomotomy (coagulative necrosis)	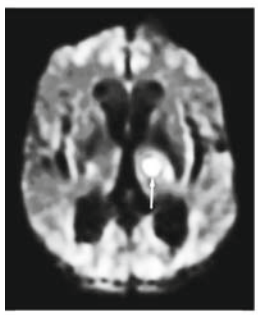 Fig. 11.10 b	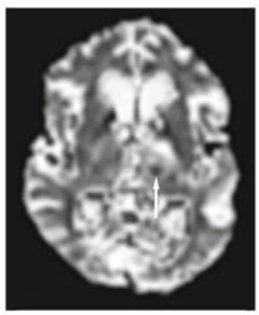 Fig. 11.10 c	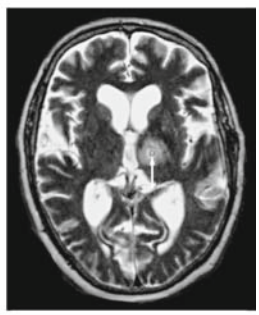 Fig. 11.10 a
Vasculitis/vasculopathy			
Primary angiitis of central nervous system (PACNS)	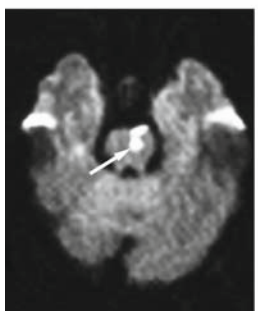 Fig. 7.4 e	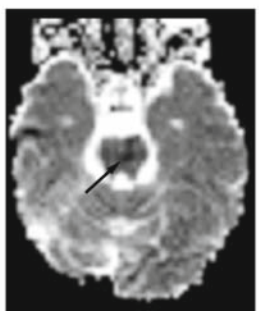 Fig. 7.4 f	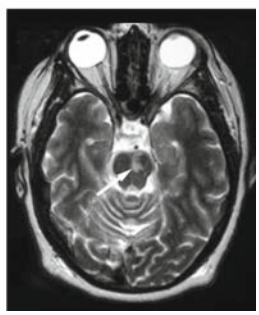 Fig. 7.4 b

Table 16.3

Differential diagnoses for lesions with a **high diffusion** signal associated with a **low ADC** and **high intense T2** signal

Diagnoses	Reference images		
	DWI high	ADC iso-high	T2 high
Pneumococcal meningitis and vasculitis	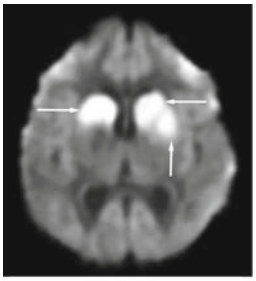 Fig. 7.10 b	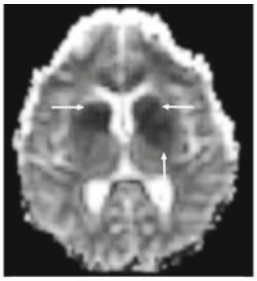 Fig. 7.10 c	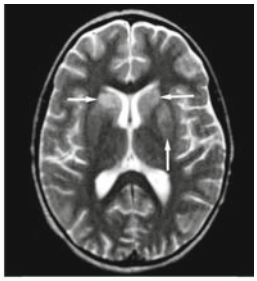 Fig. 7.10 a
Sickle cell disease	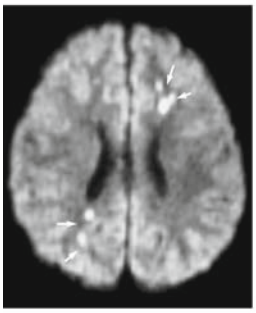 Fig. 14.6 b	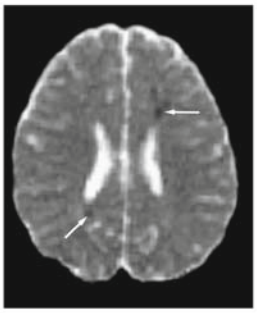 Fig. 14.6 c	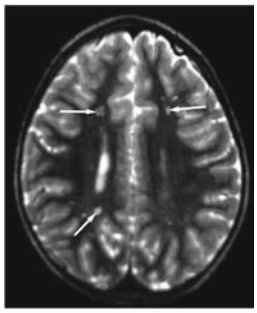 Fig. 14.6 a
Hemolytic uremic syndrome (HUS)	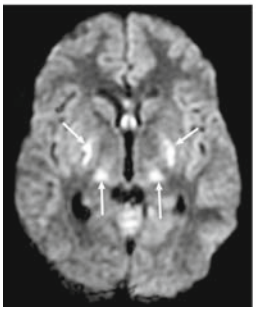 Fig. 7.21 b	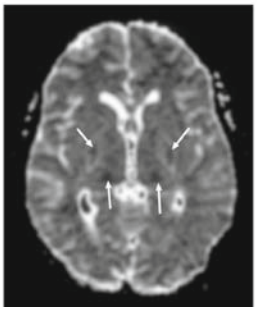 Fig. 7.21 c	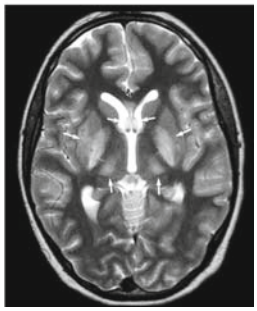 Fig. 7.21 a

Table 16.4

Differential diagnoses for lesions with an **iso diffusion** signal associated with a **high ADC** and **high intense T2** signal

Diagnoses	Reference images		
	DWI iso	ADC high	T2 high
Vasculitis/Vasculopathy			
Posterior reversible encephalopathy syndrome (PRES)	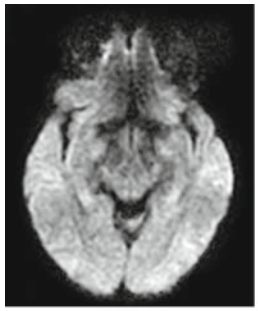 Fig. 3.4 c	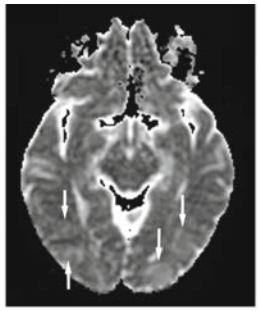 Fig. 3.4 d	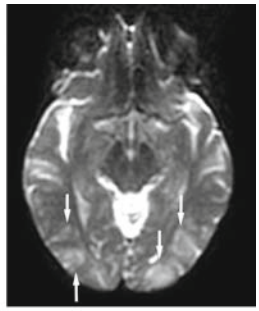 Fig. 3.4 b
Vasogenic edema (metastasis)	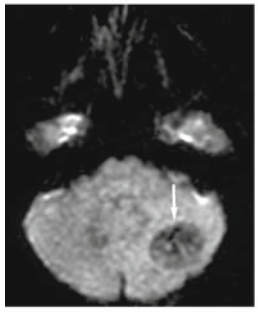 Fig. 3.5 e	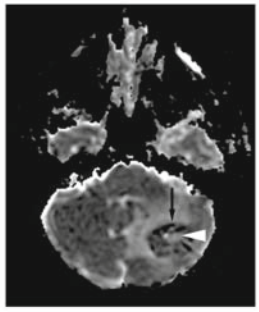 Fig. 3.5 d	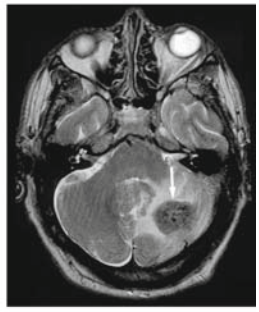 Fig. 3.5 a
Tacrolimus neurotoxicity	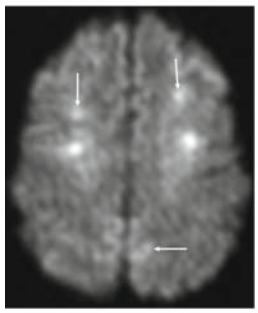 Fig. 7.19 b	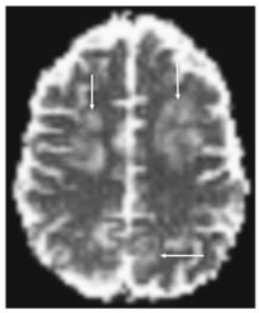 Fig. 7.19 c	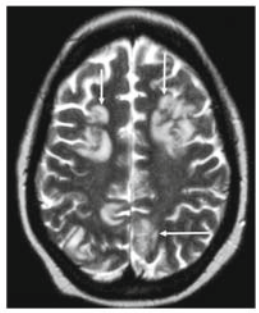 Fig. 7.19 a
Postictal encephalopathy	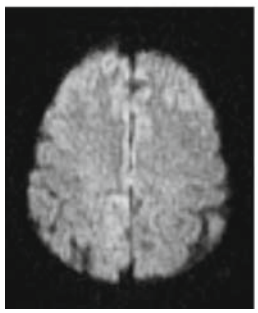 Fig. 8.3 d	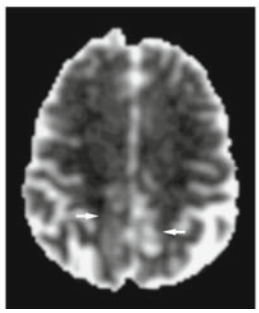 Fig. 8.3 e	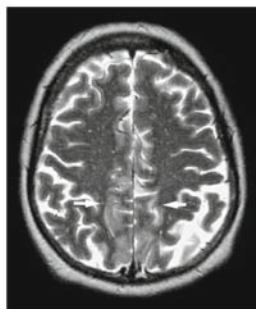 Fig. 8.3 a

Table 16.4

Differential diagnoses for lesions with an **iso diffusion** signal associated with a **high ADC** and **high intense T2** signal

Diagnoses	Reference images		
	DWI iso	ADC high	T2 high
Metabolic disease			
Wernicke encephalopathy	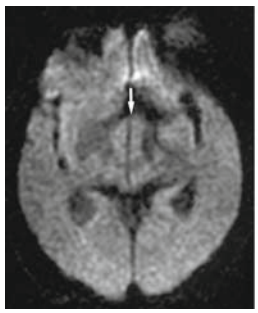 Fig. 10.16 b	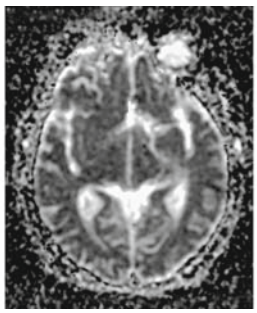 Fig. 10.16 c	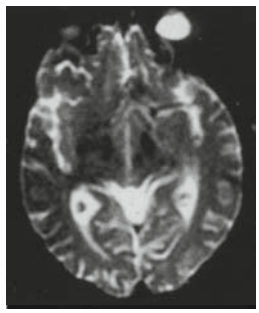 Fig. 10.16 a

Table 16.5

Differential diagnoses for lesions with a **low diffusion** signal associated with a **high ADC** and **high intense T2** signal

Diagnoses	Reference images		
	DWI low	ADC high	T2 high
Infarction			
Chronic infarction (10 months)	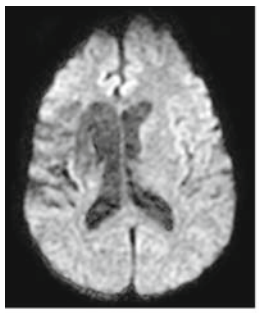 Fig. 5.4 c	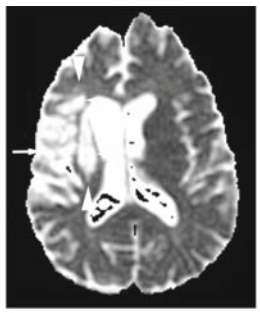 Fig. 5.4 d	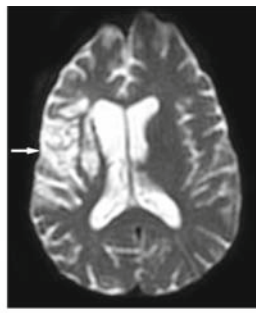 Fig. 5.4 b
Turmor			
Glioblastoma (necrosis)	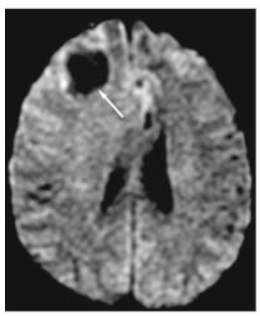 Fig. 11.8 c	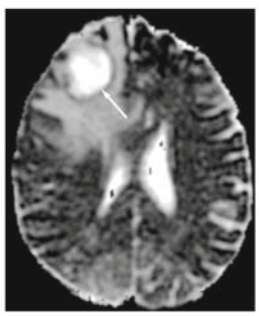 Fig. 11.8 d	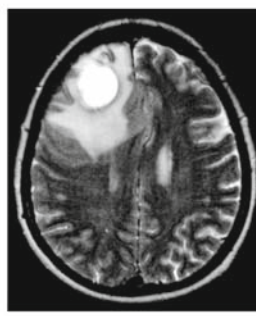 Fig. 11.8 a
Craniopharyngioma	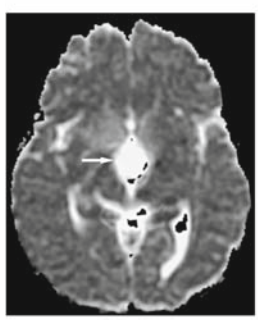 Fig. 13.46 c	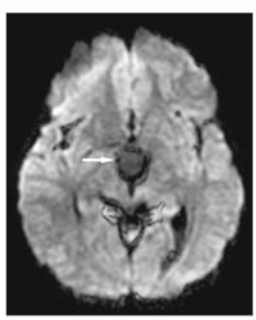 Fig. 13.46 b	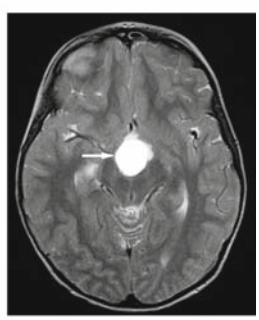 Fig. 13.46 a
Metastasis (lung)	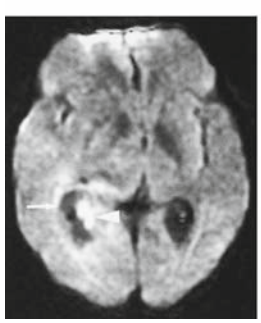 Fig. 13.51 c	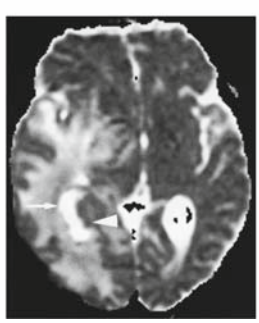 Fig. 13.51 d	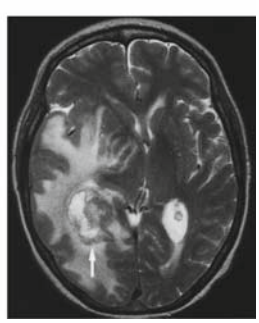 Fig. 13.51 a

Table 16.5

Differential diagnoses for lesions with a **low diffusion** signal associated with a **high ADC** and **high intense T2** signal

Diagnoses	Reference images		
	DWI low	ADC high	T2 high
Arachnoid cyst	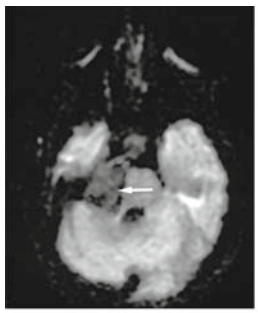 Fig. 13.45 c	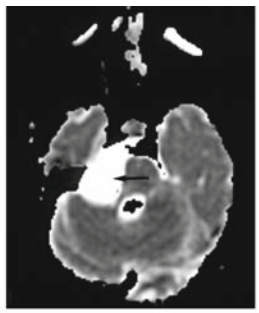 Fig. 13.45 d	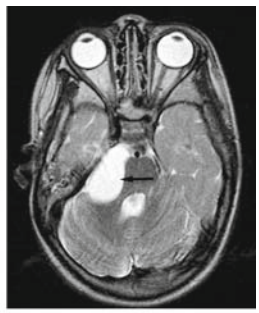 Fig. 13.45 a
Vanishing white matter disease	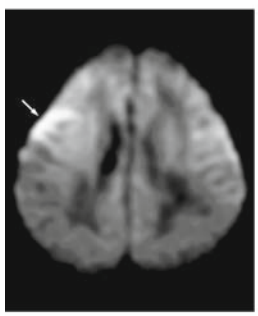 Fig. 14.43 b	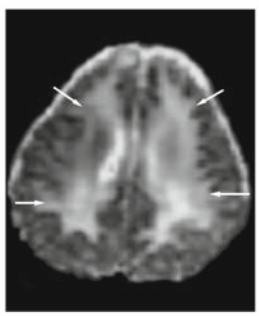 Fig. 14.43 c	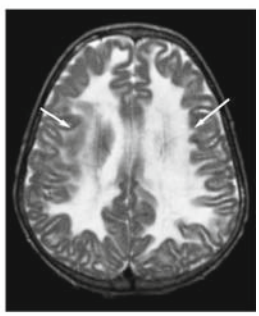 Fig. 14.43 a
Van der Knaap disease	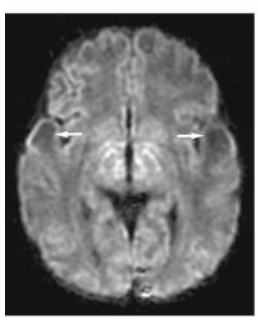 Fig. 10.24 b	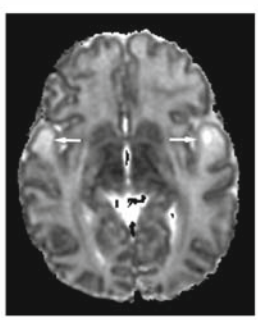 Fig. 10.24 c	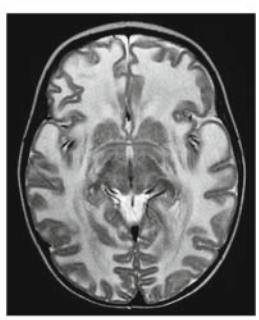 Fig. 10.24 a
Vasogenic edema (toxoplasmosis)	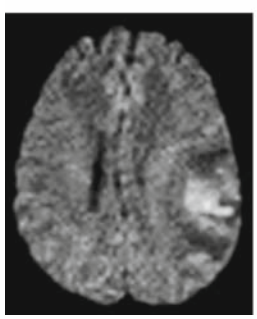 Fig. 4.20 b	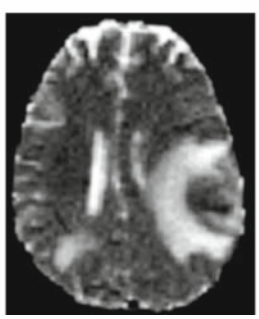 Fig. 4.20 c	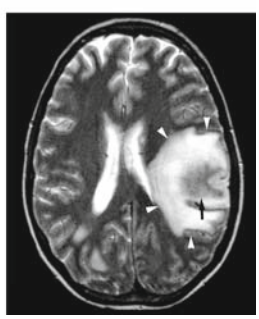 Fig. 4.20 a

Table 16.6

Differential diagnoses for lesions with a **low diffusion** signal associated with a **high ADC** and **isointense T2** signal

Diagnoses	Reference images		
	DWI low	ADC high	T2 iso
Normal			
Neonate	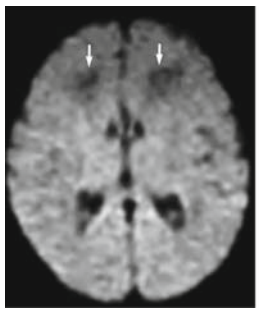 Fig. 2.4 a	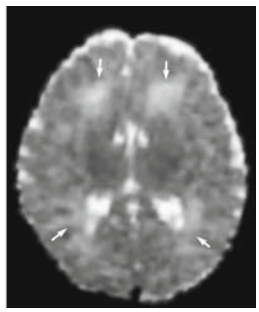 Fig. 2.4 b	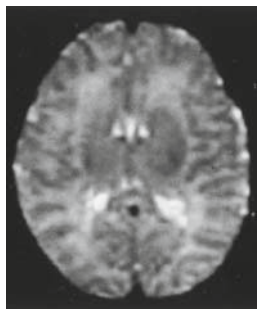 Fig. 2.4 c

Table 16.7

Differential diagnoses for lesions with **artifacts**

Diagnoses	Reference images		
	DWI	ADC	T2
Susceptibility artifacts			
Physiological iron deposition	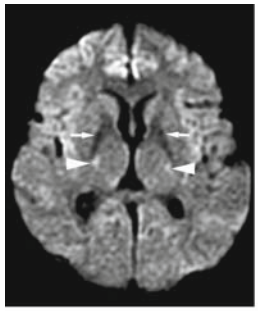 Fig. 2.1 a	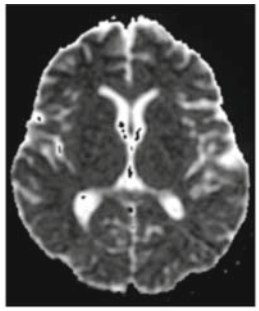 Fig. 2.1 b	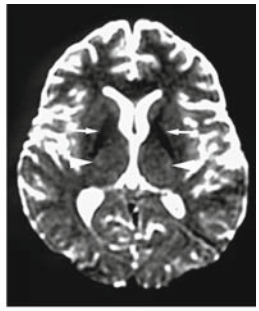 Fig. 2.1 c
Oxy/deoxy hemoglobin	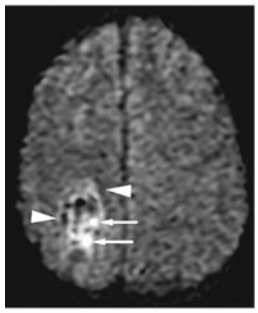 Fig. 6.2 d	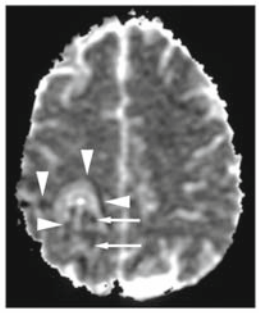 Fig. 6.2 f	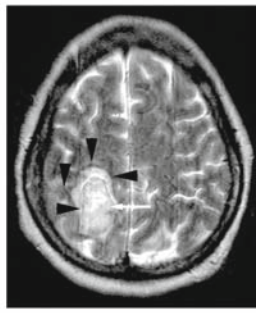 Fig. 6.2 b
Deoxy/intracellular met-hemoglobin	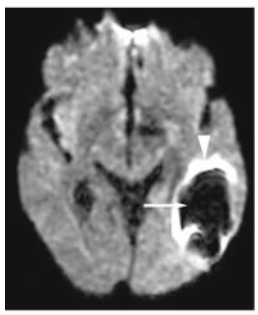 Fig. 6.3 c	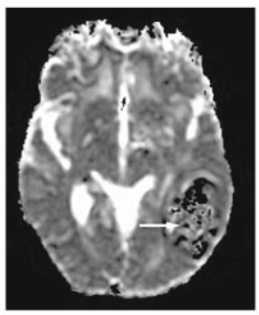 Fig. 6.3 e	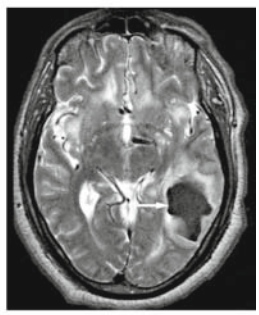 Fig. 6.3 a
Epidural hematoma (EDH)	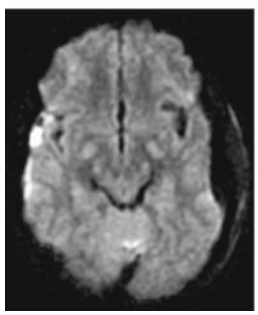 Fig. 12.12 c	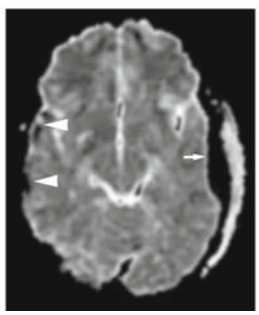 Fig. 12.12 d	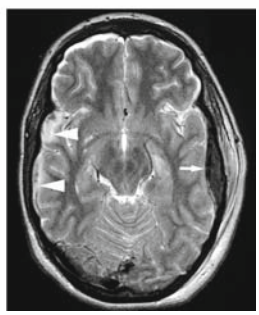 Fig. 12.12 b

Table 16.7
Differential diagnoses for lesions with **artifacts**

Diagnoses	Reference images		
	DWI	ADC	T2
Hemosiderin/ferritin	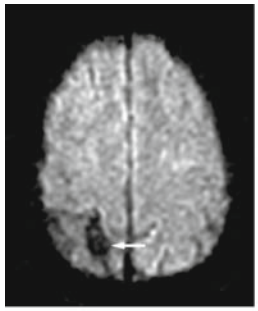 Fig. 6.2 k	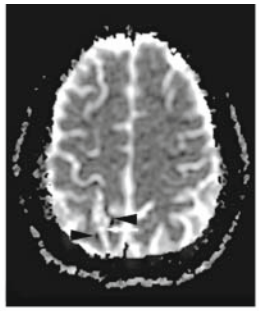 Fig. 6.2 m	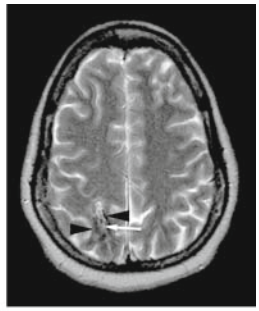 Fig. 6.2 i
Hemorrhagic infarction	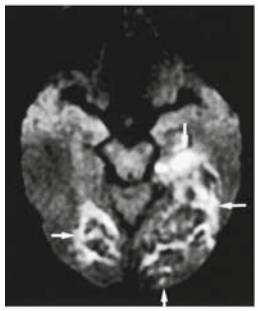 Fig. 5.14 b	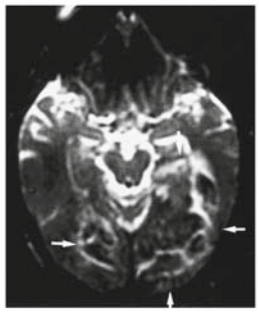 Fig. 5.14 c	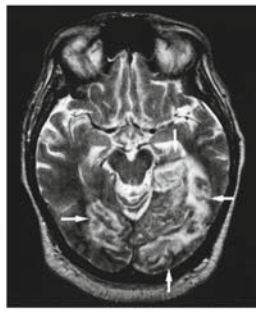 Fig. 5.14 a
Disseminated aspergillosis	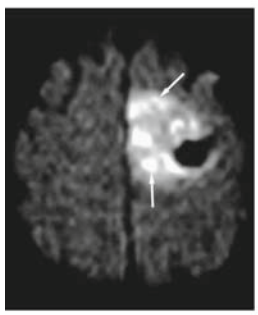 Fig. 7.11 c	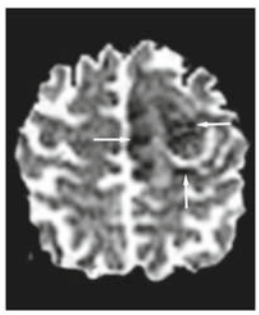 Fig. 7.11 d	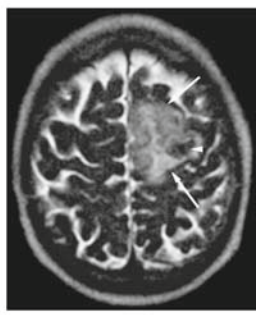 Fig. 7.11 a
Metastasis (melanoma)	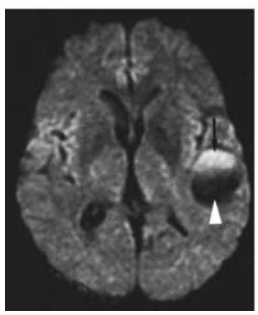 Fig. 13.52 d	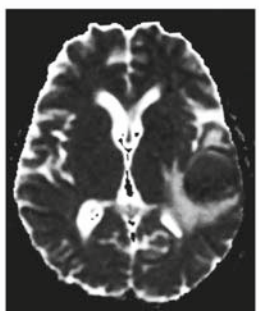 Fig. 13.52 e	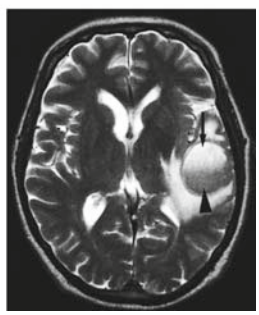 Fig. 13.52 b

Table 16.7

Differential diagnoses for lesions with **artifacts**

Diagnoses	Reference images		
	DWI	ADC	T2
Contusion	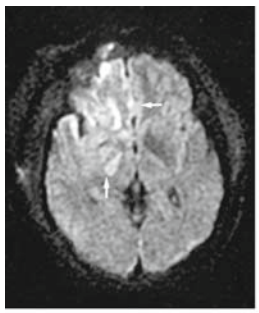 Fig. 12.9 c	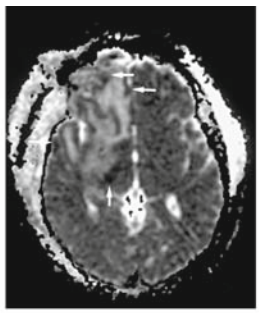 Fig. 12.9 d	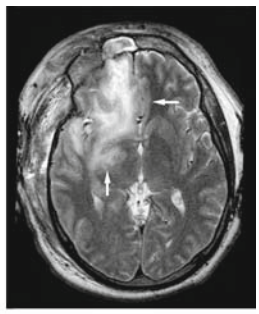 Fig. 12.9 b
Eddy current artifacts	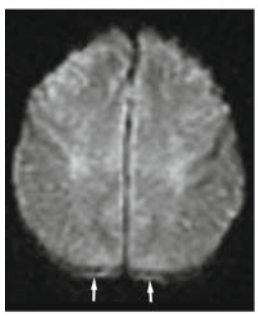 Fig. 3.7 a	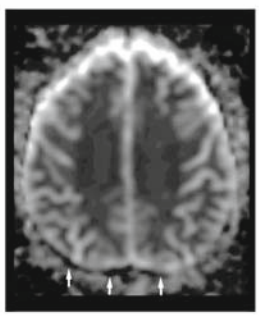 Fig. 3.7 b	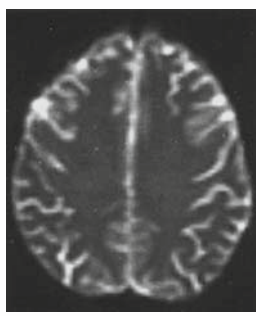 Fig. 3.7 c
N/2 ghosting artifacts	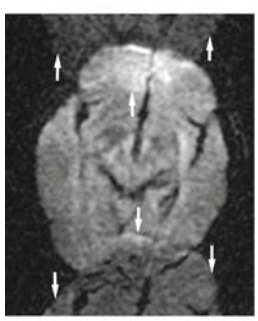 Fig. 3.10 a	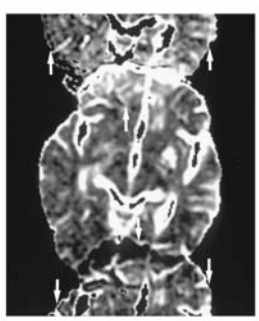 Fig. 3.10 b	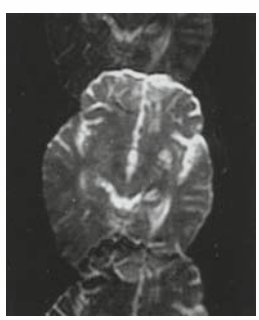 Fig. 3.10 c
Motion artifacts	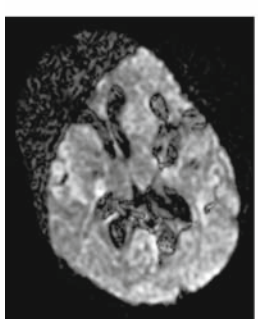 Fig. 3.12 a	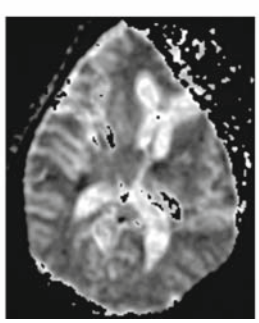 Fig. 3.12 b	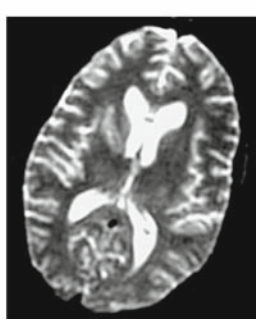 Fig. 3.12 c

Subject Index

D

E

F

N

O

P

R

S

T

U

V

W

X